

## Special Collection on Cancer Therapeutics

Differential effects of PI3K inhibitors on obesity in ob/ob mice, see Lopez-Guadamillas et al. - “PI3K $\alpha$  inhibition reduces obesity in mice.”

**Cancer  
Therapeutics**

**AGING**

# AGING

www.aging-us.com

## EDITORIAL BOARD

### EDITORS-IN-CHIEF

[Jan Vijg](#) - Albert Einstein College of Medicine, Bronx, NY, USA

[David A. Sinclair](#) - Harvard Medical School, Boston, MA, USA

[Vera Gorbunova](#) - University of Rochester, Rochester, NY, USA

[Judith Campisi](#) - The Buck Institute for Research on Aging, Novato, CA, USA

[Mikhail V. Blagosklonny](#) - Roswell Park Cancer Institute, Buffalo, NY, USA

### EDITORIAL BOARD

[Frederick Alt](#) - Harvard Medical School, Boston, MA, USA

[Vladimir Anisimov](#) - Petrov Institute of Oncology, St.Petersburg, Russia

[Johan Auwerx](#) - Ecole Polytechnique Federale de Lausanne, Switzerland

[Andrzej Bartke](#) - Southern Illinois University, Springfield, IL, USA

[Nir Barzilai](#) - Albert Einstein College of Medicine, Bronx, NY, USA

[Elizabeth H. Blackburn](#) - University of California, San Francisco, CA, USA

[Maria Blasco](#) - Spanish National Cancer Center, Madrid, Spain

[Vilhelm A. Bohr](#) - National Institute on Aging, NIH, Baltimore, MD, USA

[William M. Bonner](#) - National Cancer Institute, NIH, Bethesda, MD, USA

[Robert M. Brosh, Jr.](#) - National Institute on Aging, NIH, Baltimore, MD, USA

[Anne Brunet](#) - Stanford University, Stanford, CA, USA

[Rafael de Caba](#) - NIA, NIH, Baltimore, MD, USA

[Ronald A. DePinho](#) - Dana-Farber Cancer Institute, Boston, MA, USA

[Jan van Deursen](#) - Mayo Clinic, Rochester, MN, USA

[Lawrence A. Donehower](#) - Baylor College of Medicine, Houston, TX, USA

[Caleb E. Finch](#) - University of Southern California, Los Angeles, CA, USA

[Toren Finkel](#) - National Institutes of Health, Bethesda, MD, USA

[Luigi Fontana](#) - Washington University, St. Louis, MO, USA

[Claudio Franceschi](#) - University of Bologna, Bologna, Italy

[David Gems](#) - Inst. of Healthy Ageing, Univ. College London, UK

[Myriam Gorospe](#) - National Institute on Aging, NIH, Baltimore, MD, USA

[Leonard Guarente](#) - MIT, Cambridge, MA, USA

[Andrei Gudkov](#) - Roswell Park Cancer Institute, Buffalo, NY, USA

[Michael Hall](#) - University of Basel, Basel, Switzerland

[Philip Hanawalt](#) - Stanford University, CA, USA

[Nissim Hay](#) - University of Illinois at Chicago, Chicago, IL, USA



[Siegfried Hekimi](#) - McGill University, Montreal, Canada

[Stephen L. Helfand](#) - Brown University, Providence, RI, USA

[Jan H.J. Hoeijmakers](#) - Erasmus MC, Rotterdam, The Netherlands

[John O. Holloszy](#) - Washington University, St. Louis, MO, USA

[Stephen P. Jackson](#) - University of Cambridge, Cambridge, UK

[Heinrich Jasper](#) - The Buck Institute for Research on Aging, Novato, CA, USA

[Pankaj Kapahi](#) - The Buck Institute for Research on Aging, Novato, CA, USA

[Jan Karlseder](#) - The Salk Institute, La Jolla, CA, USA

[Cynthia Kenyon](#) - University of California San Francisco, San Francisco, CA, USA

[James L. Kirkland](#) - Mayo Clinic, Rochester, MN, USA

[Guido Kroemer](#) - INSERM, Paris, France

[Titia de Lange](#) - Rockefeller University, New York, NY, USA

[Arnold Levine](#) - The Institute for Advanced Study, Princeton, NJ, USA

[Michael P. Lisanti](#) - University of Salford, Salford, UK

[Lawrence A. Loeb](#) - University of Washington, Seattle, WA, USA

[Valter Longo](#) - University of Southern California, Los Angeles, CA, USA

[Gerry Melino](#) - University of Rome, Rome, Italy

[Simon Melov](#) - The Buck Institute for Research on Aging, Novato, CA, USA

[Alexey Moskalev](#) - Komi Science Center of RAS, Syktyvkar, Russia

[Masashi Narita](#) - University of Cambridge, Cambridge, UK

[Andre Nussenzweig](#) - National Cancer Institute, NIH, Bethesda, MD, USA

[William C. Orr](#) - Southern Methodist University, Dallas, TX, USA

[Daniel S. Peeper](#) - The Netherlands Cancer Institute, Amsterdam, The Netherlands

[Thomas Rando](#) - Stanford University School of Medicine, Stanford, CA, USA

[Michael Ristow](#) - Swiss Federal Institute of Technology, Zurich, Switzerland

[Igor B. Roninson](#) - Ordway Research Institute, Albany, NY, USA

[Michael R. Rose](#) - University of California, Irvine, CA, USA

[K Lenhard Rudolph](#) - Hannover Medical School, Hannover, Germany

[Paolo Sassone-Corsi](#) - University of California, Irvine, CA, USA

[John Sedivy](#) - Brown University, Providence, RI, USA

[Manuel Serrano](#) - Spanish National Cancer Research Center, Madrid, Spain

[Gerald S. Shadel](#) - Yale University School of Medicine, New Haven, CT, USA

[Norman E. Sharpless](#) - University of North Carolina, Chapel Hill, NC, USA

[Vladimir P. Skulachev](#) - Moscow State University, Moscow, Russia

[Sally Temple](#) - NY Neural Stem Cell Institute, Albany, NY, USA

[George Thomas](#) - University of Cincinnati, Cincinnati, OH, USA

[Jonathan L. Tilly](#) - Massachusetts General Hospital, Boston, MA, USA

[John Tower](#) - University of Southern California, LA, CA, USA

[Eric Verdin](#) - University of California, San Francisco, CA, USA

[Thomas von Zglinicki](#) - Newcastle University, Newcastle, UK

[Alex Zhavoronkov](#) - Insilico Medicine, Baltimore, MD, USA

[Aging](#) (ISSN: 1945 - 4589) is published monthly by Impact Journals, LLC.  
6666 East Quaker St., Suite 1B, Orchard Park, NY 14127

Abstracted and/or indexed in: PubMed/Medline (abbreviated as "Aging (Albany NY)"), PubMed Central (abbreviated as "Aging (Albany NY)"), Web of Science/Science Citation Index Expanded (abbreviated as Aging-US) & listed in the Cell Biology-SCIE and Geriatrics & Gerontology category, Scopus /Rank Q1(the highest rank) (abbreviated as Aging)- Aging and Cell Biology category, Biological Abstracts, BIOSIS Previews, EMBASE, META (Chan Zuckerberg Initiative), Dimensions (Digital Science's).

This publication and all its content, unless otherwise noted, is licensed under CC-BY 3.0 Creative Commons Attribution License.  
Impact Journals, LLC meets Wellcome Trust Publisher requirements.  
IMPACT JOURNALS is a registered trademark of Impact Journals, LLC.

### **Editorial and Publishing Office Aging**

6666 E. Quaker St., Suite 1,  
Orchard Park, NY 14127  
Phone: 1-800-922-0957  
Fax: 1-716-508-8254  
e-Fax: 1-716-608-1380

### **Submission**

Please submit your manuscript on-line at <http://aging.msubmit.net>

### **Editorial**

For editorial inquiries, please call us or email [editors@impactaging.com](mailto:editors@impactaging.com)

### **Production**

For questions related to preparation of your article for publication, please call us or email [krasnova@impactaging.com](mailto:krasnova@impactaging.com)

### **Indexing**

If you have questions about the indexing status of your paper, please email [kurenova@impactaging.com](mailto:kurenova@impactaging.com)

### **Billing/Payments**

If you have questions about billing/invoicing or would like to make a payment, please call us or email [payment@impactaging.com](mailto:payment@impactaging.com)

### **Media**

If you have questions about post publication promotion, Altmetric, video interviews or social media, please email [media@impactjournals.com](mailto:media@impactjournals.com)

### **Printing**

Each issue or paper can be printed on demand. To make a printing request, please call us or email [printing@impactjournals.com](mailto:printing@impactjournals.com)

### **Publisher's Office**

Aging is published by Impact Journals, LLC  
To contact the Publisher's Office, please email: [publisher@impactjournals.com](mailto:publisher@impactjournals.com), visit [www.impactjournals.com](http://www.impactjournals.com), or call 1-800-922-0957

*Aging* (ISSN: 1945 - 4589) is published twice a month by Impact Journals, LLC.  
6666 East Quaker St., Suite 1B, Orchard Park, NY 14127

**Abstracted and/or indexed in:** PubMed/Medline (abbreviated as "Aging (Albany NY)"), PubMed Central (abbreviated as "Aging (Albany NY)"), Web of Science/Science Citation Index Expanded (abbreviated as Aging-US) & listed in the Cell Biology-SCIE and Geriatrics & Gerontology category, Scopus /Rank Q1(the highest rank) (abbreviated as Aging) - Aging and Cell Biology category, Biological Abstracts, BIOSIS Previews, EMBASE, META (Chan Zuckerberg Initiative), Dimensions (Digital Science's).

This publication and all its content, unless otherwise noted, is licensed under CC-BY 3.0 Creative Commons Attribution License.  
Impact Journals, LLC meets Wellcome Trust Publisher requirements.  
IMPACT JOURNALS is a registered trademark of Impact Journals, LLC.



# Table of Contents

Physiological frailty index (PFI): quantitative in-life estimate of individual biological age in mice

[Originally published in Volume 9, Issue 3 pp 615-626](#)

Delivery of sFIT-1 engineered MSCs in combination with a continuous low-dose doxorubicin treatment prevents growth of liver cancer

[Originally published in Volume 8, Issue 12 pp 3520-3534](#)

RelA NF- $\kappa$ B subunit activation as a therapeutic target in diffuse large B-cell lymphoma

[Originally published in Volume 8, Issue 12 pp 3321-3340](#)

Discovery of piperlongumine as a potential novel lead for the development of senolytic agents

[Originally published in Volume 8, Issue 11 pp 2915-2926](#)

PI3K $\alpha$  inhibition reduces obesity in mice

[Originally published in Volume 8, Issue 11 pp 2747-2753](#)

Mitophagy-driven mitochondrial rejuvenation regulates stem cell fate

[Originally published in Volume 8, Issue 7 pp 1330-1349](#)

Potential targeted therapeutic approaches in liposarcoma

[Originally published in Volume 8, Issue 4 pp 569-570](#)

Apoptosis as anticancer mechanism: function and dysfunction of its modulators and targeted therapeutic strategies

[Originally published in Volume 8, Issue 4 pp 603-619](#)

Fasting plus tyrosine kinase inhibitors in cancer

[Originally published in Volume 7, Issue 12 pp 1026-1027](#)

A novel autosomal recessive TERT T1129P mutation in a dyskeratosis congenita family leads to cellular senescence and loss of CD34<sup>+</sup> hematopoietic stem cells not reversible by mTOR-inhibition

[Originally published in Volume 7, Issue 11 pp 911-927](#)

The p53 tumor suppressor protein protects against chemotherapeutic stress and apoptosis in human medulloblastoma cells

[Originally published in Volume 7, Issue 10 pp 854-867](#)

Kinase overexpressing cancers responsive to drug withdrawal

[Originally published in Volume 7, Issue 10 pp 752-753](#)

Sonic Hedgehog in SCLC

[Originally published in Volume 7, Issue 9 pp 605-606](#)

Targeting of non-oncogene addiction

[Originally published in Volume 7, Issue 8 pp 525-526](#)

Caloric restriction induces heat shock response and inhibits B16F10 cell tumorigenesis both *in vitro* and *in vivo*

[Originally published in Volume 7, Issue 4 pp 233-240](#)

Clearance of senescent hepatocytes in a neoplastic-prone microenvironment delays the emergence of hepatocellular carcinoma

[Originally published in Volume 6, Issue 1 pp 26-34](#)

Therapeutic and space radiation exposure of mouse brain causes impaired DNA repair response and premature senescence by chronic oxidant production

[Originally published in Volume 5, Issue 8 pp 607-622](#)

Rapamycin extends lifespan and delays tumorigenesis in heterozygous p53+/- mice

[Originally published in Volume 4, Issue 10 pp 709-714](#)

Reversing the aging stromal phenotype prevents carcinoma initiation

[Originally published in Volume 3, Issue 4 pp 407-416](#)

Naringin targets Zeb1 to suppress osteosarcoma cell proliferation and metastasis

[Originally published in Volume 10, Issue 12 pp 4141-4151](#)

Long noncoding RNA B3GALT5-AS1 suppresses colon cancer liver metastasis via repressing microRNA-203

[Originally published in Volume 10, Issue 12 pp 3662-3682](#)

A four-methylated mRNA signature-based risk score system predicts survival in patients with hepatocellular carcinoma

[Originally published in Volume 11, Issue 1 pp 160-173](#)

First-in-class candidate therapeutics that target mitochondria and effectively prevent cancer cell metastasis: mitoriboscins and TPP compounds

[Originally published in Volume 12, Issue 11 pp 10162-10179](#)

Loss of AKR1B10 promotes colorectal cancer cells proliferation and migration via regulating FGF1-dependent pathway

[Originally published in Volume 12, Issue 13 pp 13059-13075](#)

Coupled immune stratification and identification of therapeutic candidates in patients with lung adenocarcinoma

[Originally published in Volume 12, Issue 16 pp 16514-16538](#)

Mimetics of extra virgin olive oil phenols with anti-cancer stem cell activity

[Originally published in Volume 12, Issue 21 pp 21057-21075](#)

Targeting FTO for cancer therapy and more

[Originally published in Volume 13, Issue 15 pp 19080-19082](#)

Impact of aging on primary liver cancer: epidemiology, pathogenesis and therapeutics

[Originally published in Volume 13, Issue 19 pp 23416-23434](#)

Identification of a novel immune signature for optimizing prognosis and treatment prediction in colorectal cancer

[Originally published in Volume 13, Issue 23 pp 25518-25549](#)

TIMP-2 regulates 5-Fu resistance via the ERK/MAPK signaling pathway in colorectal cancer

[Originally published in Volume 14, Issue 1 pp 297-315](#)

Binding of the angiogenic/senescence inducer CCN1/CYR61 to integrin  $\alpha_6\beta_1$  drives endocrine resistance in breast cancer cells

[Originally published in Volume 14, Issue 3 pp 1200-1213](#)

Mechanisms of action of triptolide against colorectal cancer: insights from proteomic and phosphoproteomic analyses

[Originally published in Volume 14, Issue 7 pp 3084-3104](#)

Synergistic blocking of RAS downstream signaling and epigenetic pathway in *KRAS* mutant pancreatic cancer

[Originally published in Volume 14, Issue 8 pp 3597-3606](#)

microRNA-569 inhibits tumor metastasis in pancreatic cancer by directly targeting NUSAP1

[Originally published in Volume 14, Issue 8 pp 3652-3665](#)

Hallmarks of cancer and hallmarks of aging

[Originally published in Volume 14, Issue 9 pp 4176-4187](#)

## Physiological frailty index (PFI): quantitative in-life estimate of individual biological age in mice

Marina P. Antoch<sup>1</sup>, Michelle Wrobel<sup>1,2</sup>, Karen K. Kuropatwinski<sup>1</sup>, Ilya Gitlin<sup>3</sup>, Katerina I. Leonova<sup>3</sup>, Ilya Toshkov<sup>2</sup>, Anatoli S. Gleiberman<sup>2</sup>, Alan D. Hutson<sup>4</sup>, Olga B. Chernova<sup>2</sup>, Andrei V. Gudkov<sup>3</sup>

<sup>1</sup>Department of Pharmacology and Therapeutics, Roswell Park Cancer Institute, Buffalo, NY 14263, USA

<sup>2</sup>Everon Biosciences, Inc., Buffalo, NY 14203, USA

<sup>3</sup>Department of Cell Stress Biology, Roswell Park Cancer Institute, Buffalo, NY 14263, USA

<sup>4</sup>Biostatistics and Bioinformatics, Roswell Park Cancer Institute, Buffalo, NY 14263, USA

**Correspondence to:** Marina P. Antoch; email: [marina.antoch@roswellpark.org](mailto:marina.antoch@roswellpark.org)

**Keywords:** aging, high fat diet, obesity, rapamycin, rapatar, chronological age

**Received:** January 12, 2017

**Accepted:** March 11, 2017

**Published:** March 19, 2017

### ABSTRACT

The development of healthspan-extending pharmaceuticals requires quantitative estimation of age-related progressive physiological decline. In humans, individual health status can be quantitatively assessed by means of a *frailty index* (FI), a parameter which reflects the scale of accumulation of age-related deficits. However, adaptation of this methodology to animal models is a challenging task since it includes multiple subjective parameters. Here we report a development of a quantitative non-invasive procedure to estimate biological age of an individual animal by creating *physiological frailty index* (PFI). We demonstrated the dynamics of PFI increase during chronological aging of male and female NIH Swiss mice. We also demonstrated acceleration of growth of PFI in animals placed on a high fat diet, reflecting aging acceleration by obesity and provide a tool for its quantitative assessment. Additionally, we showed that PFI could reveal anti-aging effect of mTOR inhibitor rapatar (bioavailable formulation of rapamycin) prior to registration of its effects on longevity. PFI revealed substantial sex-related differences in normal chronological aging and in the efficacy of detrimental (high fat diet) or beneficial (rapatar) aging modulatory factors. Together, these data introduce PFI as a reliable, non-invasive, quantitative tool suitable for testing potential anti-aging pharmaceuticals in pre-clinical studies.

### INTRODUCTION

Mammalian aging is characterized by a gradual decline of numerous health parameters with multiple biochemical, physiological and behavioral manifestations [1]. These include reduced muscle strength, bone degeneration, osteoporosis, an increase in systemic inflammation, vascular calcification, hair loss, cataracts, cognitive decline, etc. [2]. Several animal models including *C.elegans*, yeast, *Drosophila* and rodents (rats and mice) have been successfully used over the last several decades to address mechanistic aspects of aging and development of age-related diseases. In most of these studies the major metric parameter for assessing pro-/anti-aging effect

of genetic, nutritional or pharmacological manipulation has been the animals' lifespan.

While being informative, longevity by itself however, cannot provide an assessment of the animal's health status, which, like in humans, can significantly decline at older ages and therefore reduce the quality of life. This concern is particularly relevant to research focused on developing the "healthspan"-extending pharmaceuticals, efficacy of which may not be necessarily translated in increased longevity but rather in prolongation of healthy life and require quantitative objective assessment. Clinical studies in humans measure age-related declines in performance by quan-

tifying the frailty index (FI), which reflects accumulation of health deficits during chronological aging [3].

Since numerous studies have shown that many age-associated changes that occur in humans are also present in aged mice, FI was recently introduced as a measure of mouse aging to pre-clinical models [4]. However, standardized and comprehensive approaches for FI measurements, which will address changes in a broad spectrum of physiological functions, are still missing. Here we describe development of an alternative scoring system, based on a selected set of non-invasive quantitative and physiological parameters, which could be repetitively used in the same animal over the course of its entire lifespan. We refer to this set of parameters as physiological frailty index (PFI). We show that similar to results of human studies older mice have much greater PFI reflecting age-related accumulation of deficits. We also validated our approach of PFI by testing detrimental (feeding high fat diet, HFD) and beneficial (treatment with mTOR inhibitor rapamycin) factors on animals' longevity and healthspan and revealed significant sex-dependent differences, thus emphasizing the importance of including both male and female animals in pre-clinical studies. The results of our study provide a feasible tool applicable for pre-clinical studies to test the efficacy of anti-aging pharmaceuticals.

## RESULTS

### Choosing informative parameters for creating PFI

To select which physiological parameters to choose for creating reliable FI we used several criteria. First, we wanted them to be diverse to reflect the status of different health-related physiological systems. Second, we wanted them to be objective and quantitative and not to involve any visual scoring. Finally, we wanted them to be minimally invasive so they can be applied in longitudinal studies. Based on these considerations, we selected 29 variables reflective of physical fitness (body weight and grip strength), cardiovascular system (systolic, diastolic and mean blood pressure, heart rate, tail blood flow and tail blood volume), total blood cell composition (white and red blood cell counts and differentials), plasma concentration of CXCL1/KC, triglycerides and glucose. All variables were measured in male and female NIH Swiss mice of different chronological ages (CA) of 26, 52, 78 and 104 weeks in a cross-sectional study. Next, using one-way ANOVA analysis, we identified those variables that demonstrate statistically significant changes during aging ( $p$ -value  $<0.05$ ). Out of total of 29 parameters, 16 and 18 qualified these criteria in males and females respectively. These parameters and corresponding mean values for each age group are summarized in Tables 1 and 2. Interestingly, the two lists have only partial overlap pointing to sex-specific differences in the process of aging.

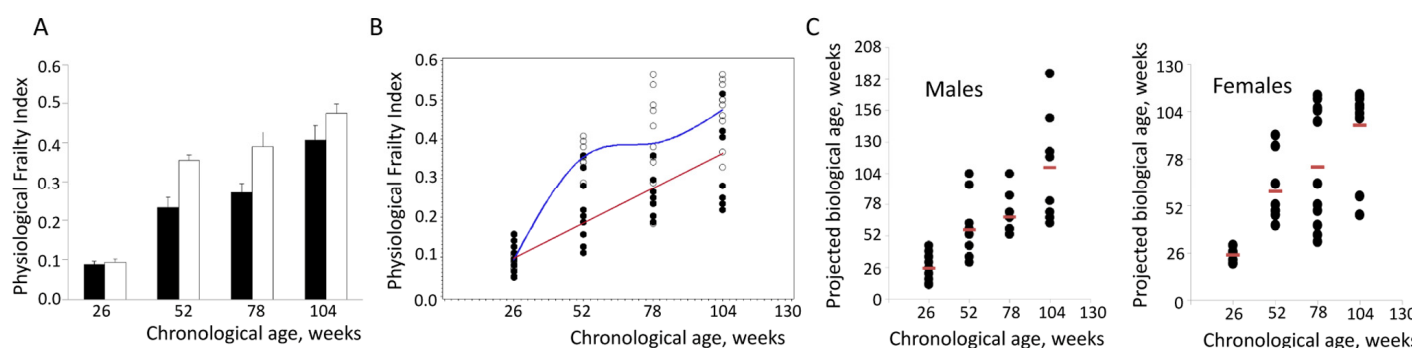


**Figure 1. Assessment of individual biological age of NIH Swiss mice.** (A) Age-related increase in PFI in male (closed bars) and female (open bars) NIH Swiss mice ( $n=10-12$ /group). PFI indices were measured as described using 16 or 18 parameters for males and females respectively. Data is presented as mean  $\pm$ SEM. One-way ANOVA detects significant effect of age on FI value ( $p<0.001$  for both sexes). (B) PFI values for individual male (closed circles) and female (open circles) mice. A cubic regression performed on this set of data generated the best fitting model as:  $PFI=0.00684+0.0034 \times BA$  for males (red line) and  $PFI=-0.67372+0.04277 \times CA-0.00057899 \times CA^2+0.00000263 \times CA^3$  for females (blue line). All regression coefficients presented were significantly different from 0 at the 0.05 alpha-level. (C) Projected biological age of individual mice calculated from the PFI values using the fitting model predictions.



## Quantification of PFI in chronologically aged male and female NIH/Swiss mice

To quantitatively evaluate age-dependent accumulation of health deficits, male and female NIH Swiss mice were allowed to age in the animal facility under normal husbandry conditions. Separate groups of male and female mice were tested for their overall health status at the ages of 26, 52, 78, and 104 weeks as described in Materials and Methods section. PFI was created using the 26-week old mice as a reference so that deviation of each parameter from the mean value was calculated. As shown in Fig.1A, PFI demonstrates gradual increase with age in both males and females; however, dynamics of this process was different. Consistent with previous studies, both in mice and humans [5], females show a more rapid accumulation of health deficits than males and average PFI values were higher compared to the males of the corresponding age.

Although average value of PFI showed highly statistically significant increase with age, within each age-matched group it demonstrated considerable individual variability (Fig. 1B). This is consistent with widely accepted concept originated from human and animal model studies stating that chronological age (CA, the actual age from the date of birth) and biological age (BA, reflecting individual's health status) are different [6-8]. To test whether PFI value can be used as a predictor of an individual animal's BA, polynomial regression of order 3 was fit to the data using a stepwise regression approach.

The best fitting models were given as:

$$\begin{aligned} \text{PFI} &= 0.00684 + 0.0034 \times \text{BA} \text{ for males and} \\ \text{FI} &= -0.67372 + 0.04277 \times \text{CA} - 0.00057899 \times \text{CA}^2 \\ &+ 0.00000263 \times \text{CA}^3 \text{ for females.} \end{aligned}$$

Next, we used these equations to calculate BA of each individual animal based on its PFI. Fig. 1C presents results of this analysis showing high degree of variability of estimated BA within the group of chronologically age-matched male and female mice. Overall these data indicate that our scoring system allows for an unbiased and reliable quantitation of age-related accumulation of deficits. They also suggest that PFI may be used as a tool for evaluating health status of an individual animal and determining its BA. This tool may be applied for quantitative assessment of the effects of various environmental, nutritional and pharmacological interventions on healthspan.

## Sex-dependent effect of high fat diet on PFI and longevity

To validate our approach for assessing animal's BA, we subjected them to two treatments known to cause detrimental (feeding high fat diet, HFD) or beneficial (administration of rapamycin) effects on health and longevity. Fifty two week old male and female NIH Swiss mice were randomly assigned to four groups. Group 1 remained on regular chow and drinking water; group 2 remained on regular chow but started receiving rapamycin in drinking water. Group 3 started receiving HFD in combination with normal drinking water and group 4 was fed HFD in combination with rapamycin.

**Table 1. Physiological parameters used to create PFI in male NIH Swiss mice. Data is presented as mean  $\pm$  SEM.**

Age, weeks	GS, g	Dia	Mean	Flow	NE (K/ $\mu$ l)	LY (K/ $\mu$ l)	MO (K/ $\mu$ l)	KC (pg/ml)
26	76.96 $\pm$ 3.42	79.28 $\pm$ 3.98	88.93 $\pm$ 3.49	15.81 $\pm$ 2.17	1.45 $\pm$ 0.12	3.24 $\pm$ 0.30	0.19 $\pm$ 0.02	595.9 $\pm$ 57.22
52	72.17 $\pm$ 3.42	76.95 $\pm$ 2.24	85.63 $\pm$ 2.17	22.07 $\pm$ 1.56	1.02 $\pm$ 0.17	2.52 $\pm$ 0.30	0.217 $\pm$ 0.02	905.07 $\pm$ 234.12
78	78.74 $\pm$ 4.14	72.70 $\pm$ 4.16	84.17 $\pm$ 4.36	15.86 $\pm$ 1.7	2.65 $\pm$ 0.56	4.32 $\pm$ 0.77	0.309 $\pm$ 0.10	372.10 $\pm$ 39.58
104	49.92 $\pm$ 3.15	88.75 $\pm$ 3.33	97.81 $\pm$ 3.34	21.04 $\pm$ 1.6	0.55 $\pm$ 0.14	2.25 $\pm$ 0.82	0.271 $\pm$ 0.08	705.93 $\pm$ 94.94

**Table 1. (continued)**

Age, weeks	NE %	MO %	RBC (M/ $\mu$ l)	HB (g/dl)	HCT %	MCV(fl)	MCH (Pg)	MCHC (g/dl)
26	24.16 $\pm$ 4.04	3.02 $\pm$ 0.30	8.91 $\pm$ 0.41	13.09 $\pm$ 0.69	39.60 $\pm$ 2.20	44.27 $\pm$ 0.72	14.66 $\pm$ 0.23	32.90 $\pm$ 0.29
52	26.01 $\pm$ 2.09	6.03 $\pm$ 0.57	7.97 $\pm$ 0.46	11.83 $\pm$ 0.73	37.85 $\pm$ 2.37	47.34 $\pm$ 0.69	14.81 $\pm$ 0.21	31.28 $\pm$ 0.30
78	34.18 $\pm$ 2.12	3.83 $\pm$ 0.48	9.94 $\pm$ 0.59	15.23 $\pm$ 0.87	49.20 $\pm$ 2.60	49.71 $\pm$ 0.98	15.33 $\pm$ 0.22	30.91 $\pm$ 0.27
104	18.10 $\pm$ 3.16	8.78 $\pm$ 1.41	6.6 $\pm$ 0.63	9.50 $\pm$ 0.97	34.01 $\pm$ 3.23	51.73 $\pm$ 1.00	14.33 $\pm$ 0.16	27.77 $\pm$ 0.45

GS – grip strength; Dia – diastolic pressure; Mean – mean pressure; NE – neutrophils; LY – lymphocytes; MO – monocytes; RBC – red blood cells count; HB – hemoglobin; HCT – hematocrit; MCV – mean corpuscular volume; MCH – mean corpuscular hemoglobin; MCHC – mean corpuscular hemoglobin concentration

It is well established that HFD-induced obesity has a detrimental effect on health increasing the risk of diabetes, heart disease, high blood pressure and cancer [9]. As shown in Fig. 2A, feeding HFD results in significant increase in body weight in both males and females (40% and 30% for males and females respectively). Nevertheless, effect on longevity was very different. Whereas feeding HFD reduced lifespan of male NIH Swiss mice from  $121.1 \pm 9.2$  to  $91.5 \pm 5.9$  weeks ( $p=0.008$ , Kaplan-Meier log-rank test), it had no effect on longevity of female mice ( $109.6 \pm 6.9$  and  $104.9 \pm 7.7$  weeks for mice fed regular or high fat chow respectively; Fig. 2B). This result is consistent with previous studies showing that female mice are protected against HFD-induced metabolic changes by maintaining an anti-inflammatory environment in the intra-abdominal adipose tissue, whereas HFD-fed male mice develop adipose tissue inflammation, glucose intolerance, hyperinsulinemia, and islet hypertrophy [10].

To further test whether reduction in lifespan in males correlates with an increase in accumulation of health deficits, after 26 weeks of feeding HFD (at the age of 78 weeks) we created PFI for each individual animal.

Consistent with longevity data, feeding HFD significantly increased PFI in male but not in female mice (Fig. 2C). These data indicate that HFD-induced obesity produces stronger damaging effect in male mice affecting both their longevity and health status and that our approach can reliably detect overall health decline in a quantitative manner.

### Chronic treatment with rapamycin increases the lifespan of female NIH Swiss mice without affecting their health status

To further validate our method, we decided to test whether we can reliably measure the beneficial effects of lifespan increasing approaches on animals' health. For this we chose to use rapamycin, which has been shown to extend lifespan of inbred and genetically heterogeneous mice [11, 12] as well as of mice that develop syndrome of premature aging [13]. Several studies performed in cancer-prone animal models suggest that rapamycin extends lifespan by delaying tumor development and progression [11, 14, 15]. In our previous work, we successfully used nanoformulated water soluble rapamycin (rapatar), which can be admi-

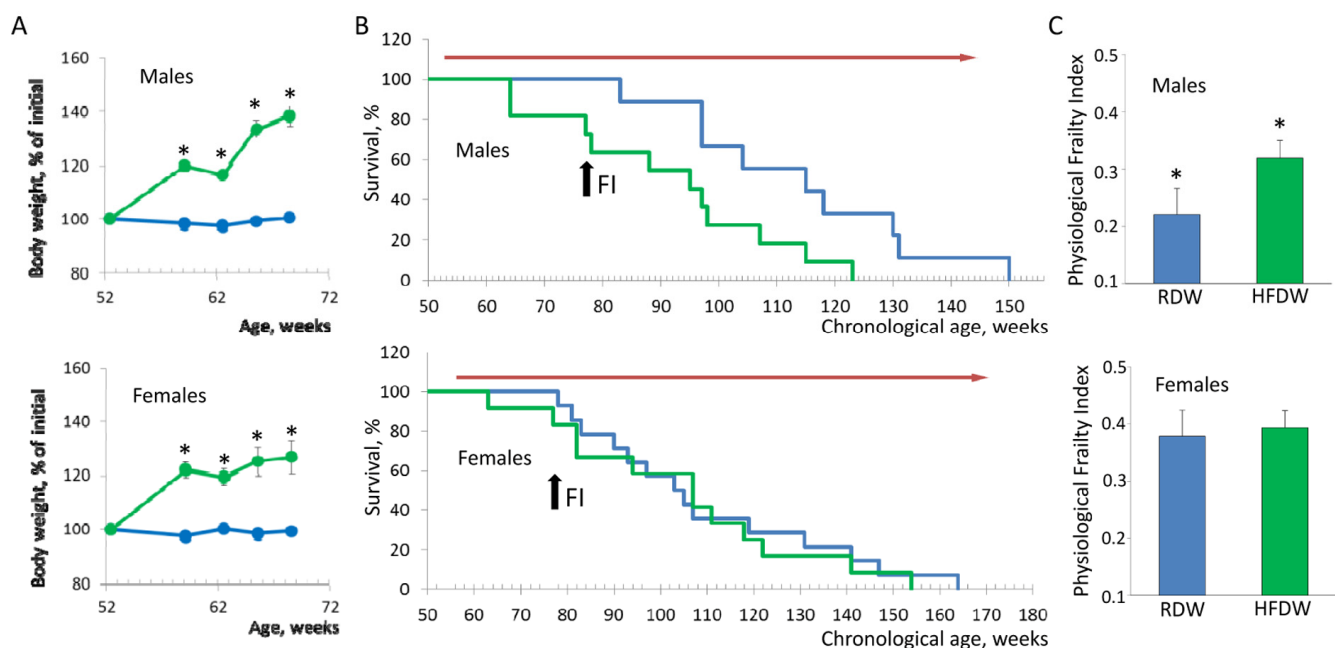


**Figure 2. Sex-specific effects of HFD on lifespan and health of NIH Swiss mice.** (A) HFD-induced body weight gain in male and female mice. Feeding HFD results in 40% and 30% increase in body weight in males and females respectively ( $p<0.001$ , Student's t-test). Since mortality is usually preceded by rapid weight loss, data is shown for the initial period of treatment before the first case of death in each group was recorded. Blue line – regular diet; green line – HFD. (B) Feeding HFD reduces lifespan of male mice from  $121.1 \pm 9.2$  to  $91.5 \pm 5.9$  weeks ( $p=0.008$ , Kaplan-Meier log-rank test) but had no effect on longevity of female mice ( $109.6 \pm 6.9$  and  $104.9 \pm 7.7$  weeks for mice fed regular or high fat chow respectively). Blue line – regular diet; green – HFD. Red arrow indicates the period of time when mice received HFD. Black arrow indicates time when PFI was measured (at the age of 78 weeks). (C) PFI created at 78 weeks of age using 16 or 18 parameters for male and female mice respectively. Feeding HFD significantly increases PFI of male ( $p=0.019$ , Student's t-test) but not female mice. RDW - regular diet in combination with water (group 1), HFDW – HFD in combination with water (group 3).

nistered with drinking water and demonstrated high bioavailability [14]. In concurrence with the previous study, chronic administration of rapamycin did not cause any toxicity as both male and female mice in control and experimental groups maintained similar body weight (Fig. 3A). However, there was a significant difference in the effect of rapamycin on longevity between the sexes. Chronic rapamycin treatment had no effect on longevity of male mice (mean survival  $113.91 \pm 6.98$  and  $100.8 \pm 6.96$  weeks for control and rapamycin-treated mice respectively) whereas in females, it increased lifespan from  $110.09 \pm 7.12$  to  $131.23 \pm 8.29$  weeks ( $p=0.05$ , Kaplan-Meier log-rank test; Fig. 3B). Surprisingly, this effect was not translated into improved health status between the groups as monitored by PFI (Fig. 3C). Thus, our data provides an additional support for the concept that chronological and biological aging may not be intrinsically identical and that other factors besides time may affect the pace of age-dependent functional decline.

### Rapamycin alleviates detrimental effect of high fat diet on male mice longevity and healthspan

Our data show that HFD-induced obesity shortens lifespan and deteriorates health status of NIH Swiss male mice (Fig. 1). It has been previously demonstrated that in rodents HFD-induced obesity increases activation of mTOR pathway in liver and skeletal muscle [16]. Therefore, we hypothesize that treatment with rapamycin can ameliorate detrimental effects of HFD. Comparison of the dynamics of body weight change showed that chronic treatment with rapamycin did not affect HFD-induced obesity in male mice but did prevent it in females (Fig. 4A). Longevity was not affected in mice of both sexes (Fig. 4B) constituting  $91.45 \pm 5.87$  and  $100.55 \pm 6.26$  weeks for male ( $p=0.26$ ) and  $105.01 \pm 7.74$  and  $110.50 \pm 7.58$  weeks for female mice ( $p=0.6$ ). Strikingly, rapamycin administration significantly alleviated detrimental effects of HFD in male mice as judged by a significant decrease in PFI

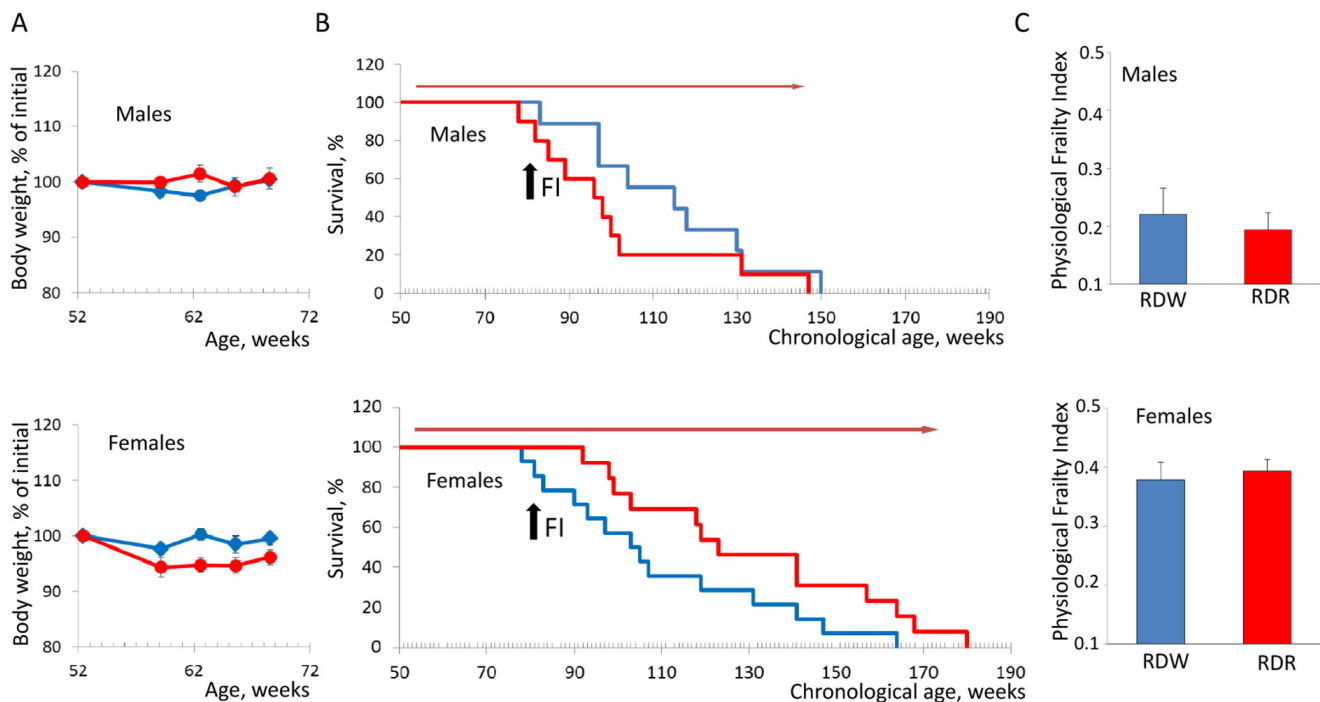


**Figure 3. Sex-specific effects of rapamycin on lifespan and health of NIH Swiss mice.** (A) Animals receiving rapamycin in drinking water maintain their body weights comparable to control mice. Blue line – normal drinking water; red line – water with rapamycin. (B) Kaplan-Meier survival curves for mice fed regular chow in combination with normal drinking water (blue line) or rapamycin (red line). Chronic administration of rapamycin has no effect on longevity of male mice (mean survival is  $113.91 \pm 6.98$  and  $100.8 \pm 6.96$  weeks for control and rapamycin-treated mice respectively). In females, rapamycin administration increases lifespan from  $110.09 \pm 7.12$  to  $131.23 \pm 8.29$  weeks ( $p=0.05$ , Kaplan-Meier log-rank test). Red arrow indicates the period of time when mice received rapamycin. Black arrow indicates time when PFI was measured. (C) PFI created at described above. No effect of rapamycin on health status was detected in male and female mice fed regular chow. RDW – regular diet in combination with normal drinking water (group1); RDR – regular diet in combination with rapamycin (group 2).

(Fig. 4C). Thus, whereas chronic treatment with rapamycin had no effect on lifespan and health status of male mice under standard diet conditions, it did prevent development of HFD-induced decline in health.

**Table 2. Physiological parameters used to create PFI in female NIH Swiss mice. Data is presented as mean +SEM**

Age, weeks	BW, g	GS, g	Dia	Flow	WBC (K/ $\mu$ l)	NE (K/ $\mu$ l)	NE %	LY %	MO %
26	26.61 $\pm$ 0.31	76.96 $\pm$ 3.42	79.28 $\pm$ 3.98	15.81 $\pm$ 2.17	5.19 $\pm$ 0.27	0.86 $\pm$ 0.07	16.56 $\pm$ 0.96	77.82 $\pm$ 0.81	4.90 $\pm$ 0.37
52	32.20 $\pm$ 1.15	72.17 $\pm$ 3.42	76.95 $\pm$ 2.24	22.07 $\pm$ 1.56	4.41 $\pm$ 0.46	1.28 $\pm$ 0.14	30.50 $\pm$ 4.22	61.90 $\pm$ 4.27	7.06 $\pm$ 0.66
78	37.17 $\pm$ 1.86	78.74 $\pm$ 4.14	72.70 $\pm$ 4.16	15.86 $\pm$ 1.7	7.47 $\pm$ 0.91	2.57 $\pm$ 0.42	34.23 $\pm$ 3.36	59.59 $\pm$ 3.90	4.01 $\pm$ 0.29
104	35.71 $\pm$ 1.17	49.92 $\pm$ 3.15	88.75 $\pm$ 3.33	21.04 $\pm$ 1.6	6.55 $\pm$ 2.32	1.57 $\pm$ 0.50	22.86 $\pm$ 3.69	63.99 $\pm$ 4.12	7.90 $\pm$ 0.83

**Table 2. (continued)**

Age, weeks	EO%	RBC (M/ $\mu$ l)	HB (g/dl)	HCT %	MCV(fl)	MCH (Pg)	MCHC (g/dl)	PLT	MPV
26	0.11 $\pm$ 0.02	9.86 $\pm$ 0.25	14.95 $\pm$ 0.19	49.05 $\pm$ 2.13	49.47 $\pm$ 1.34	14.72 $\pm$ 0.15	30.15 $\pm$ 0.86	1134.53 $\pm$ 28.53	4.83 $\pm$ 0.04
52	0.50 $\pm$ 0.1	11.21 $\pm$ 0.27	16.33 $\pm$ 0.31	61.13 $\pm$ 1.43	54.65 $\pm$ 1.16	14.60 $\pm$ 0.31	26.75 $\pm$ 0.37	706.00 $\pm$ 97.92	4.76 $\pm$ 0.11
78	1.70 $\pm$ 0.58	10.11 $\pm$ 0.42	15.39 $\pm$ 0.76	49.12 $\pm$ 2.45	48.44 $\pm$ 0.77	15.16 $\pm$ 0.20	31.35 $\pm$ 0.19	1285.09 $\pm$ 134.26	5.26 $\pm$ 0.09
104	3.95 $\pm$ 0.67	9.63 $\pm$ 1.07	9.50 $\pm$ 0.97	33.49 $\pm$ 3.65	48.15 $\pm$ 1.05	13.83 $\pm$ 0.30	28.72 $\pm$ 0.22	876.25 $\pm$ 96.58	5.57 $\pm$ 0.19

WBC – white blood cells, NE – neutrophils; LY – lymphocytes; MO – monocytes; EO – eosinophils; RBC – red blood cells count; HB – hemoglobin; HCT – hematocrit; MCV – mean corpuscular volume; MCH – mean corpuscular hemoglobin; MCHC – mean corpuscular

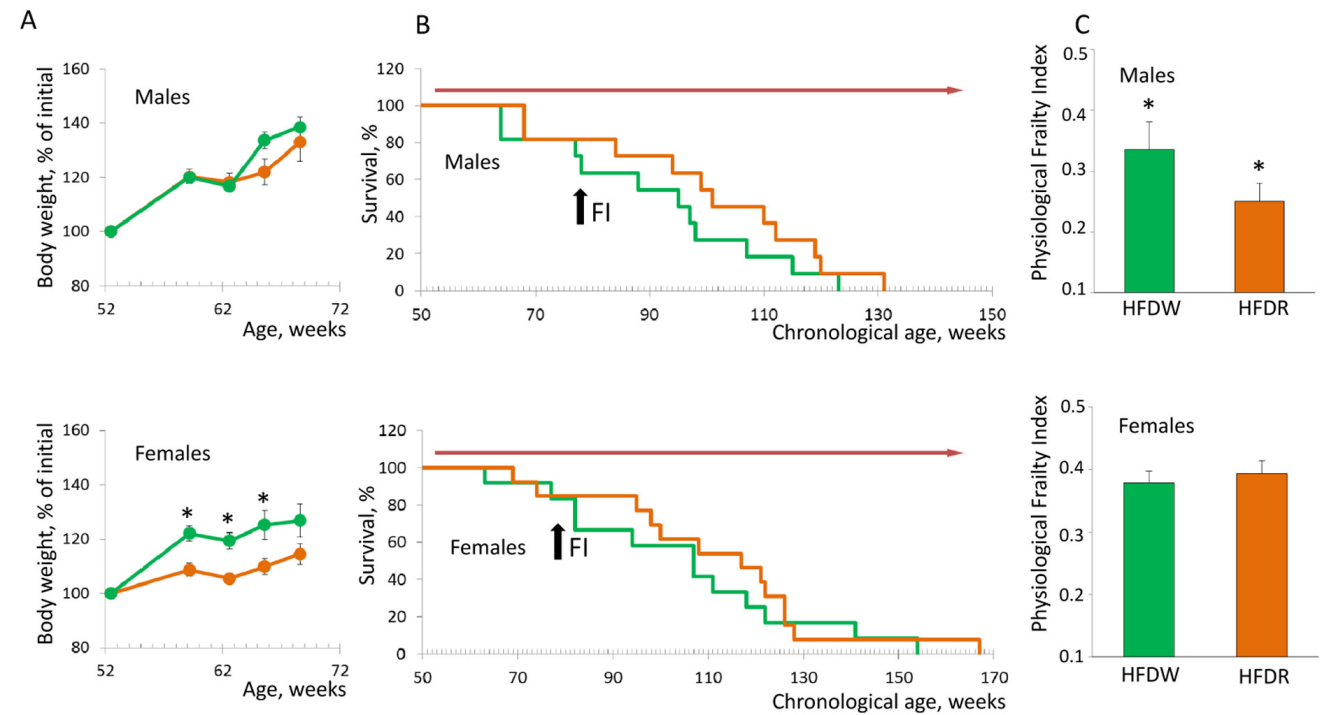


**Figure 4. Chronic treatment with rapamycin ameliorates HFD-induced health decline in male mice. (A)** Rapamycin prevents HFD-induced weight gain in female but not in male mice ( $p < 0.01$ , Student's  $t$ -test). Green – HFD given with normal water, orange – HFD given in combination with rapamycin. **(B)** Kaplan-Meier survival curves for mice fed HFD in combination with normal drinking water (green line) or rapamycin (orange line). Chronic administration of rapamycin has no effect on longevity of both male (mean survival is  $91.5 \pm 5.9$  and  $100.5 \pm 6.26$  weeks) and female mice (mean survival is  $104.9 \pm 7.7$  and  $110.5 \pm 7.6$  weeks for control and rapamycin-treated mice respectively). Red arrow indicates the period of time when mice received rapamycin. Black arrow indicates time when PFI was measured. **(C)** PFI created at 78 weeks of age using 16 or 18 parameters for male and female mice respectively. Chronic administration of rapamycin ameliorates detrimental effect of HFD and brings the PFI values down to the normal range characteristic for this age ( $p = 0.014$ , Student's  $t$ -test). HFDW – high-fat diet in combination with regular drinking water (group 3), HFDR – high-fat diet in combination with rapamycin (group 4).



To further illustrate the complex effects of diet and rapamycin on animal's health, we calculated projected biological age of each 78 week old male and female mouse based on their PFI. Results of this analysis are presented in Fig. 5. Similar to our data for chronologically aged mice, we observed a significant individual variability within each experimental group of age-matched animals. The data showed that feeding HFD increases mean BA of male mice by 34 weeks (from  $62.7 \pm 13.3$  to  $96.4 \pm 8.8$  weeks;  $p=0.03$ , Student's

t-test; Fig. 5A). Chronic treatment with rapamycin improves animals' health status and reduces their BA to values characteristic for control group (from  $96.4 \pm 8.8$  to  $71.5 \pm 9.6$  weeks ( $p=0.04$ , Student's t-test; Fig. 5B). No difference between groups was detected in female mice, in which BA was very close to their CA in all groups. Slight reduction of BA in rapamycin treated group from  $71.8 \pm 7.8$  to  $62.6 \pm 7.0$  weeks was not statistically significant ( $p=0.3$  Student's t-test).

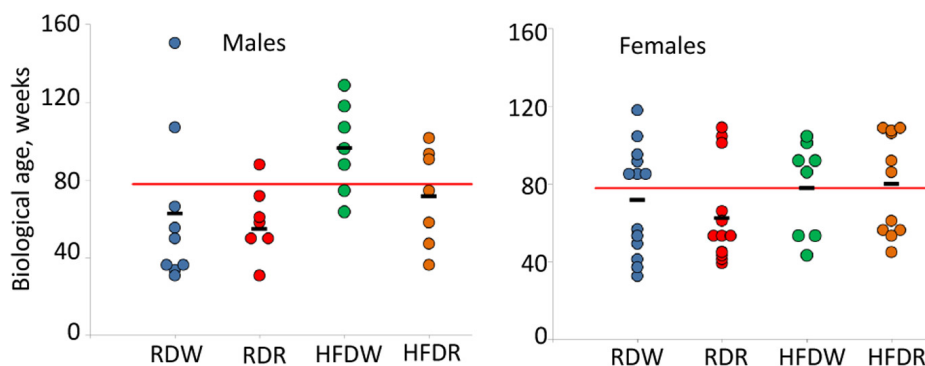


**Figure 5. Sex-specific effects of detrimental (HFD) and beneficial (rapamycin) factors on BA of NIH Swiss mice.** Feeding HFD accelerates aging of NIH Swiss male mice whereas rapamycin counteracts this process. Projected biological age of individual mice (shown by circles) and mean BA for the group (black marker) were calculated from the corresponding FI value using the fitting model predictions. Red line designates chronological age of all mice at the time of testing (78 weeks). Data show that projected BA of all mice that received HFD (green circles) is significantly higher than their actual chronological age and mean BA age for control group on regular diet ( $62.7 \pm 13.3$  and  $96.4 \pm 8.8$  weeks for RDW and HFDW groups respectively ( $p=0.03$ , Student's t-test). Chronic administration of rapamycin reduces BA of males fed HFD to values characteristic for control group (from  $96.4 \pm 8.8$  to  $71.5 \pm 9.6$  weeks;  $p=0.04$ , Student's t-test). No difference between groups was detected in female mice, in which BA was very close to their CA. Slight reduction in BA in rapamycin treated group from  $71.8 \pm 7.8$  to  $62.6 \pm 7.0$  weeks was not statistically significant ( $p=0.3$  Student's t-test).

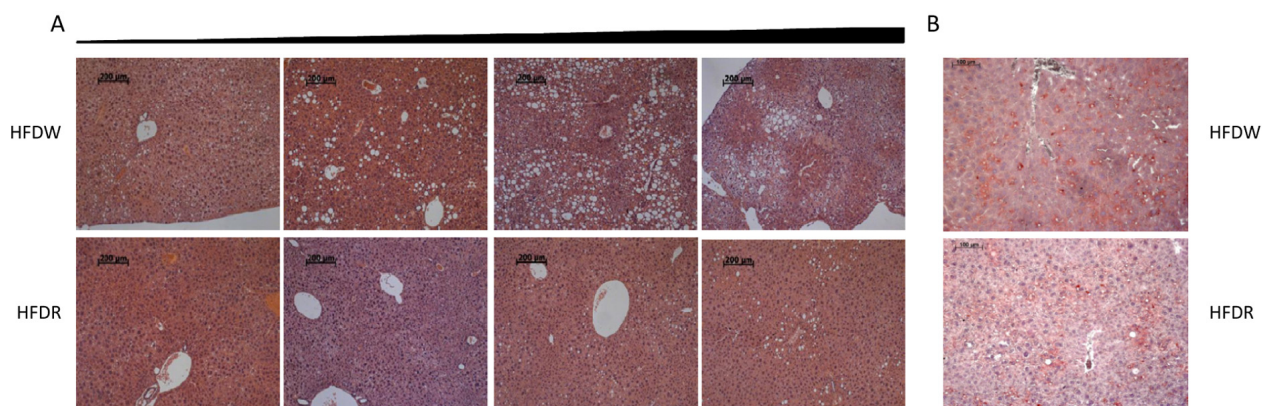


**Figure 6. Rapamycin prevents development of HFD-induced hepatic steatosis in male mice.** (A) H&E staining of representative liver sections graded from the least affected (left) to the worst affected (right) within each group. (B) Representative oil-red O stained sections of livers. HFDW – mice fed with HFD; HFDR – mice received HFD in combination with rapamycin.

To confirm the preventive role of rapamycin in the development of diet-induced obesity, at completion of the experiment we performed hematoxylin-eosin and Oil Red O staining of livers of male mice fed HFD in combination with either normal water or rapamycin. Fig. 6A shows examples of H&E staining that were graded from the best to the worst within each group demonstrating larger and more lipid droplet accumulation in liver parenchyma in high-fat diet group and significant improvement of hepatic steatosis by rapamycin administration. These conclusions were consistent with the results of the Oil Red O staining (Fig. 6B). Taken together, these data suggest that our approach for frailty assessment allows for reliable and quantitative evaluation of animal's health status both during normal aging process as well as after various interventions.

## DISCUSSION

Aging is characterized by accumulation of deficits and increased frailty, which in turn increases vulnerability of an older organism to various stressors. In clinical gerontology two major tools were developed to evaluate frailty in elderly: the phenotype model and FI (reviewed in [17]). The phenotype model describes frailty as a phenotype that can be scored using 5 criteria of patient's physical performance [18]. In contrast, FI represents cumulative score of a degree of deviation that multiple behavioral, physical and physiological parameters developed with age compared to normal values characteristic to healthy young individuals [3]. Since FI was introduced to human gerontology, it was used in many epidemiological and clinical studies to evaluate the risk of adverse health events in elderly. These include a decline in overall activity, reduced muscle strength, bone degeneration, osteoporosis, an increase in inflammation, vascular calcification, hair loss, cataracts, cognitive decline, etc.

The strategy of estimating FI as a measurement of health status has been also applied to the mouse models [19, 20]. However, the majority of frailty assessment tools use multiple observational approaches such as recording and scoring of visible pathologies (eye inflammation or cataracts, high respiratory rate, visible tumors, alopecia, dermatitis, distended abdomen etc.), or behavioral signs (circling behavior, reduced or excessive grooming, etc.). Although informative, this approach has some significant limitations and researcher bias. First, these parameters are subjective by nature and require scoring by several independent raters in consistent manner [21-23]. Secondly, many health problems start a lot earlier than could be detected by their visual manifestation. Therefore, the goal of our study was to develop a reliable, quantitative scoring

system, physiological frailty index (PFI) that would be based on non-invasive quantitative measurements of various physiological parameters, which could be repetitively used in the same animal during the course of its entire lifespan and would represent its overall health status.

Several previous studies suggest that the more diverse variables are used for creating the FI, more reliable FI value is [24]. At the same time to optimize the robustness of the procedure in order to make it applicable to a large number of animals, we were inclined to minimize the number of variables. This rationale was supported by several previous studies, which reported good correlation between FI calculated with 8 and 31 items [24]. Therefore, after measuring 29 diverse physiological parameters including physical (body weight and grip strength), blood cell composition, metabolic, and immune, we selected those that show statistically significant change with age. These parameters were used to create PFI of individual mice of different chronological age. The observed gradual increase in mean PFI values with age suggests that our approach can reliably detect the scale of age-dependent health deterioration in a quantitative manner.

Interestingly, the dynamics of deficit accumulation appeared to be very gender-specific. Thus, in male NIH Swiss mice increase in PFI can be approximated by linear function suggesting that health deficits are evenly accumulated with age. In females the dynamics of increase in PFI is more complicated with sharp increase observed between 26 and 52 weeks of age followed by a period of almost no change (between 52 and 78 weeks) and a second increase after 78 weeks. This is an important observation that has to be considered in both pre-clinical and clinical studies. First, it points to fundamental sex-related differences in the process of aging and consequently, has to be taken into account when developing strategies for treatment of aging and age-related diseases. Second, our data provide an additional explanation for numerous examples of sexual dimorphism in response to life-extending genetic or pharmacological interventions. Although clear mechanistic details of this phenomenon are still not understood, most of the previous reports linked it to interactions of the interventions with sex hormones, sex differences in immune function or in distribution of adipose tissue and accordingly differences in the effects of its secretory activity (reviewed in [25]). Our results suggest that in addition to basic gender differences, females' response to treatments may vary depending on the age at which it is applied. Thus, based on observed sex-related differences in the pattern of deficits accumulation, the lack of effects of both detrimental and beneficial interventions on the health status of

female mice may be explained by the fact that treatments started at 52 weeks of age (beginning of “no-change” period in females) and the FI was measured at the end of this phase (78 weeks).

Our results in the experiment with chronic rapamycin treatment showing an increase in lifespan of female NIH Swiss mice without improvement in their health, underscores the importance of using health status as the major metrics in development of anti-aging therapeutics. These data are consistent with previous observations made in different model systems demonstrating that increase in longevity is not necessarily accompanied by improved health status. Such as, caloric restriction extends lifespan in *Drosophila* without improving their cognitive function [26]. Long-lived calorie-restricted mice and IGF-1 knockout mice develop multiple health deficits [27, 28]. Recent work in *C. elegans*, which measured simultaneously worms’ longevity and health status, demonstrated that four different long-lived mutants that were used in the study increased the proportion of time spent in a frail state [29]. Altogether, we suggest that our approach allows for unbiased and reliable assessment of healthspan by quantitation of age-related accumulation of deficits during chronological aging than may serve as a valuable tool in a variety of pre-clinical aging studies. Importantly, experimental validation of this approach demonstrated its ability to quantitatively evaluate detrimental effect of HFD on animal’s health as well as the ability of rapamycin to mitigate it, thereby providing an alternative age-accelerated model for testing the effects of various environmental, nutritional and pharmacological interventions on healthspan.

## MATERIALS AND METHODS

### Animals

Male and female Cr:NIH(S) Mice (NIH Swiss) mice were purchased from Charles River at the age of 6-8 weeks and were allowed to age at the RPCI Animal Facility. During this time mice were housed 1-3 per cage and were fed ad lib with standard chow (Tekland Global 18% Protein Rodent Diet). To quantitatively evaluate age-dependent decline in animals’ health, FI was created for individual male and female mouse at 26, 52, 78 and 104 weeks of age as described below using cross-sectional experimental design (10-14 mice per group). In a separate experiment, male and female mice (9-14 per group) were randomly assigned to four groups. Group 1 remained on regular chow and drinking water; group 2 remained on regular chow but started receiving rapamycin in drinking water. Group 3 started receiving high fat diet (Harlan Laboratories, TD.03584,

35% Lard Diet) in combination with normal drinking water and group 4 received HFD in combination with rapamycin. Rapamycin was delivered in the form of Rapatar (polymeric formulation developed by Everon Biosciences as previously described [14] at a concentration of 125 mg/L (corresponds to 2.5 mg/L rapamycin). Based on the assumption that mice drink 3-5ml water per day, we estimated that in average each animal received 7.5-12.5 µg rapamycin daily. To preserve rapamycin stability in was delivered in non-acidified water in light-protected water bottles, which were replaced twice/week. When mice were 78 weeks of age FI was created for each individual animal as described below. Mice remained on their designated feeding/water schedules for the rest of the experiments and their longevity was recorded. Data for males and females were analyzed separately. All animal studies were conducted in accordance with the regulations of the Committee on Animal Care and Use at Roswell Park Cancer Institute.

### Grip strength measurement

Fore limb grip strength measurements were performed using Animal Grip Strength System (San Diego Instruments). Five measurements were recorded for each individual animal and the average value was assigned.

### Non-invasive measurement of hemodynamic parameters

Non-invasive measurement of hemodynamic parameters was performed using CODA apparatus (Kent Scientific) according to manufacturer’s protocol. Mice were placed into cylinder-shaped restraint devices and allowed to acclimate for 5 min on a heating platform before blood pressure measurements begin. Body temperature was continuously monitored by observation of animal behavior, tail blood volume and an infrared thermometer. Recorded hemodynamic parameters include systolic, diastolic and mean blood pressure, heart rate, tail blood flow and tail blood volume.

### Blood samples collection

To evaluate age-dependent changes in blood composition, blood samples were collected using the least invasive method that does not require anesthesia or restraining. Twenty µl of blood was collected from a single submandibular vein bleed into EDTA-treated Vacutainer tubes (BD) and used for whole blood cell counts and glucose measurements. Another 75ul of blood was collected into Li-Heparin treated plasma separator tubes; plasma was purified by centrifugation at 5000 x g for 5 min and used for measuring con-



centration of circulating pro-inflammatory cytokines and triglycerides.

### **Whole blood cell counts, blood chemistry and inflammatory cytokines**

Whole blood cell analysis was performed in 20  $\mu$ l of blood using Hemavet 950 Analyzer (Drew Scientific). The following parameters were measured: white blood cell counts (WBC), neutrophil (NE), lymphocyte (LY), monocyte (MO) and eosinophil (EO) counts and percentage, red blood cell (RBC) counts, hemoglobin (Hb), hematocrit (HCT), mean corpuscular volume (MCV), mean corpuscular hemoglobin (MCH), mean corpuscular hemoglobin concentration (MCHC), red cell distribution width (RDW), platelet (PLT) counts and mean platelet volume (MPV). Plasma concentration of chemokine (C-X-C motif) ligand 1 (CXCL1/KC) was measured using ELISA kit (R&D) according to manufacturer's protocol. Plasma concentration of triglycerides was measured using triglyceride quantification Kit (Abcam) according to manufacturer's protocol. In both assays reactions were run in duplicates and concentrations were calculated from a calibration curve generated for each experiment. Glucose concentration was measured using AlphaTRAK 2 Blood Glucose Monitoring Kit (Abbott Laboratories).

### **Creating physiological Frailty Index**

Frailty Index was created for each individual mouse as previously described [20] using 26 week-old group as a "young mouse" reference. For each parameter mean value and standard deviation were calculated. Animals differing in more than one standard deviation (STDEV) from mean value in any single parameter were excluded from the reference group. Value for each parameter measured for mice of older ages (52, 78 and 104 weeks) was compared with corresponding value for the reference group and assigned a score. Values that differ less than 1 STDEV were assigned the score of 0 (no deficit, within the range of the reference group). Values that were different for one STDEV were scored as 0.25 (minimal deficit). Values that differ from the corresponding values in the reference group by 2 STDEV were scored as 0.5 and those that differ by 3 STDEV were scored as 0.75. If the value is above 3 STDEV it was scored as 1 (extreme deficit). The number of deficits the individual mouse is expressed was calculated as a ratio of total number of parameters measured and was referred to as Physiological Frailty Index (PFI).

### **Histological evaluation**

After completion of the experiment mouse livers were fixed in 10% neutral formalin for 24 h. For

morphological observations samples were transferred to 70% ethanol and processed in an automated processor (Leica ASP 300) and embedded in paraffin using LEICA EG 1150H embedding unit according to manufacturer's protocols. Five micron sections were obtained using rotary microtome (LEICA RM 2235) and stained with hematoxylin and eosin (H&E). Neutral lipids were revealed by Oil Red O staining according to standard protocol on 12 micron cryo-sections prepared from formalin-fixed material using CM1900 cryostat. Histopathological examination was performed using Zeiss AxioImager A1 with AxioCam MRc digital camera.

### **Statistics**

Survival curves were generated using Kaplan-Meier estimators and compared using the log-rank test. Continuous data are expressed as mean  $\pm$  SEM. Statistical analyses were performed using one or two-way ANOVA with Tukey post hoc tests for multiple comparisons, ANOVA on ranks with Dunn's tests or Student's t-test where appropriate. P-values  $<0.05$  were considered significant. To generate a trend line that would best describe age-dependent increase in FI, a cubic regression was fit regressing the PFI on chronological age (CA), CA<sup>2</sup> and CA<sup>3</sup>. A stepwise selection procedure was then used to eliminate unnecessary terms for any or all of the higher order polynomial terms. The models were fit individually by sex.

### **AUTHOR CONTRIBUTIONS**

Marina P. Antoch conceived the study, designed and carried out experiments, analyzed and interpreted data, generated the figures and table and wrote the manuscript; Michelle Wrobel, Karen Kuropatwinski, Ilya Gitlin and Katerina Leonova carried out experiments, analyzed and interpreted data; Iliia Toshkov and Anatoli Gleiberman performed histological evaluation of tissue sections; Alan Hutson performed statistical data analysis; Olga Chernova and Andrei Gudkov analyzed and interpreted data, and reviewed the manuscript.

### **ACKNOWLEDGEMENTS**

We would like to thank Eugene Kononov for his excellent assistance with animal experiments. We also thank the staff of the Laboratory Animal Shared Resources at Roswell Park Cancer Institute for their veterinary and technical assistance. We are very grateful to the research team of Everon Biosciences and all members of A.V.G. laboratory for constructive discussions

## CONFLICTS OF INTEREST

O.B.C. and A.V.G. are co-founders and shareholders of Everon Biosciences.

## FUNDING

This work was supported by National Cancer Institute (NCI) grant P30CA016056 involving the use of Roswell Park Cancer Institute's Laboratory Animals Shared Resource, by Roswell Park Alliance Foundation and Everon Biosciences, Inc. (M.P.A. and A.V.G.)

## REFERENCES

1. López-Otín C, Blasco MA, Partridge L, Serrano M, Kroemer G. The hallmarks of aging. *Cell*. 2013; 153:1194–217. doi: 10.1016/j.cell.2013.05.039
2. Rodier F, Campisi J. Four faces of cellular senescence. *J Cell Biol*. 2011; 192:547–56. doi: 10.1083/jcb.201009094
3. Mitnitski A, Rockwood K. Aging as a process of deficit accumulation: its utility and origin. *Interdiscip Top Gerontol*. 2015; 40:85–98. doi: 10.1159/000364933
4. Howlett SE. Assessment of Frailty in Animal Models. *Interdiscip Top Gerontol Geriatr*. 2015; 41:15–25.
5. Rockwood K, McMillan M, Mitnitski A, Howlett SE. A Frailty Index Based on Common Laboratory Tests in Comparison With a Clinical Frailty Index for Older Adults in Long-Term Care Facilities. *J Am Med Dir Assoc*. 2015; 16:842–47. doi: 10.1016/j.jamda.2015.03.027
6. Jonker MJ, Melis JP, Kuiper RV, van der Hoeven TV, Wackers PF, Robinson J, van der Horst GT, Dollé ME, Vijg J, Breit TM, Hoeijmakers JH, van Steeg H. Life spanning murine gene expression profiles in relation to chronological and pathological aging in multiple organs. *Aging Cell*. 2013; 12:901–09. doi: 10.1111/acer.12118
7. Melis JP, Jonker MJ, Vijg J, Hoeijmakers JH, Breit TM, van Steeg H. Aging on a different scale--chronological versus pathology-related aging. *Aging (Albany NY)*. 2013; 5:782–88. doi: 10.18632/aging.100606
8. Mitnitski A, Collerton J, Martin-Ruiz C, Jagger C, von Zglinicki T, Rockwood K, Kirkwood TB. Age-related frailty and its association with biological markers of ageing. *BMC Med*. 2015; 13:161. doi: 10.1186/s12916-015-0400-x
9. Ogden CL, Carroll MD, Fryar CD, Flegal KM. Prevalence of Obesity Among Adults and Youth: united States, 2011-2014. *NCHS Data Brief*. 2015; 219:1–8.
10. Pettersson US, Waldén TB, Carlsson PO, Jansson L, Phillipson M. Female mice are protected against high-fat diet induced metabolic syndrome and increase the regulatory T cell population in adipose tissue. *PLoS One*. 2012; 7:e46057. doi: 10.1371/journal.pone.0046057
11. Anisimov VN, Zabezhinski MA, Popovich IG, Piskunova TS, Semchenko AV, Tyndyk ML, Yurova MN, Antoch MP, Blagosklonny MV. Rapamycin extends maximal lifespan in cancer-prone mice. *Am J Pathol*. 2010; 176:2092–97. doi: 10.2353/ajpath.2010.091050
12. Spong A, Bartke A. Rapamycin slows aging in mice. *Cell Cycle*. 2012; 11:845. doi: 10.4161/cc.11.5.19607
13. Khapre RV, Kondratova AA, Patel S, Dubrovsky Y, Wrobel M, Antoch MP, Kondratov RV. BMAL1-dependent regulation of the mTOR signaling pathway delays aging. *Aging (Albany NY)*. 2014; 6:48–57. doi: 10.18632/aging.100633
14. Comas M, Toshkov I, Kuropatwinski KK, Chernova OB, Polinsky A, Blagosklonny MV, Gudkov AV, Antoch MP. New nanoformulation of rapamycin Rapatar extends lifespan in homozygous p53-/- mice by delaying carcinogenesis. *Aging (Albany NY)*. 2012; 4:715–22. doi: 10.18632/aging.100496
15. Komarova EA, Antoch MP, Novototskaya LR, Chernova OB, Paszkiewicz G, Leontieva OV, Blagosklonny MV, Gudkov AV. Rapamycin extends lifespan and delays tumorigenesis in heterozygous p53+/- mice. *Aging (Albany NY)*. 2012; 4:709–14. doi: 10.18632/aging.100498
16. Khamzina L, Veilleux A, Bergeron S, Marette A. Increased activation of the mammalian target of rapamycin pathway in liver and skeletal muscle of obese rats: possible involvement in obesity-linked insulin resistance. *Endocrinology*. 2005; 146:1473–81. doi: 10.1210/en.2004-0921
17. Kane AE, Hilmer SN, Mach J, Mitchell SJ, de Cabo R, Howlett SE. Animal models of frailty: current applications in clinical research. *Clin Interv Aging*. 2016; 11:1519–29. doi: 10.2147/CIA.S105714
18. Fried LP, Tangen CM, Walston J, Newman AB, Hirsch C, Gottdiener J, Seeman T, Tracy R, Kop WJ, Burke G, McBurnie MA, and Cardiovascular Health Study Collaborative Research Group. Frailty in older adults: evidence for a phenotype. *J Gerontol A Biol Sci Med Sci*. 2001; 56:M146–56. doi: 10.1093/gerona/56.3.M146
19. Liu H, Graber TG, Ferguson-Stegall L, Thompson LV. Clinically relevant frailty index for mice. *J Gerontol A Biol Sci Med Sci*. 2014; 69:1485–91. doi: 10.1093/gerona/glt188

20. Parks RJ, Fares E, Macdonald JK, Ernst MC, Sinal CJ, Rockwood K, Howlett SE. A procedure for creating a frailty index based on deficit accumulation in aging mice. *J Gerontol A Biol Sci Med Sci*. 2012; 67:217–27. doi: 10.1093/gerona/qlr193
21. Feridooni HA, Sun MH, Rockwood K, Howlett SE. Reliability of a Frailty Index Based on the Clinical Assessment of Health Deficits in Male C57BL/6J Mice. *J Gerontol A Biol Sci Med Sci*. 2015; 70:686–93. doi: 10.1093/gerona/glu161
22. Howlett SE, Rockwood K. Factors that influence reliability of the mouse clinical frailty index. *J Gerontol A Biol Sci Med Sci*. 2015; 70:696. doi: 10.1093/gerona/glv045
23. Kane AE, Hilmer SN, Huizer-Pajkos A, Mach J, Nines D, Boyer D, Gavin K, Mitchell SJ, de Cabo R. Factors that Impact on Interrater Reliability of the Mouse Clinical Frailty Index. *J Gerontol A Biol Sci Med Sci*. 2015; 70:694–95. doi: 10.1093/gerona/glv032
24. Whitehead JC, Hildebrand BA, Sun M, Rockwood MR, Rose RA, Rockwood K, Howlett SE. A clinical frailty index in aging mice: comparisons with frailty index data in humans. *J Gerontol A Biol Sci Med Sci*. 2014; 69:621–32. doi: 10.1093/gerona/glt136
25. Austad SN, Bartke A. Sex Differences in Longevity and in Responses to Anti-Aging Interventions: A Mini-Review. *Gerontology*. 2015; 62:40–46. doi: 10.1159/000381472
26. Burger JM, Buechel SD, Kawecki TJ. Dietary restriction affects lifespan but not cognitive aging in *Drosophila melanogaster*. *Aging Cell*. 2010; 9:327–35. doi: 10.1111/j.1474-9726.2010.00560.x
27. Longo VD, Finch CE. Evolutionary medicine: from dwarf model systems to healthy centenarians? *Science*. 2003; 299:1342–46. doi: 10.1126/science.1077991
28. Partridge L, Gems D, Withers DJ. Sex and death: what is the connection? *Cell*. 2005; 120:461–72. doi: 10.1016/j.cell.2005.01.026
29. Bansal A, Zhu LJ, Yen K, Tissenbaum HA. Uncoupling lifespan and healthspan in *Caenorhabditis elegans* longevity mutants. *Proc Natl Acad Sci USA*. 2015; 112:E277–86. doi: 10.1073/pnas.1412192112

# Delivery of sFIT-1 engineered MSCs in combination with a continuous low-dose doxorubicin treatment prevents growth of liver cancer

Jian Niu<sup>1</sup>, Yue Wang<sup>1</sup>, Ji Wang<sup>1</sup>, Bin Liu<sup>1</sup>, Xin Hu<sup>2</sup>

<sup>1</sup>General Surgery of the Hospital Affiliated Hospital of Xuzhou Medical University, Digestive Disease Research Laboratory of Xuzhou Medical University, Xuzhou, Jiangsu 221002, PR China

<sup>2</sup>The University of Texas Graduate School of Biomedical Sciences at Houston, MD Anderson Cancer Center, Houston, TX 77030, USA

**Correspondence to:** Jian Niu; **email:** [njni\\_001@163.com](mailto:njni_001@163.com)

**Keywords:** liver cancer, gene therapy, mesenchymal stem cells, vascular endothelial growth factor, soluble Fms-like tyrosine kinase-1 (sFlt1)

**Received:** November 7, 2016

**Accepted:** December 12, 2016

**Published:** December 28, 2016

## ABSTRACT

One important process in liver cancer growth and progression is angiogenesis. Vascular endothelial growth factor (VEGF) has the significant role in liver cancer angiogenesis. sFlt1 (soluble Fms-like tyrosine kinase-1) is the promising inhibitor of VEGF and can be used as the new method of inhibiting angiogenesis. MSCs (Mesenchymal stem cells) can infiltrate into tumor tissue and function as the efficient transgene delivery mediator. Here, we engineered murine MSCs to express sFlt1 and examined the anti-tumor effect of MSC- sFlt1 in combination with continues low-dose doxorubicin treatment. We found that this combination therapy significantly inhibited liver cancer cells proliferation. Above all, HepG2 xenografts treated with this combination therapy went into remission. It is of note that this inhibition effect was not p53 binding and by increasing caspase8. This study suggests that this combination treatment has novel therapeutic potential for liver cancer because of significantly inhibiting cancer cells growth and anti-angiogenesis in vitro and in vivo.

## INTRODUCTION

Despite aggressive treatment with operation and combination with chemotherapy, the prognosis of liver cancer remains poor. Most liver cancers are of rich blood supply and there is the close correlation between angiogenesis and tumor progression [1–2]. Recently, anti-angiogenesis has been proved to be the hopeful strategy for liver cancer treatment [3–4].

VEGF is the significant angiogenic factor and plays its roles by interacting with its receptors including Flt-1 (Fms-like tyrosine kinase-1) and Flk-1 /KDR (fetal liver kinase-1/kinase insert domain containing receptor). sFlt1 is a spliced form of the Flt1 receptor and it comes from the Flt1 transmembrane domain. sFlt1 binds to VEGF as a part of the full-length receptor and this binding blocks signal transduction. Importantly, Flt1 protein is expressed in liver cancer cells [5–8].

Reports have shown that transferring of sFlt1 into tumor

can inhibit tumor angiogenesis and growth [9–10]. MSCs can be engineered to express genes and are known to infiltrate into tumor tissues [11–14]. Therefore, MSCs may provide an avenue for sFlt1 delivery in liver cancer.

Doxorubicin leads to DNA damage and cell apoptosis in a lot of cancer cells .Doxorubicin has also the distinct antitumor effect for liver cancer cells. In this study, we used the treatment of continuous low-dose doxorubicin combination with MSC.sFlt1 to demonstrate the additive inhibition of liver cancer cells growth and anti-angiogenesis in vitro and in vivo.

## RESULTS

### sFlt1 is expressed by MSCs and released into the culture media

To measure transient expression of sFlt1 in MSCs, 24 hours after adv-sFIT1 transduction into MSCs, sFlt1 protein (100.0±18.7mg/ml) was found from cell

culture supernatant and the expression of sFlt1 was detected for more than 7 days (Figure 1).

### Endothelial cells are sensitive to low dose doxorubicin treatment

Since most endothelial cell assays utilize HUVEC (human umbilical vein endothelial cells) [15], we tested the sensitivity of HUVEC cells to doxorubicin which is widely used in liver cancer chemotherapy. Our data suggested that HUVEC cells proliferation were significantly more inhibited at low-dose doxorubicin ( $0.02\mu\text{M}$ ) than HepG2 cells (Figure 2).

### Combination treatment had more inhibitory effect on HUVEC cells functions

To prove that sFlt1 engineered MSCs can inhibit the growth of HUVEC cells, we investigated the effect of sFlt1 and/or low-dose doxorubicin on HUVEC cells functions in vitro. The results showed single-agent sFlt1 (concentrated conditioned medium) or low concentration doxorubicin inhibited the migration and proliferation of HUVEC cells. Interestingly, the combination therapy exerted a significant enhanced inhibitory effect on HUVEC cells proliferation and migration (Figure 3).

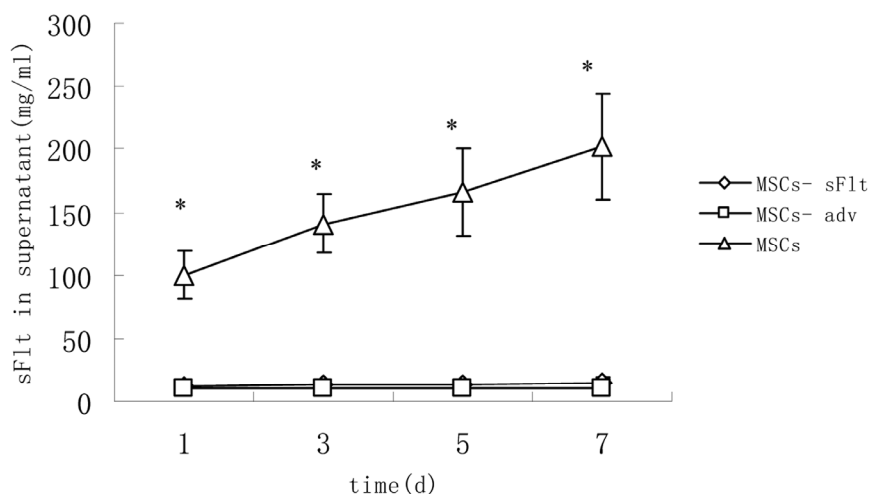


**Figure 1. The content of sFlt1 in supernatant increased significantly in MSCs-sFlt1 group as compared with day-matched MSCs-adv group or MSCs group.** Data from 3 independent experiments are shown. \* $P < 0.05$  versus MSC-sFlt1 group.

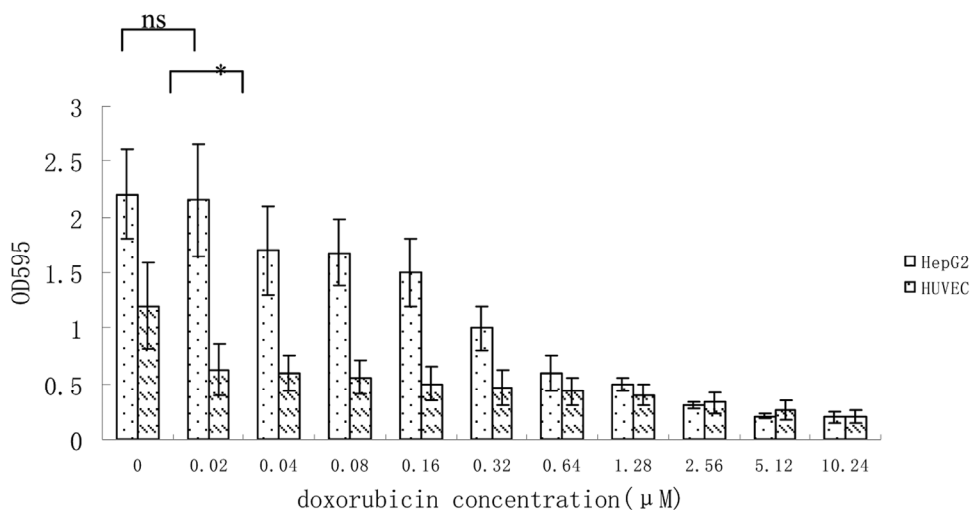


**Figure 2. Growth inhibition of HUVEC and HepG2 cells at different concentration of doxorubicin.** Data from 3 independent experiments are shown. \* $p < 0.05$ , n.s. not significant, vs  $0.02\mu\text{M}$ .

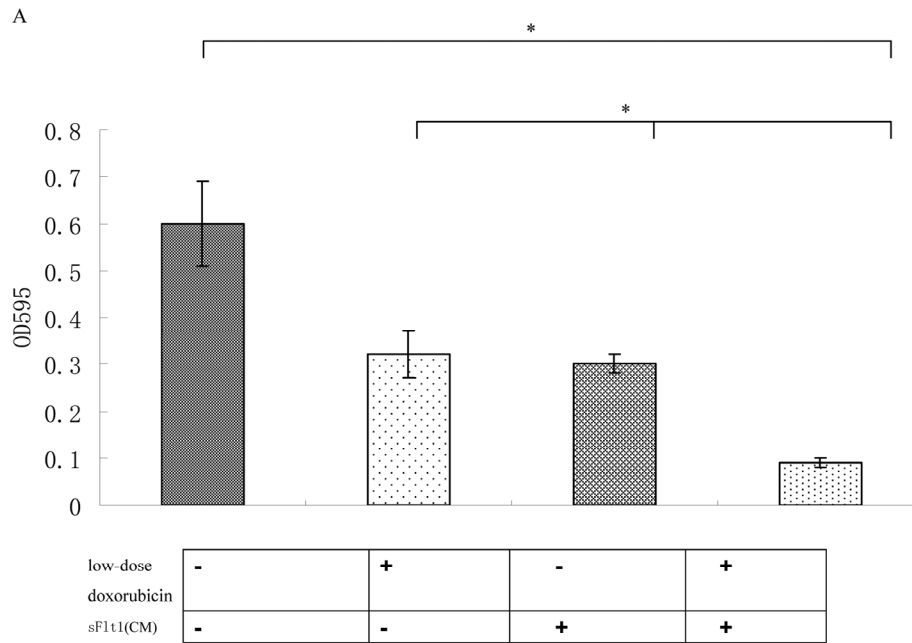


**Figure 3. (A)** The combination therapy enhanced the proliferation inhibition of HUVECs cells in vitro.

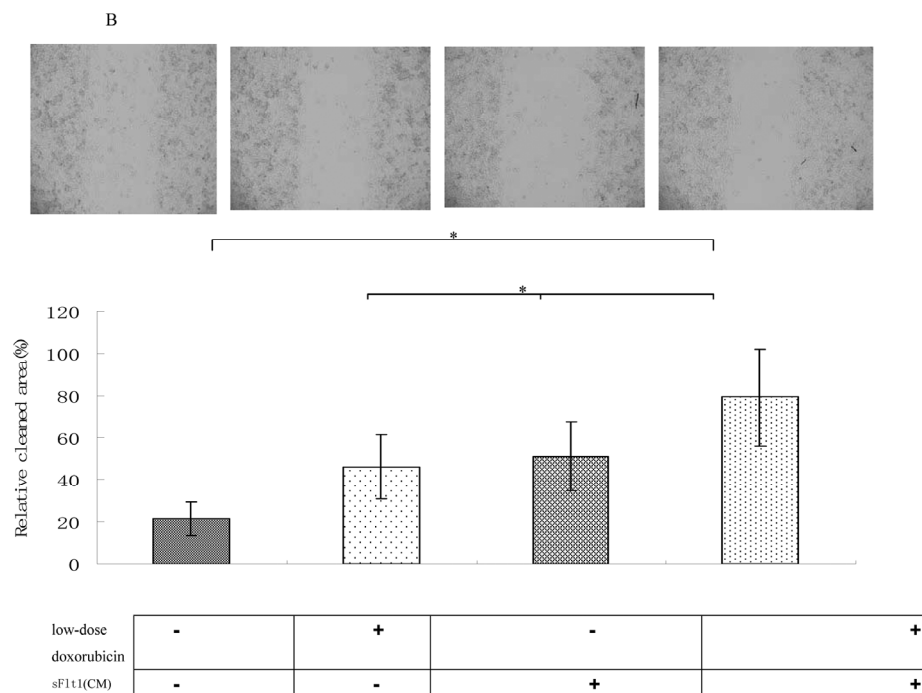


**Figure 3. (B)** Wound healing assays were performed. The amount of migrating cells of sFlt1 (1.5 ml of concentrated conditioned medium) plus low-dose doxorubicin group were much lower than control. Magnification, 200×. Picture of one representative experiment of 3 is shown. Data from 3 independent experiments are shown. \*p < 0.05 , vs sFlt1 plus low-dose doxorubicin group.



**Combination therapy of doxorubicin and sFlt1 leads to additive apoptosis induction**

Because low-dose doxorubicin (0.02μM) alone was not efficient to inhibit HepG2 cells, we began to test sFlt1 -based treatment utilizing combination with low-dose doxorubicin. We treated HepG2 cells with sFlt1 (1.0 ml of concentrated conditioned medium) plus 0.02 μM

doxorubicin for 48h before we measured cell apoptosis. This combination therapy resulted in 37±0.6% apoptosis as compared with 2.6±0.4% (sFlt1 group) and 10.5± 0.4% (low-dose doxorubicin group). Apoptosis could be inhibited by zVAD (carbobenzoxy-valyl-alanyl-aspartyl- [O-methyl] -fluoromethylketone), showing that apoptosis was correlate with caspase (Figure 4A).

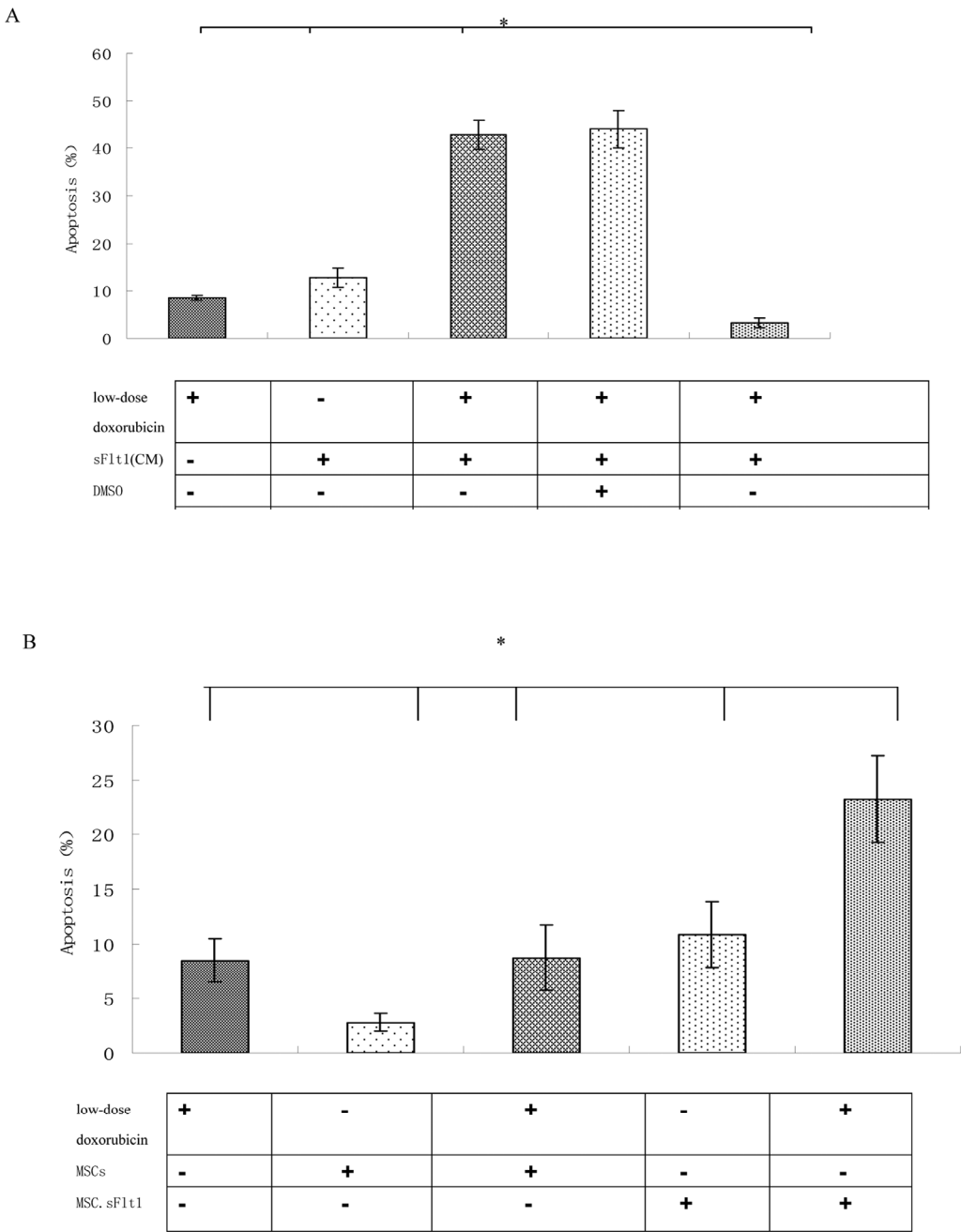


**Figure 4. HepG2 cells can be sensitized to low-dose doxorubicin inducing by MSC. sFlt1. (A)** Apoptosis measurement was conducted after the combination treatment. Addition of zVAD to the HepG2 cells before combination treatment can inhibite apoptosis. **(B)** Mixing HepG2 cells with MSC.sFlt1 (in a ratio of 10:1) plus 0.02μM doxorubicin treated for 48 h showed significantly increased apoptosis as compared with other group. Data from 3 independent experiments are shown. \*p < 0.05 , vs sFlt1 plus low-dose doxorubicin group.



One important step for clinical use of sFlt1 is effective delivery and sufficient bioavailability in carcinoma. The carcinoma-infiltrating properties of MSCs could be used to deliver sFlt1. We had to determine whether MSCs could effectively deliver sFlt1. To test this in vitro, we mixed MSC.sFlt1 with HepG2 cells for 48 h. This gave rise to apoptosis levels significantly (Figure 4B).

### Combined therapy of MSC.sFlt1 plus continuous low-dose doxorubicin is efficacious and safe *in vivo*

We established HepG2 xenografts in immune-deficient Balb/c mice. Although the tumors in saline group , grew almost exponentially, xenografts either treated with continuous low-dose doxorubicin or MSC.sFlt1 showed

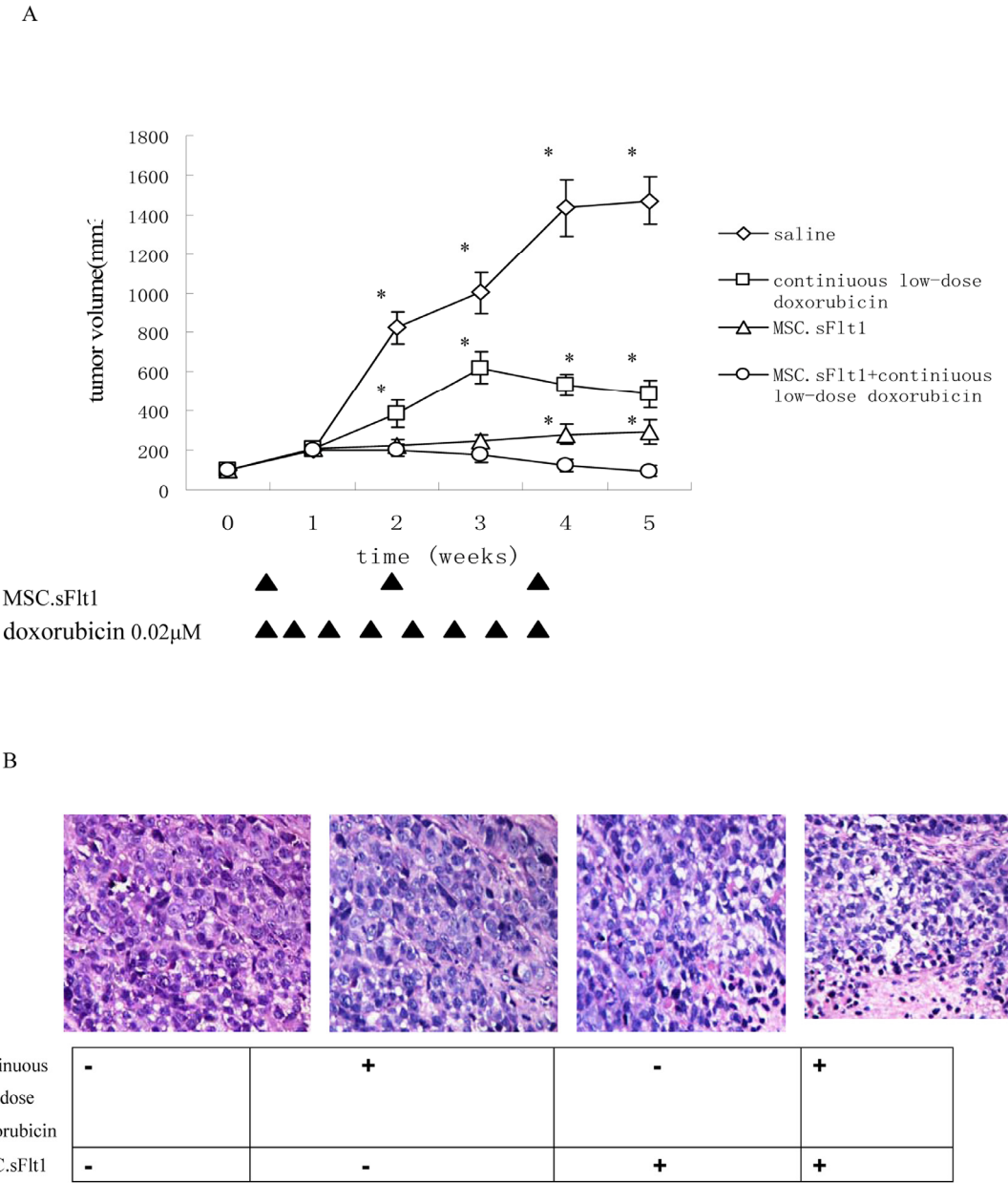


**Figure 5. Treatment with continuous low-dose doxorubicin plus MSC.sFlt1 led to tumor remission and was safe *in vivo*.** (A) Animals bearing HepG2 xenografts began treatments when tumor diameters reached 5 mm as described in "Materials and Methods." Arrows: days on which treatment was administered. Results are given as mean tumor volume of 7 mice /group. \*p < 0.05 , vs MSC.sFlt1 plus continuous low-dose doxorubicin group. (B) HE staining was to examine general tumor tissue morphology from saline group, continuous low-dose doxorubicin group, MSC.sFlt1 group and MSC.sFlt1 plus continuous low-dose doxorubicin group. Magnification, 200×.

obvious growth inhibition. Surprisingly, xenografts treated with combination therapy went into remission (Figure 5A). Nonencapsulated tumor with cancer cells infiltration was found in sample sections of saline group by HE analysis. In contrast, MSC.sFlt1 plus continuous low-dose doxorubicin group clearly showed cellular necrosis and fibrosis instead of cancer cells (Figure 5B). Moreover, PCNA (nuclear proliferating cell nuclear antigen) protein was detected by immunohistochemistry. PCNA levels decreased significantly from the combination therapy group compared with other group (Figure 5C). To determine whether combination therapy inhibit tumor angiogenesis, tissue specimens were immunostained with CD31 mAb to count microvessels density (MVD). The data showed MVD was significantly lower in combination therapy group than other group (Figure 5D).

Then, we detected the safety of combination therapy on MSCs. We incubated MSCs with 0.02μM doxorubicin plus sFlt1 (concentrated conditioned medium) for 48h. MSCs were resistant to the single treatment as well as to the combination therapy by detecting apoptosis (Figure 5E).

Moreover, we detected the liver tissue of mice that had treated with combination therapy and could not detect any signs of tissue damage showing that this treatment is safe relatively (Figure 5F).

**The molecular mechanism of the combination therapy is not p53 binding**

To further improve sFlt1-based combination treatments, the better knowing of the molecular mechanisms is

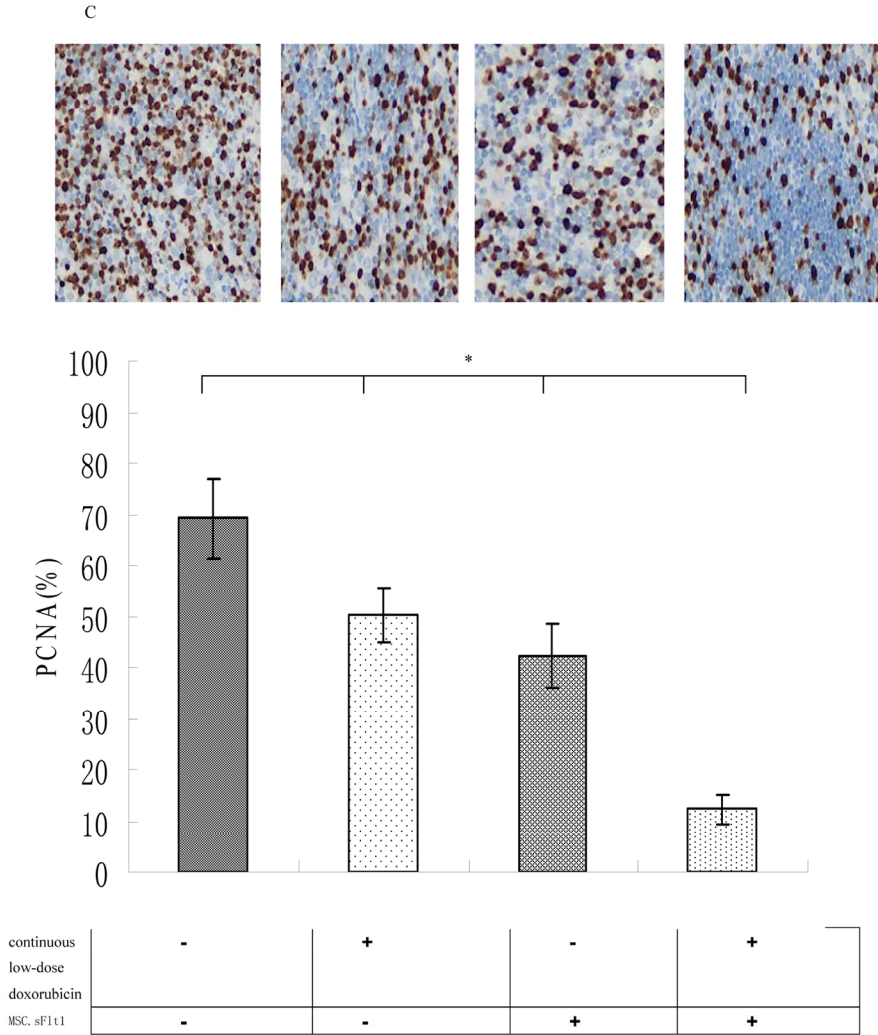


**Figure 5.** (C) Immunohistochemical detection of PCNA protein expression (brown color) of saline group, continuous low-dose doxorubicin group, MSC.sFlt1 group and MSC.sFlt1 plus continuous low-dose doxorubicin group. Combination therapy enhanced the inhibition of tumor cell proliferation in vivo. Magnification, 200×. Data from 3 independent experiments are shown. \*p < 0.05 , vs MSC.sFlt1 plus continuous low-dose doxorubicin group.

necessary. First, caspase8 was tested which is the important molecular event in the apoptosis pathway. Caspase8 activation is markedly increased in sFlt1 treated group compared to saline group. Additionally, caspase8 level increased further in sFlt1 plus low-dose doxorubicin group compared with other groups. In order to further testify that the sFlt1 sensitization effect is by caspase8, we cloned stable cell lines of caspase8 knockdown, named HepG2.shc8 (Figure 6A). HepG2.shc8 were treated with 0.02μM doxorubicin plus sFlt1 for 48 h, then the apoptosis was measured. Results showed that the apoptosis of HepG2.shc8 was decreased, showing that caspase8 is the initiator in this process (Figure 6B). Next, we want to prove the apoptosis induced by the combination treatment is p53 independent. We found that low-dose doxorubicin plus sFlt1-triggered apoptosis reached the same level in

HepG2 p53<sup>-/-</sup> cells as in HepG2 cells. To test that combination treatment-induced apoptosis is not cell specific, we also analyzed huh7 cells, which express p53 mutation, and found that huh7 cells could exhibit increased apoptosis in response to combination treatment (Figure 6C).

### DISCUSSION

As a lot of tumor growth are correlate on angiogenesis, antiangiogenic therapy shows the great promise for tumor treatment.

Recently, scientists found that blocking VEGF/VEGFR signaling pathway can inhibit tumor growth [16, 17]. As we all know, human liver cancer cells produce lots of proangiogenic factors including VEGF/ VEGFR that

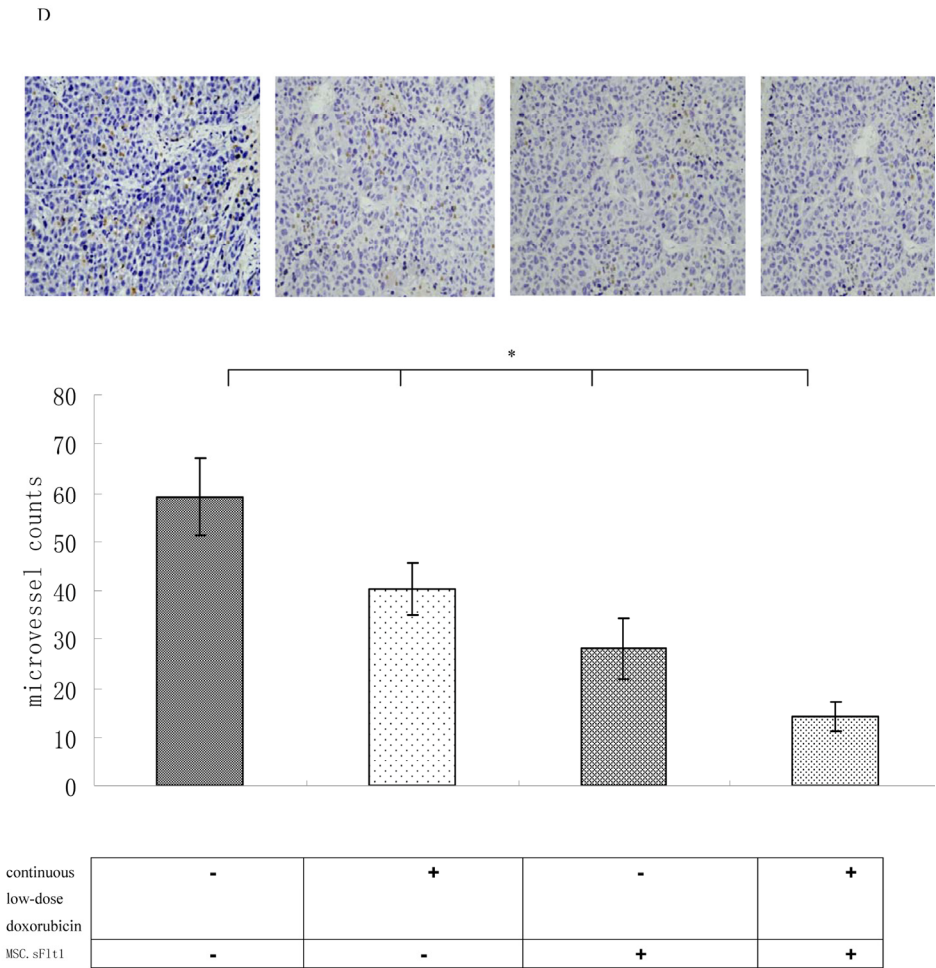


**Figure 5. (D)** Immunohistochemical analysis for MVD in HepG2 xenografts and combination therapy enhanced the inhibition of tumor angiogenesis in vivo. Magnification , 200×. \*p < 0.05 , vs MSC.sFlt1 plus continuous low-dose doxorubicin group.

may serve as therapeutic targets. For example, some synthesized drugs in the market by targeting VEGF receptors can suppress the proliferation of liver cancer cells [18-21].

But all of these drugs have many side effects and with only moderate therapeutic activities. The possible explanation is that these drugs have the short half time or limited accessibility to liver cancer tissue.

Tumor-targeted therapy is one of the major strategies for pharmacotherapy of cancer today. sFlt1 is the potent

antagonist of VEGF. sFlt1 could selectively incorporate with VEGF and inhibit VEGF activity [22, 23].

As MSCs can infiltrate into tumor tissue, they have been applied in cancer treatment [24-26]. In this study, we successfully constructed sFlt1 engineered MSCs as verified by ELISA assay (Figure 1) and explored the potential of MSC-sFlt1 to target tumor angiogenesis and growth.

Previous reports showed that withdrawal of neutralizing anti-VEGF antibody treatment resulted in tumor recur-

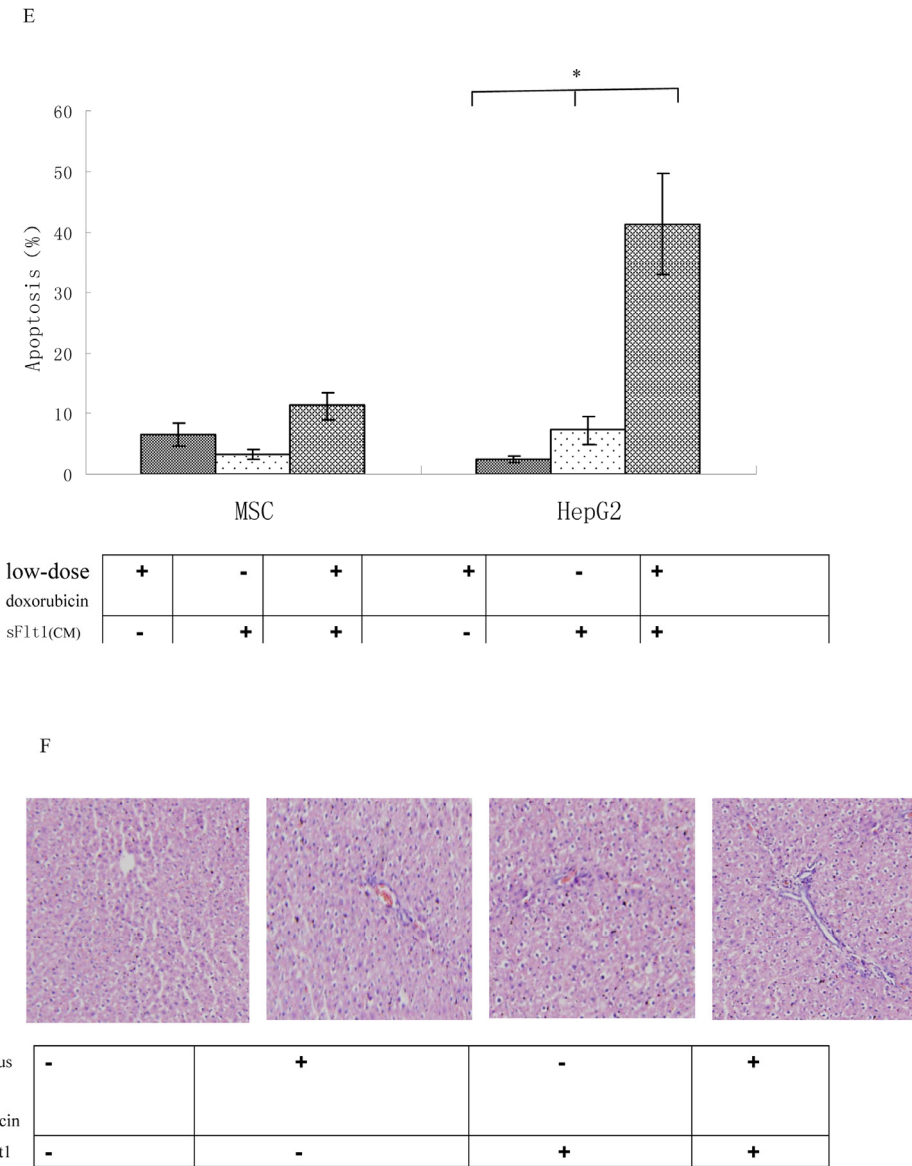


**Figure 5.** (E) Apoptosis was measured after exposure of MSCs or HepG2 cells to 0.02μM doxorubicin plus sFlt1 (1.0 ml of concentrated conditioned medium) for 48 h. \*p < 0.05 , vs sFlt1 plus low-dose doxorubicin group. (F) HE staining of liver sections from mice treated with saline, continuous low-dose doxorubicin, MSC.sFlt1 and MSC.sFlt1plus continuous low-dose doxorubicin, respectively. Magnification, 200×.

rence [16-17]. These experiments proved that antiangiogenic therapy is insufficient and combination with chemotherapy is needed. Antiangiogenic-schedule chemotherapy is recommended because this kind of chemotherapy enable clinicians to give lower doses of drugs and has less side effects [27-28]. This novel strategy is explored as anti-tumor treatment effectively [29-31].

Doxorubicin has the significant anti-tumor effect for human liver cancer, either as a single agent or in combination with other cytotoxic agents [32]. Our data prove that low-dose doxorubicin inhibited HUVEC cells growth significantly more than HepG2 cell growth (Figure 2). And low dose doxorubicin plus sFlt1 can

inhibit proliferation and migration of HUVEC cells more efficiently in vitro (Figure 3). Moreover, we observed the direct inhibition effect of this combination treatment on proliferation of HepG2 cells in vitro (Figure 4).

Next, we conducted animal experiments to test whether MSC.sFlt1 plus continuous low dose doxorubicin treatment can induce growth retardation or remission of xenografts with less side effects.

Our data showed that this combination treatment inhibited the growth of HepG2 xenografts in nude mice and had no toxicity as represented by liver histology examination (Figure 5). To prove whether the inhibitory

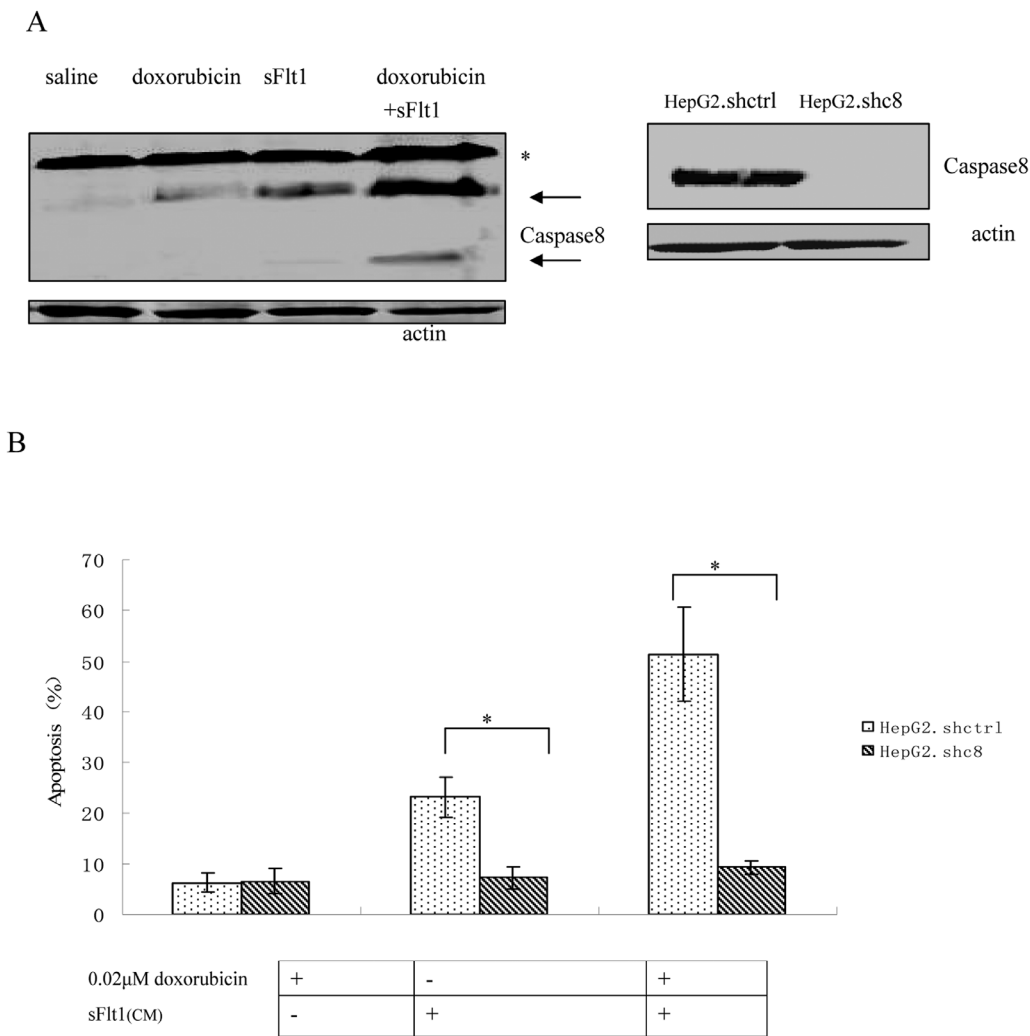


**Figure 6. (A)** Western blot of Caspase8 that HepG2 cells were either treated with saline, 0.02μM doxorubicin, sFlt1, or 0.02μM doxorubicin plus sFlt1 for 48 h. Pro-caspase bands are marked by an (\*), whereas Caspase8 are labeled by arrows. **(B)**Caspase8 knockdown clone (HepG2.shc8) and control clone (HepG2.shctrl1) were treated with doxorubicin plus sFlt1 before the apoptosis was measured. The apoptosis of HepG2.shc8 was decreased. \*p < 0.05, vs sFlt1 plus 0.02μM doxorubicin group.



effect was related with anti-angiogenesis, we tested MVD in tumor samples and found this combination treatment led to significant decreasing in MVD compared with other group (Figure 5).The mechanisms of anti-tumor growth of MSC.sFlt1 plus continuous low dose doxorubicin includes the elevated apoptosis of cancer cells and endothelial cells (Figure 4, 5).

HepG2 cells express wild p53 but many kinds of liver cancer cells express p53 mutated and/or dysfunctional. Hence, in order to evaluate the combination treatment, we analyzed huh7 p53 mutated cells and HepG2 p53<sup>-/-</sup> cells. We observed the increased apoptosis following the combination treatment in both cancer cell lines. These results proved that the therapy is effective in cancer cells expressing p53 mutated and/or dysfunc-

tional (Figure 6). Subsequently, we want to clarify the mechanism in this progress to improve the MSC. sFlt1 system. Silencing of caspase8 resulted in the apoptosis inhibition of huh7 p53 mutated cells or HepG2 P53<sup>-/-</sup> cells. This result showed that the inhibition of cancer cells was correlate with caspase8 (Figure 6).

In conclusion, MSC.sFlt1 plus low-dose doxorubicin therapy effectively suppressed the progression of liver cancer cells with less side effects in the mice xenograft model. The mechanism lies in its anti-angiogenesis and anti-cancer cells effect. This treatment might be more practical for clinical application and can be of the development of the targeted therapy for liver cancer.

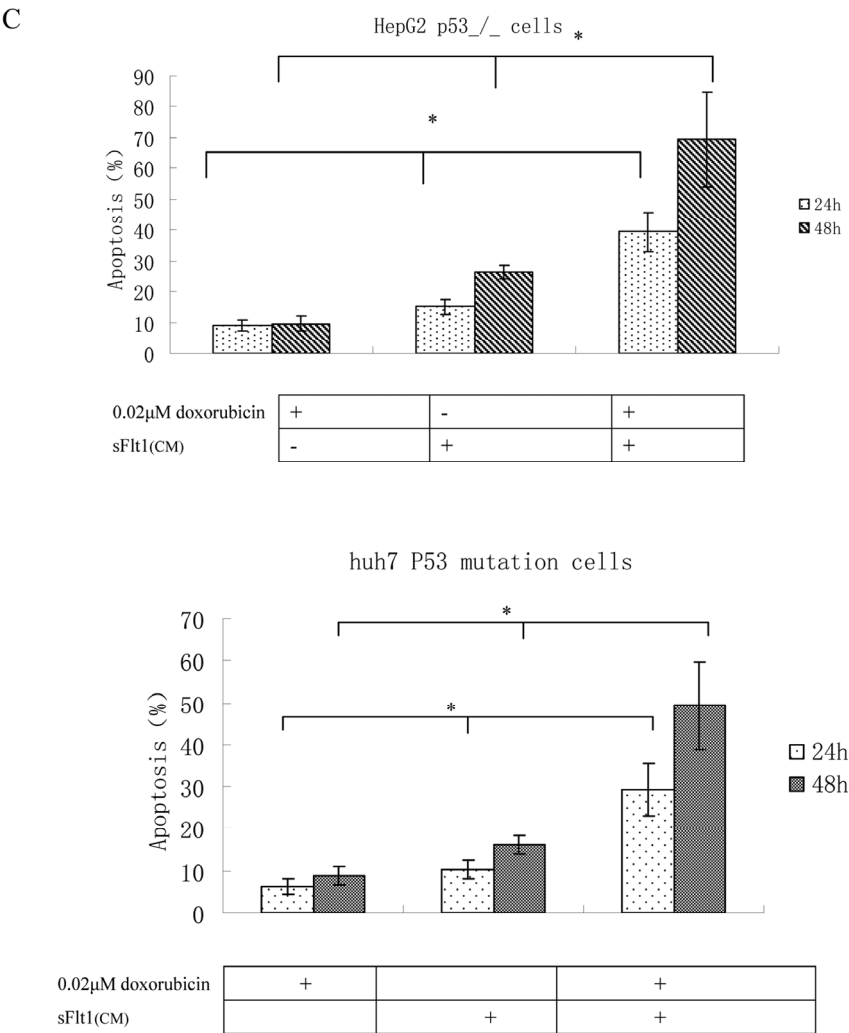


**Figure 6. (C)** Apoptosis measurements in HepG2 p53<sup>-/-</sup> cells or huh cells after treatment with 0.02µM doxorubicin plus sFlt1 (concentrated conditioned medium) for 24h and for 48h. HepG2 p53<sup>-/-</sup>cells and huh7 cells exhibited increased apoptosis in response to combination treatment \*p < 0.05 , vs sFlt1 plus low-dose doxorubicin group.

## METHODS

### Materials and reagents

Recombinant adenovirus (adv-sFlt) was provided by Dr. S Luo (Zhongshan University, Guangdong, China). Adv-sFlt contained the 1–3 Ig-like domains of Flt according to the sequence information from GenBank (accession No. X51602) [33]. Cell lines HepG2, huh7 and HUVEC were obtained from Chinese national human genome center (Shanghai, China). With regard to P53 status, HepG2 cells carry wild-type P53 and huh7 cells carry mutation P53 [34]. HepG2 cells were maintained in MEM and huh7 cells in DMEM containing 100U/ml of penicillin and 100 µg/ml of streptomycin in a humidified chamber at 37°C in 5% CO<sub>2</sub>. HUVEC cells were cultured in DMEM with 10% fetal bovine serum, 100 unit/ml heparin, and 75 µg/ml of endothelial cell growth supplement (ECGs; SIGMA, Saint Louis, MI) in 5% CO<sub>2</sub> at 37°C. MSCs from 4 to 6 week old female BALB/c nu/nu mice were prepared based on the method of Peister et al [37]. The cells were grown in Dulbecco's modified Eagle's medium (DMEM)–low glucose with 100 U/ml penicillin, 100µg/ml streptomycin and 10% fetal bovine serum. The mice bone marrow mesenchymal stem cells (BMMSCs) are generally referred to as MSCs throughout the text.

### Generation of secreted MSC-sFlt1 and ELISA

The adenovirus hosting sFlt was introduced into the MSCs at a multiplicity of infection (MOI) of 100 in DMEM for 24 hours with 8µg/mL polybrene. After 24hours, the collected supernatant was concentrated by a centrifugal filter (Millipore, Schwalbach, Germany) at 4000 rpm for 30 min at 4°C. The concentrated conditioned medium (CM) was then filtered through 0.2 µm filters and stored at –80°C for further use. MSCs were infected with adv-sFlt for 24 hours, then washed twice and the culture supernatant containing secreted sFlt was examined for 7 days. sFlt1 expression was verified via ELISA using a commercial kit (Invitrogen, USA) according to the instructions provided by the manufacturer. The sFlt1 concentration in the cell supernatant samples was calculated based on the standard curve.

### Cell proliferation assay

Cell proliferation were examined by MTT assay [35]. 20 ml of MTT solution (5 mg/ml in PBS) (Aqueous One Solution Assay, Promega, USA) was added to each well, and the cells were incubated for 4 h at 37°C. Then, absorbances were measured at 595 nm using a microtitre plate reader (Titertek Multiskan MCC, USA). The percentage of cell proliferation was calculated by

defining the absorption of cells not treated with doxorubicin (control) as 100%. A total of three independent experiments were performed, and the means were used to depict the survival curve.

### Apoptosis assay

Apoptosis was measured as previously described [36]. In brief,  $3 \times 10^4$  HepG2 cells were cultured in a 24-well plate for 24h. We treated HepG2 cells with sFlt1 (1.5 ml of concentrated conditioned medium, CM) plus 0.02µM doxorubicin for 48h, then we measured cell apoptosis. Cells were collected by trypsinization and washed twice with cold  $1 \times$  PBS. Then, Nicoletti buffer (Sodium citrate 0.1 % containing 0.1 % Triton X-100) and propidium iodide (50g/ml) was added to the cell pellets. Tubes were vortexed for 10s at medium speed and left for 5 h in the dark (4°C). The fluorescence intensity was then measured in a flow cytometer (BD, USA).

### Wound healing assay

$3 \times 10^4$  HUVEC cells were cultured in a 24-well plate for 24 h. After a tight cell monolayer was formed, the cells were incubated with serum-free medium for 24 h and the cell monolayer was wounded with a plastic pipette tip [37]. The remaining cells were washed twice with fresh medium to remove cell debris, and further incubated with 1.5ml CM for 12h, purified recombinant human VEGF165 (R&D Systems, Minneapolis, USA) at 10 ng/ml was added to HUVEC cells, which were assayed for migratory ability. After 24h, the migrant cells at the wound front were photographed with a microscope.

### Mixture of MSC-sFlt with liver cancer cells

Tumor cells were plated in six-well plates at  $1 \times 10^6$  cells per well and left overnight to adhere. Then, HepG2 cells were treated with  $1 \times 10^5$  MSC.sFlt1 and doxorubicin (0.02µM) for 48h (in a ratio of 10:1). Then cells were collected for apoptosis assays.

### Animal studies

The animal study was performed to verify the effects of MSC.sFlt1 plus continuous low-dose doxorubicin in inhibiting the growth of liver tumors in vivo. Balb/c nu/nu mice (4–6 weeks old, 18–20 g body weight) were purchased from the experimental animal center of Shanghai, Chinese Academy of Sciences (Shanghai, China) and kept at a specific pathogen-free facility.

The nude mice were implanted subcutaneously with  $1 \times 10^6$  HepG2 cells. When the tumor diameters reach 5mm, the animals were intraperitoneally injected with



doxorubicin (1 mg/kg, American Pharmaceutical Partners, USA ). Doxorubicin was administered every 3 days for a total of eight dosages (continuous low-dose schedule dosage).  $1 \times 10^5$  MSC.sFlt1 were delivered intravenously to the mice 24hrs after MSC transduction with adv-sFlt1. The injections with  $1 \times 10^5$  MSC.sFlt1 were repeated two weeks later. Combined treatment consisted of at the beginning of  $1 \times 10^5$  MSC.sFlt1 treatment, 1 mg/kg doxorubicin given once every 3 days for a total of eight times.

The animals were randomly assigned into four groups (n=12/group): (i) saline group (ii) continuous low-dose doxorubicin group (iii) MSC.sFlt1 group (iv) MSC.sFlt1 plus continuous low-dose doxorubicin group. Tumor diameters were measured with a caliper and tumor volumes were calculated by using the equation  $V(\text{mm}^3) = 0.5 \times a \times b^2$ , where a=length, b=width. All procedures with animals were reviewed and approved by the Instructional Animal Care and Use Committee at Xuzhou Medical University.

The mice were sacrificed 42 days after HepG2 cells injection. The tumors were excised. A section of the tumor was fixed in paraformaldehyde (4%) and paraffin-embedded, and HE was performed. Tissue specimens were also used for immunohistochemical analyses. The animal study was repeated independently once.

#### Immunohistochemistry for expression of PCNA and microvessel density (MVD)

Tumor tissue sections (5  $\mu\text{m}$ ) were prepared for immunohistochemistry following reports [38]. Mouse anti-PCNA monoclonal antibody (1:100) (Leica Biosystems, UK) or goat anti-mouse CD31 polyclonal antibody (1:100) (Santa Cruz, USA) were used as primary antibodies. PBS instead of primary antibody was used as a negative control. The intensity of PCNA immunostaining was quantified using a computerized imaging system with 5 randomly selected fields at 200 times magnification. Staining was considered negative when the percentage of cells positive for PCNA staining was less than 10%. For MVD quantitation, 5 fields containing CD31 staining were selected and the number of CD31 positive cells in a field was quantified.

#### Western blot

Western blots were principally carried out as described previously [35]. In brief, the protein lysate was mixed with loading buffer, boiled for 5 mins, and loaded into sodium dodecyl sulfate-polyacrylamide gels (SDS-PAGE) with equal amounts of protein. The gel was run at 200 V for 60mins, followed by transfer to nitro-

cellulose membrane (Amersham Biosciences, USA) at 100 V for 30 min at room temperature and incubation with primary antibodies. The primary antibodies include anti-caspase8 (1:100), anti-wtP53 (1:100) (Santa Cruz Biotechnology, CA). The secondary antibodies, anti-goat/rabbit/mouse immunoglobulin G (IgG)-HRP, were purchased from Zhongshan Company (Beijing, China). The protein expression levels were detected by chemiluminescence (ECL system, Amersham, UK) and quantified using Quantity One software (Bio-Rad). The expression level of the genes of interest were normalized using  $\beta$ -actin.

#### pSUPER-siRNA constructs and stable cell lines generation

The caspase8 siRNA and wtP53 siRNA hairpin oligos were designed by Ambion website (www.ambion.com) and synthesized by Shanghai SBS Genetech. Inc. (Shanghai, China). The sense strand oligo sequences were: caspase8: 5'-GGGTCATGCTCTATCAGAT-3' and wtP53: 5'-TCTGTGACTTGACGTA CTTT-3'. The synthesized siRNA specific to the caspase8 or wtP53 gene was inserted into pSUPER vector according to our previous procedures[39], which was co-transfected with pSUPER-caspase8-siRNA or pSUPER-P53-siRNA and pEGFP vectors using Lipofectamine 2000 (Invitrogen, USA) to generate the HepG2-caspase8-siRNA or HepG2-P53-siRNA cell line. Clones that did not show a knock-down were used as controls.

#### Statistical analysis

The results were expressed as means  $\pm$  standard error of means of at least 3 independent experiments, unless stated otherwise. Experimental values are expressed as mean value  $\pm$ SD. For significance analyses, analysis of variance (ANOVA) between groups was used (SAS 6.12, SAS Institute, USA). \*P<0.05 was considered significant.

#### Abbreviations

BCA, Bicinchoninic acid; FBS, Fetal bovine serum; PBS, Phosphate buffered saline; PVDF, Polyvinylidene difluoride; HE, Hematoxylin and eosin; MTT 3, 4,5-dimethylthiazol-2yl)-2,5-diphenyltetra-zoliumbromide; VEGF, Vascular endothelial growth factor; Flk-1 /KDR, fetal liver kinase-1/kinase insert domain containing receptor; MSCs, Mesenchymal stem cells; HUVEC, human umbilical vein endothelial cells; Zvad, carbobenzoxy -valyl- alanyl-aspartyl- [O-methyl] - fluo-romethylketone; PCNA, nuclear proliferating cell nuclear antigen; MVD, microvessels density; CM,

concentrated conditioned medium; sFlt1, soluble Fms-like tyrosine kinase-1.

## AUTHOR CONTRIBUTIONS

Jian Niu made critical intellectual contributions that formed the central concept of this study and were involved in the writing process of the manuscript. Wang Yue, Wang-ji, Liu bin, Xin Hu did part of the experiments and collected data.

## CONFLICTS OF INTEREST

No conflicts of interest, financial or otherwise, are declared by the authors.

## FUNDING

This study was supported by grants from of the National Science Foundation of China (30801125 ) and Jiangsu province natural science foundation of China (BK20161176). No support has been received from any company and the author has no financial conflict of benefits.

## REFERENCES

1. Marshall A, Alexander G. Vascular invasion leaves its mark in hepatocellular carcinoma. *J Hepatol.* 2011; 55:1174–75. doi: 10.1016/j.jhep.2011.05.005
2. Kaseb AO, Hanbali A, Cotant M, Hassan MM, Wollner I, Philip PA. Vascular endothelial growth factor in the management of hepatocellular carcinoma: a review of literature. *Cancer.* 2009; 115:4895–906. doi: 10.1002/cncr.24537
3. Cao Y. Future options of anti-angiogenic cancer therapy. *Chin J Cancer.* 2016; 35:21. doi: 10.1186/s40880-016-0084-4
4. Vasudev NS, Reynolds AR. Anti-angiogenic therapy for cancer: current progress, unresolved questions and future directions. *Angiogenesis.* 2014; 17:471–94. doi: 10.1007/s10456-014-9420-y
5. Peng S, Wang Y, Peng H, Chen D, Shen S, Peng B, Chen M, Lencioni R, Kuang M. Autocrine vascular endothelial growth factor signaling promotes cell proliferation and modulates sorafenib treatment efficacy in hepatocellular carcinoma. *Hepatology.* 2014; 60:1264–77. doi: 10.1002/hep.27236
6. Sia D, Alsinet C, Newell P, Villanueva A. VEGF signaling in cancer treatment. *Curr Pharm Des.* 2014; 20:2834–42. doi: 10.2174/13816128113199990590
7. Waidmann O, Trojan J. Novel drugs in clinical development for hepatocellular carcinoma. *Expert Opin Investig Drugs.* 2015; 24:1075–82. doi: 10.1517/13543784.2015.1058776
8. Li T, Zhu Y, Qin CY, Yang Z, Fang A, Xu S, Ren W. Expression and prognostic significance of vascular endothelial growth factor receptor 1 in hepatocellular carcinoma. *J Clin Pathol.* 2012; 65:808–14. doi: 10.1136/jclinpath-2012-200721
9. Farnia P, Ghanavi J, Bahrami A, Bandehpour M, Kazemi B, Velayati AA. Increased production of soluble vascular endothelial growth factors receptor-1 in CHO-cell line by using new combination of chitosan-protein lipid nanoparticles. *Int J Clin Exp Med.* 2015; 8:1526–33.
10. Zhu H, Li Z, Mao S, Ma B, Zhou S, Deng L, Liu T, Cui D, Zhao Y, He J, Yi C, Huang Y. Antitumor effect of sFlt-1 gene therapy system mediated by Bifidobacterium Infantis on Lewis lung cancer in mice. *Cancer Gene Ther.* 2011; 18:884–96. doi: 10.1038/cgt.2011.57
11. Zhou YL, Li YM, He WT. Application of Mesenchymal Stem Cells in the Targeted Gene Therapy for Gastric Cancer. *Curr Stem Cell Res Ther.* 2016; 11:434–39. doi: 10.2174/1574888X10666151026113818
12. Rhee KJ, Lee JI, Eom YW. Mesenchymal Stem Cell-Mediated Effects of Tumor Support or Suppression. *Int J Mol Sci.* 2015; 16:30015–33. doi: 10.3390/ijms161226215
13. Bhare D, Shah K. Stem Cell-Based Therapies for Cancer. *Adv Cancer Res.* 2015; 127:159–89. doi: 10.1016/bs.acr.2015.04.012
14. Shah K. Mesenchymal stem cells engineered for cancer therapy. *Adv Drug Deliv Rev.* 2012; 64:739–48. doi: 10.1016/j.addr.2011.06.010
15. Liu J, Li J, Su C, Huang B, Luo S. Soluble Fms-like tyrosine kinase-1 expression inhibits the growth of multiple myeloma in nude mice. *Acta Biochim Biophys Sin (Shanghai).* 2007; 39:499–506. doi: 10.1111/j.1745-7270.2007.00310.x
16. Niu J, Qian H, Han Z. siRNA-mediated type 1 insulin-like growth factor receptor silencing induces chemosensitization of a human liver cancer cell line with mutant P53. *Cell Biol Int.* 2006; 10:1016–19.
17. Peister A, Mellad JA, Larson BL, Hall BM, Gibson LF, Prockop DJ. Adult stem cells from bone marrow (MSCs) isolated from different strains of inbred mice vary in surface epitopes, rates of proliferation, and differentiation potential. *Blood.* 2004; 103:1662–68. doi: 10.1182/blood-2003-09-3070
18. Mohr A, Büneker C, Gough RP, Zwacka RM. MnSOD protects colorectal cancer cells from TRAIL-induced apoptosis by inhibition of Smac/DIABLO release. *Oncogene.* 2008; 27:763–74.

doi: 10.1038/sj.onc.1210673

19. Wang Y-H, Dong Y-Y, Wang W-M, Xie X-Y, Wang Z-M, Chen R-X, Chen J, Gao D-M, Cui J-F, Ren Z-G. Vascular endothelial cells facilitated HCC invasion and metastasis through the Akt and NF- $\kappa$ B pathways induced by paracrine cytokines. *J Exp Clin Cancer Res*. 2013; 32:51. doi: 10.1186/1756-9966-32-51
20. Niu J, Yue W, Song Y, Zhang Y, Qi X, Wang Z, Liu B, Shen H, Hu X. Prevention of acute liver allograft rejection by IL-10-engineered mesenchymal stem cells. *Clin Exp Immunol*. 2014; 176:473–84. doi: 10.1111/cei.12283
21. Zhou J-R, Yu L, Mai Z, Blackburn GL. Combined inhibition of estrogen-dependent human breast carcinoma by soy and tea bioactive components in mice. *Int J Cancer*. 2004; 108:8–14. doi: 10.1002/ijc.11549
22. Niu J. Xiangnong-Li, Zeguag-Han. siRNA mediated the type 1 insulin-like growth factor receptor and Epidermal Growth Factor Receptor silencing induces chemosensitization of liver cancer cells. *J Cancer Res Clin Oncol*. 2008; 26:703–08.
23. Zhu B, Lin N, Zhang M, Zhu Y, Cheng H, Chen S, Ling Y, Pan W, Xu R. Activated hepatic stellate cells promote angiogenesis via interleukin-8 in hepatocellular carcinoma. *J Transl Med*. 2015; 13:365. doi: 10.1186/s12967-015-0730-7
24. Tsai AC, Pan SL, Liao CH, Guh JH, Wang SW, Sun HL, Liu YN, Chen CC, Shen CC, Chang YL, Teng CM. Moscatilin, a bibenzyl derivative from the India orchid *Dendrobium loddigesii*, suppresses tumor angiogenesis and growth in vitro and in vivo. *Cancer Lett*. 2010; 292:163–70. doi: 10.1016/j.canlet.2009.11.020
25. Barral M, Raballand A, Dohan A, Soyer P, Pocard M, Bonnin P. Preclinical Assessment of the Efficacy of Anti-Angiogenic Therapies in Hepatocellular Carcinoma. *Ultrasound Med Biol*. 2016; 42:438–46. doi: 10.1016/j.ultrasmedbio.2015.10.012
26. Zhang Z, Zhang H, Peng T, Li D, Xu J. Melittin suppresses cathepsin S-induced invasion and angiogenesis via blocking of the VEGF-A/VEGFR-2/MEK1/ERK1/2 pathway in human hepatocellular carcinoma. *Oncol Lett*. 2016; 11:610–18.
27. Ye ZL, Huang Y, Li LF, Zhu HL, Gao HX, Liu H, Lv SQ, Xu ZH, Zheng LN, Liu T, Zhang JL, Jin HJ, Qian QJ. Argonaute 2 promotes angiogenesis via the PTEN/VEGF signaling pathway in human hepatocellular carcinoma. *Acta Pharmacol Sin*. 2015; 36:1237–45. doi: 10.1038/aps.2015.18
28. Liu L, Yu H, Huang X, Tan H, Li S, Luo Y, Zhang L, Jiang S, Jia H, Xiong Y, Zhang R, Huang Y, Chu CC, Tian W. A novel engineered VEGF blocker with an excellent pharmacokinetic profile and robust anti-tumor activity. *BMC Cancer*. 2015; 15:170. doi: 10.1186/s12885-015-1140-1
29. Torimura T, Iwamoto H, Nakamura T, Abe M, Ikezono Y, Wada F, Sakaue T, Masuda H, Hashimoto O, Koga H, Ueno T, Yano H. Antiangiogenic and Antitumor Activities of Aflibercept, a Soluble VEGF Receptor-1 and -2, in a Mouse Model of Hepatocellular Carcinoma. *Neoplasia*. 2016; 18:413–24. doi: 10.1016/j.neo.2016.05.001
30. Farnia P, Ghanavi J, Bahrami A, Bandehpour M, Kazemi B, Velayati AA. Increased production of soluble vascular endothelial growth factors receptor-1 in CHO-cell line by using new combination of chitosan-protein lipid nanoparticles. *Int J Clin Exp Med*. 2015; 8:1526–33.
31. Goi T, Nakazawa T, Hirono Y, Yamaguchi A. The anti-tumor effect is enhanced by simultaneously targeting VEGF and PROK1 in colorectal cancer. *Oncotarget*. 2015; 6:6053–61. doi: 10.18632/oncotarget.3474
32. Maleki M, Ghanbarvand F, Reza Behvarz M, Ejtemaei M, Ghadirkhomi E. Comparison of mesenchymal stem cell markers in multiple human adult stem cells. *Int J Stem Cells*. 2014; 7:118–26. doi: 10.15283/ijsc.2014.7.2.118
33. Zhou YL, Li YM, He WT. Application of Mesenchymal Stem Cells in the Targeted Gene Therapy for Gastric Cancer. *Curr Stem Cell Res Ther*. 2016; 11:434–39. doi: 10.2174/1574888X10666151026113818
34. Bhere D, Shah K. Stem Cell-Based Therapies for Cancer. *Adv Cancer Res*. 2015; 127:159–89. doi: 10.1016/bs.acr.2015.04.012
35. Rico MJ, Perroud HA, Mainetti LE, Rozados VR, Scharovsky OG. Comparative effectiveness of two metronomic chemotherapy schedules-our experience in the preclinical field. *Cancer Invest*. 2014; 32:92–98. doi: 10.3109/07357907.2013.877480
36. Albertsson P, Lennernäs B, Norrby K. Dose effects of continuous vinblastine chemotherapy on mammalian angiogenesis mediated by VEGF-A. *Acta Oncol*. 2008; 47:293–300. doi: 10.1080/02841860701558781
37. Rico MJ, Perroud HA, Mainetti LE, Rozados VR, Scharovsky OG. Comparative effectiveness of two metronomic chemotherapy schedules-our experience in the preclinical field. *Cancer Invest*. 2014; 32:92–98. doi: 10.3109/07357907.2013.877480
38. Tseng JC, Granot T, DiGiacomo V, Levin B, Meruelo D. Enhanced specific delivery and targeting of oncolytic Sindbis viral vectors by modulating vascular leakiness

in tumor. *Cancer Gene Ther.* 2010; 17:244–55. doi: 10.1038/cgt.2009.70

39. Al-Abbasi FA, Alghamdi EA, Baghdadi MA, Alamoudi AJ, El-Halawany AM, El-Bassossy HM, Aseeri AH, Al-Abd AM. Gingerol Synergizes the Cytotoxic Effects of Doxorubicin against Liver Cancer Cells and Protects from Its Vascular Toxicity. *Molecules.* 2016; 21:580–91. doi: 10.3390/molecules21070886

## RelA NF- $\kappa$ B subunit activation as a therapeutic target in diffuse large B-cell lymphoma

Mingzhi Zhang<sup>1,2\*</sup>, Zijun Y. Xu-Monette<sup>2\*</sup>, Ling Li<sup>1\*</sup>, Ganiraju C. Manyam<sup>3</sup>, Carlo Visco<sup>4</sup>, Alexandar Tzankov<sup>5</sup>, Jing Wang<sup>3</sup>, Santiago Montes-Moreno<sup>6</sup>, Karen Dybkaer<sup>7</sup>, April Chiu<sup>8</sup>, Attilio Orazi<sup>9</sup>, Youli Zu<sup>10</sup>, Govind Bhagat<sup>11</sup>, Kristy L. Richards<sup>12</sup>, Eric D. Hsi<sup>13</sup>, William W.L. Choi<sup>14</sup>, J. Han van Krieken<sup>15</sup>, Jooryung Huh<sup>16</sup>, Maurilio Ponzoni<sup>17</sup>, Andrés J.M. Ferreri<sup>17</sup>, Michael B. Møller<sup>18</sup>, Ben M. Parsons<sup>19</sup>, Jane N. Winter<sup>20</sup>, Miguel A. Piris<sup>6</sup>, L. Jeffrey Medeiros<sup>2</sup>, Lan V. Pham<sup>2</sup>, Ken H. Young<sup>2,21</sup>

<sup>1</sup>Department of Oncology, The First Affiliated Hospital Zhengzhou University, Zhengzhou, Henan, China;

<sup>2</sup>Department of Hematopathology, The University of Texas MD Anderson Cancer Center, Houston, TX 77030, USA

<sup>3</sup>Department of Bioinformatics and Computational Biology, The University of Texas MD Anderson Cancer Center, Houston, TX 77030, USA

<sup>4</sup>San Bortolo Hospital, Vicenza, Italy

<sup>5</sup>University Hospital, Basel, Switzerland

<sup>6</sup>Hospital Universitario Marques de Valdecilla, Santander, Spain

<sup>7</sup>Aalborg University Hospital, Aalborg, Denmark

<sup>8</sup>Memorial Sloan-Kettering Cancer Center, New York, NY 10065, USA

<sup>9</sup>Weill Medical College of Cornell University, New York, NY 10065, USA

<sup>10</sup>The Methodist Hospital, Houston, TX 77030, USA

<sup>11</sup>Columbia University Medical Center and New York Presbyterian Hospital, New York, NY 10032, USA

<sup>12</sup>University of North Carolina School of Medicine, Chapel Hill, NC 27514, USA

<sup>13</sup>Cleveland Clinic, Cleveland, OH 44195, USA

<sup>14</sup>University of Hong Kong Li Ka Shing Faculty of Medicine, Hong Kong, China

<sup>15</sup>Radboud University Nijmegen Medical Centre, Nijmegen, the Netherlands

<sup>16</sup>Asan Medical Center, Ulsan University College of Medicine, Seoul, Korea

<sup>17</sup>San Raffaele H. Scientific Institute, Milan, Italy

<sup>18</sup>Odense University Hospital, Odense, Denmark

<sup>19</sup>Gundersen Medical Foundation, La Crosse, WI 54601, USA

<sup>20</sup>Feinberg School of Medicine, Northwestern University, Chicago, IL 60611, USA

<sup>21</sup>The University of Texas School of Medicine, Graduate School of Biomedical Sciences, Houston, TX 77030, USA

\*Equal contribution

**Correspondence to:** Mingzhi Zhang; Ken H. Young; email: [mingzhi\\_zhang@126.com](mailto:mingzhi_zhang@126.com), [khyoung@mdanderson.org](mailto:khyoung@mdanderson.org)

**Keywords:** NF- $\kappa$ B; p65; diffuse large B-cell lymphoma; TP53, GCB, gene expression profiling, proteasome inhibitor

**Received:** October 29, 2016

**Accepted:** November 11, 2016

**Published:** December 8, 2016

### ABSTRACT

It has been well established that nuclear factor kappa-B (NF- $\kappa$ B) activation is important for tumor cell growth and survival. RelA/p65 and p50 are the most common NF- $\kappa$ B subunits and involved in the classical NF- $\kappa$ B pathway. However, the prognostic and biological significance of RelA/p65 is equivocal in the field. In this study, we assessed RelA/p65 nuclear expression by immunohistochemistry in 487 patients with *de novo* diffuse large



B-cell lymphoma (DLBCL), and studied the effects of molecular and pharmacological inhibition of NF- $\kappa$ B on cell viability. We found RelA/p65 nuclear expression, without associations with other apparent genetic or phenotypic abnormalities, had unfavorable prognostic impact in patients with stage I/II DLBCL. Gene expression profiling analysis suggested immune dysregulation and antiapoptosis may be relevant for the poorer prognosis associated with p65 hyperactivation in germinal center B-cell-like (GCB) DLBCL and in activated B-cell-like (ABC) DLBCL, respectively. We knocked down individual NF- $\kappa$ B subunits in representative DLBCL cells in vitro, and found targeting p65 was more effective than targeting other NF- $\kappa$ B subunits in inhibiting cell growth and survival. In summary, RelA/p65 nuclear overexpression correlates with significant poor survival in early-stage DLBCL patients, and therapeutic targeting RelA/p65 is effective in inhibiting proliferation and survival of DLBCL with NF- $\kappa$ B hyperactivation.

## INTRODUCTION

Diffuse large B-cell lymphoma (DLBCL), the most common form of aggressive non-Hodgkin lymphoma, accounts for nearly 40% of non-Hodgkin lymphomas [1]. Although most cases of DLBCL are curable with the standard immunochemotherapy regimen, rituximab plus cyclophosphamide, hydroxydaunomycin, vincristine, and prednisone (R-CHOP), 30-40% of patients have drug-resistant disease or recurrence [2]. DLBCL is a highly heterogeneous disease. Based on gene expression profiling (GEP), DLBCL can be classified into two molecular subtypes: germinal center B-cell-like (GCB) and activated B-cell-like (ABC) DLBCL [3]. The ABC subtype of DLBCL typically exhibits constitutive activation of the nuclear factor- $\kappa$ B (NF- $\kappa$ B) pathway [4, 5] and patients have inferior clinical outcomes compared with patients with GCB-DLBCL [6, 7]. Recent studies have shown that NF- $\kappa$ B expression is not limited to ABC-DLBCL but also can occur in GCB-DLBCL [8-10].

The NF- $\kappa$ B/Rel family contains five transcription factors: RelA (p65), NF- $\kappa$ B1 (p50; p105), NF- $\kappa$ B2 (p52; p100), RelB, and c-Rel. Only RelA/p65, RelB, and c-Rel had transactivation domains [11]. NF- $\kappa$ B activity is controlled by inhibitors of NF- $\kappa$ B (such as I $\kappa$ B $\alpha$  which inhibits p65/p50 dimers) that keep NF- $\kappa$ B inactive in the cytoplasm. Constitutive activation of NF- $\kappa$ B in ABC-DLBCL is caused by chronic activation of B-cell-receptor (BCR) signaling and elevated I $\kappa$ B kinase (IKK) activities which phosphorylate I $\kappa$ B $\alpha$ . As a result, I $\kappa$ B $\alpha$  is degraded releasing homo- or heterodimers of NF- $\kappa$ B to enter the nucleus where NF- $\kappa$ B activates gene transcription [4, 12-14]. *In vivo* the most abundant NF- $\kappa$ B dimers are p50/p65 heterodimers which are ubiquitously expressed in mammalian tissue [11, 15-17], consistent with the highest level of nuclear p50/p65 in DLBCL samples among all NF- $\kappa$ B subunits by our previous studies [10, 18]. Detection of p65/p50 nuclear expression in tumor cells has been considered as

homodimers with distinct DNA-binding modes and functions [19-21].

NF- $\kappa$ B activation suppresses apoptosis and promotes tumor cell survival and proliferation, leading to treatment resistance. Different NF- $\kappa$ B subunits had distinct and overlapping functions [22-24]. In addition, transcriptional and functional crosstalk between antiapoptotic NF- $\kappa$ B and proapoptotic p53 (an essential tumor suppressor) plays a critical role in determining the fate of tumor cells [25, 26]. The p65 subunit of NF- $\kappa$ B and p53 counteract each other's function in regulating cell proliferation, metabolism and apoptosis [25, 27-29]. p65 increases MDM2 levels, which decrease the stabilization of p53 and cell death induced by cytotoxic chemotherapy [25]. However, cooperation between p65 and p53 has been also reported [30-33], making interactions between p65/NF- $\kappa$ B and p53 much more complicated. Both p53 and p65 were unexpectedly found necessary for either p53 or NF- $\kappa$ B-directed gene transcription under replicational stress or atypical and classical stimuli for NF- $\kappa$ B. Induced p65 in stimulated cancer cells by pro-inflammatory tumor necrosis factor  $\alpha$  (TNF- $\alpha$ ) binds to p53 and the p65/p53 complex transcriptionally activates NF- $\kappa$ B target genes (*survivin/BIRC5*, *BCL2*, *BCL-XL*, and *FASL*) [32]. Moreover, p65 and p53 co-regulate induction of proinflammatory genes in monocytes and macrophages [33].

Despite the well-established role of NF- $\kappa$ B signaling in lymphoma pathogenesis and treatment resistance, conflicting results on the prognostic significance of NF- $\kappa$ B and RelA/p65 expression (as a surrogate marker of NF- $\kappa$ B activation) in DLBCL have been reported by previous clinical studies [8, 9, 34-36]. To help clarify the prognostic effect of RelA/p65 nuclear expression, in this study we evaluated nuclear expression of RelA/p65 by immunohistochemistry (IHC) in a large cohort of DLBCL treated with R-CHOP, and studied the prognostic effects and gene expression profiles associated



with p65 nuclear expression. Moreover, we inactivated individual NF- $\kappa$ B subunits in vitro and investigated their differential effects on proliferation and apoptosis of DLBCL cells which highlighted the important therapeutic value of RelA/p65.

## RESULTS

### p65 hyperactivation has significant adverse impact in early-stage DLBCL

p65 expression was evaluable in 487 DLBCL patients, including 287 men and 200 women. GCB/ABC ratio was close to 1 (243 GCB and 239 ABC). The median age of the patients in the study group was 63 years, and 58% of the study cohort had elderly age ( $\geq 60$ ). Immunohistochemical results showed that 58% of DLBCL samples had p65 nuclear expression indicative of p65 activation at various levels (Fig. 1A) with a mean level of 14%. p65 nuclear expression was not specific for ABC-DLBCL. In fact, the GCB-DLBCL group had a slightly higher mean level of p65 nuclear expression (16.1%) than the ABC-DLBCL group (12.6%) (Fig. 1A). Table 1 showed the clinical and pathological features of the study cohort.

Low levels (10-40%) of p65 nuclear expression did not have significant prognostic impact in DLBCL (Fig. 1B). However, high p65 nuclear expression (p65<sup>high</sup>,  $\geq 50\%$  tumor cells with p65 positive nuclei) correlated with significantly shorter PFS and OS durations in patients with stage I/II DLBCL and in patients with an International Prognostic Index score (IPI)  $\leq 2$  (Fig. 1B, Fig. 2A). In contrast, in patients with stage III/IV DLBCL or an IPI  $> 2$ , p65 expression was not prognostic. p65<sup>high</sup> patients with stage I/II DLBCL had similar survival rates compared with p65<sup>high</sup> patients with stage III/IV DLBCL (Fig. 2B).

When analyzed individually in GCB and ABC subtypes, in GCB-DLBCL only, the p65<sup>high</sup> group frequently had large ( $\geq 5$ cm) tumors (65% vs. 37%,  $P = 0.011$ ) (Table 1), and significantly decreased PFS ( $P = 0.04$ , Fig. 2C) and OS ( $P = 0.015$ ) rates than other patients (p65<sup>low</sup> group, IHC  $< 50\%$ ). However, the unfavorable prognostic effect manifested in GCB-DLBCL was limited in stage I/II (Fig. 1C) and minimal in stage III/IV GCB-DLBCL ( $P = 0.95$  for PFS and  $P = 0.60$  for OS); also, in stage I/II ABC-DLBCL patients, p65<sup>high</sup> expression also significantly correlated with worse PFS (Fig. 1C).

### p65 nuclear expression correlates with p50 nuclear expression in DLBCL

We found high p65 nuclear expression was significantly

associated with p50<sup>+</sup> and p50<sup>high</sup> nuclear expression in overall DLBCL, GCB-DLBCL, and ABC-DLBCL (Table 1), suggesting the predominance of p65/p50 dimer activation via the canonical NF- $\kappa$ B pathway [9]. Significant association with c-Rel<sup>+</sup> nuclear expression was also found in overall DLBCL and GCB-DLBCL (p50/c-Rel is another dimer activated via the canonical pathway [37, 38]). No significant association was observed between p65<sup>high</sup> and RelB<sup>+</sup>. p65<sup>high</sup> showed significant association with p52<sup>+</sup> in overall DLBCL but not in either GCB or ABC subset.

Nuclear expression of p50, p52, and c-Rel did not show further prognostic effects among the p65<sup>high</sup> patients. We did not observe associations of p65<sup>high</sup> with any other adverse biomarkers such as *TP53* mutations, *MYC/BCL2* translocation, and Myc/Bcl-2 overexpression which may confound the prognostic effects [39-42]. In contrast, in the GCB but not the ABC subgroup, p65<sup>high</sup> compared with p65<sup>low</sup> patients less frequently had Bcl-2 overexpression (18% vs. 40%,  $P = 0.036$ ).

### p65 hyperactivation has significant adverse impact in patients with wild-type *TP53*

Cases of DLBCL with wild-type *TP53* (*WT-TP53*) had significantly lower levels of *RELA* mRNA ( $P = 0.018$ , Fig. 1D) and a trend toward lower nuclear p65 levels ( $P = 0.11$ ) than those with mutated *TP53* (*MUT-TP53*), suggesting that wild-type p53 suppressed *RELA* NF- $\kappa$ B expression. Conversely, p65 antagonized p53 function as suggested by survival analysis: in *WT-TP53* DLBCL, patients with p65<sup>high</sup> expression correlated with significantly decreased PFS ( $P = 0.0076$ , Fig. 2C) and OS ( $P = 0.0082$ ) rates than patients with p65<sup>low</sup> tumors, independent of GCB and ABC cell-of-origin. However, when subdivided cohorts by disease stages, we found the prognostic impact was only significant in patients with stage I/II disease ( $P < 0.0001$  for PFS,  $P = 0.0004$  for OS). Also in *MUT-TP53* patients with stage I/II DLBCL, positive p65 nuclear expression was associated with significant poorer survival; in contrast, opposite trends were observed in *MUT-TP53* patients with stage III/IV DLBCL (Fig. 1E).

### Multivariate survival analysis

Multivariate survival analysis (Cox regression) for high p65 nuclear expression with adjustments for clinical variables confirmed that p65<sup>high</sup> was an independent adverse prognostic factor in patients with GCB-DLBCL and in patients with *WT-TP53* DLBCL, but not in the overall study group, the ABC-DLBCL subgroup, or the *MUT-TP53* DLBCL subgroup (Table 2).

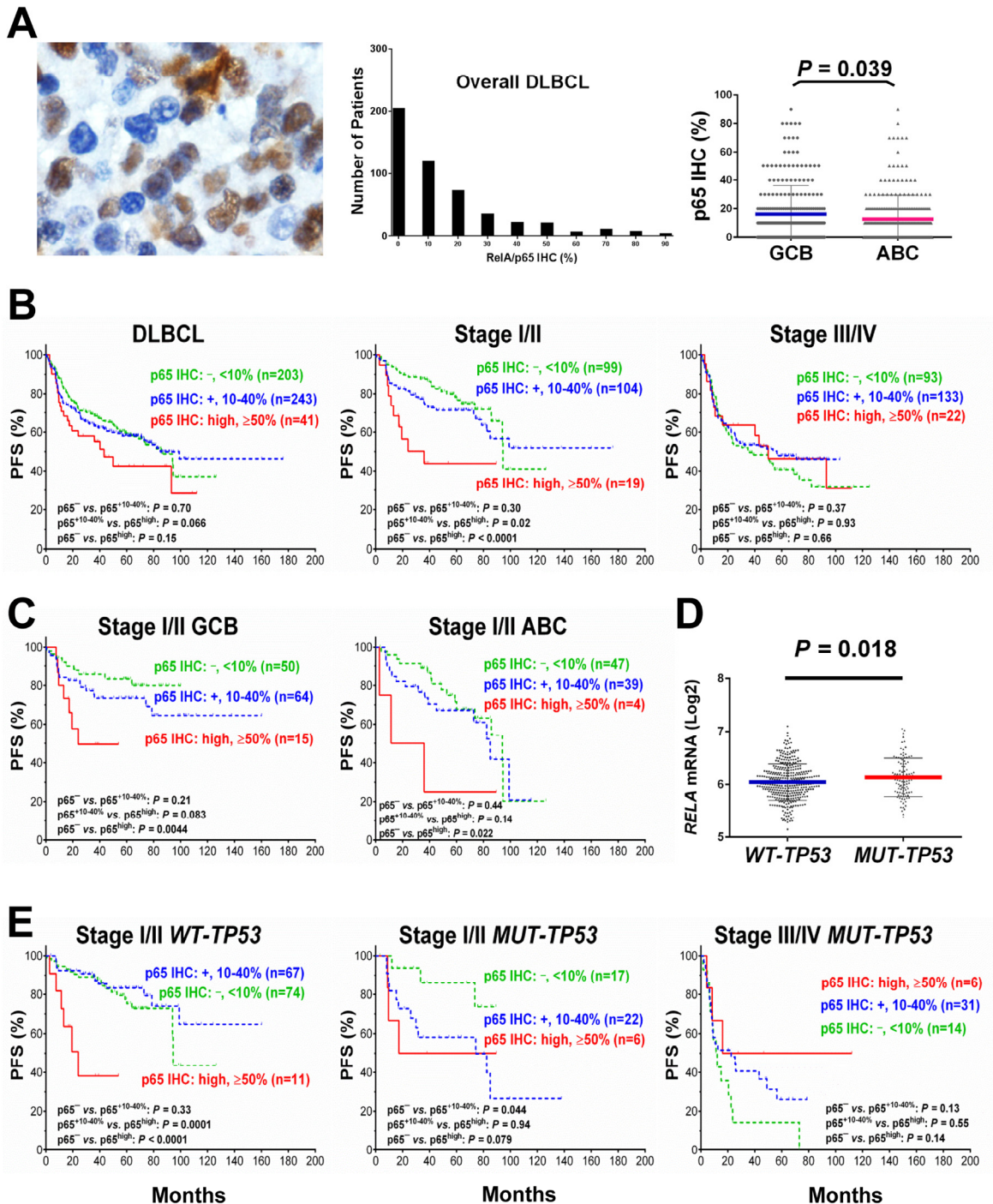


**Figure 1. Nuclear expression of p65 and its effect on progression-free survival (PFS) in diffuse large B-cell lymphoma (DLBCL)** (A) Representative immunohistochemical analysis (IHC) and histograms for p65 nuclear expression in DLBCL. The mean expression of nuclear p65 was significantly higher in the germinal center B-cell-like (GCB) subtype than in the activated B-cell-like (ABC) subtype. (B) In overall DLBCL, high p65 nuclear expression ( $p65^{high}$ ,  $\geq 50\%$  nuclear expression) was associated with a trend towards worse PFS. In patients with stage I/II DLBCL,  $p65^{high}$  correlated with significantly shorter PFS. In patients with stage III/IV DLBCL,  $p65^{high}$  did not show significant prognostic impact. (C)  $p65^{high}$  correlate with significantly shorter PFS in patients with stage I/II DLBCL independent of GCB/ABC subtypes. (D) *TP53* mutation status was significantly associated with higher *RELA* mRNA expression. (E) In patients with stage I/II DLBCL,  $p65^{high}$  correlate with significantly shorter PFS independent of *TP53* mutation status although more significant in patients with wild-type *TP53* (WT-*TP53*). In patients with mutated *TP53* (MUT-*TP53*) and stage III/IV DLBCL,  $p65^{high}$  was associated with a trend of better PFS.

**Table 1. Clinical characteristics of 487 patients with *de novo* diffuse large B-cell lymphoma (DLBCL).**

	DLBCL			GCB-DLBCL			ABC-DLBCL			WT-TP53			MUT-TP53		
	p65 <sup>high</sup>	p65 <sup>low</sup>	P	p65 <sup>high</sup>	p65 <sup>low</sup>	P	p65 <sup>high</sup>	p65 <sup>low</sup>	P	p65 <sup>high</sup>	p65 <sup>low</sup>	P	p65 <sup>high</sup>	p65 <sup>low</sup>	P
Characteristics	N (%)	N (%)		N (%)	N (%)		N (%)	N (%)		N (%)	N (%)		N (%)	N (%)	
Patients	41	446		28	215		13	226		26	312		12	84	
Age (years)															
<60	21 (51)	183 (41)	0.21	16 (57)	106 (49)	0.44	5 (39)	74 (33)	0.67	13 (50)	124 (40)	0.31	7 (58)	30 (36)	0.13
≥60	20 (49)	263 (59)		12 (43)	109 (51)		8 (61)	152 (67)		13 (50)	188 (60)		5 (42)	54 (64)	
Gender															
Female	8 (20)	192 (43)	0.003	6 (21)	95 (44)	0.022	2 (15)	95 (42)	0.057	6 (30)	130 (42)	0.063	2 (17)	38 (45)	0.06
Male	33 (80)	254 (57)		22 (79)	120 (56)		11 (85)	131 (58)		20 (70)	182 (58)		10 (83)	46 (55)	
Stage															
I/II	19 (46)	203 (47)	0.90	15 (54)	114 (56)	0.84	4 (31)	86 (39)	0.54	11 (42)	141 (48)	0.60	6 (50)	39 (46)	0.82
III/IV	22 (54)	226 (53)		13 (46)	91 (45)		9 (69)	133 (61)		15 (58)	155 (52)		6 (50)	45 (54)	
B-symptoms															
No	25 (61)	272 (64)	0.67	18 (64)	141 (70)	0.55	7 (54)	127 (59)	0.73	16 (61)	196 (66)	0.61	7 (58)	54 (68)	0.53
Yes	16 (39)	151 (36)		10 (36)	61 (30)		6 (46)	89 (41)		10 (39)	99 (34)		5 (42)	26 (33)	
LDH levels															
Normal	14 (34)	161 (40)	0.51	8 (29)	86 (44)	0.12	6 (46)	74 (36)	0.44	10 (39)	121 (43)	0.65	3 (25)	28 (36)	0.46
Elevated	27 (66)	247 (60)		20 (71)	109 (56)		7 (54)	134 (64)		16 (61)	160 (57)		9 (75)	50 (64)	
Extranodal sites (n)															
0–1	35 (85)	327 (77)	0.22	23 (82)	160 (80)	0.75	12 (92)	163 (74)	0.15	21 (81)	231 (79)	0.79	11 (92)	64 (78)	0.27
≥2	6 (15)	98 (23)		5 (18)	41 (20)		1 (8)	56 (26)		5 (19)	63 (21)		1 (8)	18 (22)	
Performance status															
0–1	34 (87)	329 (83)	0.53	23 (85)	158 (86)	0.87	11 (92)	166 (80)	0.33	22 (85)	231 (85)	0.93	10 (91)	69 (90)	0.89
≥2	5 (13)	66 (17)		4 (15)	25 (14)		1 (8)	41 (20)		4 (15)	40 (15)		1 (9)	8 (10)	
Size of largest tumor															
<5cm	14 (44)	192 (58)	0.11	8 (35)	97 (63)	0.011	6 (67)	93 (54)	0.47	8 (38)	146 (62)	0.035	5 (50)	33 (49)	0.96
≥5cm	18 (56)	137 (42)		15 (65)	58 (37)		3 (33)	78 (46)		13 (62)	91 (38)		5 (50)	34 (51)	
IPI risk group															
0–2	29 (71)	267 (62)	0.25	21 (75)	144 (71)	0.82	8 (61)	118 (54)	0.78	17 (65)	189 (63)	1.0	10 (83)	47 (57)	0.12
3–5	12 (29)	162 (38)		7 (25)	60 (29)		5 (39)	102 (46)		9 (35)	109 (37)		2 (17)	43 (35)	
Therapy response															
CR	29 (71)	343 (77)	0.37	17 (61)	166 (77)	0.057	12 (92)	172 (76)	0.18	17 (65)	257 (82)	0.034	9 (75)	49 (58)	0.27
Non-CR	12 (29)	103 (23)		11 (39)	49 (23)		1 (8)	22 (24)		9 (35)	55 (18)		3 (25)	35 (42)	
Primary origin															
Extranodal	20 (49)	149 (34)	0.058	14 (50)	68 (32)	0.063	6 (46)	79 (36)	0.44	14 (54)	102 (33)	0.035	4 (33)	26 (32)	0.91
Nodal	21 (51)	289 (66)		14 (50)	143 (68)		7 (54)	143 (64)		12 (46)	204 (67)		8 (67)	56 (68)	

Cell-of-origin															
GCB	28 (68)	215 (49)	<b>0.022</b>	-	-	-	-	-	-	18 (69)	143 (46)	<b>0.039</b>	9 (75)	49 (58)	0.35
ABC	13 (32)	226 (51)		-	-	-	-	-	-	8 (31)	165 (54)		3 (25)	35 (42)	
p50 nuclear expression															
<20%	15 (40)	278 (67)	<b>0.002</b>	12 (46)	149 (74)	<b>0.005</b>	3 (27)	129 (60)	<b>0.05</b>	9 (41)	188 (65)	<b>0.037</b>	6 (50)	57 (71)	0.18
≥20%	22 (60)	138 (33)		14 (54)	52 (26)		8 (73)	85 (40)		13 (59)	102 (35)		6 (50)	23 (29)	
p52 nuclear expression															
-	21 (55)	300 (71)	<b>0.043</b>	14 (54)	142 (71)	0.11	7 (58)	157 (72)	0.33	14 (58)	208 (71)	0.25	5 (46)	59 (74)	0.078
+	17 (45)	120 (29)		12 (46)	58 (29)		5 (42)	61 (28)		10 (42)	86 (29)		6 (54)	21 (26)	
c-Rel nuclear expression															
-	17 (46)	297 (72)	<b>0.002</b>	11 (44)	147 (74)	<b>0.004</b>	6 (50)	150 (70)	0.20	9 (41)	207 (73)	<b>0.003</b>	7 (58)	55 (67)	0.53
+	20 (54)	117 (28)		14 (56)	52 (26)		6 (50)	64 (30)		13 (59)	78 (27)		5 (42)	27 (33)	
Bcl-2 expression															
<70%	27 (66)	229 (52)	0.10	23 (82)	127 (60)	<b>0.036</b>	4 (31)	99 (44)	0.40	17 (65)	164 (53)	0.31	7 (58)	40 (48)	0.55
≥70%	14 (34)	208 (48)		5 (18)	83 (40)		9 (69)	125 (56)		9 (35)	143 (47)		5 (42)	44 (52)	

Abbreviations: p65<sup>high</sup>, high levels of nuclear p65; p65<sup>low</sup>, low levels of p65 nuclear expression; LDH, lactate dehydrogenase; IPI, international prognostic index; CR, complete remission; PR, partial response; GCB, germinal center B-cell-like; ABC, activated B-cell-like; *WT-TP53*, wild-type *TP53*; *MUT-TP53*, mutated *TP53*. Some of the clinicopathologic data were not available. Percentages are calculated among cases with specific data available. Significant *P* values in bold.

**Table 2. Multivariate analysis of clinicopathologic parameters for survival of patients with diffuse large B-cell lymphoma (DLBCL) treated with R-CHOP.**

		Overall survival			Progression-free survival		
	HR	95% CI	<i>P</i>		HR	95% CI	<i>P</i>
DLBCL ( <i>n</i> = 497)							
IPI > 2	2.41	1.70–3.42	< <b>0.001</b>		2.29	1.64–3.19	< <b>0.001</b>
Female sex	1.03	0.72–1.49	0.86		0.99	0.70–1.41	0.98
Tumor size ≥ 5	1.28	0.91–1.81	0.16		1.23	0.89–1.71	0.21
B-symptoms	1.35	0.94–1.94	0.099		1.31	0.93–1.85	0.12
p65 <sup>high</sup>	1.56	0.91–2.68	0.11		1.44	0.85–2.42	0.18
GCB-DLBCL ( <i>n</i> = 243)							
IPI > 2	2.47	1.40–4.38	<b>0.002</b>		2.39	1.39–4.09	<b>0.002</b>
Female sex	1.00	0.55–1.82	1.00		0.98	0.56–1.71	0.95
Tumor size ≥ 5	1.30	0.88–1.91	0.19		1.40	0.82–2.40	0.22
B-symptoms	1.44	0.80–2.58	0.22		1.34	0.77–2.33	0.31
p65 <sup>high</sup>	2.30	1.14–4.62	<b>0.02</b>		2.01	1.06–3.82	<b>0.034</b>
WT-TP53 DLBCL ( <i>n</i> = 338)							
IPI > 2	2.54	1.66–3.88	< <b>0.001</b>		2.33	1.57–3.46	< <b>0.001</b>
Female sex	0.98	0.63–1.53	0.92		0.99	0.65–1.51	0.96
Tumor size ≥ 5	1.20	0.79–1.84	0.39		1.09	0.73–1.63	0.18
B-symptoms	1.59	1.04–2.43	<b>0.034</b>		1.57	1.05–2.33	<b>0.028</b>
p65 <sup>high</sup>	1.91	1.04–3.52	<b>0.037</b>		1.94	1.08–3.48	<b>0.026</b>

Abbreviations: R-CHOP, rituximab with cyclophosphamide, doxorubicin, vincristine, and prednisone; HR, hazard ratio; CI, confidence interval; IPI, International Prognostic Index; p65<sup>high</sup>, high levels of nuclear p65; GCB, germinal center B-cell-like; ABC, activated B-cell-like; WT-TP53, wild-type TP53. \*Significant *P* values in bold.



## GEP analysis suggests different signaling pathways activated in GCB- and ABC-DLBCL

To gain insight into the molecular mechanisms underlying the prognostic effects of p65 hyperactivation in DLBCL, we compared gene expression profiles of p65<sup>high</sup> and p65<sup>low</sup> tumors. p65<sup>high</sup> patients showed GEP signatures compared with other DLBCL including p65<sup>low</sup> DLBCL patients (IHC <10%), stronger in GCB-DLBCL than in ABC-DLBCL subset (Fig. 3A, Fig. 4, Tables 3-4).

In line with the unfavorable prognosis of patients with p65<sup>high</sup> DLBCL, GEP analysis found that *JUN* and *PTPRD* (involved in cell cycle progression) were upregulated (1.43-fold and 1.31-fold respectively) whereas pro-apoptotic *NOXA/PMAIP1* and *BTG3* which negatively regulates proliferation and cell cycle progression were downregulated (1.62-fold and 1.45-fold, respectively) in p65<sup>high</sup> DLBCL compared with p65<sup>low</sup> DLBCL. *RBMS1* which transactivates *MYC* was upregulated (1.48-fold) in p65<sup>high</sup> compared with p65<sup>low</sup> GCB-DLBCL (Table 3). Paradoxically, antiapoptotic

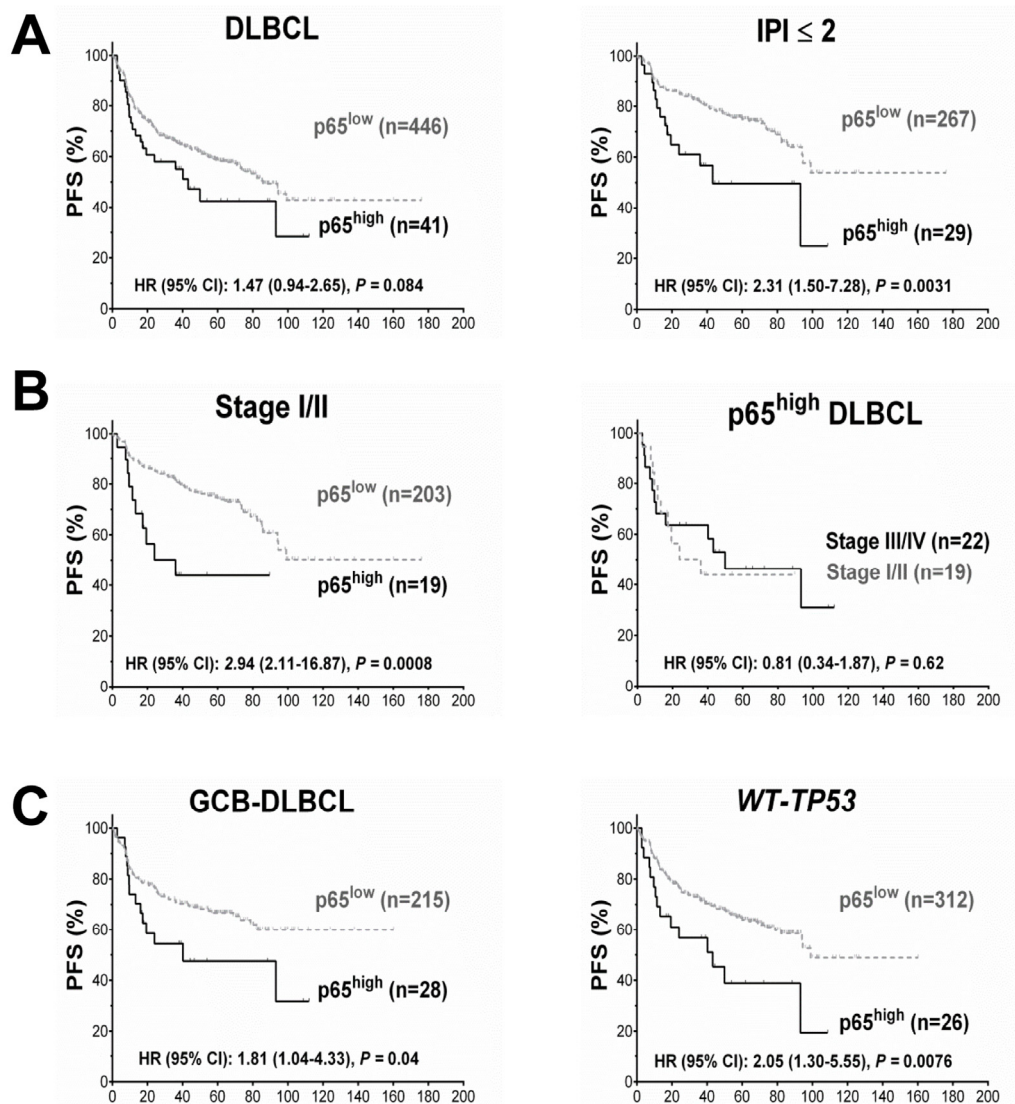


**Figure 2. Prognosis for p65 hyperactivation in diffuse large B-cell lymphoma (DLBCL).** (A) In overall DLBCL, high p65 nuclear expression (p65<sup>high</sup>, ≥50% nuclear expression) was associated with unfavorable progression-free survival (PFS). The adverse prognostic impact was significant in patients with an international prognostic index score (IPI) ≤2. (B) In patients with stage I/II DLBCL, p65<sup>high</sup> correlated with significantly poorer PFS. Among p65<sup>high</sup> DLBCL patients, disease stages did not show further prognostic impact. (C) p65<sup>high</sup> correlated with significantly poorer PFS in patients with GCB-DLBCL and patients with wild-type *TP53* (WT-*TP53*).

*BIRC6*, *MCM10* (involved in the initiation of eukaryotic genome replication), *CARS* (cysteinyI-tRNA synthetase) and *PA2G4* (involved in growth regulation) were downregulated in p65<sup>high</sup> patients, and *TENC1* (which inhibits AKT1 signaling) was upregulated in p65<sup>high</sup> DLBCL.

When analyzed in GCB and ABC subtypes individually, we found such paradoxical association was limited in

the GCB subset. *RNF130* involved in apoptosis showed 1.81-fold upregulation in p65<sup>high</sup> GCB-DLBCL patients. In contrast, in p65<sup>high</sup> ABC-DLBCL, antiapoptotic *BIRC5* and *BCL2L2* were significantly upregulated whereas pro-apoptotic *NOXA/PMAIP1* was significantly downregulated (Fig. 3B-C), in addition to the proliferative signatures (such as upregulation of genes involved in replication, transcription, translation, and metabolism) in ABC-DLBCL (Table 3).

**Table 3. Differentially expressed (canonical activation) genes between p65<sup>high</sup> vs. p65<sup>low</sup> patients with diffuse large B-cell lymphoma (DLBCL).**

Functional categories	p65 <sup>high</sup> vs. p65 <sup>low</sup>		
	In overall DLBCL (FDR <0.30)	In GCB-DLBCL (FDR <0.05)	In ABC-DLBCL (FDR <0.20)
Signaling, ion channels	<i>TNFRSF1A</i> ↑ <i>FYN</i> ↑ <i>LCP2</i> ↑ <i>PTPRD</i> ↑ <i>GTPBP2</i> ↑ <i>PROCR</i> ↑ <i>TENC1</i> ↑ <i>ITPR3</i> ↑ <i>TEK</i> ↑ <i>CACNA2D1</i> ↑ <i>AGTRAP</i> ↑ <i>LPAR3</i> ↓	<i>MTIX</i> ↑ <i>MT1G</i> ↑ <i>SERPING1</i> ↑ <i>PSEN1</i> ↑	<i>ARHGEF2</i> ↑ <i>FGFBP1</i> ↑ <i>EPHA1</i> ↑ <i>MS4A3</i> ↑
Immune responses, inflammation		<i>CD163</i> ↑ <i>FCER1G</i> ↑ <i>CYBB</i> ↑ <i>GRN</i> ↑ <i>CD84</i> ↑ <i>LILRB1</i> ↑	<i>DEFB4</i> ↑
Cell cycle, DNA metabolism, transcription and translation regulation	<i>JUN</i> ↑ <i>MLLT10</i> ↑ <i>GATAD2A</i> ↑ <i>HOXD10</i> ↑ <i>NFRKB</i> ↑ <i>ZWINT</i> ↓ <i>MCM10</i> ↓ <i>HMGB1</i> ↓ <i>PPP2CA</i> ↓ <i>UHRF1</i> ↓ <i>BTG3</i> ↓ <i>ZNF254</i> ↓ <i>CARS</i> ↓ <i>PA2G4</i> ↓ <i>SERBP1</i> ↓	<i>RBMS1</i> ↑ <i>ANKRD11</i> ↑ <i>FAM89B</i> ↑	<i>ESRP1</i> ↑ <i>DPPA4</i> ↑
Apoptosis	<i>PMAIP1</i> ↓ <i>BIRC6</i> ↓	<i>RNF130</i> ↑	
Metabolism	<i>SULT1A1</i> ↑ <i>SPTLC2</i> ↑ <i>SLC25A16</i> ↑ <i>SLC9A9</i> ↑	<i>GLUL</i> ↑ <i>SERINC1</i> ↑ <i>CAT</i> ↑ <i>SLC9A9</i> ↑	<i>S100A16</i> ↑ <i>SLC9A5</i> ↑
Transport, trafficking, protein folding, chaperone	<i>CPNE8</i> ↑ <i>DNAJC5</i> ↑ <i>RHD</i> ↑ <i>AGFG2</i> ↑	<i>SLC8A1</i> ↑ <i>NPC2</i> ↑ <i>VAMP5</i> ↑ <i>DNAJC5</i> ↑	
Cell adhesion, cytoskeleton, collagen, extracellular matrix	<i>SH3D19</i> ↑ <i>ITGA6</i> ↑ <i>MYLK</i> ↑ <i>COL6A1</i> ↑ <i>UTRN</i> ↑ <i>FMOD</i> ↑	<i>UTRN</i> ↑	<i>CCDC151</i> ↑ <i>KRT13</i> ↑ <i>ANTXR2</i> ↑ <i>COL17A1</i> ↑
Degradation, ubiquitination	<i>RNASE1</i> ↑	<i>SCARB2</i> ↑ <i>CTSB</i> ↑ <i>UBA7</i> ↑	<i>PSMB1</i> ↑
lncRNA genes, unknown function	<i>NCRNA00185</i> ↑ <i>C19orf6</i> ↑ <i>PLEKHO2</i> ↑ <i>FAM124A</i> ↑	<i>MT1P2</i> ↑ <i>ZDHHC20</i> ↑ <i>PLEKHO2</i> ↑	<i>FAM105B</i> ↓ <i>CG030</i> ↑ <i>NCRNA00185</i> ↑ <i>IQCG</i> ↑

Abbreviations: p65<sup>high</sup>, p65 immunohistochemistry results: ≥50% nuclear expression; p65<sup>low</sup>, p65 immunohistochemistry results: <50% nuclear expression; GCB, germinal center B-cell-like; ABC, activated B-cell-like; FDR, false discovery rate.

\*Upregulated genes in bold.



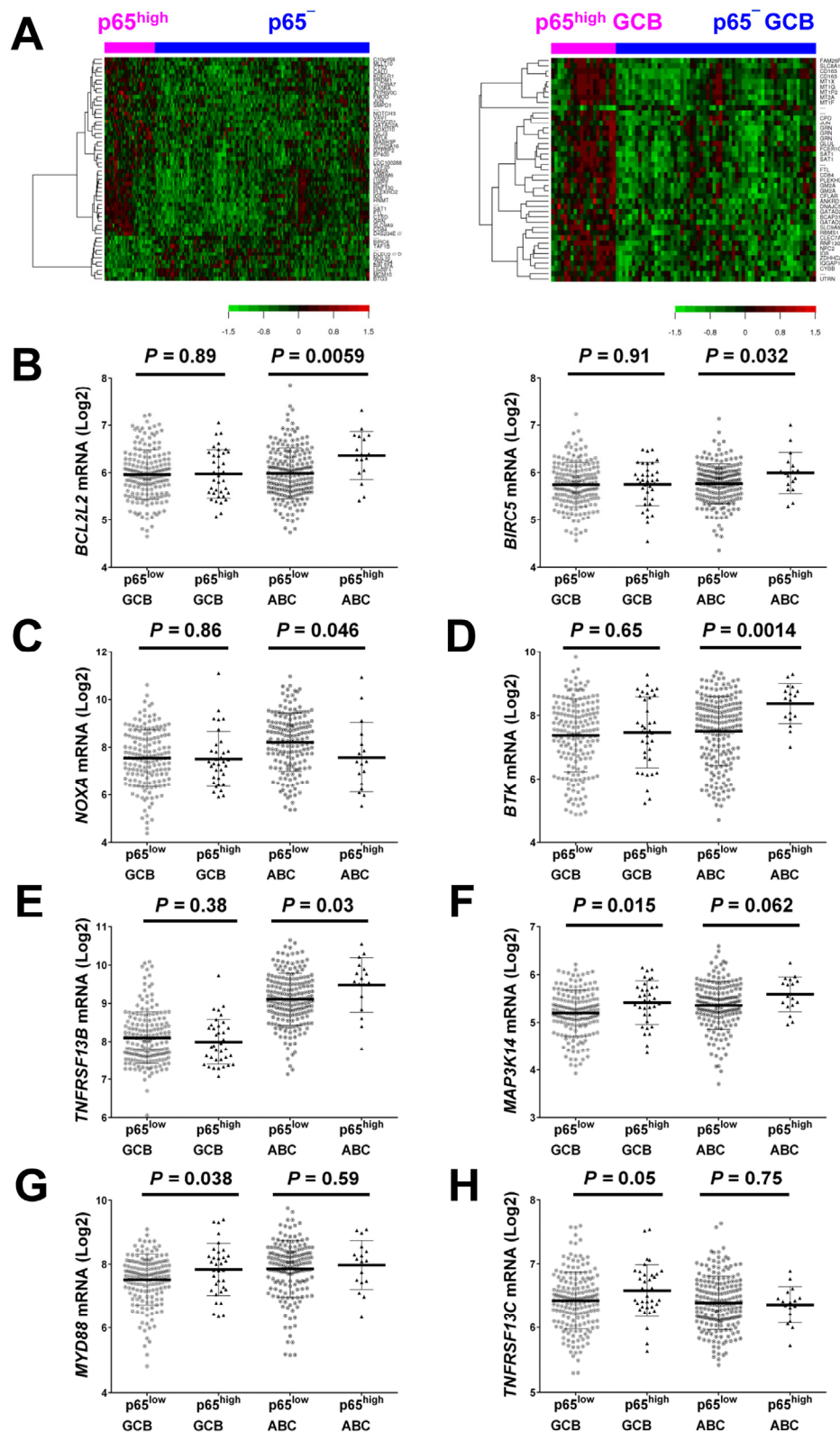


**Figure 3. Gene expression profiling analysis.** (A) Heatmaps for comparisons between DLBCL patients with p65<sup>high</sup> expression (IHC ≥50%) and those without p65 nuclear expression (IHC <10%) in the overall and GCB-DLBCL cohorts (FDR <0.15 and FDR <0.05, respectively). (B) *BIRC5/survivin* and *BCL2L2* were significantly upregulated in p65<sup>high</sup> ABC-DLBCL. (C) *NOXA/PMAIP1* was significantly downregulated in p65<sup>high</sup> ABC-DLBCL. (D-E) *BTK* and *TNFRSF13B* were significantly upregulated in the p65<sup>high</sup> group in ABC-DLBCL but not in GCB-DLBCL. (F-H) *MAP3K14/NIK*, *MYD88*, and *TNFRSF13C* were significantly upregulated in the p65<sup>high</sup> group in GCB-DLBCL but not in ABC-DLBCL.

GEP suggested that in GCB-DLBCL, instead of antiapoptotic mechanisms, dysregulations in immune responses and tumor microenvironment may be relevant for the poor prognosis associated with p55<sup>high</sup>. Such immune signatures included *FCER1G* (Fc fragment of IgE high affinity I receptor for gamma subunit), 2.21-fold upregulation, *CYBB* (critical component of phagocytes generating superoxide), 1.77-fold upregulation, granulin gene *GRN*, 1.63-fold upregulation, *LILRB1* (a MHC class I receptor resulting in immunosuppression), 1.49-fold upregulation, *CD163* (an antigen exclusively expressed in monocytes and macrophages), 2.46-fold upregulation, and *CD84* (an

adhesion molecule involved in regulating receptor-mediated signaling in immune cells), 1.55-fold upregulation. In the GEP comparison in overall DLBCL, a few immune-related genes were also found up- or down-regulated in p55<sup>high</sup> DLBCL compared with p55<sup>low</sup> DLBCL, including upregulation of *LCP2* (lymphocyte cytosolic protein 2, involved in T cell receptor signaling, 1.27-fold) and *TEK* (anti-inflammatory, 1.21-fold), and downregulation of *UHRF1* (an epigenetic regulator promoting proliferation of immunosuppressive Treg cell, 1.48-fold downregulation) [43] in p55<sup>high</sup> DLBCL (Table 3).

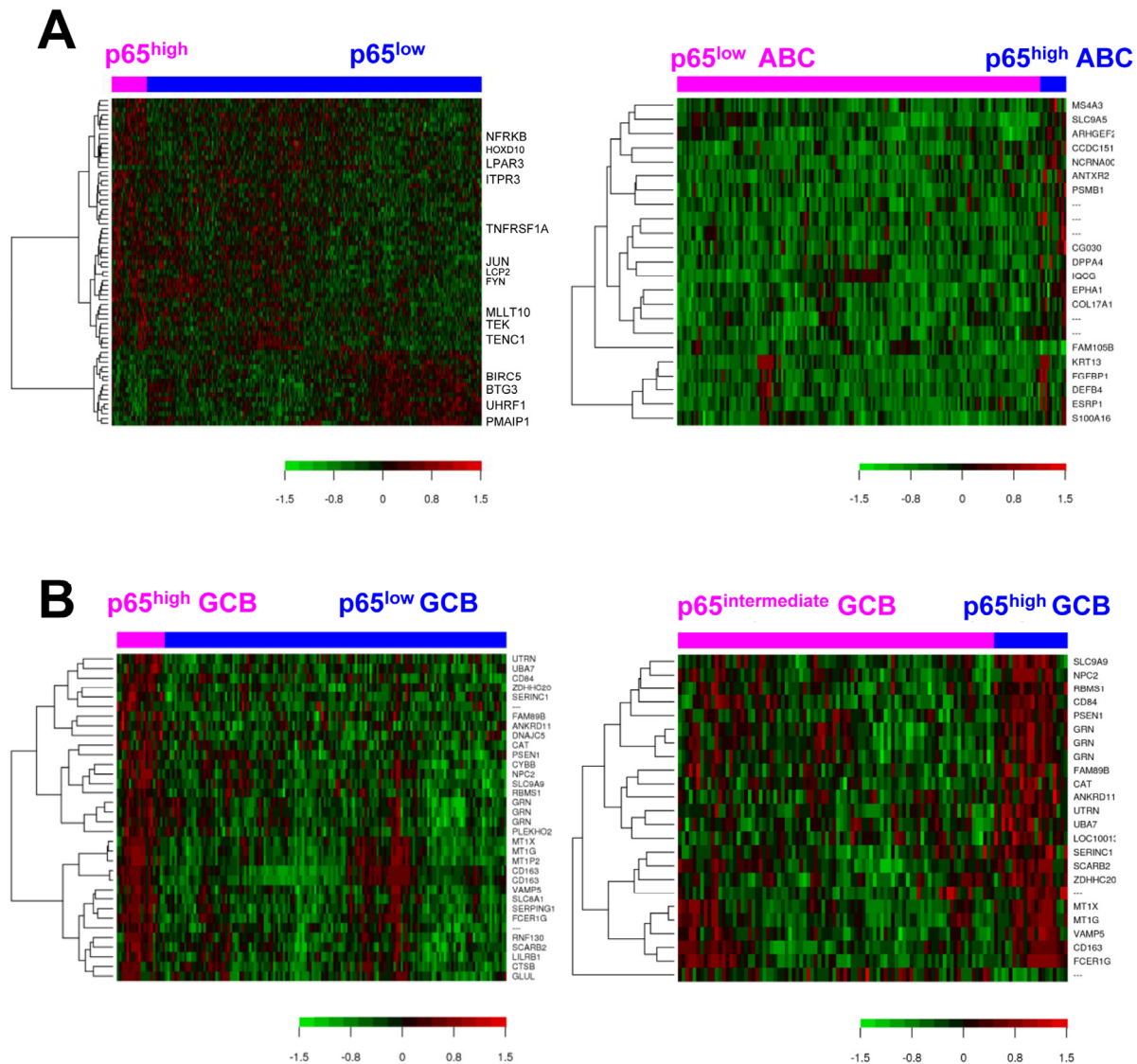


**Figure 4. Gene expression analysis for p55 hyperactivation in diffuse large B-cell lymphoma (DLBCL).** (A) Heatmaps for gene differentially expressed between p55<sup>high</sup> (IHC ≥50%) and p55<sup>low</sup> (IHC <50%) patients in DLBCL overall and in ABC-DLBCL (false discovery rate <0.30 and <0.20, respectively). (B) Heatmaps for genes differentially expressed between p55<sup>high</sup> (IHC ≥50%) and p55<sup>low</sup> (IHC <50%) patients and between p55<sup>high</sup> (IHC ≥50%) and p55<sup>intermediate</sup> (IHC 10-40%) patients with germinal center B-cell-like DLBCL (false discovery rate <0.05 and <0.20, respectively).

**Table 4. Differentially expressed genes between p65<sup>high</sup> vs. p65<sup>-</sup> patients with diffuse large B-cell lymphoma (DLBCL) in the overall cohort and in the germinal-center-B-cell-like subgroup.**

Functional categories	p65 <sup>high</sup> vs. p65 <sup>-</sup> DLBCL (FDR <0.15)	p65 <sup>high</sup> GCB vs. p65 <sup>-</sup> GCB (FDR <0.05)
Signaling, ion channels	<i>IL10RA</i> ↑ <i>GPS2</i> /// <i>D4S234E</i> ↑ <i>NOTCH3</i> ↑ <i>VAV1</i> ↑	<i>FAM26F</i> ↑ <i>MT1X</i> ↑ <i>MT1G</i> ↑ <i>MT2A</i> ↑ <i>MT1F</i> ↑ <i>CFLAR</i> ↑ <i>CLEC7A</i> ↑
Immune responses, inflammation	<i>GRN</i> ↑	<i>CD163</i> ↑ <i>GRN</i> ↑ <i>FCER1G</i> ↑ <i>CD84</i> ↑ <i>CYBB</i> ↑
Cell cycle, DNA metabolism, transcription and translation regulation	<i>JUN</i> ↑ <i>PRDM1</i> ↑ <i>GATAD2A</i> ↑ <i>TCF25</i> ↑ <i>MLLT10</i> ↑ <i>EP400</i> ↑ <i>HOXD10</i> ↑ <i>TAF1B</i> ↓ <i>ZNF254</i> ↓ <i>RPL37A</i> ↓ <i>UHRF1</i> ↓ <i>MCM10</i> ↓ <i>BTG3</i> ↓	<i>JUN</i> ↑ <i>GATAD2A</i> ↑ <i>RBMS1</i> ↑
Apoptosis	<i>TMBIM6</i> ↑ <i>RNF130</i> ↑ <i>BIRC6</i> ↓	<i>RNF130</i> ↑
Metabolism, redox regulation	<i>SLC9A9</i> ↑ <i>ATP6V0C</i> ↑ <i>SLC25A16</i> ↑ <i>SAT1</i> ↑ <i>SMPD1</i> ↑ <i>C10orf58</i> ↑ <i>HNMT</i> ↑ <i>GTPBP2</i> ↑	<i>CPD</i> ↑ <i>GLUL</i> ↑ <i>SAT1</i> ↑ <i>FTL</i> ↑ <i>ANKRD11</i> ↑ <i>SLC9A9</i> ↑
Transport, trafficking, protein folding, modification	<i>NPC2</i> ↑ <i>WASH3P</i> ↑ <i>FTL</i> ↑ <i>GM2A</i> ↑ <i>KDELR1</i> ↑ <i>SLC39A7</i> ↑ <i>CTSD</i> ↑ <i>CALU</i> ↑	<i>SLC8A1</i> ↑ <i>GM2A</i> ↑ <i>DNAJC5</i> ↑ <i>BCAP31</i> ↑ <i>NPC2</i> ↑
Cell adhesion, cytoskeleton, collagen, extracellular matrix	<i>ITGB2</i> ↑ <i>MYLK</i> ↑ <i>CD84</i> ↑ <i>FMOD</i> ↑	<i>IQGAP1</i> ↑ <i>UTRN</i> ↑
Degradation	<i>CTSZ</i> ↑ <i>IDS</i> ↑	<i>IDS</i> ↑
lncRNA genes, other function	<i>PLEKHO2</i> ↑ <i>LOC100288142</i> /// <i>NBPF1</i> /// <i>NBPF10</i> ↑ <i>CCHCR1</i> ↑ <i>IGLJ3</i> ↑ <i>DLEU2</i> /// <i>DLEU2L</i> ↓ <i>NOL10</i> ↓	<i>MT1P2</i> ↑ <i>PLEKHO2</i> ↑ <i>ZDHHC20</i> ↑

Abbreviations: p65<sup>high</sup>, high p65 nuclear expression (immunohistochemistry results: ≥50%); p65<sup>-</sup>, negative p65 nuclear expression (immunohistochemistry results: <10%); FDR, false discovery rate. \*Upregulated genes in bold.

These data indicated that the antiapoptotic and proliferation function of p65 was primarily activated in ABC-DLBCL, whereas immune dysregulation might be more relevant for the significantly adverse impact of p65 hyperactivation in GCB-DLBCL. We further analyzed the expression of p65-activating upstream signals in GCB- and ABC-DLBCL. *TNFRSF1A* encoding a TNF-α receptor which can activate NF-κB by degrading inhibitory IκBα (canonical activation), was upregulated in the overall p65<sup>high</sup> group than in the overall p65<sup>low</sup> group ( $P = 0.0001$ ). *LPAR3* which encodes a receptor for lyso-phosphatidic acid/LPA was downregulated in p65<sup>high</sup> DLBCL. In the ABC-DLBCL subset only, *PSMB1*, which encodes a 20S core beta subunit of the proteasome B-type family, was upregulated in p65<sup>high</sup> compared with p65<sup>low</sup> patients (suggesting canonical activation of NF-κB). Bruton tyrosine kinase gene *BTK* which plays an important role in BCR signaling activation (canonical activation), and *TNFRSF13B* which encodes the tumor necrosis factor

receptor for APRIL and BAFF were significantly upregulated in p65<sup>high</sup> ABC-DLBCL but not in p65<sup>high</sup> GCB-DLBCL (Fig. 3D-E). In comparison, in GCB-DLBCL but not in ABC-DLBCL, *TNFRSF13C* which encodes the receptor specific for BAFF (non-canonical activation), *MYD88* which encodes an adapter protein essential for the Toll-like receptor (TLR) and interleukin-1 receptor signaling pathways, and *MAP3K14/NIK* which is involved in non-canonical activation of NF-κB were significantly upregulated in the p65<sup>high</sup> compared with p65<sup>low</sup> group (Fig. 3F-H).

### Targeting NF-κB in DLBCL cells

#### Molecular inhibition of constitutive NF-κB activation in DLBCL cell lines

First, we examined whether specific inhibition of NF-κB was sufficient to block cell survival by over-expressing a super repressor mutant form of IκBα

(pCMV-I $\kappa$ B $\alpha$ M) in a representative DLBCL cell line, MS, that has been previously shown to have constitutive NF- $\kappa$ B activation [44]. I $\kappa$ B $\alpha$ M binds to NF- $\kappa$ B subunits but cannot be phosphorylated on the basis of alanine substitution for serines 32 and 36, acting as a dominant negative (DN) and thereby preventing the NF- $\kappa$ B subunits from translocating into the nucleus. Transient

transfection (70-80 efficiency and 75% viability) of a DLBCL-MS cell line with the DN-I $\kappa$ B $\alpha$ M leads to the induction of I $\kappa$ B $\alpha$  protein level while suppressing constitutive NF- $\kappa$ B activation (Fig. 5A). In addition, cells over-expressing the DN-I $\kappa$ B $\alpha$ M are prone to apoptosis as demonstrated by Annexin V binding assays (Fig. 5B). This result suggests that constitutive NF- $\kappa$ B

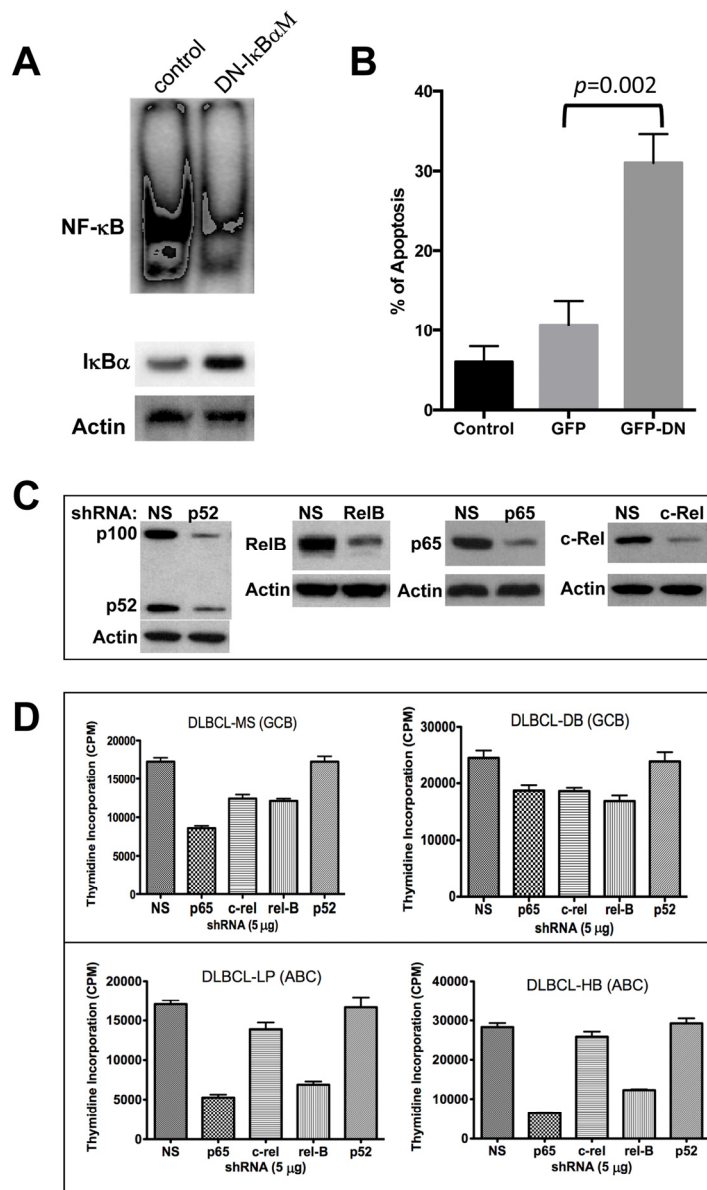


**Figure 5. Molecular targeting of NF- $\kappa$ B in diffuse large B-cell lymphoma (DLBCL) cell lines.** (A) DLBCL-MS cells were transfected with empty control vector or a pCMV-I $\kappa$ B $\alpha$ M vector for 24 hrs. Nuclear extracts (10  $\mu$ g) were analyzed for NF- $\kappa$ B expression by EMSA. Cytoplasmic extracts were assessed for I $\kappa$ B $\alpha$  and actin protein expression by Western blotting. (B) Transfected cells from part A were also assessed for apoptosis after 24 hours of incubation using annexin V assays. (C) MS cells were transfected with plasmids expressing the p52, RelB, p65, c-Rel, or a non-specific (NS) shRNA. Forty-eight hours post-transfection, proteins were extracted and analyzed for NF- $\kappa$ B component inhibition by Western blot. (D) Indicated DLBCL cell lines were transfected with the validated green fluorescent protein (GFP)-plasmid-based shRNA for each of the NF- $\kappa$ B subunits. After 16 hours, GFP-positive cells were sorted and assessed using proliferation assays. Data represent two independent experiments with triplicate samples. **Abbreviations:** GCB, germinal center B-cell-like; ABC, activated B-cell-like, DN, dominant negative.



activation is required for the survival of this cell line. To determine the functional significance of each NF- $\kappa$ B subunit on growth and survival regulation in DLBCL, we used specific validated shRNAs to selectively silence each NF- $\kappa$ B component individually in four representative DLBCL cell lines (two GCB-DLBCLs, two ABC-DLBCLs). These validated shRNAs inhibited endogenous NF- $\kappa$ B by more than 70% (Fig. 5C). Except for p52, downregulation of p65, c-Rel, and RelB protein expression with individual shRNAs inhibited DLBCL cell growth (thymidine incorporation assay), and inhibition of p65 was most effective (Fig. 5D), particularly in cell lines with mutated p53 (MS, LP and HB).

### Pharmacological targeting of constitutive NF- $\kappa$ B activation in DLBCL cells

To evaluate the effects of pharmacological inhibition of NF- $\kappa$ B activation on transcription activities of NF- $\kappa$ B subunits and DLBCL cell growth and survival, we select-

ed the proteasome inhibitor bortezomib (BZ), and the small molecule NF- $\kappa$ B inhibitor BAY 11-7082 (BAY-11) that selectively inhibits the phosphorylation and degradation of I $\kappa$ B $\alpha$  [45-47] in MS (GCB-DLBCL) cells.

To ascertain whether BZ or BAY-11 has an effect on constitutive NF- $\kappa$ B activation in DLBCL cells, we performed EMSA with nuclear extracts purified from BZ- or BAY-11-treated GCB-DLBCL cell line (MS). After BZ or BAY-11 treatment, NF- $\kappa$ B DNA-binding activity (Fig. 6A) and the level of phosphorylated-I $\kappa$ B $\alpha$  (Fig. 6B) gradually declined in a dose-dependent manner in the MS DLBCL cell line. Confocal microscopy analysis also demonstrated that BZ or BAY-11 treatment inhibits the nuclear accumulation of p50 and p65 NF- $\kappa$ B subunits, leading to DNA fragmentation, indicative of cells undergoing apoptosis (Fig. 6C). Next, we evaluated the effects of BZ or BAY-11 on DLBCL cell viability using *in vitro* proliferation assays in four representative DLBCL cell

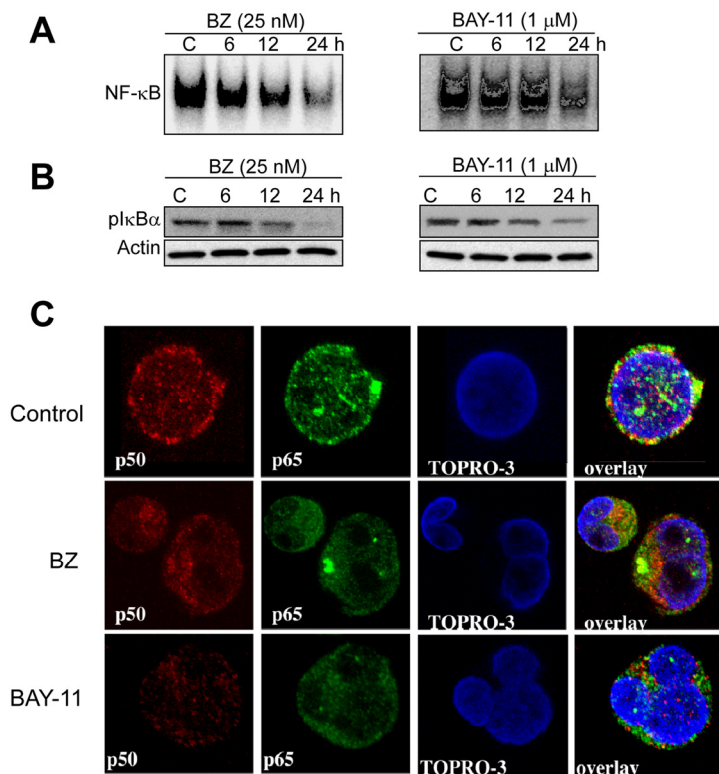


**Figure 6. Pharmacological inhibition of constitutive NF- $\kappa$ B activation in DLBCL cells.** (A-B) DLBCL cells (MS) were cultured in the presence of bortezomib (BZ, 25 nM) or BAY-11 (1  $\mu$ M) for the indicated time points (hours). Nuclear extracts were purified and subjected to EMSA analyzed for NF- $\kappa$ B DNA binding activity; cytoplasmic extracts were subjected to immunoblotting for pI $\kappa$ B $\alpha$  and actin. (C) DLBCL-MS cells cultured in the presence of bortezomib (BZ, 25 nM) or BAY-11 (1  $\mu$ M) for 24 hours and then analyzed for p50 (red) and p65 (green) protein expression by confocal microscopy analysis. Topro-3 (blue) serves as a nuclear staining marker.

lines (two ABC, two GCB). Both BZ and BAY-11 inhibited cell proliferation in the representative DLBC

cell lines in a dose-dependent manner (Fig. 7A). BZ and BAY-11 inhibit NF- $\kappa$ B by different mechanisms, as we

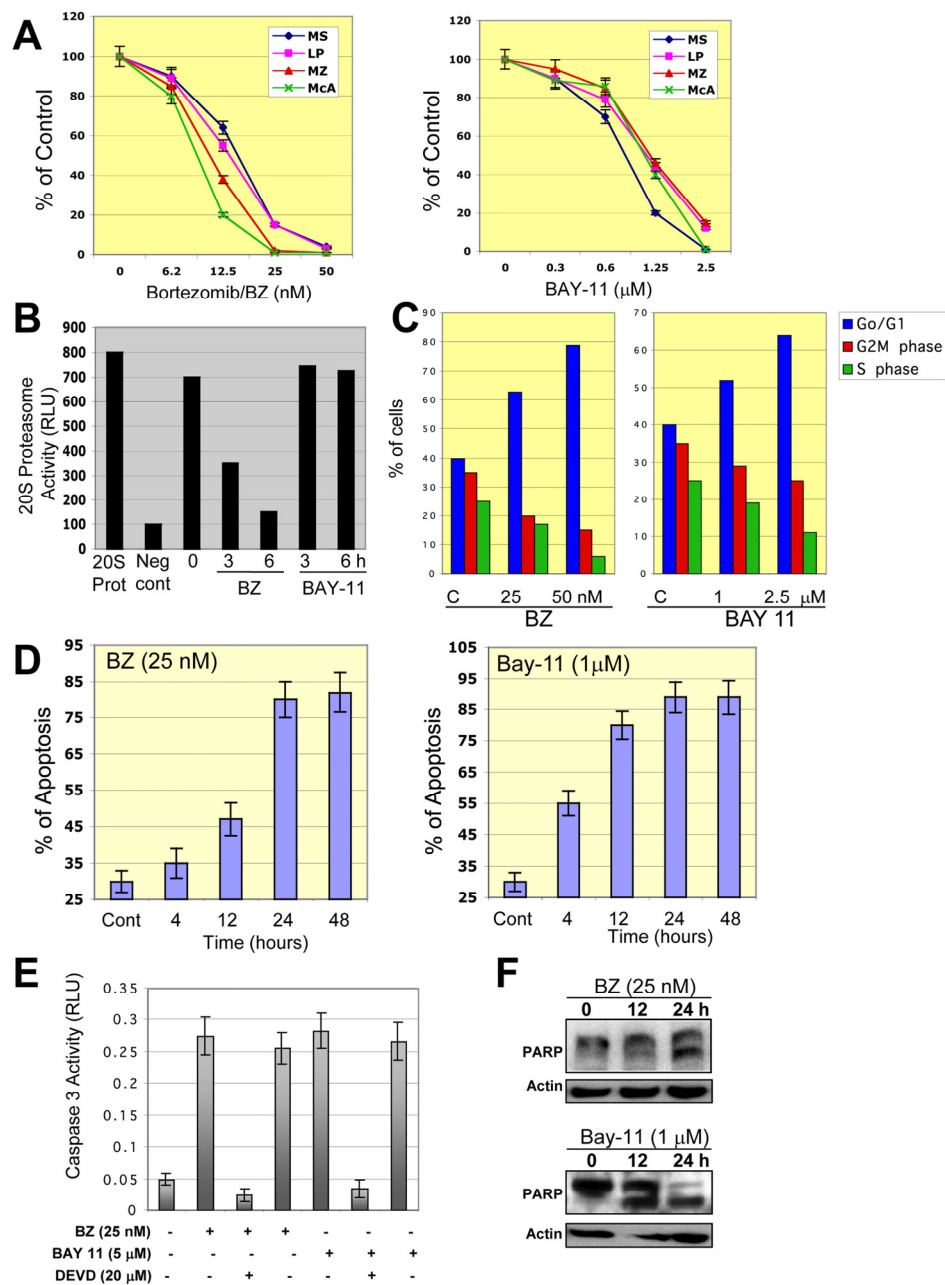


**Figure 7. Inhibition of NF- $\kappa$ B in DLBCL cells leads to cell growth inhibition, G0/G1 cell cycle arrest, and apoptosis.** (A) Representative ABC- and GCB-DLBCL cell lines were treated with bortezomib (BZ) or BAY-11 for 48 hours and cell proliferation was measured using 3H-thymidine incorporation assays. The percentages of growth inhibition of treated cells relative to untreated (control cells) were plotted. The data shown are the means and ranges of triplicate cultures from three independent experiments. (B) DLBCL-MS cells were cultured in the absence or presence of bortezomib (BZ) or BAY-11 and subjected to a 20S proteasome assay. Purified 20S proteasome was used as a positive control. **Abbreviations:** RLU, relative light unit; 20S pro, 20S proteasome, Neg Cont., negative control. (C) DLBCL-MS cells were cultured in the absence or presence of BZ (50 nM) or BAY-11 (1 μM) and analyzed for cell cycle profile. The percentages of cells in G0/G1, S, and G2M phases are shown. (D) DLBCL-MS cells were cultured in the absence or presence of BZ (50 nM) or BAY-11 (1 μM) for the indicated time points and then analyzed for apoptosis using annexin V assays. (E) DLBCL-MS cells were cultured in the presence of BZ (50 nM) or BAY-11 (1 μM) and in some cases with the caspase 3 inhibitor DEVD or the caspase 1 inhibitor VAD. Caspase 3 activity was measured after 24 hours of treatments. Caspase 3 activity was observed after 12 hours of treatment. **Abbreviations:** RLU, relative light units. (F) DLBCL-MS cells were cultured in the presence of BZ (50 nM) or BAY-11 (1 μM) for the indicated time points and cell extracts were subjected to Western blotting for a known caspase substrate, poly-(ADP-ribose) polymerase (PARP) cleavage.



analyzed the cell lysates from BZ-treated and BAY-11-treated DLBCL-MS cells to a 20S proteasome proteolysis assay, and found proteasome activity was substantially inhibited (>50%) after 3 hours of BZ treatment, whereas BAY-11 treatment did not affect proteasome activity in a similar time points (Fig. 7B). To determine whether the cell growth inhibition effects of BZ and BAY-11 involve their activity in the cell cycle regulation, we analyzed the cell cycle profile. As shown in Fig. 7C, in a representative DLBCL cell line (MS), both BZ-and BAY-11-treated DLBCL cells accumulated in the G0/G1 phase of the cell cycle, while cells in G2M and S phases were decreased. In addition, BZ or BAY-11 treatments in MS DLBCL cell line resulting in cells undergoing apoptosis in a time-dependent manner (Fig. 7D). To verify that these cells had actually undergone apoptosis, we measured the generation of caspase 3 activities. DLBCL cells treated with BZ or BAY-11 activated caspase 3 activity after 12 hours of treatment, which can be block with a caspase 3 inhibitor (DVED) but not with a caspase 1 inhibitor (VAD) (Fig. 7E). In addition, a known caspase substrate, poly-(ADP-ribose) polymerase (PARP), was cleaved after BZ or BAY-11 treatment (Fig. 7F). These experiments provide additional and interesting insights into the putative role of NF- $\kappa$ B in DLBCL cell proliferation and viability maintenance.

## DISCUSSION

In this study we studied the significance of RelA/p65 NF- $\kappa$ B in DLBCL by two ways. In the first part of this study, we evaluated the prognostic significance of RelA/p65 nuclear expression in a large cohort of *de novo* DLBCL treated with R-CHOP ( $n = 487$ ). Although p65 nuclear expression may not be a strong prognostic marker in overall DLBCL, we found p65 hyperactivation (IHC  $\geq 50\%$ ) had significant adverse impact on survival of patients with stage I/II DLBCL independent of cell-of-origin and *TP53* mutation status, even though it was not associated with apparent genetic or phenotypic abnormalities, such as *TP53* mutations, *MYC/BCL2* translocation, and *Myc/Bcl-2* overexpression.

The adverse prognostic significance of p65 hyperactivation was also seen in the GCB-DLBCL subtype overall and in the subset with wild-type *TP53*, but not in the subsets with strong unfavorable factors including advanced stages, *TP53* mutations, and ABC cell-of-origin. In addition, lower levels (10-40%) of p65 nuclear expression did not have significant prognostic impact in DLBCL. This limited significance of p65 expression in DLBCL may reflect different signaling transductions pathways activating p65, different p65 NF- $\kappa$ B dimers, and complicated p65 functions influenced by other factors including p53 in different

stimulatory signals. For example, NF- $\kappa$ B p65 activation induced by cytotoxic stimuli promotes apoptosis in mouse embryo fibroblasts, which contrasts with the prosurvival function of p65 induced by inflammatory cytokines [30]. In various cancer cell lines, p65 and p53 formed p65/p53 complex and bound to DNA targets; the function of p65 and fate of tumor cells are significantly affected by p53 and stress levels [32]. Others have shown that there is transcriptional and functional crosstalk between NF- $\kappa$ B and p53. p53 can negatively regulate NF- $\kappa$ B activation by regulating *IKK1* expression [29] and suppressing glycolysis [28]; NF- $\kappa$ B and p53 antagonize each other's function in apoptosis, proliferation and tumor invasion that appears to depend on cellular context. Overall the results in this study suggested that p65 and wild-type p53 counteracted each other in DLBCL, and that the inhibition of p53 tumor suppressor function by p65 hyperactivation had a significant adverse impact on clinical outcomes.

GEP suggested that BCR, TNF, TLR, and mitogen-activated protein kinase signaling pathways were all implicated in p65 hyperactivation in DLBCL. These upstream pathways were activated preferably in ABC-DLBCL or GCB-DLBCL, and correspondingly, resulting in different downstream pathways in ABC and GCB subtypes. In ABC-DLBCL, p65<sup>high</sup> GEP signatures were featured by proliferation and anti-apoptosis, whereas in GCB-DLBCL in which subgroup p65 hyperactivation showed significant adverse prognostic impact, p65<sup>high</sup> expression was accompanied with upregulation of some pro-apoptosis genes as well as many immune genes. Upregulation of *LILRB1* and *CD163* in p65<sup>high</sup> patients suggested immune suppression and dysregulation, which may contribute to the associated poor prognosis.

In the second part of this study, we tested whether NF- $\kappa$ B p65 subunit in particular is a potential molecular target by the proteasome inhibitor bortezomib and the small molecule NF- $\kappa$ B inhibitor BAY-11 *in vitro*. Previous studies have shown that proteasome inhibitors have better antitumor efficacy in patients with ABC-DLBCL than in patients with GCB-DLBCL, probably due to higher p65 expression in the ABC subtype [45, 48, 52]. Consistently, our GEP analysis also found the proteasome gene *PSMB1* was upregulated in ABC-DLBCL. Our *in vitro* experiments found that these anti-NF- $\kappa$ B agents can effectively inhibit p65 protein expression and DNA binding activity, leading to cell cycle arrest, decreased cell proliferation, and apoptosis induction in both GCB and ABC types of p65-overexpressing DLBCL cell lines. Intriguingly, representative DLBCL cell lines with mutated p53 are more sensitive to p65 shRNA targeting approach as compared to a cell line with wild-type p53, opposite the

prognostic effects observed in the DLBCL study cohort. These findings may suggested that although p65 subunit only manifested prognostic significance in certain DLBCL subsets due to the complexity of NF- $\kappa$ B dimers and activating mechanisms, *in vitro* experiments nonetheless demonstrated that NF- $\kappa$ B overexpressing DLBCL cells were addictive to NF- $\kappa$ B and vulnerable for NF- $\kappa$ B inhibitors. This vulnerability of DLBCL cells was also apparent in the context of mutated p53; p65 may have an important role in the oncogenic activities of mutated p53 in DLBCL. Importantly, *in vitro* p65 subunit stood out as a critical factor in controlling cell growth and survival and showed the most sensitivity to molecular and pharmacological inhibition of NF- $\kappa$ B activation. Therefore, our current study in both patient samples and DLBCL cell lines provided additional insights into the putative roles of NF- $\kappa$ B p65 in immune regulation, DLBCL cell proliferation, and viability maintenance, and the utility of p65 as a biomarker to stratify DLBCL patients to receive alternative therapeutic regimens including agents targeting NF- $\kappa$ B [52]. However, these findings warrant further investigation and validation in more representative DLBCL cell lines as well as primary DLBCL cells.

In summary, we provide clinical and experimental data that RelA/p65 NF- $\kappa$ B has prognostic and therapeutic value in DLBCL. High p65 nuclear expression is a significant adverse biomarker in patients with early-stage (I/II) DLBCL. Pharmacological p65 inactivation effectively inhibited cell growth and survival in both GCB-DLBCL and ABC-DLBCL cell lines with p65 hyperactivation.

## METHODS

### Patients

The study cohort included 487 patients with *de novo* DLBCL treated with R-CHOP, as part of the International DLBCL R-CHOP Consortium Program. All patients were diagnosed as DLBCL between 2001 and 2012 according to the World Health Organization classification criteria, and did not have a history of low-grade B-cell lymphoma, primary mediastinal, cutaneous, central nervous system DLBCL, or human immunodeficiency virus infection. Informed consent was obtained from all patients. This study was conducted in accordance with the Helsinki Declaration and was approved by the Institutional Review Boards of all participating centers. GCB/ABC subtype classification by GEP or immuno-histochemistry algorithms [49], and *TP53* mutation detection using p53 AmpliChip [39] have been described previously. Overall survival (OS) was calculated from the date of

diagnosis to the date of death from any cause or the date of last follow-up for censored patients. Progression-free survival (PFS) was calculated from the date of diagnosis to the date of disease progression, recurrence, or patient death from any cause. Survival analysis was performed using the Kaplan-Meier method and the log-rank (Mantel-Cox) test. The clinical features of DLBCL patients with high or low levels of p65 at the time of presentation were compared using the chi-square test. Univariate survival analysis was performed using the GraphPad Prism 6 (GraphPad Software, San Diego, CA). Multivariate survival analysis was performed using the Cox regression model and SPSS software (version 19.0; IBM Corporation, Armonk, NY). *P* values  $\leq 0.05$  were considered statistically significant.

### Immunohistochemical staining

Immunohistochemistry for p65 and other NF- $\kappa$ B subunits using specific antibodies (Abcam, Cambridge, MA) was performed on tissue microarrays of formalin-fixed, paraffin-embedded lymphoma samples using methods described previously [10, 49]. The immunohistochemical stains were assessed in 10% increments by three pathologists blinded to the clinical outcomes. Disagreements about the percentage of positive cells were resolved by joint review at a multi-headed microscope.

### Gene expression profiling

GEP was performed using the Affymetrix GeneChip Human Genome U133 Plus 2.0 array (Santa Clara, CA) and CEL files were deposited in the NCBI Gene Expression Omnibus repository (GSE#31312) [49]. GEP were available for 444 DLBCL patients of this study cohort with high or low levels of p65 nuclear expression. The *P* values for differential expression obtained via multiple *t*-tests were corrected for false discovery rates using the beta-uniform mixture method.

### *In vitro* studies

#### Cell lines

Human DLBCL cell lines MS (mutated *TP53*) and DB (wild-type for p53) (GCB subtype), as well as LP (mutated *TP53*) and HB (mutated *TP53*) (ABC subtype) were previously characterized and described [44, 50]. The DLBCL cells were cultured in Roswell Park Memorial Institute medium (Life Technologies, Carlsbad, CA) containing 15% fetal calf serum and 1% penicillin/streptomycin (HyClone Laboratories, Logan, UT).

#### Antibodies and small hairpin RNA plasmids

The following primary antibodies were used: p50, p65, c-Rel and p52 (Millipore, Billerica, MA), and RelB

(Santa Cruz Biotechnology, Santa Cruz, CA). The SureSilencing small hairpin RNA (shRNA) green fluorescent protein (GFP)-based plasmids for the NF- $\kappa$ B subunits p52, p65, c-Rel, and RelB were purchased from SuperArray Biosciences (Frederick, MD). pCMV-I $\kappa$ B $\alpha$ M and control vectors were purchased from Clontech Laboratories (Mountain View, CA).

### Transfection

Transfection experiments in DLBCL cells with validated green fluorescent protein (GFP)-shRNAs were performed *in vitro* in representative transfectable DLBCL cells, using the Neon transfection system from Invitrogen (Life Technologies Corporation, Grand Island, NY) as described previously [44], and were repeated at least twice to verify reproducible experimental results. Twenty-four hours after transfection, GFP<sup>+</sup> cells were sorted by a fluorescence-activated cell sorter (FACS) flow cytometer and plated. Cell proliferation was measured 96 hours after sorting by thymidine incorporation assays, while some cells were lysed for Western blot analysis for NF- $\kappa$ B subunit inhibition. A set of four shRNA plasmids for each NF- $\kappa$ B subunit was tested and the optimal (>75%) gene knock-down shRNA plasmid was selected.

### Therapeutic NF- $\kappa$ B inhibition experiment

DLBCL cells were treated with increasing doses of bortezomib (0–50 nM), or organic compounds BAY 11-7082/BAY-11 (1  $\mu$ M) for 6–48 hours and subjected to cell proliferation assays, electromobility gel shift assay (EMSA), immunofluorescence, apoptosis detection assay, and cell cycle analysis according to the manufacturer's instructions or procedures as previously described [51]. Data are representative of three independent experiments.

### Thymidine incorporation assays

*In vitro* thymidine incorporation proliferation assays were performed as described previously<sup>1</sup>. Briefly, cells were plated (in triplicate) at  $4.0 \times 10^4$  cells/well in 200  $\mu$ l of RPMI 1640 with 10% FCS and the indicated reagents in a 96-well plate and incubated in 5% CO<sub>2</sub> at 37°C. After 72 h, each well was pulsed with 0.5  $\mu$ Ci/10  $\mu$ l of [<sup>3</sup>H]thymidine (Amersham, Arlington Heights, IL) for 16 h. Cells were harvested and the radioactivity was measured.

### CONFLICTS OF INTEREST

KHY receives research support from Roche Molecular System, Gilead Sciences Pharmaceutical, Seattle Genetics, Dai Sanyo Pharmaceutical, Adaptive Biotechnology, Incyte Pharmaceutical, and HTG Molecular Diagnostics. EDH is a Consultant for HTG

Molecular Diagnostics. BMP joins speakers Bureau for Celgene and Amgen, and a Consultant for Celgene.

### FUNDING

The work was supported by the National Cancer Institute/National Institutes of Health (R01CA138688, R01CA187415, and 1RC1CA146299 to KHY). This work was also partially supported by NSFC (81570203 to MZ and 81570204 to LL), the National Cancer Institute and National Institutes of Health grants P50CA136411 and P50CA142509, and by MD Anderson's Cancer Center Support Grant CA016672. MZ is the recipient of professorship award. KHY is also supported by The University of Texas MD Anderson Cancer Center Institutional Research and Development Fund, an Institutional Research Grant Award, an MD Anderson Cancer Center Lymphoma Specialized Programs on Research Excellence (SPORE) Research Development Program Award, an MD Anderson Cancer Center Myeloma SPORE Research Development Program Award, a Gundersen Lutheran Medical Foundation Award, the University Cancer Foundation via the Sister institution network Fund at The University of Texas MD Anderson Cancer Center and is partially supported by grants from the National Cancer Institute/National Institutes of Health (P50CA136411 and P50CA142509).

### REFERENCES

1. Abramson JS, Shipp MA. Advances in the biology and therapy of diffuse large B-cell lymphoma: moving toward a molecularly targeted approach. *Blood*. 2005; 106:1164–74. doi: 10.1182/blood-2005-02-0687
2. Sehn LH, Donaldson J, Chhanabhai M, Fitzgerald C, Gill K, Klasa R, MacPherson N, O'Reilly S, Spinelli JJ, Sutherland J, Wilson KS, Gascoyne RD, Connors JM. Introduction of combined CHOP plus rituximab therapy dramatically improved outcome of diffuse large B-cell lymphoma in British Columbia. *J Clin Oncol*. 2005; 23:5027–33. doi: 10.1200/JCO.2005.09.137
3. Alizadeh AA, Eisen MB, Davis RE, Ma C, Lossos IS, Rosenwald A, Boldrick JC, Sabet H, Tran T, Yu X, Powell JI, Yang L, Marti GE, et al. Distinct types of diffuse large B-cell lymphoma identified by gene expression profiling. *Nature*. 2000; 403:503–11. doi: 10.1038/35000501
4. Davis RE, Brown KD, Siebenlist U, Staudt LM. Constitutive nuclear factor kappaB activity is required for survival of activated B cell-like diffuse large B cell



- lymphoma cells. *J Exp Med.* 2001; 194:1861–74. doi: 10.1084/jem.194.12.1861
5. Kloo B, Nagel D, Pfeifer M, Grau M, Düwel M, Vincendeau M, Dörken B, Lenz P, Lenz G, Krappmann D. Critical role of PI3K signaling for NF-kappaB-dependent survival in a subset of activated B-cell-like diffuse large B-cell lymphoma cells. *Proc Natl Acad Sci USA.* 2011; 108:272–77. doi: 10.1073/pnas.1008969108
6. Roschewski M, Staudt LM, Wilson WH. Diffuse large B-cell lymphoma-treatment approaches in the molecular era. *Nat Rev Clin Oncol.* 2014; 11:12–23. doi: 10.1038/nrclinonc.2013.197
7. Ben-Neriah Y, Karin M. Inflammation meets cancer, with NF- $\kappa$ B as the matchmaker. *Nat Immunol.* 2011; 12:715–23. doi: 10.1038/ni.2060
8. Odqvist L, Montes-Moreno S, Sánchez-Pacheco RE, Young KH, Martín-Sánchez E, Cereceda L, Sánchez-Verde L, Pajares R, Mollejo M, Fresno MF, Mazon F, Ruiz-Marcellán C, Sánchez-Beato M, Piris MA. NF $\kappa$ B expression is a feature of both activated B-cell-like and germinal center B-cell-like subtypes of diffuse large B-cell lymphoma. *Mod Pathol.* 2014; 27:1331–37. doi: 10.1038/modpathol.2014.34
9. Espinosa I, Briones J, Bordes R, Brunet S, Martino R, Sureda A, Sierra J, Prat J. Activation of the NF-kappaB signalling pathway in diffuse large B-cell lymphoma: clinical implications. *Histopathology.* 2008; 53:441–49. doi: 10.1111/j.1365-2559.2008.03139.x
10. Ok CY, Xu-Monette ZY, Li L, Manyam GC, Montes-Moreno S, Tzankov A, Visco C, Dybkær K, Routbort MJ, Zhang L, Chiu A, Orazi A, Zu Y, et al. Evaluation of NF- $\kappa$ B subunit expression and signaling pathway activation demonstrates that p52 expression confers better outcome in germinal center B-cell-like diffuse large B-cell lymphoma in association with CD30 and BCL2 functions. *Mod Pathol.* 2015; 28:1202–13. doi: 10.1038/modpathol.2015.76
11. Oeckinghaus A, Ghosh S. The NF-kappaB family of transcription factors and its regulation. *Cold Spring Harb Perspect Biol.* 2009; 1:a000034. doi: 10.1101/cshperspect.a000034
12. Davis RE, Ngo VN, Lenz G, Tolar P, Young RM, Romesser PB, Kohlhammer H, Lam Y, Zhao H, Yang Y, Xu W, Shaffer AL, Wright G, et al. Chronic active B-cell-receptor signalling in diffuse large B-cell lymphoma. *Nature.* 2010; 463:88–92. doi: 10.1038/nature08638
13. Wan F, Lenardo MJ. The nuclear signaling of NF-kappaB: current knowledge, new insights, and future perspectives. *Cell Res.* 2010; 20:24–33. doi: 10.1038/cr.2009.137
14. Scheidereit C. I kappa B kinase complexes: gateways to NF-kappaB activation and transcription. *Oncogene.* 2006; 25:6685–705. doi: 10.1038/sj.onc.1209934
15. Chen FE, Huang DB, Chen YQ, Ghosh G. Crystal structure of p50/p65 heterodimer of transcription factor NF-kappaB bound to DNA. *Nature.* 1998; 391:410–13. doi: 10.1038/34356
16. Schmidt-Ullrich R, Mémet S, Lilienbaum A, Feuillard J, Raphaël M, Israel A. NF-kappaB activity in transgenic mice: developmental regulation and tissue specificity. *Development.* 1996; 122:2117–28.
17. Geymayer S, Doppler W. Activation of NF-kappaB p50/p65 is regulated in the developing mammary gland and inhibits STAT5-mediated beta-casein gene expression. *FASEB J.* 2000; 14:1159–70.
18. Li L, Xu-Monette ZY, Ok CY, Tzankov A, Manyam GC, Sun R, Visco C, Zhang M, Montes-Moreno S, Dybkær K, Chiu A, Orazi A, Zu Y, et al. Prognostic impact of c-Rel nuclear expression and REL amplification and crosstalk between c-Rel and the p53 pathway in diffuse large B-cell lymphoma. *Oncotarget.* 2015; 6:23157–80. doi: 10.18632/oncotarget.4319
19. Ganchi PA, Sun SC, Greene WC, Ballard DW. A novel NF-kappa B complex containing p65 homodimers: implications for transcriptional control at the level of subunit dimerization. *Mol Cell Biol.* 1993; 13:7826–35. doi: 10.1128/MCB.13.12.7826
20. Chen YQ, Sengchanthalangsy LL, Hackett A, Ghosh G. NF-kappaB p65 (RelA) homodimer uses distinct mechanisms to recognize DNA targets. *Structure.* 2000; 8:419–28. doi: 10.1016/S0969-2126(00)00123-4
21. Tsui R, Kearns JD, Lynch C, Vu D, Ngo KA, Basak S, Ghosh G, Hoffmann A. I $\kappa$ B $\beta$  enhances the generation of the low-affinity NF $\kappa$ B/RelA homodimer. *Nat Commun.* 2015; 6:7068. doi: 10.1038/ncomms8068
22. Kim HJ, Hawke N, Baldwin AS. NF-kappaB and IKK as therapeutic targets in cancer. *Cell Death Differ.* 2006; 13:738–47. doi: 10.1038/sj.cdd.4401877
23. Baldwin AS. Control of oncogenesis and cancer therapy resistance by the transcription factor NF-kappaB. *J Clin Invest.* 2001; 107:241–46. doi: 10.1172/JCI11991
24. Gasparini C, Celeghini C, Monasta L, Zauli G. NF-kappaB pathways in hematological malignancies. *Cellular and molecular life sciences. Cell Mol Life Sci.* 2014; 71:2083–102. doi: 10.1007/s00018-013-1545-4
25. Tergaonkar V, Pando M, Vafa O, Wahl G, Verma I. p53 stabilization is decreased upon NFkappaB activation: a role for NFkappaB in acquisition of resistance to chemotherapy. *Cancer Cell.* 2002; 1:493–503.

doi: 10.1016/S1535-6108(02)00068-5

26. Ak P, Levine AJ. p53 and NF- $\kappa$ B: different strategies for responding to stress lead to a functional antagonism. *FASEB J*. 2010; 24:3643–52. doi: 10.1096/fj.10-160549
27. Huang WC, Ju TK, Hung MC, Chen CC. Phosphorylation of CBP by IKK $\alpha$  promotes cell growth by switching the binding preference of CBP from p53 to NF- $\kappa$ B. *Mol Cell*. 2007; 26:75–87. doi: 10.1016/j.molcel.2007.02.019
28. Kawauchi K, Araki K, Tobiume K, Tanaka N. p53 regulates glucose metabolism through an IKK-NF- $\kappa$ B pathway and inhibits cell transformation. *Nat Cell Biol*. 2008; 10:611–18. doi: 10.1038/ncb1724
29. Gu L, Zhu N, Findley HW, Woods WG, Zhou M. Identification and characterization of the IKK $\alpha$  promoter: positive and negative regulation by ETS-1 and p53, respectively. *J Biol Chem*. 2004; 279:52141–49. doi: 10.1074/jbc.M407915200
30. Campbell KJ, Rocha S, Perkins ND. Active repression of antiapoptotic gene expression by RelA(p65) NF- $\kappa$ B. *Mol Cell*. 2004; 13:853–65. doi: 10.1016/S1097-2765(04)00131-5
31. Bohuslav J, Chen LF, Kwon H, Mu Y, Greene WC. p53 induces NF- $\kappa$ B activation by an IKK $\alpha$  kinase-independent mechanism involving phosphorylation of p65 by ribosomal S6 kinase 1. *J Biol Chem*. 2004; 279:26115–25. doi: 10.1074/jbc.M313509200
32. Schneider G, Henrich A, Greiner G, Wolf V, Lovas A, Wiecek M, Wagner T, Reichardt S, von Werder A, Schmid RM, Weih F, Heinzel T, Saur D, Krämer OH. Cross talk between stimulated NF- $\kappa$ B and the tumor suppressor p53. *Oncogene*. 2010; 29:2795–806. doi: 10.1038/onc.2010.46
33. Lowe JM, Menendez D, Bushel PR, Shatz M, Kirk EL, Troester MA, Garantzios S, Fessler MB, Resnick MA. p53 and NF- $\kappa$ B coregulate proinflammatory gene responses in human macrophages. *Cancer Res*. 2014; 74:2182–92. doi: 10.1158/0008-5472.CAN-13-1070
34. Zhao Q, Fu W, Jiang H, Du J, Zhang C, Xi H, Zhou F, Li R, Hou J. Clinicopathological implications of nuclear factor  $\kappa$ B signal pathway activation in diffuse large B-cell lymphoma. *Hum Pathol*. 2015; 46:524–31. doi: 10.1016/j.humpath.2014.06.032
35. Bavi P, Uddin S, Bu R, Ahmed M, Abubaker J, Balde V, Qadri Z, Ajarim D, Al-Dayel F, Hussain AR, Al-Kuraya KS. The biological and clinical impact of inhibition of NF- $\kappa$ B-initiated apoptosis in diffuse large B cell lymphoma (DLBCL). *J Pathol*. 2011; 224:355–66. doi: 10.1002/path.2864
36. Hu CR, Wang JH, Wang R, Sun Q, Chen LB. Both FOXP1 and p65 expression are adverse risk factors in diffuse large B-cell lymphoma: a retrospective study in China. *Acta Histochem*. 2013; 115:137–43. doi: 10.1016/j.acthis.2012.06.001
37. Shaffer AL 3rd, Young RM, Staudt LM. Pathogenesis of human B cell lymphomas. *Annu Rev Immunol*. 2012; 30:565–610. doi: 10.1146/annurev-immunol-020711-075027
38. Staudt LM. Oncogenic activation of NF- $\kappa$ B. *Cold Spring Harb Perspect Biol*. 2010; 2:a000109. doi: 10.1101/cshperspect.a000109
39. Xu-Monette ZY, Wu L, Visco C, Tai YC, Tzankov A, Liu WM, Montes-Moreno S, Dybkaer K, Chiu A, Orazi A, Zu Y, Bhagat G, Richards KL, et al. Mutational profile and prognostic significance of TP53 in diffuse large B-cell lymphoma patients treated with R-CHOP: report from an International DLBCL Rituximab-CHOP Consortium Program Study. *Blood*. 2012; 120:3986–96. doi: 10.1182/blood-2012-05-433334
40. Hu S, Xu-Monette ZY, Tzankov A, Green T, Wu L, Balasubramanyam A, Liu WM, Visco C, Li Y, Miranda RN, Montes-Moreno S, Dybkaer K, Chiu A, et al. MYC/BCL2 protein coexpression contributes to the inferior survival of activated B-cell subtype of diffuse large B-cell lymphoma and demonstrates high-risk gene expression signatures: a report from The International DLBCL Rituximab-CHOP Consortium Program. *Blood*. 2013; 121:4021–31. doi: 10.1182/blood-2012-10-460063
41. Tzankov A, Xu-Monette ZY, Gerhard M, Visco C, Dirnhofer S, Gisin N, Dybkaer K, Orazi A, Bhagat G, Richards KL, Hsi ED, Choi WW, van Krieken JH, et al. Rearrangements of MYC gene facilitate risk stratification in diffuse large B-cell lymphoma patients treated with rituximab-CHOP. *Mod Pathol*. 2014; 27:958–71. doi: 10.1038/modpathol.2013.214
42. Xu-Monette ZY, Dabaja BS, Wang X, Tu M, Manyam GC, Tzankov A, Xia Y, Zhang L, Sun R, Visco C, Dybkaer K, Yin L, Chiu A, et al. Clinical features, tumor biology, and prognosis associated with MYC rearrangement and Myc overexpression in diffuse large B-cell lymphoma patients treated with rituximab-CHOP. *Mod Pathol*. 2015; 28:1555–73. doi: 10.1038/modpathol.2015.118
43. Obata Y, Furusawa Y, Endo TA, Sharif J, Takahashi D, Atarashi K, Nakayama M, Onawa S, Fujimura Y, Takahashi M, Ikawa T, Otsubo T, Kawamura YI, et al. The epigenetic regulator Uhrf1 facilitates the proliferation and maturation of colonic regulatory T cells. *Nat Immunol*. 2014; 15:571–79. doi: 10.1038/ni.2886



44. Pham LV, Fu L, Tamayo AT, Bueso-Ramos C, Drakos E, Vega F, Medeiros LJ, Ford RJ. Constitutive BR3 receptor signaling in diffuse, large B-cell lymphomas stabilizes nuclear factor- $\kappa$ B-inducing kinase while activating both canonical and alternative nuclear factor- $\kappa$ B pathways. *Blood*. 2011; 117:200–10. doi: 10.1182/blood-2010-06-290437
45. Dunleavy K, Pittaluga S, Czuczman MS, Dave SS, Wright G, Grant N, Shovlin M, Jaffe ES, Janik JE, Staudt LM, Wilson WH. Differential efficacy of bortezomib plus chemotherapy within molecular subtypes of diffuse large B-cell lymphoma. *Blood*. 2009; 113:6069–76. doi: 10.1182/blood-2009-01-199679
46. Mori N, Yamada Y, Ikeda S, Yamasaki Y, Tsukasaki K, Tanaka Y, Tomonaga M, Yamamoto N, Fujii M. Bay 11-7082 inhibits transcription factor NF- $\kappa$ B and induces apoptosis of HTLV-I-infected T-cell lines and primary adult T-cell leukemia cells. *Blood*. 2002; 100:1828–34. doi: 10.1182/blood-2002-01-0151
47. Buhrmann C, Mobasher A, Busch F, Aldinger C, Stahlmann R, Montaseri A, Shakibaei M. Curcumin modulates nuclear factor  $\kappa$ B (NF- $\kappa$ B)-mediated inflammation in human tenocytes in vitro: role of the phosphatidylinositol 3-kinase/Akt pathway. *J Biol Chem*. 2011; 286:28556–66. doi: 10.1074/jbc.M111.256180
48. Wilson WH. Treatment strategies for aggressive lymphomas: what works? *Hematology (Am Soc Hematol Educ Program)*. 2013; 2013:584–90. doi: 10.1182/asheducation-2013.1.584
49. Visco C, Li Y, Xu-Monette ZY, Miranda RN, Green TM, Li Y, Tzankov A, Wen W, Liu WM, Kahl BS, d'Amore ES, Montes-Moreno S, Dybkær K, et al. Comprehensive gene expression profiling and immunohistochemical studies support application of immunophenotypic algorithm for molecular subtype classification in diffuse large B-cell lymphoma: a report from the International DLBCL Rituximab-CHOP Consortium Program Study. *Leukemia*. 2012; 26:2103–13. doi: 10.1038/leu.2012.83
50. Pham LV, Tamayo AT, Li C, Bueso-Ramos C, Ford RJ. An epigenetic chromatin remodeling role for NFATc1 in transcriptional regulation of growth and survival genes in diffuse large B-cell lymphomas. *Blood*. 2010; 116:3899–906. doi: 10.1182/blood-2009-12-257378
51. Pham LV, Tamayo AT, Yoshimura LC, Lo P, Ford RJ. Inhibition of constitutive NF- $\kappa$ B activation in mantle cell lymphoma B cells leads to induction of cell cycle arrest and apoptosis. *J Immunol*. 2003; 171:88–95. doi: 10.4049/jimmunol.171.1.88
52. Yu L, Li L, Medeiros LJ, Young KH. NF- $\kappa$ B signaling pathway and its potential as a target for therapy in lymphoid neoplasms. *Blood Rev*. 2016; S0268-960X(16)30046-7.

## Discovery of piperlongumine as a potential novel lead for the development of senolytic agents

Yingying Wang<sup>1,2</sup>, Jianhui Chang<sup>1,2</sup>, Xingui Liu<sup>1</sup>, Xuan Zhang<sup>1</sup>, Suping Zhang<sup>1,2</sup>, Xin Zhang<sup>1,2</sup>, Daohong Zhou<sup>1,2</sup>, Guangrong Zheng<sup>1</sup>

<sup>1</sup>Department of Pharmaceutical Sciences, College of Pharmacy, University of Arkansas for Medical Sciences, Little Rock, AR 72205, USA

<sup>2</sup>Winthrop P. Rockefeller Cancer Institute, University of Arkansas for Medical Sciences, Little Rock, AR 72205, USA

**Correspondence to:** Daohong Zhou, Guangrong Zheng; **email:** [dzhou@uams.edu](mailto:dzhou@uams.edu), [gzheng@uams.edu](mailto:gzheng@uams.edu)

**Keywords:** piperlongumine, aging, senescent cells, senolytic agents, ABT-263, reactive oxygen species, synergistic effect

**Received:** July 13, 2016    **Accepted:** November 4, 2016    **Published:** November 19, 2016

### ABSTRACT

Accumulating evidence indicates that senescent cells play an important role in many age-associated diseases. The pharmacological depletion of senescent cells (SCs) with a “senolytic agent”, a small molecule that selectively kills SCs, is a potential novel therapeutic approach for these diseases. Recently, we discovered ABT-263, a potent and highly selective senolytic agent, by screening a library of rationally-selected compounds. With this screening approach, we also identified a second senolytic agent called piperlongumine (PL). PL is a natural product that is reported to have many pharmacological effects, including anti-tumor activity. We show here that PL preferentially killed senescent human WI-38 fibroblasts when senescence was induced by ionizing radiation, replicative exhaustion, or ectopic expression of the oncogene *Ras*. PL killed SCs by inducing apoptosis, and this process did not require the induction of reactive oxygen species. In addition, we found that PL synergistically killed SCs in combination with ABT-263, and initial structural modifications to PL identified analogs with improved potency and/or selectivity in inducing SC death. Overall, our studies demonstrate that PL is a novel lead for developing senolytic agents.

### INTRODUCTION

Cellular senescence, an essentially irreversible arrest of cell proliferation, can be triggered when cells experience a potential risk for malignant transformation due to the activation of oncogenes and/or DNA damage [1-7]. While eliminating aged or damaged cells by inducing senescence is an effective barrier to tumorigenesis, the accumulation of senescent cells (SCs) over time compromises normal tissue function and contributes to aging and the development of age-associated diseases [6, 8, 9]. Often, SCs secrete a broad spectrum of pro-inflammatory cytokines, chemokines, growth factors, and extracellular matrix proteases, a feature collectively termed the senescence-associated secretory phenotype. These factors degrade the local tissue environment and induce inflammation in various tissues and organs if SCs are not effectively cleared by immune system [6, 8-11].

Studies have shown that the genetic clearance of SCs extends the lifespan of mice and delays the onset of several age-associated diseases in both progeroid and naturally-aged mice [12-15]. It has also been shown that rapamycin and metformin increase lifespan in mice and marmoset monkeys, by suppressing the induction of senescence [16-20]. These findings support the hypothesis that SCs play a causative role in aging and age-associated diseases [6, 21, 22] and, importantly, highlight the tremendous therapeutic potential of pharmacologically targeting SCs [23, 24]. Consistent with these findings, we have shown that ABT-263 (navitoclax), an inhibitor of the antiapoptotic Bcl-2 family proteins, acts as a potent senolytic agent to deplete SCs *in vivo* and functionally rejuvenates hematopoietic stem cells in both sublethally irradiated and naturally-aged mice [25]. Complementary studies from other labs have confirmed that the Bcl-2 protein

family is a promising molecular target for the development of senolytic drugs [26, 27]. These studies further establish the concept that the pharmacological depletion of SCs is a promising, novel approach for treating age-associated diseases [28].

ABT-263 was identified by screening a small library of structurally diverse, rationally-selected small molecules that target pathways predicted to be important for SC survival [25]. By titrating their cytotoxicity against normal human WI-38 fibroblasts and ionizing radiation (IR)-induced senescent WI-38 fibroblasts, this targeted screen also identified the promising senolytic agent piperlongumine (PL, Fig. 1A); PL is a natural product isolated from a variety of species in the genus *Piper* [29]. Here, we report the characterization of PL as a potential novel lead for the development of senolytic agents.

## RESULTS

### Piperlongumine is a potential senolytic agent

Because we identified PL as a potential senolytic agent by screening a library of rationally-selected compounds with IR-induced senescent WI-38 fibroblasts, we tested its ability to selectively kill senescent human WI-38 fibroblasts induced by different means. PL exhibited moderate selectivity in reducing the viability of IR-induced WI-38 SCs (IR-SCs) compared to non-senescent WI-38 cells (NCs) (Fig. 1B and Table 1), and PL induced cell death in a time-dependent manner (Fig. 1C). We also assessed the survival of WI-38 cells in which senescence was induced by replicative exhaustion or by ectopic expression of the oncogene *Ras* (Fig. 1B). Replicative WI-38 SCs, which were previously

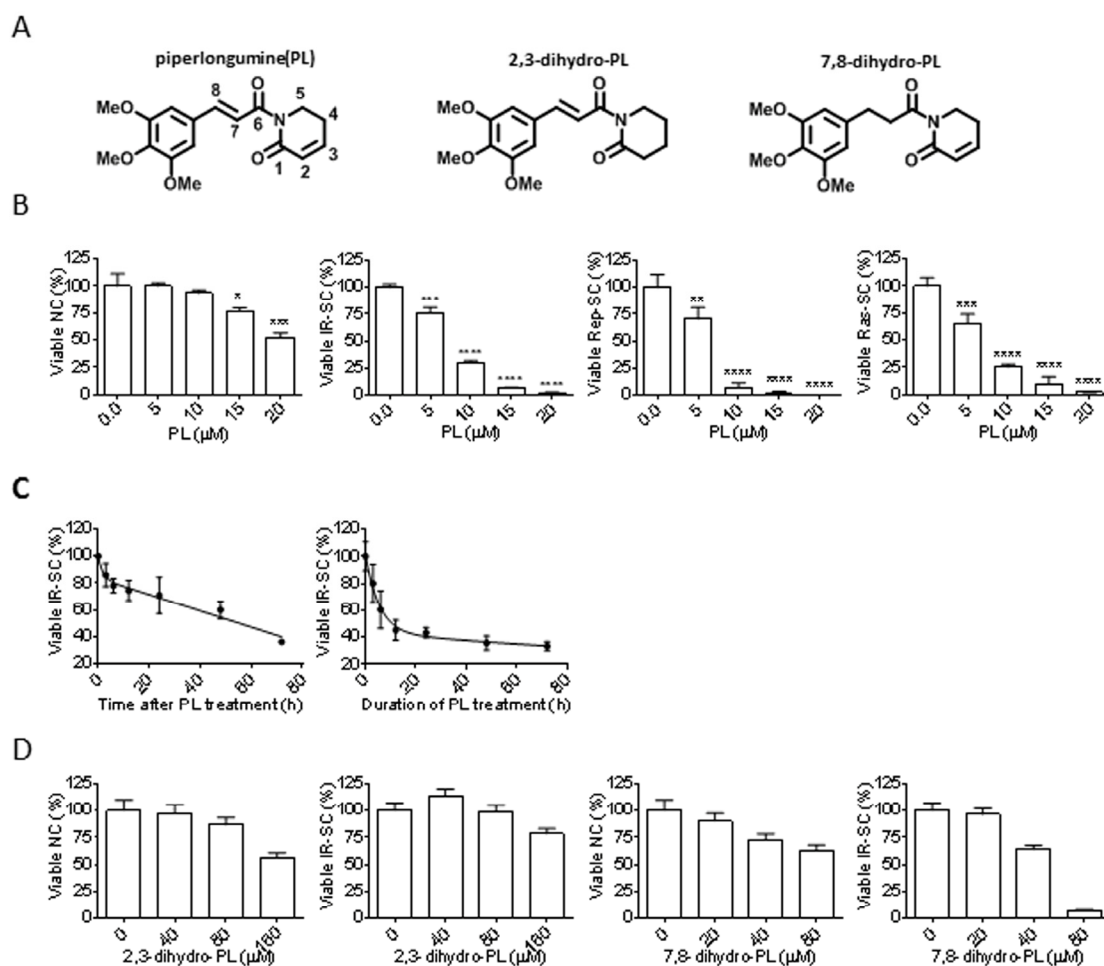


**Figure 1. Senolytic activity of piperlongumine (PL).** (A) Structures of PL, 2,3-dihydro-PL, and 7,8-dihydro-PL. (B) Quantification of viable WI-38 non-senescent cells (NC), IR-induced senescent cells (IR-SC), replication-exhausted senescent cells (Rep-SC), or Ras-induced senescent cells (Ras-SC) 72 h after treatment with increasing concentrations of PL ( $n = 3$ ). (C) Quantification of viable IR-SCs over time after treatment with 10  $\mu$ M PL (left) or after incubation with 10  $\mu$ M PL, removal of the drug, and further culture for 72 h (right) ( $n = 3$ ). (D) Quantification of viable WI-38 NCs and IR-SCs 72 h after treatment with increasing concentrations of 2,3-dihydro-PL or 7,8-dihydro-PL ( $n = 3$ ). Data are represented as the mean  $\pm$  SEM.

shown to be more resistant to ABT-263 [25], were slightly more sensitive to PL (Fig. 1B) than IR- and Ras-induced SCs. The mechanisms underlying the difference of SCs induced by different stimuli have yet to be elucidated.

**Table 1. EC<sub>50</sub> values and selectivity of PL in WI-38 cells**

Cell types	EC <sub>50</sub> (μM)	EC <sub>50</sub> Ratio (NC/SC)
NC	20.28	-
IR-SC	7.97	2.54
Rep-SC	6.24	3.25
Ras-SC	7.09	2.86

Structurally, PL contains two electrophiles, the C2-C3 and C7-C8 α,β-unsaturated imides, both of which are important for the toxicity of PL in cancer cells [30]. Thus, we investigated whether the integrity of the two-electrophile system was also important for the ability of PL to kill SCs. Consistent with the findings in cancer cells, 2,3-dihydro-PL and 7,8-dihydro-PL (Figure 1A), in which the C2-C3 olefin or the C7-C8 olefin was saturated, respectively, showed little or no senolytic activity toward IR-SCs (Fig. 1D).

**Piperlongumine induces apoptosis in SCs**

Next, we investigated the mechanism by which PL selectively kills SCs. Because PL induces apoptosis in cancer cells [31-41], we hypothesized that the same is true for SCs. We used Annexin V and propidium iodide staining and subsequent fluorescence-activated cell sorting to detect apoptosis, respectively, in senescent WI-38 cells. PL treatment increased the number of Annexin-V-positive cells in SCs by 5.5-fold when compared to the vehicle group (Fig. 2A). To further confirm that PL killed cells by apoptosis, we treated IR-induced WI-38 SCs with the pan-caspase inhibitor Q-VD-Oph (QVD) [42] to inhibit apoptosis. Ten μM QVD, in the presence of PL, significantly reduced apoptosis and partially rescued SCs from PL-induced death (Fig. 2A, B). In addition, western blot analysis showed elevated levels of activated caspase-3 and degradation of poly(ADP-ribose) polymerase (PARP) in PL-treated IR-SCs (Fig. 2C), confirming the apoptotic cell-death mechanism. Furthermore, PL had no effect on the levels of receptor-interacting protein kinase 1 and 3 (RIP1 and RIP3), indicating that PL did not induce necroptosis in IR-SCs (Fig. 2D) [43].

**Piperlongumine kills senescent cells through an ROS-independent mechanism**

Initially, PL has been proposed to selectively induce cancer cell death by increasing reactive oxygen species

(ROS) production, based on the observation that PL elevates cellular ROS levels in various cancer cells, but not in normal cells [31]. However, structural modifications to PL have revealed that there is no correlation between a PL analog’s ability to increase ROS and its toxicity toward cancer cells, leading to the conclusion that ROS-independent mechanisms are also involved in cancer cell death [30]. We hypothesized that the same scenario is true for the PL-induced killing of SCs. We used the non-fluorescent ROS indicator dihydrorhodamine 123 (DHR 123), which can passively diffuse across membranes where it is oxidized to green fluorescent rhodamine 123 in the presence of ROS, and flow cytometry to determine if PL increased ROS in IR-SCs. Treatment with 10 μM PL for 6 or 24 h significantly elevated ROS levels in IR-SCs compared to vehicle-treated IR-SCs or non-senescent WI-38 cells with PL treatment, whereas IR-SCs have a higher baseline level of ROS (Fig. 3A). In addition, similar to the results obtained in cancer cells [31, 33-35, 41, 44-47], co-treatment with 2 mM N-acetyl-L-cysteine (NAC), an antioxidant, fully reversed PL-induced ROS elevation and cell death (Fig. 3B), suggesting that the selective induction of ROS in SCs may be the basis for the senolytic activity of PL. However, a number of small molecules, including hydrogen peroxide, pargenolide, arsenic trioxide, phenethyl isothiocyanate, auranofin [a thioredoxin reductase inhibitor], buthionine sulfoximine [a γ-glutamylcysteine synthetase inhibitor], and decyl-triphenylphosphonium, that were previously shown to kill cancer cells by inducing oxidative stress were not able to selectively kill IR-SCs [25]. This finding suggests that ROS elevation alone is insufficient to selectively kill SCs. Interestingly, it has been reported that PL can chemically react with the sulfhydryl group of methyl thioglycolate to form the product of conjugate addition at C3 [30]. Based on this, we hypothesized that NAC, rather than acting as an ROS scavenger, inactivates PL through a similar reaction in cell culture media. In support of this hypothesis, we observed that PL (10 μM) disappeared within 2 h after co-incubation with NAC (2 mM) in cell culture media under conditions mimicking a cell viability assay (Fig. 3C), forming the corresponding hetero-conjugated product, NAC-PL (Fig. 3C). NAC-PL was isolated from this reaction, and it exhibited diminished toxicity toward IR-SCs (Fig. 3C). To further investigate the role of ROS in PL-induced SC death, we treated IR-SCs with PL in the presence of a different, potent antioxidant, γ-tocotrienol (GT3, 5 μM) [48]. GT3 did not decrease PL-induced cell death in IR-SCs, although GT3 reversed the PL-induced increase in ROS (Fig. 3D). These data suggest that ROS were not involved in the SC death induced by PL.

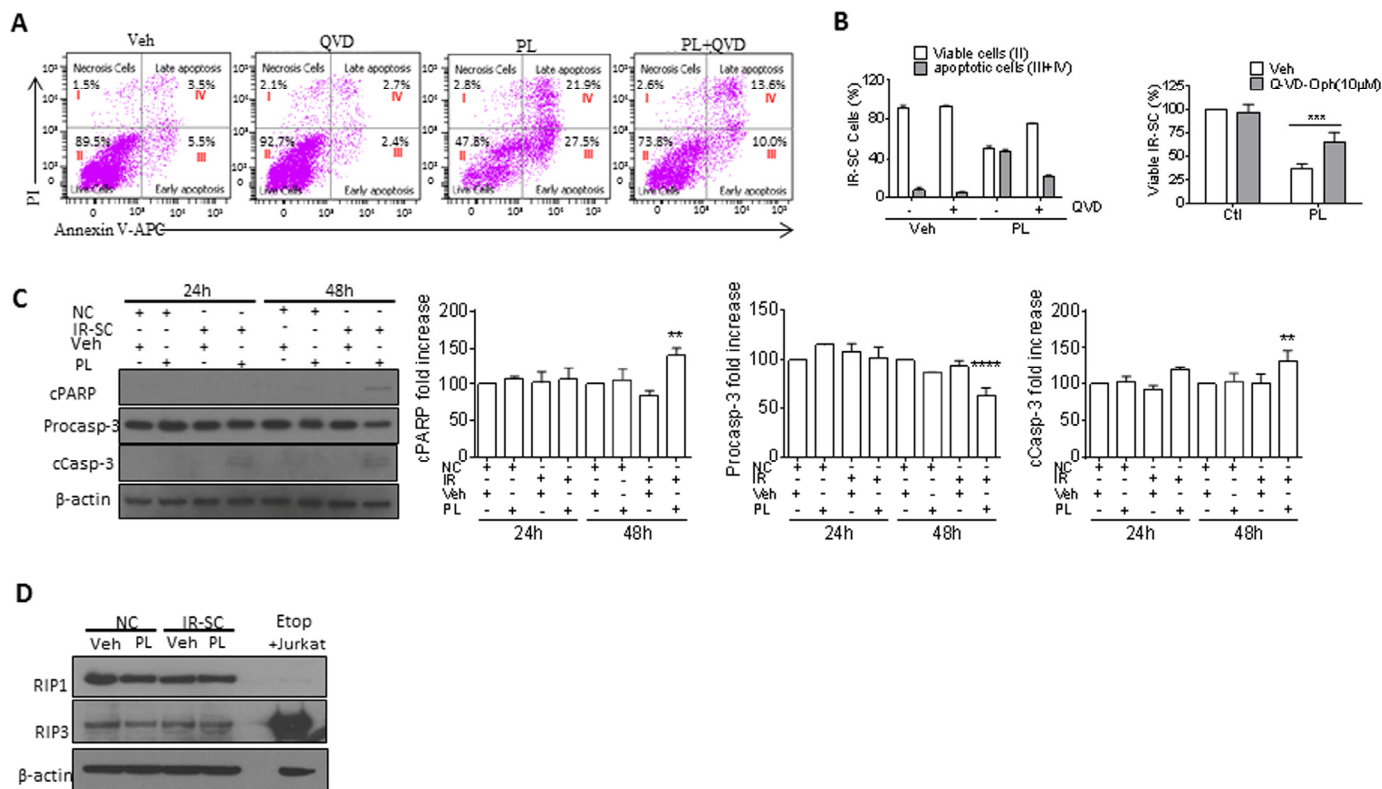


**Figure 2. PL kills SCs by apoptosis.** (A) Representative flow cytometric plots to measure apoptotic WI-38 IR-SCs at 48 h after treatment with vehicle (Veh), 10  $\mu$ M PL, 10  $\mu$ M Q-VD-Oph (QVD), or the combination of PL and QVD. (B) Quantification of the percentage of viable (gate II: PI<sup>-</sup> Annexin V<sup>-</sup>) and apoptotic (gates III and IV: PI<sup>-</sup> Annexin V<sup>+</sup> and PI<sup>+</sup> Annexin V<sup>+</sup>) (right) IR-SCs 48 h after treatment as in (A) (left), and quantification of the percentage of viable IR-SCs 72 h after treatment as in (A) (right). (C) Representative western blot and quantitative analysis of cleaved-poly(ADP-ribose) polymerase (cPARP), procaspase-3 (Procasp-3), cleaved caspase-3 (cCasp-3), and  $\beta$ -actin in NCs and WI-38 IR-SCs 24 h and 48 h after incubation with Veh or 10  $\mu$ M PL. (D) Representative western blot analysis of RIP1, RIP3, and  $\beta$ -actin in WI-38 NCs and IR-SCs 24 h after incubation with Veh or 10  $\mu$ M PL. A cell lysate of etoposide-treated Jurkat cells was used as a positive control. Data are represented as the mean  $\pm$  SEM.

To determine if PL-based senolytic agents with increased potency/selectivity could be developed, we synthesized a series of PL analogs that have been reported as potent anti-cancer agents. No obvious correlation between ROS induction and senolytic potency was observed in these analogs. Specifically, BRD4809 [49], an abbreviated PL analog (Fig. 3E), and PL-DI [30], a PL dimer (Fig. 3F), showed unchanged or increased potency against IR-SCs, respectively, compared to PL; however, these analogs did not affect ROS levels in SCs at concentrations near their EC<sub>50</sub> values for SC viability (Table 2). On the other hand, PL-FPh [30], which contains an alkenyl substituent at C2 of PL, selectively induced ROS production in IR-SCs and had increased potency and selectivity in killing these SCs when compared to PL (Fig. 3G). Finally, PL-7 [30], a PL analog with an enlarged ring, inhibited ROS production, yet retained the senolytic potency of PL toward IR-SCs (Fig. 3H). Taken together, these

results further confirm that PL and its analogs kill SCs in an ROS-independent manner.

**Table 2. EC<sub>50</sub> values and selectivity of PL analogs in WI-38 cells**

PL analogs	EC <sub>50</sub> ( $\mu$ M)		EC <sub>50</sub> ratio (NC/IR)
	NC	IR	
BRD4809	35.7	9.7	3.68
PL-DI	1.53	0.76	2.01
PL-7	12.96	8.85	1.46
PL-FPh	5.87	1.11	5.29

### The synergistic senolytic effect of piperlongumine and ABT-263

PL has been tested for its synergistic anti-tumor effect in combination with TNF-related apoptosis-inducing



ligand [46], ataxia telangiectasia and Rad3-related protein inhibition [50], or a chemotherapeutic agent, such as cisplatin [33, 34], paclitaxel [34], docetaxel [51], and gemcitabine [39]. Thus, we investigated the synergistic senolytic effect of PL and ABT-263 on IR-SCs. We tested 1.25  $\mu$ M ABT-263 with 5 or 10  $\mu$ M PL and 10  $\mu$ M PL with 0.08-1.25  $\mu$ M ABT-263; the ABT-263 concentrations were selected based on our recent studies [25]. The combination of 10  $\mu$ M PL with 1.25  $\mu$ M ABT-263 did not induce significant toxicity in non-

senescent WI-38 cells (Fig. 4A). When the combinations were applied to IR-SCs, however, we observed significant synergistic effects (Fig. 4B-C). For example, treatment of SCs with 10  $\mu$ M PL or 1.25  $\mu$ M ABT-263 individually resulted in cell viability of 30.4% and 25.8%, respectively. However, the combined treatment with PL and ABT-263 killed almost all IR-SCs (Fig. 4C). The coefficient of drug interaction (CDI) method [52] was then used to evaluate the effects of PL and ABT-263; Table 3 gives the CDI values for these

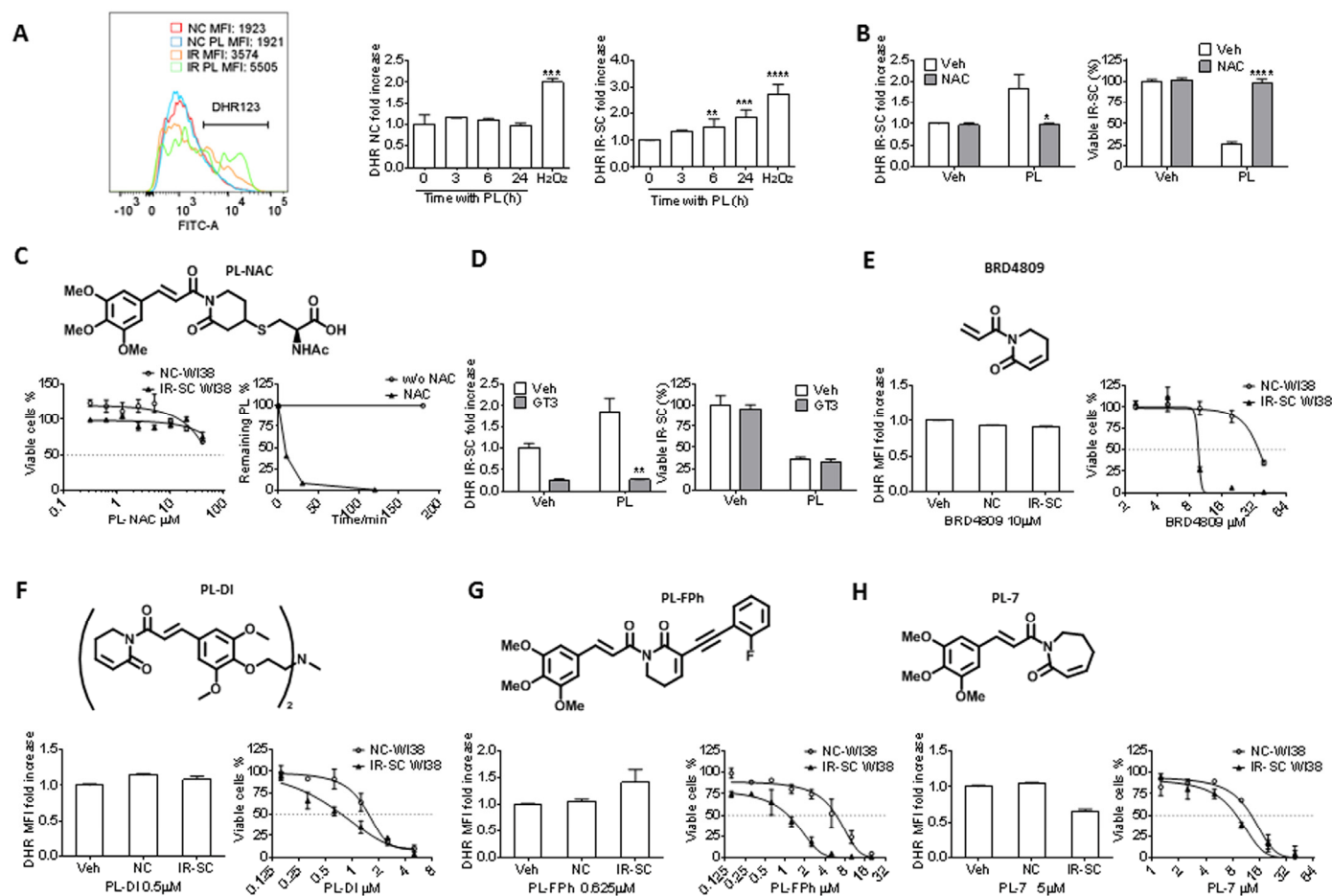


**Figure 3. Effect of PL and its analogs on ROS production and senolytic activity in WI-38 IR-SCs.** (A) Representative flow cytometric analysis of ROS production in NCs and IR-SCs 24 h after incubation with or without PL by DHR (left) (MFI, mean fluorescence intensity) and quantification of the fold increase of ROS levels in WI-38 NCs and WI-38 IR-SCs cells at the indicated times (middle and right) after incubation with 10  $\mu$ M PL. As a positive control, cells were treated with 100  $\mu$ M of  $H_2O_2$  for 2 h, the  $H_2O_2$  was removed, and cells were cultured for an additional 24 h ( $n = 3$ ). (B) Quantification of the fold increase in DHR-123 MFI (left) in WI-38 IR-SCs 24 h after treatment with Veh, 10  $\mu$ M PL, 2 mM NAC (pretreatment overnight), or the combination of PL and NAC, and (right) the percentage of viable WI-38 IR-SCs 72 h after treatment with Veh, 10  $\mu$ M PL, 2 mM NAC (pretreatment overnight), or the combination of PL and NAC ( $n = 3$ ). (C) Structure of PL-NAC and (Left) quantification of viable WI-38 NCs and WI-38 IR-SCs 72 h after treatment with increasing concentrations of PL-NAC ( $n = 3$ ). (Right) Percentage of 10  $\mu$ M PL remaining in the culture medium vs. time with or without 2mM NAC. (D) Left panel: quantification of the fold increase in DHR MFI (left) of WI-38 IR-SCs 24 h after treatment with Veh, 10  $\mu$ M PL, 5  $\mu$ M  $\gamma$ -tocotrienol (GT3, pretreatment overnight), or the combination of PL and GT3; and right panel: the percentage of viable WI-38 IR-SCs 72 h after treatment with Veh, 10  $\mu$ M PL, 5  $\mu$ M GT3 (pretreatment overnight), or the combination of PL and GT3 ( $n = 3$ ). (E-H) Quantification of the fold increase in DHR-123 MFI after 24 h treatment (left) and viability of WI-38 NCs and WI-38 IR-SCs 72 h treatment (right) after they were treated with increasing concentrations or (E) 10  $\mu$ M BRD4809, (F) 0.5  $\mu$ M PL-DI, (G) 0.625  $\mu$ M PL-FPh, and (H) 5  $\mu$ M PL-7 ( $n = 3$ ). Data are represented as the mean  $\pm$  SEM.

combinations. An additive effect for the combination of 10  $\mu$ M PL and 0.08  $\mu$ M ABT-263 ( $CDI = 0.99$ ) was observed. The  $CDI$  values for the other combinations ranged from 0.02-0.41, indicating that PL and ABT-263 exerted a strong synergistic senolytic effect on IR-SCs. It is worth noting that, in our previous studies, increasing the concentration of ABT-263 from 1.25  $\mu$ M to 5  $\mu$ M did not increase cell killing in WI-38 SCs. PL appeared to eliminate the subpopulation of IR-SCs that was resistant to ABT-263.

**Table 3. CDI values for the combination of PL and ABT-263**

ABT-263 ( $\mu$ M)	PL ( $\mu$ M)	CDI
0.08	10	0.99
0.156	10	0.20
0.313	10	0.05
0.625	10	0.02
1.25	10	0.38
1.25	5	0.41

### DISCUSSION

Selective depletion of SCs is a potentially novel anti-aging strategy that may prevent cancer and various human diseases associated with aging and rejuvenate the body to live a longer, healthier life. As such, several senolytic agents, including ABT-263, have been identified recently [23, 25-27], demonstrating the feasibility of pharmacologically targeting SCs. However, ABT-263 induces thrombocytopenia [53], and it remains to be determined whether ABT-263 can be used to safely treat age-related diseases, since individuals may require long-term treatment with a senolytic drug. Thus, it is necessary to identify a safer

senolytic drug. In the present study, we evaluated PL as a novel senolytic agent. PL induced caspase-mediated apoptosis in SCs and effectively killed SCs induced by IR, replicative exhaustion, or ectopic expression of the oncogene *Ras*. Similar to the observations in cancer cells versus normal cells, PL elevated ROS levels in IR-SCs, but not in non-senescent WI-38 cells.

Because NAC blocks PL-induced ROS elevation in cancer cells and abolishes the anti-tumor effect of PL, it has been proposed that induction of ROS production is a key mechanism of PL-induced cancer cell apoptosis [31, 33-35, 41, 45-47]. Indeed, we showed that co-treatment of IR-SCs with PL and NAC fully reversed the senolytic effect of PL. However, we found that PL was chemically inactivated by NAC in culture media through a conjugated addition reaction between the sulfhydryl group of NAC and the C2-C3  $\alpha,\beta$ -unsaturated imide group of PL; the resulting adduct, NAC-PL, was not senolytic. Based on these findings, caution is warranted when using NAC or similar compounds that contain a nucleophilic sulfhydryl group, such as dithiothreitol [54], as an ROS scavenger to study ROS inducers such as PL. In contrast, GT3, a potent ROS scavenger that does not react with PL, effectively blocked PL-induced ROS elevation but had no inhibitory effect on PL-induced SC death. In addition, through evaluation of PL analogs, we found that there is no correlation between senolytic potency and ROS-induction in IR-SCs. These results led us to conclude that the senolytic activity of PL is ROS independent.

Unlike ABT-263, the precise mechanism of action (MOA) by which PL induces SC apoptosis remains unclear. PL modulates the activity of many cell signaling and survival pathways in cancer cells [31], and a number of studies have investigated the MOA by

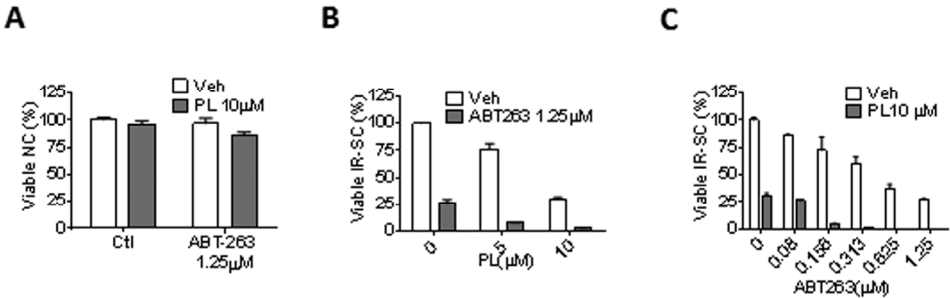


**Figure 4. PL synergistically and selectively kills SCs in combination with ABT-263.** (A) Quantification of NC viability 72 h after the cells incubation with vehicle, 1.25  $\mu$ M ABT-263, 10  $\mu$ M PL, or the combination of ABT-263 and PL ( $n = 3$ ). (B) Quantification of WI-38 IR-SC viability 72 h after incubation with vehicle, 1.25  $\mu$ M ABT-263, 5 or 10  $\mu$ M PL, or the combination of ABT-263 and PL ( $n = 3-5$ ). (C) Quantification of WI-38 IR-SC viability 72 h after incubation with vehicle, 10  $\mu$ M PL, 0.08-1.25  $\mu$ M ABT-263, or the combination of ABT-263 and PL ( $n = 3-6$ ). Data are represented as the mean  $\pm$  SEM.

which PL induces apoptosis in these cells [30, 35-40, 45, 54-69]. Data from these studies may be translatable to PL-induced SC apoptosis because SCs and cancer cells share some common pro-survival pathways [23]. In addition, mass spectrometry-based proteomic approaches using probes derived from PL could be used to identify direct molecular target(s) of PL in SCs. In this regard, novel anti-senescent protein target(s) and MOAs could be identified, making it possible to develop promising novel classes of senolytic agents. Importantly, PL appears to be safe; the maximum tolerated dose in mice is very high, and it maintains high bioavailability after oral administration [31]. Furthermore, our initial structural modifications to PL demonstrate that we can develop PL analogs with increased potency and selectivity toward SCs (Fig. 3), supporting the use of PL as a lead for further drug discovery and development.

Another potential use of PL and its derivatives is in combination with ABT-263, or other inhibitors of Bcl-2 family proteins, for a synergistic senolytic effect. Although ABT-263 is a highly specific senolytic agent, it causes transient thrombocytopenia and neutropenia in patients [70]; this results from its inhibitory effect on Bcl-xL, which is important for platelet survival [71, 72]. We showed that PL had a strong synergistic effect on the senolytic activity of ABT-263 *in vitro*, potentially reducing the dose of ABT-263 needed to effectively deplete SCs. We expect this therapeutic approach would significantly reduce ABT-263-induced thrombocytopenia, making senolytic treatment with ABT-263 safer.

Although clearance of SCs with a senolytic drug may be used to treat some age-related diseases, it is well recognized that cellular senescence is also functionally linked to many beneficial physiological processes, such as wound healing, tissue remodeling, and embryonic development [73]. Attempt to clear SCs in certain situations may produce some side effects. Therefore, we should proceed with caution to use senolytic drugs to treat age-related diseases before we have a better understanding of their risks.

## MATERIALS AND METHODS

### Cells, induction of senescence, and senolytic agents

Human WI-38 fibroblasts (WI-38, catalog no. CCL-75, American Type Culture Collection, Manassas, VA) were cultured in a complete cell culture medium (CM) (Dulbecco's Modified Eagle Medium supplemented with 10% Fetal Bovine Serum, FBS; catalog no. 16000044, Thermo Fisher Scientific, Waltham, MA) supplemented with 100 U/ml penicillin and 100 µg/ml streptomycin (purchased from Atlanta Biologicals,

Norcross, GA) in a 37°C, humidified incubator with 5% CO<sub>2</sub>.

Low-passage WI-38 (< 25 passages) cells were used as controls or for the induction of senescence.

### Replicative senescence

To induce replicative senescence (Rep-SC), WI-38 cells were subcultured until they stopped dividing and became senescent (after approximately 38 passages for WI-38).

### Ionizing radiation-induced senescence

To induce senescence with ionizing radiation (IR), WI-38 cells, roughly 70% confluent, were exposed to 15 Gy of IR in a J.L. Shepherd Model Mark I <sup>137</sup>Cesium γ-irradiator (J.L. Shepherd, Glendale, CA) at a dose rate of 1.080 Gy/min. Three days after irradiation, cells were passaged once at a 1:3 dilution. WI-38 cells became fully senescent 10 d after irradiation.

### Ras-induced senescence

WI-38 cells were made senescent by ectopically expressing the oncogene *Ras* (Ras-SC), as previously described [25].

PL was purchased from Biovision (catalog no. 1919-10; Milpitas, CA). ABT-263 was purchased from Selleckchem (catalog no. S1001; Houston, TX). The PL analogs 2,3-dihydro-PL, 7,8-dihydro-PL, BRD4809, PL-DI, PL-FPh, and PL-7 were synthesized according to reported methods, with minor modifications [30, 49]. PL-NAC was obtained by incubating equal volume of 20 µM PL with 4 mM NAC in culture media at 37°C for 30 min, followed by extraction with methylene chloride and silica gel column purification. The structure of PL-NMR was characterized by NMR and MS: <sup>1</sup>H NMR (400 MHz, CDCl<sub>3</sub>) δ 7.59 (d, *J* = 15.6 Hz, 1H), 7.28 (d, *J* = 15.6 Hz, 1H), 6.86 (br, 1H), 6.76 (s, 2H), 4.68 (s, 1H), 3.99 (m, 1H), 3.88–3.75 (m, 9H), 3.63 (m, 1H), 3.27 (m, 1H), 3.13–2.87 (m, 3H), 2.69–2.44 (m, 1H), 2.25 (m, 1H), 2.04 (s, 3H), 1.81 (m, 1H) ppm; ESI-MS *m/z* 479.2 [M-H]<sup>+</sup>.

### Cell viability assays

Cell viability was measured with flow cytometry, as previously described [25].

### Calculation of EC<sub>50</sub> values

Dose-response curves were generated for each senolytic agent, and the half-maximal effective concentrations (EC<sub>50</sub> values) were calculated with GraphPad Prism 6 software.

## ROS assay

Control, non-senescent WI-38 cells were plated in 24-well plates (60,000 cells/well). IR-induced WI-38 senescent cells (10 d after 15 Gy IR) were plated in 6-well plates (50,000 cells/well) and allowed to recover. Cells were incubated overnight with NAC (2 mM; catalog no. 138061, Sigma-Aldrich, St. Louis, MO) and GT3 (5  $\mu$ M; isolated from annatto oil). The next day, the cells were treated with dilutions of compounds in DMSO and incubated for 24 h, or as indicated. The medium was then replaced with pre-warmed DMEM (no supplements) containing 1  $\mu$ M dihydrorhodamine 123 (DHR 123, catalog no. D632, Thermo Fisher Scientific), and the cells were incubated at 37°C for 30 min. The cells were then harvested with trypsin and washed twice with PBS. Mean fluorescence intensity (MFI) was determined with a BD LSR II flow cytometer (BD Biosciences, San Jose, CA).

## Apoptosis assay

WI-38 cells were pretreated with vehicle or 10  $\mu$ M Q-VD-Oph (QVD, catalog no. A1901, APEXBio, Houston, TX) for 4 h. Cells were then treated with 10  $\mu$ M PL for the indicated time. The cells were harvested and washed twice with Annexin V binding buffer and then stained with Alexa Fluor 647-Annexin V (1: 50, catalog no. 640912, BioLegend, San Diego, CA) and propidium iodide (PI, 10  $\mu$ g/ml, catalog no. P4170, Sigma-Aldrich), according to the manufacturer's instructions (Biotium, Hayward, CA). All of the stained cells were analyzed with the BD LSR II flow cytometer.

## Western blot analysis

Cells were lysed in RIPA buffer with EDTA and EGTA (catalog no. BP-115DG, Boston BioProducts, Ashland, MA), supplemented with 1% Phosphatase Inhibitor Cocktail 3 (catalog no. P0044, Sigma-Aldrich) and 1% Protease Inhibitor Cocktail (catalog no. P8340, Sigma-Aldrich). An equal amount of protein (15–30  $\mu$ g/lane) from each cell extract was resolved on a 12% SDS-PAGE gel. Proteins were blotted to a NOVEL PVDF membrane (catalog no. LC2002, Life Technologies) by electrophoresis. The membranes were blocked with TBS-T blocking buffer (5% nonfat milk in 25 mM Tris-HCl, pH 7.4; 3 mM KCl; 140 mM NaCl; and 0.05% Tween) and probed with primary antibodies (at a predetermined optimal concentration) overnight at 4°C or for 1 h at room temperature. After extensive washing with TBS-T, the membranes were incubated with an appropriate peroxidase-conjugated secondary antibody (Jackson ImmunoResearch Europe, Suffolk, UK) for 1 h at room temperature. After three washes with TBS-T, the proteins of interest were detected with ECL Western

Blotting Detection Reagents (catalog no. WBKLS0100, EMD Millipore, Newmarket, Suffolk, UK) and recorded with autoradiography (Pierce Biotech, Rockford, IL, USA). The primary antibodies included cleaved-Poly (ADP-ribose) polymerase (catalog no. 9541, Cell Signaling Technology, Boston, MA), Procaspase-3 (catalog no. 9662S, Cell Signaling Technology), cleaved-caspase 3 (catalog no. 9664S, Cell Signaling Technology), RIP1 (D94C12, catalog no. 3493S, Cell Signaling Technology),  $\beta$ -actin (catalog no. SC-1615, Santa Cruz Biotechnology, Dallas, TX), and RIP3 (catalog no. IMG-5846A, IMGENEX, San Diego, CA).

## Statistical analysis

The data displayed normal variance. The data were analyzed by analysis of variance (ANOVA) with Graphpad Prism from GraphPad Software (San Diego, CA). In the event that ANOVA justified post hoc comparisons between group means, the comparisons were made with Neuman-Keuls or Tukey's multiple-comparisons test.  $P < 0.05$  was considered to be significant. CDI was calculated as:  $CDI = AB / (A \times B)$ . AB represents the percent of viable cells remaining after the treatment with the combined drugs, while A and B represent the percent of viable cells remaining after the treatment with each drug independently.  $CDI < 1$  indicates a synergistic effect,  $CDI = 1$  indicates an additive effect, and  $CDI > 1$  indicates antagonism.  $CDI < 0.7$  indicates that the drugs are significantly synergistic.

## CONFLICTS OF INTEREST

Y.W., J.C., X.L., G.Z., and D.Z. filed a patent application for the use of PL and PL analogs as anti-aging agents. A potential royalty stream to Y.W., J.C., X.L., G.Z., and D.Z. may occur consistent with University of Arkansas for Medical Sciences policy. G.Z. is a consultant and D.Z. is a co-founder and advisor of UNITY Biotechnology that develops senolytic drugs.

## FUNDING

This work was initially supported in part by grants from the National Institutes of Health (R01CA122023 and P20GM109005) and a scholarship from the Arkansas Research Alliance. The development of various PL analogs was supported by a sponsored research agreement between UNITY Biotechnology and the University of Arkansas for Medical Sciences. This manuscript was edited in the Office of Grants and Scientific Publications at the University of Arkansas for Medical Sciences.



## REFERENCES

- Braig M, Lee S, Loddenkemper C, Rudolph C, Peters AH, Schlegelberger B, Stein H, Dörken B, Jenuwein T, Schmitt CA. Oncogene-induced senescence as an initial barrier in lymphoma development. *Nature*. 2005; 436:660–65. doi: 10.1038/nature03841
- Chen Z, Trotman LC, Shaffer D, Lin HK, Dotan ZA, Niki M, Koutcher JA, Scher HI, Ludwig T, Gerald W, Cordon-Cardo C, Pandolfi PP. Crucial role of p53-dependent cellular senescence in suppression of Pten-deficient tumorigenesis. *Nature*. 2005; 436:725–30. doi: 10.1038/nature03918
- Campisi J, d'Adda di Fagagna F. Cellular senescence: when bad things happen to good cells. *Nat Rev Mol Cell Biol*. 2007; 8:729–40. doi: 10.1038/nrm2233
- Prieur A, Peeper DS. Cellular senescence in vivo: a barrier to tumorigenesis. *Curr Opin Cell Biol*. 2008; 20:150–55. doi: 10.1016/j.ceb.2008.01.007
- Kuilman T, Michaloglou C, Mooi WJ, Peeper DS. The essence of senescence. *Genes Dev*. 2010; 24:2463–79. doi: 10.1101/gad.1971610
- Campisi J. Aging, cellular senescence, and cancer. *Annu Rev Physiol*. 2013; 75:685–705. doi: 10.1146/annurev-physiol-030212-183653
- Aravintan A. Cellular senescence: a hitchhiker's guide. *Hum Cell*. 2015; 28:51–64. doi: 10.1007/s13577-015-0110-x
- Rodier F, Campisi J. Four faces of cellular senescence. *J Cell Biol*. 2011; 192:547–56. doi: 10.1083/jcb.201009094
- Ohtani N, Takahashi A, Mann DJ, Hara E. Cellular senescence: a double-edged sword in the fight against cancer. *Exp Dermatol*. 2012 (Suppl 1); 21:1–4. doi: 10.1111/j.1600-0625.2012.01493.x
- Tchkonia T, Zhu Y, van Deursen J, Campisi J, Kirkland JL. Cellular senescence and the senescent secretory phenotype: therapeutic opportunities. *J Clin Invest*. 2013; 123:966–72. doi: 10.1172/JCI64098
- Salama R, Sadaie M, Hoare M, Narita M. Cellular senescence and its effector programs. *Genes Dev*. 2014; 28:99–114. doi: 10.1101/gad.235184.113
- Baker DJ, Wijshake T, Tchkonia T, LeBrasseur NK, Childs BG, van de Sluis B, Kirkland JL, van Deursen JM. Clearance of p16Ink4a-positive senescent cells delays ageing-associated disorders. *Nature*. 2011; 479:232–36. doi: 10.1038/nature10600
- Baker DJ, Childs BG, Durik M, Wijers ME, Sieben CJ, Zhong J, Saltness RA, Jeganathan KB, Verzosa GC, Pezeshki A, Khazaie K, Miller JD, van Deursen JM. Naturally occurring p16(Ink4a)-positive cells shorten healthy lifespan. *Nature*. 2016; 530:184–89. doi: 10.1038/nature16932
- Xu M, Tchkonia T, Ding H, Ogrodnik M, Lubbers ER, Pirtskhalava T, White TA, Johnson KO, Stout MB, Mezera V, Giorgadze N, Jensen MD, LeBrasseur NK, Kirkland JL. JAK inhibition alleviates the cellular senescence-associated secretory phenotype and frailty in old age. *Proc Natl Acad Sci USA*. 2015; 112:E6301–10. doi: 10.1073/pnas.1515386112
- Hall BM, Balan V, Gleiberman AS, Strom E, Krasnov P, Virtuoso LP, Rydkina E, Vujcic S, Balan K, Gitlin I, Leonova K, Polinsky A, Chernova OB, Gudkov AV. Aging of mice is associated with p16(Ink4a)- and  $\beta$ -galactosidase-positive macrophage accumulation that can be induced in young mice by senescent cells. *Aging (Albany NY)*. 2016; 8:1294–315. doi: 10.18632/aging.100991
- Johnson SC, Rabinovitch PS, Kaeblerlein M. mTOR is a key modulator of ageing and age-related disease. *Nature*. 2013; 493:338–45. doi: 10.1038/nature11861
- Anisimov VN. Metformin for aging and cancer prevention. *Aging (Albany NY)*. 2010; 2:760–74. doi: 10.18632/aging.100230
- Komarova EA, Antoch MP, Novototskaya LR, Chernova OB, Paszkiewicz G, Leontieva OV, Blagosklonny MV, Gudkov AV. Rapamycin extends lifespan and delays tumorigenesis in heterozygous p53+/- mice. *Aging (Albany NY)*. 2012; 4:709–14. doi: 10.18632/aging.100498
- Menendez JA, Joven J. One-carbon metabolism: an aging-cancer crossroad for the gerosuppressant metformin. *Aging (Albany NY)*. 2012; 4:894–98. doi: 10.18632/aging.100523
- Ross C, Salmon A, Strong R, Fernandez E, Javors M, Richardson A, Tardif S. Metabolic consequences of long-term rapamycin exposure on common marmoset monkeys (*Callithrix jacchus*). *Aging (Albany NY)*. 2015; 7:964–73. doi: 10.18632/aging.100843
- van Deursen JM. The role of senescent cells in ageing. *Nature*. 2014; 509:439–46. doi: 10.1038/nature13193
- Sharpless NE, Sherr CJ. Forging a signature of in vivo senescence. *Nat Rev Cancer*. 2015; 15:397–408. doi: 10.1038/nrc3960
- Zhu Y, Tchkonia T, Pirtskhalava T, Gower AC, Ding H, Giorgadze N, Palmer AK, Ikeno Y, Hubbard GB, Lenburg M, O'Hara SP, LaRusso NF, Miller JD, et al. The Achilles' heel of senescent cells: from transcriptome to senolytic drugs. *Aging Cell*. 2015; 14:644–58. doi: 10.1111/ace.12344



24. Kirkland JL, Tchkonina T. Clinical strategies and animal models for developing senolytic agents. *Exp Gerontol*. 2015; 68:19–25. doi: 10.1016/j.exger.2014.10.012
25. Chang J, Wang Y, Shao L, Laberge RM, Demaria M, Campisi J, Janakiraman K, Sharpless NE, Ding S, Feng W, Luo Y, Wang X, Aykin-Burns N, et al. Clearance of senescent cells by ABT263 rejuvenates aged hematopoietic stem cells in mice. *Nat Med*. 2016; 22:78–83. doi: 10.1038/nm.4010
26. Zhu Y, Tchkonina T, Fuhrmann-Stroissnigg H, Dai HM, Ling YY, Stout MB, Pirtskhalava T, Giorgadze N, Johnson KO, Giles CB, Wren JD, Niedernhofer LJ, Robbins PD, Kirkland JL. Identification of a novel senolytic agent, navitoclax, targeting the Bcl-2 family of anti-apoptotic factors. *Aging Cell*. 2016; 15:428–35. doi: 10.1111/acer.12445
27. Yosef R, Pilpel N, Tokarsky-Amiel R, Biran A, Ovadya Y, Cohen S, Vadai E, Dassa L, Shahar E, Condiotti R, Ben-Porath I, Krizhanovsky V. Directed elimination of senescent cells by inhibition of BCL-W and BCL-XL. *Nat Commun*. 2016; 7:11190. doi: 10.1038/ncomms11190
28. Geiger H. Depleting senescent cells to combat aging. *Nat Med*. 2016; 22:23–24. doi: 10.1038/nm.4024
29. Bezerra DP, Pessoa C, de Moraes MO, Saker-Neto N, Silveira ER, Costa-Lotufo LV. Overview of the therapeutic potential of piplartine (piperlongumine). *Eur J Pharm Sci*. 2013; 48:453–63. doi: 10.1016/j.ejps.2012.12.003
30. Adams DJ, Dai M, Pellegrino G, Wagner BK, Stern AM, Shamji AF, Schreiber SL. Synthesis, cellular evaluation, and mechanism of action of piperlongumine analogs. *Proc Natl Acad Sci USA*. 2012; 109:15115–20. doi: 10.1073/pnas.1212802109
31. Raj L, Ide T, Gurkar AU, Foley M, Schenone M, Li X, Tolliday NJ, Golub TR, Carr SA, Shamji AF, Stern AM, Mandinova A, Schreiber SL, Lee SW. Selective killing of cancer cells by a small molecule targeting the stress response to ROS. *Nature*. 2011; 475:231–34. doi: 10.1038/nature10167
32. Han SS, Son DJ, Yun H, Kamberos NL, Janz S. Piperlongumine inhibits proliferation and survival of Burkitt lymphoma in vitro. *Leuk Res*. 2013; 37:146–54. doi: 10.1016/j.leukres.2012.11.009
33. Roh JL, Kim EH, Park JY, Kim JW, Kwon M, Lee BH. Piperlongumine selectively kills cancer cells and increases cisplatin antitumor activity in head and neck cancer. *Oncotarget*. 2014; 5:9227–38. doi: 10.18632/oncotarget.2402
34. Gong LH, Chen XX, Wang H, Jiang QW, Pan SS, Qiu JG, Mei XL, Xue YQ, Qin WM, Zheng FY, Shi Z, Yan XJ. Piperlongumine induces apoptosis and synergizes with cisplatin or paclitaxel in human ovarian cancer cells. *Oxid Med Cell Longev*. 2014; 2014:906804. doi: 10.1155/2014/906804
35. Liu JM, Pan F, Li L, Liu QR, Chen Y, Xiong XX, Cheng K, Yu SB, Shi Z, Yu AC, Chen XQ. Piperlongumine selectively kills glioblastoma multiforme cells via reactive oxygen species accumulation dependent JNK and p38 activation. *Biochem Biophys Res Commun*. 2013; 437:87–93. doi: 10.1016/j.bbrc.2013.06.042
36. Randhawa H, Kibble K, Zeng H, Moyer MP, Reindl KM. Activation of ERK signaling and induction of colon cancer cell death by piperlongumine. *Toxicol In Vitro*. 2013; 27:1626–33. doi: 10.1016/j.tiv.2013.04.006
37. Ginzburg S, Golovine KV, Makhov PB, Uzzo RG, Kutikov A, Kolenko VM. Piperlongumine inhibits NF- $\kappa$ B activity and attenuates aggressive growth characteristics of prostate cancer cells. *Prostate*. 2014; 74:177–86. doi: 10.1002/pros.22739
38. Jin HO, Lee YH, Park JA, Lee HN, Kim JH, Kim JY, Kim B, Hong SE, Kim HA, Kim EK, Noh WC, Kim JI, Chang YH, et al. Piperlongumine induces cell death through ROS-mediated CHOP activation and potentiates TRAIL-induced cell death in breast cancer cells. *J Cancer Res Clin Oncol*. 2014; 140:2039–46. doi: 10.1007/s00432-014-1777-1
39. Wang Y, Wu X, Zhou Y, Jiang H, Pan S, Sun B. Piperlongumine Suppresses Growth and Sensitizes Pancreatic Tumors to Gemcitabine in a Xenograft Mouse Model by Modulating the NF-kappa B Pathway. *Cancer Prev Res (Phila)*. 2016; 9:234–44. doi: 10.1158/1940-6207.CAPR-15-0306
40. Zheng J, Son DJ, Gu SM, Woo JR, Ham YW, Lee HP, Kim WJ, Jung JK, Hong JT. Piperlongumine inhibits lung tumor growth via inhibition of nuclear factor kappa B signaling pathway. *Sci Rep*. 2016; 6:26357. doi: 10.1038/srep26357
41. Chen SY, Liu GH, Chao WY, Shi CS, Lin CY, Lim YP, Lu CH, Lai PY, Chen HR, Lee YR. Piperlongumine Suppresses Proliferation of Human Oral Squamous Cell Carcinoma through Cell Cycle Arrest, Apoptosis and Senescence. *Int J Mol Sci*. 2016; 17:E616. doi: 10.3390/ijms17040616
42. Caserta TM, Smith AN, Gultice AD, Reedy MA, Brown TL. Q-VD-OPh, a broad spectrum caspase inhibitor with potent antiapoptotic properties. *Apoptosis*. 2003; 8:345–52. doi: 10.1023/A:1024116916932
43. Walsh CM. Grand challenges in cell death and survival: apoptosis vs. necroptosis. *Front Cell Dev Biol*. 2014; 2:3. doi: 10.3389/fcell.2014.00003
44. Wang Y, Wang JW, Xiao X, Shan Y, Xue B, Jiang G, He

- Q, Chen J, Xu HG, Zhao RX, Werle KD, Cui R, Liang J, et al. Piperlongumine induces autophagy by targeting p38 signaling. *Cell Death Dis.* 2013; 4:e824. doi: 10.1038/cddis.2013.358
45. Liu QR, Liu JM, Chen Y, Xie XQ, Xiong XX, Qiu XY, Pan F, Liu D, Yu SB, Chen XQ. Piperlongumine inhibits migration of glioblastoma cells via activation of ROS-dependent p38 and JNK signaling pathways. *Oxid Med Cell Longev.* 2014; 2014:653732. doi: 10.1155/2014/653732
46. Li J, Sharkey CC, King MR. Piperlongumine and immune cytokine TRAIL synergize to promote tumor death. *Sci Rep.* 2015; 5:9987. doi: 10.1038/srep09987
47. Duan C, Zhang B, Deng C, Cao Y, Zhou F, Wu L, Chen M, Shen S, Xu G, Zhang S, Duan G, Yan H, Zou X. Piperlongumine induces gastric cancer cell apoptosis and G2/M cell cycle arrest both in vitro and in vivo. *Tumour Biol.* 2016; 37:10793–804. doi: 10.1007/s13277-016-4792-9
48. Cerecetto H, López GV. Antioxidants derived from vitamin E: an overview. *Mini Rev Med Chem.* 2007; 7:315–38. doi: 10.2174/138955707780059871
49. Boskovic ZV, Hussain MM, Adams DJ, Dai M, Schreiber SL. Synthesis of piperlogs and analysis of their effects on cells. *Tetrahedron.* 2013; 69:7559–67. doi: 10.1016/j.tet.2013.05.080
50. Cottini F, Hideshima T, Suzuki R, Tai YT, Bianchini G, Richardson PG, Anderson KC, Tonon G. Synthetic Lethal Approaches Exploiting DNA Damage in Aggressive Myeloma. *Cancer Discov.* 2015; 5:972–87. doi: 10.1158/2159-8290.CD-14-0943
51. Patel K, Chowdhury N, Doddapaneni R, Boakye CH, Godugu C, Singh M. Piperlongumine for Enhancing Oral Bioavailability and Cytotoxicity of Docetaxel in Triple-Negative Breast Cancer. *J Pharm Sci.* 2015; 104:4417–26. doi: 10.1002/jps.24637
52. Hao JQ, Li Q, Xu SP, Shen YX, Sun GY. Effect of lumiracoxib on proliferation and apoptosis of human nonsmall cell lung cancer cells in vitro. *Chin Med J (Engl).* 2008; 121:602–07.
53. Kaefer A, Yang J, Noertersheuser P, Mensing S, Humerickhouse R, Awni W, Xiong H. Mechanism-based pharmacokinetic/pharmacodynamic meta-analysis of navitoclax (ABT-263) induced thrombocytopenia. *Cancer Chemother Pharmacol.* 2014; 74:593–602. doi: 10.1007/s00280-014-2530-9
54. Han JG, Gupta SC, Prasad S, Aggarwal BB. Piperlongumine chemosensitizes tumor cells through interaction with cysteine 179 of IκBα kinase, leading to suppression of NF-κB-regulated gene products. *Mol Cancer Ther.* 2014; 13:2422–35. doi: 10.1158/1535-7163.MCT-14-0171
55. Bharadwaj U, Eckols TK, Kolosov M, Kasembeli MM, Adam A, Torres D, Zhang X, Dobrolecki LE, Wei W, Lewis MT, Dave B, Chang JC, Landis MD, et al. Drug-repositioning screening identified piperlongumine as a direct STAT3 inhibitor with potent activity against breast cancer. *Oncogene.* 2015; 34:1341–53. doi: 10.1038/onc.2014.72
56. Chen Y, Liu JM, Xiong XX, Qiu XY, Pan F, Liu D, Lan SJ, Jin S, Yu SB, Chen XQ. Piperlongumine selectively kills hepatocellular carcinoma cells and preferentially inhibits their invasion via ROS-ER-MAPKs-CHOP. *Oncotarget.* 2015; 6:6406–21. doi: 10.18632/oncotarget.3444
57. Golovine K, Makhov P, Naito S, Raiyani H, Tomaszewski J, Mehrazin R, Tulin A, Kutikov A, Uzzo RG, Kolenko VM. Piperlongumine and its analogs down-regulate expression of c-Met in renal cell carcinoma. *Cancer Biol Ther.* 2015; 16:743–49. doi: 10.1080/15384047.2015.1026511
58. Golovine KV, Makhov PB, Teper E, Kutikov A, Canter D, Uzzo RG, Kolenko VM. Piperlongumine induces rapid depletion of the androgen receptor in human prostate cancer cells. *Prostate.* 2013; 73:23–30. doi: 10.1002/pros.22535
59. Han SS, Tompkins VS, Son DJ, Kamberos NL, Stunz LL, Halwani A, Bishop GA, Janz S. Piperlongumine inhibits LMP1/MYC-dependent mouse B-lymphoma cells. *Biochem Biophys Res Commun.* 2013; 436:660–65. doi: 10.1016/j.bbrc.2013.06.012
60. Jarvius M, Fryknäs M, D’Arcy P, Sun C, Rickardson L, Gullbo J, Haglund C, Nygren P, Linder S, Larsson R. Piperlongumine induces inhibition of the ubiquitin-proteasome system in cancer cells. *Biochem Biophys Res Commun.* 2013; 431:117–23. doi: 10.1016/j.bbrc.2013.01.017
61. Kong EH, Kim YJ, Kim YJ, Cho HJ, Yu SN, Kim KY, Chang JH, Ahn SC. Piplartine induces caspase-mediated apoptosis in PC-3 human prostate cancer cells. *Oncol Rep.* 2008; 20:785–92.
62. Lee HN, Jin HO, Park JA, Kim JH, Kim JY, Kim B, Kim W, Hong SE, Lee YH, Chang YH, Hong SI, Hong YJ, Park IC, et al. Heme oxygenase-1 determines the differential response of breast cancer and normal cells to piperlongumine. *Mol Cells.* 2015; 38:327–35. doi: 10.14348/molcells.2015.2235
63. Li W, Wen C, Bai H, Wang X, Zhang X, Huang L, Yang X, Iwamoto A, Liu H. JNK signaling pathway is involved in piperlongumine-mediated apoptosis in human colorectal cancer HCT116 cells. *Oncol Lett.* 2015; 10:709–15.

64. Makhov P, Golovine K, Teper E, Kutikov A, Mehrazin R, Corcoran A, Tulin A, Uzzo RG, Kolenko VM. Piperlongumine promotes autophagy via inhibition of Akt/mTOR signalling and mediates cancer cell death. *Br J Cancer*. 2014; 110:899–907. doi: 10.1038/bjc.2013.810
65. Niu M, Shen Y, Xu X, Yao Y, Fu C, Yan Z, Wu Q, Cao J, Sang W, Zeng L, Li Z, Liu X, Xu K. Piperlongumine selectively suppresses ABC-DLBCL through inhibition of NF- $\kappa$ B p65 subunit nuclear import. *Biochem Biophys Res Commun*. 2015; 462:326–31. doi: 10.1016/j.bbrc.2015.04.136
66. Ryu J, Kim MJ, Kim TO, Huh TL, Lee SE. Piperlongumine as a potential activator of AMP-activated protein kinase in HepG2 cells. *Nat Prod Res*. 2014; 28:2040–43. doi: 10.1080/14786419.2014.919283
67. Shrivastava S, Jeengar MK, Thummuri D, Naidu VG. Piperlongumine inhibits growth potential of gastric cancer cells by targeting PI3K/Akt/mTOR signaling pathway. *Eur J Cancer*. 2014; 50:S9–9. doi: 10.1016/S0959-8049(14)70032-2
68. Shrivastava S, Kulkarni P, Thummuri D, Jeengar MK, Naidu VG, Alvala M, Redddy GB, Ramakrishna S. Piperlongumine, an alkaloid causes inhibition of PI3 K/Akt/mTOR signaling axis to induce caspase-dependent apoptosis in human triple-negative breast cancer cells. *Apoptosis*. 2014; 19:1148–64. doi: 10.1007/s10495-014-0991-2
69. Wang F, Mao Y, You Q, Hua D, Cai D. Piperlongumine induces apoptosis and autophagy in human lung cancer cells through inhibition of PI3K/Akt/mTOR pathway. *Int J Immunopathol Pharmacol*. 2015; 28:362–73. doi: 10.1177/0394632015598849
70. Rudin CM, Hann CL, Garon EB, Ribeiro de Oliveira M, Bonomi PD, Camidge DR, Chu Q, Giaccone G, Khaira D, Ramalingam SS, Ranson MR, Dive C, McKeegan EM, et al. Phase II study of single-agent navitoclax (ABT-263) and biomarker correlates in patients with relapsed small cell lung cancer. *Clin Cancer Res*. 2012; 18:3163–69. doi: 10.1158/1078-0432.CCR-11-3090
71. Schoenwaelder SM, Jarman KE, Gardiner EE, Hua M, Qiao J, White MJ, Josefsson EC, Alwis I, Ono A, Willcox A, Andrews RK, Mason KD, Salem HH, et al. Bcl-xL-inhibitory BH3 mimetics can induce a transient thrombocytopathy that undermines the hemostatic function of platelets. *Blood*. 2011; 118:1663–74. doi: 10.1182/blood-2011-04-347849
72. Vogler M, Hamali HA, Sun XM, Bampton ET, Dinsdale D, Snowden RT, Dyer MJ, Goodall AH, Cohen GM. BCL2/BCL-X(L) inhibition induces apoptosis, disrupts cellular calcium homeostasis, and prevents platelet activation. *Blood*. 2011; 117:7145–54. doi: 10.1182/blood-2011-03-344812
73. Lujambio A. To clear, or not to clear (senescent cells)? That is the question. *BioEssays*. 2016 (Suppl 1); 38:S56–64. doi: 10.1002/bies.201670910

## PI3K $\alpha$ inhibition reduces obesity in mice

Elena Lopez-Guadamillas<sup>1</sup>, Maribel Muñoz-Martin<sup>1</sup>, Sonia Martinez<sup>2</sup>, Joaquin Pastor<sup>2</sup>, Pablo J. Fernandez-Marcos<sup>3</sup>, Manuel Serrano<sup>1</sup>

<sup>1</sup>Tumor Suppression Group, Spanish National Cancer Research Center (CNIO), Madrid E28029, Spain

<sup>2</sup> Experimental Therapeutics Programme, Spanish National Cancer Research Center (CNIO), Madrid E28029, Spain

<sup>3</sup>Bioactive Products and Metabolic Syndrome Group, Madrid Institute of Advanced Studies (IMDEA) in Food, CEI UAM+CSIC, Madrid E28049, Spain

**Correspondence to:** Manuel Serrano; email: [mserrano@cnio.es](mailto:mserrano@cnio.es)

**Keywords:** PI3K, obesity, energy expenditure, diabetes, metabolism

**Received:** August 19, 2016

**Accepted:** October 18, 2016

**Published:** November 4, 2016

### ABSTRACT

Partial inhibition of PI3K is one of the best-validated and evolutionary conserved manipulations to extend longevity. The best known health beneficial effects of reduced PI3K are related to metabolism and include increased energy expenditure, reduced nutrient storage, and protection from obesity. We have previously shown that a dual chemical inhibitor of the alpha and delta PI3K isoforms (CNIO-PI3Ki) reduces obesity in mice and monkeys, without evident toxic effects after long-term treatment. Here, we dissect the role of the alpha and delta PI3K isoforms by making use of selective inhibitors against PI3K $\alpha$  (BYL-719 also known as alpelisib) or PI3K $\delta$  (GS-9820 also known as acalisib). Treatment of mice with the above mentioned inhibitors indicated that BYL-719 increases energy expenditure in normal mice and efficiently reduces body weight in obese (ob/ob) mice, whereas these effects were not observed with GS-9820. Of note, the dose of BYL-719 required to reduce obesity was 10-times higher than the equivalent dose of CNIO-PI3Ki, which could suggest that simultaneous inhibition of PI3K alpha and delta is more beneficial than single inhibition of the alpha isoform. In summary, we conclude that inhibition of PI3K $\alpha$  is sufficient to increase energy expenditure and reduce obesity, and suggest that concomitant PI3K $\delta$  inhibition could play an auxiliary role.

### INTRODUCTION

The first gene mutation found to extend longevity in an animal was in the age-1 gene of *Caenorhabditis elegans* [1], which was later shown to encode the catalytic p110 $\alpha$  subunit of class I phosphatidylinositol-4,5-bisphosphate 3-kinase (PI3K $\alpha$ ) [2]. PI3K $\alpha$  mediates the signaling of numerous factors, being insulin and insulin-like growth factor 1 (IGF1) of special relevance. Indeed, partial genetic reduction of the insulin and IGF1 signaling (IIS) pathways at different levels extends longevity in worms, flies and mice [3]. For example, similar to worms, heterozygous inactivation of the gene encoding PI3K $\alpha$  also extends longevity in mice [4]. Despite the strong link between PI3K down-modulation and longevity, it remains unclear which of its multiple physiological consequences are responsible for the beneficial effects on health and aging. A main function of the PI3K pathway is to activate anabolism and nutrient

storage and, conversely, a consistent observation in a variety of genetic mouse models with partial PI3K down-modulation is their higher energy expenditure and protection from obesity [5]. Therefore, the beneficial metabolic effects of reduced PI3K signaling could explain, at least in part, the improved healthspan and delayed aging. Furthermore, inhibition of the PI3K downstream effector mTOR by rapamycin also increases longevity [6] and reduces body weight [7].

The above-described genetic evidences make very attractive the possibility that moderate inhibition of PI3K with small chemical compounds could have beneficial health effects. Indeed, two selective inhibitors of PI3K $\alpha$ , PIK75 and A66, reduce body weight in normal lean mice but present negative effects including reduced locomotor activity [8]. On the other hand, we have shown that a chemical PI3K inhibitor with good

oral bioavailability and pharmacokinetics, named CNIO-PI3Ki, can efficiently reduce adiposity in obese mice and in obese Rhesus monkeys in the absence of detectable toxicities [9]. Of note, CNIO-PI3Ki not only inhibits PI3K $\alpha$  but also PI3K $\delta$  [9]. PI3K $\delta$  is one of the four class I PI3K isoforms [10] and is mainly involved in the regulation of immune cells [11]. Interestingly, there is a strong association between inflammation of the adipose tissue and the pathological manifestations of obesity [12]. Based on this, it is conceivable that the inhibition of PI3K $\delta$  could also contribute to the beneficial metabolic effects of CNIO-PI3Ki.

In this report, we use selective inhibitors of PI3K $\alpha$  and PI3K $\delta$  in mice to determine their efficacy in reducing obesity and elevating energy expenditure.

## RESULTS

### Differential effects of PI3K inhibitors on obesity in ob/ob mice

To dissect the relative contribution of PI3K $\alpha$  and PI3K $\delta$  inhibition in the reduction of obesity, we treated obese hyperphagic ob/ob mice with a selective PI3K $\alpha$  inhibitor, BYL-719 [13], or with a selective PI3K $\delta$  inhibitor, GS-9820 (also known as CAL-120) [14]. Remarkably, BYL-719 reduced body weight after 15 days of treatment to a similar extent as CNIO-PI3Ki, whereas GS-9820 had no significant effect at the same doses as BYL-719 (Figure 1A and 1B). It should be noted that 10 mg/kg of GS-9820 is sufficient to reduce the growth of multiple myeloma xenografts in mice [15]. Interestingly, CNIO-PI3Ki at 1 mg/kg was as effective as BYL-719 at 10 mg/kg. The higher efficiency of CNIO-PI3Ki may be due to a number of reasons, such as for example a better pharmacokinetics, but it could also reflect a contribution of PI3K $\delta$  inhibition in the reduction of obesity in the context of simultaneous PI3K $\alpha$  inhibition. We conclude that inhibition of PI3K $\alpha$  is sufficient to reduce obesity, but we cannot exclude an additional auxiliary benefit due to the concomitant inhibition of PI3K $\delta$ .

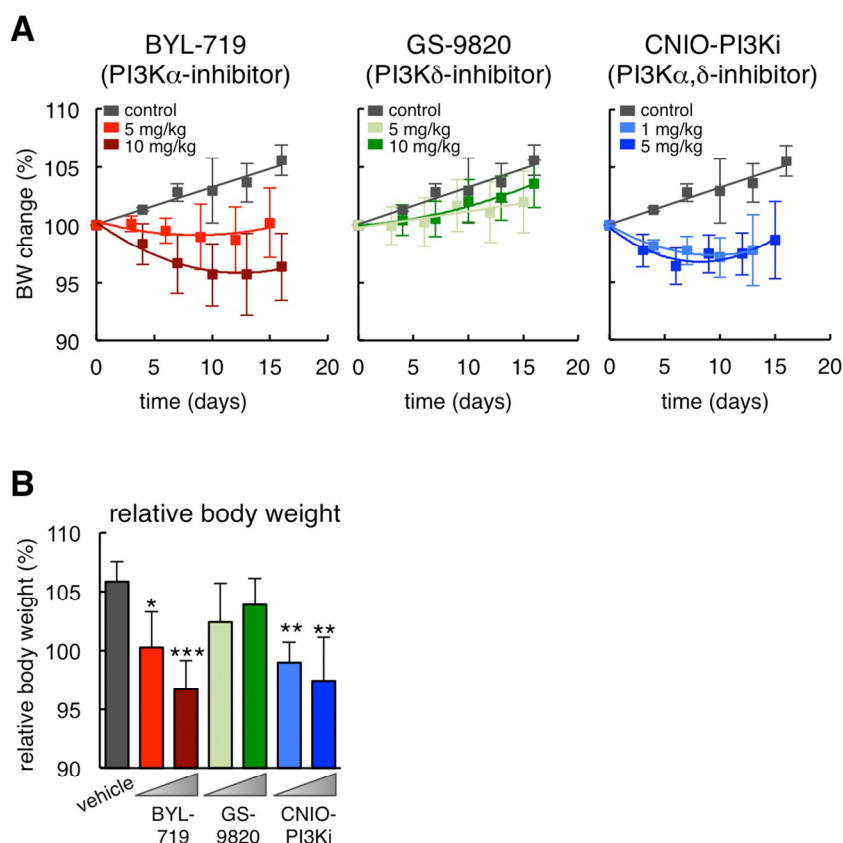


**Figure 1. Differential effects of PI3K inhibitors on obesity in ob/ob mice.** (A) Body weight change relative to day 0 during daily dosing of the indicated PI3K inhibitors (n=10 per group, ob/ob males, 20 weeks old). The vehicle treated group is the same for the three graphs. (B) Relative body weight change at the end of the treatment (day 15 or 16) of the same experimental groups shown in panel A. Values correspond to average  $\pm$  s.d. Statistical significance was determined by the two-tailed Student's t-test relative to vehicle controls: \* $p < 0.05$ , \*\* $p < 0.01$ , \*\*\* $p < 0.001$ .



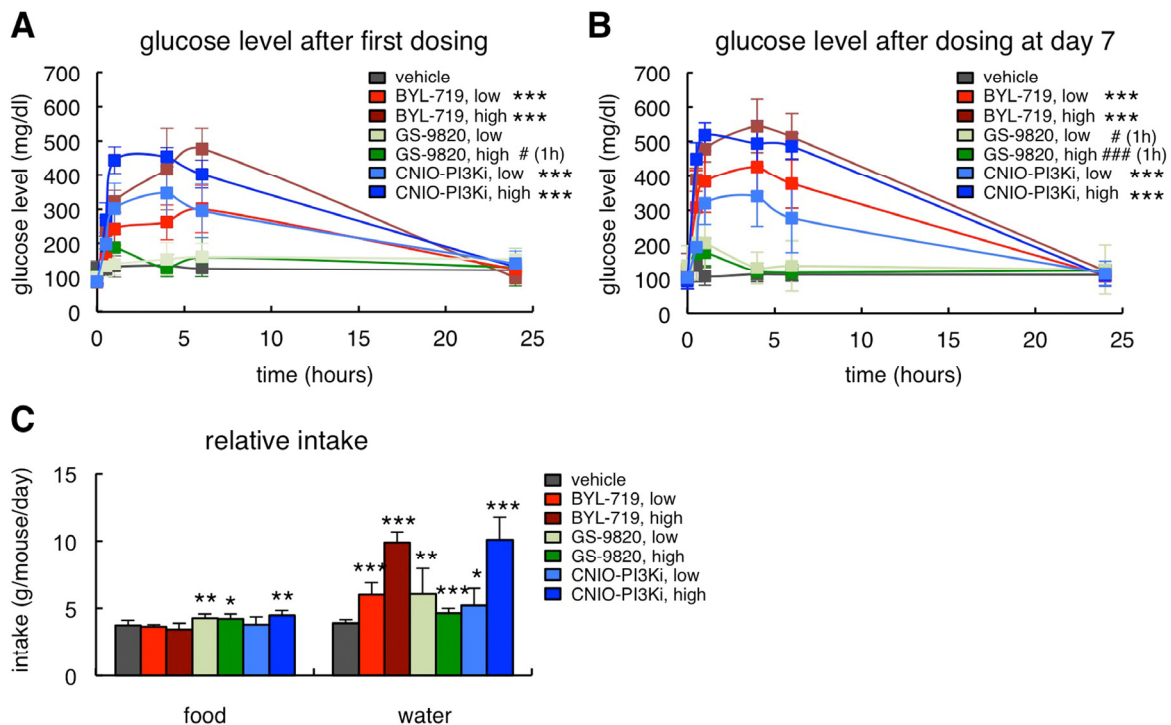


**Figure 2. On-target effects of PI3K $\alpha$  inhibition in ob/ob mice.** (A) Glucose serum excursions after a single administration of vehicle, BYL-719 (5 or 10 mg/kg), GS-9820 (5 or 10 mg/kg) or CNIO-PI3Ki (1 or 5 mg/kg) by oral gavage (n=10 per group, ob/ob males, 20 weeks old). Treatments and measurements were done under ad libitum feeding. (B) Glucose serum excursions measured 7 days after the beginning of the treatment in the same mice as in Figure 2A. (C) Relative food and water intake in the same mice as in Figure 1A. The results correspond to the average daily food and water intake from days 7 to 12. Values correspond to the average  $\pm$  s.d. Statistical significance was determined by the two-tailed Student's t-test relative to vehicle controls: \*  $p < 0.05$ , \*\*  $p < 0.01$ , \*\*\*  $p < 0.001$ . In Figures 2A and 2B, significant differences were found from 0.5 h to 6 h post-gavage, except for acalisib that is significant only at 1 h, indicated with # (1h).

### On-target effects of PI3K $\alpha$ inhibition in ob/ob mice

PI3K $\alpha$  is involved in the signaling of insulin and, therefore, hyperglycemia is an expected on-target effect of PI3K $\alpha$  inhibitors. In this regard, we have previously reported that, in lean mice, CNIO-PI3Ki at 15 mg/kg produces a moderate glycemic excursion, within physiological range (up to 150 mg/dl of serum glucose), and reversible within 8 h [9]. Obese ob/ob mice are insulin resistant and therefore their glycemic excursions were severe (up to 500 mg/dl) in the case of the two PI3K $\alpha$  inhibitors, CNIO-PI3Ki and BYL-719, whereas GS-9820 had a comparatively minor effect (Figure 2A). It is important to note that the hyperglycemia produced by 1 mg/kg CNIO-PI3Ki was less severe than the one produced by 10 mg/kg BYL-719 (Figure 2A), being both treatments equally efficient in reducing obesity (Figures 1A and 1B). The hyperglycemic peaks were in all cases fully normalized after 24 h (Figure 2A). Furthermore, in mice that had been treated daily with the PI3K inhibitors for 7 days, glucose levels were

also normal 24 h after the last administration of inhibitors (Figure 2B). The severe hyperglycemia produced in ob/ob mice was also reflected by their increased water intake, a compensatory response to reduce hyperglycemia (Figure 2C). Finally, we observed a modest increase in food intake in mice treated with GS-9820 or with high-dose CNIO-PI3Ki (Figure 2C).

Inhibition of insulin signaling not only affects glucose homeostasis but also lipid metabolism. Therefore, another anticipated on-target effect of PI3K $\alpha$  inhibition in the white adipose tissue is a reduction in the uptake of dietary triglycerides (TG) and an increase in lipolysis that results in elevated serum free fatty acids (FFA) [16,17]. These effects are recapitulated by treatment with rapamycin, which inhibits mTOR, a key downstream effector of PI3K [18]. In agreement with this, mice treated for 15 days with BYL-719 or CNIO-PI3Ki presented increased serum TG (Figure 3A) and FFA (Figure 3B), while GS-9820 had no detectable effect on serum lipids.

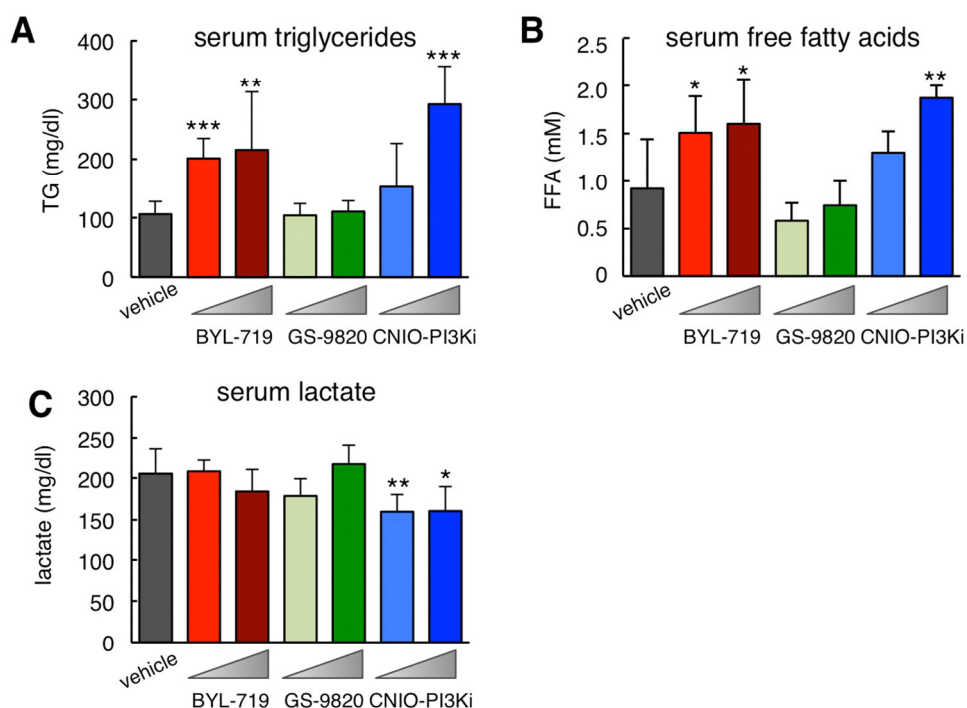


**Figure 3. Biochemical serum profile of ob/ob mice after treatment with PI3K inhibitors.** (A) Serum triglycerides (TG) in the same mice as in Figure 1A measured 3-4 hours after the last dosing at the end of the treatment (always under ad libitum feeding). (B) Serum free fatty acids (FFA) as in panel A. (C) Serum lactate as in panel A. Values correspond to average  $\pm$  s.d. Statistical significance was determined by the two-tailed Student's t-test relative to vehicle controls: \*  $p < 0.05$ , \*\*  $p < 0.01$ , \*\*\*  $p < 0.001$ .

Partial down-modulation of PI3K has been reported to reduce serum lactate levels due to increased mitochondrial oxidative phosphorylation [19] and this effect has also been observed upon treatment with rapamycin [20]. Interestingly, mice treated for 15 days with 1 mg/kg CNIO-PI3Ki had a significant reduction in serum lactate, whereas this was not observed with BYL-719 or with GS-9820 at 10 mg/kg (Figure 3C). All together, we validate that BYL-719 and CNIO-PI3Ki are inhibiting PI3K $\alpha$  *in vivo* by using a number of on-target readouts (hyperglycemia, increased serum lipids, and reduced serum lactate), whereas these effects are absent upon treatment with GS-9820.

#### Differential effect of PI3K inhibitors in energy expenditure

The PI3K pathway is a major inducer of anabolism and, therefore, genetic down-modulation of PI3K by PTEN or treatment of mice with CNIO-PI3Ki elevates energy expenditure [19,21]. We used lean wild-type mice to test the effect of a single dose (15 mg/kg) of each of the three PI3K inhibitors on energy expenditure. Interestingly, BYL-719, but not GS-9820, elevated energy expenditure during 7 h after oral administration in a similar way as CNIO-PI3Ki (Figure 4A). No chan-

ges in locomotor activity were observed in any of the treated mice (Figure 4B). Normal locomotor activity suggests the absence of severe toxic effects, and also excludes the possibility that increased physical activity could be the underlying reason for the increased energy expenditure. We conclude that PI3K $\alpha$ , but not PI3K $\delta$ , regulates energy expenditure in mice.

## DISCUSSION

Previous work by us has shown that a dual PI3K $\alpha$  and PI3K $\delta$  inhibitor, namely CNIO-PI3Ki, reduces obesity and elevates energy expenditure in mice. Here, we have used selective inhibitors of PI3K $\alpha$  and PI3K $\delta$  and we have concluded that PI3K $\alpha$  is the main isoform responsible for these beneficial metabolic effects. These observations are in agreement with the reported protection against aging-associated obesity of mice with reduced expression of PI3K $\alpha$  [4]. It should be noted that CNIO-PI3Ki seems more efficient than BYL-719 in reducing obesity. Although the differential efficacy of the two inhibitors can have several explanations, one possibility is that PI3K $\delta$  inhibition, although not sufficient by itself, contributes to reduce obesity in the context of simultaneous PI3K $\alpha$  inhibition.

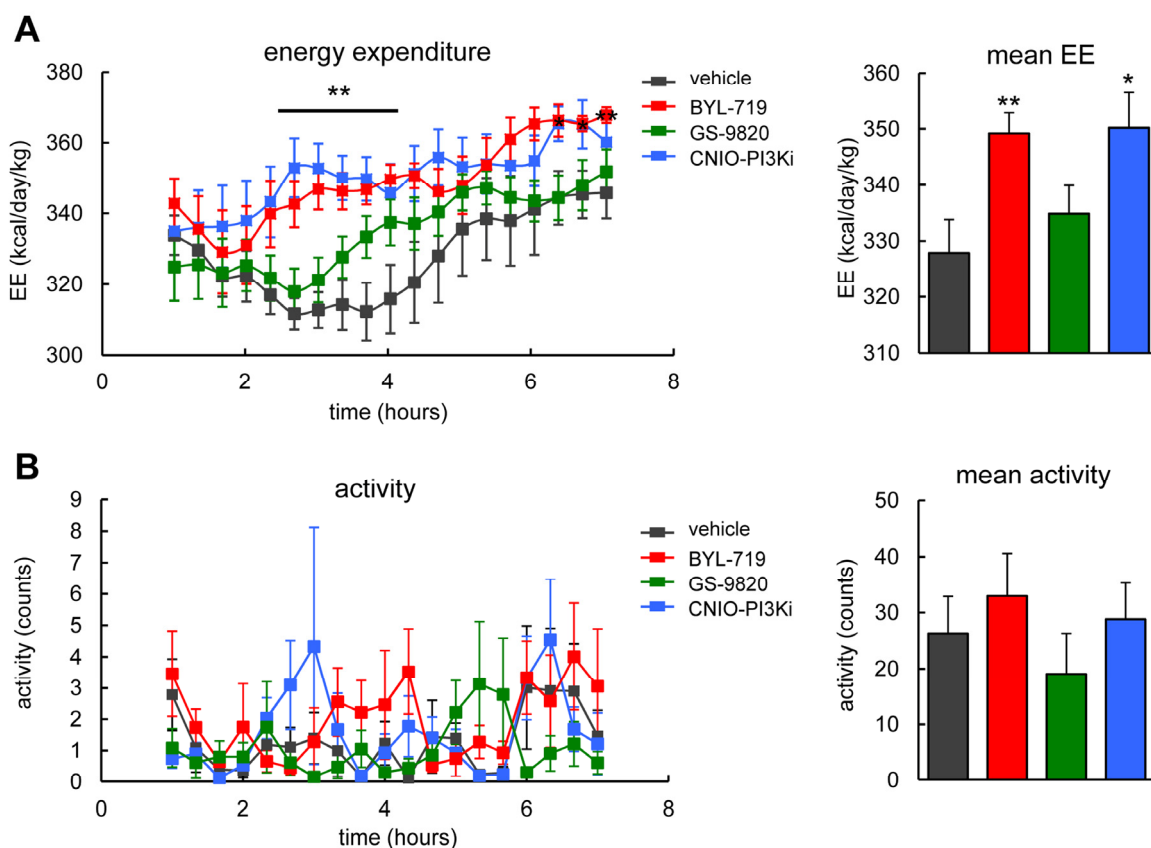


**Figure 4. Energy expenditure and activity of wild-type mice after treatment with PI3K inhibitors.** (A) *Left*, energy expenditure (EE). *Right*, mean EE. Calorimetry of male WT mice, under ad libitum feeding, after a single oral dose of 15 mg/kg of the indicated PI3K inhibitors (n=7-8 per group, C57BL6 males, 20 weeks old). The line and asterisks indicate that CNIO-PI3Ki and BYL-719 are significantly different relative to vehicle at these time points. (B) *Left*, activity. *Right*, mean activity. Activity was measured in the same mice as in panel A. Values correspond to average  $\pm$  s.e.m. Statistical significance was determined by the two-tailed Student's t-test relative to vehicle controls: \*  $p < 0.05$ . \*\*  $p < 0.01$ .

In addition, we have validated some on-target effects of PI3K $\alpha$  inhibition produced as a consequence of reduced insulin signaling, including elevated levels of serum glucose, and serum lipids. In contrast, PI3K $\delta$  inhibition by GS-9820 did not produce any of these effects even administered at a dose that was shown to have anti-tumoral effectiveness [15], thereby confirming its minor role in insulin signaling. The most dramatic on-target effect of PI3K $\alpha$  inhibition was hyperglycemia, which in the case of the ob/ob mice was severe due to their diabetic condition. However, it is important to note that in normal lean mice, the glycemia induced by PI3K $\alpha$  inhibition is within physiological range [9]. In summary, we conclude that moderate pharmacological inhibition of PI3K $\alpha$  is sufficient to elicit the metabolic beneficial effects of reduced PI3K signaling. Our results, however, leave open the possibility that inhibition of PI3K $\delta$  could also contribute to these effects in the context of concomitant PI3K $\alpha$  inhibition.

## MATERIALS AND METHODS

### Ethics statement

All animal procedures were approved by the CNIO-ISCIII Ethics Committee for Research and Animal Welfare (CEIyBA) and the Community of Madrid, and conducted in accordance to the recommendations of the Federation of European Laboratory Animal Science Associations (FELASA) and the institutional guidelines.

### Mouse experimentation

Mice were housed under specific pathogen free (SPF) conditions, at 22°C, and with 12 hours dark/light cycles (light cycle from 8 am to 8 pm). Mice were fed with standard chow diet (Harlan Teklad 2018, 18% of fat-based caloric content). Ob/ob C57BL6J mice were purchased from Charles River Laboratories. Wild-type C57BL6J/Ola.Hsd mice were purchased from Harlan.

All mice used were males of 20 weeks of age. PI3K inhibitors were administered daily by oral gavage during 15 or 16 days as follows, BYL-719 (5 and 10 mg/kg) and GS-9820 (5 and 10 mg/kg), CNIO-PI3Ki (1 and 5 mg/kg), dissolved in PEG-300 (Sigma) and 10% N-methyl-2-pyrrolidone (Sigma).

### Serum analyses

For glucose excursions (Figure 2 A and B), mice under ad libitum feeding were treated with a single dose of the indicated PI3K inhibitors by oral gavage (at 10:00 am) and blood was collected from the tail tip for the determination of glucose (Glucocard strips; A. Meranini). For all the other serum analyses, mice at the end of their corresponding daily treatments for 15-16 days received a final dose of treatment and were sacrificed 3-4 h later (always under ad libitum feeding). Blood was collected from post-mortem heart puncture. Serum free fatty acids were quantified by a colorimetric assay (BioVision #K612-100). Triglycerides and lactate levels were measured using the ABX PENTRA 400 clinical chemical analyzer (Horiba ABX Diagnostics).

### Indirect calorimetry and activity

Indirect calorimetry was performed following standard methods using Oxylet System metabolic chambers (Panlab Harvard Apparatus). Acclimatization of mice to the measurement cages was three days prior to data recording. Mice under ad libitum feeding were treated with a single dose of 15 mg/kg for each PI3K inhibitor (BYL-719, GS-9820 and CNIO-PI3Ki) by gavage. The volumes of consumed O<sub>2</sub> (VO<sub>2</sub>) and eliminated CO<sub>2</sub> (VCO<sub>2</sub>) were recorded every 24 min (8 simultaneous metabolic chambers) for the following 7 hrs. Room temperature was constantly kept at 21°C. Energy Expenditure (EE) was calculated as  $EE = 3.815 + (1.232 \times (VCO_2/VO_2)) \times VO_2 \times 1.44$ . Mouse activity was recorded in time intervals of 20 min during the whole measurement period.

### Statistical analyses

Values are expressed as mean  $\pm$  s.d. (Figures 1 to 3) or mean  $\pm$  s.e.m (Figure 4). Statistical analyses were performed using unpaired two-tailed Student's t-test and differences with *P* values of <0.05 were considered to be statistically significant (\* *p*<0.05, \*\* *p*<0.01, \*\*\* *p*<0.001). Statistical analyses were performed using Excel or GraphPad Prism software.

### AUTHOR CONTRIBUTIONS

E.L.-G. participated in the conceptual and experimental design, carried out and analyzed most of the

experiments, and wrote the manuscript; M.M.-M. helped with animal experimentation; S.M. and J.P. synthesized the PI3K inhibitors; P.J.F.-M. carried out the calorimetry; M.S. conceived, designed, supervised the work and wrote the manuscript. All authors discussed the results and commented on the manuscript.

### ACKNOWLEDGEMENTS

We thank Cristina Pantoja for her help. We also thank Gema Iglesias for animal handling.

### CONFLICTS OF INTEREST

The authors have no conflict of interests to declare.

### FUNDING

E.L.-G. was recipient of a predoctoral contract from the Spanish Ministry of Education. P.J.F.-M. has been funded by the Spanish Association Against Cancer (aecc). Work in the laboratory of M.S. is funded by the CNIO and by grants from the Spanish Ministry of Economy co-funded by the European Regional Development Fund (SAF project), the European Research Council (ERC Advanced Grant), the Regional Government of Madrid co-funded by the European Social Fund (ReCaRe project), the Botin Foundation and Banco Santander (Santander Universities Global Division), the Ramon Areces Foundation, and the AXA Foundation.

### REFERENCES

1. Friedman DB, Johnson TE. A mutation in the age-1 gene in *Caenorhabditis elegans* lengthens life and reduces hermaphrodite fertility. *Genetics*. 1988; 118:75–86.
2. Morris JZ, Tissenbaum HA, Ruvkun G. A phosphatidylinositol-3-OH kinase family member regulating longevity and diapause in *Caenorhabditis elegans*. *Nature*. 1996; 382:536–39. doi: 10.1038/382536a0
3. Fontana L, Partridge L, Longo VD. Extending healthy life span—from yeast to humans. *Science*. 2010; 328:321–26. doi: 10.1126/science.1172539
4. Foukas LC, Bilanges B, Bettledi L, Pearce W, Ali K, Sancho S, Withers DJ, Vanhaesebroeck B. Long-term p110 $\alpha$  PI3K inactivation exerts a beneficial effect on metabolism. *EMBO Mol Med*. 2013; 5:563–71. doi: 10.1002/emmm.201201953
5. Ortega-Molina A, Serrano M. PTEN in cancer, metabolism, and aging. *Trends Endocrinol Metab*. 2013; 24:184–89. doi: 10.1016/j.tem.2012.11.002



6. Harrison DE, Strong R, Sharp ZD, Nelson JF, Astle CM, Flurkey K, Nadon NL, Wilkinson JE, Frenkel K, Carter CS, Pahor M, Javors MA, Fernandez E, Miller RA. Rapamycin fed late in life extends lifespan in genetically heterogeneous mice. *Nature*. 2009; 460:392–95. doi: 10.1038/nature08221
7. Leontieva OV, Paszkiewicz GM, Blagosklonny MV. Comparison of rapamycin schedules in mice on high-fat diet. *Cell Cycle*. 2014; 13:3350–56. doi: 10.4161/15384101.2014.970491
8. Smith GC, Ong W-K, Costa JL, Watson M, Cornish J, Grey A, Gamble GD, Dickinson M, Leung S, Rewcastle GW, Han W, Shepherd PR. Extended treatment with selective phosphatidylinositol 3-kinase and mTOR inhibitors has effects on metabolism, growth, behaviour and bone strength. *FEBS J*. 2013; 280:5337–49. doi: 10.1111/febs.12428
9. Ortega-Molina A, Lopez-Guadamillas E, Mattison JA, Mitchell SJ, Muñoz-Martin M, Iglesias G, Gutierrez VM, Vaughan KL, Szarowicz MD, González-García I, López M, Cebrián D, Martinez S, et al. Pharmacological inhibition of PI3K reduces adiposity and metabolic syndrome in obese mice and rhesus monkeys. *Cell Metab*. 2015; 21:558–70. doi: 10.1016/j.cmet.2015.02.017
10. Vanhaesebroeck B, Guillermet-Guibert J, Graupera M, Bilanges B. The emerging mechanisms of isoform-specific PI3K signalling. *Nat Rev Mol Cell Biol*. 2010; 11:329–41. doi: 10.1038/nrm2882
11. Hawkins PT, Stephens LR. PI3K signalling in inflammation. *Biochim Biophys Acta*. 2015; 1851:882–97. doi: 10.1016/j.bbalip.2014.12.006
12. Pellegrinelli V, Carobbio S, Vidal-Puig A. Adipose tissue plasticity: how fat depots respond differently to pathophysiological cues. *Diabetologia*. 2016; 59:1075–88. doi: 10.1007/s00125-016-3933-4
13. Furet P, Guagnano V, Fairhurst RA, Imbach-Weese P, Bruce I, Knapp M, Fritsch C, Blasco F, Blanz J, Aichholz R, Hamon J, Fabbro D, Caravatti G. Discovery of NVP-BYL719 a potent and selective phosphatidylinositol-3 kinase alpha inhibitor selected for clinical evaluation. *Bioorg Med Chem Lett*. 2013; 23:3741–48. doi: 10.1016/j.bmcl.2013.05.007
14. Lannutti BJ, Meadows SA, Herman SE, Kashishian A, Steiner B, Johnson AJ, Byrd JC, Tyner JW, Loriaux MM, Deininger M, Druker BJ, Puri KD, Ulrich RG, Giese NA. CAL-101, a p110 $\delta$  selective phosphatidylinositol-3-kinase inhibitor for the treatment of B-cell malignancies, inhibits PI3K signaling and cellular viability. *Blood*. 2011; 117:591–94. doi: 10.1182/blood-2010-03-275305
15. Ikeda H, Hideshima T, Fulciniti M, Perrone G, Miura N, Yasui H, Okawa Y, Kiziltepe T, Santo L, Vallet S, Cristea D, Calabrese E, Gorgun G, et al. PI3K/p110delta is a novel therapeutic target in multiple myeloma. *Blood*. 2010; 116:1460–68. doi: 10.1182/blood-2009-06-222943
16. Dimitriadis G, Mitrou P, Lambadiari V, Maratou E, Raptis SA. Insulin effects in muscle and adipose tissue. *Diabetes Res Clin Pract*. 2011 (Suppl 1); 93:S52–59. doi: 10.1016/S0168-8227(11)70014-6
17. Frayn KN. Adipose tissue as a buffer for daily lipid flux. *Diabetologia*. 2002; 45:1201–10. doi: 10.1007/s00125-002-0873-y
18. Blagosklonny MV. Rapamycin-induced glucose intolerance: hunger or starvation diabetes. *Cell Cycle*. 2011; 10:4217–24. doi: 10.4161/cc.10.24.18595
19. Garcia-Cao I, Song MS, Hobbs RM, Laurent G, Giorgi C, de Boer VC, Anastasiou D, Ito K, Sasaki AT, Rameh L, Carracedo A, Vander Heiden MG, Cantley LC, et al. Systemic elevation of PTEN induces a tumor-suppressive metabolic state. *Cell*. 2012; 149:49–62. doi: 10.1016/j.cell.2012.02.030
20. Leontieva OV, Blagosklonny MV. M(o)TOR of pseudo-hypoxic state in aging: rapamycin to the rescue. *Cell Cycle*. 2014; 13:509–15. doi: 10.4161/cc.27973
21. Ortega-Molina A, Efeyan A, Lopez-Guadamillas E, Muñoz-Martin M, Gómez-López G, Cañamero M, Mulero F, Pastor J, Martinez S, Romanos E, Mar Gonzalez-Barroso M, Rial E, Valverde AM, et al. Pten positively regulates brown adipose function, energy expenditure, and longevity. *Cell Metab*. 2012; 15:382–94. doi: 10.1016/j.cmet.2012.02.001



# Mitophagy-driven mitochondrial rejuvenation regulates stem cell fate

Alejandro Vazquez-Martin<sup>1</sup>, Chris Van den Haute<sup>2</sup>, Sílvia Cufi<sup>3</sup>, Bruna Corominas-Faja<sup>4</sup>, Elisabet Cuyàs<sup>4</sup>, Eugeni Lopez-Bonet<sup>5</sup>, Esther Rodriguez-Gallego<sup>6</sup>, Salvador Fernández-Arroyo<sup>6</sup>, Jorge Joven<sup>6</sup>, Veerle Baekelandt<sup>2</sup>, and Javier A. Menendez<sup>4,7</sup>

<sup>1</sup>Cancer Research Group, Latvian Biomedical Research & Study Centre, Riga, Latvia

<sup>2</sup>Laboratory for Neurobiology and Gene Therapy, Department of Neurosciences, Katholieke Universiteit Leuven, Leuven, Flanders, Belgium

<sup>3</sup>Josep Carreras Leukemia Research Institute, Stem Cell Lab, Barcelona, Spain

<sup>4</sup>Molecular Oncology Group, Girona Biomedical Research Institute (IDIBGI), Girona, Spain

<sup>5</sup>Department of Anatomical Pathology, Dr. Josep Trueta Hospital of Girona, Girona, Catalonia, Spain

<sup>6</sup>Unitat de Recerca Biomèdica, Hospital Universitari Sant Joan, Institut d'Investigació Sanitària Pere Virgili (IISPV), Universitat Rovira i Virgili, Reus, Spain

<sup>7</sup>ProCURE (Program Against Cancer Therapeutic Resistance), Metabolism and Cancer Group, Catalan Institute of Oncology, Girona, Spain

**Key words:** mitophagy, mitochondria, stem cells, pluripotency, cancer, epigenetics

**Received:** 02/11/16; **Accepted:** 05/30/16; **Published:** 06/13/16

**Correspondence to:** Javier A. Menendez, PhD; Veerle Baekelandt, PhD; Alejandro Vazquez-Martin, PhD

**E-mail:** [jmenendez@idibgi.org](mailto:jmenendez@idibgi.org); [veerle.baekelandt@med.kuleuven.be](mailto:veerle.baekelandt@med.kuleuven.be); [jandraes@yahoo.es](mailto:jandraes@yahoo.es)

**Abstract:** Our understanding on how selective mitochondrial autophagy, or mitophagy, can sustain the archetypal properties of stem cells is incomplete. PTEN-induced putative kinase 1 (PINK1) plays a key role in the maintenance of mitochondrial morphology and function and in the selective degradation of damaged mitochondria by mitophagy. Here, using embryonic fibroblasts from *PINK1* gene-knockout (KO) mice, we evaluated whether mitophagy is a causal mechanism for the control of cell-fate plasticity and maintenance of pluripotency. Loss of *PINK1*-dependent mitophagy was sufficient to dramatically decrease the speed and efficiency of induced pluripotent stem cell (iPSC) reprogramming. Mitophagy-deficient iPSC colonies, which were characterized by a mixture of mature and immature mitochondria, seemed unstable, with a strong tendency to spontaneously differentiate and form heterogeneous populations of cells. Although mitophagy-deficient iPSC colonies normally expressed pluripotent markers, functional monitoring of cellular bioenergetics revealed an attenuated glycolysis in mitophagy-deficient iPSC cells. Targeted metabolomics showed a notable alteration in numerous glycolysis- and TCA-related metabolites in mitophagy-deficient iPSC cells, including a significant decrease in the intracellular levels of  $\alpha$ -ketoglutarate -a key suppressor of the differentiation path in stem cells. Mitophagy-deficient iPSC colonies exhibited a notably reduced teratoma-initiating capacity, but fully retained their pluripotency and multi-germ layer differentiation capacity *in vivo*. *PINK1*-dependent mitophagy pathway is an important mitochondrial switch that determines the efficiency and quality of somatic reprogramming. Mitophagy-driven mitochondrial rejuvenation might contribute to the ability of iPSCs to suppress differentiation by directing bioenergetic transition and metabolome remodeling traits. These findings provide new insights into how mitophagy might influence the stem cell decisions to retain pluripotency or differentiate in tissue regeneration and aging, tumor growth, and regenerative medicine.

## INTRODUCTION

Mitochondrial autophagy, or mitophagy, is a key cellular pathway for mitochondrial quality control that

functions to clear mitochondria [1-4]. Because the selective autophagosome-based mitochondrial degradation process eliminates unwanted or dysfunctional mitochondria after cell stress [5-9],

abnormal mitophagy has a deleterious impact on cell homeostasis and may lead to cell death, which causally contributes to the pathogenesis of degenerative disorders [10-16]. Although our knowledge of mitophagy in somatic cell physiology is extensive, the role of mitophagy in the physiology of stem cells, which have the unique ability to self-renew and differentiate into various cell types, is less understood. Thus, while mitophagy is believed to play a pivotal role in stem cell functions during aging, tissue regeneration, and cancer [17-24], our current understanding on how mitophagy can sustain the archetypal properties of stem cells is rudimentary.

Mitochondria appear to play crucial roles during stemness factor-mediated nuclear reprogramming of somatic cells into induced pluripotent stem cells (iPSCs), a convenient “in a dish” model that allows a comprehensive understanding of stem cell biology. Functional metamorphosis of somatic oxidative phosphorylation into glycolytic metabolism plays a causal role in enabling the reprogramming process of acquisition and maintenance of stemness to occur [25-35]. It is also apparent that the intrinsic metabolic demands that drive reprogramming to stemness involve substantial structural mitochondrial reorganization, transforming mitochondria into a cristae-poor, immature phenotype [36-45]. Paradoxically, the establishment of induced pluripotency requires a transient and early energy-demanding metabolic state characterized by increased mitochondrial oxidative phosphorylation and hyperactive mitophagy [46, 47]. Because the unique metabolic state required to achieve cell plasticity is accompanied by significant temporal changes in mitochondrial function, composition, structure, and maturation, it might appear elementary to suggest that mitophagy is a prerequisite of induced pluripotency. Nonetheless, recent studies have shed light on how interlinked processes critical for mitochondrial health, including mitochondrial fragmentation and mitochondrial fission/fusion, significantly alter the efficiency and speed of induced pluripotency [48-51], but little information is available on the role of mitophagy in the acquisition and maintenance of stemness.

PTEN-induced putative kinase 1 (*PINK1*) encodes a key mitochondrial protein that specifically identifies and commits mitochondria to degradation via selective autophagy [52-63]. Using embryonic fibroblasts from *PINK1* gene-knockout (KO) mice, we here tested the hypothesis that mitophagy is a pivotal mechanism of cell-fate plasticity by converting functionally mature mitochondrial networks into immature states and vice versa during nuclear reprogramming to stemness and

commitment to differentiation, respectively. By examining the ability of mitophagy to causally modulate cell fate decisions during the entry to and exit from pluripotency, we have identified a hitherto unrecognized role of the mitophagy pathway as a critical mitochondrial switch that directs bioenergetic transition and metabolome remodeling traits to ultimately determine the efficiency and quality of nuclear reprogramming and stemness transition in somatic cells.

## RESULTS

### **PINK1-mediated mitophagy is necessary for efficient nuclear reprogramming of somatic cells into iPSCs**

Because the initial stages of reprogramming trigger a stress response involving repression of mitochondrial functions and oxidative stress [36-45, 66], we hypothesized that the critical ability of PINK1 to identify and selectively trim impaired mitochondria from the mitochondrial network might determine the efficiency of reprogramming. To test whether *PINK1*-KO mouse embryonic fibroblasts (MEFs) constitute a useful model to dissect the role of mitophagy in the establishment of induced pluripotency, we first mimicked mitochondrial damage by experimentally depolarizing mitochondria with the uncoupler carbonyl cyanide *m*-chlorophenylhydrazone (CCCP) and then monitoring loss of MitoTracker staining after mitophagy stimulation [62, 67]. Collectively, our findings show that PINK1 is necessary to efficiently drive the mitophagic digestion of damaged mitochondria (Supplemental data; supplemental Fig. 1).

We then used *PINK1*<sup>-/-</sup> MEFs to explore whether PINK1-mediated mitophagy might constitute part of the molecular roadmap facilitating reprogramming. To do this, we compared iPSC generation in early-passage *PINK1*<sup>+/+</sup> and *PINK1*<sup>-/-</sup> MEFs using a three-factor induction protocol (*Oct4*, *Sox2*, and *Klf4*, hereafter referred to as OSK). We transduced MEFs with OSK at a 1:1:1 ratio on day 0 and repeated the transduction up to four times (one infection every 12 h using the same batch of all three retroviruses), after which the regular media was replaced with standard mESC media supplemented with the knockout serum replacement (KSR). As early as 7 days after transduction, clearly recognizable flat, packed, tight colonies characteristic of ES-like cells appeared in OSK-transduced *PINK1*<sup>+/+</sup> MEF cultures (Fig. 1A). Conversely, OSK-transduced *PINK1*<sup>-/-</sup> MEFs mostly failed to display the typical compact ES cell colony morphology (Fig. 1A). Indeed, using a parallel live cell-imaging 96-well-plate-based screening assay to rapidly assess the expression of the

pluripotency-associated surface marker Ssea-1 during reprogramming, we found that the appearance of Ssea-1<sup>+</sup> clusters was delayed by 3-4 days in *PINK1*<sup>-/-</sup> MEFs compared with *PINK1*<sup>+/+</sup> isogenic counterparts (data not shown). We combined the observations of ES cell-like morphological changes (e.g., defined boundaries and high nucleus-to-cytoplasm ratio within individual cells) with alkaline phosphatase (AP) activity, a commonly used pluripotency indicator, to quantify *bona fide* iPSC colonies. From 50,000 *PINK1*<sup>+/+</sup> MEFs transduced, 150±10 colonies were AP-positive at day 14 after transduction, resulting in an iPSC generation efficiency

of 0.3% (Fig. 1A). In contrast, only 30±4 colonies were generated from an equivalent number of *PINK1*<sup>-/-</sup> MEFs, equivalent to an iPSC generation efficiency of 0.06% (Fig. 1A). Concerning the transduction efficiency, we did not observe any significant differences between the two groups (data not shown), thus confirming that the observed decrease in reprogramming efficiency is due to the absence of *PINK1*. These findings show that loss of PINK1-dependent mitophagy is sufficient to dramatically decrease the speed and efficiency of nuclear reprogramming.

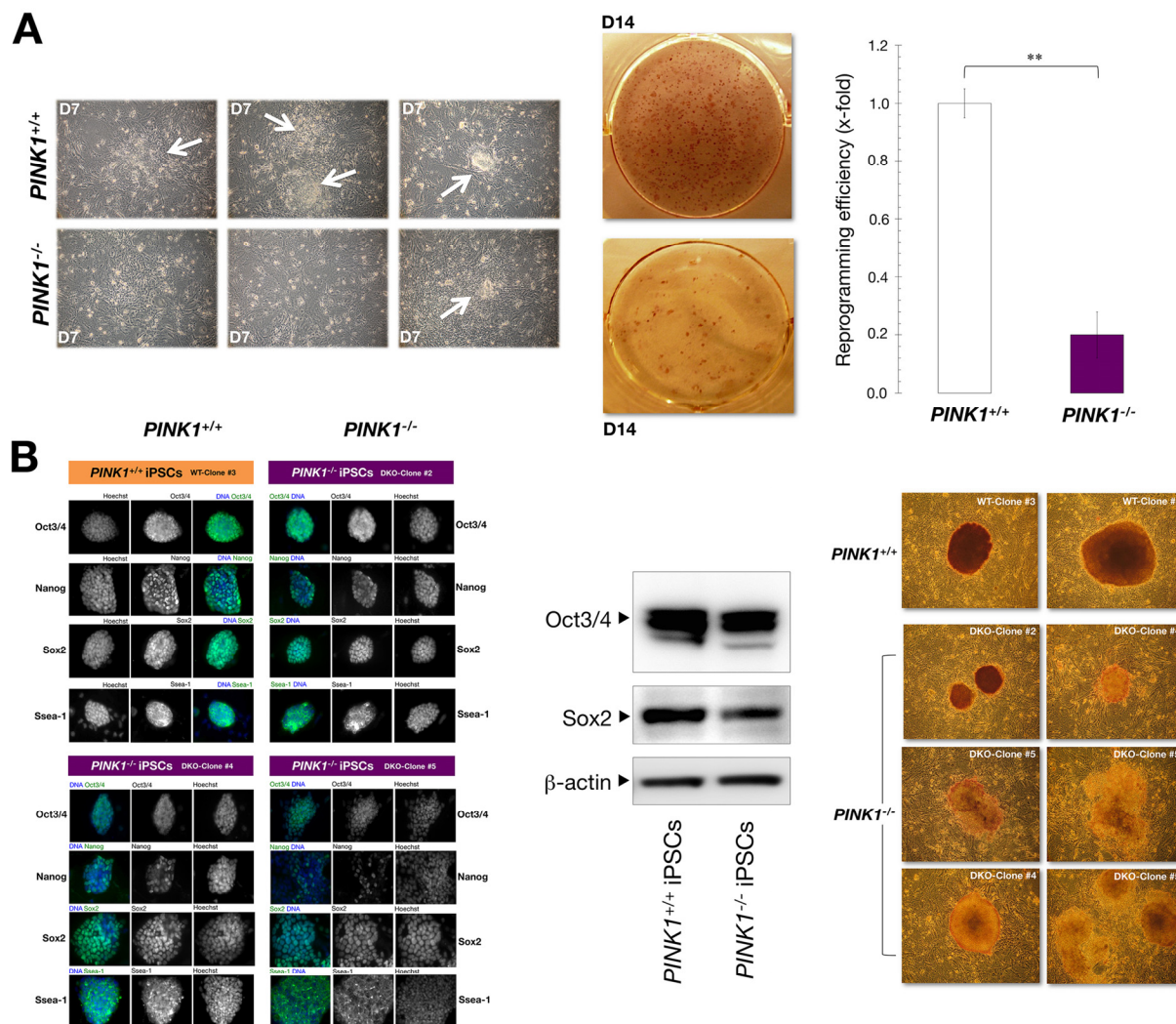


**Figure 1. Mitophagy deficiency is a reprogramming barrier.** (A) Early passage *PINK1*<sup>+/+</sup> and *PINK1*<sup>-/-</sup> MEFs were transduced with retroviral vectors encoding for Oct4, Sox2, and Klf4 and cultured in ES medium. Phase-contrast microphotographs of representative *PINK1*<sup>+/+</sup> and *PINK1*<sup>-/-</sup> MEFs at day 7 (D7) after the initial transduction with OSK are shown (white arrows indicate emerging iPSC-like colonies). Representative photographs of colonies of AP-stained OSK-transduced *PINK1*<sup>+/+</sup> and *PINK1*<sup>-/-</sup> MEFs. The number of AP<sup>+</sup> colonies was counted 14 days after the initial infection and represent reprogramming efficiency relative to *PINK1*<sup>+/+</sup> MEFs (x-fold) (n=6 for each condition). \*\*, P<0.01. (B) Individual iPSC-like colonies were randomly selected from each *PINK1* subtype, cultured on 6-well plates coated with MEF feeder layers, and stained either for AP activity (left) or with antibodies against Oct3/4, Nanog, Sox2, and Ssea-1 (right), as indicated in the “Methods” section. Nuclear staining was performed with Hoechst 33258. Panel depicts representative images of iPSC colonies that were captured using different channels for Oct3/4 (green), Nanog (green), Sox2 (green), Ssea-1 (green), or Hoechst 33258 (blue), as specified. Representative Western blots for Oct3/4 and Sox2 protein expression in *PINK1*<sup>+/+</sup> - *PINK1*<sup>-/-</sup> iPSCs are shown (middle; n = 2).

## Loss of PINK1-mediated mitophagy destabilizes the undifferentiated state in iPSCs

To verify that loss of PINK1-driven mitophagy dampens the reprogramming process, we picked random colonies from the previous experiment and established *PINK1*<sup>+/+</sup>-iPSC and *PINK1*<sup>-/-</sup>-iPSC clonal cell lines on pre-seeded MEF feeder layers, which are known to encourage induced stem cells to remain in an undifferentiated state. Immunofluorescence staining analysis of early-passage iPSCs failed to reveal major differences in the expression level of Oct3/4, Nanog, Sox2, and Ssea-1 of individual cells within *PINK1*<sup>-/-</sup>- and *PINK1*<sup>+/+</sup>-iPSC colonies (Fig. 1B, right). Indeed, immunoblotting procedures demonstrated a similar expression profile of the pluripotency markers Oct3/4 and Sox2 in early-passage *PINK1*<sup>-/-</sup> and *PINK1*<sup>+/+</sup>-iPSCs (Fig. 1B, middle). Both early- and late-passage *PINK1*<sup>+/+</sup>-iPSC colonies were large and well-rounded and stained strongly for AP, reflective of a high percentage of non-differentiated cells (Fig. 1B). The majority of relatively late-passage *PINK1*<sup>-/-</sup>-iPSC colonies, however, were slightly smaller upon colony expansion, with very few showing a smooth, circular and distinct edge, and in many cases displaying irregular morphologies and undefined edges. Indeed, late-passage *PINK1*<sup>-/-</sup>-iPSC colonies tended to rapidly lose AP activity and failed to stably retain the compact colony morphology typical of undifferentiated iPSCs [50, 68] (Fig. 1B, right).

Given that the apparent destabilization of the undifferentiated state of *PINK1*<sup>-/-</sup>-iPSCs occurred without drastic changes in the expression of several pluripotency markers, we explored whether loss of PINK1-driven mitophagy significantly altered the well-known ability of nuclear reprogramming to transform the mitochondrial infrastructure and induce iPSC-associated bioenergetic transition and metabolome remodeling traits [30].

## Mitophagy deficient-iPSCs cannot “rejuvenate” the morphological characteristics of the mitochondria network

We first confirmed that loss of *PINK1* induces a moderate mitochondrial fragmentation in MEFs [52] as well as a more prominent accumulation of mitochondrial aggregates due to impaired mitophagy (Fig. 2A). Given that cell reprogramming leads to mitochondrial structural and functional alterations described as “rejuvenation” [36-42, 44, 45, 66], we used transmission electron microscopy (TEM) to examine whether the decreased capacity of *PINK1*<sup>-/-</sup>-iPSCs to maintain their undifferentiated state involves alterations

in the morphology of the mitochondrial network. Although we could detect a small decrease in the length and area of mitochondria in *PINK1*<sup>-/-</sup> MEFs, together with an increase in the number of mitochondria per cell (Fig. 2B), the majority of mitochondria in both MEF populations had a similar morphology characterized by mature mitochondrial networks with tubular structures and densely-packed cristae (Fig. 2B).

*PINK1*<sup>+/+</sup>-iPSC mitochondria exhibited a dramatically decreased long diameter and increased short diameter relative to *PINK1*<sup>-/-</sup> MEFs (Fig. 2B). Interestingly, though nuclear reprogramming of *PINK1*<sup>+/+</sup>-iPSCs led to the acquisition of an immature mitochondrial phenotype characterized by a rounded morphology with sparse cristae, it was noteworthy that reprogramming failed to fully reset the mitochondrial morphology of *PINK1*<sup>-/-</sup> MEFs to a *bona fide* embryonic-like state. Consequently, *PINK1*<sup>-/-</sup> iPSCs accumulated larger, irregular mitochondria containing different inclusions and more cristae (Fig. 2B). These findings, altogether, strongly suggest that mitophagy deficient-iPSCs fail to fully rejuvenate the morphological characteristics of the mitochondrial network.

## Loss of PINK1-driven mitophagy impairs the bioenergetic transition associated with nuclear reprogramming

Mitochondrial rejuvenation is a key mechanism to protect cells from reprogramming factor-induced oxidative stress and reactive oxygen species (ROS) accumulation, a well-known roadblock to reprogramming [36-42, 44, 45, 66]. We therefore speculated that blockade of PINK1-driven mitophagy might lead to a detrimental accumulation of ROS during the initial stages of reprogramming (Supplemental data; supplemental Fig. 2). Only when forced expression of c-Myc, which can override the cell cycle checkpoints imposed in response to ROS accumulation [69-71], was combined with the exogenous addition of vitamin C *PINK1*<sup>-/-</sup> MEFs reached reprogramming efficiencies equivalent to those observed in OSK-transduced *PINK1*<sup>+/+</sup> MEFs in the absence of this antioxidant (Supplemental data; supplemental Fig. 2). Because the incapacity of the ROS scavenger and epigenetic regulator vitamin C [72-75] to fully bypass the reprogramming roadblock imposed by the loss of *PINK1* suggested that mitophagy-driven remodeling of the mitochondria network into an immature state might constitute a critical barrier during somatic reprogramming, we performed a multimodal metabolic characterization of *PINK1*<sup>-/-</sup> and *PINK1*<sup>+/+</sup> iPSCs at the level of cellular bioenergetics and intracellular metabolome.



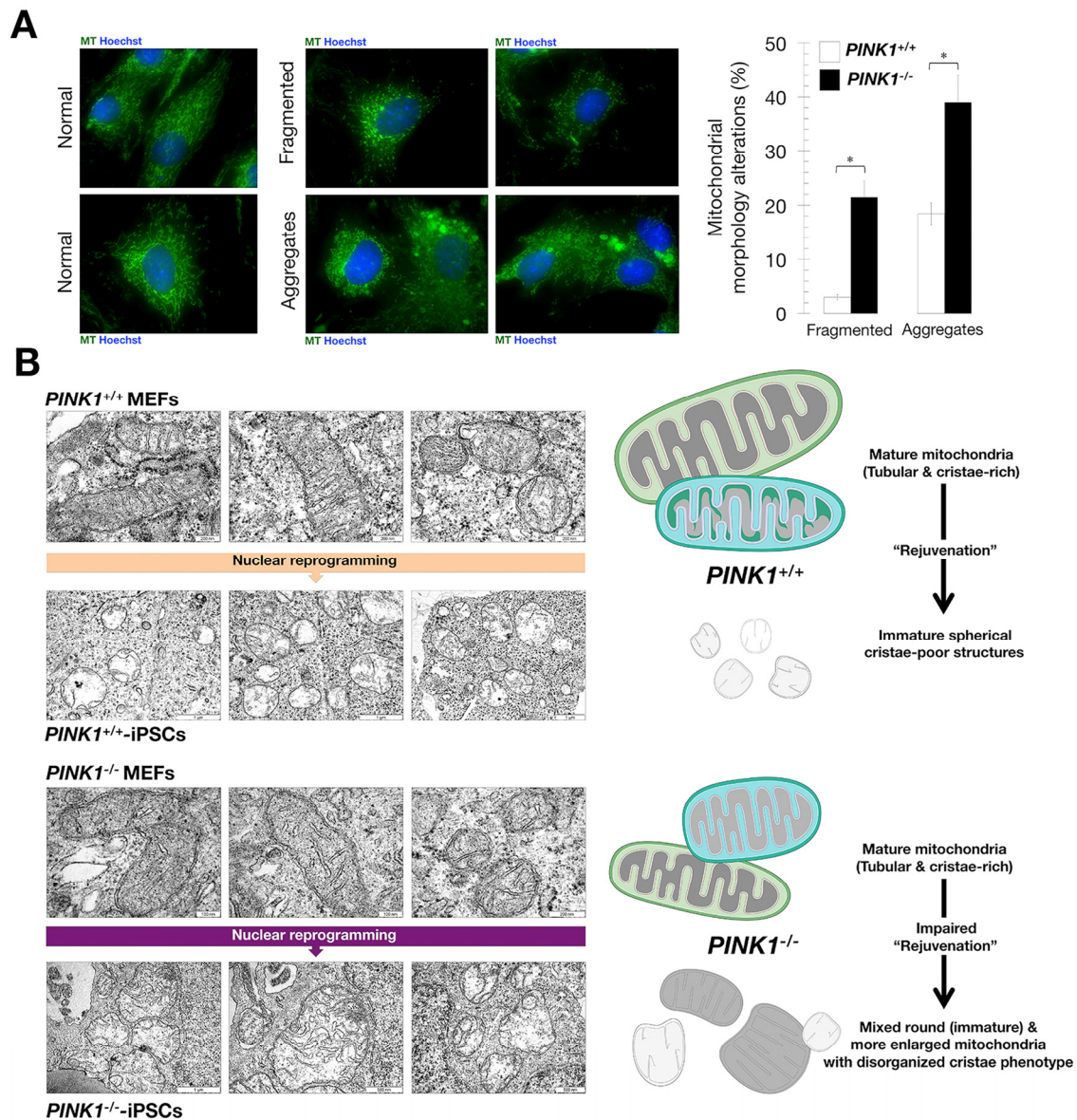


**Figure 2. Mitophagy deficiency impedes the rejuvenation of mitochondria networks in iPSCs.** (A) Loss of *PINK1* induces moderate mitochondrial fragmentation and aggregation in MEFs (MT: MitoTracker). Bar chart depicts the average percentages of cells showing fragmentation and/or aggregation (n=3). \*, P<0.05. (B) Representative TEM images of mitochondria in all cell lines. *PINK1*<sup>+/+</sup> and *PINK1*<sup>-/-</sup> MEFs display a preponderance of tubular and cristae-rich mature mitochondria. *PINK1*<sup>+/+</sup> iPSCs display a preponderance of "rejuvenated" spherical cristae-poor immature mitochondria, whereas *PINK1*<sup>-/-</sup> iPSCs display an impaired "rejuvenation" characterized by an assortment of mitochondrial configurations including round (immature) and more enlarged mitochondria with disorganized cristae.

First, a well-validated extracellular flux technology was employed to establish functional monitoring of cellular bioenergetics in *PINK1*<sup>-/-</sup> and *PINK1*<sup>+/+</sup> iPSCs. Measurement of the extracellular acidification rate (ECAR) enabled real-time assessment of the glycolytic phenotype associated with iPSCs (Fig. 3A). Sequential

supplementation of the glycolytic fuel glucose, the ATP synthase complex V mitochondrial inhibitor oligomycin, and the competitive inhibitor of glucose 2-deoxy-glucose (2-DG), dissected key parameters of glycolytic function, including glycolysis (i.e., the ECAR rate reached by iPSCs after the addition of saturating



amounts of glucose), glycolytic capacity (i.e., the maximum ECAR rate reached upon blockade of oxidative phosphorylation), and glycolytic reserve (i.e., the capability of iPSCs to respond to an energetic demand). *PINK1*<sup>-/-</sup>-iPSCs were found to be significantly less glycolytic than *PINK1*<sup>+/+</sup>-iPSCs

(Fig. 3A), suggesting that the reduced capacity of mitophagy deficient-iPSCs to efficiently drive mitochondrial metamorphosis translate into a reduced capacity to bioenergetically transitioning from somatic cellular respiration to glycolysis during iPSC derivation [30].

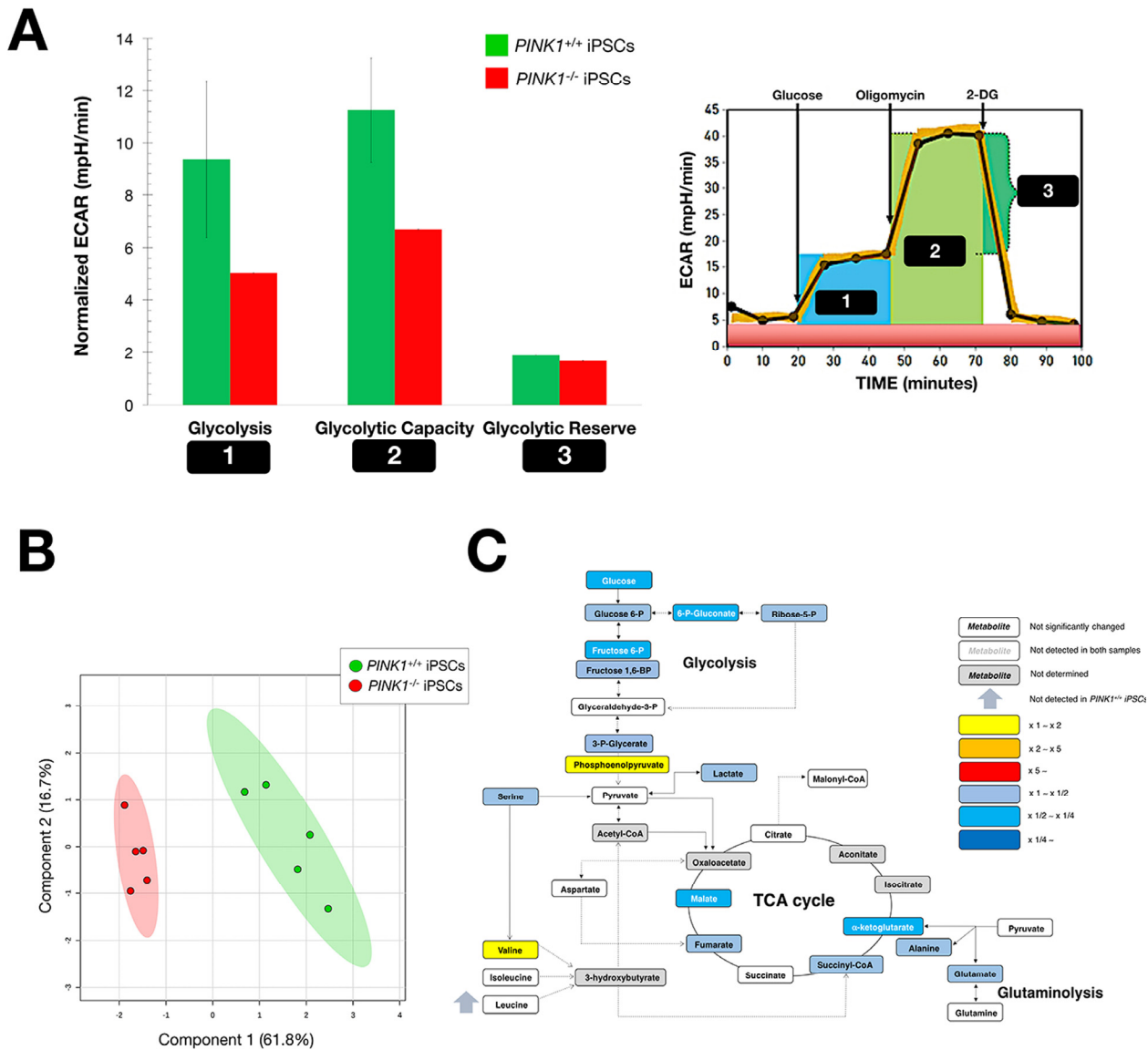


**Figure 3. Mitophagy deficiency impairs the bioenergetic transition associated with nuclear reprogramming.** (A) Calculated glycolysis (maximum rate measurement before oligomycin injection – Last rate measurement before glucose injection [1]), glycolytic capacity (maximum rate measurement after oligomycin injection – Last rate measurement before glucose injection [2]), and glycolytic reserve (glycolytic capacity – glycolysis [3]) were calculated with normalized ECAR values in *PINK1*<sup>+/+</sup>- and *PINK1*<sup>-/-</sup>-iPSCs (n = 2). (B) Two-dimensional PLS-DA models to view the separation of the two groups (*PINK1*<sup>+/+</sup>- and *PINK1*<sup>-/-</sup>-iPSCs) following GC-ESI-QTOF-MS-based metabolomic profiling. (C) Metabolites in *PINK1*<sup>+/+</sup>-iPSCs were extracted and quantitatively analyzed by GC-ESI-QTOF-MS and compared with metabolites from *PINK1*<sup>-/-</sup>-iPSCs (n = 2). Significantly increased and decreased metabolites are shown using yellow-red and light blue-dark blue color scales, respectively (see also Table 1).

**Loss of PINK1-driven mitophagy impairs the metabolome remodeling associated with nuclear reprogramming**

We utilized our recently developed targeted metabolomics platform coupling gas chromatography with quadrupole time-of-flight mass spectrometry and an electron impact source (GC-EI-QTOF-MS), which allows the simultaneous measurement of selected metabolites representative of the catabolic and anabolic status of key metabolic nodes. These metabolites include not only representatives of glycolysis and the mitochondrial tricarboxylic acid (TCA) cycle, but also other biosynthetic routes such as pentose phosphate pathway, amino acid metabolism and *de novo* fatty acid biogenesis [76, 77]. Metabolite-based clustering obtained by partial least squares-discriminant analysis (PLS-DA) model revealed a clear and significant separation between *PINK1*<sup>-/-</sup>-iPSCs and *PINK1*<sup>+/+</sup>-iPSCs in two-dimensional (2D) score plots (Fig. 3B). Profiling of the intracellular metabolome supported a *PINK1*<sup>-/-</sup> iPSCs signature distinct from the *PINK1*<sup>+/+</sup> iPSCs counterpart, which apparently involved a notable decrease in a majority of the measured glycolysis- and TCA-related biochemicals (Fig. 3C).

Heatmap visualization, commonly used for unsupervised clustering, likewise revealed distinct segregation of metabolites in *PINK1*<sup>-/-</sup>-iPSCs and *PINK1*<sup>+/+</sup>-iPSCs groups, pointing to an altered metabolic signature associated with the loss of *PINK1*-dependent mitophagy in iPSCs (Fig. 4). Unsupervised hierarchical clustering of all pairwise comparisons among individual metabolites revealed several “hot spots” of highly correlated metabolites in a correlation matrix (Fig. 4). When VIP scores  $\geq 1$  in the PLS-DA model were used to maximize the difference of metabolic profiles between *PINK1*<sup>-/-</sup>- and *PINK1*<sup>+/+</sup>-iPSCs, the TCA metabolite  $\alpha$ -ketoglutarate was the metabolite majorly impacted in mitophagy-deficient *PINK1*<sup>-/-</sup>-iPSCs (Fig. 5). Quantitative assessment of metabolite concentrations confirmed that *PINK1*<sup>-/-</sup>-iPSCs significantly accumulated > 3-fold less  $\alpha$ -ketoglutarate than *PINK1*<sup>+/+</sup>-iPSCs (Table 1), suggesting that the reduced capacity of mitophagy deficient-iPSCs to efficiently drive mitochondrial metamorphosis during nuclear reprogramming translate into a reduced capacity to achieve the embryonic stem cell-like metabolome that characterizes generated iPSCs.

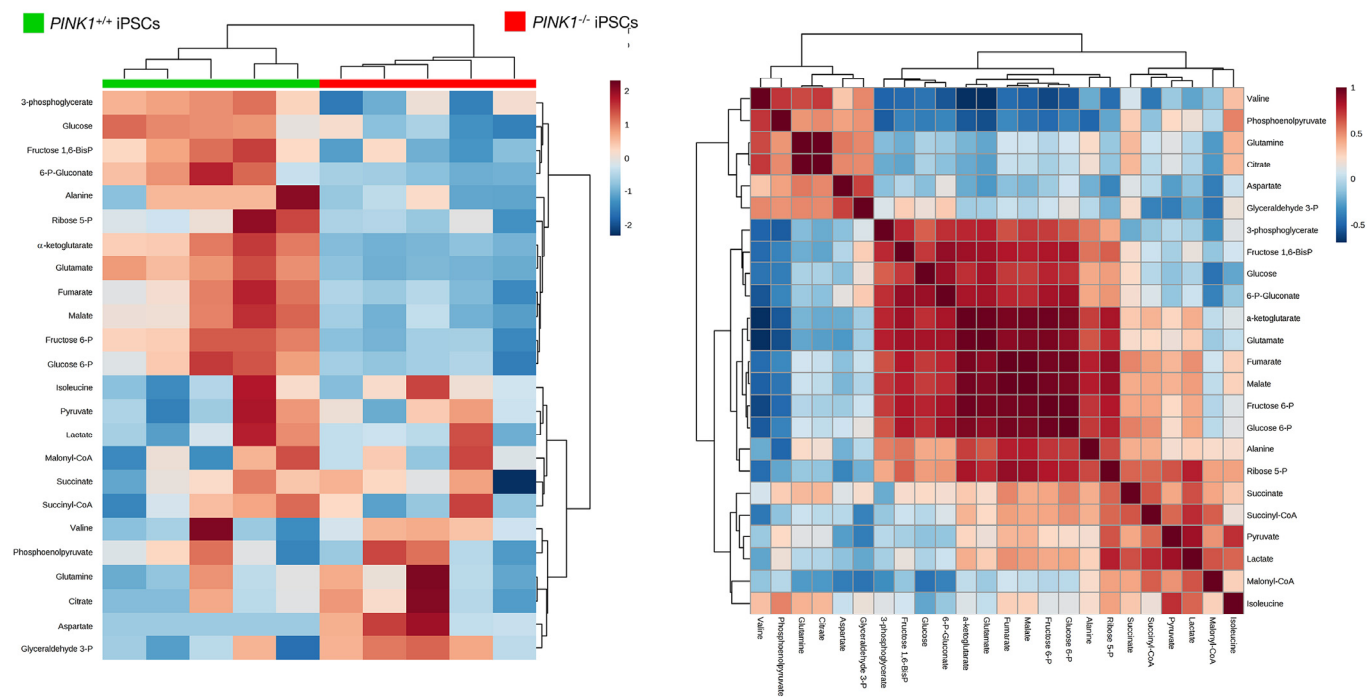


**Figure 4. Mitophagy deficiency impairs the metabolome remodeling associated with nuclear reprogramming.** *Left.* Heatmap to view the agglomerative hierarchical clustering of the *PINK1*<sup>+/+</sup>- and *PINK1*<sup>-/-</sup>-iPSCs groups analyzed with MetaboAnalyst’s data annotation tool [103]. Rows: metabolites; columns: samples; color key indicates metabolite expression value (blue: lowest; red: highest). *Right.* Heatmap of correlations between iPSCs metabolites. Each square represents the Spearman’s correlation coefficient between the metabolite of the column with that of the row. Metabolite order is determined as in hierarchical clustering using the distance function 1-correlation. Self-self correlations are identified in dark brown.

**Table 1. Concentration (in  $\mu\text{M}/\text{mg}$  protein) and fold-change of bioenergetic metabolites in *PINK1*<sup>-/-</sup> vs *PINK1*<sup>+/+</sup>-iPSCs cells.**

Metabolite	<i>PINK1</i> <sup>+/+</sup> iPSCs	<i>PINK1</i> <sup>-/-</sup> iPSCs	Fold-change
3-phosphoglycerate*	136.079 $\pm$ 16.415	77.173 $\pm$ 15.581	-1.76
6-P-Gluconate*	11.045 $\pm$ 3.159	5.715 $\pm$ 0.397	-1.93
$\alpha$ -ketoglutarate*	0.364 $\pm$ 0.111	0.116 $\pm$ 0.005	-3.14
Alanine	2.435 $\pm$ 1.029	1.415 $\pm$ 0.335	-1.72
Aspartate	102.883 $\pm$ 11.692	106.727 $\pm$ 3.873	1.04
Citrate	4.533 $\pm$ 0.531	5.104 $\pm$ 1.146	1.13
Fructose 1,6-BisP*	144.329 $\pm$ 29.863	80.327 $\pm$ 20.233	-1.80
Fructose 6-P*	12.079 $\pm$ 2.511	5.499 $\pm$ 0.759	-2.20
Fumarate*	1.814 $\pm$ 0.389	1.130 $\pm$ 0.116	-1.61
Glucose*	40.668 $\pm$ 7.493	20.546 $\pm$ 6.196	-1.98
Glucose 6-P*	9.085 $\pm$ 1.600	5.877 $\pm$ 0.587	-1.55
Glutamate*	338.181 $\pm$ 2.622	322.962 $\pm$ 0.710	-1.05
Glutamine	5.122 $\pm$ 0.630	5.643 $\pm$ 1.159	1.10
Glyceraldehyde 3-P	54.602 $\pm$ 5.824	55.356 $\pm$ 7.668	1.01
Isoleucine	24.623 $\pm$ 7.773	25.745 $\pm$ 5.453	1.05
Lactate	212.007 $\pm$ 24.712	182.187 $\pm$ 18.347	-1.16
Leucine*	ULOQ	4.693 $\pm$ 1.384	-
Malate*	10.379 $\pm$ 3.172	4.824 $\pm$ 0.693	-2.15
Malonyl-CoA	24.615 $\pm$ 3.858	25.290 $\pm$ 2.881	1.03
Phosphoenolpyruvate*	0.315 $\pm$ 0.124	0.541 $\pm$ 0.134	1.72
Pyruvate	2.245 $\pm$ 0.946	2.136 $\pm$ 0.443	-1.05
Ribose 5-P*	6.136 $\pm$ 1.768	4.286 $\pm$ 0.499	-1.43
Serine*	36.239 $\pm$ 1.181	22.870 $\pm$ 0.448	-1.59
Succinate	35.714 $\pm$ 3.785	34.638 $\pm$ 5.498	-1.03
Succinyl-CoA	1.142 $\pm$ 0.296	1.044 $\pm$ 0.341	-1.09
Valine*	2.943 $\pm$ 0.001	3.856 $\pm$ 0.761	1.31

Data are expressed as mean  $\pm$  SD.

\* Metabolite statistically significant ( $p < 0.005$ ). ULOQ: under limit of quantitation

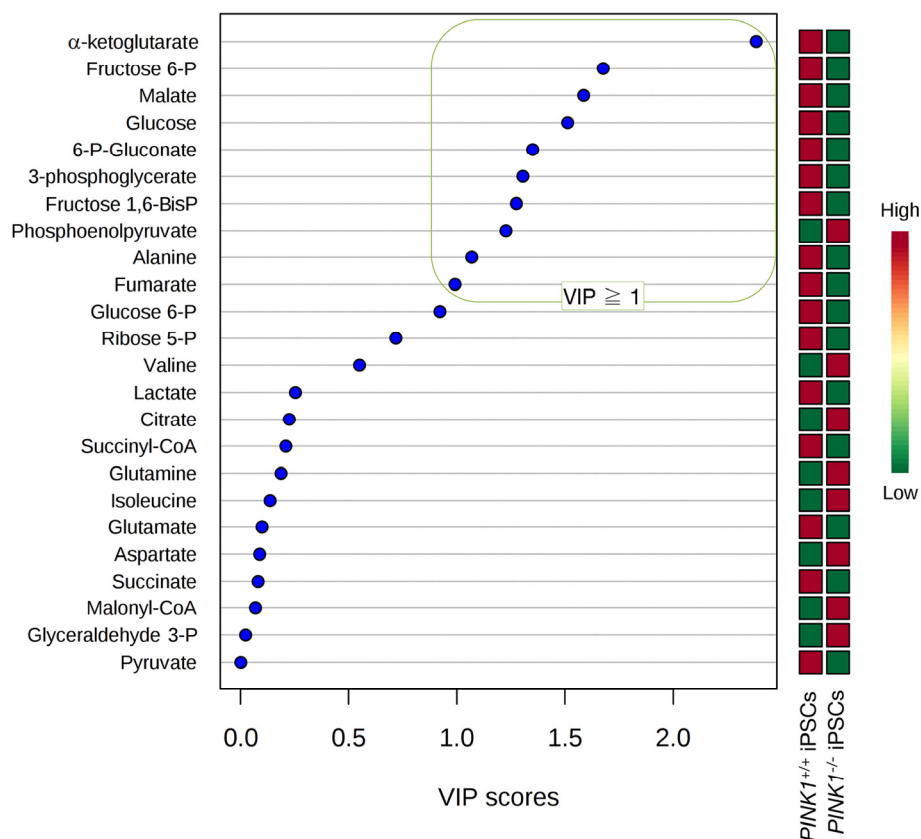


**Figure 5. α-ketoglutarate is the most impacted metabolite in mitophagy deficient-iPSCs.** VIP rank-score of quantified metabolites in the *PINK1*<sup>+/+</sup>- and *PINK1*<sup>-/-</sup>-iPSCs groups. Green box indicates metabolites that achieved VIP scores above 1.0.

### Mitophagy-deficient iPSC colonies exhibit a significantly reduced teratoma-initiating capacity

The ability to derive the three germ layers generated during development, (ectoderm, mesoderm and endoderm), is the gold standard for determining whether potential iPSC candidates are fully pluripotent [78-80]. We thus examined the teratoma initiating and differentiation potential of *PINK1*<sup>+/+</sup>- and *PINK1*<sup>-/-</sup>-iPSCs *in vivo*. To exclude the possibility that any uncoupling of pluripotent capacity from tumorigenesis might be dose-dependent, i.e., with differentiation occurring at lower cell doses but tumors forming at higher cell doses, we injected 4- to 5-week-old athymic nude mice subcutaneously either with  $5 \times 10^5$  undifferentiated iPSCs or with  $2 \times 10^6$  cells, the latter being a saturating concentration to ensure the development of teratoma masses within a few weeks [64, 81]. We then analyzed efficiency, latency, and

histology of teratoma composition. The rate of teratoma formation in *PINK1*<sup>+/+</sup>-iPSCs was 100% (6/6 mice in each group) regardless of the number of cells injected (Fig. 6A). In contrast, we observed a cell number-independent reduction in the rate of teratoma formation following the injection of *PINK1*<sup>-/-</sup>-iPSCs (60%; 4/6 mice in each group). Thus, the time required for 50% of animals to develop palpable teratomas was lengthened by 161% (from 26 to 68 days) upon injection of  $5 \times 10^5$  *PINK1*<sup>-/-</sup>-iPSCs, and by 166% (from 21 to 56 days) upon injection of  $2 \times 10^6$  *PINK1*<sup>-/-</sup>-iPSCs *in vivo* (Fig. 6A). Indeed, injection of *PINK1*<sup>-/-</sup>-iPSCs resulted in drastically smaller teratomas than those observed upon injection of *PINK1*<sup>+/+</sup>-iPSCs, i.e., the lesions in *PINK1*<sup>-/-</sup>-iPSC-injected mice were 15-fold smaller in size compared to the mean teratoma size observed in the *PINK1*<sup>+/+</sup>-iPSC group (78 mm<sup>3</sup> versus 1166 mm<sup>3</sup>, respectively) (Fig. 6B).

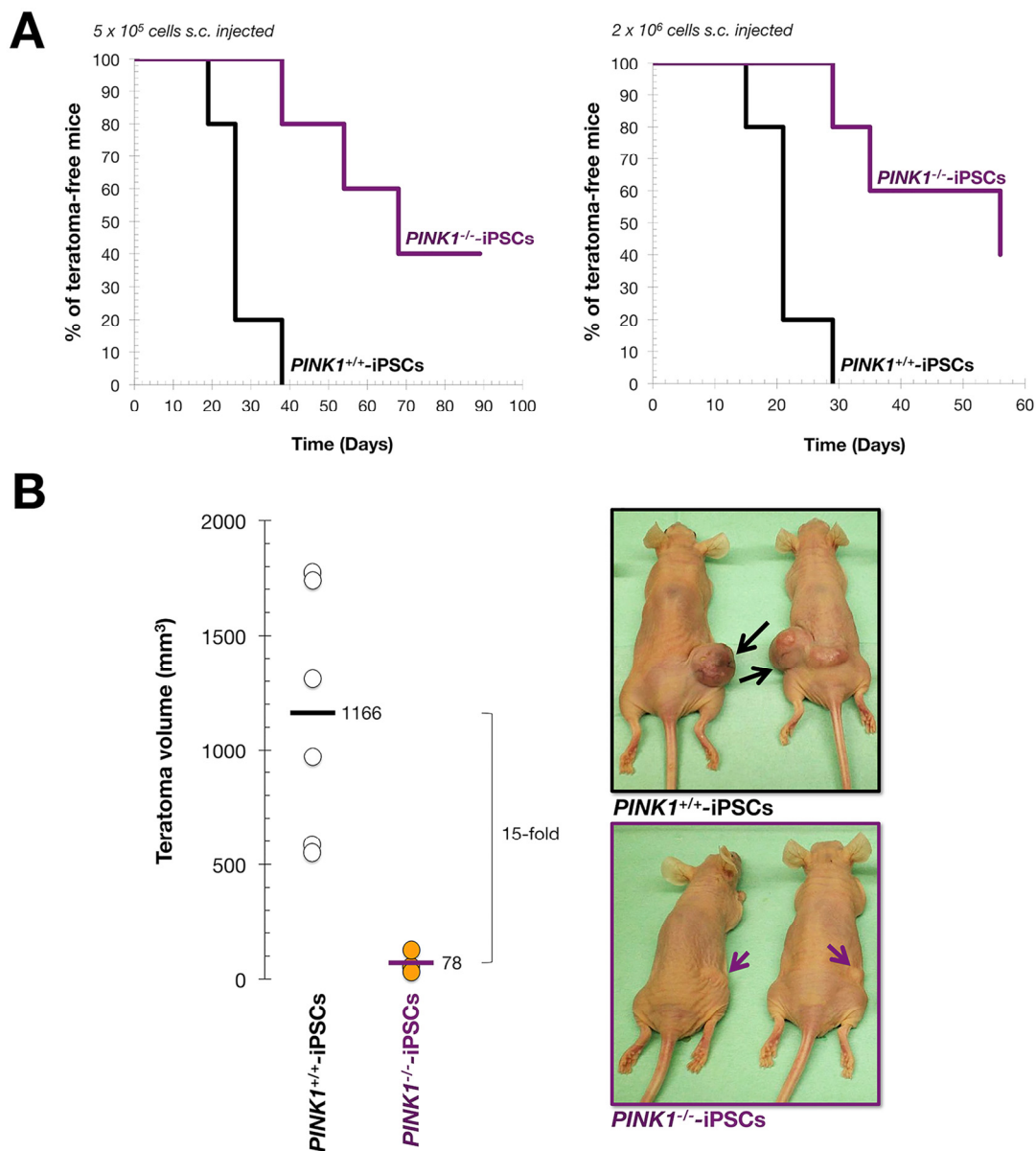


**Figure 6. Mitophagy deficiency reduces tumorigenicity of iPSC colonies.** Athymic mice were injected with  $5 \times 10^5$  or  $2 \times 10^6$  cells obtained from *PINK1<sup>+/-</sup>*-iPSC or *PINK1<sup>-/-</sup>*-iPSC colonies. Teratoma growth rate was calculated by measuring teratoma volume. **(A)** Kaplan-Meier plots show the percentage of mice that remained teratoma-free after subcutaneous injection of iPSCs obtained as described in Fig. 2. **(B)** Mean teratoma volumes obtained at the end of the experiment (left) as well as representative images of animals bearing *PINK1<sup>+/-</sup>*-iPSC- and *PINK1<sup>-/-</sup>*-iPSC-derived teratomas after injection with  $2 \times 10^6$  cells (right). Note that teratomas formed from *PINK1<sup>+/-</sup>*-iPSCs present a dramatically higher growth rate that those derived from *PINK1<sup>-/-</sup>*-iPSCs.

### Mitophagy-deficient iPSC colonies retain pluripotency and multi-germ layer differentiation potential

Given the above results, it might be argued that blockade of teratoma formation upon loss of PINK1-

dependent mitophagy was due to the failure of *PINK1<sup>-/-</sup>*-iPSCs to differentiate into primitive tissues representing all three germ layers. To question this, we carried out an ultrastructure analysis of teratomas from both groups of mice. Despite the lower efficiency in teratoma formation and the longer latency, tissue composition of



*PINK1*<sup>-/-</sup>-teratomas was not noticeably different from equivalent *PINK1*<sup>+/+</sup>-teratomas at the histological level. Hematoxylin-eosin staining showed various tissue derivatives of the three germ layers, including neural rosettes (ectoderm), gut-like epithelial tissues (endoderm), and smooth muscle, adipocytes, bone, and cartilage (mesoderm), in both teratoma groups (Fig. 7), confirming the full pluripotency and multi-germ layer differentiation potential of the iPSCs regardless of the PINK1-mediated mitophagy status. These findings, together with the fact that *PINK1*<sup>-/-</sup>-iPSCs normally expressed pluripotent markers confirmed that mitophagy-deficient iPSCs re-established pluripotency at the molecular and cellular level.

Although *PINK1*<sup>+/+</sup>- and *PINK1*<sup>-/-</sup>-iPSCs gave rise to teratomas composed of various recognizable tissue elements, we observed striking differences in the embryonal carcinoma (EC)-like component of poorly differentiated, primitive-appearing, blast-like teratocarcinoma stem cells. Accordingly, the large teratomas originating from *PINK1*<sup>+/+</sup>-iPSCs displayed extensive areas of undifferentiated tissue, e.g., abundant embryonic-appearing neuroepithelium with a high number of mitotic figures, which were considered as malignant based on the examination by a pathologist (Fig. 7). Conversely, *PINK1*<sup>-/-</sup>-iPSCs developed teratomas consisting almost exclusively of fully committed adult tissues, forming very small, morpho-

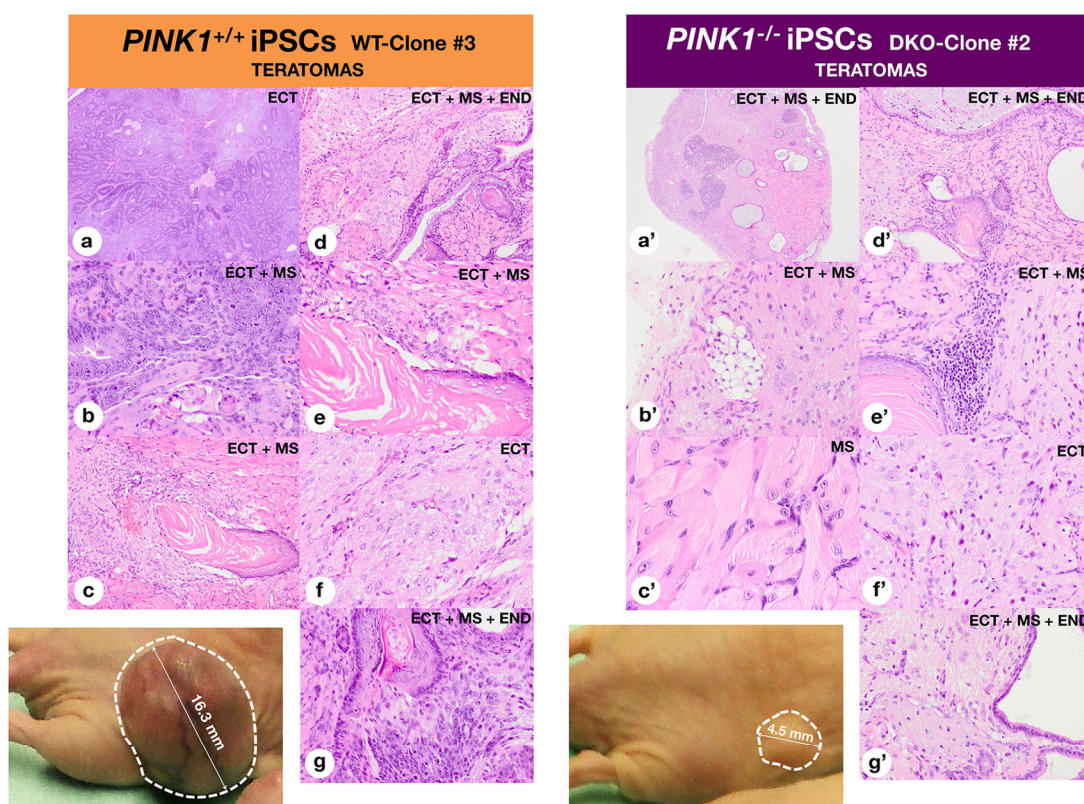


**Figure 7. Mitophagy deficiency preserves the pluripotency of iPSCs.** Histological analyses of *PINK1*<sup>+/+</sup>- and *PINK1*<sup>-/-</sup>-iPSC-derived teratomas. Representative photographs of teratomas (circled with white dotted lines) are shown. *PINK1*<sup>+/+</sup>-iPSC-derived teratomas: (a) Primitive neural tissue, (b) Primitive neural tissue and skeletal muscle tissue, (c) Squamous epithelium, immature neural and glial tissue, (d) Mature nervous tissue, squamous keratinized epithelium, skeletal muscle tissue, mucinous glands, (e) Squamous keratinized epithelium, skeletal muscle tissue, (f) Mature nervous tissue, (g) Squamous keratinized epithelium, skeletal muscle tissue, respiratory epithelium. *PINK1*<sup>-/-</sup>-iPSC-derived teratomas; (a') Whole-tumor section with dark areas of primitive neuroepithelium mixed with skeletal muscle tissue and seromucinous glands, (b') Mature nervous tissue, (c') Skeletal muscle tissue, (d') Mature nervous tissue, squamous keratinized epithelium, skeletal muscle tissue, mucinous glands, (e') Mature nervous tissue, squamous keratinized epithelium, skeletal muscle tissue, (f') Mature nervous tissue, (g') Mature nervous tissue, mucinous glands, osteoid substance. Note that teratomas from *PINK1*<sup>+/+</sup>-iPSCs and *PINK1*<sup>-/-</sup>-iPSCs similarly show mixed tissues apparently derived from the three germ layers, i.e., ECT: Ectoderm, MS: Mesoderm, and END: Endoderm.

logically benign, mature, and well-differentiated cystic lesions. Using TEM, we found that the cytoplasm of the extensive undifferentiated regions in *PINK1*<sup>+/+</sup>-iPSC-generated teratomas exhibited a simple architecture typical of embryonic-like cells in the early stages of development. Consequently, these regions were devoid of most organelles except for the presence of numerous ribosomes, a well-developed Golgi apparatus, and rough endoplasmic reticulum (Fig. 8). These regions contained few mitochondria and, when found, presented a globular shape with poorly developed cristae and electron-lucid matrix, and perinuclear localization, all indicative of functionally immature mitochondria. Conversely, tera-

tomas from *PINK1*<sup>-/-</sup>-iPSCs generated tissues with conspicuous and numerous mitochondria, possessing a complex morphology with well-developed cristae, denser matrix, and elongated or branched appearance (Fig. 8).

Although it might be argued that, because mitophagy-deficient iPSC colonies tended to rapidly differentiate *in vitro* and exhibited a significantly reduced teratoma-initiating capacity, the percentage of fully reprogrammed cells might be significantly lower within *PINK1*<sup>-/-</sup>-iPSC colonies, these findings are also consistent with a more rapid differentiation of mitophagy-deficient iPSCs *in vivo*.

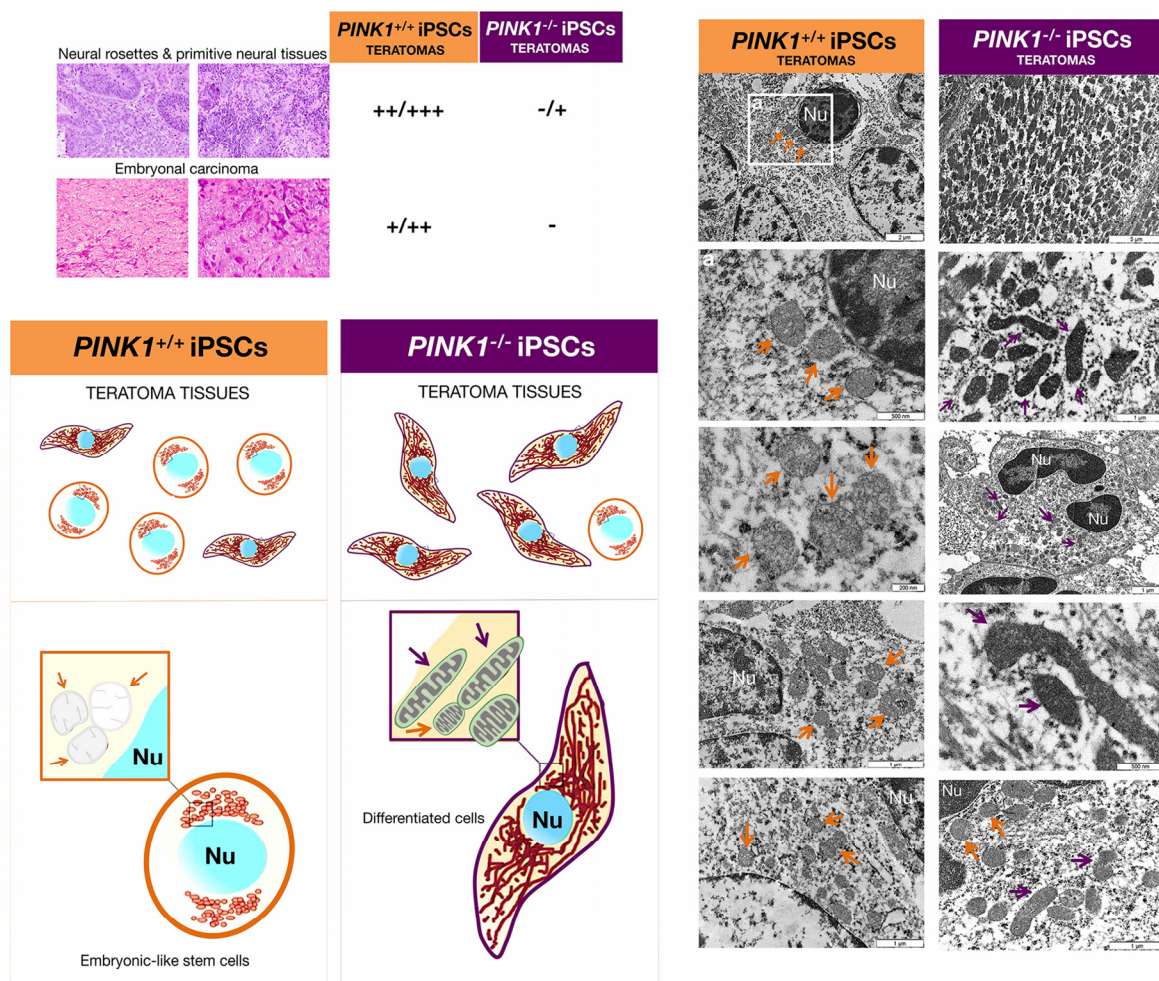


**Figure 8. Mitophagy-deficient iPSC colonies are prone to direct differentiation *in vivo*.** *Left.* Analyses of histopathological features associated with the malignant behavior of iPSC-derived teratomas including the presence of neural rosettes/primitive neural tissues and embryonal carcinoma. Note that small *PINK1*<sup>-/-</sup>-iPSC-derived teratomas lack all the malignant features of iPSCs, which were highly abundant in *PINK1*<sup>+/+</sup>-iPSC-derived teratomas. “-” means that no features are present, “+” a small number present, “++” a medium number, and “+++” a large number. *Right.* Representative TEM images of mitochondria in *PINK1*<sup>+/+</sup>- and *PINK1*<sup>-/-</sup>-iPSC-derived teratomas. While the mitochondria in many tissue sections from *PINK1*<sup>+/+</sup>-iPSCs-derived teratomas were characterized by a punctate, perinuclear arrangement, an electron-lucid matrix and poorly developed cristae, mitochondria in the majority of tissue sections from *PINK1*<sup>-/-</sup>-iPSC-derived teratomas formed more developed networks, had an electron-dense matrix and developed cristae. (Nu: Nucleus).



## DISCUSSION

Here we provide the first demonstration that mitophagy is a necessary mechanism for the conversion of somatic cells to a pluripotent cell fate with maximum efficiency. Our discovery that mitophagy-driven mitochondrial rejuvenation is required for induction and maintenance of stem cell pluripotency and that the mitophagy pathway plays a critical mitochondrial switch that determines the efficiency and quality of somatic reprogramming, illustrates how mitophagy can play a pivotal role in stem cell functions during aging and tissue regeneration.

We first addressed the question of whether mitophagy is a crucial process during nuclear reprogramming. Our findings reveal that the sole loss of PINK1-dependent mitophagy was sufficient to dramatically decrease the efficiency (~80% reduction) and speed of the nuclear reprogramming process (Fig. 9). Deficiency of PINK1-regulated mitochondrial quality control constitutes a previously unrecognized barrier to reprogramming. This fact, taken together with recent studies showing that whereas activation of DRP1-driven mitochondrial fragmentation contributes to the acquisition and maintenance of stem cell pluripotency [48, 50], deficiency of mitofusins Mfn1 and Mfn2 (which co-

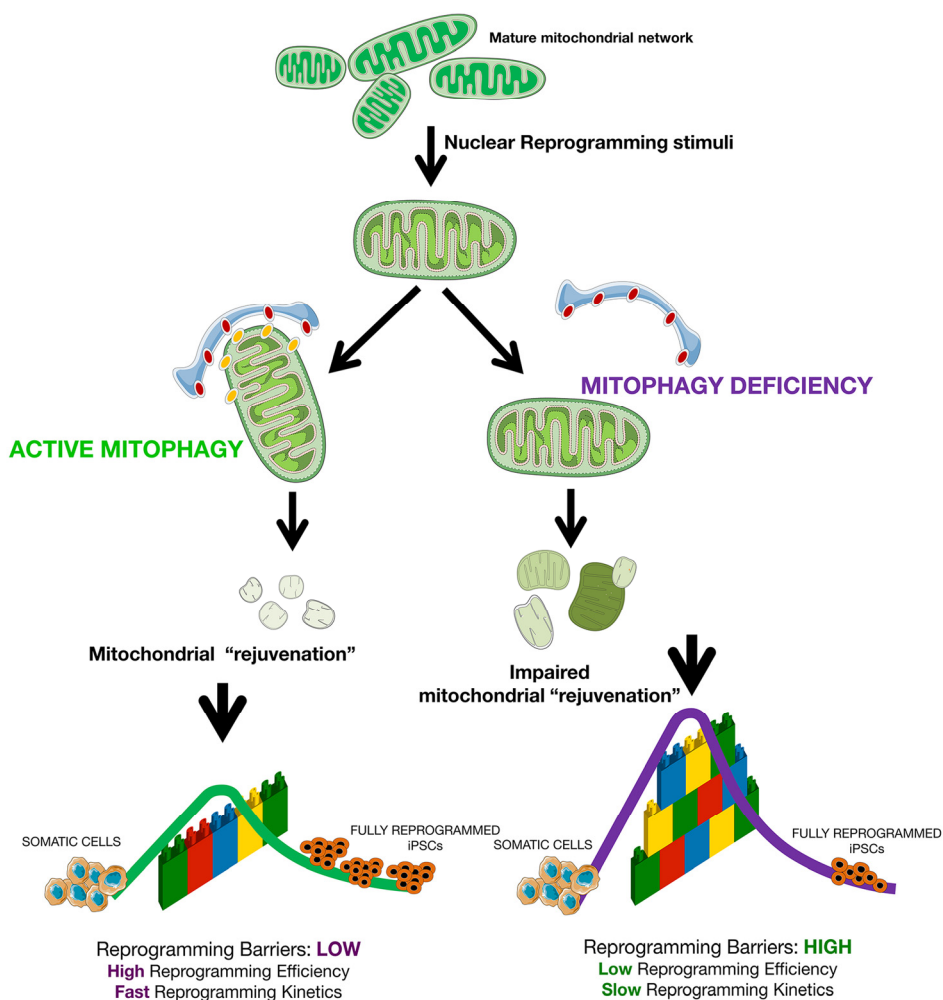


**Figure 9. Mitophagy-regulated nuclear reprogramming of somatic cells into pluripotent stem cells.** Mitophagy is part of the roadmap during nuclear reprogramming of somatic cells to pluripotency and, as such, its blockade is sufficient to dramatically alter the speed and efficiency of iPSC reprogramming by “elevating” the “reprogramming barriers” of the epigenetic landscape and decreasing the size of the stem cell state basin of attraction, which results in the deceleration (i.e., lower efficiency and slower kinetics) of the nuclear reprogramming process. This conceptual figure represent cells stabilized in an initial non-pluripotent, somatic attractor and how nuclear reprogramming can make cells exceed the “reprogramming barriers”, represented as a wall of interlocking bricks, easier or harder in the presence or absence of PINK1-dependent mitophagy, respectively, and fall down in a final attractor of fully reprogrammed, induced pluripotent stem cell states. The cellular reprogramming process is presented as a colored line from the initial to the final cellular state.

ordinately regulate mitochondrial fusion) instead elicits mitochondrial metabolic reprogramming to pluripotency [49], bolsters the notion that the ability of mitochondrial fission/fusion and mitophagy to restructure mitochondrial dynamics is central for the control of cell-fate plasticity. Accordingly, it was reported that a restricted 2-day burst of autophagy (causing mitophagy) at the early stages of reprogramming was vital for iPSC generation [47].

We next focused on whether mitophagy is the driving mechanism for the conversion of functionally mature mitochondria to an immature state and vice versa, during reprogramming to stemness and commitment to terminal differentiation, respectively. The fact that loss of *PINK1*-dependent mitophagy impeded the full rejuvenation of the mitochondrial network during reprogramming indicates that mitophagy operates as a key mechanism in generating the immature mitochondrial structure commonly found in stem cells. Because a high level of mitophagy has recently been found to be a requisite for the high quality of mitochondria required for the stem cell state [82], and given that the number of AP<sup>+</sup> colonies during early stages of reprogramming is used as an initial indicator of successful reprogramming of cells, the fact that cells within *PINK1*<sup>-/-</sup> iPSC colonies appeared to inherit a mixture of mature (“old”) and immature (“young”) mitochondria when compared with *PINK1*<sup>+/+</sup>-iPSCs colonies whose cells almost exclusively inherited immature mitochondria might suggest that the ratio of fully reprogrammed colonies among AP<sup>+</sup> colonies is significantly lower in the absence of *PINK1*-dependent mitophagy. Furthermore, because AP expression levels is a less sensitive measure to differentiate between undifferentiated and early differentiating cells, the fact that mitophagy-deficient iPSC colonies normally expressed the pluripotent markers Oct4 and Sox2 together with their strong tendency to spontaneously differentiate and form heterogeneous populations of cells strongly suggest that *PINK1*-dependent mitophagy might be necessary for the iPSCs to remain in undifferentiated state. Indeed, with growing evidence for remodeling of energy metabolism in cell fate decisions, the fact that functional monitoring of cellular bioenergetics revealed an attenuated glycolytic capacity in mitophagy-deficient iPSC cells strongly suggest that the mitophagy pathway is an operating mechanism of mitochondrial switching that directs bioenergetic transition from somatic oxidative in somatic cells to glycolysis in iPSCs. While mitophagy might ultimately determine the efficiency and quality of nuclear reprogramming and stemness transition in somatic cells by participating in the bioenergetic conversion for establishing functional pluripotency, it remains to be

unambiguously defined whether the ultimate role of mitophagy in stem cells is to regulate the preferential, asymmetric apportion of younger mitochondria during self-renewal [82].

The main characteristics of iPSC mitochondria are their rounded morphology with condensed cristae and their poor oxidative activity due to the low membrane potential [36-45, 65]. Given that mitophagy is triggered by mild oxidative stress in a mitochondrial fission-dependent manner [83], we hypothesized that abnormal mitophagy might lead to the accumulation of “old”, ROS-generating mitochondria, and this, in turn, might impair the efficiency of reprogramming. Our results showed that the mitophagy deficiency-imposed roadblock for reprogramming is bypassed, in part, by the ROS scavenger vitamin C upon the inclusion of oncogenic c-Myc, which is a key inducer of glycolytic reconfiguration [31, 84]. Interestingly, c-Myc also functions as the major contributor of reprogramming-mediated oxidative stress [38, 85]. Therefore, while it seems likely that ROS partially contribute to the lower reprogramming efficiency of *PINK1*<sup>-/-</sup> MEFs, other ROS-independent mitochondrial changes imposed by the loss of *PINK1*-driven mitophagy seem to operate as a dominant roadblock during reprogramming. Because histone demethylases have been shown to be the direct downstream effectors of vitamin C-dependent enhancement of cell reprogramming, in addition to its antioxidant activity [72-75], it is possible that mitophagy deficiency might impede reprogramming by inhibiting histone demethylation. In this regard, it was noteworthy that the iPSC metabolite majorly impacted by loss of *PINK1*-dependent mitophagy was  $\alpha$ -ketoglutarate, a key mitochondrial metabolite that is siphoned from the TCA cycle to support rapid cell proliferation via lipid and amino acid biosynthesis that can exit also the mitochondria to function as a cofactor for dioxygenase enzymes including Jumonji-family histone demethylases, TET-family DNA hydroxylases, and prolyl hydroxylases [86-88]. Indeed, the intracellular  $\alpha$ -ketoglutarate levels have been shown to contribute to the maintenance of cellular identity and have a mechanistic role in the transcriptional and epigenetic state of stem cells [89]. Further research, however, is needed to evaluate the precise epigenetic modifications associated with mitophagy-related changes in mitochondrial biogenesis, structure, and function, i.e., how mitophagy might drive the acquisition and maintenance of stemness by metabolically regulating the epigenetic landscape of the nuclear genome [90-92].

The fact that *PINK1*<sup>-/-</sup>-iPSCs possessed a normal capacity to differentiate into mature tissue confirmed

that deficiency of PINK1-driven mitophagy does not interfere with the pluripotent quality of iPSCs. Because the kinetics of teratoma formation is dependent on the number of remaining pluripotent stem cells during the differentiation procedure [93-98], it might be tempting to suggest that loss of PINK1-driven mitophagy facilitates the depletion of residual undifferentiated pluripotent cells (teratocarcinoma-initiating cells) during *in vivo* teratoma formation. Moreover, because the retention of the embryonal character is considered the basis for continuous and progressive growth of malignant teratomas, loss of biological aggressiveness in *PINK1*<sup>-/-</sup>-iPSC-derived teratomas apparently suggest that mitophagy deficiency impedes the retention of undifferentiated pluripotent stem cells by promoting their differentiation and inhibiting potential dedifferentiation of committed cells. Accordingly, the highly significant more active mitochondrial state of tissues from *PINK1*<sup>-/-</sup> teratomas might be indicative of rapid, most committed differentiation of otherwise pluripotent *PINK1*<sup>-/-</sup>-iPSCs. Conversely, it might be argued that these findings reflect that the percentage of fully reprogrammed cells might be significantly lower within mitophagy-deficient *PINK1*<sup>-/-</sup>-iPSC colonies. Forthcoming studies should evaluate whether rapidly differentiating, mitophagy-deficient heterogeneous colonies of *PINK1* KO-iPSCs might illuminate new mitochondria-centered mechanisms aimed to restore or stimulate a differentiation checkpoint capable of limiting the aberrant self-renewal of life-threatening cancer stem cells in tumor tissues.

We are beginning to dissect the roles of mitochondria in the establishment and homeostasis of stemness, which may help to uncover novel insights into our understanding of a wide variety of degenerative diseases, aging, and aging-related diseases including cancer. Although we are still far from a comprehensive understanding of the physiological functions of mitochondria in stem cells, our findings extend previous studies into the causal mechanism behind the well-recognized metabolic switch during the establishment of pluripotency, which is accompanied by significant changes in mitochondrial function, composition, structure, maturation, and signaling. Mitophagy appears to be a crucial cellular process for the conversion of functionally mature mitochondria to an immature state and vice versa during reprogramming and differentiation, respectively. In this regard, mitophagy may ensure a metabolic transition to meet the specific energetic and anabolic demands of the stemness state, e.g., mitophagy-induced repression of mitochondrial functions including mitochondrial clearance might accelerate the onset of the glycolytic metabolism [99]. Furthermore, mitophagy-driven mitochondrial rejuvena-

tion might contribute to the ability of stem cells to suppress differentiation by orchestrating the mitochondria function as signaling organelles of diverse biological functions [100, 101], including not only bioenergetic transitions but, perhaps more importantly, metabolome remodeling traits connecting mitochondrial metabolites with epigenetics [100-102]. Further studies are warranted to determine the causal role of mitophagy-driven mitochondrial rejuvenation as part of the mechanism involved in the maintenance and asymmetric transmission of the pluripotency and differentiation fate of stem cells. Our discovery that mitophagy-controlled mitochondrial quality is a critical director of cell-fate plasticity and stem-cell fate should provide new insights into how mitophagy might influence the stem cell decisions to retain pluripotency or differentiate in tissue regeneration and aging, tumor growth, and regenerative medicine.

## MATERIALS AND METHODS

***PINK1*-knockout mouse embryonic fibroblasts.** *PINK1*-knockout mice were generated by targeted deletion of exon 1 as described [52]. Loss of *Pink1* mRNA expression in primary embryonic fibroblasts (MEFs) was confirmed by quantitative RT-PCR [52].

***Generation of iPSCs.*** Mouse primary iPSCs were created by transducing MEFs deficient for *PINK1* (*PINK1*<sup>-/-</sup>) and wild-type (*PINK1*<sup>+/+</sup>) counterparts with the pMXs-based retroviruses that individually encode the mouse transcription factors Oct3/4, Sox2, and Klf4 following a previously-described protocol [64, 65]. Characterization of iPSC-like colonies was carried out by analyzing pluripotent marker expression by alkaline phosphatase (AP) staining using the StemTAG™ Alkaline Phosphatase Staining and Activity Assay Kit (Cell Biolabs, Inc. Cat. No. CBA-302) and the expression of Oct3/4, Nanog, Sox2, and Ssea-1 by immunofluorescence (see below).

To generate feeder-free iPSC cultures for teratoma assays, culture plates were coated with 0.3 mg/mL Matrigel (growth factor-reduced, BD Biosciences, San Jose, CA) at 4°C overnight. Unbound Matrigel was aspirated, and the cells were washed with DMEM/F12 medium. iPSCs were seeded on Matrigel-coated plates in MEF-conditioned ES cell medium supplemented with leukemia inhibitory factor (LIF) and bFGF (4 ng/mL). The medium was changed every day.

***Immunofluorescence staining.*** High-content confocal imaging was performed in 96-well clear bottom imaging tissue culture plates (BD Biosciences) optimized for automated imaging applications. Triton®



X-100 permeabilization and blocking, primary antibody staining, secondary antibody staining using Alexa Fluor® 488 goat anti-rabbit/mouse IgG (Invitrogen, Molecular Probes, Eugene, OR) and counterstaining (Hoechst 33258; Invitrogen) were performed following BD Biosciences protocols. Images were captured in different channels for Alexa Fluor® 488 (pseudocolored green) and Hoechst 33258 (pseudocolored blue) on a BD Pathway™ 855 Bioimager System (BD Biosciences) with 20× or 40× objectives (NA 075, Olympus). Merged images were obtained according to the Recommended Assay Procedure using BD Attovision™ software.

**Reactive Oxygen Species (ROS) detection.** Cells were incubated for 60 min with 10 µmol/L 2',7'-dihydro-dichlorofluorescein-diacetate (H2DCF-DA) (Invitrogen, Molecular Probes) at 37°C. Cellular green fluorescence was then measured by flow cytometry. Cell-permeant non-fluorescent H2DCF-DA, upon cleavage of the acetate moiety by intercellular esterases and oxidation by ROS, is converted to strongly fluorescent DCF and thus reports the ROS abundance.

**Immunoblotting.** Equal concentration of proteins (50 µg) was loaded into a 10% SDS-polyacrylamide gel and then electrotransferred. After blocking (5% nonfat powder milk in TBS plus 0.1% TritonX100 for 1 h at room temperature), the nitrocellulose membranes were incubated for 16-20 h at 4°C with the primary antibody (Oct3/4, Abcam ab-1985, 1:600; Sox2, Abcam ab-97959, 1:1000; β-actin, Santa Cruz sc-47778, 1:500). The detection of the immune complexes after incubation with the appropriate peroxidase-conjugated secondary antibody (Cell Signaling #7074, 1:1000; Calbiochem #401215, 1:5000) was performed with the Clarity™ Western ECL Substrate (Bio-Rad).

**Extracellular flux bioenergetic assays.** Extracellular acidification rates were measured using an XF Extracellular Flux Seahorse Analyzer (Seahorse Bioscience). XFp Glycolysis Stress tests were performed in accordance with manufacturer's instructions. Each plotted value is the mean of at least 6 replicates and was normalized to Hoechst signal in each well.

**Targeted metabolomics and data analysis.** Measurements of bioenergetics metabolites obtained from *PINK1*<sup>+/+</sup>-iPSC and *PINK1*<sup>-/-</sup>-iPSC clonal cell lines were performed by employing a previously described simple and quantitative method based on gas chromatography coupled to quadrupole-time of flight mass spectrometry and an electron ionization interface (GC-EI-QTOF-MS) [76, 77].

Raw data were processed and compounds were detected and quantified using the Qualitative and Quantitative Analysis B.06.00 software (Agilent Technologies), respectively. MetaboAnalyst 3.0 (<http://www.metaboanalyst.ca>) was used to generate scores/loading plots, Heatmaps, and correlation maps [103].

**Teratoma assays.** To form teratomas, iPSCs were harvested from Matrigel-coated culture dishes and injected subcutaneously (s.c.) into the dorsal flank of female athymic nude mice (four- to five-weeks-old, 23-25g; Harlan Laboratories, France). Mice were weighed once per week. Teratomas were measured daily with electronic calipers and tumour volumes were calculated using the formula: volume (mm<sup>3</sup>) = length × width<sup>2</sup> × 0.5. General health of the mice in response to teratoma development (e.g., subcutaneous teratomas cause ulceration on the skin) was monitored daily by a specialized veterinarian. Teratomas were carefully dissected and removed in entirety, fixed in 10% phosphate buffered formalin (3.6% formaldehyde) for 24 hours, and paraffin-embedded. For histopathological analysis, consecutive sections (4 µm) were cut and stained with haematoxylin and eosin according to standard procedures.

The Institutional Animal Care and Use Committee (IACUC) of the Institut d'Investigació Biomèdica de Bellvitge (IDIBELL; Animal Use Protocol #6302 authorized by the Animal Experimental Commission from the Catalan Government, Barcelona, Spain) approved the experiments.

**Transmission electron microscopy.** Small pieces of teratomas were fixed in a 2% glutaraldehyde solution in 0.1 M cacodylate buffer, pH 7.4. Samples were then post-fixed in 1% osmium tetroxide (OsO<sub>4</sub>) for 2 h and dehydrated through a graded series of acetone prior to impregnation in increasing concentrations of resin in acetone over a 24 h period. Semi-thin sections (500 nm) were stained with 1% toluidine blue. Ultrathin sections (70 nm) were subsequently cut using a diamond knife, double-stained with uranyl acetate and lead citrate, and examined with a transmission electron microscope (Hitachi, Tokyo, Japan).

**Statistical analysis.** The results are presented as the mean ± SD of at least three repeated individual experiments for each group. The analyses were performed using XLSTAT 2010 (Addinsoft™). A P-value ≤ 0.05 was considered statistically significant.

## ACKNOWLEDGEMENTS

The authors would like to thank Dr. Kenneth McCreath for editorial support.

## Funding

This work was supported by grants from the Ministerio de Ciencia e Innovación (Grant SAF2012-38914), Plan Nacional de I+D+I, Spain and the Agència de Gestió d'Ajuts Universitaris i de Recerca (AGAUR) (Grant 2014 SGR229), Departament d'Economia i Coneixement, Catalonia, Spain to Javier A. Menendez. And by the FP7 RTD MEFOPA HEALTH-2009-241791 and EC-FP7/2007-2013 project, HEALTH-F2-2011-278850 (INMiND) to VB.

## Author contributions

A. V-M. and J.A.M conceived the idea for this project. C. VdH. and V. B. provided essential study materials. A. V-M. designed and conducted the nuclear reprogramming assays and carried out the confocal fluorescence microscopy experiments. A. V-M. and J.A.M designed and analyzed the experiments on living cells. S.C. performed all the teratoma formation assays. E. L-B. performed all the histopathological tissue analyses. E. R-G, S. F-A. and J. J. conducted and analyzed the experiments with the transmission electron microscopy. B. C-F. and E. C. participated in the nuclear reprogramming and ROS experiments. E. C. performed and analyzed the immunoblotting and cell energy phenotyping procedures. B. C-F., E. C., J.J., E. R-G, and S. F-A. designed, conducted and analyzed the metabolomic experiments. J.A.M and J. J. wrote the manuscript. We confirm that the manuscript has been read and approved by all named authors and that there are no other persons who satisfied the criteria for authorship but are not listed. We further confirm that the order of authors listed in the manuscript has been approved by all of us. Correspondence and requests for materials should be addressed to corresponding authors.

## Conflict of interest statement

The authors confirm that there are no known conflicts of interest associated with this publication and there has been no significant financial support for this work that could have influenced its outcome. We further confirm that any aspect of the work covered in this manuscript that has involved experimental animals has been conducted with the ethical approval of all relevant bodies and that such approvals are acknowledged within the manuscript.

## REFERENCES

1. Ding WX, Yin XM. Mitophagy: mechanisms, pathophysiological roles, and analysis. *Biol Chem*. 2012; 393: 547-64.
2. Kim I, Rodriguez-Enriquez S, Lemasters JJ. Selective degradation of mitochondria by mitophagy. *Arch Biochem Biophys*. 2007; 462: 245-53.
3. Novak I. Mitophagy: a complex mechanism of mitochondrial removal. *Antioxid Redox Signal*. 2012; 17: 794-802.
4. Tolkovsky AM. Mitophagy. *Biochim Biophys Acta*. 2009; 1793: 1508-15.
5. Ashrafi G, Schwarz TL. The pathways of mitophagy for quality control and clearance of mitochondria. *Cell Death Differ*. 2013; 20: 31-42.
6. Feng D, Liu L, Zhu Y, Chen Q. Molecular signaling toward mitophagy and its physiological significance. *Exp Cell Res*. 2013; 319: 1697-1705.
7. Gomes LC, Scorrano L. Mitochondrial morphology in mitophagy and macroautophagy. *Biochim Biophys Acta*. 2013; 1833: 205-12.
8. Mishra P, Chan DC. Mitochondrial dynamics and inheritance during cell division, development and disease. *Nat Rev Mol Cell Biol*. 2014; 15: 634-46.
9. Wei H, Liu L, Chen Q. Selective removal of mitochondria via mitophagy: distinct pathways for different mitochondrial stresses. *Biochim Biophys Acta*. 2015; 1853: 2784-90.
10. Dupuis L. Mitochondrial quality control in neurodegenerative diseases. *Biochimie*. 2014; 100: 177-83.
11. Itoh K, Nakamura K, Iijima M, Sesaki H. Mitochondrial dynamics in neurodegeneration. *Trends Cell Biol*. 2013; 23: 64-71.
12. Osellame LD, Duchon MR. Defective quality control mechanisms and accumulation of damaged mitochondria link Gaucher and Parkinson diseases. *Autophagy*. 2013; 9: 1633-35.
13. Osellame LD, Duchon MR. Quality control gone wrong: mitochondria, lysosomal storage disorders and neurodegeneration. *Br J Pharmacol*. 2014; 171: 1958-1972.
14. Pickrell AM, Youle RJ. The roles of PINK1, parkin, and mitochondrial fidelity in Parkinson's disease. *Neuron*. 2015; 85: 257-73.
15. Ryan BJ, Hoek S, Fon EA, Wade-Martins R. Mitochondrial dysfunction and mitophagy in Parkinson's: from familial to sporadic disease. *Trends Biochem Sci*. 2015; 40: 200-10.
16. Zhu J, Wang KZ, Chu CT. After the banquet: mitochondrial biogenesis, mitophagy, and cell survival. *Autophagy*. 2013; 9: 1663-76.
17. Guan JL, Simon AK, Prescott M, Menendez JA, Liu F, Wang F, Wang C, Wolvetang E, Vazquez-Martin A, Zhang J. Autophagy in stem cells. *Autophagy*. 2013; 9: 830-49.
18. Joshi A, Kundu M. Mitophagy in hematopoietic stem cells: the case for exploration. *Autophagy*. 2013; 9: 1737-49.
19. Menendez JA, Joven J. Energy metabolism and metabolic sensors in stem cells: the metabostem crossroads of aging and cancer. *Adv Exp Med Biol*. 2014; 824: 117-40.
20. Menendez JA, Vellon L, Oliveras-Ferreros C, Cufi S, Vazquez-Martin A. mTOR-regulated senescence and autophagy during reprogramming of somatic cells to pluripotency: a roadmap from energy metabolism to stem cell renewal and aging. *Cell Cycle*. 2011; 10: 3658-77.

21. Michel S, Wanet A, De Pauw A, Rommelaere G, Arnould T, Renard, P. Crosstalk between mitochondrial (dys)function and mitochondrial abundance. *J Cell Physiol.* 2012; 227: 2297-10.
22. Pan H, Cai N, Li M, Liu GH, Izpisua Belmonte JC. Autophagic control of cell 'stemness'. *EMBO Mol Med.* 2013; 5: 327-31.
23. Phadwal K, Watson AS, Simon AK. Tighrope act: autophagy in stem cell renewal, differentiation, proliferation, and aging. *Cell Mol Life Sci.* 2013; 70: 89-103.
24. Vessoni AT, Muotri AR, Okamoto OK. Autophagy in stem cell maintenance and differentiation. *Stem Cells Dev.* 2012; 21: 513-20.
25. Chen CT, Hsu SH, Wei YH. Mitochondrial bioenergetic function and metabolic plasticity in stem cell differentiation and cellular reprogramming. *Biochim Biophys Acta.* 2012; 1820: 571-76.
26. Folmes CD, Nelson TJ, Martinez-Fernandez A, Arrell DK, Lindor JZ, Dzeja PP, Ikeda Y, Perez-Terzic C, Terzic, A. Somatic oxidative bioenergetics transitions into pluripotency-dependent glycolysis to facilitate nuclear reprogramming. *Cell Metab.* 2011; 14: 264-71.
27. Folmes CD, Nelson TJ, Terzic A. Energy metabolism in nuclear reprogramming. *Biomark Med.* 2011; 5: 715-29.
28. Folmes CD, Dzeja PP, Nelson TJ, Terzic, A. Metabolic plasticity in stem cell homeostasis and differentiation. *Cell Stem Cell.* 2012; 11: 596-06.
29. Folmes CD, Nelson TJ, Dzeja PP, Terzic A. Energy metabolism plasticity enables stemness programs. *Ann N Y Acad Sci.* 2012; 1254: 82-89.
30. Folmes CD, Arrell DK, Zlatkovic-Lindor J, Martinez-Fernandez A, Perez-Terzic C, Nelson TJ, Terzic A. Metabolome and metaboloproteome remodeling in nuclear reprogramming. *Cell Cycle.* 2013; 12: 2355-65.
31. Folmes CD, Martinez-Fernandez A, Faustino RS, Yamada S, Perez-Terzic C, Nelson TJ, Terzic A. Nuclear reprogramming with c-Myc potentiates glycolytic capacity of derived induced pluripotent stem cells. *J Cardiovasc Transl Res.* 2013; 6: 10-21.
32. Ito K, Suda T. Metabolic requirements for the maintenance of self-renewing stem cells. *Nat Rev Mol Cell Biol.* 2014; 15: 243-56.
33. Panopoulos AD, Yanes O, Ruiz S, Kida YS, Diep D, Tautenhahn R, Herreras A, Batchelder EM, Plongthongkum N, Lutz M, Berggren WT, Zhang K, Evans RM, Siuzdak G, Izpisua Belmonte JC. The metabolome of induced pluripotent stem cells reveals metabolic changes occurring in somatic cell reprogramming. *Cell Res.* 2012; 22: 168-177.
34. Son MJ, Jeong BR, Kwon Y, Cho YS. Interference with the mitochondrial bioenergetics fuels reprogramming to pluripotency via facilitation of the glycolytic transition. *Int J Biochem Cell Biol.* 2013; 45: 2512-18.
35. Teslaa T, Teitell MA. Pluripotent stem cell energy metabolism: an update. *EMBO J.* 2015; 34: 138-53.
36. Bukowiecki R, Adjaye J, Prigione, A. Mitochondrial function in pluripotent stem cells and cellular reprogramming. *Gerontology.* 2014; 60: 174-82.
37. Prigione A, Adjaye J. Modulation of mitochondrial biogenesis and bioenergetic metabolism upon in vitro and in vivo differentiation of human ES and iPS cells. *Int J Dev Bio.* 2010; 54: 1729-41.
38. Prigione A, Adjaye J. A mitochondrial strategy for safeguarding the reprogrammed genome. *Cell Regen (Lond).* 2014; 3: 5.
39. Prigione A, Fauler B, Lurz R, Lehrach H, Adjaye J. The senescence-related mitochondrial/oxidative stress pathway is repressed in human induced pluripotent stem cells. *Stem Cells.* 2010; 28: 721-33.
40. Prigione A, Hossini AM, Lichtner B, Serin A, Fauler B, Megges M, Lurz R, Lehrach H, Makrantonaki E, Zouboulis CC, Adjaye J. Mitochondrial-associated cell death mechanisms are reset to an embryonic-like state in aged donor-derived iPS cells harboring chromosomal aberrations. *PLoS One.* 2011; 6: e27352.
41. Prigione A, Ruiz-Pérez MV, Bukowiecki R, Adjaye J. Metabolic restructuring and cell fate conversion. *Cell Mol Life Sci.* 2015; 72: 1759-77.
42. Suhr ST, Chang EA, Tjong J, Alcasid N, Perkins GA, Goissis MD, Ellisman MH, Perez GI, Cibelli JB. Mitochondrial rejuvenation after induced pluripotency. *PLoS One.* 2010; 5: e14095.
43. Vazquez-Martin A, Corominas-Faja B, Cufi S, Vellon L, Oliveras-Ferraro C, Menendez OJ, Joven J, Lupu R, Menendez JA. The mitochondrial H(+)-ATP synthase and the lipogenic switch: new core components of metabolic reprogramming in induced pluripotent stem (iPS) cells. *Cell Cycle.* 2013; 12: 207-18.
44. Wang Y, Mah N, Prigione A, Wolfrum K, Andrade-Navarro MA, Adjaye J. A transcriptional roadmap to the induction of pluripotency in somatic cells. *Stem Cell Rev.* 2010; 6: 282-96.
45. Xu X, Duan S, Yi F, Ocampo A, Liu GH, Izpisua Belmonte JC. Mitochondrial regulation in pluripotent stem cells. *Cell Metab.* 2013; 18: 325-32.
46. Kida YS, Kawamura T, Wei Z, Sogo T, Jacinto S, Shigeno A, Kushige H, Yoshihara E, Liddle C, Ecker JR, Yu RT, Atkins AR, Downes M, Evans RM. ERRs Mediate a Metabolic Switch Required for Somatic Cell Reprogramming to Pluripotency. *Cell Stem Cell.* 2015; 16: 547-55.
47. Wang S, Xia P, Ye B, Huang G, Liu J, Fan Z. Transient activation of autophagy via Sox2-mediated suppression of mTOR is an important early step in reprogramming to pluripotency. *Cell Stem Cell.* 2013; 13: 617-25.
48. Son MY, Choi H, Han YM, Cho YS. Unveiling the critical role of REX1 in the regulation of human stem cell pluripotency. *Stem Cells.* 2013; 31: 2374-87.
49. Son MJ, Kwon Y, Son MY, Seol B, Choi HS, Ryu SW, Choi C, Cho YS. Mitofusins deficiency elicits mitochondrial metabolic reprogramming to pluripotency. *Cell Death Differ.* 2015; 22: 1957-69.
50. Vazquez-Martin A, Cufi S, Corominas-Faja B, Oliveras-Ferraro C, Vellon L, Menendez JA. Mitochondrial fusion by pharmacological manipulation impedes somatic cell reprogramming to pluripotency: new insight into the role of mitophagy in cell stemness. *Aging (Albany NY).* 2012; 4: 393-401. doi: 10.18632/aging.100465.
51. Wang L, Ye X, Zhao Q, Zhou Z, Dan J, Zhu Y, Chen Q, Liu L. Drp1 is dispensable for mitochondria biogenesis in induction to pluripotency but required for differentiation of embryonic stem cells. *Stem Cells Dev.* 2014; 23: 2422-34.
52. Heeman B, Van den Haute C, Aelvoet SA, Valsecchi F, Rodenburg RJ, Reumers V, Debyser Z, Callewaert G, Koopman WJ, Willems PH, Baekelandt V. Depletion of PINK1 affects mitochondrial metabolism, calcium homeostasis and energy maintenance. *J Cell Sci.* 2011; 124: 1115-25.
53. Oliveras-Salv  M, Van Rompuy AS, Heeman B, Van den Haute C, Baekelandt V. Loss-of-function rodent models for parkin and PINK1. *J Parkinsons Dis.* 2011; 1: 229-51.

54. Chu CT. A pivotal role for PINK1 and autophagy in mitochondrial quality control: implications for Parkinson disease. *Hum Mol Genet.* 2010; 19: R28-R37.
55. Clark IE, Dodson MW, Jiang C, Cao JH, Huh JR, Seol JH, Yoo SJ, Hay BA, Guo M. Drosophila pink1 is required for mitochondrial function and interacts genetically with parkin. *Nature.* 2006; 441: 1162-66.
56. Deng H, Dodson MW, Huang H, Guo M. The Parkinson's disease genes pink1 and parkin promote mitochondrial fission and/or inhibit fusion in Drosophila. *Proc Natl Acad Sci U S A.* 2008; 105: 14503-508.
57. Eiyama A, Okamoto K. PINK1/Parkin-mediated mitophagy in mammalian cells. *Curr Opin Cell Biol.* 2015; 33: 95-101.
58. Gautier CA, Kitada T, Shen J. Loss of PINK1 causes mitochondrial functional defects and increased sensitivity to oxidative stress. *Proc Natl Acad Sci U S A.* 2008; 105: 11364-369.
59. Gegg ME, Cooper JM, Chau KY, Rojo M, Schapira AH, Taanman JW. Mitofusin 1 and mitofusin 2 are ubiquitinated in a PINK1/parkin-dependent manner upon induction of mitophagy. *Hum Mol Genet.* 2010; 19: 4861-70.
60. Geisler S, Holmström KM, Skujat D, Fiesel FC, Rothfuss OC, Kahle PJ, Springer W. PINK1/Parkin-mediated mitophagy is dependent on VDAC1 and p62/SQSTM1. *Nat Cell Biol.* 2010; 12: 119-31.
61. Kawajiri S, Saiki S, Sato S, Sato F, Hatano T, Eguchi H, Hattori N. PINK1 is recruited to mitochondria with parkin and associates with LC3 in mitophagy. *FEBS Lett.* 2010; 584: 1073-79.
62. Springer W, Kahle PJ. Regulation of PINK1-Parkin-mediated mitophagy. *Autophagy.* 2011; 7: 266-78.
63. Vives-Bauza C, Zhou C, Huang Y, Cui M, de Vries RL, Kim J, May J, Tocilescu MA, Liu W, Ko HS, Magrané J, Moore DJ, Dawson VL, et al. PINK1-dependent recruitment of Parkin to mitochondria in mitophagy. *Proc Natl Acad Sci U S A.* 2010; 107: 378-83.
64. Vazquez-Martin A, Cufi S, Lopez-Bonet E, Corominas-Faja B, Oliveras-Ferreros C, Martin-Castillo B, Menendez JA. Metformin limits the tumorigenicity of iPS cells without affecting their pluripotency. *Sci Rep.* 2012; 2: 964.
65. Vazquez-Martin A, Vellon L, Quirós PM, Cufi S, Ruiz de Galarreta E, Oliveras-Ferreros C, Martin AG, Martin-Castillo B, López-Otín C, Menendez JA. Activation of AMP-activated protein kinase (AMPK) provides a metabolic barrier to reprogramming somatic cells into stem cells. *Cell Cycle.* 2012; 11: 974-89.
66. Rehman J. Empowering self-renewal and differentiation: the role of mitochondria in stem cells. *J Mol Med (Berl).* 2010; 88: 981-86.
67. Rodriguez-Enriquez S, Kim I, Currin RT, Lemasters JJ. Tracker dyes to probe mitochondrial autophagy (mitophagy) in rat hepatocytes. *Autophagy.* 2006; 2: 39-46.
68. Jiang J, Chan YS, Loh YH, Cai J, Tong GQ, Lim CA, Robson P, Zhong S, Ng HH. A core Klf circuitry regulates self-renewal of embryonic stem cells. *Nat Cell Biol.* 2008; 10: 353-60.
69. Vafa O, Wade M, Kern S, Beeche M, Pandita TK, Hampton GM, Wahl GM. c-Myc can induce DNA damage, increase reactive oxygen species, and mitigate p53 function: a mechanism for oncogene-induced genetic instability. *Mol Cell.* 2002; 9: 1031-44.
70. Prochownik EV, Li Y. The ever expanding role for c-Myc in promoting genomic instability. *Cell Cycle.* 2007; 6: 1024-29.
71. Sancho P, Burgos-Ramos E, Tavera A, Bou Kheir T, Jagust P, Schoenhals M, Barneda D, Sellers K, Campos-Olivas R, Graña O, Viera CR, Yuneva M, Sainz B Jr, Heeschen C. MYC/PGC-1 $\alpha$  Balance Determines the Metabolic Phenotype and Plasticity of Pancreatic Cancer Stem Cells. *Cell Metab.* 2015; 22: 590-605.
72. Chung TL, Brena RM, Kolle G, Grimmond SM, Berman BP, Laird PW, Pera MF, Wolvetang EJ. Vitamin C promotes widespread yet specific DNA demethylation of the epigenome in human embryonic stem cells. *Stem Cells.* 2010; 28: 1848-55.
73. Esteban MA, Wang T, Qin B, Yang J, Qin D, Cai J, Li W, Weng Z, Chen J, Ni S, Chen K, Li Y, Liu X, Xu J, et al. Vitamin C enhances the generation of mouse and human induced pluripotent stem cells. *Cell Stem Cell.* 2010; 6: 71-79.
74. Monfort A, Wutz A. Breathing-in epigenetic change with vitamin C. *EMBO Rep.* 2013; 14: 337-46.
75. Wang T, Chen K, Zeng X, Yang J, Wu Y, Shi X, Qin B, Zeng L, Esteban MA, Pan G, Pei D. The histone demethylases Jhdm1a/1b enhance somatic cell reprogramming in a vitamin-C-dependent manner. *Cell Stem Cell.* 2011; 9: 575-87.
76. Cuyàs E, Fernández-Arroyo S, Corominas-Faja B, Rodríguez-Gallego E, Bosch-Barrera J, Martin-Castillo B, De Llorens R, Joven J, Menendez JA. Oncometabolic mutation IDH1 R132H confers a metformin-hypersensitive phenotype. *Oncotarget.* 2015; 6:12279-296. doi: 10.18632/oncotarget.3733.
77. Riera-Borrull M, Rodríguez-Gallego E, Hernández-Aguilera A, Luciano F, Ras R, Cuyàs E, Camps J, Segura-Carretero A, Menendez JA, Joven J, Fernández-Arroyo S. Exploring the Process of Energy Generation in Pathophysiology by Targeted Metabolomics: Performance of a Simple and Quantitative Method. *J Am Soc Mass Spectrom.* 2016;27:168-77.
78. Gutierrez-Aranda I, Ramos-Mejia V, Bueno C, Munoz-Lopez M, Real PJ, Mácia A, Sanchez L, Ligerio G, Garcia-Perez JL, Menendez P. Human induced pluripotent stem cells develop teratoma more efficiently and faster than human embryonic stem cells regardless the site of injection. *Stem Cells.* 2010; 28: 1568-70.
79. Knoepfler PS. Deconstructing stem cell tumorigenicity: a roadmap to safe regenerative medicine. *Stem Cells.* 2009; 27: 1050-56.
80. Müller FJ, Goldmann J, Löser P, Loring JF. A call to standardize teratoma assays used to define human pluripotent cell lines. *Cell Stem Cell.* 2010; 6: 412-14.
81. Menendez S, Camus S, Herreria A, Paramonov I, Morera LB, Collado M, Pekarik V, Maceda I, Edel M, Consiglio A, Sanchez A, Li H, Serrano M, Belmonte JC. Increased dosage of tumor suppressors limits the tumorigenicity of iPS cells without affecting their pluripotency. *Aging Cell.* 2012; 11: 41-50.
82. Katajisto P, Döhla J, Chaffer CL, Pentimikko N, Marjanovic N, Iqbal S, Zoncu R, Chen W, Weinberg RA, Sabatini DM. Stem cells. Asymmetric apportioning of aged mitochondria between daughter cells is required for stemness. *Science.* 2015; 348: 340-43.
83. Frank M, Duvezin-Caubet S, Koob S, Occhipinti A, Jagasia R, Petcherski A, Ruonala MO, Priault M, Salin B, Reichert AS. Mitophagy is triggered by mild oxidative stress in a mitochondrial fission dependent manner. *Biochim Biophys Acta.* 2012; 1823: 2297-2310.
84. Miller DM, Thomas SD, Islam A, Muench D, Sedoris K. c-Myc and cancer metabolism. *Clin Cancer Res.* 2012; 18: 5546-53.
85. Ji J, Sharma V, Qi S, Guarch ME, Zhao P, Luo Z, Fan W, Wang Y, Mbabaali F, Neculai D, Esteban MA, McPherson JD, Batada NN. Antioxidant supplementation reduces genomic aberrations in human induced pluripotent stem cells. *Stem Cell Reports.* 2014; 2: 44-51.

86. Teperino R, Schoonjans K, Auwerx J. Histone methyl transferases and demethylases; can they link metabolism and transcription? *Cell Metab.* 2010;12:321-27.
87. Cascella B, Mirica LM. Kinetic analysis of iron-dependent histone demethylases:  $\alpha$ -ketoglutarate substrate inhibition and potential relevance to the regulation of histone demethylation in cancer cells. *Biochemistry.* 2012;51:8699-701.
88. Salminen A, Kauppinen A, Hiltunen M, Kaarniranta K. Krebs cycle intermediates regulate DNA and histone methylation: epigenetic impact on the aging process. *Ageing Res Rev.* 2014;16:45-65.
89. Carey BW, Finley LW, Cross JR, Allis CD, Thompson CB. Intracellular  $\alpha$ -ketoglutarate maintains the pluripotency of embryonic stem cells. *Nature.* 2015;518:413-16.
90. Minocherhomji S, Tollefsbol TO, Singh KK. Mitochondrial regulation of epigenetics and its role in human diseases. *Epigenetics.* 2012;7:326-34.
91. Salminen A, Kaarniranta K, Hiltunen M, Kauppinen A. Krebs cycle dysfunction shapes epigenetic landscape of chromatin: novel insights into mitochondrial regulation of aging process. *Cell Signal.* 2014;26:1598-1603.
92. Merkwirth C, Jovaisaite V, Durieux J, Matilainen O, Jordan SD, Quiros PM, Steffen KK, Williams EG, Mouchiroud L, Tronnes SU, Murillo V, Wolff SC, Shaw RJ, Auwerx J, Dillin A. Two Conserved Histone Demethylases Regulate Mitochondrial Stress-Induced Longevity. *Cell.* 2016; 165:1209-23.
93. Ben-David U, Benvenisty N. Chemical ablation of tumor-initiating human pluripotent stem cells. *Nat Protoc.* 2014; 9: 729-40.
94. Ben-David U, Gan QF, Golan-Lev T, Arora P, Yanuka O, Oren YS, Leikin-Frenkel A, Graf M, Garippa R, Boehringer M, Gromo G, Benvenisty N. Selective elimination of human pluripotent stem cells by an oleate synthesis inhibitor discovered in a high-throughput screen. *Cell Stem Cell.* 2013; 12: 167-79.
95. Chen F, Cai B, Gao Y, Yuan X, Cheng F, Wang T, Jiang M, Zhou Y, Lahn BT, Li W, Xiang AP. Suicide gene-mediated ablation of tumor-initiating mouse pluripotent stem cells. *Biomaterials.* 2013; 34: 1701-11.
96. Lee MO, Moon SH, Jeong HC, Yi JY, Lee TH, Shim SH, Rhee YH, Lee SH, Oh SJ, Lee MY, Han MJ, Cho YS, Chung HM, Kim KS, Cha HJ. Inhibition of pluripotent stem cell-derived teratoma formation by small molecules. *Proc Natl Acad Sci U S A.* 2013; 110: E3281-E3290.
97. Menendez JA. Metabolic control of cancer cell stemness: Lessons from iPS cells. *Cell Cycle.* 2015; 14: 3801-11.
98. Tang C, Lee AS, Volkmer JP, Sahoo D, Nag D, Mosley AR, Inlay MA, Ardehali R, Chavez SL, Pera RR, Behr B, Wu JC, Weissman IL, Drukker M. An antibody against SSEA-5 glycan on human pluripotent stem cells enables removal of teratoma-forming cells. *Nat Biotechnol.* 2011; 29: 829-34.
99. Ma T, Li J, Xu Y, Yu C, Xu T, Wang H, Liu K, Cao N, Nie BM, Zhu SY, Xu S, Li K, Wei WG, Wu Y, Guan KL, Ding S. Atg5-independent autophagy regulates mitochondrial clearance and is essential for iPSC reprogramming. *Nat Cell Biol.* 2015; 17: 1379-87.
100. Chandel NS. Evolution of Mitochondria as Signaling Organelles. *Cell Metab.* 2015;22:204-06.
101. Martínez-Reyes I, Diebold LP, Kong H, Schieber M, Huang H, Hensley CT, Mehta MM, Wang T, Santos JH, Woychik R, Dufour E, Spelbrink JN, Weinberg SE, Zhao Y, DeBerardinis RJ, Chandel NS. TCA Cycle and Mitochondrial Membrane Potential Are Necessary for Diverse Biological Functions. *Mol Cell.* 2016;61:199-209.
102. Fernández-Arroyo S, Cuyàs E, Bosch-Barrera J, Alarcón T, Joven J, Menendez JA. Activation of the methylation cycle in cells reprogrammed into a stem cell-like state. *Oncoscience.* 2016;2:958-67.
103. Xia J, Sinelnikov IV, Han B, Wishart DS. MetaboAnalyst 3.0--making metabolomics more meaningful. *Nucleic Acids Res.* 2015; 43:W251-W257.



## Potential targeted therapeutic approaches in liposarcoma

Deepika Kanojia, Manoj Garg, and H. Phillip Koeffler

Liposarcoma (LPS) is rare malignant tumor of fat cells in deep soft tissue that affects adults between the ages of 40 and 60 [1]. This tumor is extremely aggressive with high morbidity and mortality. World Health organization classifies LPS into five subtypes: well-differentiated (WDLPS)/Atypical lipomatous tumors (ALT); dedifferentiated (DDLPS); myxoid (MLPS); pleomorphic (PLPS); and mixed type LPS [2]. Most common modality of treatment is surgical removal of tumor followed by radiation and chemotherapy. The five year survival rate of LPS patients vary from 56%-100% based on different subtypes [3]. Previous genetic studies have focused either on a subset of target genes or one subtype of LPS. Till now no reports have provided a detailed genomic analysis of LPS which included all different subtypes of LPS. Therefore, recently we defined the genomic landscape of LPS using SNP array and whole exome sequencing and identified a spectrum of altered genes and pathways in different subtypes of LPS patients and cell lines [4].

WDLPS and DDLPS subtypes have a characteristic feature of amplified region of chromosome 12q13-15 containing several well-known oncogenes such as MDM2, CDK4 and HMGA2 [5]. SNP array analysis of LPS patients and cell lines identified recurrent amplification of Carboxypeptidase M (CPM) gene only in WDLPS and DDLPS subtypes. We studied in detail CPM gene in vitro and in vivo and showed its involvement in liposarcomagenesis. CPM is a membrane bound enzyme and we found it expressed on the cell surface of LPS cells suggesting it as a potential therapeutic target. Carboxypeptidase activity of CPM is known to regulate the processing of EGF [6]. We found downregulation of CPM expression leads to reduced EGFR signalling and induces apoptosis of LPS cells. Future studies are ongoing detailing further role of enzymatic activity of CPM in EGFR signaling and enhancement of tumor growth. Further, we are developing both a quantitative PCR assay and an ELISA to measure CPM activity in the serum to develop a biomarker to measure minimal residual disease which might aid in monitoring therapy. Specific and selective inhibitors of CPM are not available in the market; therefore, we are also aiming to do screening to find selective and specific small molecules to inhibit

CPM enzymatic activity. We proposed CPM as potential therapeutic candidate which could be used as targeted approach to manage CPM amplified WDLPS or DDLPS patients.

Next, whole exome sequencing and targeted exome sequencing identified various known cancer related and novel genes recurrently mutated in different subtypes of LPS. MAPK, ErbB, JAK-STAT, Wnt, apoptosis, cell cycle, DNA replication and repair and axon guidance pathways were found to be potentially involved in liposarcomagenesis. We identified recurrent mutations in previously unidentified genes in LPS associated with DNA damage repair pathways. LPS tumors with DNA repair mutations could be completely dependent on other backup repair pathways for the survival which may be exploited to induce synthetic lethality as therapeutic approach in these tumors.

Interestingly, we reported for the first time multi-region genomic analysis of single LPS patient's tumor signifying intra-tumor mutational and copy number heterogeneity. The current basis for most of the personalized medicine approaches depends on the genomic landscape of a single tumor biopsy sample. Due to the frequent large size of LPS tumors compared to other solid tumors, intra-tumor heterogeneity will lead to difficulties in identifying biomarkers and therapeutic targets. Our preliminary analysis of intra-tumor heterogeneity mandates the need for future detailed studies exploring the evolution of LPS tumors leading to progression.

In summary, our recent work gave insights into global genomic spectrum of LPS cohort for development of novel therapeutic strategies and for understanding the pathogenesis this deadly disease.

## REFERENCES

1. Mack TM. Cancer. 1995; 75:211-244.
2. Fletcher CDM BJ, Hogendoorn PCW, Mertens F eds. Lyon: IARC Press. 2013; (4th ed).
3. Dalal KM, et al. J Surg Oncol. 2008; 97:298-313.
4. Kanojia D, et al. Oncotarget. 2015; 6:42429-42444. doi: 10.18632/oncotarget.6464.
5. Barretina J, et al. Nat Gen. 2010; 42:715-721.
6. McGwire GB and Skidgel RA. J Biol Chem. 1995; 270:17154-17158.

**Deepika Kanojia:** Cancer Science Institute of Singapore,  
National University of Singapore, Singapore

***Correspondence:*** Deepika Kanojia

***Email:*** [csidk@nus.edu.sg](mailto:csidk@nus.edu.sg)

***Keywords:*** liposarcoma, therapeutics, exome sequencing,  
tumor heterogeneity, genomic landscape

**Received:** April 8, 2016

**Published:** April 14, 2016

## Apoptosis as anticancer mechanism: function and dysfunction of its modulators and targeted therapeutic strategies

Giuseppa Pistritto<sup>1</sup>, Daniela Trisciuglio<sup>2</sup>, Claudia Ceci<sup>1</sup>, Alessia Garufi<sup>2,3</sup>, and Gabriella D'Orazi<sup>2,3</sup>

<sup>1</sup>Department of Systems Medicine, University "Tor Vergata", 00133 Rome, Italy

<sup>2</sup>Department of Research, Advanced Diagnostics, and Technological Innovation, Regina Elena National Cancer Institute, 00158 Rome, Italy

<sup>3</sup>Department of Medical Oral and Biotechnological Sciences, Tumor Biology Unit, University "G. d'Annunzio", 66013 Chieti, Italy

**Key words:** apoptosis, defective apoptotic pathways, cancer, small molecules, miRNAs, p53

**Received:** 01/04/16; **Accepted:** 03/08/16; **Published:** 03/27/16

**Correspondence to:** Gabriella D'Orazi, MD/PhD; Giuseppa Pistritto, MD/PhD; **E-mail:** [gabriella.dorazi@unich.it](mailto:gabriella.dorazi@unich.it); [pistritto@med.uniroma2.it](mailto:pistritto@med.uniroma2.it)

**Copyright:** Pistritto et al. This is an open-access article distributed under the terms of the Creative Commons Attribution License, which permits unrestricted use, distribution, and reproduction in any medium, provided the original author and source are credited

**Abstract:** Apoptosis is a form of programmed cell death that results in the orderly and efficient removal of damaged cells, such as those resulting from DNA damage or during development. Apoptosis can be triggered by signals from within the cell, such as genotoxic stress, or by extrinsic signals, such as the binding of ligands to cell surface death receptors. Deregulation in apoptotic cell death machinery is an hallmark of cancer. Apoptosis alteration is responsible not only for tumor development and progression but also for tumor resistance to therapies. Most anticancer drugs currently used in clinical oncology exploit the intact apoptotic signaling pathways to trigger cancer cell death. Thus, defects in the death pathways may result in drug resistance so limiting the efficacy of therapies. Therefore, a better understanding of the apoptotic cell death signaling pathways may improve the efficacy of cancer therapy and bypass resistance. This review will highlight the role of the fundamental regulators of apoptosis and how their deregulation, including activation of anti-apoptotic factors (i.e., Bcl-2, Bcl-xL, etc) or inactivation of pro-apoptotic factors (i.e., p53 pathway) ends up in cancer cell resistance to therapies. In addition, therapeutic strategies aimed at modulating apoptotic activity are briefly discussed.

### INTRODUCTION

Apoptosis, the programmed cell death, is finely regulated at gene level resulting in the orderly and efficient removal of damaged cells such as those occurring following DNA damage or during development [1]. The machinery of apoptosis is complex and involves many signaling pathways. Apoptosis can be triggered in a cell through either the caspase-mediated extrinsic or intrinsic pathways. Both pathways converge to activate the effector apoptotic caspases resulting ultimately in morphological and biochemical cellular alterations, characteristics of apoptosis [2]. Usually, the balance between the pro-apoptotic and anti-apoptotic protein regulators is a

critical key point to determine if a cell undergoes apoptosis. The induction of apoptosis as result of DNA damage in precancerous lesions can remove potentially harmful cells, thereby blocking tumor growth. Deregulation of this death process is associated with unchecked cell proliferation, development and progression of cancer and cancer resistance to drug therapies [3,4]. For that reason, deregulation of apoptosis is considered one of the hallmarks of cancer [5]. Therapeutic strategies targeting molecules involved in apoptotic resistance therefore represent a valid approach to be pursued in order to restore cancer cells sensitivity to apoptosis and overcome the ineffectiveness of the treatments [6,7]. This article focuses on the mechanisms of apoptosis, how defects along the

apoptotic pathway contribute to cancer development and drug resistance and, briefly, how apoptosis can be used as a vehicle of targeted treatment in cancer.

### **Morphological and biochemical changes in apoptosis**

From the morphological point of view apoptotic cells show a characteristic cytoplasmic cell shrinkage, budding of plasma membrane, membrane exposure of phosphatidylserine (PS) on extracellular side, chromatin condensation and DNA fragmentation [8,9]. The plasma membrane is intact throughout the total process. The expression of PS in the outer layers of the cell membrane allows early recognition of dead cells by macrophages, resulting in phagocytosis without the release of proinflammatory cellular components [10]. At the later stage of apoptosis some of the morphological features include membrane blebbing, ultrastructural modification of cytoplasmic organelles and loss of membrane integrity [11]. Usually phagocytic cells engulf apoptotic cells before apoptotic bodies occur [12]. Apoptosis is primarily executed by a family of proteases known as the caspases (cysteiny, aspartate-specific proteases) [13]. Caspases are central to the mechanism of apoptosis as they are both the initiators (caspase-2, -8, -9 and -10, primarily responsible for the beginning of the apoptotic pathway) and the executors (caspase-3, -6 and -7, responsible for the definite cleavage of cellular components) of cell death [14]. After being produced as inactive proteins (zymogens or pro-caspases), the initiator caspases auto-activate through auto-proteolysis, a process that is facilitated by their interaction with specific adapter molecules [15]. Once activated, the initiator caspases cleave off the executors caspases that perform critical cleavage of specific cellular substrates resulting in the final apoptotic cell death [16]. This caspases activity is responsible of the apoptotic hallmarks, such as chromatin condensation, plasma membrane asymmetry and cellular blebbing. The extensive and irreversible proteolytic activity mediated by executor caspases represents the ultimate outcome of both the extrinsic and the intrinsic apoptotic pathways (see below). Thus, both pathways converge on caspases-3, 6, or -7 that allow disruption of DNA and cellular components inducing the typical morphological changes in apoptosis [17]. Of note, caspases activity has been also extended to non-apoptotic functions such as cell differentiation/maturation suggesting that the caspase cascade may become activated independently of- or without inducing- an apoptotic cascade [18-20].

### **Extrinsic apoptotic pathway**

The extrinsic apoptotic pathway (death receptor-dependent) is initiated by the interaction of cell surface

exposed death receptors, belonging to the superfamily of tumor necrosis factor receptor (TNFR), with their respective protein TNF family ligands [21]. Death receptors are structurally defined by an intracellular protein-protein interaction domain, called the death domain (DD), which is critically involved in apoptosis-inducing signalling [22]. The more broadly characterized signaling systems of death receptor-ligands include TNFR1-TNF $\alpha$ , FAS (CD95, APO-1)-FasL, TRAILR1 (DR4)-TRAIL, TRAILR2 (DR5)-TRAIL. Upon death receptor stimulation by its corresponding ligand, the same receptor undergoes oligomerization and a conformational change to reveal its cytoplasmic DD to support homotypic interactions with other DD-containing proteins [21]. The role of adapter proteins (FADD/TRADD) is to sequester, at level of this protein complex, the initiator pro-caspase-8 and/or -10 resulting in the formation of the so-called death-inducing signaling complex (DISC), increasing the local concentration of pro-caspase and promoting the mutual auto-activation [23]. The activation of initiator caspases results in the processing of the downstream effector caspases-3, -6 and -7 whose activation leads to the cleavage of essential substrates for cell viability, inducing cell death (Figure 1) [17]. Some cells do not die in response to the extrinsic pathway alone and require an amplification step that is induced by caspase-8. In this situation, caspase-8 targets the BH3-only protein Bid (BH3-interacting-domain death agonist) for cleavage and generate the activated fragment t-Bid; t-Bid then directly activates pro-apoptotic multi-domain proteins to induce mitochondrial outer membrane permeability (MOMP), so this co-engages the intrinsic pathway [3] (Figure 1) (see below).

### **Intrinsic apoptotic pathway**

The intrinsic apoptotic pathway (mitochondria-dependent) is mediated by intracellular signals that converge at the mitochondrial level in response to different stress conditions (i.e., irradiation, treatment with chemotherapeutic agents, etc.) [24]. Internal stimuli such as irreparable genetic damage, hypoxia, extremely high concentrations of cytosolic Ca<sup>+</sup> and severe oxidative stress are some triggers of the initiation of the intrinsic mitochondrial pathway [25]. Subsequent activation of pro-apoptotic BH3-only members of the Bcl-2 family (Bax, Bak) neutralizes the antiapoptotic proteins Bcl-2, Bcl-xL, and Mcl-1, leading to disruption of mitochondrial membrane outer membrane permeability (MOMP) so that proteins normally confined in the intermembrane space spread into the cytosol. These proteins include the so-called apoptogenic factors, such as cytochrome-c, which plays a

crucial role in activating the mitochondrial-dependent death in the cytosol [26]. Cytochrome-*c* binds to the cytosolic Apaf-1 (apoptosis protease activating factor-1) and triggers the formation of a complex named apoptosome, which recruits initiator pro-caspase-9 to its caspase recruitment domain (CARD), allowing auto-activation and then proteolysis. The process in turn activates downstream executor caspases-3, -6 and -7 for cleavage of cellular substrates leading to apoptotic cell death (Figure 1) [27,28].

### The B-cell lymphoma 2 (Bcl-2) family proteins

The intrinsic pathway is closely regulated by the B-cell lymphoma 2 (Bcl-2) family of intracellular proteins. This proteins family regulates both pro-apoptotic and anti-apoptotic intrinsic pathways controlling the alteration of MOMP [29]. Therefore, by mediating per-

meabilization of the mitochondrial membrane, the Bcl-2 proteins serve as an “apoptotic switch” [30]. The Bcl-2 proteins are classified into three subgroups, one group with anti-apoptotic and two with pro-apoptotic function, depending on the composition of typical BH (Bcl-2 Homology) domains, listed from BH1 to BH4 [31,32] (Figure 2). Whereas the BH1 and BH2 domains of *bcl-2* are required for dimerization with pro-apoptotic proteins, BH3 domain is crucially important to the interaction between pro-apoptotic and anti-apoptotic proteins and is contained by all family members. The amino-terminal BH4 domain is mainly found in the *bcl-2* family members with death-repressing activity, but is also present in some pro-apoptotic molecules. The anti-apoptotic multi-domain group includes Bcl-2, Bcl-xL, Bcl-W, Mcl-1, A1, and Bcl-B, containing from three to four BH domains; the pro-apoptotic multi-domain group includes Bax, Bak and Bok proteins, containing three

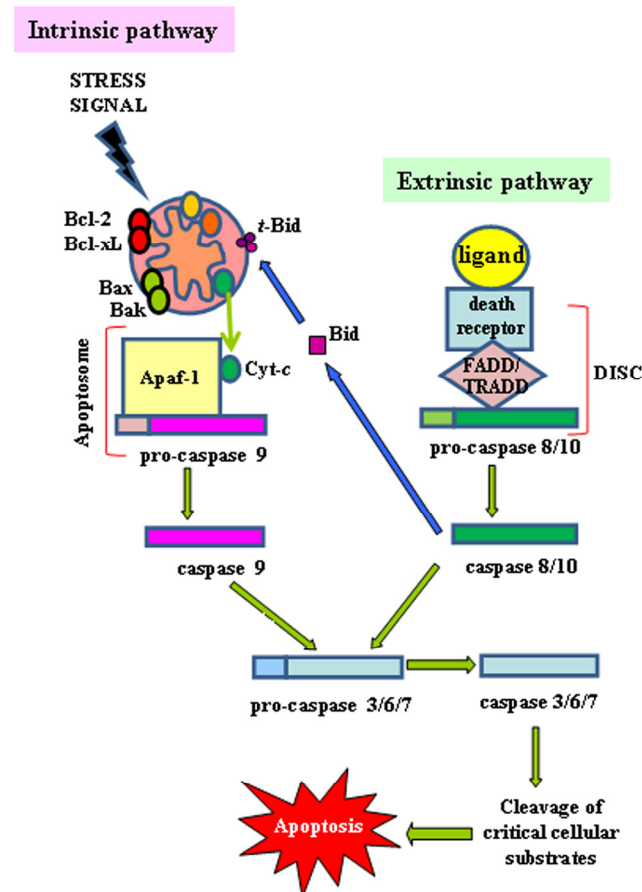


**Figure 1. Intrinsic and extrinsic apoptotic pathways.** The intrinsic (mitochondrial) and the extrinsic (ligands/death receptors) cell death pathways and their convergence through t-Bid are depicted (see text for details).



BH-domains (BH1, BH2 and BH3); and the pro-apoptotic BH3-only proteins group includes Bid (BH3 interacting-domain death agonist), Bim (Bcl-2-like protein 11), Bad (Bcl-2-associated death promoter), Puma (p53 upregulated modulator of apoptosis), Noxa, BMF, HRK and BIK (Figure 3) [33]. While the anti-apoptotic proteins regulate apoptosis by blocking the mitochondrial release of cytochrome-c, the pro-apoptotic proteins act by promoting such release.

The balance and protein-protein interactions between Bcl-2 family members is required to determine whether a cell undergoes cell survival or apoptosis. The activation of Bax (cytosolic protein that translocates into mitochondria during induction of apoptosis), and Bak (integral membrane protein located in the mitochondria and endoplasmic reticulum) involves conformational changes that trigger the formation of homo-oligomeric protein complexes that end up altering

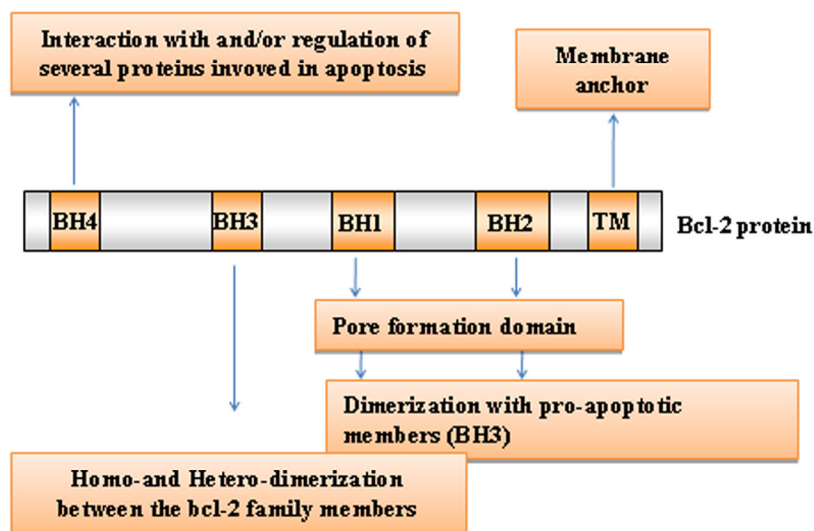


**Figure 2. Bcl-2 family members domain composition and function.** Typical BH (Bcl-2 Homology) domains, listed from BH1 to BH4, are shown. TM: transmembrane domain.

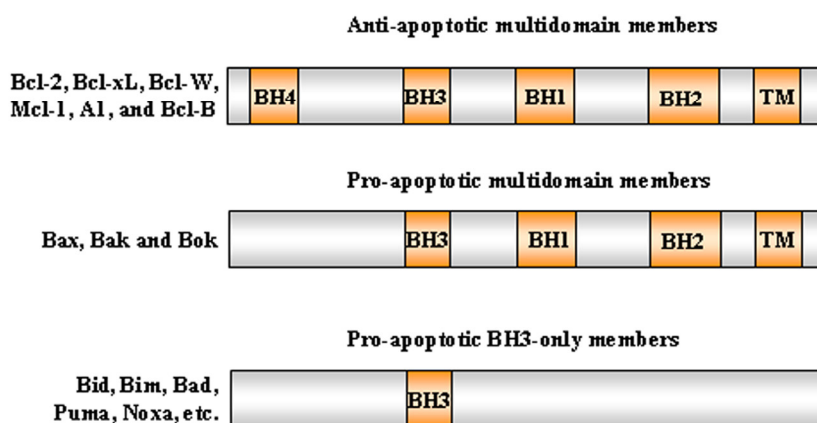


**Figure 3. Bcl-2 protein subgroups.** The Bcl-2 proteins are classified into three subgroups, one group with anti-apoptotic and two with pro-apoptotic function, depending on the composition of the typical BH domains, listed from BH1 to BH4. Representative members of each subfamily are shown.

the mitochondrial membrane permeability [34,35]. The pro-apoptotic BH3-only proteins act upstream of this event binding with high affinity to anti-apoptotic Bcl-2 family members thereby allowing Bax/Bak to elicit MOMP and activation of the caspase cascade [36,37]. Anti-apoptotic multidomain members of the Bcl-2 protein family not only counteract the pore-forming activity of Bax and Bak by engaging in direct inhibitory interactions, but also prevent the generation of pro-apoptotic cytosolic  $\text{Ca}^{2+}$  waves either by reducing capacity of endoplasmic reticulum (ER)  $\text{Ca}^{2+}$  storage, an effect that is antagonized by Bax and Bak or by interacting with inositol 1,4,5- trisphosphate (IP3) receptor [38,39]. Other apoptotic factors that are released from the mitochondrial intermembrane space into the cytoplasm include apoptosis inducing factor (AIF), second mitochondria-derived activator of caspase (Smac), direct IAP Binding protein with Low pI (DIABLO) and Omi/high temperature requirement protein A (HtrA2) [40].

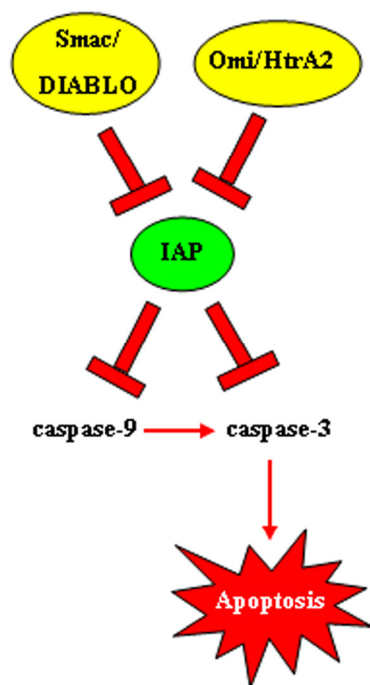


**Figure 4. Function of inhibitors of apoptosis proteins (IAPs).** IAPs are often overexpressed in cancer and they have the ability to bind and inactivate caspases 9 and 3. The activities of IAPs, on the other hand, may be suppressed by mitochondrial proteins, such as Omi/HtrA2 and Smac/DIABLO, released into the cytosol during apoptosis.

## The inhibitors of apoptosis proteins (IAPs)

Considering that proteolysis is an irreversible process, strict control of caspases-mediated proteolytic cleavage is imperative to prevent inappropriate cell destruction [41]. Negative regulation of caspases function is achieved by IAP proteins family whose principal members in humans are NAIP (BIRC1), cIAP1 (BIRC2), cIAP2 (BIRC3), X-linked IAP (XIAP, BIRC4), Survivin (BIRC5), Apollon (BRUCE, BIRC6), Livin/ML-IAP (BIRC7), and IAP-like protein 2 (ILP2 – BIRC8) [42]. Their characteristic BIR (baculovirus IAP repeat) domain mediates the interaction with various proteins and gives them the ability to bind and inactivate caspases [43]. The activities of IAPs, however, may be suppressed by mitochondrial proteins, such as Omi/HtrA2 and Smac/DIABLO, released into the cytosol during apoptosis (Figure 4). These endogenous IAPs antagonists are able to bind to the BIR domain of IAPs reducing their ability to interact with caspase-3 or -9 thereby restoring their activity [44]. XIAP is the best characterized IAP so far and is generally recognized as the most potent endogenous caspase inhibitor. XIAP anti-apoptotic activity involves inhibition of active executor caspases as well as prevention of initiator caspase-9 activation [45].

## Alterations of the apoptotic pathways

There are many ways through which both the extrinsic and the intrinsic apoptotic pathways may be altered, resulting in reduction of apoptosis or acquisition of apoptosis resistance. They include impaired death receptor signaling, disrupted balance between pro-apoptotic and anti-apoptotic proteins, reduced caspase function and impaired p53 function (Figure 5). Alteration of extrinsic apoptotic signaling has been associated with different types of human tumors, underscoring how the loss of activity of Fas-FasL system [46] or the aberrant expression of cytosolic components of this death receptor apoptotic pathway (i.e., FADD) [47] can contribute to the tumor transformation. Several genetic defects have been proven to contribute to the resistance of tumor cells to Fas-mediated apoptosis. Fas transcriptional silencing is a common oncogenic event in the epithelial transformation, while its mutation has been often associated with B-cell germinal center-derived lymphomas [48]. In acute myelogenous leukemia (AML) reduced or absent expression of FADD has been frequently observed, resulting in resistance to chemotherapy and poor patient prognosis [47,49]. Moreover, in several cancers including neuroblastoma, medulloblastoma, and small cell lung cancer (SCLC), absent or reduced expression of caspase-8 was reported

[50-52]. Another resistance mechanism reported in a variety of human tumors is the overexpression of anti-apoptotic protein c-Flip, recruited at the DISC level, that prevents the pro-caspase-8 auto-activation thereby rendering cell resistant to death receptor-mediated apoptosis [53-55].

As for the extrinsic pathway, alteration of some components of the intrinsic apoptotic pathway can play a fundamental role in the development of resistance to chemotherapy in different types of tumors. Disruption in the balance of anti-apoptotic and pro-apoptotic members of the Bcl-2 family results in deregulated apoptosis in the affected cells. This can be due to overexpression of one or more anti-apoptotic proteins or downregulation of one or more pro-apoptotic proteins or a combination of both. Anti-apoptotic Bcl-2 over-expression has been reported in several human cancers, including prostate cancer, diffuse large B-cell lymphoma (DLBCL), melanoma, etc. [56-58], resulting in protection of cancer cells from apoptosis or inhibition of TRAIL-induced apoptosis [59,60]. Overexpression of Bcl-xL has also been reported in colorectal cancer and Kaposi's sarcoma [61,62]. Such

overexpression confers a multi-drug resistance phenotype in tumor cells and prevents them from undergoing apoptosis [63]. Thus, high expression levels of anti-apoptotic proteins Bcl-2 and Bcl-xL have been reported to correlate with cisplatin resistance and tumor recurrence in different cancers including non-small cell lung cancer (NSCLC), head and neck, ovarian, and breast [64-68]. On the other hand, mutations in the pro-apoptotic Bax gene have been reported in colorectal cancers and contribute to resistance to anticancer treatments [69]. Increased Bcl-2/Bax ratio has been reported in chronic lymphocytic leukaemia (CLL) patients. [70]. Other examples of alteration of the intrinsic pathway include reduced expression of the basic component of the apoptosome, Apaf-1, in melanomas [71,72], as result of promoter aberrant methylation. In addition, tumor cells resistance to apoptosis also occurs as a result of alteration of mediators that control the intrinsic apoptotic pathway downstream from the apoptosome formation, i.e. acting on caspase activity. In this regard, high level of IAPs expression has been found in different types of cancers, and this evidence is considered a marker of poor prognosis for patients [73,74].

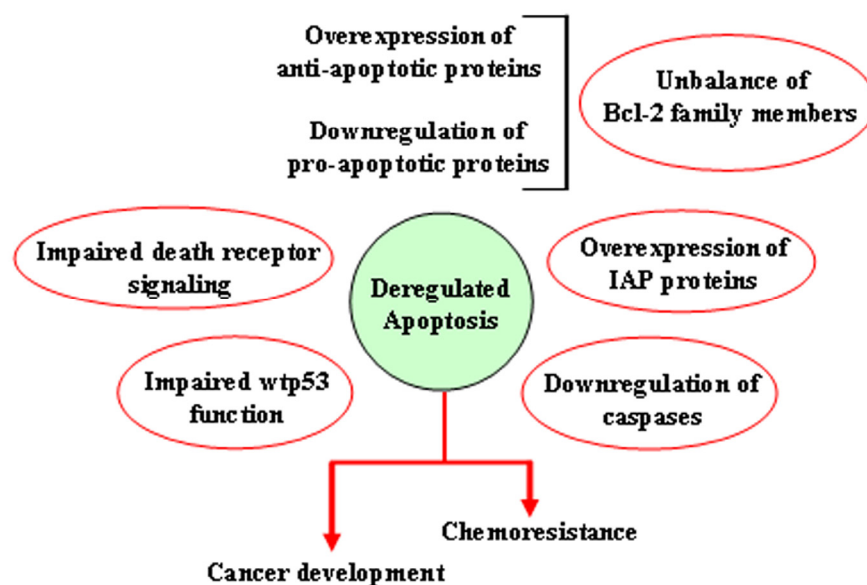


**Figure 5. Mechanisms leading to deregulation of apoptosis.** Schematic representation of the different ways through which both the extrinsic and the intrinsic apoptotic pathways may be altered, resulting in reduction of apoptosis or acquisition of apoptosis resistance.

## Pharmacological targeting of the apoptotic pathways

Based on this evidence, restoration of apoptotic pathway by drugs targeting both apoptotic pathways constitutes a promising anticancer therapeutic approach. Regarding the extrinsic pathway, the down-regulation of c-Flip by metabolic inhibitors and the promotion of caspase-8 activation by interferon, are some examples of strategies aimed at making tumors responsive to death receptor-induced apoptosis, and more generally, to chemotherapy-induced apoptosis [55,75,76]. The therapeutic importance of inducing apoptosis through the extrinsic pathway also extends to cancer cells that do not show defects in components of that pathway. Indeed, inducing the apoptosis by stimulating the extrinsic pathway can overcome the resistance to therapeutic agents that act by causing DNA damage, as death receptor-dependent apoptosis may occur regardless of the stress response. An example of such therapeutic strategy is represented by the ligand TRAIL known to induce apoptosis in different tumor cell lines [77]. The preferential destructive effect against tumor cells and the apparent absence of systemic toxicity through TRAIL-induced apoptosis, led to the development of antibodies with agonistic activity against the TRAIL death receptors (DR4 and DR5) or soluble recombinant derivatives of TRAIL (sTRAIL) as promising chemotherapeutic agents [78]. An attractive strategy to sensitize resistant malignancies to TRAIL-induced cell death is the design of small molecules that target and promote caspase-8 activation. Through an *in silico* screening some authors successfully found a small molecule activator of caspase-8 [79]. Experimental validation performed in multiple cell lines, such as leukemic and prostate cells, revealed that CaspPro small molecule promotes caspase-8 activation, caspase-3 activation and PARP cleavage, in the presence of TRAIL, leading to cell death [79]. Owing to its different toxicity for transformed as opposed to normal cells, Apo2/TRAIL shows promise as potential cancer therapy agent [80,81].

As in the extrinsic pathway, mediators of the intrinsic pathway involved both in tumorigenesis and chemoresistance, are targeted for therapeutic approaches. These anticancer strategies attempt to develop drug-designed inhibitors of anti-apoptotic proteins typically overexpressed in cancer cells, such as Bcl-2, Bcl-xL and IAPs [82]. Efforts to target Bcl-2 proteins involve the development of agents that disrupt Bcl-2 complexes. BH3 mimetics bind to the hydrophobic groove of antiapoptotic proteins mimicking the action of BH3-only proteins in binding to pro-survival proteins, leading to the release of BH3-only proteins from complexes and activation of BAX and BAK. So far,

nearly a dozen BH3 mimetics are under investigation as Bcl-2 inhibitors in different phases of human clinical trials such as AT-101 (R-(-)-gossypol) [83,84], ABT-199 (venetoclax) [85], ABT-737 [86], ABT-263 (navitoclax, orally available derivative of ABT-737) [87,88], GX15-070 (obatoclax) [89,90] and TW37 [91]. The field of inhibitors of Bcl-2 family members is in continuous development [92,93], underscoring the importance of these molecules as potent anticancer agents. Moreover, targeting the specific BH4 domain of Bcl-2 is also emerging as a novel strategy for anticancer therapy [94]. Thus, Bcl-2, via its BH4 domain, cooperates with numerous proteins regulating different cellular pathways involved in tumor progression and chemoresistance such as hypoxia and angiogenesis [95-97]. Recently, a small molecule namely BDA-366 was discovered as a potent and effective BH4 domain antagonist, displaying remarkable anticancer activity *in vitro* and *in vivo*, thus providing the proof-of-concept of this approach [98]. Another innovative approach to inhibit Bcl-2 comes from the evidence that human bcl-2 gene contains a GC-rich sequence located in its promoter with the potential to form G-quadruplex structures [99] and functions as a transcriptional repressor element. Therefore, G-quadruplex-specific ligands can regulate the transcription of bcl-2 through stabilization of quadruplex structure [100,101].

Interestingly, it has been shown that the tumor suppressor p53, at least in part by transcription independent mechanisms, contributes to cell death induction by BH3 mimetic inhibitors of BCL-xL. In addition to mildly facilitating the ability of compounds to derepress BAX from BCL-xL, p53 also provides a death signal downstream of anti-apoptotic proteins inhibition that is independent from PUMA, as enhanced p53 can substitute for PUMA to promote BAX activation in response to BH3 mimetics [102]. It is thus of particular relevance that p53, even when expressed constitutively under conditions where it does not influence the expression of its pro-apoptotic transcription targets, enhances cell death induced by BCL-xL inhibition [102]. Such results suggest on one hand that BH3 mimetics may not totally substitute for the lack of an active p53 tumor suppressor in cancer cells; on the other hand, they imply that healthy tissues may be more harmed than anticipated when BCL-xL inhibitors are combined with chemotherapeutic agents that even mildly affect p53.

Among the therapeutic strategies targeting IAPs two approaches have been developed, that is the use of antisense oligonucleotides and of small-molecule inhibitors. The XIAP down-regulation through administration of antisense agents carried by an

adenoviral vector has been proven effective in inducing apoptosis in chemoresistant ovarian cancer cells [103] and sensitizing lung cancer cells to the radiation treatment [104]. Similarly, the inhibition of XIAP expression with specific oligomers has been shown to induce caspase-3 activity, boosting the apoptotic effect of cisplatin and TRAIL in human prostate androgen-insensitive cancer cells [105]. Moreover, preclinical studies have shown that Smac mimetics can directly trigger cancer cell death or sensitize tumor cells to various cytotoxic therapies, including conventional chemotherapy, radiotherapy, or novel agents. They promote activation of caspases by neutralizing XIAP-mediated caspase inhibition [106]. Therefore, the success of each therapeutic strategy depends mainly on the ability of the therapeutic tool to induce apoptosis either by targeting the overexpressed anti-apoptotic proteins or by stimulating the expression of the pro-apoptotic molecules.

However, it is worth to mention that the cancer genetic background may induce failure of apoptosis by drugs. In this regard, KRAS and the PI3K/AKT/mTOR pathway are frequently dysregulated in cancer and, for such reason, are the most critical targets in clinical oncology. Thus, direct targeting of KRAS has not been successful so far and, similarly, inhibition of the PI3K/AKT/mTOR pathway often results in apoptosis resistance. Using a panel of 20 human KRAS-mutant NSCLC (non-small cell lung cancer) cell lines Hata and collaborators show that most human KRAS-mutant cell lines fail to undergo marked apoptosis in response to AZD6244 (Selumetinib, a potent, selective, and ATP-uncompetitive inhibitor of MEK1/2 kinases) [107] in combination with GDC-0941 (an orally bioavailable inhibitor of class I PI3K) [108], thus suggesting that failure to induce apoptosis may limit the efficacy of combined MEK and PI3K inhibition for KRAS-mutant NSCLCs. This differential apoptotic response induced by MEKi/PI3Ki is not simply explained by variable inhibition of RAS effector pathways but results from differential ability of the MEK and PI3K pathways to modulate the BCL-2 family of apoptotic regulatory proteins [109]. Another recent study reveals that Bcl-xL upregulation is an important mechanism of apoptosis resistance in mutant KRAS cells. Concurrent induction of pro-apoptotic Noxa/Bik and antagonism of Bcl-xL have been shown to synergistically interact to overcome KRAS-mediated apoptosis resistance [110]. These findings highlight a promising therapeutic strategy to overcome apoptosis resistance in KRAS-mutant colorectal cancer cells. Moreover, Corcoran and collaborators identified, by a pooled shRNA-drug screen, a synthetic, lethal interaction of combined Bcl-xL and MEK inhibition to promote tumor regressions in

KRAS mutant cancer models [111]. Therefore, a dual-targeted or multitargeted strategy may be more efficient to overcome the resistance due to cancer genetic background.

### Oncosuppressor p53 and apoptosis

The tumor suppressor p53 is a transcription factor that, upon DNA damage, is activated to induce sequence-specific target genes involved in either cancer cell growth arrest or apoptosis [112]. Activation of wild-type (wt) p53 occurs in response to genotoxic stress essentially through posttranslational modifications, such as acetylation and phosphorylation, resulting in protein stabilization (by escape from proteasome-mediated degradation) and nuclear localization leading to binding to sequence-specific promoters of target genes as final outcome of its function as transcription factor [113]. The induction of apoptosis by p53 in response to cellular stress is its most conserved function and is crucial for p53 tumor suppression [114]. The apoptotic activation of p53 is central not only for preventing tumor transformation but also for efficient response to therapies aiming at tumor eradication. In response to cellular stress p53 regulates molecules involved in both the death receptor (extrinsic) and mitochondria-dependent (intrinsic) apoptotic pathways [115]. In response to multiple chemotherapeutic drugs two pro-apoptotic members of the TNFR superfamily, Fas/Apo1 and Killer/DR5, are regulated in a p53-dependent manner [116,117]. In addition to stimulating Fas transcription, activated p53 may enhance levels of Fas at the cell surface promoting trafficking of the Fas receptor from the Golgi [118]. Another membrane-bound protein that was identified as a p53 target gene is p53 apoptosis effector related PMP-22 (PERP), although the precise mechanism by which its induction occurs has not been fully elucidated [119] (Figure 6). Regarding the apoptotic function of the intrinsic pathway, p53 seems to play a pivotal role because it modulates both pro-survival and pro-apoptotic Bcl-2 family members. Indeed, a key subset of the Bcl-2 family genes are p53 targets, including *Bax*, *Noxa*, *PUMA* and *Bid* [120-122] (Figure 6). *PUMA* gene is extremely effective in inducing apoptotic cell death within few hours and, more importantly, knockout experiments in human colorectal cancer cells showed that *PUMA* is required for p53-induced apoptosis [123]. Moreover, p53 appears to promote the convergence of the intrinsic and extrinsic pathways through *Bid* regulation. Indeed, *Bid* gene has been found to be transcriptionally induced by p53 in response to  $\gamma$ -irradiation [124]. Interestingly, cellular chemosensitivity to the DNA-damaging agents doxorubicin and 5-fluorouracil appears to be critically dependent on



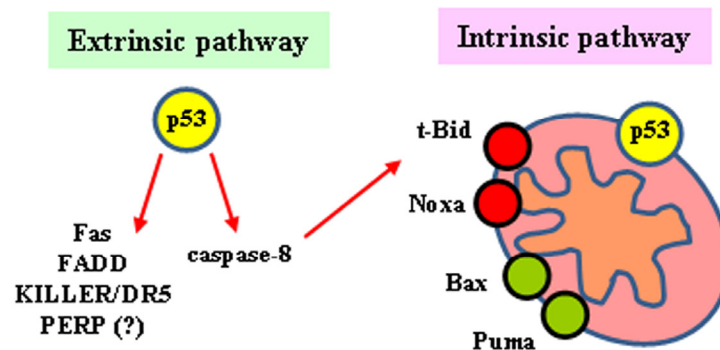


**Figure 6. p53-mediated apoptosis.** Role of p53 in both the extrinsic and the intrinsic pathway and their convergence through t-Bid.

the presence of wtp53 and Bid. Therefore, the induction of Bid by p53 helps to sensitize the cells to the toxic effects of chemotherapeutic drugs [124]. While the induction of some p53 target genes appears to be sufficient to initiate apoptosis, another class of p53 target genes (i.e., Apaf-1, caspase-6, and Bid) does not efficiently induce apoptosis per se but rather sensitizes cancer cells to the effects of chemotherapeutic agents, improving the apoptotic outcome [124-127]. Moreover, p53 also participates in apoptosis induction in a transcription-independent way by acting directly at mitochondria [128]; mechanistically, p53 interacts with anti-apoptotic Bcl-xL as well as pro-apoptotic Bcl-2 family proteins resulting in releasing of the pro-apoptotic effectors Bax/Bak that elicit cytochrome-*c* release and procaspase-3 activation [129].

### Waking up the guardian: p53 as a druggable target

Because of its critical antitumor function, p53 is frequently targeted for inactivation and suffers disabling mutations or deletions in about 50% of all malignant tumors. The other half of human cancers express wild-type p53 protein that, however, can be inactivated by deregulation of regulatory proteins [130]. Stimulation of disabled p53 pathways has been suggested as a valuable anticancer strategy and, interestingly, activated wtp53 may target cancer cells though sparing the normal ones [131] which is an important concern in clinical studies. The p53 oncosuppressor protein is normally kept at low level because subject to negative regulation by MDM2-dependent proteasome degradation [132]; in response to genotoxic stress, however, p53 undergoes post-translational modifications that allow the protein to escape MDM2 control, accumulate, and become active

[133]. The *mdm2* gene is amplified in a significant proportion of human tumor types, thereby contributing to tumor development by efficiently reducing the availability of a functional p53 protein [134]. The MDM2-negative regulation of p53 protein can be neutralized by specific protein modifications such as serine 46 (Ser46) phosphorylation [135], a key determinant in shifting the p53 pro-apoptotic transcription in response, for instance, to UV irradiation and chemotherapy [136,137]. In particular, p53-Ser46 phosphorylation by kinase HIPK2 is able to neutralize MDM2-mediated p53 inhibition rescuing p53 transcriptional activity of pro-apoptotic factors such as *p53AIP1*, *PIG3*, *Bax*, *Noxa*, *Puma* and *Killer/DR5* [138-142]. The interaction between p53 and MDM2 is a promising target in anticancer therapy [143]. To this aim, various peptidomimetic small molecules have been developed as protein-protein interaction blockers [144]. Among these is Nutlin-3, an imidazoline-based MDM2 antagonist that potentially inhibits the p53/MDM2 interaction though maintaining MDM2 E3 ligase activity [145]. The pharmacological action of Nutlin-3 is through both the transcription-dependent and -independent p53 apoptotic pathways [128,146,147]. MDM2 can also trigger, in response to low genotoxic damage, the downregulation of p53 apoptotic activator HIPK2 [148]. In agreement, the use of Nutlin-3 has been shown to mainly induce mitotic arrest rather than apoptosis [149]. Interestingly, co-treatment of cancer cells with zinc ion in the presence of Nutlin-3 can interfere with the interplay between HIPK2, p53 and MDM2 favoring HIPK2 stabilization and induction of p53 apoptotic activity through inhibition of MDM2 ligase activity [150]. In addition, p53 apoptotic activation can be achieved by zinc combination with

low-dose doxorubicin (ADR) that used alone does not achieve such effect; mechanistically, zinc supplementation reduces the p53 binding to MDM2, improving the low-dose drug-induced cytotoxic effect and cancer cell apoptosis [151]. Additionally, zinc ion restores the HIPK2/p53 apoptotic pathway that is inhibited by hypoxia [152]. Co-treatment with Nutlin-3 and Bcl-2 inhibitor ABT-737 has been shown to greatly enhance the sensitivity to apoptosis of cancer cells with high MDM2 levels [153], suggesting that the combined inhibition of MDM2 and Bcl-2 could be a multi-target-based anticancer strategy to trigger tumor death [154]. Some p53 activators as small-molecules MDM2 antagonist are in clinical trials [155] (<https://clinicaltrials.gov>). In contrast with the majority of the approaches that target the interaction between p53 and MDM2, a new method has been developed aimed at inhibiting the activity of the MDM2/MDM4 complexes by interfering with their heterodimerization [156]. The binding of the peptide mimicking the MDM4 C-terminus tail to MDM2 impairs MDM2-mediated p53 ubiquitination and activates p53-dependent transcription and oncosuppressive activities [156]. MDM4 (also known as HDM4, MDMX or HDMX) is a cytoplasmic protein with p53-activating function under DNA damage conditions. Particularly, MDM4 promotes mitochondrial localization of p53 phosphorylated at Ser46 through MDM4/HIPK2/p53 cytoplasmic assembly, uncovering coordinated repression of molecules with anti-apoptotic activity such as Bcl-2, release of cytochrome-*c* and apoptosis [157,158]. The existence of nuclear and cytoplasmic complexes able to stimulate the same p53 modification, that is Ser46<sup>P</sup>, may indicate the presence of overlapping pathways to ensure the proper realization of a crucial process as the apoptosis. These findings highlight the potential therapeutic value of targeting the MDM2/MDM4 heterodimers for p53 apoptotic function.

Pharmacological reactivation of mutant (mut) p53 is an interesting field of research under continuous development aimed at designing new drugs. Some of them exploit the intrinsically unstable nature of mutp53 and therefore the possibility to stabilize the wild-type conformation thus restoring wild-type function and tumor response to therapies. Numerous findings about this subject have been shown and summarized in different reviews [159-161].

### MicroRNA and apoptosis

MicroRNAs (miRNAs) are highly conserved, small noncoding RNA molecules, which post-transcriptionally regulate gene expression via inhibition of mRNA translation or inducing degradation of target

mRNAs [162]. They are key regulators of many cell processes often deregulated in cancer, including apoptosis. Indeed, it is becoming clear that miRNAs might act as both anti-apoptotic and pro-apoptotic by directly targeting, respectively, pro- or anti-apoptotic mRNAs or their positive regulators [163]. The currently known apoptosis-regulating miRNAs list is expected to expand quickly and hopefully also their therapeutic use; therefore, we just highlight here some miRNAs involved in apoptosis regulation. Among the microRNAs involved in regulating the extrinsic apoptotic pathway, miR-20a, miR-21, miR-196b and miR-590 were reported as potential modulator of Fas/FasL system in different cancer types [164-167], while MiR-34a, miR-181c and miR-187 were shown to directly target TNF- $\alpha$  mRNA [168-170]. Among the microRNAs involved in regulating the intrinsic pathway there are the let-7 family, miR-15a, miR-16-1, miR-204, and miR-608, just to mention a few. The Let-7 family is highly conserved in sequence across animal species and is one of the first identified miRNA families. Let-7 miRNAs have been shown to negatively regulate Bcl-xL expression in human hepatocellular carcinomas and induce apoptosis in cooperation with anti-cancer drug targeting Mcl-1 [171]. Bcl-2 mRNA may be targeted by miR-204 with consequent increase in cells responsiveness to both 5-fluorouracil and oxaliplatin treatments and therefore to apoptotic cell death [172]. MiR-608 has been reported to target Bcl-xL in chordoma malignancy and lung cancer [173]. Notably, numerous miRNAs are also transcriptionally modulated by wtp53 [174] and among them is miR-34a [175,176], a member of the MiR-34 family implicated in cell death/survival signaling. MiR-34a is associated with G1 cell cycle arrest, senescence and apoptosis, thereby possessing a tumor suppressor activity. Deregulation of MiR-34a has been reported in several types of cancers [175,176]. Mutant (mut) p53 was also found to play a role in the regulation of miRNA processing. Garibaldi and collaborators demonstrate that mutp53 proteins modulate the biogenesis of several miRNAs in cancer cells directly interfering with Drosha-p72 association and promoting cell survival and cell migration [177]. They demonstrate a global impact of mutp53 on miRNA biogenesis and suggest that miRNAs are downregulated by mutp53 in order to inactivate tumor suppressive pathways. Of note they found that the endogenous wtp53 has an opposite effect on the expression of mutp53 repressed miRNAs on colon cancer cell lines confirming the contribution of mutp53 gain of oncogenic function (GOF) on miRNA repression [177]. Additional studies on a large scale would help in identifying the entire repertoire of miRNAs negatively downregulated by different mutp53 in different tumor models. According to the authors, the

characterization of the entire gene-regulatory networks governed by mutp53-miRNA cross-talks will offer a molecular basis for diagnostic and therapeutic strategies based on miRNA biology. In the meanwhile, developing strategies to block mutp53 GOF may have clinical impact in cancer treatment.

Delivery of miRNAs as synthetic miRNA mimics or antagomirs has emerged as a promising approach to treat cancer. Although different miRNAs are currently in the preclinical stage and ready to enter Phase I clinical trials, to date, only two miRNA therapeutics are registered for the treatment of cancers [https://clinicaltrials.gov]. The first therapeutic trial began in 2013 and is a Phase I, open-label, multicenter, dose-escalation study to investigate the safety, pharmacokinetics and pharmacodynamics of MRX34 in patients with unresectable primary liver cancer or advanced/metastatic cancer with or without liver involvement or in patients with hematologic malignancies (Mirna Therapeutics). MRX34 is based on the formulation of miR-34 mimic and the liposomal delivery technology SMARTICLES (Marina Biotech). The second one, began in early 2015, and is an early stage clinical trial of a new therapeutical approach for selected patients with malignant pleural mesothelioma or non-small cell lung cancer. The trial aims to test optimal dose of TargomiRs, an experimental medication consisting of three components, that is, miR-16-based microRNA mimic, a nanoparticle drug delivery system using nonliving bacterial minicells, and an anti-epidermal growth factor receptor antibody as a targeting moiety. The trial is being carried out in three different hospitals in Australia and the study is expected to be completed in mid 2016.

### Concluding remarks

Intensive investigation in the last decades on the molecular mechanisms of apoptosis in cancer cells has led to the identification of the several molecules involved in both the intrinsic and the extrinsic apoptotic pathways. This is underscored by the extensive literature that those studies have produced in the last years. Those findings also reported how the many different alterations of key players of the apoptotic mechanisms are responsible of evasion from apoptosis and therefore of tumor development and resistance to therapies. For that reason, evasion from apoptosis is an hallmark of cancer and apoptotic proteins are interesting therapeutic targets. Therefore, this insight into the deregulation of apoptosis has focused the research attention towards the development of apoptosis-reactivating strategies, to be used in the treatment of various types of cancer, that hold great promise for the

benefit of patients, although the mechanisms defining their mode of action still need to be unveiled, as recently highlighted [178]. Some molecules or therapeutic strategies are in preclinical trial, others are already in clinical trials, though underscoring the usefulness of such discoveries.

However, the study of apoptosis still presents challenges that should be addressed in future studies. They include, for instance, the study of 3-D cellular models, since most of the findings have been so far produced in 2-D cell culture systems. Knowing that the tumor is a three-dimensional entity and that the environment plays a big role in the cross-talk with cancer cells, it is likely that more physiological studying approach for the manipulation of the apoptotic machinery might give us novel insight into the mechanisms of tumor development and response to therapies. Moreover, additional studies on the development of drugs aiming at targeting, for instance, IAP proteins or mutp53 should take in consideration also the in vivo toxicity and the fact that they should selectively induce apoptosis in malignant and not in normal cells. In conclusion, there is little doubt that drugs that target the deregulated apoptotic pathways could have wide application in the treatment of cancer. The intense effort devoted lately to target the apoptotic pathway is encouraging and supportive for the development of new approaches to drug discovery and therapy.

### Funding

This work was supported by AIRC Grant (IG 2015 Id.16742) to GDO.

### Conflict of interest statement

The authors declare no conflict of interest.

### REFERENCES

1. Fuchs Y, Steller H. Programmed cell death in animal development and disease. *Cell*. 2011; 147: 742–758.
2. Wong RSY. Apoptosis in cancer: from pathogenesis to treatment. *JECCR*. 2011; 30:87.
3. Plati J, Bucur O, Khosravi-Far R. Dysregulation of apoptotic signaling in cancer. *Molecular mechanisms and therapeutic opportunities*. *J Cell Biochem*. 2008; 104:1124-1149.
4. Fulda S. Tumor resistance to apoptosis. *Int J Cancer*. 2009; 124:515-515.
5. Hanahan D, Weinberg RA. Hallmarks of cancer: The next generation. *Cell*. 2011; 144:646-674.
6. Gimenez-Bonafe P, Tortosa A, Perez-Tomas R. Overcoming drug resistance by enhancing apoptosis of tumor cells. *Curr Cancer Drug Targ*. 2009; 9:320-340.

7. Fulda S. Targeting apoptosis for anticancer therapy. *Sem Cancer Biol.* 2015; 31:84-88.
8. Hacker G. The morphology of apoptosis. *Cell Tissue Res.* 2000; 301:5-17.
9. Saraste A, Pulkki K. Morphologic and biochemical hallmarks of apoptosis. *Cardiovasc Res.* 2000; 45:528-537.
10. Hengartner MO. Apoptosis: corralling the corpses. *Cell.* 2000; 104:325-328.
11. Kroemer G, El-Deiry WS, Golstein P, Peter ME, Vaux D, Vandenabeele P, Zhivotovsky B, Blagosklonny MV, Malorni W, Knight RA, Piacentini M, Nagata S, Melino G. Classification of cell death: recommendations of the Nomenclature Committee on Cell Death. *Cell Death Diff.* 2005; 12:1463-1467.
12. Bucur O, Nat R, Cretoiu D, Popescu LM. Phagocytosis of apoptotic cells by microglia in vitro. *J Cell Mol Med.* 2001; 5:438-441.
13. Li J, Yuan J. Caspases in apoptosis and beyond. *Oncogene.* 2008; 27:6194-6206.
14. Thornberry NA, Laxebnik Y. Caspases: enemies within. *Science* 1998; 281:1312-1316.
15. Nicholson DW. Caspase structure, proteolytic substrates, and function during apoptotic cell death. *Cell Death Diff.* 1999; 6:1028-1042.
16. Stennicke HR, Salvesen GS. Caspases - controlling intracellular signals by protease zymogen activation- *Biochim Biophys Acta-Port Struct Mol Enzimol.* 2000; 1477:299-306.
17. Degterev A, Boyce M, Yuan JY. A decade of caspases. *Oncogene.* 2003; 22:8543-8567.
18. Pistritto G, Jost M, Srinivasula SM, Baffa R, Poyet JL, Kari C, Lazebnik Y, Rodeck U, Alnemri ES. Expression and transcriptional regulation of caspase-14 in simple and complex epithelia. *Cell Death Diff.* 2002; 9:995-1006.
19. Pistritto G, Papaleo V, Sanchez P, Ceci C, Barbaccia ML. Divergent modulation of neuronal differentiation by caspase-2 and-9. *PLoS ONE.* 2012; 7:e36002.
20. Shalini S, Dorstyn L, Dawar S and Kumar S. Old, new and emerging functions of caspases. *Cell Death Diff.* 2015; 22: 526-39.
21. Guicciardi ME, Gores, Gregory J. Life and death by death receptors *FASEB J.* 2009; 23:1625-1637.
22. Fulda S, Debatin KM. Death receptor signaling in cancer therapy. *Curr Med Chem Anticancer Agents.* 2003; 3: 253-262.
23. Boatright KM, Salvesen GS. Mechanisms of caspase activation. *Curr Opin Cell Biol.* 2003; 6:725-731.
24. Green DR, Kroemer G. The pathophysiology of mitochondrial cell death. *Science* 2004; 305:626-629.
25. Kroemer G, Galluzzi L, Brenner C: Mitochondrial membrane permeabilisation in cell death. *Physiol Rev.* 2007; 87:99-163.
26. Danial NN, Korsmeyer SJ. Cell death: critical control points. *Cell.* 2004; 116:205-219.
27. Slee EA, Adrain C, Martin SJ. Serial killers: ordering caspase activation events in apoptosis. *Cell Death Diff.* 1999; 6:1067-1074.
28. Kuribayashi K, Mayes PA, El-Dery WS. What are caspases 3 and 7 doing upstream of the mitochondria? *Cancer Biol Ther.* 2006; 5:763-765.
29. Giam M, Huang DC, Bouillet P. BH3-only proteins and their roles in programmed cell death. *Oncogene.* 2008; 27:S128-36.
30. Adams JM, Cory S. The Bcl-2 apoptotic switch in cancer development and therapy. *Oncogene.* 2007; 26:1324-1337.
31. Danial NN. BCL-2 family proteins: Critical checkpoints of apoptotic cell death. *Clin Cancer Res.* 2007; 13:7254-7263.
32. Lomonosova E and G Chinnadurai. BH3-only proteins in apoptosis and beyond: an overview. *Oncogene.* 2009; 27:S2-S19.
33. Youle RJ, Strasser A. The BCL-2 protein family: opposing activities that mediate cell death. *Nat Rev Mol Cell Biol.* 2008; 9: 47-59.
34. Dewson G, Kratina T, Sim HW, Puthalakath H, Adams JM, Colman PM, Kluck RM. To trigger apoptosis, Bak exposes its BH3 domain and homodimerizes via BH3 : Groove interactions. *Mol Cell.* 2008; 30:369-380.
35. Bleicken St, Classen M, Padmavathi PVL, Ishikawa T, Zeth K, Steinhoff HJ, Bordignon E. Molecular details of Bax activation, oligomerization, and membrane insertion. *J Biol Chem.* 2010; 285: 6636-6647.
36. Gavathiotis E, Suzuki M, Davis ML, Pitter K, Bird GH, Katz SG, Tu HC, Kim H, Cheng EH, Tjandra N, Walensky LD. BAX activation is initiated at a novel interaction site. *Nature.* 2008; 455:1076-U6
37. Brunelle JK, Letai A. Control of mitochondrial apoptosis by the Bcl-2 family. *J Cell Sci.* 2009; 122:437-441.
38. Oakes SA, Scorrano L, Opferman JT, Bassik MC, Nishino M, Pozzan T, Korsmeyer SJ. Proapoptotic BAX and BAK regulate the type 1 inositol trisphosphate receptor and calcium leak from the endoplasmic reticulum. *Proc Natl Acad Sci USA.* 2005; 102:105-110.
39. Distelhorst CW, Bootman MD. Bcl-2 interaction with the inositol 1,4,5-trisphosphate receptor: Role in Ca<sup>2+</sup> signaling and disease. *Cell Calcium.* 2011; 50:234-241.
40. Hegde R, Srinivasula SM, Zhang Z, Wassell R, Mukattash R, Cilenti L, DuBois G, Lazebnik Y, Zervos AS, Fernandes-Alnemri T, Alnemri ES. Identification of Omi/HtrA2 as a mitochondrial apoptotic serine protease that disrupts inhibitor of apoptosis protein-caspase interaction. *J Biol Chem.* 2002; 277: 432-438.
41. Pop C, Salvesen GS. Human caspases: activation, specificity, and regulation. *J Biol Chem.* 2009; 284:21777-21781.
42. Salvesen GS and Duckett CS. IAP proteins: Blocking the road to death's door. *Nat Rev Mol Cell Biol.* 2002; 3:401:410.
43. Berthelet J, Dubrez L. Regulation of apoptosis by inhibitors of apoptosis (IAPs). *Cells.* 2013; 2:163-87.
44. LaCasse EC, Mahoney DJ, Cheung HH, Plenchette S, Baird S, Korneluk RG: IAP-targeted therapies for cancer. *Oncogene.* 2008; 27:6252-6275.
45. Mace PD, Shirley S, Day CL. Assembling the building blocks: structure and function of inhibitor of apoptosis proteins. *Cell Death Differ.* 2010; 17:46-53.
46. Müschen M, Beckmann MW. CD95 ligand expression as a criterion of malignant transformation in breast cancer *J Pathol.* 2000; 191: 468-470.
47. Tournier L, Buzyn A, Chiochia G. FADD adaptor in cancer. *Med Immunol.* 2005; 4:1.
48. Müschen M, Rajewsky K, Krönke M, Küppers R. The origin of CD95-gene mutations in B-cell lymphoma. *Trends Immunol.* 2002; 23:75-80.
49. Tournier L, Delluc S, Levy V, Valesi F, Radford-Weiss I, Legrand O, Vargftig J, Boix C, Macintyre EA, Varet B, Chiochia G, Buzyn A. Absence or low expression of fas-associated protein with death domain in acute myeloid leukemia cells predicts resistance to chemotherapy and poor outcome. *Cancer Res.* 2004; 64: 8101-8108.

50. Teitz T, Wei T, Valentine MB, Vanin EF, Grenet J, Valentine VA, Behm FG, Look AT, Lahti JM, Kidd VJ. Caspase 8 is deleted or silenced preferentially in childhood neuroblastomas with amplification of MYCN. *Nat Med*. 2000; 6: 529-535.
51. Shivapurkar N, Toyooka S, Eby MT, Huang CX, Sathyanarayana UG, Cunningham HT, Reddy JL, Brambilla E, Takahashi T, Minna JD, Chaudhary PM, Gazdar AF. Differential inactivation of caspase-8 in lung cancers. *Cancer Biol Ther*. 2002; 1: 65-69.
52. Zuzak TJ, Steinhoff DF, Sutton LN, Phillips PC, Eggert A, Grotzer MA. Loss of caspase-8 mRNA expression is common in childhood primitive neuroectodermal brain tumor/medulloblastoma. *Eur J Cancer*. 2002; 38: 83-91.
53. Irmeler M, Thome M, Hahne M, Schneider P, Hofmann K, Steiner V, Bodmer JL, Schröter M, Burns K, Mattmann C, Rimoldi D, French LE, Tschopp J. Inhibition of death receptor signals by cellular FLIP. *Nature*. 1997; 388: 190-195.
54. Bagnoli M, Canevari S, Mezzanzanica D. Cellular FLICE-inhibitory protein (c-FLIP) signalling: A key regulator of receptor-mediated apoptosis in physiologic context and in cancer. *Int J Biochem Cell Biol*. 2010; 42:210-213.
55. Shirley S, Mischeau O. Targeting c-FLIP in cancer. *Cancer Lett*. 2013; 332:141-150.
56. Gandour-Edwards R, Mack PC, Devere-White RW, Gumerlock PH. Abnormalities of apoptotic and cell cycle regulatory proteins in distinct histopathologic components of benign prostatic hyperplasia. *Prost Cancer Prost Dis*. 2004; 7:321-326.
57. Abramson JS, Shipp MA. Advances in the biology and therapy of diffuse large B-cell lymphoma: moving toward a molecularly targeted approach. *Blood*. 2005; 106:1164-1174.
58. Watanabe A, Yasuhira S, Inoue T, Kasai S, Shibazaki M, Takahashi K, Akasaka T, Masuda T, Maesawa C. BCL2 and BCLxL are key determinants of resistance to antitubulin chemotherapeutics in melanoma cells. *Exp Dermatol*. 2013; 22: 518-523.
59. Raffo AJ, Perlman H, Chen MW, Day ML, Streitman JS, Buttyan R. Overexpression of bcl-2 protects prostate cancer cells from apoptosis in vitro and confers resistance to androgen depletion in vivo. *Cancer Res*. 1995; 55:4438.
60. Fulda S, Meyer E, Debatin KM. Inhibition of TRAIL-induced apoptosis by Bcl-2 overexpression. *Oncogene*. 2000; 21:2283-2294.
61. Foreman KE, Wrone-Smith T, Boise LH, Thompson CB, Polverini PJ, Simonian PL, Nunez G, Nickoloff BJ. Kaposi's sarcoma tumor cells preferentially express Bcl-xL. *Am J Pathol*. 1996; 149: 795-803.
62. Krajewska M, Moss SF, Krajewski S, Song K, Holt PR, Reed JC. Elevated expression of Bcl-X and reduced Bak in primary colorectal adenocarcinomas. *Cancer Res*. 1996; 56: 2422-2427.
63. Minn AJ, Rudin CM, Boise LH, Thompson CB. Expression of Bcl-xL can confer a multidrug resistance phenotype. *Blood*. 1995; 86:1903-1910.
64. Han JY, Hong EK, Choi BG, Park JN, Kim KW, Kang JH, Jin JY, Park SY, Hong YS, Lee KS. Death receptor 5 and Bcl-2 protein expression as predictors of tumor response to gemcitabine and cisplatin in patients with advanced non-small-cell lung cancers. *Med Oncol*. 2003; 20:355-362.
65. Erovic BM, Pelzmann M, Grasl MCh, Pammer J, Kornek G, Brannath W, Selzer E, Thurnher D. Mcl-1, vascular endothelial growth factor-R2, and 14-3-3sigma expression might predict primary response against radiotherapy and chemotherapy in patients with locally advanced squamous cell carcinomas of the head and neck. *Clin Cancer Res*. 2005; 11:8632-8636.
66. Williams J, Lucas PC, Griffith KA, Choi M, Fogoros S, Hu YY, Liu JR. Expression of Bcl-xL in ovarian carcinoma is associated with chemoresistance and recurrent disease. *Gynecol Oncol*. 2005; 96: 287-295.
67. Michaud WA, Nichols AC, Mroz EA, Faquin WC, Clark JR, Begum S, Westra WH, Wada H, Busse PM, Ellisen LW, Rocco JW. Bcl-2 blocks cisplatin-induced apoptosis and predicts poor outcome following chemoradiation treatment in advanced oropharyngeal squamous cell carcinoma. *Clin Cancer Res*. 2009; 15: 1645-1654.
68. Yang D, Chen MB, Wang LQ, Yang L, Liu CY, Lu PH. Bcl-2 expression predicts sensitivity to chemotherapy in breast cancer: a systematic review and meta-analysis. *JECCR* 2013; 32:105.
69. Miquel C, Borrini F, Grandjouan S, Aupérin A, Viguier J, Velasco V, Duvillard P, Praz F, Sabourin JC. Role of bax mutations in apoptosis in colorectal cancers with microsatellite instability. *Am J Clin Pathol*. 2005; 23:562-570.
70. Pepper C, Hoy T, Bentley DP. Bcl-2/Bax ratios in chronic lymphocytic leukaemia and their correlation with in vitro apoptosis and clinical resistance. *Br J Cancer*. 1997; 76:935-938.
71. Soengas MS, Capodici P, Polsky D, Mora J, Esteller M, Opitz-Araya X, McCombie R, Herman JG, Gerald WL, Lazebnik YA, Cordon-Cardó C, Lowe SW. Inactivation of the apoptosis effector Apaf-1 in malignant melanoma. *Nature*. 2001; 409:207-211.
72. Baldi A, Santini D, Russo P, Catricala' C, Amantea A, Picardo M, Tatangelo F, Botti G, Dragonetti E, Murace R, Tonini G, Natali PG, Baldi F, Paggi MG. Analysis of APAF-1 expression in human cutaneous melanoma progression. *Exp Dermatol*. 2004; 13:93-97.
73. Schimmer AD. Inhibitor of apoptosis proteins: translating basic knowledge into clinical practice. *Cancer Res*. 2004; 64: 7183-7190.
74. Fulda S. Inhibitor of apoptosis proteins in hematological malignancies. *Leukemia*. 2009; 23:467-476.
75. Fulda S, Debatin KM. IFNgamma sensitizes for apoptosis by upregulating caspase-8 expression through the Stat1 pathway. *Oncogene*. 2002; 21:2295-2308.
76. Subramanian K, Hirpara JL, Tucker-Kellogg L, Tucker-Kellogg G, Pervaiz S. FLIP: A flop for execution signals. *Cancer Lett*. 2013; 332:151-155.
77. Almasan A, Ashkenazi A. Apo2L/TRAIL: apoptosis signaling, biology, and potential for cancer therapy. *Cytok Growth Fact Rev*. 2003; 14:337-348.
78. Amarante-Mendes GP, Griffith TS. Therapeutic applications of TRAIL receptor agonists in cancer and beyond. *Pharmacol Ther*. 2015; 155:117-131.
79. Bucur O, Gaidos G, Yatawara A, Pennarum B, Rupasinghe C, Roux J, Andrei S, Guo B, Panaititu A, Pellegrini M, Mierke DF, Khosravi-Far R. A novel caspase 8 selective small molecule potentiates TRAIL-induced cell death. *Sci Rep*. 2015; 5:9893.
80. Ashkenazi A, Pai RC, Fong S, Leung S, Lawrence DA, Marsters SA, Blackie C, Chang L, McMurtrey AE, Hebert A, DeForge L, Koumenis IL, Lewis D, et al. Safety and antitumor activity of recombinant soluble Apo2 ligand. *J Clin Invest*. 1999; 104:155-162.
81. LeBlanc H, Ashkenazi A. Apo2/TRAIL and its death and decoy receptors. *Cell Death Diff*. 2003; 10:66-75.
82. Kang MH, Reynolds CP. Bcl-2 inhibitors: targeting mitochondrial apoptotic pathways in cancer therapy. *Clin Cancer Res*. 2009; 15:1126-1132.



83. Sonpavde G, Matveev V, Burke JM, Caton JR, Fleming MT, Hutson TE, Galsky MD, Berry WR, Karlov P, Holmlund JT, Wood BA, Brookes M, Leopold L. Randomized phase II trial of docetaxel plus prednisone in combination with placebo or AT-101, an oral small molecule Bcl-2 family antagonist, as first-line therapy for metastatic castration-resistant prostate cancer. *Ann Oncol*. 2012; 23:1803-1808.
84. Stein MN, Hussain M, Stadler WM, Liu G, Tereshchenko IV, Goodin S, Jeyamohan C, Kaufman HL, Mehnert J, Di Paola RS. A Phase II study of AT-101 to overcome Bcl-2-mediated resistance to androgen deprivation therapy in patients with newly diagnosed castration-sensitive metastatic prostate cancer. *Clin Genitour Cancer*. 2016; 14:22-27.
85. Souers AJ, Levenson JD, Boghaert ER, Ackler SL, Catron ND, Chen J, Dayton BD, Ding H, Enschede SH, Fairbrother WJ, Huang DCS, Hymowitz SG, Jin S, et al. ABT-199, a potent and selective BCL-2 inhibitor, achieves antitumor activity while sparing platelets. *Nat Med*. 2013; 19:202-208.
86. Oltersdorf T, Elmore SW, Shoemaker AR, Armstrong RC, Augeri DJ, Belli BA, Bruncko M, Deckwerth TL, Dinges J, Hajduk PJ, Joseph MK, Kitada S, Korsmeyer SJ, et al. An inhibitor of Bcl-2 family proteins induces regression of solid tumors. *Nature*. 2005; 435:677-681.
87. Tse C, Shoemaker AR, Adickes J, Anderson MG, Chen J, Jin S, Johnson EF, Marsh KC, Mitten MJ, Nimmer P, Roberts L, Tahir SK, Mao Y, Yang X, Zhang HC, Fesik S, Rosenberg SH, Elmore SW. ABT-263: a potent and orally bioavailable Bcl-2 family inhibitor. *Cancer Res*. 2008; 68:3421-3428.
88. Roberts AW, Seymour JF, Brown JR, Wierda WG, Kipps TJ, Khaw SL, Carney DA, He SZ, Huang DCS, Xiong H, Cui Y, Busman TA, McKeegan EM, et al. Substantial susceptibility of chronic lymphocytic leukemia to BCL2 inhibition: results of a phase I study of navitoclax in patients with relapsed or refractory disease. *J Clin Oncol*. 2012; 30:488-496.
89. Chiappori A, Williams C, Northfelt DW, Adams JW, Malik S, Edelman MJ, Rosen P, Van Echo DA, Berger MS, Haura EB. Obatoclox mesylate, a pan-bcl-2 inhibitor, in combination with docetaxel in a phase 1/2 trial in relapsed non-small-cell lung cancer. *J Thorac Oncol*. 2014; 9:121-125.
90. Theile D, Allendorf D, Koehler BC, Jassowicz A, Weiss J. Obatoclox as a perpetrator in drug-drug interactions and its efficacy in multidrug resistance cell lines. *J Pharm Pharmacol*. 2015; 67:1575-1584.
91. Zeitlin BD, Joo E, Dong Z, Warner K, Wang G, Nikolovska-Coleska Z, Wang S, Nor JE. Antiangiogenic effect of TW37, a small-molecule inhibitor of Bcl-2. *Cancer Res*. 2006; 66:8698-8706.
92. Tao ZF, Hasvold L, Wang L, Wang X, Petros AM, Park CH, et al. Discovery of a potent and selective Bcl-xL inhibitor with in vivo activity. *ACS Med Chem Lett*. 2014; 5:1088-1093.
93. Bruncko M, Wang L, Sheppard GS, Phillips DC, Tahir SK, Xue J, et al. Structure-guided design of a series of MCL-1 inhibitors with high affinity and selectivity. *J Med Chem*. 2015; 58:2180-2194.
94. Vervloessem T, La Rovere R, Bultynck G. Antagonizing Bcl-2's BH4 domain in cancer. *Aging (Albany NY)*. 2015; 7:748-749. doi: 10.18632/aging.100828.
95. Trisciuglio D, Gabellini C, Desideri M, Ragazzoni Y, De Luca T, Ziparo E, Del Bufalo D. Involvement of BH4 domain of bcl-2 in the regulation of HIF-1-mediated VEGF expression in hypoxic tumor cells. *Cell Death Diff*. 2011; 18:1024-1035.
96. Trisciuglio D, De Luca T, Desideri M, Passeri D, Gabellini C, Scarpino S, Liang C, Orlandi A, Del Bufalo D. Removal of the BH4 domain from Bcl-2 protein triggers an autophagic process that impairs tumor growth. *Neoplasia*. 2013; 15:315-327.
97. Gabellini C, De Luca T, Trisciuglio D, Desideri M, Di Martile M, Passeri D, Candiloro A, Biffoni M, Rizzo MG, Orlandi A, Del Bufalo D. BH4 domain of bcl-2 protein is required for its proangiogenic function under hypoxic condition. *Carcinogenesis*. 2013; 34:2558-2567.
98. Han B, Park D, Li R, Xie M, Owonikoko T, Zhang G, Sica GL, Ding C, Zhou J, Magis AT, Chen ZG, Shin DM, Ramalingam S, Khuri FR, Curran WJ, Deng X. Small-molecule Bcl-2 BH4 antagonist for lung cancer therapy. *Cancer Cell*. 2015; 27:852-863.
99. Dexheimer TS, Sun D, Hurley LH. Deconvoluting the structural and drug-recognition complexity of the G-quadruplex-forming region upstream of the bcl-2 P1 promoter. *J Am Chem Soc*. 2006; 128:5404-5415.
100. Lin J, Hou JQ, Xiang HD, Yan YY, Gu YC, Tan JH, Li D, Gu LQ, Ou TM, Huang ZS. Stabilization of G-quadruplex DNA by C-5-methyl-cytosine in bcl-2 promoter: implications for epigenetic regulation. *Biochem Biophys Res Commun*. 2013; 433:368-373.
101. Sun H, Xiang J, Shi Y, Yang Q, Guan A, Li Q, Yu L, Shang Q, Zhang H, Tang Y, Xu G. A newly identified G-quadruplex as a potential target regulating Bcl-2 expression. *Biochim Biophys Acta*. 2014; 1840:3052-3057.
102. Le Pen J, Laurent M, Sarosiek K, Vuillier C, Gautier F, Montessuit S, Martinou JC, Letai A, Braun F, Juin PP. Constitutive p53 heightens mitochondrial apoptotic priming and favors cell death induction by BH3 mimetic inhibitors of BCL-xL. *Cell Death Dis*. 2016; 7:e2083.
103. Sasaki H, Sheng Y, Kotsuji F, Tsang BK. Down-regulation of X-linked inhibitor of apoptosis protein induces apoptosis in chemoresistant human ovarian cancer cells. *Cancer Res*. 2000; 60:5659-5666.
104. Holcik M, Yeh C, Korneluk RG, Chow T. Translational upregulation of X-linked inhibitor of apoptosis (XIAP) increases resistance to radiation induced cell death. *Oncogene*. 2000; 19:4174-4177.
105. Amantana A, London CA, Iversen PL, Devi GR. X-linked inhibitor of apoptosis protein inhibition induces apoptosis and enhances chemotherapy sensitivity in human prostate cancer cells. *Mol Cancer Ther*. 2004; 3:699-707.
106. Fulda S. Promises and challenges of Smac mimetics as cancer therapeutics. *Clin Cancer Res*. 2015; 21:5030-5036.
107. Davies BR, Logie A, McKay JS, Martin P, Steele S, Jenkins R, Cockerill M, Carlidge S, Smith PD. AZD6244 (ARRY-142886), a potent inhibitor of mitogen activated protein kinase/extracellular signal-regulated kinase 1/2 kinases: mechanism of action in vivo, pharmacokinetic/pharmacodynamic relationship, and potential for combination in preclinical models. *Mol Cancer Ther*. 2007; 6:2209-2219.
108. Folkes AJ, Ahmadi K, Alderton WK, Alix S, Baker SJ, Box G, Chuckowree IS, Clarke PA, Depledge P, Eccles SA, Friedman LS, Hayes A, Hancox TC, et al. The identification of 2-(1H-indazol-4-yl)-6-(4-methanesulfonyl-piperazin-1-ylmethyl)-4-morpholin-4-yl-thieno[3,2-d] pyrimidine (GDC-0941) as a potent, selective, orally bioavailable inhibitor of class I PI3 kinase for the treatment of cancer. *J Med Chem*. 2008; 51:5522-5532.
109. Hata AN, Yeo A, Faber AC, Lifshits E, Chen Z, Cheng KA, Walton Z, Sarosiek KA, Letai A, Heist RS, Mino-Kenudson M,

- Wong KK, Engelman JA. Failure to induce apoptosis via BCL-2 family proteins underlies lack of efficacy of combined MEK and PI3K inhibitors for KRAS-mutant lung cancers. *Cancer Res.* 2014; 74:3146-3156.
- 110.** Okamoto K, Zaanan A, Kawakami H, Huang S, Sinicrope FA. Reversal of mutant KRAS-mediated apoptosis resistance by concurrent Noxa/Bik induction and Bcl-2/Bcl-xL antagonism in colon cancer cells. *Mol Cancer Res.* 2015; 13:659-669.
- 111.** Corcoran RB, Cheng KA, Hata AN, Faber AC, Ebi H, Coffee EM, Greninger P, Brown RD, Godfrey JT, Cohoon TJ, Song Y, Lifshits E, Hung KE, et al. Synthetic lethal interaction of combined BCL-XL and MEK inhibition promotes tumor regressions in KRAS mutant cancer models. *Cancer Cell.* 2013; 23:121-128.
- 112.** Vousden KH, Lane DP. P53 in health and disease. *Nat Rev Mol Cell Biol.* 2007;8:275-283.
- 113.** Brooks CL, Gu W. Ubiquitination, phosphorylation and acetylation: the molecular basis for p53 regulation. *Curr Opin Cell Biol.* 2003; 15:164-171.
- 114.** Haupt S, Berger M, Goldberg Z, Haupt Y. Apoptosis – the p53 network. *J Cell Sci.* 2003; 116:4077-4085.
- 115.** Vousden KH. P53: Death Star. *Cell.* 2000; 103:691-694.
- 116.** Wu GS, Burns TF, McDonald III ER, Jiang W, Meng R, Krantz ID, Kao G, Gan DD, Zhou JY, Muschel R, Hamilton SR, Spinner NB, Matkowitz S, et al. KILLER/DR5 is a DNA damage-induced p53-regulated death receptor gene. *Nat Genet.* 1997; 17:141-143.
- 117.** Muller M, Wilder S, Bannasch D, Israeli D, Lehlbach K, Li-Weber M, Friedman SL, Galle PR, Stremmel W, Oren M, Krammer PH. P53 activates the CD95 (APO-1/Fas) gene in response to DNA damage by anticancer drugs. *J Exp Med.* 1998; 188:2033-2045.
- 118.** Bennet M, Macdonald K, Chan SW, Luzio JP, Simari R, Weissberg. Cell surface trafficking of Fas: a rapid mechanisms of p53-mediated apoptosis. *Science.* 1998; 282:290-293.
- 119.** Attardi LD, Reczek EE, Cosmas C, Demicco EG, McCurrach ME, Lowe SW, Jacks T. PERP, an apoptosis-associated target of p53, is a novel member of the PMP-22/gas3 family. *Genes Dev.* 2000; 14:704-718.
- 120.** Oda E, Ohki R, Murasawa H, Nemoto J, Shibue T, Yamashita T, Tokino T, Taniguchi T, Tanaka N. Noxa, a BH3-only member of the Bcl-2 family and candidate mediator of p53-induced apoptosis. *Science.* 2000; 288:1053-1058.
- 121.** Nakano K, Vousden KH. PUMA, a novel proapoptotic gene, is induced by p53. *Mol Cell.* 2001; 7:683-694.
- 122.** Thornborrow EC, Patel S, Mastropietro AE, Schwartzfarb EM, Manfredi JJ. A conserved intronic response element mediates direct p53-dependent transcriptional activation of both the human and murine bax gene. *Oncogene.* 2002; 21:990-999.
- 123.** Yu J, Wang Z, Kinzler KW, Vogelstein B, Zhang L. PUMA mediates the apoptotic response to p53 in colorectal cancer cells. *Proc Natl Acad Sci U S A.* 2003; 100:1931-1936.
- 124.** Sax JK, Fei P, Murphy ME, Bernhard E, Korsmeyer SJ, El-Deiry WS. BID regulation by p53 contributes to chemosensitivity. *Nat Cell Biol.* 2002; 4: 842-849.
- 125.** Moroni MC, Hickman ES, Denchi EL, Caprara G, Colli E, Cecconi F, Muller H, Helin K. Apaf-1 is a transcriptional target for E2F and p53. *Nat Cell Biol.* 2001; 3:553-558.
- 126.** MacLachlan TK, and El-Deiry WS. Apoptotic threshold is lowered by p53 transactivation of caspase-6. *Proc Natl Acad Sci.* 2002; 99: 9492-9497.
- 127.** Sax JK, El-Deiry WS. P53 downstream targets and chemosensitivity. *Cell Death Diff.* 2003; 10:413-417.
- 128.** Chi SW. Structural insights into the transcription-independent apoptotic pathway of p53. *BMB Rep.* 2014; 47:167-172.
- 129.** Tomita Y, Marchenko N, Erster S, Nemajerova A, Dehner A, Klein C, Pan H, Kessler H, Pancoska P, Moll UM. WT p53, but not tumor-derived mutants, bind to Bcl2 via the DNA binding domain and induce mitochondrial permeabilization. *JBC* 2006; 281:8600-8606.
- 130.** Brown CJ, Lain S, Verma CS, Fersht AR, Lane DP. Awakening guardian angels: drugging the p53 pathway. *Nat Rev Cancer.* 2009; 9:862-873.
- 131.** D'Orazi G, Marchetti A, Crescenzi M, Coen S, Sacchi A, Soddu S: Exogenous wt-p53 protein is active in transformed cells but not in their nontransformed counterparts: implications for cancer gene therapy without tumor targeting. *J Gene Med.* 2000; 2: 11-21.
- 132.** Momand J, Wu HH, Dasgupta G. MDM2 - master regulator of the p53 tumor suppressor protein. *Gene.* 2000; 242:15-29.
- 133.** Harris SL, Levine, AJ. The p53 pathway: positive and negative feedback loops. *Oncogene.* 2005; 24:2899-2908.
- 134.** Momand J, Jung D, Wilczynski S, Niland J. The MDM2 gene amplification database. *Nucleic Acids Res.* 1998; 26:3453-3459.
- 135.** Di Stefano V, Blandino G, Sacchi A, Soddu S, D'Orazi G. HIPK2 neutralizes MDM2 inhibition rescuing p53 transcriptional activity and apoptotic function. *Oncogene.* 2004; 23:5185-5192.
- 136.** Oda K, Arakawa H, Tanaka T, Matsuda K, Tanikawa C, Mori T, Nishimori H, Tamai K, Tokino T, Nakamura Y, Taya Y. p53AIP1, a potential mediator of p53-dependent apoptosis, and its regulation by Ser-46-phosphorylated p53. *Cell.* 2000; 102:849-862.
- 137.** Mayo LD, Seo YR, Jackson MW, Smith ML, Guzman JR, Korgaonkar CK, Donner DB. Phosphorylation of human p53 at serine 46 determines promoter selection and whether apoptosis is attenuated or amplified. *J Biol Chem* 2005; 280:25953-25959.
- 138.** D'Orazi G, Cecchinelli B, Bruno T, Manni I, Higashimoto Y, Saito S, Gostissa M, Coen S, Marchetti A, Del Sal G, Piaggio G, Fanciulli M, Appella E, et al. Homeodomain-interacting protein kinase 2 phosphorylates p53 at Ser46 and mediates apoptosis. *Nat Cell Biol.* 2002; 4:11-19.
- 139.** Di Stefano V, Rinaldo C, Sacchi A, Soddu S, D'Orazi G. Homeodomain-interacting protein kinase-2 activity and p53 phosphorylation are critical events for cisplatin-mediated apoptosis. *Exp Cell Res.* 2004; 293:311-320.
- 140.** Pistrutto G, Puca R, Nardinocchi L, Sacchi A, D'Orazi G. HIPK2-induced p53Ser46 phosphorylation activates the KILLER/DR5-mediated caspase-8 extrinsic apoptotic pathway. *Cell Death Diff.* 2007; 14:1837-1839.
- 141.** Puca R, Nardinocchi L, Sacchi A, Rechavi G, Givol D, D'Orazi G. HIPK2 modulates p53 activity towards pro-apoptotic transcription. *Mol Cancer.* 2009; 8:85.
- 142.** Garufi A, D'Orazi G. High glucose dephosphorylates serine 46 and inhibits p53 apoptotic activity. *JECCR.* 2014; 33:79.
- 143.** Jin ZG, Shen JF, He JY, Hu CQ. Combination therapy with p53-MDM2 binding inhibitors for malignancies. *Med Chem Res.* 2015; 24:1369-1379.
- 144.** Vassilev LT. MDM2 inhibitors for cancer therapy. *Trends Mol Med.* 2007; 13:23-31.
- 145.** Vassilev LT, Vu BT, Graves B, Carvajal D, Podlaski F, Filipovic Z, Kong N, Kammlot U, Lukacs C, Klein C, Fotouhi N, Liu EA. In

vivo activation of the p53 pathway by small-molecule antagonists of MDM2. *Science*. 2004; 303:844-848.

**146.** Kojima K, Konopleva M, McQueen T, O'Brien S, Plunkett W, Andreeff M. Mdm2 inhibitor Nutlin-3a induces p53-mediated apoptosis by transcription-dependent and transcription-independent mechanisms that may overcome Atm-mediated resistance to fludarabine in chronic lymphocytic leukemia. *Blood* 2006; 108:993-1000.

**147.** Vaseva AV and Moll UM. The mitochondrial p53 pathway. *Biochim Biophys Acta*. 2009; 1787: 414-420.

**148.** Rinaldo C, Prodosmo A, Mancini F, Iacovelli S, Sacchi A, Moretti F, Soddu Silvia. MDM2-regulated degradation of HIPK2 prevents p53Ser46 phosphorylation and DNA damage-induced apoptosis. *Mol Cell*. 2007; 25:739-750.

**149.** Rinaldo C, Prodosmo A, Siepi F, Moncada A, Sacchi A, Selivanova G, Soddu S. HIPK2 regulation by MDM2 determines tumor cell response to the p53-reactivating drugs Nutlin-3 and RITA. *Cancer Res*. 2009; 69:6241–6248.

**150.** Nardinocchi L, Puca R, Givol D, D'Orazi G. Counteracting MDM2-induced HIPK2 downregulation restores the HIPK2/p53 apoptotic signaling in cancer cells. *FEBS Lett*. 2010; 584:4253-4258.

**151.** Garufi A, Ubertini V, Mancini F, D'Orazi V, Baldari S, Moretti F, Bossi G, D'Orazi G. The beneficial effect of Zinc(II) on low-dose chemotherapeutic sensitivity involves p53 activation in wild-type p53-carrying colorectal cancer cells *JECCR*. 2015; 34:87.

**152.** Nardinocchi L, Puca R, D'Orazi G. HIF-1 $\alpha$  antagonizes p53-mediated apoptosis by triggering HIPK2 degradation. *Aging (Albany NY)*. 2011; 3:33-43. doi: 10.18632/aging.100254.

**153.** Kojima K, Konopleva M, Samudio IJ, Schober WD, Bornmann WG, Andreeff M. Concomitant inhibition of MDM2 and Bcl-2 protein function synergistically induces mitochondrial apoptosis in AML. *Cell Cycle* 2006; 5:2778-2786.

**154.** Wade M, Rodewald LW, Espinosa JM, Wahl G. BH3 activation blocks Hdmx suppression of apoptosis and cooperates with Nutlin to induce cell death. *Cell Cycle* 2008; 7:1973-1982.

**155.** Zhao YJ, Aguilar A, Bernard D, Wang S. Small-molecule inhibitors of the MDM2-p53 protein-protein interaction (MDM2 Inhibitors) in clinical trials for cancer treatment. *J Med Chem*. 2015; 58:1038-1052.

**156.** Pellegrino M, Mancini F, Lucà R, Coletti A, Giacchè N, Manni I, Arisi I, Florenzano F, Teveroni E, Buttarelli M, Fici L, Brandi R, Bruno T, et al. Targeting the MDM2/MDM4 interaction interface as a promising approach for p53 reactivation. *Cancer Res*. 2015; 75:4560-4572.

**157.** Mancini F, Di Conza G, Pellegrino M, Rinaldo C, Prodosmo A, Giglio S, D'Agnano I, Florenzano F, Felicioni L, Buttitta F, Marchetti A, Sacchi A, Pontecorvi A, et al. MDM4 (MDMX) localizes at the mitochondria and facilitates the p53-mediated intrinsic-apoptotic pathway. *EMBO J*. 2009; 28:1926-1939.

**158.** Mancini F, Pieroni L, Monteleone V, Luca R, Fici L, Luca E, Urbani A, Xiong S, Soddu S, Masetti R, Lozano G, Pontecorvi A, Moretti F. MDM4/ HIPK2/p53 cytoplasmic assembly uncovers coordinated repression of molecules with anti-apoptotic activity during early DNA damage response. *Oncogene*. 2016; 35:228–240.

**159.** Hoe KK, Verma CS, Lane DP. Drugging the p53 pathway: understanding the route to clinical efficacy. *Nat Rev Drug Discov*. 2014; 13:217-236.

**160.** Yu X, Narayanan S, Vazquez A, Carpizo DR. Small molecule compounds targeting the p53 pathway: are we finally making progress? *Apoptosis*. 2014; 19:1055-1068.

**161.** Zawanska-Pankau, Selivanova G. Pharmacological reactivation of p53 as a strategy to treat cancer. *J Intern Med*. 2015; 277: 248-259.

**162.** Lujambio A, Lowe SW. The microcosmos of cancer. *Nature*. 2012; 482:347-355.

**163.** Lima RT, Busacca S, Almeida GM, Gaudino G, Fennell DA, Helena Vasconcelos M MicroRNA regulation of core apoptosis pathways in cancer. *Eur J Cancer*. 2011; 47:163-174.

**164.** Huang G, Nishimoto K, Zhou Z, Hughes D, Kleinerman ES. miR-20a encoded by the miR-17–92 cluster increases the metastatic potential of osteosarcoma cells by regulating Fas expression. *Cancer Res*. 2012; 72:908–916.

**165.** Wang P, Zhuang L, Zhang J, Fan J, Luo J, Chen H, Wang K, Liu L, Chen Z, Meng Z. The serum miR-21 level serves as a predictor for the chemosensitivity of advanced pancreatic cancer, and miR-21 expression confers chemoresistance by targeting FasL. *Mol Oncol*. 2013; 7:334–345.

**166.** Li Z, Huang H, Chen P, He M, Li Y, Arnovitz S, Jiang X, He C, Hyjek E, Zhang J. miR-196b directly targets both HOXA9/MEIS1 oncogenes and FAS tumour suppressor in MLL-rearranged leukaemia. *Nat Commun*. 2012; 2:688.

**167.** Shaffiey F, Cross E, Sathyanarayana P. Mir-590 is a novel STAT5 regulated oncogenic miRNA and targets FasL in acute myeloid leukemia. *Blood*. 2013; 122:3811–3811.

**168.** Guennewig B, Roos M, Dogar AM, Gebert LF, Zagalak JA, Vongrad V, Metzner KJ, Hall J. Synthetic pre-microRNAs reveal dual-strand activity of miR-34a on TNF- $\alpha$ . *RNA*. 2014; 20:61–75.

**169.** Zhang L, Dong L, Li Y, Hong Z, Wei W. The microRNA miR-181c controls microglia-mediated neuronal apoptosis by suppressing tumor necrosis factor. *J Neuroinflamm*. 2012; 9:211.

**170.** Rossato M, Curtale G, Tamassia N, Castellucci M, Mori L, Gasperini S, Mariotti B, De Luca M, Mirolo M, Cassatella MA. IL-10-induced microRNA-187 negatively regulates TNF- $\alpha$ , IL-6, and IL-12p40 production in TLR4-stimulated monocytes. *Proc Natl Acad Sci USA*. 2012; 109:E3101–E3110.

**171.** Shimizu S, Takehara T, Hikita H, Kodama T, Miyagi T, Hosui A, Tatsumi T, Ishida H, Noda T, Nagano H, Doki Y, Mori M, Hayashi N. The let-7 family of microRNAs inhibits Bcl-xL expression and potentiates sorafenib-induced apoptosis in human hepatocellular carcinoma. *J Hepatol*. 2010; 52:698-704.

**172.** Sacconi A, Biagioni F, Canu V, Mori F, Di Benedetto A, Lorenzon L, Ercolani C, Di Agostino S, Cambria AM, Germoni S, Grasso G, Blandino R, Panebianco V, et al. miR-204 targets Bcl-2 expression and enhances responsiveness of gastric cancer. *Cell Death Dis*. 2012; 3:e423.

**173.** Zhang Y, Schiff D, Park D, Abounader R. MicroRNA-608 and MicroRNA-34a regulate chordoma malignancy by targeting EGFR, Bcl-xL and MET. *PloS ONE*. 2014; 9:e91546.

**174.** Kurataka O, Takahiro O. Genetic networks lead and follow tumor development: MicroRNA regulation of cell cycle and apoptosis in the p53 pathways. *Bio Med Res Intern*. 2014; 2014:ID749724.

**175.** Raver-Shapira N, Marciano E, Meiri E, Spector Y, Rosenfeld N, Moskovits N, Bentwich Z, Oren M. Transcriptional activation of miR-34a contributes to p53-mediated apoptosis. *Mol Cell*. 2007; 26:731-743.

**176.** Chang TC, Wentzel EA, Kent OA, Ramachandran K, Mullendore M, Lee KH, Feldmann G, Yamakuchi M, Ferlito M,

Lowenstein CJ. Transactivation of miR-34a by p53 broadly influences gene expression and promotes apoptosis. *Mol Cell*. 2007; 26:745-752.

**177.** Garibaldi F, Falcone E, Trisciuoglio D, Colombo T, Lisek K, Walerych D, Del Sal G, Paci P, Bossi G, Piaggio G, Gurtner A. Mutant p53 inhibits miRNA biogenesis by interfering with the microprocessor complex. *Oncogene* 2016. doi: 10.1038/onc.2016.51. [Epub ahead of print]

**178.** Baig S, Seevasant I, Mohamad J, Mukheem A, Huri HZ, Kamarul T. Potential of apoptotic pathway-targeted cancer thereapeutic research: Where do we stand? *Cell Death Dis*. 2016; 7:e2058.

## Fasting plus tyrosine kinase inhibitors in cancer

Irene Caffa, Valter D. Longo, and Alessio Nencioni

Tyrosine kinase inhibitors (TKIs), such as Tarceva (erlotinib), Iressa (gefitinib), Tykerb (lapatinib), and Gleevec (imatinib), are among the most broadly applied cancer therapeutics. By blocking the tyrosine kinase activity of mutated or overexpressed oncogenes, such as Epidermal Growth Factor Receptor (EGFR) and human epidermal growth factor receptor 2 (HER2), they interfere with signaling cascades which cancer cells are frequently “addicted” to, inducing vigorous and prolonged clinical responses in responsive patients [1]. Nevertheless, particularly in solid cancers, patients will sooner or later face relapses due to the emergence of resistant cell clones. Thus, strategies to safely increase the effectiveness of TKIs, but also reduce their toxicity are critically needed.

Studies show that cycles of prolonged fasting (PF, water only for more than two days) or of fasting-mimicking diets (FMDs) enhance the activity of chemo- and radiotherapy in preclinical cancer models [2, 3]. In addition, another advantage of administering chemotherapy during PF is that its overall tolerability appears to be increased [4]. As a result, several clinical trials are currently exploring the effects of PF/FMDs in patients undergoing chemotherapy (NCT01304251, NCT01175837, NCT00936364, NCT01175837, NCT01802346, NCT02126449).

Given this background, it is important to ask whether starvation would also be a useful approach to increase the efficacy of TKIs [5]. Results show that starvation strongly potentiates the antitumor activity of these agents both in vitro and in vivo in mice carrying human tumor xenografts. This goes along with a marked increase in the ability of TKIs to block signaling via the pro-tumorigenic mitogen-activated protein kinase (MAPK) cascade when they are administered under starvation conditions. Gene expression microarrays indicated that starvation and crizotinib (a TKI that is commonly used in advanced non-squamous non-small-cell lung cancer with EML4-ALK translocation) lead to similar changes in gene expression (primarily affecting cell cycle and DNA repair genes), whereas combining the two treatments compounds such effects by activating E2F6 (a dominant negative inhibitor of other E2F family members) and RB1, and by inhibiting the

cell cycle-promoting transcription factors E2F1 and E2F4.

Overall, this work indicated that PF and FMDs, recently shown to be effective in reducing IGF-1 levels in both mice and human subjects [6], may not only be effective when coupled to standard chemotherapy or to radiotherapy, but that they may also find applications in patients receiving more modern, molecularly-targeted agents, such as TKIs, making them more effective. That being said, this study also left several questions open and opportunities for investigations. Do PF/FMDs also reduce the likelihood of secondary resistance (or delay its occurrence), thereby extending progression-free survival and overall survival? Can PF/FMDs achieve cases of advanced solid cancers cured with TKIs? Do PF/FMDs also increase the activity of commonly used anti-EGFR and anti-HER2 monoclonal antibodies, such as cetuximab or trastuzumab? Last, but not least, can PF/FMDs also increase the tolerability of TKIs, as much as they do with chemotherapeutics? Indeed, although the toxicity of TKIs is typically less severe than that of chemotherapy, it can still be invalidating and lead to dose reductions or treatment discontinuations [1]. Reduced toxicity is anticipated considering the already demonstrated differential regulation of the growth of normal vs. cancer cells by PF/FMDs, which would promote entry of many normal cell types into a non-dividing and protected mode and make them less dependent on tyrosine kinase activity. Thus, if PF/FMDs helped spare healthy tissues from the toxicity of TKIs, the overall effectiveness of these agents could be strongly improved [7]. Answering these questions through preclinical and clinical studies is going to be crucial to provide a clear frame of usefulness for PF/FMDs in oncology.

## REFERENCES

1. Gridelli C et al. Clin lung cancer. 2014; 15:173-181.
2. Lee C et al. Science Translational Medicine. 2012; 4:124ra127.
3. Safdie F et al. PLoS one. 2012; 7:e44603
4. Raffaghello L et al. Proceedings of the National Academy of Sciences of the United States of America. 2008; 105:8215-8220.
5. Caffa I et al. Oncotarget. 2015; 6:11820-11832. DOI: 10.18632/oncotarget.3689



6. Brandhorst S et al. Cell Metab. 2015. pii: S1550-4131(15)00224-7.
7. Eichler HG et al. Nature Reviews Drug Discovery. 2010; 9:277-291.

**Alessio Nencioni:** Department of Internal Medicine,  
University of Genoa, 16132 Genoa, Italy

**Correspondence:** Alessio Nencioni

**Email:** [alessio.nencioni@unige.it](mailto:alessio.nencioni@unige.it)

**Keywords:** cancer; fasting; tyrosine kinase inhibitors;  
MAPK signaling; molecularly, targeted therapy

**Received:** July 11, 2015

**Published:** December 6, 2015

## A novel autosomal recessive TERT T1129P mutation in a dyskeratosis congenita family leads to cellular senescence and loss of CD34+ hematopoietic stem cells not reversible by mTOR-inhibition

Clemens Stockklausner<sup>1\*</sup>, Simon Raffel<sup>2, 3, 4\*</sup>, Julia Klermund<sup>5</sup>, Obul Reddy Bandapalli<sup>1</sup>, Fabian Beier<sup>6</sup>, Tim H. Brümmendorf<sup>6</sup>, Friederike Bürger<sup>7</sup>, Sven W. Sauer<sup>7</sup>, Georg F. Hoffmann<sup>7</sup>, Holger Lorenz<sup>5</sup>, Laura Tagliaferri<sup>1</sup>, Daniel Nowak<sup>8</sup>, Wolf-Karsten Hofmann<sup>8</sup>, Rebecca Buergermeister<sup>1, 5</sup>, Carolin Kerber<sup>1</sup>, Tobias Rausch<sup>9, 10</sup>, Jan O. Korbel<sup>10</sup>, Brian Luke<sup>5, 11\*</sup>, Andreas Trumpp<sup>2, 3, 4\*</sup> and Andreas E. Kulozik<sup>1\*</sup>

<sup>1</sup>Department of Pediatric Oncology, Hematology and Immunology, University of Heidelberg and Molecular Medicine Partnership Unit, 69120 Heidelberg, Germany;

<sup>2</sup>Division of Stem Cells and Cancer, German Cancer Research Center (DKFZ), Im Neuenheimer Feld 280, 69120 Heidelberg, Germany;

<sup>3</sup>Heidelberg Institute for Stem Cell Technology and Experimental Medicine (HI-STEM gGmbH), Im Neuenheimer Feld 280, 69120 Heidelberg, Germany;

<sup>4</sup>German Cancer Consortium (DKTK), 69120 Heidelberg, Germany;

<sup>5</sup>Zentrum für Molekulare Biologie der Universität Heidelberg (ZMBH), DKFZ-ZMBH Alliance, 69120 Heidelberg, Germany;

<sup>6</sup>Department of Hematology, Oncology, Hemostaseology and Stem Cell Transplantation, Medical Faculty of the RWTH Aachen University, 52062 Aachen, Germany;

<sup>7</sup>Center for Pediatric and Adolescent Medicine, Heidelberg University Hospital, Im Neuenheimer Feld 430, 69120 Heidelberg, Germany;

<sup>8</sup>Department of Hematology and Oncology, University Hospital Mannheim, Medical Faculty Mannheim of the University of Heidelberg, 68167 Mannheim, Germany;

<sup>9</sup>European Molecular Biology Laboratory (EMBL), Genomics Core Facility, D 69117 Heidelberg, Germany;

<sup>10</sup>European Molecular Biology Laboratory (EMBL), Genome Biology Unit and Molecular Medicine Partnership Unit, D 69117 Heidelberg, Germany;

<sup>11</sup>Institute of Molecular Biology gGmbH, gefördert durch die Böhringer Ingelheim Stiftung, 55128 Mainz, Germany;

\*Equally contributed

**Key words:** TERT, TERC, mTOR, rapamycin, sirolimus, senescence

**Received:** 09/24/15; **Accepted:** 10/30/15; **Published:** 11/06/15

**Correspondence to:** Andreas E. Kulozik, MD/PhD; **E-mail:** [andreas.kulozik@med.uni-heidelberg.de](mailto:andreas.kulozik@med.uni-heidelberg.de)

**Copyright:** Stockklausner et al. This is an open-access article distributed under the terms of the Creative Commons Attribution License, which permits unrestricted use, distribution, and reproduction in any medium, provided the original author and source are credited

**Abstract:** The TERT gene encodes for the reverse transcriptase activity of the telomerase complex and mutations in TERT can lead to dysfunctional telomerase activity resulting in diseases such as dyskeratosis congenita (DKC). Here, we describe a novel TERT mutation at position T1129P leading to DKC with progressive bone marrow (BM) failure in homozygous members of a consanguineous family. BM hematopoietic stem cells (HSCs) of an affected family member were 300-fold reduced associated with a significantly impaired colony forming capacity in vitro and impaired repopulation activity in

mouse xenografts. Recent data in yeast suggested improved cellular checkpoint controls by mTOR inhibition preventing cells with short telomeres or DNA damage from dividing. To evaluate a potential therapeutic option for the patient, we treated her primary skin fibroblasts and BM HSCs with the mTOR inhibitor rapamycin. This led to prolonged survival and decreased levels of senescence in T1129P mutant fibroblasts. In contrast, the impaired HSC function could not be improved by mTOR inhibition, as colony forming capacity and multilineage engraftment potential in xenotransplanted mice remained severely impaired. Thus, rapamycin treatment did not rescue the compromised stem cell function of TERT<sup>T1129P</sup> mutant patient HSCs and outlines limitations of a potential DKC therapy based on rapamycin.

## INTRODUCTION

Telomeres, the protective nucleoprotein structures at chromosome ends, shorten upon each cell division due to the so-called “end-replication problem” [1, 2]. The end-replication problem is compensated for by the reverse transcriptase, telomerase, which is active in germ cells, cancer cells and, to an extent in somatic stem cells [3]. Accelerated telomere shortening leads to the premature replicative senescence of cells and can be caused by mutations of the telomerase components DKC1 (dyskerin), TERC and TERT, among other genes involved in telomere maintenance [4-7]. TERC and TERT represent the RNA and catalytic protein moieties of the telomerase reverse transcriptase, respectively. Mutations affecting the function of these genes may lead to dyskeratosis congenita (DKC), a disease with a highly heterogeneous phenotype [8-11]. Affected patients suffer from a variable combination of skin, nail and mucosal dystrophies, but also life-threatening conditions such as progressive bone marrow failure, pulmonary fibrosis and an increased propensity to develop malignant tumors [12-16]. Telomere loss has been proposed to eliminate cells with a long proliferative history, and in this manner, acts as a tumor suppressor to limit replicative capacity. Telomere attrition also occurs with age and the associated accumulation of senescent cells may contribute to the aging process [13]. In disease states with reduced stem cell replicative reserve, substantially increased stem cell turnover or in the absence of telomerase activity short telomeres accumulate in hematopoietic stem cells [17]. Critically short telomeres are dysfunctional in terms of chromosome end protection and hence upon nucleolytic processing the DNA damage checkpoint is unleashed, thereby driving the onset of replicative senescence [18]. Dysfunctional telomeres are also prone to unscheduled repair events leading to chromosomal rearrangements. Therefore, in the absence of a functional DNA damage checkpoint, chronic telomere shortening could also potentially lead to pathogenic chromosomal instability.

Current treatment for patients affected by dyskeratosis congenita includes the androgen danazol [19-21]. The

use of androgens can lead to virilization in female patients and thereby limits its therapeutic range [22, 23].

Stem cell transplantation to cure the progressive bone marrow failure is challenging, and DKC patients have a poor tolerance for conditioning regimens and frequently suffer from life threatening side effects [24-26]. Future therapy options include the utilization of induced pluripotent stem cells that might be beneficial for patients that have defined mutations in telomerase components such as TERC [5].

mTOR is a protein kinase that promotes cell growth in response to nutrient supplies and growth signals, and can be specifically inhibited by rapamycin [27]. As it has been shown that inhibiting the mTOR pathway with rapamycin reduces the rate of cellular senescence onset, we hypothesized that rapamycin might have a therapeutic potential for patients suffering from mutations of the telomerase complex where senescent cells accumulate [28, 29].

In this work we describe a consanguineous Libyan family in which we identify a novel T1129P TERT mutation leading to progressive bone marrow failure in homozygous family members. In order to test our hypothesis that rapamycin may rescue or at least improve the physiology of TERT<sup>T1129P</sup> patient cells, we analyzed the effect of the mTOR inhibitor rapamycin on growth and senescence of skin fibroblasts and on hematopoietic stem cells using in vitro cultures and xenograft mouse models.

## RESULTS

### **The novel TERT T1129P mutation leads to pathological telomere shortening causing progressive bone marrow failure in homozygous patients**

Progressive bone marrow failure including transfusion dependent anemia and thrombocytopenia was first diagnosed in patient II-1 at the age of six years in a consanguineous Libyan family when a blood count was obtained to address symptoms of anemia including weak-

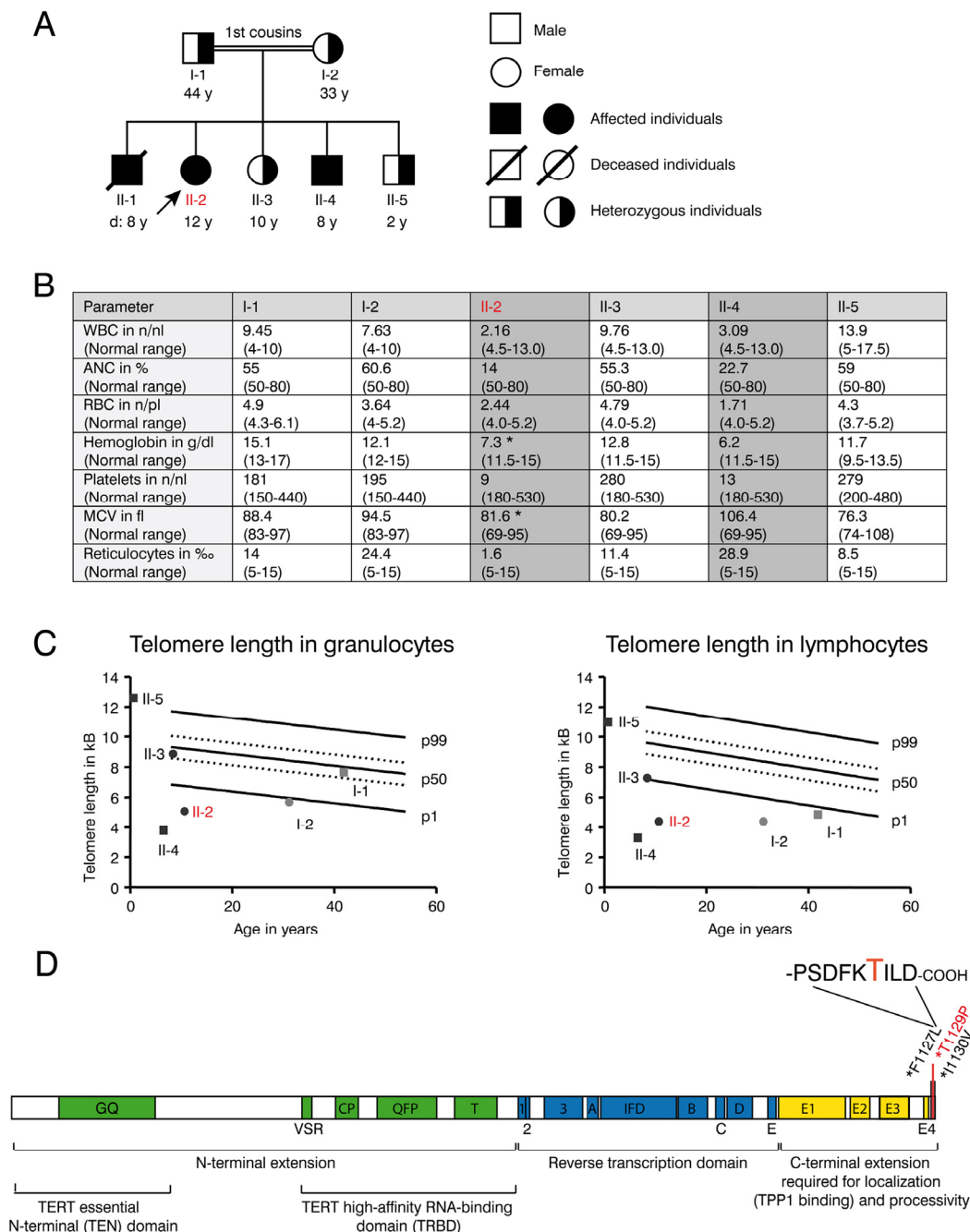


**Figure 1. Clinical features and telomere length of the DKC family with the novel T1129P TERT mutation.** (A) Family tree of the consanguineous Libyan family. Family members affected by dyskeratosis congenita (son II-1 (deceased), daughter II-2, son II-4) are indicated in black. Marked in red: patient II-2 who was analyzed in detail in the following figures. (B) Table showing complete blood counts (WBC=white blood cells (n/nl), ANC= absolute neutrophil count (% of WBC), RBC= red blood cells (n/pl), Hb=hemoglobin (g/dl), Plt=platelet count, mean corpuscular volume (MCV in fl) and reticulocytes (% of RBC) and the respective age dependent normal values in brackets of the family members I-1, I-2, II-2, II-3, II-4 and II-5 shown in (A). Family members II-2 and II-4 that were diagnosed with dyskeratosis congenita and were homozygous for the TERT<sup>T1129P</sup> mutation are highlighted with grey color. Indicated with \*: Patient II-2 was on a 3-weekly red cell transfusion regimen and had a red cell transfusion of 15 ml/kg erythrocytes 20 days before the sample was taken; patient II-4 had no history of red blood cell or platelet transfusions. (C) Telomere lengths of the described family determined in lymphocytes and granulocytes of the peripheral blood. Absolute telomere lengths in kb of lymphocytes and granulocytes of the patient II-2, her affected brother II-4, her siblings II-3, II-5 and her parents I-1 and I-2 are shown in the context of age-dependent percentiles (Females: circle, males: square. Parents: light grey, children: black. Marked in red: patient II-2 who was analyzed in detail). The solid lines represent the respective 1%, 50%, 99% percentile curves. The dashed lines represent the 25% and 75% percentile. (D) Schematic representation of the TERT gene with functional domains and known mutations at the C-terminus. Our novel T1129P mutation is depicted in red.

ness and pallor. There was no history of transfusions in the family before. The parents of II-1 were first degree cousins and family studies showed similar thrombocytopenia and anemia in two of their other offspring (II-2 and II-4) (Figure 1 A and B). Normal white blood counts, hemoglobin and platelet counts were observed from the father (I-1), mother (I-2) as well as in the second sister (II-3) and in the third brother (II-5). No family member showed any indication of nail dystrophy or skin alterations.

II-1 died at the age of eight years during conditioning regimen for intended stem cell transplantation that was performed abroad under the suspected diagnosis of aplastic anemia. His aplastic anemia was not diagnosed on a molecular basis and blood samples are no longer available.

The patient II-2 presented at our center at the age of 12 years with progressive bone marrow failure including transfusion dependent anemia and thrombocytopenia, leukopenia (Figure 1B) and hypermenorrhea. Fanconi anemia was excluded as normal results were obtained for the analysis of DNA breakage. Suspected dyskeratosis congenita was confirmed by telomere length analysis in lymphocytes and granulocytes as determined by Flow-FISH (Figure 1C). The telomere lengths in lymphocytes and granulocytes in patients II-2 and II-4 and the mother I-2 corresponded to less than the 1<sup>st</sup> percentile of age matched controls. Telomere length of the father (I-1) in lymphocytes (right panel) also corresponded to less than the 1<sup>st</sup> percentile of age-matched controls, whereas it was normal in granulocytes (left panel). The healthy sibling II-3 also displayed a decreased telomere length when compared to age matched controls, although not below the 1<sup>st</sup> percentile (Figure 1C). Pulmonary function was normal in patient II-2 and not determined in other family members.

Whole exome sequencing and validation by Sanger sequencing revealed a novel homozygous c. 3385 A>C mutation (nucleotide entry NM\_198253), resulting in the novel p.Thr1129Pro or T1129P mutation (Figure 1D) of the TERT gene in the 12-year-old patient II-2. No other homozygous mutation was found in the patient. This mutation was absent from public SNP databases (dbSNP, 1000 Genome variant catalogue), conserved and was predicted to be damaging using SIFT and PolyPhen-2 [30, 31]. The unaffected family members were heterozygous carriers of this mutation. The 8-year-old brother II-4 was detected with the same homozygous mutation by Sanger sequencing from peripheral blood.

### **The T1129P mutated TERT does not show nuclear clustering together with TERC in a ST-cell culture model**

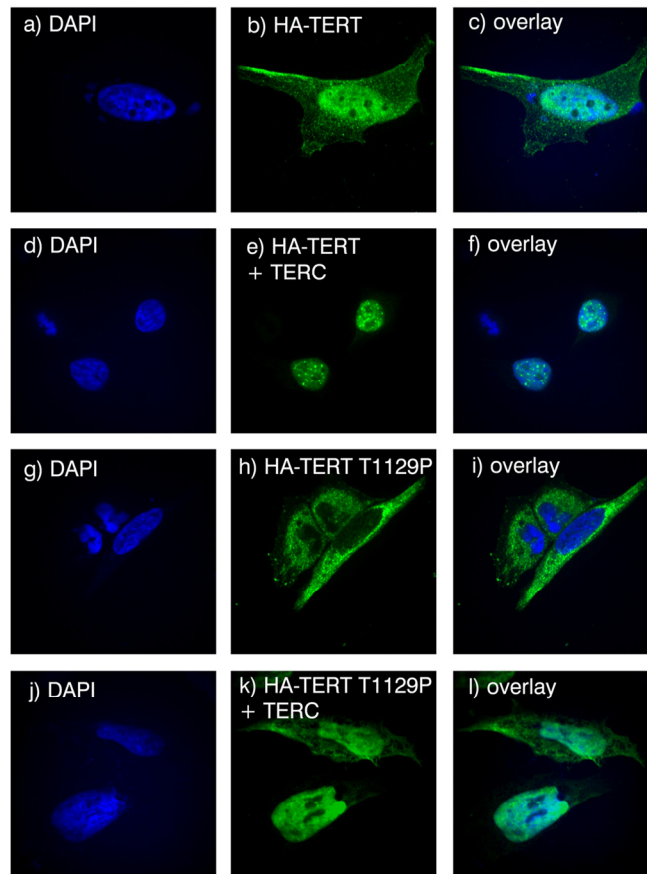
The novel T1129P mutation is located at the C-terminus of TERT altering the 4<sup>th</sup> last amino acid (Figure 1D). This region of normal TERT was shown to bind the telomeric protein TPP1, and has therefore been suggested to be required for the telomeric localization of TERT [32]. To investigate if this novel mutation would influence recruitment of the telomerase complex, we employed a modified “supertelomerase” assay (ST) that used transient, plasmid based expression of the central scaffold protein of the telomerase ribonucleoprotein TERC and hemagglutinin (HA)-tagged TERT in HeLa cells [32-35]. As shown in Figure 2, transfection of N-terminally HA-tagged TERT into HeLa cells resulted in a nucleoplasmic pattern. In line with previous findings, expression of TERC together with HA-TERT resulted in nuclear clusters that have been described as clusters with the telomeres at the chromosomal ends (Figure 2A, compare b with e) [32]. Interestingly, the mutant HA-TERT T1129P protein was detected in the cytoplasm in the absence of co-expressed TERC. When co-expressed with TERC, a nucleoplasmic pattern was observed, but it lacked the typical nuclear clustering of wild type TERT (Figure 2A, compare e to h, k, quantified in B and C) suggesting a failure to be recruited to chromosome ends. Taken together, these results strongly further support the hypothesis that the T1129P mutation impairs the recruitment of TERT to the telomerase complex located at its site of action at the chromosome ends.

### **mTOR inhibition with rapamycin influences population doublings and senescence of patient skin fibroblast cultures**

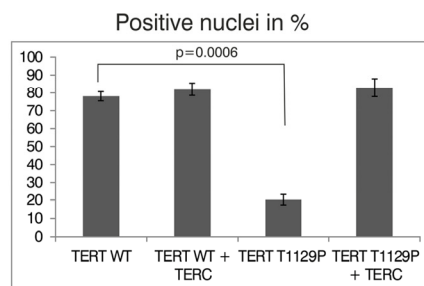
The proliferative capacity of cells can be quantified by calculating the population doublings that cells undergo during the culturing process as a function of time. Population doublings are defined as the number of times that the cell number is doubled. As telomeres shorten, the proliferative potential decreases. Generally, population doublings can be recorded in skin fibroblast cultures by plating a specific number of cells and then counting those cells after a defined period of growth as described in Material and Methods. Skin fibroblasts represent an easily accessible cell type that can be cultivated over a long time period, and were treated with either 5 nM rapamycin or DMSO as a vehicle control. Fibroblast cultures obtained from the father (I-1) fulfilled criteria of senescence from the beginning, as they did not show population doublings within 4 weeks despite frequent changes of cell culture media (not shown).



A



B



C

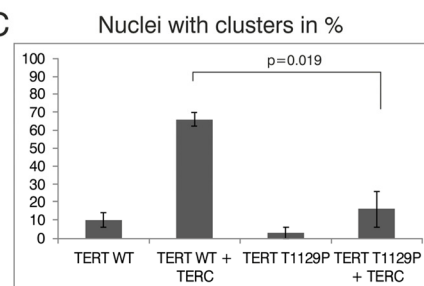


**Figure 2. Analysis of nuclear clustering of the TERT T1129P mutation in a cell culture model.** (A) Representative confocal images of transiently co-transfected HeLa-cells. HA-TERT or HA-TERT T1129P, respectively, harboring 3 HA-tag sequences in frame at the N-terminus were transfected and fixed 48h later. On the indicated pictures e) and k) equal amounts of the TERC minigene was co-transfected together with the respective TERT minigene. The HA-tag was visualized with a mouse monoclonal anti-HA antibody and an anti-mouse secondary antibody linked to Alexa 488 as described in Materials and Methods. The nucleus was visualized by DAPI staining. The panels on the right represent overlays of the TERT wild type or the T1129P mutations, respectively, with the nucleus stained with DAPI. Cells depicted represent the subcellular distribution pattern seen in >90% of the transfected cells. (B) and (C) Quantification of nuclear accumulation and clustering. For quantification of nuclear accumulation and clustering in the nuclei, 100 cells each from 3 independent transfections have been assessed and counted visually for the presence of nuclear staining and/or nuclear clustering. For statistical analysis a student's unpaired two-tailed t-test was used.

Skin fibroblast cultures of the TERT T1129P homozygous patient II-2 but also from the heterozygous mother I-2 showed impaired population doublings when compared to fibroblasts from a healthy age matched control (Figure 3A). Treatment of the control and mother (I-2) fibroblasts with rapamycin did not influence the proliferative potential measured by popula-

tion doublings over time (Figure 3A). The fibroblast culture of the patient II-2 did not show a comparable proliferation potential after day 48 and had no vital cells after day 97. In contrast, the rapamycin treated fibroblast culture of patient II-2 still divided (albeit slowly) after day 97 and showed prolonged survival until day 182 (Figure 3A).

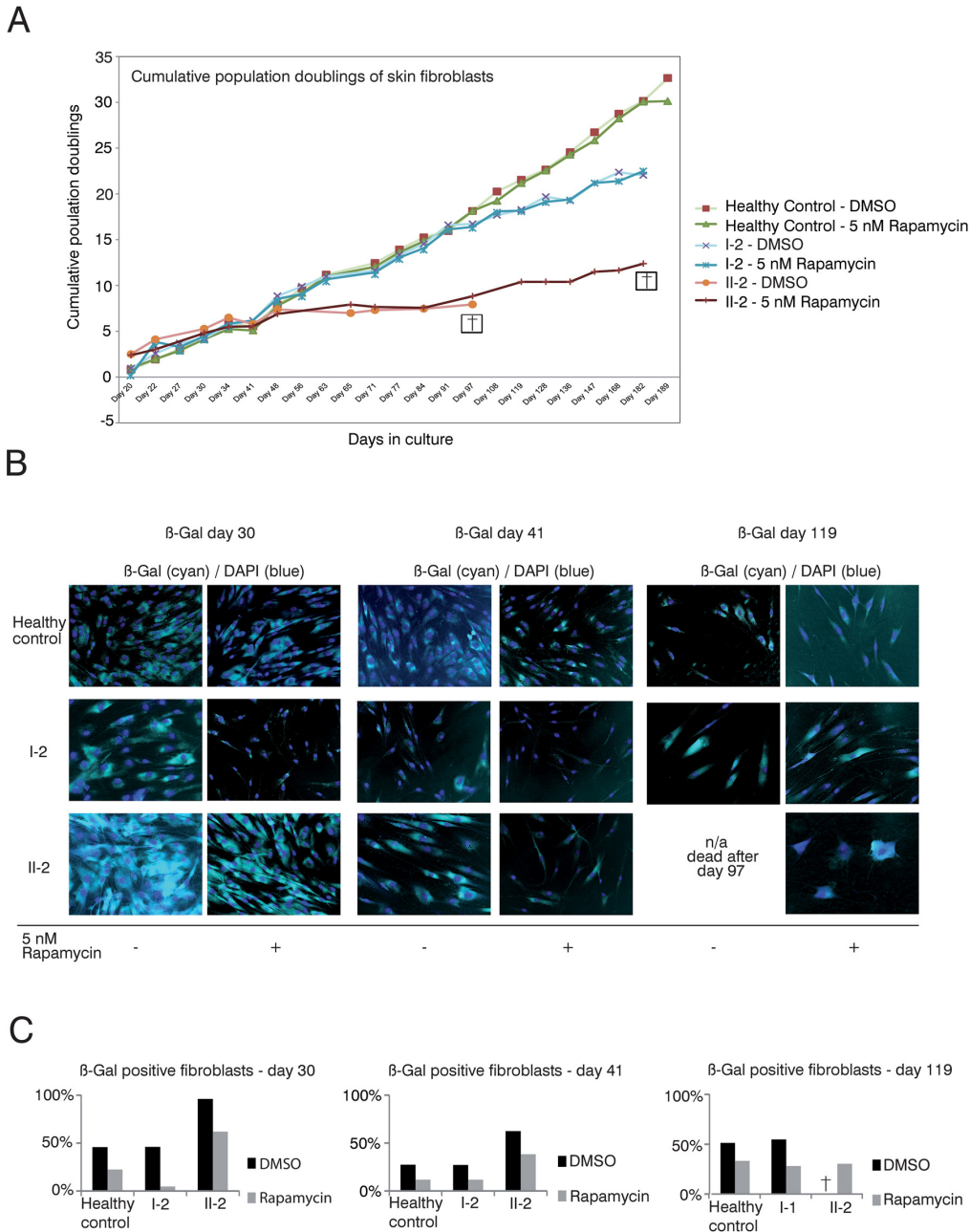


**Figure 3. Rapamycin treatment of DKC skin fibroblast cultures.** (A) Cumulative population doublings of skin fibroblasts. Fibroblast cultures from the mother I-2, the daughter II-2 and a healthy control were trypsinized and viable cells determined by trypan blue staining. Viable cells remained unstained. Population doublings were calculated using the following equation:  $PD = X + \log_2(Y/I)$  where: X = initial PD I = cell inoculum (number of cells plated in the flask) Y = final cell yield (number of cells at the end of the growth period). Cell were defined as dead (indicated with a cross) if no remaining viable cells were detected.

(B)  $\beta$ -gal senescence assay of skin fibroblasts. Fibroblasts were cultured in DMEM/10% FCS/1%PenStrep containing either 5nM rapamycin dissolved in DMSO or the equal volume of DMSO as negative control (equivalent to a 1:1,000 dilution). For the indicated timepoints, cells were fixed after 24h with 0.1% glutaraldehyde and stained for  $\beta$ -galactosidase ( $\beta$ -Gal) at pH 6 as described in Materials and Methods. Nuclei were visualized by staining with DAPI (Sigma-Aldrich), diluted 1:10,000. Coverglasses were embedded in moviol 4-88 (Carl Roth) on slides. Cells were observed at 20-fold magnification and pictures taken at brightfield and fluorescent light with a filter set suitable for DAPI on an Olympus CellR microscope. Depicted overlays of brightfield and fluorescence were merged in ImageJ. Images are representative of the indicated time points. (C) Quantification of  $\beta$ -gal assay.  $\beta$ -Gal-positive cells were detected at the indicated time points using a programmed plugin for the image editing program ImageJ as described in Materials and Methods. The quantified images were representative of the indicated time points. 200 cells counted by DAPI staining were analyzed for each time point and measurement. The fibroblasts were determined as  $\beta$ -Gal positive when blue staining in the brightfield reached a defined intensity and surrounding area of the core that was detected in the fluorescence light (Ex 330-385, Em LP420 filter set for DAPI detection).

The limited capacity of cells to divide culminates in senescence, a status that is characterized by decreased viability, enlarged cell size, altered pattern of gene expression and expression of pH dependent beta-galactosidase activity [36-38].  $\beta$ -galactosidase activity is present only in senescent cells and is not found in pre-senescent, quiescent or immortal cells [37]. Therefore, we performed  $\beta$ -galactosidase assays to test if the prolonged survival in the rapamycin treated fibroblast cultures of the patient (II-2) correlated with decreased senescence (Figure 3B and C). We detected decreased senescence in the control fibroblasts, fibroblasts of the mother I-2 and the affected patient II-2 at day 30 when treated with rapamycin (Figure 3B and C). The same effect was observed at day 41 of this experiment. At day 119 the DMSO treated fibroblast culture of our patient II-2 did not show any vital cells (no viability after day 97). In healthy control fibroblasts and the mother's fibroblasts, the rapamycin treated cultures still showed decreased senescence when compared to the respective DMSO treated cultures (Figure 3B). Taken together, these data reveal a positive correlation between proliferative potential and a decrease of the senescence marker, beta-galactosidase activity, in DC patient cells.

### **CD34+ HSPCs are reduced more than 300-fold in patient bone marrow**

Next, we sought to investigate the effect of rapamycin treatment on hematopoietic stem and progenitor cells (HSPCs), hypothesizing that in line with our previous results with fibroblasts (Figure 3), a prolonged survival of HSPCs could improve the patient's blood counts. If so, rapamycin might offer a therapeutic treatment to reduce transfusion dependence of the affected family members. Patient bone marrow derived HSPCs were characterized and quantified by flow cytometry and functionally characterized in vitro by colony forming unit (CFU) assays as well as in vivo by xeno-transplantation into immunocompromized NOD/SCID/

interleukin 2 receptor  $\gamma^{\text{null}}$  (NSG) mice. Rapamycin treatment and control groups were included in all experiments (Figure 4A). As shown in Figure 4B cellularity and HSPC frequency were strongly reduced in the bone marrow of patient II-2. Compared to a healthy female donor the patient had a 4-fold reduced bone marrow mononuclear cell count ( $1.53 \times 10^6/\text{ml}$  vs.  $0.4 \times 10^6/\text{ml}$ ) with reduced viability after gradient centrifugation (98.1 percent vs. 84.3 percent viable cells). A dramatic 300-fold reduction was observed in CD34+ HSPCs per ml bone marrow. Only 0.034 percent of all lineage negative cells were CD34+ in the patient II-2 compared to 7.04 percent in the healthy control sample, highlighting a severe HSPC depletion phenotype (Figure 4B and C). Using magnetic bead enrichment for CD34, less than 10,000 CD34+ cells could be isolated from 100 ml bone marrow aspirate, limiting functional studies with these cells.

### **Impaired clonogenic growth potential of patient II-2 HSPCs in vitro was not improved by rapamycin**

To evaluate clonogenicity and lineage differentiation potential of the patient's HSPCs and the influence of rapamycin treatment we performed colony forming unit (CFU) assays (see Figure 4A for experimental design). Plating 3,000 CD34+ cells resulted in approx. 80 colonies per plate in the healthy control. In contrast, the patient's HSPC colony forming potential was significantly reduced, revealing on average only 4 colonies in the DMSO treatment group and 2 colonies in the rapamycin treatment group (Figure 5A). Although colonies treated with rapamycin were reduced in size in both patient and healthy control, this effect was more pronounced in the patient HSPCs (Figure 5B). Furthermore, patient HSPCs showed no long-term self-renewing potential as no colonies were detected anymore in secondary CFU assays, irrespective of rapamycin treatment. In addition to a reduced abundance of HSPCs in the patient's bone marrow, results from the CFU assays indicate a severe functional

impairment including self-renewal potential of mutant progenitors. However, in contrast to our observation in fibroblasts, rapamycin treatment showed no beneficial effect on colony number, size and self-renewal activity.

**Xenotransplantation of remaining CD34-negative HSPCs from patient II-2 does not result in multilineage engraftment**

Xenotransplantation of human HSPCs into immunocompromized NSG mice is considered the gold standard to evaluate hematopoietic stem cell function. We have recently shown that co-transplantation of mesenchymal stromal cells (MSCs) can enable engraftment of functionally impaired and usually non-transplantable HSPCs derived from Myelodysplastic Syndrome patients [39]. Lacking sufficient amounts of CD34+ HSPCs and to rule out the possibility that the patient’s HSPCs are “hidden” within the CD34-negative fraction we co-injected CD34-negative BM MNCs

together with healthy human MSCs infra-femorally into sub-lethally irradiated NSG recipient mice. As control, CD34+ healthy HSPCs and MSCs were co-transplanted. In addition, 90-day slow release rapamycin or placebo pellets were implanted subcutaneously. Engraftment of human blood cells was measured by the chimerism for human CD45+ cells 90 days after transplantation. Expression of human CD19 determined lymphoid lineage output, while human CD33 expression was indicative of myeloid differentiation. As expected, healthy HSPCs reconstituted multi-lineage human hematopoiesis in bone marrow (Figure 6A, D), spleen (Figure 6B) and peripheral blood (Figure 6C) of recipient mice. Although not statistically significant, there was a clear trend showing that human CD45+ engraftment was impaired in the rapamycin treatment group in all organs analyzed. In contrast, patient II-2 derived CD34-negative bone marrow MNCs failed to engraft in both rapamycin and placebo treated animals as neither myeloid nor lymphoid cell engraftment was observed.

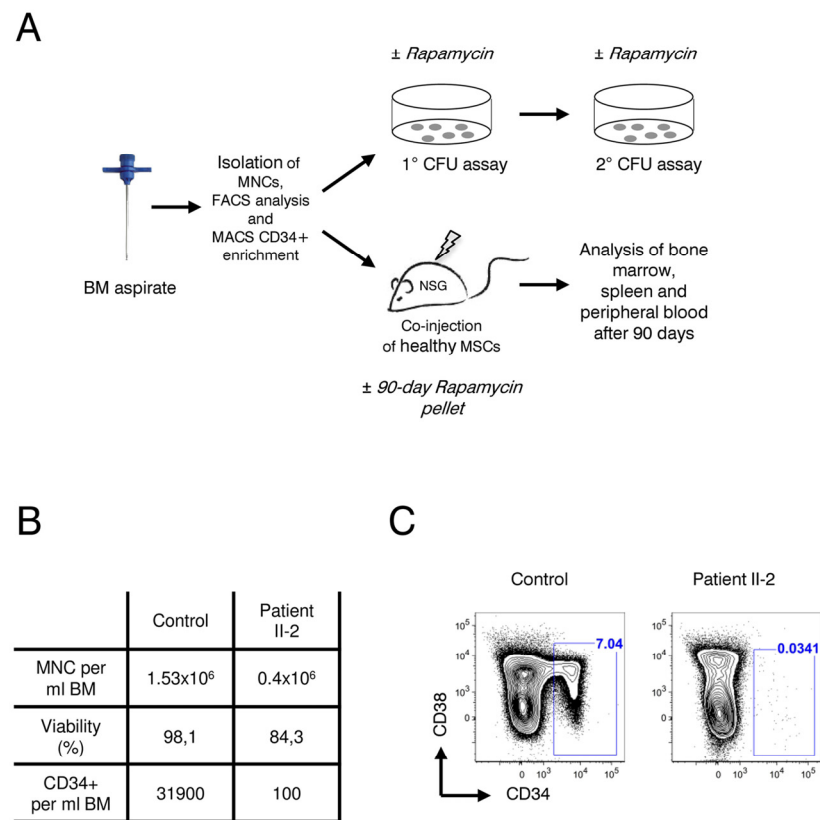


**Figure 4. Analysis of patient II-2 bone marrow.** (A) Experimental setup: Bone marrow mononuclear cells were isolated by gradient centrifugation from patient II-2 and healthy control, analyzed by FACS and either plated in colony forming unit assays (see Figure 5) or transplanted into NSG females (see Figure 6). (B) Bone marrow characteristics at time of sampling. (C) FACS plots showing CD34 and CD38 levels gated on live, lineage-negative cells. Gates show frequencies of CD34+ cells in percent.

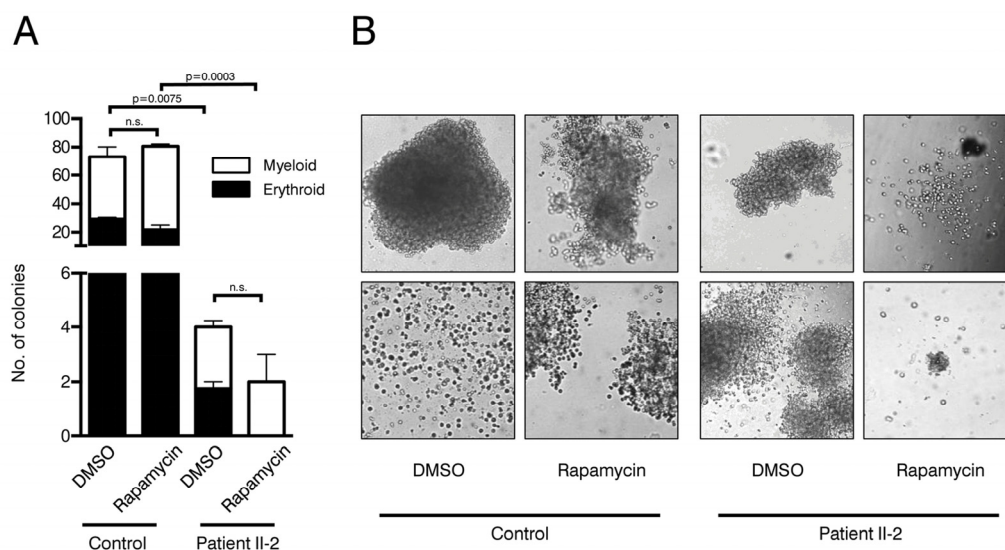


**Figure 5. Colony forming unit assays.** (A) Number of colonies in patient and control CFU assays treated with rapamycin or DMSO. Cells were plated in duplicates. Student's t-test was performed on total number of colonies, n.s. not significant. (B) Representative pictures of colonies.

However, CD3+ T cells, which were present in the transplanted CD34-negative cell fraction of patient II-2, expanded over the course of 90 days under placebo treatment leading to a clinically inapparent graft-versus-host disease. Rapamycin almost completely suppressed T cell expansion in the recipient mice, confirming the activity of the rapamycin pellets and being in line with its known mode of action as an immunosuppressive drug (Figure 6A-D).

Taken together, our experiments with bone marrow MNCs from the dyskeratosis congenita patient II-2 revealed a striking reduction in HSPCs associated with a severe functional impairment of stem cell activity that could not be improved by rapamycin treatment.

## DISCUSSION

Members of the telomerase complex such as TERC, TERT or DKC1 play fundamental roles in aging processes [4-7]. Mutations in these genes may lead to diseases associated with premature aging such as DKC and cancers. Therefore, a refined knowledge of the effects of these mutations may prove useful for understanding pathways that lead to, or mitigate, long-term health, prevention of cancer and late-stage disease. The novel germline T1129P mutation in the TERT gene identified in a consanguineous Libyan family leads to DKC with progressive bone marrow failure in all homo-

zygous individuals. Patients II-2 and II-4 showed significantly shortened telomeres below the 1<sup>st</sup> percentile when compared to healthy controls or to heterozygous family members. The pronounced telomere loss for lymphocytes in comparison to granulocytes is consistent with previous findings in healthy individuals as well as in patients with reduced telomere activity [40, 41]. Only homozygous family members showed progressive bone marrow failure. Heterozygous family members showed normal blood results. Heterozygosity of TERC- and most TERT-mutations can lead to haploinsufficiency and to the clinical phenotype of dyskeratosis congenita, although some TERT mutations cause recessive DKC with heterozygous carriers showing normal blood counts [42]. The heterozygous family members described here are phenotypically healthy despite the presence of shortened telomeres indicating a recessive mode of inheritance of the TERT T1129P mutation. This is consistent with the observation that disease severity cannot be predicted by telomere length alone [43]. However, a late onset of clinical symptoms cannot, of course, be ruled out. Strikingly, the phenotype of affected, homozygous family members only showed progressive bone marrow failure with an absence of other DKC related symptoms such as skin or nail dystrophy or pulmonary fibrosis. The localization of the mutation within the gene does not necessarily predict the phenotype, which is highly variable in various muta-



tions described throughout the TERT gene [4]. Our novel autosomal recessive T1129P mutation is in close proximity to the previously described mutations at positions 1127 and 1130 [43, 44]. When comparing the phenotypes and modes of inheritance of these two near-

by mutations, it is striking that the mutation F1127L resembles Hoyeraal-Hreidarsson-syndrome and causes autosomal dominant dyskeratosis congenita whereas the somatic I1130V mutation leads to non-severe aplastic anemia [43, 44].

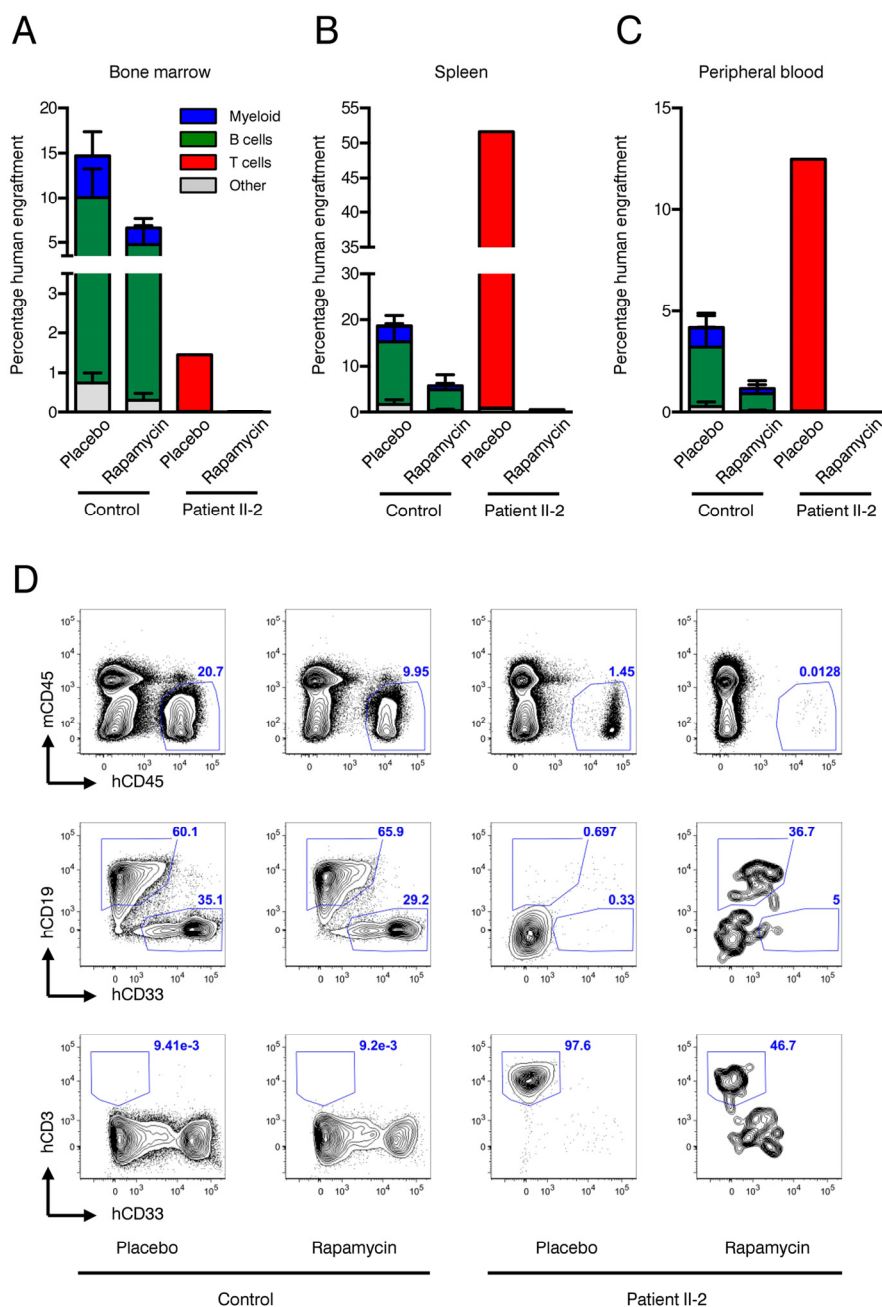


**Figure 6. Xenotransplantation experiments.** (A-C) Frequencies of human engraftment with respect to lineage differentiation in bone marrow (A), spleen (B) and peripheral blood (C) 90 days after transplantation of patient II-2 or healthy bone marrow. Mice were treated either with rapamycin or placebo. n=2 per condition in healthy donor, n=1 per condition in patient (D) Representative FACS plots depicting human (h)CD45 versus mouse (m)CD45 for blood cell chimerism (upper panel), human (h)CD19 for lymphoid differentiation and human (h)CD33 for myeloid differentiation (middle panel) and human (h)CD3 for T cell expansion. Upper panel is gated on live cells, middle and lower panels are gated on live, hCD45+ cells. Numbers represent percentage of gated events.

It still needs to be elucidated how the T1129P TERT mutation exerts its effect causing aplastic anemia in affected patients. In HeLa cell cultures the T1129P mutated TERT did not efficiently enter the nucleus without co-transfected TERC (Figure 2A and B). Together with the lack of nuclear clustering upon co-transfection with TERC, this indicates an inefficient recruitment of the telomerase complex to telomeres within the nucleus for T1129P mutated TERT. As the postulated binding site of TPP1 is within the C-terminus, binding to TPP1 or other members of the telomerase recruitment complex might be impaired by the novel T1129P mutation. A mutant of the three amino acid sequence F1127/K1128/T1129 has been shown before to display only slightly compromised telomerase catalytic activity in vitro, but its in vivo ability to elongate telomeres was highly compromised [45]. In another study, this mutant was further analyzed for its ability to localize to telomeres and to TPP1. While it did not localize to telomeres, it could still localize with TPP1 in Cajal bodies, even though the association with TPP1 was weaker compared to wild type [32].

As androgens harbor various side effects especially for female patients with DKC including virilization, there is need for substances that are safe and well tolerated antagonizing pre-mature aging processes [22, 39]. mTOR inhibition, by rapamycin, has been demonstrated to extend lifespan in a host of model organisms as well as reduce the onset of cellular senescence in cell culture [46, 47]. Moreover, recent data obtained in yeast suggest that mTOR inhibition by rapamycin can strengthen the DNA damage checkpoint and thereby increase the likelihood that cell division only occurs when damaged chromosomes are repaired [48].

Therefore, rapamycin, a substance well characterized in the clinical setting, might be an attractive target to treat DKC patients as they harbor increased numbers of senescent cells which contain dysfunctional chromosome ends. Before administering rapamycin to the patient, we assessed its effect on skin fibroblasts and on HSPCs – the cells that are most severely affected in our patient. Rapamycin had no effect on enhancing the proliferation of normal skin fibroblasts but did prolong the survival of the fibroblasts from the affected patient II-2 (Figure 3A). In our functional analysis, senescence of skin fibroblasts of patient II-2 was increased, as expected. Rapamycin showed an effect on decreasing cellular senescence in treated skin fibroblast cultures of patient II-2. Strikingly, cellular senescence was also reduced in the fibroblast culture of the mother I-2 and the fibroblasts of the healthy control (Figure 3B and C). As mTOR inhibition regulates cellular pathways that

affect senescence and aging, this might show the influence of mTOR on fundamental senescence steps even in healthy cells [47]. All fibroblast cultures showed a higher initial senescence at day 30 when compared to day 41. This can be explained by an increased senescence of the newly plated cells and later a reduced senescence of the increasingly dense cell cultures at day 41 that could have been caused by contact inhibition of geroconversion [49, 50].

Decreased frequency of HSPCs and severe impairment of these cells in functional tests such as colony-forming unit assays and xenotransplantation into immunocompromized NSG mice highlight a fundamental HSC defect in patient II-2 (Figures 4 and 5).

In contrast to fibroblasts, rapamycin treatment did not improve HSC function in these assays. The fact that rapamycin treatment resulted in a trend towards fewer and smaller colonies argues against a possible improvement of the patient's blood counts by inhibiting mTOR. However, we cannot exclude that long-term rapamycin treatment of CD34+ HSPCs may ultimately lead to restoration of HSC function as CFU assays cover only a few weeks. Due to limited availability of diseased CD34+ HSPCs (only 10,000 CD34+ cells in 100ml bone marrow aspirate) xenotransplantation had to be performed using MNCs not selected for CD34. The data thus exclude the possibility that the patient's HSCs in the diseased BM down-regulated CD34 expression. Even co-transplantation of MSCs, which typically enhance engraftment of stem cells usually not capable of initiating human hematopoiesis in NSG mice, showed no beneficial effect [39].

Interestingly, T cells present in the CD34-negative MNCs expanded in the non-treated xenografts, while the immunosuppressive agent rapamycin blocked their expansion efficiently in the treated animals (Figure 6).

Due to the nature of our biological samples (skin biopsy and bone marrow aspirate from patient II-2) repetitive sampling was not possible or useful.

Previous studies in yeast demonstrated that rapamycin was beneficial for cells with dysfunctional telomeres when cells were given the chance to repair the telomeres and eventually proliferate in the absence of rapamycin [48]. Indeed when telomere dysfunction and rapamycin treatment were chronic, there was an initial lag in growth and only at very late time points the rapamycin treatment appeared to be beneficial (J.K. and B.L. unpublished results). In the mouse experiments, rapamycin was constantly released from the pellets. In contrast, rapamycin was added to the fibroblast cultures

at the time of the splitting procedure and a possible degradation of the drug over time might have limited the toxic effects in our fibroblast experiments. Fine-tuning of rapamycin dosage might therefore be required for the anti-senescent effect and to avoid toxic effects [51]. Therefore it may be necessary to re-evaluate the dosage of rapamycin and the effects of cyclic dosing in order to see stronger effects.

The observed difference between fibroblasts and hematopoietic cells might also be explained by the different growth characteristics of the cell types studied: Fibroblasts divide much more slowly than hematopoietic cells and it is possible that hematopoietic DKC T1129P cells require a stronger therapeutic effect than DKC T1129P fibroblasts for an improvement in survival. This difference of the effect of this mutation in either fibroblast or hematopoietic cells might also be reflected by the most severely affected hematopoiesis of the homozygous TERT T1129P patients, whereas the skin and other epithelial tissues were not clinically affected.

Furthermore, the severity of the telomerase mutation may render cells completely unable to re-elongate telomeres. It should also be considered that continuous presence of rapamycin in our experiment might have had additional toxic effects preventing cell division.

In summary, we report a novel hereditary T1129P TERT mutation that leads to DKC with aplastic anemia that can be attributed to a severe reduction and functional impairment of CD34<sup>+</sup> hematopoietic stem cells. Functional analyses to find a therapeutic alternative for this serious condition revealed that rapamycin treatment prolonged survival and decreased levels of cellular senescence in treated skin fibroblasts. However, impaired HSC function could not be restored by rapamycin mediated mTOR inhibition, as colony forming capacity in vitro and multilineage engraftment potential in xenotransplanted mice was unchanged in the presence of rapamycin. Our data argue against a therapeutic use of mTOR inhibitors to treat aplastic anemia in DKC patients with TERT mutations.

## MATERIALS AND METHODS

**Ethics statement.** Investigation has been conducted in accordance with the ethical standards and according to the Declaration of Helsinki and according to national and international guidelines and has been approved by the authors' institutional review board.

**Genotype analysis.** EDTA-blood samples of the patients and their family were obtained after informed consent

had been given. DNA was prepared according to standard protocols (QIAampDNA Blood Mini Kit, Qiagen, Germany). The genebank accession number used was NM\_198253 for the cDNA and amino acid sequences.

**Telomere length measurement via flow-FISH.** Telomere length in lymphocytes and granulocytes from the peripheral blood of our patients was analyzed using flow-FISH as previously described [40, 52, 53]. Briefly, samples were analyzed in triplicates with and without Alexa488-(C3TA2) PNA staining (Panagene, Daejeon, South Korea). Granulocytes, lymphocytes and cow thymocytes were identified based on forward scatter and LDS 751 staining. Cow thymocytes with known telomere length were used as an internal control to calculate telomere length in kilobases. To determine the percentiles, linear regression on 104 blood samples from healthy donors was carried out [54, 55].

**Exome capture and Illumina sequencing.** Exome capture was carried out with the SureSelect Target Enrichment Kit v4 (Agilent, Santa Clara, CA) according to manufacturer's instructions (version 1.7, July, 2014). DNA concentration was determined with the Qubit fluorometer using the BR dsDNA Assay (Qubit 2.0, Invitrogen Life Technologies, Grand Island, NY). 3 µg of genomic DNA was sheared using Covaris S2 instrument (Covaris, Woburn, Mass, USA) to a mean size of 150-200bp. 500 ng of the library was subjected to hybridization with the SureSelect baits for 16 hours at 65 °C. Fragments captured in hybridization were indexed, amplified and sequenced in a paired end 100-bp mode using an Illumina HiSeq2000 deep sequencing instrument (v3 sequencing chemistry; Illumina, San Diego, CA).

**Analysis of the whole exome sequencing data.** Single nucleotide variant (SNV) calling was performed with the Genome Analysis Toolkit (GATK) and SAMtools mpileup [56, 57]. For GATK, the data were recalibrated with dbSNP v132 and the 1000 Genomes Project Indel release from July 5, 2011 (<http://1000genomes.org>). Subsequently, SNVs were called by using GATK's Unified Genotyper on the recalibrated data. All GATK calls were annotated for strand bias, low mapping quality, and SNV clusters. The GATK resulting SNV calls were intersected with the SAMtools mpileup SNV calls. All SNVs were intersected with information on gene coding regions by using the Annotation of Genetic Variants framework (ANNOVAR) [58]. By using RefSeq gene annotations, the SNVs were classified as nonsynonymous SNVs affecting protein-coding regions. ANNOVAR was also used to compute the overlap with dbSNP v132 ([www.ncbi.nlm.nih.gov/projects/SNP](http://www.ncbi.nlm.nih.gov/projects/SNP)), and

the October 2011 SNV releases of the 1000 Genomes Project (<http://1000genomes.org>). Additionally the SNVs were filtered using an in-house database, which is based on more than 25 deeply sequenced (>30x coverage) human genomes and which includes sites that are commonly identified as false-positive SNVs by using GATK and SAMtools mpileup. Following these additional filtering steps, candidate SNVs were evaluated computationally to assess the possible effect of an amino acid substitution on the structure and function of the respective protein by using SIFT and PolyPhen-2 [30, 59].

To verify the results obtained by whole exome sequencing, the coding regions of the TERT gene were PCR-amplified and sequenced (GATC Biotech AG, Germany). Primer sequences used for fragment amplification and sequencing are available on request.

**Plasmid constructs.** The 3xHA-TERT in pCDNA-minigene was kindly provided by Steven Artandi over addgene (pCDNA-3xHA-hTERT, addgene plasmid #51637) [60]. Functionality of this TERT construct with 3xHA at the N-terminus has been previously shown by immortalization of human fibroblasts that lack TERT expression [60].

The 3xHA-TERT T1129P minigene was constructed using the following primers:  
forward primer AscI Tert: CGGGGCGCGCCCCGCG CGCTCCCCG  
reverse primer PacI Tert: AGACTTAATTAATCAGTC CAGGATGGGCTTGAAGTCTG.

After PCR amplification, the PCR products were digested with AscI and PacI and inserted in an AscI and PacI digested pCDNA vector. The identity of all constructs was confirmed by DNA sequencing (GATC Biotech AG, Germany).

The TERC minigene (pBS U3-hTR-500, addgene plasmid #28170) was kindly provided by Kathleen Collins over addgene [61].

**Cell culture and transient transfection.** HeLa-cells were grown in Dulbecco's modified Eagle's medium (DMEM) supplemented with 10% FCS and 1% P/S at 37°C and 5% CO<sub>2</sub>. Cells were transiently transfected by calcium phosphate precipitation in 6-well plates using 3µg of the test construct DNA as described before [62].

**Immunocytochemistry.** For immunocytochemical detection of the HA-epitope, transfected cells that had been grown on coverslips in 6-well plates were fixed in 4% paraformaldehyde in phosphate-buffered saline

(PBS) for 20min at 4°C and pre-treated with 5% FCS in PBS+/-T (0.1% Triton X-100 in PBS) for 20min at RT to block unspecific antibody binding and to permeabilize the cells. The cells were then incubated with a mouse monoclonal anti-HA antibody (Sigma-Aldrich) at 1:1,000 in 3% FCS/PBS. Immunoreactivity was visualized by a goat anti-mouse secondary antibody conjugated to AlexaFluor488 (CellSignaling) (1:1,000 in 3% FCS/PBS). Before mounting the coverslips upside down in moviol 4-88 (Carl Roth) on slides, cells were washed 3x with PBS and nuclei were visualized by staining with DAPI (4'-6-Diamidino-2-phenylindole, 10mg/ml stock solution, Sigma-Aldrich), diluted 1:10,000 in PBS for 10min at RT.

**Microscopy and quantification.** Cells were imaged in the 405 and 488nm laser channels (DAPI excitation 405nm, emission 455nm; AlexaFluor excitation 488nm, emission 525nm) using a spinning-disk confocal microscope (Perkin Elmer ERS-6 with a Hamamatsu C9100-50 camera). The system incorporated a Nikon Eclipse TE2000-U inverted microscope using a Nikon 100x objective. Perkin-Elmer Ultraview ERS software and Velocity 6.3 software (Improvision, Lexington, MA) were used for acquisition. Images were subsequently cropped in Adobe Photoshop CS2. Cropped images were imported into Corel Draw X5 for the final figures presented.

For quantification of nuclear accumulation and clustering in the nuclei, 100 cells each from 3 independent transfections have been assessed and counted visually for the presence of nuclear staining and/or nuclear clustering. For statistical analysis a student's unpaired two-sided t-test was used.

**Patient data and material.** Patient data and samples were acquired and the patient was treated in accordance with the Helsinki Declaration of 1975.

After written consent, the bone marrow sample was taken according to standard procedures as a necessary routine assessment in bone marrow failure patients to determine cellularity and further cytogenetic aberrations.

Skin fibroblasts were obtained by standard procedures from underarm skin under local anesthesia and grown in DMEM (LifeTechnologies) media supplemented with 10% FCS, 1% P/S and 1% fungizone (LifeTechnologies) at 37°C in 5% CO<sub>2</sub>.

**Determination of population doublings in skin fibroblast cultures.** Monolayers were dissociated with trypsin/EDTA and resuspended cells in complete

medium. To check for viability, cells were diluted 1:2 with trypan blue (LifeTechnologies). Viable cells remained unstained. Viability and number were determined using a hemacytometer (improved Neubauer). Population doublings were calculated using the following equation:  $PD = X + \log_2(Y/I)$  where: X = initial PD I = cell inoculum (number of cells plated in the flask) Y = final cell yield (number of cells at the end of the growth period).

**Beta-galactosidase ( $\beta$ -Gal) Staining + DAPI.** Fibroblasts were cultured in DMEM/10% FCS/1%PenStrep containing either DMSO (negative control) or 5 nM rapamycin dissolved in DMSO. For several time points cells were semi-confluently seeded on 18mm-coverslips in DMEM/10%FCS/1%PenStrep at 37°C and 5% CO<sub>2</sub>. Senescence associated  $\beta$ -Gal staining was performed according to a modified published protocol [63]. After 24h cells were washed twice with PBS and fixed with 0.1% glutaraldehyde at room temperature for 15 minutes. Following two washing steps with PBS, fibroblasts were stained for  $\beta$ -galactosidase using a 0.1% $\beta$ -Gal / 5 mM Potassium hexacyano-ferrate (II)/5 mM Potassium hexacyano-ferrate (III)/2 mM MgCl<sub>2</sub> / 7.4mM Citric Acid / 150 mM NaCl- solution at pH6 for 14-16 hours at 37°C. Nuclei were visualized by staining with DAPI (4'-6-Diamidino-2-phenylindole, 10mg/ml stock solution, Sigma-Aldrich), diluted 1:10,000 in PBS for 20min at RT. Two additional washings with PBS were performed before embedding coverslips upside down in moviol 4-88 (Carl Roth) on slides. Cells were observed at 20-fold magnification on an Olympus CellR microscope and pictures taken at brightfield and fluorescent light (Ex 330-385, Em LP420), respectively. Depicted overlays of brightfield and fluorescence were merged in Fiji.

**Quantification of  $\beta$ -Gal positive cells.** The self-written macro Nuclei\_PeripheryMeasure was used to count the number of cells with a cytosolic signal above a user-defined threshold within a cell population. As output, the number of criteria-matching cell counts with respect to the total number of cells is provided. The macro works on images or image stacks with at least two channels. In short, the macro takes the nuclear signal (here DAPI) in one channel as reference for individual cells. Segmentation of nuclei is done by intensity thresholding. The corresponding nuclear areas are registered and used to create binary images as masks. In order to measure the cytosolic signal of the second channel (here  $\beta$ -Gal), dilations are performed on the binary images in a user-defined manner to match cell dimensions. The resulting mask images with intensity values 0 (background) and 1 (foreground) are multiplied with the images of the second channel to select the areas

for measurement. For the analysis, the user can specify both a general signal intensity threshold and a minimal number of pixels required above that threshold for positive counts. The software is available as ImageJ macro and can be downloaded from [http://www.zmbh.uniheidelberg.de/Central\\_Services/Imaging\\_Facility/2D\\_ImageJ\\_Macros.html](http://www.zmbh.uniheidelberg.de/Central_Services/Imaging_Facility/2D_ImageJ_Macros.html) [64]. The following settings were used to define  $\beta$ -Gal positive cells in the programmed plugin: Find and add nuclei to the ROI manger (yes). Subtract background (yes), maximum nuclei radius 80 pixels, minimum nuclei size 300 pixels, maximum nuclei size 4000 pixels, minimum circularity 0, maximum circularity 1. Clear ROI manager (yes). Surrounding analysis: surrounding distance (dilation) 5, threshold to detect intensity: 120, amount of pixels over threshold: 100. For quantification an average number of 200 DAPI stained cells were counted.

**FACS analysis, CD34+ magnetic bead enrichment and colony forming unit assays.** Bone marrow mononuclear cells were isolated by gradient centrifugation using Histopaque-1077 (Sigma) and labeled with APC-eFluor780-conjugated anti-CD34 (4H11, eBioscience), Alexa-Fluor 700-conjugated anti-CD38 (HIT2, eBioscience), a cocktail of APC-conjugated lineage antibodies consisting of anti-CD4 (RPA-T4), anti-CD8 (RPA-T8), anti-CD11b (ICRF44), anti-CD20 (2H7), anti-CD56 (B159, all BD Biosciences), anti-CD14 (61D3), anti-CD19 (HIB19) and anti-CD235a (HIR2, all eBioscience) and DAPI (Sigma). FACS analysis was performed on LSR Fortessa (BD Biosciences).

CD34+ cells from MNC were isolated using MACS enrichment columns (Miltenyi Biotec) according to the manufacturer's instructions. CD34+ cells were plated in methylcellulose medium (MethoCult H4434; StemCell Technologies) with 5nM rapamycin or DMSO. Colonies were counted after 14 days and pictures were taken with a Nikon Eclipse Ti microscope.

**Mouse transplantation and in-vivo rapamycin treatment.** Animals were housed under specific pathogen-free conditions at the central animal facility of the German Cancer Research Center (DKFZ). All animal experiments were approved by the Regierungspräsidium Karlsruhe under "Tierversuchsantrag G210/12".

Female NSG mice with 8 weeks of age were sublethally irradiated (175 cGy) one day before the cells were injected in the femoral bone marrow cavity. For the healthy control 10<sup>5</sup> CD34+ cells were injected along with 5 x10<sup>5</sup> MSCs. For the patient 10<sup>6</sup> CD34-negative MNCs cells were injected along with 5 x10<sup>5</sup> MSCs. 90 day slow release implantable pellets (Innovative



Research of America, USA) with 9mg rapamycin/pellet or placebo were implanted subcutaneously on the day of transplantation.

Recipient mice were analyzed 12 weeks post transplantation. Bone marrow cells were labeled with PE-conjugated anti-human CD45 (2D1), APC-eFluor780-conjugated anti-mouse CD45 (30-F11), PE-Cy5-conjugated anti-human CD3 (UCHT1), APC-labeled anti-human CD19 (HIB19), PE-Cy7-conjugated anti-human CD33 (WM-53, all from ebioscience) to assess multilineage human hematopoietic engraftment.

## ACKNOWLEDGEMENT

The authors acknowledge the staff at the Nikon Imaging Center at the University of Heidelberg for their assistance and for providing their excellent facility for imaging. We thank Dr. Michaela Socher and A. Rathgeb from the DKFZ Central Animal Facility for excellent mouse husbandry, and the EMBL GeneCore and EMBL IT for technical support.

## Funding

C.S. was supported by the Frontier program of the University of Heidelberg. This work was supported by the SFB 1036 of the Deutsche Forschungsgemeinschaft (DFG) and the Forschergruppe NicHem (FOR 2033) of the DFG and by the Dietmar Hopp Stiftung.

## Conflict of interest statement

The authors have no relevant conflicts of interest to disclose.

## REFERENCES

1. Hug N and Lingner J. Telomere length homeostasis. *Chromosoma*. 2006; 115:413-425.
2. Lingner J, Cooper JP and Cech TR. Telomerase and DNA end replication: no longer a lagging strand problem? *Science*. 1995; 269:1533-1534.
3. Shay JW and Wright WE. Telomeres and telomerase in normal and cancer stem cells. *FEBS Lett*. 2010; 584:3819-3825.
4. Díaz de Leon A, Cronkhite JT, Katzenstein AL, Godwin JD, Raghu G, Glazer CS, Rosenblatt RL, Girod CE, Garrity ER, Xing C and Garcia CK. Telomere lengths, pulmonary fibrosis and telomerase (TERT) mutations. *PloS one*. 2010; 5:e10680.
5. Batista LF, Pech MF, Zhong FL, Nguyen HN, Xie KT, Zaugg AJ, Cray SM, Choi J, Sebastiano V, Cherry A, Giri N, Wernig M, Alter BP, et al. Telomere shortening and loss of self-renewal in dyskeratosis congenita induced pluripotent stem cells. *Nature*. 2011; 474:399-402.
6. Agarwal S, Loh YH, McLoughlin EM, Huang J, Park IH, Miller JD, Huo H, Okuka M, Dos Reis RM, Loewer S, Ng HH, Keefe DL, Goldman FD, et al. Telomere elongation in induced pluripotent

- stem cells from dyskeratosis congenita patients. *Nature*. 2010; 464:292-296.
7. Du HY, Pumbo E, Ivanovich J, An P, Maziarz RT, Reiss UM, Chirnomas D, Shimamura A, Vlachos A, Lipton JM, Goyal RK, Goldman F, Wilson DB, et al. TERC and TERT gene mutations in patients with bone marrow failure and the significance of telomere length measurements. *Blood*. 2009; 113:309-316.
8. Dokal I. Dyskeratosis congenita in all its forms. *British journal of haematology*. 2000; 110:768-779.
9. Armanios M and Blackburn EH. The telomere syndromes. *Nat Rev Genet*. 2012; 13:693-704.
10. Mason PJ and Bessler M. The genetics of dyskeratosis congenita. *Cancer Genet*. 2011; 204:635-645.
11. Tummala H and Walne AJ. Long tails, short telomeres: Dyskeratosis congenita. *Oncotarget*. 2015; 6:13856-13857.
12. Calado RT and Young NS. Telomere maintenance and human bone marrow failure. *Blood*. 2008; 111:4446-4455.
13. Townsley DM, Dumitriu B and Young NS. Bone marrow failure and the telomeropathies. *Blood*. 2014; 124:2775-2783.
14. Savage SA and Alter BP. The role of telomere biology in bone marrow failure and other disorders. *Mechanisms of ageing and development*. 2008; 129:35-47.
15. Calado RT. Telomeres and marrow failure. *Hematology / the Education Program of the American Society of Hematology American Society of Hematology Education Program*. 2009:338-343.
16. Gadalla SM, Cawthon R, Giri N, Alter BP and Savage SA. Telomere length in blood, buccal cells, and fibroblasts from patients with inherited bone marrow failure syndromes. *Aging (Albany NY)*. 2010; 2:867-874.
17. Brummendorf TH and Balabanov S. Telomere length dynamics in normal hematopoiesis and in disease states characterized by increased stem cell turnover. *Leukemia*. 2006; 20:1706-1716.
18. Karlseder J, Smogorzewska A and de Lange T. Senescence induced by altered telomere state, not telomere loss. *Science*. 2002; 295:2446-2449.
19. Islam A, Rafiq S, Kirwan M, Walne A, Cavenagh J, Vulliamy T and Dokal I. Haematological recovery in dyskeratosis congenita patients treated with danazol. *British journal of haematology*. 2013; 162:854-856.
20. Ziegler P, Schrezenmeier H, Akkad J, Brassat U, Vankann L, Panse J, Wilop S, Balabanov S, Schwarz K, Martens UM and Brummendorf TH. Telomere elongation and clinical response to androgen treatment in a patient with aplastic anemia and a heterozygous hTERT gene mutation. *Ann Hematol*. 2012; 91:1115-1120.
21. Zlateska B, Ciccolini A and Dror Y. Treatment of dyskeratosis congenita-associated pulmonary fibrosis with danazol. *Pediatric pulmonology*. 2015.
22. Zawar V and Sankalecha C. Facial hirsutism following danazol therapy. *Cutis*. 2004; 74:301-303.
23. Riedl MA. Critical appraisal of androgen use in hereditary angioedema: a systematic review. *Ann Allergy Asthma Immunol*. 2015; 114:281-288 e287.
24. Yabe M, Yabe H, Hattori K, Morimoto T, Hinohara T, Takakura I, Shimizu T, Shimamura K, Tang X and Kato S. Fatal interstitial pulmonary disease in a patient with dyskeratosis congenita after allogeneic bone marrow transplantation. *Bone marrow transplantation*. 1997; 19:389-392.

25. Amarasinghe K, Dalley C, Dokal I, Laurie A, Gupta V and Marsh J. Late death after unrelated-BMT for dyskeratosis congenita following conditioning with alemtuzumab, fludarabine and melphalan. *Bone marrow transplantation*. 2007; 40:913-914.
26. Giri N, Lee R, Faro A, Huddleston CB, White FV, Alter BP and Savage SA. Lung transplantation for pulmonary fibrosis in dyskeratosis congenita: Case Report and systematic literature review. *BMC Blood Disord*. 2011; 11:3.
27. Laplante M and Sabatini DM. mTOR signaling in growth control and disease. *Cell*. 2012; 149:274-293.
28. Demidenko ZN and Blagosklonny MV. Growth stimulation leads to cellular senescence when the cell cycle is blocked. *Cell Cycle*. 2008; 7:3355-3361.
29. Demidenko ZN, Zubova SG, Bukreeva EI, Pospelov VA, Pospelova TV and Blagosklonny MV. Rapamycin decelerates cellular senescence. *Cell Cycle*. 2009; 8:1888-1895.
30. Adzhubei IA, Schmidt S, Peshkin L, Ramensky VE, Gerasimova A, Bork P, Kondrashov AS and Sunyaev SR. A method and server for predicting damaging missense mutations. *Nature methods*. 2010; 7:248-249.
31. Ng PC and Henikoff S. SIFT: Predicting amino acid changes that affect protein function. *Nucleic acids research*. 2003; 31:3812-3814.
32. Zhong FL, Batista LF, Freund A, Pech MF, Venteicher AS and Artandi SE. TPP1 OB-fold domain controls telomere maintenance by recruiting telomerase to chromosome ends. *Cell*. 2012; 150:481-494.
33. Abreu E, Arifonovska E, Reichenbach P, Cristofari G, Culp B, Terns RM, Lingner J and Terns MP. TIN2-tethered TPP1 recruits human telomerase to telomeres in vivo. *Molecular and cellular biology*. 2010; 30:2971-2982.
34. Cristofari G, Adolf E, Reichenbach P, Sikora K, Terns RM, Terns MP and Lingner J. Human telomerase RNA accumulation in Cajal bodies facilitates telomerase recruitment to telomeres and telomere elongation. *Molecular cell*. 2007; 27:882-889.
35. Cristofari G and Lingner J. Telomere length homeostasis requires that telomerase levels are limiting. *The EMBO journal*. 2006; 25:565-574.
36. Goldstein S. Replicative senescence: the human fibroblast comes of age. *Science*. 1990; 249:1129-1133.
37. Dimri GP, Lee X, Basile G, Acosta M, Scott G, Roskelley C, Medrano EE, Linskens M, Rubelj I, Pereira-Smith O and et al. A biomarker that identifies senescent human cells in culture and in aging skin in vivo. *Proceedings of the National Academy of Sciences of the United States of America*. 1995; 92:9363-9367.
38. Cristofalo VJ, Volker C, Francis MK and Tresini M. Age-dependent modifications of gene expression in human fibroblasts. *Critical reviews in eukaryotic gene expression*. 1998; 8:43-80.
39. Medyouf H, Mossner M, Jann JC, Nolte F, Raffel S, Herrmann C, Lier A, Eisen C, Nowak V, Zens B, Mudder K, Klein C, Oblander J, et al. Myelodysplastic cells in patients reprogram mesenchymal stromal cells to establish a transplantable stem cell niche disease unit. *Cell stem cell*. 2014; 14:824-837.
40. Rufer N, Brummendorf TH, Kolvraa S, Bischoff C, Christensen K, Wadsworth L, Schulzer M and Lansdorp PM. Telomere fluorescence measurements in granulocytes and T lymphocyte subsets point to a high turnover of hematopoietic stem cells and memory T cells in early childhood. *J Exp Med*. 1999; 190:157-167.
41. Aubert G, Baerlocher GM, Vulto I, Poon SS and Lansdorp PM. Collapse of telomere homeostasis in hematopoietic cells caused by heterozygous mutations in telomerase genes. *PLoS Genet*. 2012; 8:e1002696.
42. Marrone A, Walne A, Tamary H, Masunari Y, Kirwan M, Beswick R, Vulliamy T and Dokal I. Telomerase reverse-transcriptase homozygous mutations in autosomal recessive dyskeratosis congenita and Hoyeraal-Hreidarsson syndrome. *Blood*. 2007; 110:4198-4205.
43. Vulliamy TJ, Kirwan MJ, Beswick R, Hossain U, Baqai C, Ratcliffe A, Marsh J, Walne A and Dokal I. Differences in disease severity but similar telomere lengths in genetic subgroups of patients with telomerase and shelterin mutations. *PLoS one*. 2011; 6:e24383.
44. Vulliamy TJ, Walne A, Baskaradas A, Mason PJ, Marrone A and Dokal I. Mutations in the reverse transcriptase component of telomerase (TERT) in patients with bone marrow failure. *Blood Cells Mol Dis*. 2005; 34:257-263.
45. Banik SS, Guo C, Smith AC, Margolis SS, Richardson DA, Tirado CA and Counter CM. C-terminal regions of the human telomerase catalytic subunit essential for in vivo enzyme activity. *Molecular and cellular biology*. 2002; 22:6234-6246.
46. Blagosklonny MV. Geroconversion: irreversible step to cellular senescence. *Cell Cycle*. 2014; 13:3628-3635.
47. Komarova EA, Antoch MP, Novototskaya LR, Chernova OB, Paszkiewicz G, Leontieva OV, Blagosklonny MV and Gudkov AV. Rapamycin extends lifespan and delays tumorigenesis in heterozygous p53<sup>+/−</sup> mice. *Aging (Albany NY)*. 2012; 4:709-714.
48. Klermund J, Bender K and Luke B. High nutrient levels and TORC1 activity reduce cell viability following prolonged telomere dysfunction and cell cycle arrest. *Cell Rep*. 2014; 9:324-335.
49. Leontieva OV and Blagosklonny MV. Gerosuppression in confluent cells. *Aging (Albany NY)*. 2014; 6:1010-1018.
50. Leontieva OV, Demidenko ZN and Blagosklonny MV. Contact inhibition and high cell density deactivate the mammalian target of rapamycin pathway, thus suppressing the senescence program. *Proceedings of the National Academy of Sciences of the United States of America*. 2014; 111:8832-8837.
51. Qi H, Su FY, Wan S, Chen Y, Cheng YQ and Liu AJ. The antiaging activity and cerebral protection of rapamycin at micro-doses. *CNS Neurosci Ther*. 2014; 20:991-998.
52. Beier F, Balabanov S, Buckley T, Dietz K, Hartmann U, Rojewski M, Kanz L, Schrezenmeier H and Brummendorf TH. Accelerated telomere shortening in glycosylphosphatidylinositol (GPI)-negative compared with GPI-positive granulocytes from patients with paroxysmal nocturnal hemoglobinuria (PNH) detected by proaerolysin flow-FISH. *Blood*. 2005; 106:531-533.
53. Beier F, Masouleh BK, Buesche G, Ventura Ferreira MS, Schneider RK, Ziegler P, Wilop S, Vankann L, Gattermann N, Platzbecker U, Giagounidis A, Götze KS, Nolte F, et al. Telomere dynamics in patients with del (5q) MDS before and under treatment with lenalidomide. *Leukemia Research*. 2015.
54. Weidner CI, Lin Q, Koch CM, Eisele L, Beier F, Ziegler P, Bauerschlag DO, Jockel KH, Erbel R, Muhleisen TW, Zenke M, Brummendorf TH and Wagner W. Aging of blood can be tracked by DNA methylation changes at just three CpG sites. *Genome Biol*. 2014; 15:R24.
55. Stepensky P, Rensing-Ehl A, Gather R, Revel-Vilk S, Fischer U, Nabhani S, Beier F, Brummendorf TH, Fuchs S, Zenke S, Firat E, Pessach VM, Borkhardt A, et al. Early-onset Evans syndrome, immunodeficiency, and premature immunosenescence

associated with tripeptidyl-peptidase II deficiency. *Blood*. 2015; 125:753-761.

**56.** DePristo MA, Banks E, Poplin R, Garimella KV, Maguire JR, Hartl C, Philippakis AA, del Angel G, Rivas MA, Hanna M, McKenna A, Fennell TJ, Kernytsky AM, et al. A framework for variation discovery and genotyping using next-generation DNA sequencing data. *Nature genetics*. 2011; 43:491-498.

**57.** Li H, Handsaker B, Wysoker A, Fennell T, Ruan J, Homer N, Marth G, Abecasis G, Durbin R and Genome Project Data Processing S. The Sequence Alignment/Map format and SAMtools. *Bioinformatics*. 2009; 25:2078-2079.

**58.** Wang K, Li M and Hakonarson H. ANNOVAR: functional annotation of genetic variants from high-throughput sequencing data. *Nucleic acids research*. 2010; 38:e164.

**59.** Kumar P, Henikoff S and Ng PC. Predicting the effects of coding non-synonymous variants on protein function using the SIFT algorithm. *Nature protocols*. 2009; 4:1073-1081.

**60.** Venteicher AS, Meng Z, Mason PJ, Veenstra TD and Artandi SE. Identification of ATPases pontin and reptin as telomerase components essential for holoenzyme assembly. *Cell*. 2008; 132:945-957.

**61.** Fu D and Collins K. Distinct biogenesis pathways for human telomerase RNA and H/ACA small nucleolar RNAs. *Molecular cell*. 2003; 11(5):1361-1372.

**62.** Stockklausner C, Breit S, Neu-Yilik G, Echner N, Hentze MW, Kulozik AE and Gehring NH. The uORF-containing thrombopoietin mRNA escapes nonsense-mediated decay (NMD). *Nucleic acids research*. 2006; 34:2355-2363.

**63.** Debacq-Chainiaux F, Erusalimsky JD, Campisi J and Toussaint O. Protocols to detect senescence-associated beta-galactosidase (SA-beta-gal) activity, a biomarker of senescent cells in culture and in vivo. *Nature protocols*. 2009; 4:1798-1806.

**64.** Schneider CA, Rasband WS and Eliceiri KW. NIH Image to ImageJ: 25 years of image analysis. *Nature methods*. 2012; 9:671-675.

# The p53 tumor suppressor protein protects against chemotherapeutic stress and apoptosis in human medulloblastoma cells

Sarah Wayne<sup>1#</sup>, Aisha Naeem<sup>1#</sup>, Muhammad Umer Choudhry<sup>1#</sup>, Erika Parasido<sup>1</sup>, Lucas Tricoli<sup>1</sup>, Angiela Sivakumar<sup>1</sup>, John P. Mikhael<sup>1</sup>, Venkata Yenugonda<sup>1</sup>, Olga C. Rodriguez<sup>1</sup>, Sana D. Karam<sup>2</sup>, Brian R. Rood<sup>3</sup>, Maria Laura Avantaggiati<sup>1\*</sup>, and Chris Albanese<sup>1,4,\*</sup>

<sup>1</sup>Lombardi Comprehensive Cancer Center and Department of Oncology, Georgetown University Medical Center, Washington, DC 20057, USA;

<sup>2</sup>Department of Radiation Oncology, University of Colorado, Denver, CO 80208, USA;

<sup>3</sup>Center for Cancer and Immunology Research, Children's National Medical Center, Washington, DC 20057, USA;

<sup>4</sup>Department of Pathology, Georgetown University Medical Center, Washington, DC 20057, USA.

<sup>#</sup>These authors contributed equally

<sup>\*</sup>Equal Senior Author Contributions

**Key words:** p53, apoptosis, autophagy, medulloblastoma, Endonuclease G, BIK, p63, p73

**Received:** 08/30/15; **Accepted:** 10/02/15; **Published:** 10/27/15

**Correspondence to:** Chris Albanese, PhD; **E-mail:** [albanese@georgetown.edu](mailto:albanese@georgetown.edu)

**Copyright:** Wayne et al. This is an open-access article distributed under the terms of the Creative Commons Attribution License, which permits unrestricted use, distribution, and reproduction in any medium, provided the original author and source are credited

**Abstract:** Medulloblastoma (MB), a primitive neuroectodermal tumor, is the most common malignant childhood brain tumor and remains incurable in about a third of patients. Currently, survivors carry a significant burden of late treatment effects. The p53 tumor suppressor protein plays a crucial role in influencing cell survival in response to cellular stress and while the p53 pathway is considered a key determinant of anti-tumor responses in many tumors, its role in cell survival in MB is much less well defined. Herein, we report that the experimental drug VMY-1-103 acts through induction of a partial DNA damage-like response as well induction of non-survival autophagy. Surprisingly, the genetic or chemical silencing of p53 significantly enhanced the cytotoxic effects of both VMY and the DNA damaging drug, doxorubicin. The inhibition of p53 in the presence of VMY revealed increased late stage apoptosis, increased DNA fragmentation and increased expression of genes involved in apoptosis, including *CAPN12* and *TRPM8*, *p63*, *p73*, *BIK*, *EndoG*, *CIDEB*, *P27<sup>Kip1</sup>* and *P21<sup>cip1</sup>*. These data provide the groundwork for additional studies on VMY as a therapeutic drug and support further investigations into the intriguing possibility that targeting p53 function may be an effective means of enhancing clinical outcomes in MB.

## INTRODUCTION

Medulloblastoma (MB) is a primitive neuroectodermal tumor that arises from granule neuron precursors in the cerebellum or from neural stem cells of the rhombic lip and is the most frequently diagnosed malignant brain tumor in children [1]. Approximately 70% of MB cases occur in children under the age of 10. While less common, MB is also seen in patients between 20 and 44 years of age, with incidences falling off significantly thereafter. A combination of surgery, radiotherapy, and

chemotherapy has contributed to improved treatment outcomes, resulting in a 70-80% five-year disease-free patients with medulloblastoma remain significant and recurrence is frequently observed. As with many malignancies, disease recurrence is nearly always fatal, and late mortality remains a serious health issue in long-term MB survivors [2]. Moreover, current therapies result in significant negative impacts on neurological, cognitive and social development, especially in the youngest affected children. Significant efforts are therefore underway to develop more effective and less toxic MB treatments.

The efficacy of many anti-tumor agents relies on their ability to trigger the tumor suppressive activities of p53, which leads to the induction of cell death, frequently via cellular pathways of apoptosis, senescence or mitotic catastrophe. While the activity of the p53 tumor suppressor protein is highly complex [3], its expression is induced by a broad array of cell stressors including DNA-damaging chemotherapeutic drugs and can be an excellent target for therapeutic intervention ([4], see also [3]). Impairment of p53 signaling by gene mutation or gene silencing/loss has been shown to contribute to the induction, progression and/or recurrence of many tumor types and can confer resistance to tumor therapy. p53 plays unique roles in neural development. For example, p53 has been directly implicated in neurogenesis as well as in neural stem cell self-renewal, neurite outgrowth and axonal regeneration (reviewed in [5]), and acetylation of p53 is required for the induction of neurite outgrowth [6]. Despite this knowledge and that related to the role of p53 in many malignancies, the function of p53 in MB remains under-explored. For example, unlike lung, pancreas and bladder cancers, only a minority of primary MB patients present with p53 mutation or loss, with reported frequencies between 7% [7] and 15% [8]. Interestingly, while the frequency of p53 mutations increases upon recurrence, the percentage of cells with nuclear p53 also increases, rising from 26% at diagnosis to 33% at relapse [8], suggesting that certain mechanisms underlying p53 function may still be intact. Importantly, the MAGIC consortium identified chromosome 17 deletions, where the p53 locus is located, to be associated with chromothripsis (chromosomal fragmentation) in Group 3 MB [9], while reduced expression of p53 was seen in Group 4 MB [10]. Collectively, these findings highlight the complex and poorly defined role for p53 in human MB, and support the need for mechanistic studies into p53 activity as a possible therapeutic effector protein.

The *in vitro* [11-13] and *in vivo* [14] anti-tumor activities of an experimental CDK inhibitor, VMY-1-103 (VMY), have previously been described by us in both prostate and other solid tumors [11, 13, 15] and in MB [12, 14]. Our previous MB studies established that the extrinsic apoptotic pathway was induced by VMY, as was mitotic catastrophe in a subset of the cells [12]. In the present study, we sought to further define the molecular and genetic mechanisms by which VMY induces MB cell death. Herein, we show in both p53-wild type (D556) and p53-mutant (DAOY) MB cell lines that treatment with VMY resulted in the translocation of p53 into the nucleus, an induction of  $\gamma$ H2AX, a decrease in MDM2 protein levels and activation of non-survival macro-autophagy.

Interestingly, suppression of p53 function via shRNA knockdown or treatment with the p53 inhibitory compound Pifithrin- $\alpha$  (Pif) [16] resulted in significant increases in cell death following treatment with either VMY or doxorubicin. Gene expression analyses performed on D556 cells treated with VMY and Pif versus VMY alone revealed a significant increase in genes associated with apoptosis and necrosis, including the calcium pathway signaling genes *CAPN12* and *TRPM8* suggesting alterations in intracellular calcium signaling may play a role in enhancing cell death. In addition, p63 and its transcriptional target the pro-apoptotic gene *BIK* were induced, as were p73 and its target, the caspase-independent intranucleosomal DNase, *Endonuclease-G* (Endo-G) [17].

Given the difficulties in effectively treating MB, especially recurrent disease, targeting p53 in combination with chemotherapy potentially represents a new treatment strategy for medulloblastoma.

## RESULTS

### Treatment of MB cells induces a durable cytotoxic effect

We have previously reported that VMY induces MB cell death [12, 14]. To test whether VMY's antiproliferative effects were sustained after removal of the compound, colony forming assays were performed. D556 cells were treated with VMY or its parent compound purvalanol B (PVB) for 18 hrs, at which point the media was changed and the cells were allowed to recover in the absence of the drugs until the control plate reached 80% confluency (approximately 3-5 days). VMY treatment resulted in a significant reduction in both the number of colonies (Fig 1A, B, C) as well as the number of cells per colony (Fig 1D) versus either DMSO- or PVB- treated D556 cells, which express wild type p53. The DNA damaging drug, doxorubicin (1 $\mu$ M), effectively killed all cells (not shown).

### VMY induces a partial DNA damage-like response in DAOY and D556 MB cell lines

Our previous studies established that the induction of cell death in MB cells occurred, at least in part, through the extrinsic apoptotic pathway and mitotic disruption [12, 14]. To further investigate the mechanisms by which VMY impacts cell survival, we interrogated proteins involved in DNA damage response and stress signaling. Time course studies of VMY treatment were performed first in DAOY cells, which express mutant p53 (p53<sup>C252F</sup>). Doxorubicin was used as a positive control for induction of a DNA damage response [18],



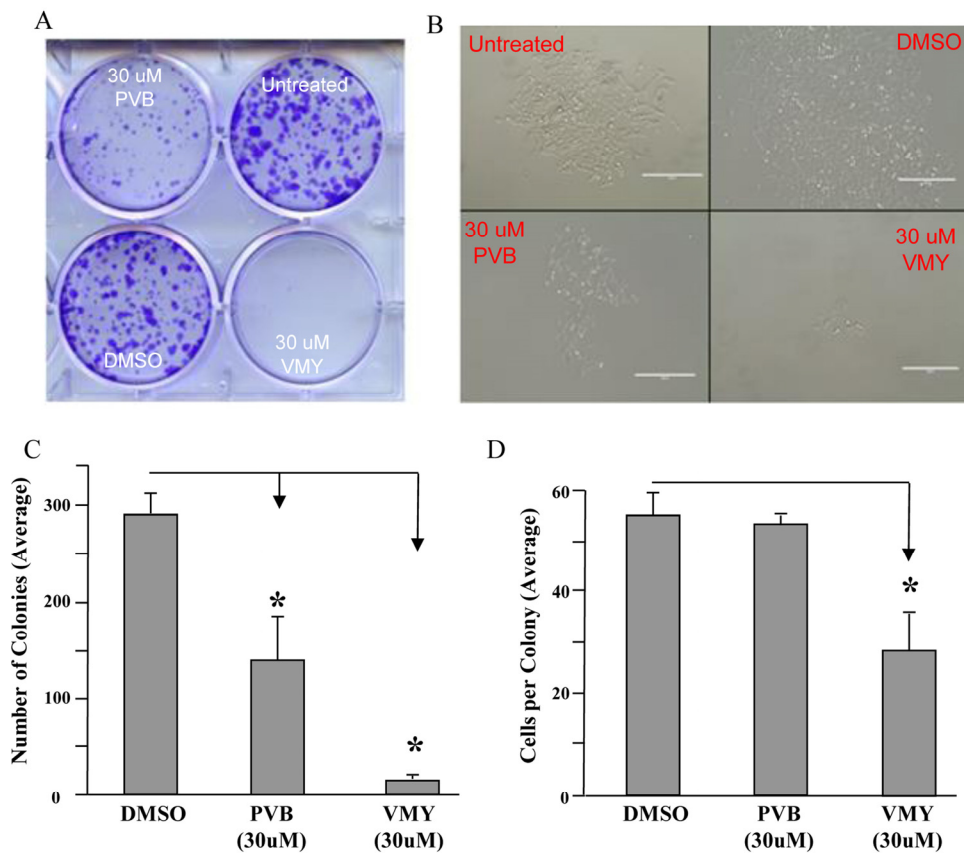


**Figure 1. VMY induced cell death.** The durability of effects of VMY on cell viability was determined via colony forming assays. D556 cells were treated with DMSO, PVB or VMY for 18 hrs. Fresh media was added and the cells cultured for an additional 3-5 days. (A) Cells stained with crystal violet. (B) Colonies as visualized by microscopy. (C) Quantification of colony number. (D) Quantification of cells per colony. The data are shown as average  $\pm$  standard deviation. PVB; purvalanol B, \*;  $p < 0.05$ .

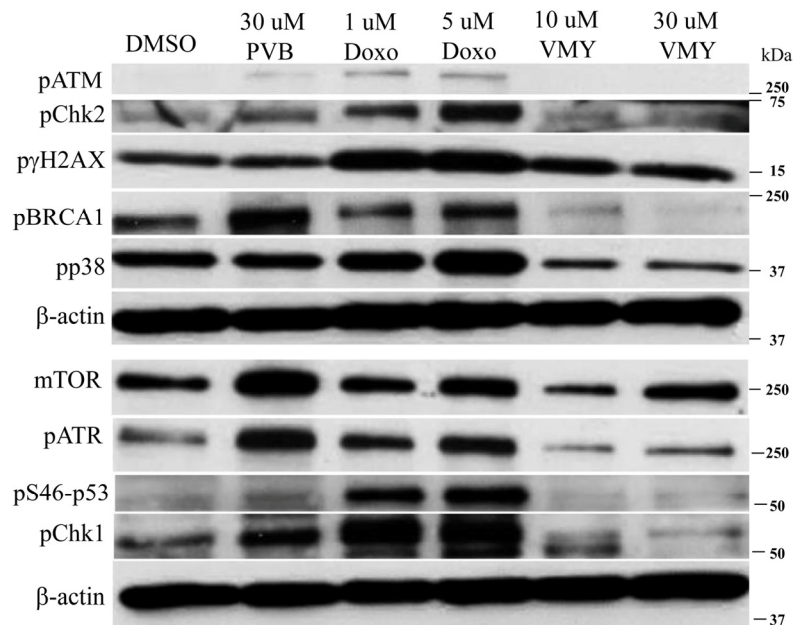


**Figure 2. Effects of VMY on stress related proteins.** DAOY cells were treated for 18 hrs with DMSO, PVB, VMY or doxorubicin at the concentrations listed and immunoblotting was performed for the proteins shown. β-actin was used as a loading control. PVB; purvalanol B, Doxo; doxorubicin.

and PVB was also tested. Compared to DMSO control, treatment with doxorubicin for 18 hours increased the levels of phosphorylated isoforms of ATM, Chk2,  $\gamma$ H2AX, BRCA1 and p38 (Fig. 2) as well as ATR, pS46-p53 and Chk1 (Fig 2). A modest increase in mTOR was also noted. In contrast, the levels of all of these proteins, with the exception of p- $\gamma$ H2AX (Fig 2) and to a lesser extent mTOR, were reduced following treatment with VMY. Interestingly, PVB behaved in a

manner similar to doxorubicin despite the fact that PVB is an inefficient inhibitor of MB cell proliferation [12]. In contrast to DAOY cells, the levels of total- and phospho- p38 remained relatively constant in D556 cells and phospho-p38 decreased slightly following 18 hrs of VMY treatment (Fig 3A), however sustained induction of  $\gamma$ H2AX was confirmed by western blot and by immunofluorescence in both DAOY and D556 cells (Fig 3A, B).

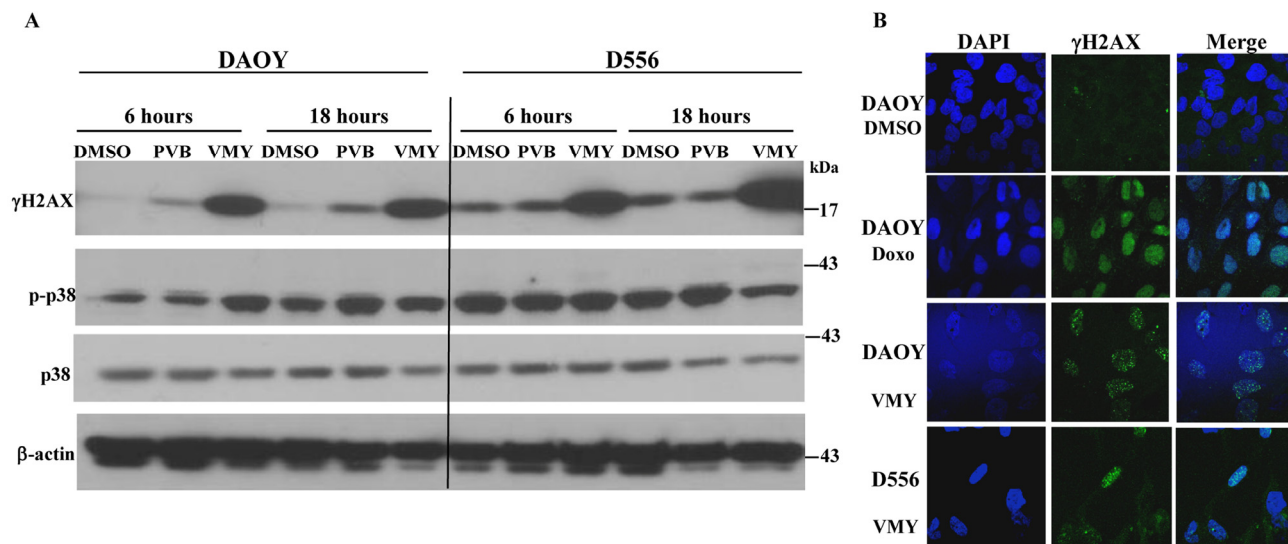


**Figure 3. Effects of VMY on stress related proteins in MB cells.** DAOY and D556 cells were treated with PVB or VMY. (A) Immunoblotting was performed for total and phosphorylated p38 and phosphorylated  $\gamma$ -H2AX following treatment for 6 or 18 hrs. (B) Immunofluorescence microscopy for  $\gamma$ -H2AX was performed on DAOY cells treated with 1  $\mu$ M doxorubicin for 18 hrs and DAOY and D556 cells treated with 10  $\mu$ M VMY for 18 hrs. DAPI was used to stain the nuclei. PVB; purvalanol B, Doxo; doxorubicin.

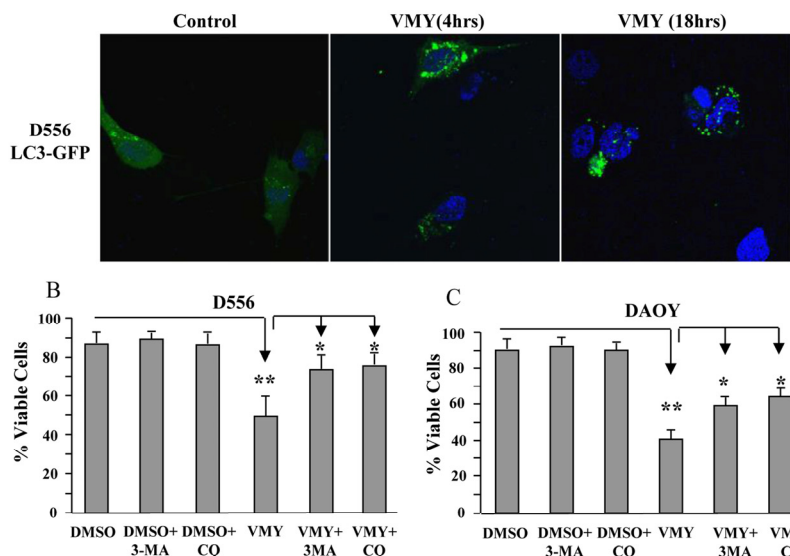


**Figure 4. Induction of Autophagy by VMY reduces cell viability.** (A) D556 cells, transfected with LC3-GFP, were treated with DMSO or VMY for 4 and 18 hrs. Autophagic LC3-GFP puncta were visualized by fluorescence microscopy. Cell nuclei were stained with DAPI. (B) D556 and (C) DAOY cells were treated with VMY for 18hrs in the presence or absence of 5  $\mu$ M 3-MA (an inhibitor of early autophagy) or 50  $\mu$ M chloroquine (an inhibitor of acidification of lysosomes and autophagosomes), and trypan blue viability assays were performed to establish cell viability. The data are shown as the average  $\pm$  standard deviation of N=3 separate experiments. \*,  $p < 0.05$ , \*\*,  $p < 0.01$ , 3-MA; 3-methyladenine, CQ; chloroquine.

## VMY induces autophagy in MB cells

VMY has the ability to block proliferation in prostate cancer cells in part through the induction of catastrophic autophagy [15]. During autophagy, LC3-I (microtubule-associated protein 1 light chain 3) becomes lipidated by the class III phosphoinositide 3-kinase, Vps34, and re-localizes from the microtubules to autophagosomal membranes (reviewed in Kang, et al. [19]). We therefore studied the pattern of subcellular localization of LC3-I in MB cells. D556 cells were transiently transfected with an LC3-GFP expression vector and subjected to fluorescence microscopy as previously described [15]. VMY treatment induced LC3-GFP re-localization and concentration into prototypical autophagic puncta (Fig 4A) with an average of 6 puncta per VMY-treated, LC3-GFP positive cell at 4 hours and 7.8 puncta per cell at 18 hrs, versus an average of 2.3 puncta per cell in control cells (Fig 4A). Our previous data established that inhibition of autophagy protected against VMY-induced cell death in prostate cancer cells [15]. We therefore investigated whether inhibitors of early (3-methyladenine, 3-MA) or late (chloroquine, CQ) autophagy influenced cell survival. Using D556 and DAOY cells, trypan blue dye exclusion assays established that neither 3-MA nor CQ influenced survival in control cells, however significant increases ( $p < 0.05$ ,  $N = 3$  separate experiments) in cell viability were seen in both cell lines when treated with VMY and the inhibitors (Fig 4B, C).

## Regulation of p53 activity is similar in DAOY and D556 MB cell lines

Our earlier investigations into the mechanisms by which VMY reduced overall cell survival in solid tumors clearly established a role for wild type p53 in inducing cell death through both apoptosis and catastrophic autophagy. For example, in adenocarcinoma cell lines with wild type p53, VMY caused a rapid induction of p53 protein levels whereas p53 levels remained constant in cells harboring p53 mutations [15]. Furthermore, the loss of p53 function via deletion, mutation or genetic silencing resulted in a complete loss of VMY-induced cytotoxicity in a variety of cancers, including prostate, breast and pancreas, while re-expression of wild type p53 in PC3 cells or treatment of DU145 cells with PRIMA1 restored VMY-induced autophagy and cell death [11, 15].

We therefore next investigated the effects of VMY on p53 expression in DAOY (p53 C242F mutant [20]) and D556 cells (p53 wild type). Unlike our previous findings in adenocarcinoma cells, p53 levels were high in both cell lines and were not affected by treatment with VMY (Supplemental Fig. 1). Similar results were seen with PVB (Supplemental Fig. 1). The levels of the p53-regulatory protein MDM2 were decreased in both cell lines (Fig 5A) and immunofluorescence microscopy demonstrated that p53 shifted from diffusely cytoplasmic with some nuclear positivity in control cells to

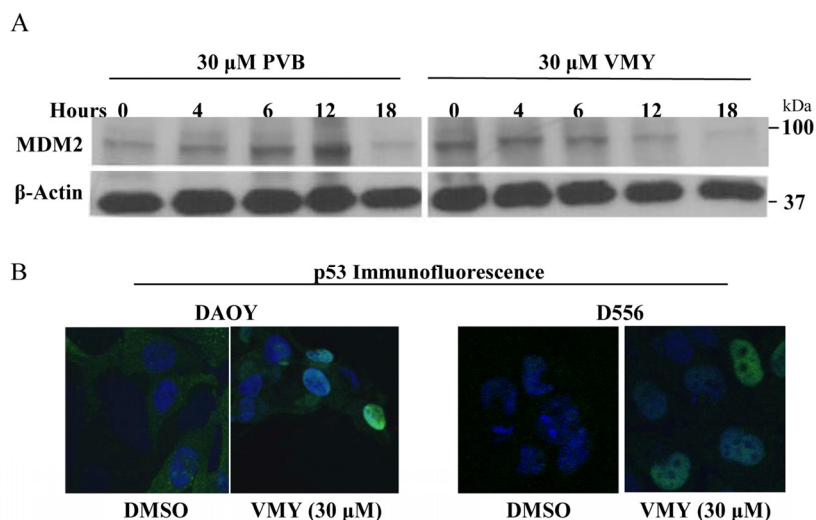


**Figure 5. VMY alters the subcellular localization of p53.** (A) Immunoblotting for MDM2 following exposure of D556 cells to PVB and VMY for the times indicated.  $\beta$ -actin was used as a loading control. (B) Immunofluorescence microscopy for p53 subcellular localization was performed on DAOY (left panels) and D556 (right panels). DAPI was used to stain the nuclei. PVB; purvalanol B.

predominantly nuclear in both cell lines following VMY treatment (Fig 5B). As both the wild type and mutant p53 proteins localize to the nucleus following exposure to VMY, these data suggest that both proteins may retain some functional activity.

### The role of p53 in inducing cell death

To determine the role of p53 in regulating MB cell survival in the presence of VMY, p53 was genetically silenced with the previously validated p53 shRNA [15] or chemically inhibited by the p53-inhibitory compound, Pifithrin- $\alpha$  (Pif), which we have used in previous experiments to investigate p53's role in regulating autophagy [16]. The silencing of p53 by shRNA resulted

in up to a 68% decrease in p53 protein levels versus pLKO control across all treatment groups in both D556 and DAOY cells (Fig 6A). Surprisingly, both the genetic and chemical silencing of p53 led to significant increases in cell death by VMY as measured by colony forming assay (Fig 6B). Equally surprising was the observation that the loss of p53 failed to protect against cell death by doxorubicin (Fig 6B, C). Dose escalation experiments performed in D556 cells in the presence and absence of Pif established that the heightened chemosensitivity was consistent across a broad range of concentrations (Fig 6D). In addition, experiments performed in DAOY showed that cell-survival declined by 33 percent in VMY-treated cells with p53 shRNA knockdown compared to VMY-treated pLKO control cells (Sup Fig S2).

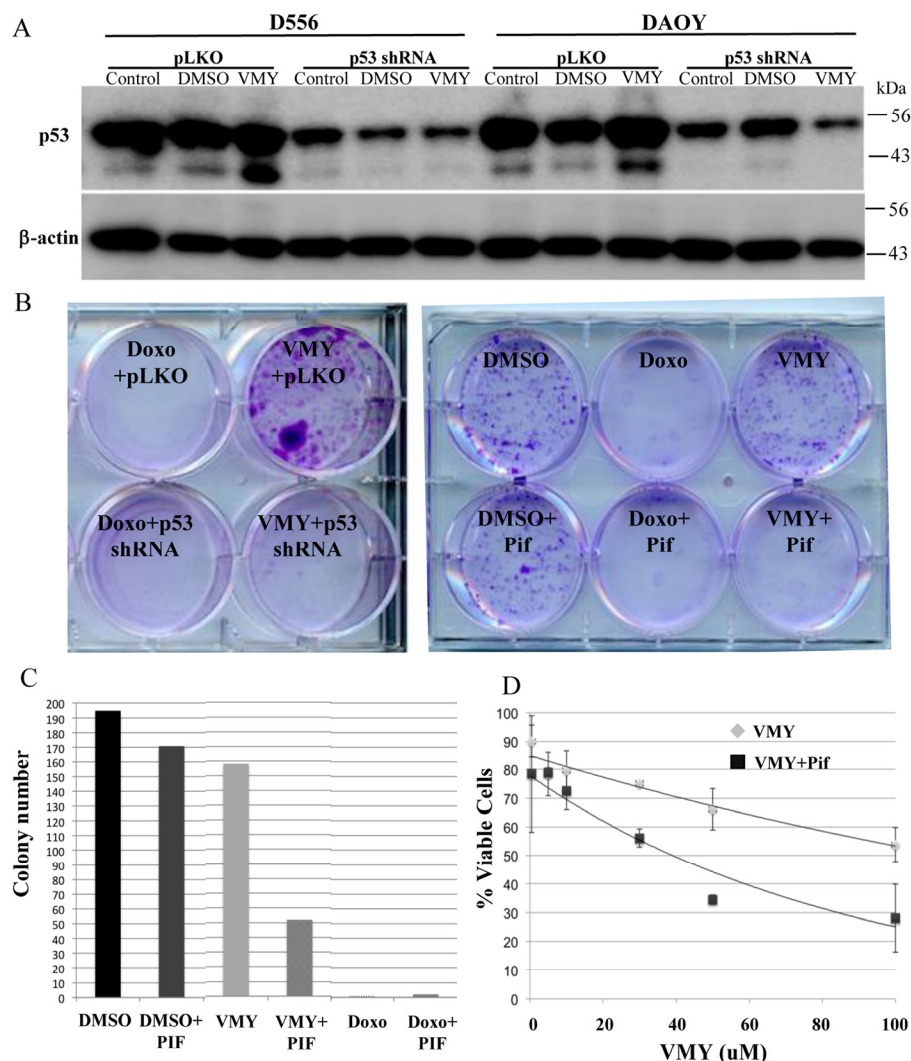


**Figure 6. Effects of silencing of p53 on cell survival.** (A) Genetic silencing of p53. D556 and DAOY cells were infected with p53siRNA or pLKO lentivirus'. The cells were left untreated or exposed for 18 hrs to DMSO or 30uM VMY as indicated, and western blots for p53 and  $\beta$ -actin were run. (B) The effects of p53shRNA knockdown (left) and Pifithrin (Pif, right) on cell viability were determined via colony forming assays. D556 cells were treated with DMSO, doxorubicin or VMY for 18 hrs. Fresh media was added and the cells cultured for an addition 3-5 days, followed by staining with crystal violet. (C) Quantification of the number of colonies in (B). (D) Dose response curves of D556 cells treated with VMY at the concentrations shown in the presence and absence of Pifithrin. The data are shown as average  $\pm$  standard deviation of N=3 separate experiments.

**Table 1. Top 25 genes altered in the presence of Pifithrin  $\alpha$  plus VMY vs. VMY alone.**

Pif + VMY vs. VMY			
Up-regulated	Fold	Down-regulated	Fold
EndoG	8.77809E+30	FIGF	-6.10476E+11
CIDEB	1.9687E+12	ANGPT4	-6.017072518
PRSS54	1299.03	GSK3A	-5.35
BIK	19.44	INCA1	-5.18
MAP3K9	18.19	TNFSF14	-4.01
ERBB3	15.17	GDF15	-4.01
BRAT1	7.48	HGF	-3.89
CISH	6.73	BIRC3	-3.41
FADD	6.73	LIF	-2.85
TP63	6.63	NTF3	-2.77
CBX6	6.23	DRD2	-2.75
SRC	5.98	SNCG	-2.67
CBX7	5.98	MAGEA9	-2.67
HDAC4	5.24	ZNF385D	-2.67
RASSF4	4.49	CRIP3	-2.67
TRPM8	4.49	TNFSF15	-2.45
ERBB2	4.06	NAP1L6	-2.45
AKT1	3.84	TENC1	-2.33
UNC5B	3.83	NRCAM	-2.23
TNFRSF10D	3.74	DNAJB7	-2.21
NLRP12-14	3.74	MAGEB2	-2.19
TP73	3.74	PPAPDC2	-2.14
ARHGEF18	3.55	PRSS12	-2.14
TNFRSF25	3.49	CFLAR	-2.07
FASTK	3.48	GADD45A	-2.07

### Loss of p53 in the presence of VMY alters calcium, p63 and p73 signaling pathways

In order to more completely define the mechanism underlying the paradoxical effect of p53 silencing, RNAseq next generation sequencing was performed on D556 cells treated with VMY in the presence or absence of Pif. RNA sequence analysis revealed an increase in expression of *calpain 12* in the VMY/Pif treated cells vs. VMY/DMSO control cells (Table 1). In addition, elevated expression of the transient receptor potential channel subfamily (*TRPM8*) gene was seen (Table 1), collectively suggesting that intracellular calcium signaling pathways were affected by p53 silencing. Dysregulation of the calcium signaling pathway downstream of stressors such as excitotoxicity can lead to necrotic cell death in neurons (reviewed in

[21, 22]), with one of the hallmarks of necrosis being Endo G induction and intranucleosomal DNA cleavage [22]. As both the pro-apoptosis regulatory genes p63 and p73 were induced by p53 silencing, as were possible downstream targets including Endo-G [23], the pro-apoptotic BH3-protein, BIK (Bcl-2-interacting killer) and CIDEB (cell death-inducing DFFA-like effector B), we assessed levels of late stage apoptosis and necrosis by flow cytometry, by gating for annexin V-positive/propidium iodide (PI)-positive cells. D556 cells were infected with either pLKO or p53shRNA as described above and treated for 18-hours with DMSO, 30uM VMY or 1uM doxorubicin, after which they were analyzed by flow cytometry as previously described [15]. While the annexin<sup>-</sup>/PI<sup>+</sup> fraction of cells was unaffected, the silencing of p53 increased the proportion of annexin V<sup>+</sup>/PI<sup>+</sup> cells following exposure to VMY or doxorubicin



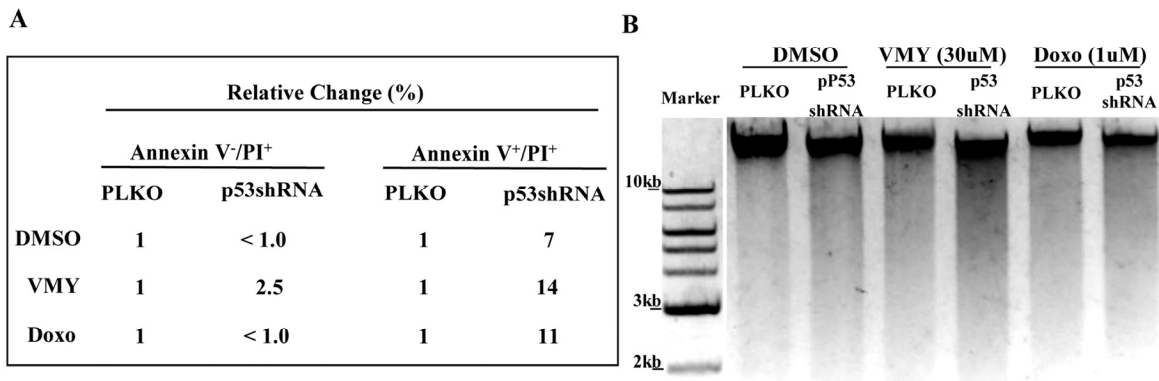


**Figure 7. Effects of p53 knockdown on apoptosis and DNA fragmentation in D556 cells.** (A) The proportion of cells undergoing apoptotic cell death as a result of p53 shRNA knockdown in D556 cells treated for 18 hrs with DMSO, VMY (30uM) or doxorubicin (1uM) as assessed using annexin V and propidium iodide (PI) staining and measured by flow cytometry. Data are shown as percent change in staining versus pLKO-control infected cells. (B) D556 cells were infected with pLKO or p53shRNA and treated with DMSO, VMY or doxorubicin for 18hrs. DNA fragmentation of nuclear DNA was assessed by ethidium bromide-agarose gel electrophoresis.

(Fig 7A). Finally, similar effects were seen using agarose gel electrophoresis assays where 18-hour treatment with VMY or doxorubicin plus p53shRNA resulted in enhanced DNA degradation, indicative of necrosis and apoptosis (Fig 7B).

Taken together, these experiments show that p53 protects against drug-induced cell death in medulloblastoma cells and its genetic- or chemical-suppression results in a significant increase in cell sensitivity to VMY and doxorubicin, an experimental and a clinical drug, respectively.

## DISCUSSION

Necrosis, apoptosis and autophagy are activated under a variety of cell stress conditions (see references [24, 25] among others), however, little is known about how these complex and partially overlapping mechanisms are induced in medulloblastoma cells. In addition, to date, there have been few publications exploring the effects in medulloblastoma cells of the synthetic modulation of p53 activity during exposure to chemotherapeutic drugs.

We have recently shown in prostate cancer cell lines as well as in primary prostate cancer cells established using our conditional cell reprogramming approach [26, 27], that the induction of p53 by VMY was a prerequisite for inducing both autophagy and apoptosis, and that silencing p53 effectively blocked cell death [15]. Additionally, our earlier studies on VMY's effects

on MB established that this experimental drug induced apoptosis and mitotic catastrophe *in vitro* [12]. Furthermore, while our *in vivo* studies showed that 20 mg/kg of VMY administered three times per week for more than four weeks was well tolerated and was effective at treating a mouse model of SHH-driven medulloblastoma [14], a detailed investigation into the mechanism of VMY-induced cell death, and the role that p53 may play had not been explored. We now show that in MB cells, VMY induces the relocalization of p53 into the nucleus, an accumulation of  $\gamma$ H2AX, a decrease in MDM2 protein levels and activation of non-survival macro-autophagy. Since the protein levels of key stress-related proteins were reduced by VMY, the possibility existed that components of the CAP-dependent protein translation pathway may be inhibited by VMY. MNK1 is a target of p38 and MAPK and acts to increase CAP-dependent translation through the phosphorylation of the elongation factor eIF4E [28]. 4E-BP1 is a negative regulator of translation and phosphorylation of 4E-BP1 by mTOR inhibits its repressor function. Thus, if VMY negatively regulated CAP-dependent translation, the phosphorylation levels of 4E-BP1 and pMNK1 would be expected to reduce, however VMY increased the levels of these proteins in both D556 and DAOY cells (S.W and C.A, unpublished data). Interestingly, rather than protecting against chemotherapeutic cell killing, the suppression of p53 through shRNA knockdown or chemical inhibition by Pifithrin- $\alpha$  resulted in a significant increase in cell death by either VMY or doxorubicin, suggesting that p53 acts as a chemoprotective protein in these primitive neuroectoderm-derived cancer cells.

Regarding its function in the neuroectoderm, p53 performs roles different to those found in other tissues. In the past decade a role for p53 has emerged in neuronal differentiation, axon guidance, neurite outgrowth and axonal regeneration [29, 30]. Analysis of p53-dependent transcriptional activation in normal development *in vivo* by using a lacZ reporter gene under the control of a p53-responsive promoter showed that p53 activity was maximal during neuronal differentiation and clustered in areas that showed little correlation with the apoptosis normally ongoing in the developing nervous system [31, 32]. Furthermore, other studies have shown that approximately one quarter of

p53-null mice developed exencephaly due to cellular overgrowth, rather than decreased apoptosis [33, 34].

The dependence of neurite outgrowth and elongation on p53 has also been shown in the developing cerebellum. Gaub et al., 2010 showed that acetylated p53 is required for neurite outgrowth in cerebellar granule cell progenitors. Conversely, the loss of the function acetyl p53 mutant (K-R) inhibits physiological neurite outgrowth in those cells [35]. In cultured rat cerebellar granule cells, Maruoka et al., 2011, showed a p53-mediated neuroprotective effect against glutathione depletion-induced oxidative stress [36].

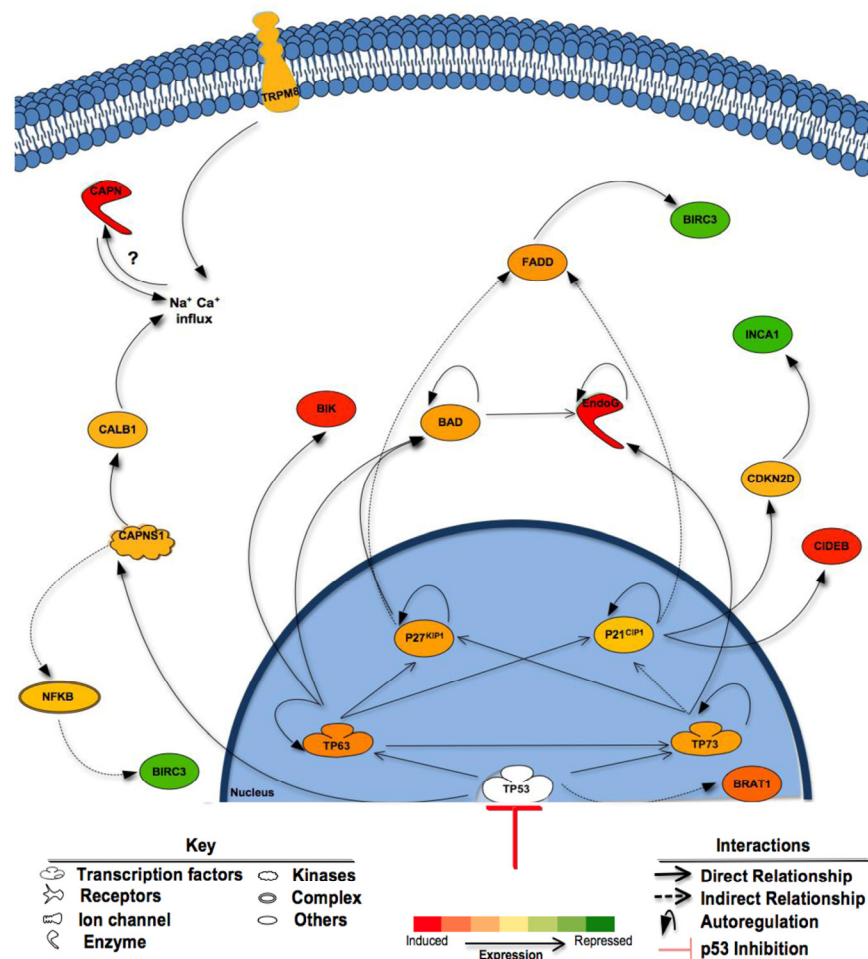


**Figure 8. Proposed mechanisms of enhanced cell death following inhibition of p53.** Shown are the effects of p53 suppression on components of cell death pathways in Pif + VMY vs. VMY treated D556 cells. p53 inhibition by Pifithrin resulted in the induction of *p63* and *p73* genes and subsequent enhanced cell death via apoptosis. Induction of the *p63* and *p73* genes leads to the activation of *p21<sup>CIP1</sup>* and *p27<sup>KIP1</sup>* both of which can indirectly trigger FADD, reducing the expression of BIRC3 (cIAP2). Induction of *p73* led to large increases in EndoG and CIDEB expression leading to DNA fragmentation while increased levels of *p63* induced apoptosis through BIRC3 and BIK, the latter of which along with TRPM8 can influence intracellular calcium levels. BAD; BCL2-Associated Agonist Of Cell Death, BIK; BCL2-Interacting Killer (Apoptosis-Inducing), BIRC3; baculoviral IAP repeat containing 3 (cIAP2), BRAT1; BRCA1-Associated ATM Activator 1, CAPN; Calpain, CALB1; Calbindin 1, CDKN2D; Cyclin-Dependent Kinase Inhibitor 2D (*p19<sup>Ink4D</sup>*), CIDEB; Cell Death-Inducing DFFA-Like Effector B, EndoG; Endonuclease G, FADD; Fas-Associated Via Death Domain, INCA1; Inhibitor Of CDK, Cyclin A1 Interacting Protein 1, NF-KappaB; Nuclear Factor Of Kappa Light Polypeptide Gene Enhancer In B-Cells, TRPM8, Transient receptor potential cation channel subfamily M member 8.

Further validation of the role for p53 in neurite outgrowth and neuronal differentiation and maturation comes from studies establishing p53 as a downstream target of neurotrophic receptors. Loss of function experiments of p53 via either gene silencing or dominant negative p53 proteins lacking transactivation capacity have been shown to block NGF-dependent neurite outgrowth and differentiation in PC-12 cells [6, 37]. Another neurotrophic factor, BDNF, has also been shown to stimulate p53 phosphorylation and transcriptional activation in primary cortical neurons [30]. Activation of signaling molecules downstream of NGF or BDNF that are known to induce p53 post-translational modifications and enhance its transcriptional activity has been reported, including ERK1 and ERK2, p38MAPK, JNK1-2 (c-Jun N-terminal kinases 1-2), cytoskeleton remodeling genes, such as GAP-43, the actin-binding protein Coronin 1b and the RAS family member Rab13 [6, 38].

Unresolved however is an actual role for p53 in the biology of human MB. Frequencies of *p53* mutations are low in primary MB but increase significantly in recurrences, and mutant p53 proteins and Myc may collaborate to drive aggressive disease [8]. Additionally, modifications of p53 function are required in *Myc*- [39, 40] but not *Smoothed*- based mouse models to drive MB. The genetic silencing of *p53* in mice with conditional deletion of the *BRCA2-interacting protein (BCCIP)* gene also resulted in MB [41]; however the resulting tumor formation was predicated upon the loss of the BCCIP knockdown cassette, which restored BCCIP expression in the neuroectoderm, supporting a role for p53 in neuronal genomic stability. Interestingly, p53 expression levels are lower in group 4 MB, due to the iso-dicentric (17)(p11.2) recombination events frequently seen in this group [10]. However, neither the levels of p53 expression nor its subcellular localization were reported following chemotherapy. It should be noted that etoposide induced p53 activity in D283, MEDI and D458 MB cell lines *in vitro* [42] and the p53 target miR-34a was able to reduce the viability in the p53-impaired MB cell line, MEB-Med8a [43], however the effects of silencing of p53 *per se* were not reported. Furthermore, docosahexaenoic acid and etoposide were found to reduce the levels of MDM2 in both p53-mutant DAOY cells as well as in p53-wildtype D283 cells [44] and we also observe decreases in MDM2 with VMY, along with rapid translocation of p53 into the nucleus. Collectively these published studies and our new data suggest that components of the p53 pathway remain intact in a variety of p53-mutant and p53-wild type MB cells.

It was therefore surprising that rather than causing chemotherapeutic resistance, the suppression of p53

function by either shRNA knockdown or Pif sensitized DAOY and D556 cells to both VMY and doxorubicin. Mechanistically, the induction of the *p63* and *p73* and their targeted genes by VMY in the Pif-treated cells was one of the most prominent features (Table 1 and Figure 8). These p53 family-member genes, and their various splice variants, play both similar and distinct roles in development as well as in cancer (reviewed in [45]) and can interact with each other with a high degree of complexity. There is abundant evidence that modulation of p53 function can influence the activity of p63 and p73 (reviewed in [46]) and conversely that p63 and p73 can influence p53 activity in adult neural precursor cells [47]. While the mechanism(s) by which the genetic knockdown or chemical suppression of p53 regulates *p63* and *p73* expression in MB cells has yet to be elucidated, our data suggest that the induction of *p63* and *p73* following p53 suppression fundamentally alters the pro-apoptotic machinery in MB cells (Fig 8). It is also unknown whether the increased sensitivity seen in the cell lines tested extends to a broader array of clinical samples or to the chemo-radiation interventions currently used for treating MB. However as both DAOY and D556 cells show similar sensitivities to p53 functional blockade, the possibility exists that at least a subset of the p53 mutations found in MB patients may not adversely impact p53-targeting regimens. Additional experiments assessing whether the p53 mutant proteins identified in recurrent MB exhibit similar responses to combined p53 suppression and exposure to VMY, doxorubicin or other drugs are clearly warranted.

## MATERIALS AND METHODS

**Cell lines and cell culture.** The human medulloblastoma (MB) cell lines D556 and DAOY were maintained in complete DMEM containing 10% FBS, L-glutamine, and 100 U/ml Penicillin-Streptomycin as previously described [12]. DNA STR fingerprint analyses were performed on both cell lines as a quality control measure. The DAOY data matched the ATCC database for this line, while early and late passage D556 cultures were compared with no significant changes observed and no matches with the available STR database (not shown).

**Cell viability and growth.** Cell viability was determined using trypan blue dye exclusion and viable and total cell counting using a hemocytometer as previously described [11, 12, 15].

**Colony forming assays.** A total of 1000 cells were plated in 6 well plates. Cells were allowed to adhere for 24 hrs before treatment, at which point they were

treated with VMY or Doxorubicin for 18 hrs. The media was changed after 18hrs and the plates were incubated in the absence of drug for 3-5 days to reach 80% confluency in the negative control wells. Cells were washed with PBS, fixed with 10% neutral buffered formalin solution for 15-30 minutes and stained with 0.5% (w/v) crystal violet for 30-60 minutes. The crystal violet was aspirated, cells were washed with PBS and dried for one hour before counting.

Flow cytometry. The prostate cells were fixed and stained with 20ug/ml propidium iodide (PI) and 5 U RNase A, and the DNA content and subG1 DNA fragmentation was measured using a FACStar Plus system (Becton-Dickson, Franklin Lakes, NJ) as previously described [11, 12]. Cellular apoptosis was also assessed by APC-Annexin V antibody (Biolegend, San Diego, CA) staining immediately after treatment with VMY and analyzed using FACStar Plus dual laser FACS sort system (Becton-Dickson, Franklin Lakes, NJ) as previously described by us [11, 12, 48, 49].

Immunoblotting. Protein extracts were prepared and separated on 4-20% Tris-glycine gels and electroblotted onto PVDF membranes as previously described [11, 12, 50]. Protein levels were assessed using antibodies against p53 (Millipore, Bellerica, MA #05-224), p-ATM (Cell Signaling, Danvers, MA #5883P), p-Chk2 (Cell Signaling, Danvers, MA #2661P), p-Chk1 (Cell Signaling, Danvers, MA #2348P), p38 (Cell Signaling, Danvers, MA #8690), histone  $\gamma$ -H2AX (Cell Signaling, Danvers, MA #7631), p-histone  $\gamma$ H2AX (Cell Signaling, Danvers, MA #9718P), p-BRCA1 (Ser1524) (Cell Signaling, Danvers, MA #9009P), p-P38 MAPK (Cell Signaling, Danvers, MA #9216S), mTOR (Cell Signaling, Danvers, MA #2983), p-ATR (Cell Signaling, Danvers, MA #2853P), p-p53 (Cell Signaling, Danvers, MA #9286P), p-MNK1 (cell signaling, #2111S), p-4E-BP1 (Cell Signaling, Danvers, MA #2855S), MDM2 (Santa Cruz Biotechnology, #sc-965),  $\beta$ -actin (Cell Signaling, Danvers, MA #4967). Densitometry was performed using ImageJ analysis software (NIH, Bethesda, MD) as previously described [11, 12, 50].

Immunofluorescent imaging. Cells were seeded on glass coverslips and treated with DMSO or VMY for 4 or 18 hrs. Cells were washed with PBS and fixed in 10% formalin for 10 min. The coverslips were washed three times with PBS, the cells were permeabilized with 0.1% Triton X-100 and washed three times with PBS. The samples were blocked with 1% BSA for 20 minutes and washed an additional three times in PBS. The cells were exposed to anti-p53 (1:150, Millipore #05-224) or anti- $\gamma$ H2AX (1:150, Cell Signaling #7631) antibodies for 1

hr at room temperature. The slides were washed with PBS an additional three times and stained with the secondary antibody Alexa Fluor goat 488 anti-mouse (1:150, Life Technologies, A-10667) for 30 min at room temperature. Slides were then counter-stained with DAPI for 5 min. The coverslips were mounted onto glass slides with Tris-buffered fluoro-gel (Electron Microscopy Sciences). Confocal microscopy was performed on a Zeiss (Thornwood, NY) LSM510 Meta microscope using a 40x lens.

LC3-GFP. LC3 translocation was detected using the green fluorescent protein (GFP)-fused LC3 construct that was generously donated by Dr Robert Clarke [51]. Briefly, cells were seeded in 6 well plates containing glass coverslips and allowed to attach overnight. The LC3-GFP expression plasmid (14ug) was transfected using Lipofectamine LTX reagent (Life Technologies, Carlsbad, CA #15338-100) as previously described by us [15]. 24 hours after transfection, the cells were treated with VMY or vehicle. After 18 hours, the coverslips with attached cells were stained with DAPI and rinsed 3 times with PBS and the coverslips mounted. Imaging was performed by confocal microscopy as previously described [12, 15].

Autophagy inhibitors. For autophagy inhibition, 3-methyladenine (3-MA) (Sigma-Aldrich, St Louis, MO #M921) was used at 5mM and chloroquine diphosphate (CQ) (Sigma-Aldrich, St Louis, MO #C6628) was used at 50  $\mu$ M as previously described [15]. Cells were exposed to these inhibitors for 20 minutes prior to treatment with either DMSO or VMY [15].

p53 expression and shRNA knockdown. For lentivirus knockdown experiments, the p53shRNA and pLKO vectors were purchased commercially (Vector Biolabs, Philadelphia, PA, #1854) and used as described by the manufacturer as previously described [15]. Briefly, 293T cells (ATCC, Manassas, VA) were cotransfected with shRNA constructs along with the pHR'8.2 $\Delta$ R and pCMV-VSV-G helper constructs. After 24 hours, the media was changed and the virus-containing media was harvested after an additional 24 hours of incubation. The MB cells were seeded at 30% confluency and viral infections were performed for 72 hours prior to treatment with VMY or DMSO. Efficiency of the knockdown was monitored by p53 immunoblotting and quantification by ImageJ as previously described [15, 52, 53].

Chemical inhibition of p53. For chemical inhibition of p53, 30uM Pifithrin- $\alpha$  (Sigma-Aldrich, St Louis, MO #P4359) was added one hour prior to treatment with VMY, doxorubicin or DMSO.



**DNA fragmentation.** D556 cells were infected with pLKO or p53shRNA virus's for 72 hrs prior to treatment with VMY or DMSO. Doxorubicin was used as a positive control. The genomic DNA was isolated after 18 hr treatment with VMY or doxorubicin using the DNeasy blood and tissue kit (Qiagen, MD #69506). 500ng of DNA was run on 1% agarose gel containing ethidium bromide with the electrophoresis carried out at 100V for one hour.

**RNAseq and pathway analyses.** Total RNA was extracted from D556 cells treated with Pif and VMY as described above using an RNeasy Plus Mini Kit (Qiagen, MD, #74134) and submitted to Orogenetics Corporation (Norcross, GA USA) for RNA-Seq assays. Sequencing was performed on the Illumina HiSeq 2500 (20 million reads, Rapid run, Illumina, CA USA) with chemistry v1.0 and using the 2×106bp paired-end read mode and original chemistry from Illumina according to the manufacturer's instructions. The initial data analysis was started directly on the HiSeq 2500 System during the run. The HiSeq Control Software 2.0.5 in combination with RTA 1.17.20.0 (real time analysis) performed the initial image analysis and base calling. Quality control (QC) was performed using FastQC software. All the samples passed the "Basic Statistics", "Per Base Sequence Quality", "Per Sequence Quality Scores", "Per Base N Content", and "Sequence Length Distribution". No specific filtering was done for the samples. The final FASTQ files comprising the sequence information which was used for all subsequent bioinformatics analyses. Sequences were demultiplexed according to the 6bp index code with 1 mismatch allowed. After QC, Tophat2 was used for the alignment, and BAM files were obtained. Partek Genomics Suite (6.6 version 6.12.0713 software (Partek Inc.) was utilized to calculate RPKM as normalization, and fold changes were calculated based on the RPKM results. The pathways analysis was performed through the use of QIAGEN's Ingenuity<sup>®</sup> Pathway Analysis (Qiagen, Redwood City, CA).

## ACKNOWLEDGEMENTS

Cell cycle analyses were performed in the Lombardi Comprehensive Cancer Center's Flow Cytometry Shared Resource, microscopy was performed in the Lombardi Comprehensive Cancer Center's Microscopy and Imaging Shared Resource, the DNA fingerprint analyses were done through the Lombardi Comprehensive Cancer Center's Tissue Culture Shared Resource and the RNAseq was performed through the Lombardi Comprehensive Cancer Center's Genomics and Epigenomics Shared Resource.

## Funding

Funding was provided by; ABCC (Albanese), R01CA193698 (Avantaggiati) and NIH P30 CA51008-18 (Weiner). This work was also supported by the Paul Calabresi Career Development Award for Clinical Oncology (K12, Karam) an American Cancer Society Institutional Grant (Karam) and a Howard Hughes Medical Institute University Grant (Waye). We thank Milton Brown for supplying VMY-1-103.

## Conflict of interest statement

Georgetown University has submitted a patent application on VMY-1-103 where V.Y. is an inventor.

## REFERENCES

1. Samkari A, White JC and Packer RJ. Medulloblastoma: toward biologically based management. *Semin Pediatr Neurol.* 2015; 22:6-13.
2. Ning MS, Perkins SM, Dewees T and Shinohara ET. Evidence of high mortality in long term survivors of childhood medulloblastoma. *J Neurooncol.* 2015; 122:321-327.
3. Soussi T and Wiman KG. TP53: an oncogene in disguise. *Cell Death Differ.* 2015; 22:1239-1249.
4. Muller PA and Vousden KH. Mutant p53 in cancer: new functions and therapeutic opportunities. *Cancer Cell.* 2014; 25:304-317.
5. Quadrato G and Di Giovanni S. Gatekeeper between quiescence and differentiation: p53 in axonal outgrowth and neurogenesis. *Int Rev Neurobiol.* 2012; 105:71-89.
6. Di Giovanni S, Knights CD, Rao M, Yakovlev A, Beers J, Catania J, Avantaggiati ML and Faden AI. The tumor suppressor protein p53 is required for neurite outgrowth and axon regeneration. *Embo J.* 2006; 25:4084-4096.
7. Pfaff E, Remke M, Sturm D, Benner A, Witt H, Milde T, von Bueren AO, Wittmann A, Schottler A, Jorch N, Graf N, Kulozik AE, Witt O, Scheurlen W, von Deimling A, Rutkowski S, et al. TP53 mutation is frequently associated with CTNNB1 mutation or MYCN amplification and is compatible with long-term survival in medulloblastoma. *J Clin Oncol.* 2010; 28:5188-5196.
8. Hill RM, Kuijper S, Lindsey JC, Petrie K, Schwalbe EC, Barker K, Boulton JK, Williamson D, Ahmad Z, Hallsworth A, Ryan SL, Poon E, Robinson SP, Ruddle R, Raynaud FI, Howell L, et al. Combined MYC and P53 defects emerge at medulloblastoma relapse and define rapidly progressive, therapeutically targetable disease. *Cancer Cell.* 2015; 27:72-84.
9. Rausch T, Jones DT, Zapatka M, Stutz AM, Zichner T, Weischenfeldt J, Jager N, Remke M, Shih D, Northcott PA, Pfaff E, Tica J, Wang Q, Massimi L, Witt H, Bender S, et al. Genome sequencing of pediatric medulloblastoma links catastrophic DNA rearrangements with TP53 mutations. *Cell.* 2012; 148:59-71.
10. Bien-Willner GA and Mitra RD. Mutation and expression analysis in medulloblastoma yields prognostic variants and a putative mechanism of disease for i17q tumors. *Acta Neuropathol Commun.* 2014; 2:74.



11. Ringer L, Yenugonda VM, Ghosh A, Divito K, Trabosh V, Patel Y, Brophy A, Grindrod S, Lisanti MP, Rosenthal D, Brown ML, Avantaggiati ML, Rodriguez O and Albanese C. VMY-1-103, a dansylated analog of purvalanol B, induces caspase-3-dependent apoptosis in LNCaP prostate cancer cells. *Cancer Biol Ther.* 2010; 10:320-325.
12. Ringer L, Sirajuddin P, Heckler M, Ghosh A, Suprynowicz F, Yenugonda VM, Brown ML, Toretzky JA, Uren A, Lee Y, MacDonald TJ, Rodriguez O, Glazer RI, Schlegel R and Albanese C. VMY-1-103 is a novel CDK inhibitor that disrupts chromosome organization and delays metaphase progression in medulloblastoma cells. *Cancer Biol Ther.* 2011; 12:818-826.
13. Smahi A, Courtois G, Vabres P, Yamaoka S, Solange H, Munnich A, Israël A, Heiss NS, Klauck SKP and Wiemann Sea. Genomic rearrangement in NEMO impairs NF- $\kappa$ B activation and is a cause of incontinentia pigmenti (IP). *Nature.* 2000; 405:466-472.
14. Sirajuddin P, Das S, Ringer L, Rodriguez O, Sivakumar A, Lee Y, Uren A, Fricke S, Rood B, Ozcan A, Wang SS, Karam S, Yenugonda VM, Salinas P, Petricoin EF, 3rd, Lisanti MP, et al. Quantifying the CDK inhibitor VMY-1-103's activity and tissue levels in an in vivo tumor model by LC-MS/MS and by MRI. *Cell Cycle.* 2012; 11:3801-3809.
15. Ringer L, Sirajuddin P, Tricoli L, Wayne S, Parasido E, Lee RJ, Feldman A, Wu C-L, Dritschilo A, Lynch J, Schlegel R, Rodriguez O, Pestell RG, Avantaggiati ML and Albanese C. The Induction of the p53 Tumor Suppressor Protein Bridges the Apoptotic and Autophagic Signaling Pathways to Regulate Cell Death in Prostate Cancer Cells. *Oncotarget.* 2014; 5:10678-10691.
16. Garufi A, Pucci D, D'Orazi V, Cirone M, Bossi G, Avantaggiati ML and D'Orazi G. Degradation of mutant p53H175 protein by Zn(II) through autophagy. *Cell Death Dis.* 2014; 5:e1271.
17. Li LY, Luo X and Wang X. Endonuclease G is an apoptotic DNase when released from mitochondria. *Nature.* 2001; 412:95-99.
18. Petrucci LA, Pettersson F, Del Rincon SV, Guilbert C, Licht JD and Miller WH, Jr. Expression of leukemia-associated fusion proteins increases sensitivity to histone deacetylase inhibitor-induced DNA damage and apoptosis. *Mol Cancer Ther.* 2013; 12:1591-1604.
19. Kang R, Zeh HJ, Lotze MT and Tang D. The Beclin 1 network regulates autophagy and apoptosis. *Cell Death Differ.* 2011; 18:571-580.
20. Raffel C, Thomas GA, Tishler DM, Lassoff S and Allen JC. Absence of p53 mutations in childhood central nervous system primitive neuroectodermal tumors. *Neurosurgery.* 1993; 33:301-305; discussion 305-306.
21. Hara MR and Snyder SH. Cell signaling and neuronal death. *Annu Rev Pharmacol Toxicol.* 2007; 47:117-141.
22. Fujikawa DG. The role of excitotoxic programmed necrosis in acute brain injury. *Comput Struct Biotechnol J.* 2015; 13:212-221.
23. Kitagawa K and Niikura Y. Caspase-independent mitotic death (CIMD). *Cell Cycle.* 2008; 7:1001-1005.
24. Galluzzi L, Vitale I, Abrams JM, Alnemri ES, Baehrecke EH, Blagosklonny MV, Dawson TM, Dawson VL, El-Deiry WS, Fulda S, Gottlieb E, Green DR, Hengartner MO, Kepp O, Knight RA, Kumar S, et al. Molecular definitions of cell death subroutines: recommendations of the Nomenclature Committee on Cell Death 2012. *Cell Death Differ.* 2012; 19:107-120.
25. Klionsky DJ, Abdalla FC, Abeliovich H, Abraham RT, Acevedo-Arozena A, Adeli K, Agholme L, Agnello M, Agostinis P, Aguirre-Ghiso JA, Ahn HJ, Ait-Mohamed O, Ait-Si-Ali S, Akematsu T, Akira S, Al-Younes HM, et al. Guidelines for the use and interpretation of assays for monitoring autophagy. *Autophagy.* 2012; 8:445-544.
26. Liu X, Ory V, Chapman S, Yuan H, Albanese C, Kallakury B, Timofeeva O, Nealon C, Dalic A, Simic V, Haddad B, Rhim J, Dritschilo A, Riegel A, McBride A and Schlegel R. ROCK inhibitor and feeder cells induce the conditional reprogramming of epithelial cells. *American Journal of Pathology.* 2012; 180:590-607.
27. Palechor-Ceron N, Suprynowicz FA, Upadhyay G, Dakic A, Minas T, Simic V, Johnson M, Albanese C, Schlegel R and Liu X. Radiation Induces Diffusible Feeder Cell Factor(s) That Cooperate with ROCK Inhibitor to Conditionally Reprogram and Immortalize Epithelial Cells. *Am J Pathol.* 2013; 183:1862-1870.
28. Bhat M, Robichaud N, Hulea L, Sonenberg N, Pelletier J and Topisirovic I. Targeting the translation machinery in cancer. *Nat Rev Drug Discov.* 2015; 14:261-278.
29. Arakawa H. p53, apoptosis and axon-guidance molecules. *Cell Death Differ.* 2005; 12:1057-1065.
30. Tedeschi A and Di Giovanni S. The non-apoptotic role of p53 in neuronal biology: enlightening the dark side of the moon. *EMBO Rep.* 2009; 10:576-583.
31. Komarova EA, Chernov MV, Franks R, Wang K, Armin G, Zelnick CR, Chin DM, Bacus SS, Stark GR and Gudkov AV. Transgenic mice with p53-responsive lacZ: p53 activity varies dramatically during normal development and determines radiation and drug sensitivity in vivo. *Embo J.* 1997; 16:1391-1400.
32. Gottlieb E, Haffner R, King A, Asher G, Gruss P, Lonai P and Oren M. Transgenic mouse model for studying the transcriptional activity of the p53 protein: age- and tissue-dependent changes in radiation-induced activation during embryogenesis. *Embo J.* 1997; 16:1381-1390.
33. Sah VP, Attardi LD, Mulligan GJ, Williams BO, Bronson RT and Jacks T. A subset of p53-deficient embryos exhibit exencephaly. *Nat Genet.* 1995; 10:175-180.
34. Armstrong JF, Kaufman MH, Harrison DJ and Clarke AR. High-frequency developmental abnormalities in p53-deficient mice. *Curr Biol.* 1995; 5:931-936.
35. Gaub P, Tedeschi A, Puttagunta R, Nguyen T, Schmandke A and Di Giovanni S. HDAC inhibition promotes neuronal outgrowth and counteracts growth cone collapse through CBP/p300 and P/CAF-dependent p53 acetylation. *Cell Death Differ.* 2010; 17(9):1392-1408.
36. Maruoka H, Sasaya H, Sugihara K, Shimoke K and Ikeuchi T. Low-molecular-weight compounds having neurotrophic activity in cultured PC12 cells and neurons. *J Biochem.* 2011; 150:473-475.
37. Knights CD, Catania J, Di Giovanni S, Muratoglu S, Perez R, Swartzbeck A, Quong AA, Zhang X, Beerman T, Pestell RG and Avantaggiati ML. Distinct p53 acetylation cassettes differentially influence gene-expression patterns and cell fate. *J Cell Biol.* 2006; 173:533-544.
38. Tedeschi A, Nguyen T, Puttagunta R, Gaub P and Di Giovanni S. A p53-CBP/p300 transcription module is required for GAP-43 expression, axon outgrowth, and regeneration. *Cell Death Differ.* 2009; 16:543-554.

39. Kawauchi D, Robinson G, Uziel T, Gibson P, Rehg J, Gao C, Finkelstein D, Qu C, Pounds S, Ellison DW, Gilbertson RJ and Roussel MF. A mouse model of the most aggressive subgroup of human medulloblastoma. *Cancer Cell*. 2012; 21:168-180.
40. Pei Y, Moore CE, Wang J, Tewari AK, Eroshkin A, Cho YJ, Witt H, Korshunov A, Read TA, Sun JL, Schmitt EM, Miller CR, Buckley AF, McLendon RE, Westbrook TF, Northcott PA, et al. An animal model of MYC-driven medulloblastoma. *Cancer Cell*. 2012; 21:155-167.
41. Huang YY, Dai L, Gaines D, Droz-Rosario R, Lu H, Liu J and Shen Z. BCCIP suppresses tumor initiation but is required for tumor progression. *Cancer Res*. 2013; 73:7122-7133.
42. Meley D, Spiller DG, White MR, McDowell H, Pizer B and See V. p53-mediated delayed NF-kappaB activity enhances etoposide-induced cell death in medulloblastoma. *Cell Death Dis*. 2010; 1:e41.
43. Fan YN, Meley D, Pizer B and See V. Mir-34a mimics are potential therapeutic agents for p53-mutated and chemo-resistant brain tumour cells. *PLoS One*. 2014; 9:e108514.
44. Wang F, Bhat K, Doucette M, Zhou S, Gu Y, Law B, Liu X, Wong ET, Kang JX, Hsieh TC, Qian SY and Wu E. Docosahexaenoic acid (DHA) sensitizes brain tumor cells to etoposide-induced apoptosis. *Curr Mol Med*. 2011; 11:503-511.
45. Moll UM and Slade N. p63 and p73: roles in development and tumor formation. *Mol Cancer Res*. 2004; 2:371-386.
46. Pflaum J, Schlosser S and Muller M. p53 Family and Cellular Stress Responses in Cancer. *Front Oncol*. 2014; 4:285.
47. Fatt MP, Cancino GI, Miller FD and Kaplan DR. p63 and p73 coordinate p53 function to determine the balance between survival, cell death, and senescence in adult neural precursor cells. *Cell Death Differ*. 2014; 21:1546-1559.
48. Albanese C, D'Amico M, Reutens AT, Fu M, Watanabe G, Lee RJ, Kitsis RN, Henglein B, Avantaggiati M, Somasundaram K, Thimmapaya B and Pestell RG. Activation of the *cyclin D1* gene by the E1A-associated protein p300 through AP-1 inhibits cellular apoptosis. *J Biol Chem*. 1999; 274:34186-34195.
49. Albanese C, Wu K, D'Amico M, Jarrett C, Joyce D, Hughes J, Hult J, Sakamaki T, Fu M, Ben-Ze'ev A, Bromberg JF, Lamberti C, Verma U, Gaynor RB, Byers SW and Pestell RG. IKKalpha Regulates Mitogenic Signaling through Transcriptional Induction of Cyclin D1 via Tcf. *Mol Biol Cell*. 2003; 14:585-599.
50. Rodriguez OC, Choudhury S, Kolukula V, Vietsch EE, Catania J, Preet A, Reynoso K, Bargonetti J, Wellstein A, Albanese C and Avantaggiati ML. Dietary downregulation of mutant p53 levels via glucose restriction: mechanisms and implications for tumor therapy. *Cell Cycle*. 2013; 11:4436-4446.
51. Schwartz-Roberts JL, Shajahan AN, Cook KL, Warri A, Abu-Asab M and Clarke R. GX15-070 (obatoclax) induces apoptosis and inhibits cathepsin D- and L-mediated autophagosomal lysis in antiestrogen-resistant breast cancer cells. *Mol Cancer Ther*. 2013; 12:448-459.
52. Perez RE, Knights CD, Sahu G, Catania J, Kolukula VK, Stoler D, Graessmann A, Ogryzko V, Pishvaian M, Albanese C and Avantaggiati ML. Restoration of DNA-binding and growth-suppressive activity of mutant forms of p53 via a PCAF-mediated acetylation pathway. *J Cell Physiol*. 2010; 225:394-405.
53. Catalina-Rodriguez O, Kolukula VK, Tomita Y, Preet A, Palmieri F, Wellstein A, Byers S, Giaccia AJ, Glasgow E, Albanese C and Avantaggiati ML. The mitochondrial citrate transporter, CIC, is essential for mitochondrial homeostasis. *Oncotarget*. 2012; 3:1220-1235.

**Kinase overexpressing cancers responsive to drug withdrawal****Amit Dipak Amin, Soumya S. Rajan, and Jonathan H. Schatz**

Aberrant protein kinase activity promotes tumor survival and proliferation, and targeted kinase inhibitors that halt growth and promote apoptosis demonstrate some cancers are truly kinase addicted. Clinically, this is best exemplified by chronic myeloid leukemia (CML), driven by the fusion kinase BCR-ABL, where tyrosine kinase inhibitor (TKI) therapy can control the disease for years, perhaps indefinitely in many patients. For other cancers, however, the success of kinase inhibition has been more modest. Despite great strides in drug design and delivery, resistance invariably develops, typically limiting median progression free survival (PFS) to a period of months. Development of new-generation inhibitors therefore has focused on increasing potency, overcoming resistance-conferring mutations to the drug target, and hitting parallel signaling pathways that bypass the target altogether. While sequential treatments and/or combination cocktails to circumvent resistance may work in some cases, concerns arise regarding toxicity and cost, prompting exploration of innovative new strategies to prolong PFS. Two recent studies in different cancers propose an alternative with a potential to increase the duration of tumor control by several already approved TKIs.

Approximately 70% anaplastic large cell lymphoma (ALCL) cases are driven by the constitutively activated fusion kinase NPM-ALK [1]. To investigate resistance mechanisms, our laboratory grew patient-derived NPM-ALK-driven cell lines in one of two FDA approved ALK TKIs, crizotinib or ceritinib, at increasing concentrations. Resistance reliably arose due to overexpression of NPM-ALK even if resistance-conferring mutations also began to arise. Strikingly, characterization of resistant phenotypes showed viability of these cells was actually stimulated by – indeed required – continued presence of ALK TKI, as drug withdrawal rapidly induced apoptosis. Concomitantly we observed massive ALK activation, suggesting over-activation provides as much of a fitness deficit as inhibition [2]. These results echo the findings of a prominent study investigating mutant-BRAF inhibition with vemurafenib in melanoma, where resistance also arose due to target overexpression [3]. As in our study, resistant cells underwent apoptosis in response to inhibitor withdrawal. Oncogene over-

expression in both reports therefore promoted a dual phenotype of drug resistance and dependence.

Both studies demonstrate potential therapeutic exploitation of the paradoxically toxic response of resistant-dependent cells to drug withdrawal. Xenografted resistant cells in both reports underwent apoptosis leading to tumor regressions upon discontinuation of drug dosing to host animals. After time tumors resumed growth, but sampling showed drug-target expression had returned to baseline – a requirement for their growth without inhibitor. At the same time dependence went away, so did resistance, as re-initiation of inhibitor dosing to host animals led to new rounds of tumor regressions. This suggested cycling of drug through discontinuous dosing could forestall onset of fatal resistance, and was explored in both reports, but especially in the melanoma models [2, 3]. Here both pre-scheduled and individualized intermittent dosing strategies greatly prolonged tumor control compared to continuous drug administration. Patients at risk of developing resistance due to up-regulation of some oncogenes may therefore benefit from intermittent dosing, a strategy carrying both low cost and low toxicity.

A randomized phase 2 trial comparing intermittent vs. continuous inhibitor dosing in melanoma already is enrolling patients (NCT02196181), and one is in planning for ALK+ ALCL. More preclinical assessment, however, also is needed in these and other cancers. Supporting the approach, drug holidays already may be employed to counter toxicity, and some second remissions to the ALK TKI crizotinib have been reported in lung cancer patients whose tumors were previously resistant [4, 5].

Great care must be taken, when determining appropriate timing of drug administration and withdrawal with such strategies, as the onset of resistance may be unpredictable, and drug interruption or re-initiation too early could exacerbate the onset of other resistance pathways [6]. An intriguing alternative, however, is identifying the specific mechanisms by which over-activity of particular oncogenes promote toxicity, and then pharmacologically inducing them as either a direct means of cellular toxicity or to prime the cells for other therapies. Indeed, a recent study showed pharmacological induction of SYK hyper-activation caused

BCR-ABL+ acute lymphoblastic leukemia (ALL) cell death [7]. Targeted inhibition of several signaling pathway targets downstream failed to rescue resistant cells from NPM-ALK overdose in our systems (unpublished observations), but unbiased approaches are ongoing to determine the mechanisms.

Finally, it is important to keep in mind that intermittent dosing is not a cure and drug cycling eventually will prove futile. Such strategy gives a patient more time, however, delaying the need to change inhibitors, initiate combination cocktails, or a move to traditional therapies like chemotherapy or radiation, all of which may be significantly more toxic. In the ever-expanding arsenal of weapons against cancer, strategies exploiting oncogene overdose appear to hold promise, and in the case of intermittent dosing don't even require development of new drugs.

## REFERENCES

1. Pearson JD, et al. J Signal Transduct. 2012; 2012:123253.
2. Amin AD, et al. Cancer research. 2015; 75:2916-2927.
3. Das Thakur M, et al. Nature. 2013; 494:251-255.
4. Browning ET, et al. Journal of thoracic oncology: official publication of the International Association for the Study of Lung Cancer. 2013; 8:e21.
5. Schrödl K, et al. Respiration; international review of thoracic diseases. 2014; 88:262-264.
6. Foo J, et al. Journal of thoracic oncology: official publication of the International Association for the Study of Lung Cancer. 2012; 7:1583-1593.
7. Chen Z, et al. Nature. 2015; 521:357-361.

**Jonathan H. Schatz**: Department of Medicine, Division of Hematology-Oncology, Sylvester Comprehensive Cancer Center, University of Miami Miller School of Medicine, Miami, FL, 33136

**Correspondence:** Jonathan H. Schatz

**Email:** [jschatz@miami.edu](mailto:jschatz@miami.edu)

**Keywords:** *oncogene overdose, ALK, BRAF, cancer therapeutics*

**Received:** September 27, 2015

**Published:** October 22, 2015

## Sonic Hedgehog in SCLC

Mikko O. Laukkanen, J Silvio Gutkind, and Maria Domenica Castellone

The Hedgehog (Hh) signal transduction pathway has been discovered as a central regulator of embryonic development, tissue maintenance and repair [1]. Moreover, several recent evidences have highlighted its key function in tumorigenesis [2]. In some familial cancers, such as basal cell carcinoma and medulloblastoma, Hh pathway activation represents the initial tumorigenic event, whereas in other human malignancies, including gastrointestinal, lung, brain, breast and prostate cancers, deregulation of Hh signaling occurs during tumor progression and participates in tumor maintenance. Clinical trials using molecular inhibitors targeting Hh pathway components, in particular the Smo receptor, have often yielded limited clinical benefits unless they are used for the treatment of tumors harboring defined genetic mutations inactivating tumor suppressors (e.g. Ptch receptor) or activating oncogenes (e.g. Smo receptor, Gli transcription factor, Shh ligand) within the Hh pathway. In these specific cases, promising results led to FDA approval of Vismodegig (GDC0449, Genentech), a Smo inhibitor, in the treatment of basal cell carcinoma and medulloblastoma [3]. Notwithstanding, several clinical studies using the same compound in tumors exhibiting Hh overactivity without identified Hh mutations have resulted in discouraging outcome and discontinuation of the trials because of lack of objective response [2]. These unexpected results have been related to drug resistance due to the presence of activating mutations or genetic alterations driving Hh signaling bypassing Smo function. These evidences emphasize the need for further characterization of Hh signaling in tumorigenesis and for a more precise identification of the interaction between Hh and other signaling pathways involved in tumor development and response to therapy.

Small cell lung carcinoma (SCLC) is a very aggressive cancer with extremely poor prognosis, whose genetic events, such as oncogenic driver mutations, have not been defined yet. Classified as neuroendocrine tumors, SCLCs secrete factors of the bombesin (BN)/ Gastrin-Releasing Peptide (GRP) family and express their cognate receptors activating an autocrine loop that increases proliferation and survival [4]. The positivity for this ligand/receptor pair is considered to be a marker

of aggressiveness and unfavorable tumor outcome. Recent reports have described the Hh pathway as a key regulator of lung embryogenesis and SCLCs maintenance, although no mutations in Hh signal transduction pathway molecules have been identified, suggesting a ligand-dependent pathway activation [5, 6]. The ligand-dependent activation of Hh signaling can occur in an autocrine manner, where cancer cells express both the ligand and the receptor, or in a paracrine manner, where ligand produced from cancer cells is activating Hh signaling in tumor stroma or vice versa.

To characterize Hh function in SCLC and to evaluate the therapeutic potential of Hh inhibitors in this cancer, we have investigated the possibility of a direct interaction between Hh and BN/GRPR signaling pathways. According to our initial observations, Cyclopamine, an inhibitor of Smo, attenuated BN induced cell proliferation. In support of these data, RNA interference for Sonic Hedgehog (Shh), upstream activator of Smo, reduced BN stimulated growth, matrigel spreading and soft agar colony formation [7]. Surprisingly, when testing the activation of Gli transcription factor upon BN stimulation, we revealed the existence of a direct crosstalk between the two pathways. In order to dissect the signaling molecular events mediating this interaction, we discovered that BN, through its G protein coupled receptor (GRPR) linked to  $G\alpha_q/G\alpha_{12/13}$  large G proteins, and their downstream target, the Rho small GTPase, was able to stimulate NF $\kappa$ B-mediated transcription of Shh, thus initiating an autocrine signaling loop that links BN/GRPR pathway to production of Shh ligand, and the autocrine Hh signaling activation (Figure 1, left panel) [7].

Our findings, besides shedding new light on the mechanisms of Hh signaling activation in SCLC, may suggest a more general application for other BN/GRPR positive tumors over-expressing Shh pathway, such as pancreatic cancer, neuroblastomas and glioblastomas. Interestingly, use of Hh inhibitors alone in these tumors has not reached positive results that may indicate existence of functional parallel pathways able to counteract the effect of the drug. Moreover, recent re-



ports have highlighted a role for Hh signaling in tumor-stroma interactions, with production of Shh ligand from cancer cells and stimulation of Gli transcription factor in tumor microenvironment (myofibroblasts, endothelial cells, and CSC) [8]. In our study, we have investigated the existence of an autocrine ligand-dependent Hh signaling in SCLC. We certainly believe that it would be interesting to study also the paracrine activation of Hh signaling, which could have the double effect of stimulating proliferation and survival of stroma cells, leading to increased angiogenesis and metastasis and, at the same time, produce growth factors acting on cancer cells to sustain their proliferation, epithelial-to-mesenchymal transition (EMT), dissemination and survival (Figure 1, right panel). Our data connecting BN/GRPR and the Hh signaling pathway may therefore provide valuable knowledge on the complex interaction between tumor cells and cancer microenvironment and may offer the scientific basis for developing novel therapeutic strategies that, by combining different anti-tumor approaches, could be more effective than single agent treatments. In this case, novel co-targeting strategies would target not only cancer cells but also other component of tumor microenvironment. Moreover, simultaneous targeting of BN/GRPR and Hh pathway could help in counteracting mechanisms of cell-autonomous and non-cell autonomous (stroma-dependent) resistance to targeted therapies.

6. Park KS, et al. Nat Med. 2011; 17: 1504-1508.
7. Castellone MD, et al. Oncogene. 2015; 34:1679-1687.
8. Bailey JM, et al. Oncogene. 2009; 28: 3513-3525.

**Maria Domenica Castellone:** Istituto di Endocrinologia ed Oncologia Sperimentale "G. Salvatore" (IEOS), C.N.R. 80131- Naples; Italy

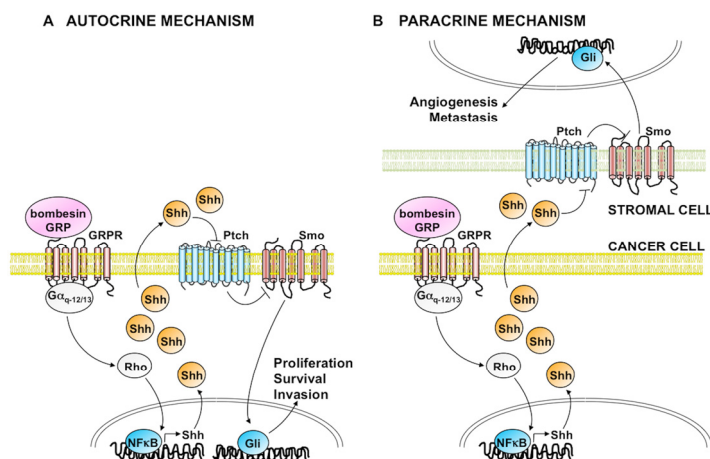
**Correspondence:** Maria Domenica Castellone

**Email:** [mcastell@unina.it](mailto:mcastell@unina.it)

**Key words:** Sonic Hedgehog, SCLC, BN/GRPR

**Received:** September 9, 2015

**Published:** September 26, 2015



## REFERENCES

1. Hahn H, et al. J Biol Chem. 1996; 271: 12125-12128.
2. Amakye D, et al. Nat. Med. 2013; 19: 1410-1422.
3. Gould S.E, et al. Expert Opin. Drug. Discov. 2014; 9: 969-984.
4. Carney DN, et al. Cancer Res. 1987; 47: 821-825.
5. Pepicelli CV, et al. Curr Biol. 1998; 8: 1083-1086.

### Targeting of non-oncogene addiction

Ana Igea, Jalaj Gupta, and Angel R. Nebreda

Signaling pathways control all phases of tumor development and are critical in cancer therapy as they are largely responsible for the ability of tumor cells to survive or die in response to chemotherapy and radiotherapy. The p38 MAPK signaling pathway is one of the routes that cells use extensively to interpret extracellular signals and orchestrate appropriate responses. This pathway was originally characterized as a key regulator of stress and inflammatory processes, which prompted the development of chemical inhibitors mainly targeting the p38 $\alpha$  and p38 $\beta$  family members. These inhibitors were expected to curtail production of inflammatory mediators and be useful for the treatment of inflammatory diseases such as rheumatoid arthritis. Unfortunately, the available information indicates rather disappointing outcomes, sometimes due to toxicity and in other cases for lack of efficacy, notwithstanding that some clinical trial results are not made public [1]. However, recent clinical trials with p38 MAPK inhibitors have given promising results for Chronic Obstructive Pulmonary Disease [2].

Intensive research over the past two decades has provided good evidence for the implication of the p38 MAPK pathway in cellular processes unrelated to stress that are important for normal physiology. It is now clear, for example, that p38 MAPK can regulate the proliferation, differentiation and survival of many cell types. In addition, p38 MAPK signaling has been implicated in several pathologies including cancer. Initial studies performed using cell lines both in culture and in mouse xenografts indicated that this pathway can suppress tumorigenesis. More recent studies have included the use of genetically modified mice to address the role of p38 MAPK signaling in different cell types, showing that this pathway can regulate tumor development at different levels.

Our group has contributed to the study of how the p38 MAPK pathway regulates tumor initiation and progression *in vivo*. Using mouse models, we have shown an important role of p38 MAPK signaling in colon and breast cancer [3, 4]. As reported for other tumor types, we provided evidence that the p38 MAPK pathway suppresses tumor initiation in a mouse model of inflammation-associated colon tumorigenesis. Unexpectedly, once the tumor is formed, p38 MAPK signaling contributes to the proliferation and survival of

the malignant cells and inhibition of p38 MAPK reduces colon tumor growth [3]. Moreover, genetic and pharmacological experiments indicate that p38 MAPK inhibition cooperates with chemotherapeutic drugs such as cisplatin to kill breast and colon cancer cells in culture and to reduce tumor size *in vivo* in a mouse model of breast cancer [4]. Along the same lines, other groups have shown that inhibition of the p38 MAPK pathway potentiates the anti-tumoral effects of doxorubicin and sorafenib in mouse models of lung and liver cancer, respectively [5, 6]. Taken together, these results strongly suggest that p38 MAPK inhibitors can be potentially exploited for cancer therapy in combination with chemotherapeutic drugs.

The results obtained in mouse models of cancer are promising but any attempt to modulate p38 MAPK activity for therapeutic purposes should be carefully evaluated in preclinical models. This is always an important validation step but in the case of p38 MAPK signaling is critical, given the many functions that this pathway can perform depending on the cellular context. We have started to use patient-derived xenografts (PDX) as preclinical models that recapitulate the complexity and heterogeneity of the human tumors. Using PDX models, we have confirmed that pharmacological inhibition of p38 MAPK impairs the growth of colon tumors derived from patients [7]. In line with the possible therapeutic interest that inhibition of p38 MAPK signaling could have for colon cancer treatment, p38 MAPK inhibitors either alone or in combination with other drugs have been used or are currently in clinical trials for different types of cancer (<https://clinicaltrials.gov>).

It therefore seems that tumor cells may become addicted to p38 MAPK signaling, perhaps to be able to tolerate homeostatic control deficiencies and the kind of permanent stressful conditions in which they have to thrive. Considering that sustained activation of the p38 MAPK pathway in normal cells usually leads to cell cycle arrest and apoptosis, it cannot be considered an oncogenic route. However, the ability of this pathway to perform a variety of functions makes tumor cells to rely on it, illustrating a good example of non-oncogene addiction.

In summary, results obtained by our group and others support that the p38 MAPK pathway could act as an

accessory component of oncogenic networks, which can be potentially exploited in combination therapies to effectively shut down pro-tumorigenic pathways and facilitate tumor cell death. Thus, pharmacological inhibitors of p38 MAPK are worth exploring for cancer therapy and combined with chemotherapeutic drugs could improve current treatments and reduce side effects.

## REFERENCES

1. Coulthard LR et al. Trends Mol Med. 2009; 15:369-379.
2. Norman P. Expert Opin Investig Drugs. 2015; 24:383-392.
3. Gupta J et al. Cancer Cell. 2014; 25:484-500.
4. Pereira L et al. EMBO Mol Med. 2013; 5:1759-1774.
5. Morandell S et al. Cell Rep. 2013; 5:868-877.
6. Rudalska R et al. Nature Med. 2014; 20:1138-1146.
7. Gupta J et al. Oncotarget. 2015; 6:8539-8551.

Angel R. Nebreda: Institute for Research in Biomedicine (IRB Barcelona), 08028 Barcelona, Spain

**Correspondence:** Angel R. Nebreda

**Email:** [angel.nebreda@irbbarcelona.org](mailto:angel.nebreda@irbbarcelona.org)

**Received:** August 6, 2015

**Published:** August 18, 2015

## Caloric restriction induces heat shock response and inhibits B16F10 cell tumorigenesis both *in vitro* and *in vivo*

Marta G. Novelle<sup>1,3</sup>, Ashley Davis<sup>1</sup>, Nathan L. Price<sup>1</sup>, Ahmed Ali<sup>1</sup>, Stefanie Fürer-Galvan<sup>1</sup>, Yongqing Zhang<sup>2</sup>, Kevin Becker<sup>2</sup>, Michel Bernier<sup>1</sup>, and Rafael de Cabo<sup>1</sup>

<sup>1</sup>Translational Gerontology Branch, National Institute on Aging, National Institutes of Health, Baltimore, MD 21224, USA;

<sup>2</sup>Gene Expression and Genomics Unit, National Institute on Aging, National Institutes of Health, Baltimore, MD 21224, USA;

<sup>3</sup>Department of Physiology, CIMUS, University of Santiago de Compostela-Instituto de Investigación Sanitaria, 15782 Santiago de Compostela, Spain; CIBER Fisiopatología de la Obesidad y Nutrición (CIBERObn), 15706 Santiago de Compostela, Spain.

**Key words:** caloric restriction, heat shock, stress response, tumorigenesis, aging

**Received:** 12/01/14; **Accepted:** 03/24/15; **Published:** 04/05/15

**Correspondence to:** Rafael de Cabo, PhD; **E-mail:** decabora@grc.nia.nih.gov

**Copyright:** Novelle et al. This is an open-access article distributed under the terms of the Creative Commons Attribution License, which permits unrestricted use, distribution, and reproduction in any medium, provided the original author and source are credited

**Abstract:** Caloric restriction (CR) without malnutrition is one of the most consistent strategies for increasing mean and maximal lifespan and delaying the onset of age-associated diseases. Stress resistance is a common trait of many long-lived mutants and life-extending interventions, including CR. Indeed, better protection against heat shock and other genotoxic insults have helped explain the pro-survival properties of CR. In this study, both *in vitro* and *in vivo* responses to heat shock were investigated using two different models of CR. Murine B16F10 melanoma cells treated with serum from CR-fed rats showed lower proliferation, increased tolerance to heat shock and enhanced HSP-70 expression, compared to serum from *ad libitum*-fed animals. Similar effects were observed in B16F10 cells implanted subcutaneously in male C57BL/6 mice subjected to CR. Microarray analysis identified a number of genes and pathways whose expression profile were similar in both models. These results suggest that the use of an *in vitro* model could be a good alternative to study the mechanisms by which CR exerts its anti-tumorigenic effects.

## INTRODUCTION

Aging is a complex multifactorial process, whereby organisms undergo major cell degeneration and loss of function. During aging, irreversible and deleterious processes are triggered by accumulation of damaged cellular macromolecules [1, 2]. Several theories have been proposed to explain these processes [3, 4], but the exact molecular mechanisms behind aging remains unknown. Cellular damage may result from oxidative stress, toxic metabolic byproducts, endoplasmic reticulum stress and mitochondrial unfolded protein responses, or exposure to heat stress, among others. Several heat shock proteins (HSP) function as molecular

chaperones by preventing misfolding and aggregation of other proteins. This induction of cytoprotective responses promotes longevity [5, 6]; conversely, aging is associated with down-regulation in HSP expression in neuronal tissue, skeletal and cardiac muscle, and the liver [7, 8]. Stimulation of HSP synthesis has been suggested as a viable strategy to counteract the negative effects of aging and eliciting a ‘low-grade’ stress response may help organisms live longer and improve their survival [9].

More than 8 decades ago, McCay and colleagues observed that severe reduction in calorie intake while maintaining sufficient micronutrient levels for optimum health resulted in lifespan extension [10]. Since then,

numerous studies have reported that lifelong caloric restriction (CR) extends mean and maximum lifespan and delays age-associated diseases in a wide variety of species [11, 12]. Many of the beneficial effects of CR are mediated by altering the expression of several HSPs, notably Hsp70, and the activation of heat shock transcription factor 1 [13-15]. In this context, our group has demonstrated that exposure of HepG2 cells to human serum from CR participants conferred significant cytoprotection against heat stress [7]. Moreover, cells treated with human serum from CR volunteers trigger a transcriptional up-regulation of numerous genes and pathways implicated in stress resistance through activation of the transcription factor NF-E2-related factor (NRF2) [16]. NRF2 plays a key role in maintaining homeostasis during oxidative stress and exposure to carcinogens by coordinately regulating the expression of antioxidants and detoxification enzymes [17] that boost protection against cancer [18].

The anti-tumorigenic properties of CR on spontaneously arising tumors and in experimental cancer models are well-documented [19]. For example, 15 days of 40% CR significantly reduces the growth of brain tumors in mice by reducing angiogenesis and increasing tumor cell apoptosis [20]. The combination of fasting and chemotherapy retards the growth of human breast cancer tumors in mice [21] and delays the progression of pancreatic cancer lesions in a mouse model [22]. The use of the mouse as an experimental tool in cancer research is cumbersome, time-consuming and expensive, and, therefore, has compelled us to explore an alternative approach to study anti-cancer therapies.

In this manuscript we present a new approach to investigate a central mechanism by which CR activates a stress response pathway to combat tumorigenesis. The stress response of murine B16F10 melanoma cells maintained in culture medium supplemented with serum from rats fed CR and *ad libitum* (AL) diet was evaluated and compared to that of mice injected with B16F10 melanoma cells and maintained on either CR or AL. In the latter experimental model, mice were subjected to heat stress followed by the monitoring of a melanoma-specific Hsp70 reporter expression. These results combined with microarray analysis illustrated alteration of a common set of cancer-related genes using *in vitro* and *in vivo* testing.

## RESULTS

### Growth rate and heat shock response of B16F10 melanoma cells maintained in serum from CR-fed animals

Proliferation of B16F10 melanoma cells was carried out

in the presence of serum from rats fed either AL or CR diet. A significant reduction in cell growth was observed following incubation with CR serum as compared to AL serum controls (Fig. 1a). Exposure of B16F10 cells to heat stress (45°C) for 1 h caused a significant difference in survival depending on whether these cells were maintained in CR or AL serum (Fig. 1b). Our observations that CR serum decreased heat-dependent cellular cytotoxicity support previously published results from this laboratory [23].

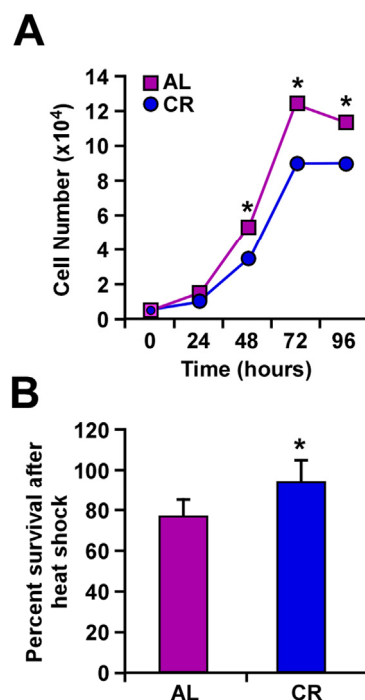


**Figure 1. Caloric restriction slows cellular growth and improves response to heat shock.** (A) B16F10 melanoma cells were maintained in culture with serum from AL- and CR-fed rats over a period of 96 h. The number of cells was counted at 24-h intervals. (B) Percent of cells surviving a 1-h treatment at 45°C when maintained in culture with serum from either AL- or CR-fed rats. Data are represented as the mean  $\pm$  SEM. \*,  $p < 0.05$ .

### Reduction in the number and size of tumors in mice on caloric restriction

To evaluate the effect of CR on tumor growth *in vivo*, mouse B16F10 melanoma cells that were stably transfected with Hsp70-GFP plasmid, were implanted subcutaneously in male C57BL/6 mice fed either a CR or AL diet. A significant decrease in the size and weight of tumors was observed in CR-fed mice along with delayed tumor growth both in the periscapular region and lower back area (Fig. 2).



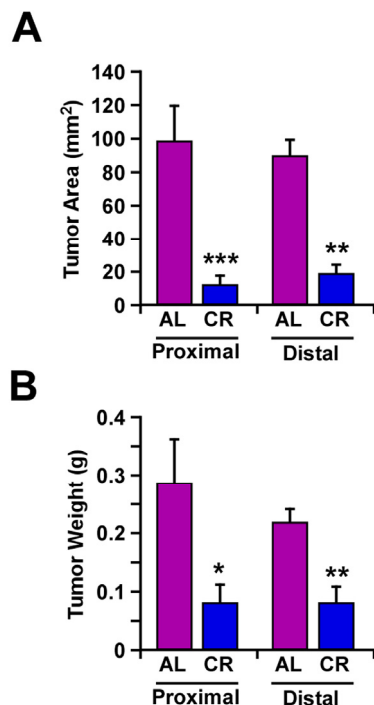


**Figure 2. Caloric restriction decreased melanoma tumor growth *in vivo*.** In AL- and CR-fed mice, mouse tumor xenografts were formed by implanting B16F10 melanoma cells, at the periscapular region (proximal area) and in the lower back over the hip (distal area). Tumor area (mm<sup>2</sup>) (A) and individual tumor weight (g) (B) were determined after 14 days. Data are represented as the mean  $\pm$  SEM. n=10/per group. \*, p<0.05, \*\*, p<0.01, \*\*\* p<0.001.

## Heat stress-mediated induction of Hsp70 expression both in *in vitro* and *in vivo* models

Changes in HSP expression play an important role in the ability of cells to respond to environmental stressors. Earlier work has shown an elevation in Hsp70 expression in B16F10 melanoma cells cultured with serum from CR-fed animals [23]. Here, we compared the effects of CR alone, heat shock alone or the combination ‘CR + heat shock’ using B16F10 melanoma cells stably expressing GFP-tagged Hsp70 construct under the control of rat *hsp70.1* promoter [24]. The results indicate that the heat-mediated induction of Hsp70 expression was significantly higher when B16F10 cells and tumor-bearing animals were subjected to CR (Fig. 3).

## Microarray analysis of B16F10 melanoma cells used in *in vitro* and *in vivo* settings

DNA microarray analysis was performed to compare the global transcriptional effect of CR in B16F10 melanoma cells either grown in culture or implanted in mice. Principal Component Analysis (PCA) revealed inherent *in vivo* and *in vitro* differences that must be taken into account when comparing the impact of CR in gene expression profile. Nevertheless, Venn diagram indicated that both models shared 55 up-regulated and 17 down-regulated transcripts, which were significantly enriched in the CR versus AL pairwise comparisons (Fig. 4a, Supplemental Table 1). Among these shared transcripts, MAP Kinase Interacting Serine/Threonine

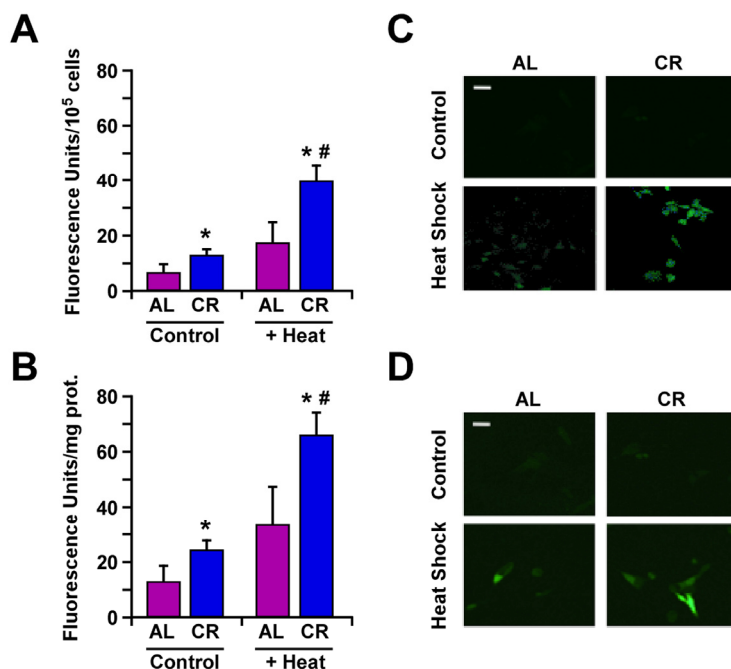


**Figure 3. Caloric restriction improves protection against heat shock through increased expression of Hsp70.** (A) B16F10 melanoma cells stably transfected with a plasmid encoding GFP-tagged Hsp70 construct were maintained in medium supplemented with 10% serum from AL- or CR-fed rats and then subjected or not to heat shock stress for 45 min. Bars represent fluorescence intensity per 10<sup>5</sup> cells. Cell culture experiments were performed as three or more replicates. (B) B16F10 tumor xenografts from mice fed either AL or CR diet were subjected to heat shock stress for 45 min and sacrificed after 4h. Bars represent fluorescence intensity per mg of tumor proteins; n=10 per group. Data, obtained by fluorimetry, are represented as the means  $\pm$  SEM. \*, p<0.05 vs. AL group; #, p<0.05 vs. CR group. (C) Images of B16F10 cells and (D) tumor cells depicting GFP fluorescence were detected by confocal microscopy. White bar, 20  $\mu$ m.

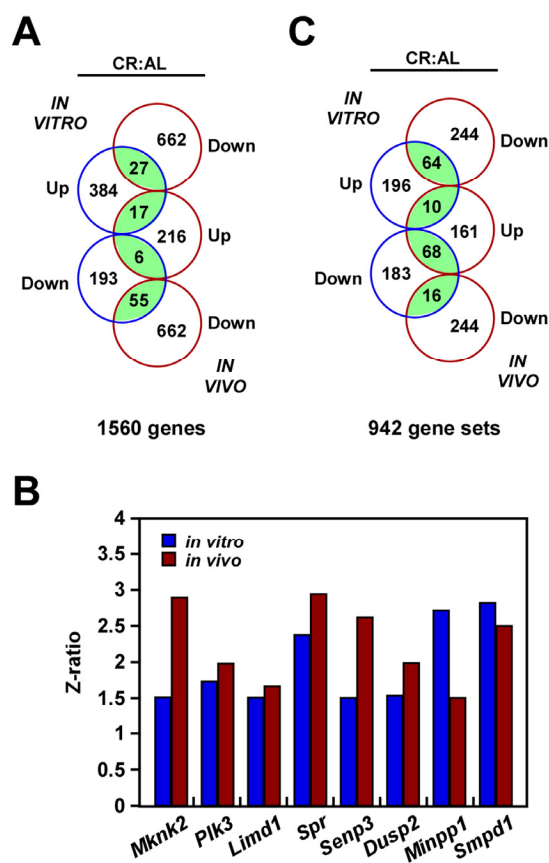


**Figure 4. Gene expression profiling in response to caloric restriction.** (A) Venn diagram showing the overlap of gene transcripts with significant change in expression in the CR versus AL pairwise comparisons by both B16F10 melanoma cells growing in culture (*in vitro*) and as tumor xenografts (*in vivo*). (B) Effect of CR on the expression of a select group of transcripts. (C) Venn diagram showing the overlap of gene sets with significant change in expression in the CR versus AL pairwise comparisons.

Kinase 2 (*Mknk2*) [25], polo-like kinase 3 (*Plk3*) [26] and LIM Domains Containing 1 (*Limd1*) [27] are implicated in tumorigenesis, whereas *Spr* and *Semp3*, which encode for Sepiapterin Reductase and SUMO1/Sentrin/SMT3 Specific Peptidase 3, are involved in stress response [28, 29]. DUSP2 is an important member of the dual-specificity protein phosphatase subfamily, which is implicated in inflammatory response and reported to be upregulated both with CR and heat shock [30]. Moreover, there is an increased expression of *Minpp1*, which encodes for Multiple Inositol Polyphosphate Phosphatase 1. This phosphatase is induced in response to heat shock, osmotic and oxidative stress conditions, thereby contributing to the regulation of ER stress and apoptosis

[31]. Finally, upregulation of *Smpd1* (Sphingomyelin phosphodiesterase 1, also known as ASM) was also observed in both experimental models with CR (Fig. 4b). Its activity is expressed at high levels in cancer cells under the control of an inducible expression of hsp70.1 protein [32]. Using parametric analysis of gene set enrichment, 26 gene sets were identified whose expression levels were significantly altered in the same direction by CR in both experimental models (Fig. 4c, Supplemental Table S2).

## DISCUSSION

The aging process involves multiple physiological mechanisms and represents one of the main risk factors for several human pathologies, such as cancer, diabetes, and cardiovascular disease. Dietary CR retards the aging process and age-related disease pathogenesis [33, 34], and many studies have tried to elucidate the exact mechanism(s) by which CR acts (reviewed in [35]). Our work demonstrates that CR significantly decreases tumor cell proliferation, in agreement with previous studies [36, 37], and this phenomenon takes place whether B16F10 melanoma cells were cultured with serum from CR-fed animals or these tumor cells were implanted in CR-fed mice. Moreover, the process of tumorigenesis was significantly decreased in CR-fed animals after heat stress. Hsp70 is one of several heat-shock proteins implicated in the regulation of cancer cell growth. HSPs sustain tumor survival and drive tumor growth [38]; however, induction of Hsp70 family members results in cellular protection against unfavorable environmental conditions, including elevated temperatures, oxidative stress, exposure to heavy metals, proteasome inhibitors, and infection [39]. CR has been previously shown to restore the ability of cells to mount a heat shock response through increase in Hsp70-mediated thermotolerance [40], an observation that was confirmed in the present study. Moreover, B16F10 melanoma cells subjected to heat shock stress showed greater survival when maintained in CR serum as compared to serum from AL-fed animals. It would appear that heat stress and CR acted cooperatively to enhance cell survival, possibly via activation of the deacetylase SIRT1 [40, 41]. It is interesting to note that the combination of heat stress with CR caused a synergistic increase in Hsp70-GFP expression when compared to either condition alone both *in vitro* and *in vivo*.

Microarray results reinforce the idea that despite significant genome-wide gene expression variation between the two experimental models, the expression profile of several transcripts implicated in tumorigenesis and stress response exhibited a comparable pattern,

whether B16F10 melanoma cells were cultured in CR serum or implanted in mice fed a CR diet. Although this *in vitro* model is quite distant from a physiological setting, it displayed a number of molecular pathways similar to the ones observed *in vivo*.

In conclusion, our findings indicate that the impact of CR on the regulation of several pathways implicated in tumorigenesis on an *in vivo* model of heat stress response can be replicated *in vitro* using tumor cells incubated with serum from CR-fed animals. The idea that hormones and nutrients present in serum, whose levels are altered during CR, are involved in homeostasis control mechanisms, including the aging process, has been suggested [7, 16, 23]. These results support the notion that *in vitro* testing may be well suited for the study of molecular aspects of CR that have not been elucidated yet.

## MATERIALS AND METHODS

**Animals and Dietary Manipulation.** The mice were single-housed in duplex caging in a room maintained at a constant temperature (20-22 °C) and humidity (30-70%) in a light:dark 12:12-h schedule, according to established animal protocols and NIH guidelines. Male C57BL/6 mice (3 month old) were fed on a standard purified mouse diet (NIH-31) *ad libitum* (AL; n=10) or maintained on a 40% calorie restriction regimen (CR; n=10) during six weeks. Body weight and food intake was recorded weekly (supplemental figure 1 a, b).

**Cell culture.** B16F10 melanoma cells (ATCC® CRL-6475™) were purchased from American Type Culture Collection (Manassas, VA); they were cultured in Dulbecco's Modified Essential Medium (DMEM) supplemented with 10% fetal bovine serum and penicillin/streptomycin (Gibco, Gaithersburg, MD) under standard cell culture conditions. Cells were incubated in media with 10% serum from AL- or CR-fed rats (as described previously [23]). Briefly, serum was obtained from overnight fasted, anesthetized 6-month-old male Fisher 344 rats from three different cohorts. The blood collection took place between 7-11:00 a.m. After a 1-h incubation in a water bath at 45°C, cells were trypsinized, washed twice with phosphate-buffered saline (Invitrogen, Grand Island, NY), and then seeded at  $1.5 \times 10^5$  cells/well in 96-well plates. Cell proliferation assays were carried out during 96 h by the addition of a tetrazolium salt solution, WST-8, to each well according to the manufacturer's protocol (Dojindo, Indianapolis, IN). The absorbance of the formazan dye formed was measured at 450nm using the Perkin Elmer HTS 7000 Plus BioAssay reader.

**Heat shock treatment of B16F10 melanoma xenografts *in vivo*.** One month into the study, mice were injected with  $1 \times 10^6$  B16F10 melanoma cells stably transfected with a plasmid containing *GFP* gene linked to rat stress-inducible *hsp70.1* gene promoter [24] in the periscapular region (proximal) and in the lower back over the hip (distal area). After a two-week period, five mice were randomly chosen from each group and placed in a tumor hyperthermia induction chamber (THIC) constructed in our facility. Mice were anesthetized with isoflurane droplets in a closed chamber prior to being placed in the THIC and maintained under anesthesia for the reminder of the experiment. Two membranous tubes filled with pre-warmed water were placed over the proximal (45°C) and distal (27°C) tumors of the anesthetized mice (supplemental figure 1 c, d). The water temperature was maintained throughout the duration of the experiment. After a 45-min heat treatment, the mice recovered for 4 h and then euthanized by cervical dislocation, according to the AAALAC guidelines.

**Melanoma tumor growth *in vivo*.** Tumor xenografts were formed by implanting murine B16F10 melanoma cells at the periscapular region and in the lower back of AL- and CR-fed mice. Fourteen days later, animals were euthanized and tumors were excised for the determination of the tumor area using a caliper. Tumor weight was also recorded.

**GFP fluorescence detection.** Experiments were carried out as indicated, using B16F10 melanoma cells stably expressing a plasmid encoding GFP-tagged Hsp70 that were either maintained in culture or used as tumor xenografts in mice. GFP fluorescence was monitored using both a confocal microscope (Axiovert-200, Zeiss LSM 510) to obtain images and a fluorimeter (Perkin-Elmer LS-55 and HTS 7000 Plus BioAssay reader) to accurately quantify GFP expression levels, which were normalized per  $10^5$  cells (in culture) or mg of tumor proteins.

**Microarray analysis.** RNA was isolated from B16F10 melanoma cells maintained in culture and as tumor xenografts. For microarray analysis, RNA was processed, reverse transcribed, labeled and hybridized to Mouse 15K cDNA arrays and read on an Illumina BeadArray 500GX reader. Raw data were subjected to Z normalization to ensure compatibility using the formula:  $z(\text{raw data}) = [\ln(\text{raw data}) - \text{avg}(\ln(\text{raw data}))] / [\text{std dev}(\ln(\text{raw data}))]$ , where  $\ln$  is natural logarithm, avg is the average over all genes of an array, and std dev is the standard deviation over all genes of an array (Cheadle et al., 2003). The Z ratio (between treatment A and B) is given by  $z(A) - z(B) / \text{std dev}$ .

Individual genes with Z ratio > 1.5 in both directions, *P* value < 0.05, and false discovery rate > 0.3 were considered significantly changed. All raw data were deposited in the NCBI Gene Expression Omnibus under accession number GSE67430.

**Statistical analysis.** Statistical analyses were performed using Microsoft Excel software (Microsoft Corp., Redmond, WA). Unpaired t-tests were used for all analyses. Statistical significance was established at *p*<0.05. Data are expressed as means ± standard error of the mean (SEM).

## ACKNOWLEDGEMENTS

We would like to thank Dr. Zdzislaw Krawczyk for giving us the plasmid encoding GFP-tagged Hsp70. This work has been supported by the Intramural Research Program of the National Institute on Aging, National Institutes of Health. MGN was supported by CIBER de Fisiopatología de la Obesidad y Nutrición (CIBERobn), an initiative of ISCIII, Spain.

## Conflict of interest statement

The authors have no conflict of interests to declare.

## REFERENCES

1. Chondrogianni N, Sakellari M, Lefaki M, Papaevgeniou N and Gonos ES. Proteasome Activation Delays Aging in Vitro and in Vivo. *Free Radic Biol Med*. 2014; 71:303-320.
2. López -Otin C, Blasco MA, Partridge L, Serrano M and Kroemer G. The hallmarks of aging. *Cell*. 2013; 153:1194-1217.
3. Jin K. Modern Biological Theories of Aging. *Aging Dis*. 2010; 1:72-74.
4. Wiggins J and Bitzer M. Slowing the aging process. *Clin Geriatr Med*. 2013; 29:721-730.
5. Shore DE, Carr CE and Ruvkun G. Induction of cytoprotective pathways is central to the extension of lifespan conferred by multiple longevity pathways. *PLoS Genet*. 2012; 8:e1002792.
6. Shore DE and Ruvkun G. A cytoprotective perspective on longevity regulation. *Trends Cell Biol*. 2013; 23:409-420.
7. Allard JS, Heilbronn LK, Smith C, Hunt ND, Ingram DK, Ravussin E and de CR. In vitro cellular adaptations of indicators of longevity in response to treatment with serum collected from humans on calorie restricted diets. *PLoS One*. 2008; 3:e3211.
8. Hall DM, Xu L, Drake VJ, Oberley LW, Oberley TD, Moseley PL and Kregel KC. Aging reduces adaptive capacity and stress protein expression in the liver after heat stress. *J Appl Physiol* (1985). 2000; 89:749-759.
9. Rattan SI, Fernandes RA, Demirovic D, Dymek B and Lima CF. Heat stress and hormetin-induced hormesis in human cells: effects on aging, wound healing, angiogenesis, and differentiation. *Dose Response*. 2009; 7:90-103.
10. McCay CM, Crowell MF and Maynard LA. The effect of retarded growth upon the length of life span and upon the ultimate body size. 1935. *Nutrition*. 1989; 5:155-171.
11. McDonald RB and Ramsey JJ. Honoring Clive McCay and 75 years of calorie restriction research. *J Nutr*. 2010; 140:1205-1210.
12. Mercken EM, Carboneau BA, Krzysik-Walker SM and de Cabo R. Of mice and men: the benefits of caloric restriction, exercise, and mimetics. *Ageing Res Rev*. 2012; 11:390-398.
13. Brown MK and Naidoo N. The endoplasmic reticulum stress response in aging and age-related diseases. *FPHYS*. 2012; 3:263.
14. Morimoto RI and Cuervo AM. Proteostasis and the aging proteome in health and disease. *J Gerontol A Biol Sci Med Sci*. 2014; 69 Suppl 1:S33-38.
15. Sinclair DA. Toward a unified theory of caloric restriction and longevity regulation. *Mech Ageing Dev*. 2005; 126:987-1002.
16. Omodei D, Licastro D, Salvatore F, Crosby SD and Fontana L. Serum from humans on long-term calorie restriction enhances stress resistance in cell culture. *Aging (Albany NY)*. 2013; 5:599-606.
17. Martin-Montalvo A, Villalba JM, Navas P and de Cabo R. NRF2, cancer and calorie restriction. *Oncogene*. 2011; 30:505-520.
18. Jaramillo MC and Zhang DD. The emerging role of the Nrf2-Keap1 signaling pathway in cancer. *Genes Dev*. 2013; 27:2179-2191.
19. Hursting SD, Smith SM, Lashinger LM, Harvey AE and Perkins SN. Calories and carcinogenesis: lessons learned from 30 years of calorie restriction research. *Carcinogenesis*. 2010; 31:83-89.
20. Mukherjee P, Abate LE and Seyfried TN. Antiangiogenic and proapoptotic effects of dietary restriction on experimental mouse and human brain tumors. *Clin Cancer Res*. 2004; 10:5622-5629.
21. Lee C, Safdie FM, Raffaghello L, Wei M, Madia F, Parrella E, Hwang D, Cohen P, Bianchi G and Longo VD. Reduced levels of IGF-I mediate differential protection of normal and cancer cells in response to fasting and improve chemotherapeutic index. *Cancer Res*. 2010; 70:1564-1572.
22. Lanza-Jacoby S, Yan G, Radice G, LePhong C, Baliff J and Hess R. Calorie restriction delays the progression of lesions to pancreatic cancer in the LSL-KrasG12D; Pdx-1/Cre mouse model of pancreatic cancer. *Exp Biol Med (Maywood)*. 2013; 238:787-797.
23. De Cabo R, Fürer-Galban S, Anson RM, Gilman C, Gorospe M and Lane MA. An in vitro model of caloric restriction. *Exp Gerontol*. 2003; 38:631-639.
24. Wysocka A and Krawczyk Z. Green fluorescent protein as a marker for monitoring activity of stress-inducible hsp70 rat gene promoter. *Mol Cell Biochem*. 2000; 215:153-156.
25. Ueda T, Sasaki M, Elia AJ, Chio II, Hamada K, Fukunaga R and Mak TW. Combined deficiency for MAP kinase-interacting kinase 1 and 2 (Mnk1 and Mnk2) delays tumor development. *PNAS*. 2010; 107(32):13984-13990.
26. Strebhardt K. Multifaceted polo-like kinases: drug targets and antitargets for cancer therapy. *Nat Rev Drug Discov*. 2010; 9:643-660.
27. Sharp TV, Munoz F, Bourbouli D, Presneau N, Darai E, Wang HW, Cannon M, Butcher DN, Nicholson AG, Klein G, Imreh S and Boshoff C. LIM domains-containing protein 1 (LIMD1), a tumor suppressor encoded at chromosome 3p21.3, binds pRB and represses E2F-driven transcription. *PNAS*. 2004; 101:16531-16536.
28. Rochette L, Lorin J, Zeller M, Guillaud JC, Lorgis L, Cottin Y and Vergely C. Nitric oxide synthase inhibition and oxidative

stress in cardiovascular diseases: possible therapeutic targets? *Pharmacol Ther.* 2013; 140:239-257.

**29.** Wang Y, Yang J and Yi J. Redox sensing by proteins: oxidative modifications on cysteines and the consequent events. *Antioxid Redox Signal.* 2012; 16:649-657.

**30.** Lang R, Hammer M and Mages J. DUSP meet immunology: dual specificity MAPK phosphatases in control of the inflammatory response. *J Immunol.* 2006; 177:7497-7504.

**31.** Kilaparty SP and Ali N. Changes in expression of Multiple Inositol Polyphosphate Phosphatase1 (Minpp1) under Apoptotic and Cellular Stress Conditions. *FASEB J.* 2013; 27:834.14

**32.** Zhu H, Yoshimoto T and Yamashima T. Heat shock protein 70.1 (Hsp70.1) affects neuronal cell fate by regulating lysosomal acid sphingomyelinase. *J Biol Chem.* 2014; 289:27432-27443.

**33.** Mercken EM, Crosby SD, Lamming DW, JeBailey L, Krzysik-Walker S, Villareal DT, Capri M, Franceschi C, Zhang Y, Becker K, Sabatini DM, de Cabo R and Fontana L. Calorie restriction in humans inhibits the PI3K/AKT pathway and induces a younger transcription profile. *Aging Cell.* 2013; 12:645-651.

**34.** Omodei D and Fontana L. Calorie restriction and prevention of age-associated chronic disease. *FEBS Lett.* 2011; 585:1537-1542.

**35.** De Cabo R, Carmona-Gutierrez D, Bernier M, Hall MN and Madeo F. The search for antiaging interventions: from elixirs to fasting regimens. *Cell.* 2014; 157:1515-1526.

**36.** De Lorenzo MS, Baljinnyam E, Vatner DE, Abarzua P, Vatner SF and Rabson AB. Caloric restriction reduces growth of mammary tumors and metastases. *Carcinogenesis.* 2011; 32:1381-1387.

**37.** Minor RK, López M, Younts CM, Jones B, Pearson KJ, Anson RM, Dieguez C and de Cabo R. The arcuate nucleus and neuropeptide Y contribute to the antitumorigenic effect of calorie restriction. *Aging Cell.* 2011; 10:483-492.

**38.** Daugaard M, Jaattela M and Rohde M. Hsp70-2 is required for tumor cell growth and survival. *Cell Cycle.* 2005; 4:877-880.

**39.** Westerheide SD and Morimoto RI. Heat shock response modulators as therapeutic tools for diseases of protein conformation. *J Biol Chem.* 2005; 280:33097-33100.

**40.** Raynes R, Leckey BD, Jr., Nguyen K and Westerheide SD. Heat shock and caloric restriction have a synergistic effect on the heat shock response in a sir2.1-dependent manner in *Caenorhabditis elegans*. *J Biol Chem.* 2012; 287:29045-29053.

**41.** Westerheide SD, Anckar J, Stevens SM, Jr., Sistonen L and Morimoto RI. Stress-inducible regulation of heat shock factor 1 by the deacetylase SIRT1. *Science.* 2009; 323:1063-1066.



# Clearance of senescent hepatocytes in a neoplastic-prone microenvironment delays the emergence of hepatocellular carcinoma

Fabio Marongiu\*, Maria Paola Serra\*, Marcella Sini, Fabrizio Angius, and Ezio Laconi

Department of Biomedical Sciences, Unit of Experimental Medicine, University of Cagliari, 09124 Cagliari, Italy

\*These two authors contributed equally to this work.

**Key words:** cell transplantation, tumor microenvironment, cell senescence, cell competition, liver repopulation, liver carcinogenesis

**Received:** 11/19/13; **Accepted:** 1/20/14; **Published:** 1/23/14

**Correspondence to:** Ezio Laconi, MD/PhD; **E-mail:** [elaconi@unica.it](mailto:elaconi@unica.it)

**Copyright:** © Marongiu et al. This is an open-access article distributed under the terms of the Creative Commons Attribution License, which permits unrestricted use, distribution, and reproduction in any medium, provided the original author and source are credited

**Abstract:** Increasing evidence indicates that carcinogenesis is dependent on the tissue context in which it occurs, implying that the latter can be a target for preventive or therapeutic strategies. We tested the possibility that re-normalizing a senescent, neoplastic-prone tissue microenvironment would exert a modulatory effect on the emergence of neoplastic disease. Rats were exposed to a protocol for the induction of hepatocellular carcinoma (HCC). Using an orthotopic and syngeneic system for cell transplantation, one group of animal was then delivered 8 million normal hepatocytes, via the portal circulation. Hepatocytes transplantation resulted in a prominent decrease in the incidence of both pre-neoplastic and neoplastic lesions. At the end of 1 year 50% of control animals presented with HCC, while no HCC were observed in the transplanted group. Extensive hepatocyte senescence was induced by the carcinogenic protocol in the host liver; however, senescent cells were largely cleared following infusion of normal hepatocytes. Furthermore, levels of Il-6 increased in rats exposed to the carcinogenic protocol, while they returned to near control values in the group receiving hepatocyte transplantation. These results support the concept that strategies aimed at normalizing a neoplastic-prone tissue landscape can modulate progression of neoplastic disease.

## INTRODUCTION

Population The role of the microenvironment in the pathogenesis of neoplastic disease is increasingly being appreciated. Starting from the report of Mintz and Illmensee [1], describing the generation of normal genetically mosaic mice from malignant teratocarcinoma cells, several studies have demonstrated that the phenotype of pre-neoplastic and neoplastic cell populations can be profoundly modulated by external cues emanating from the surrounding microenvironment [2-5]. Furthermore, it has been documented that specific gene-expression profiles in non-cancerous tissue are able to predict recurrence and survival in patients with hepatocellular carcinoma (HCC), again pointing to the critical role of the surrounding microenvironment in the natural history of neoplastic disease [6-7]. Along this line, studies from

our laboratory have indicated that a growth-constrained/senescent tissue environment is able to generate a powerful driving force for the selective expansion of pre-neoplastic hepatocytes in the liver, leading to their progression to HCC [8]. Exposure to retrorsine (RS), a naturally-occurring pyrrolizidine alkaloid, impairs liver regeneration and induces extensive hepatocyte senescence in rat liver [9-10]. When pre-neoplastic cells isolated from hepatic nodules were transplanted in RS-treated livers, they grew rapidly and evolved into HCC; however, the same cell preparation was unable to expand and progress following injection into untreated, syngeneic normal hosts [8].

These observations provide a rationale for the hypothesis that targeting a neoplastic-prone tissue

landscape may represent a valuable approach to modulate the evolution of carcinogenic process [11-13]. Recently, we have obtained evidence to indicate that orthotopic transplantation of normal hepatocytes in animals previously exposed to a carcinogenic regimen exerts a delaying effect on the growth of early preneoplastic lesions [14]. In the present studies, we have extended this observation and explored the possible biological and molecular mechanisms underlying this phenomenon. Neoplastic process was induced in rat liver through sequential exposure to diethylnitrosamine (DENA) and RS. Normal hepatocytes transplanted following the carcinogenic protocol were able to reduce the incidence of preneoplastic and neoplastic lesions at the end of 1 year. This was associated with clearance of RS-induced senescent hepatocytes by transplanted normal cells.

## RESULTS

### The induction of hepatocellular carcinoma following exposure to DENA+RS

As already mentioned, naturally occurring pyrrolizidine alkaloids, including RS, are known for their ability to promote the growth of early hepatic nodules in initiated rat liver [15]. However, no studies have been reported to date on the long term effects of these agents in animals previously given a carcinogen. In the present experiments, rats were administered DENA and RS (two single injections, 10 days apart), and they were killed 1 year later. As predicted, multiple pre-neoplastic and neoplastic hepatocellular lesions, ranging in size from a few mm to 2.5 cm in diameter, were observed in all animals exposed to this protocol (figure 1, panel A). Furthermore, histological analysis confirmed the pre-

sence of large, advanced hepatocyte nodules in all liver samples in this group, while trabecular HCC was diagnosed in 4 out of 8 rats (figure 1, panel B).

### Normal hepatocyte transplantation delays the emergence of HCC induced by DENA+RS

Based on the above findings, we next considered the effect of normal hepatocyte transplantation on the incidence of hepatic nodules and HCC following exposure to DENA+RS. Results are reported figure 2 and table 1. Major differences were already evident upon macroscopic examination. The liver of DENA+RS-treated animals displayed slightly increased stiffness compared to normal, with irregular margins and finely granular surface; however, these changes were largely reversed in rats receiving the infusion of normal cells (figure 2, panels A and B). Most notably, the presence of large nodular lesions and overall tumour burden in the liver were greatly reduced in the latter group (figure 2, panel C); only 2 out of 8 rats in this group had nodules >5mm in diameter; strikingly, in 2 animals no macroscopic lesions were observed. Histological analysis on H&E stained liver samples confirmed and extended these results: overt HCC was found in 4 out of 8 animals given DENA+RS, as mentioned in the preceding paragraphs; however, no HCCs were present in the group receiving normal hepatocyte transplantation following the carcinogenic protocol (table 1). Proliferating hepatocytes were readily observed in hepatic nodules and HCC in animals exposed to DENA+RS, as expected (figure 2, panel D); however, they were fewer in GST 7-7-positive lesions from the group receiving hepatocyte transplantation (figure 2, panel E); in the latter group, areas of repopulated liver displayed scattered BrdU-positive hepatocytes (figure 2, panel F).

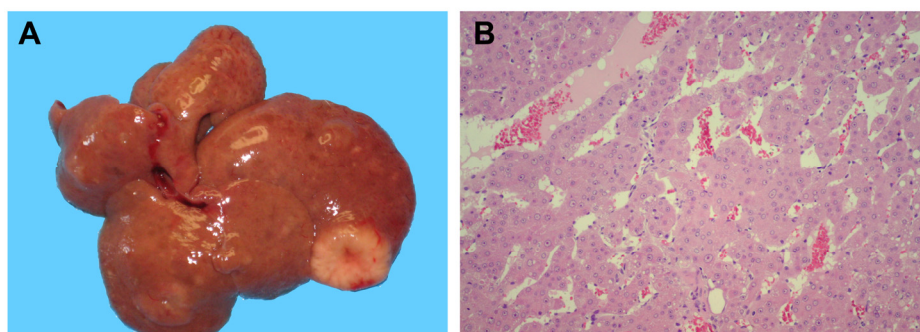


**Figure 1.** The development of HCC in rats exposed to DENA+RS and killed after one year. Panel **A**: macroscopic appearance, with whitish-grey lesions displaying prominent vasculature; panel **B**: trabecular HCC with discrete cellular pleomorphism (100x).

**Table 1.** Incidence of nodules and HCC in the two experimental groups

	Number of animals with:		
	Preneoplastic nodules		HCC
	$\leq 5\text{mm}$	$> 5\text{mm}$	
DENA + RS	8/8	7/8	4/8
DENA + RS + Tx	6/8	2/8	0/8
Relative Risk	0.7500	0.2857	0
P value	ns	$<0.05$	$<0.05$

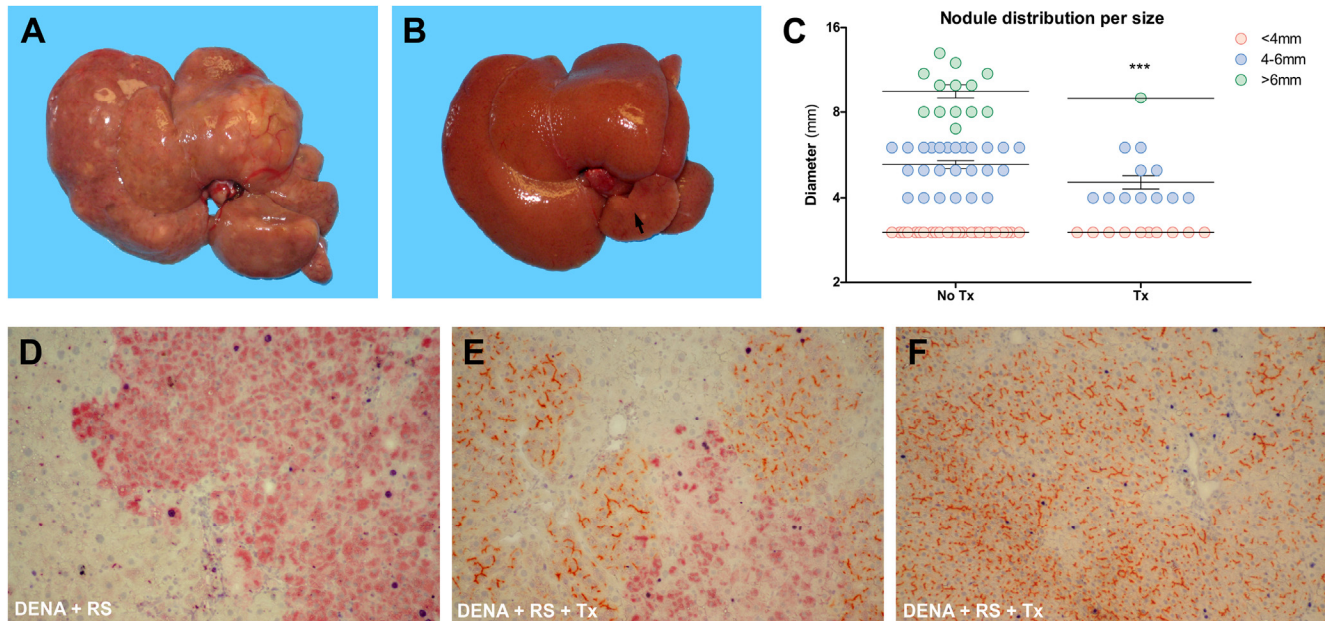


**Figure 2. Analysis of liver lesions.** Macroscopic appearance of livers from animals exposed to either DENA+RS (panel **A**) or DENA+RS followed by hepatocyte transplantation (panel **B**); both animals were killed 1 year post-treatment. Note the presence of large lesions in panel **A**, while the liver in panel **B** appears normal and shows only one tiny nodule in the caudate lobe. Panel **C** shows the size distribution of hepatic lesions in both experimental groups; note that the largest lesion found in one animal in DENA+RS-treated group is not included in this plot. \*\*\*Significantly different from non-transplanted animals: nodules  $<4\text{mm}$ ,  $P<0.005$ ; nodules  $4\text{-}6\text{mm}$ ,  $P<0.001$ ; nodules  $>6\text{mm}$ ,  $P<0.005$ . Panels **D-F**: immunohistochemical analysis of liver sections from animals exposed to either DENA+RS (panel **D**) or DENA+RS followed by hepatocyte transplantation (panels **E** and **F**); sections were stained for glutathione-S-transferase 7-7 (GST 7-7, a marker of preneoplastic nodules), BrdU and DPP-IV (orange-rust). Note the presence of BrdU-labelled hepatocytes (dark blue) in GST 7-7-positive lesions (red color, panels **D** and **E**) and in areas of repopulated liver (orange-rust, panel **E** and **F**).

## Normal hepatocyte transplantation results in the clearance of DENA+RS-induced senescent hepatocytes

As mentioned in the Introduction, recent findings have indicated that exposure to RS induces extensive hepatocyte senescence in rat liver [10]. Although cell senescence can represent a fail safe mechanism to halt neoplastic progression of altered cells [17], it is now well established that it can also contribute to the emergence of the neoplastic phenotype, possibly through secretion of a host of factors, variably referred to as senescence-associated secretory phenotype (SASP) [18] or senescence-messaging secretome (SMS) [19], and comprising cytokines, growth factors and proteases. Based on this information, it became important to determine the presence of hepatocyte senescence in animals treated with DENA+RS or DENA+RS+Tx. As reported in figure 3, markers relat-

ed to cell senescence were highly expressed in animals treated with DENA+RS and killed 4 months later; these included the senescence-associated  $\beta$ -galactosidase (SA- $\beta$ -gal), (panel A); and the phosphorylated form of H2A histone family, member X ( $\gamma$ -H2AX), which is considered as a marker of persistent activation of a DNA damage response and a trigger of cell senescence (panel D). However, both changes were almost completely reversed in animals given DENA+RS followed by hepatocyte transplantation. Transplanted hepatocytes were able to extensively repopulate the host liver; this effect was already prominent at 4 months post-injection (Figure 3, panel C), and persisted after 1 year (data not shown); it was associated with decreased expression of both SA- $\beta$ -gal and  $\gamma$ -H2AX, which were virtually absent in repopulated areas of the liver and were only detected in residual portions of endogenous parenchyma (figure 3, panels B, C, E, F, G and H).

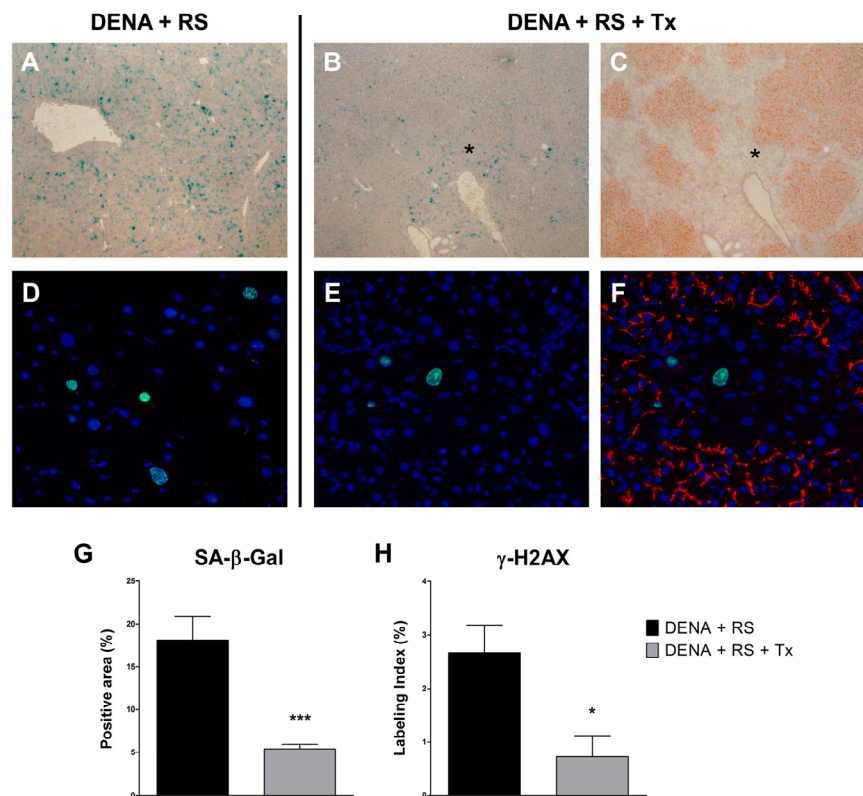


**Figure 3. Hepatocyte transplantation reverses the RS-induced senescent phenotype.** Expression of SA- $\beta$ -gal (panels A, B, C and G) and  $\gamma$ -H2AX (panels D, E, F and H), in rat liver exposed to either DENA+RS or DENA+RS followed by normal hepatocyte transplantations. Markers of cell senescence were highly expressed in DENA+RS-treated livers (panels A, D), while their levels were markedly reduced in animals receiving hepatocyte transplantation (panels B, C, E, F). In the latter group, extensive repopulation of the recipient liver was observed (panels C, histochemical staining for DPP-IV, orange-rust; panel F, immunofluorescence staining for CD26, red); note the residual expression of senescence markers in non-repopulated areas (panel C and F). Panels A, B and C: magnification 40x; panels D, E and F: magnification 200x. Panels G and H: \*\*\*P<0.001; \*P<0.05.



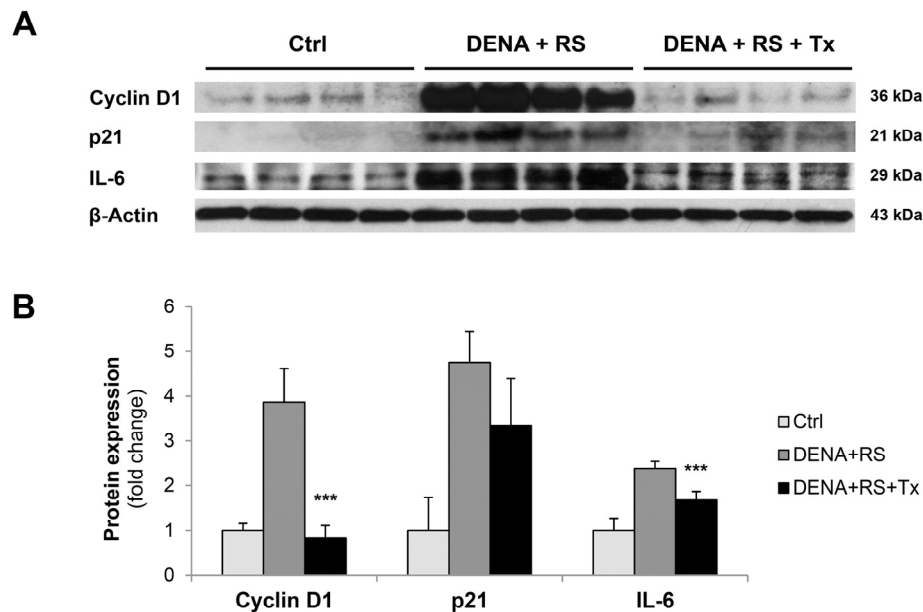


**Figure 4. Hepatocyte transplantation reverses the RS-induced senescent phenotype.**

Expression of cyclin D1, p21 and IL-6 in control rat liver and rat liver exposed to either DENA+RS or DENA+RS followed by normal hepatocyte transplantations. All gene products were highly expressed in DENA+RS-treated livers, while their levels were near control values in animals receiving hepatocyte transplantation (panels A and B). \*\*\*Significantly different from non-transplanted animals:  $P < 0.005$ .

### Hepatocyte transplantation reverses biochemical markers of hepatocyte senescence and SASP

An intriguing interpretation of cell senescence postulates that this unique phenotype emerges when a cell integrates two types of signals: one that reads for growth and one that imposes a block in the replicative cycle [20,21]. For example, DNA damaging agents do not induce senescence in quiescent cells; however, they do so if the presence of persistent DNA damage and cell cycle arrest is coupled with growth promoting stimuli [21]. Under these conditions, cells switch on the senescence program and express markers related to both cell cycle block and growth stimulation. In line with this postulation, both the cyclin-dependent kinase inhibitor, p21, and the positive regulator cyclin D1 were found to be over-expressed in rats exposed to DENA+RS and killed 4 months thereafter (figure 4, panels A and B). Furthermore, a main component of SASP/SMS, namely the pro-inflammatory cytokine IL-6, was also over-expressed in DENA+RS-treated animals. Both findings were in agreement with those reported following exposure to RS alone [10].

Remarkably, these changes were strongly counteracted by transplantation of normal hepatocytes: in fact, the expression of p21, cyclin D1 and IL-6 returned to near-control levels in animals receiving normal cells following exposure to the carcinogenic protocol. (figure 4, panels A and B).

### DISCUSSION

The results of these studies indicate that transplantation of normal hepatocytes in a neoplastic-prone liver microenvironment delays the growth of hepatic nodules and the emergence of HCC; furthermore, this effect is associated with clearance of senescent hepatocytes induced by the carcinogenic protocol.

Over a decade ago, we reported that pre-neoplastic hepatocytes grew very rapidly and progressed to HCC upon transplantation into a host liver pre-treated with RS; however, the same cell population was unable to expand following implantation into the liver of a normal, un-treated recipient [8]. Recent studies, aimed at defining the biological and molecular determinants of



the RS-induced effect, revealed the presence of extensive hepatocyte senescence in rat liver exposed to the alkaloid. Based on those findings, it was suggested that cell senescence and the associated SASP/SMS are possibly involved in the induction of the RS-associated neoplastic-prone tissue microenvironment [10]. In fact, it is now widely recognized that the senescence phenotype, while representing a fail-safe mechanism to avoid the risk of malignant transformation in cells harbouring damaged DNA or activated oncogenes [16,17,22,23], can also foster the emergence of premalignant and malignant cells [18,19,24,25], including their acquisition of metastatic potential [26] and resistance to chemotherapy [27,28]. These effects are at least partly mediated by a host of secreted factors, referred to as SASP/SMS and comprising cytokines, growth factors and proteases [18,19]. Among other products, the pro-inflammatory cytokine IL-6 has been attributed a prominent role both as a mediator of SASP effects and in reinforcing the senescence phenotype [24]. Moreover, cell senescence and SASP have been linked to chronic inflammation [29], adding yet another facet to the complex relationship between cancer, aging, and the immune response [30,31]. Interestingly, cell senescence has been reported in association with major risk factors for human neoplasia, including aging, cigarette smoke [32], UV light [33] and liver cirrhosis [34]. Indeed, the presence of hepatocyte senescence has long been documented during the evolution of chronic liver disease [35]. A recent study suggests that parameters related to cell senescence predict progression in non-alcoholic fatty liver disease (NAFLD) [36]. Moreover, a specific role for IL-6, together with TNF, has been proposed in the pathogenesis of liver inflammation and cancer associated with dietary and genetic obesity [37]. Thus, it appears that the tissue microenvironment induced by RS in rat liver, which strongly promotes the neoplastic process, shares intriguing similarities with chronic alterations associated with increased risk of liver cancer in humans.

In the present studies we tested the possibility that normal hepatocyte transplantation would reverse alterations induced by RS in the liver microenvironment, thereby modulating its tumour promoting potential. To this end, animals were sequentially exposed to DENA and RS, followed by two injections of hepatocytes freshly isolated from normal syngenic donors [14]. At end of 1 year, all animals treated with DENA+RS developed large liver tumours, with 50% (4/8) incidence of HCC. By contrast, the number of nodules were greatly reduced in rats receiving normal hepatocyte transplantation; most importantly, no animal in this group showed histological evidence of HCC (figure 2 and Table 1).

The liver of transplanted animals was extensively repopulated by donor-derived cells, resulting in the clearance of DENA+RS-induced senescent hepatocytes. Only residual hepatocytes expressing SA- $\beta$ -Gal or  $\gamma$ -H2AX were found in these animals, and they were confined to areas of non-repopulated liver (figure 3); furthermore, the expression of cyclin D1, p21 and the SASP-associated cytokine IL-6 were markedly reduced to near control values. In summary, normal hepatocyte transplantation is able to delay DENA+RS-induced carcinogenic process and it is also associated with extensive remodeling of the tissue landscape, consisting in the massive replacement of resident senescent hepatocytes with phenotypically normal cells. It is noteworthy that our results are reminiscent of those reported by the group of the DeGregori in the hematopoietic system: it was observed that transplantation of young, normal bone marrow cells was able to prevent the clonal expansion and leukemogenesis mediated by initiated progenitors in the context of an aged or previously irradiated bone marrow microenvironment [38,39].

In a recent report, Kang et al. described the protective effect of immune-mediated clearance of N-ras-expressing senescent hepatocytes on liver cancer development in mice [40]. The effect was attributed to the putative preneoplastic nature of oncogene-transduced senescent cells, whose removal by a T-cell specific response was therefore considered as directly responsible for the reduced incidence of HCC [40]. While any direct involvement of the immune system was not investigated in our present study, our findings appear difficult to reconcile with the above proposition. In fact, there is no evidence that RS-induced senescent hepatocytes display any direct pre-neoplastic potential [41]; on the other hand, they are able to support the growth of transplanted nodular hepatocytes and their progression to HCC [8]. Thus, it appears that, under the conditions described in our studies, the role of cell senescence is to promote the growth of carcinogen-induced altered cells, possibly through the effect(s) of SASP/SMS components, including IL-6 [42]. Replacement of senescent hepatocytes by normal transplanted cells results in the attenuation of such promoting effect and a delay in the emergence of preneoplastic and neoplastic lesions. Interestingly, a similar paradigm could be applicable to the increased cancer incidence associated with aging [43].

Taken together, these findings reinforce the concept that strategies aimed at preserving and/or re-establishing a normal tissue microenvironment represent an effective approach towards limiting the impact of neoplastic disease. Furthermore, they highlight the role of

senescent cells in fuelling carcinogenesis in a neoplastic-prone tissue landscape.

## EXPERIMENTAL PROCEDURES

**Animals and treatments.** Liver carcinogenesis was induced using a sequential exposure to diethylnitrosamine (DENA) and retrorsine (RS) [14]. Male Fischer 344, rats of 4 weeks of age were injected with DENA (160 mg/kg, i.p.), followed by a single dose of RS (30 mg/kg, i.p.), given 10 days after DENA administration. Two weeks later, animals were divided into 2 groups of 12 rats each: group 1 received no further treatment, while group 2 was given two injections of hepatocytes isolated from a normal syngenic donor, containing  $4 \times 10^6$  cells each, two weeks apart. Animals from each group were killed at either 4 months (4 rats) or 12 months (the remaining 8 rats) after DENA administration. Starting 24 hours before killing, animals were given 3 injections of 5'-bromo-deoxyuridine (BrdU, 50 mg/kg, i.p.) every 8 hours. All experiments were approved by the University of Cagliari Ethical Committee for Animal Experimentation; all animals received humane care in accordance with NIH Guidelines for the care and use of animals. Hepatic lesions were microscopically classified according to published criteria [44].

**Hepatocyte isolation and transplantation.** Hepatocytes for transplantation were isolated from a 6-wk old donor, according to a two-step collagenase perfusion technique [45]. Cell viability, determined by trypan blue exclusion at the end of the isolation procedure, was >90%. Animals were anesthetized and a small incision (about 1 cm) was performed in the upper abdominal wall; hepatocytes, suspended in PBS ( $1 \times 10^7$ /ml), were then delivered through a branch of the mesenteric veins, using a syringe with a 26-gauge needle. The fate of donor-derived cells in the recipient liver was followed using the F344-dipeptidyl-peptidase type IV (DPP-IV)-deficient model for cell transplantation [46]. Donor hepatocytes were isolated from animals expressing the marker enzyme (DPP-IV-positive), while DPP-IV-deficient rats were used as recipients. Since the Fischer 344 rat is a syngenic strain, no immunosuppression was required for successful cell transplantation.

**Histochemical and immunohistochemical methods.** After sacrifice, livers were removed and samples were taken from each lobe to be either frozen for cryostat sections or fixed in buffered formalin for standard histological analysis and immunohistochemistry. In animals killed at 12 months, liver lobes were cut into 1-2 mm-thick slices and were macroscopically examined for the presence of hepatic nodules/tumors or any other

evident lesion. The extent of liver repopulation in transplanted animals was monitored in cryostat sections stained for DPP-IV expression, using histochemical detection methods. Double staining for BrdU (DAKO, Glostrup, Denmark) and glutathione-S-transferase 7-7 (GST 7-7, Santa Cruz, Santa Cruz, CA) was performed on frozen sections, previously fixed in cold 1% acetic acid/ethyl alcohol and boiled in 0.01M Sodium Citrate, pH 6.0.

Staining for SA- $\beta$ -gal was performed according to published procedures [47]. Immediately before staining, X-Gal stock solution was prepared by dissolving 20mg/ml X-Gal (Invitrogen, Carlsbad, CA) in dimethylformamide. SA- $\beta$ -Gal staining solution was prepared as follows: 1 mg/ml of X-Gal stock solution were dissolved in 40 mM citric acid in sodium phosphate, pH 6.0/5 mM potassium ferrocyanide/5 mM potassium ferricyanide/150 mM NaCl/2 mM  $MgCl_2$ . Frozen sections of 10- $\mu$ m thickness were fixed for 5' in 4% formaldehyde/0.5% glutaraldehyde at 4°C, washed in PBS and incubated in fresh SA- $\beta$ -Gal staining solution for 16h at 37°C. Sections were counterstained with Hematoxylin.

**Immunofluorescence.** Immunofluorescence staining for  $\gamma$ -H2AX and CD26 was performed on frozen sections, following fixation in acetone. Slides were blocked for 30', incubated with primary antibodies (H2AX: Abcam, Cambridge, MA; CD26: BD Pharmingen, San Jose, CA) for 1 h at RT, then incubated with Alexa 488- and Alexa 555-conjugated secondary antibodies (Life Technologies, Carlsbad, CA). Slides were counterstained with DAPI and images were acquired with an IX71 fluorescence microscope with CCD camera (Olympus, Tokyo, Japan).

**Western Blot.** Liver tissue samples were homogenized in RIPA lysis buffer containing Protease Inhibitors, then centrifuged at 12000 rpm for 30' at 4°C. Protein concentration in supernatants was measured using the BCA method [48]. Samples (20 $\mu$ g protein) were prepared in Laemmli buffer, boiled at 95°C for 5' then loaded into SDS-PAGE precast gels (Biorad, Hercules, CA) and run under denaturing conditions. Proteins were transferred onto nitrocellulose membranes (GE, Fairfield, CT), blocked with 5% non-fat milk for 1 h, then incubated with primary antibodies for Cyclin D1 (Sigma, St. Louis, MO), p21 (Santa Cruz, Santa Cruz, CA) NF- $\kappa$ B, TNF- $\alpha$ , IL-6 and  $\beta$ -Actin (Abcam) overnight at 4°C. Membranes were washed and incubated for 2 h with the appropriate secondary antibody conjugated with HRP. Protein bands were detected using a chemoluminescent substrate (Biorad) and imaged onto Kodak film.

Imaging and Statistical analysis. Relative risk of developing preneoplastic/neoplastic lesions was calculated for both experimental groups, as shown in table 1. Chi-square test was used to evaluate statistical significance. Histological images and western blots were processed for quantification with Image Pro Premier software (Media Cybernetics, Rockville, MD). Results are presented as mean±S.E; two-tailed Student t test was used to evaluate results, with a lowest level of significance of  $p<0.05$ .

## ACKNOWLEDGEMENTS

We thank Mrs. Anna Saba and Mr. Roberto Marras for their technical contribution. Grant Support: this work was supported by AIRC (Italian Association for Cancer Research, grant No. IG 10604) and by Sardinian Regional Government (RAS).

## Conflicts of Interest Statement

The authors declare no conflict of interest.

## REFERENCES

- Mintz B, Illmensee K. Normal genetically mosaic mice produced from malignant teratocarcinoma cells. *Proc Natl Acad Sci U S A* 1975;72:3585-3589.
- Barcellos-Hoff MH, Ravani SA. Irradiated mammary gland stroma promotes the expression of tumorigenic potential by unirradiated epithelial cells. *Cancer Res* 2000;60:1254-1260.
- Laconi E. The evolving concept of tumor microenvironments. *Bioessays* 2007;29:738-744.
- Bissell MJ, Hines WC. Why don't we get more cancer? A proposed role of the microenvironment in restraining cancer progression. *Nat Med* 2011;17:320-329.
- PM, Kasemeier-Kulesa JC, Teddy JM, Margaryan NV, Seftor EA, Seftor REB, Hendrix MJC. Reprogramming metastatic melanoma cells to assume a neural crest cell-like phenotype in an embryonic microenvironment. *Proc Natl Acad Sci U S A* 2006;103:3752-3757.
- Hoshida Y, Villanueva A, Kobayashi M, Peix J, Chiang DY, Camargo A, Gupta S, Moore J, Wrobel MJ, Lerner J, Reich M, Chan JA, Glickman JN, Ikeda K, Hashimoto M, Watanabe G, et al. Gene expression in fixed tissues and outcome in hepatocellular carcinoma. *N Engl J Med*. 2008; 359: 1995-2004.
- Okamoto M, Utsunomiya T, Wakiyama S, Hashimoto M, Fukuzawa K, Ezaki T, Hanai T, Inoue H, Mori M. Specific gene-expression profiles of noncancerous liver tissue predict the risk for multicentric occurrence of hepatocellular carcinoma in hepatitis C virus-positive patients. *Ann Surg Oncol*. 2006; 13: 947-54.
- Laconi S, Pani P, Pillai S, Pasciu D, Sarma DS, Laconi E. A growth-constrained environment drives tumor progression invivo. *Proc Natl Acad Sci U S A* 2001;98:7806-7811.
- Laconi S, Curreli F, Diana S, Pasciu D, De Filippo G, Sarma DS, Pani P, Laconi E. Liver regeneration in response to partial hepatectomy in rats treated with retrorsine: a kinetic study. *J Hepatol*. 1999; 31: 1069-1074
- Serra MP, Marongiu F, Sini M, Laconi E. Hepatocyte senescence in vivo following preconditioning for liver repopulation. *Hepatology* 2012;56:760-768.
- Place AE, Jin Huh S, Polyak K. The microenvironment in breast cancer progression: biology and implications for treatment. *Breast Cancer Res*. 2011; 13: 227.
- Correia AL, Bissell MJ (2012) The tumor microenvironment is a dominant force in multidrug resistance. *Drug Resist Updat* 15: 39-49.
- Hernandez-Gea V, Toffanin S, Friedman SL, Llovet JM. Role of the Microenvironment in the Pathogenesis and Treatment of Hepatocellular Carcinoma. *Gastroenterology* 2013;144:512-27.
- Serra MP, Doratiotto S, Marongiu F, Laconi E. Normal hepatocyte transplantation delays the emergence of chemically-induced pre-neoplastic nodules in rat liver. *Cell Transplant*. 2012; 21 :671-7
- Hayes MA, Roberts E, Farber E. Initiation and selection of resistant hepatocyte nodules in rats given the pyrrolizidine alkaloids lasiocarpine and senecionine. *Cancer Res*. 1985; 45: 3726-3734.
- Narita M, Lowe SW. Senescence comes of age. *Nature Med*. 2005; 11: 920-922.
- Suram A, Kaplunov J, Patel PL, Ruan H, Cerutti A, Boccardi V, Fumagalli M, Di Micco R, Mirani N, Gurung RL, Hande MP, d'Adda di Fagagna F, Herbig U. Oncogene-induced telomere dysfunction enforces cellular senescence in human cancer precursor lesions. *EMBO J*. 2012; 31:2839-2851.
- Coppé JP, Patil CK, Rodier F, Sun Y, Muñoz DP, Goldstein J, Nelson PS, Desprez PY, Campisi J. Senescence-associated secretory phenotypes reveal cell-nonautonomous functions of oncogenic RAS and the p53 tumor suppressor. *PLoS. Biol*. 2008; 6: 2853-2868.
- Kuilman T, Peeper DS. Senescence-messaging secretome: SMS-ing cellular stress. *Nat Rev Cancer*. 2009; 9: 81-94.
- Demidenko ZN, Blagosklonny MV. Growth stimulation leads to cellular senescence when the cell cycle is blocked. *Cell Cycle*. 2008; 7: 3355-3361.
- Leontieva OV, Natarajan V, Demidenko ZN, Burdelya LG, Gudkov AV, Blagosklonny MV. Hypoxia suppresses conversion from proliferative arrest to cellular senescence. *Proc Natl Acad Sci USA*. 2008; 109: 13314-13318.
- Van Nguyen T, Puebla-Orsorio N, Pang H, Dujka ME, Zhu C. DNA damage-induced cellular senescence is sufficient to suppress tumorigenesis: a mouse model. *J Exp Med*. 2007; 204: 1453-1461.
- Xue W, Zender L, Miething C, Dickins RA, Hernando E, Krizhanovsky V, Cordon-Cardo C, Lowe SW. Senescence and tumour clearance is triggered by p53 restoration in murine liver carcinomas. *Nature*. 2007; 445:656-60
- Kuilman T, Michaloglou C, Vredeveld LC, Douma S, van Doorn R, Desmet CJ, Aarden LA, Mooi WJ, Peeper DS. Oncogene-induced senescence relayed by an interleukin-dependent inflammatory network. *Cell*. 2008; 133: 1019-1031.
- Rodier F, Coppé JP, Patil CK, Hoeijmakers WA, Muñoz DP, Raza SR, Freund A, Campeau E, Davalos AR, Campisi J. Persistent DNA damage signalling triggers senescence-associated inflammatory cytokine secretion. *Nat Cell Biol*. 2009; 11: 973-979.

26. Angelini PD, Zacarias Fluck MF, Pedersen K, Parra-Palau JL, Guiu M, Bernadó Morales C, Vicario R, Luque-García A, Navalpotro NP, Giralt J, Canals F, Gomis RR, Tabernero J, Baselga J, Villanueva J, Arribas J. Constitutive HER2 signaling promotes breast cancer metastasis through cellular senescence. *Cancer Res.* 2013; 73: 450-458.
27. Gilbert LA, Hemann MT. DNA damage-mediated induction of a chemoresistant niche. *Cell.* 2010; 143: 355-366.
28. Sun Y, Campisi J, Higano C, Beer TM, Porter P, Coleman I, True L, Nelson PS. Treatment-induced damage to the tumor microenvironment promotes prostate cancer therapy resistance through WNT16B. *Nat Med.* 2012; 18: 1359-1368.
29. MM, Weyand CM, Goronzy JJ. Chronic inflammation and aging: DNA damage tips the balance. *Curr Opin Immunol.* 2012; 24: 488-493.
30. Coussens LM, Zitvogel L, Palucka AK. Neutralizing tumor-promoting chronic inflammation: a magic bullet? *Science.* 2013; 339: 286-291.
31. Takahashi H, Ogata H, Nishigaki R, Broide DH, Karin M. Tobacco smoke promotes lung tumorigenesis by triggering IKK $\beta$ - and JNK1-dependent inflammation. *Cancer Cell.* 2010; 17:89-97.
32. Tsuji T, Aoshiba K, Nagai A. Cigarette smoke induces senescence in alveolar epithelial cells. *Am J Respir Cell Mol Biol.* 2004; 31: 643-649.
33. Lewis DA, Yi Q, Travers JB, Spandau DF. UVB-induced senescence in human keratinocytes requires a functional insulin-like growth factor-1 receptor and p53. *Mol Biol Cell.* 2008; 19: 1346-1353.
34. Wiemann SU, Satyanarayana A, Tsahuridu M, Tillmann HL, Zender L, Klempnauer J, Flemming P, Franco S, Blasco MA, Manns MP, Rudolph KL. Hepatocyte telomere shortening and senescence are general markers of human liver cirrhosis. *FASEB J.* 2002; 16: 935-942.
35. Paradis V, Youssef N, Dargère D, Bâ N, Bonvoust F, Deschatrette J, Bedossa P. Replicative senescence in normal liver, chronic hepatitis C, and hepatocellular carcinomas. *Hum Pathol.* 2001; 32: 327-332.
36. Aravinthan A, Scarpini C, Tachtatzis P, Verma S, Penrhyn-Lowe S, Harvey R, Davies SE, Allison M, Coleman N, Alexander G. Hepatocyte senescence predicts progression in non-alcohol-related fatty liver disease *J Hepatol.* 2013; 58: 549-56.
37. Park EJ, Lee JH, Yu GY, He G, Ali SR, Holzer RG, Osterreicher CH, Takahashi H, Karin M. Dietary and genetic obesity promote liver inflammation and tumorigenesis by enhancing IL-6 and TNF expression. *Cell.* 2010; 140: 197-208.
38. Marusyk A, Casás-Selves M, Henry CJ, Zaberezhnyy V, Klawitter J, Christians U, DeGregori J. Irradiation alters selection for oncogenic mutations in hematopoietic progenitors. *Cancer Res.* 2009; 69:7262-7269.
39. Henry CJ, Marusyk A, Zaberezhnyy V, Adane B, DeGregori J. Declining lymphoid progenitor fitness promotes aging-associated leukemogenesis. *Proc Natl Acad Sci U S A.* 2010; 107:21713-21718.
40. Kang TW, Yevsa T, Woller N, Hoenicke L, Wuestefeld T, Dauch D, Hohmeyer A, Gereke M, Rudalska R, Potapova A, Iken M, Vucur M, Weiss S, Heikenwalder M, Khan S, Gil J, Bruder D, Manns M, Schirmacher P, Tacke F, Ott M, Luedde T, Longerich T, Kubicka S, Zender L. Senescence surveillance of pre-malignant hepatocytes limits liver cancer development. *Nature.* 2011; 479: 547-551.
41. Laconi S, Montisci S, Doratiotto S, Greco M, Pasciu D, Pillai S, Pani P, Laconi E. Liver repopulation by transplanted hepatocytes and risk of hepatocellular carcinoma. *Transplantation.* 2006; 82: 1319-1323.
42. Galun E, Axelrod JH. The role of cytokines in liver failure and regeneration: potential new molecular therapies. *Biochim Biophys Acta.* 2002; 1592: 345-358.
43. Pasciu D, Montisci S, Greco M, Doratiotto S, Pitzalis S, Pani P, Laconi S, Laconi E. Aging is associated with increased clonogenic potential in rat liver in vivo. *Aging Cell.* 2006; 5: 373-377.
44. Squire RA, Levitt MH. Report of a workshop on classification of specific hepatocellular lesions in rats. *Cancer Res.* 1975; 35: 3214-3223.
45. Seglen PO. Preparation of isolated rat liver cells. *Methods Cell Biol.* 1976; 13:29-83.
46. Thompson NL, Hixson DC, Callanan H, Panzica M, Flanagan D, Faris RA, Hong WJ, Hartel-Schenk S, Doyle D. A Fischer rat substrain deficient in dipeptidyl peptidase IV activity makes normal steady-state RNA levels and an altered protein. Use as a liver-cell transplantation model. *Biochem J.* 1991; 273 (Pt 3): 497-502.
47. Itahana K, Campisi J, Dimri GP. Methods to detect biomarkers of cellular senescence: the senescence-associated beta-galactosidase assay. *Methods Mol Biol.* 2007; 371: 21-31.
48. Smith PK, Krohn RI, Hermanson GT, Mallia AK, Gartner FH, Provenzano MD, Fujimoto EK, Goeke NM, Olson BJ, Klenk DC. Measurement of protein using bicinchoninic acid. *Anal Biochem.* 1985; 150:76-85.

## Therapeutic and space radiation exposure of mouse brain causes impaired DNA repair response and premature senescence by chronic oxidant production

Shubhankar Suman<sup>1</sup>, Olga C. Rodriguez<sup>2</sup>, Thomas A. Winters<sup>3</sup>, Albert J. Fornace Jr<sup>1,2,4</sup>, Chris Albanese<sup>2</sup>, and Kamal Datta<sup>1,2</sup>

<sup>1</sup> Department of Biochemistry and Molecular & Cell Biology, Georgetown University Medical Center, Washington, DC 20057, USA;

<sup>2</sup> Lombardi Comprehensive Cancer Center, Georgetown University, Washington, DC 20057, USA;

<sup>3</sup> Nuclear Medicine Department, Warren Grant Magnuson Clinical Center, National Institutes of Health, Bethesda, Maryland 20892;

<sup>4</sup> Center of Excellence In Genomic Medicine Research (CEGMR), King Abdulaziz University, Jeddah, SA

**Key words:** Radiation, heavy ion radiation, premature aging, senescence, oxidative stress, DNA damage, cerebral cortex, long-term effects

**Received:** 6/21/13; **Accepted:** 8/5/13; **Published:** 8/6/13

**Correspondence to:** Kamal Datta, MD; **E-mail:** [kd257@georgetown.edu](mailto:kd257@georgetown.edu)

**Copyright:** © Suman et al. This is an open-access article distributed under the terms of the Creative Commons Attribution License, which permits unrestricted use, distribution, and reproduction in any medium, provided the original author and source are credited

**Abstract:** Despite recent epidemiological evidences linking radiation exposure and a number of human ailments including cancer, mechanistic understanding of how radiation inflicts long-term changes in cerebral cortex, which regulates important neuronal functions, remains obscure. The current study dissects molecular events relevant to pathology in cerebral cortex of 6 to 8 weeks old female C57BL/6J mice two and twelve months after exposure to a  $\gamma$  radiation dose (2 Gy) commonly employed in fractionated radiotherapy. For a comparative study, effects of 1.6 Gy heavy ion  $^{56}\text{Fe}$  radiation on cerebral cortex were also investigated, which has implications for space exploration. Radiation exposure was associated with increased chronic oxidative stress, oxidative DNA damage, lipid peroxidation, and apoptosis. These results when considered with decreased cortical thickness, activation of cell-cycle arrest pathway, and inhibition of DNA double strand break repair factors led us to conclude to our knowledge for the first time that radiation caused aging-like pathology in cerebral cortical cells and changes after heavy ion radiation were more pronounced than  $\gamma$  radiation.

## INTRODUCTION

Radiation exposure to normal brain tissue during therapeutic and diagnostic procedures is unavoidable and radiation has been shown to affect brain function [1-3]. Radiation therapy remains the main mode of treatment for both the primary and secondary brain tumors and fractionated radiation therapy commonly uses a 2 Gy daily dose-fraction [1,4]. Although important advances have been made in the field of radiation therapy to make it more focused, radiation exposure to normal brain tissue is inescapable leading to long-term functional deficit such as cognitive, visual,

and motor impairments. Among the diagnostic procedures, computerized tomographic (CT) scan due to its multiple exposure sequences exposes tissues to a higher radiation doses per scan than a single exposure procedures such as x-ray chest. A single head and neck CT scan, depending on age, could expose brain to radiation doses between 20 and 100 mGy and with marked increase in radiation based diagnostic procedures [5-7], the cumulative radiation dose to brain due to repeated exposure could be high enough to raise long-term health concern such as functional decline and cancer [8]. Epidemiological studies in atom bomb survivors have shown increased cancer risk after



exposure to radiation dose between 50 and 200 mGy and exposure at an early age has the highest risk [9]. Cerebral cortex, the outermost layer of the mammalian brain, regulates important functions such as awareness, motor and sensory functions, memory, language, and visual perceptions through its connections to various sub-cortical structures such as the thalamus and basal ganglia. Therefore, any perturbation in cerebral cortical cells caused by radiation exposure would lead to impairment of at least some of these neurological functions compromising quality of life. Studies in mice have shown significant structural alterations of the cerebral cortex eight weeks after exposure to four 5 Gy fractions of  $\gamma$  radiation [1]. However, long-term follow up *in vivo* data on underlying mechanisms of changes in cerebral cortex after exposure to a clinically relevant dose of  $\gamma$  radiation is not available in the literature.

Radiation exposure is intimately linked to the production of reactive oxygen species (ROS) and due to its high oxygen consumption and metabolic rate, the brain is more susceptible to ROS and oxidative stress than other organs [10]. Increased ROS could react with lipids, DNA, and proteins leading to the generation of more reactive species and the establishment of a state of perpetual oxidative stress in cells compromising cerebral cortex function [11,12]. Brain due to its high lipid content is particularly vulnerable to oxidative stress-induced lipid peroxidation, which not only generates lipid-based free radicals but also produces a number of highly reactive aldehydes such as malondialdehyde and 4-hydroxy-2-nonenal (4-HNE). These reactive aldehydes in turn react with cellular proteins to form adducts, which have been implicated in neurodegenerative diseases including Alzheimer's disease [13]. When produced in excess of cellular antioxidant capacity, ROS are known to induce, apart from other damages, DNA double strand breaks (DSB), the most lethal form of DNA damage. Experimental evidence indicates that unrepaired DSB could induce cell death, and misrepaired DSB has the potential of causing genomic instability [14,15]. DNA DSB in non-dividing cells is commonly repaired by non-homologous end joining (NHEJ) and aging has been associated with a decline in Ku70, Ku80, and DNAPKcs which are considered major players of the NHEJ pathway [16-22].

Persistent induction of DNA damage due to sustained ROS production results in a perpetual DNA damage response [23,24]. The tumor suppressor gene p53 due to its pivotal role in DNA damage response such as cell cycle arrest, DNA repair, and cell death induction remains an important player in maintenance of cellular homeostasis and genomic integrity after radiation

exposure. Upon radiation-induced ROS generation and ensuing DNA damage, p53 is activated leading to alterations in the level of its downstream effectors such as Bax, Bcl2, and p21 resulting in the induction of apoptosis and growth arrest [25]. p53, which is mutated in >50% of human cancers, has also been reported to play important roles in aging and increased p53 activity could usher in premature aging [24,26]. However, cellular senescence and aging is a complex process involving multiple signaling pathways [27-30] and association of the tumor suppressors p16<sup>Ink4a</sup> and p19<sup>Arf</sup> with senescence is well documented in literature [31,32].

Radiation injury to the brain has been shown to upregulate intermediate filament proteins such as nestin and glial fibrillary acidic protein (GFAP), which are also reported to be associated with oxidative stress, aging, and neurodegeneration [33,34]. The intermediate filament proteins nestin and vimentin are associated with the developing central nervous system (CNS) and upon terminal differentiation of neural precursor cells to astrocytes and neurons, nestin is no longer expressed and is substituted by GFAP and vimentin [35]. Re-expression of embryonic proteins such as nestin and upregulation of GFAP, which reflects proliferative activation of astroglial cells have been observed in radiation-induced CNS injury and increased cellular stress in brain [12,35-41].

Radiation environment in outer space, compared to that on earth, mostly consists of high-energy protons and heavy ions such as <sup>56</sup>Fe, <sup>28</sup>Si, <sup>16</sup>O, and <sup>12</sup>C and associated secondary particle radiation [42-44]. While solar particle events (SPE) with mostly proton radiation are sporadic, the galactic cosmic radiation (GCR) with most of its dose equivalent contributed by heavy ion radiation is ambient in space. Heavy ion radiation with high linear energy transfer (high-LET - deposits more energy per unit volume of tissue compared to low-LET  $\gamma$  radiation prevalent on earth) characteristics is vastly more damaging compared to proton and  $\gamma$  radiation not only due to its densely ionizing primary track but also due to the greater number of highly ionizing secondary delta ray tracks [45-47]. Consequently, from astronauts' health point of view, a major concern for the National Aeronautics and Space Administration (NASA) during long duration space missions is exposure to heavy ion radiation and its consequences on the CNS. Additionally, heavy ion radiation therapy of brain tumors has been shown to inflict subsequent neurological deficits such as cognitive and memory loss that are predicted to be in part due to alterations in cerebral cortex [48-50]. Also, exposure to high-LET neutron radiation has been shown to induce hypoplasia

of the cerebral cortex in the developing mouse brain [51]. While most of the animal studies involving high-LET radiation focused on hippocampus [11,52-58], very few have dealt with cerebral cortex and fewer have reported underlying mechanisms. The current study undertakes long-term follow up investigations of molecular events in cerebral cortex associated with  $\gamma$  radiation exposure and how these events relate to heavy ion radiation exposure. We have shown that there were increased oxidative stress and accelerated senescence signaling after 2 Gy  $\gamma$  radiation. Importantly, we also showed that the effects of oxidative stress and accelerated aging were more pronounced in mice exposed to heavy ions compared to  $\gamma$  radiation.

## RESULTS

### Persistently raised levels of ROS in cerebral cortical cells after radiation exposure

ROS levels were distinctly increased in freshly isolated cerebral cortical cells two and twelve months after exposure to 1.6 Gy (equitoxic to 2 Gy  $\gamma$  radiation; [59]) of  $^{56}\text{Fe}$  radiation compared to shams and 2 Gy  $\gamma$ -irradiated samples. (Figure 1A, B, D, and E). Quantification of flow cytometry data demonstrates a significant increase in ROS levels after  $^{56}\text{Fe}$  exposure at both time points relative to control and  $\gamma$  radiation (for 2-month post-radiation:  $p < 0.008$  compared to control

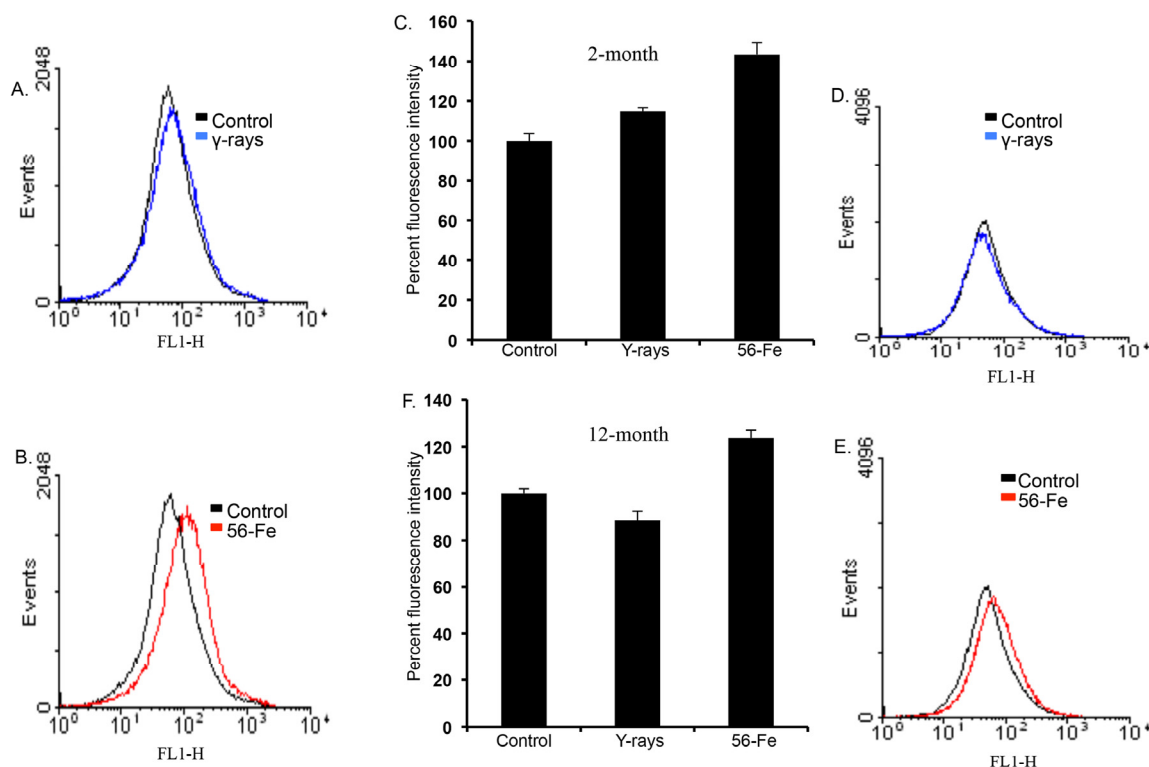


**Figure 1.** Increased reactive oxygen species (ROS) in cerebral cortical cells after  $^{56}\text{Fe}$  radiation. (A) Flow cytometry histogram showing ROS level two months after  $\gamma$  radiation. (B) Flow cytometry histogram showing ROS level two months after  $^{56}\text{Fe}$  radiation. (C) Quantification of ROS level two months after radiation presented as mean  $\pm$  standard error of mean (SEM). (D) Flow cytometry histogram showing ROS level twelve months after  $\gamma$  radiation. (E) Flow cytometry histogram showing ROS level twelve months after  $^{56}\text{Fe}$  radiation. (F) Quantification of ROS level twelve months after radiation presented as mean  $\pm$  SEM.

and  $p < 0.05$  compared to  $\gamma$  radiation; for 12-month post-radiation:  $p < 0.04$  compared to control and  $p < 0.01$  compared to  $\gamma$  radiation; Figure 1C and F). There was a statistically significant increase in ROS levels two month after  $\gamma$  radiation (Figure 1A and C;  $p < 0.03$  compared to control). We did not observe any detectable alterations in ROS levels in twelve-month post- $\gamma$ -irradiation groups relative to controls (Figure 1D and F).

### Increased lipid peroxidation, oxidative DNA damage and apoptosis after radiation exposure was associated with a decrease in cortical thickness

Persistently elevated levels of 4-HNE indicated by brown

coloration visible in the cytoplasm around nuclei both two and twelve months after  $^{56}\text{Fe}$  radiation were observed (Figure 2A and C). Although less than  $^{56}\text{Fe}$  radiation, we also observed increased 4-HNE levels after  $\gamma$  radiation (Figure 2A and C). Quantification of 4-HNE staining showed significantly more staining in two as well as twelve months post- $^{56}\text{Fe}$  irradiation samples relative to  $\gamma$  radiation and controls (for 2-month  $p < 0.0000001$  compared to control and  $p < 0.0006$  compared to  $\gamma$  radiation; for 12-month  $p < 0.00000006$  compared to control and  $p < 0.000006$  compared to  $\gamma$  radiation; Figure 2B and D). There was also a significant increase in 4-HNE staining two- and twelve-month post- $\gamma$ -irradiation relative to controls (for 2-month  $p < 0.00003$  and for 12-month  $p < 0.02$ ; Figure 2B and D).

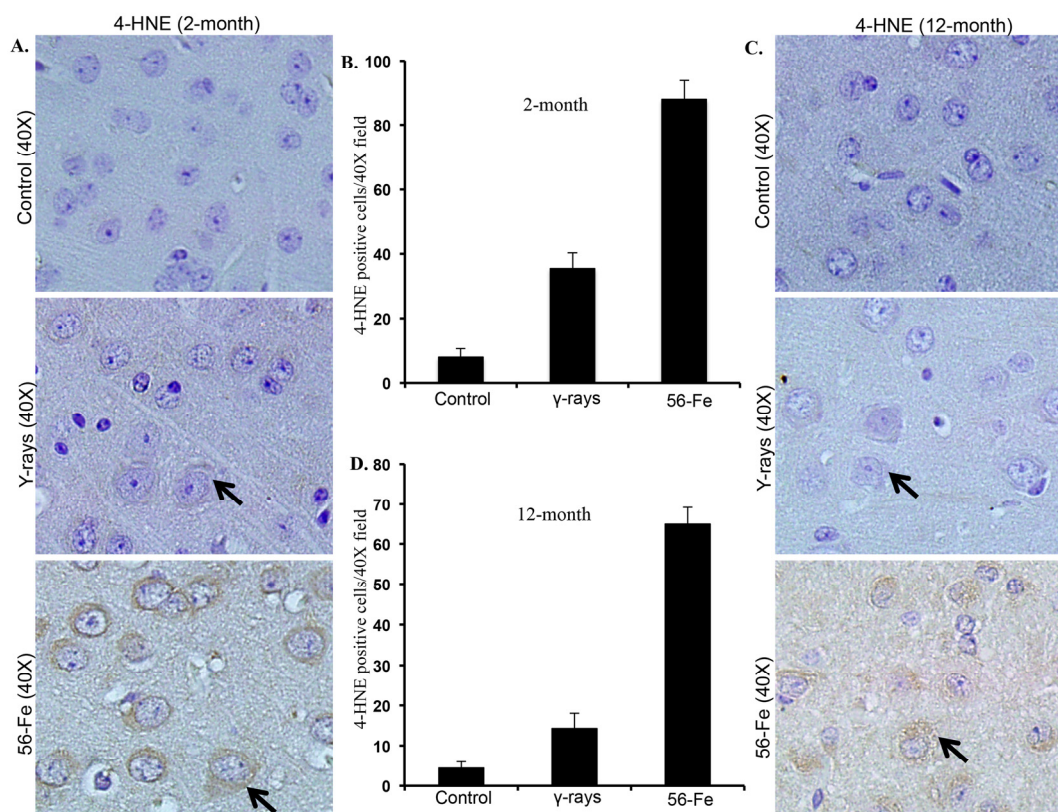


**Figure 2.** Lipid peroxidation in cerebral cortex was greater after  $^{56}\text{Fe}$  radiation. (A) Immunohistochemical staining (arrow) of cerebral cortex for 4-hydroxy-2-nonenal (4-HNE) two months after radiation. (B) Quantification of 4-HNE staining two months after exposure presented as mean  $\pm$  SEM. (C) Immunohistochemical staining (arrow) for 4-HNE twelve months after radiation. (D) Quantification of 4-HNE staining twelve months after radiation presented as mean  $\pm$  SEM.

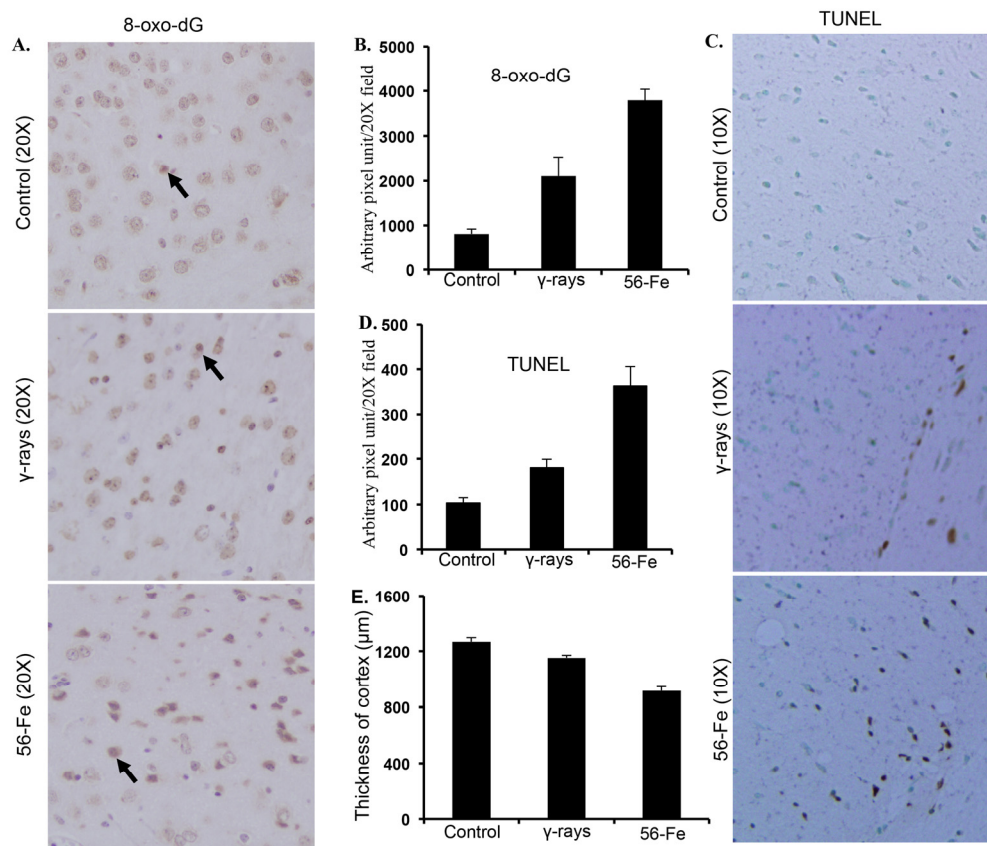


**Figure 3.** Assessing oxidative DNA damage and cell death in cerebral cortex twelve months after radiation. (A) Immunohistochemical staining of cerebral cortex for 8-oxo-dG after exposure to  $\gamma$  and  $^{56}\text{Fe}$  radiation. (B) Quantification of 8-oxo-dG staining in cerebral cortex presented as mean  $\pm$  SEM. (C) TUNEL staining of cerebral cortex after exposure to  $\gamma$  and  $^{56}\text{Fe}$  radiation. (D) Quantification of TUNEL staining of cerebral cortex after exposure to  $\gamma$  and  $^{56}\text{Fe}$  radiation presented as mean  $\pm$  SEM. (E) Measurement of cerebral cortex thickness in H&E stained histological sections presented as mean  $\pm$  SEM.

Markedly increased 8-oxo-dG staining in cerebral cortex twelve months after irradiation was observed (Figure 3A). Quantification showed significant difference in 8-oxo-dG staining between  $\gamma$  and  $^{56}\text{Fe}$ -irradiated samples (for  $^{56}\text{Fe}$  radiation  $p < 0.0001$  compared to control and  $p < 0.04$  compared to  $\gamma$  radiation; Figure 3B). Although less than  $^{56}\text{Fe}$  radiation, we also observed significantly more 8-oxo-dG staining after  $\gamma$  radiation compared to control ( $p < 0.001$ ; Figure 3A and B). TUNEL stain indicating cell death also showed greater number of positive cells twelve months after  $^{56}\text{Fe}$  radiation compared to  $\gamma$  radiation and quantification showed significant difference between the two types of radiation (for  $^{56}\text{Fe}$  radiation  $p < 0.0003$  compared to control and  $p < 0.01$  compared to  $\gamma$  radiation; Figure 3C and D). Small but significant increase in TUNEL positive cells was also observed after  $\gamma$  radiation relative to control ( $p < 0.01$ ; Figure 3C). Measurements of cortical thickness showed significantly greater decrease twelve months after ex-

posure to  $^{56}\text{Fe}$  radiation relative to control and  $\gamma$  radiation ( $p < 0.00001$  compared to control and  $p < 0.0002$  compared to  $\gamma$  radiation; Figure 3E). Cortical thickness twelve months after  $\gamma$  radiation was also decreased which was statistically significant relative to control ( $p < 0.008$ ; Figure 3E). Volumetric measurement using magnetic resonance imaging (MRI) also showed decreased brain volume twelve months after radiation exposure (Supplementary figure 1A). While  $\gamma$  radiation showed small but statistically significant decrease in brain volume ( $p < 0.05$  compared to control), the  $^{56}\text{Fe}$  radiation showed greater decrease than  $\gamma$  radiation ( $p < 0.04$  compared to control and  $\gamma$  radiation; Supplementary materials and methods and Supplementary figure 1A). Physical activity assay performed using a barrier (12" in length and width and 3" in height) showed irradiated mice taking significantly more time to climb the barrier relative to controls and  $^{56}\text{Fe}$  irradiated mice needed the most time (for  $\gamma$  radiation  $p < 0.004$  compared to control and for  $^{56}\text{Fe}$  radiation  $p < 0.01$  compared to control and  $\gamma$



radiation; Supplementary materials and methods and Supplementary figure 1B). Additionally,  $\gamma$  irradiated mice also showed increased time required climbing the barrier relative to controls ( $p < 0.02$  compared to control; Supplementary figure 1B).

### Exposure to radiation decreased DNA repair proteins and increased DNA damage response and senescence markers in cerebral cortex

Proteins involved in DNA DSB repair, DNA damage response, and senescence were markedly altered two

and twelve months after radiation exposure (Figure 4A). Quantitatively, a significant decrease in DNAPKcs level, relative to control and  $\gamma$  radiation, was observed after  $^{56}\text{Fe}$  radiation at both the time points (Figure 4B and C). Compared to control, Ku70 levels were significantly decreased two months after  $\gamma$  and  $^{56}\text{Fe}$  radiation. However, compared to  $\gamma$  radiation, there was greater decrease in Ku70 levels after  $^{56}\text{Fe}$  radiation (Figure 4B and C). Although, compared to control, Ku70 was decreased significantly in both the radiation types, its levels were similar in  $\gamma$  and  $^{56}\text{Fe}$  radiation at the twelve-month time point (Figure 4B and C).

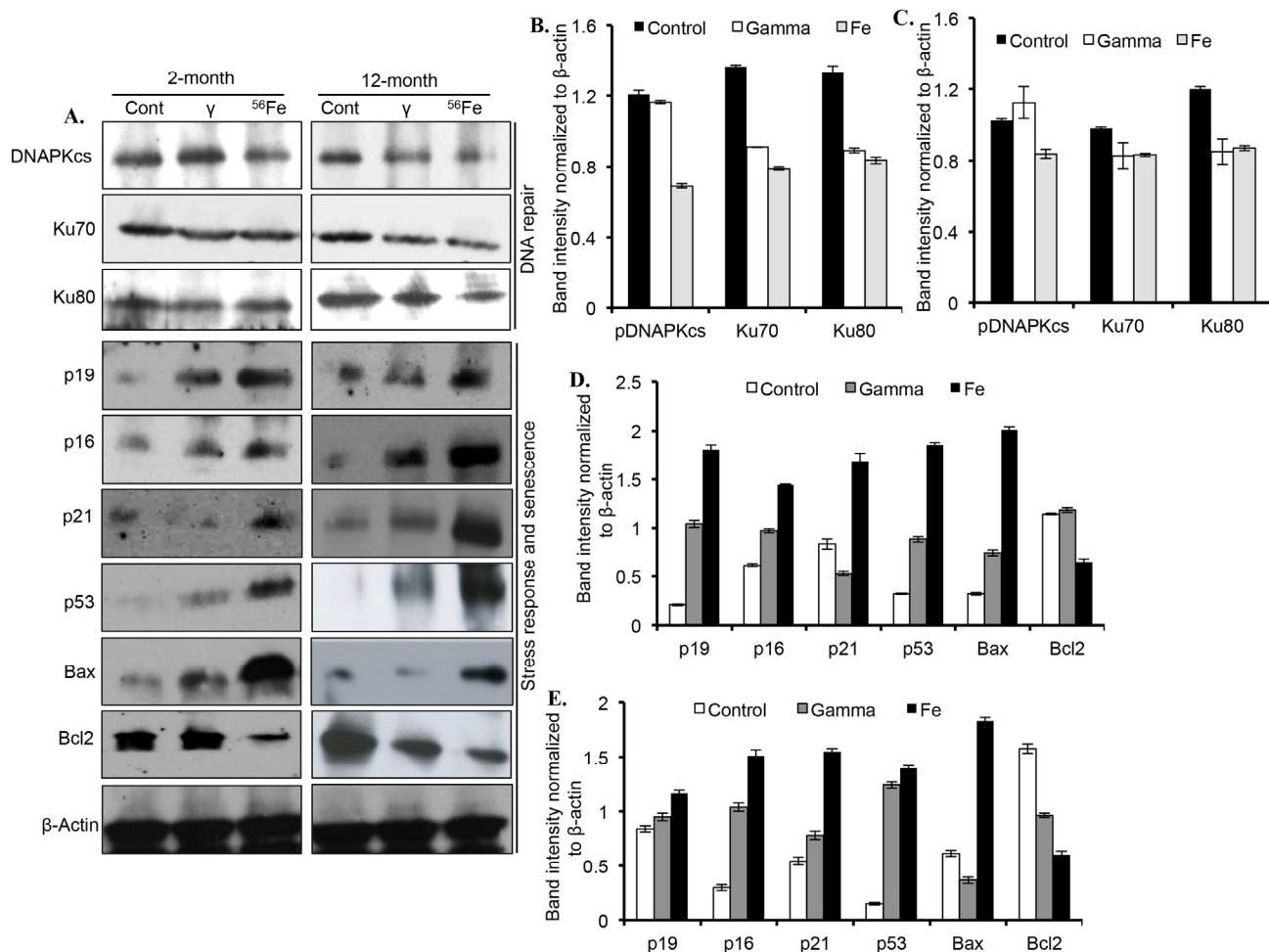


**Figure 4.** Assessing DNA repair and senescence markers in cerebral cortex. (A) Immunoblot images of DNA double strand break repair (Ku70, Ku80, and DNAPKcs), and senescence and DNA damage response (p19, p16, p21, p53, Bax, and Bcl2) proteins two and twelve months after radiation. (B) Quantification of Ku70, Ku80, and DNAPKcs two months after radiation. (C) Quantification of Ku70, Ku80, and DNAPKcs twelve months after radiation. (D) Quantification of p19, p16, p21, p53, Bax, and Bcl2 two months after radiation. (E) Quantification of p19, p16, p21, p53, Bax, and Bcl2 twelve months after radiation. Quantification data (panel B to E) is presented as mean  $\pm$  SEM.



Compared to controls, the levels of Ku80 were reduced in both the radiation types two and twelve months after exposure. (Figure 4B and C). At both the time points, however, the levels of Ku80 were not different between the two radiation types (Figure 4B and C). While compared to controls the levels of cell-cycle arrest and DNA damage response marker proteins p19, p16, and p53 were noticeably increased two and twelve months after  $\gamma$  radiation, the levels of these proteins after  $^{56}\text{Fe}$  radiation showed greater increase than  $\gamma$  radiation (Figure 4D and E). Although p21 is decreased at two months after  $\gamma$  radiation, its level was increased at twelve months post-exposure relative to controls. Bax level was increased at two months but decreased at twelve months after  $\gamma$  radiation. While Bcl2 level two months after  $\gamma$  radiation was similar to control, its level relative to control was lowered at twelve months after  $\gamma$  radiation (Figure 4D and E). However, after  $^{56}\text{Fe}$  radiation at both the time points p21 and Bax were increased and Bcl2 was decreased relative to control and

$\gamma$  radiation (Figure 4D and E).

### Reactive gliosis was associated with re-expression of nestin and upregulation of GFAP

Stressful stimuli in brain are associated with activation of astroglial cells resulting in re-expression of nestin and upregulation of GFAP [60]. Our observations showed that there was a significant enhancement of nestin staining in the twelve-month post- $^{56}\text{Fe}$  radiation exposure samples (for  $^{56}\text{Fe}$  radiation  $p < 0.0007$  compared to control and  $p < 0.003$  compared to  $\gamma$  radiation; Figure 5A and B). Also, significantly higher expression of GFAP was observed in cerebral cortex twelve months after  $^{56}\text{Fe}$  irradiation (for  $^{56}\text{Fe}$  radiation  $p < 0.02$  compared to control and  $p < 0.05$  compared to  $\gamma$  radiation; Figure 5C and D). Compared to control, statistically significant increase in nestin ( $p < 0.01$ ; Figure 5A and B) and GFAP ( $p < 0.002$ ; Figure 5C and D) staining was also observed twelve months after  $\gamma$  radiation exposure.

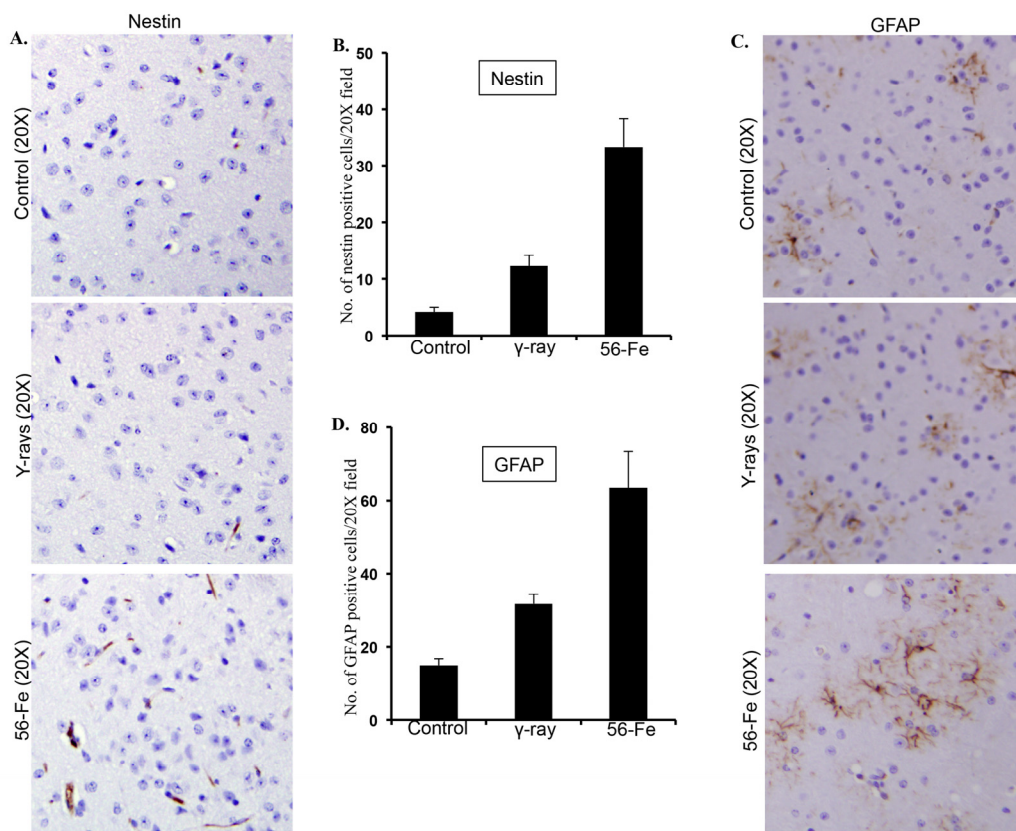


**Figure 5.** Assessing reactive gliosis twelve months after radiation exposure. (A) Comparing immunohistochemical staining of nestin in cerebral cortex after radiation. (B) Quantification of nestin staining in cerebral cortex presented as mean  $\pm$  SEM. (C) Comparing immunohistochemical staining of GFAP in cerebral cortex after radiation. (D) Quantification of GFAP staining in cerebral cortex presented as mean  $\pm$  SEM.

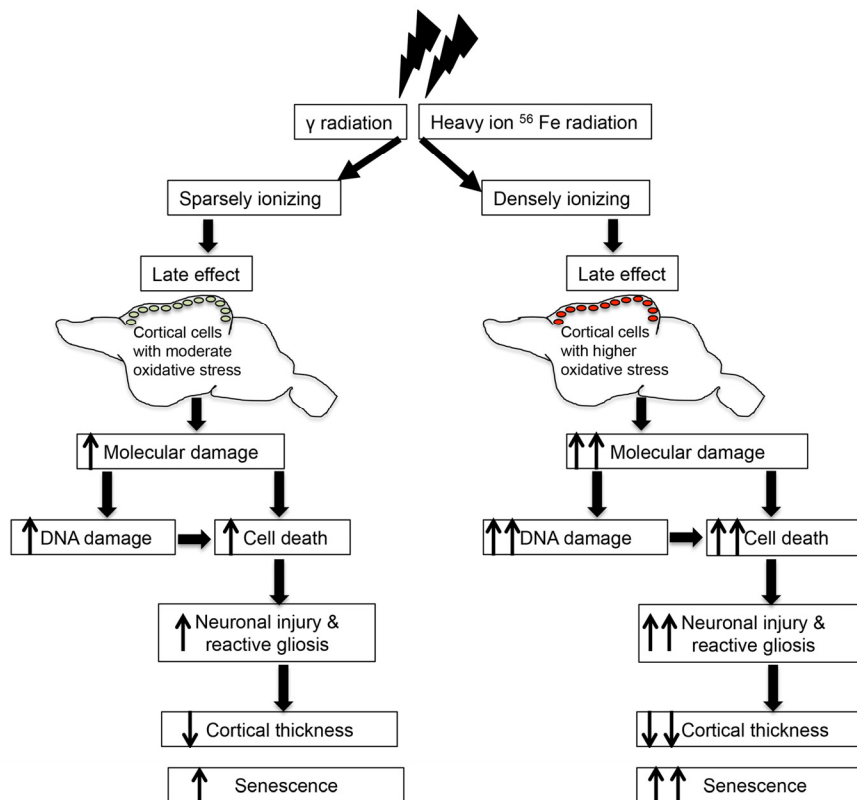


**Figure 6.** Schematic overview of radiation-induced chronic oxidative stress and accelerated aging.

## DISCUSSION

Radiation exposure on one hand has been reported to induce long-term changes in CNS resulting in functional impairments such as motor and sensory disturbances, and learning and memory deficits [61,62] and on the other it has also been associated with risk of initiation and promotion of brain tumor [7,8,63]. However, we still lack a clear mechanistic understanding required to comprehend the persistent molecular events, which unfold in the brain after radiation exposure and has the potential to cause overt neurological deficits or tumor later in life. Importantly, due to its structural makeup and functional demands, the brain is vulnerable to oxidative stress and persistent oxidative stress has been implicated in neurodegeneration and cancer [64]. Although there are reports relating radiation, both  $\gamma$  and  $^{56}\text{Fe}$ , to changes in the cellular redox status in brain, most of the studies are relatively short term [65-68], very few have involved cerebral cortex, and fewer had long-term follow up investigation at the molecular level in the cerebral

cortex. Here we demonstrated that, relative to control, there was persistently higher ROS production after  $\gamma$  radiation. We also observed that persistent ROS production was markedly more after  $^{56}\text{Fe}$  radiation relative to control and  $\gamma$  irradiation in cerebral cortical cells. While we observed increased lipid peroxidation, DNA damage, and apoptosis along with decreased cortical thickness and brain volume after  $\gamma$  radiation, these effects were more prominent after  $^{56}\text{Fe}$  radiation. We also demonstrated that there was increased p21, p19, and p16, and decreased DNA repair proteins in cerebral cortex after radiation exposure suggesting premature senescence.

Radiation-induced damage to biomolecules such as proteins and DNA has mostly been attributed to generation of ROS and consequent oxidative stress, which has been implicated in neurodegeneration, aging, and cancer [64,69-71]. Indeed, oxidative stress associated modifications of biomolecules are known hallmarks of the aging brain [11,72] and it is expected that heavy ion radiation with its propensity to cause

higher oxidative stress and increased damage to biomolecules could accelerate changes in brain commonly associated with aging. Our results of ROS measurement in cerebral cortical cells confirm the notion that heavy ion radiation induces higher oxidative stress relative to  $\gamma$  radiation and are consistent with our earlier results in intestinal epithelial cells [73]. Importantly, chronic oxidative stress leading to sustained DNA damage and continued activation of p53 dependent DNA damage response has been reported to induce chronic elevation of p21 level that could result in continued growth arrest leading to cellular senescence and short life span [24,74,75,75-78]. Indeed, our immunoblot results showed increased p53 and consequent increase in p21 suggesting senescence of cortical cells after radiation exposure. Interestingly, while persistent elevation of p21 is induced by oxidative stress-mediated DNA damage response, its sustained higher level is also known to result in the activation of signaling events promoting mitochondrial perturbation and increased ROS production [79]. Persistent elevation of p53 in  $\gamma$  as well as in  $^{56}\text{Fe}$ -irradiated mice also illustrates a state of perpetual DNA damage response (DDR), which is supported not only by elevated p21 but also by alterations of other p53 effectors such as Bax and Bcl2. Our observations of increased Bax and decreased Bcl2 in irradiated mice led us to believe that the balance of pro- and anti-apoptotic factors in cerebral cortex is in favor of cell death. It has been reported that with advancing age there is a gradual decline in normal brain volume and in neurodegenerative diseases a marked cerebral atrophy with decline in cognitive function have been observed [80,81]. Reduction of cortical thickness, a hallmark of degenerative changes, observed after radiation exposure is probably due to cell death (confirmed by our TUNEL assay) mediated by p53-induced alterations of Bax and Bcl2 levels. Taken together our results in this study demonstrated that radiation exposure caused chronic oxidative stress, persistent oxidative DNA damage, and such DNA damages were associated with increased DDR leading to growth arrest as well as cell death in cerebral cortex. Considering the fact that ROS generated immediately after radiation are due to radiolysis of water molecules and are short lived, we believe that the persistent oxidative stress in cerebral cortex observed in our study is due to metabolically regenerated ROS of which mitochondria are the major source [82]. Oxidative stress-associated damage to biomolecules such as oxidative proteins and DNA damage has been implicated in a decline in functional competence of cerebral cortex [11,72,83]. Consequently, our results in cerebral cortex demonstrated a potential risk of developing long-term functional deficit as well as cellular transformation after radiation exposure.

Effects on CNS from heavy ion space radiation exposure due to its higher damaging capacity than  $\gamma$  radiation is a major health concern for astronauts undertaking long duration space missions. Apprehension about acute and long-term heavy ion radiation exposure risks to CNS is primarily due to lack of *in vivo* data in humans and animal models. However, in recent years, substantial work has been published which sheds lights on the effects of heavy ion radiation on different parts of the brain [11,52-58,84,85]. Evidence based on *in vivo* and *in vitro* studies has demonstrated that high-LET radiation adversely alters spatial learning, cognitive, memory, and other CNS faculties [11,54,55,85-88]. Our results also suggest that heavy ion space radiation with higher oxidative stress and greater associated changes has elevated risk of developing neuronal deficit and transformation and will require additional studies.

Radiation-induced persistently increased ROS and DNA damage could lead to sustained cell-cycle arrest potentially leading to senescence [89] and the cell's capability to repair DNA damage including DSB have been reported to decline with advancing age [17,19-21]. Additionally, decreased DSB repair proteins has been associated with enhanced cellular senescence and non-functional DSB repair proteins are known to accelerate organismal aging [16-22]. Our results showing decreased Ku70, Ku80, and DNAPKcs proteins in cerebral cortex, we speculate, is due to sustained higher oxidative stress, which could affect transcription, translation, and stability of repair proteins. Decreased repair proteins leading to reduction in DNA repair, we believe, would accelerate the onset of aging after  $^{56}\text{Fe}$  radiation [90]. Additionally, cellular stress has also been reported to consistently upregulate two other well-characterized aging markers, p19<sup>Arf</sup> and p16<sup>Ink4a</sup>, heralding stress-induced senescence. Importantly, p19<sup>Arf</sup> is activated in cells under stress including radiation exposure and is associated with the augmentation of p53-dependent DNA damage response through sequestration of MDM2 and thus stabilization of p53 [91]. Indeed, marked upregulation of p19<sup>Arf</sup> after both  $\gamma$  and  $^{56}\text{Fe}$  radiation may have played a prominent role in enhanced p53-dependent DNA damage response in our experimental setting to affect cellular senescence. Although the regulation of p16<sup>Ink4a</sup>, which is a cyclin-dependent kinase inhibitor and is progressively upregulated with advancing age, is not well understood [32], chronic upregulation of both p19<sup>Arf</sup> as well as p16<sup>Ink4a</sup> further confirms cellular senescence in cerebral cortex after radiation exposure. Additionally, decreased brain volume in MRI and increased time required to climb the physical barrier after radiation exposure provided further evidence linking premature senescence

and radiation (Supplementary figure 1A and B). However, additional functional studies will be required to relate observed changes in cerebral cortex after radiation to alterations in spatial learning, cognition, memory, and other CNS faculties of the organism.

Radiation-induced cellular damage in brain not only cause enhanced DNA damage response and senescence, but it also triggers repair and remodeling process through a proliferative response known as reactive gliosis [35,36]. Our results are consistent with previous reports relating nestin and GFAP to both  $\gamma$  and heavy ion radiation exposure [36,84]. We demonstrated that these two embryonic proteins showed higher expression in response to both  $\gamma$  and heavy ion radiation exposure suggesting activation of astroglial cells in cerebral cortex. Upregulation of both nestin and GFAP after radiation support a state of reactive gliosis in cerebral cortex. However, reactive gliosis denoted by increased nestin and GFAP does not support regeneration of neurons but instead leads to glial scar formation [36,84], which along with apoptosis may have aggravated shrinkage of cerebral cortex after radiation exposure. Glial scar formation rather than neuronal regeneration is further supported by the upregulation of GFAP that indicates that radiation-induced activation of astroglial proliferative response in cerebral cortex is committed to astrogliosis and subsequent scar tissue formation [84]. Our study has provided evidence that radiation exposure in the mouse brain accelerates the appearance of biological indicators of aging at the molecular level (Figure 6). Knowledge of adverse long-term sequelae of radiation exposure on cerebral cortex will not only allow us to assess risk but will also permit us to design strategies to minimize the effects of radiation on normal tissues.

## METHODS

Ethics statement on mice. Six to eight weeks old female C57BL/6J mice were purchased from Jackson Laboratories (Bar Harbor, ME). Mice were housed at the Georgetown University (GU) and Brookhaven National Laboratory (BNL) animal care facilities. Both the facilities are Association for Assessment and Accreditation of Laboratory and Animal Care International (AAALACI)-accredited and all animal procedures were performed as per protocols approved by the Institutional Animal Care and Use Committees (IACUC) at the GU and at the BNL. Mice were housed in groups of five in autoclaved cages and bedding materials in a separate room with 12-h dark and light cycle maintained at 22 °C in 50% humidity. All animals were provided certified rodent diet (LabDiet #5053, Brentwood, MO) with filtered water *ad libitum* and CO<sub>2</sub>

asphyxiation was used for euthanasia. Our research followed Guide for the Care and Use of Laboratory Animals, prepared by the Institute of Laboratory Animal Resources, National Research Council, and U.S. National Academy of Sciences. Investigation has been conducted in accordance with the ethical standards and according to the Declaration of Helsinki and according to national and international guidelines and has been approved by the authors' institutional review board.

Radiation. Exposure to heavy ion radiation (<sup>56</sup>Fe; energy: 1GeV/nucleon; dose rate: 1 Gy/min) was performed at the NASA Space Radiation Laboratory (NSRL) at BNL and <sup>137</sup>Cs was used as a source of  $\gamma$  radiation (dose rate: 1 Gy/min) and control mice were sham irradiated. During radiation exposure mice (n=15) were placed in small transparent plastic boxes (3"x1.5"x1.5") with holes for ventilation. Mice were exposed either to 1.6 Gy of <sup>56</sup>Fe or to 2 Gy of  $\gamma$  radiation and irradiation experiments was performed three times. The <sup>56</sup>Fe radiation dose is equitoxic to  $\gamma$  radiation and was calculated using a relative biological effectiveness (RBE) factor of 1.25 determined earlier [59]. For <sup>56</sup>Fe irradiation, the NSRL beam physics team performed the dosimetry, dose rate, and beam uniformity and mice were exposed to constant LET by placing them at the entrance plateau region of the Bregg peak [92-95]. Mice were shipped directly from the vendor to BNL one week prior to radiation and on the day after irradiation all the mice were shipped in a temperature controlled environment to GU for a same day delivery. Mice were followed for up to twelve months, brain surgically removed at two and twelve months post-exposure, washed and cleaned in phosphate buffered saline (PBS), two hemispheres separated in the middle, and one half fixed in 10% buffered formalin. While immersed in sterile PBS, multiple coronal sections of the other half of the brain were made and the cerebral cortex was separated from the rest of the brain under a dissecting scope (MZ6, Leica Microsystem, Wetzlar, Germany) as per protocol described earlier [96]. Cerebral cortex was either used for preparation of cortical single cell suspension for measuring reactive oxygen species (ROS) or flash frozen in liquid N<sub>2</sub> and stored at -80 °C for immunoblots.

Measuring ROS in cerebral cortical cells. Separated cerebral cortex (n=5 mice per group) was mechanically dissociated into single cell suspensions in Hank's balanced salt solution (HBSS) and filtered through a sterile 70  $\mu$ m nylon mesh (BD Biosciences, Sparks, MD) as per protocol described previously [1,97]. Cells were centrifuged (200xg) for 10 min at room temperature (RT) and supernatant discarded. Cell pellet

was resuspended in 1 ml of PBS at RT. A 2 mM solution of H2DCFDA (Invitrogen, Carlsbad, CA) was freshly prepared in ethanol and 5 µl were added to the cell suspension (final concentration 10 µM) and incubated at 37 °C for 20 min. Cells were centrifuged at 200xg for 5 min, supernatant discarded, and cell pellet resuspended in 500 µl of PBS. Flow cytometric analysis was performed in duplicate using FACSCalibur (BD Biosciences) and acquired data were analyzed using WinMDI v2.8 software.

**Immunoblot analysis.** Immunoblots were performed using standardized protocol. Flash-frozen cerebral cortical samples isolated two and twelve months after exposure to 2 Gy  $\gamma$  radiation and equitoxic 1.6 Gy of  $^{56}\text{Fe}$  radiation were used for immunoblots. Cortical tissues from 5 mice in each group were pooled and homogenized in ice cold lysis buffer (0.5% sodium deoxycholate; 0.5% NP-40; 10mM EDTA in PBS and protease inhibitor cocktail (Sigma, St. Louis, MO)), centrifuged at 12000xg at 4 °C for 15 min, and protein concentration was estimated in the supernatant by the Bradford method. Equal amount proteins with appropriate volume of loading buffer were loaded onto SDS-PAGE. Separated proteins were transferred to polyvinylidene fluoride (PVDF) membrane, treated with 5% non-fat milk in tris-buffered saline with 0.1% Tween (TBST), and exposed to specific primary antibodies for DNAPKcs (Sc-5282; diltion-1:200; Santa Cruz Biotechnology, Santa Cruz, CA), Ku70 (Sc-17789; diltion-1:200; Santa Cruz Biotechnology), Ku80 (Sc-9034; diltion-1:400; Santa Cruz Biotechnology), p53 (Sc-99; diltion-1:500; Santa Cruz Biotechnology), Bax (Sc-7480; diltion-1:250; Santa Cruz Biotechnology), Bcl2 (Sc-7382; diltion-1:250; Santa Cruz Biotechnology), p21 (Sc-6246; diltion-1:500; Santa Cruz Biotechnology), p16 (Sc-1661; diltion-1:200; Santa Cruz Biotechnology), p19 (07-543; diltion-1:200; EMD Millipore, Billerica, MA), and  $\beta$ -actin (Sc-47778; diltion-1:2000; Santa Cruz Biotechnology) and developed by chemiluminescence (Thermo Scientific, Rockford, IL) detection system. Results were recorded by autoradiography, images scanned and displayed. We used ImageJ v1.46 software for densitometric quantification of immunoblot images and band intensity of each protein normalized to  $\beta$ -actin is presented in bar graphs.

**Cerebral cortex histology.** Twelve months post-irradiation brain samples were fixed in 10% buffered formalin for 72 hours, paraffin embedded, and 4 µm sagittal sections were obtained for further processing. For histologic analysis, slides were stained with hematoxylin and eosin (H&E) using a standard protocol

and visualized by bright field microscopy at 4X microscopic magnification. Cortical thickness was measured using a protocol described previously [1]. Briefly, slide images were captured with an Olympus DP70 camera on an Olympus BX61 microscope and the thickness of the cerebral cortex was measured using ImageScope (Aperio Technologies, Vista, CA) software and results expressed in µm. For each study group, sections from seven mice were measured and three sections from each mouse were used. Unstained sections were used for terminal deoxynucleotidyl transferase dUTP nick end labeling (TUNEL) assay and immunohistochemistry.

**TUNEL assay.** TUNEL assay on brain sections (6 sections from 6 separate mouse from each group) was performed using ApopTag plus peroxidase in situ apoptosis detection kit (Millipore, Billerica, MA) as per manufacturer's instruction. Stained sections were visualized under bright field microscopy at 20X magnification and twelve random fields per group were captured for analysis.

**Immunohistochemistry.** Anti-8-oxo-dG antibody (clone 2E2; 4354-MC-050) was purchased from Trevigen (Gaithersburg, MD) and immunostaining was performed using recommended protocol. Briefly, following incubation with primary antibody overnight at 4 °C and necessary washing steps, sections were incubated with HRP-conjugated secondary antibody for 30 min at room temperature [73]. Diaminobenzidine (DAB) detection system (Invitrogen, Carlsbad, CA) was used to visualize staining. Bright field microscopy was used to capture the images of the cerebral cortex at 10X magnification and twelve images from randomly selected visual fields were captured from each group. For nestin, GFAP, and 4-HNE, immunostaining was performed as per protocol described previously [73,98,99]. Briefly, sections were deparaffinized, antigen retrieval performed, endogenous peroxidase activity quenched, and incubated in blocking buffer (0.1% bovine serum albumin in PBS). Sections were then exposed to anti-nestin (Sc-23927; dilution-1:100; Santa Cruz Biotechnology), anti-GFAP (PA5-16291; dilution-1:150; Thermo Scientific) and anti-4-HNE (Ab-46545; 1:200; Abcam, Cambridge, MA) antibodies for 1.5 hr at RT. Signal detection and color development was performed using SuperPicture™ 3<sup>rd</sup> Gen IHC detection kit (Cat# 87-9673; Invitrogen) and slides were mounted and visualized under bright field microscopy and twelve images from randomly selected visual fields were captured from each group for quantification. Six slides from six mice in each group were stained for each protein and a representative image from one animal is presented in results.



**Data Analysis and statistics.** Images were analyzed for TUNEL, 8-oxo-dG, 4-HNE, nestin, and GFAP positive cells using color deconvolution and Image-based Tool for Counting Nuclei (ITCN) plug-ins of ImageJ v1.46 software as per protocol described earlier [73,100,101]. Average number of TUNEL (20X), 8-oxo-dG (20X), nestin (20X), and GFAP (20X) positive nuclei per visual field is presented graphically. Data is presented as mean  $\pm$  standard error of mean (SEM) and statistical significance between two groups was determined by student's t-test and  $p < 0.05$  was considered significance.

### Supplementary methods

**Activity tests.** Mice ( $n=5$  mice per study group) were irradiated with 2 Gy  $\gamma$  or 1.6 Gy of  $^{56}\text{Fe}$  radiation and twelve months after irradiation each mouse were placed inside a barrier (12" in length and width and 3" in height) and time taken to come out of the barrier was noted in seconds. Results are presented as average time (sec) per mouse relative to sham-irradiated controls.

**Mouse brain magnetic resonance imaging (MRI).** The MRI was performed on a horizontal Bruker 7T spectrometer with a 20 cm bore run by Paravision 4.0 software as per protocol standardized in the Preclinical Imaging Research Laboratory at the Lombardi Comprehensive Cancer Center at the Georgetown University. Mice ( $n=3$ ) were anesthetized and anesthesia maintained with 1.5% isoflurane, 30% oxygen and 70% nitrous oxide and animals were placed on a custom-made stereotaxic animal holder equipped with temperature and respiration monitoring and imaged in a 35 mm birdcage radiofrequency coil. The sequence used to assess brain volume was a 3D RARE, matrix: 256x256x256, RARE factor: 8, TR: 500 ms, TE: 7.45 ms, FOV: 3 cm. Volumetric measurement of the brain was determined from MRI stacked images using the Measure Stack plugin tool (developed by Dougherty RF and available at <http://www.optinav.com/imagej.html>) of the ImageJ v1.46 software as per developer's instruction.

### ACKNOWLEDGEMENTS

We are very much thankful to the members of the NASA Space Radiation Laboratory especially to Drs. Peter Guida and Adam Rusek for their excellent support in conducting  $^{56}\text{Fe}$  radiation exposures. This study is supported in part by NASA Grant# NNX07AH70G and NNX09AU95G. We also thank the Histopathology and Tissue Shared Resources at the Lombardi Comprehensive Cancer Center at Georgetown University for histology services supported by Award Number P30CA051008 from the National Cancer

Institute (NCI). The funders had no role in study design, data collection and analysis, decision to publish, or preparation of the manuscript.

### Conflicts of Interest Statement

Authors have no competing financial interest to declare.

### REFERENCES

1. Joo KM, Jin J, Kang BG, Lee SJ, Kim KH, Yang H, Lee YA, Cho YJ, Im YS, Lee DS, Lim DH, Kim DH, Um HD, Lee SH, Lee JI, and Nam DH. Trans-differentiation of neural stem cells: a therapeutic mechanism against the radiation induced brain damage. *PLoS One*. 2012; 7:e25936.
2. Butler JM, Rapp SR, and Shaw EG. Managing the cognitive effects of brain tumor radiation therapy. *Curr Treat Options Oncol*. 2006; 7:517-523.
3. Gourmelon P, Marquette C, Agay D, Mathieu J, and Clarencon D. Involvement of the central nervous system in radiation-induced multi-organ dysfunction and/or failure. *BJR Suppl*. 2005; 27:62-68.
4. Jacob R, Gilligan D, Robinson M, and Harmer C. Hyper-fractionated radiotherapy for soft tissue sarcoma: results of the second study of hyper-fractionated radiotherapy. *Sarcoma*. 1999; 3:157-165.
5. Redberg RF. Cancer risks and radiation exposure from computed tomographic scans: how can we be sure that the benefits outweigh the risks? *Arch Intern Med*. 2009; 169:2049-2050.
6. Berrington de Gonzalez A, Mahesh M, Kim KP, Bhargavan M, Lewis R, Mettler F, and Land C. Projected cancer risks from computed tomographic scans performed in the United States in 2007. *Arch Intern Med*. 2009; 169:2071-2077.
7. Smith-Bindman R, Lipson J, Marcus R, Kim KP, Mahesh M, Gould R, Berrington de Gonzalez A, and Miglioretti DL. Radiation dose associated with common computed tomography examinations and the associated lifetime attributable risk of cancer. *Arch Intern Med*. 2009; 169:2078-2086.
8. Brenner DJ, and Hall EJ. Computed tomography--an increasing source of radiation exposure. *N Engl J Med*. 2007; 357:2277-2284.
9. Pierce DA, Shimizu Y, Preston DL, Vaeth M, and Mabuchi K. Studies of the mortality of atomic bomb survivors. Report 12, Part I. Cancer: 1950-1990. *Radiat Res*. 1996; 146:1-27.
10. Noseworthy MD, and Bray TM. Effect of oxidative stress on brain damage detected by MRI and in vivo  $^{31}\text{P}$ -NMR. *Free Radic Biol Med*. 1998; 24:942-951.
11. Manda K, Ueno M, and Anzai K. Memory impairment, oxidative damage and apoptosis induced by space radiation: ameliorative potential of alpha-lipoic acid. *Behav Brain Res*. 2008; 187:387-395.
12. Poulouse SM, Bielinski DF, Carrihill-Knoll K, Rabin BM, and Shukitt-Hale B. Exposure to  $^{16}\text{O}$ -particle radiation causes aging-like decrements in rats through increased oxidative stress, inflammation and loss of autophagy. *Radiat Res*. 2011; 176:761-769.
13. Butterfield DA, Reed T, and Sultana R. Roles of 3-nitrotyrosine- and 4-hydroxynonenal-modified brain proteins in

the progression and pathogenesis of Alzheimer's disease. *Free Radic Res.* 2011; 45:59-72.

14. Datta K, Purkayastha S, Neumann RD, Pastwa E, and Winters TA. Base damage immediately upstream from double-strand break ends is a more severe impediment to nonhomologous end joining than blocked 3'-termini. *Radiat Res.* 2011; 175:97-112.

15. Khanna KK, and Jackson SP. DNA double-strand breaks: signaling, repair and the cancer connection. *Nat Genet.* 2001; 27:247-254.

16. Li H, Vogel H, Holcomb VB, Gu Y, and Hasty P. Deletion of Ku70, Ku80, or both causes early aging without substantially increased cancer. *Mol Cell Biol.* 2007; 27:8205-8214.

17. Canugovi C, Yoon JS, Feldman NH, Croteau DL, Mattson MP, and Bohr VA. Endonuclease VIII-like 1 (NEIL1) promotes short-term spatial memory retention and protects from ischemic stroke-induced brain dysfunction and death in mice. *Proc Natl Acad Sci U S A.* 2012; 109:14948-14953.

18. Zhao B, Benson EK, Qiao R, Wang X, Kim S, Manfredi JJ, Lee SW, and Aaronson SA. Cellular senescence and organismal ageing in the absence of p21(CIP1/WAF1) in ku80(-/-) mice. *EMBO Rep.* 2009; 10:71-78.

19. Engels WR, Johnson-Schlitz D, Flores C, White L, and Preston CR. A third link connecting aging with double strand break repair. *Cell Cycle.* 2007; 6:131-135.

20. Lombard DB, Chua KF, Mostoslavsky R, Franco S, Gostissa M, and Alt FW. DNA repair, genome stability, and aging. *Cell.* 2005; 120:497-512.

21. Gilchrest BA, and Bohr VA. Aging processes, DNA damage, and repair. *FASEB J.* 1997; 11:322-330.

22. Rao KS, and Loeb LA. DNA damage and repair in brain: relationship to aging. *Mutat Res.* 1992; 275:317-329.

23. von Zglinicki T, Saretzki G, Ladhoff J, d'Adda di Fagagna F, and Jackson SP. Human cell senescence as a DNA damage response. *Mech Ageing Dev.* 2005; 126:111-117.

24. Frontini M, and Proietti-De-Santis L. Interaction between the Cockayne syndrome B and p53 proteins: implications for aging. *Aging (Albany NY).* 2012; 4:89-97.

25. Liu B, Chen Y, and St Clair DK. ROS and p53: a versatile partnership. *Free Radic Biol Med.* 2008; 44:1529-1535.

26. O'Neill M, Nunez F, and Melton DW. p53 and a human premature ageing disorder. *Mech Ageing Dev.* 2003; 124:599-603.

27. Blagosklonny MV. Answering the ultimate question "what is the proximal cause of aging?". *Aging (Albany NY).* 2012; 4:861-877.

28. Kolosova NG, Vitovtov AO, Muraleva NA, Akulov AE, Stefanova NA, and Blagosklonny MV. Rapamycin suppresses brain aging in senescence-accelerated OXYS rats. *Aging (Albany NY).* 2013; 5:474-484.

29. Suh Y. Cell signaling in aging and apoptosis. *Mech Ageing Dev.* 2002; 123:881-890.

30. Greer EL, and Brunet A. Signaling networks in aging. *J Cell Sci.* 2008; 121:407-412.

31. Wong ES, Le Guezennec X, Demidov ON, Marshall NT, Wang ST, Krishnamurthy J, Sharpless NE, Dunn NR, and Bulavin DV. p38MAPK controls expression of multiple cell cycle inhibitors and islet proliferation with advancing age. *Dev Cell.* 2009; 17:142-149.

32. Ressler S, Bartkova J, Niederegger H, Bartek J, Scharffetter-Kochanek K, Jansen-Durr P, and Wlaschek M. p16INK4A is a

robust in vivo biomarker of cellular aging in human skin. *Aging Cell.* 2006; 5:379-389.

33. Porchet R, Probst A, Bouras C, Draberova E, Draber P, and Riederer BM. Analysis of glial acidic fibrillary protein in the human entorhinal cortex during aging and in Alzheimer's disease. *Proteomics.* 2003; 3:1476-1485.

34. Morgan TE, Rozovsky I, Goldsmith SK, Stone DJ, Yoshida T, and Finch CE. Increased transcription of the astrocyte gene GFAP during middle-age is attenuated by food restriction: implications for the role of oxidative stress. *Free Radic Biol Med.* 1997; 23:524-528.

35. Jin JK, Jeong BH, Na YJ, Kim YS, Carp RI, Wie MB, Moon C, and Shin T. Increased expression of the embryonic intermediate filament, nestin, in the brains of scrapie-infected mice. *Neurosci Lett.* 2004; 367:254-258.

36. Shi M, Wei LC, Cao R, and Chen LW. Enhancement of nestin protein-immunoreactivity induced by ionizing radiation in the forebrain ependymal regions of rats. *Neurosci Res.* 2002; 44:475-481.

37. Champagne D, Pearson D, Dea D, Rochford J, and Poirier J. The cholesterol-lowering drug probucol increases apolipoprotein E production in the hippocampus of aged rats: implications for Alzheimer's disease. *Neuroscience.* 2003; 121:99-110.

38. Chiang CS, McBride WH, and Withers HR. Radiation-induced astrocytic and microglial responses in mouse brain. *Radiother Oncol.* 1993; 29:60-68.

39. Hwang SY, Jung JS, Kim TH, Lim SJ, Oh ES, Kim JY, Ji KA, Joe EH, Cho KH, and Han IO. Ionizing radiation induces astrocyte gliosis through microglia activation. *Neurobiol Dis.* 2006; 21:457-467.

40. Rola R, Fishman K, Baure J, Rosi S, Lamborn KR, Obenaus A, Nelson GA, and Fike JR. Hippocampal neurogenesis and neuroinflammation after cranial irradiation with (56)Fe particles. *Radiat Res.* 2008; 169:626-632.

41. Mao XW, Favre CJ, Fike JR, Kubinova L, Anderson E, Campbell-Beachler M, Jones T, Smith A, Rightnar S, and Nelson GA. High-LET radiation-induced response of microvessels in the Hippocampus. *Radiat Res.* 2010; 173:486-493.

42. Badhwar GD, and Cucinotta FA. Depth dependence of absorbed dose, dose equivalent and linear energy transfer spectra of galactic and trapped particles in polyethylene and comparison with calculations of models. *Radiat Res.* 1998; 149:209-218.

43. Cucinotta FA, Wilson JW, Shinn JL, Badavi FF, and Badhwar GD. Effects of target fragmentation on evaluation of LET spectra from space radiations: implications for space radiation protection studies. *Radiat Meas.* 1996; 26:923-934.

44. Setlow RB. The hazards of space travel. *EMBO Rep.* 2003; 4:1013-1016.

45. Cucinotta FA, Nikjoo H, and Goodhead DT. The effects of delta rays on the number of particle-track traversals per cell in laboratory and space exposures. *Radiat Res.* 1998; 150:115-119.

46. Cucinotta FA, Nikjoo H, and Goodhead DT. Applications of amorphous track models in radiation biology. *Radiat Environ Biophys.* 1999; 38:81-92.

47. Durante M, and Cucinotta FA. Heavy ion carcinogenesis and human space exploration. *Nat Rev Cancer.* 2008; 8:465-472.

48. Butler RW, and Haser JK. Neurocognitive effects of treatment for childhood cancer. *Ment Retard Dev Disabil Res Rev.* 2006; 12:184-191.

49. Castro JR, Chen GT, and Blakely EA. Current considerations in heavy charged-particle radiotherapy: a clinical research trial of the University of California Lawrence Berkeley Laboratory, Northern California Oncology Group, and Radiation Therapy Oncology Group. *Radiat Res Suppl.* 1985; 8:S263-71.
50. Suit H, Goitein M, Munzenrider J, Verhey L, Blitzer P, Gragoudas E, Koehler AM, Urie M, Gentry R, Shipley W, Urano M, Duttonhaver J, and Wagner M. Evaluation of the clinical applicability of proton beams in definitive fractionated radiation therapy. *Int J Radiat Oncol Biol Phys.* 1982; 8:2199-2205.
51. Ohmachi Y, Ishida Y, Hiraoka T, Hamano T, Fushiki S, and Ogiu T. Postnatal Changes in Mice Exposed In Utero to Fast Neutrons. *Journal of Toxicologic Pathology.* 2004; 17:63-68.
52. Pecaut MJ, Haerich P, Miller CN, Smith AL, Zendejas ED, and Nelson GA. The effects of low-dose, high-LET radiation exposure on three models of behavior in C57BL/6 mice. *Radiat Res.* 2004; 162:148-156.
53. Manda K, Ueno M, and Anzai K. Space radiation-induced inhibition of neurogenesis in the hippocampal dentate gyrus and memory impairment in mice: ameliorative potential of the melatonin metabolite, AFMK. *J Pineal Res.* 2008; 45:430-438.
54. Denisova NA, Shukitt-Hale B, Rabin BM, and Joseph JA. Brain signaling and behavioral responses induced by exposure to (56)Fe-particle radiation. *Radiat Res.* 2002; 158:725-734.
55. Shukitt-Hale B, Casadesus G, McEwen JJ, Rabin BM, and Joseph JA. Spatial learning and memory deficits induced by exposure to iron-56-particle radiation. *Radiat Res.* 2000; 154:28-33.
56. Haerich P, Nelson GA, and Pecaut MJ. HZE radiation and dopaminergic modification of startle and prepulse inhibition in mice. *Physiol Behav.* 2005; 86:103-110.
57. Rola R, Sarkissian V, Obenaus A, Nelson GA, Otsuka S, Limoli CL, and Fike JR. High-LET radiation induces inflammation and persistent changes in markers of hippocampal neurogenesis. *Radiat Res.* 2005; 164:556-560.
58. Rice OV, Grande AV, Dehktar N, Bruneus M, Robinson JK, and Gatley SJ. Long-term effects of irradiation with iron-56 particles on the nigrostriatal dopamine system. *Radiat Environ Biophys.* 2009; 48:215-225.
59. Datta K, Suman S, Trani D, Doiron K, Rotolo JA, Kallakury BV, Kolesnick R, Cole MF, and Fornace AJ. Accelerated hematopoietic toxicity by high energy (56)Fe radiation. *Int J Radiat Biol.* 2012; 88:213-222.
60. Eliasson C, Sahlgren C, Berthold CH, Stakeberg J, Celis JE, Betsholtz C, Eriksson JE, and Pekny M. Intermediate filament protein partnership in astrocytes. *J Biol Chem.* 1999; 274:23996-24006.
61. Monje ML, and Palmer T. Radiation injury and neurogenesis. *Curr Opin Neurol.* 2003; 16:129-134.
62. DeAngelis LM, Delattre JY, and Posner JB. Radiation-induced dementia in patients cured of brain metastases. *Neurology.* 1989; 39:789-796.
63. Kleinerman RA. Cancer risks following diagnostic and therapeutic radiation exposure in children. *Pediatr Radiol.* 2006; 36 Suppl 2:121-125.
64. Waris G, and Ahsan H. Reactive oxygen species: role in the development of cancer and various chronic conditions. *J Carcinog.* 2006; 5:14.
65. Limoli CL, Giedzinski E, Rola R, Otsuka S, Palmer TD, and Fike JR. Radiation response of neural precursor cells: linking cellular sensitivity to cell cycle checkpoints, apoptosis and oxidative stress. *Radiat Res.* 2004; 161:17-27.
66. Limoli CL, Giedzinski E, Baure J, Rola R, and Fike JR. Redox changes induced in hippocampal precursor cells by heavy ion irradiation. *Radiat Environ Biophys.* 2007; 46:167-172.
67. Veeraraghavan J, Natarajan M, Herman TS, and Aravindan N. Low-dose gamma-radiation-induced oxidative stress response in mouse brain and gut: regulation by NFkappaB-MnSOD cross-signaling. *Mutat Res.* 2011; 718:44-55.
68. Manda K, Anzai K, Kumari S, and Bhatia AL. Melatonin attenuates radiation-induced learning deficit and brain oxidative stress in mice. *Acta Neurobiol Exp (Wars).* 2007; 67:63-70.
69. Ames BN, Shigenaga MK, and Hagen TM. Oxidants, antioxidants, and the degenerative diseases of aging. *Proc Natl Acad Sci U S A.* 1993; 90:7915-7922.
70. Datta K, Sinha S, and Chattopadhyay P. Reactive oxygen species in health and disease. *Natl Med J India.* 2000; 13:304-310.
71. Harman D. Role of free radicals in aging and disease. *Ann N Y Acad Sci.* 1992; 673:126-141.
72. Balu M, Sangeetha P, Murali G, and Panneerselvam C. Modulatory role of grape seed extract on age-related oxidative DNA damage in central nervous system of rats. *Brain Res Bull.* 2006; 68:469-473.
73. Datta K, Suman S, Kallakury BV, and Fornace AJ. Exposure to heavy ion radiation induces persistent oxidative stress in mouse intestine. *PLoS One.* 2012; 7:e42224.
74. Larsson O. Cellular senescence-an integrated perspective. *Cancer Therapy.* 2005; 3:495-510.
75. Atadja P, Wong H, Garkavtsev I, Veillette C, and Riabowol K. Increased activity of p53 in senescing fibroblasts. *Proc Natl Acad Sci U S A.* 1995; 92:8348-8352.
76. Jia L, Li H, and Sun Y. Induction of p21-dependent senescence by an NAE inhibitor, MLN4924, as a mechanism of growth suppression. *Neoplasia.* 2011; 13:561-569.
77. Kagawa S, Fujiwara T, Kadowaki Y, Fukazawa T, Sok-Joo R, Roth JA, and Tanaka N. Overexpression of the p21 sdi1 gene induces senescence-like state in human cancer cells: implication for senescence-directed molecular therapy for cancer. *Cell Death Differ.* 1999; 6:765-772.
78. Edwards MG, Anderson RM, Yuan M, Kendzierski CM, Weindrich R, and Prolla TA. Gene expression profiling of aging reveals activation of a p53-mediated transcriptional program. *BMC Genomics.* 2007; 8:80.
79. Passos JF, Nelson G, Wang C, Richter T, Simillion C, Proctor CJ, Miwa S, Olijslagers S, Hallinan J, Wipat A, Saretzki G, Rudolph KL, Kirkwood TB, and von Zglinicki T. Feedback between p21 and reactive oxygen production is necessary for cell senescence. *Mol Syst Biol.* 2010; 6:347.
80. Miller AK, Alston RL, and Corsellis JA. Variation with age in the volumes of grey and white matter in the cerebral hemispheres of man: measurements with an image analyser. *Neuropathol Appl Neurobiol.* 1980; 6:119-132.
81. Mouton PR, Martin LJ, Calhoun ME, Dal Forno G, and Price DL. Cognitive decline strongly correlates with cortical atrophy in Alzheimer's dementia. *Neurobiol Aging.* 1998; 19:371-377.
82. Kim GJ, Fiskum GM, and Morgan WF. A role for mitochondrial dysfunction in perpetuating radiation-induced genomic instability. *Cancer Res.* 2006; 66:10377-10383.
83. Campisi J. Senescent cells, tumor suppression, and organismal aging: good citizens, bad neighbors. *Cell.* 2005; 120:513-522.
84. Cummings P, Obenaus A, Heffron D, and Mandell J. High-energy (HZE) radiation exposure causes delayed exonal

degeneration and astrogliosis in the central nervous system of rats. *Gravit Space Biol Bull.* 2007; 20:89-90.

**85.** Tseng B, Giedzinski E, Izadi A, Suarez T, Lan M, Tran K, Acharya M, Nelson G, Raber J, Parihar VK, and Limoli C. Functional consequences of radiation-induced oxidative stress in cultured neural stem cells and the brain exposed to charged particle irradiation. *Antioxid Redox Signal.* 2013;

**86.** Rabin BM, Joseph JA, and Shukitt-Hale B. Effects of age and diet on the heavy particle-induced disruption of operant responding produced by a ground-based model for exposure to cosmic rays. *Brain Res.* 2005; 1036:122-129.

**87.** Rabin BM, Joseph JA, and Shukitt-Hale B. A longitudinal study of operant responding in rats irradiated when 2 months old. *Radiat Res.* 2005; 164:552-555.

**88.** Vlkolinsky R, Titova E, Krucker T, Chi BB, Staufenbiel M, Nelson GA, and Obenaus A. Exposure to <sup>56</sup>Fe-particle radiation accelerates electrophysiological alterations in the hippocampus of APP23 transgenic mice. *Radiat Res.* 2010; 173:342-352.

**89.** Blagosklonny MV. Cell cycle arrest is not yet senescence, which is not just cell cycle arrest: terminology for TOR-driven aging. *Aging (Albany NY).* 2012; 4:159-165.

**90.** Liu GH, Barkho BZ, Ruiz S, Diep D, Qu J et al. Recapitulation of premature ageing with iPSCs from Hutchinson-Gilford progeria syndrome. *Nature.* 2011; 472:221-225.

**91.** Ben-Porath I, and Weinberg RA. The signals and pathways activating cellular senescence. *Int J Biochem Cell Biol.* 2005; 37:961-976.

**92.** Hamilton SA, Pecaut MJ, Gridley DS, Travis ND, Bandstra ER, Willey JS, Nelson GA, and Bateman TA. A murine model for bone loss from therapeutic and space-relevant sources of radiation. *J Appl Physiol.* 2006; 101:789-793.

**93.** Obenaus A, Huang L, Smith A, Favre CJ, Nelson G, and Kendall E. Magnetic resonance imaging and spectroscopy of the rat hippocampus 1 month after exposure to <sup>56</sup>Fe-particle radiation. *Radiat Res.* 2008; 169:149-161.

**94.** Peng Y, Brown N, Fannon R, Warner CL, Liu X, Genik PC, Callan MA, Ray FA, Borak TB, Badie C, Bouffler SD, Ullrich RL, Bedford JS, and Weil MM. Radiation leukemogenesis in mice: loss of PU.1 on chromosome 2 in CBA and C57BL/6 mice after irradiation with 1 GeV/nucleon <sup>56</sup>Fe ions, X rays or gamma rays. Part I. Experimental observations. *Radiat Res.* 2009; 171:474-483.

**95.** Tucker JD, Marples B, Ramsey MJ, and Lutze-Mann LH. Persistence of chromosome aberrations in mice acutely exposed to <sup>56</sup>Fe+<sup>26</sup> ions. *Radiat Res.* 2004; 161:648-655.

**96.** Matsumura N, Yoshida N, Ohta A, Miyamoto Y, and Hisatsune T. Neural precursor cells from adult mouse cerebral cortex differentiate into both neurons and oligodendrocytes. *Cytotechnology.* 2003; 43:19-25.

**97.** Aguirre A, and Gallo V. Reduced EGFR signaling in progenitor cells of the adult subventricular zone attenuates oligodendrogenesis after demyelination. *Neuron Glia Biol.* 2007; 3:209-220.

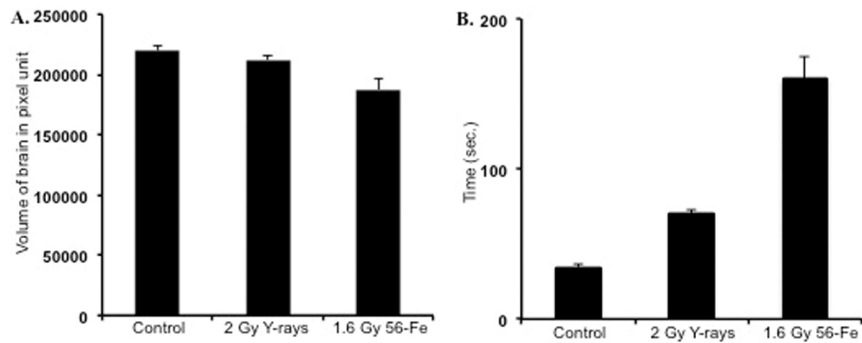
**98.** Cerbai F, Lana D, Nosi D, Petkova-Kirova P, Zecchi S, Brothers HM, Wenk GL, and Giovannini MG. The neuron-astrocyte-microglia triad in normal brain ageing and in a model of neuroinflammation in the rat hippocampus. *PLoS One.* 2012; 7:e45250.

**99.** Poncin S, Van Eeckoudt S, Humblet K, Colin IM, and Gerard AC. Oxidative stress: a required condition for thyroid cell proliferation. *Am J Pathol.* 2010; 176:1355-1363.

**100.** Shillingford JM, Piontek KB, Germino GG, and Weimbs T. Rapamycin ameliorates PKD resulting from conditional inactivation of Pkd1. *J Am Soc Nephrol.* 2010; 21:489-497.

**101.** Skaland I, Janssen EA, Gudlaugsson E, Klos J, Kjellekvold KH, Soiland H, and Baak JP. Phosphohistone H3 expression has much stronger prognostic value than classical prognosticators in invasive lymph node-negative breast cancer patients less than 55 years of age. *Mod Pathol.* 2007; 20:1307-1315.

## SUPPLEMENTARY FIGURE



**Supplementary Figure 1.** Radiation exposure caused decreased brain volume and increased time to cross a barrier. A) Volumetric measurement of brain performed using magnetic resonance imaging (MRI) showed decrease brain volume after radiation exposure. Brain volume was decreased more after <sup>56</sup>Fe radiation. B) Activity experiment performed using a physical barrier showed increased time required by the irradiated mice to climb the barrier. <sup>56</sup>Fe irradiated mice needed more time to come out of the barrier. Data presented as mean  $\pm$  SEM.



## Rapamycin extends lifespan and delays tumorigenesis in heterozygous p53<sup>+/-</sup> mice

Elena A. Komarova<sup>1</sup>, Marina P. Antoch<sup>2</sup>, Liliya R. Novototskaya<sup>1</sup>, Olga B. Chernova<sup>3</sup>, Geraldine Paszkiewicz<sup>1</sup>, Olga V. Leontieva<sup>1</sup>, Mikhail V. Blagosklonny<sup>1</sup>, and Andrei V. Gudkov<sup>1</sup>

<sup>1</sup> Department of Cell Stress Biology, Roswell Park Cancer Institute, BLSC, L3-312, Buffalo, NY 14263, USA;

<sup>2</sup> Department of Molecular & Cellular Biology, Roswell Park Cancer Institute, BLSC, L3-312, Buffalo, NY 14263, USA

<sup>3</sup> Tartis Aging, Inc., Buffalo, NY 14203, USA

**Key words:** cancer, mutations, DNA damage, aging, mTOR

**Received:** 8/30/12; **Accepted:** 10/27/12; **Published:** 10/29/12

**Correspondence to:** Andrei V. Gudkov, PhD; **E-mail:** [andrei.gudkov@roswellpark.org](mailto:andrei.gudkov@roswellpark.org) and Mikhail V. Blagosklonny, MD/PhD;

**E-mail:** [blagosklonny@oncotarget.com](mailto:blagosklonny@oncotarget.com)

**Copyright:** © Komarova et al. This is an open-access article distributed under the terms of the Creative Commons Attribution License, which permits unrestricted use, distribution, and reproduction in any medium, provided the original author and source are credited

**Abstract:** The TOR (Target of Rapamycin) pathway accelerates cellular and organismal aging. Similar to rapamycin, p53 can inhibit the mTOR pathway in some mammalian cells. Mice lacking one copy of p53 (p53<sup>+/-</sup> mice) have an increased cancer incidence and a shorter lifespan. We hypothesize that rapamycin can delay cancer in heterozygous p53<sup>+/-</sup> mice. Here we show that rapamycin (given in a drinking water) extended the mean lifespan of p53<sup>+/-</sup> mice by 10% and when treatment started early in life (at the age less than 5 months) by 28%. In addition, rapamycin decreased the incidence of spontaneous tumors. This observation may have applications in management of Li-Fraumeni syndrome patients characterized by heterozygous mutations in the p53 gene.

### INTRODUCTION

The mTOR (mammalian Target of Rapamycin) pathway plays a crucial role in the geroconversion from cell cycle arrest to senescence (geroconversion) [1]. Rapamycin suppresses or decelerates geroconversion, maintaining quiescence instead [2-8]. Furthermore, inhibition of the TOR pathway prolongs lifespan in model organisms, including mice [9-13]. In an organism, nutrients activate mTOR [14-16], whereas fasting or calorie restriction deactivates mTOR [17-19]. Calorie restriction slows down aging [20] and postpones tumorigenesis in several animal models [21, 22], including p53-deficient mice [23-25].

Similar to other tumor suppressors, p53 can inhibit mTOR in mammalian cells [26-31]. While causing cell cycle arrest, p53 can suppress geroconversion, thus preventing a senescent phenotype in the arrested cells [30, 31]. Therefore, it is not surprising that p53 inhibits hyper-secretory phenotype, a hallmark of senescence

[32] whereas p53-deficiency resulted in pro-inflammatory phenotype [33, 34]. Noteworthy, the activity of p53 is decreased with aging [35]. Lack of one p53-allele (p53<sup>+/-</sup>) accelerates carcinogenesis and shortens lifespan [36-41]. We propose that rapamycin can decelerate cancer development in p53<sup>+/-</sup> mice. Here we show experimental evidence supporting this hypothesis.

### RESULTS

Rapamycin (approximate dose, 1.5 mg/kg/day) was given in drinking water. 75 mice were divided into two groups: control (n=38) and rapamycin-treated (n=37). The mean lifespan of animals in control group was 373 days and the last 10% of survivals lived as long as 520 days (Fig. 1 A). In rapamycin-treated mice, the mean lifespan was 410 days and lifespan of the last 10% of survivals could not be determined (Fig. 1 A). Mice in both groups were also monitored for tumor development. The data presented in Fig. 1B

demonstrate that carcinogenesis was significantly delayed in rapamycin-treated mice compared to control mice.

Since in our experiments animals started to receive rapamycin at different age, we sought to test whether this affected the outcome of the treatment.

For this, we further subdivided all mice used into two groups: “young” (receiving rapamycin from the age of 5 months or earlier) and “old” (receiving rapamycin starting at 5 months of age or older). Results of the data analysis for the “young” group are shown in Figure 1C and D. The mean lifespan in control group was 373 days, whereas in rapamycin-treated “young” mice the mean lifespan reached 480 days, 3.5 months increase over the control group. Furthermore, 40% of rapamycin-treated “young” mice survived 550 days (Fig. 1C) and by this age developed 2 times less tumors than control mice (Fig. 1D). In the “old” group the difference between control and treated group was blunted (data not shown).

Thus, the life-extending effect of rapamycin is more pronounced when treatment starts earlier in life. In order to confirm that rapamycin administered with drinking water has biological activity in vivo, we measured levels of phosphorylated ribosomal protein S6 (pS6), a marker of the mTOR activity in tissues of control and rapamycin-treated mice. After receiving rapamycin in drinking water for 2 days, mice were sacrificed and the levels of total S6 and pS6 were estimated by Western blot analysis and immunocytochemistry (Fig. 2).

As shown in Fig. 2A, levels of pS6 were reduced in the heart, kidney and liver of rapamycin-treated mice. Also, pS6/S6 ratios were lower in rapamycin-treated mice (Fig. S1).

These results were confirmed by immunohistochemical staining showing lower levels of pS6 in tissues of rapamycin-treated mice (Fig. 2B). The variability of pS6 levels among mice may explain the variability of biological effects of rapamycin.

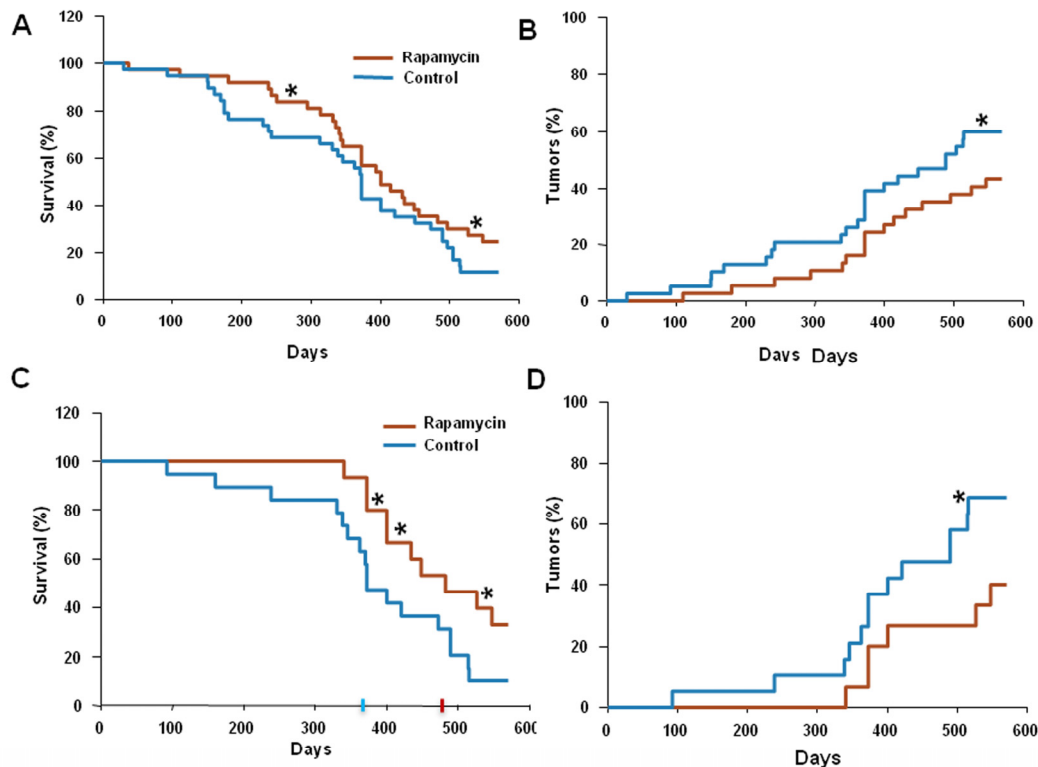


**Figure 1. Administration of rapamycin extends lifespan and delays carcinogenesis in p53<sup>+/-</sup> male mice.** (A) Kaplan Meier survival curve of rapamycin-treated (red line) and control (blue line) mice. (B) Incidence of tumors in rapamycin-treated (red) and control (blue) mice. Animals received rapamycin starting at various ages at 1.5 mg/kg per day in drinking water throughout entire life. \* p<0.05. (C) Kaplan Meier survival curve of rapamycin-treated (red line) and control (blue line) mice that start receiving rapamycin early in life (<5 months). (D) Incidence of tumors in rapamycin-treated (red) and control (blue) mice that start receiving rapamycin early in life (<5 months). \* p<0.05

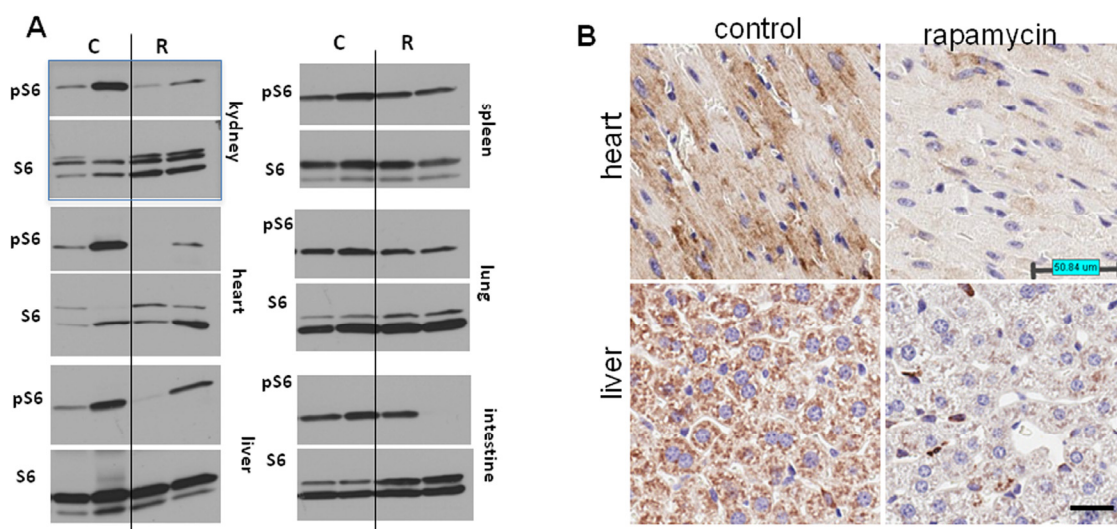


**Figure 2. Administration of rapamycin in drinking water inhibits the mTOR pathway in p53<sup>+/-</sup> male mice.** (A) Western blot analysis of whole cell lysates of 6 organs of rapamycin-treated and control mice probed with antibodies specific to S6 and phospho-S6 (Ser240/244). Mice received rapamycin in drinking water for 2 days. (B) Immunohistochemistry. pS6 in the heart and the liver. Mice received rapamycin in drinking water for 2 days.

## DISCUSSION

Previously it was shown that rapamycin prolongs lifespan in genetically heterogeneous mice [11], [12], inbred mice [42] and Her2-expressing mice [13]. In normal genetically heterogeneous mice, rapamycin extended life span even when its administration was started later in life [11]. Our data in p53<sup>+/-</sup> mice show that the effect of rapamycin was blunted when treatment started at the age of 5 months or older.

This indicates that the anti-cancer effect of rapamycin is likely to be indirect and is imposed via its systemic effect at the level of an organism rather than through direct inhibition of tumor growth. To further address this question we plan to test the effect of rapamycin on animals with established tumors (by measuring tumor growth) along with evaluating the functional status of mTOR and the ability of rapamycin to suppress it in tumors and normal tissues. As we report here, administration of rapamycin starting early in life increased mean lifespan in p53<sup>+/-</sup> male mice by 28%. Previous work has demonstrated that the life-extending effects of rapamycin [11, 12] as well as metformin [43, 44], calorie restriction [45] and genetic inhibition of the IGF-I/mTOR/S6K pathway [46, 47] were less pronounced in male mice compared with female mice. Moreover, in some cases, life span extension was achieved in female mice only [43, 47]. Therefore, the

observed increase in the median lifespan is dramatic, taking into account that it was achieved in male mice. However, because of low bioavailability of rapamycin, it was given constantly (in drinking water) without interruptions, whereas intermittent schedules may be more appropriate for future clinical developments as cancer-preventive interventions. In fact, a novel formulation of rapamycin (Rapatar) may be given intermittently, which still reveal even more pronounced extension of life span in p53-deficient mice (Comas et al, Aging 2012; this issue).

Our study suggests that rapamycin can be considered for cancer prevention in patients with Li-Fraumeni syndrome. Li-Fraumeni syndrome is an autosomal dominant disorder with a germline p53 mutation [48]. The incidence of cancer in carriers of mutation reaches 50% at the age of 40 and 90% at the age 60. Children of affected parents have an approximate 50% risk of inheriting the familial mutation [48]. Although functional assays have been established allowing for easy genetic testing for TP53 mutation, no effective chemopreventive therapy is currently available. The p53 rescue compounds may hold some promise in the future [48-50]; however these are not clinically approved drugs. In contrast, rapamycin has been used in the clinic for over a decade mostly in renal transplant patients. It was reported that rapamycin significantly decreased cancer incidence in renal transplant patients [51-53].

Our data suggest that rapamycin or its analogs can be considered for cancer prevention in Li-Fraumeni syndrome.

## METHODS

**Mice.** All animal studies were conducted in accordance with the regulations of the Committee of Animal Care and Use at Roswell Park Cancer Institute. The colony of p53-knockout mice on a C57Bl/6 background (originally obtained from Jackson Laboratories, Bar Harbor, ME) was maintained by crossing p53<sup>+/−</sup> females with p53<sup>−/−</sup> males followed by genotyping of the progeny (PCR) as described previously [54]. Heterozygous p53<sup>+/−</sup> mice were generated by crossing p53<sup>−/−</sup> males with wild type p53 females. Male mice were kept in polypropylene cages (30x21x10 cm) under standard light/dark regimen (12 hours light : 12 hours darkness) at 22 ± 2 °C, And received standard laboratory chow and water ad libitum.

**Rapamycin treatment.** Rapamycin (LC Laboratories, USA) was diluted in ethanol at concentration 15 mg/ml. Then the stock was diluted 1:1000 in drinking water. Drinking water was changed every week. Male mice were randomly divided into two groups. Mice of the first group (n=37) were given rapamycin in drinking water (approximately 1.5 mg/kg per day), whereas mice of the second group (n=38) were given tap water without rapamycin and served as control. Once a week all mice were palpated for detection of tumor mass appearance.

**Pathomorphological examination.** All animals were autopsied. Site, number and size of tumors were checked. All tumors, as well as the tissues and organs with suspected tumor development were excised and fixed in 10% neutral formalin. After the routine histological processing the tissues were embedded into paraffin. 5-7 µm thin histological sections were stained with haematoxylin and eosine and were microscopically examined. Tumors were classified according to International Agency for Research on Cancer recommendations.

**Western blot analysis.** Tissues were homogenized in Bullet blender using stainless steel 0.5 mm diameter beads (Next Advantage, Inc. NY, USA) and RIPA lysis buffer supplemented with protease and phosphatase inhibitors tablets (Roche Diagnostics, Indianapolis, IN, USA). Lysates were cleared by centrifugation at 4°C at 13000 rpm. Equal amounts of protein were separated on gradient Criterion gels (BioRad) and immunoblotting was performed with rabbit anti-phospho S6 (Ser 240/244) and mouse anti-S6 antibodies from Cell

Signaling Biotechnology as described previously [55], [56].

**Immunohistochemistry.** Dissected tissue samples were fixed in 10% buffered formalin, embedded into paraffin. 5-7 µm thin histological sections were stained with anti-phospho S6 (Ser240/244) antibody (Cell Signaling) and counterstained with Hematoxylin.

**Statistical analyses.** The SigmaStat software package was used for analysis. The P values were calculated using Fisher's Exact Test (2-tail). P<0.05 was considered as statistically significant.

## Conflict of Interest Statement

The authors of this manuscript have no conflict of interests to declare.

## REFERENCES

1. Blagosklonny MV. Cell cycle arrest is not yet senescence, which is not just cell cycle arrest: terminology for TOR-driven aging. *Aging* (Albany NY). 2012; 4: 159-165.
2. Demidenko ZN, Zubova SG, Bukreeva EI, Pospelov VA, Pospelova TV, Blagosklonny MV. Rapamycin decelerates cellular senescence. *Cell Cycle*. 2009; 8: 1888-1895.
3. Gan B, Sahin E, Jiang S, Sanchez-Aguilera A, Scott KL, Chin L, Williams DA, Kwiatkowski DJ, DePinho RA. mTORC1-dependent and -independent regulation of stem cell renewal, differentiation, and mobilization. *Proc Natl Acad Sci U S A*. 2008; 105: 19384-19389.
4. Gan B, DePinho RA. mTORC1 signaling governs hematopoietic stem cell quiescence. *Cell Cycle*. 2009; 8: 1003-1006.
5. Chen C, Liu Y, Liu R, Ikenoue T, Guan KL, Zheng P. TSC-mTOR maintains quiescence and function of hematopoietic stem cells by repressing mitochondrial biogenesis and reactive oxygen species. *J Exp Med*. 2008; 205: 2397-2408.
6. Chen C, Liu Y, Zheng P. mTOR regulation and therapeutic rejuvenation of aging hematopoietic stem cells. *Sci Signal*. 2009; 2: ra75.
7. Adhikari D, Zheng W, Shen Y, Gorre N, Hamalainen T, Cooney AJ, Huhtaniemi I, Lan ZJ, Liu K. Tsc/mTORC1 signaling in oocytes governs the quiescence and activation of primordial follicles. *Human Molecular Genet*. 2010; 19:397-410.
8. Kolesnichenko M, Hong L, Liao R, Vogt PK, Sun P. Attenuation of TORC1 signaling delays replicative and oncogenic RAS-induced senescence. *Cell Cycle*. 2012; 11: 2391-2401.
9. Kapahi P, Zid BM, Harper T, Koslover D, Sapin V, Benzer S. Regulation of lifespan in *Drosophila* by modulation of genes in the TOR signaling pathway. *Curr Biol*. 2004; 14: 885-890.
10. Bjedov I, Toivonen JM, Kerr F, Slack C, Jacobson J, Foley A, Partridge L. Mechanisms of life span extension by rapamycin in the fruit fly *Drosophila melanogaster*. *Cell Metab*. 2010; 11: 35-46.
11. Harrison DE, Strong R, Sharp ZD, Nelson JF, Astle CM, Flurkey K, Nadon NL, Wilkinson JE, Frenkel K, Carter CS, Pahor M, Javors MA, Fernandez E, Miller RA. Rapamycin fed late in life extends

lifespan in genetically heterogenous mice. *Nature*. 2009; 460: 392-396.

12. Miller RA, Harrison DE, Astle CM, Baur JA, Boyd AR, de Cabo R, Fernandez E, Flurkey K, Javors MA, Nelson JF, Orihuela CJ, Pletcher S, Sharp ZD, Sinclair D, Starnes JW, Wilkinson JE et al. Rapamycin, but not resveratrol or simvastatin, extends life span of genetically heterogeneous mice. *J Gerontol A Biol Sci Med Sci*. 2011; 66: 191-201.

13. Anisimov VN, al. e, Antoch M, Blagosklonny MV. *Am J Pathol*. 2010: in press.

14. Khamzina L, Veilleux A, Bergeron S, Marette A. Increased activation of the mammalian target of rapamycin pathway in liver and skeletal muscle of obese rats: possible involvement in obesity-linked insulin resistance. *Endocrinology*. 2005; 146: 1473-1481.

15. Tremblay F, Krebs M, Dombrowski L, Brehm A, Bernroider E, Roth E, Nowotny P, Walddhussl W, Marette A, Roden M. Overactivation of S6 kinase 1 as a cause of human insulin resistance during increased amino acid availability. *Diabetes*. 2005; 54: 2674-2684.

16. Krebs M, Brunmair B, Brehm A, Artwohl M, Szendroedi J, Nowotny P, Roth E, Fyrsinn C, Promintzer M, Anderwald C, Bischof M, Roden M. The Mammalian target of rapamycin pathway regulates nutrient-sensitive glucose uptake in man. *Diabetes*. 2007; 56: 1600-1607.

17. Jiang W, Zhu Z, Thompson HJ. Dietary energy restriction modulates the activity of AMP-activated protein kinase, Akt, and mammalian target of rapamycin in mammary carcinomas, mammary gland, and liver. *Cancer Res*. 2008; 68: 5492-5499.

18. Estep PWR, Warner JB, Bulyk ML. Short-term calorie restriction in male mice feminizes gene expression and alters key regulators of conserved aging regulatory pathways. *PLoS One*. 2009; 4: e5242.

19. Masternak MM, Panici JA, Bonkowski MS, Hughes LF, Bartke A. Insulin sensitivity as a key mediator of growth hormone actions on longevity. *J Gerontol A Biol Sci Med Sci*. 2009; 64: 516-521.

20. Wang C, Maddick M, Miwa S, Jurk D, Czapiewski R, Saretzki G, Langie SA, Godschalk RW, Cameron K, von Zglinicki T. Adult-onset, short-term dietary restriction reduces cell senescence in mice. *Aging (Albany NY)*. 2010; 2: 555-566.

21. Dirx MJ, Zeegers MP, Dagnelie PC, van den Bogaard T, van den Brandt PA. Energy restriction and the risk of spontaneous mammary tumors in mice: a meta-analysis. *Int J Cancer*. 2003; 106: 766-770.

22. Sarkar NH, Fernandes G, Telang NT, Kourides IA, Good RA. Low-calorie diet prevents the development of mammary tumors in C3H mice and reduces circulating prolactin level, murine mammary tumor virus expression, and proliferation of mammary alveolar cells. *Proc Natl Acad Sci U S A*. 1982; 79: 7758-7762.

23. Berrigan D, Perkins SN, Haines DC, Hursting SD. Adult-onset calorie restriction and fasting delay spontaneous tumorigenesis in p53-deficient mice. *Carcinogenesis*. 2002; 23: 817-822.

24. Hursting SD, Perkins SN, Phang JM. Calorie restriction delays spontaneous tumorigenesis in p53-knockout transgenic mice. *Proc Natl Acad Sci U S A*. 1994; 91: 7036-7040.

25. Hursting SD, Perkins SN, Brown CC, Haines DC, Phang JM. Calorie restriction induces a p53-independent delay of spontaneous carcinogenesis in p53-deficient and wild-type mice. *Cancer Res*. 1997; 57: 2843-2846.

26. Feng Z, Hu W, de Stanchina E, Teresky AK, Jin S, Lowe S, Levine AJ. The regulation of AMPK beta1, TSC2, and PTEN expression by p53: stress, cell and tissue specificity, and the role of these gene products in modulating the IGF-1-AKT-mTOR pathways. *Cancer Res*. 2007; 67: 3043-3053.

27. Feng Z, Zhang H, Levine AJ, Jin S. The coordinate regulation of the p53 and mTOR pathways in cells. *Proc Natl Acad Sci U S A*. 2005; 102: 8204-8209.

28. Levine AJ, Feng Z, Mak TW, You H, Jin S. Coordination and communication between the p53 and IGF-1-AKT-TOR signal transduction pathways. *Genes Dev*. 2006; 20: 267-275.

29. Budanov AV, Karin M. p53 target genes sestrin1 and sestrin2 connect genotoxic stress and mTOR signaling. *Cell*. 2008; 134: 451-460.

30. Demidenko ZN, Korotchikina LG, Gudkov AV, Blagosklonny MV. Paradoxical suppression of cellular senescence by p53. *Proc Natl Acad Sci U S A*. 2010; 9660-4: 9660-9664.

31. Korotchikina LG, Leontieva OV, Bukreeva EI, Demidenko ZN, Gudkov AV, Blagosklonny MV. The choice between p53-induced senescence and quiescence is determined in part by the mTOR pathway. *Aging (Albany NY)*. 2010; 2: 344-352.

32. Coppž JP, Patil CK, Rodier F, Sun Y, Mu-oz DP, Goldstein J, Nelson PS, Desprez PY, Campisi J. Senescence-associated secretory phenotypes reveal cell-nonautonomous functions of oncogenic RAS and the p53 tumor suppressor. *PLoS Biol*. 2008; 6: 2853-2868.

33. Komarova EA, Krivokrysenko V, Wang K, Neznanov N, Chernov MV, Komarov PG, Brennan ML, Golovkina TV, Rokhlin OW, Kuprash DV, Nedospasov SA, Hazen SL, Feinstein E, Gudkov AV. p53 is a suppressor of inflammatory response in mice. *FASEB J*. 2005; 19: 1030-1032.

34. Gudkov AV, Gurova KV, Komarova EA. Inflammation and p53: A Tale of Two Stresses. *Genes Cancer*. 2011; 2: 503-516.

35. Feng Z, Hu W, Teresky AK, Hernando E, Cordon-Cardo C, Levine AJ. Declining p53 function in the aging process: a possible mechanism for the increased tumor incidence in older populations. *Proc Natl Acad Sci U S A*. 2007; 104: 16633-16638.

36. Donehower LA, Harvey M, Slagle BL, McArthur MJ, Montgomery CA, Jr., Butel JS, Bradley A. Mice deficient for p53 are developmentally normal but susceptible to spontaneous tumours. *Nature*. 1992; 356: 215-221.

37. Harvey M, McArthur MJ, Montgomery CA, Jr., Butel JS, Bradley A, Donehower LA. Spontaneous and carcinogen-induced tumorigenesis in p53-deficient mice. *Nat Genet*. 1993; 5: 225-229.

38. Jacks T, Remington L, Williams BO, Schmitt EM, Halachmi S, Bronson RT, Weinberg RA. Tumor spectrum analysis in p53-mutant mice. *Curr Biol*. 1994; 4: 1-7.

39. Donehower LA, Harvey M, Vogel H, McArthur MJ, Montgomery CA, Jr., Park SH, Thompson T, Ford RJ, Bradley A. Effects of genetic background on tumorigenesis in p53-deficient mice. *Mol Carcinog*. 1995; 14: 16-22.

40. Venkatachalam S, Shi YP, Jones SN, Vogel H, Bradley A, Pinkel D, Donehower LA. Retention of wild-type p53 in tumors from p53 heterozygous mice: reduction of p53 dosage can promote cancer formation. *Embo J*. 1998; 17: 4657-4667.

41. Hinkal G, Parikh N, Donehower LA. Timed somatic deletion of p53 in mice reveals age-associated differences in tumor progression. *PLoS One*. 2009; 4: e6654.

42. Anisimov VN, Zabezhinski MA, Popovich IG, Piskunova TS, Semenchenko AV, Tyndyk ML, Yurova MN, Rosenfeld SV,



Blagosklonny MV. Rapamycin increases lifespan and inhibits spontaneous tumorigenesis in inbred female mice. *Cell Cycle*. 2011; 10: 4230-4236.

43. Anisimov VN, Piskunova TS, Popovich IG, Zabezhinski MA, Tyndyk ML, Egormin PA, Yurova MV, Rosenfeld SV, Semenchenko AV, Kovalenko IG, Poroshina TE, Berstein LM. Gender differences in metformin effect on aging, life span and spontaneous tumorigenesis in 129/Sv mice. *Aging (Albany NY)*. 2010; 2: 945-958.

44. Blagosklonny MV. Metformin and sex: Why suppression of aging may be harmful to young male mice. *Aging (Albany NY)*. 2010; 2: 897-899.

45. Turturro A, Duffy P, Hass B, Kodell R, Hart R. Survival characteristics and age-adjusted disease incidences in C57BL/6 mice fed a commonly used cereal-based diet modulated by dietary restriction. *J Gerontol A Biol Sci Med Sci*. 2002; 57: B379-389.

46. Holzenberger M, Dupont J, Ducos B, Leneuve P, Geloën A, Even PC, Cervera P, Le Bouc Y. IGF-1 receptor regulates lifespan and resistance to oxidative stress in mice. *Nature*. 2003; 421: 182-187.

47. Selman C, Tullet JM, Wieser D, Irvine E, Lingard SJ, Choudhury AI, Claret M, Al-Qassab H, Carmignac D, Ramadani F, Woods A, Robinson IC, Schuster E, Batterham RL, Kozma SC, Thomas G et al. Ribosomal protein S6 kinase 1 signaling regulates mammalian life span. *Science*. 2009; 326: 140-144.

48. Upton B, Chu Q, Li BD. Li-Fraumeni syndrome: the genetics and treatment considerations for the sarcoma and associated neoplasms. *Surg Oncol Clin N Am*. 2009; 18: 145-156, ix.

49. Glazer RI. A new therapeutic basis for treating Li-Fraumeni Syndrome breast tumors expressing mutated TP53. *Oncotarget*. 2010; 1: 470-471.

50. Herbert BS, Chanoux RA, Liu Y, Baenziger PH, Goswami CP, McClintick JN, Edenberg HJ, Pennington RE, Lipkin SM, Kopelovich L. A molecular signature of normal breast epithelial and stromal cells from Li-Fraumeni syndrome mutation carriers. *Oncotarget*. 2010; 1: 405-422.

51. Mathew T, Kreis H, Friend P. Two-year incidence of malignancy in sirolimus-treated renal transplant recipients: results from five multicenter studies. *Clin Transplant*. 2004; 18: 446-449.

52. Campistol JM, Eris J, Oberbauer R, Friend P, Hutchison B, Morales JM, Claesson K, Stallone G, Russ G, Rostaing L, Kreis H, Burke JT, Brault Y, Scarola JA, Neylan JF. Sirolimus Therapy after Early Cyclosporine Withdrawal Reduces the Risk for Cancer in Adult Renal Transplantation. *J Am Soc Nephrol*. 2006; 17: 581-589.

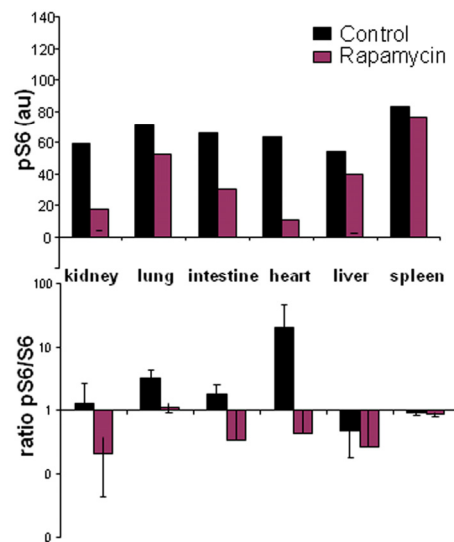
53. Blagosklonny MV. Prevention of cancer by inhibiting aging. *Cancer Biol Ther*. 2008; 7: 1520-1524.

54. Leonova KI, Shneyder J, Antoch MP, Toshkov IA, Novototskaya LR, Komarov PG, Komarova EA, Gudkov AV. A small molecule inhibitor of p53 stimulates amplification of hematopoietic stem cells but does not promote tumor development in mice. *Cell Cycle*. 2010; 9: 1434-1443.

55. Leontieva O, Gudkov A, Blagosklonny M. Weak p53 permits senescence during cell cycle arrest. *Cell Cycle*. 2010; 9: 4323-4327.

56. Leontieva OV, Blagosklonny MV. DNA damaging agents and p53 do not cause senescence in quiescent cells, while consecutive re-activation of mTOR is associated with conversion to senescence. *Aging (Albany NY)*. 2010; 2: 924-935.

## SUPPLEMENTAL FIGURE



**Supplemental Figure S1. Quantitative analysis of data shown in Figure 2A.** Top panel - Intensity of phosphorylated S6 (pS6) signal was quantified using ImageJ program (intensity units, IU). Bottom panel - Intensity of pS6 and S6 signals were quantified and the ratio pS6/S6 was calculated.

## Reversing the aging stromal phenotype prevents carcinoma initiation

Davina A. Lewis<sup>1</sup>, Jeffrey B. Travers<sup>1,2,3</sup>, Christiane Machado<sup>1</sup>, Ally-Khan Somani<sup>1</sup>, and Dan F Spandau<sup>1,5</sup>

<sup>1</sup> Departments of Dermatology, Indiana University School of Medicine, Indianapolis, Indiana

<sup>2</sup> Pharmacology and Toxicology, Indiana University School of Medicine, Indianapolis, Indiana

<sup>3</sup> Herman B. Wells Center for Pediatric Research, Indiana University School of Medicine, Indianapolis, Indiana

<sup>4</sup> Richard L. Roudebush V.A. Medical Center, Indiana University School of Medicine, Indianapolis, Indiana

<sup>5</sup> Biochemistry & Molecular Biology, Indiana University School of Medicine, Indianapolis, Indiana

**Key words:** Senescence, aging, photocarcinogenesis, therapy, UVB

**Received:** 4/1/11; **Accepted:** 4/20/11; **Published:** 4/21/11

**Corresponding author:** Dan F Spandau, PhD; **E-mail:** [dspanda@iupui.edu](mailto:dspanda@iupui.edu)

**Copyright:** © Lewis et al. This is an open-access article distributed under the terms of the Creative Commons Attribution License, which permits unrestricted use, distribution, and reproduction in any medium, provided the original author and source are credited

**Abstract:** The accumulation of senescent stromal cells in aging tissue changes the local microenvironment from normal to a state similar to chronic inflammation. This inflammatory microenvironment can stimulate the proliferation of epithelial cells containing DNA mutations which can ultimately lead to cancer. Using geriatric skin as a model, we demonstrated that senescent fibroblasts also alter how epithelial keratinocytes respond to genotoxic stress, due to the silencing of IGF-1 expression in geriatric fibroblasts. These data indicate that in addition to promoting epithelial tumor growth, senescent fibroblasts also can promote carcinogenic initiation. We hypothesized that commonly used therapeutic stromal wounding therapies can reduce the percentage of senescent fibroblasts and consequently prevent the formation of keratinocytes proliferating with DNA mutations following acute genotoxic (UVB) stress. Sun-protected skin on the lower back of geriatric human volunteers was wounded by dermabrasion and the skin was allowed to heal for three months. In geriatric skin, we found that dermabrasion wounding decreases the proportion of senescent fibroblasts found in geriatric dermis, increases the expression of IGF-1, and restores the appropriate UVB response to epidermal keratinocytes in geriatric skin. Therefore, dermal rejuvenation therapies may play a significant role in preventing the initiation of skin cancer in geriatric patients.

## INTRODUCTION

Cancer is an age-dependent disease in most mammalian species; in humans over 50% of cancers are found in people over 70 years of age [1]. Recently, the accumulation of senescent cells in aging tissues have been shown to acquire a chronic inflammatory phenotype (called SASP, Senescence-Associated Secretory Phenotype) that serves to promote the growth of initiated tumorigenic epithelial cells [2]. Additional reports have demonstrated that in the skin, the accumulation of senescent fibroblasts also increases the susceptibility of epidermal keratinocytes to carcinogenic initiation [3]. Therefore, while investigations into the role of stromal tissue on the initiation and promotion of cancer are in their infancy,

they may serve as potential emerging opportunities for interventional and prophylactic therapeutic strategies [4-6]. Our lab is investigating the role of aging in the development of non-melanoma skin cancer (NMSC) as a model for the effect that aging stromal tissue has in controlling carcinogenesis initiation [3, 6-10]. As such, the skin is an excellent model system for these studies; it is accessible, it has a relevant environmental carcinogen (UVB), and it is possible to easily interrogate human disease.

NMSC has the highest incidence rate of all cancers worldwide, including an estimated 2 million newly diagnosed patients in the United States this year alone [11-12]. Although the mortality of NMSC is relatively low compared to other types of cancer, the morbidity

and the cost of treating NMSC is enormous [11, 13]. As NMSC occurs primarily in geriatric individuals, it has been estimated that up to nearly 1% of total Medicare expenses in the United States go towards the treatment of NMSC [13]. Therefore, NMSC is a major burden on our healthcare system [14]. Despite our understanding for decades that sunlight is the main etiologic agent responsible for NMSC (over 90%), the incidence of NMSC continues to rise at an alarming rate [11].

The primary environmental factor that influences the development of skin cancer is exposure to the spectrum of ultraviolet wavelengths found in sunlight. Furthermore, as we age our chances of developing NMSC greatly increases so that at age 65 we have a 50% chance of acquiring a NMSC [15-16]. In fact, 80% of all NMSC are diagnosed in individuals greater than 60 years old [15-16]. While the correlation between aged epidermis and NMSC is apparent, the mechanism responsible for this relationship remains obscure. Early hypotheses describing why the incidence of NMSC increases with age, suggested that excessive sun exposure during adolescence causes mutations in clones of keratinocytes. Subsequently over many decades of genetic selection, these initiated keratinocytes will form detectable tumors [17-18]. However, recent studies have shown that more than 77% of our lifetime sun exposure occurs *after* the age of 18 [19], indicating the vast majority of damaging UVB-irradiation takes place later in life. In fact, more sun exposure occurs after age 59 (26%) than before age 18 (23%) [19]. Recent data from a variety of labs have proposed a modification in the latency theory of carcinogenesis [20-21] based on changes in the effects of stromal cells (i.e. fibroblasts) on epithelial cells in aged individuals [22-23]. This new hypothesis states that the selection of initiated epithelial cells is accelerated in aged tissue due to alterations in gene expression by senescent fibroblasts supporting epithelial cell growth [24-26]. In addition, the aged state of cells may play a greater role in the initiation of carcinogenic DNA mutations than was previously considered [27]. Previously we have shown that the activation of the insulin-like growth factor-1 receptor (IGF-1R) is critical for determining the response of skin keratinocytes to UVB irradiation *in vitro* and *in vivo* [3, 6-10]. If the IGF-1R is functionally inactive *in vitro* at the time of UVB-irradiation, surviving keratinocytes can continue to proliferate with the potential of converting the damaged DNA into initiating carcinogenic mutations [3, 5-6, 10]. Recent data from our laboratories have indicated that similar IGF-1R-dependent UVB responses occur in epidermal keratinocytes *in vivo* [3, 5-6, 10]. Because keratinocytes do not produce IGF-1, the majority of the IGF-1 supplied to the epidermis is

produced by dermal fibroblasts. Therefore, any deficiencies in dermal IGF-1 production could have profound effects on the response of epidermal keratinocytes to UVB irradiation. We have demonstrated that such an instance occurs in aged skin, as senescent dermal fibroblasts produce significantly lower levels of IGF-1 than youthful, proliferating fibroblasts [3]. Geriatric skin with lower IGF-1 levels responds inappropriately to UVB exposure and results in the production of keratinocytes that can proliferate with DNA damage. Moreover, we demonstrate that therapeutic treatment of geriatric skin can result in increased levels of dermal IGF-1 and protection against acute UVB-mediated formation of keratinocytes proliferating with DNA damage. We hypothesize that the reduced activation of the IGF-1R in aging skin due to silencing of IGF-1 expression in senescent fibroblasts is an important factor in the dramatic increase in NMSC observed in geriatric patients. The incorporation of recent data from our laboratories and these new ideas on the origins of cancer has led us to a new paradigm to explain non-melanoma skin carcinogenesis [3, 5-6, 10]. This new paradigm indicates that the accumulation of senescent fibroblasts in geriatric dermis leads to a silencing of IGF-1 expression in the skin, resulting in a deficient activation of the IGF-1R in epidermal keratinocytes, causing an inappropriate UVB-response in keratinocytes, leading to proliferating keratinocytes containing DNA mutations, and subsequently photocarcinogenesis [3, 5-6]. Therefore, the susceptibility to develop NMSC is dependent on both the exposure of skin to UVB and the biologic age of the skin.

Given our findings that the lack of endogenous IGF-1 [3] in geriatric skin resulted in an inappropriate pro-carcinogenic response to relatively low doses of UVB [3], and that this inappropriate response was reversed by local injections of *exogenous* IGF-1 [3], these studies have examined the ability of dermal wounding to upregulate *endogenous* IGF-1 levels and restore the appropriate UVB response in geriatric skin. We assayed whether ablation of both the epidermis and papillary dermis by dermabrasion could upregulate IGF-1 expression in geriatric skin and restore the appropriate UVB response. The successful development of the prophylactic therapies as described here could have a major impact on how NMSCs can be prevented in susceptible individuals.

## RESULTS

### Senescent human fibroblasts *in vitro* contain markers of the DNA damage response

Normal human fibroblasts that are continually cultured

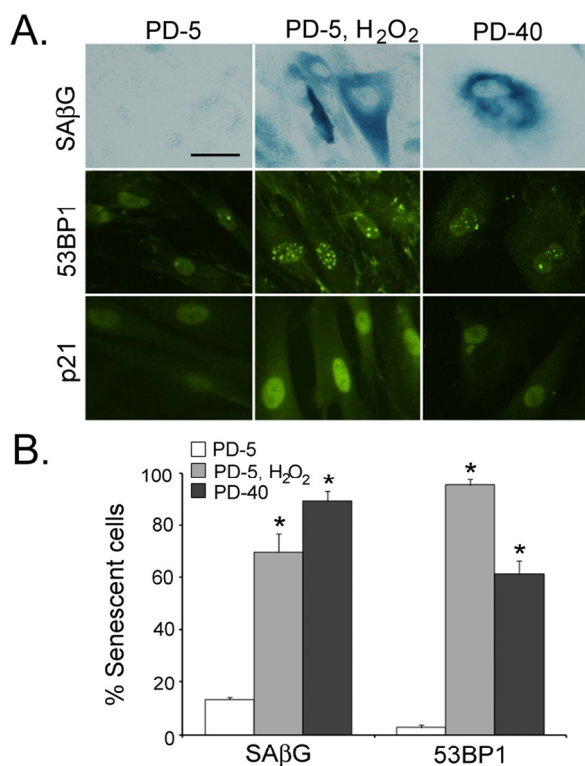


**Figure 1. Senescent human fibroblasts contain markers of DNA damage response *in vitro*.** (A) Low passage neonatal normal human fibroblasts (PD-5), stress-induced senescent fibroblasts (PD-5, H<sub>2</sub>O<sub>2</sub>), and replicatively senescent fibroblasts (PD-40) were stained for the presence of senescence-associated  $\beta$ -galactosidase activity (blue), with  $\alpha$ -53BP1 antibodies (multiple punctate nuclear staining), or  $\alpha$ -p21 antibodies (bar = 20  $\mu$ m). (B) The percentage of senescent cells were determined for senescence-associated  $\beta$ -galactosidase and 53BP1 staining. 53BP1-positive cells contained at least four individual fluorescent pin-point spots per nucleus (asterisks indicate significant difference from PD-5 cells,  $p < 0.001$ , two-tailed t-test).

*in vitro* until they reach replicative senescence have historically been identified by their expression of senescence-associated  $\beta$ -galactosidase [28]. Similarly, replicating fibroblasts treated with DNA-damaging chemotherapeutic drugs or pro-oxidative stressors to induce stress-induced senescence have been assayed for senescence-associated  $\beta$ -galactosidase activity to verify their senescence phenotype [3]. However, because identifying senescent cells using senescence-associated  $\beta$ -galactosidase requires an assay of enzymatic activity, its use in specimens from human tissues is not as effective. Recently, it has been described that markers

of a DNA-damage response (DDR) are found in most types of senescent cells, whether induced by replication exhaustion, reactive oxygen species, or oncogene expression [29-32]. To determine the reliability of DDR markers to identify senescent fibroblasts in skin, replicating, stress-induced senescent, and replicative senescent fibroblasts were stained for the traditional senescence-associated  $\beta$ -galactosidase activity, for the presence of 53BP1, and for the expression of cell cycle inhibitor p21 (Fig. 1A). As seen in Fig. 1A, senescent fibroblasts can be identified by nuclei which have greater than four 53BP1-positive foci. When the numbers of senescent fibroblasts were counted in stress-induced senescent and replicatively senescent fibroblasts, the use of either senescence-associated  $\beta$ -galactosidase or 53BP1 foci yielded similar results (Fig. 1B). Therefore, markers of DDR may be useful in identifying senescent fibroblasts *in vivo*.

### Senescent fibroblasts accumulate in geriatric dermis *in vivo*

As we age, the skin becomes altered both phenotypically and biologically. The undulating structure of the dermal-epidermal junction in young skin becomes significantly flattened with age [33-34; Supplemental Fig. 1A]. Both the epidermis and the papillary dermis become atrophied in geriatric skin [33-37; Fig. 2D] and the transcriptome in the geriatric dermis becomes altered, including the relative silencing of the IGF-1 and collagen I genes [3; Fig. 2B]. Additionally, fibroblast morphology transforms from a spindle-shaped cell body and elliptical nucleus to a more rounded cell body and a rounded nucleus [37-38; Supplemental Fig. 1A, white circles]. These morphological changes in fibroblast shape are associated with increasing proportions of senescent fibroblasts in the papillary dermis (Fig. 2C). These senescent fibroblasts can be defined *in vivo* by increased expression of DDR markers (Fig. 2A). Previously, we and others have shown that senescent fibroblasts *in vitro* silence IGF-1 expression [3]. Similarly, intrinsic aging of skin *in vivo* can be characterized by a significantly increased proportion of senescent fibroblasts in the papillary dermis and a corresponding silencing of IGF-1 expression in geriatric dermis.

### Dermabrasion restores young adult function in geriatric dermis

Cosmetic dermal rejuvenation techniques have been widely used to stimulate the production of new collagen synthesis by inducing a 'wounding response' in the skin [39-40]. As such, it was of interest to determine if these dermal rejuvenation techniques restored a more youth-



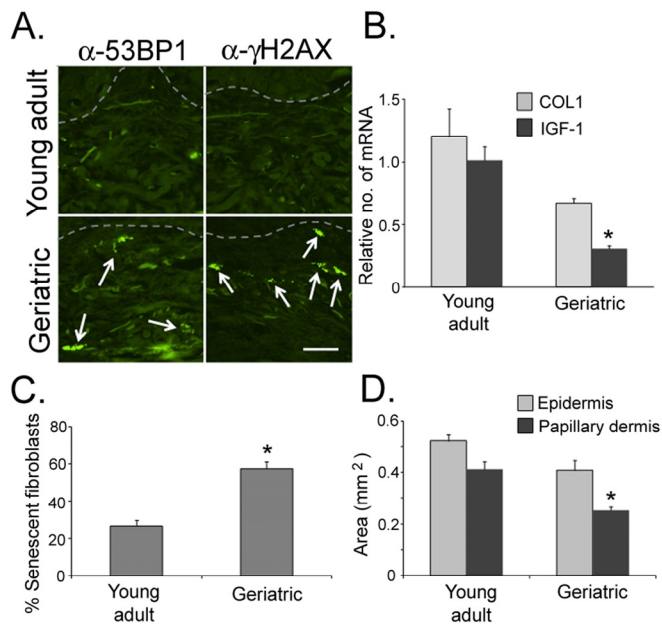


**Figure 2. Senescent fibroblasts accumulate in geriatric dermis *in vivo*.**

Biopsies of sun-protected skin were obtained from six young adult (20-28 years old) and six geriatric ( $\geq 65$  years old) volunteers. (A) Sections of skin were stained with antibodies to 53BP1 and  $\gamma$ H2AX. Positive nuclei are indicated by white arrows; dashed line specifies the location of the basement membrane; bar = 25  $\mu$ m. (B) Quantitative PCR analysis of mRNA isolated from skin biopsies, normalized to actin expression. Asterisk indicate statistical significance from young adult values (IGF-1  $p=0.005$ , COL1  $p=0.091$ ; two-tailed t-test). (C) The number of senescent fibroblasts (based on circular or elliptical nuclear morphology as determined using Nikon Elements Image Analysis software) was counted in the papillary dermis. Asterisk indicates statistical significance from young adult values ( $p=0.001$ ; two-tailed t-test). (D) The area of the epidermis and papillary dermis were calculated from 3mm punch biopsies using Nikon Elements image analysis software. Asterisk indicates statistical significance from young adult values (Epidermis  $p=0.0577$ , Papillary dermis  $p=0.022$ ; two-tailed t-test).

ful phenotype and biology to geriatric skin, and specifically to determine if these techniques could restore the appropriate DNA-damage response found in young skin to UVB-irradiated geriatric skin. Small areas of sun-protected skin on geriatric volunteers were treated by dermabrasion. Biopsies of dermabrased and untreated skin were analyzed after the treated sites were allowed to heal for three months. Consistent with previous reports, dermabrased skin demonstrated increased synthesis of collagen [39-40; Supplemental Fig. 2] and a restoration of the dermal collagen structure similar to that found in young adults (Fig. 3A, panels *i* and *iv*). Dermabrasion also reversed the aging-associated

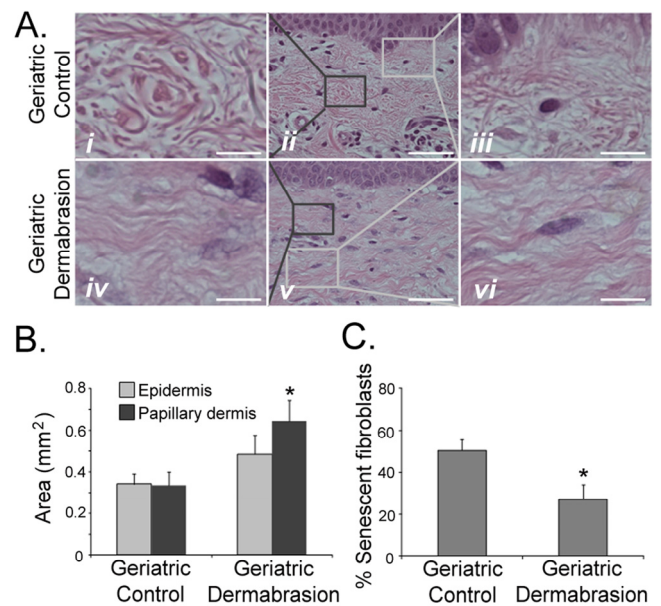


**Figure 3. Dermabrasion restores young adult fibroblast function in geriatric dermis.**

A 5 cm<sup>2</sup> area of sun-protected skin on geriatric ( $\geq 65$  years old) volunteers was dermabrased. After a healing period of three months, biopsies of untreated and dermabrased skin were obtained. (A) Representative H&E sections from untreated and dermabrased geriatric skin. Panels *i* and *iv* are higher magnification images of dark boxes indicated in panels *ii* and *v*. Panels *iii* and *vi* are higher magnification images of light boxes indicated in panels *ii* and *v*. Panels *i* and *iv*, bar=10  $\mu$ m; panels *ii* and *v*, bar=50  $\mu$ m; panels *iii* and *vi*, bar=12.5  $\mu$ m. (B) The area of epidermis and papillary dermis were calculated as described in Fig. 2. Asterisk indicates statistical significance from geriatric control values (Epidermis  $p=0.287$ , Papillary dermis  $p=0.013$ ; two-tailed t-test). (C) The number of senescent fibroblasts in the papillary dermis was determined as described in Fig. 2. Asterisk indicates statistical significance from control values ( $p=0.018$ , two-tailed t-test).

ed atrophy of the papillary dermis (Fig. 2D) by significantly increasing the area of the papillary dermis (Fig. 3B). The thickness of the epidermis was modestly increased by dermabrasion, although this result was not statistically significant (Fig. 3B). Increased thickness of the papillary dermis was accompanied by an increase in fibroblast density in the dermabrased geriatric skin (Fig. 4B; see Supplemental Fig. 3 for example of fibroblast verification) and statistically greater numbers of replicating keratinocytes and fibroblasts (Fig. 4C). The increased proliferative potential of fibroblasts in the dermis corresponded with a decrease in the proportion of dermal senescent fibroblasts (Fig. 3C). The round phenotype of the senescent fibroblast nuclei in control geriatric dermis was replaced with increasing percentages of replicating elliptical fibroblast nuclei



(Fig. 3A, panels *iii* and *vi*). The loss of senescent cells in dermabraded skin can also be observed by assaying for DDR markers. In contrast to the abundant expression of DDR markers in senescent fibroblasts of control geriatric dermis, DDR-positive fibroblasts are not detected in dermabraded geriatric dermis (Fig. 4A).

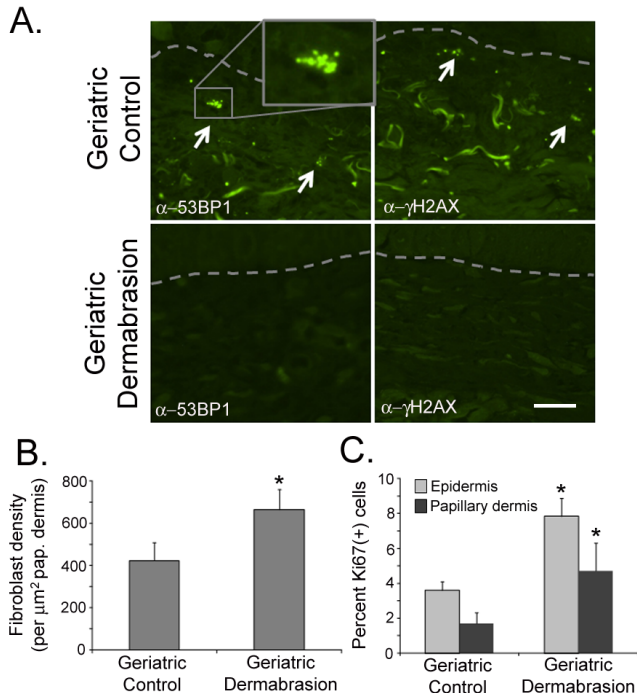


**Figure 4. Dermabrasion stimulates fibroblast replication and suppresses senescence in geriatric dermis.** (A) Skin biopsies described in Fig. 3 were stained with antibodies to 53BP1 and  $\gamma$ H2AX. Senescent nuclei are indicated by white arrows, the basement membrane is designated by a dashed grey line, bar=25  $\mu\text{m}$ . (B) The density of fibroblasts in the papillary dermis was determined using the Nikon Elements Image Analysis software. Asterisk indicates statistical significance from control values ( $p=0.0048$ , two-tailed t-test). (C) Sections of biopsies were stained with antibodies to Ki67. The percentage of Ki67(+) fibroblasts in the papillary dermis and the percentage of Ki67(+) keratinocytes in the basal layer of the epidermis were calculated using Nikon Elements image analysis software. Asterisks indicate statistical significance from control values (papillary dermis,  $p=0.039$ ; epidermis  $p=0.058$ , two-tailed t-test).

Our previous data had shown that the silencing of endogenous IGF-1 in geriatric skin resulted in an inappropriate pro-carcinogenic response to relatively low doses of UVB which could be reversed by local injections of exogenous IGF-1 [3]. Therefore, it was important to determine whether IGF-1 expression was upregulated in geriatric skin treated with dermabrasion.

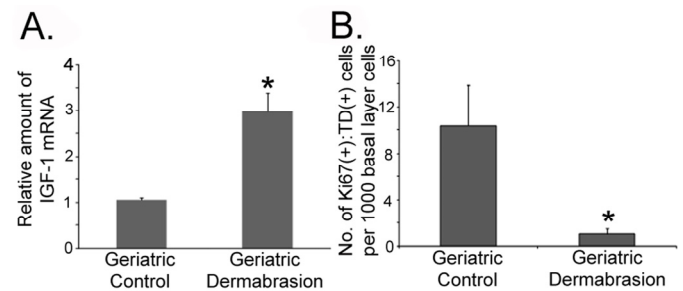


**Figure 5. Dermabrasion upregulates IGF-1 expression and restores the appropriate UVB response to geriatric skin.** Small areas of dermabraded and untreated skin on geriatric volunteers described in Fig. 2 were irradiated with UVB (dose of 350  $\text{J}/\text{m}^2$ ). Twenty-four hours post-UVB, the irradiated skin was biopsied. (A) Total mRNA was isolated and the relative level of IGF-1 expression was determined by quantitative PCR (normalized to actin expression). Asterisk indicates statistically significant differences from control values ( $p<0.006$ , two-tailed t-test). (B) Sections of biopsies were stained with antibodies to Ki67 and thymine dimers (TD). The number of dual Ki67(+):TD(+) basal keratinocytes were determined for both sets of biopsies. Asterisk indicates statistically significant differences from control values ( $p<0.05$ , two-tailed t-test).

At three months following dermabrasion, IGF-1 expression was three-fold higher in treated dermis compared to geriatric controls (Fig. 5A). To assay the UVB-response, small areas of the dermabraded skin and untreated skin on the opposing hip/buttock were irradiated with 350  $\text{J}/\text{m}^2$  (one MED) of UVB. Twenty-four hours post-irradiation (the time required to clear TD lesions), the UVB-irradiated areas were biopsied and the basal layer keratinocytes were assayed for co-expression of proliferation (Ki67) markers and UVB-induced DNA damage (TD; see examples of scored keratinocytes in Supplemental Figure 4). Consistent with the ability of dermabrasion to upregulate IGF-1 levels, UVB irradiation of control versus dermabraded skin were similar to our findings using young skin or geriatric skin treated with exogenous IGF-1 (i.e., no keratinocytes proliferating with DNA damage in the dermabraded skin in contrast to significant numbers of Ki67+:TD+ basal keratinocytes in untreated UVB-irradiated skin; Fig. 5B). These findings indicate that dermal rejuvenation upregulates IGF-1 levels and normalizes the UVB response in geriatric skin.

## DISCUSSION

We have demonstrated *in vivo* that geriatric skin accumulates increasing proportions of senescent fibroblasts as measured by changes in cellular and

nuclear morphology [3; Fig. 3] as well as the induction of DNA-damage recognition proteins associated with cellular senescence [3; Fig. 3]. Furthermore, we have shown that geriatric skin silences IGF-1 expression [3] leading to deficient activation of the IGF-1R [3] on geriatric epidermal keratinocytes. Therefore, when geriatric skin is irradiated with UVB, a portion of the epidermal keratinocytes respond inappropriately by allowing replication of UVB-damaged DNA and potentially creating 'initiated' tumor cells [3, 5-6]. The role of IGF-1 *in vivo* was confirmed by its ability to correct this inappropriate UVB response in geriatric skin by injection of IGF-1 into the dermis prior to UVB irradiation [3]. Thus, therapies that can restore IGF-1 expression to levels seen in young adult dermis could potentially prevent the initiation of carcinogenesis in geriatric skin. Skin rejuvenation techniques, including dermabrasion, have been widely used to stimulate dermal collagen production and promote a youthful appearance of the skin. We found that dermabrasion of sun-protected geriatric skin decreased the proportion of senescent fibroblasts resulting in increased IGF-1 expression. Most importantly, dermabrasion corrected the inappropriate UVB response normally observed in geriatric skin. These results suggest that dermabrasion of geriatric skin can prophylactically prevent non-melanoma skin carcinogenesis.

It is interesting to note that the use of dermabrasion to prophylactically treat actinic keratosis and NMSC was described over 40 years ago [41]. A number of reports have demonstrated that dermabrasion can reduce the incidence of actinic keratosis and NMSC up to 95% in susceptible individuals for many years after treatment [42-44]. However, the use of dermabrasion has fallen out of favor as a primary method for the prophylaxis of NMSC despite the fact that newer methods of prophylactic therapy, i.e. lasers, topical chemotherapy (5-fluorouracil, imiquimod), have never achieved the same level of effectiveness as dermabrasion [45-49]. In fact, studies of the efficacy of these modalities often use dermabrasion as the gold standard for NMSC prophylaxis [50].

Although the early studies on dermabrasion demonstrated its success in NMSC prophylaxis, the mechanism of how it prevented NMSC was unclear. It was hypothesized (but unproven) that the effectiveness of dermabrasion was due to the removal of previously initiated carcinogenic keratinocytes. However, if this hypothesis was true, other ablative procedures should be just as successful in treating NMSC, but they are not. Our studies suggest a new mechanism by which dermabrasion can prevent NMSC carcinogenesis which focuses on its effect on dermal fibroblasts. The

accumulation of senescent fibroblasts in geriatric dermis alters the susceptibility of epidermal keratinocytes to accumulate and fix UVB-induced mutations in their genomes. Furthermore, senescent fibroblasts have been shown to provide an enhanced environment for the growth of carcinogenically initiated epithelial cells via their upregulation of inflammatory cytokines [22-24]. Therefore, the preponderance of senescent fibroblasts in geriatric dermis not only promotes initiating mutations in UVB-exposed keratinocytes but they also promote the expansion of initiated clones of keratinocytes. As demonstrated in these studies, dermabrasion can dramatically reduce the proportion of senescent fibroblasts in treated geriatric dermis. Importantly, the elimination of senescent fibroblasts restores the expression of IGF-1 to normal levels, increases the production of collagen, and prevents the inappropriate UVB response in epidermal keratinocytes. These studies demonstrate an alternative mechanism, other than just removal of initiated keratinocytes, by which dermabrasion can protect geriatric skin from actinic neoplasia.

## METHODS

Human subjects. Geriatric volunteers were recruited from patients treated at Indiana University dermatology clinics. These studies were approved by the Indiana University School of Medicine Institutional Review Board and subjects have signed approved consent forms. Specific requirements for inclusion/exclusion from these studies can be found in the Supplemental Materials.

Dermabrasion. Prior to treatment, a region of sun-protected hip/buttock skin was photographed. Next, an approximately 5 x 5 cm area of the subject's lower hip/buttock skin was isolated and anesthetized with xylocaine anesthesia. Under sterile conditions the localized area of skin was then abraded with sterile, coarse (#60) sandpaper down to the mid dermis, with complete removal of all epidermis and superficial dermis. The wounded area was bandaged with moist, occlusive dressings and the volunteer was instructed to change the dressing twice daily until the wound is re-epithelized in 1-2 weeks. Approximately three months later (~Day 90 +/- 7 days) the volunteer returned to the clinic and a localized area 1 x 1 cm of either dermabrasion or untreated normal skin on the opposite hip/buttock was irradiated with dose of 350 J/m<sup>2</sup> of UVB. In Fitzpatrick Skin Types I and II, this dose of UVB is sufficient to cause a minimal erythematous reaction. Permanent marker was used to outline the areas of skin that was irradiated. Twenty-four hours following UVB exposure, photographs were taken of

the skin to document the extent of the UVB reaction. The irradiated skin, as well as unirradiated adjacent skin, was removed by punch biopsy, (4 mm punch biopsies of the UVB-treated skin and 3 mm punch biopsies of unirradiated skin; 4 biopsies per individual).

**Human UVB response assay.** The epidermal response to UVB irradiation was assayed as previously described [3]. Briefly, thin paraffin-embedded sections from unirradiated and UVB-irradiated biopsies were simultaneously stained with antibodies to Ki67 and thymine dimers. Secondary antibodies that specifically detect only one of the primary antibodies are conjugated to the fluorescent dyes AlexaFluor 488 (detecting Ki67, emitting green wavelengths), and AlexaFluor 568 (detecting thymine dimers, emitting red wavelengths). Images were captured sequentially along the entire length of the biopsy specimen (3mm non-irradiated, 4mm irradiated) using a Nikon Eclipse 80i microscope with Intensilight epifluorescence. These images were analyzed by counting the number of keratinocytes in contact with the basement membrane that are Ki67(+), thymine dimer(+), and Ki67(+):thymine dimer(+). These numbers were expressed as a percentage of total basal layer keratinocytes in the biopsy specimen (determined by counting basal layer keratinocytes for each specimen on H&E-stained slides).

**Statistical analysis.** Statistical analyses were done by two-tailed Student's t test. Statistical significance was defined as  $p < 0.05$  unless otherwise noted in the figure legend.

**Supplemental Material.** Four additional figures and specific protocols for quantitative reverse-transcription PCR, immunofluorescence, growth of human fibroblasts, and senescence-associated  $\beta$ -galactosidase assays can be found in the Supplemental Material.

## ACKNOWLEDGEMENTS

We are grateful to Dr. Raymond Konger for his valuable suggestions. This work was supported by grants from the National Institutes of Health (R21CA131901 to DFS; R01HL062996; U19A1070448 to JBT), VA Merit Award (JBT), and a Dermatology Foundation Career Development Award (AKS). The authors have no conflicts of interest in regard to the data presented in this manuscript.

## CONFLICT OF INTERESTS STATEMENT

The authors declare no conflicts of interest with the data or ideas presented in this manuscript.

## REFERENCES

1. Parkin DM, Bray FI, Devesa SS. Cancer burden in the year 2000. the global picture. *Euro J Cancer* 2001; 37: S4–S66.
2. Coppe JP, Desprez PY, Krtolica A, Campisi J. The senescence-associated secretory phenotype: the dark side of tumor suppression. *Ann Rev Path Mech Dis* 2010; 5: 99-118.
3. Lewis DA, Travers JB, Somani AK, Spandau DF. The IGF-1/IGF-1R signaling axis in the skin: a new role for the dermis in aging-associated skin cancer. *Oncogene* 2010; 29: 1475-1485.
4. Anisimov VN. Carcinogenesis and aging 20 years after: escaping horizon. *Mech of Ageing Develop* 2009; 130: 105-121.
5. Lewis DA, Travers JB, Spandau DF. A new paradigm for the role of aging in the development of skin cancer. *J Invest Dermatol* 2008; 129: 787-791.
6. Lewis DA, Travers JB, Spandau DF. (2010) Aging-associated non-melanoma skin cancer: a role for the dermis. In *Textbook of Aging Skin*, MA Farage, KW Miller and HI Maibach, eds. (Springer Berlin Heidelberg), pp 588-599.
7. Chuang T-Y, Lewis DA, Spandau DF. Decreased incidence of non-melanoma skin cancer in patients with type 2 diabetes mellitus using insulin: a pilot study. *Br J Dermatol* 2005; 153: 552-557.
8. Kuhn C, Kumar M, Hurwitz SA, Cotton J, Spandau DF. Activation of the insulin-like growth factor-1 receptor promotes the survival of human keratinocytes following ultraviolet B irradiation. *Intl J Cancer* 1999; 80: 431-438.
9. Lewis DA, Spandau DF. UVB-induced activation of NF- $\kappa$ B is regulated by the IGF-1R and dependent on p38 MAPK. *J Invest Dermatol* 2008; 128: 1022-1029.
10. Lewis DA, Yi Q, Travers JB, Spandau DF. UVB-induced senescence in human keratinocytes requires a functional IGF-1R and p53. *Mol Biol Cell* 2008; 19:1346-1353.
11. American Cancer Society. Cancer Facts and Figures 2010. [www.cancer.org/downloads/STT/Cancer\\_Facts\\_and\\_Figures\\_2010.pdf](http://www.cancer.org/downloads/STT/Cancer_Facts_and_Figures_2010.pdf)
12. Rogers HW, Weinstock MA, Harris AR, Hinckley MR, Feldman SR, Fleischer AB, et al. Incidence estimate of nonmelanoma skin cancer in the United States, 2006. *Arch Dermatol* 2010; 146: 283-287.
13. Bickers DR, Lim HW, Margolis D, Weinstock MA, Goodman C, Faulkner E, et. al. The burden of skin diseases. *J Am Acad Dermatol* 2006; 55: 490-500.
14. Housman TS, Feldman SR, Williford PM, Fleischer AB, Goldman ND, Acostamadiedo JM, et. al. Skin cancer is among the most costly of all cancers to treat for the Medicare population. *J Am Acad Dermatol* 2003; 48: 425-429.
15. Kraemer KH. Sunlight and skin cancer: another link revealed. *Proc Natl Acad Sci USA* 1997; 94: 11-14.
16. National Institutes of Health, Sun Protection in Cancer Trends Progress Report – 2009/2010, [www.cancer.gov](http://www.cancer.gov)
17. Brash DE, Ziegler A, Jonason AS, Simon JA, Kunala S, Leffell DJ. Sunlight and sunburn in human skin cancer: p53, apoptosis, and tumor progression. *J Invest Dermatol Symp Proc* 1996; 1: 136-142.
18. Jeffes EWB, Tang EH: Actinic keratosis: current treatment options. *Am J Clin Dermatol* 2000; 1: 167-179.
19. Godar DE, Urbach F, Gasparro FP, van der Leun JC. UV doses of young adults. *Photochem. Photobiol.* 2003; 77: 453-457.

20. Vogelstein B, Kinzler KW. Cancer genes and the pathways they control. *Nature Med* 2004; 10: 789-799.
21. Sjoblom T, Jones S, Wood LD, Parsons DW, Lin J, Barber TD, et. al. The consensus coding sequences of human breast and colorectal cancers. *Science* 2006; 314: 268-274.
22. Krtolica A, Parrinello S, Lockett S, Desprez PY, Campisi J. Senescent fibroblasts promote epithelial cell growth and tumorigenesis: A link between cancer and aging. *Proc Natl Acad Sci USA* 2001; 98: 12072-12077.
23. Parrinello S, Coppe J-P, Krtolica A, Campisi J. Stromal-epithelial interactions in aging and cancer: senescent fibroblasts alter epithelial cell differentiation. *J Cell Sci* 2005; 118: 485-496.
24. Campisi J. Senescent cells, tumor suppression, and organismal aging: good citizens, bad neighbors. *Cell* 2005; 120: 513-522.
25. Campisi J. Suppressing cancer: the importance of being senescent. *Science* 2005; 309: 886-887.
26. Dimri GP. What has senescence got to do with cancer? *Cancer Cell* 2005; 7: 505-512.
27. Feng Z, Hu W, Teresky AK, Hernando E, Cordon-Dardo C, Levine AJ. Declining p53 function in the aging process: a possible mechanism for the increased tumor incidence in older populations. *Proc Natl Acad Sci USA* 2007; 104: 16633-16638.
28. Dimri GP, Lee X, Basile G, Acosta M, Scott G, Roskelley C, et. al. A biomarker that identifies senescent human cells in culture and in aging skin in vivo. *Proc Natl Acad Sci USA* 1995; 92: 9363-9367.
29. d'Adda di Fagagna, F. Living on a break: cellular senescence as a DNA-damage response. *Nat Rev Cancer* 2008; 8: 512-522.
30. Pospelova TV, Demidenko ZN, Bukreeva EI, Pospelov VA, Gudkov AV, Blagosklonny MV. Pseudo-DNA damage response in senescent cells. *Cell Cycle* 2009; 8: 4112-4118.
31. Seviour EG, Lin SY. The DNA damage response: balancing the scale between cancer and ageing. *Aging* 2010; 2: 900-907.
32. Redon CE, Nakamura AJ, Martin OA, Parekh PR, Weyemi US, Bonner WM. Recent developments in the use of  $\gamma$ -H2AX as a quantitative DNA double-strand break biomarker. *Aging* 2011; 3: 168-174.
33. Makrantonaki E, Zouboulis CC. (2010). Pathomechanisms of endogenously aged skin. In *Textbook of Aging Skin*, MA Farage, KW Miller and HI Maibach, eds. (Springer Berlin Heidelberg), pp 93-99.
34. Ramos-e-Silva M, da Silva Carneiro SC. Elderly skin and its rejuvenation: products and procedures for the aging skin. *J Cosmetic Dermatol* 2007; 6: 40-50.
35. Helmbold P. (2010). Basophilic (actinic) degeneration of the dermis: an easy histological scoring approach in dermal photoaging. In *Textbook of Aging Skin*, MA Farage, KW Miller and HI Maibach, eds. (Springer Berlin Heidelberg), pp 19-21.
36. Farage MA, Miller KW, Maibach HI. (2010). Degenerative changes in aging skin. In *Textbook of Aging Skin*, MA Farage, KW Miller and HI Maibach, eds. (Springer Berlin Heidelberg), pp 25-35.
37. Mine S, Fortunel NO, Pigeon H, Asselineau D. Aging alters functionally human dermal papillary fibroblasts but not reticular fibroblasts: a view of skin morphogenesis and aging. *PLoS ONE* 2008; 3: e4066 (1-13).
38. Fisher GJ, Varani J, Voorhees JJ. Looking older: fibroblast collapse and therapeutic implications. *Arch Dermatol* 2008; 144: 666-672.
39. Lawrence N, Mandy S, Yarborough J, Alt T. History of dermabrasion. *Dermatol Surg* 2000; 26: 95-101.
40. Friedman S, Lippitz J. Chemical peels, dermabrasion, and laser therapy. *Dis Mon* 2009; 55: 223-235.
41. Epstein, E. Planing for precancerous skin: a ten-year evaluation. *California Med* 1966; 105: 26-27.
42. Benedetto AV, Griffin TD, Benedetto EA, Humeniuk HM. Dermabrasion: therapy and prophylaxis of the photoaged face. *J Am Acad Dermatol* 1992; 27: 439-447.
43. Coleman WP, Yarborough JM, Mandy SH. Dermabrasion for prophylaxis and treatment of actinic keratoses. *Dermatol Surg* 1996; 22: 17-21.
44. Field LM. Dermabrasion and premalignant disease. *Dermatol Surg* 1997; 23: 714.
45. Cooley JE, Casey DL, Kauffman CL. Manual resurfacing and trichloroacetic acid for the treatment of patients with widespread actinic damage. *Dermatol Surg* 1997; 23: 373-379.
46. Hantash BM, Stewart DB, Cooper ZA, Rehms WE, Koch RJ, Swetter SM. Facial resurfacing for nonmelanoma skin cancer prophylaxis. *Arch Dermatol* 2006; 142: 976-982.
47. Ostertag JU, Quaedvlieg PJF, Neumann MHAM, Kerkels GA. Recurrence rates and long-term follow-up after laser resurfacing as a treatment for widespread actinic keratoses in the face and on the scalp. *Dermatol Surg* 2006; 32: 261-267.
48. Halachmi S, Lapidoth M. Lasers in skin cancer prophylaxis. *Exp Rev Anticancer Therapy* 2008; 8: 1713-1715.
49. Love WE, Bernhard JD, Bordeaux JS. Topical imiquimod or fluorouracil therapy for basal and squamous cell carcinoma. *Arch Dermatol* 2009; 145: 1431-1438.
50. Field LM. The superiority of dermabrasion over laser abrasion in the prophylaxis of malignant and premalignant disease. *Dermatol Surg* 2007; 33: 258-259.



## SUPPLEMENTAL MATERIAL

### Supplemental Experimental Procedures

**Quantitative Reverse-Transcriptase PCR.** Homogenized tissue from dissected dermal sections was lysed using RNeasy kit (Qiagen) buffers. Cell lysates were then further homogenized using Shredder columns (Qiagen) and RNA isolation continued with RNeasy kit. All of the reagents used for RT and PCR are obtained from SuperArray Biosciences, Frederick, MD. The following were added to a 0.2 ml tube where first a genomic DNA elimination step was performed on 2 µg RNA total volume 10 µl was heated to 42°C for 5 minutes and chilled on ice. Next the reverse transcription cocktail was prepared and 10 µl added to the RNA; 2 µl RT enzyme mix, 4 µl RT buffer, 1 µl primer and external control mix, 3 µl RNase free water. Mixture was heated 42°C for 15 minutes, 95°C for 5 minutes and chilled on ice for experiments, the final volume of cDNA was 20 µl. qRT-PCR is performed using a LightCycler PCR (Roche Scientific, Fishers IN). Quantization of experimental qRT-PCR products was determined by comparison with external control qRT-PCR products from templates of a known copy number. Relative copy numbers of experimental mRNA are then determined following adjustment with actin controls from the same tissue.

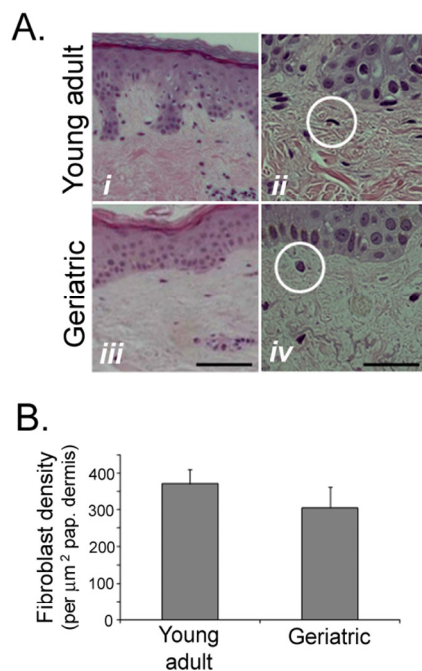
**Immunofluorescence.** Paraffin-embedded sections were deparaffinized, hydrated, and rinsed with tris-buffered saline with tween 20 (TBS) (DAKO, Carpinteria, CA). Antigen retrieval was performed using a water bath at 95°C for 20 minutes with DAKO Target Retrieval buffer. After cooling, the slides are rinsed with TBS, and the slides were then transferred to a clean 100 mm bacterial glass petri dish containing PBS-saturated filter paper under a strip of Parafilm. Primary antibodies (1:50) diluted in 3% BSA in TSB was added to the tissues. The lid was placed on the petri dish and the coverslips incubated for 1 hour at room temperature. The tissues were rinsed in PBS (three 10 minutes washes), and then the appropriate secondary antibody conjugated to the desired fluorochrome was added for 30 minutes at room temperature in the dark. The sections were washed as before, the edges blotted dry, and then mounted with coverslips using Fluoromount G. Antibodies used included: α-53BP1 (Abcam, Cambridge, MA), α-p21 (Cell Signaling, Danvers, MA), α-γH2AX (Millipore, Temecula, CA), α-prolyl-4-hydroxylase (Millipore, Temecula, CA), α-Ki67 (NeoMarkers, Fremont, CA), and α-thymine dimers (Kamiya Biomedical, Seattle, WA).

**Senescence-associated β-galactosidase assays.** Fibroblasts were washed twice with PBS and fixed with 2% formaldehyde/0.2% glutaraldehyde at room temperature for 10 minutes. After two additional washes with PBS, 2 ml of staining solution (150 mM sodium chloride, 25.2 mM sodium phosphate dibasic, 7.36 mM citric acid, 5 mM potassium ferricyanide, 5 mM potassium ferrocyanide, 2 mM magnesium chloride, 1 ng/ml 5-bromo-4-chloro-3-indolyl-β-D-galactoside, pH 6.0)<sup>25</sup>, were added to the cells and they were incubated at 37°C overnight. The cells were again washed with PBS and photographed by bright field microscopy to count blue cells and phase contrast microscopy to count total cells. At least four fields (100X magnification, approximately 200 cells/field) were counted for each plate of cells; at least two plates of cells for each condition (or cell type) were assayed in each experiment.

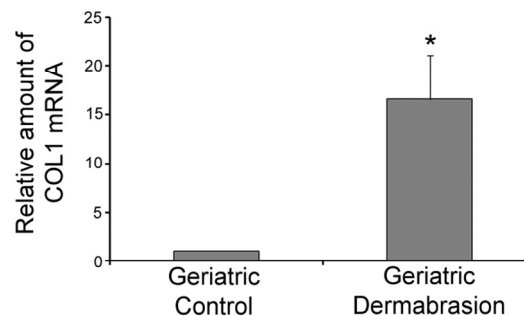
**Isolation and culture of normal human fibroblasts.** Excised foreskin tissue was washed with antibiotics, the tissue minced, and individual cells released from the tissue by trypsin digestion (8). Keratinocytes and fibroblasts were separated by differential resistance to treatment with EDTA. Fibroblasts were grown in Dulbecco's Modified Eagles medium containing 10% fetal calf serum. All relevant procedures using human tissue have been approved by the Indiana University School of Medicine Institutional Review Board.



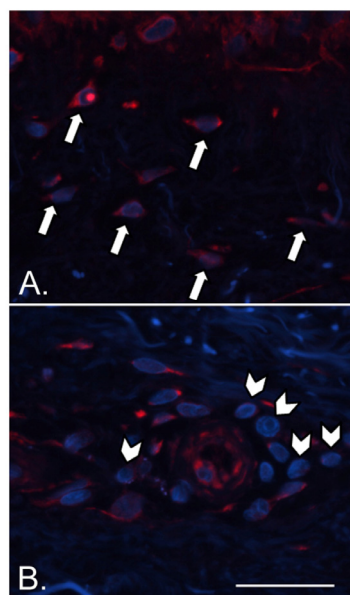
## SUPPLEMENTAL FIGURES



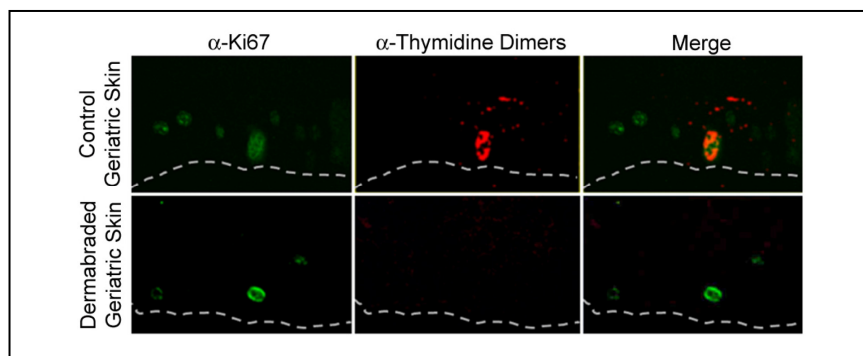
**Supplementary Figure 1. Phenotypic changes in geriatric skin.** (A) H&E sections of the biopsies described in Fig. 2. White circles indicate elliptical nucleus of a replicating fibroblast in panel *ii* and the spherical nucleus of a senescent fibroblast in panel *iv*. Bar=100  $\mu\text{m}$  in panels *i* and *iii*; bar=25  $\mu\text{m}$  in panels *ii* and *iv*. (B) The density of fibroblasts was determined in young adult and geriatric skin as described in Fig. 2 ( $p=0.093$ ; two-tailed t-test).



**Supplementary Figure 2. Dermabrasion increases collagen expression.** Quantitative PCR was conducted on biopsies described in Fig. 2. The relative amount of collagen I mRNA (normalized to actin expression) is shown. Asterisk indicates statistical significance from young adult values ( $p=0.018$ , two-tailed t-test).



**Supplementary Figure 3. Identification of dermal fibroblasts in geriatric dermis.** Example of how the identity of fibroblasts was confirmed in the papillary dermis. Sections were stained with antibodies to  $\alpha$ -prolyl-4-hydroxylase (red) and DAPI (nuclear-specific stain, blue). Fibroblasts stain positive for  $\alpha$ -prolyl-4-hydroxylase and are indicated by arrows in panel **A**. Non-fibroblasts are indicated in panel **B** by chevrons.



**Supplementary Figure 4. Example of the UVB-response assay.** Two  $\text{cm}^2$  areas on the lower backs of volunteers were irradiated with UVB (350  $\text{J}/\text{m}^2$ ). Twenty-four hours following irradiation, a four mm punch biopsy was obtained from the irradiated skin. Sections of formalin-fixed, paraffin-embedded tissue were stained with both  $\alpha$ -Ki67 (staining green) and  $\alpha$ -thymine dimer antibodies (staining red). The merged images are shown to the right of the figure. The top series of panels is an example of a cell positive for both Ki67 and thymine dimers (staining yellow, inappropriate UVB response) while the cell indicated in bottom panels is only positive for Ki67 (staining green, appropriate UVB response). The location of the basement membrane is indicated by a grey dashed line. Similar sections were stained with H&E to determine the total number of basal layer keratinocytes in each biopsy.

# Naringin targets Zeb1 to suppress osteosarcoma cell proliferation and metastasis

He Ming<sup>1</sup>, Qiu Chuang<sup>1</sup>, Wang Jiashi<sup>1</sup>, Li Bin<sup>1</sup>, Wang Guangbin<sup>1</sup>, Ji Xianglu<sup>1</sup>

<sup>1</sup>Department of Orthopedic Surgery, Shengjing Hospital of China Medical University, Heping District, Shenyang 110004, People's Republic of China

**Correspondence to:** Ji Xianglu; email: [jixiangludor@163.com](mailto:jixiangludor@163.com)

**Keywords:** naringin, osteosarcoma, Zeb1, proliferation, metastasis

**Received:** July 10, 2018 **Accepted:** December 6, 2018 **Published:** December 22, 2018

**Copyright:** Ming et al. This is an open-access article distributed under the terms of the Creative Commons Attribution License (CC BY 3.0), which permits unrestricted use, distribution, and reproduction in any medium, provided the original author and source are credited.

## ABSTRACT

Naringin, a citrus bioflavonoid, has anti-inflammatory actions and cardio- and neuroprotective effects. In addition, naringin exhibits multiple antitumor actions in several cancer types, including osteosarcoma, the most common type of bone cancer. Here, we show that naringin inhibits proliferation and invasion and induces apoptosis in human osteosarcoma cells by inhibiting zinc finger E-box binding homeobox 1 (Zeb1), a transcriptional repressor of epithelial differentiation involved in tumor metastasis. Our expression analyses confirm that Zeb1 is highly expressed in osteosarcoma specimens and cell lines. The effects of naringin, which included downregulation of Cyclin D1, MMP2, and bcl-2, were reproduced by siRNA-mediated Zeb1 silencing, whereas Zeb1 overexpression increased proliferation, migration, and Cyclin D1, MMP2, and bcl-2 levels. In addition, naringin administration reduced tumor nodule formation and attenuated the expression of the above proteins in the livers of mice injected with MG63 osteosarcoma cells. Our study provides preclinical evidence for the potential therapeutic application of naringin in the treatment of osteosarcoma.

## INTRODUCTION

Although adjuvant chemotherapy has improved osteosarcoma survival rate in recent years, development of multidrug resistance severely impacts prognosis and restricts success of curative attempts [1-3]. Therefore, new and effective drugs to treat osteosarcoma are clearly needed.

Naringin, a bioflavonoid abundant in grapefruit and other citrus, has multiple biological activities. It possesses sedative, antifungal, antispasmodic, and analgesic properties, and provides cardioprotective, neuroprotective, and anticancer effects [4]. In addition, naringin has been demonstrated to inhibit inflammatory responses, prevent bone degeneration, and exert anabolic effects on bone cells [5, 6]. Naringin promotes the expression of  $\beta$ -catenin and increase Ser552 phosphorylation on  $\beta$ -catenin in UMR-106 osteosar-

coma cells. This led to activation of lymphoid enhancer factor (LEF)/T-cell factor (TCF) transcription factors to stimulate bone development [7]. Naringin abrogates osteoclastogenesis and bone resorption by inhibiting RANKL-induced NF- $\kappa$ B and ERK activation [8], and demonstrated therapeutic potential to attenuate polymethylmethacrylate-induced osteoclastogenesis and osteolysis. There is substantial evidence supporting a role for naringin as an anticancer agent. Studies also indicated that naringin could reduce the release of inflammatory factors and inhibit the growth of W256 carcinosarcoma in rats [4, 9, 10]. Moreover, growth arrest and apoptosis were common effects of naringin in several *in vitro* and *in vivo* studies conducted on breast, cervical, ovarian, bladder, hepatic, skin, colorectal, and gastric cancer cells [11, 12].

Zeb1 (zinc finger E-box binding homeobox 1) is a transcription factor that represses epithelial differentia-

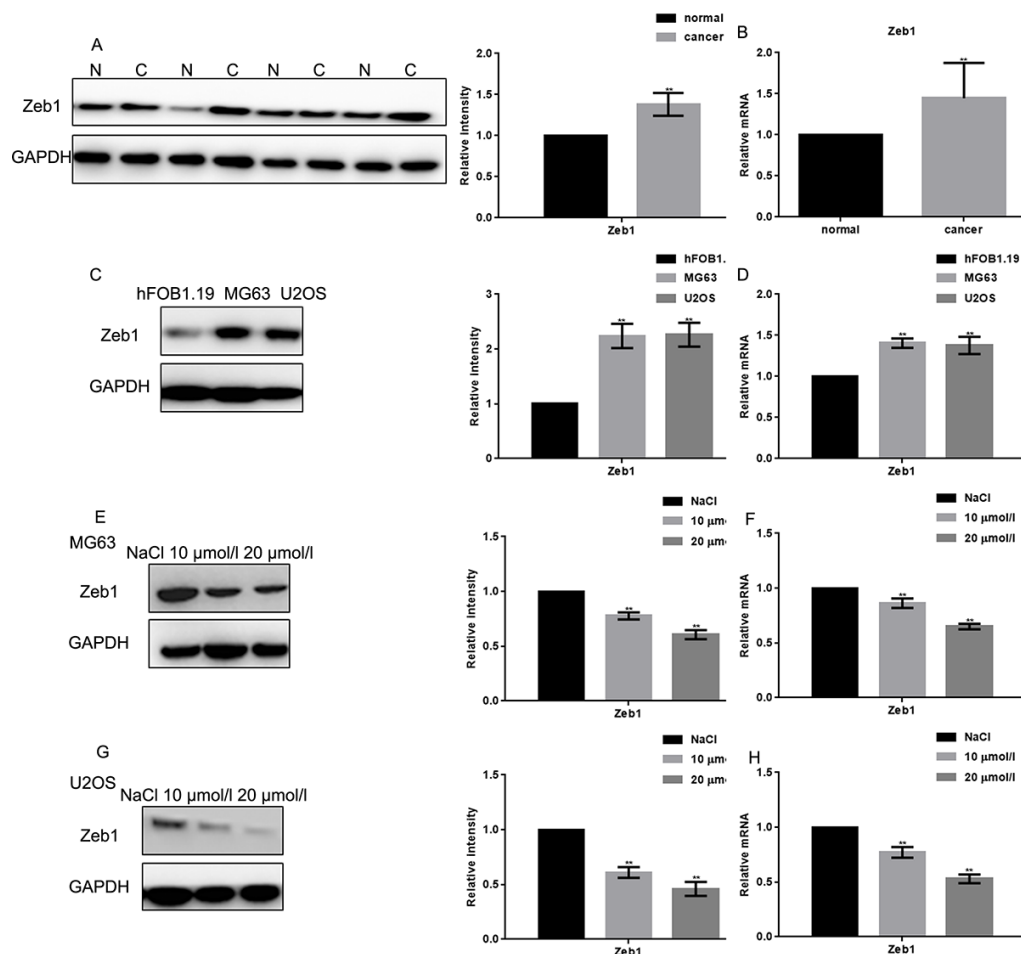


**Figure 1: Naringin inhibits the expression of Zeb1 in osteosarcoma cells.** (A, B) Zeb1 expression in 30 human osteosarcoma specimens and their adjacent normal tissue counterparts was detected by Western blot and real-time PCR.  $**P < 0.05$ , vs normal tissues. (C, D) Zeb1 expression in MG63, U2OS and hFOB1.19 cells, detected by Western blot and real-time PCR.  $**P < 0.05$ , vs hFOB1.19 cells. (E-H) Zeb1 expression detected by Western blot and real-time PCR in MG63 and U2OS cells treated with NaCl or indicated concentrations of naringin for 24 h.  $**P < 0.05$ , compared with NaCl.

tion and promotes a mesenchymal phenotype [13]. Zeb1 is upregulated in several cancers, where it influences cell motility, cell cycle, and survival, and is an important contributor to tumor invasion and metastasis [14, 15].

Studies have shown that Zeb1 can override the G1 checkpoint directly, by stimulating Cyclin D1 expression, and indirectly, by regulating the Wnt signaling pathway [16, 17]. Zeb1 was shown to promote the progression of lung cancer by increasing the expression of MMP2, a member of the matrix metalloproteinases family that play an important role in cell migration and facilitate invasion and metastasis of tumor cells [18, 19]. Zeb1 has also been shown to be upregulated in osteosarcoma, and to contribute to its development [20, 21].

Using human osteosarcoma cell lines as experimental model, in the present study we provide *in vitro* and *in vivo* evidence that naringin suppresses proliferation and metastasis of osteosarcoma cells by inhibiting the expression of Zeb1. Our findings highlight the potential of naringin, a safe and natural flavonoid, for osteosarcoma therapy.

## RESULTS

### Naringin inhibits the expression of Zeb1 in osteosarcoma cells

The expression of Zeb1 in human osteosarcoma samples was assessed by Western blot and real-time PCR (Figs. 1A, B). Both assays showed that Zeb1 was overexpressed in most samples, although heterogeneity

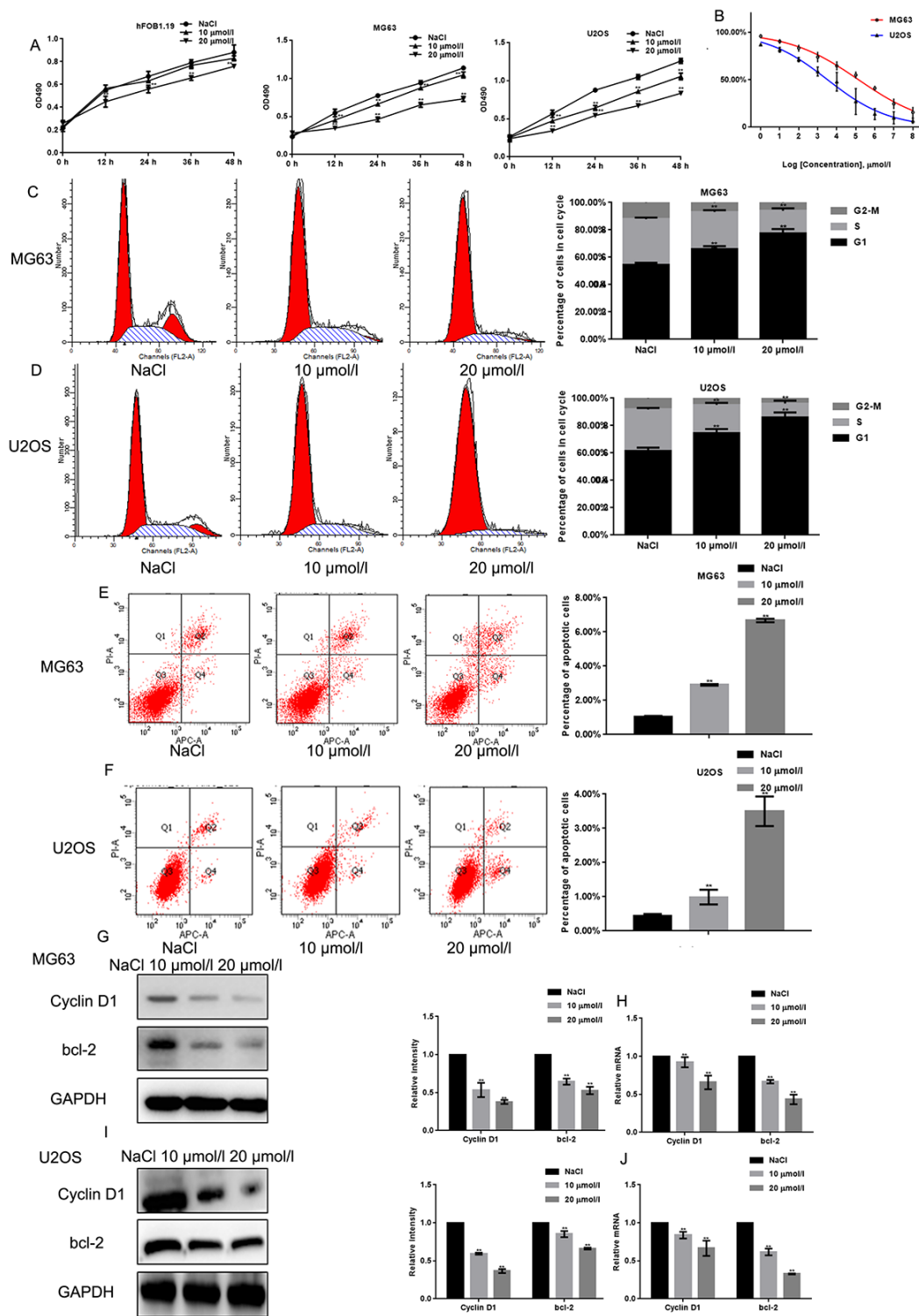


**Figure 2: Naringin inhibits the proliferation of osteosarcoma cells.** (A) Results of MTT proliferation assays in hFOB1.19, MG63, and U2OS cells cultured with various concentrations of naringin for different times. Results represent the mean  $\pm$  SD of three experiments done in triplicate.  $**P < 0.05$ , compared with NaCl. (B) Proliferation inhibition rates induced by naringin on MG63 and U2OS cells.  $\text{IC}_{50}$  values were calculated through linear regression. (C, D) Flow cytometric analysis of cell cycle distribution in MG63 and U2OS cells pre-incubated with or without naringin for 24 h and stained with PI. The experiment was repeated three times.  $**P < 0.05$ , compared with NaCl. (E, F) Flow cytometric assay of apoptosis in MG63 and U2OS cells pre-incubated with or without naringin for 24 h and stained with Annexin V-FITC/PI. The experiment was repeated three times.  $**P < 0.05$ , compared with NaCl. (G-J) Expression of Cyclin D1 and bcl-2 detected by Western blot and real-time PCR in MG63 and U2OS cells treated with NaCl or naringin for 24 h.  $**P < 0.05$ , compared with NaCl.

was evident. In cultured cells, both Western blot and real-time PCR showed much stronger Zeb1 expression in osteosarcoma MG63 and U2OS cells than in control hFOB1.19 osteoblasts (Figs. 1C, D). Upon exposure to naringin (10 or 20  $\mu\text{mol/L}$ ) for 24 h, Zeb1 protein and mRNA levels were dramatically decreased, in dose-dependent manner, in both osteosarcoma cell lines (Figs. 1 E-H).

### **Naringin inhibits proliferation and induces apoptosis in osteosarcoma cells**

The MTT assay revealed that naringin treatment inhibited the proliferation of MG63 and U2OS cells in a concentration dependent manner (Fig. 2A). The inhibitory effect of naringin on the proliferation of hFOB1.19 was only obvious when the concentration of naringin was 20  $\mu\text{mol/L}$ . The  $\text{IC}_{50}$  of naringin on MG63 and U2OS cells at 24 h was  $\sim 50 \mu\text{mol/L}$  and  $\sim 30 \mu\text{mol/L}$ , respectively (Fig. 2B). Next, we used flow cytometry to evaluate cell cycle staging in PI-stained MG63 and U2OS cells previously exposed to various concentrations of naringin for 24 h. Naringin induced a dose-dependent increase in the percentage of cells in  $G_1$  phase, and decreased the number of cells in S phase, compared to control (Figs. 2C, D). To assess whether naringin can promote apoptosis, flow cytometry was used in Annexin-V-FITC-stained osteosarcoma cells. Results showed a dose-dependent increase in apoptotic cells treated with naringin (Figs. 2E, F). In line with these antiproliferative and pro-apoptotic effects, both Western blot and real-time PCR assays showed that exposure to 10 or 20  $\mu\text{mol/L}$  naringin for 24 h dramatically decreased the expression of Cyclin D1 and bcl-2 (Figs. 2G-J).

### **Naringin inhibits migration of osteosarcoma cells**

The effects of naringin on osteosarcoma cell migration and invasion was assessed using Transwell assays in the absence or presence, respectively, of Matrigel. Results showed that naringin exposure (10 or 20  $\mu\text{mol/L}$  for 24 h) significantly decreased both migration and invasion of MG63 and U2OS cells in a dose-dependent manner (Figs. 3A-D). These effects were consistent with a decrease in MMP2 expression, detected in both cell lines in Western blot, real-time PCR, and zymography gel assays (Figs. 3E-H).

### **Naringin suppresses osteosarcoma cell proliferation and migration by inhibiting Zeb1**

To test the hypothesis that naringin exerts antiproliferative and anti-invasive effects by inhibiting Zeb1, its effects were tested in MG63 cells transfected with a plasmid encoding Zeb1 (Zeb1 overexpression) or

an empty vector backbone (control). Conversely, siRNAs were introduced to downregulate Zeb1 (si-Zeb1), and to serve as non-targeted, negative control (si-NC). MTT assays showed that proliferation was stimulated by Zeb1 overexpression, and decreased to control inhibition levels by naringin (20  $\mu\text{mol/L}$ ) (Fig. 4A). On the other hand, Zeb1 suppression, although partial, decreased cell proliferation, and naringin induced no further inhibition in these cells. (Fig. 4B). We next examined whether migration was affected in Zeb1-overexpressing and Zeb1-suppressed cells. Transwell assay results indicated that Zeb1 overexpression enhances the migration of MG63 cells, while Zeb1 silencing recapitulates the inhibitory effect of naringin on control cells (Figs. 4C, D). Finally, we analyzed the effects of Zeb1 overexpression and downregulation on Cyclin D1, MMP2, and bcl-2 expression. The results showed that expression of these proteins increased upon Zeb1 upregulation (Figs. 4 E-F). Meanwhile, Zeb1 silencing lowered protein expression to levels like those observed in naringin-treated control cells (Figs. 4 G-H).

### **Naringin inhibits the invasion of MG63 cells *in vivo***

To examine the effect of naringin on osteosarcoma cell tumorigenesis *in vivo*, MG63 cells were injected into nude mice via the tail vein. After daily administration of naringin (5 or 10 mg/kg) or 0.9% NaCl for 16 days, mice were sacrificed and lung tissues processed for microscopic histological analysis. Results showed that naringin significantly prevented lung degeneration and reduced the incidence of metastatic nodules (Fig. 5A). Moreover, Western blots (Fig. 5B) and real-time PCR assays (Fig. 5C) showed that the expression of Zeb1, Cyclin D1, MMP2, and bcl-2 was decreased in the livers of mice treated with naringin.

## **DISCUSSION**

Naringin, a flavonoid present in citrus fruits, has HMG-CoA reductase inhibitor activity, and at low (nM) doses increases osteogenic activities in an osteoblast cell model *in vitro* [22]. Moreover, naringin-induced osteogenic differentiation has been recently described in bone marrow stromal cells and stem cells[23]. On the other hand, naringin has been shown to inhibit cell proliferation and promote cell apoptosis in breast cancer, cervical cancer, melanoma, and bladder cancer cells [24]. Thus, we speculated that naringin may have therapeutic effect on osteosarcoma as well.

In this study, we tested the hypothesis that naringin has anticancer actions through inhibition of Zeb1, a zinc finger homeodomain transcription factor implicated in invasiveness and metastasis development in several



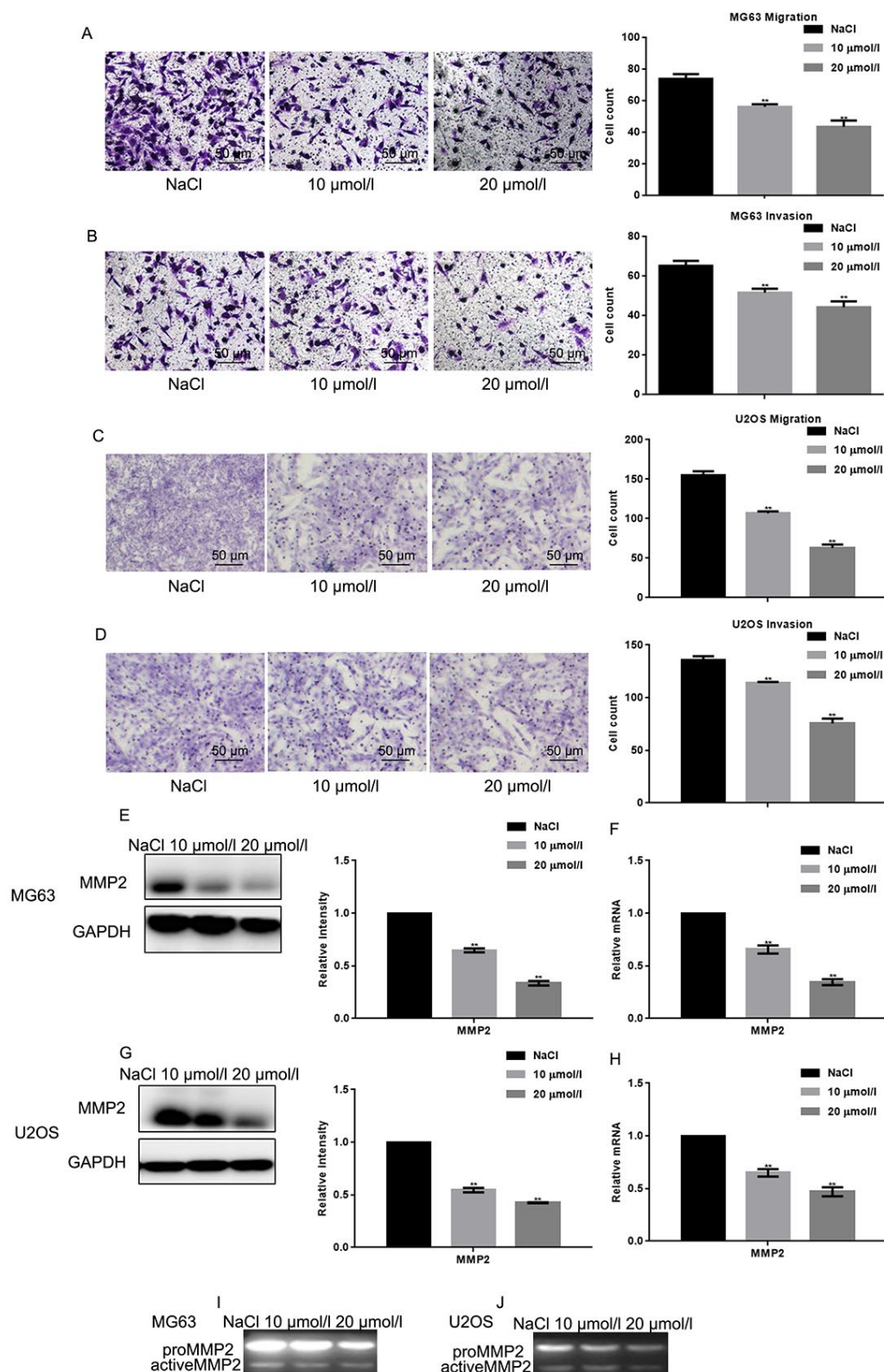


**Figure 3: Naringin inhibits migration and invasion of osteosarcoma cells.** (A-D) Migration and invasion were studied, respectively, using Transwell assays with or without Matrigel, in naringin-treated MG63 and U2OS cells. Cell count results represent the mean  $\pm$  SD of three experiments.  $**P < 0.05$ , compared with NaCl. (E-H) MMP2 expression by Western blot and real-time PCR in MG63 and U2OS cells treated with NaCl or naringin for 24 h.  $**P < 0.05$ , compared with NaCl. (I, J) Zymography gel assay showing the inhibitory effect of naringin on MMP2 activity in MG63 and U2OS cells.

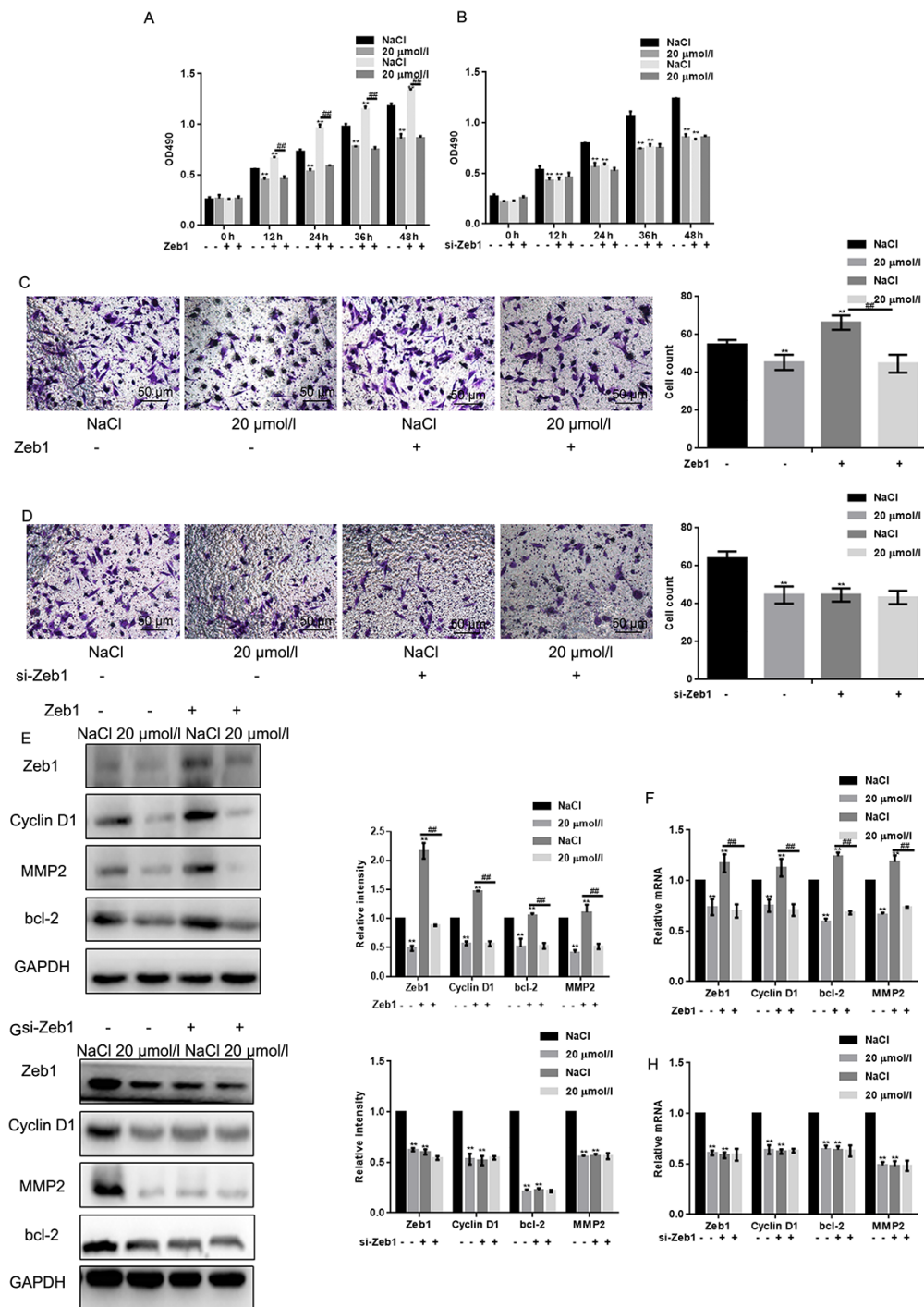


**Figure 4: Naringin suppresses osteosarcoma cell proliferation and migration by inhibiting Zeb1.** (A) MTT proliferation assay of MG63 cells expressing a control vector or Zeb1. Cells were incubated with 20  $\mu\text{mol/L}$  of naringin or NaCl and assayed at the indicated times. Results represent the mean  $\pm$  SD of three experiments done in triplicate. \*\* $P < 0.05$ , compared with NaCl. ##  $P < 0.05$ , compared with Zeb1 overexpressed group. (B) MTT proliferation assay of MG63 cells transfected with si-Zeb1 (Zeb1 silencing) or si-NC (negative control). Cells were treated with 20  $\mu\text{mol/L}$  of naringin or NaCl and assayed at the indicated times. Results represent the mean  $\pm$  SD of three experiments done in triplicate. \*\* $P < 0.05$ , compared with NaCl. (C) Results of Transwell migration assays (without Matrigel) performed in MG63 cells expressing control vectors or Zeb1. Cells were treated with 20  $\mu\text{mol/L}$  of naringin or NaCl. \*\* $P < 0.05$ , compared with NaCl; ##  $P < 0.05$ , compared with Zeb1 overexpressed group. (D) Results of Transwell migration assays (without Matrigel) performed in MG63 cells transfected with si-Zeb1 (Zeb1 silencing) or si-NC (negative control). Cells were treated with 20  $\mu\text{mol/L}$  of naringin or NaCl. \*\* $P < 0.05$ , compared with NaCl. (E, F) Western blot and real-time PCR assay results for Zeb1, Cyclin D1, bcl-2, and MMP2 expression in MG63 cells expressing Zeb1 or empty vector. Cells were incubated with 20  $\mu\text{mol/L}$  of naringin or NaCl (control). \*\* $P < 0.05$ , compared with NaCl; ##  $P < 0.05$ , compared with Zeb1 overexpressed group. (G, H) Western blot and real-time PCR assay results for Zeb1, Cyclin D1, bcl-2, and MMP2 expression in MG63 cells transfected with si-Zeb1 or si-NC. Cells were treated with 20  $\mu\text{mol/L}$  of naringin or NaCl. \*\* $P < 0.05$ , compared with NaCl.

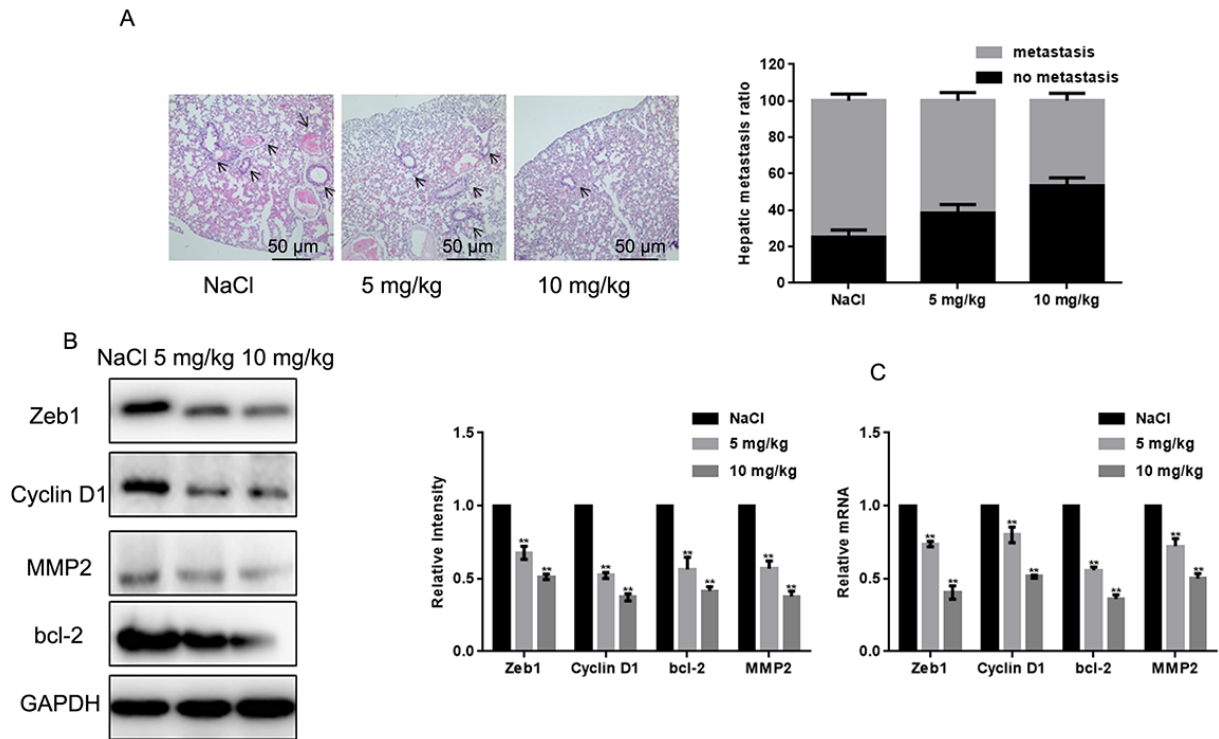


**Figure 5: Naringin inhibits lung invasion by MG63 cells *in vivo*.** (A) Representative images of lung histopathology (H&E staining; 400x) from mice injected with MG63 cells and treated daily with two different doses of naringin or NaCl (control) for 16 days. (B, C) Zeb1, Cyclin D1, bcl-2, and MMP2 expression in liver tumor samples, detected by Western blot (B) and real-time PCR (C). \*\* $P < 0.05$ , compared with NaCl-treated controls.

tumor types, including osteosarcoma and lung cancer [25-27]. We first confirmed high Zeb1 expression in human specimens and in human MG63 and U2OS osteosarcoma cell lines. In these cells, naringin dose-dependently inhibited the expression of Zeb1, reduced proliferation by arresting the cell cycle in the G1 phase, and promoted apoptosis. In contrast, naringin had weaker effects on normal osteoblasts. The induction of apoptosis by naringin correlated with a decrease in anti-apoptotic bcl-2 protein expression; the latter was also observed in a study evaluating naringin's effects in an ovarian cancer mouse model [12]. Naringin-mediated apoptosis has been documented in cervical cancer cells, in two studies that implicated NF- $\kappa$ B/COX-2-caspase-1 pathway repression [9] and expression of caspases, p53, Bax, and Fas death receptor [28] respectively.

Our results also showed that both naringin exposure and Zeb1 silencing significantly suppressed osteosarcoma cell migration in Transwell assays. This is consistent with the down-regulation of MMP2, observed under both conditions, and the stimulation of MMP2 expression seen instead after ectopic expression of Zeb1 in these cells. These effects may be related to a well-known role of Zeb1 in promoting metastasis through

epithelial-to-mesenchymal transition (EMT), although more research is needed to clarify the mechanisms at play in osteosarcoma [29].

Importantly, we demonstrated that naringin's effects *in vitro* correlated with antimetastatic actions *in vivo*, as its administration to nude mice injected with osteosarcoma MG63 cells attenuated the formation of tumor nodules in the liver. In summary, our data showed that naringin inhibits the malignant phenotype of osteosarcoma cells by inhibiting the expression of Zeb1 and Zeb1-associated proteins such as Cyclin D1 and MMP2. The present findings support the potential of naringin as a novel therapeutic strategy for osteosarcoma.

## MATERIALS AND METHODS

### Drugs and reagents

Naringin, 3-(4,5-dimethyl-2-thiazolyl)-2,5-diphenyl-2-H-tetrazolium bromide (MTT), propidium iodide (PI), and Trypan Blue were purchased from Beyotime Biotechnology (Shanghai, China). Fetal bovine serum (FBS), Dulbecco's modified Eagle's medium (DMEM), Lipofectamine 2000, and TRIzol were obtained from

Invitrogen (Carlsbad, CA, USA). RT-PCR kits were obtained from Promega (Beijing, China). SYBR Premix Ex Taq reagents were obtained from TaKaRa (Dalia, China). Anti-Zeb1, anti-cyclin D1, anti-bcl-2, anti-MMP2, and anti-GAPDH antibodies were purchased from Santa Cruz Biotechnology (Dallas, TX, USA). HRP-conjugated secondary antibody, BCA protein assay kit, and enhanced chemiluminescence (ECL) solution were purchased from Beyotime Biotechnology. All experiments were completed in the Central Laboratory of our hospital.

## Human samples

Tissue samples were obtained from patients undergoing surgery at Shengjing Hospital of China Medical University (Table 1). The original histopathologic reports were obtained from each case, and the diagnosis of osteosarcoma was confirmed. Part of the excised tissue was embedded in paraffin, and part of the sample was snap-frozen at  $-80^{\circ}\text{C}$ . Clinical samples were collected after written informed consent was obtained, and the study was approved by the Ethics Committee at the Academic Medical Center of Shengjing Hospital of China Medical University.

**Table 1. Patient information.**

Group		N	Percent
Sex	Male	13	65%
	Female	7	35%
Age	<20	12	60%
	>20	8	40%
History	Yes	1	5%
	No	19	95%
Site of primary disease	Tibia	11	55%
	Femur	7	35%
	Humerus	2	10%
TNM	I	9	45%
	II	7	35%
	III	5	25%

## Cell culture

Human osteosarcoma MG63 and U2OS cells, and human hFOB1.19 osteoblasts (SV40-transfected), used as control, were supplied by the Cell Pool Bank of China (Guangzhou, China). The cells were cultured in DMEM supplemented with 10% FBS at  $37^{\circ}\text{C}$  under an atmosphere of 5%  $\text{CO}_2$  and 95% air.

## Cell viability assay

The MTT assay was employed to assess cell viability. Cells were cultured in 96-well plates at a concentration of  $1 \times 10^4$  cells/ml and incubated with 10 or 20  $\mu\text{mol/L}$  naringin for 12, 24, 36, or 48h. At those time intervals,

0.01 ml of MTT solution (5 mg/ml) was added to each well. After a 4 h incubation at  $37^{\circ}\text{C}$ , medium was replaced by 0.15 ml DMSO. After 15 min incubation at  $37^{\circ}\text{C}$ , optical densities (490 nm) were measured.

## Cell cycle assay

Cells were incubated with 10 or 20  $\mu\text{mol/L}$  naringin for 24 h and fixed in 75% ethanol at  $4^{\circ}\text{C}$  overnight. After resuspension in 10  $\mu\text{g/ml}$  PI, cell cycle stages were determined using a FACS Vantage flow cytometer using CellQuest (Becton Dickinson and Co., San Jose, CA, USA).

## Apoptosis assay

Cells were incubated with 10 or 20  $\mu\text{mol/L}$  naringin for 24 h, washed twice with cold PBS, and stained with 5  $\mu\text{l}$  ANNEXIN-V-FITC/10  $\mu\text{l}$  PI for 15 min. After addition of 400  $\mu\text{l}$  binding buffer to each tube, the apoptosis rate was measured by flow cytometry within 1 h.

## Transwell migration assay

Transwell assays were performed using a modified Boyden chamber with Nuclepore polycarbonate membranes. After 24 h treatment with 10 or 20  $\mu\text{mol/L}$  naringin,  $1 \times 10^5$  cells in 100  $\mu\text{l}$  FBS-free DMEM were placed in the upper part of the chamber with or without Matrigel, whereas the lower compartment was filled with 600  $\mu\text{l}$  DMEM containing 10% FBS. After 8 h incubation at  $37^{\circ}\text{C}$ , the invading cells on the lower surface of the filter were fixed, stained with Trypan Blue, and counted under high-power magnification ( $400\times$ ).

## Zymography

Cells were cultured in 12-well plates and treated with 10 or 20  $\mu\text{mol/L}$  naringin. After 24 h, media was changed into DMEM containing 5% FBS (the source of proMMP2). After another 24 h, the media were harvested, cleared by centrifugation at 12,000 rpm for 10 min, and subjected to analysis by SDS-PAGE impregnated with 1 mg/ml gelatin. The gels were incubated at  $37^{\circ}\text{C}$  overnight, stained with Coomassie Blue, destained, and then scanned.

## Transfection

To stably overexpress and silence Zeb1, cells were transfected with a pcDNA3.1 vector encoding Zeb1, and with a Zeb1-targeted siRNA, respectively (Shanghai GeneChem Company, Shanghai, China). An empty pcDNA3.1 vector and a non-targeted siRNA were transfected as respective controls, and cells were



**Table 2: Primers for RT-PCR.**

Name	Forward primer (5'→3')	Reverse primer (5'→3')
Zeb1 (NM_001323643.1)	GCACAACCAAGTGCAGAAG	CATTTGCAGATTGAGGCTG
Cyclin D1 (NM_053056.2)	CCGAGGAGCTGCTGCAAATGGAGCT	TGAAATCGTGCGGGGTCATTGCGGC
MMP2 (NM_004530.5)	CGCATCTGGGGCTTTAAACAT	TCAGCACAAACAGGTTGCAG
GAPDH (NM_002046.6)	GAAGGCTGGGGCTCATTTG	AGGGGCCATCCACAGTCTTC

selected with puromycin (1.5 µg/mL). Lipofectamine 2000 was used for cell transfection according to the manufacturer's protocols. We extracted protein and total RNA at 24 h after transfection.

### Real-time PCR

Total RNA was extracted after the indicated treatments (24 h) using TRIzol according to the manufacturer's protocol. Cells or tissues were lysed by 0.2 mL chloroform and centrifuged (12,000 × g at 4°C for 15 min). The supernatant was then treated with 0.5 mL isopropanol and centrifuged (12,000 × g at 4°C for 10 min). The RNA pellet was dissolved in 1 mL 75% ethanol, centrifuged (7,500 × g at 4°C for 5 min), and the supernatant discarded. After resuspension in DEPC water, 1 µg of RNA was reverse transcribed to cDNA using a RT-PCR kit. Real-time PCR was performed using an Mx 3000P real-time PCR system (Applied Biosystems, Shanghai, China) and SYBR Premix Ex Taq as a DNA-specific fluorescent dye. PCR was carried out for 40 cycles of 95°C for 10 s and 60°C for 30 s. Primer sequences for detection of mRNA expression were synthesized (Table 2). All the reactions were repeated at least three times. Gene expression levels were calculated relative to the housekeeping gene GAPDH using Stratagene Mx 3000P software.

### Western blot

Tissues (homogenized by grinding) and treated cells were lysed with lysis solution at 4°C for 30 min, followed by centrifugation (12,000 × g at 4°C for 15 min). From each sample, 20 µg of protein was fractionated by 10% sodium dodecyl sulphate-polyacrylamide gel electrophoresis (SDS-PAGE) and transferred onto polyvinylidene difluoride (PVDF) membranes (Amersham, Beijing, China). After blocking with 5% nonfat dry milk in TBST for 1 h at room temperature, proteins were probed with specific antibodies against Zeb1, Cyclin D1, or MMP2. To assure equal loading, gels were stripped and reprobed

with an anti-GAPDH antibody. Following incubation with HRP-conjugated secondary antibodies, signals were detected by chemiluminescence. All the reactions were repeated at least three times.

### *In vivo* experiments

Five- to six-week-old female, athymic nude BALB/c mice (Vital River Laboratory Animal Technology Co. Ltd., Shanghai, China) were split into three groups of six and received tail vein injections containing 2×10<sup>6</sup> MG63 cells in 0.1 ml saline. The following day, and once a day thereafter, the mice were given intravenous injections of naringin (5 or 10 mg/kg) or 0.9% NaCl (control). On day 16 following tumor cell injection, liver samples were collected for histological examination.

All experimental procedures involving animals were conducted in accordance with the Guide for the Care and Use of Laboratory Animals (NIH publication no. 80-23, revised 1996) and followed institutional ethical guidelines. The study was approved by the Ethics Committee at the Academic Medical Center of Shengjing Hospital of China Medical University.

### Histopathology

Lung specimens were fixed with 4% paraformaldehyde. Serial sections were cut using a microtome and affixed onto positively charged slides. Tissues were deparaffinized and rehydrated through graded xylene and alcohol. The sections were lightly counterstained with hematoxylin–eosin, dehydrated through an ethanol series, cleared in xylene and mounted. Stained sections were viewed using a light microscope (400×).

### Statistical analysis

All data are presented as the mean ± SD. Statistical significance between two groups of data was evaluated by Student's t test (two-tailed) using GraphPad Prism



software (GraphPad, Inc., La Jolla, CA, USA).  $P < 0.05$  was considered significant.

### Ethics statement and consent to participate

Research involving human subjects, human material, or human data has been performed in accordance with the Declaration of Helsinki and was approved by the Research Ethics Committee of Shengjing Hospital (R20160965).

### Compliance with ethical standards

For the use of clinical materials for research purposes, written consent and approval from patients were obtained from the Shengjing Hospital of China Medical University. Patient consent was obtained in writing according to institutional regulations.

### Consent to publish

We have obtained consent to publish from the participants to report individual patient data.

## AUTHOR CONTRIBUTIONS

Ming He: conceived of the study and carried out molecular studies. Qiu Chuang: carried out molecular studies. Wang Jiashi: participated in the design of the study and performed statistical analysis. Li Bin: participated in the study design and coordination and helped to draft the manuscript. Wang Guangbin: conceived the study. Ji Xianglu: helped to draft the manuscript.

## ACKNOWLEDGMENTS

All personnel who have contributed to this article are in the list of authors.

## CONFLICTS OF INTEREST

The authors declare no conflicts of interest.

## REFERENCES

1. Degnan AJ, Chung CY, Shah AJ. Quantitative diffusion-weighted magnetic resonance imaging assessment of chemotherapy treatment response of pediatric osteosarcoma and Ewing sarcoma malignant bone tumors. *Clin Imaging*. 2018; 47:9–13. <https://doi.org/10.1016/j.clinimag.2017.08.003>
2. Shi J, Fu Q, Yang P, Liu H, Ji L, Wang K. Downregulation of microRNA-15a-3p is correlated with clinical outcome and negatively regulates cancer proliferation and migration in human osteosarcoma. *J Cell Biochem*. 2018; 119:1215–22. <https://doi.org/10.1002/jcb.26294>
3. Davis JC, Daw NC, Navid F, Billups CA, Wu J, Bahrami A, Jenkins JJ, Snyder SE, Reddick WE, Santana VM, McCarville MB, Guo J, Shulkin BL. (18)F-FDG uptake during early adjuvant chemotherapy predicts histologic response in pediatric and young adult patients with osteosarcoma. *J Nucl Med*. 2018; 59:25–30. <https://doi.org/10.2967/jnumed.117.190595>
4. Raha S, Yumnam S, Hong GE, Lee HJ, Saralamma VV, Park HS, Heo JD, Lee SJ, Kim EH, Kim JA, Kim GS. Naringin induces autophagy-mediated growth inhibition by downregulating the PI3K/Akt/mTOR cascade via activation of MAPK pathways in AGS cancer cells. *Int J Oncol*. 2015; 47:1061–69. <https://doi.org/10.3892/ijo.2015.3095>
5. Yin FM, Xiao LB, Zhang Y. [Research progress on *Drynaria fortunei* naringin on inflammation and bone activity]. *Zhongguo Gu Shang*. 2015; 28:182–86.
6. Chen R, Qi QL, Wang MT, Li QY. Therapeutic potential of naringin: an overview. *Pharm Biol*. 2016; 54:3203–10. <https://doi.org/10.1080/13880209.2016.1216131>
7. Wang D, Ma W, Wang F, Dong J, Wang D, Sun B, Wang B. Stimulation of Wnt/ $\beta$ -Catenin Signaling to Improve Bone Development by Naringin via Interacting with AMPK and Akt. *Cell Physiol Biochem*. 2015; 36:1563–76. <https://doi.org/10.1159/000430319>
8. Ang ES, Yang X, Chen H, Liu Q, Zheng MH, Xu J. Naringin abrogates osteoclastogenesis and bone resorption via the inhibition of RANKL-induced NF- $\kappa$ B and ERK activation. *FEBS Lett*. 2011; 585:2755–62. <https://doi.org/10.1016/j.febslet.2011.07.046>
9. Zeng L, Zhen Y, Chen Y, Zou L, Zhang Y, Hu F, Feng J, Shen J, Wei B. Naringin inhibits growth and induces apoptosis by a mechanism dependent on reduced activation of NF  $\kappa$ B/COX 2 caspase-1 pathway in HeLa cervical cancer cells. *Int J Oncol*. 2014; 45:1929–36. <https://doi.org/10.3892/ijo.2014.2617>
10. Kawaguchi K, Kikuchi S, Hasegawa H, Maruyama H, Morita H, Kumazawa Y. Suppression of lipopolysaccharide-induced tumor necrosis factor-release and liver injury in mice by naringin. *Eur J Pharmacol*. 1999; 368:245–50. [https://doi.org/10.1016/S0014-2999\(98\)00867-X](https://doi.org/10.1016/S0014-2999(98)00867-X)
11. Guo B, Zhang Y, Hui Q, Wang H, Tao K. Naringin suppresses the metabolism of A375 cells by inhibiting the phosphorylation of c-Src. *Tumour Biol*.

- 2016; 37:3841–50. <https://doi.org/10.1007/s13277-015-4235-z>
12. Cai L, Wu H, Tu C, Wen X, Zhou B. Naringin inhibits ovarian tumor growth by promoting apoptosis: An in vivo study. *Oncol Lett*. 2018; 16:59–64.
13. Aigner K, Dampier B, Descovich L, Mikula M, Sultan A, Schreiber M, Mikulits W, Brabletz T, Strand D, Obrist P, Sommergruber W, Schweifer N, Wernitznig A, et al. The transcription factor ZEB1 (deltaEF1) promotes tumour cell dedifferentiation by repressing master regulators of epithelial polarity. *Oncogene*. 2007; 26:6979–88. <https://doi.org/10.1038/sj.onc.1210508>
14. Browne G, Sayan AE, Tulchinsky E. ZEB proteins link cell motility with cell cycle control and cell survival in cancer. *Cell Cycle*. 2010; 9:886–91. <https://doi.org/10.4161/cc.9.5.10839>
15. Caramel J, Ligier M, Puisieux A. Pleiotropic Roles for ZEB1 in Cancer. *Cancer Res*. 2018; 78:30–35. <https://doi.org/10.1158/0008-5472.CAN-17-2476>
16. Wang M, He SF, Liu LL, Sun XX, Yang F, Ge Q, Wong WK, Meng JY. Potential role of ZEB1 as a DNA repair regulator in colorectal cancer cells revealed by cancer-associated promoter profiling. *Oncol Rep*. 2017; 38:1941–48. <https://doi.org/10.3892/or.2017.5888>
17. Hanrahan K, O'Neill A, Principe M, Bugler J, Murphy L, Fabre A, Puhr M, Culig Z, Murphy K, Watson RW. The role of epithelial-mesenchymal transition drivers ZEB1 and ZEB2 in mediating docetaxel-resistant prostate cancer. *Mol Oncol*. 2017; 11:251–65. <https://doi.org/10.1002/1878-0261.12030>
18. Bae GY, Choi SJ, Lee JS, Jo J, Lee J, Kim J, Cha HJ. Loss of E-cadherin activates EGFR-MEK/ERK signaling, which promotes invasion via the ZEB1/MMP2 axis in non-small cell lung cancer. *Oncotarget*. 2013; 4:2512–22. <https://doi.org/10.18632/oncotarget.1463>
19. Shan Y, Zhang L, Bao Y, Li B, He C, Gao M, Feng X, Xu W, Zhang X, Wang S. Epithelial-mesenchymal transition, a novel target of sulforaphane via COX-2/MMP2, 9/Snail, ZEB1 and miR-200c/ZEB1 pathways in human bladder cancer cells. *J Nutr Biochem*. 2013; 24:1062–69. <https://doi.org/10.1016/j.jnutbio.2012.08.004>
20. Wang H, Xing D, Ren D, Feng W, Chen Y, Zhao Z, Xiao Z, Peng Z. MicroRNA 643 regulates the expression of ZEB1 and inhibits tumorigenesis in osteosarcoma. *Mol Med Rep*. 2017; 16:5157–64. <https://doi.org/10.3892/mmr.2017.7273>
21. Yi L, Liu M, Tang Z. MicroRNA 130a inhibits growth and metastasis of osteosarcoma cells by directly targeting ZEB1. *Mol Med Rep*. 2017; 16:3606–12. <https://doi.org/10.3892/mmr.2017.6968>
22. Li H, Yang B, Huang J, Xiang T, Yin X, Wan J, Luo F, Zhang L, Li H, Ren G. Naringin inhibits growth potential of human triple-negative breast cancer cells by targeting  $\beta$ -catenin signaling pathway. *Toxicol Lett*. 2013; 220:219–28. <https://doi.org/10.1016/j.toxlet.2013.05.006>
23. Wang H, Li C, Li J, Zhu Y, Jia Y, Zhang Y, Zhang X, Li W, Cui L, Li W, Liu Y. Naringin enhances osteogenic differentiation through the activation of ERK signaling in human bone marrow mesenchymal stem cells. *Iran J Basic Med Sci*. 2017; 20:408–14.
24. Wong RW, Rabie AB. Effect of naringin on bone cells. *J Orthop Res*. 2006; 24:2045–50. <https://doi.org/10.1002/jor.20279>
25. Zhang X, Zhang Z, Zhang Q, Zhang Q, Sun P, Xiang R, Ren G, Yang S. ZEB1 confers chemotherapeutic resistance to breast cancer by activating ATM. *Cell Death Dis*. 2018; 9:57. <https://doi.org/10.1038/s41419-017-0087-3>
26. Yu P, Shen X, Yang W, Zhang Y, Liu C, Huang T. ZEB1 stimulates breast cancer growth by up-regulating hTERT expression. *Biochem Biophys Res Commun*. 2018; 495:2505–11. <https://doi.org/10.1016/j.bbrc.2017.12.139>
27. Langer EM, Kendsersky ND, Daniel CJ, Kuziel GM, Pelz C, Murphy KM, Capecchi MR, Sears RC. ZEB1-repressed microRNAs inhibit autocrine signaling that promotes vascular mimicry of breast cancer cells. *Oncogene*. 2018; 37:1005–19. <https://doi.org/10.1038/onc.2017.356>
28. Ramesh E, Alshatwi AA. Naringin induces death receptor and mitochondria-mediated apoptosis in human cervical cancer (SiHa) cells. *Food Chem Toxicol*. 2013; 51:97–105. <https://doi.org/10.1016/j.fct.2012.07.033>
29. Liu Y, El-Naggar S, Darling DS, Higashi Y, Dean DC. Zeb1 links epithelial-mesenchymal transition and cellular senescence. *Development*. 2008; 135:579–88. <https://doi.org/10.1242/dev.007047>

# Long noncoding RNA B3GALT5-AS1 suppresses colon cancer liver metastasis via repressing microRNA-203

Liang Wang<sup>1,\*</sup>, Zhewei Wei<sup>1,\*</sup>, Kaiming Wu<sup>1</sup>, Weigang Dai<sup>1</sup>, Changhua Zhang<sup>1</sup>, Jianjun Peng<sup>1</sup>, Yulong He<sup>1</sup>

<sup>1</sup>Department of Gastrointestinal Surgery, The First Affiliated Hospital, Sun Yat-sen University, Guangzhou 510080, China

\*Equal contribution

**Correspondence to:** Yulong He; email: [yulong\\_he123@163.com](mailto:yulong_he123@163.com)

**Keywords:** long noncoding RNA, colon cancer, liver metastasis, microRNA, epithelial-to-mesenchymal transition

**Received:** August 28, 2018

**Accepted:** October 27, 2018

**Published:** December 10, 2018

**Copyright:** Wang et al. This is an open-access article distributed under the terms of the Creative Commons Attribution License (CC BY 3.0), which permits unrestricted use, distribution, and reproduction in any medium, provided the original author and source are credited.

## ABSTRACT

Long noncoding RNAs (lncRNAs) are implicated in various cancers, including colon cancer. Liver metastasis is the main cause of colon cancer-related death. However, the roles of lncRNAs in colon cancer liver metastasis are still largely unclear. In this study, we identified a novel lncRNA B3GALT5-AS1, which is reduced in colon cancer tissues and further reduced in colon cancer liver metastasis tissues. Reduced expression of B3GALT5-AS1 is associated with liver metastasis and poor outcome of colon cancer patients. Gain-of-function and loss-of-function assays revealed that B3GALT5-AS1 inhibited proliferation but promoted migration and invasion of colon cancer cells. Further investigation revealed that B3GALT5-AS1 directly bound to the promoter of *miR-203*, repressed *miR-203* expression, upregulated *miR-203* targets ZEB2 and SNAI2, and induced epithelial-to-mesenchymal transition (EMT). *In vivo* study revealed that B3GALT5-AS1 suppressed colon cancer liver metastasis via its binding on *miR-203* promoter and the repression of *miR-203*. *miR-203* is increased and epithelial phenotype is preferred in colon cancer liver metastasis tissues. Collectively, our data revealed the suppressive roles of B3GALT5-AS1/*miR-203*/EMT regulation axis in colon cancer liver metastasis. Our data suggested that the activating B3GALT5-AS1/*miR-203*/EMT axis may be potential therapeutic strategy for colon cancer liver metastasis.

## INTRODUCTION

Colon cancer is one of the most prevalent malignancies and causes of cancer-related deaths worldwide [1]. Distant metastasis, especially liver metastasis accounts for the major cause of deaths of colon cancer patients [2]. Most colon cancer patients with liver metastasis are not suitable for surgery [3]. In addition, there is a lack of effective treatments for colon cancer patients with liver metastasis [4]. Thus, the prognoses of colon cancers with liver metastases are very poor with a 5-year survival rate of 10-15% [5]. Therefore, further revealing critical molecular mechanisms driving colon

cancer liver metastasis and developing more effective therapies for colon cancers with liver metastasis are urgently needed.

Colon cancer liver metastasis is a complex and multistep process [6]. Many molecules are contradictorily involved in this process [7, 8]. The detailed molecular mechanisms mediating the process are largely unclear [9]. Epithelial-to-mesenchymal transition (EMT) plays critical roles during the process of colon liver metastasis [10, 11]. EMT permits the migration and invasion of various tumor cells, which is beneficial for the early invasion of primary cancers

[12]. EMT may also discount proliferative capacity of cancer cells [13]. In the distant metastatic locations, disseminated cancer cells require mesenchymal-to-epithelial transition (MET), a reverse process of EMT, to settle and growth [7]. MET enables metastatic cancer cells to acquire epithelial phenotype and colonize in distant organs [14-16]. Epithelial marker E-cadherin is reported to be elevated in lymph node metastases and distant metastases relative to primary tumors [17]. Therefore, identifying critical EMT-MET regulators during colon cancer liver metastasis cascade are beneficial for appropriate therapy of colon cancer liver metastasis.

Genomic and transcriptomic sequencings have demonstrated that although 70% of human genome transcribe RNA molecules, only about 2% of human genome encode proteins [18]. Therefore, most of human transcriptome are non-coding RNAs [19]. Many of these non-coding RNAs have critical regulatory roles in cancers [20]. Long noncoding RNA (lncRNA) is a class of RNA transcript with limited protein coding ability and greater than 200 nucleotides in length [21]. Accumulating evidences displayed that lncRNAs are commonly deregulated in many pathological states and have important roles during various pathophysiological processes [22-27]. As to colon cancer, several lncRNAs are revealed to regulate colon cancer cells proliferation, apoptosis, migration, invasion, chemoresistance, and so on, such as lncRNA N-BLR, GAS5, HNF1A-AS1, CRNDE, LINC01133 [28-32]. However, the roles of lncRNAs in EMT and liver metastasis of colon cancer are largely unclear.

microRNA (miRNA) is another class of non-coding RNA transcript with 20-25 nucleotides in length [33]. Similarly, miRNAs are reported to have important regulatory roles during various pathophysiological processes [34-38]. Several miRNAs are well-known EMT regulators through repressing EMT-inducing transcription factors [39, 40]. miR-200 family have been reported to inhibit EMT by directly repressing ZEB1 and ZEB2 [39, 41-43]. miR-203 has been reported to inhibit EMT via repressing ZEB2 and SNAI2 [44, 45]. However, miR-203 has different roles in different cancers [40, 46-49]. miR-203 is revealed to exert tumor suppressive roles in prostate, lung, nasopharyngeal, and colorectal cancer [50-52]. However, miR-203 is also revealed to be increased in colorectal cancer tissues compared with adjacent normal mucosa [46]. Furthermore, miR-203 is also revealed to be upregulated in colorectal cancer liver metastasis tissues compared with primary colorectal cancer tissues [46]. Meta-analysis indicated that the upregulation of miR-203 indicted worse prognosis in colorectal cancer [49]. These controversial results suggested that more

investigations of the expression and roles of miR-203 in EMT and liver metastasis of colon cancer are needed.

In this study, using public available RNA-seq dataset of colon cancer [53], we identified that lncRNA B3GALT5-AS1 is reduced in colon cancer tissues, and further reduced in colon cancer liver metastasis tissues. In clinical specimens, we further confirmed the expression pattern of B3GALT5-AS1 in colon cancer and liver metastasis. Furthermore, we confirmed the negative correlation between miR-203 and B3GALT5-AS1 expression pattern in colon cancer liver metastasis. In addition, biological roles of B3GALT5-AS1 and miR-203 in EMT and liver metastasis of colon cancer were explored using gain-of-function and loss-of-function experiments.

## RESULTS

### **B3GALT5-AS1 is reduced in colon cancer and further reduced in liver metastasis tissues**

Analyzing the RNA-seq dataset from GSE50760 which containing 18 normal colonic epithelium, 18 primary colorectal cancers, and 18 metastasized cancers in liver, we noted that lncRNA B3GALT5-AS1 (C21orf88) is reduced in primary colorectal cancers compared with normal colonic epithelium and is further reduced in metastasized cancers in liver (Fig. 1A). To further explore B3GALT5-AS1 expression pattern in human colon cancer, we collected 64 pairs of primary colon cancer tissues and corresponding adjacent colonic epithelium tissues. Through searching the National Center for Biotechnology Information (NCBI), we found two transcript variants of B3GALT5-AS1. qRT-PCR results displayed that transcript variant 2 (NCBI Reference Sequence: NR\_026543.1) is the main transcript of B3GALT5-AS1 in both normal colon tissues and colon cancer tissues (Figure S1). Furthermore, transcript variant 2 is reduced in colon cancer, and while transcript variant 1 doesn't have significant difference between colon cancer and normal colonic epithelium tissues (Figure S1). Therefore, we focused our attention on transcript variant 2 of B3GALT5-AS1.

The expression of B3GALT5-AS1 in 64 pairs of primary colon cancer tissues and corresponding normal colonic epithelium tissues was measured via qRT-PCR. As displayed in Fig. 1B, B3GALT5-AS1 is markedly reduced in primary colon cancer tissues compared with colonic epithelium tissues. Analyses of the association between the expression of B3GALT5-AS1 and clinicopathologic features of colon cancers displayed that lower B3GALT5-AS1 expression is correlated with larger tumor size, distant metastasis, and advanced

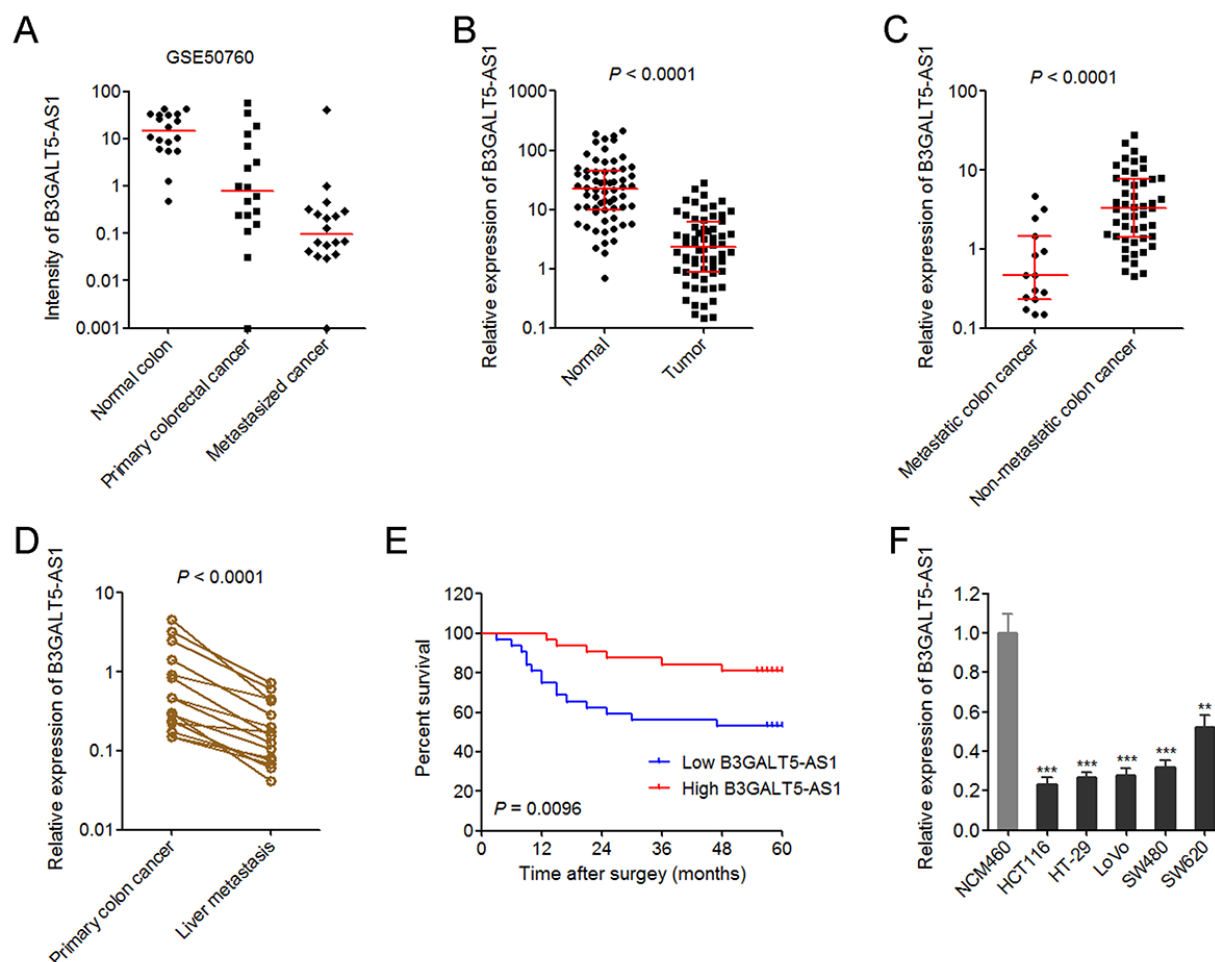


**Figure 1. The expression pattern of B3GALT5-AS1 in colon cancer and its association with prognosis.** (A) The expression intensity of B3GALT5-AS1 in 18 pairs of normal colonic epithelium, primary colorectal cancers, and metastasized cancers in liver from GSE50760. (B) The expression of B3GALT5-AS1 in 64 pairs of primary colon cancer tissues and adjacent colonic epithelium tissues was detected using qRT-PCR.  $P < 0.0001$ , Wilcoxon signed-rank test. (C) The expression of B3GALT5-AS1 in 15 colon cancer tissues with metastasis and 49 colon cancer tissues without metastasis.  $P < 0.0001$ , Mann-Whitney test. (D) The expression of B3GALT5-AS1 in 15 pairs of primary colon cancer tissues and corresponding liver metastasis tissues was measured using qRT-PCR.  $P < 0.0001$ , Wilcoxon signed-rank test. (E) Kaplan-Meier survival analysis of the correlation between B3GALT5-AS1 expression level and overall survival of 64 colon cancer patients. The median expression level of B3GALT5-AS1 was used as cut-off.  $P = 0.0096$ , Log-rank test. (F) The expression of B3GALT5-AS1 in normal colonic epithelial cell line NCM460 and colon cancer cell lines HCT116, HT-29, LoVo, SW480 and SW620 was measured using qRT-PCR. Results are displayed as mean  $\pm$  s.d. of three independent experiments.  $**P < 0.01$ ,  $***P < 0.001$ , Student's *t*-test.

AJCC stages (Table 1). To confirm the association between B3GALT5-AS1 expression and distant metastasis, we re-analyzed the expression of B3GALT5-AS1 in colon cancer tissues with ( $n = 15$ ) or without ( $n = 49$ ) metastasis. The results displayed that B3GALT5-AS1 is significantly reduced in primary colon cancer tissues with metastasis compared with that without metastasis (Fig. 1C). For these 15 colon cancers with metastasis, we collected their corresponding liver metastasis tissues. The expression of B3GALT5-AS1 in these 15 pairs of primary colon cancer tissues and corresponding liver metastasis tissues was measured via

qRT-PCR. As displayed in Fig. 1D, B3GALT5-AS1 is markedly reduced in liver metastasis tissues compared with primary colon cancer tissues. Kaplan-Meier survival analysis of these 64 colon cancer patients displayed that colon cancer patients with lower B3GALT5-AS1 expression had worse survival than those with higher B3GALT5-AS1 expression (Fig. 1E). Moreover, the expression of B3GALT5-AS1 in normal colonic epithelial cell line NCM460 and colon cancer cell lines HCT116, HT-29, LoVo, SW480 and SW620 was measured by qRT-PCR. As displayed in Fig. 1F, B3GALT5-AS1 was also significantly reduced in colon



**Table 1. Correlation between B3GALT5-AS1 expression and clinicopathologic features of colon cancers.**

Features	N of cases	B3GALT5-AS1		<i>P</i> -value
		Low	High	
Total	64	32	32	0.316
Age (years)				
>65	34	19	15	
≤65	30	13	17	0.802
Gender				
Male	31	15	16	
Female	33	17	16	0.802
Location				
Right	35	17	18	<b>0.002</b>
Left	29	15	14	
Tumor size (cm)				
>3	36	24	12	0.757
≤3	28	8	20	
Depth of invasion				
T1	2	1	1	0.523
T2	9	6	3	
T3	25	12	13	
T4	28	13	15	<b>0.008</b>
Lymph node metastasis				
N0	25	12	13	
N1	22	13	9	<b>0.043</b>
N2	17	7	10	
Distant metastasis				
M0	49	20	29	
M1	15	12	3	
AJCC stage				
I	8	4	4	
II	17	8	9	
III	24	8	16	
IV	15	12	3	

The median expression level of B3GALT5-AS1 was used as cut-off.

*P*-value was acquired by Pearson chi-square tests.

cancer cell lines compared with normal colonic epithelial cell line. These data suggested that B3GALT5-AS1 is reduced in colon cancer and further reduced in liver metastasis tissues. Low expression of B3GALT5-AS1 indicates poor outcome of colon cancers.

### **B3GALT5-AS1 suppresses colon cancer cell proliferation**

To explore the effects of B3GALT5-AS1, we stably overexpressed B3GALT5-AS1 in HCT116 cells by transfecting B3GALT5-AS1 overexpression plasmid (Fig. 2A), and stably knocked-down B3GALT5-AS1 in SW620 cells by transfecting two independent shRNAs against B3GALT5-AS1 (Fig. 2B). Glo cell viability assays displayed that B3GALT5-AS1 overexpression markedly reduced cell viability, and while B3GALT5-

AS1 knockdown significantly upregulated cell viability of colon cancer cells (Fig. 2C, D). EdU incorporation assays further displayed that enhanced expression of B3GALT5-AS1 markedly suppressed cell proliferation, and while B3GALT5-AS1 knockdown markedly promoted proliferation of colon cancer cells (Fig. 2E, F). Due to B3GALT5-AS1 is highly expressed in normal colonic epithelial cell line NCM460, we further determined the effects of B3GALT5-AS1 knockdown on NCM460 cell viability and cell proliferation using Glo cell viability assay and EdU incorporation assay. As displayed in Figure S2A-C, transient knockdown of B3GALT5-AS1 also promoted NCM460 cell proliferation. Collectively, these data suggested that B3GALT5-AS1 suppresses cell viability and cell proliferation of colon cancer and colonic epithelial cells.

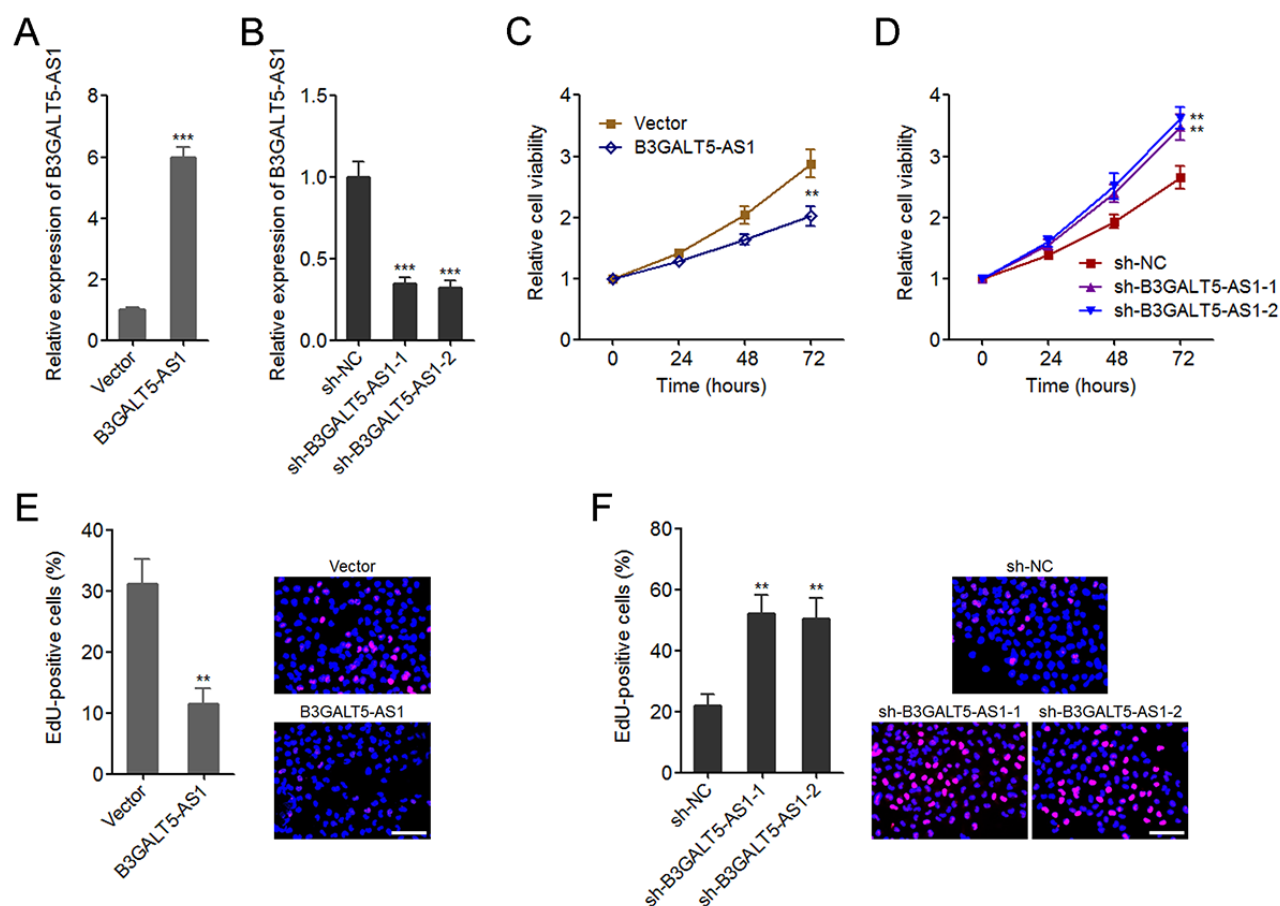


**Figure 2. B3GALT5-AS1 suppressed colon cancer cell proliferation.** (A) The expression of B3GALT5-AS1 in B3GALT5-AS1 stably overexpressed and control HCT116 cells was detected using qRT-PCR. (B) The expression of B3GALT5-AS1 in B3GALT5-AS1 stably depleted and control SW620 cells was detected using qRT-PCR. (C) Cell viability of B3GALT5-AS1 stably overexpressed and control HCT116 cells was detected using Glo cell viability assay. (D) Cell viability of B3GALT5-AS1 stably depleted and control SW620 cells was detected using Glo cell viability assay. (E) Cell proliferation of B3GALT5-AS1 stably overexpressed and control HCT116 cells was detected using EdU incorporation assay. The red color indicates EdU-positive cells. Scale bars = 100  $\mu$ m. (F) Cell proliferation of B3GALT5-AS1 stably depleted and control SW620 cells was detected using EdU incorporation assay. The red color indicates EdU-positive cells. Scale bars = 100  $\mu$ m. Results are displayed as mean  $\pm$  s.d. of three independent experiments. \*\* $P$  < 0.01, \*\*\* $P$  < 0.001, Student's  $t$ -test.

## B3GALT5-AS1 promotes colon cancer cell migration, invasion and EMT

We then further explored the roles of B3GALT5-AS1 in migration and invasion of colon cancer cells. Transwell migration assays displayed that B3GALT5-AS1 overexpression promoted cell migration, and while B3GALT5-AS1 knockdown inhibited cell migration of colon cancer cells (Fig. 3A, B). Transwell invasion assays displayed that enhanced expression of B3GALT5-AS1 promoted invasion, and while B3GALT5-AS1 knockdown repressed invasion of colon cancer cells (Fig. 3C, D). Similarly, B3GALT5-AS1 knockdown also repressed migration and invasion of NCM460 cells (Figure S2D, E). The opposing effects of B3GALT5-AS1 on cell proliferation and migration,

invasion implied that EMT may mediate the roles of B3GALT5-AS1 in colon cancer. Thus, we further explored the roles of B3GALT5-AS1 in EMT of colon cancer cells. The results displayed that B3GALT5-AS1 overexpression reduced the expression of epithelial marker E-cadherin and increased mesenchymal marker N-cadherin (Fig. 3E, F), suggesting that B3GALT5-AS1 overexpression induced EMT of colon cancer cells. B3GALT5-AS1 knockdown upregulated the expression of E-cadherin and downregulated N-cadherin (Fig. 3G, H), suggesting that B3GALT5-AS1 knockdown repressed EMT of colon cancer cells. Similarly, B3GALT5-AS1 knockdown also repressed EMT of NCM460 cells (Figure S2F). These data demonstrated that B3GALT5-AS1 promotes migration, invasion and EMT of colon cancer and colonic epithelial cells.

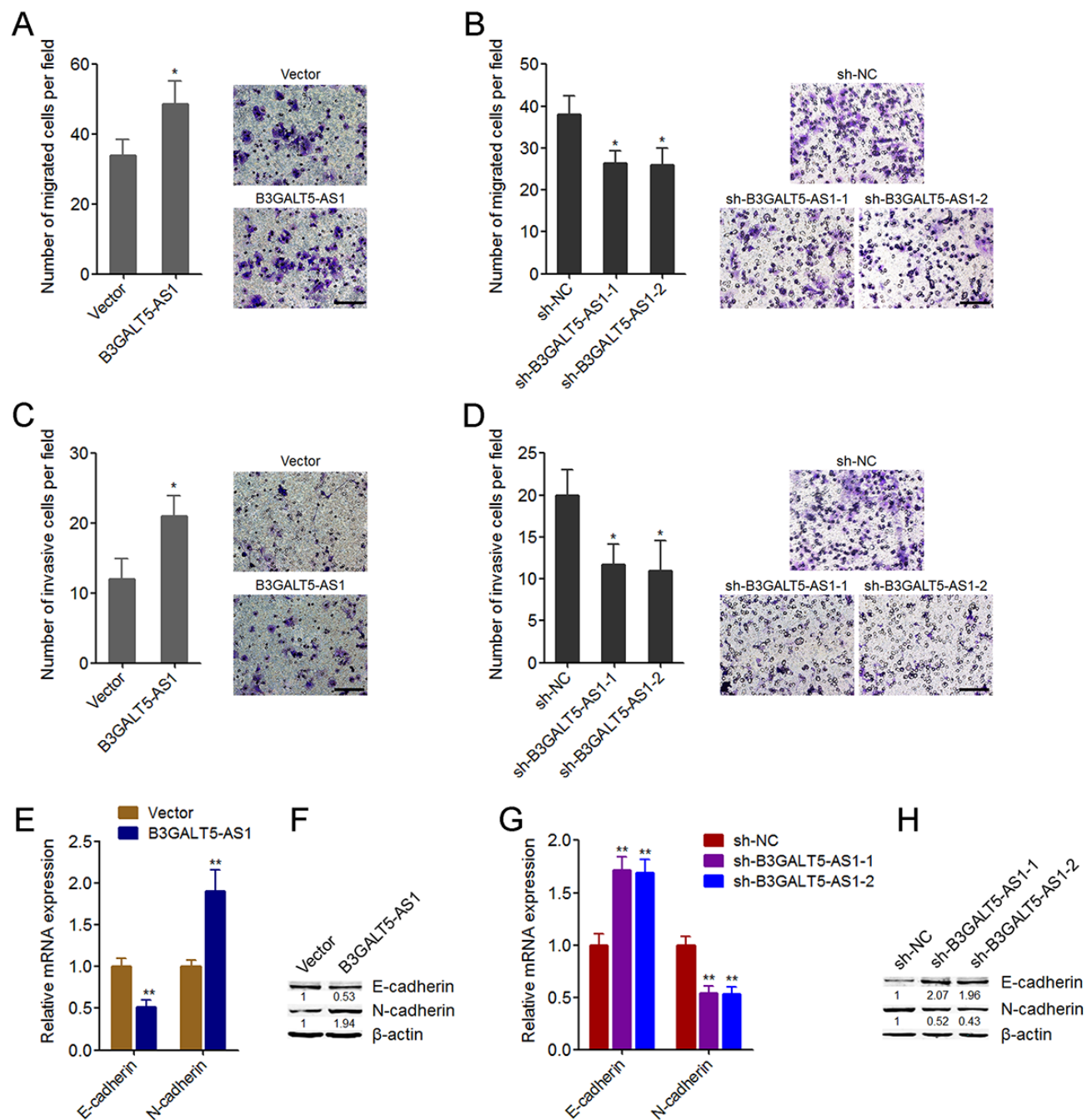


**Figure 3. B3GALT5-AS1 promoted migration, invasion, and EMT of colon cancer cells.** (A) Cell migration of B3GALT5-AS1 stably overexpressed and control HCT116 cells was detected using transwell migration assay. Scale bars = 100  $\mu$ m. (B) Cell migration of B3GALT5-AS1 stably depleted and control SW620 cells was detected using transwell migration assay. Scale bars = 100  $\mu$ m. (C) Cell invasion of B3GALT5-AS1 stably overexpressed and control HCT116 cells was detected using transwell invasion assay. Scale bars = 100  $\mu$ m. (D) Cell invasion of B3GALT5-AS1 stably depleted and control SW620 cells was detected using transwell invasion assay. Scale bars = 100  $\mu$ m. (E) E-cadherin and N-cadherin mRNA levels in B3GALT5-AS1 stably overexpressed and control HCT116 cells were detected using qRT-PCR. (F) E-cadherin and N-cadherin protein levels in B3GALT5-AS1 stably overexpressed and control HCT116 cells were detected using western blot. (G) E-cadherin and N-cadherin mRNA levels in B3GALT5-AS1 stably depleted and control SW620 cells were detected using qRT-PCR. (H) E-cadherin and N-cadherin protein levels in B3GALT5-AS1 stably depleted and control SW620 cells were detected using western blot. Results are displayed as mean  $\pm$  s.d. of three independent experiments. \* $P$  < 0.05, \*\* $P$  < 0.01, Student's  $t$ -test.

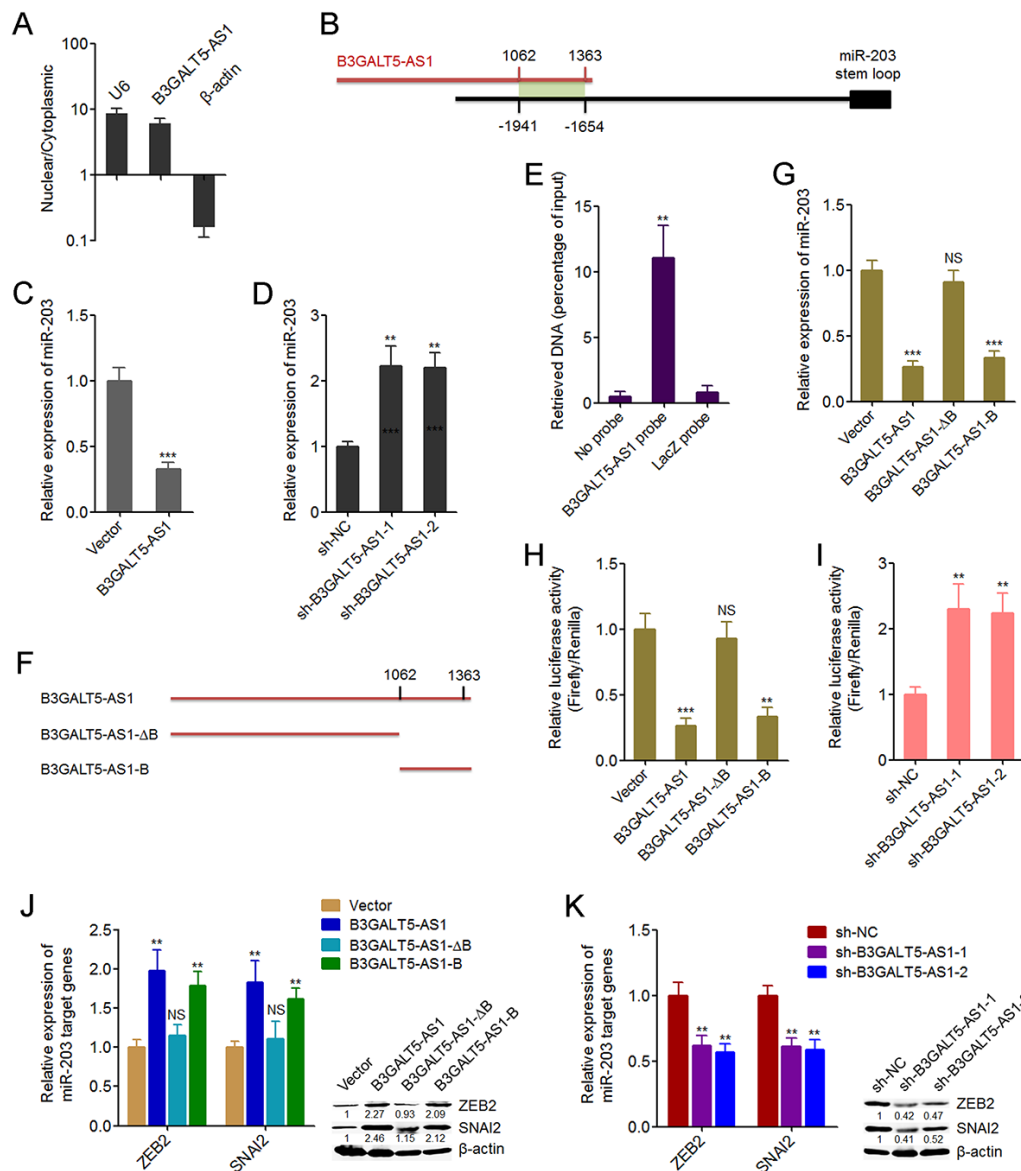


**Figure 4. B3GALT5-AS1 bound to the promoter of *miR-203* and repressed the expression of *miR-203*.** (A) The subcellular distribution of B3GALT5-AS1 in the cytoplasmic and nuclear fractions of HCT116 cells was evaluated using cytoplasmic and nuclear RNA isolation followed by qRT-PCR. β-actin and U6 were used as cytoplasmic and nuclear controls, respectively. (B) Schematic outline of the predicted interaction sites between B3GALT5-AS1 and the promoter of *miR-203*. (C) The expression of *miR-203* in B3GALT5-AS1 stably overexpressed and control HCT116 cells was detected using qRT-PCR. (D) The expression of *miR-203* in B3GALT5-AS1 stably depleted and control SW620 cells was detected using qRT-PCR. (E) ChIP assays in HCT116 cells were carried out with anti-sense probe sets specific for B3GALT5-AS1 or LacZ (negative control). The enriched DNA was measured using qRT-PCR with specific primers against *miR-203* promoter. (F) Schematic outline of the constructed different depletion transcripts of B3GALT5-AS1. (G) After transient transfections of the different B3GALT5-AS1 expressing plasmids into HCT116 cells, *miR-203* expression was measured using qRT-PCR. (H) After transient co-transfection of the firefly luciferase reporter containing the promoter of *miR-203*, renilla luciferase expression plasmid pRL-TK, and the different B3GALT5-AS1 expression plasmids into HCT116 cells, luciferase activities were detected using dual luciferase reporter assays. Results are displayed as the relative ratio of firefly luciferase activity to renilla luciferase activity. (I) After transient co-transfection of the firefly luciferase reporter containing the promoter of *miR-203* and pRL-TK into B3GALT5-AS1 stably depleted and control SW620 cells, luciferase activities were measured by dual luciferase reporter assays. Results are shown as the relative ratio of firefly luciferase activity to renilla luciferase activity. (J) After transient transfections of the different B3GALT5-AS1 expressing plasmids into HCT116 cells, the expression of ZEB2 and SNAI2 was detected using qRT-PCR and western blot. (K) The expression of ZEB2 and SNAI2 in B3GALT5-AS1 stably depleted and control SW620 cells was detected using qRT-PCR and western blot. Data are displayed as mean ± s.d. of three independent experiments. \*\* $P < 0.01$ , \*\*\* $P < 0.001$ , NS, not significant, Student's  $t$ -test.

### **B3GALT5-AS1 directly binds the promoter of *miR-203* and represses the expression of *miR-203***

To investigate the underpinning mechanism mediating the roles of B3GALT5-AS1 in colon cancer, we first confirmed the subcellular distribution of B3GALT5-AS1 in colon cancer cells using cytoplasmic and nuclear RNA purification. As displayed in Fig. 4A, B3GALT5-AS1 was dominantly localized in the nucleus. Several miRNAs are reported to be involved in EMT [11]. *miR-203*, *miR-200* family (including *miR-200a*, *miR-200b*, *miR-200c*, *miR-141*, *miR-429*), *miR-34a*, *miR-9* are reported to inhibit EMT [11, 44]. *miR-29a* is reported to promote EMT. Therefore, we predicted the potential roles of B3GALT5-AS1 on these miRNAs via searching the potential binding sites of B3GALT5-AS1 on the promoters of these miRNAs using Basic Local Alignment Search Tool (BLAST) (<https://blast.ncbi.nlm.nih.gov/Blast.cgi>). As displayed in Figure S3, the promoter of *miR-203* has the strongest binding potential with B3GALT5-AS1. The predicted interaction region covers 1062-1363 nucleotides of B3GALT5-AS1 (Fig. 4B). Then, we investigated whether B3GALT5-AS1 regulates *miR-203* expression in colon cancer cells. qRT-PCR results displayed that B3GALT5-AS1 overexpression significantly suppressed *miR-203* expression, and while depletion of B3GALT5-AS1 markedly upregulated *miR-203* expression (Fig. 4C, D). ChIRP assays displayed that *miR-203* promoter was specifically enriched by B3GALT5-AS1 antisense probe sets (Fig. 4E). Next, we expressed the truncated B3GALT5-AS1 fragments with or without the binding sites, which encode 1062-1363 nucleotides or 1-1061 nucleotides of B3GALT5-AS1, respectively (Fig. 4F). Transient transfections of the full-length or truncated B3GALT5-AS1 expression plasmids into HCT116 cells revealed that the depletion of the binding sites abolished the repressive roles of B3GALT5-AS1 on *miR-203* expression, and while only the binding sites of B3GALT5-AS1 could sufficiently repress *miR-203* expression (Fig. 4G). These results suggested that the binding region is responsible for the effects of B3GALT5-AS1 on *miR-203*. To further investigate whether B3GALT5-AS1 regulates the promoter activity of *miR-203*, we cloned *miR-203* promoter containing the binding region into luciferase reporter. Dual luciferase reporter assays displayed that B3GALT5-AS1 overexpression significantly downregulated the promoter activity of *miR-203*, which was abolished by the depletion of binding sites of B3GALT5-AS1, and while only the binding sites of B3GALT5-AS1 could sufficiently downregulated *miR-203* promoter activity (Fig. 4H). Conversely, B3GALT5-AS1 knockdown significantly upregulated *miR-203* promoter activity (Fig. 4I). *miR-203* is

reported to inhibit EMT via repressing the expression of EMT-inducing transcription factor ZEB2 and SNAI2 [44, 45]. Therefore, we further investigate the roles of B3GALT5-AS1 on *miR-203* targets ZEB2 and SNAI2. Transient transfections of the different B3GALT5-AS1 expression plasmids into HCT116 cells demonstrated that B3GALT5-AS1 overexpression upregulated ZEB2 and SNAI2, which were abolished by the depletion of binding sites of B3GALT5-AS1, and while only the binding sites of B3GALT5-AS1 could sufficiently upregulated ZEB2 and SNAI2 (Fig. 4J). Conversely, B3GALT5-AS1 knockdown downregulated ZEB2 and SNAI2 (Fig. 4K). All these results suggested that B3GALT5-AS1 inhibited *miR-203* and upregulated *miR-203* targets ZEB2 and SNAI2 via interacting with *miR-203* promoter.

### ***miR-203* is increased in colon cancer and further increased in liver metastasis**

To explore whether the regulation of *miR-203* and EMT by B3GALT5-AS1 exists *in vivo*, we measured *miR-203* expression in the same 64 pairs of primary colon cancer tissues and corresponding adjacent colonic epithelium tissues used in Fig. 1B. As displayed in Fig. 5A, *miR-203* was markedly upregulated in colon cancer tissues compared with colonic epithelium tissues. Analyses of the correlation between the expression of B3GALT5-AS1 and *miR-203* in these 64 colon cancer tissues displayed that the expression of *miR-203* was inversely correlated with that of B3GALT5-AS1 in colon cancer tissues (Fig. 5B). *miR-203* expression in 15 pairs of primary colon cancer tissues and corresponding liver metastasis tissues used in Fig. 1D was also detected. As displayed in Fig. 5C, *miR-203* was significantly upregulated in liver metastasis tissues compared with primary colon cancer tissues. In addition, the expressions of ZEB2 and SNAI2 were measured in the same 15 pairs of primary colon cancer tissues and corresponding liver metastasis tissues. The results displayed that ZEB2 and SNAI2 were both downregulated in liver metastasis tissues compared with primary colon cancer tissues (Fig. 5D, E). The expression of EMT markers E-cadherin and N-cadherin were also measured in these paired primary colon cancer tissues and liver metastasis tissues. As displayed in Fig. 5F, G, E-cadherin was upregulated and while N-cadherin was downregulated in liver metastasis tissues compared with primary colon cancer tissues. These data suggested that *miR-203* is increased in colon cancer and further increased in liver metastasis tissues, which is inversely associated with B3GALT5-AS1. ZEB2 and SNAI2 were reduced, and epithelial feature was preferred in liver metastasis tissues.



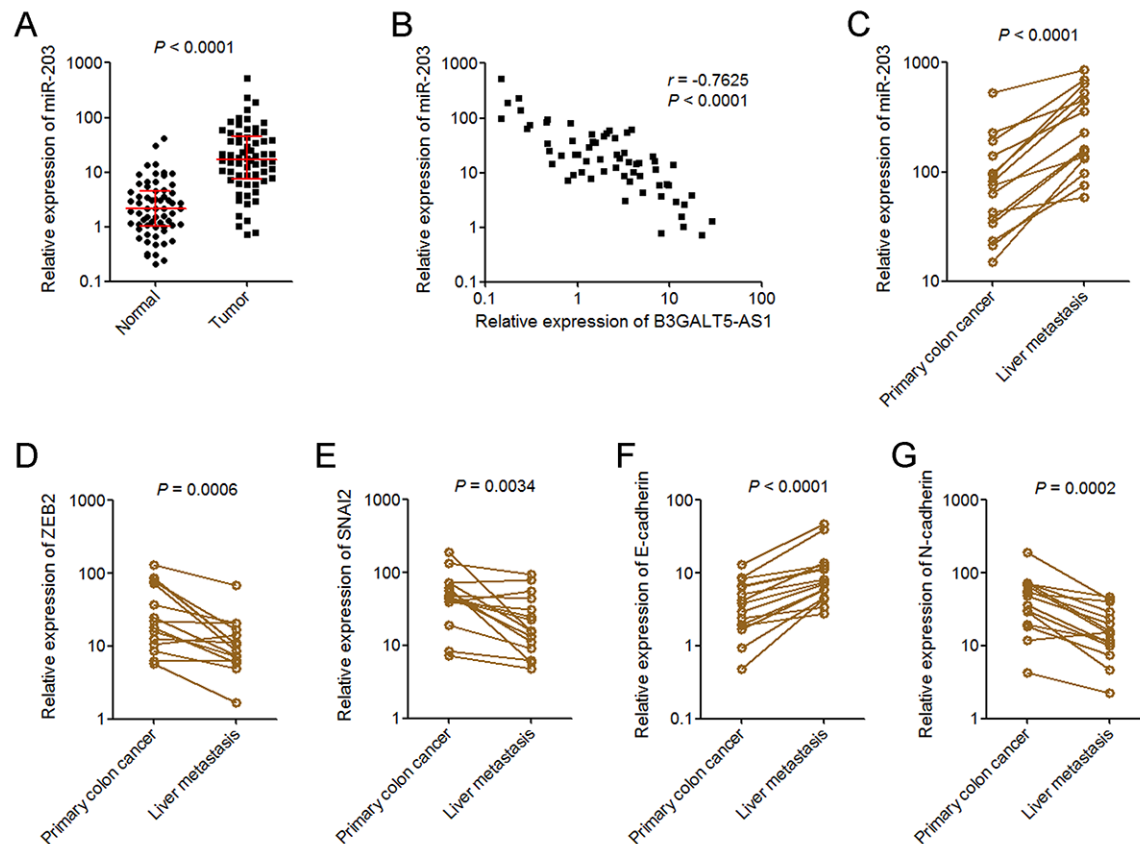


**Figure 5. miR-203 expression pattern in colon cancer.** (A) miR-203 expression in 64 pairs of primary colon cancer tissues and adjacent colonic epithelium tissues was measured by qRT-PCR.  $P < 0.0001$ , Wilcoxon signed-rank test. (B) The correlation between B3GALT5-AS1 and miR-203 expression level in colon cancer tissues.  $n = 64$ ,  $r = -0.7625$ ,  $P < 0.0001$ , Pearson's correlation analysis. (C) The expression of miR-203 in 15 pairs of primary colon cancer tissues and corresponding liver metastasis tissues was measured using qRT-PCR.  $P < 0.0001$ , Wilcoxon signed-rank test. (D) The expression of ZEB2 in 15 pairs of primary colon cancer tissues and corresponding liver metastasis tissues was measured using qRT-PCR.  $P = 0.0006$ , Wilcoxon signed-rank test. (E) The expression of SNAI2 in 15 pairs of primary colon cancer tissues and corresponding liver metastasis tissues was measured using qRT-PCR.  $P = 0.0034$ , Wilcoxon signed-rank test. (F) The expression of E-cadherin in 15 pairs of primary colon cancer tissues and corresponding liver metastasis tissues was measured using qRT-PCR.  $P < 0.0001$ , Wilcoxon signed-rank test. (G) The expression of N-cadherin in 15 pairs of primary colon cancer tissues and corresponding liver metastasis tissues was measured using qRT-PCR.  $P = 0.0002$ , Wilcoxon signed-rank test.

### B3GALT5-AS1 suppresses colon cancer liver metastasis

Next, we explored whether B3GALT5-AS1 have effects on colon cancer liver metastasis. The binding sites depleted B3GALT5-AS1 was stably overexpressed in HCT116 cells with a similar overexpression level to B3GALT5-AS1 full length overexpression clone (Fig. 6A). B3GALT5-AS1 stably overexpressed and control HCT116 cells were injected through the spleen to establish liver metastasis model in nude mice. The results displayed that ectopic expression of B3GALT5-AS1 decreased the amount of liver metastatic foci, which was abolished by the depletion of binding sites (Fig. 6B). The expressions of B3GALT5-AS1 and miR-

203 were measured in the liver metastatic foci formed by these different HCT116 clones. The results confirmed the overexpression of B3GALT5-AS1 and the downregulation of miR-203 in the liver metastatic foci formed by B3GALT5-AS1 stably overexpressed cells (Fig. 6C). Depletion of the binding sites abolished the effects of B3GALT5-AS1 on miR-203 *in vivo* (Fig. 6C). Proliferation marker Ki67 immunohistochemical staining of the liver metastatic foci displayed that B3GALT5-AS1 overexpression decreased the proportion of Ki67-positive cells, which was abolished by the depletion of binding sites (Fig. 6D). The expressions of ZEB2 and SNAI2 were measured in the liver metastatic foci, and the results displayed that ZEB2 and SNAI2 were upregulated in the liver

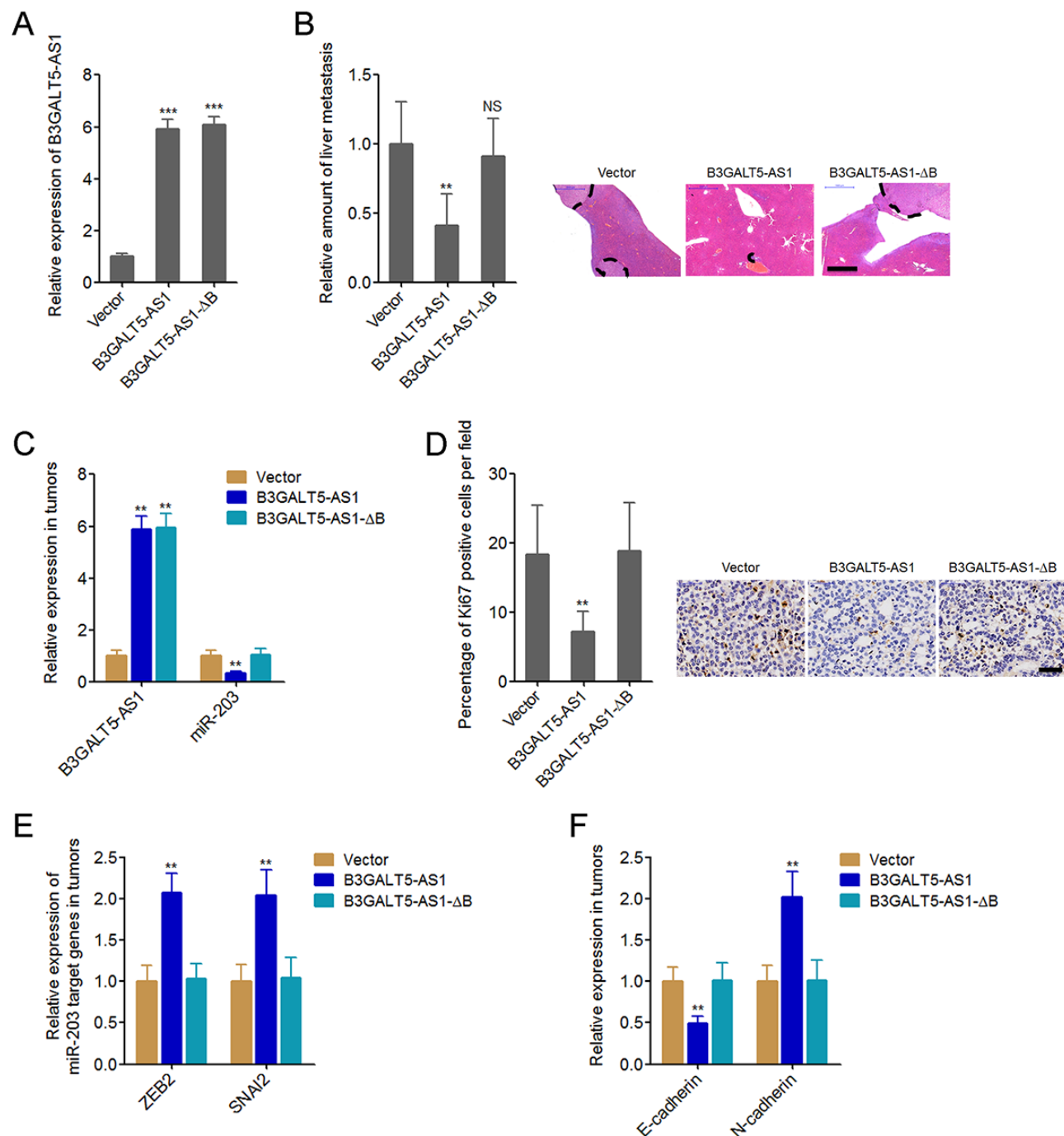


**Figure 6. B3GALT5-AS1 inhibited colon cancer liver metastasis.** (A) B3GALT5-AS1 expression in different B3GALT5-AS1 stably overexpressed HCT116 cells clones was measured using qRT-PCR. Data are displayed as mean  $\pm$  s.d. of three independent experiments. \*\*\* $P < 0.001$ , Student's  $t$ -test. (B) Indicated B3GALT5-AS1 stably overexpressed HCT116 cells were intra-splenic injected to establish liver metastasis. The amount of liver metastatic foci was assessed at the 42<sup>th</sup> day after intra-splenic injection using HE staining. Scale bars = 1000  $\mu$ m. (C) The expression of B3GALT5-AS1 and miR-203 in liver metastatic foci formed by these indicated B3GALT5-AS1 stably overexpressed HCT116 cells was detected using qRT-PCR. (D) Immunohistochemical staining of Ki67 in liver metastatic foci formed by these indicated B3GALT5-AS1 stably overexpressed HCT116 cells. Scale bars = 50  $\mu$ m. (E) The expression of ZEB2 and SNAI2 in liver metastatic foci formed by these indicated B3GALT5-AS1 stably overexpressed HCT116 cells was measured using qRT-PCR. (F) The expression of E-cadherin and N-cadherin in liver metastatic foci formed by these indicated B3GALT5-AS1 stably overexpressed HCT116 cells was detected using qRT-PCR. For B-F, data are displayed as mean  $\pm$  s.d. of six mice in each group. \*\* $P < 0.01$ , NS, not significant, Mann-Whitney test.

metastatic foci formed by B3GALT5-AS1 stably overexpressed cells, which were abolished by the depletion of binding sites of B3GALT5-AS1 (Fig. 6E). The expression of EMT markers E-cadherin and N-cadherin were also measured in the liver metastatic foci. The results displayed that E-cadherin was downregulated and while N-cadherin was upregulated in the liver metastatic foci formed by B3GALT5-AS1 stably overexpressed cells, which were also abolished by the depletion of binding sites of B3GALT5-AS1 (Fig. 6F). All these results suggested that B3GALT5-AS1 inhibited miR-203, upregulated ZEB2 and SNAI2, induced EMT, and suppressed colon cancer liver metastasis *in vivo*.

### Depletion of B3GALT5-AS1 promotes colon cancer liver metastasis in a miR-203-dependent manner

To further investigate whether the inhibition of miR-203 mediates the roles of B3GALT5-AS1 in colon cancer liver metastasis, we stably inhibited miR-203 expression in B3GALT5-AS1 stably depleted SW620 cells (Fig. 7A). The constructed cell clones were injected through the spleen to establish liver metastasis model in nude mice. The results displayed that B3GALT5-AS1 knockdown increased the amount of liver metastatic foci, which was attenuated by the inhibition of miR-203 (Fig. 7B). The expressions of B3GALT5-AS1 and miR-203 were measured in the liver metastatic foci formed by these stable clones. The results confirmed the downregulation of B3GALT5-AS1 and the upregulation of miR-203 in liver metastatic foci formed by B3GALT5-AS1 stably depleted cells, and also the inversion of miR-203 in the liver metastatic foci formed by B3GALT5-AS1 and miR-203 concurrently depleted cells (Fig. 7C). Proliferation marker Ki67 immunohistochemical staining of the liver metastatic foci displayed that B3GALT5-AS1 knockdown increased the proportion of Ki67-positive cells, which was attenuated by the inhibition of miR-203 (Fig. 7D). The expressions of ZEB2 and SNAI2 were measured in the liver metastatic foci, and the results displayed that ZEB2 and SNAI2 were downregulated in the liver metastatic foci formed by B3GALT5-AS1 stably depleted cells, which were abolished by the inhibition of miR-203 (Fig. 7E). The expression of EMT markers E-cadherin and N-cadherin were also measured in the liver metastatic foci. The results displayed that E-cadherin was upregulated and while N-cadherin was downregulated in the liver metastatic foci formed by B3GALT5-AS1 stably depleted cells, which were also abolished by the inhibition of miR-203 (Fig. 7F). All these results demonstrated that B3GALT5-AS1 knockdown increased miR-203, downregulated ZEB2 and SNAI2, and inhibited EMT *in vivo*. These data also suggested

that B3GALT5-AS1 knockdown promoted colon cancer liver metastasis at least partially via the upregulation of miR-203.

## DISCUSSION

Distant metastasis, particular liver metastasis, is the major cause of colon cancer-related death [4]. However, the critical molecular mechanisms underpinning colon cancer liver metastasis are largely unknown. In the present study, we found a novel regulation axis in the process of colon cancer liver metastasis, which is the induction of EMT by lncRNA B3GALT5-AS1 via repressing miR-203. Our data revealed that B3GALT5-AS1 directly binds to the promoter of *miR-203*, represses *miR-203* expression, upregulates miR-203 targets ZEB2 and SNAI2, induces EMT, and finally suppresses colon cancer liver metastasis. Consistent with the suppressive roles of B3GALT5-AS1/miR-203/ZEB2-SNAI2/EMT in colon cancer liver metastasis, B3GALT5-AS1 is reduced, miR-203 is increased, ZEB2 and SNAI2 are reduced, epithelial marker E-cadherin is increased, mesenchymal marker N-cadherin is reduced in liver metastasis tissues compared with primary colon cancer tissues.

In the liver metastatic foci, the metastasized colon cancer cells undergo MET and regain epithelial phenotype to permit their settlement and proliferation [54]. Our data support this theory. Our *in vivo* liver metastasis assays demonstrated that overexpression of B3GALT5-AS1 induced mesenchymal phenotype of liver metastasized colon cancer cells and inhibited liver metastasis of colon cancer. Depletion of B3GALT5-AS1 induced epithelial phenotype of liver metastasized colon cancer cells and promoted liver metastasis of colon cancer. Therefore, the opposing roles of EMT in early invasion and late settlement of colon cancer liver metastasis processes imply that disease stage-specific therapies are warranted.

Mechanistically, we identified a long interaction region with about 300 nucleotides between the last 300 nucleotides of B3GALT5-AS1 and the promoter of *miR-203*. ChIRP assays revealed the physical binding between B3GALT5-AS1 and the promoter of *miR-203*. Dual luciferase reporter assays and depletion mapping assays revealed that B3GALT5-AS1 inhibited the promoter activity of *miR-203*, which was dependent on the interaction region. Consistently, B3GALT5-AS1 repressed miR-203 expression both *in vitro* and in liver metastasized colon cancer cells *in vivo*, which were also dependent on the interaction region. The inverse correlation between B3GALT5-AS1 and miR-203 expression in colon cancer tissues supported the negative regulation of miR-203 by B3GALT5-AS1.

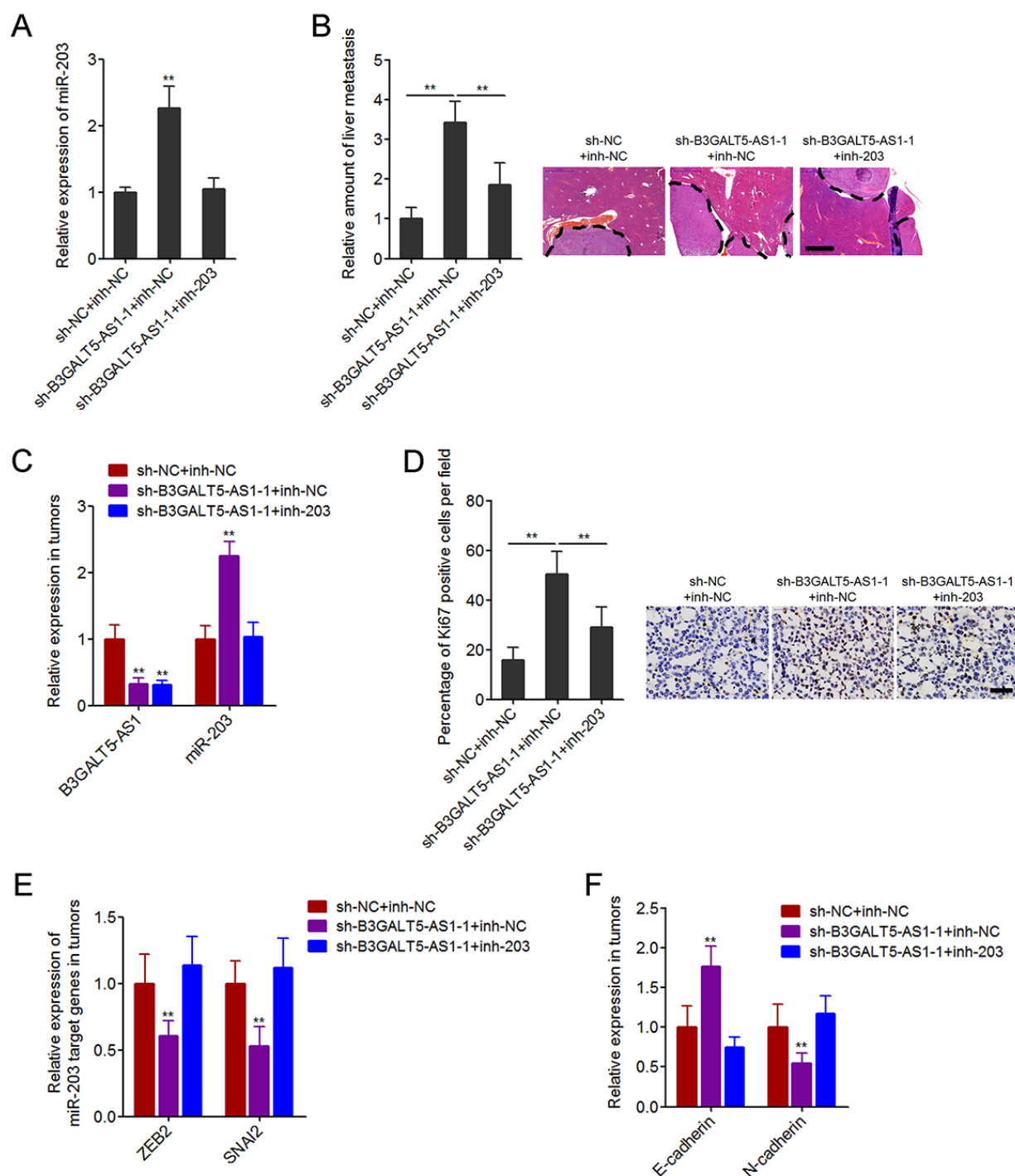


**Figure 7. Depletion of B3GALT5-AS1 promoted colon cancer liver metastasis in a miR-203-dependent manner.** (A) miR-203 expression in B3GALT5-AS1 and miR-203 concurrently depleted and control SW620 cells was measured using qRT-PCR. Data are displayed as mean  $\pm$  s.d. of three independent experiments.  $^{**}P < 0.01$ , Student's *t*-test. (B) B3GALT5-AS1 and miR-203 concurrently depleted and control SW620 cells were intra-splenic injected to establish liver metastasis. The amount of liver metastatic foci was detected at the 42<sup>th</sup> day after intra-splenic injection using HE staining. Scale bars = 1000  $\mu$ m. (C) The expression of B3GALT5-AS1 and miR-203 in liver metastatic foci formed by B3GALT5-AS1 and miR-203 concurrently depleted and control SW620 cells was detected using qRT-PCR. (D) Immunohistochemical staining of Ki67 in liver metastatic foci formed by B3GALT5-AS1 and miR-203 concurrently depleted and control SW620 cells. Scale bars = 50  $\mu$ m. (E) The expression of ZEB2 and SNAI2 in liver metastatic foci formed by B3GALT5-AS1 and miR-203 concurrently depleted and control SW620 cells was measured using qRT-PCR. (F) The expression of E-cadherin and N-cadherin in liver metastatic foci formed by B3GALT5-AS1 and miR-203 concurrently depleted and control SW620 cells was detected using qRT-PCR. For B-F, data are displayed as mean  $\pm$  s.d. of six mice in each group.  $^{**}P < 0.01$ , Mann-Whitney test.



Furthermore, *in vivo* functional assays revealed that inhibition of miR-203 attenuated the pro-metastatic roles of B3GALT5-AS1 depletion in colon cancer liver metastasis. Except for miR-203, other EMT regulators may also be B3GALT5-AS1 downstream targets, which need further investigation. Excluding EMT, other mechanisms may also mediate the roles of B3GALT5-AS1 in colon cancer cell proliferation, which also need further investigation. Nonetheless, our results suggested that the negative regulation of miR-203 and positive regulation of EMT by B3GALT5-AS1 at least partially mediated the roles of B3GALT5-AS1 in colon cancer liver metastasis.

In summary, we demonstrated that lncRNA B3GALT5-AS1 is reduced in colon cancer tissues, and further reduced in colon cancer liver metastasis tissues. Low expression of B3GALT5-AS1 indicates poor outcome of colon cancer patients. B3GALT5-AS1 inhibits proliferation, promotes migration and invasion, induces EMT, and inhibits liver metastasis of colon cancer cells via repressing miR-203. Our data suggested that B3GALT5-AS1/miR-203/EMT axis may be potential therapeutic target for colon cancer liver metastasis.

## MATERIALS AND METHODS

### Patient and tissue specimens

Sixty-four pairs of primary colon cancer tissues and adjacent normal colonic epithelium tissues, and 15 colon cancer liver metastasis tissues were collected from colon cancer patients with written informed consent who received surgical resection at The First Affiliated Hospital, Sun Yat-sen University (Guangzhou, China). These tissue samples were diagnosed with pathological examination. All resected tissues were immediately snap-frozen in liquid nitrogen and stored at -80 °C until use. The Research Review Board of The First Affiliated Hospital, Sun Yat-sen University reviewed and approved this study.

### Cell culture

The human normal colonic epithelial cell line NCM460 and colon cancer cell lines HCT116, HT-29, LoVo, SW480 and SW620 were acquired from the Institute of Biochemistry and Cell Biology of the Chinese Academy of Sciences (Shanghai, China). NCM460 was maintained in Dulbecco's Modified Eagle's Medium (Gibco, Grand Island, NY, USA). HCT116 and HT-29 were cultured in McCoy's 5A Medium (Sigma-Aldrich, Saint Louis, MO, USA). LoVo was cultured in Ham's F-12K Medium (Invitrogen, Carlsbad, CA, USA). SW480 and SW620 were maintained in L-15 Medium (Gibco). These cells were maintained in the above described

medium added with 10% fetal bovine serum (Gibco) at 37°C in a humidified incubator with 5% CO<sub>2</sub>.

### RNA isolation and quantitative real-time PCR (qRT-PCR)

Total RNA was isolated from indicated tissues and cells with TRIzol Reagent (Invitrogen) according to the manufacturer's instruction. The isolated RNA was deal with DNase I (Takara, Dalian, China) to get rid of genomic DNA. Next, reverse transcription was carried out using the RNA and the M-MLV Reverse Transcriptase (Invitrogen) following the manufacturer's instruction. Quantitative real-time PCR (qRT-PCR) assays were performed using SYBR® Premix Ex Taq™ II (Takara) on ABI StepOnePlus Real-Time PCR System (Applied Biosystems, Foster City, CA, USA) following the manufacturers' protocols. β-actin was employed as an endogenous control for the quantitation of mRNAs and lncRNAs. Primers' sequences were as follows: for transcript variant 1 of B3GALT5-AS1, 5'-ATTCACGGATGAGACGAC-3' (forward) and 5'-CCTTGAGAGACGAAGCAC-3' (reverse); for transcript variant 2 of B3GALT5-AS1, 5'-TCACGGATGAGACGACTC-3' (forward) and 5'-AAGGCTTCCAAACACGAAAA-3' (reverse); for E-cadherin, 5'-GCCCCATCAGGCCTCCGTTT-3' (forward) and 5'-ACCTTGCCTTCTTTGTCTTTGTTGGA-3' (reverse); for N-cadherin, 5'-TGGACCATCACTCGGCTTA-3' (forward) and 5'-ACACTGGCAAACCTTCACG-3' (reverse); for ZEB2, 5'-TGAGGATGACGGTATTGC-3' (forward) and 5'-ATCTCGTTGTTGTGCCAG-3' (reverse); for SNAIL2, 5'-GGCAAGGCGTTTTCCAG-3' (forward) and 5'-CAGCCAGATTCCTCATGTTT-3' (reverse); and for β-actin, 5'-GGGAAATCGTGCGTGACATTAAG-3' (forward) and 5'-TGTGTTGGCGTACAGGTCTTTG-3' (reverse). For miRNAs quantitation, qRT-PCR was carried out as above described with TaqMan microRNA assays following the manufacturer's instruction (Applied Biosystems). U6 served as an endogenous control for the quantitation of miRNAs. The quantitation of RNA was calculated with the comparative Ct method.

### Western blot

Total proteins were isolated from tissues or cells using RIPA buffer (Beyotime, Shanghai, China). Identical quantity of protein samples were separated using sodium dodecyl sulfate-polyacrylamide gel electrophoresis (SDS-PAGE). Then, proteins were transferred to nitrocellulose filter membrane (Millipore, Bedford, MA, USA). Next, the membranes were blocked with 5% bovine serum albumin, followed by being incubated with primary antibodies against β-actin



(Sigma-Aldrich), E-cadherin (Abcam, Hong Kong, China), or N-cadherin (Abcam). After three washes using TBS buffer, the membranes were incubated with IRdye 700-conjugated goat anti-mouse IgG or IRdye800-conjugated goat anti-rabbit IgG (Li-Cor, Lincoln, NE, USA). Last, immunoreactive bands were detected using an Odyssey infrared scanner (Li-Cor).

### Plasmids construction

For construction of different B3GALT5-AS1 overexpression plasmids, B3GALT5-AS1 full-length nucleotides, 1-1061 nucleotides of B3GALT5-AS1, and 1062-1363 nucleotides of B3GALT5-AS1 were PCR amplified with Thermo Scientific Phusion Flash High-Fidelity PCR Master Mix (Thermo-Fisher Scientific, Waltham, MA, USA). Then, the PCR products were subcloned into the Hind III and Xba I, Hind III and BamH I, or BamH I and Xba I sites of the pcDNA3.1 plasmid (Invitrogen), termed as pcDNA3.1-B3GALT5-AS1, pcDNA3.1-B3GALT5-AS1-ΔB, pcDNA3.1-B3GALT5-AS1-B, respectively. The PCR primers' sequences are as follows: for pcDNA3.1-B3GALT5-AS1, 5'-CCCAAGCTTGACGCGGCGGGCGGCTCC-3' (forward) and 5'-GCTCTAGAAATTTTACTTTTTTTGGAGACAGGG-3' (reverse); for pcDNA3.1-B3GALT5-AS1-ΔB, 5'-CCCAAGCTTGACGCGGCGGGCGGCTCC-3' (forward) and 5'-CGGGATCCTATGGAGGTTCTGTTTGCTTCTGCA-3' (reverse); for pcDNA3.1-B3GALT5-AS1-B, 5'-CGGGATCCAAATGTAATGATGTCTTGTGCC-3' (forward) and 5'-GCTCTAGAAATTTTACTTTTTTTGGAGACAGGG-3' (reverse). Empty plasmid pcDNA3.1 was employed as negative control. Two pairs of cDNA oligonucleotides suppressing B3GALT5-AS1 expression were inserted into the SuperSilencing shRNA expression plasmid pGPU6/Neo (GenePharma, Shanghai, China), named sh-B3GALT5-AS1-1 and sh-B3GALT5-AS1-2. The target sites are 5'-GCAAGACAGCGCATTGATTGG-3' and 5'-GCATAAGAGAGACCAACTTGG-3', respectively. A scrambled shRNA was employed as negative control and named sh-NC. The promoter of *miR-203* containing the predicted B3GALT5-AS1 binding sites was PCR amplified using the Thermo Scientific Phusion Flash High-Fidelity PCR Master Mix and subcloned into the Kpn I and Hind III sites of firefly luciferase reporter pGL3-Basic plasmid (Promega, Madison, WI, USA), named pGL3-miR203-pro. The PCR primers' sequences are as follows: 5'-GGGGTACCTCCTCTCCATCACGACTACT-3' (forward) and 5'-CCCAAGCTTGTTTCTGCTTCTCAGACCCT-3' (reverse).

### Stable cell lines construction

For construction of B3GALT5-AS1 stably overexpressed HCT116 cells, pcDNA3.1-B3GALT5-AS1, pcDNA3.1-B3GALT5-AS1-ΔB, or pcDNA3.1 was transfected into HCT116 cells with Lipofectamine 3000 (Invitrogen) following the manufacturer's protocols. Next, the cells were selected with neomycin for four weeks. For construction of B3GALT5-AS1 stably depleted SW620 cells, sh-B3GALT5-AS1-1, sh-B3GALT5-AS1-2, or sh-NC was transfected into SW620 cells with Lipofectamine 3000 (Invitrogen). Next, the cells were selected with neomycin for four weeks. Recombinant lentiviruses containing miR-203 inhibitor or the control were purchased from GenePharma (Shanghai, China). B3GALT5-AS1 stably depleted SW620 cells were transfected with  $2 \times 10^6$  transducing units of miR-203 inhibition lentiviruses and selected with puromycin for four weeks. The stably cell lines were identified by qRT-PCR.

### Cell proliferation assay

Cell proliferation was assessed by Glo cell viability assay and Ethynyl deoxyuridine (EdU) incorporation assay. For Glo cell viability assay, 2,000 colon cancer cells per-well were plated into 96-well plates and maintained for indicated time. At the end of the incubation period, luminescence values were measured with the CellTiter-Glo<sup>®</sup> Luminescent Cell Viability Assay (Promega) following the manufacturer's protocol. EdU incorporation assay was carried out using the EdU kit (Roche, Mannheim, Germany) following the manufacturer's instruction. The results were collected with the Zeiss fluorescence photomicroscope (Carl Zeiss, Oberkochen, Germany) and measured via counting at least ten random fields.

### Cell migration and invasion assays

Cell migration and invasion were evaluated by transwell assays. For transwell migration assay, 40,000 indicated colon cancer cells resuspended in serum-free medium with 1 μg/ml Mitomycin C to repress cell proliferation were seeded into the upper chambers of transwell inserts (Millipore). Medium supplemented with 10% FBS was added to the lower chambers. After incubation for 24 hours, colon cancer cells remaining on the upper membranes were fully removed. The colon cancer cells migrated through the membranes were fixed in methanol, stained using 0.1% crystal violet, and imaged with the Zeiss fluorescence photomicroscope (Carl Zeiss). The results were measured via counting at least ten random fields. Transwell invasion assay was performed with the Cell Invasion Assay Kit from CHEMICON (Millipore) according to the

manufacturer's protocol. The results were analyzed as transwell migration assay.

### Purification of cytoplasmic and nuclear RNA

Cytoplasmic and nuclear RNA was purified with Cytoplasmic & Nuclear RNA Purification Kit (Norgen, Belmont, CA, USA) following the manufacturer's protocol. The purified RNA was measured using qRT-PCR.

### Chromatin isolation by RNA purification (ChIRP)

ChIRP was carried out using Magna ChIRP RNA Interactome Kit (Millipore) following the manufacturer's protocol. Anti-sense DNA probes specific for B3GALT5-AS1 were synthesized by Biosearch Technologies. Probes sequences are as follows: 1, 5'-aaactcaagaaccggcctc-3'; 2, 5'-ggcatctggggttgagaag-3'; 3, 5'-ttgcatgactttggctcatt-3'; 4, 5'-taagtattgtccagcattc-3'; 5, 5'-gaagatagcctctctgacag-3'; 6, 5'-atacctcttttgacagagct-3'; 7, 5'-ccacctcaaaggatgatcaa-3'; 8, 5'-ttctgcaccttggtctaatc-3'. ChIRP enriched DNA was measured by qRT-PCR to assess *miR-203* promoter enrichment. Primers' sequences were as follows: 5'-ACTGGGAAGATGGAGGTTG-3' (forward) and 5'-GATGGAAGTGGGCATAGGG-3' (reverse).

### Dual luciferase reporter assay

The constructed firefly luciferase reporter pGL3-miR203-pro was cotransfected with renilla luciferase expression vector pRL-TK into indicated SW620 cells. The different B3GALT5-AS1 expression plasmids were cotransfected with pGL3-miR203-pro and pRL-TK into HCT116 cells. Forty-eight hours after transfection, the luciferase activity was detected by Dual-Luciferase<sup>®</sup> Reporter Assay System (Promega) following the manufacturer's protocols.

### Animal study

To establish *in vivo* liver metastasis model, 2×10<sup>6</sup> indicted colon cancer cells in 100 µL phosphate buffered saline were intra-splenic injected into 6-week old nude mice acquired from Laboratory Animal Center of Sun Yat-sen University (Guangzhou, China). The mice were housed in a temperature and light controlled pathogen-free animal facility with free access to food and water to being allowed to grow for 6 weeks. Then the mice were sacrificed and the livers were resected. The resected livers were fixed in formalin, paraffin embedded, deparaffinized, rehydrated, and antigen retrieved. The amount of liver metastatic foci was counted via hematoxylin-eosin (HE) staining. The sections were incubated with primary antibody specific

for Ki67 (Abcam) and horseradish peroxidase-conjugated secondary antibody (Beyotime, Shanghai, China), followed by being visualized with 3, 3'-diaminobenzidine. The animal care and use committee of The First Affiliated Hospital, Sun Yat-sen University reviewed and approved the experimental protocols concerning the handling of mice.

### Statistical analysis

Statistical analyses were performed using GraphPad Prism Software (GraphPad Software, La Jolla, CA, USA). Student's *t*-test, Wilcoxon signed-rank test, Mann-Whitney test, Pearson chi-square test, Pearson's correlation analysis, or Log-rank test was carried out as indicated. *P*-values < 0.05 were considered as statistically significant.

### Abbreviations

lncRNAs, long noncoding RNAs; miR-203, microRNA-203; EMT, epithelial-to-mesenchymal transition; MET, mesenchymal-to-epithelial transition; miRNA, microRNA; qRT-PCR, quantitative real-time PCR; SDS-PAGE, sodium dodecyl sulfate-polyacrylamide gel electrophoresis; EdU, Ethynyl deoxyuridine; ChIRP, chromatin isolation by RNA purification; HE, hematoxylin-eosin.

### AUTHOR CONTRIBUTIONS

YH, LW, and ZW conceived the study; LW, ZW, KW, WD, CZ, and JP carried out the experiments; YH, LW, and ZW collected and analyzed the data. YH and LW wrote the manuscript. All authors read and approved the final manuscript.

### CONFLICTS OF INTEREST

All authors declare no conflict of interest.

### REFERENCES

1. Torre LA, Bray F, Siegel RL, Ferlay J, Lortet-Tieulent J, Jemal A. Global cancer statistics, 2012. *CA Cancer J Clin.* 2015; 65:87–108. <https://doi.org/10.3322/caac.21262>
2. Geng L, Chaudhuri A, Talmon G, Wisecarver JL, Are C, Brattain M, Wang J. MicroRNA-192 suppresses liver metastasis of colon cancer. *Oncogene.* 2014; 33:5332–40. <https://doi.org/10.1038/onc.2013.478>
3. Akgül Ö, Çetinkaya E, Ersöz Ş, Tez M. Role of surgery in colorectal cancer liver metastases. *World J Gastroenterol.* 2014; 20:6113–22.

<https://doi.org/10.3748/wjg.v20.i20.6113>

4. Manfredi S, Lepage C, Hatem C, Coatmeur O, Faivre J, Bouvier AM. Epidemiology and management of liver metastases from colorectal cancer. *Ann Surg*. 2006; 244:254–59. <https://doi.org/10.1097/01.sla.0000217629.94941.cf>
5. Landreau P, Drouillard A, Launoy G, Ortega-Deballon P, Jooste V, Lepage C, Faivre J, Facy O, Bouvier AM. Incidence and survival in late liver metastases of colorectal cancer. *J Gastroenterol Hepatol*. 2015; 30:82–85. <https://doi.org/10.1111/jgh.12685>
6. Urošević J, García-Albéniz X, Planet E, Real S, Céspedes MV, Guiu M, Fernández E, Bellmunt A, Gawrzak S, Pavlovic M, Mangues R, Dolado I, Barriga FM, et al. Colon cancer cells colonize the lung from established liver metastases through p38 MAPK signalling and PTHLH. *Nat Cell Biol*. 2014; 16:685–94. <https://doi.org/10.1038/ncb2977>
7. Polyak K, Weinberg RA. Transitions between epithelial and mesenchymal states: acquisition of malignant and stem cell traits. *Nat Rev Cancer*. 2009; 9:265–73. <https://doi.org/10.1038/nrc2620>
8. Rokavec M, Horst D, Hermeking H. Cellular model of colon cancer progression reveals signatures of mRNAs, miRNA, lncRNAs, and epigenetic modifications associated with metastasis. *Cancer Res*. 2017; 77:1854–67. <https://doi.org/10.1158/0008-5472.CAN-16-3236>
9. Mehlen P, Puisieux A. Metastasis: a question of life or death. *Nat Rev Cancer*. 2006; 6:449–58. <https://doi.org/10.1038/nrc1886>
10. Spaderna S, Schmalhofer O, Hlubek F, Berx G, Eger A, Merkel S, Jung A, Kirchner T, Brabletz T. A transient, EMT-linked loss of basement membranes indicates metastasis and poor survival in colorectal cancer. *Gastroenterology*. 2006; 131:830–40. <https://doi.org/10.1053/j.gastro.2006.06.016>
11. Vu T, Datta PK. Regulation of EMT in colorectal cancer: a culprit in metastasis. *Cancers (Basel)*. 2017; 9:E171. <https://doi.org/10.3390/cancers9120171>
12. Yuan JH, Yang F, Wang F, Ma JZ, Guo YJ, Tao QF, Liu F, Pan W, Wang TT, Zhou CC, Wang SB, Wang YZ, Yang Y, et al. A long noncoding RNA activated by TGF- $\beta$  promotes the invasion-metastasis cascade in hepatocellular carcinoma. *Cancer Cell*. 2014; 25:666–81. <https://doi.org/10.1016/j.ccr.2014.03.010>
13. Ocaña OH, Córcoles R, Fabra A, Moreno-Bueno G, Acloque H, Vega S, Barrallo-Gimeno A, Cano A, Nieto MA. Metastatic colonization requires the repression of the epithelial-mesenchymal transition inducer Prrx1. *Cancer Cell*. 2012; 22:709–24. <https://doi.org/10.1016/j.ccr.2012.10.012>
14. Zhang W, Zhou P, Meng A, Zhang R, Zhou Y. Down-regulating Myoferlin inhibits the vasculogenic mimicry of melanoma via decreasing MMP-2 and inducing mesenchymal-to-epithelial transition. *J Cell Mol Med*. 2018; 22:1743–54. <https://doi.org/10.1111/jcmm.13455>
15. Kahlert UD, Joseph JV, Kruyt FA. EMT- and MET-related processes in nonepithelial tumors: importance for disease progression, prognosis, and therapeutic opportunities. *Mol Oncol*. 2017; 11:860–77. <https://doi.org/10.1002/1878-0261.12085>
16. Korpál M, Ell BJ, Buffa FM, Ibrahim T, Blanco MA, Celià-Terrassa T, Mercatali L, Khan Z, Goodarzi H, Hua Y, Wei Y, Hu G, Garcia BA, et al. Direct targeting of Sec23a by miR-200s influences cancer cell secretome and promotes metastatic colonization. *Nat Med*. 2011; 17:1101–08. <https://doi.org/10.1038/nm.2401>
17. Jeschke U, Mylonas I, Kuhn C, Shabani N, Kunert-Keil C, Schindlbeck C, Gerber B, Friese K. Expression of E-cadherin in human ductal breast cancer carcinoma in situ, invasive carcinomas, their lymph node metastases, their distant metastases, carcinomas with recurrence and in recurrence. *Anticancer Res*. 2007; 27:1969–74.
18. Iyer MK, Niknafs YS, Malik R, Singhal U, Sahu A, Hosono Y, Barrette TR, Prensner JR, Evans JR, Zhao S, Poliakov A, Cao X, Dhanasekaran SM, et al. The landscape of long noncoding RNAs in the human transcriptome. *Nat Genet*. 2015; 47:199–208. <https://doi.org/10.1038/ng.3192>
19. Yan X, Hu Z, Feng Y, Hu X, Yuan J, Zhao SD, Zhang Y, Yang L, Shan W, He Q, Fan L, Kandalaft LE, Tanyi JL, et al. Comprehensive genomic characterization of long non-coding RNAs across human cancers. *Cancer Cell*. 2015; 28:529–40. <https://doi.org/10.1016/j.ccell.2015.09.006>
20. Schmitt AM, Chang HY. Long noncoding RNAs in cancer pathways. *Cancer Cell*. 2016; 29:452–63. <https://doi.org/10.1016/j.ccell.2016.03.010>
21. Ponting CP, Oliver PL, Reik W. Evolution and functions of long noncoding RNAs. *Cell*. 2009; 136:629–41. <https://doi.org/10.1016/j.cell.2009.02.006>
22. Lin A, Hu Q, Li C, Xing Z, Ma G, Wang C, Li J, Ye Y, Yao J, Liang K, Wang S, Park PK, Marks JR, et al. The LINK-A lncRNA interacts with PtdIns(3,4,5)P3 to

- hyperactivate AKT and confer resistance to AKT inhibitors. *Nat Cell Biol.* 2017; 19:238–51. <https://doi.org/10.1038/ncb3473>
23. Lin A, Li C, Xing Z, Hu Q, Liang K, Han L, Wang C, Hawke DH, Wang S, Zhang Y, Wei Y, Ma G, Park PK, et al. The LINK-A lncRNA activates normoxic HIF1 $\alpha$  signalling in triple-negative breast cancer. *Nat Cell Biol.* 2016; 18:213–24. <https://doi.org/10.1038/ncb3295>
24. Grelet S, Link LA, Howley B, Obellianne C, Palanisamy V, Gangaraju VK, Diehl JA, Howe PH. A regulated PNUITS mRNA to lncRNA splice switch mediates EMT and tumour progression. *Nat Cell Biol.* 2017; 19:1105–15. <https://doi.org/10.1038/ncb3595>
25. Yuan JH, Liu XN, Wang TT, Pan W, Tao QF, Zhou WP, Wang F, Sun SH. The MBNL3 splicing factor promotes hepatocellular carcinoma by increasing PXN expression through the alternative splicing of lncRNA-PXN-AS1. *Nat Cell Biol.* 2017; 19:820–32. <https://doi.org/10.1038/ncb3538>
26. Kaur P, Tan JR, Karolina DS, Sepramaniam S, Armugam A, Wong PT, Jeyaseelan K. A long non-coding RNA, BC048612 and a microRNA, miR-203 coordinate the gene expression of neuronal growth regulator 1 (NEGR1) adhesion protein. *Biochim Biophys Acta.* 2016; 1863:533–43. <https://doi.org/10.1016/j.bbamcr.2015.12.012>
27. Ellis BC, Graham LD, Molloy PL. CRNDE, a long non-coding RNA responsive to insulin/IGF signaling, regulates genes involved in central metabolism. *Biochim Biophys Acta.* 2014; 1843:372–86. <https://doi.org/10.1016/j.bbamcr.2013.10.016>
28. Rigoutsos I, Lee SK, Nam SY, Anfossi S, Pasculli B, Pichler M, Jing Y, Rodriguez-Aguayo C, Telonis AG, Rossi S, Ivan C, Catela Ivkovic T, Fabris L, et al. N-BLR, a primate-specific non-coding transcript leads to colorectal cancer invasion and migration. *Genome Biol.* 2017; 18:98. <https://doi.org/10.1186/s13059-017-1224-0>
29. Fang C, Qiu S, Sun F, Li W, Wang Z, Yue B, Wu X, Yan D. Long non-coding RNA HNF1A-AS1 mediated repression of miR-34a/SIRT1/p53 feedback loop promotes the metastatic progression of colon cancer by functioning as a competing endogenous RNA. *Cancer Lett.* 2017; 410:50–62. <https://doi.org/10.1016/j.canlet.2017.09.012>
30. Han P, Li JW, Zhang BM, Lv JC, Li YM, Gu XY, Yu ZW, Jia YH, Bai XF, Li L, Liu YL, Cui BB. The lncRNA CRNDE promotes colorectal cancer cell proliferation and chemoresistance via miR-181a-5p-mediated regulation of Wnt/ $\beta$ -catenin signaling. *Mol Cancer.* 2017; 16:9. <https://doi.org/10.1186/s12943-017-0583-1>
31. Kong J, Sun W, Li C, Wan L, Wang S, Wu Y, Xu E, Zhang H, Lai M. Long non-coding RNA LINC01133 inhibits epithelial-mesenchymal transition and metastasis in colorectal cancer by interacting with SRSF6. *Cancer Lett.* 2016; 380:476–84. <https://doi.org/10.1016/j.canlet.2016.07.015>
32. Pickard MR, Mourtada-Maarabouni M, Williams GT. Long non-coding RNA GAS5 regulates apoptosis in prostate cancer cell lines. *Biochim Biophys Acta.* 2013; 1832:1613–23. <https://doi.org/10.1016/j.bbadis.2013.05.005>
33. Ge Y, Zhang L, Nikolova M, Reva B, Fuchs E. Strand-specific in vivo screen of cancer-associated miRNAs unveils a role for miR-21(\*) in SCC progression. *Nat Cell Biol.* 2016; 18:111–21. <https://doi.org/10.1038/ncb3275>
34. Jeong JH, Cheol Kang Y, Piao Y, Kang S, Pak YK. miR-24-mediated knockdown of H2AX damages mitochondria and the insulin signaling pathway. *Exp Mol Med.* 2017; 49:e313. <https://doi.org/10.1038/emm.2016.174>
35. Cho YM, Kim TM, Hun Kim D, Hee Kim D, Jeong SW, Kwon OJ. miR-148a is a downstream effector of X-box-binding protein 1 that silences Wnt10b during adipogenesis of 3T3-L1 cells. *Exp Mol Med.* 2016; 48:e226. <https://doi.org/10.1038/emm.2016.3>
36. Yuan JH, Yang F, Chen BF, Lu Z, Huo XS, Zhou WP, Wang F, Sun SH. The histone deacetylase 4/SP1/microrna-200a regulatory network contributes to aberrant histone acetylation in hepatocellular carcinoma. *Hepatology.* 2011; 54:2025–35. <https://doi.org/10.1002/hep.24606>
37. Werner TV, Hart M, Nickels R, Kim YJ, Menger MD, Bohle RM, Keller A, Ludwig N, Meese E. MiR-34a-3p alters proliferation and apoptosis of meningioma cells in vitro and is directly targeting SMAD4, FRAT1 and BCL2. *Aging (Albany NY).* 2017; 9:932–54. <https://doi.org/10.18632/aging.101201>
38. Penolazzi L, Lambertini E, Bergamin LS, Roncada T, De Bonis P, Cavallo M, Piva R. MicroRNA-221 silencing attenuates the degenerated phenotype of intervertebral disc cells. *Aging (Albany NY).* 2018; 10:2001–15. <https://doi.org/10.18632/aging.101525>
39. Gregory PA, Bert AG, Paterson EL, Barry SC, Tsykin A, Farshid G, Vadas MA, Khew-Goodall Y, Goodall GJ. The miR-200 family and miR-205 regulate epithelial to mesenchymal transition by targeting ZEB1 and SIP1. *Nat Cell Biol.* 2008; 10:593–601. <https://doi.org/10.1038/ncb1722>



40. Zhao G, Guo Y, Chen Z, Wang Y, Yang C, Dudas A, Du Z, Liu W, Zou Y, Szabo E, Lee SC, Sims M, Gu W, et al. miR-203 functions as a tumor suppressor by inhibiting epithelial to mesenchymal transition in ovarian cancer. *J Cancer Sci Ther.* 2015; 7:34–43. 10.4172/1948-5956.1000322
41. Brabletz S, Brabletz T. The ZEB/miR-200 feedback loop--a motor of cellular plasticity in development and cancer? *EMBO Rep.* 2010; 11:670–77. <https://doi.org/10.1038/embor.2010.117>
42. Renthal NE, Chen CC, Williams KC, Gerard RD, Prange-Kiel J, Mendelson CR. miR-200 family and targets, ZEB1 and ZEB2, modulate uterine quiescence and contractility during pregnancy and labor. *Proc Natl Acad Sci USA.* 2010; 107:20828–33. <https://doi.org/10.1073/pnas.1008301107>
43. Wang G, Guo X, Hong W, Liu Q, Wei T, Lu C, Gao L, Ye D, Zhou Y, Chen J, Wang J, Wu M, Liu H, Kang J. Critical regulation of miR-200/ZEB2 pathway in Oct4/Sox2-induced mesenchymal-to-epithelial transition and induced pluripotent stem cell generation. *Proc Natl Acad Sci USA.* 2013; 110:2858–63. <https://doi.org/10.1073/pnas.1212769110>
44. Duan X, Fu Z, Gao L, Zhou J, Deng X, Luo X, Fang W, Luo R. Direct interaction between miR-203 and ZEB2 suppresses epithelial-mesenchymal transition signaling and reduces lung adenocarcinoma chemoresistance. *Acta Biochim Biophys Sin (Shanghai).* 2016; 48:1042–49. <https://doi.org/10.1093/abbs/gmw099>
45. Qu Y, Li WC, Hellem MR, Rostad K, Popa M, McCormack E, Oyan AM, Kalland KH, Ke XS. MiR-182 and miR-203 induce mesenchymal to epithelial transition and self-sufficiency of growth signals via repressing SNAI2 in prostate cells. *Int J Cancer.* 2013; 133:544–55. <https://doi.org/10.1002/ijc.28056>
46. Hur K, Toiyama Y, Okugawa Y, Ide S, Imaoka H, Boland CR, Goel A. Circulating microRNA-203 predicts prognosis and metastasis in human colorectal cancer. *Gut.* 2017; 66:654–65. <https://doi.org/10.1136/gutjnl-2014-308737>
47. Zhang A, Lakshmanan J, Motameni A, Harbrecht BG. MicroRNA-203 suppresses proliferation in liver cancer associated with PIK3CA, p38 MAPK, c-Jun, and GSK3 signaling. *Mol Cell Biochem.* 2017; 441:89–98. <https://doi.org/10.1007/s11010-017-3176-9>
48. Wan D, Shen S, Fu S, Preston B, Brandon C, He S, Shen C, Wu J, Wang S, Xie W, Chen B, Liya A, Guo Y, et al. miR-203 suppresses the proliferation and metastasis of hepatocellular carcinoma by targeting oncogene ADAM9 and oncogenic long non-coding RNA HULC. *Anticancer Agents Med Chem.* 2016; 16:414–23. <https://doi.org/10.2174/1871520615666150716105955>
49. Shao Y, Gu W, Ning Z, Song X, Pei H, Jiang J. Evaluating the Prognostic Value of microRNA-203 in Solid Tumors Based on a Meta-Analysis and the Cancer Genome Atlas (TCGA) Datasets. *Cell Physiol Biochem.* 2017; 41:1468–80. <https://doi.org/10.1159/000470649>
50. Saini S, Majid S, Yamamura S, Tabatabai L, Suh SO, Shahryari V, Chen Y, Deng G, Tanaka Y, Dahiya R. Regulatory Role of mir-203 in Prostate Cancer Progression and Metastasis. *Clin Cancer Res.* 2011; 17:5287–98. <https://doi.org/10.1158/1078-0432.CCR-10-2619>
51. Funamizu N, Lacy CR, Kamada M, Yanaga K, Manome Y. MicroRNA-203 induces apoptosis by upregulating Puma expression in colon and lung cancer cells. *Int J Oncol.* 2015; 47:1981–88. <https://doi.org/10.3892/ijo.2015.3178>
52. Jiang Q, Zhou Y, Yang H, Li L, Deng X, Cheng C, Xie Y, Luo X, Fang W, Liu Z. A directly negative interaction of miR-203 and ZEB2 modulates tumor stemness and chemotherapy resistance in nasopharyngeal carcinoma. *Oncotarget.* 2016; 7:67288–301. <https://doi.org/10.18632/oncotarget.11691>
53. Kim SK, Kim SY, Kim JH, Roh SA, Cho DH, Kim YS, Kim JC. A nineteen gene-based risk score classifier predicts prognosis of colorectal cancer patients. *Mol Oncol.* 2014; 8:1653–66. <https://doi.org/10.1016/j.molonc.2014.06.016>
54. Hur K, Toiyama Y, Takahashi M, Balaguer F, Nagasaka T, Koike J, Hemmi H, Koi M, Boland CR, Goel A. MicroRNA-200c modulates epithelial-to-mesenchymal transition (EMT) in human colorectal cancer metastasis. *Gut.* 2013; 62:1315–26. <https://doi.org/10.1136/gutjnl-2011-301846>



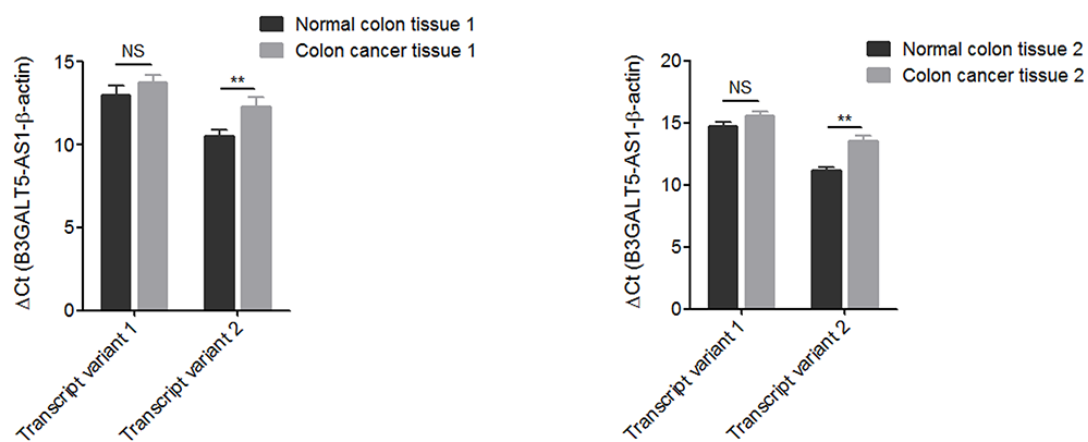


**Figure S1. The expression of transcript variants of B3GALT5-AS1 in colon cancer.** The expression of B3GALT5-AS1 in 2 pairs of primary colon cancer tissues and adjacent normal colonic epithelium tissues was measured using qRT-PCR. Data are displayed as mean  $\pm$  s.d. of three independent experiments. \*\* $P < 0.01$ , NS, not significant, Student's  $t$ -test.

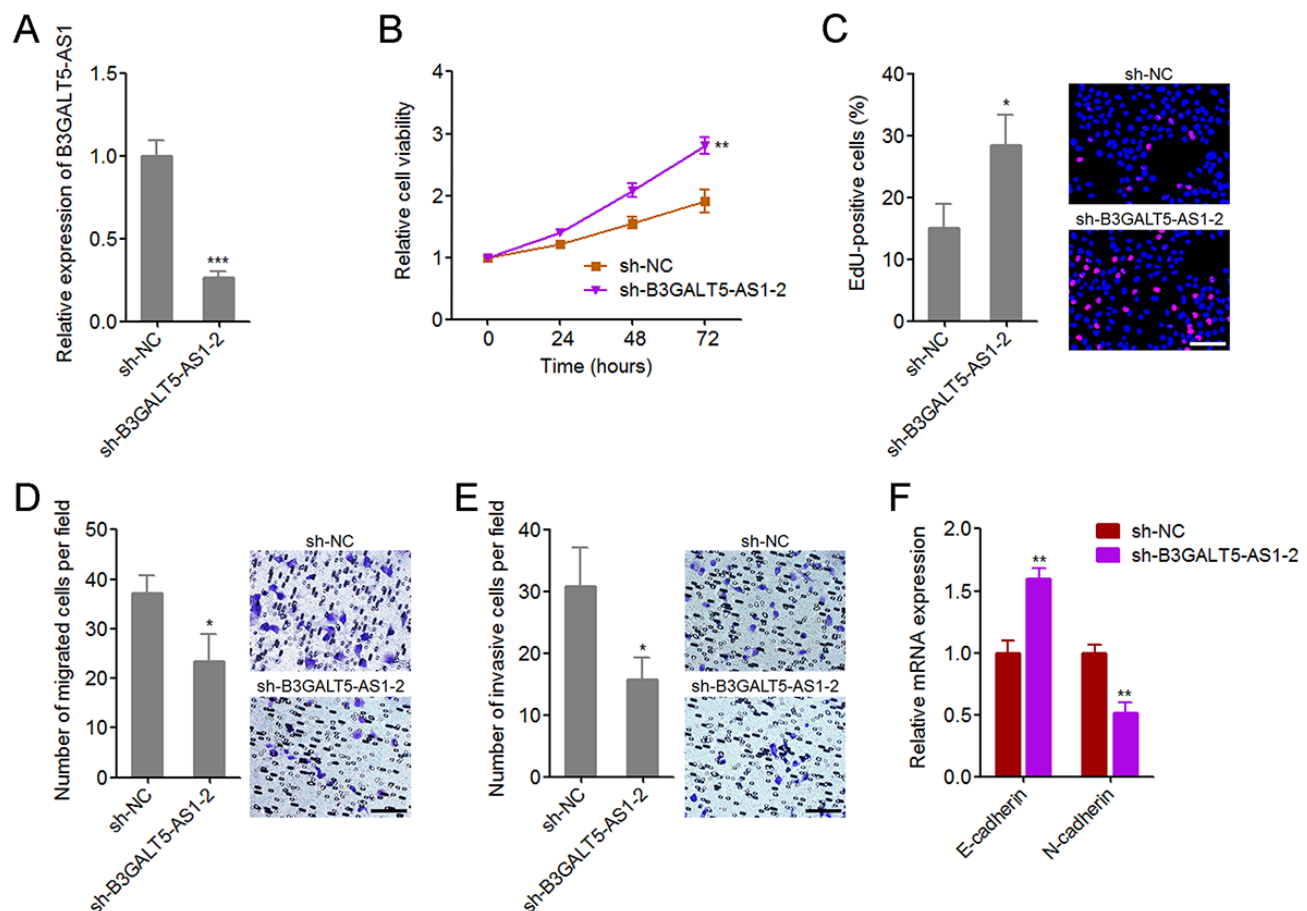


**Figure S2. Knockdown of B3GALT5-AS1 promoted proliferation and suppressed migration, invasion, and EMT of NCM460 cells.** (A) After transient transfection of B3GALT5-AS1 specific or control shRNA into NCM460 cells, the expression of B3GALT5-AS1 was detected using qRT-PCR. (B) After transient transfection of B3GALT5-AS1 specific or control shRNA into NCM460 cells, cell viability was detected using Glo cell viability assay. (C) After transient transfection of B3GALT5-AS1 specific or control shRNA into NCM460 cells, cell proliferation was detected using EdU incorporation assay. The red color indicates EdU-positive cells. Scale bars = 100  $\mu$ m. (D) After transient transfection of B3GALT5-AS1 specific or control shRNA into NCM460 cells, cell migration was detected using transwell migration assay. Scale bars = 100  $\mu$ m. (E) After transient transfection of B3GALT5-AS1 specific or control shRNA into NCM460 cells, cell invasion was detected using transwell invasion assay. Scale bars = 100  $\mu$ m. (F) After transient transfection of B3GALT5-AS1 specific or control shRNA into NCM460 cells, the expression of E-cadherin and N-cadherin was detected using qRT-PCR. Data are displayed as mean  $\pm$  s.d. of three independent experiments. \* $P$  < 0.05, \*\* $P$  < 0.01, \*\*\* $P$  < 0.001, Student's  $t$ -test.

A

Promoter of miRNAs	Predicted expect
miR-203	1e-30
miR-34a	5e-20
miR-200b/200a/429	0.32
miR-200c/141	0.097
miR-9	0.003
miR-29a	0.041

B

Range 1: 1060 to 1347 <a href="#">Graphics</a>					▼ Next Match
Score	Expect	Identities	Gaps	Strand	
122 bits(134)	1e-30	213/305(70%)	20/305(6%)	Plus/Plus	
Query 1062	CCTGCAATCCTAGTCTTTCAGAGGCCAAGGTGGGAAGATTCCTTGAAGCTCAGGAGTTCG				1121
Sbjct 1060	CCTGCAATCCAGCAGCTTTGGGAGGCCGAGGCGGTGGATAGCTTGAAGCTCAGGAGTTCG				1119
Query 1122	AGACCAGCCTGAACAACACACAAGACCTCGTATCTATGAAAAAATAAATAAATAAATAA				1181
Sbjct 1120	AGAACAGCC-----AACATGGCGAAAC-TC-TGCTCTTAAAAAATAAATAAATAAATAA				1170
Query 1182	TAGCTGCACACCTATTGGTGGCACACACCTGTGGTCCAGGTACTCGGGAGGCTGAGAT				1241
Sbjct 1171	TAGC-----CAGGTGTGGTGGTTTGTGTCTGTGGTCCAGGTACTCGGGAGGCTGAGAT				1224
Query 1242	GAGATCAT---TTGAGCCAGGAGATCAAGGTGCAATCAGCTGTGATCATGCCACTGCC				1298
Sbjct 1225	GGGAGAATCGCTTGAAGTGGGAGATGGAGGTTCAGCGAGCCAGATCGCACCAGTCCA				1284
Query 1299	CTCCAGCCTGGACAAGTGAAGGAGACCTGTCTCCAAAAAAGTAAATAAATAAATAAATAA				1358
Sbjct 1285	CTCCAGCCTGGGCAACACAGCAAGACTAGGTCTCAAAAAAAGAAAAAATAAATAAATAA				1342
Query 1359	AAAAA 1363				
Sbjct 1343	AAGAA 1347				

**Figure S3. The binding potential between B3GALT5-AS1 and promoters of miRNAs involved in EMT.** (A) The binding potential between B3GALT5-AS1 and promoters of miRNAs was predicted by Basic Local Alignment Search Tool (BLAST) (<https://blast.ncbi.nlm.nih.gov/Blast.cgi>). (B) Schematic outline of the predicted interaction sites between B3GALT5-AS1 (query) and the promoter of *miR-203* (subject).

# A four-methylated mRNA signature-based risk score system predicts survival in patients with hepatocellular carcinoma

Yu Wang<sup>1</sup>, Zhiping Ruan<sup>1</sup>, Sizhe Yu<sup>1</sup>, Tao Tian<sup>1</sup>, Xuan Liang<sup>1</sup>, Li Jing<sup>1</sup>, Wenyuan Li<sup>1</sup>, Xiao Wang<sup>1</sup>, LCL Xiang<sup>1</sup>, F.X. Claret<sup>2</sup>, Kejun Nan<sup>1</sup>, Hui Guo<sup>1</sup>

<sup>1</sup>Department of Medical Oncology, The First Affiliated Hospital of Xi'an Jiaotong University, Xi'an, Shaanxi, PR China

<sup>2</sup>Department of Systems Biology, The University of Texas MD Anderson Cancer Center, Houston, TX 77030, USA

**Correspondence to:** Hui Guo; **email:** [guohuihappy97@163.com](mailto:guohuihappy97@163.com)

**Keywords:** score system, nomogram, prognosis, methylation, hepatocellular carcinoma

**Received:** September 16, 2018    **Accepted:** December 19, 2018    **Published:** January 10, 2019

**Copyright:** Wang et al. This is an open-access article distributed under the terms of the Creative Commons Attribution License (CC BY 3.0), which permits unrestricted use, distribution, and reproduction in any medium, provided the original author and source are credited.

## ABSTRACT

Evidence suggests that altered DNA methylation plays a causative role in the pathogenesis of various cancers, including hepatocellular carcinoma (HCC). Thus, methylated differently expressed genes (MDEGs) could potentially serve as biomarkers and therapeutic targets in HCC. In the present study, screening four genomics profiling datasets (GSE62232, GSE84402, GSE73003 and GSE57956) enabled us to identify a total of 148 MDEGs. A signature was then established based on the top four MDEGs (BRCA1, CAD, CDC20 and RBM8A). Taking clinical variables into consideration, we constructed a risk score system consisting of the four-MDEG signature and the patients' clinical features, which was predictive of prognosis in HCC. The prognostic value of the HCC risk score system was confirmed using TCGA HCC samples. The scores were then used to construct a nomogram, performance of which was evaluated using Harrel's concordance index (C-index) and a calibration curve. The signature-based nomogram for prediction of overall survival in HCC patients exhibited good performance and was superior to traditional staging systems (C-index: 0.676 vs 0.629,  $P < 0.05$ ). We have thus established a novel risk score system that is predictive of prognosis and is a potentially useful guide for personalized treatment of HCC patients.

## INTRODUCTION

Hepatocellular carcinoma (HCC) is the fifth most common cancer in China, where it is estimated to have killed 140 million people [1]. The leading cause of HCC is chronic infection with a hepatitis virus, alcohol abuse, exposure aflatoxin, tobacco smoking and diabetes [2]. Although there are a large number of studies examining HCC formation and progression, the precise mechanism underlying its pathogenesis remains unclear [3]. Moreover, the rate of early diagnosis of HCC is low; most patients are diagnosed with advanced disease. TNM stage at diagnosis is still regarded as the best predictor of survival [4]. However, because HCC is a

highly heterogeneous malignancy, the prognoses of patients with the same stage disease may differ due to inherent clinical and molecular diversities [5]. Therefore, new valid and reliable prognostic and predictive biomarkers are needed to improve risk prediction and offer better information for guiding personalized therapy.

Alterations in epigenetic modifications such as DNA methylation, histone acetylation and RNA interference are important heritable contributory factors in tumor development [6]. For example, altered DNA methylation is thought to contribute to the pathogenesis of a variety of cancers, including HCC [7]. However,

multiple studies indicate that a variety of genes are aberrantly hyper- or hypomethylated in HCC [8], but a comprehensive profile of the pathways within the interaction network remains to be elucidated. Several genes encoding epigenetic regulatory proteins, including EZH2 and HBV, have been shown to be involved in hepatocellular malignancy [9-10]. In addition, evidence now suggests that methylated mRNA may be a valid predictor of HCC [11]. But to the best of our knowledge, there are no prior studies examining methylated differentially expressed genes (MDEGs) on a genome-wide scale and focusing on predicting prognosis in HCC. In the present study, therefore, we comprehensively analyzed high-dimensional data from the Gene Expression Omnibus (GEO) and The Cancer Genome Atlas (TCGA) to build a novel MDEG-based risk score system that is predictive of prognosis and could potentially guide personalized therapy for HCC patients.

## RESULTS

### Identification and enrichment analysis of MDEGs in HCC

The flowchart for this study is shown in Figure 1. GSE62232, GSE84402, GSE73003 and GSE57956 comprised the training cohort downloaded from the GEO

database. The mRNA expression datasets GSE62232 and GSE84402 were calculated using the limma package in R (v 3.5.1). GSE62232 included 81 HCC and 10 normal liver samples, while, GSE84402 included 14 paired HCC and non-tumor samples (Affymetrix Human Genome U133 plus 2.0 platform). The GEO2R online analysis tool was used to calculate the datasets for the methylation difference profiles GSE73003 and GSE57956. The GSE73003 series consisted of 20 paired HCC and non-tumor samples, while GSE57956 consisted of 59 paired HCC and non-tumor samples (Illumina Human Methylation27 BeadChip). With cut-off criteria of  $P < 0.05$  and  $|\log_2FC| > 1$ , a total of 130 hypomethylation-high expression genes were detected by overlapping 3476 hypomethylated genes (4869 in GSE57956, 3748 in GSE73003) and 1945 upregulated genes (3972 in GSE62232, 3213 in GSE84402). Similarly, 18 hypermethylation-high expression genes were detected by overlapping 1689 hypermethylated genes (2651 in GSE67956, 1881 in GSE73003) and 338 downregulated genes (583 in GSE62232, 745 in GSE73003) (Figure 2A). To confirm that the  $P$  value and  $|\log_2FC|$  conform to logic using a different test, a representative volcano plot was constructed for GSE84402 (Figure 2B).

To obtain a deeper understanding of MDEGs, enrichment analysis with the Database for Annotation,

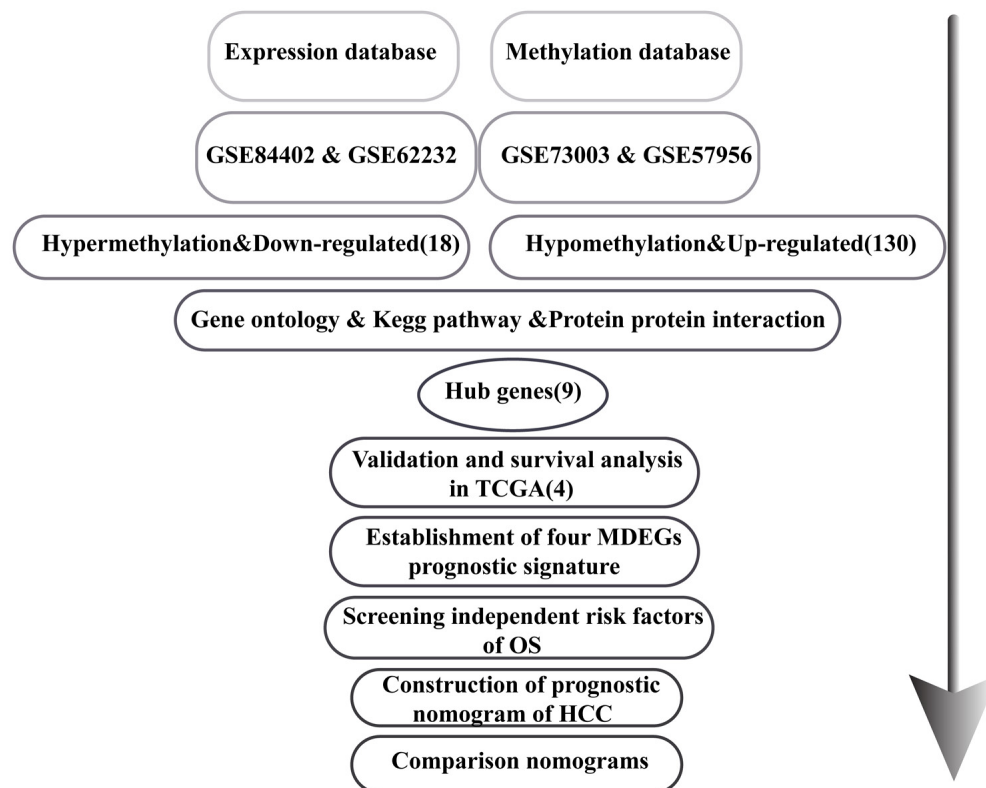


Figure 1. Flowchart of the study.



Visualization and Integrated Discovery (DAVID, <https://david.ncifcrf.gov/>) was used to elucidate biological function. The top significant terms emerging from the gene ontology enrichment analysis are shown in Figure 2C. MDEGs were enriched in “biological processes of cellular response to DNA damage stimulus,” “liver development,” “viral process,” “angiogenesis,” and “cell cycle.” Regarding molecular function, MDEGs showed enrichment in “protein binding,” “ATP binding,” “enzyme binding,” and “protein kinase activity.” Enrichment of cell components was mostly “nucleus region,” which suggests MDEGs may play an important role in transcription in HCC. Kyoto Encyclopedia of Genes and Genomes (KEGG) analysis suggested that MDEGs were significantly enriched in pathways in “cancer,” “leukocyte transendothelial migration,” and “chemokine signaling pathway.” (Figure 2D).

## Identification of hub MDEGs and their clinical value in HCC

To identify the connections among MDEGs, a protein-protein interaction (PPI) network for MDEGs was constructed using STRING protein databases (Figure 3A). The top hub genes were CDC20, CDKN3, GNAI1, RBM8A, BRCA1, CAD, ACLY, MMP9, and MAPK1 based on a combined score  $>0.7$  and connection numbers  $>8$ . To verify the hub genes, 371 HCC and 50 non-tumor samples were downloaded from TCGA as a validation cohort. Within this group, the expression and methylation values of most hub genes were consistent with the training group, with the exception of MMP9 (Figure 3B, C). We then further investigated the association between gene methylation and expression. The results showed a mild or moderate negative correlation,

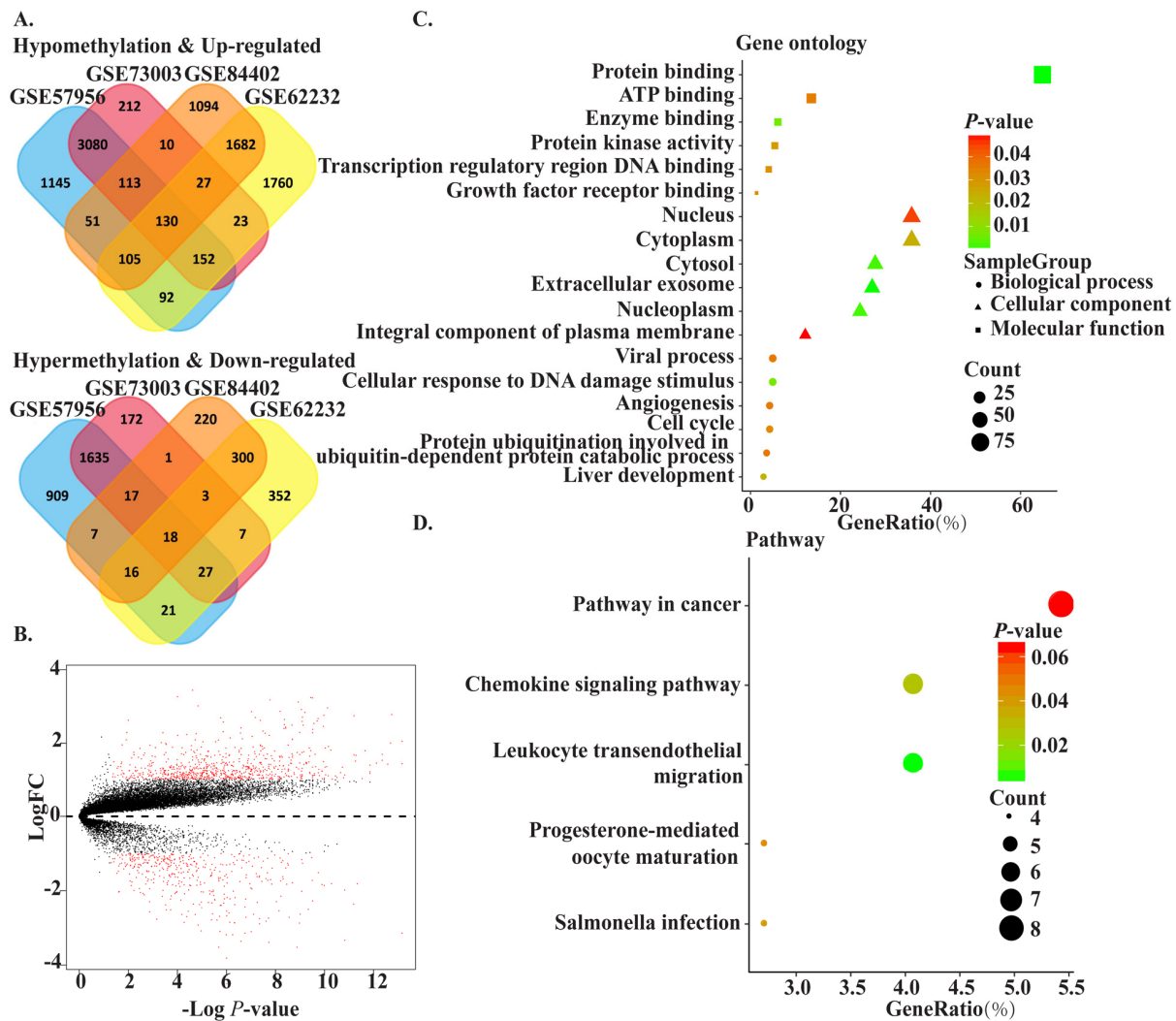


**Figure 2. The methylated-differentially expressed genes identification and function.** (A) Venn of methylated-differentially expressed genes in gene expression datasets (GSE62232, GSE84402) and gene methylation datasets (GSE73003, GSE57956). (B) The volcano plot of GSE84402. Log<sub>2</sub> (FC) vs. -log<sub>10</sub> (p value) for differentially expressed mRNA. Red dot represents significant mRNA ( $\log_2|FC|>1$ ,  $P<0.05$ ). (C) The significant enriched gene ontology of MDEGs. (D) The significant enriched KEGG pathways of MDEGs.

which suggests methylation leads to decreased gene expression (Figure 3D-E). Expression of CDC20, CDKN3, GNAI1, RBM8A, BRCA1, and CAD showed a significant negative correlation with expression ( $p < 0.05$ ), whereas expression of ACLY, MMP9 and

MAPK1 showed no correlation or was positively correlated. And results also were verified in MethHC, a database of DNA Methylation and gene expression in Human Cancer (<http://methhc.mbc.nctu.edu.tw/php/index.php>) (Supplementary Figure 1).

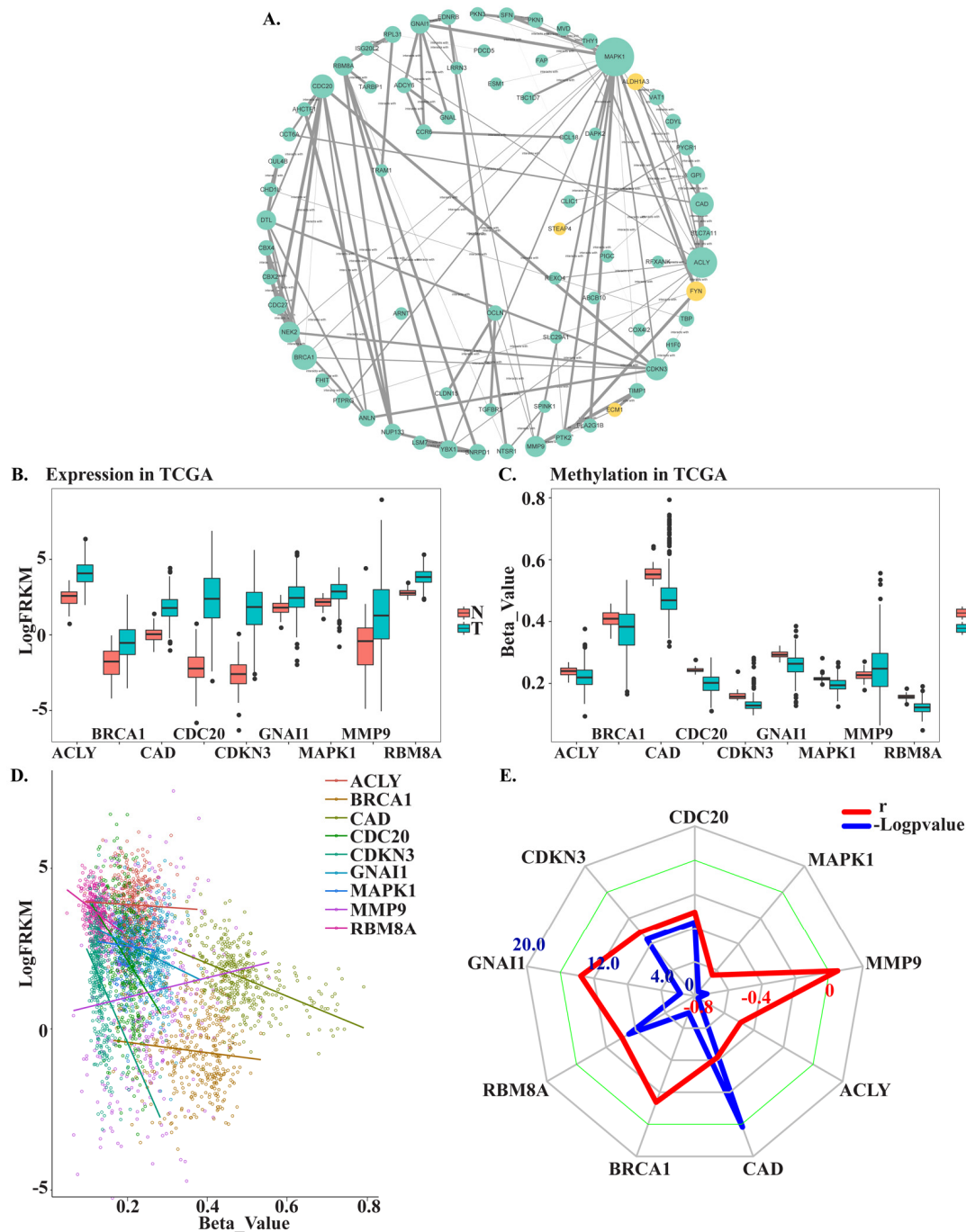


**Figure 3. Screening and verifying hub MDEGs.** (A) Protein-protein interaction network of MDEGs. Green dot represents hypo methylation-high expression gene. Yellow dot represents hyper methylation- low expression. The size of dot was decided by the connection degree of gene and the width of line between genes was decided by connectivity between two genes. (B) Expression of hub genes in TCGA. (C) Methylation of hub genes in TCGA. Beta-Value represents ratio of methylation. T represents tumor tissue, N represents normal tissue. (D) Correlation of expression and methylation of hub genes. (E) Radar map of hub genes correlation. Red line represents  $r$  and blue line represents  $-\text{Logpvalue}$ .

To identify hub MDEGs with potential prognostic value, we used the Kaplan-Meier method with the Log-rank test to evaluate the relation between expression of the aforementioned genes and the patients' overall survival (OS). Details of the clinical characteristics are presented in Supplementary Table 1. We found that OS was negatively related to expression of CDC20, RBM8A, BRCA1 and CAD, but had no relation with CDKN3 or GNAI1. Ultimately, the top four hub MDEGs were identified: CDC20, RBM8A, BRCA1 and

CAD. To further confirm the results, we verified the four hub genes in Gene Expression Profiling Interactive Analysis (GEPIA, <http://gepia.cancer-pku.cn/>) (Supplementary Figure 2). Receiver operating characteristic curve (ROC) analysis showed that all four of these genes have high sensitivity and specificity, which suggests high diagnostic value for distinguishing HCC patients from healthy individuals (Figure 4E). These four MDEGs may thus be useful as biomarkers for early diagnosis of HCC.

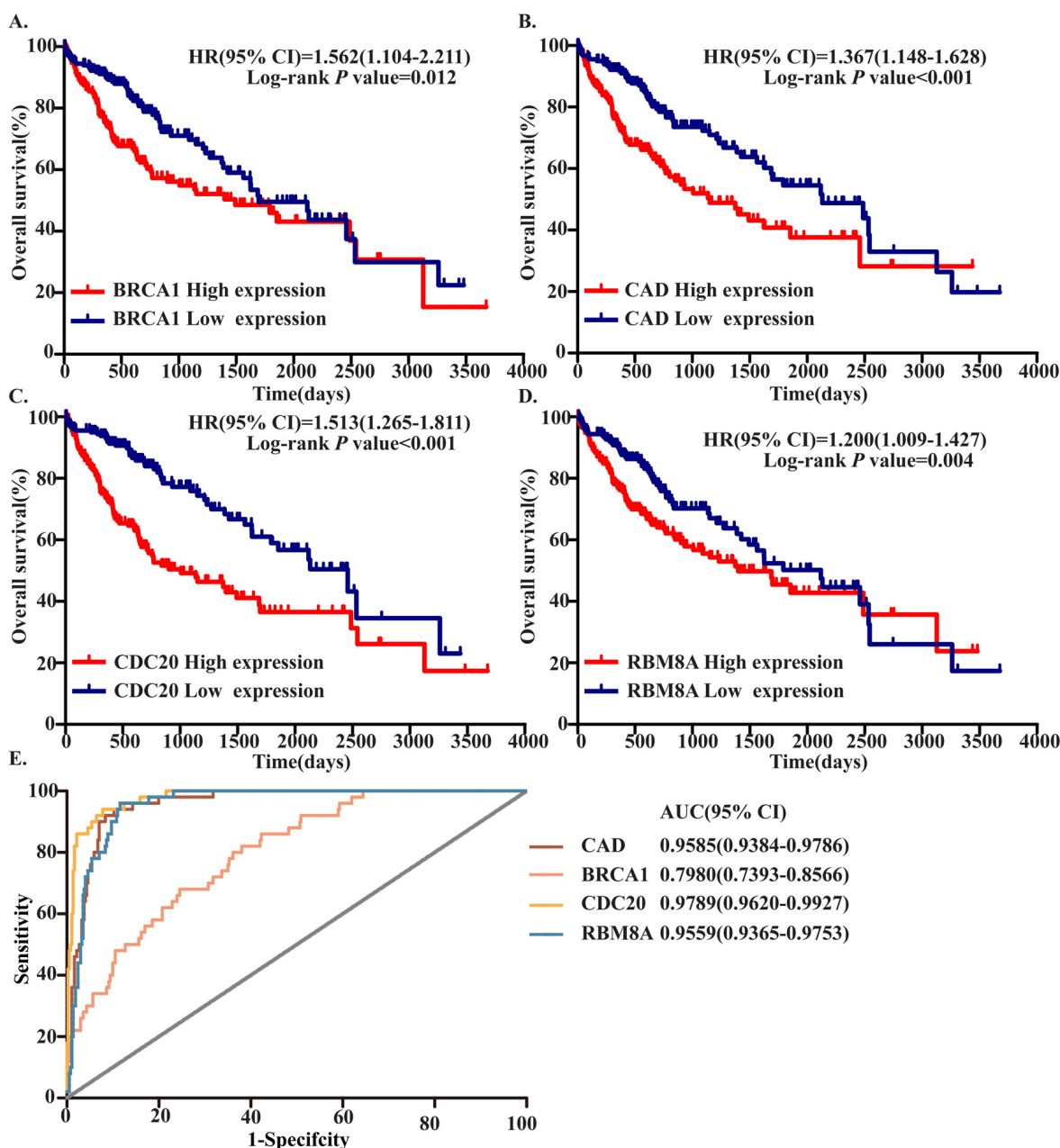


**Figure 4. Four hub MDEGs were associated with overall survival in HCC patients by using Kaplan-Meier curve and Log-rank test.** The patients were stratified into high expression group and low expression group according to median expression of each mRNA. (A) BRCA1; (B) CAD; (C) CDC20; (D) RBM8A. (E) ROC curves of the 4 hub MDEGs in HCC. The X axis shows false positive rate, presented as "1-Specificity". The Y axis indicates true positive rate, shown as "Sensitivity".

## Prognostic value of a four-MDEG signature risk score in HCC

To assess the prognostic value of CDC20, RBM8A, BRCA1 and CAD, we constructed a prognostic signature by integrating the expression of these four MDEGs using a regression coefficient. We then calculated a risk score for each patient and ranked them based on increasing score, after which patients were classified into a high-risk ( $n = 179$ ) or a low risk ( $n = 179$ ) group based on the median risk score. The risk score distribution, survival status, and expression profile of the four prognostic MDEGs are shown in Figure 5A. OS and progression-free survival (PFS) rates among patients were 60.7% and 53.3%, respectively, in the high-risk group, as compared to 69.2% and 67.2% in the low-risk group (Figure 5B, C). The hazard ratio (HR) of

high-risk group versus low-risk group was 1.515 for OS ( $P = 0.001$ , 95% confidence interval (CI) = 0.8075-2.222) and 2.559 for PFS ( $P < 0.001$ , 95%CI = 1.891-3.227). Thus, patients in the high-risk group had significantly poorer OS and PFS than patients in the low-risk group (Figure 5D, E).

A ROC analysis of the predictive efficiency of the four-MDEG signature suggested it had good performance with respect to both death and progression prediction (Figure 5F). Taking into consideration the patients' clinical features, including age, gender, clinical stage, T stage, grade, adjacent hepatic tissue inflammation, and HCC risk factors (virus infection, alcohol abuse, non-alcoholic fatty liver disease, hemochromatosis, alpha-1 antitrypsin deficiency), univariate and multivariate Cox regression analysis were used to assess the signature

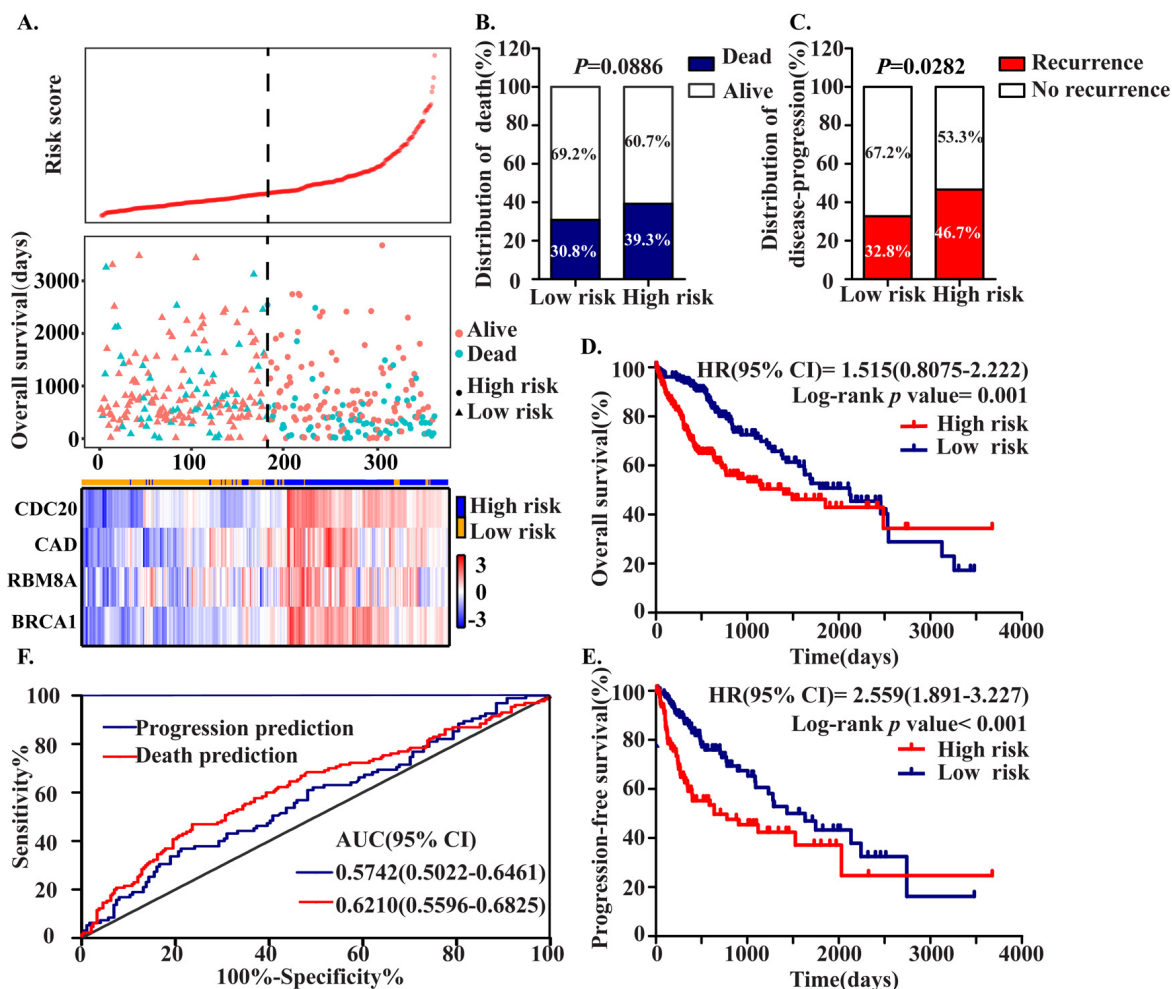


**Figure 5. Construction of the Four MDEGs signature of HCC.** The patients were stratified into high risk group and low risk group based on median of risk score. (A) Risk score distribution of HCC patients, Survival status of each patient and Expression heatmap of the four hub MDEGs corresponding to each sample above. Red: high expression; Blue: low expression. (B, C) The distribution of death (B) and disease-progression (C) in high and low risk group. (D, E) Kaplan-Meier estimates of the overall survival (D) and progression-free survival (E) time of patients using the four MDEGs signature based risk score. (F) The ROC curve of the four MDEGs signature.



(high-risk vs. low-risk) with respect to OS. In the univariate analysis, clinical stage (HR = 2.229,  $P < 0.001$ ), T stage (HR = 2.534,  $P < 0.001$ ), HCC risk factors (HR = 0.631,  $P = 0.011$ ), fibrosis (HR = 0.542,  $P = 0.002$ ) and the four-MDEG signature (HR = 4.467,  $P < 0.001$ ) were all significantly associated with OS in HCC patients. To integrate all independent risk factors affecting OS for construction of a HCC prognostic nomogram, significant clinicopathological factors from the univariate analyses were entered into multivariate COX regression analyses. The results indicated that the four-MDEG signature (HR = 2.022,  $P < 0.001$ ) was a significant independent factor of OS, as were T stage (HR = 2.149,  $P < 0.001$ ) and HCC risk factors (HR = 0.651,  $P = 0.019$ ) (Table 1).

#### Establishment of a nomogram for OS prediction in HCC

To provide a clinically associated quantitative method that could be used to predict the probabilities of 3- and 5-year OS in HCC, a prognostic nomogram was established in which the score integrated the three indepen-

dent prognostic factors, T stage, HCC risk factors and the four-MDEG signature (Figure 6A). Harrel's concordance index (C-index) for OS prediction was 0.676. The calibration curves for the nomogram for the 3- and 5- year OS rates showed good agreement between the prediction and the actual observation (Figure 6B). Each patient for whom there was complete clinical information about T stage, HCC risk factors, and the four-MDEG signature would obtain a Nomogram score reflecting total points. Using the Nomogram score, patients were divided into three risk groups based on the tertiles, which had cut-off values of 28.50 and 44.60. From KM analysis of the TCGA dataset, significant differences were observed between the high-, intermediate- and low-risk groups ( $P = 0.0003$ ) (Figure 6C).

#### Comparison of predictive accuracy between the nomogram and a single independent factor

The TNM stage system is regarded as the best predictor of survival. Moreover, we found that T stage was an independent prognostic factor for OS in HCC. The predictive power of the nomogram for HCC prognosis

**Table 1. Univariate/multivariate COX regression analyses of clinicopathologic factors associated with OS.**

Variables	Univariate analysis		Multivariate analysis	
	HR(95%CI)	P	HR(95%CI)	P
Age( $\geq 65$ vs. $< 65$ )	1.265(0.893-1.791)	0.235		
Gender(Male vs. Female)	0.817(0.573-1.164)	0.262		
Clinical stage( III +IV vs. I+II)	2.229(1.559-3.188)	$<0.001^*$		
Grade(G3+G4 vs. G1+G2)	1.113(0.774-1.601)	0.564		
T stage(T3+T4 vs. T1+T2)	2.534(1.783-3.601)	$<0.001^*$	2.149(1.499-3.081)	$<0.001^*$
AFP( $<25$ ng/ml vs. $\geq 25$ ng/ml)	1.002(0.697-1.442)	0.991		
Adjacent hepatic tissue inflammation( Yes vs. No)	0.699(0.468-1.044)	0.699		
Fibrosis(Yes vs. No)	0.542(0.366-0.803)	0.002*		
Child-Pugh(A vs. B+C)	1.141(0.578-2.251)	0.703		
BMI( $\geq 25$ vs $<25$ )	0.733(0.515-1.043)	0.084		
Family history(Yes vs. No)	1.225(0.858-1.748)	0.264		
HCC risk factors(Yes vs. No)	0.631(0.443-0.898)	0.011*	0.651(0.454-0.933)	0.019*
Four MDEGs signature (high risk vs. low risk)	4.467(1.995-10.002)	$<0.001^*$	2.022(1.486-2.753)	$<0.001^*$

Abbreviations: OS, overall survival; HR, hazard ratio; 95% CI, 95% confidence interval.

\*Statistically significant; AFP, Alpha-fetoprotein; BMI, body mass index.



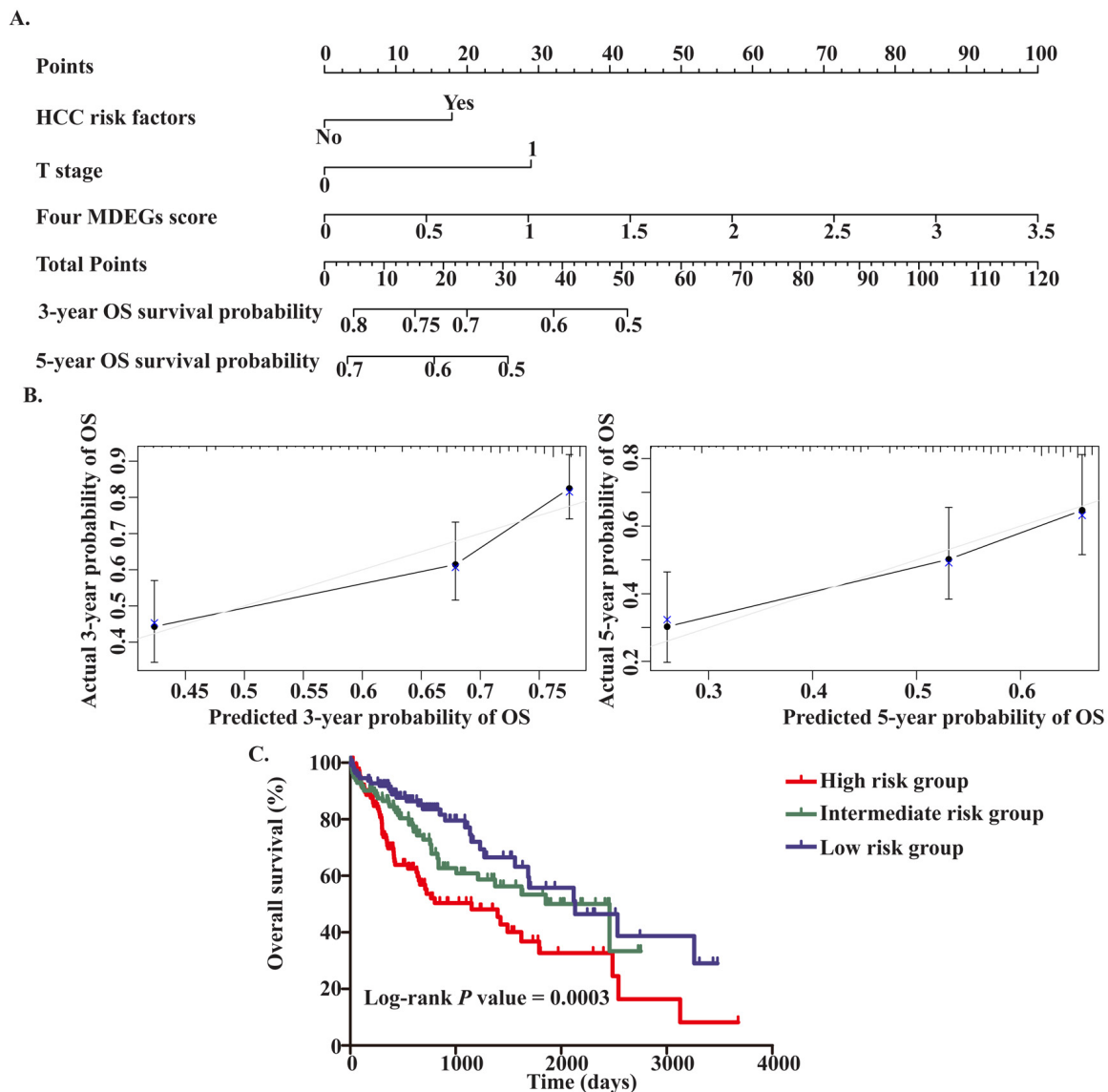


**Figure 6. Establishment of the OS nomogram for HCC patients.** (A) Nomogram for predicting OS of HCC. There are three components in this nomogram: the four MDEGs score, HCC risk factor and T stage. Each of them generates points according to the line drawn upward. And the total points of the three components of an individual patient lie on "Total Points" axis which corresponds to the probability of 3-year and 5-year OS rate plotted on the two axes below. (B) Calibration plots of the nomogram for predicting OS rate at 3 year (Left) and 5 years (Right). The predicted and the actual probabilities of OS were plotted on the x- and y-axis, respectively. (C) Kaplan-Meier curves of three risk subgroups stratified by the total points the nomogram gives.

was compared with that of T stage. The C-index for OS prediction based on T stage was 0.629, which was significantly lower than the C-index for the nomogram (0.676,  $P < 0.05$ ). This suggests our nomogram is a more accurate predictor of OS in HCC than conventional staging systems and is potentially valuable for predicting survival of HCC patients.

## DISCUSSION

A valid and accurate molecule-based method for identifying patients who have a poor prognosis is ur-

gently needed to optimize their individual therapy. Therefore, effective and credible biomarkers and genetic signatures that can serve as prognostic predictors and treatment targets are critically needed for HCC. In the last decade, methylation has come to be recognized as an important epigenetic regulator of gene expression in eukaryotes, and it is now well established that methylation, especially DNA methylation, is crucially involved in multiple cancers, including HCC [12, 13]. Nishida showed that alterations in DNA methylation are a common feature of hepatocarcinogenesis [14]. Although some studies have identified

MDEGs in HCC [15, 16], their predictive value for HCC patients has not been systematically investigated until now. To our knowledge, this is the first study to develop a MDEG-based risk score that is predictive of prognosis in HCC.

We used methylation and expression microarrays with GEO databases to screen for MDEGs and were able to obtain a set of MDEGs through *in silico* analysis. Enrichment analysis of the MDEGs suggested they were involved in key biological processes, including DNA damage, viral processes, angiogenesis, and cell cycling. Given that hepatitis virus is a main cause of HCC, the presence of DNA damage due to integration of the virus genome into the host DNA is reasonable [17]. Also reasonable is the involvement of angiogenesis, since HCC is a highly vascular tumor. In addition, KEGG enrichments suggested that significantly enriched pathways include chemokine signaling pathways, which suggests that inflammation and immunity are critical factors in the pathogenesis, progression and metastasis of HCC [18]. Chemokine signaling reportedly influences HCC invasion and/or metastasis through effects on the tumor microenvironment [19, 20]. Evidence indicates, for example, that chemokines such as CCL5, CCL7, CXCL8 act via CCRs on myeloid-derived suppressor cells (MDSCs) to form an inhibitory tumor microenvironment that promotes tumor pathogenesis, progression and resistance [21-23].

Based on PPI analysis, we identified nine hub genes, which were verified and analyzed in a validation cohort from TCGA. Four of these hub genes, which were significantly associated with OS of HCC patients, were ultimately selected. Earlier research has consistently demonstrated that upregulation of BRCA1, CDC20, RBM8A and CAD promotes progression, invasion, metastasis and chemoresistance in HCC [24-27]. While the efficacy of any single marker is limited, a multiple-marker signature could have greater diagnostic and prognostic value. We therefore constructed a four-MDEG signature that was an independent prognostic factor for HCC patients. This signature was predictive of both OS and PFS. If applied, relatively minor examination using our risk score system could help identify high- and low-risk HCC patients and provide useful information that could aid in selecting a therapeutic strategy.

To increase the accuracy of the prediction of prognosis, both genetic and clinically-related variables were integrated into the nomogram. Ultimately, the OS nomogram included the four-MDEG signature, T stage and HCC risk factors. The nomogram for HCC performed well when used to predict OS, and its pre-

dictive ability was verified using a C-index and a calibration curve. Indeed, the nomogram provides greater predictive accuracy for OS than traditional systems. As regards the prognostic signature or nomogram, if we are able to put it into clinical practice in the future, we anticipate being able to identify patients at high-risk of cancer-related death before treatment, and recommend a more aggressive therapeutic strategies with dynamic surveillance. However, there are limitations to our study. First, whether the prognostic signature or nomogram can be applied to patients must be confirmed in larger groups of HCC patients. Second, the molecular mechanism of the four MDEGs in HCC remains to be explored further.

In summary, we have developed a novel four-MDEG expression-based risk score system for objectively and accurately predicting survival and prognosis in HCC patients. In addition, the MDEG signature could also shed new light on the role of methylation in the pathogenesis and progression of HCC, which may provide information helpful for selection of therapeutic strategies. The four MDEGs could potentially serve as biomarkers and therapeutic targets for dynamic surveillance and treatment of HCC patients.

## MATERIALS AND METHODS

### Data processing

The raw data and clinical information were download from the GEO (<https://www.ncbi.nlm.nih.gov/geo/>) and TCGA (<https://cancergenome.nih.gov/>). Gene methylation profiling of the GSE73003 and GSE57956 datasets was conducted using the GPL8490 platform (Illumina Human Methylation27 BeadChip), which included 27,578 highly informative CpG sites and more than 14476 genes (<http://www.illumina.com/pages.ilmn?ID=243>). Gene expression profiling of the GSE84402 and GSE62232 datasets was conducted using the GPL570 platform (Affymetrix Human Genome U133 plus 2.0 Array), which included 54675 unique probes and tested more than 23517 genes (<http://www.affymetrix.com/support/technical/byproduct.affx?product=hg-u133-plus>). The GSE73003 series consisted of 20 paired HCC and non-tumor samples. The GSE57956 series consisted of 59 paired HCC and non-tumor samples. The GSE84402 series included 14 paired HCC and non-tumor samples. And the GSE62232 series included 81 HCC and 10 normal liver samples. From TCGA, we downloaded 371 HCC and 50 non-tumor samples. The mRNA-seq data were preprocessed and submitted for analysis as the upper quantile normalized FPKM values. GEO2R was used to screen for genes differentially methylated between tumor and non-tumor samples. The differentially

expressed genes were identified using the limma package in R. Values of  $P < 0.05$  and  $|FC| \geq 1$  were considered significant. Finally, hypomethylation-high expression genes were detected by overlapping hypomethylated and upregulated genes; similarly, hypermethylation-low expression genes were detected by overlapping hypermethylated and downregulated genes.

### Functional and pathway enrichment analysis

Functional annotations in MDEGs were done using The Database for Annotation, Visualization and Integrated Discovery (DAVID; <https://david.ncifcrf.gov/>), which enriched gene oncology and pathways. Gene oncology involved three categories: cellular components, molecular function, and biological processes. Pathway enrichment was carried out using the Kyoto Encyclopedia of Genes and Genomes (KEGG, <https://www.kegg.jp/>), which contains information about genomes, biological pathways, diseases, and chemical substances. The criterion for significant enrichment of biological processes and pathways was  $P = 0.05$ .

### Hub MDEG screening and verification

STRING protein databases (<https://string-db.org/>) were used to evaluate interactive relationships among the MDEGs. We used Cytoscape software to construct a network based on the STRING results. Combined scores  $> 0.7$  and connection numbers  $> 8$  were deemed to indicate hub genes. To confirm the results, the hub MDEGs were validated in TCGA. The Pearson correlation test was used to assess the relationship between hub gene methylation and expression in HCC.

### Formulation of MDEG signatures and association of signatures and clinical features

ROC curve analysis was used to evaluate the diagnostic effectiveness of hub MDEGs. The prognostic value of hub MDEGs were evaluated using the Kaplan-Meier method with the Log-rank test. Hub MDEGs related to OS were considered to be prognostic. Using the combination of weighted MDEG expression values, independent hub MDEG biomarkers were integrated into a MDEG signature using a risk scoring method as shown in the following equation: Risk Score (patient) =  $\sum_{i=1}^n \frac{\text{expression}(mRNA_i)}{\text{median}} * \text{coefficient}(mRNA_i)$ . Here, Risk Score (patient) is a MDEG signature risk score for a HCC patient. In addition,  $mRNA_i$  represents the  $i$ th prognostic mRNA, while expression ( $mRNA_i$ ) is the expression value of  $mRNA_i$  for the patient. Coefficient ( $mRNA_i$ ) is the regression coefficient of  $mRNA_i$ , which represents the contribution of  $mRNA_i$  to the prognostic risk score. Based on the risk score, patients can be assigned to a high-risk or low-risk group. Subsequently,

a risk score system was constructed, and the median risk score was regarded as the cutoff point. HCC patients were then divided into high- and low-risk groups. Kaplan-Meier survival curves were calculated to compare survival and recurrence risk between the high- and low-risk groups.

### Statistical analysis

To identify independent predictors of OS in HCC, univariate Cox regression analysis was performed to evaluate the prognostic value of signatures with a threshold value of 0.2. Multivariate Cox regression analyses were conducted using Forward LR. Hazard ratios (HRs) and 95% confidence intervals (CIs) were computed based on the Cox regression analysis. A nomogram was constructed based on the results of the multivariate Cox regression analyses using rms version 3.5.1 (<http://www.r-project.org/>). The performance of the nomogram was assessed using Harrel's concordance index (C-index) and comparing the predicted and actual probabilities for OS. Bootstraps with 1,000 resamples were used for these activities. Comparisons between the nomogram and other staging systems were made using the rcorr.cens package in Hmisc and were evaluated using the C-index. Each patient received the total points from the nomogram (Nomo-score). KM curve analysis was performed to evaluate the performance of the nomogram by dividing patients into high-, intermediate- and low-risk groups using tertiles of the Nomo-scores as cut-off points. Values of  $P < 0.05$  were considered significant. Statistical analysis was performed using the IBM SPSS Statistics software program version 22.0 (IBM Corp., NY, USA).

### Abbreviations

MDEG: methylated differently expressed gene; HCC: hepatocellular carcinoma; OS: overall survival; PFS: progression-free survival; HR: hazard ratio; CI: confidence interval; KM curve: Kaplan-Meier curve.

### AUTHOR CONTRIBUTIONS

Hui Guo and Yu Wang designed the research and performed analysis; Zhiping Ruan, Sizhe Yu, Tao Tian and Xuan Liang collected and analyzed data and constructed figures; Li Jing, Wenyuan Li, Xiao Wang, LCL Xiang performed statistical analyses; F.X. Claret and Kejun Nan guided experiments; Hui Guo and Yu Wang drafted and revised the manuscript.

### ACKNOWLEDGEMENTS

This work benefited from the Gene Expression Omnibus (GEO) database and the Cancer Genome Atlas

(TCGA) database. We were grateful to the access to the resources and the efforts of the staff to expand and improve the two databases.

## CONFLICTS OF INTEREST

The authors declare that there are no financial or other relationships that might lead to a conflict of interest of the present article.

## FUNDING

This study was supported in part by grant 81672432 from the National Natural Science Foundation of China (to H.G).

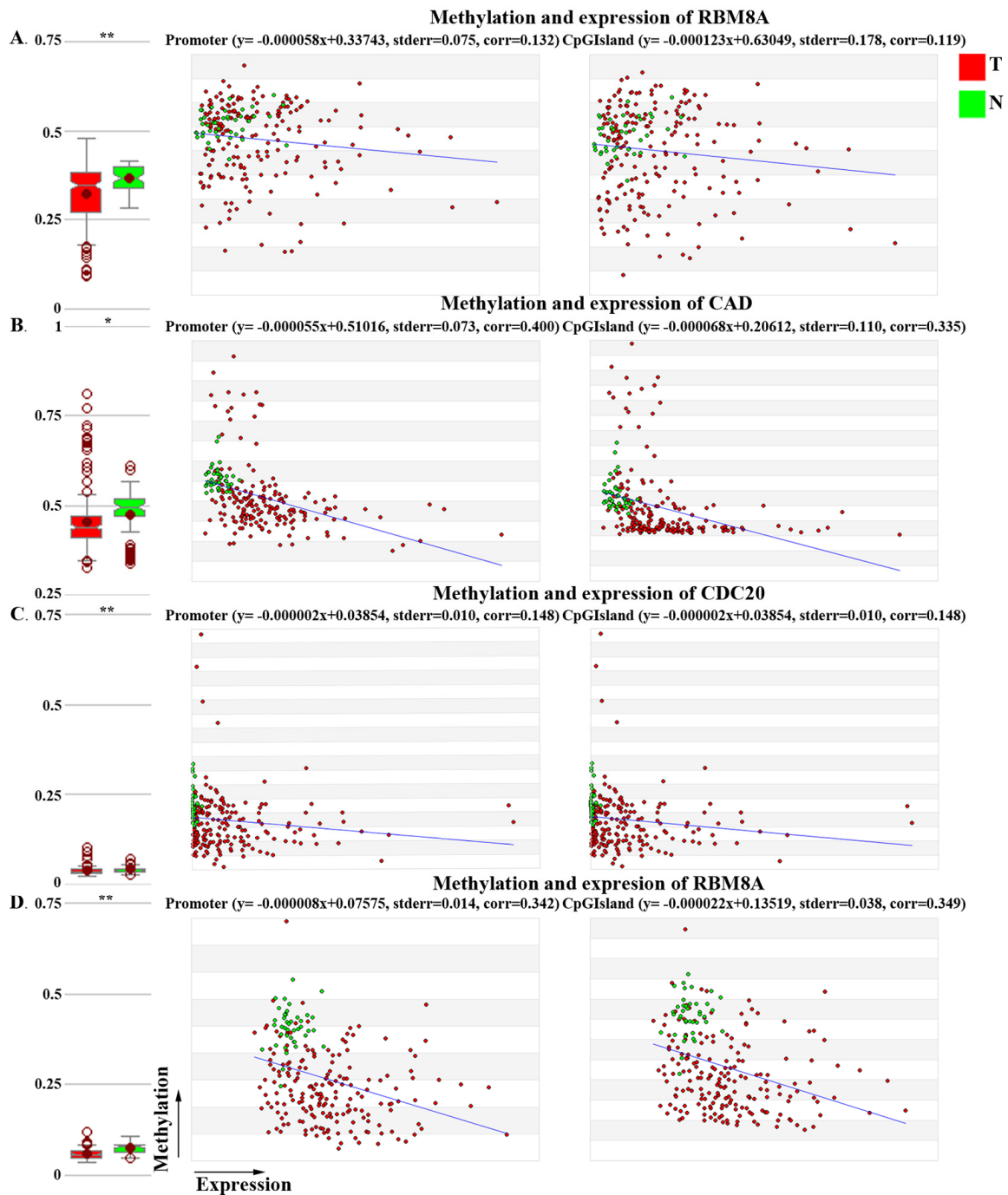
## REFERENCES

1. Siegel RL, Miller KD, Jemal A. Cancer Statistics, 2017. *CA Cancer J Clin*. 2017; 67:7–30. <https://doi.org/10.3322/caac.21387>
2. Forner A, Llovet JM, Bruix J. Hepatocellular carcinoma. *Lancet*. 2012; 379:1245–55. [https://doi.org/10.1016/S0140-6736\(11\)61347-0](https://doi.org/10.1016/S0140-6736(11)61347-0)
3. Guo H, Jing L, Cheng Y, Atsaves V, Lv Y, Wu T, Su R, Zhang Y, Zhang R, Liu W, Rassidakis GZ, Wei Y, Nan K, Claret FX. Down-regulation of the cyclin-dependent kinase inhibitor p57 is mediated by Jab1/Csn5 in hepatocarcinogenesis. *Hepatology*. 2016; 63:898–913. <https://doi.org/10.1002/hep.28372>
4. Amin MB, Greene FL, Edge SB, Compton CC, Gershenwald JE, Brookland RK, Meyer L, Gress DM, Byrd DR, Winchester DP. The Eighth Edition AJCC Cancer Staging Manual: Continuing to build a bridge from a population-based to a more "personalized" approach to cancer staging. *CA Cancer J Clin*. 2017; 67:93–99. <https://doi.org/10.3322/caac.21388>
5. Bruix J, Gores GJ, Mazzaferro V. Hepatocellular carcinoma: clinical frontiers and perspectives. *Gut*. 2014; 63:844–55. <https://doi.org/10.1136/gutjnl-2013-306627>
6. Chen Z, Li S, Subramaniam S, Shyy JY, Chien S. Epigenetic Regulation: A New Frontier for Biomedical Engineers. *Annu Rev Biomed Eng*. 2017; 19:195–219. <https://doi.org/10.1146/annurev-bioeng-071516-044720>
7. Nordlund J, Syvänen AC. Epigenetics in pediatric acute lymphoblastic leukemia. *Semin Cancer Biol*. 2018; 51:129–38. <https://doi.org/10.1016/j.semcancer.2017.09.001>
8. Sang L, Wang XM, Xu DY, Zhao WJ. Bioinformatics analysis of aberrantly methylated-differentially expressed genes and pathways in hepatocellular carcinoma. *World J Gastroenterol*. 2018; 24:2605–16. <https://doi.org/10.3748/wjg.v24.i24.2605>
9. Cai MY, Tong ZT, Zheng F, Liao YJ, Wang Y, Rao HL, Chen YC, Wu QL, Liu YH, Guan XY, Lin MC, Zeng YX, Kung HF, Xie D. EZH2 protein: a promising immunomarker for the detection of hepatocellular carcinomas in liver needle biopsies. *Gut*. 2011; 60:967–76. <https://doi.org/10.1136/gut.2010.231993>
10. Lee SM, Lee YG, Bae JB, Choi JK, Tayama C, Hata K, Yun Y, Seong JK, Kim YJ. HBx induces hypomethylation of distal intragenic CpG islands required for active expression of developmental regulators. *Proc Natl Acad Sci USA*. 2014; 111:9555–60. <https://doi.org/10.1073/pnas.1400604111>
11. Xu RH, Wei W, Krawczyk M, Wang W, Luo H, Flagg K, Yi S, Shi W, Quan Q, Li K, Zheng L, Zhang H, Caughey BA, et al. Circulating tumour DNA methylation markers for diagnosis and prognosis of hepatocellular carcinoma. *Nat Mater*. 2017; 16:1155–61. <https://doi.org/10.1038/nmat4997>
12. Casadevall D, Kilian AY, Bellmunt J. The prognostic role of epigenetic dysregulation in bladder cancer: A systematic review. *Cancer Treat Rev*. 2017; 61:82–93. <https://doi.org/10.1016/j.ctrv.2017.10.004>
13. Hlady RA, Sathyanarayan A, Thompson JJ, Zhou D, Wu Q, Pham K, Lee JH, Liu C, Robertson KD. Integrating the Epigenome to Identify Drivers of Hepatocellular Carcinoma. *Hepatology*. 2019. <https://doi.org/10.1002/hep.30211>
14. Nishida N, Nishimura T, Nakai T, Chishina H, Arizumi T, Takita M, Kitai S, Yada N, Hagiwara S, Inoue T, Minami Y, Ueshima K, Sakurai T, Kudo M. Genome-wide profiling of DNA methylation and tumor progression in human hepatocellular carcinoma. *Dig Dis*. 2014; 32:658–63. <https://doi.org/10.1159/000367982>
15. Sun XJ, Wang MC, Zhang FH, Kong X. An integrated analysis of genome-wide DNA methylation and gene expression data in hepatocellular carcinoma. *FEBS Open Bio*. 2018; 8:1093–103. <https://doi.org/10.1002/2211-5463.12433>
16. Liu S, Miao C, Liu J, Wang CC, Lu XJ. Four differentially methylated gene pairs to predict the prognosis for early stage hepatocellular carcinoma patients. *J Cell Physiol*. 2018; 233:6583–90. <https://doi.org/10.1002/jcp.26256>
17. Lee WY, Bachtar M, Choo CC, Lee CG. Comprehensive review of Hepatitis B Virus-associated hepatocellular carcinoma research through text mining and big data analytics. *Biol Rev Camb Philos Soc*. 2018. <https://doi.org/10.1111/brv.12457>
18. Yu S, Wang Y, Jing L, Claret FX, Li Q, Tian T, Liang X,

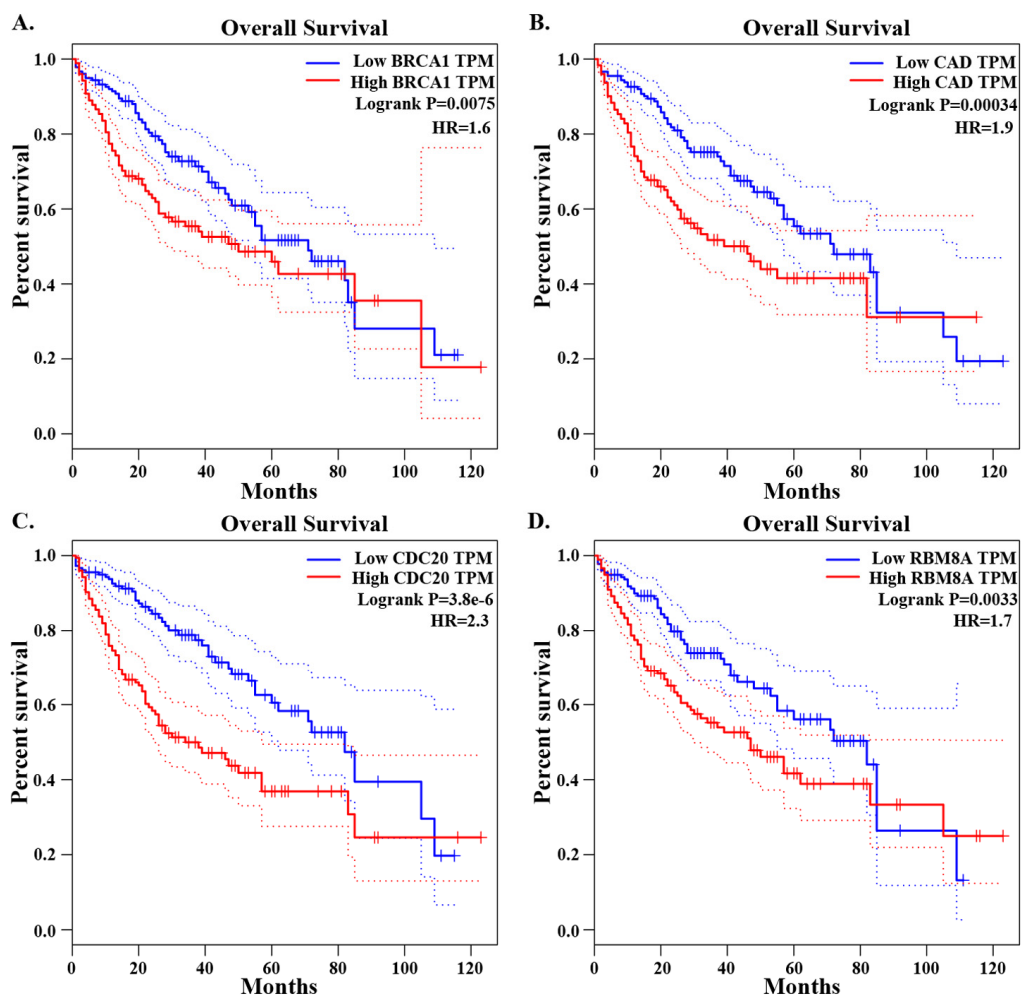
- Ruan Z, Jiang L, Yao Y, Nan K, Lv Y, Guo H. Autophagy in the “inflammation-carcinogenesis” pathway of liver and HCC immunotherapy. *Cancer Lett.* 2017; 411:82–89. <https://doi.org/10.1016/j.canlet.2017.09.049>
19. Zhu Y, Gao XM, Yang J, Xu D, Zhang Y, Lu M, Zhang Z, Sheng YY, Li JH, Yu XX, Zheng Y, Dong QZ, Qin LX. C-C chemokine receptor type 1 mediates osteopontin-promoted metastasis in hepatocellular carcinoma. *Cancer Sci.* 2018; 109:710–23. <https://doi.org/10.1111/cas.13487>
  20. Liu J, Chen S, Wang W, Ning BF, Chen F, Shen W, Ding J, Chen W, Xie WF, Zhang X. Cancer-associated fibroblasts promote hepatocellular carcinoma metastasis through chemokine-activated hedgehog and TGF- $\beta$  pathways. *Cancer Lett.* 2016; 379:49–59. <https://doi.org/10.1016/j.canlet.2016.05.022>
  21. Thakur A, Schalk D, Tomaszewski E, Kondadasula SV, Yano H, Sarkar FH, Lum LG. Microenvironment generated during EGFR targeted killing of pancreatic tumor cells by ATC inhibits myeloid-derived suppressor cells through COX2 and PGE2 dependent pathway. *J Transl Med.* 2013; 11:35. <https://doi.org/10.1186/1479-5876-11-35>
  22. Qin Y, Vasilatos SN, Chen L, Wu H, Cao Z, Fu Y, Huang M, Vlad AM, Lu B, Oesterreich S, Davidson NE, Huang Y. Inhibition of histone lysine-specific demethylase 1 elicits breast tumor immunity and enhances antitumor efficacy of immune checkpoint blockade. *Oncogene.* 2018. <https://doi.org/10.1038/s41388-018-0451-5>. Epub ahead of print.
  23. Kumar D, Xu ML. Microenvironment Cell Contribution to Lymphoma Immunity. *Front Oncol.* 2018; 8:288. <https://doi.org/10.3389/fonc.2018.00288>
  24. Liao Y, Yuan S, Chen X, Zhu P, Li J, Qin L, Liao W. Up-regulation of BRCA1-associated RING Domain 1 Promotes Hepatocellular Carcinoma Progression by Targeting Akt Signaling. *Sci Rep.* 2017; 7:7649. <https://doi.org/10.1038/s41598-017-07962-7>
  25. Cui X, Li X, Li J, Wang X, Sun W, Cheng Z, Ding J, Wang H. inFRank: a ranking-based identification of influential genes in biological networks. *Oncotarget.* 2017; 8:43810–21. <https://doi.org/10.18632/oncotarget.11878>
  26. Liang R, Lin Y, Ye JZ, Yan XX, Liu ZH, Li YQ, Luo XL, Ye HH. High expression of RBM8A predicts poor patient prognosis and promotes tumor progression in hepatocellular carcinoma. *Oncol Rep.* 2017; 37:2167–76. <https://doi.org/10.3892/or.2017.5457>
  27. Zhai X, Zhu H, Wang W, Zhang S, Zhang Y, Mao G. Abnormal expression of EMT-related proteins, S100A4, vimentin and E-cadherin, is correlated with clinicopathological features and prognosis in HCC. *Med Oncol.* 2014; 31:970. <https://doi.org/10.1007/s12032-014-0970-z>



## SUPPLEMENTARY MATERIAL



**Supplementary Figure 1. Methylation and correlation with expression of the four hub genes. (A) BRCA1 (B) CAD (C) CDC20 (D) RBM8A** Red dot represents tumor sample; green dot represents normal sample. Horizontal axis is expression and vertical axis is methylation. \*:  $P < 0.05$ ; \*\*:  $P < 0.005$ .



**Supplementary Figure 2. Relation between expression of the four hub genes and OS. (A) BRCA1 (B) CAD (C) CDC20 (D) RBM8A.**

## SUPPLEMENTARY TABLE

Please browse the link in Full Text version to find the data of **Supplementary Table 1. The clinical characteristics of TCGA.**

# First-in-class candidate therapeutics that target mitochondria and effectively prevent cancer cell metastasis: Mitoriboscins and TPP compounds

Béla Ózsvári<sup>1</sup>, Federica Sotgia<sup>1</sup>, Michael P. Lisanti<sup>1</sup>

<sup>1</sup>Translational Medicine, School of Science, Engineering and Environment (SEE), University of Salford, Greater Manchester, United Kingdom

**Correspondence to:** Federica Sotgia, Michael P. Lisanti; email: [fsotgia@gmail.com](mailto:fsotgia@gmail.com), [michaelp.lisanti@gmail.com](mailto:michaelp.lisanti@gmail.com)

**Keywords:** cancer stem-like cells (CSCs), mitochondrial inhibitors, treatment failure, breast cancer, metastasis prophylaxis

**Received:** April 25, 2020

**Accepted:** May 14, 2020

**Published:** May 24, 2020

**Copyright:** Ózsvári et al. This is an open-access article distributed under the terms of the Creative Commons Attribution License (CC BY 3.0), which permits unrestricted use, distribution, and reproduction in any medium, provided the original author and source are credited.

## ABSTRACT

Cancer stem cells (CSCs) have been proposed to be responsible for tumor recurrence, distant metastasis and drug-resistance, in the vast majority of cancer patients. Therefore, there is an urgent need to identify new drugs that can target and eradicate CSCs. To identify new molecular targets that are unique to CSCs, we previously compared MCF7 2D-monolayers with 3D-mammospheres, which are enriched in CSCs. We observed that 25 mitochondrial-related proteins were >100-fold over-expressed in 3D-mammospheres. Here, we used these 25 proteins to derive short gene signatures to predict distant metastasis (in N=1,395 patients) and tumor recurrence (in N=3,082 patients), by employing a large collection of transcriptional profiling data from ER(+) breast cancer patients. This analysis resulted in a 4-gene signature for predicting distant metastasis, with a hazard ratio of 1.91-fold ( $P=2.2e-08$ ). This provides clinical evidence to support a role for CSC mitochondria in metastatic dissemination. Next, we employed a panel of mitochondrial inhibitors, previously shown to target mitochondria and selectively inhibit 3D-mammosphere formation in MCF7 cells and cell migration in MDA-MB-231 cells. Remarkably, these five mitochondrial inhibitors had only minor effects or no effect on MDA-MB-231 tumor formation, but preferentially and selectively inhibited tumor cell metastasis, without causing significant toxicity. Mechanistically, all five mitochondrial inhibitors have been previously shown to induce ATP-depletion in cancer cells. Since 3 of these 5 inhibitors were designed to target the large mitochondrial ribosome, we next interrogated whether genes encoding the large mitochondrial ribosomal proteins (MRPL) also show prognostic value in the prediction of distant metastasis in both ER(+) and ER(-) breast cancer patients. Interestingly, gene signatures composed of 6 to 9 MRPL mRNA-transcripts were indeed sufficient to predict distant metastasis, tumor recurrence and Tamoxifen resistance. These gene signatures could be useful as companion diagnostics to assess which patients may benefit most from anti-mito-ribosome therapy. Overall, our studies provide the necessary proof-of-concept, and *in vivo* functional evidence, that mitochondrial inhibitors can successfully and selectively target the biological process of cancer cell metastasis. Ultimately, we envision that mitochondrial inhibitors could be employed to develop new treatment protocols, for clinically providing metastasis prophylaxis, to help prevent poor clinical outcomes in cancer patients.

## INTRODUCTION

Today, breast cancer treatment requires a multi-disciplinary approach, involving an extensive medical

team consisting of specialized surgeons, medical oncologists, oncology nurses, as well as radiologists and radiology technicians, to perform anti-cancer therapy, which consists of tumor excision, chemo- or hormonal-

therapy, as well as radiation therapy. Despite these major advances, many patients still ultimately undergo treatment failure, in the form of tumor recurrence and distant metastasis. Unfortunately, distant metastasis causes premature death, in >90% of cancer patients with treatment failure [1–5]. Therefore, there is a clear need to develop new strategies to prevent cancer cell metastasis.

Local and distant metastases are thought to be caused by a small sub-population of cancer cells, known as cancer stem cells (CSCs) [1–5]. These CSCs are unique, in the sense that they can regenerate tumors in immune-deficient mice, as xenografts, and they undergo anchorage-independent proliferation and the EMT, allowing them to disseminate throughout the body, thereby creating local and distant metastatic lesions, which are largely chemo- and radio-therapy resistant [1–5]. However, it remains largely unknown, what are the precise vulnerabilities of CSCs.

Recently, we identified cancer cell mitochondria as a new promising therapeutic target for the eradication of CSCs [6–8]. New evidence suggests that CSCs have elevated levels of mitochondrial biogenesis, that helps to energetically drive their rapid propagation and anchorage-independent growth [6–10]. In support of this notion, metastatic breast cancer cells in positive lymph nodes, removed from patients, show a significant increase in mitochondrial Complex IV activity, as seen by histochemical- and immuno-staining [11, 12].

Importantly, mitochondrial biogenesis is strictly dependent on the function of the mitochondrial ribosome, which consists of both large and small subunits, to effectively carry out the mitochondrial protein translation of 13 key genes that are absolutely required for OXPHOS and mitochondrial ATP production [13]. Interestingly, in eukaryotic cells, mitochondria originally evolved from engulfed aerobic bacteria, an event estimated to have occurred approximately 1.5 billion years ago. Because of this close evolutionary relationship, certain FDA-approved drugs inhibit mitochondrial protein translation as an off-target side effect. For example, Doxycycline (a Tetracycline family member) negatively affects the small mito-ribosome, while Azithromycin (an Erythromycin family member) inhibits the large mito-ribosome. Both Doxycycline and Azithromycin effectively inhibit the anchorage-independent propagation of CSCs, as assessed using the 3D-tumor-sphere assay, in 12 cell lines derived from 8 different cancer types, including breast cancers (MCF7, T47D, MDA-MB-231 and MCF10.DCIS.COM) [13].

Therefore, we proposed that these off-target side-effects could be clinically “re-purposed” as a therapeutic effect.

A recent Phase II clinical trial also showed that Doxycycline treatment (200-mg/day for 2-weeks) of early stage breast cancer patients reduced their CSC tumor load (as assessed by CD44 immuno-staining), between ~17% and ~67%, with a positive response rate approaching nearly 90% [14]. Therefore, inhibition of mitochondrial protein translation may be a new valuable target for eradicating CSCs in patients [14].

To design novel therapeutics to more effectively target the mitochondria, we used the known 3D-structure of the large mammalian mito-ribosome, to perform *in silico* library screening, coupled with phenotypic drug screening, to develop a new family of drug-like compounds, called the Mitoriboscins [15]. Importantly, as predicted, the Mitoriboscins inhibited mitochondrial oxygen consumption rates, resulting in cellular ATP-depletion, and potently inhibited 3D-mammosphere formation, all with an IC-50 in the low micro-molar range [15].

Here, we now show that the Mitoriboscins have only minor effects (23/G4) or no inhibitory effects (24/D4, 24/F9) on tumor growth, but functionally prevent metastatic progression. Quantitatively similar results were obtained with another independent class of mitochondrial inhibitors, namely Butene-1,4-bis-triphenyl-phosphonium (Bis-TPP) and Dodecyl-triphenyl-phosphonium (Dodecyl-TPP) [16, 17]. Bis-TPP and Dodecyl-TPP both contain a TPP moiety, which functions as a chemical signal for mitochondrial targeting [16, 17]. These data provide *in vivo* functional evidence that five mitochondrial inhibitors can successfully and preferentially target the biological process of cancer cell metastasis, without significant toxicity.

## RESULTS

### Cancer stem cell (CSC) based mitochondrial signatures for predicting distant metastasis and tumor recurrence

After a breast cancer diagnosis, most patients undergo surgical resection of the primary tumor and are then subsequently treated with hormone-, chemo- and/or radio-therapy, depending on the breast cancer subtype. However, many patients ultimately experience treatment failure, resulting in tumor recurrence and distant metastasis. Unfortunately, distant metastasis is responsible for the premature deaths in the vast majority of cancer patients, approaching >90% (Figure 1). Therefore, new diagnostics and therapeutics are urgently needed to prevent and treat metastatic disease,

which has been attributed to the existence and resurgence of a small sub-population of cancer cells, known as cancer stem cells (CSCs).

In order to identify new molecular targets that are selectively up-regulated in CSCs, we previously carried out unbiased proteomics analysis on MCF7 cell 2D-monolayers, as directly compared with MCF7 3D-mammospheres, which are known to be highly enriched in CSCs and progenitor cells [6]. As a consequence, we observed that 25 mitochondrial proteins were highly up-regulated by >100-fold, specifically in 3D-mammospheres [6].

Here, we interrogated whether the mRNA transcripts of these mitochondrial proteins show any prognostic value in large numbers of ER(+) human breast cancer patients. Interestingly, we observed that 13 of these 25 gene transcripts showed prognostic value in predicting distant metastasis. We then used these 13 gene transcripts to create a mitochondrial-related gene signature, that effectively predicted distant metastasis in 1,395 patients (HR=1.79; P=3.4e-07). See Supplementary Table 1 and Figure 2.

To optimize its predictive value, we next selected the top 4 gene transcripts, with the largest hazard ratios, to construct a short 4-gene signature, which revealed an increase in prognostic value, related to distant

metastasis (HR=1.91; P=2.2e-08). Remarkably, this 4-gene signature was also able to predict tumor recurrence in the same patient population (HR=1.68; P=1.2e-15; Supplementary Table 2 and Figure 3).

Therefore, we conclude that these CSC-based mitochondrial signatures may provide a new prognostic approach for predicting distant metastasis and tumor recurrence in breast cancer patients. Most importantly, these results may also biologically and functionally implicate CSC mitochondria in the process of metastasis and tumor recurrence.

**Mitochondrial inhibitors metabolically target and prevent cancer cell metastasis, without significant toxicity**

To functionally evaluate the role of mitochondria in cancer metastasis, we used a series of mitochondrial inhibitors that were previously developed to specifically target the propagation of CSCs, known as the

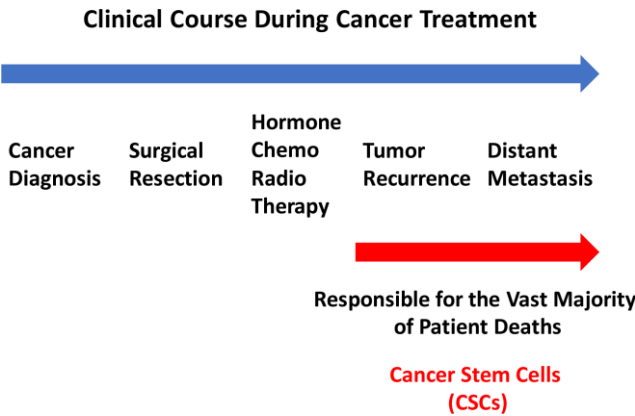
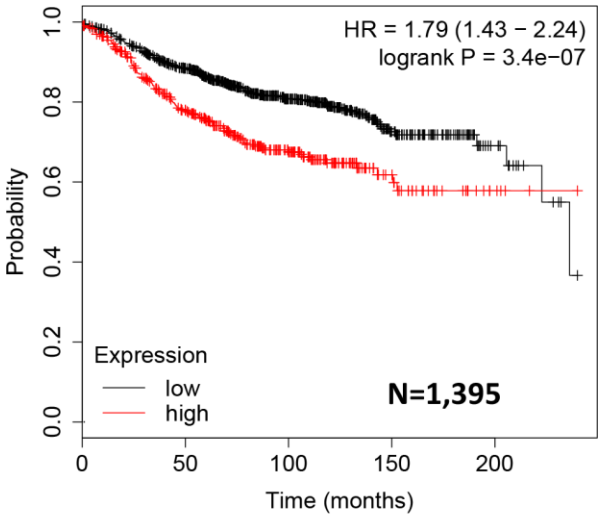


**Figure 1. Clinical course of cancer therapy: Focus on the causes of treatment failure.** After diagnosis, breast cancer patients undergo surgical resection of the primary tumor and then are treated with a specific therapy (hormone/chemo/radio), depending on the breast cancer subtype and clinical staging. However, a significant number of patients ultimately undergo treatment failure, resulting in tumor recurrence and distant metastasis. Distant metastasis is responsible for the premature deaths of >90% of cancer patients, undergoing treatment failure. This phenomenon has been attributed to the propagation and dissemination of CSCs.

**CSC-Mito-Genes**

**ER(+)**

**Distant Metastasis  
(13 Gene Signature)**



**DMFS**

**Figure 2. A CSC-based mitochondrial 13-gene signature predicts distant metastasis in ER(+) breast cancer patients.** We used 13 gene transcripts to create a CSC-based mitochondrial-related gene signature, that effectively predicted distant metastasis in N=1,395 patients (HR=1.79; P=3.4e-07). See also Supplementary Table 1. DMFS, distant metastasis free survival.



Mitoriboscins [15]. These inhibitors were developed via *in silico* screening of a library of 45,000 compounds, to identify positive hits that bound to the 3D-structure of the large mitochondrial ribosome [15]. After 880 positive hits were identified, these compounds were then subjected to phenotypic drug screening, using an ATP-depletion assay, and directly validated using the Seahorse Metabolic Flux analyser, to confirm their specificity as *bonafide*

mitochondrial inhibitors [15]. Ultimately, this screening approach led to the identification of three major compounds, known as 23/G4, 24/D4 and 24/F9, which all inhibited 3D-mammosphere formation in MCF7 cells and significantly blocked cell migration in MDA-MB-231 cells, all in the low micro-molar range [15]. The structures of 23/G4, 24/D4 and 24/F9 are shown in Figure 4.

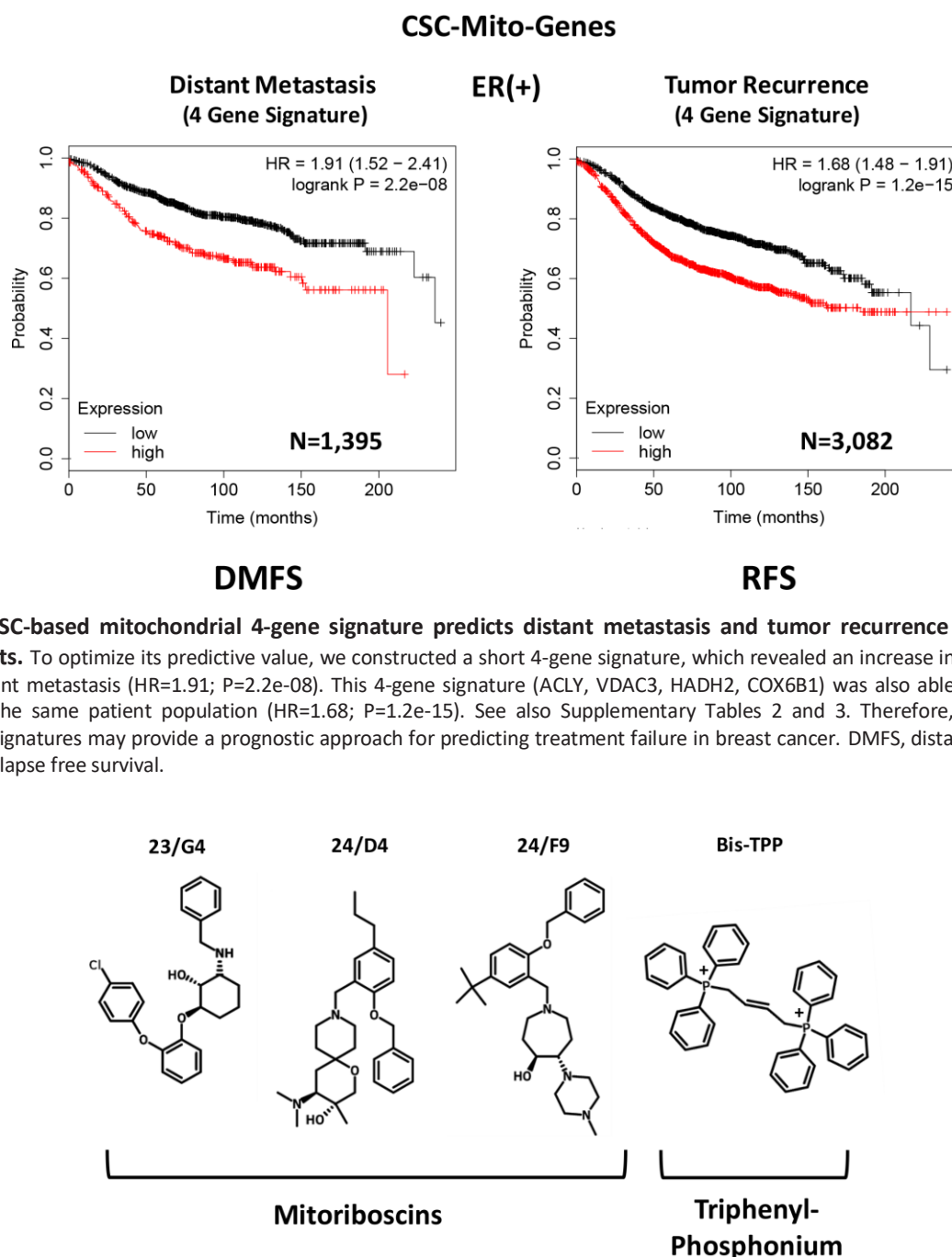


**Figure 4. Mitochondrial inhibitors: Mitoriboscins and Bis-1,4-butene-TTP.** The chemical structures of the three Mitoriboscins (23/G4, 24/D4 and 24/F9) and Bis-TTP are shown.

To experimentally evaluate their functional effects *in vivo*, we used MDA-MB-231 cells and the well-established chorio-allantoic membrane (CAM) assay in chicken eggs, to quantitatively measure tumor growth and distant metastasis. An inoculum of  $1 \times 10^6$  MDA-MB-231 cells was added onto the CAM of each egg (day E9) and then eggs were randomized into groups. On day E10, tumors were detectable and they were then treated daily for 8 days with vehicle alone (1% DMSO in PBS) or the three Mitoriboscins compounds. In parallel, we also evaluated the activity of another mitochondrial inhibitor, namely butane-1,4-bis-triphenyl-phosphonium (Bis-TPP), which we identified as an inhibitor of 3D-mammosphere formation in MCF7 cells, with an IC-50 of less than  $0.5 \mu\text{M}$  [16]. It is well-established that the TPP-moiety acts as a chemical signal for mitochondrial targeting [16, 17].

After 8 days of drug administration, on day E18 all tumors were weighed, and the lower CAM was collected to evaluate the number of metastatic cells, as analyzed by qPCR with specific primers for Human Alu sequences.

Figure 5 shows the effects of the three Mitoriboscins (23/G4, 24/D4, 24/F9) and Bis-TPP on MDA-MB-231 tumor growth. Note that none of the four inhibitors tested showed any significant effects on tumor growth, as a result of the 8-day period of drug administration.

However, all four mitochondrial inhibitors showed significant effects on MDA-MB-231 cancer cell metastasis. Figure 6 illustrates that all three Mitoriboscins were clearly effective in inhibiting metastatic progression, although 24/D4 and 24/F9 were the most effective. In addition, Bis-TPP also significantly prevented metastasis.

As 23/G4 was minimally effective at a concentration of  $0.5 \text{ mM}$ , we also tested it at higher concentrations of  $0.75$ ,  $1$  and  $2 \text{ mM}$ . Importantly, our results show that 23/G4, at these concentrations, significantly inhibited both tumor growth (by 40% to 60%; Figure 7) and metastatic progression (by 70-75%; Figure 8). Interestingly, as expected, the effects of 23/G4 on metastasis were significantly more pronounced.

Remarkably, in this series of experiments, little or no embryo toxicity was observed, otherwise tumor growth and cancer metastasis assays could not have been completed (Tables 1–3). Therefore, we conclude that mitochondrial inhibitors can be used experimentally, to preferentially inhibit the initiation of tumor metastasis, without significant toxicity.

Finally, we also tested another more potent mitochondrially-targeted TPP compound, namely Dodecyl-TPP, using low micro-molar concentrations ( $6.25$ - and  $25\text{-}\mu\text{M}$ ). Figures 9 and 10 demonstrate that Dodecyl-TPP significantly inhibited tumor growth (by

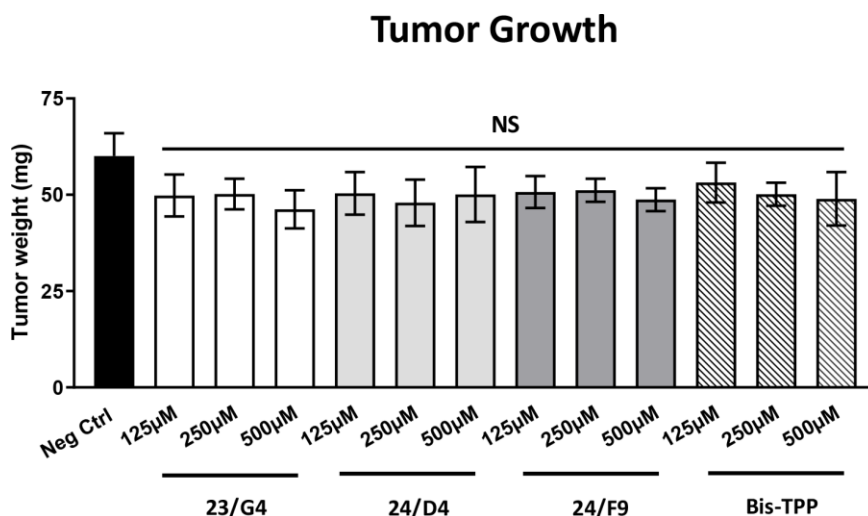


**Figure 5. Mitochondrial inhibitors have no effect on tumor growth.** MDA-MB-231 cells and the well-established chorio-allantoic membrane (CAM) assay in chicken eggs were used to quantitatively measure tumor growth. An inoculum of  $1 \times 10^6$  MDA-MB-231 cells was added onto the CAM of each egg (on Day E9) and then eggs were then randomized into groups. On day E10, tumors were detectable and they were then treated daily for 8 days with vehicle alone (1% DMSO in PBS) or the four mitochondrial inhibitors. After 8 days of drug administration, on day E18 all tumors were weighed. Note that none of the mitochondrial inhibitors tested had any significant effects on tumor growth. Averages are shown  $\pm$  SEM. NS, not significant.

12% to 40%; Figure 9) and metastatic progression (by 25 to 65%; Figure 10). As predicted, Dodecyl-TPP preferentially targeted metastasis, rather than tumor growth. It is worth noting that Dodecyl-TPP showed some toxicity, but only at 62.5- $\mu$ M, preventing reliable analysis of its effects on tumor growth and metastasis, at this higher concentration (Table 3). However, Dodecyl-TPP showed little or no toxicity at 6.25- and 25- $\mu$ M (Table 3).

## Mito-Ribosome based signatures for predicting distant metastasis and tumor recurrence: Implications as companion diagnostics

Given the functional effects of the Mitoriboscins on metastasis, we next evaluated if the gene mRNA transcripts of the large mitochondrial ribosomal proteins (MRPL) show any prognostic value in ER(+) and ER(-)/basal breast cancer patients.

## Metastasis

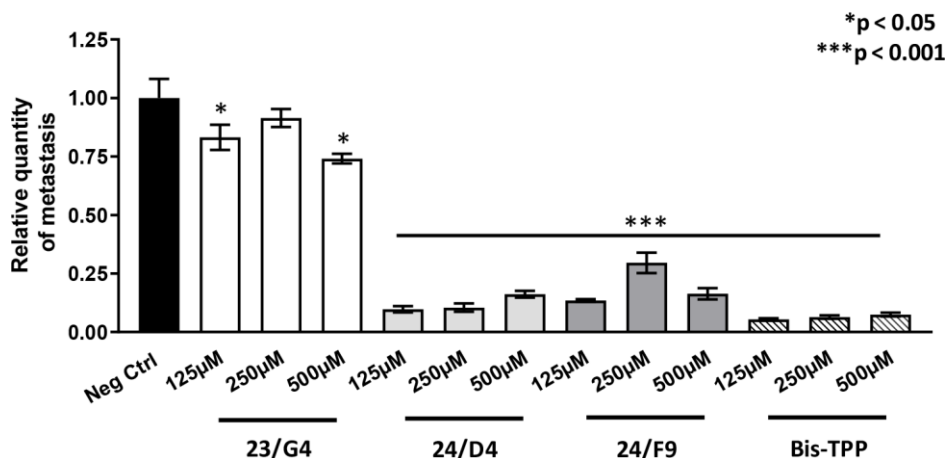


**Figure 6. Mitochondrial inhibitor compounds selectively target and prevent cancer metastasis.** MDA-MB-231 cells and the well-established chorio-allantoic membrane (CAM) assay in chicken eggs were used to quantitatively measure spontaneous tumor metastasis. An inoculum of  $1 \times 10^6$  MDA-MB-231 cells was added onto the CAM of each egg (on day E9) and then eggs were then randomized into groups. On day E10, tumors were detectable and they were then treated daily for 8 days with vehicle alone (1% DMSO in PBS) or the four mitochondrial inhibitors. After 8 days of drug administration, the lower CAM was collected to evaluate the number of metastatic cells, as analyzed by qPCR with specific primers for Human Alu sequences. Note that all four mitochondrial inhibitors showed significant effects on MDA-MB-231 metastasis. More specifically, all three Mitoriboscins were clearly effective in inhibiting metastasis, although 24/D4 and 24/F9 were the most effective. In addition, Bis-TPP also significantly prevented metastasis. Averages are shown  $\pm$  SEM. \* $p < 0.05$ ; \*\*\* $p < 0.001$ .

## Tumor Growth

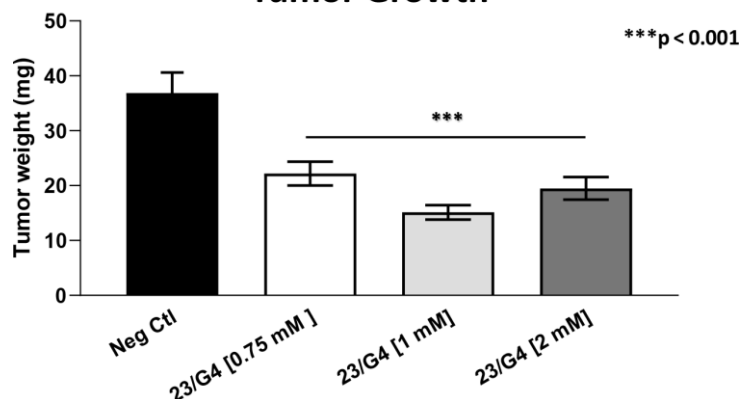


**Figure 7. Effects of the Mitoriboscins 23/G4 on tumor growth.** The Mitoriboscins 23/G4 was tested at higher concentrations of 0.75, 1 and 2 mM. Note that 23/G4, at these concentrations, inhibited tumor growth (by 40% to 60%). Averages are shown  $\pm$  SEM. \*\*\* $p < 0.001$ .

**Table 1. Chick embryo toxicity of Mitoriboscins and Bis-TPP at a concentration of 0.5 mM.**

Group #	Group Description	Total	Alive	Dead	% Alive	% Dead
1	Neg. Ctrl.	18	16	2	88.89	11.11
2	23/G4	10	7	3	70	30
3	24/D4	12	12	0	100	0
4	24/F9	10	8	2	80	20
5	Bis-TPP	12	7	5	58.33	41.67

**Table 2. Chick embryo toxicity of Mitoriboscins 23/G4 at higher concentrations.**

Group #	Group Description	Total	Alive	Dead	% Alive	% Dead
1	Neg. Ctrl.	17	12	5	70.59	29.41
2	23/G4 [0.75 mM]	14	10	4	71.43	28.57
3	23/G4 [1 mM]	15	12	3	80	20
4	23/G4 [2 mM]	15	10	5	66.67	33.33

**Table 3. Chick embryo toxicity of Dodecyl-TPP.**

Group #	Group Description	Total	Alive	Dead	% Alive	% Dead
1	Neg. Ctrl.	18	13	5	72.22	27.78
2	d-TPP [6.25 $\mu$ M]	19	13	6	68.42	31.58
3	d-TPP [25 $\mu$ M]	19	13	6	68.42	31.58
4	d-TPP [62.5 $\mu$ M]	19	3	16	15.79	84.21

In ER(+) breast cancer, a 9-gene mito-ribosome signature was able to effectively predict distant metastasis in N=1,395 patients (HR=1.59; P=5e-05) and tumor recurrence in N=3,082 patients (HR=1.71; P<1e-16) (See Supplementary Tables 4 and 5; Figure 11). Importantly, a closely related mito-ribosome signature was also

able to predict treatment failure in a sub-set of ER(+) patients undergoing Tamoxifen treatment, which resulted in distant metastasis (N=618 patients; HR=2.16; P=1.7e-05) and tumor recurrence (N=799 patients; HR=3.45; P=1.6e-08) (Supplementary Tables 6 and 7; Figure 12).

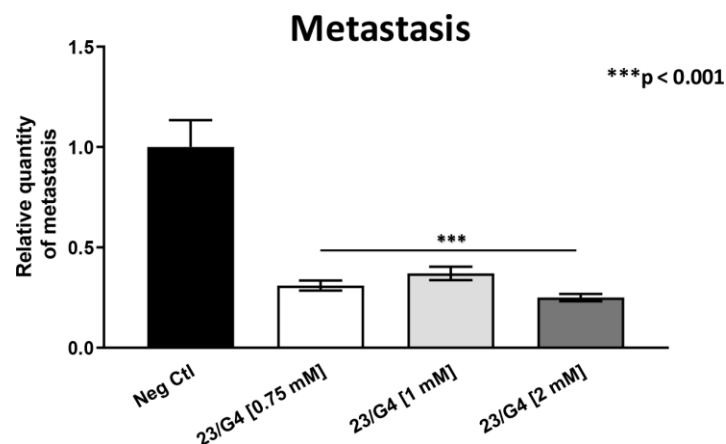


**Figure 8. Effects of the Mitoriboscins 23/G4 on cancer metastasis.** The Mitoriboscins 23/G4 was tested at higher concentrations, namely 0.75, 1 and 2 mM. Note that 23/G4, at these concentrations, significantly inhibited metastasis (by 70-75%). Interestingly, the effects of 23/G4 on metastasis were significantly more pronounced than its effects on tumor growth. Averages are shown  $\pm$  SEM. \*\*\*p<0.001.

In ER(-)/basal breast cancer, a distinct 6-gene mito-ribosome MRPL signature was also able to effectively predict distant metastasis in N=145 patients (HR=2.95; P=0.0018) and tumor recurrence in N=360 patients (HR=2.19; P=1.9e-06), as well as overall survival in N=153 patients (HR=3.17; P=0.00033) (Supplementary Table 8; Figures 13 and 14).

In summary, these short mito-ribosome gene signatures may also be useful as companion diagnostics to assess which patient populations may benefit most from the administration of the Mitoriboscins compounds.

## DISCUSSION

Current thinking indicates that CSCs are the etiological cause of treatment failure in most cancer patients, as they are the cellular drivers of tumor recurrence, metastasis and drug-resistance [1–5]. As a consequence, new therapeutic approaches are needed to effectively eliminate CSCs. Our previous studies identified CSC mitochondria as a potential new therapeutic target. More specifically, we experimentally observed that

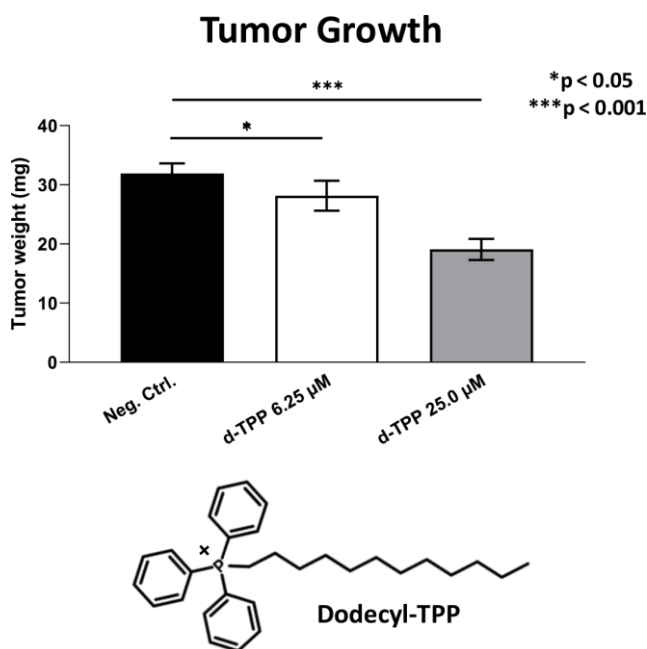


**Figure 9. Effects of Dodecyl-TPP on tumor growth.** Dodecyl-TPP, another more potent mitochondrially-targeted TPP compound, was tested using low micro-molar concentrations (6.25- and 25- $\mu$ M). Note that Dodecyl-TPP significantly inhibited tumor growth (by 12% to 40%). Averages are shown  $\pm$  SEM. \*p<0.05; \*\*\*p<0.001. The structure of Dodecyl-TPP (d-TPP) is also shown. Note the 12-carbon alkyl-chain attached to the lipophilic cation, triphenyl-phosphonium (TPP).

MCF7-derived 3D-mammospheres are specifically enriched in mitochondrial proteins; 25 mitochondrial proteins showed greater than 100-fold over-expression, while 9 of these proteins were infinitely up-regulated, as compared with 2D-monolayers [6]. In this report, we used these proteomic data as possible candidates to generate short mitochondrial gene signatures that could be employed as prognostic tools to predict distant metastasis (in N=1,395 patients) and tumor recurrence (in N=3,082 patients), in a large collection of ER(+) breast cancer patients. For example, we developed a 4-gene signature for predicting distant metastasis, resulting in a hazard ratio of 1.91-fold (P=2.2e-08). This clinical evidence supports the idea that CSC mitochondria may play a critical functional role in the metastatic dissemination of cancer cells.

To further test this hypothesis experimentally, we next employed a well-established animal model, namely the chorio-allantoic membrane (CAM) in chicken eggs, to test a series of mitochondrial inhibitors. These mitochondrial inhibitors, including the Mitoriboscins, have been previously described to effectively inhibit 3D-mammosphere formation in MCF7 cells and cell migration in MDA-MB-231 cells. All five of these

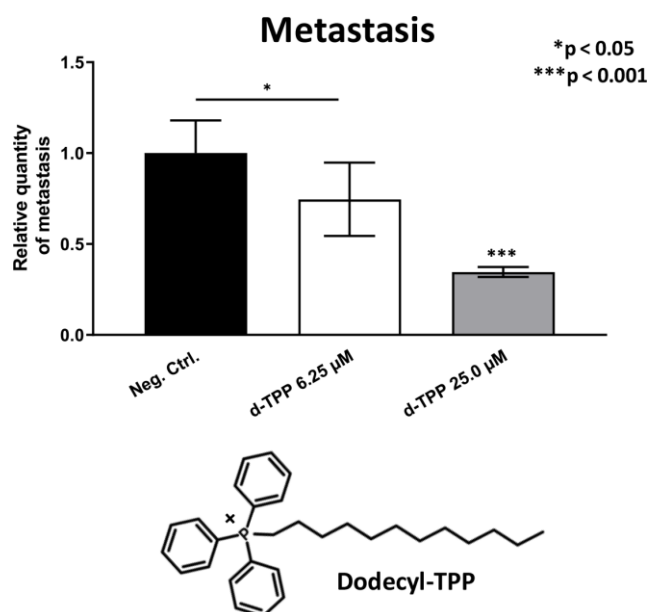


**Figure 10. Effects of Dodecyl-TPP on cancer metastasis.** Dodecyl-TPP was tested using low micro-molar concentrations (6.25- and 25- $\mu$ M). Note that Dodecyl-TPP significantly inhibited metastasis (by 25% to 65%). Averages are shown  $\pm$  SEM. \*p<0.05; \*\*\*p<0.001. Importantly, little or no toxicity was observed for Dodecyl-TPP at 6.25- and 25- $\mu$ M (Table 3). The structure of Dodecyl-TPP (d-TPP) is also shown.



## Large-Mito-Ribosome-Genes

ER(+)

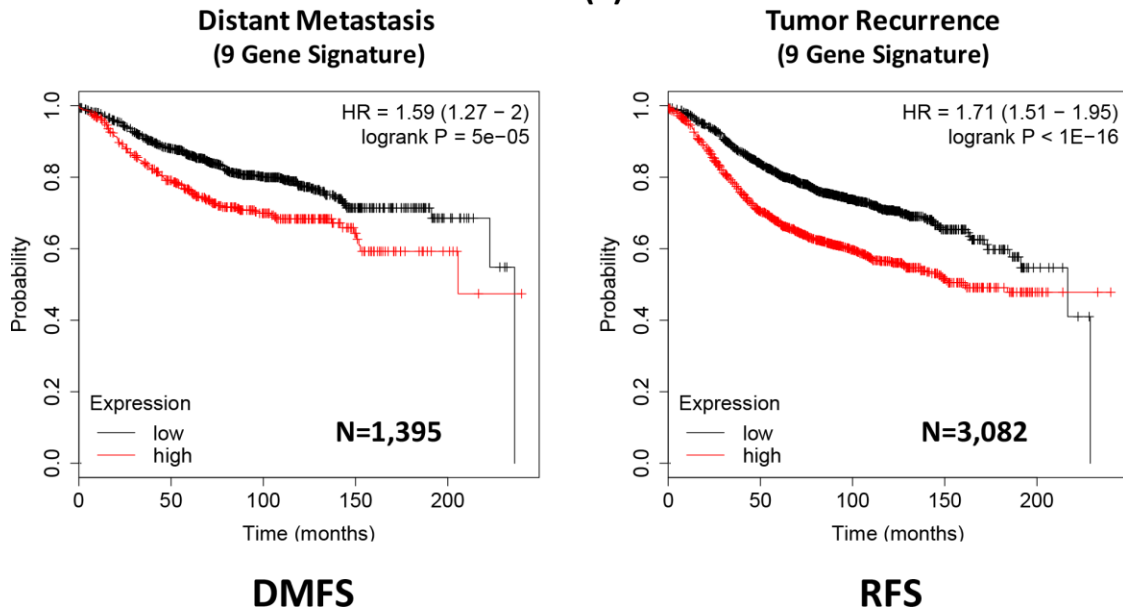


**Figure 11. A large mito-ribosome 9-gene signature predicts metastasis and recurrence in ER(+) breast cancer patients.** A 9-gene mito-ribosome signature effectively predicts distant metastasis in N=1,395 patients (HR=1.59; P=5e-05) and tumor recurrence in N=3,082 patients (HR=1.71; P<1e-16). See Supplementary Tables 4 and 5. DMFS, distant metastasis free survival; RFS, relapse free survival.

## Large-Mito-Ribosome-Genes

Tamoxifen-Treated Patients

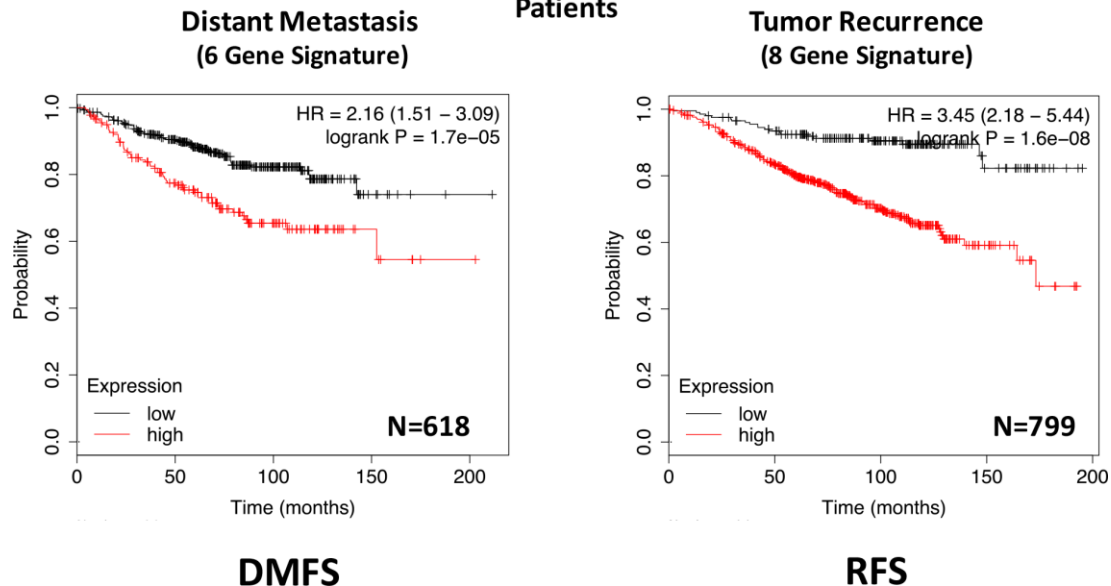


**Figure 12. A large mito-ribosome gene signature predicts metastasis and recurrence in ER(+) breast cancer patients, treated with Tamoxifen.** A mito-ribosome signature predicts treatment failure in a sub-set of ER(+) patients undergoing Tamoxifen treatment, which resulted in distant metastasis (N=618 patients; HR=2.16; P=1.7e-05) and tumor recurrence (N=799 patients; HR=3.45; P=1.6e-08). See also Supplementary Tables 6 and 7. DMFS, distant metastasis free survival; RFS, relapse free survival.

## Large-Mito-Ribosome-Genes

ER(-)/Basal Sub-type

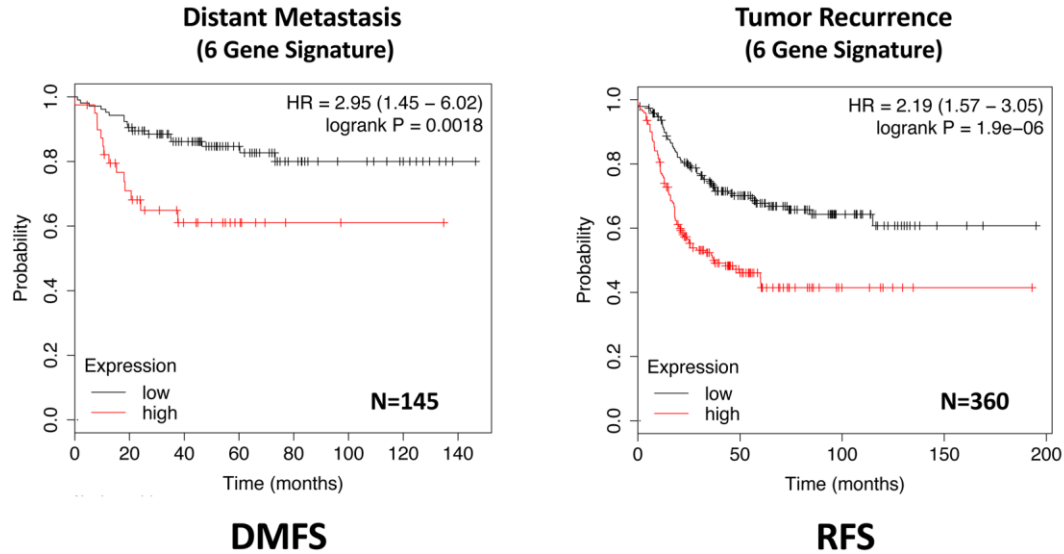


**Figure 13. A large mito-ribosome gene signature predicts distant metastasis and tumor recurrence in ER(-)/basal breast cancer patients.** In ER(-)/basal breast cancer, a 6-gene mito-ribosome signature was also able to effectively predict distant metastasis in N=145 patients (HR=2.95; P=0.0018) and tumor recurrence in N=360 patients (HR=2.19; P=1.9e-06). See also Supplementary Table 8.

## Large-Mito-Ribosome-Genes

ER(-)/Basal Sub-type

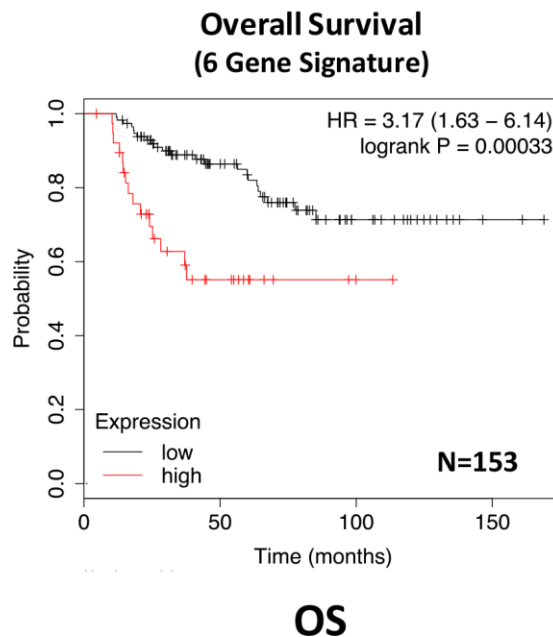


**Figure 14. A large mito-ribosome gene signature predicts overall survival in ER(-)/basal breast cancer patients.** In ER(-)/basal breast cancer, a 6-gene mito-ribosome signature was also able to effectively predict overall survival in N=153 patients (HR=3.17; P=0.00033). OS, overall survival.

mitochondrial inhibitors selectively prevented MDA-MB-231 tumor cell metastasis, but had only minor effects or no effect on tumor formation. More specifically, we have previously shown that these mitochondrial inhibitors successfully induce ATP-depletion in cancer cells, by targeting mitochondrial protein translation and/or OXPHOS activity [15–17]. Our current studies provide the necessary *in vivo* functional evidence, that mitochondrial inhibitors can successfully prevent cancer metastasis. These findings could have important clinical implications, for ultimately preventing treatment failure in breast cancer patients, via metastasis prophylaxis (Figure 15).

Since the Mitoriboscins were originally engineered to inhibit the large mitochondrial ribosome [15], we also focused on whether the large mitochondrial ribosomal gene transcripts (MRPL) have any prognostic value, for predicting distant metastasis in ER(+) breast cancer patients. Importantly, signatures containing MRPL gene transcripts were effective in predicting metastasis, recurrence and Tamoxifen-resistance. Similar results were also obtained in ER(-) breast cancer patients. As a consequence of the success of this approach, these MRPL gene signatures may ultimately be useful as new companion diagnostics, to guide decisions to determine which patients would benefit from anti-mito-ribosome therapy.

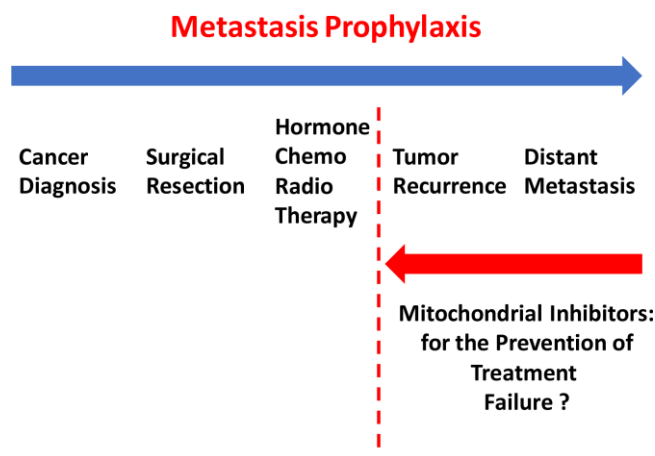


**Figure 15. Metastasis prophylaxis: Clinical implications of mitochondrial inhibitors for the prevention of treatment failure and cancer metastasis.** Based on our current results, that mitochondrial inhibitors can selectively prevent metastasis, we suggest that these findings could be applied clinically to help prevent treatment failure in breast cancer patients.

## MATERIALS AND METHODS

### Materials

MDA-MB-231 cells, a human breast cancer cell line, were obtained from the American Type Culture Collection (ATCC). Mitoriboscins (23/G4, 24/D4, 24/F9), Butene-1,4-bis-triphenyl-phosphonium (Bis-TPP), and Dodecyl-TPP, were all as we previously described [15–17].

### Kaplan-Meier (K-M) analyses

To perform K-M analysis on gene transcripts, we used an open-access online survival analysis tool to interrogate publically available microarray data from up to 3,951 breast cancer patients (18). This allowed us to determine their prognostic value. For this purpose, we primarily analyzed data from ER(+)s and ER(-)/basal patients. Biased array data were excluded from the analysis. This allowed us to identify mitochondrial gene transcripts, with significant prognostic value. Hazard-ratios were calculated, at the best auto-selected cut-off, and p-values were calculated using the Log-rank test and plotted in R. K-M curves were also generated online using the K-M-plotter (as high-resolution TIFF files), using univariate analysis: <https://kmplot.com/analysis/index.php?p=service&cancer=breast>.

This approach allowed us to directly perform *in silico* validation of these mitochondrial biomarker candidates. The multi-gene classifier function of the program was used to test the prognostic value of short mitochondrial gene signatures, using the mean expression of the selected probes. The latest 2020 version of the database was utilized for all these analyses.

### Assays for tumor growth, metastasis and embryo toxicity

#### Preparation of chicken embryos

Fertilized White Leghorn eggs were incubated at 37.5°C with 50% relative humidity for 9 days. At that moment (E9), the chorioallantoic membrane (CAM) was dropped down by drilling a small hole through the eggshell into the air sac, and a 1 cm<sup>2</sup> window was cut in the eggshell above the CAM (19–23).

#### Amplification and grafting of tumor cells

The MDA-MB-231 tumor cell line was cultivated in DMEM medium supplemented with 10% FBS and 1% penicillin/streptomycin. On day E9, cells were detached with trypsin, washed with complete medium and suspended in graft medium. An inoculum of 1 X 10<sup>6</sup> cells was added onto the upper CAM of each egg (E9) and then eggs were randomized into groups [19–23].

### ***Tumor growth assays***

At day 18 (E18), the upper portion of the CAM was removed from each egg, washed in PBS and then directly transferred to paraformaldehyde (fixation for 48 h) and weighed [19–23]. For tumor growth assays, at least 8 tumor samples were collected and analysed per group ( $n \geq 8$ ).

### ***Metastasis assays***

On day E18, a 1 cm<sup>2</sup> portion of the lower CAM was collected to evaluate the number of metastatic cells in 8 samples per group ( $n=8$ ). Genomic DNA was extracted from the CAM (commercial kit) and analyzed by qPCR with specific primers for Human Alu sequences. Calculation of Cq for each sample, mean Cq and relative amounts of metastases for each group are directly managed by the Bio-Rad® CFX Maestro software. A one-way ANOVA analysis with post-tests was performed on all the data [19–23].

### ***Embryo tolerability assays***

Before each administration, the treatment tolerability was evaluated by scoring the number of dead embryos. This approach is summarized schematically in Supplementary Figures 1 and 2.

## **ACKNOWLEDGMENTS**

We are grateful to Rumana Rafiq, for her kind and dedicated assistance, in keeping the Translational Medicine Laboratory at the University of Salford running very smoothly. We would like to thank the Foxpoint Foundation (Canada) and the Healthy Life Foundation (UK) for their philanthropic donations towards new equipment and infrastructure, in the Translational Medicine Laboratory at the University of Salford. We are thankful to Inovotion, Inc. (Grenoble, France), for independently performing the tumor growth and metastasis studies, using the CAM assay, as well as evaluating chicken embryo toxicity, through a research contract with Lunella Biotech, Inc (Ottawa, Canada).

## **CONFLICTS OF INTEREST**

MPL and FS hold a minority interest in Lunella Biotech, Inc.

## **FUNDING**

This work was supported by research grant funding, provided by Lunella Biotech, Inc.

## **REFERENCES**

1. Sotgia F, Ozsvari B, Fiorillo M, De Francesco EM, Bonuccelli G, Lisanti MP. A mitochondrial based oncology platform for targeting cancer stem cells (CSCs): MITO-ONC-RX. *Cell Cycle*. 2018; 17:2091–100. <https://doi.org/10.1080/15384101.2018.1515551> PMID:30257595
2. De Francesco EM, Sotgia F, Lisanti MP. Cancer stem cells (CSCs): metabolic strategies for their identification and eradication. *Biochem J*. 2018; 475:1611–34. <https://doi.org/10.1042/BCJ20170164> PMID:29743249
3. Martinez-Outschoorn UE, Peiris-Pagès M, Pestell RG, Sotgia F, Lisanti MP. Cancer metabolism: a therapeutic perspective. *Nat Rev Clin Oncol*. 2017; 14:11–31. <https://doi.org/10.1038/nrclinonc.2016.60> PMID:27141887
4. Peiris-Pagès M, Martinez-Outschoorn UE, Pestell RG, Sotgia F, Lisanti MP. Cancer stem cell metabolism. *Breast Cancer Res*. 2016; 18:55. <https://doi.org/10.1186/s13058-016-0712-6> PMID:27220421
5. Yu Z, Pestell TG, Lisanti MP, Pestell RG. Cancer stem cells. *Int J Biochem Cell Biol*. 2012; 44:2144–51. <https://doi.org/10.1016/j.biocel.2012.08.022> PMID:22981632
6. Lamb R, Harrison H, Hult J, Smith DL, Lisanti MP, Sotgia F. Mitochondria as new therapeutic targets for eradicating cancer stem cells: quantitative proteomics and functional validation via MCT1/2 inhibition. *Oncotarget*. 2014; 5:11029–37. <https://doi.org/10.18632/oncotarget.2789> PMID:25415228
7. Farnie G, Sotgia F, Lisanti MP. High mitochondrial mass identifies a sub-population of stem-like cancer cells that are chemo-resistant. *Oncotarget*. 2015; 6:30472–86. <https://doi.org/10.18632/oncotarget.5401> PMID:26421710
8. Lamb R, Bonuccelli G, Ozsvári B, Peiris-Pagès M, Fiorillo M, Smith DL, Bevilacqua G, Mazzanti CM, McDonnell LA, Naccarato AG, Chiu M, Wynne L, Martinez-Outschoorn UE, et al. Mitochondrial mass, a new metabolic biomarker for stem-like cancer cells: understanding Wnt/FGF-driven anabolic signaling. *Oncotarget*. 2015; 6:30453–71. <https://doi.org/10.18632/oncotarget.5852> PMID:26421711
9. De Luca A, Fiorillo M, Peiris-Pagès M, Ozsvari B, Smith DL, Sanchez-Alvarez R, Martinez-Outschoorn UE, Cappello AR, Pezzi V, Lisanti MP, Sotgia F. Mitochondrial biogenesis is required for the anchorage-independent survival and propagation of stem-like cancer cells. *Oncotarget*. 2015; 6:14777–95. <https://doi.org/10.18632/oncotarget.4401> PMID:26087310

10. Peiris-Pagès M, Oszvári B, Sotgia F, Lisanti MP. Mitochondrial and ribosomal biogenesis are new hallmarks of stemness, oncometabolism and biomass accumulation in cancer: mito-stemness and ribo-stemness features. *Aging* (Albany NY). 2019; 11:4801–35.  
<https://doi.org/10.18632/aging.102054>  
PMID: [31311889](https://pubmed.ncbi.nlm.nih.gov/31311889/)
11. Sotgia F, Whitaker-Menezes D, Martinez-Outschoorn UE, Flomenberg N, Birbe RC, Witkiewicz AK, Howell A, Philp NJ, Pestell RG, Lisanti MP. Mitochondrial metabolism in cancer metastasis: visualizing tumor cell mitochondria and the “reverse warburg effect” in positive lymph node tissue. *Cell Cycle*. 2012; 11:1445–54.  
<https://doi.org/10.4161/cc.19841> PMID: [22395432](https://pubmed.ncbi.nlm.nih.gov/22395432/)
12. Whitaker-Menezes D, Martinez-Outschoorn UE, Flomenberg N, Birbe RC, Witkiewicz AK, Howell A, Pavlides S, Tsigos A, Ertel A, Pestell RG, Broda P, Minetti C, Lisanti MP, Sotgia F. Hyperactivation of oxidative mitochondrial metabolism in epithelial cancer cells in situ: visualizing the therapeutic effects of metformin in tumor tissue. *Cell Cycle*. 2011; 10:4047–64.  
<https://doi.org/10.4161/cc.10.23.18151>  
PMID: [22134189](https://pubmed.ncbi.nlm.nih.gov/22134189/)
13. Lamb R, Oszvari B, Lisanti CL, Tanowitz HB, Howell A, Martinez-Outschoorn UE, Sotgia F, Lisanti MP. Antibiotics that target mitochondria effectively eradicate cancer stem cells, across multiple tumor types: treating cancer like an infectious disease. *Oncotarget*. 2015; 6:4569–84.  
<https://doi.org/10.18632/oncotarget.3174>  
PMID: [25625193](https://pubmed.ncbi.nlm.nih.gov/25625193/)
14. Scatena C, Roncella M, Di Paolo A, Aretini P, Menicagli M, Fanelli G, Marini C, Mazzanti CM, Ghilli M, Sotgia F, Lisanti MP, Naccarato AG. Doxycycline, an inhibitor of mitochondrial biogenesis, effectively reduces cancer stem cells (CSCs) in early breast cancer patients: a clinical pilot study. *Front Oncol*. 2018; 8:452.  
<https://doi.org/10.3389/fonc.2018.00452>  
PMID: [30364293](https://pubmed.ncbi.nlm.nih.gov/30364293/)
15. Oszvari B, Fiorillo M, Bonuccelli G, Cappello AR, Frattaruolo L, Sotgia F, Trowbridge R, Foster R, Lisanti MP. Mitoriboscins: mitochondrial-based therapeutics targeting cancer stem cells (CSCs), bacteria and pathogenic yeast. *Oncotarget*. 2017; 8:67457–72.  
<https://doi.org/10.18632/oncotarget.19084>  
PMID: [28978045](https://pubmed.ncbi.nlm.nih.gov/28978045/)
16. Oszvari B, Sotgia F, Lisanti MP. Exploiting mitochondrial targeting signal(s), TPP and bis-TPP, for eradicating cancer stem cells (CSCs). *Aging* (Albany NY). 2018; 10:229–40.  
<https://doi.org/10.18632/aging.101384>  
PMID: [29466249](https://pubmed.ncbi.nlm.nih.gov/29466249/)
17. De Francesco EM, Ószvári B, Sotgia F, Lisanti MP. Dodecyl-TPP targets mitochondria and potentially eradicates cancer stem cells (CSCs): synergy with FDA-approved drugs and natural compounds (Vitamin C and berberine). *Front Oncol*. 2019; 9:615.  
<https://doi.org/10.3389/fonc.2019.00615>  
PMID: [31440463](https://pubmed.ncbi.nlm.nih.gov/31440463/)
18. Györfy B, Lanczky A, Eklund AC, Denkert C, Budczies J, Li Q, Szallasi Z. An online survival analysis tool to rapidly assess the effect of 22,277 genes on breast cancer prognosis using microarray data of 1,809 patients. *Breast Cancer Res Treat*. 2010; 123:725–31.  
<https://doi.org/10.1007/s10549-009-0674-9>  
PMID: [20020197](https://pubmed.ncbi.nlm.nih.gov/20020197/)
19. Alsamri H, El Hasasna H, Al Dhaheer Y, Eid AH, Attoub S, Iratni R. Carnosol, a natural polyphenol, inhibits migration, metastasis, and tumor growth of breast cancer via a ROS-dependent proteasome degradation of STAT3. *Front Oncol*. 2019; 9:743.  
<https://doi.org/10.3389/fonc.2019.00743>  
PMID: [31456939](https://pubmed.ncbi.nlm.nih.gov/31456939/)
20. Nascimento BF, Laranjo M, Pereira NA, Dias-Ferreira J, Piñeiro M, Botelho MF, Pinho E Melo TM. Ring-fused diphenylchlorins as potent photosensitizers for photodynamic therapy applications: in vitro tumor cell biology and in vivo chick embryo chorioallantoic membrane studies. *ACS Omega*. 2019; 4:17244–50.  
<https://doi.org/10.1021/acsomega.9b01865>  
PMID: [31656898](https://pubmed.ncbi.nlm.nih.gov/31656898/)
21. Gilson P, Couvet M, Vanwonterghem L, Henry M, Voltaire J, Baulin V, Werner M, Orłowska A, Josserand V, Mahuteau-Betzer F, Lafanechère L, Coll JL, Busser B, Hurbini A. The pyrrolopyrimidine colchicine-binding site agent PP-13 reduces the metastatic dissemination of invasive cancer cells in vitro and in vivo. *Biochem Pharmacol*. 2019; 160:1–13.  
<https://doi.org/10.1016/j.bcp.2018.12.004>  
PMID: [30529691](https://pubmed.ncbi.nlm.nih.gov/30529691/)
22. El Hasasna H, Saleh A, Al Samri H, Athamneh K, Attoub S, Arafat K, Benhalilou N, Alyan S, Viallet J, Al Dhaheer Y, Eid A, Iratni R. Rhus coriaria suppresses angiogenesis, metastasis and tumor growth of breast cancer through inhibition of STAT3, NFκB and nitric oxide pathways. *Sci Rep*. 2016; 6:21144.  
<https://doi.org/10.1038/srep21144>  
PMID: [26888313](https://pubmed.ncbi.nlm.nih.gov/26888313/)
23. Al Dhaheer Y, Attoub S, Arafat K, Abuqamar S, Viallet J, Saleh A, Al Agha H, Eid A, Iratni R. Anti-metastatic and anti-tumor growth effects of origanum majorana on highly metastatic human breast cancer cells: inhibition



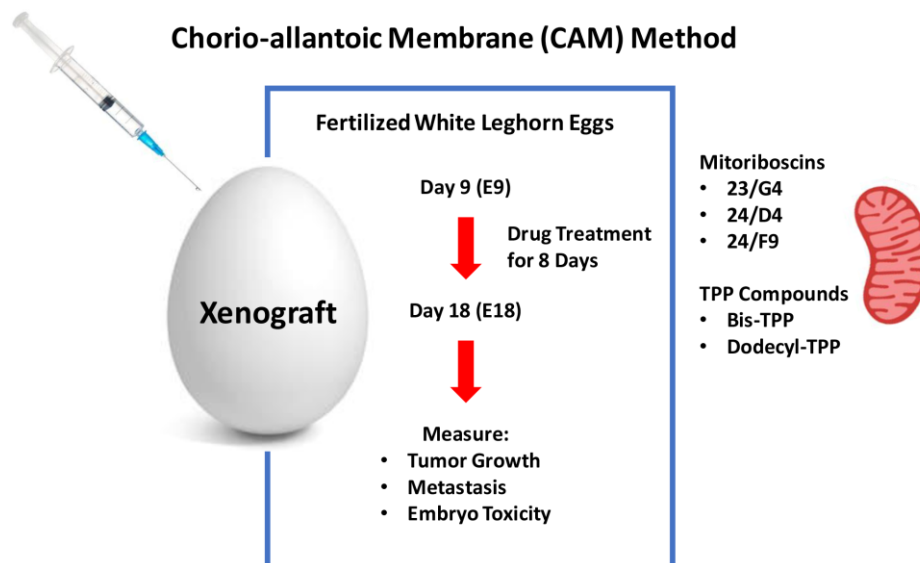
of NFκB signaling and reduction of nitric oxide production. PLoS One. 2013; 8:e68808.

<https://doi.org/10.1371/journal.pone.0068808>

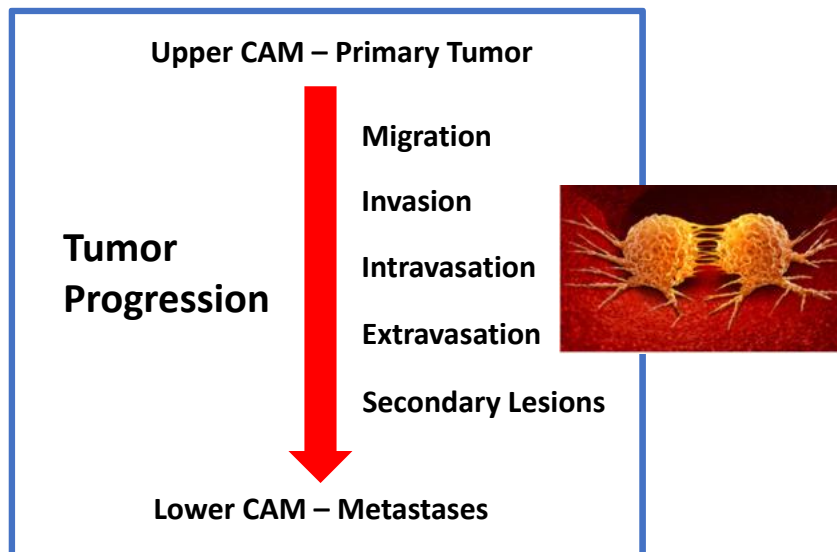
PMID:[23874773](https://pubmed.ncbi.nlm.nih.gov/23874773/)

## SUPPLEMENTARY MATERIALS

### Supplementary Figures



**Supplementary Figure 1. Summary: The Chorio-allantoic Membrane (CAM) Method.** Fertilized White Leghorn eggs were as used the xenograft host for growing human MDA-MB-231 cells to measure i) tumor growth (weight), ii) metastatic invasion/progression (by qPCR with specific primers for Human Alu sequences) and iii) drug toxicity (by evaluating chicken embryo viability). MDA-MB-231 cells were implanted on embryonic day 9 (E9). Then, tumor growth and metastasis were evaluated on embryonic day 18 (E18). Treatments were administered for 8 days, from E10 till E17. Using this approach, the efficacy and toxicity of five mitochondrial inhibitors were evaluated, in an *in vivo* setting: Mitoriboscins (23/G4, 24/D4, 24/F9) and TPP compounds (Bis-TPP and Dodecyl-TPP). See *Materials & Methods* for specific details.



**Supplementary Figure 2. Measuring Distant Metastasis with the CAM Method.** Spontaneous metastasis from the primary tumor located in the Upper CAM was measured by quantitating the amount of metastatic cells that accumulated in the Lower CAM region, after a period of 9 days, post-tumor cell implantation, using qPCR analysis. Importantly, metastatic dissemination, from the Upper CAM to the Lower CAM, requires cell migration, invasion, intravasation, extravasation and the formation of secondary lesions.

## Supplementary Tables

**Supplementary Table 1. Distant metastasis signature (13 genes): prognostic value of mitochondrial-related proteins up-regulated in MCF7 mammospheres, evaluated in ER(+) breast cancer patients (DMFS/ER+)/N=1,395/>240-months).**

Probe	Symbol	HR (DMFS)	Log-rank test
201128_s_at	ACLY	1.72	3.1e-05
208845_at	VDAC3	1.66	1.2e-05
202282_at	HADH2	1.58	7.2e-05
201441_at	COX6B1	1.53	0.00017
201322_at	ATP5B	1.43	0.0016
218440_at	MCCC1	1.40	0.0054
218275_at	SLC25A10	1.37	0.0048
205217_at	TIMM8A	1.37	0.0072
200789_at	ECH1	1.35	0.0092
212186_at	ACACA	1.34	0.031
200690_at	HSPA9	1.29	0.046
217720_at	CHCHD2	1.28	0.028
217814_at	CCDC47	1.28	0.032
<b>Combined</b>		<b>1.79</b>	<b>3.4e-07</b>

**Supplementary Table 2. Distant metastasis signature (4 genes): prognostic value of mitochondrial-related proteins up-regulated in MCF7 mammospheres, evaluated in ER(+) breast cancer patients (DMFS/ER+)/N=1,395/>240-months).**

Probe	Symbol	HR (DMFS)	Log-rank test
201128_s_at	ACLY	1.72	3.1e-05
208845_at	VDAC3	1.66	1.2e-05
202282_at	HADH2	1.58	7.2e-05
201441_at	COX6B1	1.53	0.00017
<b>Combined</b>		<b>1.91</b>	<b>2.2e-08</b>

**Supplementary Table 3. Tumor recurrence signature (4 genes): prognostic value of mitochondrial-related proteins up-regulated in MCF7 mammospheres, evaluated in ER(+) breast cancer patients (RFS/ER+)/N=3,082/>240-months).**

Probe	Symbol	HR (RFS)	Log-rank test
208845_at	VDAC3	1.56	2.3e-11
202282_at	HADH2	1.52	1.3e-09
201441_at	COX6B1	1.51	1.3e-10
201128_s_at	ACLY	1.12	0.091
<b>Combined</b>		<b>1.68</b>	<b>1.2e-15</b>

**Supplementary Table 4. Distant metastasis signature (9 genes): prognostic value of large mito-ribosomal proteins, evaluated in ER(+) breast cancer patients (DMFS /ER(+)/N=1,395/>240-months).**

Probe	Symbol	HR (DMFS)	Log-rank test
218027_at	MRPL15	1.68	4.1e-06
218049_s_at	MRPL13	1.56	8.8e-05
222216_s_at	MRPL17	1.53	0.00044
219244_s_at	MRPL46	1.46	0.0013
217907_at	MRPL18	1.40	0.005
218281_at	MRPL48	1.38	0.0078
208787_at	MRPL3	1.37	0.0086
218270_at	MRPL24	1.33	0.021
218105_s_at	MRPL4	1.29	0.023
<b>Combined</b>		<b>1.59</b>	<b>5e-05</b>

**Supplementary Table 5. Tumor recurrence signature (9 genes): prognostic value of large mito-ribosomal proteins, evaluated in ER(+) breast cancer patients (RFS /ER(+)/N=3,082/>240-months).**

Probe	Symbol	HR (RFS)	Log-rank test
218027_at	MRPL15	1.72	<1e-16
218049_s_at	MRPL13	1.71	<1e-16
208787_at	MRPL3	1.71	<1e-16
222216_s_at	MRPL17	1.70	1.1e-16
217907_at	MRPL18	1.55	2e-11
218281_at	MRPL48	1.26	0.00041
218105_s_at	MRPL4	1.24	0.00095
219244_s_at	MRPL46	1.21	0.0083
218270_at	MRPL24	1.10	0.2
<b>Combined</b>		<b>1.71</b>	<b>&lt;1e-16</b>

**Supplementary Table 6. Distant metastasis signature (6 genes): prognostic value of large mito-ribosomal proteins, evaluated in ER(+) breast cancer patients (DMFS /ER(+)/N=618/>240-months) treated with Tamoxifen.**

Probe	Symbol	HR (DMFS)	Log-rank test
218027_at	MRPL15	2.15	1.7e-06
219244_s_at	MRPL46	1.99	0.00011
222216_s_at	MRPL17	1.99	0.0036
218270_at	MRPL24	1.94	0.00024
217907_at	MRPL18	1.71	0.0051
218049_s_at	MRPL13	1.55	0.021
<b>Combined</b>		<b>2.16</b>	<b>1.7e-05</b>

**Supplementary Table 7. Tumor recurrence signature (8 genes): prognostic value of large mito-ribosomal proteins, evaluated in ER(+) breast cancer patients (RFS /ER(+)/N=799/>240-months) treated with Tamoxifen.**

Probe	Symbol	HR (RFS)	Log-rank test
218027_at	MRPL15	2.20	7.8e-08
208787_at	MRPL3	2.04	0.00015
222216_s_at	MRPL17	2.01	2.3e-06
217907_at	MRPL18	1.92	9.1e-06
218270_at	MRPL24	1.77	0.00012
218049_s_at	MRPL13	1.66	0.0059
218281_at	MRPL48	1.55	0.0033
219244_s_at	MRPL46	1.53	0.0063
<b>Combined</b>		<b>3.45</b>	<b>1.6e-08</b>

**Supplementary Table 8. Distant metastasis signature (6 genes): prognostic value of large mito-ribosomal proteins, evaluated in ER(-)/basal breast cancer patients (DMFS/N=145/>120-months).**

<b>Probe</b>	<b>Symbol</b>	<b>HR (DMFS)</b>	<b>Log-rank test</b>
222466_s_at	MRPL42	4.00	0.0024
227186_s_at	MRPL41	3.43	0.0023
225797_at	MRPL54	2.44	0.011
218049_s_at	MRPL13	2.23	0.0022
224331_s_at	MRPL36	2.13	0.036
218339_at	MRPL22	1.75	0.029
<b>Combined</b>		<b>2.95</b>	<b>0.0018</b>



## Research Paper

# Loss of AKR1B10 promotes colorectal cancer cells proliferation and migration via regulating FGF1-dependent pathway

Yizhou Yao<sup>1,\*</sup>, Xuchao Wang<sup>1,\*</sup>, Di Yuan Zhou<sup>1,\*</sup>, Hao Li<sup>1,\*</sup>, Huan Qian<sup>1</sup>, Jiawen Zhang<sup>1</sup>, Linhua Jiang<sup>1</sup>, Bin Wang<sup>1</sup>, Qi Lin<sup>2</sup>, Xinguo Zhu<sup>1</sup>

<sup>1</sup>Department of General Surgery, The First Affiliated Hospital of Soochow University, Suzhou, Jiangsu, China

<sup>2</sup>Suzhou Emergency Center, Suzhou, Jiangsu, China

\*Equal contribution

**Correspondence to:** Xinguo Zhu, Qi Lin; **email:** [xgzhu45@163.com](mailto:xgzhu45@163.com), [linqiemer@163.com](mailto:linqiemer@163.com)

**Keywords:** AKR1B10, colorectal cancer, FGF1, targeted therapy

**Received:** December 24, 2019

**Accepted:** May 1, 2020

**Published:** July 2, 2020

**Copyright:** Yao et al. This is an open-access article distributed under the terms of the Creative Commons Attribution License (CC BY 3.0), which permits unrestricted use, distribution, and reproduction in any medium, provided the original author and source are credited.

## ABSTRACT

Colorectal cancer (CRC) is a common malignancy worldwide with poor prognosis and survival rates. The aldo-keto reductase family 1 member B10 (AKR1B10) plays an important role in metabolism, cell proliferation and mobility, and is downregulated in CRC. We hypothesized that AKR1B10 would promote CRC genesis via a noncanonical oncogenic pathway and is a novel therapeutic target. In this study, AKR1B10 expression levels in 135 pairs of CRC and para-tumor tissues were examined, and its oncogenic role was determined using *in vitro* and *in vivo* functional assays following genetic manipulation of CRC cells. AKR1B10 was downregulated in CRC tissues compared to the adjacent normal colorectal tissues, and associated with the clinicopathological status of the patients. AKR1B10 depletion promoted the proliferation and migration of CRC cells *in vitro*, while its ectopic expression had the opposite effect. AKR1B10 was also significantly correlated with FGF1 gene and protein levels. Knockdown of AKR1B10 promoted tumor growth *in vivo*, and increased the expression of FGF1. Finally, AKR1B10 inhibited FGF1, and suppressed the proliferation and migration ability of CRC cells in an FGF1-dependent manner. In conclusion, AKR1B10 acts as a tumor suppressor in CRC by inactivating FGF1, and is a novel target for combination therapy of CRC.

## INTRODUCTION

Colorectal cancer (CRC) is one of the most commonly diagnosed malignancies worldwide, and is associated with high morbidity and mortality [1]. Apart from surgical resection, several targeted therapies have been developed against CRC in order to improve prognosis. However, the complex mechanism of CRC genesis considerably limits the therapeutic outcomes in advanced cancer [2, 3]. Therefore, it is essential to determine the mechanisms underlying the development and progression of CRC in order to identify novel therapeutic targets.

Aldo-keto reductase family 1 member B10 (AKR1B10), a member of the AKR1B subfamily, is a 36-kDa cytosolic

NADPH-dependent oxidoreductase that catalyzes the reduction of intracellular reactive oxygen species (ROS), retinaldehyde, lipid peroxidation products and xenobiotics [4, 5]. It is commonly expressed in normal epithelial tissues of the digestive tract and presents at very low level in non-gastrointestinal tissues [6, 7]. Aberrant expression of AKR1B10 has been detected in multiple solid tumors such as hepatocellular cancer [8], lung cancer [9], breast cancer [10] and pancreatic cancer [11], and strongly associated with prognosis [12–15], and downregulated in malignancies of the digestive tract, such as gastric cancer and CRC [15, 16]. AKR1B10 normally exerts a gastro-protective effect by metabolizing  $\alpha$ ,  $\beta$ -unsaturated carbonyl compounds produced by gut microbiota into less toxic hydroxyl compounds [17], promoting the synthesis of fatty acids or lipids in the digestive tract mucosa for the

constant renewal of crypt cells [18], and mediating retinoid acid homeostasis and cell differentiation [10]. Thus, it is not surprising that aberrantly low level of AKR1B10 in the gastrointestinal tract is closely linked with the development of cancers [15, 16], as well as inflammatory conditions like diabetic nephropathy [19]. However, little is known regarding the role of AKR1B10 in CRC development, and the molecular mechanisms remain elusive.

Fibroblast growth factor 1 (FGF1) was first identified in brain and pituitary tissues [10], and functions as an insulin sensitizer in type 2 diabetes mellitus along with maintaining adipose tissue and metabolic homeostasis [20, 21]. Studies have also reported anti-inflammatory effects of FGF1 [21, 22], which is significant since metabolic disorders often progress to tumors due to adipose inflammation and systemic circulation of metabolic and inflammatory factors [23]. Therefore, we hypothesized that high level expression of AKR1B10 would suppress CRC development via a non-canonical FGF1-dependent pathway, and our findings demonstrated a novel role of AKR1B10 in CRC and identified its potential diagnostic and therapeutic relevance.

## RESULTS

### AKR1B10 is downregulated in CRC tissues and related to poor prognosis

The AKR1B10 protein was highly expressed in normal colorectal tissues, and significantly lower in the CRC tissues (Figure 1A–1B, Supplementary Figure 1A). Although *in situ* AKR1B10 levels were similar between the T1-2 and T3-4 tissues ( $P > 0.05$ ; Figure 1C), it was significantly decreased in patients with lymph node invasion compared with those without ( $P < 0.01$ , Figure 1D). Furthermore, AKR1B10 expression was reduced in CRC tissues with tumor-node-metastasis (TNM) staging I-II compared to III-IV ( $P < 0.01$ ; Figure 1E). Our results were confirmed with TCGA datasets in the GEPIA platform (Supplementary Figure 1B). In addition, AKR1B10 expression was significantly associated with the depth of invasion ( $P < 0.05$ ), lymph node invasion ( $P < 0.001$ ) and TNM staging ( $P < 0.001$ , Table 1), while no correlation was observed with other clinicopathological variables such as age, gender, tumor size, tumor location or degree of differentiation ( $P > 0.05$ ; Table 1). Univariate analysis further revealed that

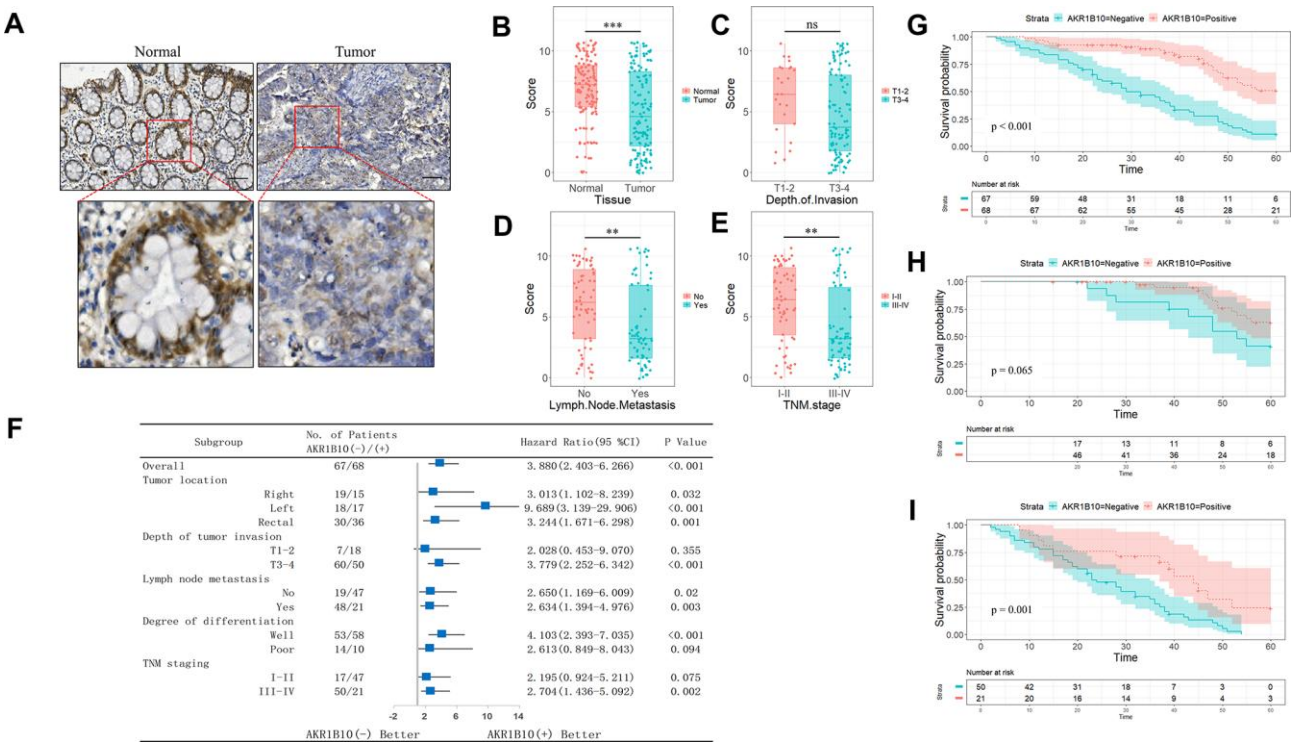


**Figure 1. Expression of AKR1B10 in CRC tissues.** (A) Representative IHC images showing *in situ* AKR1B10 expression in CRC and normal tissues (scale bar = 100μm). (B–E) IHC scores of AKR1B10 in (B) CRC vs normal tissues, (C) T I-II vs T III-IV tissues, (D) tumors with or without lymph node invasion, and (E) early vs late TNM staging. (F) OS of AKR1B10<sup>pos</sup> and AKR1B10<sup>neg</sup> CRC patients in subgroups demarcated by tumor location, depth of tumor invasion, lymph node metastasis, degree of differentiation and TNM staging. (G–I) OS of (G) AKR1B10<sup>pos</sup> and AKR1B10<sup>neg</sup> CRC patients with TNM staging I-II (H) and III-IV (I). CRC, colorectal cancer. OS, overall survival. ns, no significant difference. \*\*  $P < 0.01$ , \*\*\*  $P < 0.001$ .

**Table 1. Relationship between AKR1B10 and clinic-pathological factors in 135 CRC patients.**

Variables	AKR1B10		<i>P</i> value
	Negative	Positive	
Age (years)			
≤60	30	27	0.551
>60	37	41	
Gender			
Male	33	24	0.863
Female	44	34	
Size (cm)			
<5	26	31	0.702
≥5	33	45	
Tumor location			
Right	19	15	0.595
Left	18	17	
Rectal	30	36	
Depth of tumor invasion			
T1-2	7	18	0.017 <sup>a</sup>
T3-4	60	50	
Lymph node metastasis			
No	19	47	<0.001 <sup>b</sup>
Yes	48	21	
Degree of differentiation			
Well	53	58	0.347
Poor	14	10	
TNM staging			
I-II	17	47	<0.001 <sup>b</sup>
III-IV	50	21	

<sup>a</sup> *P* < 0.05, <sup>b</sup> *P* < 0.001

low AKR1B10 expression (*P* < 0.001), lymph node invasion (*P* < 0.001), degree of differentiation (*P* < 0.01), depth of invasion (*P* < 0.001) and TNM staging (*P* < 0.001, Table 2) were related to poor prognosis, and low AKR1B10 expression was confirmed as an independent prognostic factor for the survival of CRC patients by multivariate analysis (*P* < 0.001, Table 2). Therefore, we demarcated the patients according to AKR1B10 expression levels, and found that the survival of AKR1B10<sup>neg</sup> patients was significantly worse compared to the AKR1B10<sup>pos</sup> group (*P* < 0.05; Figure 1F–1G, Supplementary Figure 1C), regardless of age, gender, tumor size, tumor location, venous invasion, neural invasion and lymph node metastasis. In contrast, AKR1B10 expression level had no bearing on the survival of patients with staging T1-T2 invasion (*P* = 0.355), poor differentiation (*P* = 0.094) and TNM staging I-II (*P* = 0.075). Interestingly, elevated AKR1B10 expression was

associated with favorable prognosis in patients with TNM staging III-IV but not the staging I-II patients (*P* = 0.065; *P* = 0.001; Figure 1H–1I).

#### **Ectopic AKR1B10 inhibits proliferation and migration of CRC cells in vitro**

Pooled analysis of CRC and normal tissues across 7 Oncomine datasets (Figure 2A) revealed significant downregulation of *AKR1B10* mRNA in the CRC tissues, which was also consistent with the findings of Gaedcke et al, Kaiser et al and Hong et al (Supplementary Figure 2A). Furthermore, *AKR1B10* expression was also downregulated in the CRC tissues of our cohort compared to the paired normal tissues (Figure 2B, Supplementary Figure 2B–2C), as well as in multiple CRC cell lines (Figure 2C–2D, Supplementary Figure 2D). The HT29 cells expressed the highest levels

**Table 2. Results of univariate and multivariate analyses of postoperative patients' survival by Cox's proportional hazard model.**

Varieties	n	Univariate analysis			Multivariate analysis		
		HR	95% CI	P	HR	95% CI	P
Age ( $\leq 60$ or $>60$ years)	57/78	1.084	0.696-1.687	0.722			
Gender (Male / Female)	77/58	0.876	0.561-1.366	0.559			
Size of tumor ( $\leq 5$ or $>5$ cm)	59/76	0.654	0.418-1.023	0.063			
Depth of tumor invasion (T1-2 / T3-4)	25/110	0.223	0.102-0.487	$<0.001^c$	0.360	0.161-0.805	0.013 <sup>a</sup>
Lymph node metastasis (negative / positive)	66/69	0.179	0.108-0.298	$<0.001^c$	7.731	1.656-36.084	0.009 <sup>b</sup>
Degree of differentiation (moderate-well/poor)	111/24	0.461	0.270-0.787	0.005 <sup>b</sup>	0.799	0.457-1.395	0.429
TNM staging (I-II / III-IV)	64/71	0.157	0.093-0.264	$<0.001^c$	0.033	0.006-0.164	$<0.001^c$
AKR1B10 expression (negative / positive)	67/68	3.880	2.403-6.266	$<0.001^c$	2.492	1.491-4.164	$<0.001^c$

<sup>a</sup>  $P < 0.05$ , <sup>b</sup>  $P < 0.01$ , <sup>c</sup>  $P < 0.001$

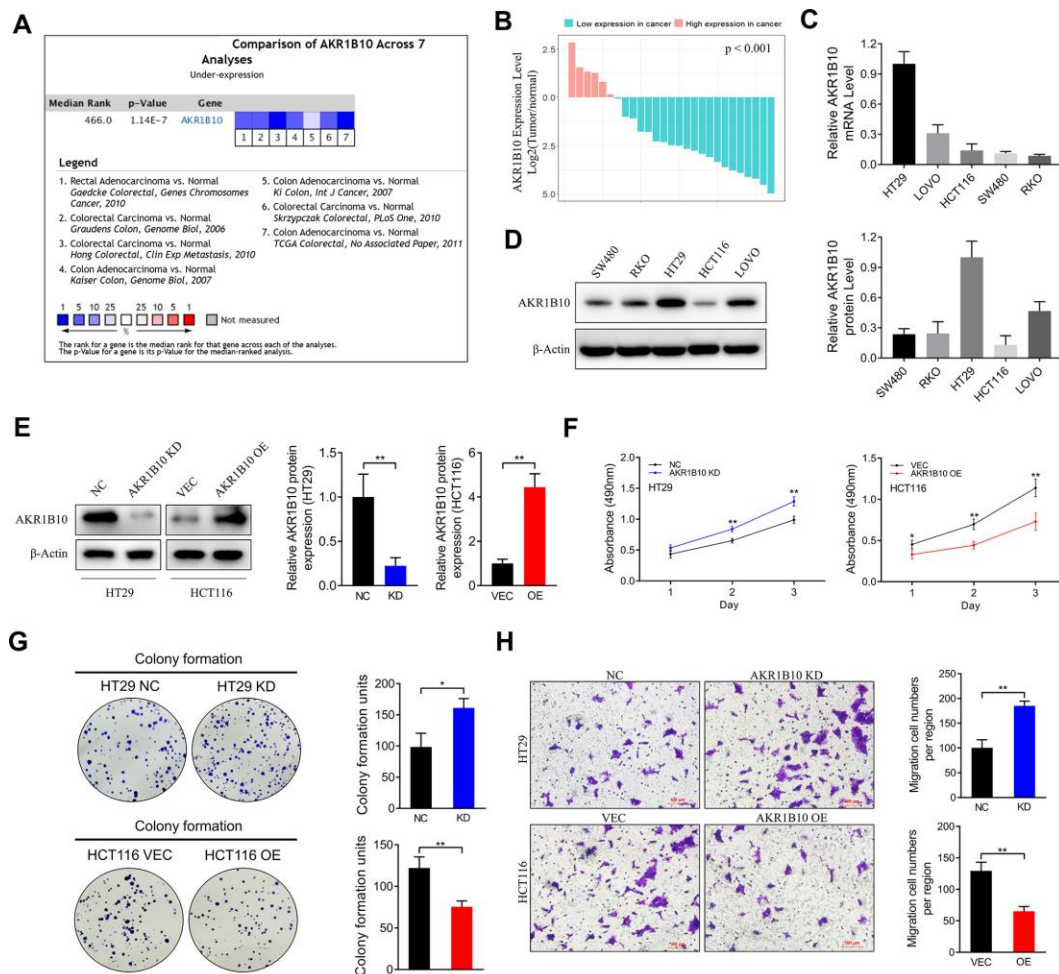


**Figure 2. Effect of AKR1B10 on CRC cell proliferation and migration ability.** (A) Comparison of AKR1B10 mRNA expression in CRC and normal tissues across 7 Oncomine datasets. (B–C) AKR1B10 mRNA levels in (B) 27 paired CRC and normal tissues and (C) 5 CRC cell lines. (D–E) Immunoblots showing AKR1B10 protein levels in (D) wild type and (E) AKR1B10-KD and AKR1B10-OE CRC cell lines. (F–H) Proliferation rates (F), colony forming capacity (G) and migration rates (H) of AKR1B10-KD and AKR1B10-OE CRC cells. CRC, colorectal cancer. CTL, control; NC, negative control; KD, AKR1B10-shRNA; VEC, vector; OE, AKR1B10 overexpression plasmid. Data are presented as mean  $\pm$  SD (n=3). \* $P < 0.05$ , \*\* $P < 0.01$ , \*\*\* $P < 0.001$ .



of AKR1B10, while that in the SW480, HCT116 and RKO cells were relatively low. The biological role of AKR1B10 was further analyzed using knockdown (KD) and overexpression (OE) constructs (Figure 2E). The proliferation rate of AKR1B10-KD cells was significantly higher, and that of AKR1B10-OE cells was inhibited compared to the negative controls (Figure 2F). Consistent with this, the AKR1B10-KD cells also showed enhanced colony-formation ability, which was markedly suppressed in the AKR1B10-OE cells (Figure 2G). Overexpression of AKR1B10 also inhibited *in vitro* migration of CRC cells, whereas its knockdown had the opposite effect (Figure 2H). Taken together, AKR1B10 acts as a tumor suppressor in CRC, and its ectopic expression promotes the growth of CRC cells *in vitro*.

### AKR1B10 is closely related with FGF1 expression levels in CRC tissues

Since FGF1 is associated with inflammation in the tumor microenvironment, we next analyzed the potential correlation between AKR1B10 and FGF1 in TCGA datasets. AKR1B10 expression levels in the CRC tissues were closely related to that of FGF1 ( $P < 0.001$ , Figure 3A). Furthermore, FGF1 mRNA levels were also significantly higher in most CRC tissue specimens compared to the paired normal tissues ( $P < 0.001$ , Figure 3B, Supplementary Figure 3A, 3B). Interestingly, high AKR1B10 levels were significantly correlated with reduced FGF1 expression in CRC tissues ( $P = 0.001$ ), while no such correlation was seen

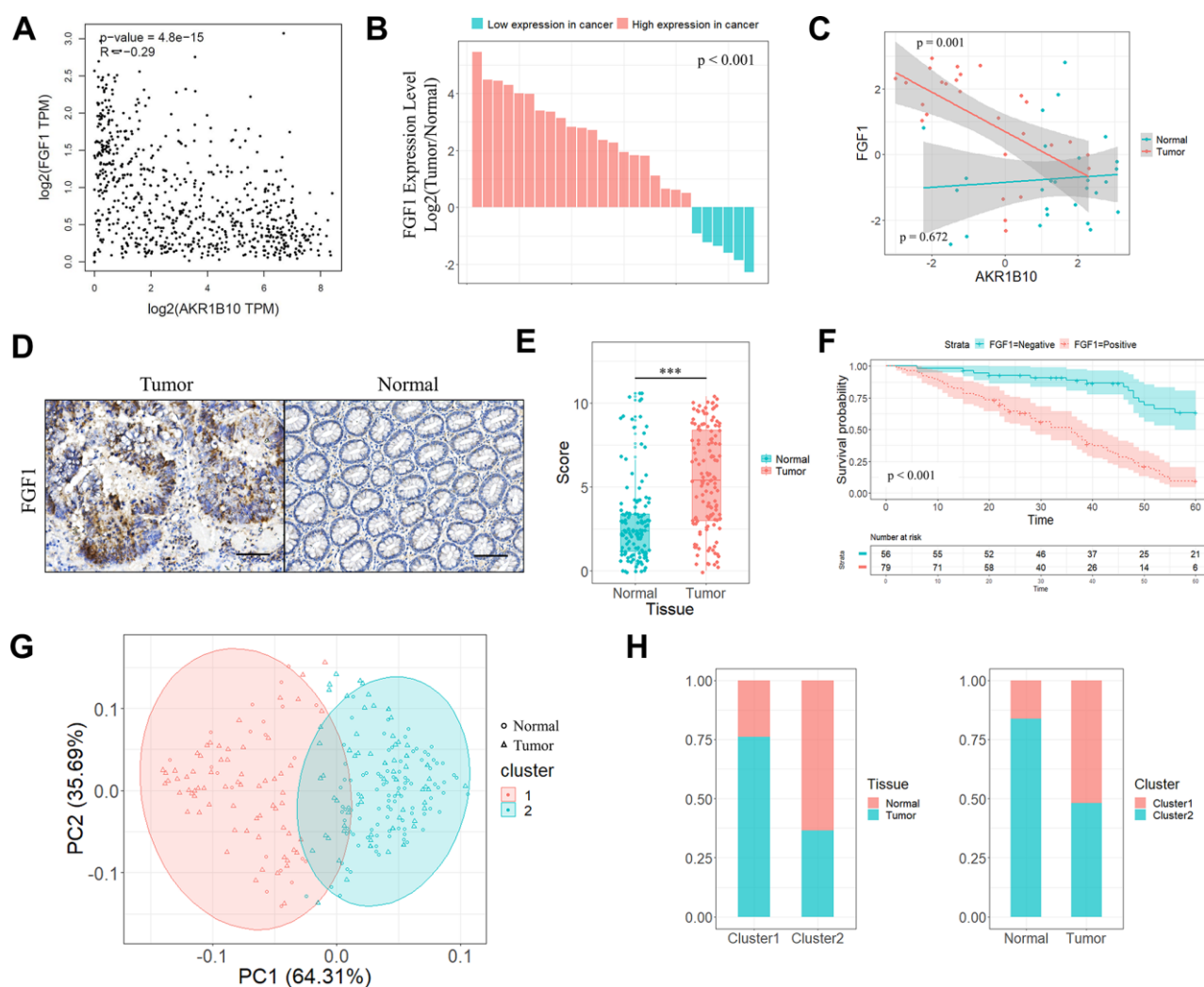


**Figure 3. Correlation between AKR1B10 and FGF1 in CRC tissues.** (A) Correlation analysis of AKR1B10 and FGF1 levels in CRC tissues from TCGA datasets by GEPIA platform. (B) FGF1 mRNA levels in 27 paired CRC and normal tissues. (C) Correlation between AKR1B10 and FGF1 levels in the above. (D) Representative IHC images showing *in situ* FGF1 expression in CRC and normal tissues (scale bar = 100 $\mu$ m) and (E) corresponding IHC scores. (F) OS of 135 CRC patients demarcated by FGF1 expression levels. (G) Stratification of 135 pairs of CRC and normal tissues into cluster 1 (red) and cluster 2 (green) according to AKR1B10 and FGF1 IHC scores. (H) Percentage of tumor and normal samples in each cluster. CRC, colorectal cancer. OS, overall survival. \*\*\*  $P < 0.001$ .



in normal tissues ( $P > 0.05$ , Figure 3C). Based on both variables, the tumor and normal groups were stratified into two clusters (Supplementary Figure 3C–3D), and most normal specimens belonged to Cluster 1 (71.4%) as opposed to Cluster 2 (28.6%) whereas the tumor samples were concentrated in Cluster 2 (63% compared to 37% in Cluster 1). The FGF1 protein levels were also significantly higher in CRC compared to the normal tissues (Figure 3D–3E), and its reduced expression was predictive of longer survival (Figure 3F). In the cluster analysis as well, the IHC scores of AKR1B10 and FGF1 were significantly different between tumor and normal tissues (Figure 3G), with 23.9% and 76.1% of the normal samples, and 51.9% and 48.1% tumor samples respectively present in Cluster 1 and Cluster 2 (Figure 3H). Taken together, AKR1B10 and FGF1 levels can distinguish between CRC and normal tissues.

## AKR1B10 inhibits colorectal tumorigenesis in vivo by targeting FGF1

The role of AKR1B10 in CRC tumor growth was analyzed by establishing an *in vivo* xenograft model using wild-type and AKR1B10-KD HT29 cells. Depletion of AKR1B10 had no obvious effect on the body weight of the mice (Figure 4A), but significantly enhanced the proliferative capacity of the CRC cells, which was manifested as increased tumor size (Figure 4B) and weight (Figure 4C–4D) compared to control group. However, the net body weights obtained after subtracting the tumor weights were significantly lower in the mice implanted with AKR1B10-KD CRC cells (Figure 4E). Furthermore, *in situ* AKR1B10 mRNA levels were markedly lower and that of FGF1 was higher in the AKR1B10-KD tumors (Figure 4F–4G),

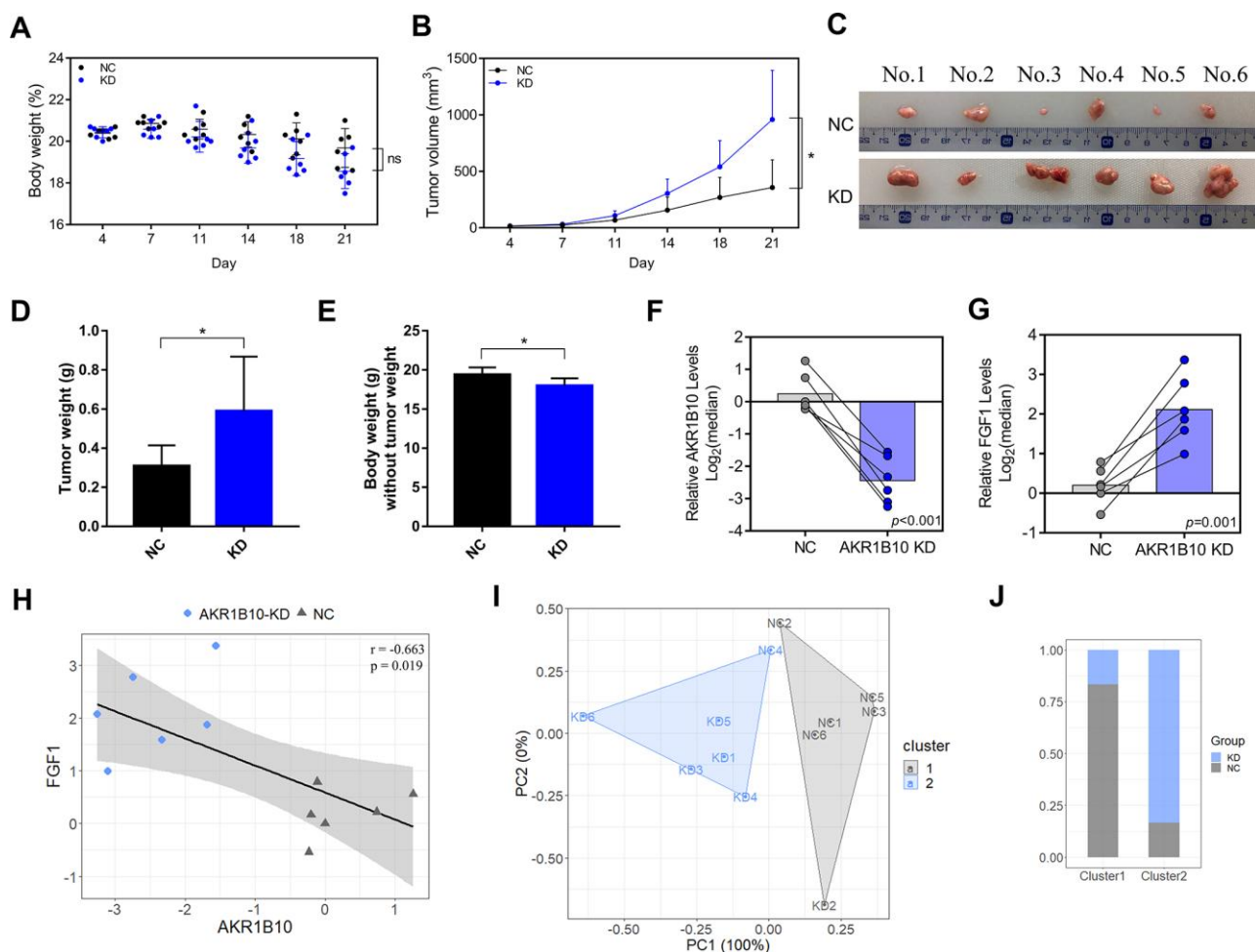


**Figure 4. AKR1B10 knockdown suppresses CRC tumor growth *in vivo*.** (A–B) Total body weight (A) and tumor volume (B) of the mice during the experiment. (C) Representative pictures of subcutaneous tumors harvested from NC and AKR1B10-KD group. (D) The weights of tumor masses. (E) Net body weight after subtracting the respective tumor weights. (F–G) Relative AKR1B10 (F) and FGF1 (G) mRNA levels in the tumors and their (H) correlation. (I) Stratification of mice into cluster 1 (grey) and cluster 2 (blue) according to body weight, tumor volume, tumor weight and AKR1B10 and FGF1 mRNA levels. (J) Percentage of NC and AKR1B10-KD mice in each cluster. Data are presented as mean  $\pm$  SD. CRC, colorectal cancer. NC, negative control; KD, AKR1B10-shRNA. \* $P < 0.05$ , \*\* $P < 0.01$ , \*\*\* $P < 0.001$ .

and showed significant statistical correlation (Figure 4H). We next performed a cluster analysis to consider the combined effects of body weight, tumor volume, tumor weight and AKR1B10/FGF1 levels (Figure 4I), and found that 16.67% of the AKR1B10-KD and 83.33% of the NC group mice were in Cluster 1 (Figure 4J). To gain further mechanism insights, we analyzed the FGF1 levels in CRC cells transfected with AKR1B10-shRNA or AKR1B10 overexpression plasmid, and found that AKR1B10 downregulated FGF1 while knocking it

down had the opposite effect (Figure 5A). To further determine the role of FGF1 in AKR1B10-mediated regulation of CRC progression, the HT29 cells were co-transfected with AKR1B10-shRNA and FGF1-shRNA. Interestingly, inhibiting AKR1B10 restored FGF1 expression levels following the latter's knockdown (Figure 5B) but its overexpression did not rescue the CRC cells from the anti-proliferative effects of FGF1 knockdown (Figure 5C–5E). Taken together, AKR1B10-mediated inhibition of CRC cells is dependent on FGF1.

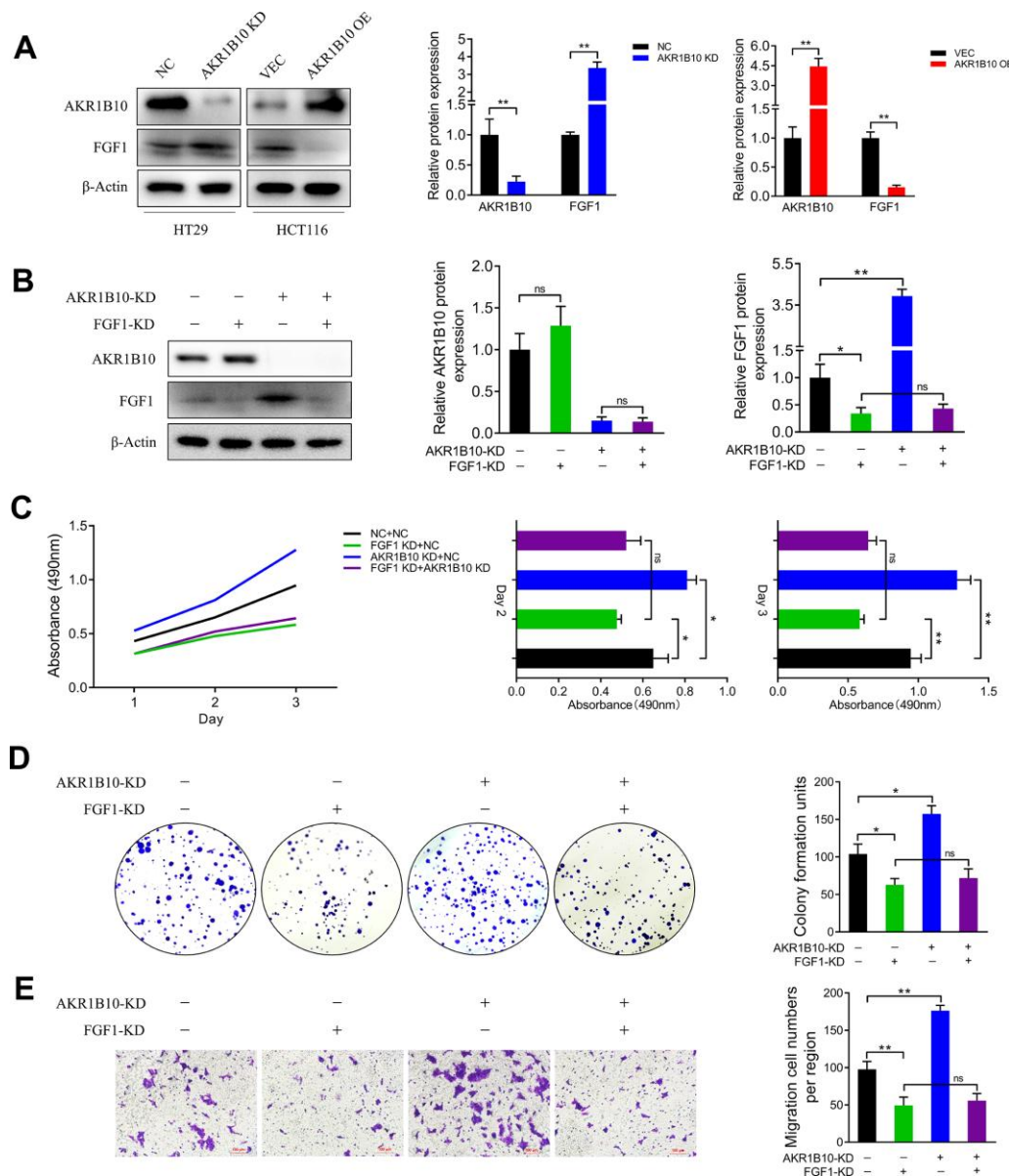


**Figure 5. AKR1B10 inhibits CRC cell growth in an FGF1-dependent manner.** (A) Immunoblot showing AKR1B10, FGF1 and GAPDH protein levels in HT29 cells transfected with AKR1B10-shRNA and in HCT116 cells transfected with AKR1B10 overexpression plasmid. (B) Immunoblot showing AKR1B10, FGF1 and GAPDH protein levels in HT29 transfected with FGF1-shRNA alone or in combination with AKR1B10-shRNA. (C–E) Proliferation rates (C), colony forming capacity (D) and migration rates (E) of the HT29 cells transfected as above. Data are presented as mean ± SD. NC, negative control; KD, AKR1B10-shRNA; VEC, vector; OE, AKR1B10 overexpression plasmid. “-”, control-shRNA. “+”, AKR1B10 or FGF1 shRNA. \* $P < 0.05$ , \*\* $P < 0.01$ , \*\*\* $P < 0.001$ .

## DISCUSSION

AKR1B10 metabolizes various substrates such as retinaldehyde, lipid peroxidation products, and xenobiotics [5, 25–27]. It is primarily expressed in normal gastrointestinal epithelial tissues, and usually non-detectable in non-digestive tract tissues [28, 29]. Recent studies have implicated AKR1B10 in tumor growth and metastasis, and reported aberrant expression levels in various cancers [14, 30]. We found that AKR1B10 levels were high in the normal colorectal tissues and decreased significantly in primary CRC tumors compared to the surrounding normal tissues. Furthermore, CRC patients overexpressing AKR1B10 had better OS compared to the low-expressing group, which is consistent with previous studies [16, 31–33]. Nevertheless, the difference in the expression levels of AKR1B10 in the gastrointestinal and other solid tumors [12, 14–16, 34–38] has limited the clinical relevance of AKR1B10 as a therapeutic target. Although a previous study correlated AKR1B10 expression to the prognosis of CRC patients [15], its role in CRC development remains unclear. We found that reduced levels of AKR1B10 in the tumor tissues correlated significantly with advanced stages, greater invasiveness, increased tumor differentiation and poor survival of CRC patients, indicating that AKR1B10 is a potential tumor suppressor in CRC. Consistent with this, ectopic expression of AKR1B10 in the CRC cells significantly inhibited their proliferation, clonal expansion and migration *in vitro*.

AKR1B10 is a potential biomarker of CRC, although the mechanisms underlying AKR1B10 down-regulation in CRC and AKR1B10-mediated tumorigenesis remain to be clarified. Overexpression of AKR1B10 significantly inhibited the proliferation and migration of CRC cells. Correlation analysis on TCGA datasets showed a significant association between AKR1B10 and FGF1. The latter is a member of the fibroblast growth factor family that is involved in cell proliferation and migration [39–41], and acts as an oncogene in several cancers. FGF1 is aberrantly expressed in pancreatic cancer, lung cancer, glioblastoma and prostate cancer [42–45]. Elevated FGF1 levels are associated with increased angiogenesis and decreased survival in serous ovarian adenocarcinoma [46], and is a potential therapeutic target for ovarian cancer [47, 48]. We found that FGF1 was overexpressed in CRC tissues and predicted poor prognosis. Furthermore, cluster analysis indicated that both FGF1 and AKR1B10 expression levels were able to distinguish between the tumor and adjacent normal tissues, and pointed to a functional relationship as well.

AKR1B10 and AKR1B1 are closely related to inflammation [15, 19], and AKR1B10 in particular regulates inflammatory factors in the tumor

microenvironment, which mobilizes the host immune response and promotes tumor suppression [15, 19, 49]. FGF1 activation is mediated via the PI3K-Akt signaling pathway that lies upstream of mTOR [50], which is related to autophagy, apoptosis and metabolism of cancer cells, as well as the NLRP3-mediated inflammatory response [51, 52]. Based on previous evidence and our findings, we hypothesized that AKR1B10 would inhibit the proliferation and migration of CRC cells by regulating FGF1-dependent signaling pathways. Indeed, AKR1B10 inhibited FGF1 in CRC cell lines, and elevated FGF1 in response to AKR1B10 depletion promoted xenograft tumor growth in a mouse model. In addition, an inverse correlation between FGF1 and AKR1B10 was also observed in human CRC tumors. The likely mechanism underlying the inhibitory effect of AKR1B10 is the induction of an anti-tumor inflammatory response [15, 53] by targeting FGF1, which is related to the growth and migration of CRC cells [54, 55]. The involvement of an FGF1-dependent pathway is significant in the context of therapeutically targeting AKR1B10 in CRC [56]. Since AKR1B10 was not able to rescue CRC cells after FGF1 knockdown, the latter is possibly a downstream target of AKR1B10. Although the exact regulatory mechanism warrants future investigation, our findings provide a rationale for targeting both as a combination therapy for CRC.

## MATERIALS AND METHODS

### Human tissue specimens

A total of 135 pairs of CRC and adjacent normal colon tissues were collected immediately after surgical resection at the Department of General Surgery of the First Affiliated Hospital of Soochow University (Suzhou, China) from 2010 to 2013. None of the patients had received radiotherapy or chemotherapy before radical surgery, and all tissue specimens were verified histo-pathologically. The study was approved by the Independent Ethics Committee of the First Affiliated Hospital of Soochow University (IRB approval number, 2020-076), and all patients provided written informed consent.

### Immunohistochemistry (IHC) evaluation

Tissue specimens were fixed with 10% formalin, embedded in paraffin, and cut into 5µm-thick sections. After cleaned in xylene and rehydrated through an ethanol gradient, the sections were treated with 3% hydrogen peroxide to quench endogenous peroxidases, and then boiled in 10mM citrate buffer (pH 6) for antigen retrieval. The processed sections were then blocked with 10% goat serum for 30 min, and incubated overnight with 1:200 diluted polyclonal anti-human

AKR1B10 (BOSTER, Wuhan, China) or anti-human FGF1 (BOSTER, Wuhan, China) at 4°C. Color was developed using a tissue staining kit (Zhongshan Biotechnology, Beijing, China). The AKR1B10 or FGF1 staining scores were evaluated in five random fields per slide by two pathologists YuHong Wang (The First Affiliated Hospital of Soochow University) and Zheng Zhi (The Soochow University) in a blinded manner as previously described [24]. The percentage of positively stained cells was scored as follows: 0 - 0-5%; 1 - 6-25%; 2 - 26-50%; 3 - 51-75%; 4 - >75%. The staining intensity was scored as 0 (negative), 1 (weak), 2 (moderate) and 3 (strong). The final score was the average of the percentage score multiplied by intensity score, and graded as follows: - (0), + (1-4), ++ (5-8) and +++ (9-12). Samples with final scores ++ or +++ were graded as positive, and - or + as negative.

### Bioinformatics analysis

CRC gene expression datasets were downloaded from the Oncomine (<https://www.oncomine.org>), CCLE (Cancer Cell Line Encyclopedia, <https://portals.broadinstitute.org/ccle>) and GEPIA (Gene Expression Profiling Interactive Analysis, <http://gepia.cancer-pku.cn>) databases, and analyzed by established protocols.

### Survival analysis

All patients were followed up by personal or telephonic interviews for 60 months, and the time point was set as the date of CRC-related death or 60 months after surgery. Self-developed R program (version 3.6.1 for Windows, <http://cran.r-project.org/>) was used for sample classification and prognostic analysis. The patients were classified into two subgroups according to the IHC staining scores, and Kaplan-Meier survival curves were plotted for both groups using the “survminer” package (version 0.4.6, <https://cran.r-project.org/web/packages/survminer/index.html>). The log-rank test was used for statistical comparison and  $P < 0.05$  was considered significant.

### Cell culture and transfection

Five human CRC cell lines (HCT116, HT29, LOVO, SW480 and RKO) were purchased from the Cell Bank of Chinese Academy of Sciences (Shanghai, China), and were cultured in RPMI 1640 medium (Hyclone) supplemented with 10% fetal bovine serum (Gibco, USA), penicillin G sodium (100U/ml) and streptomycin (100µg/ml) at 37°C under 5% CO<sub>2</sub>. The HT29 cells were grown till 70% confluency, and transfected with human AKR1B10 or human FGF1 shRNA according to the manufacturer's instructions. The transfected cells were

selected using 500µg/ml G418 (Roche, Switzerland) for 3-4 weeks, and clones with a stable knockdown of AKR1B10 or FGF1 were selected for further experiments. Control cells were stably transfected with scrambled shRNA. In addition, 70% confluent HCT116 cells were transfected with the AKR1B10 cDNA or empty plasmid using X-tremegene HP at 1:1 ratio, and harvested after 24h. Transient overexpression and silencing were confirmed by RT-PCR and Western blotting. All stable transfectants were used by the 8th passage.

### RNA isolation and quantitative real-time PCR (qRT-PCR)

Total RNA was extracted from the tissues or cells using TRIzol reagent (Invitrogen, Life Technologies, USA) according to the manufacturer's protocol. Following DNase I (Thermo Fisher Scientific, USA) treatment to remove genomic DNA, 1µg RNA was reverse transcribed using a RevertAid First Strand cDNA Synthesis Kit (Thermo Fisher Scientific, USA). The qRT-PCR was performed using Power SYBR® Green PCR Master Mix (ABI, USA) on the 7500 real time PCR system (ABI, USA) according to the manufacturer's instructions. Fold changes were calculated relative to  $\beta$ -actin (internal control) using the  $2^{-\Delta\Delta C_T}$  method. The following primers were used: AKR1B10 forward (5'-CCCAAAGATGATAAAG GTAATGCCATCGGT-3') and reverse (5'-CGATCT GGAAGTGGCTGAAATTGGAGA-3'); FGF1 forward (5'-GTGGATGGGACAAGGGACAG-3') and reverse (5'-GGCAGGGGGAGAAACAAGAT-3');  $\beta$ -actin forward (5'-CCACACTGTGCCCATCTACG-3') and reverse (5'-AGGATCTTCATGAGGTAGTCAGTCAG-3'). The PCR conditions were: initial denaturation at 95°C for 5 min, followed by 40 cycles of denaturation at 95°C for 30 sec, annealing at 55°C for 30 sec and extension at 72°C for 30 sec, and final extension at 72°C for 7 min.

### Protein isolation and Western blotting

Cells were lysed in ice-cold RIPA lysis buffer supplemented with protease and phosphatase inhibitors (KeyGEN Inc., Nanjing, China) according to the manufacturer's protocol. The extracted proteins were separated by SDS-PAGE and transferred onto PVDF membranes (Millipore, USA). After blocking with 5% non-fat milk for 1h, the membranes were probed overnight with anti-AKR1B1 (1:1000, Cell Signaling Technology), anti-FGF1 (1:1000, Cell Signaling Technology) and anti- $\beta$ -Actin (1:5000, Cell Signaling Technology) antibodies at 4°C with gentle shaking, followed by horseradish peroxidase-conjugated secondary antibodies. The protein bands were visualized by chemiluminescence and quantified by ImageJ for Windows (NIH, USA).



## MTT assay

Cell viability was determined using an MTT assay kit (Amresco, USA) according to the manufacturer's instructions. Briefly, 2000 transfected cells were seeded in 96-well plates, and cultured for 12, 24, 36, 48, 60 and 72h. The MTT solution was added 4h prior to the termination of each time point, and the supernatants were removed. The formazan crystals were dissolved in 150µl DMSO per well for 10 min with gentle shaking, and the absorbance at 490nm was measured using a microplate reader.

## Cell migration assay

Cell migration was assessed using Transwell inserts (pore size 8µm; Corning, New York, USA). The cells were seeded into the upper chambers of the inserts at the density of 50,000 cells/200µl in serum-free RPMI 1640 medium, and the lower chambers were filled with 750µl complete medium per well. After incubating for 24h at 37°C, the cells remaining on the upper surface of the membrane were removed using a cotton swab. The filters were then fixed with 4% paraformaldehyde, and the cells on the lower surface were stained with 0.1% crystal violet and counted in 5 random fields per sample.

## Colony formation assay

The suitably transfected cells were seeded in 6-well plates at the density of 1000 cells/well, and cultured for 10 days before being fixed and stained with 0.1% crystal violet. The colonies with more than 100 cells were counted at 40x magnification under an optical microscope (Nikon, Japan) fitted with a digital camera (Nikon, Japan).

## Subcutaneous xenograft establishment

SPF male BALB/c nude mice (3-5weeks old and weighing 16-18 g) were purchased from Shanghai SLRC laboratory Animal Co. Ltd. (Shanghai, China). The mice were randomly divided into the AKR1B10 knock down (KD) and negative control (NC) groups (n = 6 per group), and accordingly injected subcutaneously with 5×10<sup>6</sup> AKR1B10-KD or NC-shRNA HT29 into the left and right dorsal flank on day 0. All animal experiments were approved by the Animal Ethics Committee of Soochow University (Suzhou, China).

## Statistical analysis

All data were presented as mean ± SD of three independent experiments. Statistical analyses were performed using SPSS 22.0 software (SPSS Inc., Chicago, IL, USA), GraphPad Prism 8 (San Diego, CA)

and R programs. The Student's t-test (unpaired, two-tailed), Mann–Whitney *U* test or one-way ANOVA were used to compare means between groups. IHC results were analyzed by Chi-squared or Fisher's exact tests. Unsupervised learning cluster analysis was performed using the “cluster” package (version 2.1.0, <https://cran.r-project.org/web/packages/cluster/index.html>) in R programs. *P* < 0.05 was considered statistically significant.

## ACKNOWLEDGMENTS

We gratefully acknowledge the valuable cooperation of YuHong Wang (The First Affiliated Hospital of Soochow University) and Zheng Zhi (The Soochow University) in assessing the IHC score. This work was supported by Project of National Science Foundation of Jiangsu Province, China [grant number BK20161225]. Nanjing Medical University Science and Technology Development Fund (NMUB2018231), Suzhou Special Project of Diagnosis and Treatment for key Clinical Disease (LCZX201814) and Suzhou Science and Technology Development Project (SYSD2018144).

## CONFLICTS OF INTEREST

The authors declare no conflicts of interest.

## FUNDING

This work was supported by Project of National Science Foundation of Jiangsu Province, China [grant number BK20161225]. Nanjing Medical University Science and Technology Development Fund (NMUB2018231), Suzhou Special Project of Diagnosis and Treatment for key Clinical Disease (LCZX201814) and Suzhou Science and Technology Development Project (SYSD2018144).

## REFERENCES

1. Siegel RL, Miller KD, Jemal A. Cancer statistics, 2019. *CA Cancer J Clin.* 2019; 69:7–34. <https://doi.org/10.3322/caac.21551> PMID:30620402
2. Punt CJ, Koopman M, Vermeulen L. From tumour heterogeneity to advances in precision treatment of colorectal cancer. *Nat Rev Clin Oncol.* 2017; 14:235–46. <https://doi.org/10.1038/nrclinonc.2016.171> PMID:27922044
3. Tiwari A, Saraf S, Verma A, Panda PK, Jain SK. Novel targeting approaches and signaling pathways of colorectal cancer: an insight. *World J Gastroenterol.* 2018; 24:4428–35. <https://doi.org/10.3748/wjg.v24.i39.4428> PMID:30357011



4. Huang L, He R, Luo W, Zhu YS, Li J, Tan T, Zhang X, Hu Z, Luo D. Aldo-keto reductase family 1 member B10 inhibitors: potential drugs for cancer treatment. *Recent Pat Anticancer Drug Discov*. 2016; 11:184–96. <https://doi.org/10.2174/1574892811888160304113346> PMID: [26844556](#)
5. Zhong L, Liu Z, Yan R, Johnson S, Zhao Y, Fang X, Cao D. Aldo-keto reductase family 1 B10 protein detoxifies dietary and lipid-derived alpha, beta-unsaturated carbonyls at physiological levels. *Biochem Biophys Res Commun*. 2009; 387:245–50. <https://doi.org/10.1016/j.bbrc.2009.06.123> PMID: [19563777](#)
6. Hyndman DJ, Flynn TG. Sequence and expression levels in human tissues of a new member of the aldo-keto reductase family. *Biochim Biophys Acta*. 1998; 1399:198–202. [https://doi.org/10.1016/s0167-4781\(98\)00109-2](https://doi.org/10.1016/s0167-4781(98)00109-2) PMID: [9765596](#)
7. Cao D, Fan ST, Chung SS. Identification and characterization of a novel human aldose reductase-like gene. *J Biol Chem*. 1998; 273:11429–35. <https://doi.org/10.1074/jbc.273.19.11429> PMID: [9565553](#)
8. Han C, Gao L, Zhao L, Sheng Q, Zhang C, An Z, Xia T, Ding Y, Wang J, Bai H, Dou X. Immunohistochemistry detects increased expression of aldo-keto reductase family 1 member B10 (AKR1B10) in early-stage hepatocellular carcinoma. *Med Sci Monit*. 2018; 24:7414–23. <https://doi.org/10.12659/MSM.910738> PMID: [30328412](#)
9. Hung JJ, Yeh YC, Hsu WH. Prognostic significance of AKR1B10 in patients with resected lung adenocarcinoma. *Thorac Cancer*. 2018; 9:1492–99. <https://doi.org/10.1111/1759-7714.12863> PMID: [30253058](#)
10. Huang C, Cao Z, Ma J, Shen Y, Bu Y, Khoshaba R, Shi G, Huang D, Liao DF, Ji H, Jin J, Cao D. AKR1B10 activates diacylglycerol (DAG) second messenger in breast cancer cells. *Mol Carcinog*. 2018; 57:1300–10. <https://doi.org/10.1002/mc.22844> PMID: [29846015](#)
11. Chung YT, Matkowskyj KA, Li H, Bai H, Zhang W, Tsao MS, Liao J, Yang GY. Overexpression and oncogenic function of aldo-keto reductase family 1B10 (AKR1B10) in pancreatic carcinoma. *Mod Pathol*. 2012; 25:758–66. <https://doi.org/10.1038/modpathol.2011.191> PMID: [22222635](#)
12. Cheng BY, Lau EY, Leung HW, Leung CO, Ho NP, Gurung S, Cheng LK, Lin CH, Lo RC, Ma S, Ng IO, Lee TK. IRAK1 augments cancer stemness and drug resistance via the AP-1/AKR1B10 signaling cascade in hepatocellular carcinoma. *Cancer Res*. 2018; 78:2332–42. <https://doi.org/10.1158/0008-5472.CAN-17-2445> PMID: [29483095](#)
13. Jung YJ, Lee EH, Lee CG, Rhee KJ, Jung WS, Choi Y, Pan CH, Kang K. AKR1B10-inhibitory selaginella tamariscina extract and amentoflavone decrease the growth of A549 human lung cancer cells in vitro and in vivo. *J Ethnopharmacol*. 2017; 202:78–84. <https://doi.org/10.1016/j.jep.2017.03.010> PMID: [28286104](#)
14. Li J, Guo Y, Duan L, Hu X, Zhang X, Hu J, Huang L, He R, Hu Z, Luo W, Tan T, Huang R, Liao D, et al. AKR1B10 promotes breast cancer cell migration and invasion via activation of ERK signaling. *Oncotarget*. 2017; 8:33694–703. <https://doi.org/10.18632/oncotarget.16624> PMID: [28402270](#)
15. Taskoparan B, Seza EG, Demirkol S, Tuncer S, Stefek M, Gure AO, Banerjee S. Opposing roles of the aldo-keto reductases AKR1B1 and AKR1B10 in colorectal cancer. *Cell Oncol (Dordr)*. 2017; 40:563–78. <https://doi.org/10.1007/s13402-017-0351-7> PMID: [28929377](#)
16. Yao HB, Xu Y, Chen LG, Guan TP, Ma YY, He XJ, Xia YJ, Tao HQ, Shao QS. AKR1B10, a good prognostic indicator in gastric cancer. *Eur J Surg Oncol*. 2014; 40:318–24. <https://doi.org/10.1016/j.ejso.2013.12.014> PMID: [24406159](#)
17. Ames BN. Dietary carcinogens and anti-carcinogens. *J Toxicol Clin Toxicol*. 1984; 22:291–301. <https://doi.org/10.3109/15563658408992561> PMID: [6502792](#)
18. Laffin B, Petrash JM. Expression of the aldo-ketoreductases AKR1B1 and AKR1B10 in human cancers. *Front Pharmacol*. 2012; 3:104. <https://doi.org/10.3389/fphar.2012.00104> PMID: [22685431](#)
19. Shaw N, Yang B, Millward A, Demaine A, Hodgkinson A. AKR1B10 is induced by hyperglycaemia and lipopolysaccharide in patients with diabetic nephropathy. *Cell Stress Chaperones*. 2014; 19:281–87. <https://doi.org/10.1007/s12192-013-0455-6> PMID: [23975544](#)
20. Gasser E, Moutos CP, Downes M, Evans RM. FGF1 - a new weapon to control type 2 diabetes mellitus. *Nat Rev Endocrinol*. 2017; 13:599–609. <https://doi.org/10.1038/nrendo.2017.78> PMID: [28664920](#)
21. Suh JM, Jonker JW, Ahmadian M, Goetz R, Lackey D, Osborn O, Huang Z, Liu W, Yoshihara E, van Dijk TH,

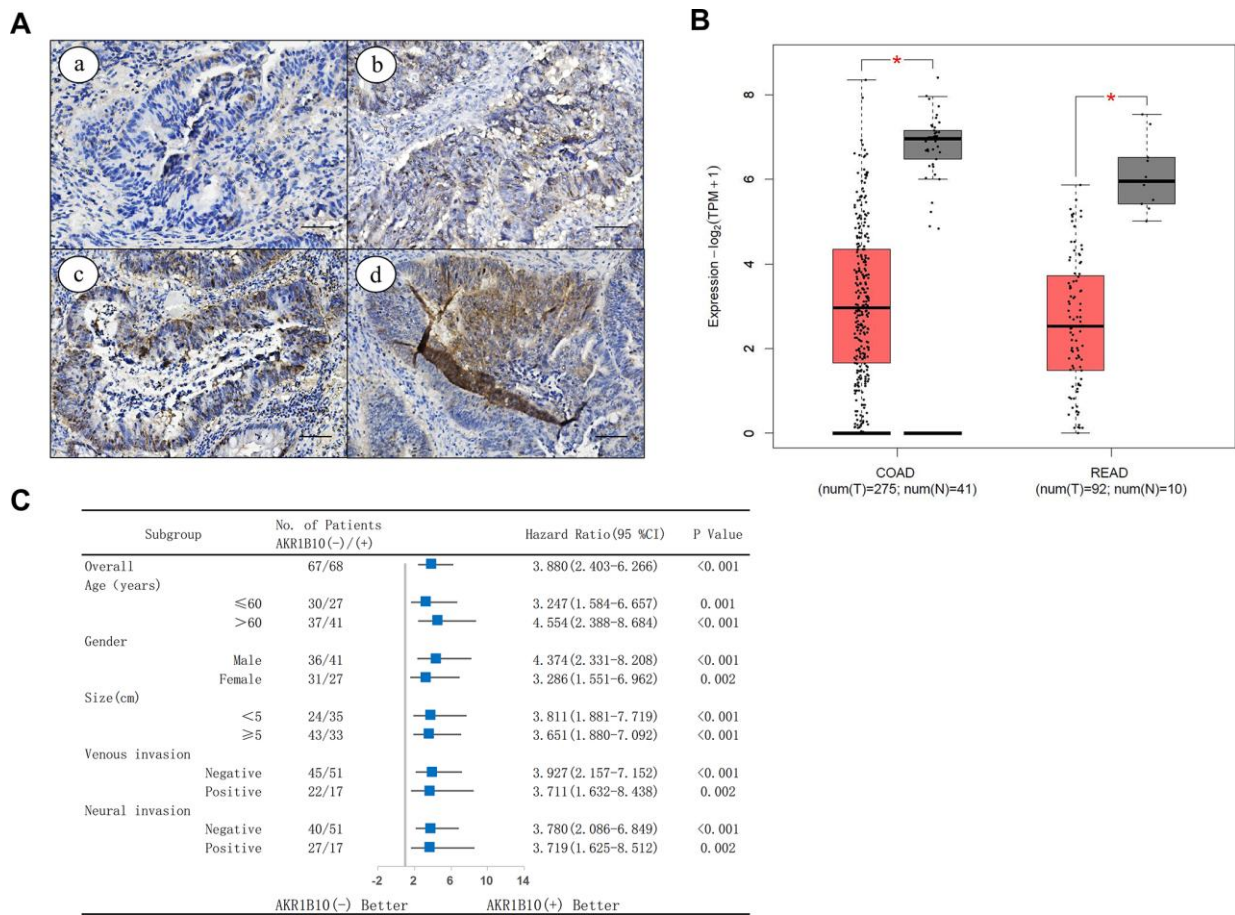
- Havinga R, Fan W, Yin YQ, et al. Endocrinization of FGF1 produces a neomorphic and potent insulin sensitizer. *Nature*. 2014; 513:436–39.  
<https://doi.org/10.1038/nature13540>  
PMID:25043058
22. Liang G, Song L, Chen Z, Qian Y, Xie J, Zhao L, Lin Q, Zhu G, Tan Y, Li X, Mohammadi M, Huang Z. Fibroblast growth factor 1 ameliorates diabetic nephropathy by an anti-inflammatory mechanism. *Kidney Int*. 2018; 93:95–109.  
<https://doi.org/10.1016/j.kint.2017.05.013>  
PMID:28750927
23. Iyengar NM, Gucalp A, Dannenberg AJ, Hudis CA. Obesity and cancer mechanisms: tumor microenvironment and inflammation. *J Clin Oncol*. 2016; 34:4270–76.  
<https://doi.org/10.1200/JCO.2016.67.4283>  
PMID:27903155
24. Yao Y, Yang X, Sun L, Sun S, Huang X, Zhou D, Li T, Zhang W, Abumrad NA, Zhu X, He S, Su X. Fatty acid 2-hydroxylation inhibits tumor growth and increases sensitivity to cisplatin in gastric cancer. *EBioMedicine*. 2019; 41:256–67.  
<https://doi.org/10.1016/j.ebiom.2019.01.066>  
PMID:30738828
25. Crosas B, Hyndman DJ, Gallego O, Martras S, Parés X, Flynn TG, Farrés J. Human aldose reductase and human small intestine aldose reductase are efficient retinal reductases: consequences for retinoid metabolism. *Biochem J*. 2003; 373:973–79.  
<https://doi.org/10.1042/BJ20021818>  
PMID:12732097
26. Spite M, Baba SP, Ahmed Y, Barski OA, Nijhawan K, Petrash JM, Bhatnagar A, Srivastava S. Substrate specificity and catalytic efficiency of aldo-keto reductases with phospholipid aldehydes. *Biochem J*. 2007; 405:95–105.  
<https://doi.org/10.1042/BJ20061743>  
PMID:17381426
27. Shen Y, Zhong L, Johnson S, Cao D. Human aldo-keto reductases 1B1 and 1B10: a comparative study on their enzyme activity toward electrophilic carbonyl compounds. *Chem Biol Interact*. 2011; 191:192–98.  
<https://doi.org/10.1016/j.cbi.2011.02.004>  
PMID:21329684
28. Penning TM. The aldo-keto reductases (AKRs): overview. *Chem Biol Interact*. 2015; 234:236–46.  
<https://doi.org/10.1016/j.cbi.2014.09.024>  
PMID:25304492
29. DiStefano JK, Davis B. Diagnostic and prognostic potential of AKR1B10 in human hepatocellular carcinoma. *Cancers (Basel)*. 2019; 11:486.  
<https://doi.org/10.3390/cancers11040486>  
PMID:30959792
30. Endo S, Xia S, Suyama M, Morikawa Y, Oguri H, Hu D, Ao Y, Takahara S, Horino Y, Hayakawa Y, Watanabe Y, Gouda H, Hara A, et al. Synthesis of potent and selective inhibitors of aldo-keto reductase 1B10 and their efficacy against proliferation, metastasis, and cisplatin resistance of lung cancer cells. *J Med Chem*. 2017; 60:8441–55.  
<https://doi.org/10.1021/acs.jmedchem.7b00830>  
PMID:28976752
31. Matsunaga T, Suzuki A, Kezuka C, Okumura N, Iguchi K, Inoue I, Soda M, Endo S, El-Kabbani O, Hara A, Ikari A. Aldo-keto reductase 1B10 promotes development of cisplatin resistance in gastrointestinal cancer cells through down-regulating peroxisome proliferator-activated receptor-γ-dependent mechanism. *Chem Biol Interact*. 2016; 256:142–53.  
<https://doi.org/10.1016/j.cbi.2016.07.008>  
PMID:27417252
32. Shen Y, Liao DF, Cao D. AKR1B10 in gastrointestinal diseases. *Aging (Albany NY)*. 2015; 7:221–22.  
<https://doi.org/10.18632/aging.100737>  
PMID:25885766
33. Zu X, Yan R, Pan J, Zhong L, Cao Y, Ma J, Cai C, Huang D, Liu J, Chung FL, Liao DF, Cao D. Aldo-keto reductase 1B10 protects human colon cells from DNA damage induced by electrophilic carbonyl compounds. *Mol Carcinog*. 2017; 56:118–29.  
<https://doi.org/10.1002/mc.22477>  
PMID:26969882
34. Hashimoto Y, Imanishi K, Tokui N, Okamoto T, Okamoto A, Hatakeyama S, Yoneyama T, Koie T, Kamimura N, Ohyama C. Carboplatin-gemcitabine combination chemotherapy upregulates AKR1B10 expression in bladder cancer. *Int J Clin Oncol*. 2013; 18:177–82.  
<https://doi.org/10.1007/s10147-011-0363-7>  
PMID:22198799
35. He YC, Shen Y, Cao Y, Tang FQ, Tian DF, Huang CF, Tao H, Zhou FL, Zhang B, Song L, He L, Lin LM, Lu FG, et al. Overexpression of AKR1B10 in nasopharyngeal carcinoma as a potential biomarker. *Cancer Biomark*. 2016; 16:127–35.  
<https://doi.org/10.3233/CBM-150548>  
PMID:26835713
36. Ko HH, Cheng SL, Lee JJ, Chen HM, Kuo MY, Cheng SJ. Expression of AKR1B10 as an independent marker for poor prognosis in human oral squamous cell carcinoma. *Head Neck*. 2017; 39:1327–32.  
<https://doi.org/10.1002/hed.24759>  
PMID:28301069

37. Reddy KA, Kumar PU, Srinivasulu M, Triveni B, Sharada K, Ismail A, Reddy GB. Overexpression and enhanced specific activity of aldoketo reductases (AKR1B1 & AKR1B10) in human breast cancers. *Breast*. 2017; 31:137–43.  
<https://doi.org/10.1016/j.breast.2016.11.003>  
PMID:[27855345](https://pubmed.ncbi.nlm.nih.gov/27855345/)
38. Sinreih M, Štupar S, Čemažar L, Verdenik I, Frković Grazio S, Smrkolj Š, Rižner TL. STAR and AKR1B10 are down-regulated in high-grade endometrial cancer. *J Steroid Biochem Mol Biol*. 2017; 171:43–53.  
<https://doi.org/10.1016/j.jsbmb.2017.02.015>  
PMID:[28232277](https://pubmed.ncbi.nlm.nih.gov/28232277/)
39. Sun Y, Fan X, Zhang Q, Shi X, Xu G, Zou C. Cancer-associated fibroblasts secrete FGF-1 to promote ovarian proliferation, migration, and invasion through the activation of FGF-1/FGFR4 signaling. *Tumour Biol*. 2017; 39:1010428317712592.  
<https://doi.org/10.1177/1010428317712592>  
PMID:[28718374](https://pubmed.ncbi.nlm.nih.gov/28718374/)
40. Wang Z, Li R, Zhong R. Extracellular matrix promotes proliferation, migration and adhesion of airway smooth muscle cells in a rat model of chronic obstructive pulmonary disease via upregulation of the PI3K/AKT signaling pathway. *Mol Med Rep*. 2018; 18:3143–52.  
<https://doi.org/10.3892/mmr.2018.9320>  
PMID:[30066869](https://pubmed.ncbi.nlm.nih.gov/30066869/)
41. Weaver AN, Burch MB, Cooper TS, Della Manna DL, Wei S, Ojesina AI, Rosenthal EL, Yang ES. Notch signaling activation is associated with patient mortality and increased FGF1-mediated invasion in squamous cell carcinoma of the oral cavity. *Mol Cancer Res*. 2016; 14:883–91.  
<https://doi.org/10.1158/1541-7786.MCR-16-0114>  
PMID:[27353029](https://pubmed.ncbi.nlm.nih.gov/27353029/)
42. Kawano M, Miura T, Fujita M, Koike S, Imadome K, Ishikawa A, Yasuda T, Imamura T, Imai T, Nakayama F. The FGF1/CPP-C chimera protein protects against intestinal adverse effects of c-ion radiotherapy without exacerbating pancreatic carcinoma. *Clin Transl Radiat Oncol*. 2018; 14:8–16.  
<https://doi.org/10.1016/j.ctro.2018.10.004>  
PMID:[30406211](https://pubmed.ncbi.nlm.nih.gov/30406211/)
43. Wu D, Yang B, Chen J, Xiong H, Li Y, Pan Z, Cao Y, Chen J, Li T, Zhou S, Ling X, Wei Y, Li G, et al. Upregulation of long non-coding RNA RAB1A-2 induces FGF1 expression worsening lung cancer prognosis. *Cancer Lett*. 2018; 438:116–25.  
<https://doi.org/10.1016/j.canlet.2018.09.016>  
PMID:[30217564](https://pubmed.ncbi.nlm.nih.gov/30217564/)
44. Hsu YC, Kao CY, Chung YF, Lee DC, Liu JW, Chiu IM. Activation of aurora a kinase through the FGF1/FGFR signaling axis sustains the stem cell characteristics of glioblastoma cells. *Exp Cell Res*. 2016; 344:153–66.  
<https://doi.org/10.1016/j.yexcr.2016.04.012>  
PMID:[27138904](https://pubmed.ncbi.nlm.nih.gov/27138904/)
45. Shain SA, Sarić T, Ke LD, Nannen D, Yoas S. Endogenous fibroblast growth factor-1 or fibroblast growth factor-2 modulate prostate cancer cell proliferation. *Cell Growth Differ*. 1996; 7:573–86.  
PMID:[8732667](https://pubmed.ncbi.nlm.nih.gov/8732667/)
46. Birrer MJ, Johnson ME, Hao K, Wong KK, Park DC, Bell A, Welch WR, Berkowitz RS, Mok SC. Whole genome oligonucleotide-based array comparative genomic hybridization analysis identified fibroblast growth factor 1 as a prognostic marker for advanced-stage serous ovarian adenocarcinomas. *J Clin Oncol*. 2007; 25:2281–87.  
<https://doi.org/10.1200/JCO.2006.09.0795>  
PMID:[17538174](https://pubmed.ncbi.nlm.nih.gov/17538174/)
47. King ML, Lindberg ME, Stodden GR, Okuda H, Ebers SD, Johnson A, Montag A, Lengyel E, MacLean II JA, Hayashi K. Wnt7A/ $\beta$ -catenin signaling induces FGF1 and influences sensitivity to niclosamide in ovarian cancer. *Oncogene*. 2015; 34:3452–62.  
<https://doi.org/10.1038/onc.2014.277>  
PMID:[25174399](https://pubmed.ncbi.nlm.nih.gov/25174399/)
48. Smith G, Ng MT, Shepherd L, Herrington CS, Gourley C, Ferguson MJ, Wolf CR. Individuality in FGF1 expression significantly influences platinum resistance and progression-free survival in ovarian cancer. *Br J Cancer*. 2012; 107:1327–36.  
<https://doi.org/10.1038/bjc.2012.410>  
PMID:[22990650](https://pubmed.ncbi.nlm.nih.gov/22990650/)
49. Segeritz CP, Rashid ST, de Brito MC, Serra MP, Ordonez A, Morell CM, Kaserman JE, Madrigal P, Hannan NR, Gatto L, Tan L, Wilson AA, Lilley K, et al. hiPSC hepatocyte model demonstrates the role of unfolded protein response and inflammatory networks in  $\alpha_1$ -antitrypsin deficiency. *J Hepatol*. 2018; 69:851–60.  
<https://doi.org/10.1016/j.jhep.2018.05.028>  
PMID:[29879455](https://pubmed.ncbi.nlm.nih.gov/29879455/)
50. Mossmann D, Park S, Hall MN. mTOR signalling and cellular metabolism are mutual determinants in cancer. *Nat Rev Cancer*. 2018; 18:744–57.  
<https://doi.org/10.1038/s41568-018-0074-8>  
PMID:[30425336](https://pubmed.ncbi.nlm.nih.gov/30425336/)
51. Cosin-Roger J, Simmen S, Melhem H, Atrott K, Frey-Wagner I, Hausmann M, de Vallière C, Spalinger MR, Spielmann P, Wenger RH, Zeitz J, Vavricka SR, Rogler G, Ruiz PA. Hypoxia ameliorates intestinal inflammation through NLRP3/mTOR downregulation and autophagy activation. *Nat Commun*. 2017; 8:98.  
<https://doi.org/10.1038/s41467-017-00213-3>  
PMID:[28740109](https://pubmed.ncbi.nlm.nih.gov/28740109/)

52. Li X, Zhang X, Pan Y, Shi G, Ren J, Fan H, Dou H, Hou Y. mTOR regulates NLRP3 inflammasome activation via reactive oxygen species in murine lupus. *Acta Biochim Biophys Sin (Shanghai)*. 2018; 50:888–96.  
<https://doi.org/10.1093/abbs/gmy088>  
PMID:[30060081](https://pubmed.ncbi.nlm.nih.gov/30060081/)
53. Sinreih M, Štupar S, Čemažar L, Verdenik I, Frković Grazio S, Smrkolj Š, Lanišnik Rižner T. Data on expression of genes involved in estrogen and progesterone action, inflammation and differentiation according to demographic, histopathological and clinical characteristics of endometrial cancer patients. *Data Brief*. 2017; 12:632–43.  
<https://doi.org/10.1016/j.dib.2017.04.050>  
PMID:[28540356](https://pubmed.ncbi.nlm.nih.gov/28540356/)
54. Henriksson ML, Edin S, Dahlin AM, Oldenborg PA, Öberg Å, Van Guelpen B, Rutegård J, Stenling R, Palmqvist R. Colorectal cancer cells activate adjacent fibroblasts resulting in FGF1/FGFR3 signaling and increased invasion. *Am J Pathol*. 2011; 178:1387–94.  
<https://doi.org/10.1016/j.ajpath.2010.12.008>  
PMID:[21356388](https://pubmed.ncbi.nlm.nih.gov/21356388/)
55. Huang YF, Niu WB, Hu R, Wang LJ, Huang ZY, Ni SH, Wang MQ, Yang Y, Huang YS, Feng WJ, Xiao W, Zhu DJ, Xian SX, Lu L. FIBP knockdown attenuates growth and enhances chemotherapy in colorectal cancer via regulating GSK3β-related pathways. *Oncogenesis*. 2018; 7:77.  
<https://doi.org/10.1038/s41389-018-0088-9>  
PMID:[30275459](https://pubmed.ncbi.nlm.nih.gov/30275459/)
56. Loeffler-Ragg J, Mueller D, Gamerith G, Auer T, Skvortsov S, Sarg B, Skvortsova I, Schmitz KJ, Martin HJ, Krugmann J, Alakus H, Maser E, Menzel J, et al. Proteomic identification of aldo-keto reductase AKR1B10 induction after treatment of colorectal cancer cells with the proteasome inhibitor bortezomib. *Mol Cancer Ther*. 2009; 8:1995–2006.  
<https://doi.org/10.1158/1535-7163.MCT-08-0987>  
PMID:[19567817](https://pubmed.ncbi.nlm.nih.gov/19567817/)

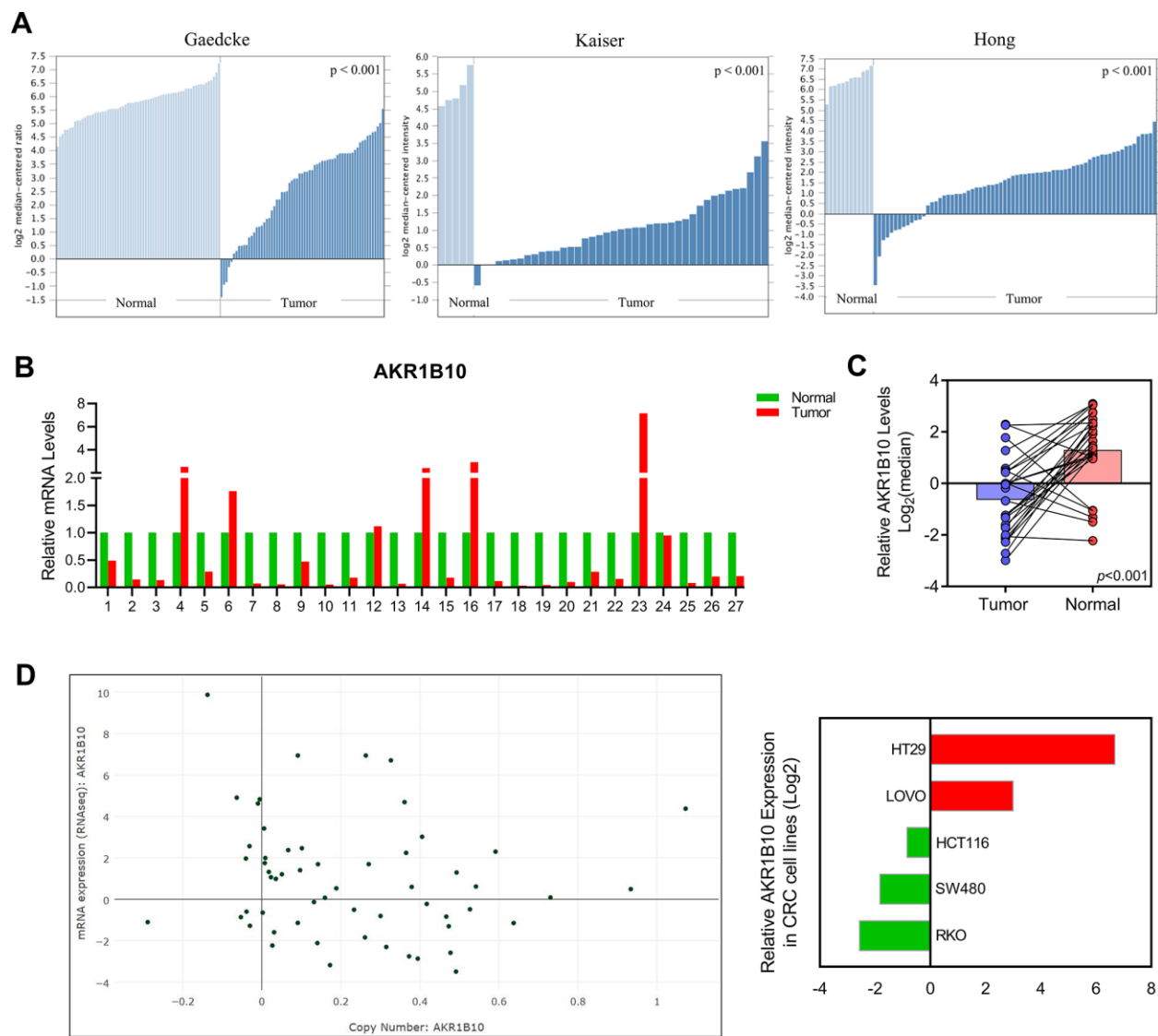
SUPPLEMENTARY MATERIALS

Supplementary Figures

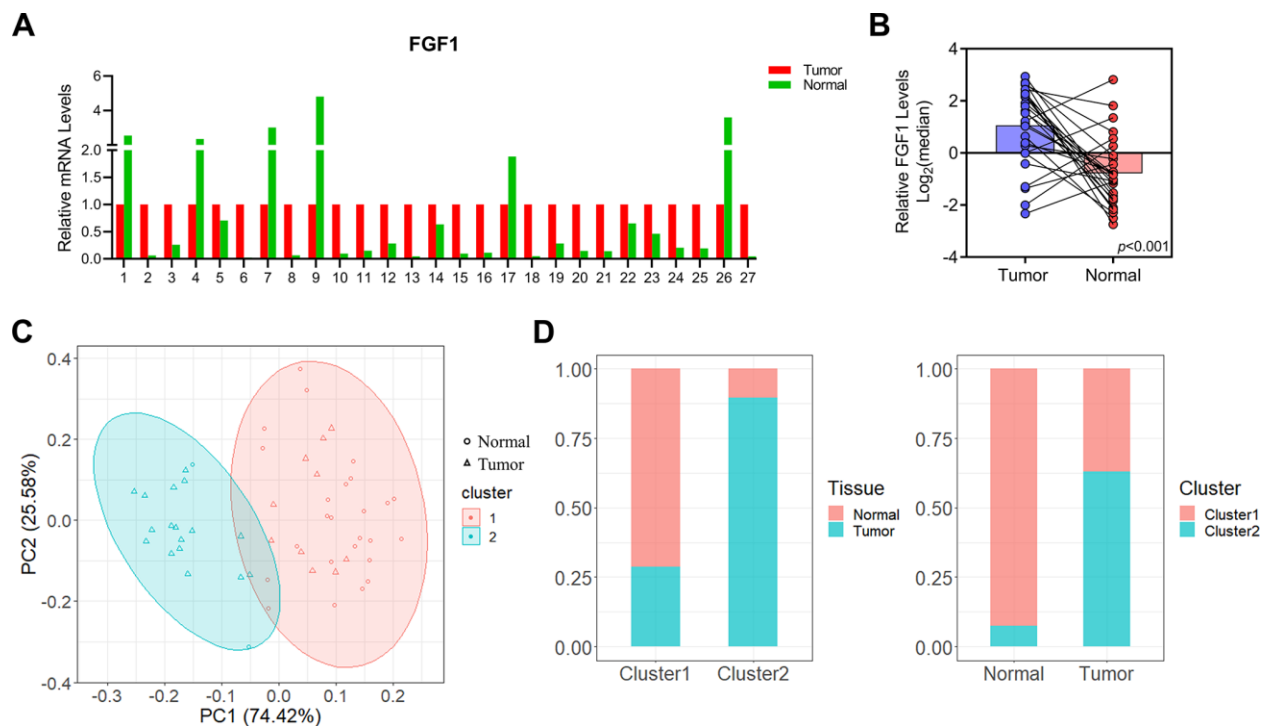


**Supplementary Figure 1. Expression of AKR1B10 in CRC in TCGA datasets.** (A) IHC images showing *in situ* AKR1B10 expression in CRC tissues (scale bar = 100µm). Negative (a), weak (b), positive (c), strong positive (d). (B) Comparison of AKR1B10 levels between CRC and paired normal tissues in TCGA datasets by GEPIA platform. (C) OS of AKR1B10<sup>POS</sup> and AKR1B10<sup>NEG</sup> CRC patients in the subgroups of age, gender, tumor size, venous invasion and neural invasion. CRC, colorectal cancer. \* *P* < 0.05.





**Supplementary Figure 2. AKR1B10 expression in CRC tissues and cell lines.** (A–B) AKR1B10 mRNA levels in (A) CRC and non-tumor tissues in OncoPrint datasets and (B) 27 paired CRC and normal tissues. (C) Relative AKR1B10 expression in 27 paired CRC and normal tissues. (D) AKR1B10 expression in 5 CRC cell lines from the CCLE platform. CRC, colorectal cancer. CCLE, Cancer Cell Line Encyclopedia.



**Supplementary Figure 3. FGF1 expression in CRC and paired normal tissues.** (A) FGF1 mRNA levels in 27 paired CRC and normal tissues and (B) the relative expression levels. (C) Stratification of the 27 pairs of CRC and normal tissues into cluster 1 (red) and cluster 2 (green) according to AKR1B10 and FGF1 mRNA levels. (D) Percentage of tumor and normal samples in each cluster. CRC, colorectal cancer.

# Coupled immune stratification and identification of therapeutic candidates in patients with lung adenocarcinoma

Weilei Hu<sup>1,2,\*</sup>, Guosheng Wang<sup>3,\*</sup>, Yundi Chen<sup>3</sup>, Lonny B. Yarmus<sup>4</sup>, Biao Liu<sup>5</sup>, Yuan Wan<sup>3</sup>

<sup>1</sup>Institute of Translational Medicine, Zhejiang University, Hangzhou 310029, China

<sup>2</sup>Center for Disease Prevention Research and Department of Pharmacology and Toxicology, Medical College of Wisconsin, Milwaukee, WI 53226, United States

<sup>3</sup>The Pq Laboratory of Micro/Nano BiomeDx, Department of Biomedical Engineering, Binghamton University—SUNY, Binghamton, NY 13902, United States

<sup>4</sup>Division of Pulmonary and Critical Care, Department of Medicine, Johns Hopkins School of Medicine, Baltimore, MD 21218, United States

<sup>5</sup>Department of Pathology, Nanjing Medical University Affiliated Suzhou Hospital, Suzhou 215006, Jiangsu, China

\*Equal contribution

**Correspondence to:** Yuan Wan, Biao Liu; **email:** [ywan@binghamton.edu](mailto:ywan@binghamton.edu), [georgebliu@126.com](mailto:georgebliu@126.com); <https://orcid.org/0000-0003-3477-6782>

**Keywords:** personalized cancer immunotherapies, drug repositioning, cold tumor, patient stratification, tumor microenvironment  
**Received:** February 8, 2020      **Accepted:** July 14, 2020      **Published:** August 27, 2020

**Copyright:** Hu et al. This is an open-access article distributed under the terms of the Creative Commons Attribution License (CC BY 3.0), which permits unrestricted use, distribution, and reproduction in any medium, provided the original author and source are credited.

## ABSTRACT

In recent years, personalized cancer immunotherapy, especially stratification-driven precision treatments have gained significant traction. However, due to the heterogeneity in clinical cohorts, the uncombined analysis of stratification/therapeutics may lead to confusion in determining ideal therapeutic options. We report that the coupled immune stratification and drug repurposing could facilitate identification of therapeutic candidates in patients with lung adenocarcinoma (LUAD). First, we categorized the patients into four groups based on immune gene profiling, associated with distinct molecular characteristics and clinical outcomes. Then, the weighted gene co-expression network analysis (WGCNA) algorithm was used to identify co-expression modules of each groups. We focused on C3 group which is characterized by low immune infiltration (cold tumor) and wild-type EGFR, posing a significant challenge for treatment of LUAD. Five drug candidates against the C3 status were identified which have potential dual functions to correct aberrant immune microenvironment and also halt tumorigenesis. Furthermore, their steady binding affinity against the targets was verified through molecular docking analysis. In sum, our findings suggest that such coupled analysis could be a promising methodology for identification and exploration of therapeutic candidates in the practice of personalized immunotherapy.

## INTRODUCTION

Current understanding of cancer immunology has promoted the stratification of patients for identifying and exploring new cancer immunotherapeutic strategies [1, 2]. Immunohistochemical staining-based immunoscore system is a possible approach in the classification of malignant tumors [3–5]. For example, lymphocyte infiltration and high expression level of IFN- $\gamma$  (T cell-inflamed tumors, *i.e.*, hot tumors) may segregate tumors, indicate patients may benefit from PD-1/PD-L1

inhibitors, and help predict immunotherapy responsiveness [6, 7]. On the contrary, the non-T cell-inflamed phenotype, *i.e.*, cold tumors, lacks expression of the type I IFN signature, CD8+ T cells, and IFN-inducible inhibitory factors, correlated with treatment resistance. In addition, bulk gene expression profiling methods, such as CIBERSORT, TIMER, and integrated immunogenomic methods [8–13] have also been developed to characterize the immune landscape of cancer and to help guide cancer immunotherapy. However, these stratification approaches are mainly

limited by heterogeneity in clinical cohorts, probably leading to confusion in determining ideal therapeutic options. Theoretically, the limitations can be partially offset by coupled analysis of stratification/therapeutics, which is relatively straightforward and efficient. However, no attempt has been undertaken.

Drug repurposing is a strategy for identifying new uses for approved or investigational drugs that are outside the scope of the original medical indication [14, 15]. Compared to *de novo* drug discovery, drug repurposing can significantly reduce the cost and time to bring a new treatment to patients. It is possible now to link gene-expression profiling data and screens for drug repurposing [16, 17]. Moreover, the Connectivity Map (CMap) database, based on a computational drug repurposing approach, has been demonstrated as an efficient tool for drug repurposing [18–20]. Therefore, combining genome polymorphisms and pharmacology may lead to promising new therapeutic strategies [21], and several drugs have been repurposed to treat cancers [22–24]. Of note, a careful selection of pertinent groups for evaluation of drug candidates remains essential, which reversely requires the rational stratification

before drug repurposing. In this work, patient stratification and drug repurposing were coupled to explore novel therapeutic candidates for treatment of LUAD which accompanied with marked genetic and genomic heterogeneity [25, 26]. Following the steps shown in Figure 1, we categorized the patients into four groups based on immune gene profiling and then identified five drugs targeting four known targets with a computational drug repurposing approach. These identified agents could correct aberrant gene expression in a class of patients referred to as the C3 group, which is characterized by cold tumors and expression of wild-type EGFR. The binding affinity between these potential drugs and paired targets were also investigated with molecular docking methods.

## RESULTS

### Four LUAD subtypes were delineated based on the immune-associated genes

The gene expression profiles of 790 immune-associated genes were used to classify the TCGA cohort data into different LUAD subtypes. Initially, we assigned all

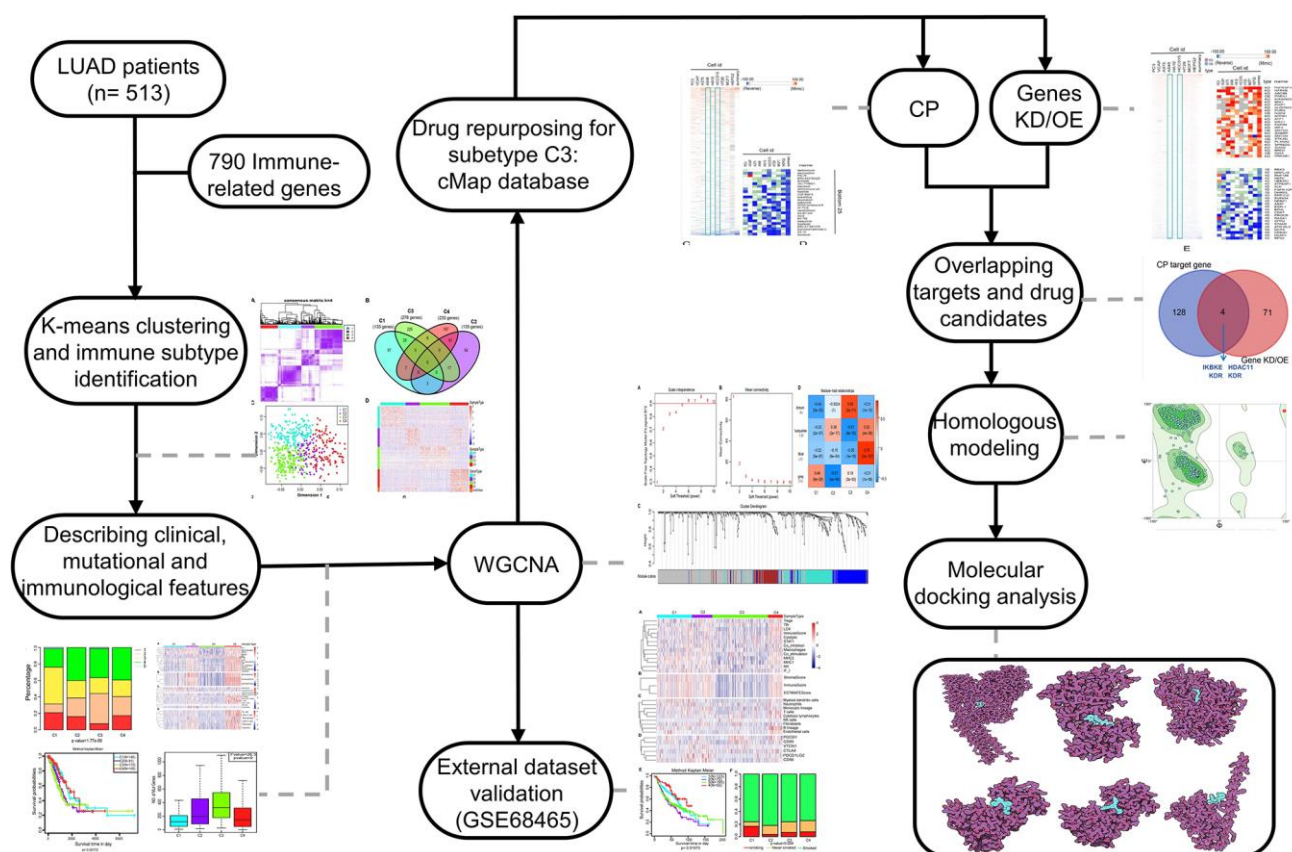


**Figure 1. The workflow of the study.** CMap, connectivity Map; WGCNA, Weighted correlation network analysis; CP, compound; Genes KD/OE, genes knockdown/overexpress.

tumor specimens into  $k$  ( $k = 2, 3, 4, 5, 6, 7, 8$ ) subtypes. A value of  $k = 4$  was set to represent stable clusters according to the CDF curves of the consensus score (Figure 2A and Supplementary Figure 1). A total of 513 LUAD tumor samples were finally assigned to four categories. The Kolmogorov-Smirnov test was used to calculate the upregulated genes in each subtype ( $FDR < 0.05$ ). Of the 790 immune-associated genes, 133, 135, 276, and 233 genes were remarkably enriched in subtypes C1, C2, C3, and C4, respectively (Figure 2B). It is worth noting that only a few genes overlapped between pairs of subsets (Figure 2B). Next, principal component analysis (PCA) was employed to calculate the top 100 highly expressed genes in each cluster. The four subsets were distinguished from each other based on the two-dimensional scaling plotting of the first two principal components (Figure 2C). Furthermore, the top 100 enriched genes in each subtype were used to describe their immune gene expression profiles (Figure 2D). In addition, the R package *sigclust* was utilized to analyze the clustering significance between the four consensus clusters. It was found that the comparison between C2 and C3 was not significant ( $p=0.192$ ), but marked differences were observed in expression distribution of C1 vs C4, C3 vs C4 ( $p < 0.05$ ) (Supplementary Table 1). Therefore, the 513 LUAD patients extracted from TCGA cohort were classified into five molecular subtypes depending on the expression pattern of immune-associated genes.

### Clinical profile of the four subtypes

To investigate the clinical relevance of tumor immune microenvironment, demographic distributions of age, gender, smoking status, tumor stage and the degree of progression of the primary tumor (T), tumor cells invasion into regional lymph nodes (N) and metastatic dissemination (M) were compared between patients with the four immune subtypes. Clinically, we observed that C3 subtype have a markedly lower median age at diagnosis ( $p = 0.025$  Pearson's chi-square test, Figure 2E), and the highest proportion of male patients ( $p=0.028$  Pearson's chi-square test, Figure 2F) and smokers ( $1.77 \times 10^{-9}$  Pearson's chi-square test, Figure 2G). Groups C2 and C3 showed a similar frequency of Stage II, Stage III and Stage IV, which is significantly higher than that of group C3 or C4 ( $p=3.172 \times 10^{-5}$  Pearson's chi-square test, Figure 2H). Specifically, groups C2 and C3 displayed a higher proportion of T3 and T4 ( $p=0.025$  Pearson's chi-square test, Figure 2I), and a much lower percentage of N0 ( $p=0.001$  Pearson's chi-square test, Figure 2J) compared to C1 or C4. Interestingly, the metastatic dissemination rate at diagnosis was not different among the four groups ( $p = 0.762$  Pearson's chi-square test, Figure 2K).

### Distinct characteristics of immunogenicity of the LUAD subtypes

We further examined the immunogenic and microenvironmental variables including immune cell metagene expression level, immune cells, tumor purity, immune and stromal score, and the abundance of tumor-infiltrating lymphocytes using RNA expression data as previously described [27]. All immunogenic and microenvironmental factors scores were considerably lower in subtype C3 compared to C4. Immune metagenes corresponding to macrophages, NK, Treg, Tfh and LCK cells, and expression of co-stimulation/co-inhibition signal-associated genes, MHC class I/II, interferon and interferon regulated genes (STAT1) were markedly lower in subtype C3 than in C4 (Figure 3A and Supplementary Figure 2). In terms of tumor microenvironment factors (stromal score, immune score, tumor purity), subtypes C2 and C4 showed upregulated stromal and immune genes and estimated tumor purity, while the subtype C3 tumors exhibited low levels of immune and stromal genes and estimated tumor cell fraction (Figure 3B and Supplementary Figure 2).

Additionally, a higher number of immune-associated cells such as, B lineage cells, monocytic lineage cells, T cells, and CD8 T cells were produced in subtype C4 than in other subtypes, while endothelial cells and myeloid dendritic cells responded more aggressively to subtype C3 (Figure 3C and Supplementary Figure 2). Molecular-tumor interactions were comprehensively assessed with TIMER (<https://cistrome.shinyapps.io/timer/>). Similarly, we compared the number immune infiltrating cells (dendritic cells, neutrophils, B, CD8<sup>+</sup> T, CD4<sup>+</sup> T, macrophages) in TCGA LUAD samples. We found that these immune cells were fewer in subtype C3 than in C4 (Figure 3D and Supplementary Figure 2). It was also noted that there was significant immune infiltration and higher expression of immune-associated genes in subtype 4, showing an enhanced immune microenvironment and disrupted immune microenvironment in subtype C3.

The expression profiles of eight immune checkpoint genes, which are crucial for immune modulation, were further examined (Figure 3E). The following genes were considerably lower in subtype C3 compared to C4, i.e., PDCD1 (PD1), CTLA4, CD274 (PDL1), PDCD1LG2 (PDL2), CD80 and CD86. Interestingly, the expression value of CD276 was markedly downregulated in subtype C4 whereas the expression level of VTCN1 was similar among the four subtypes.

### Prognostic values of the four LUAD subtypes

We then explored whether the immune-associated genes can predict the prognosis of patients with the four



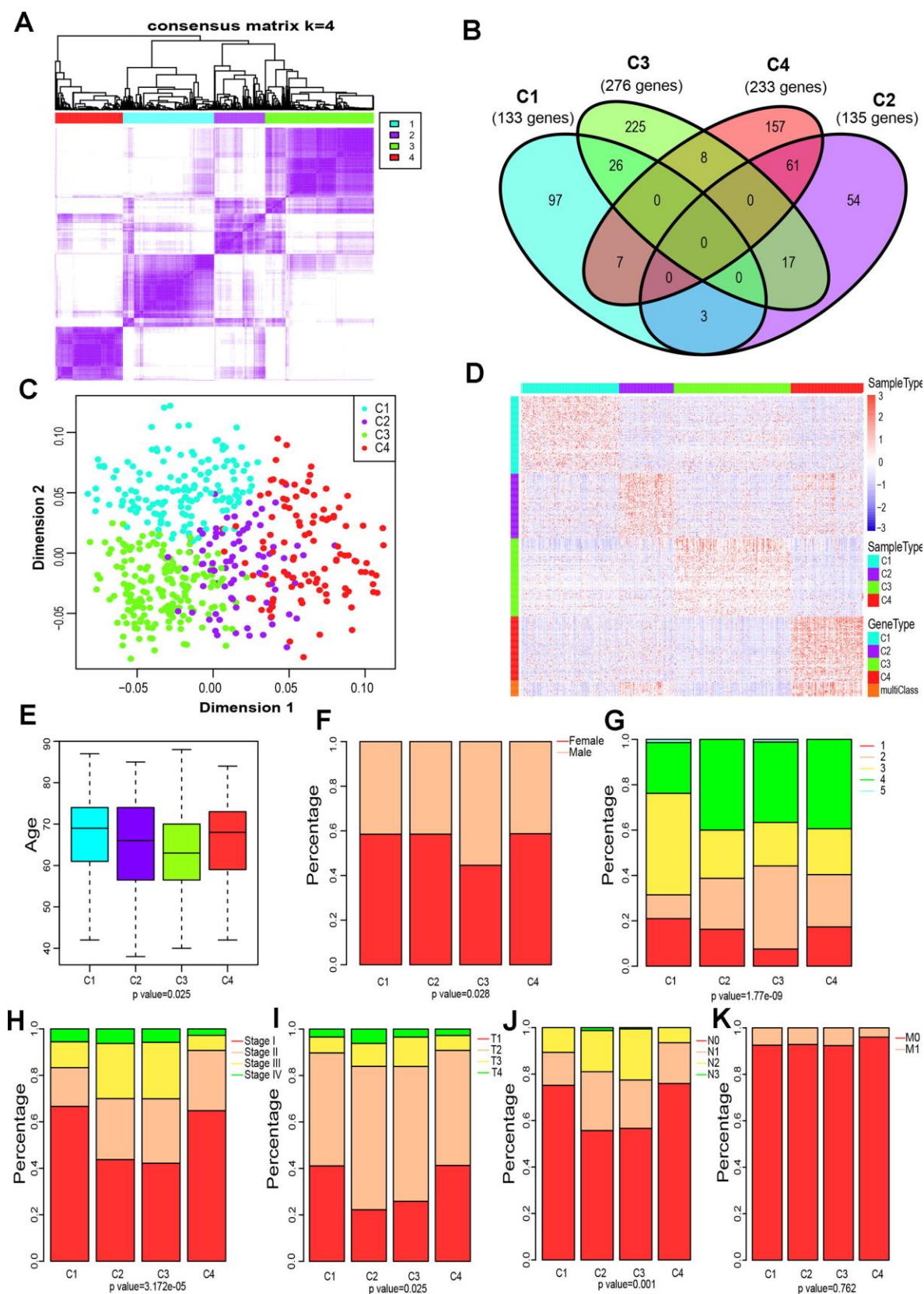


**Figure 2. Four immune subtypes of LUAD in TCGA cohort and their clinical profiles.** (A) Heatmap of consensus values when k=4. (B) Venn diagram showing the upregulated genes (FDR < 0.05) in each cluster. (C) The scatter plot of the top 100 upregulated genes in each cluster, distinguished by the first two principal components (PCs). (D) Gene expression profile of the top 100 upregulated genes in each

cluster. Heat maps showing relative gene expression values, red indicates high expression, and blue indicates low expression. (E) Age at diagnosis of the four subtypes (Kruskal-Wallis test). The Boxplot centerlines indicating the median value; box limits show the 25th (Q1) and 75th (Q3) percentiles, lower and upper whiskers extend 1.5 times the interquartile range (IQR) from Q1 and Q3, respectively. (F) Distribution of gender among the four subtypes (chi-square test). (G) Distribution of smoking status across the four subtypes (chi-square test). (H) Distribution of stage at diagnosis in the four subtypes (chi-square test). (I) The degree of progression of the primary tumor (T) at diagnosis in the four subtypes (chi-square test). (J) The degree of the invasion of regional lymph nodes (N) at diagnosis among the four subtypes (chi-square test). (K) Incidence of metastatic (M) dissemination at diagnosis among the four subtypes (chi-square test).

subtypes. The Kaplan-Meier curves were plotted to reveal the overall survival (OS) rates of patients (log-rank test, OS,  $p=0.00172$ , Figure 4A). Notably, C4 had the highest OS rate among the four subtypes. In comparison, patients with subtype C3 had a worse OS than those in other subtypes, especially in C4 (log-rank test, OS,  $p=0.00172$ , Figure 4A; log-rank test, OS,  $p=0.00171$ , Figure 4B).

### Comparison of EGFR, KRAS and ALK mutations among the four subtypes

Aberrant changes in KRAS, EGFR, ALK have been recognized as key drivers of lung cancer, and are frequently identified in LUAD [28]. To evaluate the relevance of EGFR, KRAS and ALK mutations to these four subtypes, we characterized the patterns of the EGFR, KRAS and ALK mutations in LUAD data from TCGA. Subtype C3 and C4 showed a markedly lower proportion of EGFR mutations compared to C1 and C2 ( $p=9.54 \times 10^{-5}$ , Pearson's chi-square test, Figure 4C). However, the KRAS mutation rate of subtype C4 was much lower than that of C1 and C3 ( $p=0.014$ , Pearson's chi-square test, Figure 4C). Interestingly, the ALK mutation did not differ in our grouping, which indicates that it is not an immune-sensitive gene. ( $p=0.352$ , Pearson's chi-square test, Figure 4C). We further analyzed the distribution of the number of all mutant genes in these four subtypes. Figure 4D shows that there were significant differences in the frequency of mutations among these groups ( $p=0$ , Pearson's chi-square test). Genetic mutations were more likely to appear in C3, and less so in C1 and C4.

### Gene co-expression network analysis for the four subtypes

To classify genes with similar expression patterns into different modules for the four subtypes. Firstly, data of 655 differentially expressed immune-related genes of the four subtypes was grouped on the basis of similarity using the weighted gene co-expression network analysis (WGCNA) method [29]. In this analysis, a soft thresholding power of 5 was used and the best parameter  $\beta$  was 5 (Figure 5A, 5B). Then, we converted the expression matrix into an adjacency matrix, and the adjacency matrix into a topological matrix (TOM). Based on TOM, we used the average-linkage

hierarchical clustering method to cluster genes according to their expression patterns across the subtypes. The dynamic shear method was employed to determine the gene modules, after which the eigengenes of each module were calculated. Subsequently, we clustered the modules and merged similar modules into one, then set height=0.25, deepSplit = 2, minModuleSize = 30. Four modules were acquired as shown in Figure 5C.

For better visualization, each gene cluster was assigned a specific color and a color code. A total of 655 genes were assigned into three co-expression modules (brown, turquoise, blue), while 316 genes that did not fit into other clusters were grouped into the fourth "grey" module. A key network was constructed using the Pearson correlation coefficients values of the four subtypes and modules (Figure 5D). Two modules were connected if they showed an absolute value of correlation  $> 0.45$ . Notably, the brown module was positively correlated with C3 ( $r=0.68$ ,  $p=2e-71$ ) and negatively correlated with C4 ( $r=-0.31$ ,  $p=1e-12$ ). In contrast, the blue module was strongly positively correlated with C4 ( $r=-0.78$ ,  $p=4e-36$ ) and negatively correlated with C3 ( $r=-0.35$ ,  $p=1e-16$ ). The turquoise module was also correlated with C4 ( $r=0.52$ ,  $p=4e-36$ ).

The KEGG enrichment analysis was performed to investigate the biological functions of the genes. Results showed that the blue module was enriched in 25 pathways, including immune-associated pathways such as primary immunodeficiency, the intestinal immune network for IgA production and T cell receptor signaling pathway. These observations were in agreement with previous reports [30, 31]. (Figure 5E). The genes in turquoise module were enriched in 32 pathways, and the top 20 pathways are shown in Figure 5F, including immune and inflammatory pathways such as Phagosome, Tuberculosis, and Inflammatory bowel disease (IBD). Interestingly, the genes in brown modules were not associated with KEGG pathways, indicating that the formation and pathogenesis of the subtype C3 are much more complicated and unknown.

### Validation of four molecular subtypes in the LUAD cohort

To validate the four molecular subtypes, we first selected the genes in the blue, turquoise, and brown

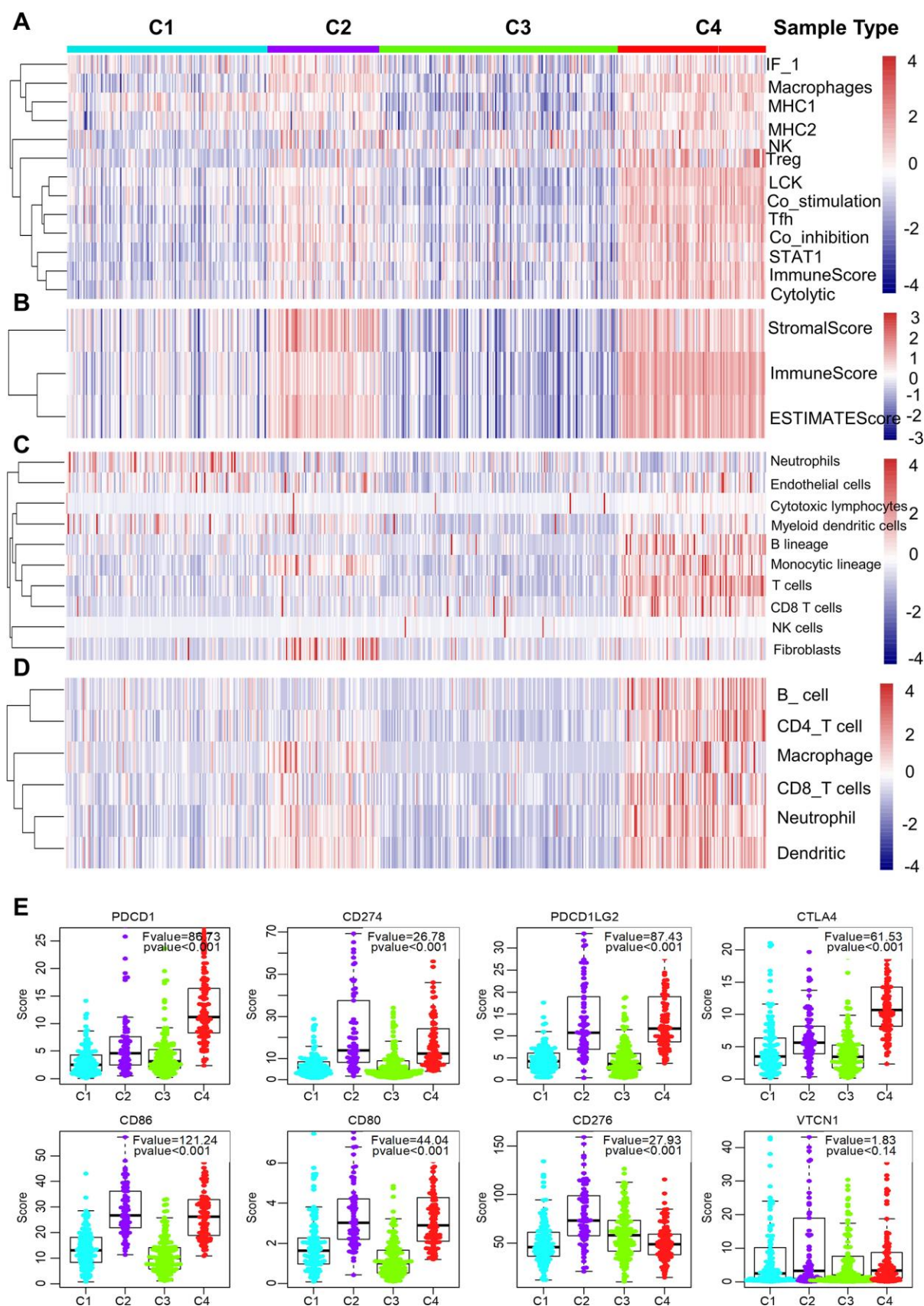


**Figure 3. Immune signature of the four subtypes in the TCGA cohort.** (A–D) Heatmaps showing the gene expression scores of immune profiles of the four subtypes. A two-color scale was used, with red indicating high expression and blue representing low expression.



(A) The expression levels of 13 immune metagenes among the four subtypes. The 13 immune metagenes: IF1, macrophages, MHC2, MHC1, NK, T regulatory cells, lymphocyte-specific kinase (LCK), STAT1, T follicular cells, T cell inhibitory and stimulatory activity, and immune score and cytolytic activity. (B) The expression scores of genes included in the ESTIMATE algorithm for determination of stromal and immune gene signatures. (C) The expression scores of 10 groups of immune-associated cells. (D) The expression levels of genes included in the TIMER algorithm for assessment of immune infiltrates. (E) Differential expression of checkpoint molecules among the four immune subtypes. Boxplots indicate 5%, 25%, 50%, 75%, and 95%, respectively. Comparisons between subtypes were performed by Analysis of Variance (ANOVA). P-values were corrected by the Bonferroni method.

modules closely related to C3 and C4 subtypes to calculate the correlation between genes and modules. Thirty-eight genes with correlation coefficients  $> 0.8$  were identified and their expression profiles were extracted as training sets. The samples were clustered with the support vector machine, at a classification accuracy of 98.83%. Subsequently, GSE68465 data was downloaded from the GEO database and standardized into quantiles. A total of 462 samples were included, comprising 19 normal samples and 442 LUAD samples.

After exclusion of 19 normal samples, 442 LUAD samples were analyzed. The expression profiles of genes in the blue, turquoise, and brown modules were extracted. The samples were subdivided into the model, of which 123, 72, 196, and 52 samples were predicted for subtype C1, C2, C3, C4, respectively. First, we analyzed the expression distribution of 13 immune metagenes in each subtype. As shown in Supplementary Figure 3, most metagenes were highly expressed in C4 and lowly expressed in C3, and this matched with the

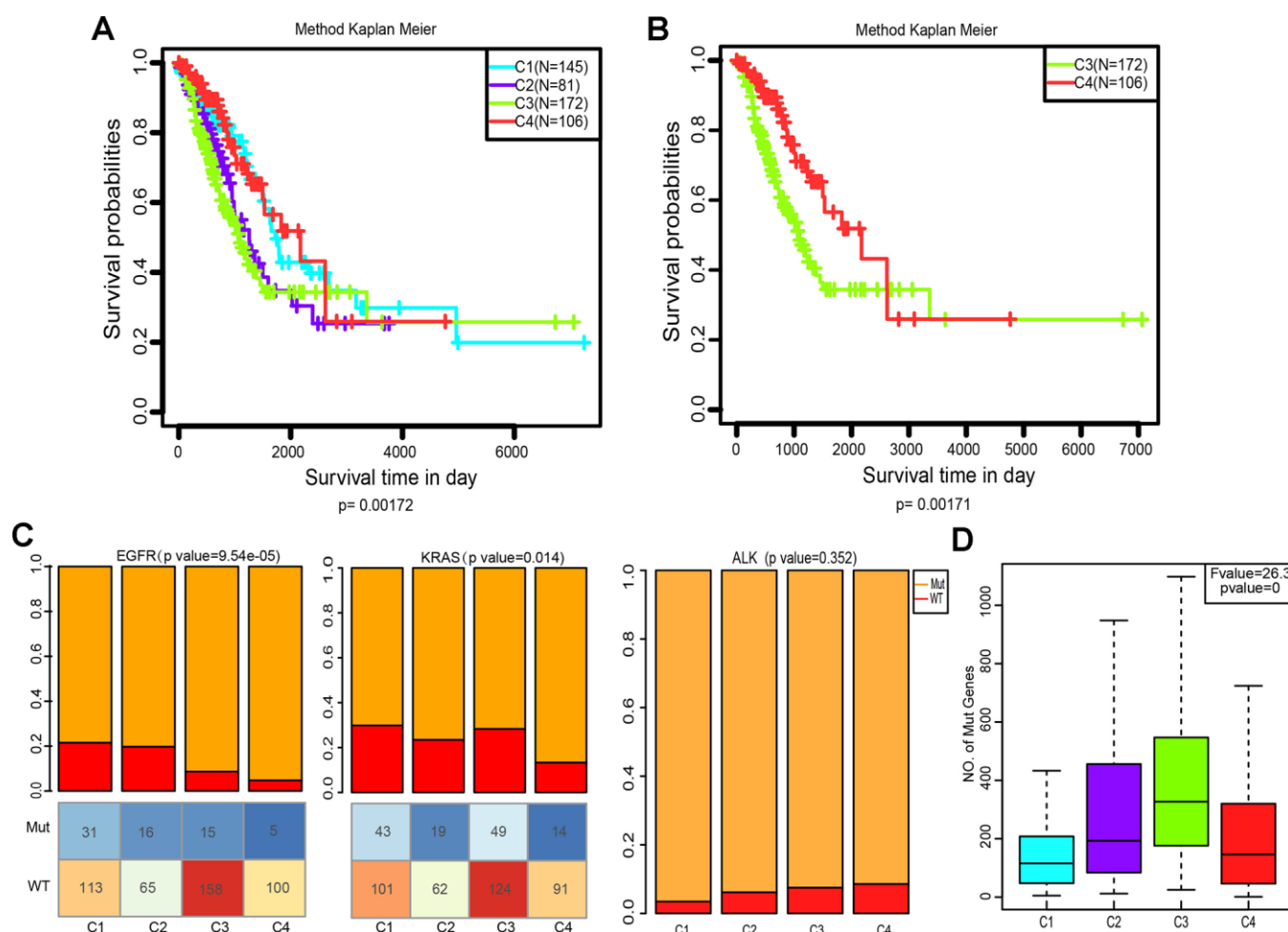


**Figure 4. Kaplan–Meier curves and mutation status of the four immune subtypes.** (A) Overall survival (OS) of the four subtypes (log-rank test). (B) Five-year Kaplan–Meier curves for OS of subtypes C3 and C4 (log-rank test). (C) Distribution of EGFR, KRAS and ALK mutant and wild-type of different subtypes (chi-square test). (D) Distribution of the number of mutant genes in the four samples (Analysis of Variance,  $p < 0.0001$ ).

validation set. Consistent with TCGA cohort, subtype C4 in the GEO cohort was considered to be highly expressed among the immune signatures (Supplementary Figure 3A–3D). Most immune metagenes were

highly expressed in C4 but lowly expressed in C3 (Supplementary Figure 3A). Analysis of immune microenvironmental factors suggested that the stromal score, immune score, and tumor purity were highest in

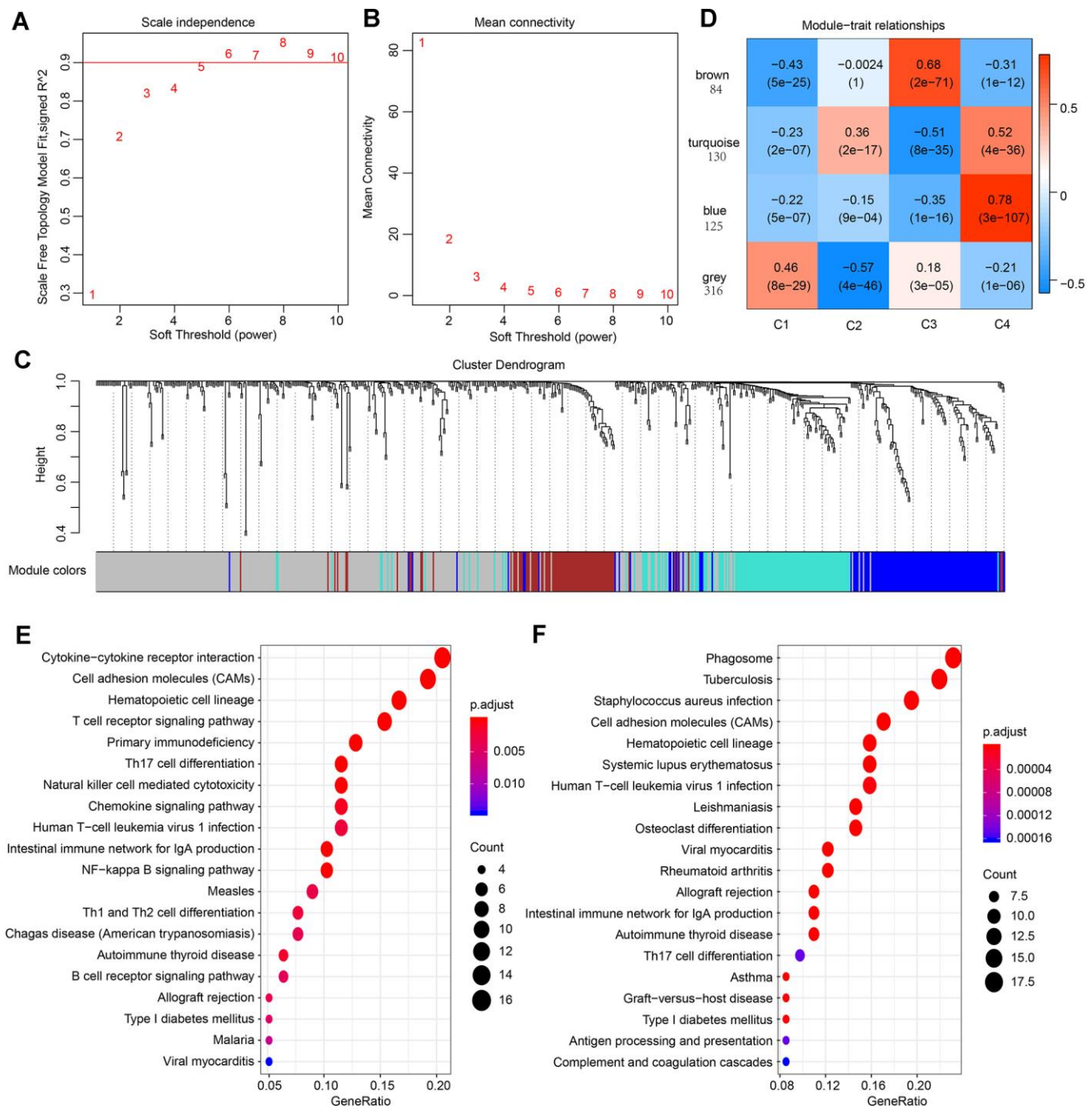


**Figure 5. Result of weighted gene correlation network analysis (WGCNA) analysis.** (A) The scale independence of WGCNA analysis and determination of parameter  $\beta$  of the adjacency function in the WGCNA algorithm. (B) The mean connectivity of WGCNA analysis. (C) Cluster results and trait heatmap of data samples. (D) Module-immune subtype weight correlations and corresponding P-values (in parenthesis). The left panel shows the four modules and the number of module member genes. (E) The top 20 pathways of genes in the blue module (ranked by FDR  $\leq 0.05$ ) in the KEGG database. (F) The top 20 pathways of genes in the turquoise module (ranked by FDR  $\leq 0.05$ ) in the KEGG database.



subtype C4, but relatively lower in C3 (Supplementary Figure 3B). Besides, B lineage cells, NK cells, T cells, cytotoxic lymphocytes and myeloid dendritic cells were higher in C4 than in C3 (Supplementary Figure 3C). In the GEO cohort, subtype C4 had higher expression levels of checkpoint receptors PD1, CTLA-4, CD86 and CD80 and lower expression of VTCN1, compared with other subtypes (Supplementary Figure 3D). The expression value of CD276 and CD274, were not detected in the GEO dataset. In addition, significant survival differences were observed among the four subtypes in the GEO cohort (Supplementary Figure 3E,  $p=0.01973$ , log-rank). In particular, C4 was associated with enhanced immune microenvironment and showed the best prognosis. Further analysis of the relationship between the four subtypes in the GEO dataset and smoking history was conducted. As shown in Supplementary Figure 3F, the smoking degree differs among the subtypes ( $p=0.004$ , Pearson's chi-square test). We further validate the four subtypes in GSE40419 dataset. Samples from GSE40419 were classified by the same method, of which 43, 40, 53, and 18 samples were predicted for subtype C1, C2, C3, C4, respectively. Consistently, most immune signatures were highly expressed in subtype C4 but lowly expressed in C3 (Supplementary Figure 4A–4D). Collectively, the findings from the GEO cohorts are in agreement with those from the TCGA cohort.

### CMap analysis for perturbagen signatures that reverse C3 immune subtype

Among the four subtypes, we focused on patients with subtype C3. Their immunosuppressive status, accompanied by EGFR wild type, has been challenging to clinical treatment due to the lack of targets for tyrosine kinase inhibitor (TKI) and immunotherapy [6, 32]. To investigate potential drugs for this subtype, we applied computational drug repurposing strategies. Subsequently, we performed CMap analysis to identify new drugs that can reverse immune-suppressed status of subtype C3. Genes in the brown module that positively correlated with C3 (Supplementary Table 2) were recognized as up-regulated genes, and genes in blue module (Supplementary Table 2) were down-regulated genes. After being queried by the next-generation CMap database (CLUE, <https://clue.io/>), small molecule compounds (CPs) and genes knockdown or overexpress (KD/OE) with positive and negative scores and exhibiting similar or opposing gene expression signatures in group C3 are shown in Figure 6A, 6B. Our analysis was carried out using cell lines A549 and HCC515, two LUAD cell lines. We then selected CPs with enrichment scores of less than -80 in both adenocarcinoma cell lines as potentially capable of reversing the C3 aberrant gene expression

(Supplementary Table 3). We next screened knockdown genes with scores lower than -80 and overexpressed genes with scores higher than 80 in the two cell lines as potential therapeutic targets against LUAD (Supplementary Table 4). This analysis identified four overlapping genes (IKBKE, KDR, HDAC11, BIRC5) among the known target genes of the selected CPs and screened genes (KD or OE). These candidates were confirmed as targets for C3 reversal and the CPs identified above (Figure 6C, 6D). Our analysis further revealed that, BX-795, ENMD-2076, midostaurin, JNJ-26854165 and alvocidib potentially reverse the C3 subtype signature (Figure 6D, 6E). Interestingly, three drug candidates were identified for KDR. The connectivity scores for BX-795 and IKBKE knockdown were relatively similar in A549 and HCC515 cells.

### Validation of affinity of the candidate drugs by molecular docking analysis

To evaluate the affinity of the candidate drugs for their targets, we performed molecular docking analysis. First, 3D models of HDAC11 and IKBKE protein structure were predicted using the template-based homology modeling approach. Consequently, 6HSK-A and 4IM0-A (PDB structures) were identified as ideal templates for modeling as they demonstrated high sequence similarity (32% and 44%) [33]. Ramachandran plot analysis demonstrated existence of 92.5% of all residues in the allowed regions for HDAC11 and 94.7% for IKBKE, highlighting the accuracy of the predicted structures (Figure 7). The binding poses and interactions of five drug candidates with four protein were obtained with Autodock Vina v.1.1.2 and binding energy for each interaction was generated (Figure 8, Supplementary Figure 5 and Table 1). Results showed that each drug candidates bound to its protein targets through visible hydrogen bonds and strong electrostatic interactions. Moreover, the hydrophobic pockets of each targets were occupied successfully by the five candidate drugs. For KDR, two candidates, JNJ-26854165 and BX-795 had low binding energy of -9.7 and -9.3 kcal/mol, indicating highly stable binding (Table 1).

## DISCUSSION

In recent years, increasing studies identifying and stratifying the immune characteristics of patients with LUAD have been reported [34–37]. Yet, most of them focused solely on the clinical relevance such as survival and prognosis, and have not been translated into routine clinical practice. This calls for a further exploration and summarization of the LUAD microenvironment to expose the molecular events underlying tumor cell–immunocyte interactions, in particular, the relevance study of drug development.

Nowadays, the combination of priming therapy to enhance T cell responses along with the removal of inhibitory signals (and/or the supply of co-stimulatory signals) has been proposed to convert “old” tumors into “hot” tumors and overcome the lack of pre-existing immune responses [7]. However, the development of novel drugs is costly and time-consuming. Consequently, drug repurposing, where existing medication are utilized for the treatment of conditions other than their original targets has emerged as a potential solution to these challenges.

**Figure 6. Connectivity mapping for the gene signature in C3 immune subtype.** (A, B) Connections of C3-driven gene signature with the small molecule compounds (A) and gene knockdown/overexpression (B) were analyzed by querying the CLUE database. Connections were viewed as a heat map ranked by the summary connectivity score. (C) The venn diagram indicating the number of target genes of screened small molecule compounds (enrichment score<-80) and gene knockdown/overexpression (gene knockdown, enrichment score<-80; gene overexpression, enrichment score>80), and the overlap between each set of genes. (D) Descriptions of overlapped gene and their corresponding drugs from screened small molecule compounds. (E) Connections of C3-driven gene signature with screened small molecules and gene knockdown/overexpression were analyzed by querying the CLUE database. Connections were viewed as a heat map with each connectivity score in individual cell line. CP, compounds. KD, knockdown. OE, overexpression.

A critical assumption of CMap analyses is that a drug that induces changes in gene expression that are opposite to those caused by a disease may have potential therapeutic benefits against the disease. Therefore, the outputs from inputting the blue and brown modules into CMap are potential targets and drugs that can reverse the cold tumor status of the C3 subgroup. Here, we identified five drugs against four targets associated with the C3 status. IKBKE has been described to impact on inflammatory and metabolic diseases as well as on cell proliferation and transformation [38]. BIRC5 (baculoviral IAP repeat containing 5) is overexpressed in various tumors and associated with poor cancer survival [39]. KDR (also called VEGFR2) is a key modulator of angiogenesis and its overexpression is frequently associated with poorer prognoses in lung cancer patients [40]. It is notable that inhibition of KDR alleviates hypoxia and remodels the immunosuppressive tumor microenvironment [41]. It

has also been reported that HDAC11 inhibition might regulate immune activation by increasing type I interferon signaling [42]. These indicates that the inhibition of these four targets has potential dual functions to correct aberrant immune microenvironment also halt tumorigenesis at the same time.

Of all drug candidates, midostaurin needs special attention because it has gained approval by the FDA for the treatment of acute myeloid leukemia (AML) [43]. Interestingly, midostaurin has been found to displayed potent antiproliferative activity in several lung cell lines [44]. Another concern is BX-795, a known multi-target kinase inhibitor [45, 46]. Researches in recent years found that it exhibited inhibitory activity against virus infection and various cancer [47–49]. In this work, we found that BX795 can inhibit IKBKE and KDR at the same time correct aberrant gene expression in the C3 subgroup. The only oral drug among all

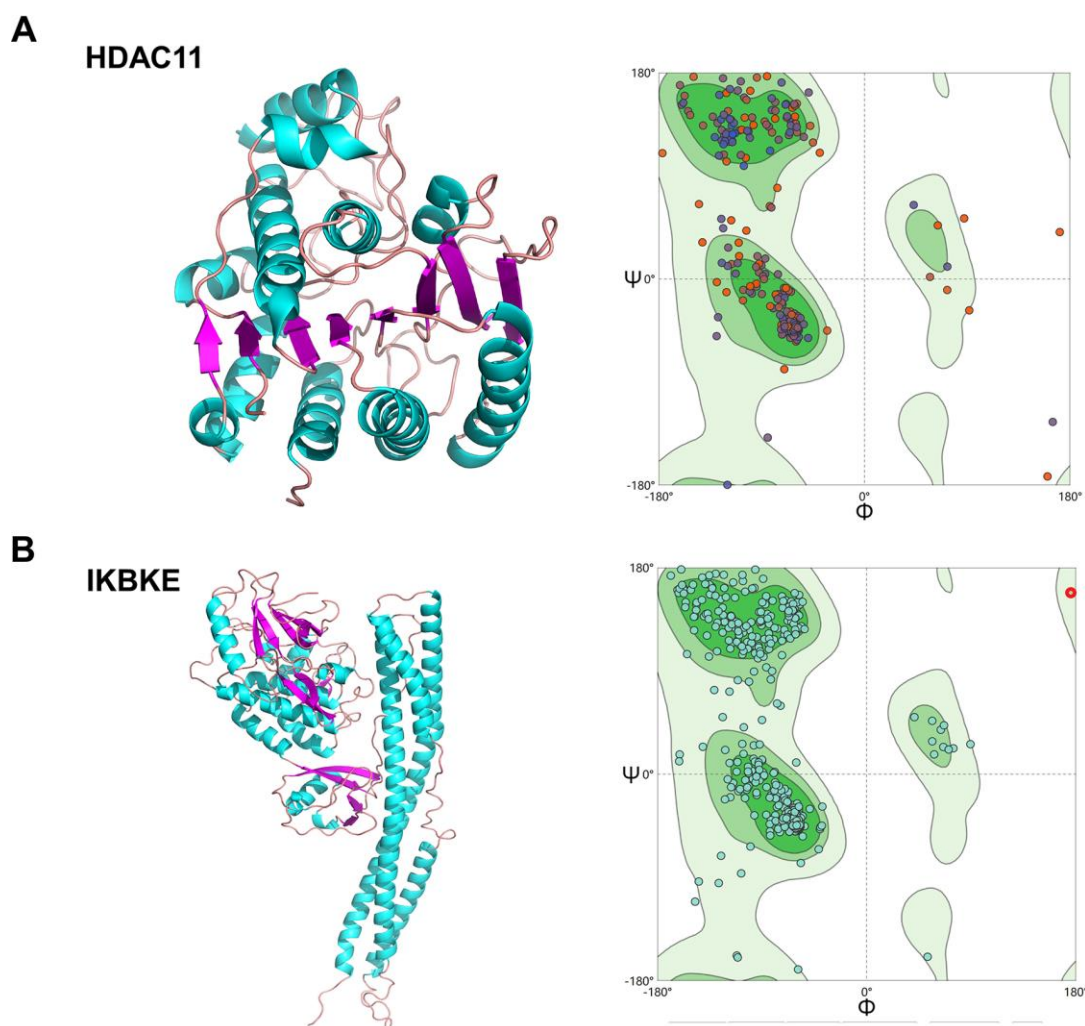


**Figure 7. Homologous modeling of HDAC11 and IKBKE protein structure. (A) 3D structure of HDAC11 and IKBKE. (B) Ramachandran plot analysis.**



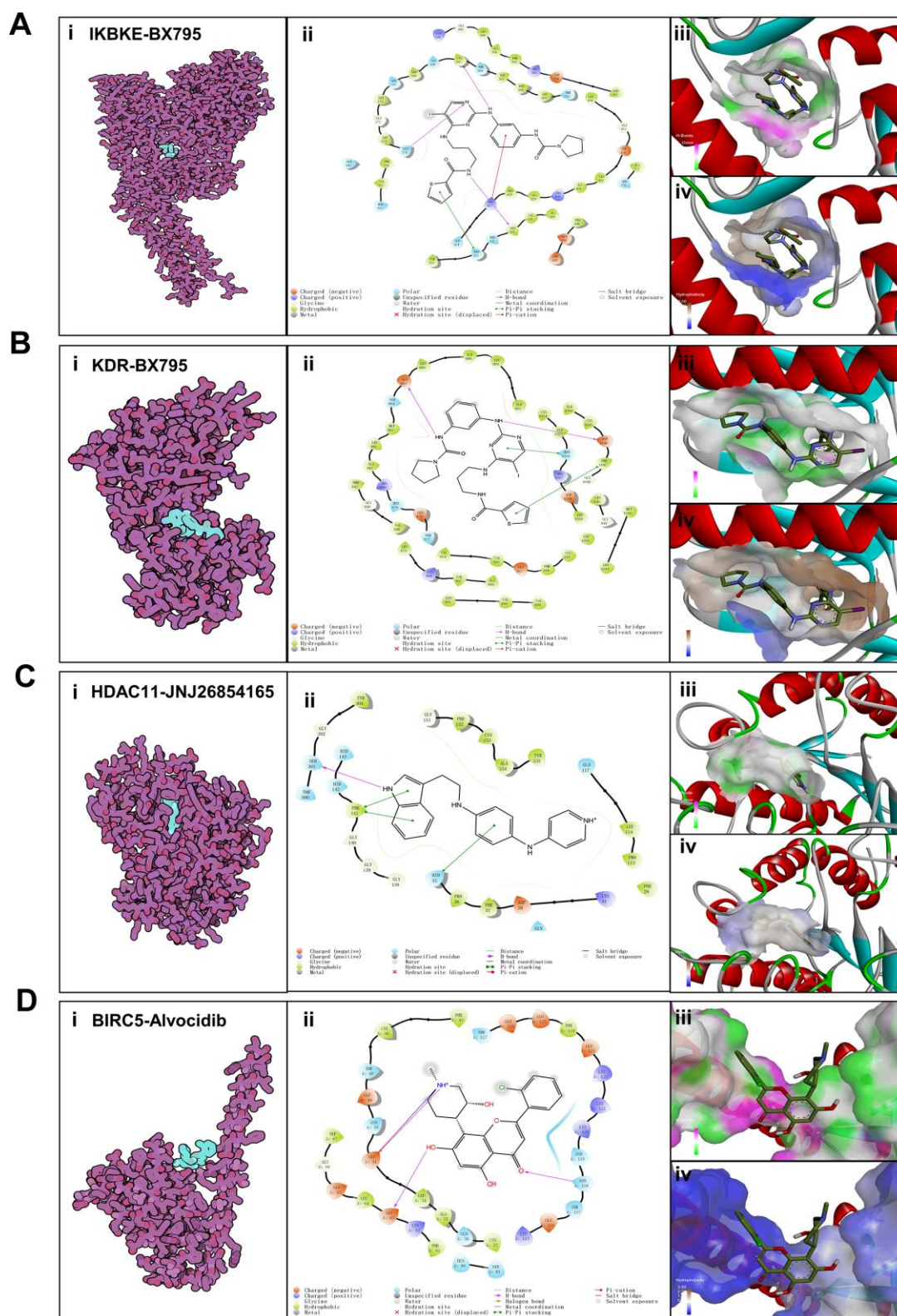


**Figure 8. Binding mode of screened drugs to their targets by molecular docking.** (A) Binding mode of BX795 to IKBKE. (B) Binding mode of BX795 to KDR. (C) Binding mode of JNJ26854165 to HDAC11. (D) Binding mode of Alvocidib to BIRC5. (i), Cartoon representation, overlay of the crystal structures of small molecule compounds and their targets were illustrated by Molecule of the Month feature. (ii), 2D interactions of compounds and their targets. (iii, iv) Three-dimensional structures of the binding pockets were showed by PyMOL software. (iii), Coloring is from carmine (for strong H-bonds) to green (for poor H-bonds). (iv), Coloring is from magenta (for strong hydrophobic regions) to blue (for poor hydrophobic regions).

**Table 1. Binding Energy for targets with their drugs.**

Target	Drug	Binding Energy (kcal/mol)
IKBKE	BX-975	-8.3
KDR	ENMD-2076	-7.8
KDR	BX-795	-9.3
KDR	Midostaurin	-0.8
HDAC11	JNJ-26854165	-8.9
BIRC5	Alvocidib	-5.4

candidates is ENMD-2076. This is a multi-target kinase inhibitor with antitumor activities against breast cancer, melanoma, colorectal cancer [50–53]. Alvocidib can be used as a metastasis inhibitor and an apoptosis inducer in KRAS mutant population especially since KRAS mutation rate of C3 group was high [54]. Over all, all identified compounds including JNJ-26854165 [55] have previously shown the potential to inhibit a variety of tumors, of which midostaurin has been clinically approved for the treatment of hematological diseases. Furthermore, their steady binding affinity against the targets was verified through molecular docking analysis at a molecular level, thus warranting further investigation to validate.

This strategy can also be used to immunotype other tumor patients and to screen for potential personalized drugs. Recently, immunotherapy, especially immune checkpoint blockade (ICB, e.g. anti-PD1/PD-L1 antibodies), has been used to treat multiple cancers, including NSCLC, melanoma, renal cell cancer, colorectal cancer, recurrent head and neck cancer (squamous cell), urothelial carcinoma, gastric cancer cervical cancer [56]. However, response to current immunotherapies and survival benefits are often seen in a subset of patients. The key to solving this problem lies in determining the individual's ability to respond to immunotherapy and to design a rational, individualized immunotherapy combined strategy. Therefore, to enhance and improve the efficacy of current immunotherapy, a better understanding of tumor immune microenvironment is required. As shown in this paper, in other tumors such as melanoma, we can also use unsupervised consensus cluster analysis, which relies on the expression profiles of immune-related genes, to reveal the immune landscape and characteristics within the tumor. Furthermore, based on immunophenotypic features, WGCNA analysis can be applied to construct co-expression networks and identify hub genes. After drug repurposing, the identified potential therapeutic candidates may help facilitate personalized immunotherapy for patients with different molecular subtypes. In conclusion, it is evident that this method can be applied to other tumor types in which therapeutic response is dependent on the immune microenvironment.

In summary, this study highlights the potential of coupling patient stratification with drug repurposing strategy as an alternative means for developing personalized immunotherapy.

## MATERIALS AND METHODS

### Sample datasets and clinical profiles

The clinical data and gene expression profiles of 513 LUAD data obtained from The Cancer Genome Atlas (TCGA) were used to analyze the immune microenvironment and molecular subtype of LUAD [57]. Data on overall survival (OS) (distant or locoregional recurrence after surgical treatment) was extracted from the TCGA cohort. The two LUAD expression datasets, including GSE68465 and GSE40419, as well as the corresponding clinical information in Gene Expression Omnibus (GEO) [58] were included to validate our results. The OS data were extracted from the GEO cohort.

### Processing of gene expression data

For the TCGA cohort, data of the fragments per kilobase of gene per million fragments (FPKM) was derived from the TCGA data portal. Next, the expression values of FPKM were converted to transcripts Per Kilobase of exon model per Million mapped reads (TPM) for subsequent analysis. The genes were annotated using the Ensembl database. The clinical information and normalized expression data of the GEO cohort was obtained from the Gene Expression Omnibus (GEO) (GSE68465). Probe annotations of BeadChips were derived from the GEO database. The expression data of the two cohorts were mapped using the Entrez Gene.

### Characterization of molecular subtypes of LUAD using immune genes

We analyzed whether the expression profile of global immune-related genes in the TCGA cohort could distinguish the LUAD subtypes. The expression data of immune-associated genes was derived from the Immunology Database and Analysis Portal (ImmPort)



database (<https://immport.niaid.nih.gov>). The immune-related genes with expression level  $> 0$  (FPKM $>0$ ) in more than 30% of samples were included, resulting in 790 genes selected for subsequent Consensus Cluster Plus analysis. The similarity distance between samples was calculated by the Euclidean distance metric. The samples were clustered using the k-means clustering algorithm, with 1000 iterations by sampling 80% of the samples in each iteration. The cluster numbers varied from 2 to 8, and the optimal partition was determined by evaluating the consensus cumulative distribution function (CDF) [59]. The pair comparisons between the identified subtypes were determined by SigClust analysis. Bonferroni correction was applied for multiple testing. The Kolmogorov-Smirnov test was used to identify highly expressed genes among the subtypes. The false discovery rate (FDR) was determined by the Benjamini-Hochberg method. FDR $<0.05$  was set as the threshold. In each subtype, the top 100 upregulated genes were employed to distinguish among the immune molecular subtypes.

### Immune signature analysis in LUAD molecular subtypes

Thirteen immune metagenes corresponding to various immune cells and related immune functions were derived from a previous publication [27]. The expression scores of micro-environmental factors (tumor, immune, and stromal purity) were obtained using the ESTIMATE algorithm [60]. The association among the tumor samples and six tumor-infiltrating lymphocytes including B, and dendritic cells, neutrophils, CD8 $^{+}$  T, macrophages, CD4 $^{+}$  T, was analyzed using TIMER (<https://cistrome.shinyapps.io/timer>). The Microenvironment Cell Populations (MCP)-counter method developed by Etienne Becht et al. was used to validate the immune profiles [61]. MCP-counter was used to estimate the inter-sample relative abundance of immune infiltrates based on gene expression profiles. The R package “MCPcounter” was utilized to calculate the MCP-counter scores. The expression score of immune signatures in each tumor sample was calculated using the log<sub>2</sub> transformed and median-centered FPKM expression values and then visualized by heatmap. The immune signature and expression level of checkpoint genes were also analyzed in all molecular subtypes. Different LUAD subtypes were compared by Analysis of Variance (ANOVA) test. Multiple testing was performed by Bonferroni correction.

### Analysis of mutations in each subtype

The EGFR-mutant, KRAS-mutant and ALK mutant data were extracted from the SNP dataset in TCGA after processing with MuTect method (<http://www.broadinstitute.org/cancer/cga/mutect>) [62]. The frequency of

mutations was assessed by calculating the number of variants annotated by ANNOVAR [63, 64].

### Weighted Gene Co-expression Network Analysis (WGCNA) Analysis

The WGCNA package in R software was employed to execute WGCNA analysis. Initially, Pearson correlation coefficients (ranging from  $-1$  to  $1$ ) were used to calculate the co-expression of all gene pairs. Due to the small sample size enrolled in the present study, Pearson correlations measuring linear relationships were chosen to minimize overfitting. To convert the correlation coefficients into a weighted adjacency matrix (values ranging from 0 to 1), we raised the co-expression similarity to a power  $\beta = 5$ . The adjacency matrix enables the determination of the strengths of connection between two nodes. The matrix is therefore used to establish a topological overlap matrix (TOM) which addresses the topological similarity factor. Here, we used the TOM to determine the corresponding dissimilarity (1-TOM) for cluster formation. Genes with clear expression patterns were classified into modules using the average linkage hierarchical clustering in concert with TOM-based dissimilarity. Specifically, gene modules (clusters of densely interconnected genes in terms of co-expression) were detected using the dynamic tree-cutting algorithm (deep split = 2, minimum number of genes per module = 30, cut height = 0.25). Unassigned genes were represented by gray color, while all other modules were assigned different colors in a random manner. Determination of modules highly correlated with subtypes was achieved using the module eigengenes (MEs). All analyses were carried out using the WGCNA package.

### Functional group analysis

ClusterProfiler software 3.6.0 was employed for KEGG pathway enrichment analysis of the genes in each module and subtype. The R package of this software helps to determine the biological functions of gene clusters and to compare several gene clusters [65].

### Connectivity map analysis

The next generation Connectivity Map (CMap, <https://clue.io/>) is a database that catalogs gene expression profiles of various human cell lines upon exposure to various small molecule compounds and genetic perturbations [66, 67]. To find perturbagens that reverse the immune-suppressed status of subtype C3, the genes listed in Supplementary Table 2 were inputted as query into the CLUE database and results downloaded from the CMap database. Compounds (CPs) with potential to reverse the C3 phenotype were

further screened by filtering for an enrichment score of  $<-80$  in both A549 and HCC515 cell lines. Gene knockdown (KD) with enrichment scores below -80 and overexpressed genes (OE) with scores above 80 in both A549 and HCC515 were also identified. Overlapping genes between target genes of CPs and genes KD or OE that perturb the C3 signature were determined by Venn diagram analysis. The overlapping genes were considered potential drug targets for C3 group. We hypothesized that these candidate genes can be pharmacologically targeted with the identified CPs with scores of  $<-80$ . Connections of C3 driven gene signature to CPs or gene KD/OE were obtained from the results and presented in the form of a heat map.

### Homologous modeling

To analyze the binding affinities and modes of interaction between the CPs and their targets, we used an in silico protein-ligand docking software (AutodockVina 1.1.2) [68]. To date, there is no complete crystal structure of HDAC11 and IKBKE, so their amino acids sequences were analyzed by EXPasy (<http://swissmodel.expasy.org/>) [69]. Ramachandran plots were used to assess stereo-chemical quality [70]. The parameters were set to default.

### Molecular docking

The molecular structures of ENMD-2076, BX-795, JNJ-26854165, midostaurin and alvocidib were retrieved from PubChem Compound (<https://pubchem.ncbi.nlm.nih.gov/>) [71]. The 3D coordinates of KDR (PDB ID, 5EW3; resolution, 2.5 Å) and BIRC5 (PDB ID, 4AOI; resolution, 1.9 Å) were downloaded from the PDB (<http://www.rcsb.org/pdb/home/home.do>). For docking analysis, all protein and molecular files were converted into PDBQT format with all water molecules excluded and polar hydrogen atoms were added using MGLTools (version 1.5.6). The grid box was centered to cover the domain of each protein and to accommodate free molecular movement. The grid box was set to 30 Å × 30 Å × 30 Å, and grid point distance was 0.05nm. Molecular docking studies were performed by Autodock Vina 1.1.2 (<http://autodock.scripps.edu/>) and Pymol software 2.3 (DeLano Scientific, Portland, USA) was used for model visualization.

### Statistical methods

Fisher's exact test or chi-square test was used to evaluate the correlation between molecular subtypes and conventional clinical variables. Benjamini-Hochberg's FDR was used for corrected multiple testing. The log-rank tests and Kaplan-Meier curves were used to calculate the OS rates for each molecular

subtype. These statistics were two-sided and were performed using R software.

### Availability of supporting data

The datasets analyzed during the current study are available in the Genomic Data Commons (GDC, <https://gdc.cancer.gov/access-data/gdc-data-portal>) and Gene Expression Omnibus (GEO, <https://www.ncbi.nlm.nih.gov/geo/>) repositories.

### Abbreviations

EGFR: Epidermal growth factor receptor; TKI: Tyrosine kinase inhibitors; LUAD: lung adenocarcinoma; TME: complex tumor microenvironment; CMap: The Connectivity Map; PCA: Principal component analysis; CPs: compounds; KD/OE: genes knockdown/overexpress; TCGA: The Cancer Genome Atlas; GEO: Gene Expression Omnibus; WGCNA: Weighted correlation network analysis; ALK: Anaplastic lymphoma kinase; FPKM: The fragments per kilobase of gene per million fragments; TPM: Transcripts Per Kilobase of exon model per Million mapped reads; ImmPort: Immunology Database and Analysis Portal; CDF: Consensus cumulative distribution function; FDR: False discovery rate; ANOVA: Analysis of Variance; TOM: Topological overlap matrix; ME: Module eigengenes; TNM: Tumor, Node, Metastasis; TOM: Topological matrix; FMT: Fecal microbiota transplantation.

### AUTHOR CONTRIBUTIONS

Conceptualization, W.H, G.W, B.L and Y.W; Formal analysis, W.H, G.W and Y.C; Funding acquisition, Y.W; Investigation, W.H, G.W, L.Y and Y.C; Methodology, W.H, G.W, L.Y, Y.C, B.L and Y.W; Software, W.H and G.W; Supervision, B.L and Y.W; Visualization, W.H and G.W; Writing – original draft, W.H, G.W, B.L and Y.W; Writing – review & editing, W.H, G.W, L.Y, Y.C, B.L and Y.W.

### CONFLICTS OF INTEREST

The authors declare that they have no conflicts of interests.

### FUNDING

This work was supported by Binghamton University Faculty Start-up Fund 910252-35, Binghamton University S3IP award ADLG195, Suzhou Science and Technology Development Project SYS2018085, and Construction Project of Suzhou Clinical Medical Center, szzx201506.

## REFERENCES

- Mlecnik B, Tosolini M, Kirilovsky A, Berger A, Bindea G, Meatchi T, Bruneval P, Trajanoski Z, Fridman WH, Pagès F, Galon J. Histopathologic-based prognostic factors of colorectal cancers are associated with the state of the local immune reaction. *J Clin Oncol*. 2011; 29:610–18.  
<https://doi.org/10.1200/JCO.2010.30.5425>  
PMID:21245428
- Pagès F, Kirilovsky A, Mlecnik B, Asslaber M, Tosolini M, Bindea G, Lagorce C, Wind P, Marliot F, Bruneval P, Zatloukal K, Trajanoski Z, Berger A, et al. In situ cytotoxic and memory T cells predict outcome in patients with early-stage colorectal cancer. *J Clin Oncol*. 2009; 27:5944–51.  
<https://doi.org/10.1200/JCO.2008.19.6147>  
PMID:19858404
- Galon J, Fridman WH, Pagès F. The adaptive immunologic microenvironment in colorectal cancer: a novel perspective. *Cancer Res*. 2007; 67:1883–86.  
<https://doi.org/10.1158/0008-5472.CAN-06-4806>  
PMID:17332313
- Galon J, Mlecnik B, Bindea G, Angell HK, Berger A, Lagorce C, Lugli A, Zlobec I, Hartmann A, Bifulco C, Nagtegaal ID, Palmqvist R, Masucci GV, et al. Towards the introduction of the ‘Immunoscore’ in the classification of Malignant tumours. *J Pathol*. 2014; 232:199–209.  
<https://doi.org/10.1002/path.4287> PMID:24122236
- D’Amico TA, Massey M, Herndon JE 2nd, Moore MB, Harpole DH Jr. A biologic risk model for stage I lung cancer: immunohistochemical analysis of 408 patients with the use of ten molecular markers. *J Thorac Cardiovasc Surg*. 1999; 117:736–43.  
[https://doi.org/10.1016/s0022-5223\(99\)70294-1](https://doi.org/10.1016/s0022-5223(99)70294-1)  
PMID:10096969
- Hegde PS, Karanikas V, Evers S. The where, the when, and the how of immune monitoring for cancer immunotherapies in the era of checkpoint inhibition. *Clin Cancer Res*. 2016; 22:1865–74.  
<https://doi.org/10.1158/1078-0432.CCR-15-1507>  
PMID:27084740
- Whiteside TL, Demaria S, Rodriguez-Ruiz ME, Zarour HM, Melero I. Emerging opportunities and challenges in cancer immunotherapy. *Clin Cancer Res*. 2016; 22:1845–55.  
<https://doi.org/10.1158/1078-0432.CCR-16-0049>  
PMID:27084738
- Ali HR, Chlon L, Pharoah PD, Markowitz F, Caldas C. Patterns of immune infiltration in breast cancer and their clinical implications: a gene-expression-based retrospective study. *PLoS Med*. 2016; 13:e1002194.  
<https://doi.org/10.1371/journal.pmed.1002194>  
PMID:27959923
- Newman AM, Liu CL, Green MR, Gentles AJ, Feng W, Xu Y, Hoang CD, Diehn M, Alizadeh AA. Robust enumeration of cell subsets from tissue expression profiles. *Nat Methods*. 2015; 12:453–57.  
<https://doi.org/10.1038/nmeth.3337> PMID:25822800
- Rooney MS, Shukla SA, Wu CJ, Getz G, Hacohen N. Molecular and genetic properties of tumors associated with local immune cytolytic activity. *Cell*. 2015; 160:48–61.  
<https://doi.org/10.1016/j.cell.2014.12.033>  
PMID:25594174
- Gentles AJ, Newman AM, Liu CL, Bratman SV, Feng W, Kim D, Nair VS, Xu Y, Khuong A, Hoang CD, Diehn M, West RB, Plevritis SK, Alizadeh AA. The prognostic landscape of genes and infiltrating immune cells across human cancers. *Nat Med*. 2015; 21:938–45.  
<https://doi.org/10.1038/nm.3909> PMID:26193342
- Li T, Fan J, Wang B, Traugh N, Chen Q, Liu JS, Li B, Liu XS. TIMER: a web server for comprehensive analysis of tumor-infiltrating immune cells. *Cancer Res*. 2017; 77:e108–10.  
<https://doi.org/10.1158/0008-5472.CAN-17-0307>  
PMID:29092952
- Thorsson V, Gibbs DL, Brown SD, Wolf D, Bortone DS, Ou Yang TH, Porta-Pardo E, Gao GF, Plaisier CL, Eddy JA, Ziv E, Culhane AC, Paull EO, et al, and Cancer Genome Atlas Research Network. The immune landscape of cancer. *Immunity*. 2018; 48:812–30.e14.  
<https://doi.org/10.1016/j.immuni.2018.03.023>  
PMID:29628290
- Li J, Zheng S, Chen B, Butte AJ, Swamidass SJ, Lu Z. A survey of current trends in computational drug repositioning. *Brief Bioinform*. 2016; 17:2–12.  
<https://doi.org/10.1093/bib/bbv020> PMID:25832646
- Shah RR, Stonier PD. Repurposing old drugs in oncology: opportunities with clinical and regulatory challenges ahead. *J Clin Pharm Ther*. 2019; 44:6–22.  
<https://doi.org/10.1111/jcpt.12759>  
PMID:30218625
- Duan Q, Reid SP, Clark NR, Wang Z, Fernandez NF, Rouillard AD, Readhead B, Tritsch SR, Hodos R, Hafner M, Niepel M, Sorger PK, Dudley JT, et al. L1000CDS<sup>2</sup>: LINCS L1000 characteristic direction signatures search engine. *NPJ Syst Biol Appl*. 2016; 2:16015.  
<https://doi.org/10.1038/npjbsa.2016.15>  
PMID:28413689
- Chen B, Ma L, Paik H, Sirota M, Wei W, Chua MS, So S, Butte AJ. Reversal of cancer gene expression correlates with drug efficacy and reveals therapeutic targets. *Nat Commun*. 2017; 8:16022.

- <https://doi.org/10.1038/ncomms16022>  
PMID:28699633
18. Ashburn TT, Thor KB. Drug repositioning: identifying and developing new uses for existing drugs. *Nat Rev Drug Discov.* 2004; 3:673–83.  
<https://doi.org/10.1038/nrd1468> PMID:15286734
  19. Chong CR, Sullivan DJ Jr. New uses for old drugs. *Nature.* 2007; 448:645–46.  
<https://doi.org/10.1038/448645a> PMID:17687303
  20. Novac N. Challenges and opportunities of drug repositioning. *Trends Pharmacol Sci.* 2013; 34:267–72.  
<https://doi.org/10.1016/j.tips.2013.03.004>  
PMID:23582281
  21. Zhao S, Iyengar R. Systems pharmacology: network analysis to identify multiscale mechanisms of drug action. *Annu Rev Pharmacol Toxicol.* 2012; 52:505–21.  
<https://doi.org/10.1146/annurev-pharmtox-010611-134520> PMID:22235860
  22. Dudley JT, Sirota M, Shenoy M, Pai RK, Roedder S, Chiang AP, Morgan AA, Sarwal MM, Pasricha PJ, Butte AJ. Computational repositioning of the anticonvulsant topiramate for inflammatory bowel disease. *Sci Transl Med.* 2011; 3:96ra76.  
<https://doi.org/10.1126/scitranslmed.3002648>  
PMID:21849664
  23. Kosaka T, Nagamatsu G, Saito S, Oya M, Suda T, Horimoto K. Identification of drug candidate against prostate cancer from the aspect of somatic cell reprogramming. *Cancer Sci.* 2013; 104:1017–26.  
<https://doi.org/10.1111/cas.12183> PMID:23600803
  24. van Noort V, Schölch S, Iskar M, Zeller G, Ostertag K, Schweitzer C, Werner K, Weitz J, Koch M, Bork P. Novel drug candidates for the treatment of metastatic colorectal cancer through global inverse gene-expression profiling. *Cancer Res.* 2014; 74:5690–99.  
<https://doi.org/10.1158/0008-5472.CAN-13-3540>  
PMID:25038229
  25. Hayes DN, Monti S, Parmigiani G, Gilks CB, Naoki K, Bhattacharjee A, Socinski MA, Perou C, Meyerson M. Gene expression profiling reveals reproducible human lung adenocarcinoma subtypes in multiple independent patient cohorts. *J Clin Oncol.* 2006; 24:5079–90.  
<https://doi.org/10.1200/JCO.2005.05.1748>  
PMID:17075127
  26. Bray F, Ferlay J, Soerjomataram I, Siegel RL, Torre LA, Jemal A. Global cancer statistics 2018: GLOBOCAN estimates of incidence and mortality worldwide for 36 cancers in 185 countries. *CA Cancer J Clin.* 2018; 68:394–424.  
<https://doi.org/10.3322/caac.21492>  
PMID:30207593
  27. Safonov A, Jiang T, Bianchini G, Györfy B, Karn T, Hatzis C, Pusztai L. Immune gene expression is associated with genomic aberrations in breast cancer. *Cancer Res.* 2017; 77:3317–24.  
<https://doi.org/10.1158/0008-5472.CAN-16-3478>  
PMID:28428277
  28. Rios Velazquez E, Parmar C, Liu Y, Coroller TP, Cruz G, Stringfield O, Ye Z, Makrigiorgos M, Fennessy F, Mak RH, Gillies R, Quackenbush J, Aerts HJ. Somatic mutations drive distinct imaging phenotypes in lung cancer. *Cancer Res.* 2017; 77:3922–30.  
<https://doi.org/10.1158/0008-5472.CAN-17-0122>  
PMID:28566328
  29. Langfelder P, Horvath S. WGCNA: an R package for weighted correlation network analysis. *BMC Bioinformatics.* 2008; 9:559.  
<https://doi.org/10.1186/1471-2105-9-559>  
PMID:19114008
  30. Matson V, Fessler J, Bao R, Chongsawat T, Zha Y, Alegre ML, Luke JJ, Gajewski TF. The commensal microbiome is associated with anti-PD-1 efficacy in metastatic melanoma patients. *Science.* 2018; 359:104–08.  
<https://doi.org/10.1126/science.aao3290>  
PMID:29302014
  31. Routy B, Le Chatelier E, Derosa L, Duong CP, Alou MT, Daillère R, Fluckiger A, Messaoudene M, Rauber C, Roberti MP, Fidelle M, Flament C, Poirier-Colame V, et al. Gut microbiome influences efficacy of PD-1-based immunotherapy against epithelial tumors. *Science.* 2018; 359:91–97.  
<https://doi.org/10.1126/science.aan3706>  
PMID:29097494
  32. Paez JG, Jänne PA, Lee JC, Tracy S, Greulich H, Gabriel S, Herman P, Kaye FJ, Lindeman N, Boggon TJ, Naoki K, Sasaki H, Fujii Y, et al. EGFR mutations in lung cancer: correlation with clinical response to gefitinib therapy. *Science.* 2004; 304:1497–500.  
<https://doi.org/10.1126/science.1099314>  
PMID:15118125
  33. Xiang Z. Advances in homology protein structure modeling. *Curr Protein Pept Sci.* 2006; 7:217–27.  
<https://doi.org/10.2174/13892030677452312>  
PMID:16787261
  34. Yue C, Ma H, Zhou Y. Identification of prognostic gene signature associated with microenvironment of lung adenocarcinoma. *PeerJ.* 2019; 7:e8128.  
<https://doi.org/10.7717/peerj.8128>  
PMID:31803536
  35. Chen H, Carrot-Zhang J, Zhao Y, Hu H, Freeman SS, Yu S, Ha G, Taylor AM, Berger AC, Westlake L, Zheng Y, Zhang J, Ramachandran A, et al. Genomic and immune



- profiling of pre-invasive lung adenocarcinoma. *Nat Commun.* 2019; 10:5472.  
<https://doi.org/10.1038/s41467-019-13460-3>  
PMID:31784532
36. Zhang C, Zhang J, Xu FP, Wang YG, Xie Z, Su J, Dong S, Nie Q, Shao Y, Zhou Q, Yang JJ, Yang XN, Zhang XC, et al. Genomic landscape and immune microenvironment features of preinvasive and early invasive lung adenocarcinoma. *J Thorac Oncol.* 2019; 14:1912–23.  
<https://doi.org/10.1016/j.jtho.2019.07.031>  
PMID:31446140
37. Zhang M, Zhu K, Pu H, Wang Z, Zhao H, Zhang J, Wang Y. An immune-related signature predicts survival in patients with lung adenocarcinoma. *Front Oncol.* 2019; 9:1314.  
<https://doi.org/10.3389/fonc.2019.01314>  
PMID:31921619
38. Ahn MJ, Sun JM, Lee SH, Ahn JS, Park K. EGFR TKI combination with immunotherapy in non-small cell lung cancer. *Expert Opin Drug Saf.* 2017; 16:465–69.  
<https://doi.org/10.1080/14740338.2017.1300656>  
PMID:28271729
39. Sah NK, Khan Z, Khan GJ, Bisen PS. Structural, functional and therapeutic biology of survivin. *Cancer Lett.* 2006; 244:164–71.  
<https://doi.org/10.1016/j.canlet.2006.03.007>  
PMID:16621243
40. Butkiewicz D, Krześniak M, Drosik A, Giglok M, Gdowicz-Kłosok A, Kosarewicz A, Rusin M, Masłyk B, Gawkowska-Suwińska M, Suwiński R. The VEGFR2, COX-2 and MMP-2 polymorphisms are associated with clinical outcome of patients with inoperable non-small cell lung cancer. *Int J Cancer.* 2015; 137:2332–42.  
<https://doi.org/10.1002/ijc.29605>  
PMID:25975224
41. Zhao S, Ren S, Jiang T, Zhu B, Li X, Zhao C, Jia Y, Shi J, Zhang L, Liu X, Qiao M, Chen X, Su C, et al. Low-dose apatinib optimizes tumor microenvironment and potentiates antitumor effect of PD-1/PD-L1 blockade in lung cancer. *Cancer Immunol Res.* 2019; 7:630–43.  
<https://doi.org/10.1158/2326-6066.CIR-17-0640>  
PMID:30755403
42. Cao J, Sun L, Aramsangtienchai P, Spiegelman NA, Zhang X, Huang W, Seto E, Lin H. HDAC11 regulates type I interferon signaling through defatty-acylation of SHMT2. *Proc Natl Acad Sci USA.* 2019; 116:5487–92.  
<https://doi.org/10.1073/pnas.1815365116>  
PMID:30819897
43. Kayser S, Levis MJ, Schlenk RF. Midostaurin treatment in FLT3-mutated acute myeloid leukemia and systemic mastocytosis. *Expert Rev Clin Pharmacol.* 2017; 10:1177–89.  
<https://doi.org/10.1080/17512433.2017.1387051>  
PMID:28960095
44. Fabbro D, Ruetz S, Bodis S, Pruschy M, Csermak K, Man A, Campochiaro P, Wood J, O'Reilly T, Meyer T. PKC412—a protein kinase inhibitor with a broad therapeutic potential. *Anticancer Drug Des.* 2000; 15:17–28.  
PMID:10888033
45. Bain J, Plater L, Elliott M, Shpiro N, Hastie CJ, McLauchlan H, Klevernic I, Arthur JS, Alessi DR, Cohen P. The selectivity of protein kinase inhibitors: a further update. *Biochem J.* 2007; 408:297–315.  
<https://doi.org/10.1042/BJ20070797> PMID:17850214
46. Clark K, Plater L, Pegg M, Cohen P. Use of the pharmacological inhibitor BX795 to study the regulation and physiological roles of TBK1 and IkappaB kinase epsilon: a distinct upstream kinase mediates ser-172 phosphorylation and activation. *J Biol Chem.* 2009; 284:14136–46.  
<https://doi.org/10.1074/jbc.M109.000414>  
PMID:19307177
47. Su AR, Qiu M, Li YL, Xu WT, Song SW, Wang XH, Song HY, Zheng N, Wu ZW. BX-795 inhibits HSV-1 and HSV-2 replication by blocking the JNK/p38 pathways without interfering with PDK1 activity in host cells. *Acta Pharmacol Sin.* 2017; 38:402–14.  
<https://doi.org/10.1038/aps.2016.160> PMID:28112176
48. Choi EA, Choi YS, Lee EJ, Singh SR, Kim SC, Chang S. A pharmacogenomic analysis using L1000CDS<sup>2</sup> identifies BX-795 as a potential anticancer drug for primary pancreatic ductal adenocarcinoma cells. *Cancer Lett.* 2019; 465:82–93.  
<https://doi.org/10.1016/j.canlet.2019.08.002>  
PMID:31404615
49. Chen W, Luo K, Ke Z, Kuai B, He S, Jiang W, Huang W, Cai Z. TBK1 promote bladder cancer cell proliferation and migration via Akt signaling. *J Cancer.* 2017; 8:1892–99.  
<https://doi.org/10.7150/jca.17638> PMID:28819387
50. Fletcher GC, Brokx RD, Denny TA, Hembrough TA, Plum SM, Fogler WE, Sidor CF, Bray MR. ENMD-2076 is an orally active kinase inhibitor with antiangiogenic and antiproliferative mechanisms of action. *Mol Cancer Ther.* 2011; 10:126–37.  
<https://doi.org/10.1158/1535-7163.MCT-10-0574>  
PMID:21177375
51. Diamond JR, Eckhardt SG, Tan AC, Newton TP, Selby HM, Brunkow KL, Kachaeva MI, Varella-Garcia M, Pitts TM, Bray MR, Fletcher GC, Tentler JJ. Predictive biomarkers of sensitivity to the aurora and angiogenic kinase inhibitor ENMD-2076 in preclinical breast cancer models. *Clin Cancer Res.* 2013; 19:291–303.

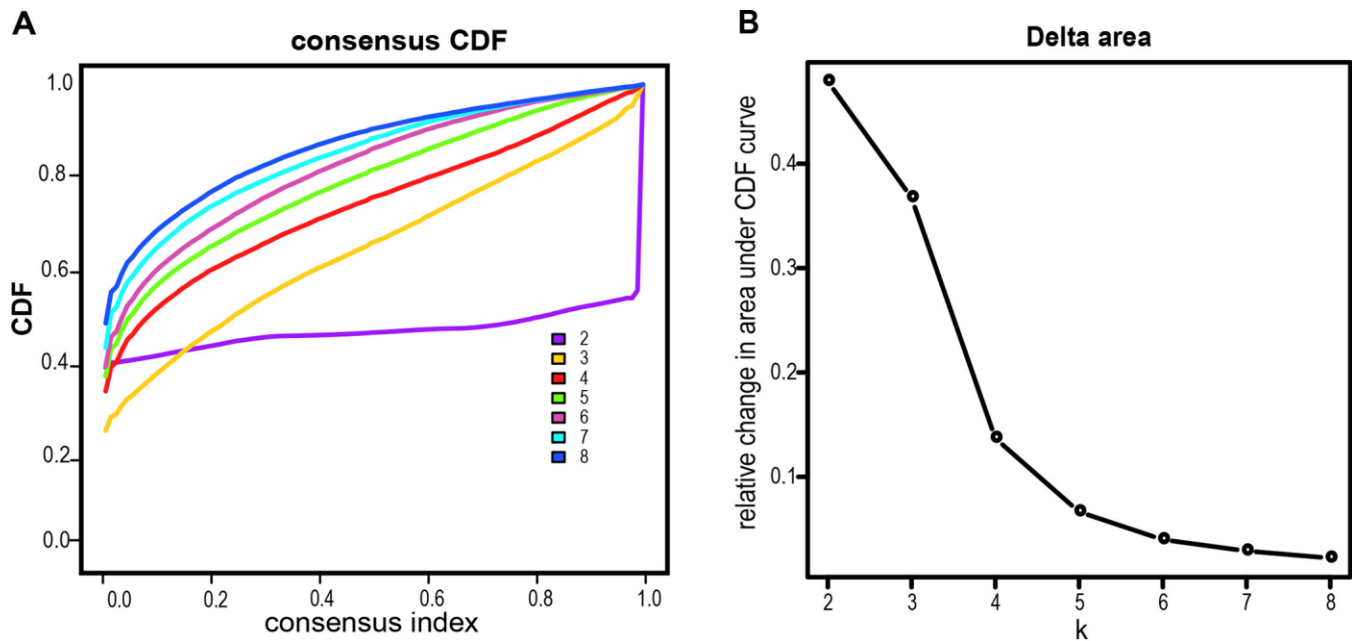


- <https://doi.org/10.1158/1078-0432.CCR-12-1611>  
PMID: [23136197](#)
52. Wang X, Sinn AL, Pollok K, Sandusky G, Zhang S, Chen L, Liang J, Crean CD, Suvannasankha A, Abonour R, Sidor C, Bray MR, Farag SS. Preclinical activity of a novel multiple tyrosine kinase and aurora kinase inhibitor, ENMD-2076, against multiple myeloma. *Br J Haematol*. 2010; 150:313–25.  
<https://doi.org/10.1111/j.1365-2141.2010.08248.x>  
PMID: [20560971](#)
  53. Capasso A, Pitts TM, Klauck PJ, Bagby SM, Westbrook L, Kaplan J, Soleimani M, Spreafico A, Tentler JJ, Diamond JR, Arcaroli JJ, Messersmith WA, Eckhardt SG, Leong S. Dual compartmental targeting of cell cycle and angiogenic kinases in colorectal cancer models. *Anticancer Drugs*. 2018; 29:827–38.  
<https://doi.org/10.1097/CAD.0000000000000673>  
PMID: [30048249](#)
  54. Dogan Turacli I, Demirtas Korkmaz F, Candar T, Ekmekci A. Flavopiridol's effects on metastasis in KRAS mutant lung adenocarcinoma cells. *J Cell Biochem*. 2019; 120:5628–35.  
<https://doi.org/10.1002/jcb.27846> PMID: [30317654](#)
  55. Tabernero J, Dirix L, Schöffski P, Cervantes A, Lopez-Martin JA, Capdevila J, van Beijsterveldt L, Platero S, Hall B, Yuan Z, Knoblauch R, Zhuang SH. A phase I first-in-human pharmacokinetic and pharmacodynamic study of serdemetan in patients with advanced solid tumors. *Clin Cancer Res*. 2011; 17:6313–21.  
<https://doi.org/10.1158/1078-0432.CCR-11-1101>  
PMID: [21831953](#)
  56. Wei SC, Duffy CR, Allison JP. Fundamental mechanisms of immune checkpoint blockade therapy. *Cancer Discov*. 2018; 8:1069–86.  
<https://doi.org/10.1158/2159-8290.CD-18-0367>  
PMID: [30115704](#)
  57. Liu J, Lichtenberg T, Hoadley KA, Poisson LM, Lazar AJ, Cherniack AD, Kovatich AJ, Benz CC, Levine DA, Lee AV, Omberg L, Wolf DM, Shriver CD, et al, and Cancer Genome Atlas Research Network. An integrated TCGA pan-cancer clinical data resource to drive high-quality survival outcome analytics. *Cell*. 2018; 173:400–16.e11.  
<https://doi.org/10.1016/j.cell.2018.02.052>  
PMID: [29625055](#)
  58. Shedden K, Taylor JM, Enkemann SA, Tsao MS, Yeatman TJ, Gerald WL, Eschrich S, Jurisica I, Giordano TJ, Misek DE, Chang AC, Zhu CQ, Strumpf D, et al, and Director's Challenge Consortium for the Molecular Classification of Lung Adenocarcinoma. Gene expression-based survival prediction in lung adenocarcinoma: a multi-site, blinded validation study. *Nat Med*. 2008; 14:822–27.  
<https://doi.org/10.1038/nm.1790>  
PMID: [18641660](#)
  59. Wilkerson MD, Hayes DN. ConsensusClusterPlus: a class discovery tool with confidence assessments and item tracking. *Bioinformatics*. 2010; 26:1572–73.  
<https://doi.org/10.1093/bioinformatics/btq170>  
PMID: [20427518](#)
  60. Yoshihara K, Shahmoradgoli M, Martínez E, Vegesna R, Kim H, Torres-García W, Treviño V, Shen H, Laird PW, Levine DA, Carter SL, Getz G, Stemke-Hale K, et al. Inferring tumour purity and stromal and immune cell admixture from expression data. *Nat Commun*. 2013; 4:2612.  
<https://doi.org/10.1038/ncomms3612>  
PMID: [24113773](#)
  61. Becht E, Giraldo NA, Lacroix L, Buttard B, Elarouci N, Petitprez F, Selves J, Laurent-Puig P, Sautès-Fridman C, Fridman WH, de Reyniès A. Estimating the population abundance of tissue-infiltrating immune and stromal cell populations using gene expression. *Genome Biol*. 2016; 17:218.  
<https://doi.org/10.1186/s13059-016-1070-5>  
PMID: [27765066](#)
  62. Cibulskis K, Lawrence MS, Carter SL, Sivachenko A, Jaffe D, Sougnez C, Gabriel S, Meyerson M, Lander ES, Getz G. Sensitive detection of somatic point mutations in impure and heterogeneous cancer samples. *Nat Biotechnol*. 2013; 31:213–19.  
<https://doi.org/10.1038/nbt.2514> PMID: [23396013](#)
  63. Wang K, Li M, Hakonarson H. ANNOVAR: functional annotation of genetic variants from high-throughput sequencing data. *Nucleic Acids Res*. 2010; 38:e164.  
<https://doi.org/10.1093/nar/gkq603> PMID: [20601685](#)
  64. Kandoth C, McLellan MD, Vandin F, Ye K, Niu B, Lu C, Xie M, Zhang Q, McMichael JF, Wyczalkowski MA, Leiserson MD, Miller CA, Welch JS, et al. Mutational landscape and significance across 12 major cancer types. *Nature*. 2013; 502:333–39.  
<https://doi.org/10.1038/nature12634>  
PMID: [24132290](#)
  65. Yu G, Wang LG, Han Y, He QY. clusterProfiler: an R package for comparing biological themes among gene clusters. *OMICS*. 2012; 16:284–87.  
<https://doi.org/10.1089/omi.2011.0118>  
PMID: [22455463](#)
  66. Subramanian A, Narayan R, Corsello SM, Peck DD, Natoli TE, Lu X, Gould J, Davis JF, Tubelli AA, Asiedu JK, Lahr DL, Hirschman JE, Liu Z, et al. A next generation connectivity map: L1000 platform and the first 1,000,000 profiles. *Cell*. 2017; 171:1437–52.e17.  
<https://doi.org/10.1016/j.cell.2017.10.049>  
PMID: [29195078](#)

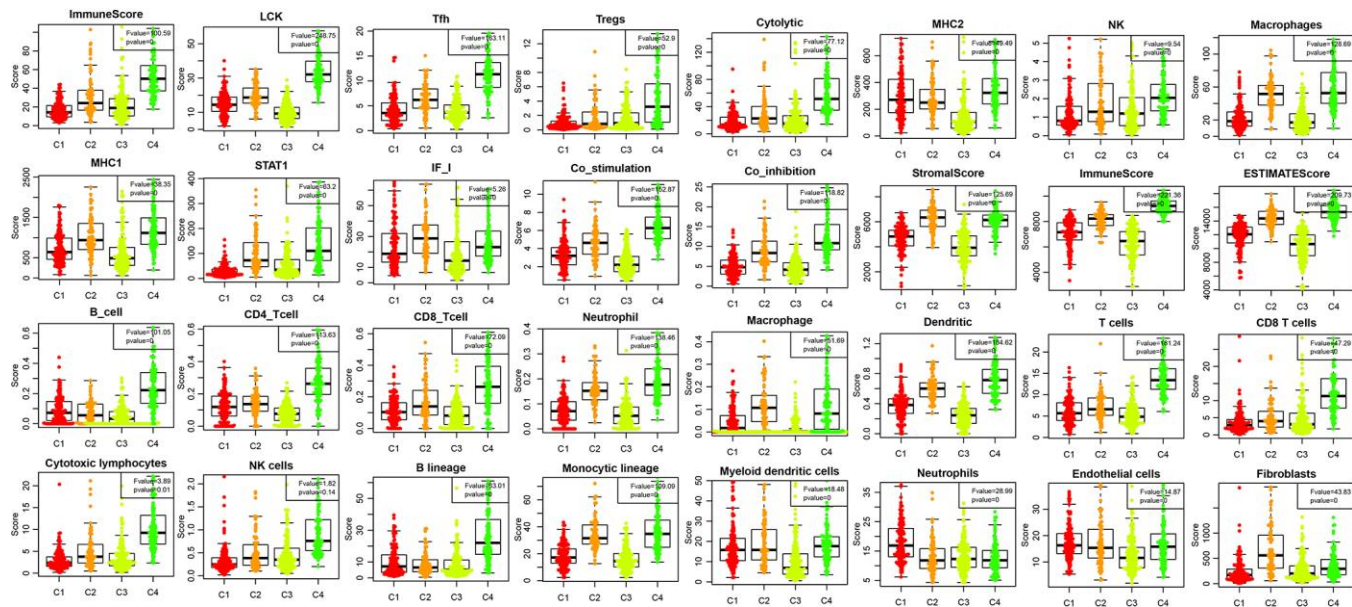
67. Lamb J, Crawford ED, Peck D, Modell JW, Blat IC, Wrobel MJ, Lerner J, Brunet JP, Subramanian A, Ross KN, Reich M, Hieronymus H, Wei G, et al. The connectivity map: using gene-expression signatures to connect small molecules, genes, and disease. *Science*. 2006; 313:1929–35.  
<https://doi.org/10.1126/science.1132939>  
PMID:[17008526](https://pubmed.ncbi.nlm.nih.gov/17008526/)
68. Morris GM, Huey R, Olson AJ. Using AutoDock for ligand-receptor docking. *Curr Protoc Bioinformatics*. 2008; 24:8.14.1–40.  
<https://doi.org/10.1002/0471250953.bi0814s24>  
PMID:[19085980](https://pubmed.ncbi.nlm.nih.gov/19085980/)
69. Schwede T, Kopp J, Guex N, Peitsch MC. SWISS-MODEL: an automated protein homology-modeling server. *Nucleic Acids Res*. 2003; 31:3381–85.  
<https://doi.org/10.1093/nar/gkg520>  
PMID:[12824332](https://pubmed.ncbi.nlm.nih.gov/12824332/)
70. Ramachandran GN, Ramakrishnan C, Sasisekharan V. Stereochemistry of polypeptide chain configurations. *J Mol Biol*. 1963; 7:95–99.  
[https://doi.org/10.1016/s0022-2836\(63\)80023-6](https://doi.org/10.1016/s0022-2836(63)80023-6)  
PMID:[13990617](https://pubmed.ncbi.nlm.nih.gov/13990617/)
71. Wang Y, Bryant SH, Cheng T, Wang J, Gindulyte A, Shoemaker BA, Thiessen PA, He S, Zhang J. PubChem BioAssay: 2017 update. *Nucleic Acids Res*. 2017; 45:D955–63.  
<https://doi.org/10.1093/nar/gkw1118>  
PMID:[27899599](https://pubmed.ncbi.nlm.nih.gov/27899599/)

SUPPLEMENTARY MATERIALS

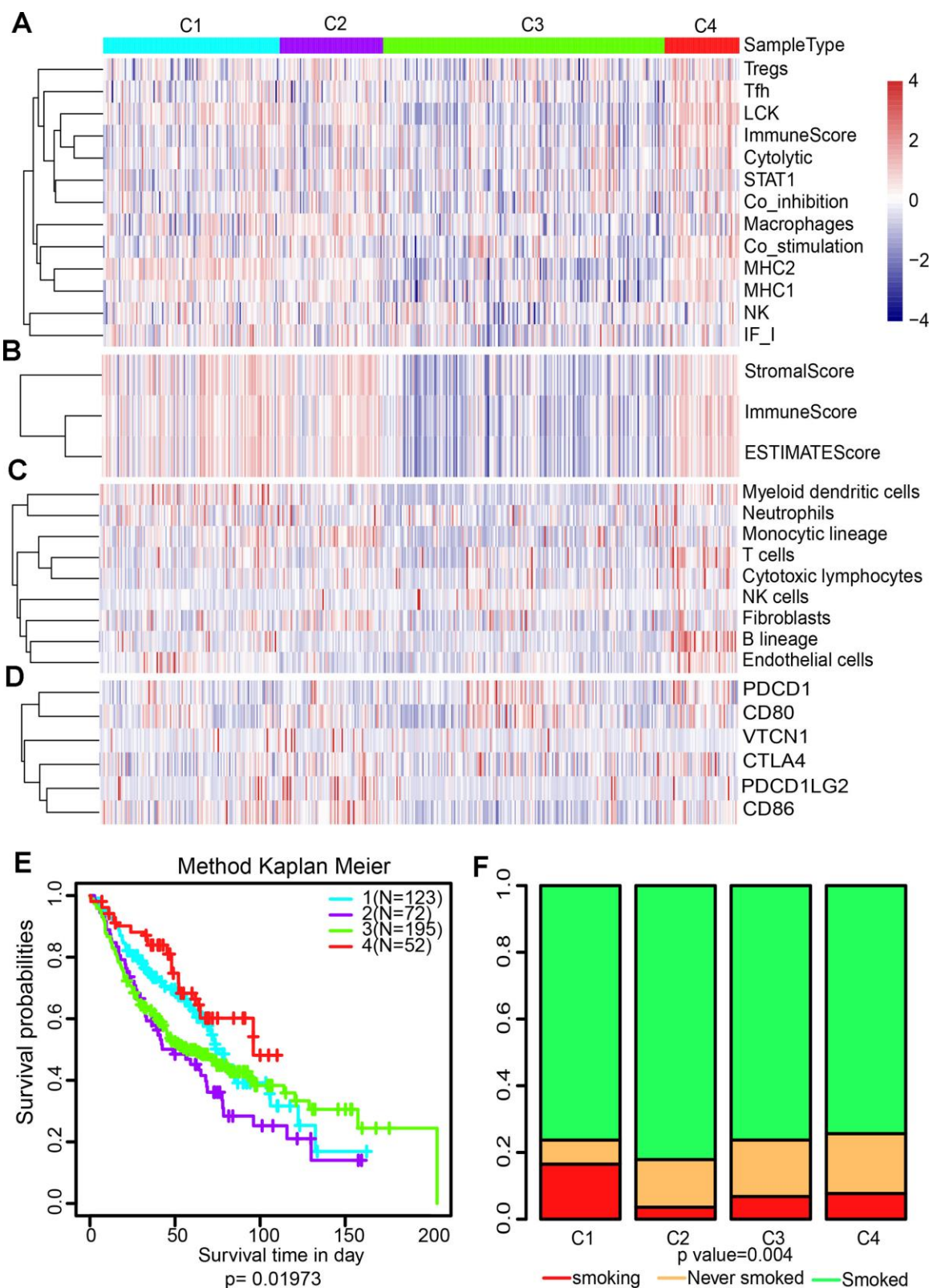
Supplementary Figures



**Supplementary Figure 1. The cumulative distribution function (CDF) curves. (A)** The CDF curves in unsupervised consensus cluster analysis. The cluster numbers ( $k = 2, 3, 4, 5, 6, 7, 8$ ) and their corresponding consensus scores. **(B)** Relative changes of the area under CDF curves. The number of clusters are shown on the x-axis. The y-axis indicates the proportion of areas under CDF curve.

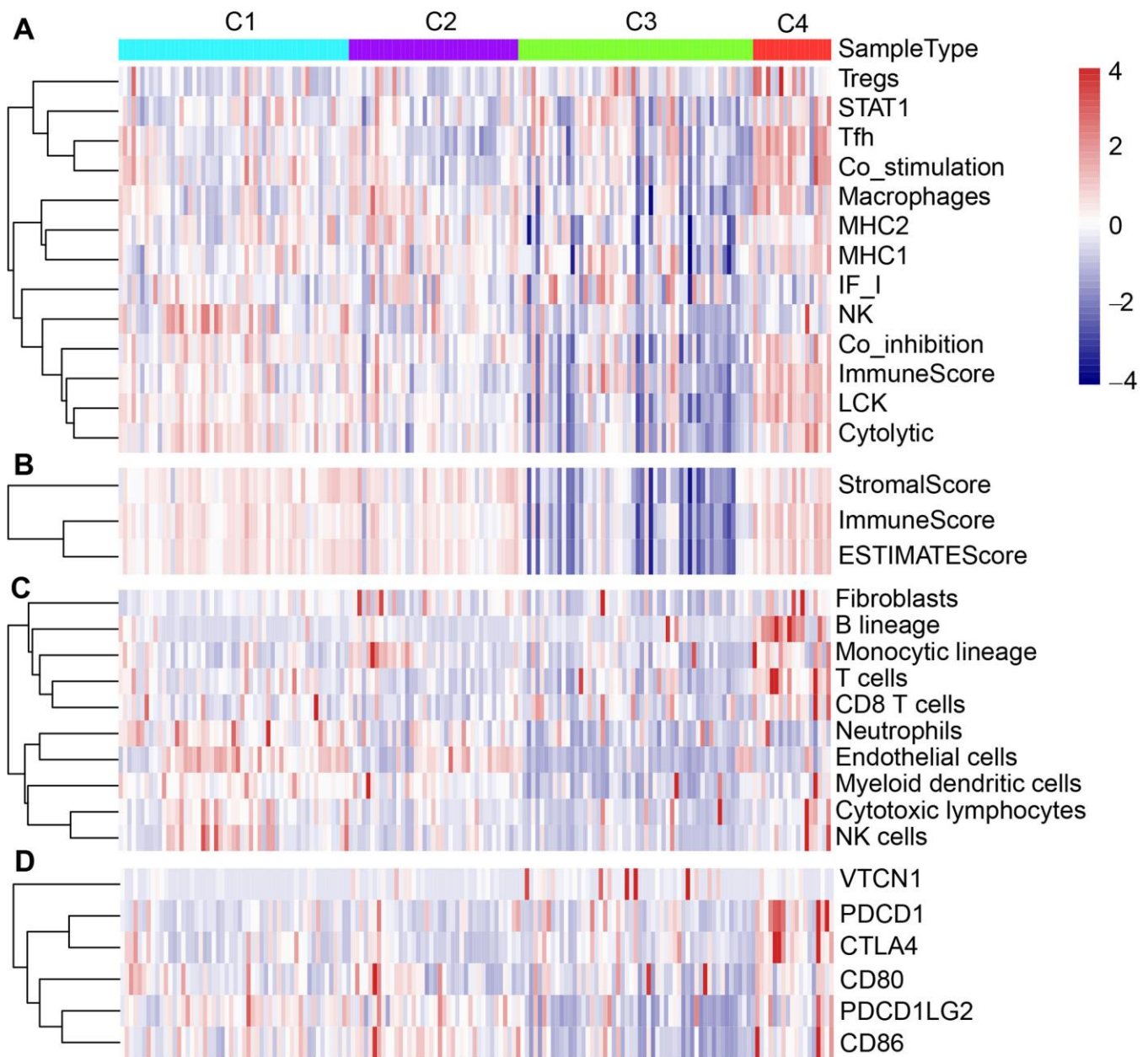


**Supplementary Figure 2. Boxplots showing the gene expression scores of immune profiles of the four subtypes.** Boxplots show 5%, 25%, 50%, 75%, and 95%, respectively.



**Supplementary Figure 3. Validation of the four immune-associated subtypes in the GEO LUAD cohort.** (A) The expression levels of 13 immune metagenes. (B) The expression levels of genes included in the ESTIMATE algorithm for determination of stromal and immune gene signatures. (C) The expression scores of genes related to 10 groups of immune cells. (D) The expression scores of checkpoint molecules among the four subtypes in the GEO LUAD cohort. (E) Kaplan-Meier curves showing the overall survival (OS) of the four subtypes (log-rank test). (F) Distribution of smoking status among the four subtypes.

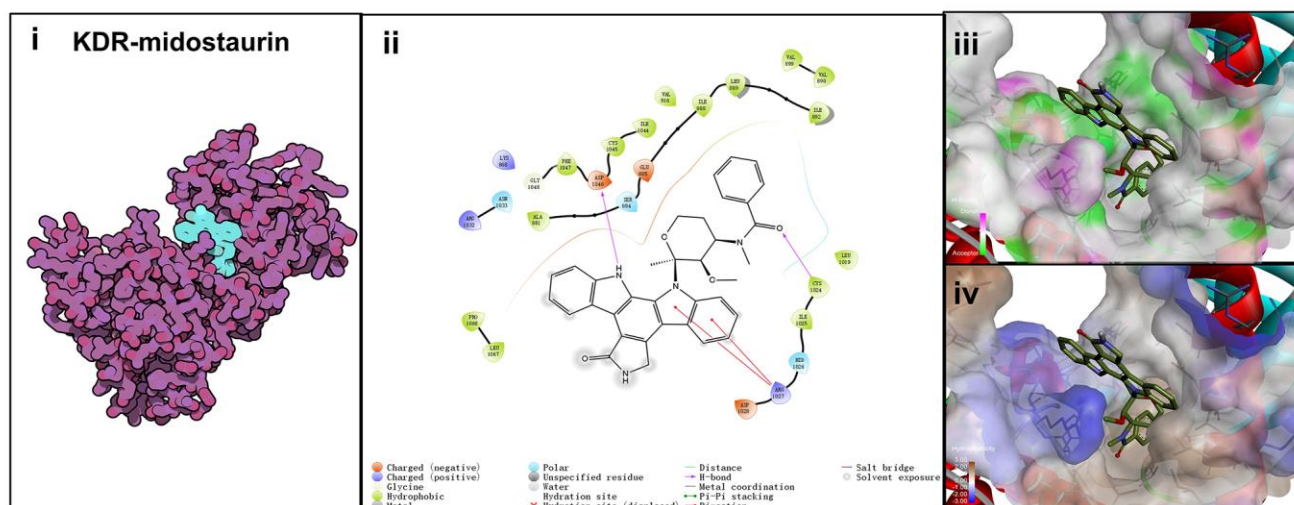




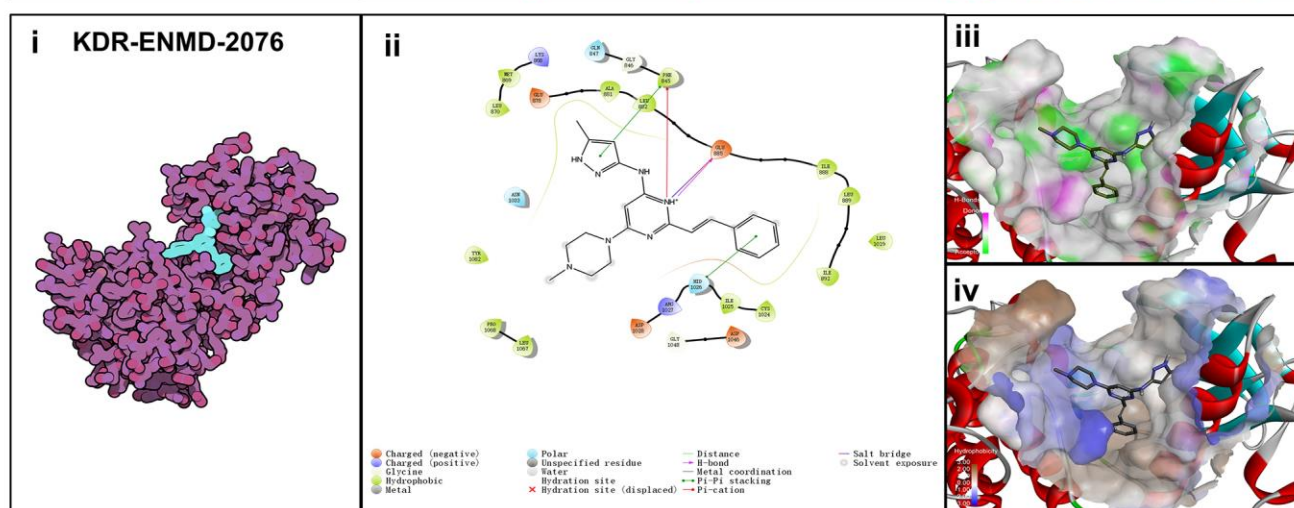
**Supplementary Figure 4. Validation of the four immune-associated subtypes in the GSE40419 dataset.** (A) The expression levels of 13 immune metagenes. (B) The expression levels of genes included in the ESTIMATE algorithm for determination of stromal and immune gene signatures. (C) The expression scores of genes related to 10 groups of immune cells. (D) The expression scores of checkpoint molecules among the four subtypes.



**A**



**B**



**Supplementary Figure 5. Binding mode of screened drugs to KDR protein by molecular docking.** (A) Binding mode of midostaurin to KDR. (B) Binding mode of ENMD-2076 to KDR. (i), Cartoon representation, overlay of the crystal structures of small molecule compounds and their targets were illustrated by Molecule of the Month feature. (ii), 2D interactions of compounds and their targets. (iii, iv) Three-dimensional structures of the binding pockets were showed by PyMOL software. (iii), Coloring is from carmine (for strong H-bonds) to green (for poor H-bonds). (iv), Coloring is from magenta (for strong hydrophobic regions) to blue (for poor hydrophobic regions).

## Supplementary Tables

Please browse Full Text version to see the data of Supplementary Tables 2 to 4.

**Supplementary Table 1. The clustering significance between the four subtypes.**

<b>P-values</b>	<b>C1</b>	<b>C2</b>	<b>C3</b>	<b>C4</b>
C1	1	0.140006283	0.062373838	0.00755249
C2	0.140006283	1	0.19246147	0.123329892
C3	0.062373838	0.19246147	1	0.000127256
C4	0.00755249	0.123329892	0.000127256	1

**Supplementary Table 2. Gens in blue, turquoise, brown and grey modules.**

**Supplementary Table 3. CPs with enrichment scores of less than -80 in A549 and HCC515 cell lines.**

**Supplementary Table 4. Knockdown genes with scores lower than -80 and overexpressed genes with scores higher than 80 in A549 and HCC515 cell lines.**

# Mimetics of extra virgin olive oil phenols with anti-cancer stem cell activity

Elisabet Cuyàs<sup>1,2</sup>, Juan Gumuzio<sup>3</sup>, Jesús Lozano-Sánchez<sup>4,5</sup>, Antonio Segura-Carretero<sup>4,6</sup>, Sara Verdura<sup>1,2</sup>, Joaquim Bosch-Barrera<sup>2,7,8</sup>, Begoña Martín-Castillo<sup>2,9</sup>, Alfons Nonell-Canals<sup>10,14</sup>, Amadeu Llebaria<sup>11</sup>, Silvia Cabello<sup>12</sup>, Carme Serra<sup>11,12</sup>, Melchor Sanchez-Martinez<sup>10,13</sup>, Ángel G. Martín<sup>3</sup>, Javier A. Menendez<sup>1,2</sup>

<sup>1</sup>Program Against Cancer Therapeutic Resistance (ProCURE), Metabolism and Cancer Group, Catalan Institute of Oncology, Girona, Spain

<sup>2</sup>Girona Biomedical Research Institute (IDIBGI), Girona, Spain

<sup>3</sup>StemTek Therapeutics, Bilbao, Spain

<sup>4</sup>Research and Development of Functional Food Centre (CIDAF), Granada, Spain

<sup>5</sup>Department of Food Science and Nutrition, University of Granada, Granada, Spain

<sup>6</sup>Department of Analytical Chemistry, University of Granada, Granada, Spain

<sup>7</sup>Medical Oncology, Catalan Institute of Oncology, Girona, Spain

<sup>8</sup>Department of Medical Sciences, Medical School University of Girona, Girona, Spain

<sup>9</sup>Unit of Clinical Research, Catalan Institute of Oncology, Girona, Spain

<sup>10</sup>Mind the Byte, Barcelona, Spain

<sup>11</sup>MCS, Laboratory of Medicinal Chemistry and Synthesis, Institute of Advanced Chemistry of Catalonia (IQAC-CSIC), Barcelona, Spain

<sup>12</sup>SIMChem, Synthesis of High Added Value Molecules, Institute of Advanced Chemistry of Catalonia (IQAC-CSIC), Barcelona, Spain

<sup>13</sup>Molomics, Barcelona Science Park, Barcelona, Spain

<sup>14</sup>Current address: The Patients Resource, Barcelona, Spain

**Correspondence to:** Javier A. Menendez; email: [jmenendez@idibgi.org](mailto:jmenendez@idibgi.org)

**Keywords:** olive oil, mTOR, DNMT, metabolism, epigenetics

**Received:** February 15, 2020

**Accepted:** September 24, 2020

**Published:** November 9, 2020

**Copyright:** © 2020 Cuyàs et al. This is an open access article distributed under the terms of the [Creative Commons Attribution License](https://creativecommons.org/licenses/by/3.0/) (CC BY 3.0), which permits unrestricted use, distribution, and reproduction in any medium, provided the original author and source are credited.

## ABSTRACT

The extra virgin olive oil (EVOO) dihydroxy-phenol oleacein is a natural inhibitor of multiple metabolic and epigenetic enzymes capable of suppressing the functional traits of cancer stem cells (CSC). Here, we used a natural product-inspired drug discovery approach to identify new compounds that phenotypically mimic the anti-CSC activity of oleacein. We coupled 3D quantitative structure-activity relationship-based virtual profiling with phenotypic analysis using 3D tumorsphere formation as a gold standard for assessing the presence of CSC. Among the top 20 computationally-predicted oleacein mimetics, four fulfilled the phenotypic endpoint of specifically suppressing the tumorsphere-initiating capacity of CSC, in the absence of significant cytotoxicity against differentiated cancer cells growing in 2D cultures in the same low micromolar concentration range. Of these, 3,4-dihydrophenetyl butyrate –a lipophilic ester conjugate of the hydroxytyrosol moiety of oleacein– and (*E*)-*N*-allyl-2-((5-nitrofur-2-yl)methylene)hydrazinecarbothioamide –an inhibitor of *Trypanosoma cruzi* triosephosphate isomerase– were also highly effective at significantly reducing the proportion of aldehyde dehydrogenase (ALDH)-positive CSC-like proliferating cells. Preservation of the mTOR/DNMT binding mode of oleacein was dispensable for suppression of the ALDH<sup>+</sup>-CSC functional phenotype in hydroxytyrosol-unrelated

**mimetics. The anti-CSC chemistry of complex EVOO phenols such as oleacein can be phenocopied through the use of mimetics capturing its physico-chemical properties.**

## INTRODUCTION

Extra virgin olive oil (EVOO) is a unique functional food with a major contribution to the health-promoting effects of the so-called Mediterranean diet. EVOO contains a group of complex phenol-conjugated compounds named oleosidic secoiridoids or oleosides that exert nutritional and beneficial effects on major aging-driven diseases including cancer [1–10]. Using a holistic approach for phenotypic drug discovery coupled with mechanism-of-action functional profiling and target deconvolution, we recently identified the dihydroxy-phenol oleacein (the dialdehydic form of decarboxymethyl elenolic acid linked to hydroxytyrosol) [11–17] as a metabolo-epigenetic inhibitor of the mammalian target of rapamycin (mTOR) kinase and DNA methyltransferases (DNMTs). Oleacein was found to specifically and potently suppressing the functional traits of tumor-initiating cancer stem cells (CSC) in genetically diverse types of cancer cell populations [18].

The anti-CSC effects of oleacein are most likely related to its chemical structure, largely due to the presence of two hydroxyl groups in the hydroxytyrosol moiety [9, 19–21]. Therefore, one could envision that its scaffold might be used as a chemical prototype to facilitate selection and advancement of new anti-CSC hits via cell-based phenotypic screenings. However, a recent delineation of the high-level functions of oleacein in terms of biomolecular interactions, signaling pathways, and protein-protein interaction networks revealed that the so-called oleacein target landscape likely involved more than 700 proteins rather than solely mTOR and DNMTs [22]. Thus, although the ability of oleacein to operate as a multi-faceted regulator of numerous metabolic processes and chromatin-modifying enzymatic activities might open new horizons for CSC-targeted therapy based on the molecular bridge that connects metabolism and epigenetics with the aberrant state of stemness in cancer tissues [23–28], a biomimicry design process of oleacein mimetics remains a highly challenging task.

Here, we used a natural-product-inspired drug discovery approach to identify new small molecules capable of phenotypically mimicking the anti-CSC actions of oleacein. Using the structure of oleacein as a “seed”, we coupled 3D quantitative structure-activity relationship (3D-QSAR)-based virtual profiling (VP) with laboratory-based phenotypic testing using tumorsphere-formation potential as a gold standard for evaluating the

presence of CSC (Figure 1). We provide evidence that oleacein can be phenocopied through the use of mimetics with anti-CSC activity, which might guide the design of synthetically tractable small molecules capable of phenotypically imitating the anti-CSC chemistry of complex EVOO phenolics.

## RESULTS

### Computer-assisted discovery of oleacein mimetics

When a 2D similarity, ligand-based VP program was executed over the ChEMBL(v19) database using the Tanimoto coefficient and 2D (Morgan/circular) fingerprints, only the closely related secoiridoid molecule oleocanthal (ChEMBL2172394) was identified. The execution of a comparative molecular similarity indices analysis (CoMSIA)-based 3D VP program, however, identified several compounds with physico-chemical similarity scores greater than 0.75 (Figure 1). Taking advantage of the previously described binding modes of oleacein to mTOR and DNMT [18], we ran rigid-docking calculations to characterize the binding modes of the top 20 oleacein mimetics (Supplementary Figure 1), both at the crystallographic sites and at additional cavities occurring within the whole protein structures of mTOR and DNMT (Supplementary Tables 1–3). Table 1 summarizes the computationally-predicted oleacein mimetics ranked according to reweighted energies based on short molecular dynamics (MD) simulations followed by molecular mechanics with generalized Born and surface area solvation (MM/GBSA) calculations, for both the crystallographic and the best mTOR/DNMT cavities for each of the selected oleacein mimetics (Supplementary Tables 4 and 5).

### Binding modes of oleacein mimetics to mTOR and DNMT

The binding mode of oleacein to mTOR was predicted to share key amino acid residues with the binding modes of second-generation ATP-competitive TORKinhibitors and, consequently, partially mimicked the binding behavior of PP242 and Torin 2 to the ATP-binding catalytic pocket [18]. But, the presence of more aromatic rings in the oleacein molecule resulted in a slightly different binding strength from that of PP242 and Torin 2. Similarly, the presence of aromatic rings notably influenced the binding of the selected oleacein mimetics to mTOR (Figure 2). In fact, we predicted three different binding modes, one of them involving 5



oleacein mimetics that apparently shared the originally described binding mode of parental oleacein; and another two models encompassing 13 compounds and 2 compounds showing a binding mode closely resembling that of TORKinhibs (Figure 2). Rigid docking calculations originally predicted that  $\pi$ - $\pi$  stacking would occur between the aromatic ring of oleacein and the Trp2239 residue (or Tyr2225 upon conformational changes of either oleacein or the mTOR catalytic pocket itself) in the catalytic site of mTOR. MD simulations confirmed the main occurrence of  $\pi$ - $\pi$  stacking with Trp2239 (and a more fluctuating interaction with Tyr2225), as well as a significant number of additional residues providing key electrostatic interactions [18]. In the case of oleacein mimetics, it was evident that Trp2239, Tyr2225, and Phe2358 played a central role in

the stabilization of their respective complexes with mTOR (Supplementary Table 6).

The binding mode of oleacein to DNMT was predicted to closely resemble that of DNMT inhibitors such as 5-azacytidine, SGI-110, and curcumin [18]. In the case of oleacein mimetics, we were able to predict two different binding modes (Figure 3): one of them shared the oleacein pattern of spatial orientation and included 17 compounds and another one involved only 3 molecules (Figure 3). Rigid docking calculations and MD simulations predicted that the main residues involved in the stabilization of the oleacein-DNMT complex were Ser1446, Pro1125, Asp1143, Phe1145, Gly1150, Leu1151, Asn1158, Val1580, and Gly1223, along with a significant number of additional residues providing key electrostatic interactions. In the case of oleacein mimetics, Phe1145, Trp1170, Pro1224, and Pro1225 were predicted as the main catalytic residues (Supplementary Table 7).

### Oleacein mimetics specifically suppress CSC-driven mammosphere formation

To explicitly test the oleacein mimetics on CSC, we measured their effect on *in vitro* tumorsphere formation in low-density non-adherent serum-free medium supplemented with growth factors [29–35], considered one of the gold standards for evaluating CSC self-renewal activity. As a source of CSC, we used the CSC-enriched triple-negative breast cancer model MDA-MB-436, which can form smooth and round tumorspheres (mammospheres) in suspension culture [33]. The Cell2Sphere™ assay [18, 36, 37] was used to evaluate the differential ability of oleacein mimetics to specifically suppress the ability of CSC to survive and proliferate as floating 3D microtumors without promoting nonspecific, cytotoxic effects on the same cells grown in 2D adherent, differentiating conditions (Figure 4).

Using the focal adhesion kinase inhibitor VS-6063 (defactinib) [38–40] and the lysine-specific demethylase KDM1A inhibitor ORY-1001 (iadademstat) [37, 41] as mechanistically distinct anti-CSC compounds and selecting a 10  $\mu$ mol/L cut-off for 2D cytotoxicity (i.e., lower than the original IC<sub>50</sub> value of oleacein [ $18 \pm 5$   $\mu$ mol/L] against CSC-driven mammosphere formation), 4 out of the 14 oleacein mimetics tested specifically suppressed mammosphere formation, namely CHEMBL1621113 (N'-[4-nitro-2-(trifluoromethyl)phenyl]propane-1,3-diamine), CHEMBL1632504 ((E)-N-allyl-2-((5-nitrofuran-2-yl)methylene)hydrazinecarbothioamide), CHEMBL126593 (N-(4-nitrobenzyl)ethanesulfonamide), and CHEMBL1950046 (3,4-dihydroxyphenethyl butyrate), while not exerting significant

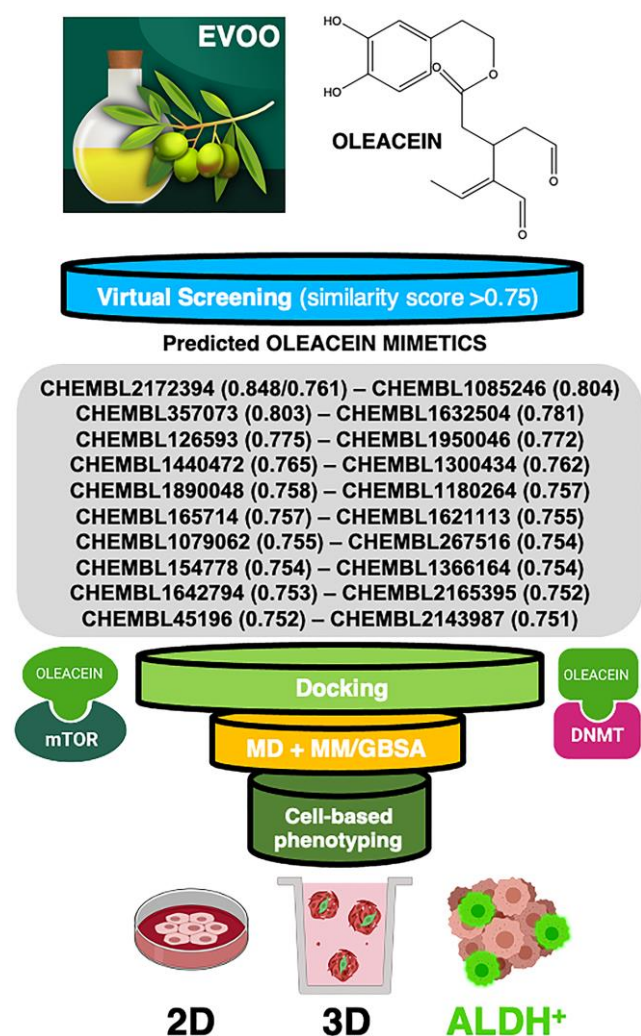


**Figure 1. Computer-assisted discovery of oleacein biomimetics with anti-CSC activity.** Schematic illustration of the computational framework coupled to laboratory-based phenotypic testing. The values in parentheses are similarity scores calculated with respect to parental oleacein.



**Table 1. MM/GBSA-based binding energy rescoring calculations over MD simulations of computationally-predicted oleacein mimetics.**

Candidates ranked by MM/GBSA energy 4JT6 (mTOR)	MM/GBSA energy Crystallographic cavity / Best cavity	Candidates ranked by MM/GBSA energy 4WXX (DNMT)	MM/GBSA energy Crystallographic cavity / Best cavity
oleacein	-26.8226 / -36.9331	oleacein	-30.567 / -36.5163
CHEMBL1300434	-38.7014 / -27.361	CHEMBL1632504	-38.2609 / -36.6319
CHEMBL2143987	-32.4070 / -40.3344	CHEMBL2143987	-36.4821 / -43.6863
CHEMBL1545778	-30.5493 / -25.0387	CHEMBL2165395	-33.4134 / -25.8227
CHEMBL126593	-29.2106 / -26.6329	CHEMBL1300434	-33.3421 / -33.9773
CHEMBL1085246	-27.4436 / -19.6725	CHEMBL267516	-32.8788 / -28.1508
CHEMBL267516	-27.3710 / -44.6454	CHEMBL1180264	-31.7196 / -32.3981
CHEMBL45196	-27.2624 / -17.1961	CHEMBL357073	-28.4676 / -27.0541
CHEMBL1632504	-25.7896 / -24.6272	CHEMBL1440472	-27.5899 / -29.3600
CHEMBL357073	-25.0102 / -33.5462	CHEMBL1621113	-26.6488 / -29.3269
CHEMBL1366164	-24.3303 / -17.8085	CHEMBL1890048	-26.0912 / -26.2952
CHEMBL1642794	-24.1435 / -19.439	CHEMBL126593	-25.7134 / -35.3592
CHEMBL1621113	-22.9663 / -21.0309	CHEMBL45196	-24.5175 / -32.1555
CHEMBL1950046	-20.2999 / -31.6794	CHEMBL1950046	-24.3167 / -21.7283
CHEMBL2165395	-19.8235 / -27.2639	CHEMBL1079062	-24.2025 / -24.4205
CHEMBL1890048	-19.6392 / -21.2089	CHEMBL1545778	-21.6215 / -22.9832
CHEMBL2172394	-18.4177 / -34.4392	CHEMBL1085246	-17.8140 / -21.8923
CHEMBL1180264	-18.2272 / -29.4140	CHEMBL1642794	-16.1264 / -20.6555
CHEMBL1079062	-17.4413 / -24.7585	CHEMBL1366164	-15.4957 / -19.6201
CHEMBL1440472	-16.6468 / -21.2853	CHEMBL165714	-12.1247 / -30.3770
CHEMBL165714	-16.1321 / -21.4634	CHEMBL2172394	-11.8887 / -31.0757

cytotoxic effects against differentiated cancer cells growing in 2D in the same low micromolar range (Figure 5). CHEMBL1085246 (*N*-(4-chloro-5-nitrothiazol-2-yl)hexanamide) exhibited anti-CSC activity due to unspecific cytotoxicity against CSC and non-CSC cells (Supplementary Figure 2).

#### Oleacein mimetics target ALDH<sup>+</sup> breast cancer stem cells

Oleacein selectively suppresses functional traits of CSC such as the expression of aldehyde dehydrogenase (ALDH) [18], a well-recognized marker of tumorigenic cell fractions enriched for proliferating, epithelial-like CSC capable of self-renewal [31, 32, 35, 42]. We next selected the 2 oleacein mimetics with the best CSC-targeted profile (i.e., anti-CSC activity at low micromolar range and lack of cytotoxic activity against differentiated cancer cells), namely CHEMBL1950046 (3,4-dihydroxyphenethyl butyrate; a.k.a. hydroxytyrosol butyrate) and CHEMBL1632504 ((*E*)-*N*-allyl-2-((5-nitrofuranyl)methylene)hydrazinecarbothioamide), to evaluate their capacity to target epithelial-like CSC cells with high levels of ALDH1 (ALDH1<sup>+</sup>). To do this, we used the Aldefluor<sup>®</sup> reagent, which quantifies ALDH activity by measuring the conversion of the ALDH substrate BODIPY aminoacetaldehyde to the fluorescent

product BODIPY aminoacetate (Figure 6A). Using HER2-overexpressing BT-474 cells as a breast cancer model naturally enriched with ALDH1<sup>+</sup> cells, we detected a significant decrease (up to 63% reduction) in the number of ALDH1<sup>+</sup> cells when BT-474 cells were treated with a non-cytotoxic concentration (10  $\mu$ mol/L) of CHEMBL1950046 (hydroxytyrosol butyrate). A more pronounced effect was seen with CHEMBL1632504 ((*E*)-*N*-allyl-2-((5-nitrofuranyl)methylene)hydrazinecarbothioamide), which significantly decreased the proportion of ALDH1<sup>+</sup> cells from 40 $\pm$ 2% in untreated BT-474 cells to levels as low as 2 $\pm$ 1% (96% reduction). To corroborate the ability of oleacein mimetics to target ALDH1<sup>+</sup> epithelial-like CSC irrespective of the mutational landscape of cancer cells, we employed triple-negative MDA-MB-436 cells as a second breast cancer model naturally enriched with ALDH1<sup>+</sup> cells. Treatment with hydroxytyrosol butyrate decreased the ALDH1<sup>+</sup> cell content of MDA-MB-436 by approximately 40%. Remarkably, the large population of ALDH1<sup>+</sup> cells in untreated MDA-MB-436 cultures (42 $\pm$ 8%) was drastically reduced by 93% (from 42 $\pm$ 8% to 3 $\pm$ 1%) in the presence of (*E*)-*N*-allyl-2-((5-nitrofuranyl)methylene)hydrazinecarbothioamide.

Preservation of the oleacein binding mode is required for a dual mTOR/DNMT inhibitory activity but not for

their anti-CSC behavior of oleacein mimetics. We finally evaluated whether the selected mimetics hydroxytyrosol butyrate and (*E*)-*N*-allyl-2-((5-nitrofur-2-yl)methylene)hydrazinecarbothioamide preserved the dual anti-mTOR/DNMT activity of the parental oleacein.

We first employed the FRET-based Z-LYTE™ Kinase Assay to test the ability of the selected oleacein mimetics to inhibit mTOR activity. Ten concentrations of hydroxytyrosol butyrate and (*E*)-*N*-allyl-2-((5-nitrofur-2-yl)methylene)hydrazinecarbothioamide spanning over five logarithmic decades were selected.

Figure 6B shows the mTOR activity rate as a function of oleacein mimetics concentration. Hydroxytyrosol butyrate inhibited mTOR activity with an IC<sub>50</sub> of ~39 μmol/L; (*E*)-*N*-allyl-2-((5-nitrofur-2-yl)methylene)hydrazinecarbothioamide was unable to decrease mTOR activity even at the maximum concentration tested.

We finally carried out a radioisotope-based methyltransferase profiling measuring the DNMT3A-catalyzed incorporation of S-adenosyl-L[methyl-<sup>3</sup>H]methionine (SAM[<sup>3</sup>H]) into DNA (DNA 5-[methyl-<sup>3</sup>H]-cytosine) in the absence or presence of oleacein

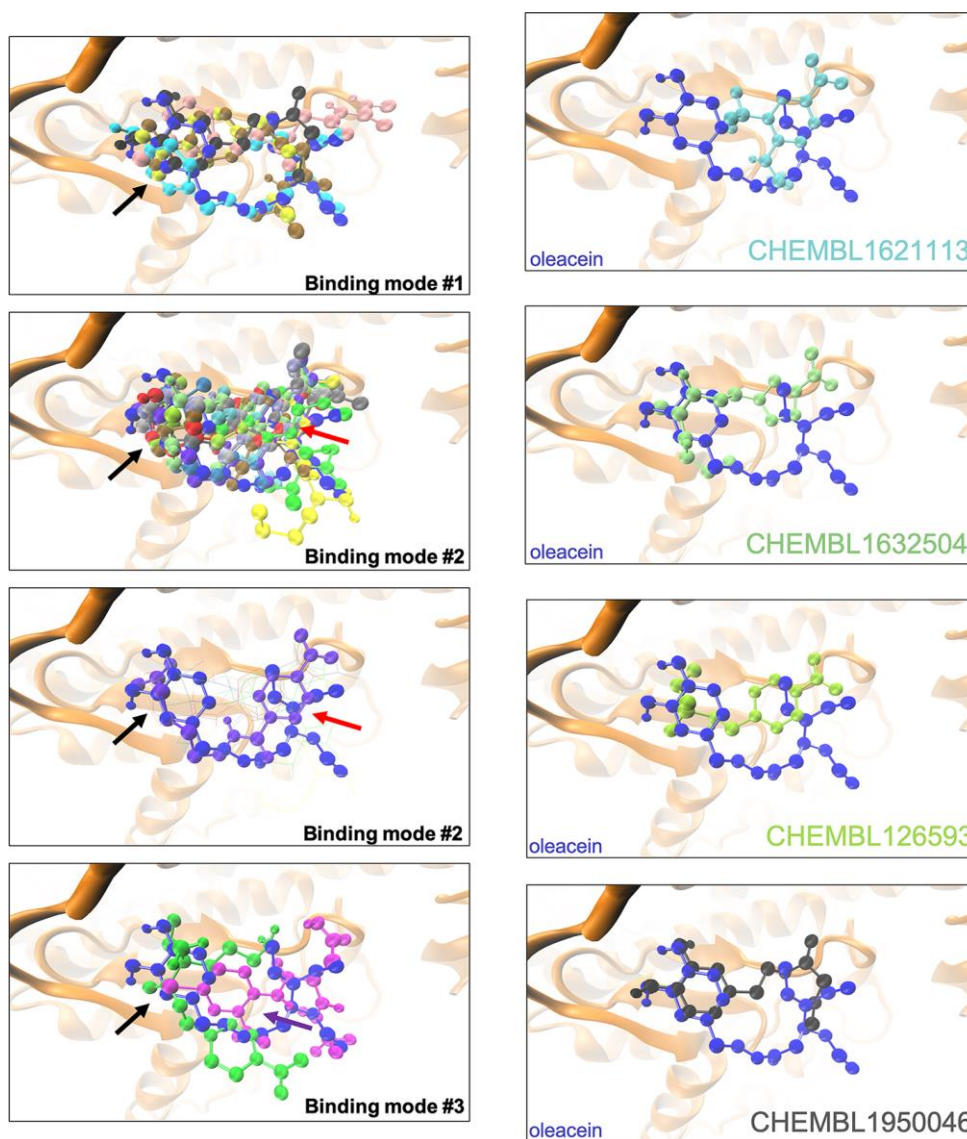


**Figure 2. Binding modes of oleacein mimetics to mTOR.** *Left panels.* Graphical representation of the binding modes of the computationally-predicted oleacein mimetics to the catalytic cavity of mTOR. The black, red, and purple arrows indicate the location of the aromatic rings in the binding modes #1, #2, and #3, respectively. *Right panels.* Graphical representation of the binding modes of parental oleacein and selected oleacein mimetics with anti-CSC activity (Figure 4, 5) to the catalytic cavity of mTOR.

mimetics. The selected oleacein mimetics were tested in 10-dose  $IC_{50}$  mode with 2-fold serial dilution and reactions were carried out at 1  $\mu\text{mol/L}$  SAM. Although hydroxytyrosol butyrate decreased DNMT3A activity in a dose-dependent manner, concentrations higher than 150  $\mu\text{mol/L}$  were necessary to reach the  $IC_{50}$  value. (*E*)-*N*-allyl-2-((5-nitrofuran-2-yl)methylene)hydrazinecarbothioamide did not reach the half maximal inhibitory concentration of DNMT3a activity even at the highest concentration tested.

## DISCUSSION

The molecular frameworks of natural products can provide feasible and innovative templates for medicinal chemistry and drug discovery [43]. But, despite the long tradition of natural product-inspired discovery of synthetic compounds, there has been little effort to utilize EVOO biophenols chemotypes as a springboard for lead discovery. Here, we carried out such a drug discovery approach to uncover new compounds capable

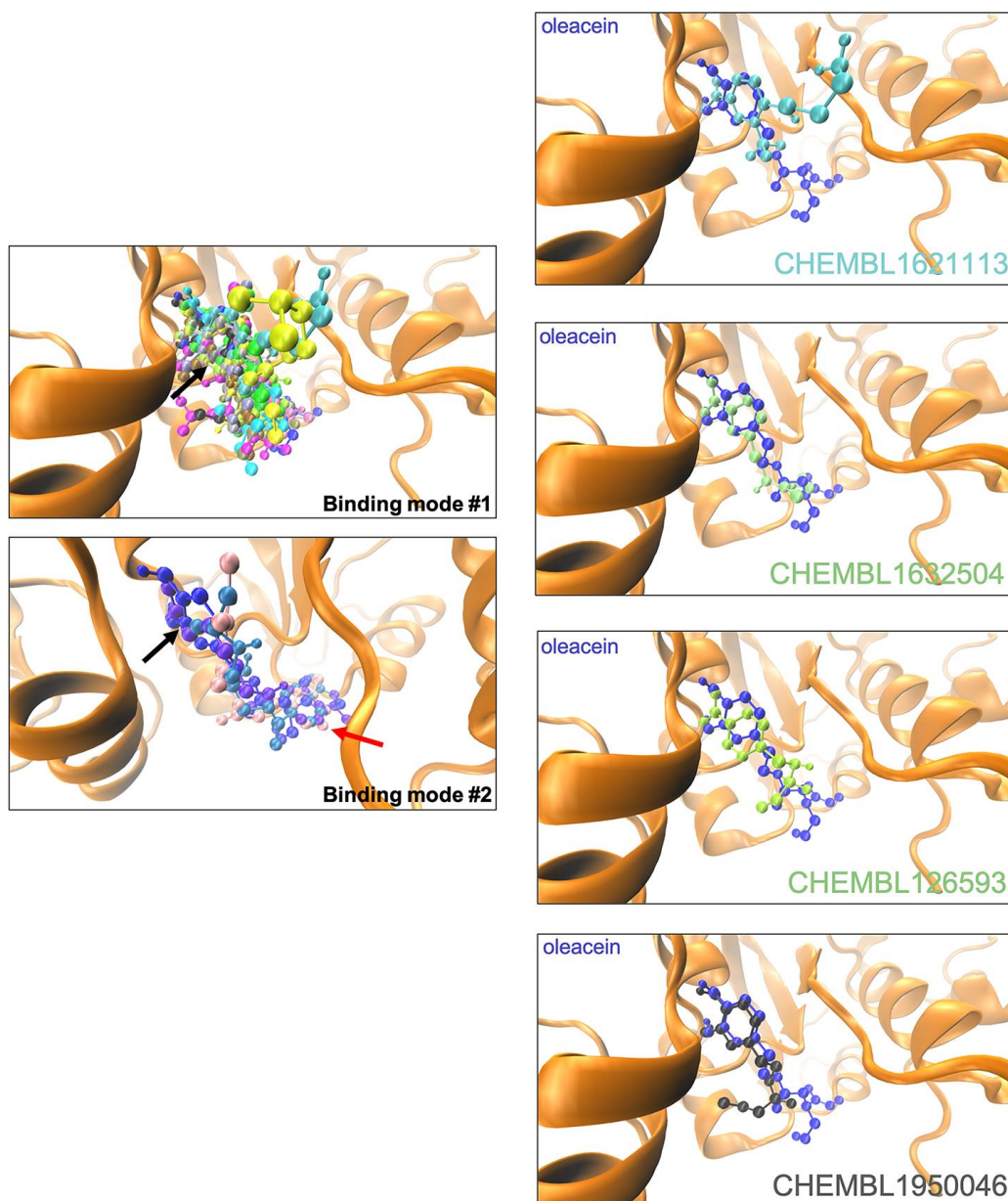


**Figure 3. Binding modes of oleacein mimetics to DNMT.** *Left panels.* Graphical representation of the binding modes of the computationally-predicted oleacein mimetics to the catalytic site of DNMT. The black and red arrows indicate the location of the aromatic rings in the binding modes #1 and #2, respectively. *Right panels.* Graphical representation of the binding modes of parental oleacein and selected oleacein mimetics with anti-CSC activity (Figures 4 and 5) to the catalytic cavity of DNMT.



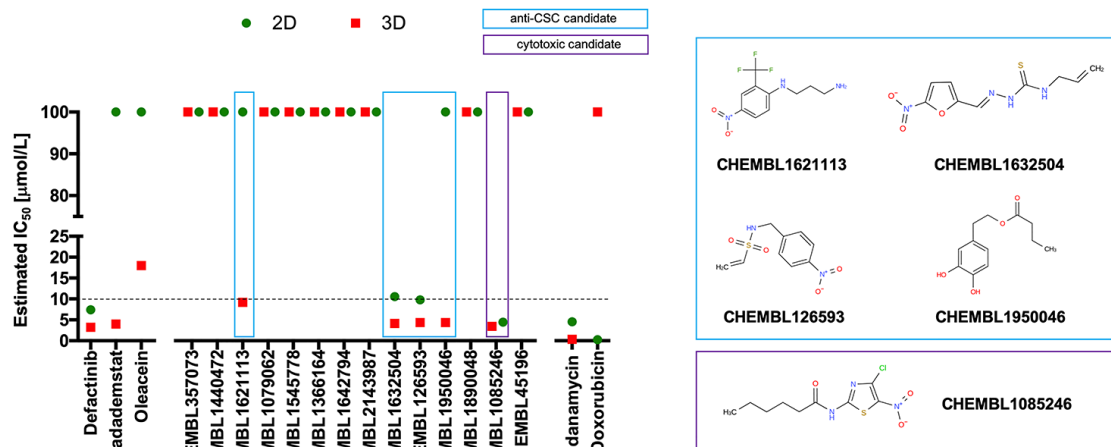


**Figure 4. Phenotypic screening of the anti-CSC activity of oleacein mimetics (I).** Left. Comparative analysis of  $IC_{50}$  values of the computationally-predicted oleacein mimetics in 2D monolayer cultures and 3D mammosphere systems. With 10  $\mu\text{mol/L}$  as a cutoff, 4/16 compounds tested were more potent in 3D than in 2D and were selected as anti-CSC candidates; 1/16 compounds tested was equally potent in 3D and in 2D and was designated as cytotoxic. Right. ChEMBL structures of the computationally-predicted oleacein mimetics with anti-CSC (blue box) and cytotoxic (red box) activity.

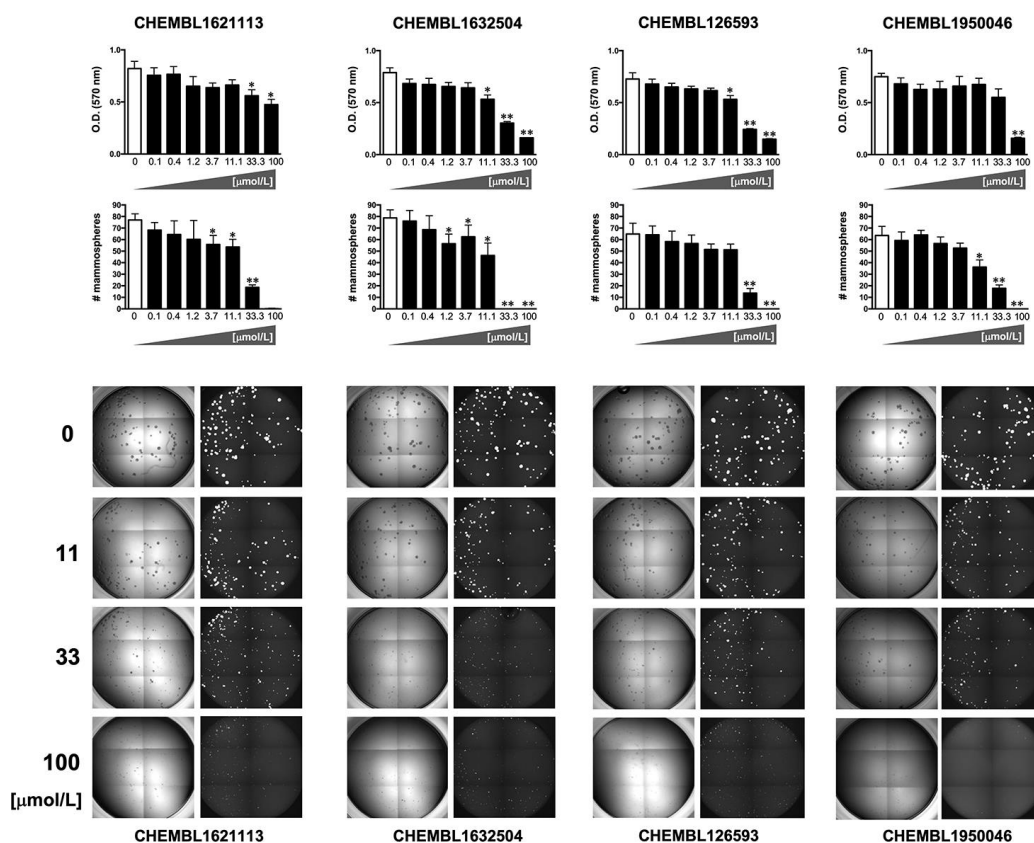


**Figure 5. Phenotypic screening of the anti-CSC activity of oleacein mimetics (II).** Top panels. MTT reduction-based measurement of cell viability is expressed as percentage uptake (OD<sub>570</sub>) relative to untreated controls (=100% cell viability). Bottom panels. Representative microscope images ( $\times 2.5$  magnification) of mammospheres formed by MDA-MB-436 cells growing in sphere medium for 6 days in the absence or presence of graded concentrations of oleacein mimetics. The number of mammospheres ( $>100 \mu\text{m}$  diameter) is expressed as means (columns)  $\pm$  SD (bars). \* $P < 0.05$  and \*\* $P < 0.005$ , statistically significant differences from the untreated (control) group.

of phenotypically mimicking the anti-CSC effects of the EVOO dihydroxy-phenol oleacein.

We took advantage of modern bioinformatics approaches with the aim of identifying physicochemical mimetics of the anti-CSC behavior of EVOO-derived oleacein. First, the somewhat structurally complex framework of the dialdehydic form of decarboxymethyl elenolic acid linked to hydroxytyrosol (i.e., oleacein) was computationally captured in terms of molecules with oleacein-like physico-chemical profiles. Second, we *in silico* compared the binding modes of the top 20 computationally-predicted oleacein mimetics to the two molecular targets originally involved in the capacity of oleacein to specifically suppress the functional traits of tumor-initiating CSC (i.e., mTOR and DNMT) [14]. Third, we phenotypically explored the computationally-discovered oleacein biomimetics in terms of their anti-CSC activity. Fourth, we evaluated the structure-mTOR/DNMT bioactivity relationship of the most promising oleacein-mimetic candidates. By doing so,

four oleacein mimetics, namely N'-[4-nitro-2-(trifluoromethyl)phenyl]propane-1,3-diamine, (*E*)-*N*-allyl-2-((5-nitrofuran-2-yl)methylene)hydrazinecarbothioamide, *N*-(4-nitrobenzyl)ethanesulfonamide, and 3,4-dihydroxyphenethyl butyrate (a.k.a. hydroxytyrosol butyrate), fulfilled the first phenotypic endpoint of the selection criteria, which was the specific suppression of the 3D mammosphere forming capability of CSC in the low micromolar range without highly significant cytotoxic effects against differentiated cancer cells growing in 2D cultures in the same range of concentrations. Moreover, non-cytotoxic concentrations of the oleacein mimetics hydroxytyrosol butyrate and (*E*)-*N*-allyl-2-((5-nitrofuran-2-yl)methylene)hydrazine carbothioamide efficiently suppressed the population of ALDH1<sup>+</sup> epithelial-like proliferating CSC [31, 32, 35, 42], a second phenotypic endpoint of the selection criteria for anti-CSC candidates.

The fact that the oleacein mimetics-responsive phenotypes were exclusively manifested under 3D stem

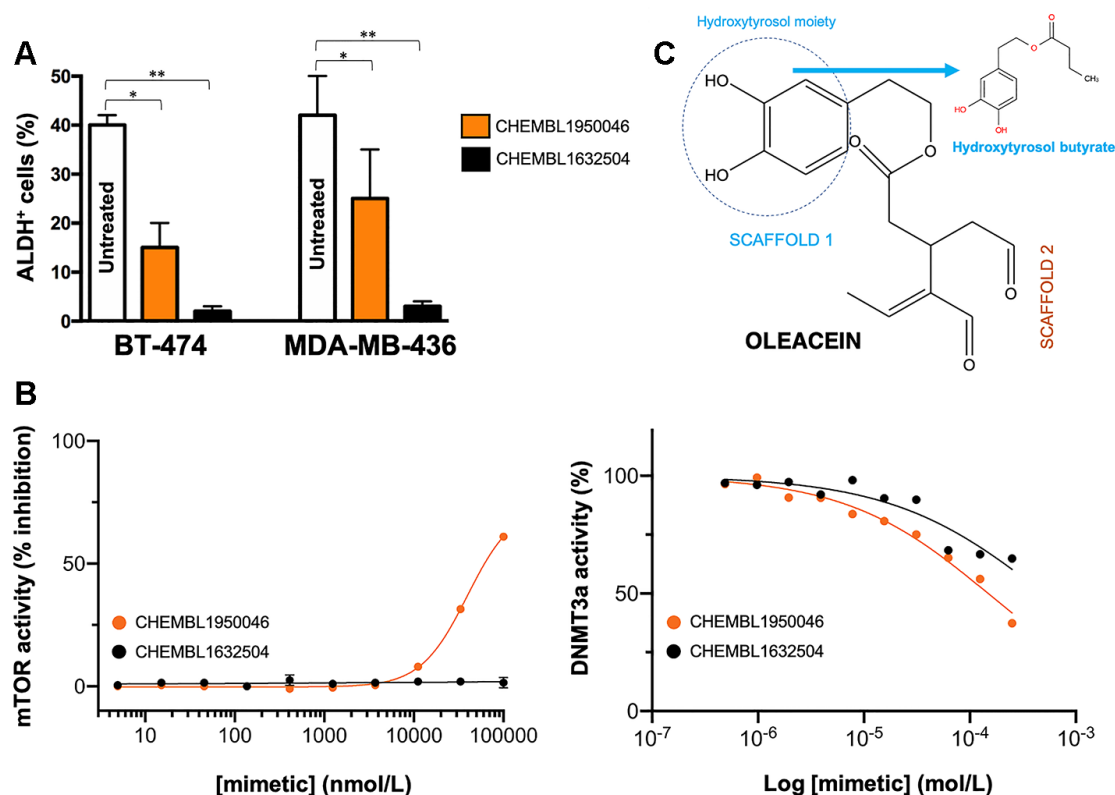


**Figure 6. Phenotypic screening of the anti-CSC activity of oleacein mimetics (III).** (A) Changes in the number of ALDH<sup>+</sup> cells in BT-474 and MDA-MB-436 populations cultured in the absence or presence of 11.1  $\mu$ mol/L of CHEMBL1950046 and CHEMBL1632504. The results are expressed as percentages means (columns)  $\pm$  SD (bars). \* $P$  < 0.05 and \*\* $P$  < 0.005, statistically significant differences from the untreated (control) group. (B) *Left*. A dose-response inhibition curve of ATP-dependent activity of mTOR kinase was created by plotting FRET signal of the Z'-LYTE Kinase assay as the function of CHEMBL1950046 and CHEMBL1632504 concentrations. *Right*. Dose-response curves of SAM-dependent methylation activity of DNMT3A were created by plotting radioisotope signals of the HotSpot<sup>SM</sup> assay as the function of CHEMBL1950046 and CHEMBL1632504 concentrations. (C) Molecular scaffolds of oleacein.



cell culture conditions along with their capacity to specifically and potently suppress (>90%) ALDH1<sup>+</sup> CSC-like cellular states irrespective of the mutational landscape of the cancer cell population strongly suggested that their mechanism of action targets the biological functioning of cancer stemness *per se*. Hydroxytyrosol butyrate is a chemically-modified (alkyl ester) lipophilic version of hydroxytyrosol that is more stable than parental hydroxytyrosol under biological conditions [44–49]. The fact that the inclusion of a short-medium lipophilic chain in the hydroxytyrosol molecule sufficed to recapitulate, at least in part, both the anti-CSC behavior and the anti-mTOR/DNMT inhibitory activity of the parental oleacein highlights the functional relevance of the dihydroxybenzene moiety within the phenolic part of oleacein, a scaffold that seems to be a crucial mediator of the metabolo-epigenetic modulatory effects of oleacein (e.g., COMT, IDH1, LSD1 [18, 22, 50–52]) *via* formation of stacking interactions, coordination with metal ions, and/or establishment of hydrophobic and/or hydrogen bond interactions through the hydroxyl groups or the aromatic ring (Figure 6C). The second oleacein scaffold, which comprises the secoiridoid dialdehyde part, might be involved in the stabilization of oleacein *via* hydrophobic interactions within the binding pocket of the targeted proteins. Accordingly, although hydroxytyrosol butyrate preserved the original double occupancy of oleacein within the catalytic sites of mTOR and DNMT, the sole dihydroxybenzene moiety does not suffice to fully preserve the low-micromolar biological activity of oleacein against mTOR and DNMT enzymatic activities. (*E*)-*N*-allyl-2-((5-nitrofuran-2-yl)methylene)hydrazinecarbothioamide, originally described as an inhibitor of the *Trypanosoma cruzi* triosephosphate isomerase [53], lacked the original binding sites of oleacein to mTOR and DNMT, thereby fully losing the original ability of oleacein to operate as a dual mTOR/DNMT inhibitor. (*E*)-*N*-allyl-2-((5-nitrofuran-2-yl)methylene)hydrazinecarbothioamide, however, appeared to operate as an optimized mimetic of oleacein capable of exhibiting a very promising and potent activity against ALDH1-positive breast CSC. These findings can be consistent with the notion that preservation of the original binding mode of oleacein to mTOR and DNMT is an obligatory requirement for a dual mTOR/DNMT inhibitory activity of hydroxytyrosol-related oleacein mimetics (e.g., hydroxytyrosol butyrate) with anti-CSC activity; for hydroxytyrosol-unrelated oleacein mimetics (e.g., (*E*)-*N*-allyl-2-((5-nitrofuran-2-yl)methylene)hydrazinecarbothioamide), however, the absence of a dual mTOR/DNMT inhibitory activity is dispensable for an efficient suppression of the ALDH<sup>+</sup>-CSC functional phenotype.

We provide, to the best of our knowledge, the first evidence that the pharma-nutritional properties of oleacein that elicit its functioning as an anti-CSC

compound can be phenocopied through the use of mimetics that capture its physico-chemical properties. Although we acknowledge that further studies are needed to validate the ability of oleacein mimetics to functionally deplete tumor-initiating CSC-like states *in vivo* and the mechanisms underlying their mode of action, it is reasonable to suggest that a biomimicry design process might guide the development of synthetically tractable small molecules capable of phenotypically imitating the anti-CSC chemistry of complex EVOO phenolics such as oleacein.

## MATERIALS AND METHODS

### Preparation and analytical characterization of oleacein mimetics

#### CHEMBL2143987 (*N*-(2-(Dimethylamino)ethyl)-2-(4-nitrophenyl)acetamide)

A mixture of 4-nitrophenylacetic acid (100 mg, 0.552 mmol) and CDI (94mg, 0.58 mmol) in DMF (1.4 mL) was stirred at 50° C for 10 min. The solution was cooled to 20° C, *N,N*-dimethylaminoethylamine (63.6 µL, 0.58 mmol) was added dropwise and the solution stirred for 2 h. The solution was poured into water and extracted with EtOAc (3×). The combined organic extracts were washed with water, brine, dried, and the solvent removed under reduced pressure. The residue was chromatographed, eluting with a DCM/MeOH (1%NH<sub>3</sub>) yielding *N*-(*N,N*-dimethylaminoethyl)-2-4-nitrophenylacetamide (27 mg, 19.5%).

#### CHEMBL1632504 ((*E*)-*N*-Allyl-2-((5-nitrofuran-2-yl)methylene)hydrazinecarbothioamide)

5-Nitrofuran-2-carbaldehyde (100 mg, 0.709 mmol), *N*-allylhydrazinecarbothioamide (93 mg, 0.709 mmol), *p*-TSA (6.74 mg, 0.035 mmol) and toluene (7.0 mL) were stirred at room temperature until the aldehyde was not present (1.5h). The solid formed (136 mg, 75%) was collected by filtration.

#### CHEMBL126593 (*N*-(4-Nitrobenzyl)ethenesulfonamide)

4-Nitrophenyl)methanamine (100 mg, 0.657 mmol) was dissolved in DCM (620 µL, dry) at 0° C with stirring under N<sub>2</sub> to which a 4-methylmorpholine (145 µL, 1.314 mmol) was added with stirring. A solution of *y* 2-chloroethanesulfonyl chloride (68.7 µL, 0.657 mmol) dissolved in DCM (620 µL, dry) was added at 0° C with stirring 10 min under N<sub>2</sub>, after which time the reaction mixture was stirred at room temperature overnight. The reaction mixture was extracted with dilute hydrochloric acid and the organic layers were collected, dried (MgSO<sub>4</sub>), filtered and the solvent removed under reduced pressure. The crude product

was purified by column chromatography (EtOAc/n-hexane 1/2). The product was obtained as a white solid (11 mg, 7%).

**CHEMBL1950046 (3,4-Dihydroxyphenethyl butyrate)**

Lipase P (25 mg) and vinyl butyrate (412  $\mu$ l, 3.24 mmol) were added to a solution of 4-(2-hydroxyethyl)benzene-1,2-diol (25 mg, 0.162 mmol) in *t*BuOMe (Volume: 5792  $\mu$ l) and the mixture was shaken at 40° C for 60 min. The reaction was quenched by filtering off enzyme and the filtrate was evaporated *in vacuo*. The resulting residue was dissolved in EtOAc and washed with sat. NaHCO<sub>3</sub> and brine then dried (MgSO<sub>4</sub>) followed by filtration and evaporation to dryness. 32 mg (89%) of compound identified as the title compound were obtained.

**CHEMBL1890048 (2-Methoxy-N-(2-methyl-5-nitrophenyl)acetamide)**

To a solution of 2-methyl-5-nitroaniline (100 mg, 0.657 mmol) in DCM (0.04 M), TEA (0.137 ml, 0.986 mmol) and 2-methoxyacetyl chloride (0.066  $\mu$ l, 0.723 mmol) were added. The reaction mixture was stirred at room temperature for 4 h. 103 mg (70%) of compound identified as the title compound were obtained.

**CHEMBL1085246 (N-(4-Chloro-5-nitrothiazol-2-yl)hexanamide)**

Hexanoyl chloride (38.2  $\mu$ l, 0.278 mmol) was dissolved in THF (0.1 M) and cooled to -78° C then 4-chloro-5-nitrothiazol-2-amine (50 mg, 0.278 mmol) was added in one portion. DIPEA (1.1 eq) was added to the resulting slurry at -78° C and the solution was held at this temperature for 10 min then allowed to warm to room temperature overnight. The solution was diluted with EtOAc and washed with sat. NaHCO<sub>3</sub>, 1M HCl and brine then dried (MgSO<sub>4</sub>) followed by filtration and evaporation to dryness. The resulting residue was purified by gradient flash column chromatography (10-60% EtOAc/hexanes or 1-2% MeOH/CH<sub>2</sub>Cl<sub>2</sub>) to obtain 22 mg (28.5%) of compound identified as the title compound.

**CHEMBL45196 (4-((5-Chloro-2-nitrophenyl)amino)-4-oxo-2-(2,2,2-trifluoroacetamido)butanoic acid)**

A mixture of 5-chloro-2-nitroaniline (50 mg, 0.290 mmol) and (*S*)-*N*-(2,5-dioxotetrahydrofuran-3-yl)-2,2,2-trifluoroacetamide (61.2 mg, 0.290 mmol) was irradiated for 60 minutes in a microwave (130° C, 200 psi, 200W). The residue was purified by reversed-phase flash chromatography, yielding 14 mg (12%) of compound identified as the title compound.

CHEMBL357073 (6-[(4-nitrophenyl)formamido]hexanoic acid), CHEMBL1545778 ([2-(methylcarbamoylamino)-2-oxo-ethyl] (E)-3-(3-bromophenyl)prop-2-

enoate), CHEMBL1366164 (ethyl 2-[(2-methyl-5-nitrophenyl)amino]-2-oxoacetate), and CHEMBL1642794 ([2-(tert-butylamino)-2-oxo-ethyl] 4-nitrobenzoate) were purchased from Enamine (EN300-302808, Z1864 6098, EN300-236023, and Z19756482, respectively; Kiev, Ukraine). CHEMBL1440472 (2-[(6-chloro-3-nitro-2-pyridinyl)amino]-3-methylbutanoic acid) was purchased from Key Organics (MS-1625; Bedford, MA). CHEMBL1621113 (N-[4-nitro-2-(trifluoromethyl)phenyl]propane-1,3-diamine) and CHEMBL1079062 ((*Z*)-4-[(4-nitrophenyl)amino]-4-oxobut-2-enoic acid) were purchased from ABCR GmbH (AB141160 and AB414326, respectively; Karlsruhe, Germany).

**Analytical and spectroscopic characterization of oleacein mimetics**

**NMR**

NMR spectra were recorded on an Agilent VNMR-400 (<sup>1</sup>H at 400.10 MHz). **HPLC-MS.** HPLC-MS were performed with a High-Performance Liquid Chromatography Thermo Ultimate 3000SD (Thermo Scientific Dionex) coupled to a photodiode array detector and a mass spectrometer LTQ XL ESI-ion trap (Thermo Scientific); 5  $\mu$ l of sample MeOH were injected (c=0.5mg/mL). Data from mass spectra were analyzed by electrospray ionization in positive and negative mode and peaks are given m/z (% of basis peak). The mobile phase used was a mixture of A = water + 0.05 formic acid and B = Acetonitrile + 0.05 formic acid with method described as follows: flow 0.5 mL/min; 5% B for 0.5 min; 5%-100% B in 5 min, 100% B for 2min.

**Virtual screening**

Virtual profiling was performed with ligand- and structure-based software tools, using the chemical structure of oleacein as a seed, as described [54]. Briefly, the 3D virtual profiling tool compares a query molecule (i.e., oleacein) with the structures present in the ChEMBL(v19) reference database using Comparative Molecular Similarity Indices Analysis (CoMSIA) fields on a 3D grid. Molecules were compared according to their relationship with their environment using the 3D descriptors topologic surface area, lipophilicity, hydrogen bond donors/acceptors count, and Van der Waals radii, among others, thereby obtaining biomimetic compounds with different structures.

**Docking and molecular dynamics calculations**

All docking, MD calculations and MM/GBSA rescoring were carried out as described [18, 22, 54].

## Cell viability

Cell viability was determined using a standard colorimetric MTT-based reduction assay 72 h after exposure to graded concentrations of oleacein mimetics.

## Mammosphere formation

Mammosphere formation was monitored using Cell2Sphere™ assays (StemTek Therapeutics, Bilbao, Spain). Graded concentrations of oleacein mimetics were added to triplicate sets of wells on day 1 and the number of 6-day-old mammospheres was recorded as a measurement of CSC content. Images were recorded using a BioTek Cytation 5 image cytometer at 2.5× magnification. Prior to image acquisition, spheroid cultures were stained with a fluorescent vital dye to increase the accuracy of spheroid detection and analysis. The system was then set to count number, size, and aspect ratio of the objects. Thresholds were set to >100 µm in size and 0.4 as aspect ratio (with 1 being the aspect ratio of a perfect circle).

## Aldefluor activity assay

The ALDEFLUOR® assay (StemCell Technologies, Vancouver, BC, Canada) was performed with or without the addition of hydroxytyrosol butyrate and (*E*)-*N*-allyl-2-((5-nitrofuranyl)methylene)hydrazinecarbothioamide for 48 h.

## mTOR and DNMT activity/inhibition assays

IC<sub>50</sub> determinations for FRAP1 (mTOR) of oleacein mimetics were outsourced to Invitrogen (Life Technologies) using the FRET-based Z-LYTE™ SelectScreen Kinase Profiling Service. The effect of oleacein mimetics on the enzymatic activities of the recombinant human DNMT3A was outsourced to Reaction Biology Corp. (Malvern, PA) using HotSpot<sup>SM</sup>, a nanoliter-scale radioisotope filter binding platform.

## Statistical analysis

All statistical analyses were performed using GraphPad Prism software (San Diego, CA). Data are presented as mean ± S.D. Comparisons of means of ≥ 3 groups were performed by analysis of variance (ANOVA) and the existence of individual differences, in case of significant *F* values at ANOVA, were assessed by multiple contrasts. *P* values < 0.05 and <0.005 were considered to be statistically significant (denoted as \* and \*\*, respectively). All statistical tests were two-sided.

## AUTHOR CONTRIBUTIONS

J.A.M. conceived the idea, directed the project, and wrote the manuscript. E. C., J.G., S. V., and A. G. M. were involved in the design, development, and analysis of all the cell-based and enzymatic experiments, and analyzed the data. J. B-B. and B. M-C. provided intellectual insights and critically read the manuscript. J. L-S. and A. S-C. provided essential materials necessary for the study. A. N-C. and M. S-M. performed virtual profiling, docking and molecular dynamics-based calculations and scorings, and examined all the chemoinformatic data. A. L., S. C., and C. S. performed chemical synthesis and analytical characterization of oleacein mimetics.

## ACKNOWLEDGMENTS

The authors would like to thank Dr. Kenneth McCreath for editorial support.

## CONFLICTS OF INTEREST

Stock ownership: Á.G.M., StemTek Therapeutics (CEO). All other authors have no competing interests to declare. The authors declare that the research was conducted in the absence of any commercial or financial relationships that could be construed as a potential conflict of interest. Ethics approval was not required for this study as per the local legislation.

## FUNDING

Work in the Menendez laboratory is supported by the Spanish Ministry of Science and Innovation (Grants SAF2016-80639-P and PID2019-104055GB-I00, Plan Nacional de I+D+I, funded by the European Regional Development Fund, Spain) and by an unrestricted research grant from the Fundació Oncolliga Girona (Lliga catalana d'ajuda al malalt de càncer, Girona). Joaquim Bosch-Barrera is the recipient of research grants from La Marató de TV3 foundation (201906) and the Health Research and Innovation Strategic Plan (SLT006/17/114; PERIS 2016-2020; Pla estratègic de recerca i innovació en salut; Departament de Salut, Generalitat de Catalunya).

## REFERENCES

1. López-Miranda J, Pérez-Jiménez F, Ros E, De Caterina R, Badimón L, Covas MI, Escrich E, Ordovás JM, Soriguer F, Abiá R, de la Lastra CA, Battino M, Corella D, et al. Olive oil and health: summary of the II international conference on olive oil and health consensus report, Jaén and Córdoba (Spain) 2008. *Nutr Metab Cardiovasc Dis.* 2010; 20:284–94.

<https://doi.org/10.1016/j.numecd.2009.12.007>  
PMID:20303720

2. Menendez JA, Joven J, Aragonès G, Barrajón-Catalán E, Beltrán-Debón R, Borrás-Linares I, Camps J, Corominas-Faja B, Cufí S, Fernández-Arroyo S, García-Heredia A, Hernández-Aguilera A, Herranz-López M, et al. Xenohormetic and anti-aging activity of secoiridoid polyphenols present in extra virgin olive oil: a new family of gerosuppressant agents. *Cell Cycle*. 2013; 12:555–78.  
<https://doi.org/10.4161/cc.23756> PMID:23370395
3. Fernández del Río L, Gutiérrez-Casado E, Varela-López A, Villalba JM. Olive oil and the hallmarks of aging. *Molecules*. 2016; 21:163.  
<https://doi.org/10.3390/molecules21020163>  
PMID:26840281
4. Reboredo-Rodríguez P, Varela-López A, Forbes-Hernández TY, Gasparrini M, Afrin S, Cianciosi D, Zhang J, Manna PP, Bompadre S, Quiles JL, Battino M, Giampieri F. Phenolic compounds isolated from olive oil as nutraceutical tools for the prevention and management of cancer and cardiovascular diseases. *Int J Mol Sci*. 2018; 19:2305.  
<https://doi.org/10.3390/ijms19082305>  
PMID:30082650
5. Gaforio JJ, Visioli F, Alarcón-de-la-Lastra C, Castañer O, Delgado-Rodríguez M, Fitó M, Hernández AF, Huertas JR, Martínez-González MA, Menendez JA, Osada J, Papadaki A, Parrón T, et al. Virgin olive oil and health: summary of the III international conference on virgin olive oil and health consensus report, JAEN (Spain) 2018. *Nutrients*. 2019; 11:2039.  
<https://doi.org/10.3390/nu11092039> PMID:31480506
6. Serreli G, Deiana M. Biological relevance of extra virgin olive oil polyphenols metabolites. *Antioxidants (Basel)*. 2018; 7:170.  
<https://doi.org/10.3390/antiox7120170>  
PMID:30469520
7. Nediani C, Ruzzolini J, Romani A, Calorini L. Oleuropein, a bioactive compound from *Olea europaea* L., as a potential preventive and therapeutic agent in non-communicable diseases. *Antioxidants (Basel)*. 2019; 8:578.  
<https://doi.org/10.3390/antiox8120578>  
PMID:31766676
8. Romani A, Ieri F, Urciuoli S, Noce A, Marrone G, Nediani C, Bernini R. Health effects of phenolic compounds found in extra-virgin olive oil, by-products, and leaf of *Olea europaea* L. *Nutrients*. 2019; 11:1776.  
<https://doi.org/10.3390/nu11081776> PMID:31374907
9. Rodríguez-López P, Lozano-Sanchez J, Borrás-Linares I, Emanuelli T, Menéndez JA, Segura-Carretero A. Structure-biological activity relationships of extra-virgin olive oil phenolic compounds: health properties and bioavailability. *Antioxidants (Basel)*. 2020; 9:685.  
<https://doi.org/10.3390/antiox9080685>  
PMID:32752213
10. Serreli G, Deiana M. Extra virgin olive oil polyphenols: modulation of cellular pathways related to oxidant species and inflammation in aging. *Cells*. 2020; 9:478.  
<https://doi.org/10.3390/cells9020478>  
PMID:32093046
11. Corominas-Faja B, Santangelo E, Cuyàs E, Micol V, Joven J, Ariza X, Segura-Carretero A, García J, Menendez JA. Computer-aided discovery of biological activity spectra for anti-aging and anti-cancer olive oil oleuropeins. *Aging (Albany NY)*. 2014; 6:731–41.  
<https://doi.org/10.18632/aging.100691>  
PMID:25324469
12. Vougiotiannopoulou K, Lemus C, Halabalaki M, Pergola C, Werz O, Smith AB 3r, Michel S, Skaltsounis L, Deguin B. One-step semisynthesis of oleacein and the determination as a 5-lipoxygenase inhibitor. *J Nat Prod*. 2014; 77:441–45.  
<https://doi.org/10.1021/np401010x>  
PMID:24568174
13. Lombardo GE, Lepore SM, Morittu VM, Arcidiacono B, Colica C, Procopio A, Maggisano V, Bulotta S, Costa N, Mignogna C, Britti D, Brunetti A, Russo D, Celano M. Effects of oleacein on high-fat diet-dependent steatosis, weight gain, and insulin resistance in mice. *Front Endocrinol (Lausanne)*. 2018; 9:116.  
<https://doi.org/10.3389/fendo.2018.00116>  
PMID:29615982
14. Polini B, Digiacocono M, Carpi S, Bertini S, Gado F, Saccomanni G, Macchia M, Nieri P, Manera C, Fogli S. Oleocanthal and oleacein contribute to the in vitro therapeutic potential of extra virgin oil-derived extracts in non-melanoma skin cancer. *Toxicol In Vitro*. 2018; 52:243–50.  
<https://doi.org/10.1016/j.tiv.2018.06.021>  
PMID:29959992
15. Celano M, Maggisano V, Lepore SM, Russo D, Bulotta S. Secoiridoids of olive and derivatives as potential adjuvant drugs in cancer: a critical analysis of experimental studies. *Pharmacol Res*. 2019; 142:77–86.  
<https://doi.org/10.1016/j.phrs.2019.01.045>  
PMID:30772463
16. Karković Marković A, Torić J, Barbarić M, Jakobišić Brala C. Hydroxytyrosol, tyrosol and derivatives and their potential effects on human health. *Molecules*. 2019; 24:2001.  
<https://doi.org/10.3390/molecules24102001>  
PMID:31137753



17. Lozano-Castellón J, López-Yerena A, Rinaldi de Alvarenga JF, Romero Del Castillo-Alba J, Vallverdú-Queralt A, Escribano-Ferrer E, Lamuela-Raventós RM. Health-promoting properties of oleocanthal and oleacein: two secoiridoids from extra-virgin olive oil. *Crit Rev Food Sci Nutr*. 2020; 60:2532–48.  
<https://doi.org/10.1080/10408398.2019.1650715>  
PMID:31423808
18. Corominas-Faja B, Cuyàs E, Lozano-Sánchez J, Cufí S, Verdura S, Fernández-Arroyo S, Borrás-Linares I, Martín-Castillo B, Martín ÁG, Lupu R, Nonell-Canals A, Sanchez-Martinez M, Micol V, et al. Extra-virgin olive oil contains a metabolite-epigenetic inhibitor of cancer stem cells. *Carcinogenesis*. 2018; 39:601–13.  
<https://doi.org/10.1093/carcin/bgy023>  
PMID:29452350
19. Bertelli M, Kiani AK, Paolacci S, Manara E, Kurti D, Dhuli K, Bushati V, Miertus J, Pangallo D, Baglivo M, Beccari T, Michelini S. Hydroxytyrosol: a natural compound with promising pharmacological activities. *J Biotechnol*. 2020; 309:29–33.  
<https://doi.org/10.1016/j.jbiotec.2019.12.016>  
PMID:31884046
20. Britton J, Davis R, O'Connor KE. Chemical, physical and biotechnological approaches to the production of the potent antioxidant hydroxytyrosol. *Appl Microbiol Biotechnol*. 2019; 103:5957–74.  
<https://doi.org/10.1007/s00253-019-09914-9>  
PMID:31177312
21. de Las Hazas MC, Rubio L, Macia A, Motilva MJ. Hydroxytyrosol: emerging trends in potential therapeutic applications. *Curr Pharm Des*. 2018; 24:2157–79.  
<https://doi.org/10.2174/1381612824666180522110314>  
PMID:29788874
22. Cuyàs E, Castillo D, Llorach-Parés L, Lozano-Sánchez J, Verdura S, Nonell-Canals A, Brunet J, Bosch-Barrera J, Joven J, Valdés R, Sanchez-Martinez M, Segura-Carretero A, Menendez JA. Computational de-orphanization of the olive oil biophenol oleacein: discovery of new metabolic and epigenetic targets. *Food Chem Toxicol*. 2019; 131:110529.  
<https://doi.org/10.1016/j.fct.2019.05.037>  
PMID:31150784
23. Menendez JA, Alarcón T. Metabostemness: a new cancer hallmark. *Front Oncol*. 2014; 4:262.  
<https://doi.org/10.3389/fonc.2014.00262>  
PMID:25325014
24. Ryall JG, Cliff T, Dalton S, Sartorelli V. Metabolic reprogramming of stem cell epigenetics. *Cell Stem Cell*. 2015; 17:651–62.  
<https://doi.org/10.1016/j.stem.2015.11.012>  
PMID:26637942
25. Menendez JA, Corominas-Faja B, Cuyàs E, García MG, Fernández-Arroyo S, Fernández AF, Joven J, Fraga MF, Alarcón T. Oncometabolic nuclear reprogramming of cancer stemness. *Stem Cell Reports*. 2016; 6:273–83.  
<https://doi.org/10.1016/j.stemcr.2015.12.012>  
PMID:26876667
26. Perusina Lanfranca M, Thompson JK, Bednar F, Halbrook C, Lyssiotis C, Levi B, Frankel TL. Metabolism and epigenetics of pancreatic cancer stem cells. *Semin Cancer Biol*. 2019; 57:19–26.  
<https://doi.org/10.1016/j.semcancer.2018.09.008>  
PMID:30273655
27. Crispo F, Condelli V, Lepore S, Notarangelo T, Sgambato A, Esposito F, Maddalena F, Landriscina M. Metabolic dysregulations and epigenetics: a bidirectional interplay that drives tumor progression. *Cells*. 2019; 8:798.  
<https://doi.org/10.3390/cells8080798> PMID:31366176
28. Dai Z, Ramesh V, Locasale JW. The evolving metabolic landscape of chromatin biology and epigenetics. *Nat Rev Genet*. 2020.  
<https://doi.org/10.1038/s41576-020-0270-8>
29. Dontu G, Abdallah WM, Foley JM, Jackson KW, Clarke MF, Kawamura MJ, Wicha MS. In vitro propagation and transcriptional profiling of human mammary stem/progenitor cells. *Genes Dev*. 2003; 17:1253–70.  
<https://doi.org/10.1101/gad.1061803> PMID:12756227
30. Dontu G, Wicha MS. Survival of mammary stem cells in suspension culture: implications for stem cell biology and neoplasia. *J Mammary Gland Biol Neoplasia*. 2005; 10:75–86.  
<https://doi.org/10.1007/s10911-005-2542-5>  
PMID:15886888
31. Ginestier C, Hur MH, Charafe-Jauffret E, Monville F, Dutcher J, Brown M, Jacquemier J, Viens P, Kleer CG, Liu S, Schott A, Hayes D, Birnbaum D, et al. ALDH1 is a marker of normal and Malignant human mammary stem cells and a predictor of poor clinical outcome. *Cell Stem Cell*. 2007; 1:555–67.  
<https://doi.org/10.1016/j.stem.2007.08.014>  
PMID:18371393
32. Korkaya H, Paulson A, Iovino F, Wicha MS. HER2 regulates the mammary stem/progenitor cell population driving tumorigenesis and invasion. *Oncogene*. 2008; 27:6120–30.  
<https://doi.org/10.1038/onc.2008.207> PMID:18591932
33. Manuel Iglesias J, Belouqui I, Garcia-Garcia F, Leis O, Vazquez-Martin A, Eguiara A, Cufí S, Pavon A, Menendez JA, Dopazo J, Martín AG. Mammosphere formation in breast carcinoma cell lines depends upon expression of e-cadherin. *PLoS One*. 2013; 8:e77281.



- <https://doi.org/10.1371/journal.pone.0077281>  
PMID:24124614
34. Weiswald LB, Bellet D, Dangles-Marie V. Spherical cancer models in tumor biology. *Neoplasia*. 2015; 17:1–15.  
<https://doi.org/10.1016/j.neo.2014.12.004>  
PMID:25622895
  35. Brooks MD, Burness ML, Wicha MS. Therapeutic implications of cellular heterogeneity and plasticity in breast cancer. *Cell Stem Cell*. 2015; 17:260–71.  
<https://doi.org/10.1016/j.stem.2015.08.014>  
PMID:26340526
  36. Cuyàs E, Martin-Castillo B, Bosch-Barrera J, Menendez JA. Metformin inhibits RANKL and sensitizes cancer stem cells to denosumab. *Cell Cycle*. 2017; 16:1022–28.  
<https://doi.org/10.1080/15384101.2017.1310353>  
PMID:28387573
  37. Cuyàs E, Gumuzio J, Verdura S, Brunet J, Bosch-Barrera J, Martin-Castillo B, Alarcón T, Encinar JA, Martín ÁG, Menendez JA. The LSD1 inhibitor iadademstat (ORY-1001) targets SOX2-driven breast cancer stem cells: a potential epigenetic therapy in luminal-B and HER2-positive breast cancer subtypes. *Aging (Albany NY)*. 2020; 12:4794–814.  
<https://doi.org/10.18632/aging.102887>  
PMID:32191225
  38. Blum W, Pecze L, Felley-Bosco E, Wu L, de Perrot M, Schwaller B. Stem cell factor-based identification and functional properties of in vitro-selected subpopulations of Malignant mesothelioma cells. *Stem Cell Reports*. 2017; 8:1005–17.  
<https://doi.org/10.1016/j.stemcr.2017.02.005>  
PMID:28285878
  39. Kolev VN, Tam WF, Wright QG, McDermott SP, Vidal CM, Shapiro IM, Xu Q, Wicha MS, Pachter JA, Weaver DT. Inhibition of FAK kinase activity preferentially targets cancer stem cells. *Oncotarget*. 2017; 8:51733–47.  
<https://doi.org/10.18632/oncotarget.18517>  
PMID:28881682
  40. Navas T, Pfister TD, Colantonio S, Aziz A, Dieckman L, Saul RG, Kaczmarczyk J, Borgel S, Alcoser SY, Hollingshead MG, Lee YH, Bottaro DP, Hiltke T, et al. Novel antibody reagents for characterization of drug- and tumor microenvironment-induced changes in epithelial-mesenchymal transition and cancer stem cells. *PLoS One*. 2018; 13:e0199361.  
<https://doi.org/10.1371/journal.pone.0199361>  
PMID:29928062
  41. Maes T, Mascaró C, Tirapu I, Estiarte A, Ciceri F, Lunardi S, Guibourt N, Perdonés A, Lufino MM, Somervaille TC, Wiseman DH, Duy C, Melnick A, et al. ORY-1001, a potent and selective covalent KDM1A inhibitor, for the treatment of acute leukemia. *Cancer Cell*. 2018; 33:495–511.e12.  
<https://doi.org/10.1016/j.ccell.2018.02.002>  
PMID:29502954
  42. Martín-Castillo B, López-Bonet E, Cuyàs E, Viñas G, Pernas S, Dorca J, Menéndez JA. Cancer stem cell-driven efficacy of trastuzumab (Herceptin): towards a reclassification of clinically HER2-positive breast carcinomas. *Oncotarget*. 2015; 6:32317–38.  
<https://doi.org/10.18632/oncotarget.6094>  
PMID:26474458
  43. Rodrigues T, Reker D, Schneider P, Schneider G. Counting on natural products for drug design. *Nat Chem*. 2016; 8:531–41.  
<https://doi.org/10.1038/nchem.2479> PMID:27219696
  44. Trujillo M, Mateos R, Collantes de Terán L, Espartero JL, Cert R, Jover M, Alcudia F, Bautista J, Cert A, Parrado J. Lipophilic hydroxytyrosyl esters. Antioxidant activity in lipid matrices and biological systems. *J Agric Food Chem*. 2006; 54:3779–85.  
<https://doi.org/10.1021/jf060520z> PMID:16719496
  45. Grasso S, Siracusa L, Spatafora C, Renis M, Tringali C. Hydroxytyrosol lipophilic analogues: enzymatic synthesis, radical scavenging activity and DNA oxidative damage protection. *Bioorg Chem*. 2007; 35:137–52.  
<https://doi.org/10.1016/j.bioorg.2006.09.003>  
PMID:17078995
  46. Calderón-Montaña JM, Madrona A, Burgos-Morón E, Orta ML, Mateos S, Espartero JL, López-Lázaro M. Selective cytotoxic activity of new lipophilic hydroxytyrosol alkyl ether derivatives. *J Agric Food Chem*. 2013; 61:5046–53.  
<https://doi.org/10.1021/jf400796p>  
PMID:23638972
  47. Reyes JJ, De La Cruz JP, Muñoz-Marin J, Guerrero A, López-Villodres JA, Madrona A, Espartero JL, González-Correa JA. Antiplatelet effect of new lipophilic hydroxytyrosol alkyl ether derivatives in human blood. *Eur J Nutr*. 2013; 52:591–99.  
<https://doi.org/10.1007/s00394-012-0361-1>  
PMID:22584413
  48. Belmonte-Reche E, Martínez-García M, Peñalver P, Gómez-Pérez V, Lucas R, Gamarro F, Pérez-Victoria JM, Morales JC. Tyrosol and hydroxytyrosol derivatives as antitrypanosomal and antileishmanial agents. *Eur J Med Chem*. 2016; 119:132–40.  
<https://doi.org/10.1016/j.ejmech.2016.04.047>  
PMID:27155468
  49. Funakoshi-Tago M, Sakata T, Fujiwara S, Sakakura A, Sugai T, Tago K, Tamura H. Hydroxytyrosol butyrate

inhibits 6-OHDA-induced apoptosis through activation of the Nrf2/HO-1 axis in SH-SY5Y cells. *Eur J Pharmacol*. 2018; 834:246–56.

<https://doi.org/10.1016/j.ejphar.2018.07.043>

PMID:[30053409](https://pubmed.ncbi.nlm.nih.gov/30053409/)

50. Cuyàs E, Verdura S, Lozano-Sánchez J, Viciano I, Llorach-Parés L, Nonell-Canals A, Bosch-Barrera J, Brunet J, Segura-Carretero A, Sanchez-Martinez M, Encinar JA, Menendez JA. The extra virgin olive oil phenolic oleacein is a dual substrate-inhibitor of catechol-O-methyltransferase. *Food Chem Toxicol*. 2019; 128:35–45.

<https://doi.org/10.1016/j.fct.2019.03.049>

PMID:[30935952](https://pubmed.ncbi.nlm.nih.gov/30935952/)

51. Cuyàs E, Gumuzio J, Lozano-Sánchez J, Carreras D, Verdura S, Llorach-Parés L, Sanchez-Martinez M, Selga E, Pérez GJ, Scornik FS, Brugada R, Bosch-Barrera J, Segura-Carretero A, et al. Extra virgin olive oil contains a phenolic inhibitor of the histone demethylase LSD1/KDM1A. *Nutrients*. 2019; 11:1656.

<https://doi.org/10.3390/nu11071656>

PMID:[31331073](https://pubmed.ncbi.nlm.nih.gov/31331073/)

52. Verdura S, Cuyàs E, Lozano-Sánchez J, Bastidas-Velez C, Llorach-Parés L, Fernández-Arroyo S, Hernández-Aguilera A, Joven J, Nonell-Canals A, Bosch-Barrera J,

Martin-Castillo B, Vellon L, Sanchez-Martinez M, et al. An olive oil phenolic is a new chemotype of mutant isocitrate dehydrogenase 1 (IDH1) inhibitors. *Carcinogenesis*. 2019; 40:27–40.

<https://doi.org/10.1093/carcin/bgy159>

PMID:[30428017](https://pubmed.ncbi.nlm.nih.gov/30428017/)

53. Alvarez G, Aguirre-López B, Varela J, Cabrera M, Merlino A, López GV, Lavaggi ML, Porcal W, Di Maio R, González M, Cerecetto H, Cabrera N, Pérez-Montfort R, et al. Massive screening yields novel and selective trypanosoma cruzi triosephosphate isomerase dimer-interface-irreversible inhibitors with anti-trypanosomal activity. *Eur J Med Chem*. 2010; 45:5767–72.

<https://doi.org/10.1016/j.ejmech.2010.09.034>

PMID:[20889239](https://pubmed.ncbi.nlm.nih.gov/20889239/)

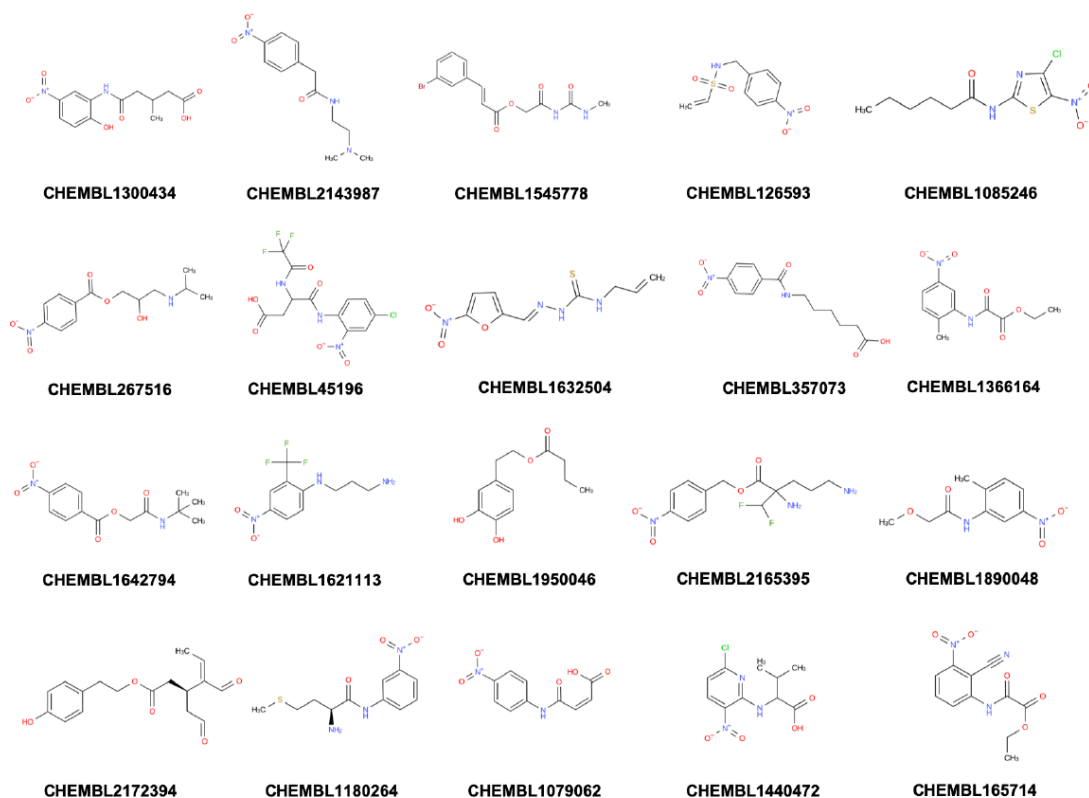
54. Cuyàs E, Verdura S, Llorach-Pares L, Fernández-Arroyo S, Luciano-Mateo F, Cabré N, Stursa J, Werner L, Martin-Castillo B, Viollet B, Neuzil J, Joven J, Nonell-Canals A, et al. Metformin directly targets the H3K27me3 demethylase KDM6A/UTX. *Aging Cell*. 2018; 17:e12772.

<https://doi.org/10.1111/acer.12772>

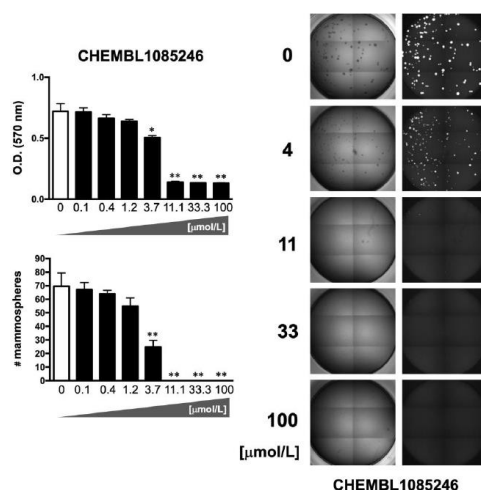
PMID:[29740925](https://pubmed.ncbi.nlm.nih.gov/29740925/)

# SUPPLEMENTARY MATERIALS

## Supplementary Figures



Supplementary Figure 1. CHEMBL structures of the computationally-predicted oleacein mimetics.



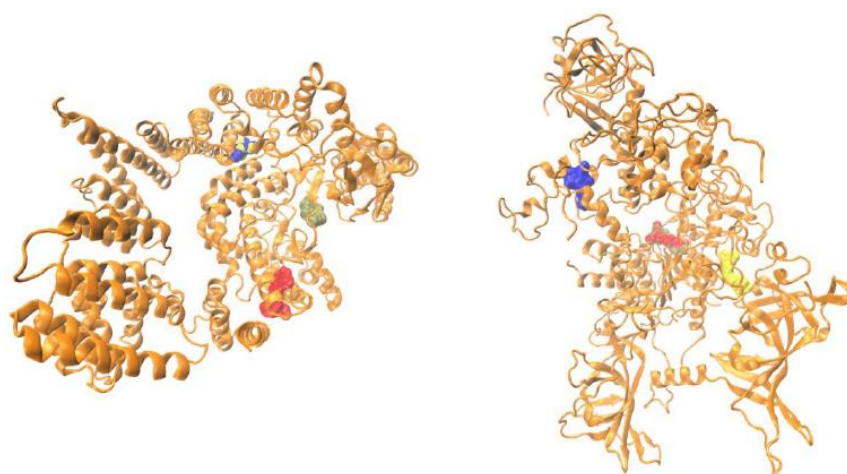
Supplementary Figure 2. *Top panels.* MTT reduction-based measurement of cell viability is expressed as percentage uptake (OD<sub>570</sub>) relative to untreated controls (=100% cell viability). *Bottom panels.* Representative microscope images (×2.5 magnification) of mammospheres formed by MDA-MB-436 cells growing in sphere medium for 6 days in the absence or presence of graded concentrations of CHEMBL1085246. The number of mammospheres (>100 μm diameter) is expressed as means (columns) ± SD (bars). \*P < 0.05 and \*\*P < 0.005, statistically significant differences from the untreated (control) group.

## Supplementary Tables

Please browse Full Text version to see the data of Supplementary Tables 6 and 7.

**Supplementary Table 1. Docking binding energies and MM/GBSA-based energy rescoring calculations of oleacein against mTOR and DNMT.**

Cavity	Docking $\Delta G$ kcal/mol	MM/GBSA $\Delta G$ kcal/mol	Target / PDBID
Crystallographic cavity	-7.1/-7.1	-26.8226	mTOR / 4JT6
Cavity1	-7.3/-6.9	-17.155	mTOR / 4JT6
Cavity4	-7.6/-7.8	-36.9931	mTOR / 4JT6
Cavity8	-7.4/-7.3	-21.8981	mTOR / 4JT6
Crystallographic cavity	-7.9/-7.6	-30.567	DNMT / 4WXX
Cavity1	-7.7/-7.7	-25.2792	DNMT / 4WXX
Cavity2	-7.2/-7.2	-36.5163	DNMT / 4WXX
Cavity3	-7.3/-7.3	-34.0772	DNMT / 4WXX



Graphical representation of parental oleacein bound to several cavities of mTOR (4JT6, *left*) and DNMT (4WXX, *right*). Oleacein is colored in gold. In the case of mTOR, oleacein poses at cavities 1, 4, and 8, colored in blue, red, and yellow, respectively. In the case of DNMT, oleacein poses at cavities 1, 2, and 3, colored in blue, red, and yellow, respectively.

**Supplementary Table 2. Docking binding energies of oleacein mimetics against the crystallographic cavities of mTOR and DNMT.**

Oleacein mimetic	Target/ PDBID	$\Delta G$ kcal/mol R0 / R1	Target / PDBID	$\Delta G$ kcal/mol R0 / R1
CHEMBL2172394	mTOR / 4JT6	-6.6 / -6.9	DNMT / 4WXX	-6.9 / -7.1
CHEMBL1085246	mTOR / 4JT6	-6.5 / -6.7	DNMT / 4WXX	-7.6 / -7.5
CHEMBL357073	mTOR / 4JT6	-7.3 / -7.2	DNMT / 4WXX	-7.8 / -7.6
CHEMBL1632504	mTOR / 4JT6	-5.9 / -6.0	DNMT / 4WXX	-7.3 / -7.2
CHEMBL126593	mTOR / 4JT6	-6.7 / -6.8	DNMT / 4WXX	-6.8 / -6.8
CHEMBL1950046	mTOR / 4JT6	-6.7 / -6.7	DNMT / 4WXX	-6.7 / -6.7
CHEMBL1440472	mTOR / 4JT6	-6.1 / -6.1	DNMT / 4WXX	-7.0 / -7.0
CHEMBL1300434	mTOR / 4JT6	-6.6 / -6.6	DNMT / 4WXX	-7.5 / -7.5
CHEMBL1890048	mTOR / 4JT6	-6.3 / -6.4	DNMT / 4WXX	-6.8 / -6.8
CHEMBL1180264	mTOR / 4JT6	-6.1 / -6.1	DNMT / 4WXX	-7.3 / -7.4
CHEMBL165714	mTOR / 4JT6	-6.3 / -6.3	DNMT / 4WXX	-7.3 / -7.3
CHEMBL1621113	mTOR / 4JT6	-6.7 / -6.6	DNMT / 4WXX	-7.0 / -7.2

CHEMBL1079062	mTOR / 4JT6	-7.2 / -7.2	DNMT / 4WXX	-7.7 / -7.7
CHEMBL267516	mTOR / 4JT6	-6.6 / -6.7	DNMT / 4WXX	-7.3 / -7.1
CHEMBL154778	mTOR / 4JT6	-8.8 / -8.6	DNMT / 4WXX	-8.1 / -8.1
CHEMBL1366164	mTOR / 4JT6	-6.9 / -6.9	DNMT / 4WXX	-7.4 / -7.4
CHEMBL1642794	mTOR / 4JT6	-7.0 / -7.0	DNMT / 4WXX	-7.6 / -7.6
CHEMBL2165395	mTOR / 4JT6	-6.5 / -6.4	DNMT / 4WXX	-7.3 / -7.3
CHEMBL45196	mTOR / 4JT6	-7.1 / -6.6	DNMT / 4WXX	-8.3 / -8.3
CHEMBL2143987	mTOR / 4JT6	-6.2 / -6.2	DNMT / 4WXX	-6.9 / -7.0

Each calculation was performed twice (R0, R1) to avoid false positives. Differences less than 1 kcal/mol are negligible.

**Supplementary Table 3. Docking binding energies of oleacein mimetics against the best cavity of mTOR and DNMT shared with oleacein.**

Oleacein mimetic	Cavity	Target / PDBID	$\Delta G$ kcal/mol R0 / R1	Cavity	Target / PDBID	$\Delta G$ kcal/mol R0 / R1
CHEMBL2172394	Cavity4	mTOR / 4JT6	-7.8 / -7.8	Cavity3	DNMT / 4WXX	-7.3 / -7.4
CHEMBL1085246	Cavity4	mTOR / 4JT6	-7.6 / -7.4	Cavity2	DNMT / 4WXX	-7.0 / -7.0
CHEMBL357073	Cavity4	mTOR / 4JT6	-7.7 / -7.6	Cavity2	DNMT / 4WXX	-7.4 / -7.6
CHEMBL1632504	Cavity8	mTOR / 4JT6	-6.8 / -6.7	Cavity2	DNMT / 4WXX	-7.2 / -7.0
CHEMBL126593	Cavity1	mTOR / 4JT6	-7.1 / -7.1	Cavity2	DNMT / 4WXX	-6.7 / -6.8
CHEMBL1950046	Cavity4	mTOR / 4JT6	-7.1 / -7.1	Cavity2	DNMT / 4WXX	-6.8 / -6.8
CHEMBL1440472	Cavity8	mTOR / 4JT6	-7.0 / -7.4	Cavity4	DNMT / 4WXX	-7.0 / -7.0
CHEMBL1300434	Cavity8	mTOR / 4JT6	-7.2 / -7.2	Cavity2	DNMT / 4WXX	-7.7 / -7.8
CHEMBL1890048	Cavity4	mTOR / 4JT6	-7.0 / -7.0	Cavity2	DNMT / 4WXX	-6.9 / -6.8
CHEMBL1180264	Cavity8	mTOR / 4JT6	-7.1 / -6.7	Cavity2	DNMT / 4WXX	-7.3 / -7.4
CHEMBL165714	Cavity8	mTOR / 4JT6	-7.2 / -7.4	Cavity1	DNMT / 4WXX	-6.9 / -6.8
CHEMBL1621113	Cavity1	mTOR / 4JT6	-7.0 / -6.5	Cavity2	DNMT / 4WXX	-7.3 / -7.3
CHEMBL1079062	Cavity8	mTOR / 4JT6	-7.3 / -7.5	Cavity2	DNMT / 4WXX	-7.5 / -7.9
CHEMBL267516	Cavity8	mTOR / 4JT6	-7.1 / -7.1	Cavity2	DNMT / 4WXX	-7.2 / -7.1
CHEMBL154778	Cavity4	mTOR / 4JT6	-8.1 / -8.2	Cavity2	DNMT / 4WXX	-8.0 / -7.8
CHEMBL1366164	Cavity4	mTOR / 4JT6	-7.2 / -7.4	Cavity2	DNMT / 4WXX	-7.2 / -7.2
CHEMBL1642794	Cavity1	mTOR / 4JT6	-7.8 / -7.6	Cavity2	DNMT / 4WXX	-7.5 / -7.5
CHEMBL2165395	Cavity8	mTOR / 4JT6	-7.6 / -7.6	Cavity2	DNMT / 4WXX	-7.4 / -7.0
CHEMBL45196	Cavity4	mTOR / 4JT6	-8.4 / -8.0	Cavity1	DNMT / 4WXX	-8.3 / -8.1
CHEMBL2143987	Cavity4	mTOR / 4JT6	-7.1 / -6.8	Cavity3	DNMT / 4WXX	-6.9 / -7.0

Each calculation was performed twice (R0, R1) to avoid false positives. Differences less than 1 kcal/mol are negligible.

**Supplementary Table 4. MM/GBSA-based binding energy rescoring calculations over MD simulations of computationally-predicted oleacein mimetics against the crystallographic cavities of mTOR and DNMT.**

Oleacein mimetic	Target/ PDBID	$\Delta G$ kcal/mol	Target / PDBID	$\Delta G$ kcal/mol
CHEMBL2172394	mTOR / 4JT6	-18.4177	DNMT / 4WXX	-11.8887
CHEMBL1085246	mTOR / 4JT6	-27.4436	DNMT / 4WXX	-17.8140
CHEMBL357073	mTOR / 4JT6	-25.0102	DNMT / 4WXX	-28.4676
CHEMBL1632504	mTOR / 4JT6	-25.7896	DNMT / 4WXX	-38.2609
CHEMBL126593	mTOR / 4JT6	-29.2106	DNMT / 4WXX	-25.7134
CHEMBL1950046	mTOR / 4JT6	-20.2999	DNMT / 4WXX	-24.3167
CHEMBL1440472	mTOR / 4JT6	-16.6468	DNMT / 4WXX	-27.5899
CHEMBL1300434	mTOR / 4JT6	-38.7014	DNMT / 4WXX	-33.3421
CHEMBL1890048	mTOR / 4JT6	-19.6392	DNMT / 4WXX	-26.0912
CHEMBL1180264	mTOR / 4JT6	-18.2272	DNMT / 4WXX	-31.7196
CHEMBL165714	mTOR / 4JT6	-16.1321	DNMT / 4WXX	-12.1247



CHEMBL1621113	mTOR / 4JT6	-22.9663	DNMT / 4WXX	-26.6488
CHEMBL1079062	mTOR / 4JT6	-17.4413	DNMT / 4WXX	-24.2025
CHEMBL267516	mTOR / 4JT6	-27.371	DNMT / 4WXX	-32.8788
CHEMBL154778	mTOR / 4JT6	-30.5493	DNMT / 4WXX	-21.6215
CHEMBL1366164	mTOR / 4JT6	-24.3303	DNMT / 4WXX	-15.4957
CHEMBL1642794	mTOR / 4JT6	-24.1435	DNMT / 4WXX	-16.1264
CHEMBL2165395	mTOR / 4JT6	-19.8235	DNMT / 4WXX	-33.4134
CHEMBL45196	mTOR / 4JT6	-27.2624	DNMT / 4WXX	-24.5175
CHEMBL2143987	mTOR / 4JT6	-32.407	DNMT / 4WXX	-36.4821

**Supplementary Table 5. MM/GBSA-based binding energy rescoring calculations over MD simulations of computationally-predicted oleacein mimetics against against the best cavity of mTOR and DNMT shared with oleacein.**

Oleacein candidate	Cavity	Target / PDBID	$\Delta G$ kcal/mol	Cavity	Target / PDBID	$\Delta G$ kcal/mol
CHEMBL2172394	Cavity4	mTOR / 4JT6	-34.392	Cavity3	DNMT / 4WXX	-31.0757
CHEMBL1085246	Cavity4	mTOR / 4JT6	-19.6725	Cavity2	DNMT / 4WXX	-36.9931
CHEMBL357073	Cavity4	mTOR / 4JT6	-33.5462	Cavity2	DNMT / 4WXX	-34.3628
CHEMBL1632504	Cavity8	mTOR / 4JT6	-24.6272	Cavity2	DNMT / 4WXX	-36.6319
CHEMBL126593	Cavity1	mTOR / 4JT6	-26.6329	Cavity2	DNMT / 4WXX	-35.3592
CHEMBL1950046	Cavity4	mTOR / 4JT6	-31.6794	Cavity2	DNMT / 4WXX	-21.7283
CHEMBL1440472	Cavity8	mTOR / 4JT6	-21.2853	Cavity4	DNMT / 4WXX	-29.360
CHEMBL1300434	Cavity8	mTOR / 4JT6	-27.361	Cavity2	DNMT / 4WXX	-33.9773
CHEMBL1890048	Cavity4	mTOR / 4JT6	-21.2089	Cavity2	DNMT / 4WXX	-26.2952
CHEMBL1180264	Cavity8	mTOR / 4JT6	-29.4140	Cavity2	DNMT / 4WXX	-32.3981
CHEMBL165714	Cavity8	mTOR / 4JT6	-21.4634	Cavity1	DNMT / 4WXX	-30.3770
CHEMBL1621113	Cavity1	mTOR / 4JT6	-21.0309	Cavity2	DNMT / 4WXX	-29.3269
CHEMBL1079062	Cavity8	mTOR / 4JT6	-24.7585	Cavity2	DNMT / 4WXX	-24.4205
CHEMBL267516	Cavity8	mTOR / 4JT6	-44.6454	Cavity2	DNMT / 4WXX	-28.1508
CHEMBL154778	Cavity4	mTOR / 4JT6	-25.0387	Cavity2	DNMT / 4WXX	-22.9832
CHEMBL1366164	Cavity4	mTOR / 4JT6	-17.8085	Cavity2	DNMT / 4WXX	-19.6201
CHEMBL1642794	Cavity1	mTOR / 4JT6	-19.439	Cavity2	DNMT / 4WXX	-20.6555
CHEMBL2165395	Cavity8	mTOR / 4JT6	-27.2639	Cavity2	DNMT / 4WXX	-25.8227
CHEMBL45196	Cavity4	mTOR / 4JT6	-17,1961	Cavity1	DNMT / 4WXX	-32,1555
CHEMBL2143987	Cavity4	mTOR / 4JT6	-40.3344	Cavity3	DNMT / 4WXX	-43.6863

**Supplementary Table 6. Key interacting residues of oleacein mimetics to the catalytic site of mTOR. Interactions other than electrostatic are highlighted in yellow (possible) or green (reliable).**

**Supplementary Table 7. Key interacting residues of oleacein mimetics to the catalytic site of DNMT. Interactions other than electrostatic are highlighted in yellow (possible) or green (reliable).**

## Targeting FTO for cancer therapy and more

Ying Qing, Rui Su, Jianjun Chen

Cancer is considered an age-related disease as the incidence rate of cancer rises with advancing age: in the United States, 80% of all cancer cases are diagnosed in the population aged 55 years and older [1]. Patients with advanced age tend to present with poorer performance status and have a worse prognosis for multiple types of cancer, including acute myeloid leukemia (AML), glioblastoma, breast cancer, and pancreatic cancer. Particularly, age is an independent prognostic factor in AML, and elderly patients are more vulnerable to treatment toxicities and have a much higher rate of developing multidrug resistance (57% - 62% for AML patients older than 56 years compared to 33% for AML patients younger than 56 years) [2]. Therefore, there is an urgent need for novel targeted therapeutics with minimal toxicity that can overcome drug resistance to improve the clinical outcomes in elderly cancer patients.

The epitranscriptional modification *N*<sup>6</sup>-Methyladenosine (m<sup>6</sup>A), the most abundant internal mark of eukaryotic mRNAs, plays critical roles in cancer development and is characterized by its reversibility and susceptibility to external regulation [3]. m<sup>6</sup>A is installed by “writers” (methyltransferases) and removed by “erasers” (demethylases), with m<sup>6</sup>A “readers” (m<sup>6</sup>A-binding proteins) responsible for recognizing the m<sup>6</sup>A-modified sites on target transcripts to mediate the downstream biological consequences. As the first identified m<sup>6</sup>A demethylase, FTO  $\alpha$ -ketoglutarate dependent dioxygenase (*FTO*) has been reported to be highly expressed in certain AML subtypes, and promotes pro-survival signaling as well as blocks myeloid differentiation by targeting a set of genes such as *ASB2*, *RARA*, *MYC* and *CEBPA* in an m<sup>6</sup>A-dependent way [4, 5]. Moreover, FTO positively regulates the glycolytic genes *PFKP* and *LDHB* to maintain aerobic glycolysis in leukemia cells [6]. *FTO* also serves as an oncogene in various solid tumors where it is aberrantly overexpressed, including glioblastoma, breast cancer, and pancreatic cancer [3]. The experimental evidences that knockdown of *FTO* effectively suppresses tumor progression, attenuates cancer cell metabolism, and improves the response of cancer cells to drug treatment strongly suggest FTO to be a promising therapeutic target for cancer treatment in elderly patients [4, 6]. Based on these data, increased efforts have been made for the discovery of effective small-molecule FTO inhibitors. However, most previously discovered FTO

inhibitors, although shown to be a potential therapeutic strategy for AML and solid tumors, only demonstrate mild/moderate efficacy and/or selectivity in inhibiting FTO (with their IC<sub>50</sub> values higher than 1  $\mu$ M), and are therefore unlikely clinically applicable (Figure 1).

Most recently, Su et al. identified two highly efficacious small-molecule FTO inhibitors, i.e., CS1 (or Bisantrone) and CS2 (or Brequinar), which display potent *in vitro* and *in vivo* anti-tumor effects in both AML and solid tumors in which *FTO* is highly expressed (including glioblastoma, breast cancer, and pancreatic cancer) [7]. By blocking the catalytic pocket and disrupting the binding of FTO to m<sup>6</sup>A modified targets, CS1 and CS2 inhibit FTO activity and signaling. The IC<sub>50</sub> values for both CS1 and CS2 are in the low nanomolar range, indicating that they are much more effective than previously discovered FTO inhibitors. Importantly, treatment with CS1 or CS2 induced minimal drug toxicity in C57BL/6 mice, even at a dose 4-fold higher than that used for cancer treatment. Since elderly cancer patients are generally less tolerant to chemotherapy and have a greater risk of drug toxicity, these FTO-targeting compounds provide a potential alternative treatment for the chemotherapy-intolerant elderly patients. Hypomethylating agents (HMAs) are also commonly used in frontline therapy for elderly AML patients unfit for intensive chemotherapy. However, most HMA-treated patients eventually develop drug resistance as a result of upregulation of immune checkpoint gene expression and subsequent immune evasion. CS1 and CS2 treatments sensitize AML cells to T cell cytotoxicity by suppressing the expression of immune checkpoint gene *LILRB4*, supporting FTO inhibition as an effective strategy to overcome immune evasion induced by HMAs (Figure 1). Pharmacological inhibition of FTO with the two compounds or genetic depletion of FTO also leads to a remarkable decrease in self-renewal capacity of the leukemia stem/initiating cells (LSCs/LICs), the major population considered to be responsible for treatment failure and disease relapse in AML (Figure 1). Hence, potent small-molecule FTO inhibitors (represented by CS1 and CS2) hold great therapeutic potential, alone or in combination with other agents such as HMAs, for the treatment of refractory and relapsed cancer in elderly patients.

The *FTO* gene is also the first genome-wide association study (GWAS)-identified locus that harbors the strongest

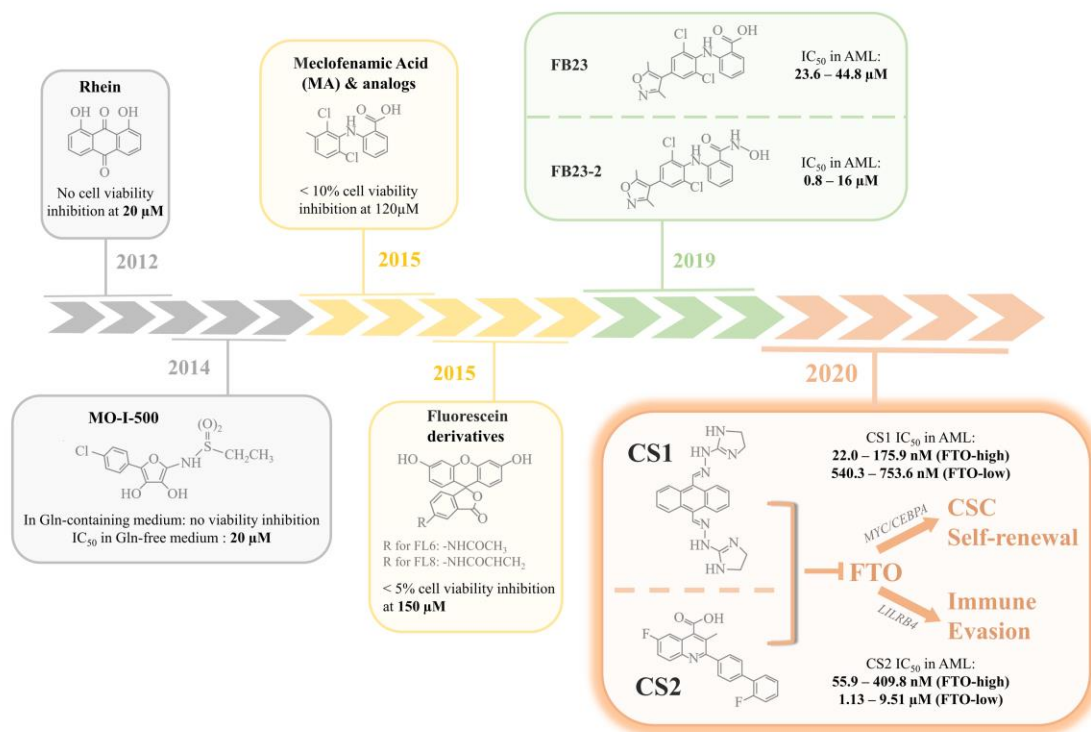


**Figure 1. Evolutional landmarks in FTO inhibitor discovery.** Rhein, the first FTO inhibitor identified in 2012, did not impair viability in BE(2)-C neuroblastoma cells at a dose of 20  $\mu\text{M}$ . MO-I-500, an inhibitor discovered in 2014, was found to inhibit survival of SUM149 breast cancer cells in glutamine (Gln)-free medium with an  $\text{IC}_{50}$  of 20  $\mu\text{M}$ , but had little effect on cells cultured in complete medium. Meclofenamic acid (MA) and its analogs were reported to be highly selective inhibitors of FTO. However, more than 90% of the Hela cells treated with 120  $\mu\text{M}$  MA2 (an MA analog) remained viable. Fluorescein and its derivatives could simultaneously inhibit and label FTO and were therefore considered “bifunctional”. At a concentration of up to 150  $\mu\text{M}$ , fluorescein derivatives FL6 and FL8 did not display inhibitory effects on Hela cells with > 95% viable cells. In 2019, guided by the structural complex of FTO/MA, FB23 and FB23-2 were designed and optimized as two more potent FTO inhibitors. But the  $\text{IC}_{50}$  for both inhibitors in acute myeloid leukemia (AML) were still in the micromolar range (23.6 – 44.8  $\mu\text{M}$  for FB23 and 0.8 – 16  $\mu\text{M}$  for the optimized FB23-2). In contrast, the most recently discovered small molecule FTO inhibitors, CS1 and CS2, have much lower  $\text{IC}_{50}$  values in AML and solid tumors, especially in cancer cells that highly express FTO (in the low nanomolar range). CS1 and CS2 exert their anti-tumor activity by suppressing the FTO-mediated upregulation of *MYC/CEBPA* as well as *LILRB4*, thereby attenuating cancer stem cell (CSC) self-renewal and overcoming tumor immune evasion.

genetic association with obesity. Although controversy exists, multiple lines of evidences support a positive relationship between *FTO* expression and the development of obesity [8]. With the continuous expansion of the obesity and overweight populations especially in the elderly, the effects of small-molecule FTO inhibitors on obesity development represent another major area of scientific inquiry to explore whether multiple health benefits (i.e. prevention of cancer and obesity/overweight) can be achieved concomitantly by targeting FTO.

## REFERENCES

1. Siegel RL, et al. CA Cancer J Clin. 2021; 71:7–33. <https://doi.org/10.3322/caac.21654> PMID:33433946
2. Appelbaum FR, et al. Blood. 2006; 107:3481–85. <https://doi.org/10.1182/blood-2005-09-3724> PMID:16455952
3. Huang H, et al. Cancer Cell. 2020; 37:270–88. <https://doi.org/10.1016/j.ccell.2020.02.004> PMID:32183948
4. Li Z, et al. Cancer Cell. 2017; 31:127–41. <https://doi.org/10.1016/j.ccell.2016.11.017> PMID:28017614
5. Su R, et al. Cell. 2018; 172:90–105.e23. <https://doi.org/10.1016/j.cell.2017.11.031> PMID:29249359
6. Qing Y, et al. Mol Cell. 2021; 81:922–939.e9. <https://doi.org/10.1016/j.molcel.2020.12.026> PMID:33434505

7. Su R, et al. Cancer Cell. 2020; 38:79–96.e11.  
<https://doi.org/10.1016/j.ccell.2020.04.017>  
PMID:[32531268](https://pubmed.ncbi.nlm.nih.gov/32531268/)
8. Deng X, et al. Front Endocrinol (Lausanne). 2018; 9:396. <https://doi.org/10.3389/fendo.2018.00396>  
PMID:[30105001](https://pubmed.ncbi.nlm.nih.gov/30105001/)

**Jianjun Chen:** Department of Systems Biology, Beckman Research Institute of City of Hope, Monrovia, CA 91016, USA

**Correspondence:** Jianjun Chen

**Email:** [jjanchen@coh.org](mailto:jjanchen@coh.org)

**Keywords:** glioblastoma, temozolomide, extended, age, survival

**Conflicts of Interest:** J.C. is a scientific founder of Genovel Biotech Corp. and holds equities with the company, and he is also a Scientific Advisor for Race Oncology.

**Copyright:** © 2021 Qing et al. This is an open access article distributed under the terms of the [Creative Commons Attribution License](https://creativecommons.org/licenses/by/3.0/) (CC BY 3.0), which permits unrestricted use, distribution, and reproduction in any medium, provided the original author and source are credited

**Received:** July 5, 2021

**Published:** August 11, 2021

# Impact of aging on primary liver cancer: epidemiology, pathogenesis and therapeutics

Rocio I.R. Macias<sup>1,5</sup>, Maria J. Monte<sup>1,5</sup>, Maria A. Serrano<sup>1,5</sup>, Jesús M. González-Santiago<sup>2</sup>, Isabel Martín-Arribas<sup>2</sup>, André L. Simão<sup>3</sup>, Rui E. Castro<sup>3</sup>, Javier González-Gallego<sup>4,5</sup>, José L. Mauriz<sup>4,5</sup>, Jose J.G. Marin<sup>1,5</sup>

<sup>1</sup>Experimental Hepatology and Drug Targeting (HEVEPHARM) Group, University of Salamanca, IBSAL, Salamanca, Spain

<sup>2</sup>Department of Gastroenterology and Hepatology, University Hospital of Salamanca, IBSAL, Salamanca, Spain

<sup>3</sup>Research Institute for Medicines (iMed.Ulisboa), Faculty of Pharmacy, Universidade de Lisboa, Lisbon, Portugal

<sup>4</sup>Institute of Biomedicine (IBIOMED), University of León, León, Spain

<sup>5</sup>Centro de Investigación Biomédica en Red de Enfermedades Hepáticas y Digestivas (CIBERehd), Carlos III National Institute of Health, Madrid, Spain

**Correspondence to:** Rocio I.R. Macias, Jose J.G. Marin; **email:** [rociorm@usal.es](mailto:rociorm@usal.es), [jigmarin@usal.es](mailto:jigmarin@usal.es)

**Keywords:** aging, cholangiocarcinoma, fragility, hepatocarcinoma, senescence

**Received:** May 24, 2021

**Accepted:** September 28, 2021

**Published:** October 11, 2021

**Copyright:** © 2021 Macias et al. This is an open access article distributed under the terms of the [Creative Commons Attribution License](https://creativecommons.org/licenses/by/3.0/) (CC BY 3.0), which permits unrestricted use, distribution, and reproduction in any medium, provided the original author and source are credited.

## ABSTRACT

Aging involves progressive physiological and metabolic reprogramming to adapt to gradual deterioration of organs and functions. This includes mechanisms of defense against pre-malignant transformations. Thus, certain tumors are more prone to appear in elderly patients. This is the case of the two most frequent types of primary liver cancer, i.e., hepatocellular carcinoma (HCC) and intrahepatic cholangiocarcinoma (iCCA). Accordingly, aging hallmarks, such as genomic instability, telomere attrition, epigenetic alterations, altered proteostasis, mitochondrial dysfunction, cellular senescence, exhaustion of stem cell niches, impaired intracellular communication, and deregulated nutrient sensing can play an important role in liver carcinogenesis in the elders. In addition, increased liver fragility determines a worse response to risk factors, which more frequently affect the aged population. This, together with the difficulty to carry out an early detection of HCC and iCCA, accounts for the late diagnosis of these tumors, which usually occurs in patients with approximately 60 and 70 years, respectively. Furthermore, there has been a considerable controversy on what treatment should be used in the management of HCC and iCCA in elderly patients. The consensus reached by numerous studies that have investigated the feasibility and safety of different curative and palliative therapeutic approaches in elders with liver tumors is that advanced age itself is not a contraindication for specific treatments, although the frequent presence of comorbidities in these individuals should be taken into consideration for their management.

## INTRODUCTION

During the last decades, there has been a marked increase in life expectancy in most developed countries. The consequence is that the population is aging in these geographical areas. For instance, in early 2018, about 20% of the total population in the European Union had

more than 65 years. This proportion is expected to reach 28.5% in 2050 [1], and a similar demographic evolution is expected to occur in the US and other developed countries. It is well-known that elders have an increased risk of developing chronic diseases, including some cancers. Primary liver cancer is the sixth most common cancer worldwide, with 80% of cases being diagnosed



among patients who are 70 years or older, and it is the third leading cause of cancer-related death worldwide according to the WHO. Approximately, 85-90% of these cancers are hepatocellular carcinoma (HCC), which is currently the third cancer-related cause of death in men worldwide, and its incidence is regularly increasing [2]. Besides, intrahepatic cholangiocarcinoma (iCCA) accounts for 10-15% of all primary liver cancers, and the number of newly diagnosed cases per year is also rising [3], although its incidence rate has important geographical variations, reflecting local differences in risk factors [4]. The increasing incidence of liver cancer is partially attributable to the increase in morbidities commonly associated with aging, such as diabetes mellitus, alcoholic liver disease, and non-alcoholic fatty liver disease [3].

Aging is characterized by cellular senescence caused by the shortening of telomeres in successive cell divisions, which leads to a halt in the proliferation of somatic cells. Several processes such as DNA damage, epigenetic alteration, oxidative stress, mitochondrial dysfunction, and alteration of metabolic pathways can contribute to the senescence of cells and tissues and, at the same time, account for higher risk of liver cancer development [5].

The main challenge in managing the growing number of elderly patients who have liver cancer is their frequent multimorbidity and hence the associated simultaneous use of several types of drugs that can result in drug-drug interactions interfering with cancer treatment. Besides, a decline in the functional reserve of several organs and the fact that the metabolism is often altered reduces the tolerance. Moreover, it can produce or aggravate adverse drug reactions [6]. Although a personalized treatment is always desirable, this is particularly required in the case of elderly patients. After evaluating their individual characteristics, the treatment must include proper monitoring in order to guarantee an adequate treatment intensity while preventing or minimizing the occurrence of adverse events and a deterioration of quality of life due to treatment [7].

The concept of elderly patients has changed over time, complicating the analysis of results published at different times. The most recent studies use as cut-off age of the elderly 75 or even 80 years, while some time ago patients more than 65 years old were included in the group of older patients and some guidelines still use this cut-off [8]. Despite these differences, most studies have shown that advanced age alone should not be a reason to dismiss the oncological evaluation for any treatment in the first place. Still, the treatment of elderly requires that, prior to designing the therapeutic strategy, oncologists carefully consider age-related comorbidities.

## Age-associated risk factors

The risk of CCA, either iCCA, distal (dCCA), or perihilar (pCCA) increases with advancing age, especially in Japan and Western countries where, without the specific risk factors of certain regions, patients present an average age at diagnosis of approximately 70, which is ten years older than the average age for patients first diagnosed with HCC [9, 10]. A recent study analyzing cancer mortality in elderly patients showed that liver cancer mortality rates were similar in most countries, with a peak of 60 per 100,000 or below for men and 25 per 100,000 or below for women in the 80-to-84 range of age. Exceptionally, these values were higher in Japan [11].

Clinical characteristics are different in elderly *versus* young HCC patients (Table 1). Elderly patients with HCC are mainly female, which has been associated with their longer life expectancy, while younger patients are predominantly male [12]. Hepatitis B virus (HBV) infection is the most frequent etiology in young HCC patients, probably because the transmission mainly occurs in the perinatal period. In contrast, the most prevalent causes of HCC in elderly patients are chronic infection with hepatitis C virus (HCV) and non-alcoholic steatohepatitis (NASH), which usually occurs later in life. The effects of alcohol consumption and HCV infection on the development of HCC appear to be stronger with advancing age, but also moderate alcohol consumption throughout life can cause HCC in the elderly [13]. In the upcoming years, due to the improvement of antiviral treatments, HCV infections are expected to decrease worldwide. In contrast, due to the predicted increased incidence of non-alcoholic fatty liver disease (NAFLD) -recently termed metabolic associated fatty liver disease (MAFLD)- predisposing for NASH, a significant growth in the number of cases of elderly patients with HCC and NASH can be predicted.

MAFLD refers to liver steatosis in addition to overweight or obesity, diabetes mellitus type 2 or metabolic dysregulation [14]. The number of studies in aging patients analyzing the relationship between MAFLD and primary liver cancer remains still limited and are mainly focused on HCC. An US study of cohorts across a 6-year period (2004 to 2009) showed a 9% annual increase on the number of NAFLD patients with HCC. NAFLD-HCC patients were older than HCC patients with other underlying diseases (73.0 years *vs.* 66.0 years), with a shorter survival time and death was more often as consequence of this primary liver cancer [15]. Similarly, the increased incidence rate of HCC between 2003 and 2011 was associated with an elevated prevalence of NAFLD in Taiwanese patients older than 65 years [16]. In addition, in U.K., patients with NAFLD-

associated HCC were older than those with other HCC etiologies (71.3 years vs 67.1 years), being liver tumors less often detected by clinical surveillance, although their survival was comparable [17]. It has been proposed a potential relationship between NAFLD and iCCA, which suggests a common pathogenesis with HCC [18, 19], however, no clear association between aging and MAFLD has already been established in this cancer.

The fact that women seem to be less prone to suffer from some liver pathologies, such as MAFLD, until post-menopausal ages, having a “lag period” when compared to male [20] can also contribute to the higher incidence in more advance age. Thus, a Taiwanese study concluded that NAFLD could constitute a possible risk factor associated to the upward trend in HCC incidence in elderly women [16]. Moreover, it has been described that depletion of cholesterol synthesis by *Cyp51* knock-out leads to HCC progression in aging female mice, indicating that sex-dependent metabolic reprogramming of cholesterol metabolism can predispose for hepatocarcinogenesis in aging females [21]. Recently, estradiol has been related to prognosis in non-surgical HCC patients leading to a better mean survival probability in women than men, but this effect is reduced after menopause. *In vitro* studies have demonstrated that estradiol is able to inhibit the proliferation of HCC cell lines [22]. Besides, it has been reported that post-menopausal hormone replacement therapy plays a protective role in HCC [23, 24]. Contrarily, high circulating levels of estradiol, commonly found in male iCCA patients, have been associated with an increased risk of this type of primary tumor in both men and women [25, 26]. Additionally, long-term oral contraceptive use and hysterectomy have been associated with increased iCCA risk (+62% and +100%, respectively) in non-menopausal women compared with women 50-54 years old at natural menopause, although no association was detected with age at natural menopause [27]. Due to the different role of estrogens in HCC and iCCA female patients, it is necessary to design adequate and specific therapeutical strategies against these types of primary liver cancer both in young and aging women.

Southeastern Asia and particularly Thailand present high incidence rates of iCCA mainly due to liver fluke infection [28], however, there is no available information regarding whether this or other risk factors affect young and older people differently.

The study of different comorbidities depending on the age and gender in patients with HCC revealed that, as could be predicted, elderly patients suffered from more comorbidities [29]. Cirrhosis was the most common condition both in young and older patients, followed by

HBV in patients aged <70 years and HCV in patients  $\geq 70$  years. The older group of HCC patients also showed a higher proportion of chronic diseases such as hypertension, diabetes mellitus, coronary disease and cerebral infarction and a worse quality of life.

In elders, HCC has lower accompanying fibrosis than in younger patients and it is usually diagnosed as single nodules and of larger size, which has been associated with lack of surveillance in patients without risk factors [30]. Moreover, HCC nodules are more frequently well-differentiated, encapsulated, and without vascular invasion [31].

## Hallmarks of aging and hepatocarcinogenesis

Hepatocarcinogenesis comprises a multistep process resulting in the malignant transformation of liver cells followed by tumor progression. Several common and critical cellular features considered “hallmarks of aging”, such as genomic instability, telomere attrition, epigenetic alterations, impairment of proteostasis, mitochondrial dysfunction, cellular senescence, exhaustion of stem cell niches, altered intracellular communication, and deregulated nutrient sensing [32] may play a crucial role in age-related hepatocarcinogenesis (Figure 1).

## Genomic instability

Liver fibrosis and its end-stage liver disease, cirrhosis, typically show persistent hepatocyte death and compensatory regeneration, chronic inflammation, and increased production of reactive oxygen species (ROS) [33]. All together, these features collaboratively create a pro-oncogenic microenvironment through induction of genetic alterations and chromosomal instability and by activating several oncogenic signaling pathways [34]. Genes involved in HCC pathogenesis have been classified into four major groups: i) genes regulating DNA damage response (e.g., p53); ii) genes involved in cell cycle control (e.g., RB1, p16INK4A, and cyclin D); iii) genes involved in growth inhibition and apoptosis (e.g., *M6P/IGF2R*, *SMAD2*, and *SMAD4*); and iv) genes responsible for cell-cell interaction and signal transduction (e.g., APC,  $\beta$ -catenin, and E-cadherin) [35].

The p53 tumor-suppressor gene responds to diverse stress signals by orchestrating specific cellular responses, including transient cell cycle arrest, cellular senescence, and apoptosis. Recent studies highlight emerging roles for p53 in modulating other cellular processes, including metabolism, stem cell maintenance, invasion, and metastasis [36]. Mutations altering p53 function, together with other cooperating events, might serve to drive alterations in the cell cycle as major defects in HCC. The most frequent mutation in the *TP53* gene consists in a

**Table 1. Characteristics of hepatocellular carcinoma in elderly compared with younger patients.**

Characteristic	Elderly	Young	Ref.
Gender	Female > Male	Male > Female	[12]
Etiology	HCV > NASH	HBV	[13]
Comorbidities	Cirrhosis, HCV Hypertension, diabetes, coronary disease, cerebral infarction	Cirrhosis, HBV	[29]
Tumors	Few nodules, big size	Multiple nodules, small size	[30, 31]
	Well-differentiated	Poorly differentiated	
	Infrequent vessel invasion	Frequent vessel invasion	
Liver fibrosis	Severe	Moderate	

HBV, hepatitis B virus; HCV, hepatitis C virus; NASH, non-alcoholic steatohepatitis.

single base substitution, which results in the substitution of arginine for serine (p53-R249S). This represents the predominant hotspot mutation identified in 34% of all detected mutations in HCCs and is the most frequent mutation (96%) of these found in high-risk regions [37]. No significant association between the presence of *TP53* mutations and age, gender, AFP level, Child-Pugh grade, tumor size, or TNM stage has been found [37].

One primary driver of HCC is the Wnt/ $\beta$ -catenin signaling pathway. Mutations targeting its components are frequent in HCC (15-33%). Activating mutations in the *CTNNB1* gene, which encodes for  $\beta$ -catenin, are

widespread in patients with well-differentiated tumors and are increased in elderly people [38]. *CTNNB1* mutations in HCC significantly co-exist with other genetic aberrant changes, such as overexpression of *MET* and *MYC* and mutations in *TERT* promoter, as well as in *NFE2L2/KEAP1*, *APOB*, and *ARID2* genes. Inactivating mutations or deletions are also frequently identified in *AXIN1* (10% of HCC), and more rarely in *APC* (1–2% of HCC) and *ZNRF3* (3% of HCC), resulting in activation of the Wnt/ $\beta$ -catenin pathway [39]. Despite the early occurrence of mutations targeting Wnt signaling components, membrane localization of  $\beta$ -catenin has been described as a dominant feature of HCC until advanced stages of the disease. At the plasma

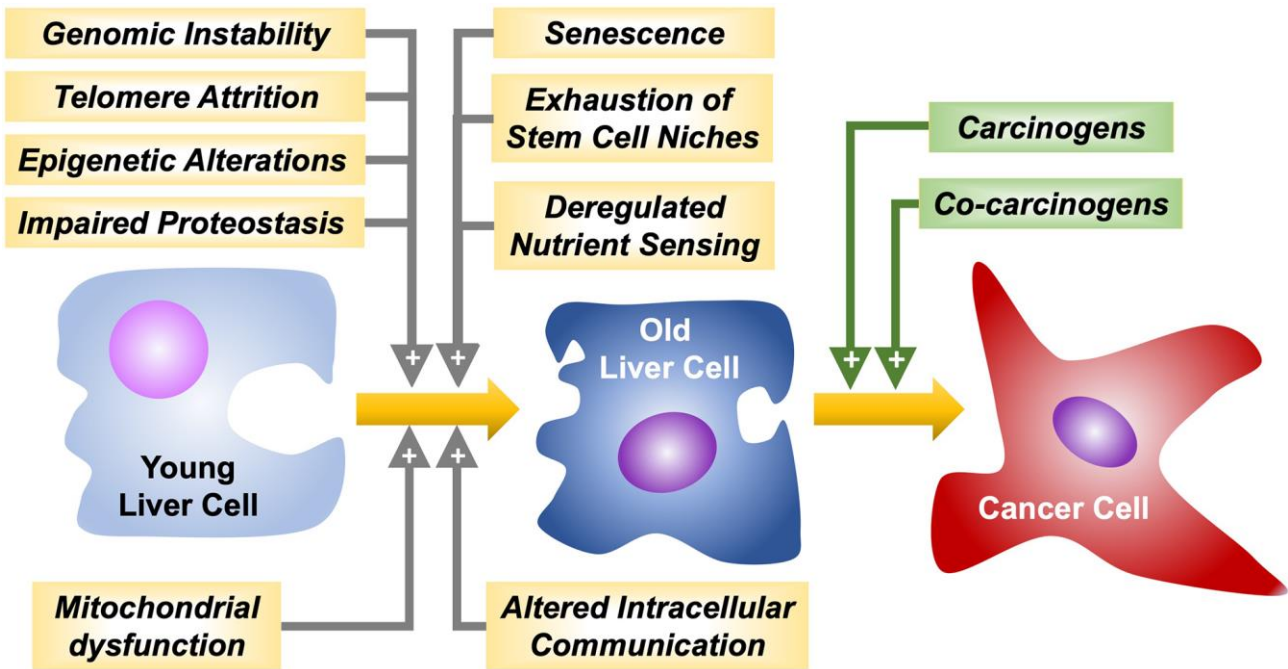


**Figure 1. Hallmarks of aging favoring liver cancer cells malignant transformation and progression by carcinogens and co-carcinogens, respectively.**

membrane,  $\beta$ -catenin interacts with multiple cadherin family members to enhance the signaling of growth factor receptors such as the epidermal growth factor receptor (EGFR). In the context of HCC, adherent junction complex disruption impairs EGFR stability to promote and support HCC cell survival. However, EGFR inhibition is not always detrimental for tumor progression as the significant level of acute tumor cell death associated with EGFR inhibition induces compensatory HCC proliferation [40]. This paradoxical mechanism of tumor progression upon  $\beta$ -catenin deficiency has been partly elucidated by establishing the connection between the adherent junction complex and EGFR signaling in HCC [41]. Moreover, patients with HCC harboring deficient levels of  $\beta$ -catenin or enhanced mutations show high rates of genomic instability, as detected by their higher frequency of loss of heterozygosity [42]. These findings suggest that abrogation of the Wnt signaling pathway could represent a divergent route to hepatocarcinogenesis. Interestingly, during aging there is a progressive deterioration in the control of the Wnt/ $\beta$ -catenin pathway affecting liver homeostasis [43].

Chromosomal instability emerges at an early stage during hepatocarcinogenesis, resulting in the acquisition of a malignant phenotype. Using complementary techniques, frequent loss and gain of chromosomal loci in HCC have been identified [44–47]. The loss of heterozygosity is an essential mechanism for the inactivation of tumor suppressor genes [48]. Allelic loss on 8p have been observed in high-grade dysplastic nodules, indicating that these deletions might occur in the early stage of hepatocarcinogenesis [49]. A high frequency of loss of heterozygosity and deletions of alleles on 8p22-p23 have been associated with metastasis and poor prognosis in HCC patients [50]. Besides, loss of 4q has been more frequently found in poorly differentiated HCC [51], which suggests that the inactivation of tumor suppressor genes on chromosome 4q, such as *ING2* (located at 4q34.3-35) [52], might be an important event that occurs during HCC progression after malignant transformation.

One particular characteristic of hepatocytes is the polyploid nature of many of these cells [53]. Changes in hepatocyte ploidy occur during liver injury and regeneration. Hepatocyte ploidy increases both with the aging process and in chronic diseases where proliferation is induced to compensate for ongoing loss of liver tissue [54]. Polyploidy is also a common feature in tumorigenesis, found in more than one third of human cancers [53]. However, in contrast to other tissues, in the liver polyploidy appears to protect from tumorigenesis. Thus, liver tumors arise mostly from poorly polyploid, mostly diploid, hepatocytes. In different carcinogen-

driven models, higher polyploidy reduces the likelihood of HCC development, which has been attributed to the increased copy numbers of tumor suppressor genes, such as p53, in polyploid cells [55].

### Telomere attrition

Telomeres shorten during aging due to the end replication inefficiency of DNA polymerase, which accounts for incomplete DNA replication [56]. Nevertheless, mechanisms for telomere maintenance exist, such as transcriptional activation of telomerase, a telomere reverse transcriptase. This holoenzyme consists of two essential components, telomerase RNA (TERC) and telomere reverse transcriptase (TERT), which is the catalytic component undertaking synthesis of telomeric sequences using TERC as a template. TERC is constitutively expressed in normal somatic cells, whereas TERT expression is epigenetically suppressed and acts as a limiting factor for telomerase activity in most human cells [57]. However, 85-95% of all cancer cells have enhanced telomerase activity due to TERT up-regulation [58, 59].

The telomere hypothesis of cellular aging suggests that during senescence telomeres reach a critically short length and lose capping function [60]. This provides a rational explanation for the limited regenerative reserve of liver cells at the senescent stage. Besides, short telomeres correlate with the development of cancer and its malignant progression [61]. Indeed, most cancers exhibit shorter telomeres compared to the surrounding non-cancerous tissue [62, 63]. The appearance of mutations affecting the *TERT* promoter has been identified as an early event, and as the most frequent somatic mutation in HCC found in 60% of cases arising either from cirrhotic or normal liver [64]. Mutations affecting *TERT* promoter and other classical driver genes, such as *TP53* (cell cycle), *CTNNB1*, *AXIN1* (Wnt signaling), *ARID1A*, *ARID2* (chromatin remodeling), *RPS6KA3*, *NFE2L2*, *KRAS*, *PIK3CA*, *CDKN2A*, *CCND1/FGF19*, and *VEGFA* are found only in HCC and not in dysplastic nodules [65, 66]. All these genes play a crucial role in a cooperative or mutually exclusive manner in regulating *TERT* expression and telomere length [67]. Nevertheless, alternative mechanisms have been suggested [68]. Recent studies have demonstrated that aging, liver fibrosis, male gender, and excessive alcohol consumption are independent determinants of liver telomere attrition, which is associated with specific clinical and molecular features of HCC [69]. Dysregulated signaling pathways and the role of various mutations in telomere shortening and reactivation of telomerase during carcinogenesis both in HCC and ICCA have been recently reviewed [70].



## Epigenetic alterations

Enzymes with “writer” (DNA methyltransferases, histone acetylases, and histone methyltransferases) and “eraser” (DNA-demethylases, histone deacetylases, and histone-demethylases) function are responsible for transferring or removing chemical groups to or from DNA and histones. On the other hand, methyl-CpG binding domain proteins and other binding proteins act as “readers” recognizing methyl-CpGs and modified histones. These epigenetic events change the expression of genes involved in aging and liver carcinogenesis [71].

DNA methylation (mainly involving CpG islands in the promoter region of genes), together with hypoacetylated and hypermethylated histones, accounts for gene silencing and has been considered a biomarker of human aging rate [72]. Whereas methylation of CpGs in promoter regions has been associated with the repression of tumor suppressor genes, the same process occurring within gene bodies has been linked to oncogene induction in tumors [73]. DNA methylation is also globally altered in HCC, and aberrant modifications are associated with poorer prognosis [74]. As commented above, mutations in *CTNNB1* are frequent in HCC, and this oncogene was recently described as a key modulator in DNA methylation by increasing CpGs hypermethylation rate during aging (+0.32% per year on average) [38]. Moreover, methylation in the promoter region of tumor suppressor genes is crucial during the early stages of carcinogenesis. It has been demonstrated that oxidative stress alters the chromatin status, which leads to abnormal methylation of promoters in tumor suppressor genes, hence contributing to hepatocarcinogenesis [75]. As these alterations are potentially reversible, epigenome-targeted therapy has become a promising strategy for the treatment of cancer [76].

Post-translational histone modifications affect tumorigenesis by modulating chromatin plasticity, genomic instability, cellular senescence, and triggering the expression of genes involved in pathways promoting carcinogenesis [77]. The interplay between large histone variants and the epigenetic alterations that characterize HCC onset has been identified in HCC cell lines. Thus, protein levels of both variants of macroH2A1 (macroH2A1.1 and macroH2A1.2), an isoform of histone H2A, are increased in the livers of elderly rodents and humans and are robust immunohistochemical markers of human cirrhosis and HCC. In response to the chemotherapeutic and DNA-demethylating agent 5-aza-deoxycytidine, transgenic expression of macroH2A1 isoforms in HCC cell lines prevented the emergence of a senescent-like phenotype and induced synergistic global DNA hypomethylation [78].

Chromatin remodeling complexes are also frequently altered in HCC. These alterations include mutations in the *BRG1*-associated factors (*BAFs*) and polybromo-associated BAF (*PBAF*) chromatin complex, specifically in AT-rich interaction domain 1A (*ARID1A*; 4–17% of cases) and in *ARID2* (3–18% of cases) [38]. Histone methyltransferase *SETDB1* overexpression in HCC promotes cancer cell growth via p53 methylation and is associated with tumor aggressiveness and a poor prognosis [79].

## Impaired proteostasis

Protein homeostasis or proteostasis involves mechanisms for the stabilization of correctly folded proteins and mechanisms for the degradation of proteins by the proteasome and the lysosomes that are affected during aging [80, 81]. A conserved feature of aging across tissues, which is a crucial component of the proteostasis network, is defective autophagy. In the liver, this event is secondary to defects in intracellular trafficking of lysosomes [82].

Proteostasis and redox homeostasis constitute interconnected branches of cellular metabolism [83]. Aging is associated with perturbed stress response and repair pathways that gradually decline. The result is increased oxidative stress that induces DNA damage, disruption of proteostasis, and altered mitochondrial function [84]. Proteomic and metabolomic profiling are essential methods to enable the characterization of the system-wide molecular changes during aging and hepatocarcinogenesis. Moreover, both HCC and its treatment induce changes in liver cell proteostasis. For instance, sorafenib inhibits mRNA translation, which might constitute an adaptive stress response in HCC cells, because it protects cancer cells from ferroptosis, a form of oxidative necrosis [83].

Chaperone-mediated autophagy (CMA) is a cellular process that contributes to protein quality control. Through this mechanism, a subset of cytosolic proteins is recognized by the chaperone hsc70 that delivers them one-by-one through LAMP-2A to lysosomes for their degradation [85]. In *LAMP-2A* knockout mice, the gradual decline in protein quality control during aging reduces stress resistance and alters metabolic homeostasis, contributing to hepatocyte dysfunction and favoring malignant transformation [86].

## Mitochondrial dysfunction

Aging-associated mitochondrial dysfunction is accompanied by increased ROS, which in turn causes further mitochondrial deterioration and global cellular damage. This has detrimental effects on hepatocyte



bioenergetics leading to oxidative stress, endoplasmic reticulum stress, inflammation, and cell death. Thus, in the progression from NASH to HCC, metabolic stress results in incomplete  $\beta$ -oxidation, impaired ketogenesis, reduced mitochondria respiratory chain activity, and ATP production, coupled with overactive tricarboxylic acid cycle. These metabolic changes favor DNA damage, the appearance of mutations, which together with the escape from cell cycle checkpoints results in enhanced risk of carcinogenesis [87].

Caspase-2 has both apoptotic and non-apoptotic functions in stress response pathways, maintaining genomic integrity, tumor suppression and aging. Progressive impaired function of this caspase is involved in age-related metabolic reprogramming, mitochondria function, and the early progression of aging [88]. In mice, the loss of caspase-2 function in older animals accelerates age-dependent alterations in mitochondrial ROS production [89]. Moreover, caspase-2-deficient mice are more susceptible to genomic instability due to their hampered ability to respond to DNA damage. Consequently, under oncogenic stress induced by diethylnitrosamine, their liver contains more damaged cells resulting in accelerated tumorigenesis [90].

### Other hallmarks of aging

The escape of hepatocytes from the senescent state is considered one primary mechanism involved in HCC development [91]. Other hallmarks of aging, such as exhaustion of stem cell niches, altered intracellular communication, and deregulated nutrient sensing, can also play a role in liver carcinogenesis. Thus, since hepatocytes play a central role in regulating the systemic response to nutrition, age-related changes in the nutrient-sensing pathways in the liver, such as insulin/IGF-1, mTOR, and sirtuins have been reported to contribute to HCC development [92, 93].

### Considerations regarding the treatment of elderly patients

Several years ago, elderly patients with liver tumors received more conservative treatments than younger patients, and, consequently, they had poorer survival [94]. However, it has been more recently accepted that the overall management strategy in the elder should not be different from that of younger patients [95]. Numerous studies have investigated the feasibility and safety of other curative (Table 2) and palliative (Table 3) therapeutic approaches in elderly patients with liver tumors, and all of them agree that advanced age itself is not a contraindication for specific treatments.

### Curative treatments

Surgical resection of the tumor is the treatment of choice in liver cancer patients diagnosed at an early stage without cirrhosis. In contrast, transplantation can be an option for cases with cirrhosis or with advanced cancer stage [96, 97]. Advances in surgical techniques and patient care have reduced morbidity while extending survival after major liver resection. The number of elderly patients who have undergone this type of surgery has increased in recent years. Most studies conclude that liver resection can be performed in selected patients aged over 70 years as safely as in younger patients [98], and that even repeat hepatectomy may be justified for recurrent cases of liver cancer [99]. In a retrospective study on 121 curative repeat hepatectomies, elderly patients displayed more comorbid conditions pre-operatively, including hypertension and cardiovascular diseases, than the younger group; however, there was no significant difference in the incidence of postoperative complications, or in the duration of postoperative hospital stay [99]. Major hepatectomy is considered safe in elderly patients with HCC, even with cirrhosis [100]. Similar criteria apply to patients with biliary tract cancer, in whom severe complications have only been reported when the remnant liver volume was lower than 45% [101].

The fact that elderly people are at higher risk of developing complications due to more frequent comorbidities justifies that a few years ago, a liver transplant was usually not offered to HCC patients above 60-65 years old. However, the average age of liver transplant recipients has been elevated more recently [102]. Moreover, since this potential curative option has been extended to patients with CCA or liver metastasis, and antiviral agents are delaying cirrhosis development in patients with chronic hepatitis B or C, the number of elderly patients requiring liver transplant is predicted to be continuously growing in the next future. Several studies have compared the outcomes in patients aged more than 60 years or younger after orthotopic liver transplantation with controversial results; some reported lower survival rates, especially in high-risk patients [103, 104], while others found no significant differences in mortality rates [105, 106]. Acceptable long-term survival after liver transplantation has been reported in selected HCC patients older than 75 years [107]. Unfortunately, the situation is different for patients with iCCA. This is still a contraindication for liver transplantation in many centers. However, a retrospective cohort multicenter study on 29 cirrhotic patients with very early iCCA, reported a satisfactory 5-year survival (73%) independently of age [108].

**Table 2. Comparison of the response to curative treatments in the elderly and young patients with hepatocellular carcinoma (HCC) or intrahepatic cholangiocarcinoma (iCCA).**

Treatment	Tumor	Findings	Ref.
Liver resection	HCC	Comparable effectiveness and safety Longer hospitalization and rehabilitation	[98–100]
	iCCA	Low mortality Severe complications when $\leq 45\%$ remnant liver	[101]
Liver transplant	HCC	Acceptable long-term survival Controversial results in high-risk patients	[103, 104, 107]
	iCCA	Similar 5-year survival when tumor size $\leq 2$ cm	[108]
Radiofrequency ablation	HCC	Comparable effectiveness and safety	[109, 110]
	iCCA	Comparable effectiveness in iCCA	[111]
Microwave ablation	HCC	Comparable effectiveness and safety in patients $>65$	[112]
	iCCA	Good survival and safety in iCCA patients when tumor size $\leq 2$ cm	[113]

Radiofrequency ablation (RFA) uses an electrical current to induce coagulative necrosis following thermal damage of tumor tissue. This treatment is considered as effective in elderly HCC patients ( $\geq 70$  years) as in younger patients [109] and provides acceptable 5-year survival rates in patients older than 75 years with good performance status. Of note, those patients with comorbidities frequently die from causes unrelated to HCC [110]. Regarding iCCA, RFA is considered effective when tumor size is  $<20$  mm independently of the patient's age [111].

Percutaneous microwave ablation therapy is a less invasive procedure than RFA to induce tumor damage by thermal effect. Only one study has described that this treatment is safe and effective for HCC patients  $\geq 65$  years and that clinical outcome is not affected by age or comorbidities [112]. Besides, this procedure has provided an excellent long-term outcome in patients with small ( $\leq 2$  cm) iCCA tumors, either under or over 65 years of age [113].

### Palliative treatments

Trans-arterial chemoembolization (TACE) is the most frequently used therapeutic approach for patients with inoperable HCC. It has been demonstrated that TACE reaches satisfactory efficacy and is well tolerated in elderly patients, including those above 85 years old [114, 115]. Recent studies have described that drug-eluting bead-TACE therapy was safe and effective in elderly patients either with HCC [116] or iCCA [117].

Regarding pharmacological treatments, although there are no specific guidelines to treat elderly patients with

liver tumors and the results of clinical trials cannot always be directly translated to the general population because the participants are selected as well-fit, which does not represent what is found in clinical practice, in general, elderly patients can benefit from all the available pharmacological treatments [118]. Nevertheless, the current pharmacological armamentarium used in systemic treatments against HCC and CCA is scarcely effective and only provides modest benefits, even in young patients. Thus, tyrosine kinase inhibitor (TKI) sorafenib has been the standard of care for advanced HCC for several years [119], despite the moderate beneficial effects and some serious adverse events in some patients. It was demonstrated that the survival benefits and the safety of sorafenib were comparable in elderly and young patients with advanced HCC [120, 121]. Another TKI, lenvatinib, is now a new therapeutic option as first-line therapy for patients with unresectable HCC, and the available data indicate that it can be used safely and efficaciously regardless of age [122]. Although there are no specific studies of the efficacy and safety of other TKIs used as second-line treatment in elders, and these patients are usually underrepresented in oncological clinical trials, the available information of subgroup analyses of regorafenib and cabozantinib is promising [123]. Regorafenib provided a survival benefit in HCC patients progressing on sorafenib treatment without differences in groups older and younger than 65 years old [124]. The randomized, double-blind, phase III trial evaluating cabozantinib vs. placebo in previously treated patients with advanced HCC found no differences in the analysis of overall survival (OS) and progression-free survival (PFS) in patients aged  $<65$  years vs.  $\geq 65$  years [125]. In another study comparing HCC patients

aged  $\geq 70$  years with younger individuals, a similar favorable middle-term outcome was obtained in both groups [126].

A recent study in patients with HCC and elevated AFP after sorafenib treatment has reported that ramucirumab, a monoclonal antibody that inhibits endothelial growth factor receptor 2 (VEGFR2), showed similar OS and safety across age subgroups, including  $\geq 75$  years old, which supports its use regardless of patient's age [127]. Regarding immune checkpoint inhibitors, the phase III CheckMate 459 trial comparing nivolumab (the first recombinant human IgG4 monoclonal antibody anti-PD-1) with sorafenib showed that OS was better in the nivolumab arm both in elderly ( $\geq 65$  years) and younger ( $< 65$  years) patients [128]. Similar results were observed with pembrolizumab, another anti-PD-1 recombinant human IgG4 monoclonal antibody [129]. The phase III open-label study of patients with locally advanced or metastatic and/or unresectable HCC comparing atezolizumab plus bevacizumab with sorafenib also showed an increase in OS and PFS together with delayed deterioration of patient quality of life in the first arm both in patients under and over 65 years [130].

It was described that biliary cancer patients aged 75 years or older tolerated standard full-dose chemotherapy with gemcitabine, and the outcomes were like those seen in younger patients [131]. More recently, it has been corroborated that the patients  $> 80$  years old with biliary malignancies, when carefully selected, can potentially undergo systemic anticancer therapy and obtain a similar benefit as younger patients [132]. Moreover, survival after gemcitabine plus cisplatin, the conventional first-line treatment for advanced CCA, has been found similar in patients with advanced age ( $\geq 70$  years) and younger [133]. Besides, capecitabine showed comparable effects when used as adjuvant chemotherapy following surgery in patients with resected biliary tract cancer either under or over 60 years old [134]. The still scarce results of the response to lenvatinib monotherapy as second-line treatment in unresectable biliary tract cancer have shown antitumor activity with a tolerable safety profile, with similar adverse events in patients under and over 65 years [135].

Data on FGFR targeted therapies in elderly patients with CCA are scarce, although subgroup analyses in some clinical trials are available and the results are interesting. Thus, the multicenter, open-label, single-arm, multicohort, phase II study FIGHT-202 investigated pemigatinib in previously treated, locally advanced or metastatic CCA and included in cohort A

patients with FGFR2 fusions or rearrangements mainly under 65 years, in fact, 23.4% were  $\geq 65$  years (25/107) and only 5 of these patients were  $\geq 75$  years. Median PFS was higher in patients  $\geq 75$  years than in those younger than 65 years, with intermediate values in patients between 65-75 years; however, the small number of older patients means that these data should be viewed with caution [136].

Ivosidenib is a potent inhibitor of mutant isocitrate dehydrogenase 1 (mIDH1). Although no studies comparing safety and activity of ivosidenib in younger and older patients have been yet performed, a phase I study showed no differences between ivosidenib pharmacokinetics and pharmacodynamics and age in patients with adequate renal/hepatic function [137].

Despite CCA mainly affects aged subjects, this population is severely underrepresented in clinical trials, which hopefully will change in the future based on available data [138]. Fortunately, the management of advanced liver cancer is changing rapidly with new options based on different kinase inhibitors and monoclonal antibodies targeting angiogenesis that have emerged, as well as novel immune checkpoint inhibitors. Thus, recent clinical trials have recruited older patients with no maximum age exclusion criteria, and age has not been found to be predictive for treatment effect in subgroup analyses [118].

## CONCLUSIONS

Aging is a dynamic process associated with a progressive reduction in the capability of all physiological functions. The liver has a remarkable regenerative potential, so the impact of aging is somewhat less relevant than in other organs, however, over time, accumulated deterioration leads to the appearance of a senescence phenotype. Our understanding of the molecular determinants involved in the characteristics of aging, as well as their interaction with the risk factors that predispose to the development of liver cancer is still incomplete. The aging of the population worldwide, together with an increased frequency of exposure to risk factors associated with the development of these tumors, such as NAFLD and obesity, suggest that in the coming years the incidence of liver tumors in the elderly will continue to increase. Fortunately, most studies to date support the concept that, in general, all available treatments can also be recommended for elderly patients, although the comorbidities that these individuals often present must be taken into account to tailor treatment to each case and, in addition, these patients should be closely monitored.

**Table 3. Comparison of the response to transarterial chemoembolization (TACE) and systemic pharmacological treatment in the elderly vs. young patients with hepatocellular carcinoma (HCC) or intrahepatic cholangiocarcinoma (iCCA).**

Tumor	Treatment	Response	Ref.
HCC	Sorafenib	Comparable survival benefits and safety	[120, 121]
	Lenvatinib	Comparable survival benefits and safety	[122]
	Regorafenib	Similar survival benefit in HCC patients progressing on sorafenib treatment	[124]
	Cabozantinib	Similar OS, PFS and middle-term outcome	[124, 126]
	Ramucirumab	Similar OS and safety	[127]
	Nivolumab	Similar OS	[128]
	Pembrolizumab	Similar OS and PFS	[129]
	Atezolizumab plus Bevacizumab	Similar OS, PFS and tolerability	[130]
	TACE	Good efficacy and tolerance even in >85	[114, 115]
iCCA	Gem/Cis	Similar OS	[133]
	Capecitabine	Similar effects when used after surgery	[134]
	Lenvatinib	Similar safety	[135]
	Pemigatinib	Better PFS	[136]
	Ivosidenib	Similar drug disposition	[137]
	TACE	Good efficacy and tolerance	[117]

Gem/Cis, Gemcitabine/Cisplatin; OS, overall survival; PFS, progression-free survival; TACE, trans-arterial chemoembolization.

## Abbreviations

CCA: cholangiocarcinoma; EGFR: epidermal growth factor receptor; HBV: hepatitis B virus; HCC: hepatocellular carcinoma; HCV: hepatitis C virus; NASH: non-alcoholic steatohepatitis; OS: overall survival; PFS progression-free survival; RFA: radiofrequency ablation; ROS: reactive oxygen species; TACE: trans-arterial chemoembolization; TERC: telomerase RNA; TERT: telomere reverse transcriptase; TKI: tyrosine kinase inhibitor.

## CONFLICTS OF INTEREST

The authors declare no conflicts of interest related to this study.

## FUNDING

The groups involved in this study were funded by the CIBERehd (EHD15PI05/2016), Carlos III Institute of Health, Spain; Centro Internacional sobre el Envejecimiento (OLD-HEPAMARKER, 0348-CIE-6-E), Spain; Fondo de Investigaciones Sanitarias, Instituto de Salud Carlos III, Spain (PI19/00819 and PI20/00189, co-funded by European Regional Development Fund/European Social Fund, “Investing in your future”), the “Junta de Castilla y León”, Spain (SA074P20); the Fundació Marató TV3 (201916-31); Fundação para a Ciência e a Tecnologia (grant PTDC/MED-PAT/31882/

2017), Portugal and “la Caixa” Banking Foundation (Grant HR17-00601, Fat2LiverTGR5). JJGM, REC and RIRM are members of COST Action CA18122 European Cholangiocarcinoma Network, EUROCHOLANGIO-NET.

## REFERENCES

1. Eurostat. Ageing Europe. Looking at the lives of older people in the EU. Publications Office of the European Union, Luxembourg. 2019.
2. Lin L, Yan L, Liu Y, Qu C, Ni J, Li H. The Burden and Trends of Primary Liver Cancer Caused by Specific Etiologies from 1990 to 2017 at the Global, Regional, National, Age, and Sex Level Results from the Global Burden of Disease Study 2017. *Liver Cancer*. 2020; 9:563–82.  
<https://doi.org/10.1159/000508568> PMID:33083281
3. Banales JM, Marin JJ, Lamarca A, Rodrigues PM, Khan SA, Roberts LR, Cardinale V, Carpino G, Andersen JB, Braconi C, Calvisi DF, Perugorria MJ, Fabris L, et al. Cholangiocarcinoma 2020: the next horizon in mechanisms and management. *Nat Rev Gastroenterol Hepatol*. 2020; 17:557–88.  
<https://doi.org/10.1038/s41575-020-0310-z> PMID:32606456
4. Khan SA, Tavolari S, Brandi G. Cholangiocarcinoma: Epidemiology and risk factors. *Liver Int*. 2019 (Suppl 1); 39:19–31.



<https://doi.org/10.1111/liv.14095>

PMID:30851228

5. Campisi J. Aging, cellular senescence, and cancer. *Annu Rev Physiol.* 2013; 75:685–705.  
<https://doi.org/10.1146/annurev-physiol-030212-183653> PMID:23140366
6. Williet N, Clavel L, Bourmaud A, Verot C, Bouarioua N, Roblin X, Merle P, Phelip JM. Tolerance and outcomes of sorafenib in elderly patients treated for advanced hepatocellular carcinoma. *Dig Liver Dis.* 2017; 49:1043–49.  
<https://doi.org/10.1016/j.dld.2017.06.008> PMID:28712860
7. Kudo M. Recent Advances in Systemic Therapy for Hepatocellular Carcinoma in an Aging Society: 2020 Update. *Liver Cancer.* 2020; 9:640–62.  
<https://doi.org/10.1159/000511001> PMID:33442538
8. Wildiers H, Heeren P, Puts M, Topinkova E, Janssen-Heijnen ML, Extermann M, Falandry C, Artz A, Brain E, Colloca G, Flamaing J, Karnakis T, Kenis C, et al. International Society of Geriatric Oncology consensus on geriatric assessment in older patients with cancer. *J Clin Oncol.* 2014; 32:2595–603.  
<https://doi.org/10.1200/JCO.2013.54.8347> PMID:25071125
9. European Association for the Study of the Liver. Electronic address: easloffice@easloffice.eu, and European Association for the Study of the Liver. EASL Clinical Practice Guidelines: Management of hepatocellular carcinoma. *J Hepatol.* 2018; 69:182–236.  
<https://doi.org/10.1016/j.jhep.2018.03.019> PMID:29628281
10. Banales JM, Cardinale V, Carpino G, Marzioni M, Andersen JB, Invernizzi P, Lind GE, Folseraas T, Forbes SJ, Fouassier L, Geier A, Calvisi DF, Mertens JC, et al. Expert consensus document: Cholangiocarcinoma: current knowledge and future perspectives consensus statement from the European Network for the Study of Cholangiocarcinoma (ENS-CCA). *Nat Rev Gastroenterol Hepatol.* 2016; 13:261–80.  
<https://doi.org/10.1038/nrgastro.2016.51> PMID:27095655
11. Hashim D, Carioli G, Malvezzi M, Bertuccio P, Waxman S, Negri E, La Vecchia C, Boffetta P. Cancer mortality in the oldest old: a global overview. *Aging (Albany NY).* 2020; 12:16744–58.  
<https://doi.org/10.18632/aging.103503> PMID:32882684
12. Hung AK, Guy J. Hepatocellular carcinoma in the elderly: Meta-analysis and systematic literature review. *World J Gastroenterol.* 2015; 21:12197–210.  
<https://doi.org/10.3748/wjg.v21.i42.12197> PMID:26576104
13. Yi SW, Choi JS, Yi JJ, Lee YH, Han KJ. Risk factors for hepatocellular carcinoma by age, sex, and liver disorder status: A prospective cohort study in Korea. *Cancer.* 2018; 124:2748–57.  
<https://doi.org/10.1002/cncr.31406> PMID:29669170
14. Myers S, Neyroud-Caspar I, Spahr L, Gkouvatsos K, Fournier E, Giostra E, Magini G, Frossard JL, Bascaron ME, Vernaz N, Zampaglione L, Negro F, Goossens N. NAFLD and MAFLD as emerging causes of HCC: A populational study. *JHEP Rep.* 2021; 3:100231.  
<https://doi.org/10.1016/j.jhepr.2021.100231> PMID:33748726
15. Younossi ZM, Otgonsuren M, Henry L, Venkatesan C, Mishra A, Erario M, Hunt S. Association of nonalcoholic fatty liver disease (NAFLD) with hepatocellular carcinoma (HCC) in the United States from 2004 to 2009. *Hepatology.* 2015; 62:1723–30.  
<https://doi.org/10.1002/hep.28123> PMID:26274335
16. Hung GY, Horng JL, Yen HJ, Lee CY, Lin LY. Changing incidence patterns of hepatocellular carcinoma among age groups in Taiwan. *J Hepatol.* 2015; 63:1390–96.  
<https://doi.org/10.1016/j.jhep.2015.07.032> PMID:26256438
17. Dyson J, Jaques B, Chattopadhyay D, Lochan R, Graham J, Das D, Aslam T, Patanwala I, Gaggar S, Cole M, Sumpter K, Stewart S, Rose J, et al. Hepatocellular cancer: the impact of obesity, type 2 diabetes and a multidisciplinary team. *J Hepatol.* 2014; 60:110–17.  
<https://doi.org/10.1016/j.jhep.2013.08.011> PMID:23978719
18. Liu SS, Ma XF, Zhao J, Du SX, Zhang J, Dong MZ, Xin YN. Association between nonalcoholic fatty liver disease and extrahepatic cancers: a systematic review and meta-analysis. *Lipids Health Dis.* 2020; 19:118.  
<https://doi.org/10.1186/s12944-020-01288-6> PMID:32475354
19. Corrao S, Natoli G, Argano C. Nonalcoholic fatty liver disease is associated with intrahepatic cholangiocarcinoma and not with extrahepatic form: definitive evidence from meta-analysis and trial sequential analysis. *Eur J Gastroenterol Hepatol.* 2021; 33:62–68.  
<https://doi.org/10.1097/MEG.0000000000001684> PMID:32091438
20. Lonardo A, Lombardini S, Scaglioni F, Ballestri S, Verrone AM, Bertolotti M, Carulli L, Ganazzi D, Carulli N, Loria P. Fatty liver, carotid disease and gallstones: a study of age-related associations. *World J Gastroenterol.* 2006; 12:5826–33.



<https://doi.org/10.3748/wjg.v12.i36.5826>

PMID:17007049

21. Cokan KB, Urlep Ž, Lorbek G, Matz-Soja M, Skubic C, Perše M, Jeruc J, Juvan P, Režen T, Rozman D. Chronic Disruption of the Late Cholesterol Synthesis Leads to Female-Prevalent Liver Cancer. *Cancers (Basel)*. 2020; 12:3302.  
<https://doi.org/10.3390/cancers12113302>  
PMID:33182326
22. Wang R, Liu Y, Sun H, Wang T, Li C, Fan J, Wang Z. Estradiol is significantly associated with prognosis in non-surgical liver cancer patients: from bench to bedside. *Aging (Albany NY)*. 2021; 13:3483–500.  
<https://doi.org/10.18632/aging.202280>  
PMID:33428602
23. Yeh SH, Chen PJ. Gender disparity of hepatocellular carcinoma: the roles of sex hormones. *Oncology*. 2010 (Suppl 1); 78:172–79.  
<https://doi.org/10.1159/000315247> PMID:20616601
24. Xu H, Wei Y, Zhang Y, Xu Y, Li F, Liu J, Zhang W, Han X, Tan R, Shen P. Oestrogen attenuates tumour progression in hepatocellular carcinoma. *J Pathol*. 2012; 228:216–29.  
<https://doi.org/10.1002/path.4009> PMID:22374713
25. Hunsawong T, Singsuksawat E, In-chon N, Chawengrattanachot W, Thuwajit C, Sripa B, Paupairoj A, Chau-in S, Thuwajit P. Estrogen is increased in male cholangiocarcinoma patients' serum and stimulates invasion in cholangiocarcinoma cell lines *in vitro*. *J Cancer Res Clin Oncol*. 2012; 138:1311–20.  
<https://doi.org/10.1007/s00432-012-1207-1>  
PMID:22476540
26. Petrick JL, Florio AA, Zhang X, Zeleniuch-Jacquotte A, Wactawski-Wende J, Van Den Eeden SK, Stanczyk FZ, Simon TG, Sinha R, Sesso HD, Schairer C, Rosenberg L, Rohan TE, et al. Associations Between Prediagnostic Concentrations of Circulating Sex Steroid Hormones and Liver Cancer Among Postmenopausal Women. *Hepatology*. 2020; 72:535–47.  
<https://doi.org/10.1002/hep.31057> PMID:31808181
27. Petrick JL, McMenamin ÚC, Zhang X, Zeleniuch-Jacquotte A, Wactawski-Wende J, Simon TG, Sinha R, Sesso HD, Schairer C, Rosenberg L, Rohan TE, Robien K, Purdue MP, et al. Exogenous hormone use, reproductive factors and risk of intrahepatic cholangiocarcinoma among women: results from cohort studies in the Liver Cancer Pooling Project and the UK Biobank. *Br J Cancer*. 2020; 123:316–24.  
<https://doi.org/10.1038/s41416-020-0835-5>  
PMID:32376888
28. Wu J, Yang S, Xu K, Ding C, Zhou Y, Fu X, Li Y, Deng M, Wang C, Liu X, Li L. Patterns and Trends of Liver Cancer Incidence Rates in Eastern and Southeastern Asian Countries (1983–2007) and Predictions to 2030. *Gastroenterology*. 2018; 154:1719–28.e5.  
<https://doi.org/10.1053/j.gastro.2018.01.033>  
PMID:29549041
29. Mu XM, Wang W, Jiang YY, Feng J. Patterns of Comorbidity in Hepatocellular Carcinoma: A Network Perspective. *Int J Environ Res Public Health*. 2020; 17:3108.  
<https://doi.org/10.3390/ijerph17093108>  
PMID:32365650
30. Cho E, Cho HA, Jun CH, Kim HJ, Cho SB, Choi SK. A Review of Hepatocellular Carcinoma in Elderly Patients Focused on Management and Outcomes. *In Vivo*. 2019; 33:1411–20.  
<https://doi.org/10.21873/invivo.11618>  
PMID:31471386
31. Nishikawa H, Kimura T, Kita R, Osaki Y. Treatment for hepatocellular carcinoma in elderly patients: a literature review. *J Cancer*. 2013; 4:635–43.  
<https://doi.org/10.7150/jca.7279> PMID:24155775
32. López-Otín C, Blasco MA, Partridge L, Serrano M, Kroemer G. The hallmarks of aging. *Cell*. 2013; 153:1194–217.  
<https://doi.org/10.1016/j.cell.2013.05.039>  
PMID:23746838
33. Elpek GÖ. Cellular and molecular mechanisms in the pathogenesis of liver fibrosis: An update. *World J Gastroenterol*. 2014; 20:7260–76.  
<https://doi.org/10.3748/wjg.v20.i23.7260>  
PMID:24966597
34. Parrinello S, Coppe JP, Krtolica A, Campisi J. Stromal-epithelial interactions in aging and cancer: senescent fibroblasts alter epithelial cell differentiation. *J Cell Sci*. 2005; 118:485–96.  
<https://doi.org/10.1242/jcs.01635> PMID:15657080
35. Röcken C, Carl-McGrath S. Pathology and pathogenesis of hepatocellular carcinoma. *Dig Dis*. 2001; 19:269–78.  
<https://doi.org/10.1159/000050693> PMID:11935086
36. Biegging KT, Mello SS, Attardi LD. Unravelling mechanisms of p53-mediated tumour suppression. *Nat Rev Cancer*. 2014; 14:359–70.  
<https://doi.org/10.1038/nrc3711> PMID:24739573
37. Qi LN, Bai T, Chen ZS, Wu FX, Chen YY, De Xiang B, Peng T, Han ZG, Li LQ. The p53 mutation spectrum in hepatocellular carcinoma from Guangxi, China : role of chronic hepatitis B virus infection and aflatoxin B1 exposure. *Liver Int*. 2015; 35:999–1009.  
<https://doi.org/10.1111/liv.12460> PMID:24461059
38. Meunier L, Hirsch TZ, Caruso S, Imbeaud S, Bayard Q, Roehrig A, Couchy G, Nault JC, Llovet JM, Blanc JF,

- Calderaro J, Zucman-Rossi J, Letouzé E. DNA Methylation Signatures Reveal the Diversity of Processes Remodeling Hepatocellular Carcinoma Methylomes. *Hepatology*. 2021; 74:816–34. <https://doi.org/10.1002/hep.31796> PMID:33713365
39. Farazi PA, DePinho RA. Hepatocellular carcinoma pathogenesis: from genes to environment. *Nat Rev Cancer*. 2006; 6:674–87. <https://doi.org/10.1038/nrc1934> PMID:16929323
40. Lanaya H, Natarajan A, Komposch K, Li L, Amberg N, Chen L, Wculek SK, Hammer M, Zenz R, Peck-Radosavljevic M, Sieghart W, Trauner M, Wang H, Sibilía M. EGFR has a tumour-promoting role in liver macrophages during hepatocellular carcinoma formation. *Nat Cell Biol*. 2014; 16:972–77. <https://doi.org/10.1038/ncb3031> PMID:25173978
41. Kim E, Lisby A, Ma C, Lo N, Ehmer U, Hayer KE, Furth EE, Viatour P. Promotion of growth factor signaling as a critical function of  $\beta$ -catenin during HCC progression. *Nat Commun*. 2019; 10:1909. <https://doi.org/10.1038/s41467-019-09780-z> PMID:31015417
42. Gross-Goupil M, Riou P, Emile JF, Saffroy R, Azoulay D, Lacherade I, Receveur A, Piatier-Tonneau D, Castaing D, Debuire B, Lemoine A. Analysis of chromosomal instability in pulmonary or liver metastases and matched primary hepatocellular carcinoma after orthotopic liver transplantation. *Int J Cancer*. 2003; 104:745–51. <https://doi.org/10.1002/ijc.11017> PMID:12640682
43. Bellanti F, Vendemiale G. The Aging Liver: Redox Biology and Liver Regeneration. *Antioxid Redox Signal*. 2021; 35:832–47. <https://doi.org/10.1089/ars.2021.0048> PMID:33789448
44. Guan XY, Fang Y, Sham JS, Kwong DL, Zhang Y, Liang Q, Li H, Zhou H, Trent JM. Recurrent chromosome alterations in hepatocellular carcinoma detected by comparative genomic hybridization. *Genes Chromosomes Cancer*. 2000; 29:110–16. PMID:10959090
45. Thorgeirsson SS, Grisham JW. Molecular pathogenesis of human hepatocellular carcinoma. *Nat Genet*. 2002; 31:339–46. <https://doi.org/10.1038/ng0802-339> PMID:12149612
46. Hwang HJ, Kim GJ, Lee GB, Oh JT, Chun YH, Park SH. A comprehensive karyotypic analysis on Korean hepatocellular carcinoma cell lines by cross-species color banding and comparative genomic hybridization. *Cancer Genet Cytogenet*. 2003; 141:128–37. [https://doi.org/10.1016/s0165-4608\(02\)00671-4](https://doi.org/10.1016/s0165-4608(02)00671-4) PMID:12606130
47. Vargas-Rondón N, Villegas VE, Rondón-Lagos M. The Role of Chromosomal Instability in Cancer and Therapeutic Responses. *Cancers (Basel)*. 2017; 10:4. <https://doi.org/10.3390/cancers10010004> PMID:29283387
48. Zhou L, Zhou W, Wu L, Yu X, Xing C, Zheng S. The association of frequent allelic loss on 17p13.1 with early metastatic recurrence of hepatocellular carcinoma after liver transplantation. *J Surg Oncol*. 2010; 102:802–08. <https://doi.org/10.1002/jso.21743> PMID:20886556
49. Zhao Z, Chen GY, Long J, Li H, Huang J. Genomic losses at 5q13.2 and 8p23.1 in dysplastic hepatocytes are common events in hepatitis B virus-related hepatocellular carcinoma. *Oncol Lett*. 2015; 9:2839–46. <https://doi.org/10.3892/ol.2015.3140> PMID:26137157
50. Zhang H, Ma H, Wang Q, Chen M, Weng D, Wang H, Zhou J, Li Y, Sun J, Chen Y, Liang X, Zhao J, Pan K, et al. Analysis of loss of heterozygosity on chromosome 4q in hepatocellular carcinoma using high-throughput SNP array. *Oncol Rep*. 2010; 23:445–55. PMID:20043106
51. Moinzadeh P, Breuhahn K, Stützer H, Schirmacher P. Chromosome alterations in human hepatocellular carcinomas correlate with aetiology and histological grade—results of an explorative CGH meta-analysis. *Br J Cancer*. 2005; 92:935–41. <https://doi.org/10.1038/sj.bjc.6602448> PMID:15756261
52. Tameda M, Sugimoto K, Shiraki K, Yamamoto N, Okamoto R, Usui M, Ito M, Takei Y, Nobori T, Kojima T, Suzuki H, Uchida M, Uchida K. Collagen triple helix repeat containing 1 is overexpressed in hepatocellular carcinoma and promotes cell proliferation and motility. *Int J Oncol*. 2014; 45:541–48. <https://doi.org/10.3892/ijo.2014.2445> PMID:24841500
53. Sladky VC, Eichin F, Reiberger T, Villunger A. Polyploidy control in hepatic health and disease. *J Hepatol*. 2021; [Epub ahead of print]. <https://doi.org/10.1016/j.jhep.2021.06.030> PMID:34228992
54. Wang MJ, Chen F, Lau JT, Hu YP. Hepatocyte polyploidization and its association with pathophysiological processes. *Cell Death Dis*. 2017; 8:e2805. <https://doi.org/10.1038/cddis.2017.167> PMID:28518148
55. Zhang S, Zhou K, Luo X, Li L, Tu HC, Sehgal A, Nguyen LH, Zhang Y, Gopal P, Tarlow BD, Siegwart DJ, Zhu H. The Polyploid State Plays a Tumor-Suppressive Role in the Liver. *Dev Cell*. 2018; 44:447–59.e5.

- <https://doi.org/10.1016/j.devcel.2018.01.010>  
PMID:29429824
56. Lundblad V. The end replication problem: more than one solution. *Nat Med.* 1997; 3:1198–99.  
<https://doi.org/10.1038/nm1197-1198> PMID:9359690
  57. Takakura M, Kyo S, Kanaya T, Hirano H, Takeda J, Yutsudo M, Inoue M. Cloning of human telomerase catalytic subunit (hTERT) gene promoter and identification of proximal core promoter sequences essential for transcriptional activation in immortalized and cancer cells. *Cancer Res.* 1999; 59:551–57.  
PMID:9973199
  58. Nakamura TM, Morin GB, Chapman KB, Weinrich SL, Andrews WH, Lingner J, Harley CB, Cech TR. Telomerase catalytic subunit homologs from fission yeast and human. *Science.* 1997; 277:955–59.  
<https://doi.org/10.1126/science.277.5328.955>  
PMID:9252327
  59. Okamoto K, Seimiya H. Revisiting Telomere Shortening in Cancer. *Cells.* 2019; 8:107.  
<https://doi.org/10.3390/cells8020107>  
PMID:30709063
  60. Harley CB, Vaziri H, Counter CM, Allsopp RC. The telomere hypothesis of cellular aging. *Exp Gerontol.* 1992; 27:375–82.  
[https://doi.org/10.1016/0531-5565\(92\)90068-b](https://doi.org/10.1016/0531-5565(92)90068-b)  
PMID:1459213
  61. Amisaki M, Tsuchiya H, Sakabe T, Fujiwara Y, Shiota G. Identification of genes involved in the regulation of TERT in hepatocellular carcinoma. *Cancer Sci.* 2019; 110:550–60.  
<https://doi.org/10.1111/cas.13884>  
PMID:30447097
  62. El Idrissi M, Hervieu V, Merle P, Mortreux F, Wattel E. Cause-specific telomere factors deregulation in hepatocellular carcinoma. *J Exp Clin Cancer Res.* 2013; 32:64.  
<https://doi.org/10.1186/1756-9966-32-64>  
PMID:24020493
  63. Yang B, Shebl FM, Sternberg LR, Warner AC, Kleiner DE, Edelman DC, Gomez A, Dagnall CL, Hicks BD, Altekruse SF, Hernandez BY, Lynch CF, Meltzer PS, McGlynn KA. Telomere Length and Survival of Patients with Hepatocellular Carcinoma in the United States. *PLoS One.* 2016; 11:e0166828.  
<https://doi.org/10.1371/journal.pone.0166828>  
PMID:27880792
  64. Schulze K, Nault JC, Villanueva A. Genetic profiling of hepatocellular carcinoma using next-generation sequencing. *J Hepatol.* 2016; 65:1031–42.  
<https://doi.org/10.1016/j.jhep.2016.05.035>  
PMID:27262756
  65. Guichard C, Amaddeo G, Imbeaud S, Ladeiro Y, Pelletier L, Maad IB, Calderaro J, Bioulac-Sage P, Letexier M, Degos F, Clément B, Balabaud C, Chevet E, et al. Integrated analysis of somatic mutations and focal copy-number changes identifies key genes and pathways in hepatocellular carcinoma. *Nat Genet.* 2012; 44:694–98.  
<https://doi.org/10.1038/ng.2256> PMID:22561517
  66. Zehir A, Benayed R, Shah RH, Syed A, Middha S, Kim HR, Srinivasan P, Gao J, Chakravarty D, Devlin SM, Hellmann MD, Barron DA, Schram AM, et al. Mutational landscape of metastatic cancer revealed from prospective clinical sequencing of 10,000 patients. *Nat Med.* 2017; 23:703–13.  
<https://doi.org/10.1038/nm.4333> PMID:28481359
  67. Nault JC, Mallet M, Pilati C, Calderaro J, Bioulac-Sage P, Laurent C, Laurent A, Cherqui D, Balabaud C, Zucman-Rossi J. High frequency of telomerase reverse-transcriptase promoter somatic mutations in hepatocellular carcinoma and preneoplastic lesions. *Nat Commun.* 2013; 4:2218.  
<https://doi.org/10.1038/ncomms3218> PMID:23887712
  68. Nakayama J, Tahara H, Tahara E, Saito M, Ito K, Nakamura H, Nakanishi T, Tahara E, Ide T, Ishikawa F. Telomerase activation by hTERT in human normal fibroblasts and hepatocellular carcinomas. *Nat Genet.* 1998; 18:65–68.  
<https://doi.org/10.1038/ng0198-65> PMID:9425903
  69. Ningarhari M, Caruso S, Hirsch TZ, Bayard Q, Franconi A, Védie AL, Noblet B, Blanc JF, Amaddeo G, Ganne N, Ziol M, Paradis V, Guettier C, et al. Telomere length is key to hepatocellular carcinoma diversity and telomerase addiction is an actionable therapeutic target. *J Hepatol.* 2021; 74:1155–66.  
<https://doi.org/10.1016/j.jhep.2020.11.052>  
PMID:33338512
  70. In der Stroth L, Tharehalli U, Günes C, Lechel A. Telomeres and Telomerase in the Development of Liver Cancer. *Cancers (Basel).* 2020; 12:2048.  
<https://doi.org/10.3390/cancers12082048>  
PMID:32722302
  71. Li D, Zeng Z. Epigenetic regulation of histone H3 in the process of hepatocellular tumorigenesis. *Biosci Rep.* 2019; 39:BSR20191815.  
<https://doi.org/10.1042/BSR20191815>  
PMID:31320544
  72. Hannum G, Guinney J, Zhao L, Zhang L, Hughes G, Sada S, Klotzle B, Bibikova M, Fan JB, Gao Y, Deconde R, Chen M, Rajapakse I, et al. Genome-wide methylation profiles reveal quantitative views of human aging rates. *Mol Cell.* 2013; 49:359–67.  
<https://doi.org/10.1016/j.molcel.2012.10.016>  
PMID:23177740

73. Arechederra M, Recalde M, Gárate-Rascón M, Fernández-Barrena MG, Ávila MA, Berasain C. Epigenetic Biomarkers for the Diagnosis and Treatment of Liver Disease. *Cancers (Basel)*. 2021; 13:1265. <https://doi.org/10.3390/cancers13061265> PMID:33809263
74. Villanueva A, Portela A, Sayols S, Battiston C, Hoshida Y, Méndez-González J, Imbeaud S, Letouze E, Hernandez-Gea V, Cornella H, Pinyol R, Solé M, Fuster J, et al, and HEPROMIC Consortium. DNA methylation-based prognosis and epidrivers in hepatocellular carcinoma. *Hepatology*. 2015; 61:1945–56. <https://doi.org/10.1002/hep.27732> PMID:25645722
75. Nishida N, Arizumi T, Takita M, Kitai S, Yada N, Hagiwara S, Inoue T, Minami Y, Ueshima K, Sakurai T, Kudo M. Reactive oxygen species induce epigenetic instability through the formation of 8-hydroxydeoxyguanosine in human hepatocarcinogenesis. *Dig Dis*. 2013; 31:459–66. <https://doi.org/10.1159/000355245> PMID:24281021
76. Rando TA, Chang HY. Aging, rejuvenation, and epigenetic reprogramming: resetting the aging clock. *Cell*. 2012; 148:46–57. <https://doi.org/10.1016/j.cell.2012.01.003> PMID:22265401
77. Berdasco M, Esteller M. Clinical epigenetics: seizing opportunities for translation. *Nat Rev Genet*. 2019; 20:109–27. <https://doi.org/10.1038/s41576-018-0074-2> PMID:30479381
78. Borghesan M, Fusilli C, Rappa F, Panebianco C, Rizzo G, Oben JA, Mazzocchi G, Faulkes C, Pata I, Agodi A, Rezaee F, Minogue S, Warren A, et al. DNA Hypomethylation and Histone Variant macroH2A1 Synergistically Attenuate Chemotherapy-Induced Senescence to Promote Hepatocellular Carcinoma Progression. *Cancer Res*. 2016; 76:594–606. <https://doi.org/10.1158/0008-5472.CAN-15-1336> PMID:26772755
79. Wong CM, Wei L, Law CT, Ho DW, Tsang FH, Au SL, Sze KM, Lee JM, Wong CC, Ng IO. Up-regulation of histone methyltransferase SETDB1 by multiple mechanisms in hepatocellular carcinoma promotes cancer metastasis. *Hepatology*. 2016; 63:474–87. <https://doi.org/10.1002/hep.28304> PMID:26481868
80. Meller A, Shalgi R. The aging proteostasis decline: From nematode to human. *Exp Cell Res*. 2021; 399:112474. <https://doi.org/10.1016/j.yexcr.2021.112474> PMID:33434530
81. Sabath N, Levy-Adam F, Younis A, Rozales K, Meller A, Hadar S, Soueid-Baumgarten S, Shalgi R. Cellular proteostasis decline in human senescence. *Proc Natl Acad Sci USA*. 2020; 117:31902–13. <https://doi.org/10.1073/pnas.2018138117> PMID:33257563
82. Bejarano E, Murray JW, Wang X, Pampliega O, Yin D, Patel B, Yuste A, Wolkoff AW, Cuervo AM. Defective recruitment of motor proteins to autophagic compartments contributes to autophagic failure in aging. *Aging Cell*. 2018; 17:e12777. <https://doi.org/10.1111/acer.12777> PMID:29845728
83. Sauzay C, Louandre C, Bodeau S, Anglade F, Godin C, Saidak Z, Fontaine JX, Usureau C, Martin N, Molinie R, Pascal J, Mesnard F, Pluquet O, Galmiche A. Protein biosynthesis, a target of sorafenib, interferes with the unfolded protein response (UPR) and ferroptosis in hepatocellular carcinoma cells. *Oncotarget*. 2018; 9:8400–14. <https://doi.org/10.18632/oncotarget.23843> PMID:29492203
84. Haigis MC, Yankner BA. The aging stress response. *Mol Cell*. 2010; 40:333–44. <https://doi.org/10.1016/j.molcel.2010.10.002> PMID:20965426
85. Klionsky DJ, Abdel-Aziz AK, Abdelfatah S, Abdellatif M, Abdoli A, Abel S, Abeliovich H, Abildgaard MH, Abudu YP, Acevedo-Arozena A, Adamopoulos IE, Adeli K, Adolph TE, et al. Guidelines for the use and interpretation of assays for monitoring autophagy (4th edition)1. *Autophagy*. 2021; 17:1–382. <https://doi.org/10.1080/15548627.2020.1797280> PMID:33634751
86. Schneider JL, Villarroya J, Diaz-Carretero A, Patel B, Urbanska AM, Thi MM, Villarroya F, Santambrogio L, Cuervo AM. Loss of hepatic chaperone-mediated autophagy accelerates proteostasis failure in aging. *Aging Cell*. 2015; 14:249–64. <https://doi.org/10.1111/acer.12310> PMID:25620427
87. Lévillé M, Estall JL. Mitochondrial Dysfunction in the Transition from NASH to HCC. *Metabolites*. 2019; 9:233. <https://doi.org/10.3390/metabo9100233> PMID:31623280
88. Wilson CH, Shalini S, Filipovska A, Richman TR, Davies S, Martin SD, McGee SL, Puccini J, Nikolic A, Dorstyn L, Kumar S. Age-related proteostasis and metabolic alterations in Caspase-2-deficient mice. *Cell Death Dis*. 2015; 6:e1615. <https://doi.org/10.1038/cddis.2014.567> PMID:25611376
89. Lopez-Cruzan M, Herman B. Loss of caspase-2 accelerates age-dependent alterations in



- mitochondrial production of reactive oxygen species. *Biogerontology*. 2013; 14:121–30.  
<https://doi.org/10.1007/s10522-013-9415-x>  
PMID:23504374
90. Shalini S, Nikolic A, Wilson CH, Puccini J, Sladojevic N, Finnie J, Dorstyn L, Kumar S. Caspase-2 deficiency accelerates chemically induced liver cancer in mice. *Cell Death Differ*. 2016; 23:1727–36.  
<https://doi.org/10.1038/cdd.2016.81> PMID:27518436
  91. Aravinthan AD, Alexander GJ. Senescence in chronic liver disease: Is the future in aging? *J Hepatol*. 2016; 65:825–34.  
<https://doi.org/10.1016/j.jhep.2016.05.030>  
PMID:27245432
  92. Su WW, Lee KT, Yeh YT, Soon MS, Wang CL, Yu ML, Wang SN. Association of circulating insulin-like growth factor 1 with hepatocellular carcinoma: one cross-sectional correlation study. *J Clin Lab Anal*. 2010; 24:195–200.  
<https://doi.org/10.1002/jcla.20320> PMID:20486202
  93. García-Rodríguez JL, Barbier-Torres L, Fernández-Álvarez S, Gutiérrez-de Juan V, Monte MJ, Halilbasic E, Herranz D, Álvarez L, Aspichueta P, Marín JJ, Trauner M, Mato JM, Serrano M, et al. SIRT1 controls liver regeneration by regulating bile acid metabolism through farnesoid X receptor and mammalian target of rapamycin signaling. *Hepatology*. 2014; 59:1972–83.  
<https://doi.org/10.1002/hep.26971> PMID:24338587
  94. Collier JD, Curless R, Bassendine MF, James OF. Clinical features and prognosis of hepatocellular carcinoma in Britain in relation to age. *Age Ageing*. 1994; 23:22–27.  
<https://doi.org/10.1093/ageing/23.1.22>  
PMID:8010166
  95. Poon RT, Fan ST, Lo CM, Liu CL, Ngan H, Ng IO, Wong J. Hepatocellular carcinoma in the elderly: results of surgical and nonsurgical management. *Am J Gastroenterol*. 1999; 94:2460–66.  
<https://doi.org/10.1111/j.1572-0241.1999.01376.x>  
PMID:10484009
  96. Forner A, Reig M, Bruix J. Hepatocellular carcinoma. *Lancet*. 2018; 391:1301–14.  
[https://doi.org/10.1016/S0140-6736\(18\)30010-2](https://doi.org/10.1016/S0140-6736(18)30010-2)  
PMID:29307467
  97. Adeva J, Sangro B, Salati M, Edeline J, La Casta A, Bittoni A, Berardi R, Bruix J, Valle JW. Medical treatment for cholangiocarcinoma. *Liver Int*. 2019 (Suppl 1); 39:123–42.  
<https://doi.org/10.1111/liv.14100> PMID:30892822
  98. Cho SW, Steel J, Tsung A, Marsh JW, Geller DA, Gamblin TC. Safety of liver resection in the elderly: how important is age? *Ann Surg Oncol*. 2011; 18:1088–95.  
<https://doi.org/10.1245/s10434-010-1404-6>  
PMID:21046265
  99. Tsujita E, Utsunomiya T, Ohta M, Tagawa T, Matsuyama A, Okazaki J, Yamamoto M, Tsutsui S, Ishida T. Outcome of repeat hepatectomy in patients with hepatocellular carcinoma aged 75 years and older. *Surgery*. 2010; 147:696–703.  
<https://doi.org/10.1016/j.surg.2009.10.054>  
PMID:20015526
  100. Wang WL, Zhu Y, Cheng JW, Li MX, Xia JM, Hao J, Yu L, Lv Y, Wu Z, Wang B. Major hepatectomy is safe for hepatocellular carcinoma in elderly patients with cirrhosis. *Eur J Gastroenterol Hepatol*. 2014; 26:444–51.  
<https://doi.org/10.1097/MEG.0000000000000046>  
PMID:24463566
  101. Watanabe Y, Kuboki S, Shimizu H, Ohtsuka M, Yoshitomi H, Furukawa K, Miyazaki M. A New Proposal of Criteria for the Future Remnant Liver Volume in Older Patients Undergoing Major Hepatectomy for Biliary Tract Cancer. *Ann Surg*. 2018; 267:338–45.  
<https://doi.org/10.1097/SLA.0000000000002080>  
PMID:27849659
  102. Durand F, Levitsky J, Cauchy F, Gilgenkrantz H, Soubrane O, Francoz C. Age and liver transplantation. *J Hepatol*. 2019; 70:745–58.  
<https://doi.org/10.1016/j.jhep.2018.12.009>  
PMID:30576701
  103. Levy MF, Somasundar PS, Jennings LW, Jung GJ, Molmenti EP, Fasola CG, Goldstein RM, Gonwa TA, Klintmalm GB. The elderly liver transplant recipient: a call for caution. *Ann Surg*. 2001; 233:107–13.  
<https://doi.org/10.1097/0000658-200101000-00016>  
PMID:11141232
  104. Herrero JL, Lucena JF, Quiroga J, Sangro B, Pardo F, Rotellar F, Álvarez-Cienfuegos J, Prieto J. Liver transplant recipients older than 60 years have lower survival and higher incidence of malignancy. *Am J Transplant*. 2003; 3:1407–12.  
<https://doi.org/10.1046/j.1600-6143.2003.00227.x>  
PMID:14525602
  105. Collins BH, Pirsch JD, Becker YT, Hanaway MJ, Van der Werf WJ, D'Alessandro AM, Knechtle SJ, Odorico JS, Levenson G, Musat A, Armbrust M, Becker BN, Sollinger HW, Kalayoglu M. Long-term results of liver transplantation in older patients 60 years of age and older. *Transplantation*. 2000; 70:780–83.  
<https://doi.org/10.1097/00007890-200009150-00012>  
PMID:11003357
  106. Aduen JF, Sujay B, Dickson RC, Heckman MG, Hewitt WR, Stapelfeldt WH, Steers JL, Harnois DM, Kramer



- DJ. Outcomes after liver transplant in patients aged 70 years or older compared with those younger than 60 years. *Mayo Clin Proc.* 2009; 84:973–78.  
[https://doi.org/10.1016/S0025-6196\(11\)60667-8](https://doi.org/10.1016/S0025-6196(11)60667-8)  
PMID:19880687
107. Taner CB, Ung RL, Rosser BG, Aranda-Michel J. Age is not a contraindication for orthotopic liver transplantation: a single institution experience with recipients older than 75 years. *Hepatol Int.* 2012; 6:403–07.  
<https://doi.org/10.1007/s12072-011-9286-7>  
PMID:21688082
  108. Sapisochin G, Rodríguez de Lope C, Gastaca M, Ortiz de Urbina J, Suarez MA, Santoyo J, Castroagudín JF, Varo E, López-Andujar R, Palacios F, Sanchez Antolín G, Perez B, Guiberteau A, et al. "Very early" intrahepatic cholangiocarcinoma in cirrhotic patients: should liver transplantation be reconsidered in these patients? *Am J Transplant.* 2014; 14:660–67.  
<https://doi.org/10.1111/ajt.12591> PMID:24410861
  109. Mirici-Cappa F, Gramenzi A, Santi V, Zambruni A, Di Micoli A, Frigerio M, Maraldi F, Di Nolfo MA, Del Poggio P, Benvegnù L, Rapaccini G, Farinati F, Zoli M, et al, and Italian Liver Cancer Group. Treatments for hepatocellular carcinoma in elderly patients are as effective as in younger patients: a 20-year multicentre experience. *Gut.* 2010; 59:387–96.  
<https://doi.org/10.1136/gut.2009.194217>  
PMID:20207642
  110. Fujiwara N, Tateishi R, Kondo M, Minami T, Mikami S, Sato M, Uchino K, Enooku K, Masuzaki R, Nakagawa H, Kondo Y, Asaoka Y, Shiina S, et al. Cause-specific mortality associated with aging in patients with hepatocellular carcinoma undergoing percutaneous radiofrequency ablation. *Eur J Gastroenterol Hepatol.* 2014; 26:1039–46.  
<https://doi.org/10.1097/MEG.000000000000161>  
PMID:25051219
  111. Brandi G, Rizzo A, Dall'Olio FG, Felicani C, Ercolani G, Cescon M, Frega G, Tavoroli S, Palloni A, De Lorenzo S, Abbati F, Mollica V, Ricci AD, Serra C. Percutaneous radiofrequency ablation in intrahepatic cholangiocarcinoma: a retrospective single-center experience. *Int J Hyperthermia.* 2020; 37:479–85.  
<https://doi.org/10.1080/02656736.2020.1763484>  
PMID:32396398
  112. Shen X, Ma S, Tang X, Wang T, Qi X, Chi J, Wang Z, Cui D, Zhang Y, Li P, Zhai B. Clinical outcome in elderly Chinese patients with primary hepatocellular carcinoma treated with percutaneous microwave coagulation therapy (PMCT): A Strobe-compliant observational study. *Medicine (Baltimore).* 2018; 97:e11618.  
<https://doi.org/10.1097/MD.00000000000011618>  
PMID:30170369
  113. Díaz-González Á, Vilana R, Bianchi L, García-Criado Á, Rimola J, Rodríguez de Lope C, Ferrer J, Ayuso C, Da Fonseca LG, Reig M, Forner A. Thermal Ablation for Intrahepatic Cholangiocarcinoma in Cirrhosis: Safety and Efficacy in Non-Surgical Patients. *J Vasc Interv Radiol.* 2020; 31:710–19.  
<https://doi.org/10.1016/j.jvir.2019.06.014>  
PMID:31685360
  114. Cohen MJ, Bloom AI, Barak O, Klimov A, Nesher T, Shouval D, Levi I, Shibolet O. Trans-arterial chemo-embolization is safe and effective for very elderly patients with hepatocellular carcinoma. *World J Gastroenterol.* 2013; 19:2521–28.  
<https://doi.org/10.3748/wjg.v19.i16.2521>  
PMID:23674854
  115. Seo JH, Kim DH, Cho E, Jun CH, Park SY, Cho SB, Park CH, Kim HS, Choi SK, Rew JS. Characteristics and Outcomes of Extreme Elderly Patients With Hepatocellular Carcinoma in South Korea. *In Vivo.* 2019; 33:145–54.  
<https://doi.org/10.21873/invivo.11451>  
PMID:30587615
  116. Yang Q, Jin X, Ye F, Zheng B, Xie X, Luo Y, Shi Z, Shi C. Safety and efficacy analysis of DEB-TACE treatment in elderly patients with hepatocellular carcinoma: a comparative cohort study. *Oncol Res.* 2018. [Epub ahead of print].  
<https://doi.org/10.3727/096504018X15223171140640> PMID:29739489
  117. Luo J, Zheng J, Shi C, Fang J, Peng Z, Huang J, Sun J, Zhou G, Li T, Zhu D, Xu H, Hou Q, Ying S, et al. Drug-eluting beads transarterial chemoembolization by CalliSpheres is effective and well tolerated in treating intrahepatic cholangiocarcinoma patients: A preliminary result from CTILC study. *Medicine (Baltimore).* 2020; 99:e19276.  
<https://doi.org/10.1097/MD.00000000000019276>  
PMID:32195932
  118. Kapacee ZA, McNamara MG, de Liguori Carino N, Lamarca A, Valle JW, Hubner RA. Systemic therapies in advanced hepatocellular carcinoma: How do older patients fare? *Eur J Surg Oncol.* 2021; 47:583–90.  
<https://doi.org/10.1016/j.ejso.2020.03.210>  
PMID:32303415
  119. Llovet JM, Ricci S, Mazzaferro V, Hilgard P, Gane E, Blanc JF, de Oliveira AC, Santoro A, Raoul JL, Forner A, Schwartz M, Porta C, Zeuzem S, et al, and SHARP Investigators Study Group. Sorafenib in advanced hepatocellular carcinoma. *N Engl J Med.* 2008; 359:378–90.

<https://doi.org/10.1056/NEJMoa0708857>

PMID:[18650514](#)

120. Wong H, Tang YF, Yao TJ, Chiu J, Leung R, Chan P, Cheung TT, Chan AC, Pang RW, Poon R, Fan ST, Yau T. The outcomes and safety of single-agent sorafenib in the treatment of elderly patients with advanced hepatocellular carcinoma (HCC). *Oncologist*. 2011; 16:1721–28.  
<https://doi.org/10.1634/theoncologist.2011-0192>  
PMID:[22135121](#)
121. Edeline J, Crouzet L, Le Sourd S, Larible C, Brunot A, Le Roy F, Cattenoz C, Latournerie M, Gédouin D, Guillygomarc'h A, Boucher E. Sorafenib use in elderly patients with hepatocellular carcinoma: caution about use of platelet aggregation inhibitors. *Cancer Chemother Pharmacol*. 2015; 75:215–19.  
<https://doi.org/10.1007/s00280-014-2645-z>  
PMID:[25477009](#)
122. Tada T, Kumada T, Hiraoka A, Michitaka K, Atsukawa M, Hirooka M, Tsuji K, Ishikawa T, Takaguchi K, Kariyama K, Itobayashi E, Tajiri K, Shimada N, et al. Safety and efficacy of lenvatinib in elderly patients with unresectable hepatocellular carcinoma: A multicenter analysis with propensity score matching. *Hepatol Res*. 2020; 50:75–83.  
<https://doi.org/10.1111/hepr.13427> PMID:[31660700](#)
123. D'Alessio A, Prete MG, Cammarota A, Personeni N, Rimassa L. The Role of Cabozantinib as a Therapeutic Option for Hepatocellular Carcinoma: Current Landscape and Future Challenges. *J Hepatocell Carcinoma*. 2021; 8:177–91.  
<https://doi.org/10.2147/JHC.S268310>  
PMID:[33824862](#)
124. Bruix J, Qin S, Merle P, Granito A, Huang YH, Bodoky G, Pracht M, Yokosuka O, Rosmorduc O, Breder V, Gerolami R, Masi G, Ross PJ, et al, and RESORCE Investigators. Regorafenib for patients with hepatocellular carcinoma who progressed on sorafenib treatment (RESORCE): a randomised, double-blind, placebo-controlled, phase 3 trial. *Lancet*. 2017; 389:56–66.  
[https://doi.org/10.1016/S0140-6736\(16\)32453-9](https://doi.org/10.1016/S0140-6736(16)32453-9)  
PMID:[27932229](#)
125. Abou-Alfa GK, Meyer T, Cheng AL, El-Khoueiry AB, Rimassa L, Ryoo BY, Cicin I, Merle P, Chen Y, Park JW, Blanc JF, Bolondi L, Klumpen HJ, et al. Cabozantinib in Patients with Advanced and Progressing Hepatocellular Carcinoma. *N Engl J Med*. 2018; 379:54–63.  
<https://doi.org/10.1056/NEJMoa1717002>  
PMID:[29972759](#)
126. Fuchigami A, Imai Y, Uchida Y, Uchiya H, Fujii Y, Nakazawa M, Ando S, Sugawara K, Nakayama N, Tomiya T, Mochida S. Therapeutic efficacy of lenvatinib for patients with unresectable hepatocellular carcinoma based on the middle-term outcome. *PLoS One*. 2020; 15:e0231427.  
<https://doi.org/10.1371/journal.pone.0231427>  
PMID:[32275701](#)
127. Kudo M, Galle PR, Llovet JM, Finn RS, Vogel A, Motomura K, Assenat E, Merle P, Brandi G, Daniele B, Okusaka T, Tomášek J, Borg C, et al. Ramucirumab in elderly patients with hepatocellular carcinoma and elevated alpha-fetoprotein after sorafenib in REACH and REACH-2. *Liver Int*. 2020; 40:2008–20.  
<https://doi.org/10.1111/liv.14462> PMID:[32279446](#)
128. El-Khoueiry AB, Sangro B, Yau T, Crocenzi TS, Kudo M, Hsu C, Kim TY, Choo SP, Trojan J, Welling TH 3rd, Meyer T, Kang YK, Yeo W, et al. Nivolumab in patients with advanced hepatocellular carcinoma (CheckMate 040): an open-label, non-comparative, phase 1/2 dose escalation and expansion trial. *Lancet*. 2017; 389:2492–502.  
[https://doi.org/10.1016/S0140-6736\(17\)31046-2](https://doi.org/10.1016/S0140-6736(17)31046-2)  
PMID:[28434648](#)
129. Finn RS, Ryoo BY, Merle P, Kudo M, Bouattour M, Lim HY, Breder V, Edeline J, Chao Y, Ogasawara S, Yau T, Garrido M, Chan SL, et al, and KEYNOTE-240 investigators. Pembrolizumab As Second-Line Therapy in Patients With Advanced Hepatocellular Carcinoma in KEYNOTE-240: A Randomized, Double-Blind, Phase III Trial. *J Clin Oncol*. 2020; 38:193–202.  
<https://doi.org/10.1200/JCO.19.01307>  
PMID:[31790344](#)
130. Li D, Toh HC, Merle P, Tsuchiya K, Hernandez S, Shao H, Mulla S, Ding B, Kudo M. Atezolizumab + bevacizumab vs sorafenib for unresectable hepatocellular carcinoma (HCC): results from older adults enrolled in IMbrave150. *ESMO-GI*. 2020; July 1–4.
131. Yukisawa S, Ishii H, Matsuyama M, Kuraoka K, Takano K, Kamei A, Ozaka M. Outcomes and tolerability of systemic chemotherapy for pancreatic or biliary cancer patients aged 75 years or older. *Jpn J Clin Oncol*. 2011; 41:76–80.  
<https://doi.org/10.1093/jjco/hyq160> PMID:[20926412](#)
132. Lewis AR, Cipriano C, Wang X, Ward R, Fitzpatrick A, Scott AR, Rashed A, Raja H, Lamarca A, Hubner RA, Valle JW, McNamara MG. Outcomes in patients ≥ 80 years with a diagnosis of a hepatopancreaticobiliary (HPB) malignancy. *Med Oncol*. 2019; 36:85.  
<https://doi.org/10.1007/s12032-019-1310-0>  
PMID:[31493088](#)
133. Shin DW, Kim MJ, Lee JC, Kim J, Woo SM, Lee WJ, Lee KH, Hwang JH. Gemcitabine Plus Cisplatin Chemotherapy Prolongs the Survival in Advanced Hilar Cholangiocarcinoma: A Large Multicenter Study.

Am J Clin Oncol. 2020; 43:422–27.  
<https://doi.org/10.1097/COC.0000000000000682>  
PMID:[32118610](https://pubmed.ncbi.nlm.nih.gov/32118610/)

134. Primrose JN, Fox RP, Palmer DH, Malik HZ, Prasad R, Mirza D, Anthony A, Corrie P, Falk S, Finch-Jones M, Wasan H, Ross P, Wall L, et al, and BILCAP study group. Capecitabine compared with observation in resected biliary tract cancer (BILCAP): a randomised, controlled, multicentre, phase 3 study. *Lancet Oncol*. 2019; 20:663–73.  
[https://doi.org/10.1016/S1470-2045\(18\)30915-X](https://doi.org/10.1016/S1470-2045(18)30915-X)  
PMID:[30922733](https://pubmed.ncbi.nlm.nih.gov/30922733/)
135. Ueno M, Ikeda M, Sasaki T, Nagashima F, Mizuno N, Shimizu S, Ikezawa H, Hayata N, Nakajima R, Morizane C. Phase 2 study of lenvatinib monotherapy as second-line treatment in unresectable biliary tract cancer: primary analysis results. *BMC Cancer*. 2020; 20:1105.  
<https://doi.org/10.1186/s12885-020-07365-4>  
PMID:[33198671](https://pubmed.ncbi.nlm.nih.gov/33198671/)
136. Abou-Alfa GK, Sahai V, Hollebecque A, Vaccaro G, Melisi D, Al-Rajabi R, Paulson AS, Borad MJ, Gallinson D, Murphy AG, Oh DY, Dotan E, Catenacci DV, et al. Pemigatinib for previously treated, locally advanced or metastatic cholangiocarcinoma: a multicentre, open-label, phase 2 study. *Lancet Oncol*. 2020; 21:671–84.  
[https://doi.org/10.1016/S1470-2045\(20\)30109-1](https://doi.org/10.1016/S1470-2045(20)30109-1)  
PMID:[32203698](https://pubmed.ncbi.nlm.nih.gov/32203698/)
137. Fan B, Mellinghoff IK, Wen PY, Lowery MA, Goyal L, Tap WD, Pandya SS, Manyak E, Jiang L, Liu G, Nimkar T, Gliser C, Prah Judge M, et al. Clinical pharmacokinetics and pharmacodynamics of ivosidenib, an oral, targeted inhibitor of mutant IDH1, in patients with advanced solid tumors. *Invest New Drugs*. 2020; 38:433–44.  
<https://doi.org/10.1007/s10637-019-00771-x>  
PMID:[31028664](https://pubmed.ncbi.nlm.nih.gov/31028664/)
138. Rizzo A, Ricci AD, Frega G, Di Federico A, Brandi G. FGFR inhibitors in elderly patients with advanced biliary tract cancer: an unsolved issue. *Expert Rev Gastroenterol Hepatol*. 2021; 15:567–74.  
<https://doi.org/10.1080/17474124.2021.1911646>  
PMID:[33787429](https://pubmed.ncbi.nlm.nih.gov/33787429/)

# Identification of a novel immune signature for optimizing prognosis and treatment prediction in colorectal cancer

Yan Li<sup>1,\*</sup>, Yiyi Li<sup>1,\*</sup>, Zijin Xia<sup>1,\*</sup>, Dun Zhang<sup>2,3</sup>, Xiaomei Chen<sup>4</sup>, Xinyu Wang<sup>1</sup>, Jing Liao<sup>5</sup>, Wei Yi<sup>6</sup>, Jun Chen<sup>1,7,8,9,10</sup>

<sup>1</sup>Zhongshan School of Medicine, Sun Yat-Sen University, Guangzhou, Guangdong, China

<sup>2</sup>Department of Medical Oncology, Sun Yat-Sen University Cancer Center, Guangzhou, Guangdong, China

<sup>3</sup>State Key Laboratory of Oncology in South China, Collaborative Innovation Center for Cancer Medicine, Sun Yat-Sen University Cancer Center, Sun Yat-Sen University, Guangzhou, Guangdong, China

<sup>4</sup>The First School of Clinical Medicine, Southern Medical University, Guangzhou, Guangdong, China

<sup>5</sup>The Sixth Affiliated Hospital, Sun Yat-Sen University, Guangzhou, Guangdong, China

<sup>6</sup>Zhongshan Ophthalmic Center, Sun Yat-Sen University, Guangzhou, Guangdong, China

<sup>7</sup>Guangdong Provincial Key Laboratory of Malignant Tumor Epigenetics and Gene Regulation, Sun Yat-Sen Memorial Hospital, Sun Yat-Sen University, Guangzhou, Guangdong, China

<sup>8</sup>Guangdong Engineering and Technology Research Center for Disease-Model Animals, Laboratory Animal Center, Zhongshan School of Medicine, Sun Yat-Sen University, Guangzhou, Guangdong, China

<sup>9</sup>Key Laboratory of Tropical Disease Control of the Ministry of Education, Sun Yat-Sen University, Guangzhou, Guangdong, China

<sup>10</sup>Center for Precision Medicine, Sun Yat-Sen University, Guangzhou, Guangdong, China

\*Equal contribution

**Correspondence to:** Wei Yi, Jun Chen; email: [yiwei@gzzoc.com](mailto:yiwei@gzzoc.com), [chenjun23@mail.sysu.edu.cn](mailto:chenjun23@mail.sysu.edu.cn)

**Keywords:** colorectal cancer, immune signature, prognosis, immunotherapy, precision medicine

**Received:** September 24, 2021 **Accepted:** November 22, 2021 **Published:** December 13, 2021

**Copyright:** © 2021 Li et al. This is an open access article distributed under the terms of the [Creative Commons Attribution License](https://creativecommons.org/licenses/by/3.0/) (CC BY 3.0), which permits unrestricted use, distribution, and reproduction in any medium, provided the original author and source are credited.

## ABSTRACT

**Background:** Globally, colorectal cancer (CRC) is one of the most lethal malignant diseases. However, the currently approved therapeutic options for CRC failed to acquire satisfactory treatment efficacy. Tailoring therapeutic strategies for CRC individuals can provide new insights into personalized prediction approaches and thus maximize clinical benefits.

**Methods:** In this study, a multi-step process was used to construct an immune-related genes (IRGs) based signature leveraging the expression profiles and clinical characteristics of CRC from the Gene Expression Omnibus (GEO) database and the Cancer Genome Atlas (TCGA) database. An integrated immunogenomic analysis was performed to determine the association between IRGs with prognostic significance and cancer genotypes in the tumor immune microenvironment (TIME). Moreover, we performed a comprehensive *in silico* therapeutics screening to identify agents with subclass-specific efficacy.

**Results:** The established signature was shown to be a promising biomarker for evaluating clinical outcomes in CRC. The immune risk score as calculated by this classifier was significantly correlated with over-riding malignant phenotypes and immunophenotypes. Further analyses demonstrated that CRCs with low immune risk scores achieved better therapeutic benefits from immunotherapy, while AZD4547, Cyclophosphamide B and S-triazotinib might have potential therapeutic implications in the immune risk score-high CRCs.

**Conclusions:** Overall, this IRGs-based signature not only afforded a useful tool for determining the prognosis and evaluating the TIME features of CRCs, but also shed new light on tailoring CRCs with precise treatment.

## INTRODUCTION

Colorectal cancer (CRC) is the third most frequently occurring cancer and the second leading cause of cancer-related deaths worldwide in 2018 [1]. The current therapeutic options for CRC include endoscopic and local surgical excision, downstaging preoperative radiotherapy and systemic therapy, extensive surgery, local ablative therapies for metastases, palliative chemotherapy, targeted therapy, and immunotherapy [2]. It's a highly heterogeneous disease on account of accumulating mutations attributed to environmental and genetic factors for years, which makes prognostic prediction and treatment to be exceedingly challenging [3, 4]. Therefore, there is an urgent need to incorporate other important elements to guide personalized therapies for CRCs, thereby improving the survival and prognosis of CRCs.

In recent years, a myriad of publications have highlighted that the tumor immune microenvironment (TIME) is critically involved in cancer initiation and progression [5, 6]. For example, tumor-infiltrating lymphocytes (TILs) were in close interaction with relapse and mortality prediction in CRC [7–9]. Besides, immune checkpoint inhibitors (ICIs) targeted programmed cell death protein 1 (PD-1)/programmed Cell Death-Ligand 1 (PD-L1) have been proved effective in the treatment of CRC [10, 11], revolutionizing oncotherapy to a great extent. Michael J et al. have demonstrated that a combination of PD-1 inhibitor (nivolumab) and cytotoxic T-lymphocyte-associated protein 4 (CTLA-4) inhibitor (ipilimumab) has comparatively better efficacy and is a promising new therapeutic option for metastatic DNA mismatch repair-deficient and microsatellite instability-high (dMMR–MSI-H) CRCs [12, 13]. As the most widely investigated marker, tumor PD-L1 expression might be useful as a predictive marker of response to anti-PD-1 treatment for non-small cell lung cancer (NSCLC), gastric cancer and gastroesophageal junction tumors [14, 15]. But in CRC, PD-L1 expression wasn't tightly associated with the response or survival in the recent studies [16]. Thus far, several other biomarkers of potential response have been demonstrated, including high tumor mutation load [17, 18], high immunoscore [19, 20], and *POLE* mutation [21, 22]. However, these biomarkers that guided the use of ICIs in patients with CRC are not always consistent in clinical practice. For example, high immunoscore were also substantiated in pMMR–MSI-L CRCs, raising queries of whether single immunophenotype might robustly predict immunotherapy benefit [23]. Consequently, integrative immunogenic features of the TIME might be more precise in predicting immunotherapeutic response than either feature alone. In conclusion, developing a novel immune signature complementary for the currently established signatures is

of great importance to optimize individual specialized immunotherapy for CRC patients.

Within the past decade, studies have aimed at elucidating the roles of immune-related genes (IRGs) in CRC. Li et al. have constructed an IRGs signature leveraging expression profiles and clinical characteristics from the GEO database and the TCGA database. Robust prognostic ability was demonstrated, meanwhile, the enrichment with cytotoxic immune cells as well as depletion of myeloid-derived suppressor cells (MDSC) and regulatory T cells (Tregs) were estimated in low-risk signature CRCs [24]. Lin et al. also comprehensively analyzed the role of IRGs in CRCs via the TCGA dataset, reporting a higher prognostic performance of 10 IRGs based signature in CRC and the infiltration degree of various immune cells [25]. Nevertheless, there has been no IRGs signature that comprehensively evaluates the TIME and predicts prognostic significance in conjunction with the response to chemotherapeutic and immunotherapeutic options of CRC.

In this study, we aimed at establishing a novel IRGs-based signature for CRC to investigate the interplay between colorectal immune activity profile and oncology genotype. Through systematic *in silico* analysis based on the constructed signature, we discovered that the IRGs risk score for CRC was associated with overall survival (OS), clinicopathological factors, and immunophenotypic characteristics. Moreover, we also assessed the efficiency of this IRGs signature in identifying chemotherapeutic compounds and immunotherapy with subtype-specific efficacy.

## MATERIALS AND METHODS

### Data preparation

Processed RNA-Seq FPKM data and clinical information of CRC were collected from the TCGA database. The TCGA colon adenocarcinoma (COAD, n = 512) cohort and rectum adenocarcinoma (READ, n = 177) cohort were obtained from the GDC data portal (<https://portal.gdc.cancer.gov/repository>). For validation, the expression profiles and detailed clinical information of GSE39582 (including 562 CRC samples based on GPL570 platform) were retrieved from the GEO database (<https://www.ncbi.nlm.nih.gov/geo/>). The immune gene lists were obtained from the ImmPort database (<https://immport.niaid.nih.gov>) [26] and overlapping genes from the TCGA dataset were defined as IRGs in the current study and extracted for the subsequent analysis.

To analyze the drug sensitivity in human CRCs, GSE17538 (including 232 CRC samples based on the



GPL570 platform) was obtained from the GEO database. The expression profiles of human cancer cell lines (CCLs) were achieved from the Broad Institute Cancer Cell Line Encyclopedia (CCLE) project (<https://portals.broadinstitute.org/ccle/>) [27]. Drug sensitivity data of CCLs were extracted from the Cancer Therapeutics Response Portal (CTRP, <https://portals.broadinstitute.org/ctrp>) and PRISM Repurposing dataset (<https://depmap.org/portal/prism/>). The PRISM is composed of sensitivity data for 1448 compounds over 482 CCLs and the CTRP comprises of sensitivity data for 481 compounds over 835 CCLs. The area under the dose-response curve (area under the curve-AUC) values as a measure of drug sensitivity are presented in both two datasets, with lower AUC values indicating higher drug sensitivity. After the exclusion of compounds with more than 20% of missing data, the missing AUC values were imputed by K-nearest neighbor (k-NN) imputation.

To investigate the response to immunotherapy, tumor expression profiles of six immunotherapeutic cohorts were obtained. Roh et al. (dataset contained melanoma patients receiving CTLA-4 or PD-1 blockade therapy was extracted from the supplementary files of reference [28]. Gene expression profiles and survival information of metastatic melanoma patients treated with CTLA-4 immuno-inhibitor were obtained from the work of Van Allen et al. (2015) [29]. The data of Ulloa Montoya et al. (2013) cohort with non-small-cell lung cancer (NSCLC) patients who were administered MAGE-A3 antigen-specific immunotherapy were downloaded from (GSE35640) [30]. The dataset of Hugo et al. (2016) included metastatic melanoma patients treated with anti-PD-1 agents was acquired from GSE78220 [31]. Moreover, patients with metastatic urothelial cancer treated with PD-L1 blockade therapy from the IMvigor210 cohort [32] and the dataset of Snyder et al. (2017) [33] were also enrolled.

### Construction of the IRGs signature for CRC

Differentially expression genes (DEGs) between tumor and normal samples from CRC patients from TCGA-COAD and TCGA-READ cohorts were first screened by limma package [34] with a cutoff value of false discovery rate (FDR)-adjusted P-value < 0.01 and  $\log_2$  | fold change (FC) | > 1. Then differentially expressed IRGs between the aforementioned CRC tumor and normal tissues were obtained using a strict criterion of FDR-adjusted P-value < 0.01 and  $\log_2$  | fold change (FC) | > 2. Heatmaps were plotted utilizing pheatmap package and volcano plots were generated via R software.

The CRC tumor samples from the TCGA cohort were enrolled as the training cohort to construct the IRGs

signature. Univariate Cox regression analysis of differentially expressed IRGs was performed by survival package in R. The prognosis-related IRGs (PRIRGs) were selected by a cutoff value of  $P < 0.01$ . To avoid the overfitting of IRGs signature and to delete highly correlated genes, dimensionality reduction analysis was conducted by the Least Absolute Shrinkage and Selection Operator (lasso) regression through survival and glmnet R packages using gene expression profiles and overall survival data. Lambda.min was set up as cutoff point to produce minimum mean cross-validated error and genes with the highest lambda values were selected for further analysis. Subsequently, multivariate Cox regression was harnessed to develop an IRGs signature based on the expression of these genes and to calculate the risk score for signature:  $\sum_{i=1}^n \beta_i * x_i$  ( $\beta$  represents the regression coefficient, and  $x$  stands for gene expression value). The training cohort samples were stratified into high- and low- risk groups according to the median value of the IRGs signature risk score.

Survival analysis for high- and low-risk subgroups was then carried out using Kaplan-Meier methods and the log-rank test was used to determine the statistical significance of differences. Time-dependent receiver operating characteristic (ROC) curves were also generated leveraging survivalROC R package to validate the prognostic ability of the IRGs signature. The IRGs signature obtained from the training cohort were used to assign the validation cohort as well as datasets containing therapeutic information into high- and low- risk score subtypes. Furthermore, to assess the independence of the constructed signature's predictive ability, we performed univariate analysis on the IRGs signature using all clinical factors in the training and validation cohort. The hazard ratio (HR) was measured by a Cox regression model using survival package in R and forest plots were drawn.

### Gene set enrichment analysis

Gene set enrichment analysis (GSEA) in the CRC cohorts was carried out by clusterProfiler R package [35]. Fold change (FC) of each gene between subgroups was firstly produced by limma R package, and input genes were then ranked in descending order according to the logFC values. GSEA was subsequently applied to enrich 50 hallmark gene sets (h.all.v7.0.symbols) achieved from the Molecular Signatures Database (MSigDB) [36]. Enrichment significance was evaluated using default settings and FDR adjusted P-value < 0.05 was considered significantly enriched. The single sample gene set enrichment analysis (ssGSEA) [37] implemented in R package GSVA, was adopted to calculate the normalized enrichment score (NES) of immune-related signatures in the training and validation cohorts.

## Collection of cancer- and immune-related data

Four consensus molecular subtypes (CMS) CMS1-CMS4 of training and validation group were classified through CMScaller R package [38]. Six immune subtypes C1-C6 of CRC were sorted out by ImmuneSubtypeClassifier package in R [39]. The ESTIMATE score, immune score, stromal score, and tumor purity for each CRCs were quantified by the estimate algorithm [40]. The cytolytic activity (CYT) score was yielded as the geometrical mean of the GZMA and PRF1 for evaluating the cytolytic T-cell activity in TIME [17], 78 immunomodulators [39], 8 fibroblasts [41], and 335 gene signatures of 10 oncogenic pathways [42] were extracted from the previously published literature, respectively.

CIBERSORT package in R was employed to estimate the proportion of 22 immune cell types based on expression profiles [43], with the perm set at 1000. The infiltration levels of 24 immune cell types in the CRC TIME were further calculated by ssGSEA implemented with deconvolution approach, applying gene signatures expressed by specific immune cell populations [44].

## Estimation of drug response in clinical samples

Large-scale drug screening and molecular data across hundreds of cancer cell lines in pharmacogenomic databases of CTRP and PRISM make it possible for precise drug response prediction in clinical samples. Ridge regression model that located in the R package pRRophetic [45] was used to evaluate the drug responses in clinical samples, with a robust predictive power assessed by 10-fold cross-validation in default. The prediction model was merely employed on expression profiles and drug response data of solid CCLs, and the AUC value of each agent in each clinical sample was ultimately estimated. Agents with NAs in more than 20% of the samples and hematopoietic as well as lymphoid tissue-derived CCLs were excluded. Subclass mapping (SubMap) analysis (Gene Pattern modules, <https://cloud.genepattern.org/>), which can assess the similarity of molecular subtypes between independent patient cohorts based on mRNA expression matrix, was utilized to determine the potential immunotherapeutic benefit of distinct subtypes employing the available clinical response data and gene expression profiles from six immunotherapy datasets.

## Statistical analysis

R statistical software (version 4.0.2) was implemented for all statistical analyses. The evaluation of normality distribution within continuous variables was performed by Shapiro-Wilk test. Comparison of a continuous variable in two or more than two groups was conducted

by parametric test (Student's t-test or analysis of variance, respectively) if the variable was normally distributed, otherwise, nonparametric test (Wilcoxon rank-sum test or Kruskal-Wallis test) was performed. Correlation between two continuous variables was evaluated by either Pearson's r correlation or Spearman's rank-order correlation. For all statistical analyses, unless otherwise noted, a two-tailed P-value < 0.05 was defined as statistically significant.

## RESULTS

### Construction of IRGs signature in CRC cohorts

A total of 638 CRC and 51 adjacent normal tissues were acquired from the TCGA database. To establish a predictive IRGs signature, we performed differential expression analysis of genes and IRGs between tumor and normal tissues. A total of 3741 DEGs were identified, including 2,502 upregulated genes and 1,239 downregulated genes (Supplementary Figure 1A, 1B). 2,483 IRGs were also collected from the ImmPort database (Supplementary Table 1). Fulfilling the screening criteria, 294 differentially expressed IRGs were obtained, containing 99 upregulated IRGs and 195 downregulated IRGs (Supplementary Figure 1C, 1D). In total, 606 CRC samples with complete gene expression profiles and intact follow-up information from the TCGA database were enrolled for establishing IRGs signature in the training cohort.

To determine the IRGs related to tumorigenesis and development in CRC, univariate Cox regression analysis was implemented on the differentially expressed IRGs in the training cohort ( $P < 0.01$ ), and 11 PRIRGs in all were obtained (Supplementary Figure 1E). Moreover, lasso regression was conducted to lessen the number of PRIRGs, and eight PRIRGs were thus filtered out (Supplementary Figure 1F, 1G and Supplementary Table 2). Through multivariate Cox regression analysis, seven-IRGs based signature was ultimately established, as depicted in Supplementary Table 3. The formula for calculating risk score is: Risk score =  $0.139 \times \text{Exp}_{\text{FABP4}} + 0.176 \times \text{Exp}_{\text{AMH}} + 0.207 \times \text{Exp}_{\text{GRP}} + 0.211 \times \text{Exp}_{\text{INHBB}} - 0.691 \times \text{Exp}_{\text{NRG1}} + 0.274 \times \text{Exp}_{\text{UCN}} + 0.366 \times \text{Exp}_{\text{MC1R}}$ . Among these IRGs, NRG1 exhibited a negative coefficient, implying that it could be considered as a protective factor for CRCs; on the contrary, FABP4, AMH, GRP, INHBB, UCN, and MC1R possess positive coefficients, implying poor prognoses in CRCs with overexpression of these six genes.

According to the median value of the risk score (0.948), the 606 CRCs in the training cohort were divided into a high-risk group ( $n = 303$ ) and a low-risk group ( $n = 303$ ). The distribution of risk scores, survival status as

well as the expression level of seven IRGs for the two subgroups in the training cohort were correspondingly displayed in Figure 1A. Kaplan-Meier survival analysis (Figure 1B) indicated dismal prognosis for patients in the high-risk group ( $P < 0.0001$ ). To assess the predictive efficiency of the constructed seven IRGs signature, time-dependent ROC curves were plotted. As shown in Figure 1C, the AUCs for 1-, 3-, 5- year survival prediction was 0.692, 0.676, and 0.721, respectively.

To evaluate the performance of the seven IRGs signature, the GSE39582 dataset ( $n=562$ ) was used for validation. On the basis of signature information acquired from the training cohort, CRCs in the validation cohort were also classified into high-risk group ( $n = 281$ ) and low-risk group ( $n = 281$ ). The distribution of risk scores, survival status, and the expression level of seven IRGs for different subclasses in the validation cohort are correspondingly displayed in Supplementary Figure 2A. Kaplan-Meier survival analysis in Supplementary Figure 2B also revealed poor prognosis in patients of high-risk score ( $P < 0.0001$ ). Similarly, time-dependent ROC curves were plotted. As exhibited in Supplementary Figure 2C, the AUC for 1-, 3-, 5- year survival prediction was 0.615, 0.616, and 0.662, respectively.

### Evaluation of the IRGs signature in CRC cohorts

A detailed summary of the training and the validation cohorts selected for univariate analysis in this study is presented in Supplementary Table 4. Univariate analysis of the TCGA dataset suggested that age ( $P = 0.003$ ), history of colon polyps ( $P = 0.020$ ), tumor stage ( $P < 0.001$ ), mismatch repair system (MMR) status ( $P = 0.045$ ), EGFR mutation ( $P = 0.003$ ), and risk score ( $P < 0.001$ ) were significantly associated with OS (Figure 1D). Meanwhile, a high-risk score was correlated with increased age, history of colon polyps, right half of CRC, dMMR as well as EGFR mutation (Supplementary Table 4). Analogous analyses in the validation dataset showed that tumor stage ( $P < 0.001$ ), KRAS mutation ( $P = 0.048$ ), and risk score ( $P < 0.001$ ) were closely connected with patient survival (Supplementary Figure 2D). As shown in Figure 1E, the risk score was significantly higher in right-side colorectal cancer than the left-side, and the risk score was significantly elevated as colorectal cancer progressed to an advanced stage.

The differences in the distribution of molecular subtypes within the IRGs risk score model were also investigated. In the TCGA cohort, there was no significant difference between the risk score and the immune subtypes (Figure 1F, 1G). Similar results were manifested in the validation dataset (Supplementary Figure 2E, 2F),

probably because six immune subtypes were generated by immunogenomics analyses encompassing multiple cancer types [39]. With regards to CMS, the CMS4 subtype had significantly higher IRGs risk score than the other three molecular subtypes, whereas the CMS2 subtype held the lowest risk score (Figure 1F, 1H). A significant difference was demonstrated among the four CMSs ( $P = 1.5e-11$ ). In the GEO validation dataset, CMS was likewise found distributed between high- and low- risk subgroups (Supplementary Figure 2E), and allied results ( $P < 2.2e-16$ ) were displayed in violin plot (Supplementary Figure 2G). Remarkably, the international CRC Subtyping Consortium proposed that superior survival was demonstrated in CMS2 patients while CMS4 patients displayed worse OS [46], consistent with our finding that a larger proportion of long-term survivors were identified in low-risk CRCs than the high-risk subset. The GSEA of 50 hallmark gene sets indicated that up-regulated genes of the high-risk group were enriched in multiple carcinogenesis related pathways, such as epithelial-mesenchymal transition (EMT), angiogenesis, Hedgehog signaling, myogenesis, transforming growth factor-beta (TGF $\beta$ ) signaling, as well as hypoxia pathway targeted HIF1A (Figure 2A and Supplementary Figure 3A). GSEA analyses revealed the enrichment of tumor proliferation-associated signatures, such as E2F targets, MYC targets, and G2M checkpoint in IRGs low-risk subgroup. Several evidences suggested that they might denote dual role of regulating anti-tumor immunity and tumor cell proliferation. It's indicated that the E2F1/SP3/STAT6 axis induced by IL-4 promoted EMT in CRC cells [47]. Activation of IL-6/p-STAT3/c-MYC signaling was demonstrated to enhance colorectal tumor growth in a TLR4-dependent manner [48]. In addition, MYC/PVT1 signaling induced immune surveillance via CD8<sup>+</sup> TILs and peripheral blood mononuclear cells in CRCs [49]. As for G2M checkpoint, *in-vitro* co-culture assays of T cells and HCT-116 colorectal cancer cells reflected that immune checkpoint TIGIT blockade suppressed G2M transit [50]. Overall, these tumor proliferation-related pathways might also exert tumor immunity associated effects on the TIME of CRC, and the underlying mechanism deserved future investigation. Metabolism-related processes consisting of oxidative phosphorylation and fatty acid metabolism, as well as immune-related signaling involved in IL6/JAK/STAT3, were observed in the low-risk group.

Besides, variation in the NES values of 10 common oncogenic pathways between the two subclasses were evaluated in the TCGA COAD and READ patients (Figure 3A). The Hippo-, Notch-, NRF2- and Wnt-related pathways exhibited significantly higher NES values in high-risk subtype than in low-risk subtype. The NES values of the PI3K, RAS, and TP53-related

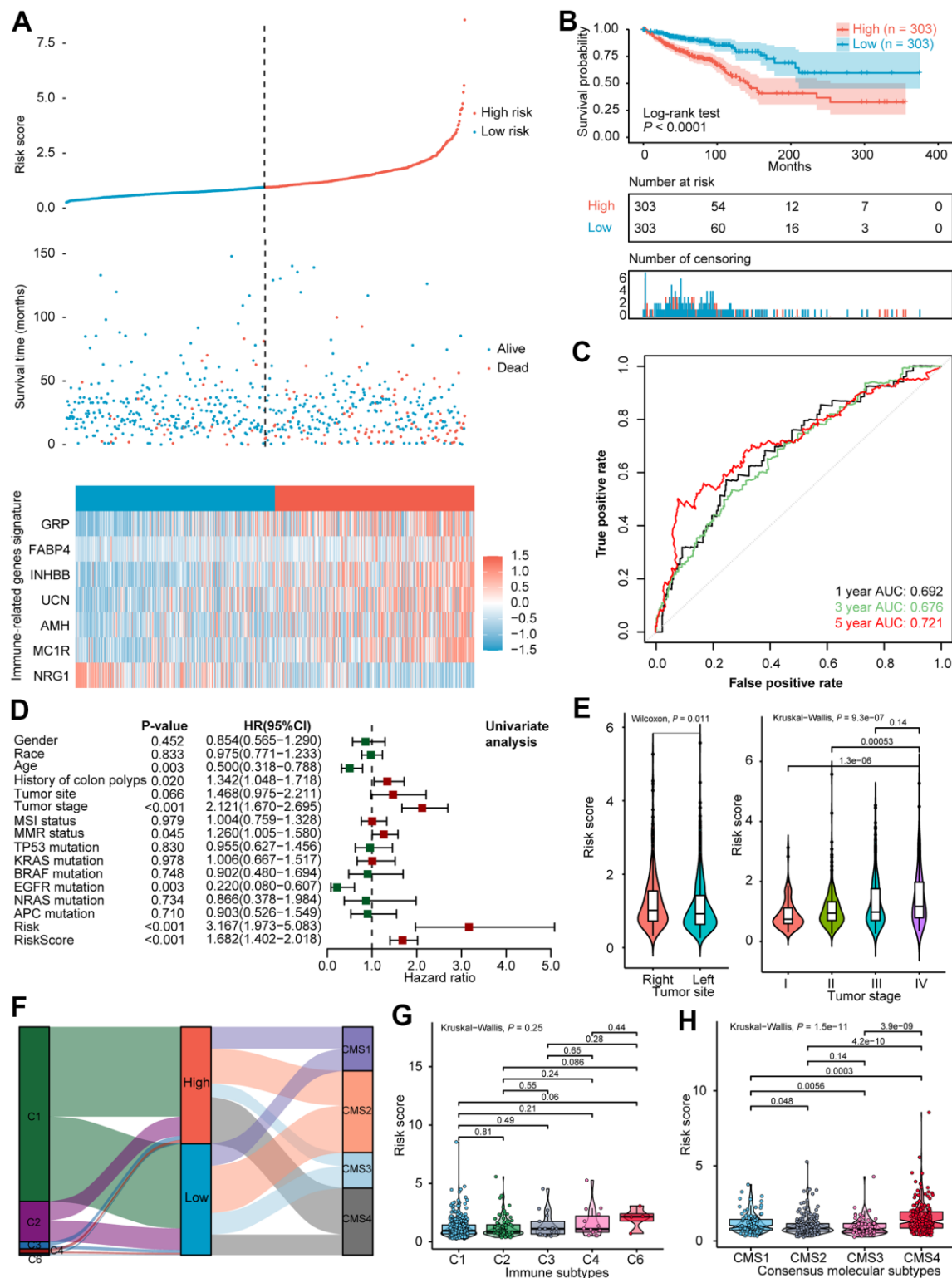


**Figure 1. Exploration of the predictive power and clinical characteristics of seven IRGs signature in the training cohort.** (A) Distribution of risk score, survival status, and expression of seven IRGs of CRCs. (B) Kaplan-Meier survival curve of the high- and low-risk subgroups. (C) ROC curve analysis of IRGs. (D) Univariate Cox analysis of prognostic factors and OS of CRCs. (E) Violin plot illustrated the correlation between risk score and tumor site as well as tumor stage. (F) Alluvial diagram for the two subtypes versus different immune subtypes and CMS. (G) Violin plot illustrated the correlation between risk score and immune subtypes, and (H) CMS. AUC, area under the curve; OS, overall survival; CRC, colorectal cancer; IRGs, immune-related genes; ROC, receiver operating characteristic; CMS, consensus molecular subtypes.



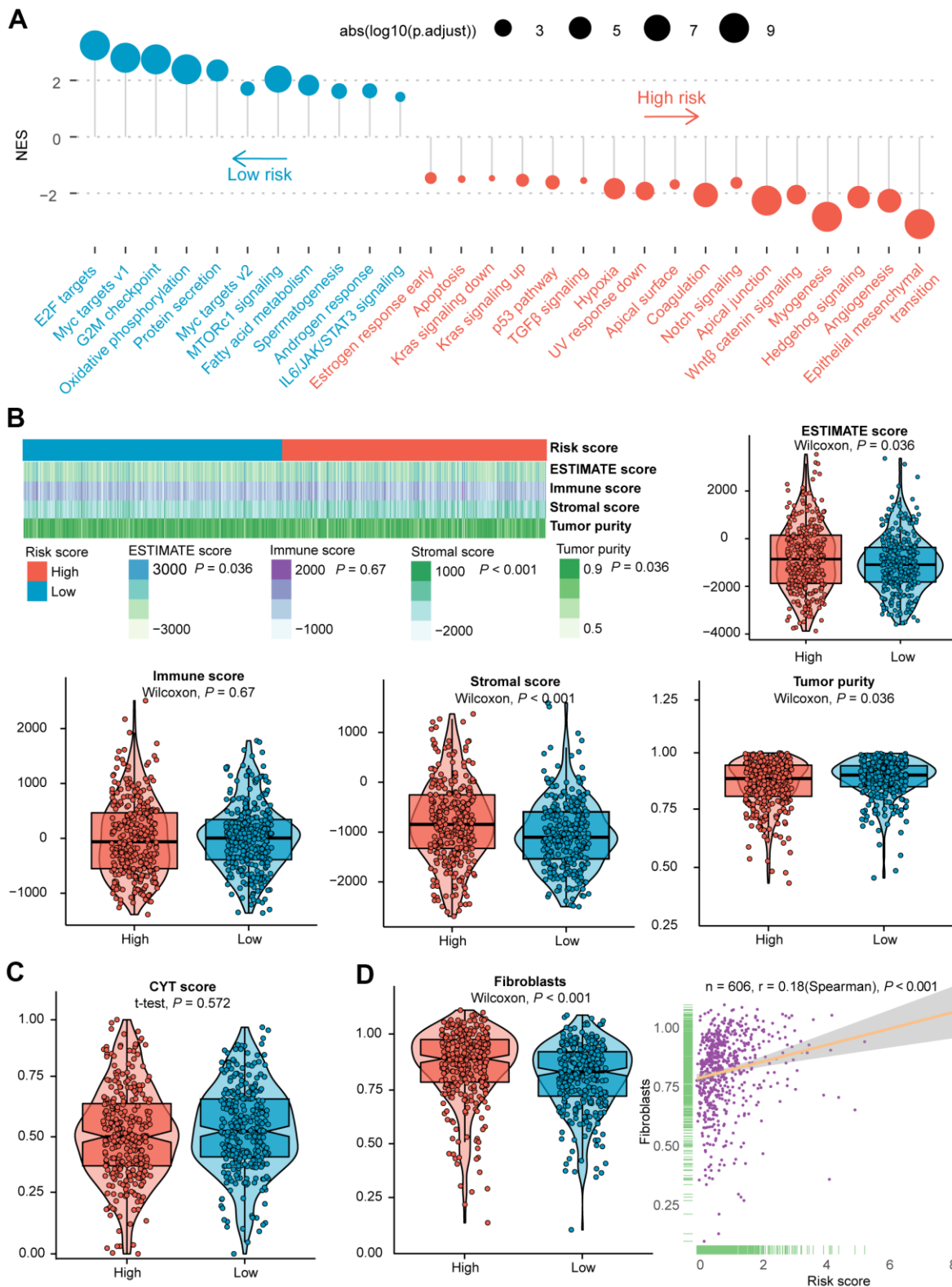


**Figure 2. Evaluation of the role of IRGs-based risk score in the training cohort.** (A) Results of GSEA of the high-risk group (red) compared with the low-risk group (blue). Color toward gray represents no statistical significance. (B) Heatmap and violin plots of the ESTIMATE score, immune score, stromal score, tumor purity between high- and low- risk subtypes. (C) Violin plot of the CYT score between high- and low- risk subtypes. (D) Violin plot of fibroblasts between two subtypes, and the association between risk score and the NES of fibroblasts. Statistical significance at the level of ns  $\geq 0.05$ , \*  $< 0.05$ , \*\*  $< 0.01$  and \*\*\*  $< 0.001$ . GSEA, gene set enrichment analysis; CYT, cytolytic activity; NES, normalized enrichment score.



pathways were significantly higher in the immune risk score-low subtype than in the immune risk score-high subtype. Analogous effects in Hippo-, Notch- and Wnt-associated pathways were investigated in the GSE39582 validation cohort (Supplementary Figure 5C).

### The immune landscape of the microenvironment in CRC subclasses

To further evaluate the potential molecular mechanism, the connection between four types of score produced by the ESTIMATE algorithm and risk score was also examined. Among the training dataset, a higher risk score was unveiled with elevated ESTIMATE score and stromal score, nevertheless, with decreased tumor purity (Figure 2B). Analogous patterns were found in the validation dataset except for a significantly positive correlation between risk score and immune score (Supplementary Figure 3B). Besides, no statistical significance was shown in the CYT score between the two subclasses (Figure 2C and Supplementary Figure 3C). It has been documented that fibroblasts are critical in multiple immunologic responses and inflammatory responses to tumor tissue injury [51, 52]. In the training group, the risk score was markedly correlated with the NES of fibroblasts (Spearman's  $r = 0.18$ ,  $P$ -value  $< 0.001$ , Figure 2D). Likewise, we found increased NES in high-risk subgroup of the validation cohort (Supplementary Figure 3D).

Immunomodulators (IM) play a determinant role in clinical oncology and plenty of IM-related agonists and antagonists are being assessed [53]. To further figure

out the underlying immune modules of the constructed IRGs model, the IM gene expression level between two subgroups in two CRC cohorts was compared. Among the IMs under investigation for cancer immunotherapy, certain of them were significantly related to the risk score (Figure 4A and Supplementary Figure 4A, 4B). In addition, we deeply investigated whether the risk score was associated with the expression level of T cell markers (CD4 and CD8A) and with six vital immune checkpoint genes (CD47, CTLA-4, LAG3, MAGE-A3, PD-1, and PD-L1). As shown in Figure 4B, the expression level of PD-1 was significantly higher in CRC of the high-risk subtype, while the risk score was negatively correlated with CD47 expression. Moreover, the differences in the expression level of CD47 and PD-1 between two subtypes of the TCGA dataset were statistically significant (Figure 4C). Even though the expression level of CD4 inclined to be elevated in high-risk subclass, no statistical difference was determined in the TCGA cohort. Statistical significance was verified in the validation cohort (Supplementary Figure 4C).

To investigate whether the immunophenotype may be shaped by immune cells, the relationship of immune infiltration with subtypes in both TCGA and GEO samples was examined in depth. We found that there was conspicuous heterogeneity in immune cell population among the established classifications, consistent with previous published TILs subpopulations in CRC [54]. As illustrated in Figure 4D and Supplementary Figure 5A, the infiltrated fractions of Tregs, activated NK cells, macrophage M0, and macrophage M2 was outstandingly augmented in the high-risk group. By contraries,

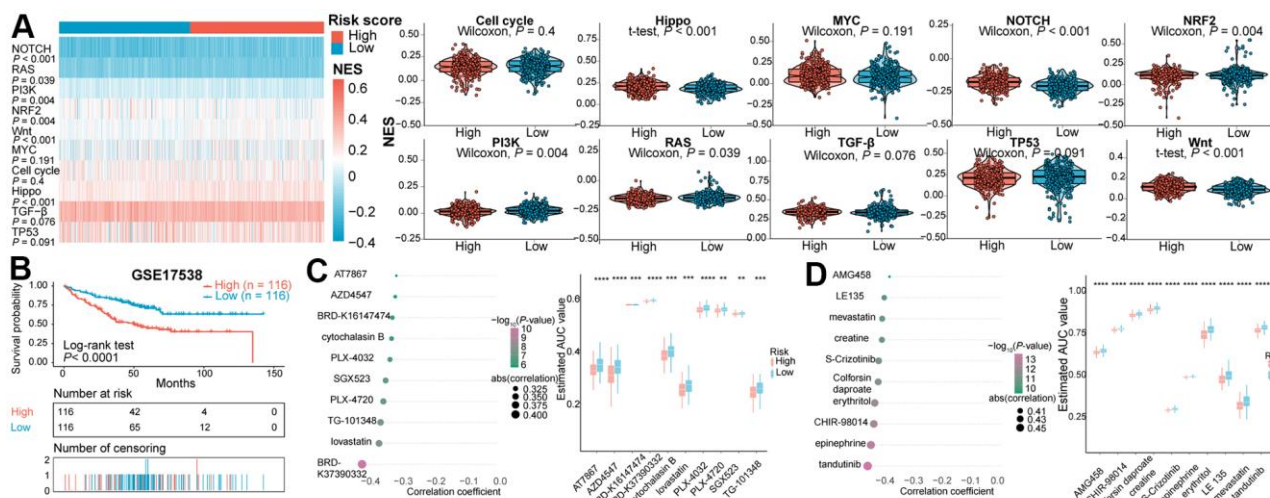


**Figure 3.** (A) Heatmap and violin plots of the NES of 10 oncogenic pathways between two subtypes in the TCGA cohort. (B) Kaplan-Meier survival curve of the high- and low- risk subgroups in GSE17538 dataset for identifying potential therapeutic agents. (C) Spearman's correlation analysis and differential drug response analysis of 10 CTRP-derived compounds. (D) Spearman's correlation analysis and differential drug response analysis of 10 PRISM-derived compounds. NES, normalized enrichment score.

markedly increased infiltration of CD4<sup>+</sup> memory resting T cells, CD4<sup>+</sup> memory activated T cells, activated dendritic cells (DCs), and neutrophils was observed in the low-risk group. Furthermore, we evaluate the correlation between the expression of seven IRGs and the infiltration of 24 types of immune cells by ssGSEA in CRC tissues. In the TCGA cohort (Figure 4E), there was a strong correlation of the FABP4 expression with the infiltration of NK cells (Spearman's  $r = 0.34$ ,  $P < 0.001$ ), GRP with NK cells (Spearman's  $r = 0.41$ ,  $P < 0.001$ ) or Th17 cells (Spearman's  $r = -0.32$ ,  $P < 0.001$ ), INKBB with NK cells (Spearman's  $r = 0.31$ ,  $P < 0.001$ ), as well as UCN with Tgd (Spearman's  $r = -0.31$ ,  $P < 0.001$ ) (Supplementary Table 5). For the training dataset and validation dataset, strong connection was confirmed between the expression of FABP4 and the infiltration of DC (Spearman's  $r = 0.38$ ,  $P < 0.001$ ), iDC (Spearman's  $r = 0.44$ ,  $P < 0.001$ ), macrophages (Spearman's  $r = 0.46$ ,  $P < 0.001$ ), and mast cells (Spearman's  $r = 0.40$ ,  $P < 0.001$ ), the expression of GRP and infiltration

of macrophages (Spearman's  $r = 0.30$ ,  $P < 0.001$ ) included (Figure 4E and Supplementary Figure 5B and Supplementary Table 5).

### Identification of potential therapeutic agents for CRCs with immune high-risk score

The CTRP and PRISM datasets shared 160 compounds, with 1770 compounds remained in total after removing duplication (Supplementary Table 6). Two approaches were utilized to screen candidate compounds with higher drug sensitivity in CRCs of high-risk score. By stratifying CRCs in GSE17538 dataset into high- and low- risk score subtypes based on seven IRGs (Figure 3B), the analyses were operated using CTRP and PRISM-derived drug response data, successively. First, differential drug response analysis between high- and low- risk groups was conducted to identify agents with differential estimated AUC values between subclasses (FDR  $< 0.05$ ). Next, the Spearman correlation test

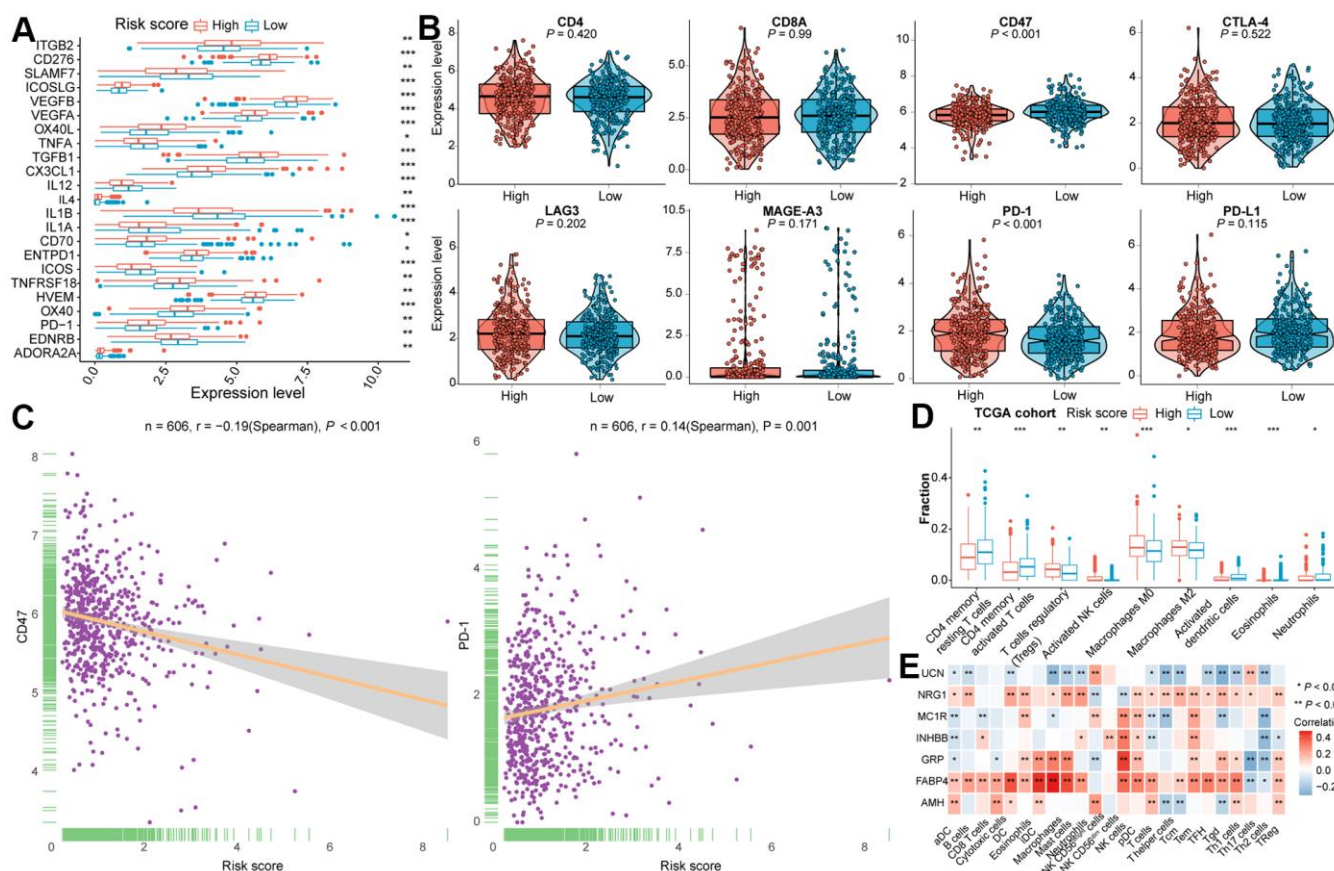


**Figure 4. The immune landscape of two distinctive subclasses in the training cohort.** (A) The differential expression level of immune checkpoint molecules between two subclasses with statistical significance. (B) Violin plots of the CD4, CD8A, CD47, CTLA4, LAG3, MAGE-A3, PD-1 and PD-L1 expression levels for two subtypes. (C) The association between risk score and CD47 as well as PD-1 expression levels. (D) Immune infiltration between high- and low- risk subtypes with statistical significance in the training cohort. (E) Correlation analysis between the expression of seven IRGs and the infiltration of immune cells. Statistical significance at the level of ns  $\geq 0.05$ , \*  $< 0.05$ , \*\*  $< 0.01$  and \*\*\*  $< 0.001$ .

between AUC value and risk score was adopted to identify drugs with negative correlation coefficient (Spearman's  $r < -0.30$  for CTRP or  $-0.40$  for PRISM). Above analyses yielded 10 CTRP-derived agents (including AT7867, AZD4547, BRD-K37390332, Cytochalasin B, PLX-4720, SGX-523, PLX-4032, TG-101348, lovastatin, and BRD-K16147474) and 10 PRISM-derived agents (including AMG458, LE135, mevastatin, creatine, S-Crizotinib, Colforsin daproate, erythritol, CHIR-98014, epinephrine, and tandutinib). All these compounds presented lower estimated AUC values in the high-risk subgroup and a negative correlation with IRGs-based risk score (Figure 3C, 3D). Although the 20 candidate agents displayed a higher drug sensitivity in IRGs score-high patients, solely the analyses above could not draw to the conclusion that these compounds are promising treatment modality for the eradication of CRC. Therefore, an integrated literature retrieval was conducted in PubMed, DrugBank [55], and HERB [56] databases to search for the experimental and clinical evidence of candidate compounds for CRC (Supplementary Table 7). BRD-K16147474, SGX-523, BRD-K37390332, AMG458, LE135, creatine, colforsin daproate, erythritol, CHIR-98014, and epinephrine without supporting evidence for CRC were firstly excluded. Secondly, PLX-4032 [57, 58] and PLX-4720 [59] targeted B-raf<sup>V600E</sup>, AT7867 targeted Akt [60], tandutinib targeted Akt/mTOR pathway [61], TG-101348 targeted the JAK2/STAT3/PIM1 pathway [62], lovastatin [63] and mevastatin [64] inhibiting 3-hydroxy-3-methylglutaryl coenzyme A (HMG-CoA) reductase weren't considered as the potential compounds for risk score-high subclass. This is because these drugs functioned inconsistently with targets enriched in the immune score-high subclass through GSEA (Figure 2A and Supplementary Figure 3A). Collectively, AZD4547, Cytochalasin B and S-crizotinib, which held true *in vitro* and *in silico* evidence, were deemed the most promising therapeutic agents for CRCs with high IRG risk scores.

### CRC subgroups have distinct responses to immunotherapy

Two different procedures were adopted in this study to identify subclass-specific candidate immunotherapies. Submap analysis was first used to find potential immunotherapeutic benefit of two subgroups through six immunotherapy datasets available with clinical response and gene expression information. As exhibited in Figure 5F, the high-risk subclass shared high similarity with anti-MAGE-A3 nonresponse group in Ulloa Montoya et al. (2013) dataset ( $P = 0.049$ ) and anti-PD-1 nonresponse group in Hugo et al. (2016) dataset ( $P = 0.002$ ), and the high-risk subgroup tended to be correlated with anti-PD-L1 nonresponse group in

IMvigor210 cohort although no statistical significance was found ( $P = 0.08$ ).

Patients received immunotherapy in Van Allen et al. (2015) dataset, Hugo et al. (2016) dataset, IMvigor210 dataset, and Snyder et al. (2017) dataset were classified into high-risk subtype and low-risk subtype using the median IRGs-based risk score as the cutoff. Then, the AUC values for classifying the responder and non-responder cases of several previous signatures, including CD8 [65], CYT [17], T cell-inflamed GEP [66], IFN $\gamma$  [66], IPRES [67], MHC [68], Chemokine [69], and PD-L1 [65] signatures as well as IRGs-based signature were calculated across all the four immunotherapeutic datasets with abundant gene expression profiles. Notably, IRGs signature outperformed the other eight signatures and the AUC values exceeded 0.7 in three out of four datasets (Figure 5A–5D). The results of performance comparison in four independent datasets suggested that the predictive power of IRGs signature ranked the highest. The association across these signatures indicated that five signatures, including IFN $\gamma$ , CD8, MHC, IPRES, and PD-L1 signatures correlated closely with each other (Figure 5E). By contrast, IRGs signature displayed relatively weak correlation with other signatures, implying its complementary role rather than the alternative as an immunotherapeutic indicator. Patients in the low-risk subclass presented significant longer OS than those in the high-risk subclass of Van Allen et al. (2015) dataset (log-rank test  $P$ -value  $< 0.001$ , Figure 5G), IMvigor210 dataset (log-rank test  $P$ -value = 0.036, Figure 5I) and Snyder et al. (2017) dataset (log-rank test  $P$ -value = 0.027, Figure 5J), however, no statistical difference was observed in Hugo et al. (2016) dataset (log-rank test  $P$ -value = 0.096, Figure 5H). These findings demonstrated that the lower risk score was associated with better survival outcomes in tumor patients treated with immunotherapy. Collecting immunotherapeutic response data in four cohorts mentioned above, we determined the correlation between immunotherapeutic response and risk score. It's shown that patients in the low-risk subtype had a dramatically higher response to immunotherapy than patients in the high-risk subtype among three datasets ( $P$ -value = 0.024 for Van Allen et al. anti-CTLA-4 cohort,  $P$ -value = 0.001 for IMvigor210 anti-PD-L1 cohort, and  $P$ -value = 0.029 for Snyder et al. anti-PD-L1 cohort;  $\chi^2$  test, Figure 5K, 5M, 5N), apart from ( $P$ -value = 0.194 for Hugo et al. anti-PD-1 cohort,  $\chi^2$  test, Figure 5L). According to Van Allen et al. (2015) anti-CTLA-4 cohort (Figure 5O), IMvigor210 anti-PD-L1 cohort (Figure 5Q), and Snyder et al. (2017) anti-PD-L1 cohort (Figure 5R), violin plots revealed that the risk score was significantly decreased in patients responsive to the immunotherapeutic intervention, compared to non-responsive patients. Nonetheless, no



statistical significance was observed in Hugo et al. (2016) anti-PD-1 cohort (Figure 5P).

## DISCUSSION

Despite the advances in treatment, CRC is a lethal disease of great heterogeneity, prompting therapeutic optimization to prolong survival outcomes and reduce mortality. Hence, it's essential to acquire reliable prognostic biomarkers to stratify survival risk and to predict subclass-specific therapeutic strategies. Tailoring specialized management for patients depends on personalized clinical and molecular features. Gaining insight into IRGs involved in CRC enables

scientists to recapitulate the underlying mechanism of carcinogenesis in CRC and identify patients who may benefit from adaptive therapy. In this study, by exploiting a compendium of IRGs, a robust prognostic immune-based signature was built using public CRC cohorts. CRC samples with intact expression profiles and clinical characteristics were downloaded from the TCGA and the GEO database. Multivariate Cox regression was utilized to calculate the risk score for each cohort based on the seven IRGs signature independently. Besides, bioinformatic analyses were separately performed in different CRC cohorts, the normalized process was thus unneeded.

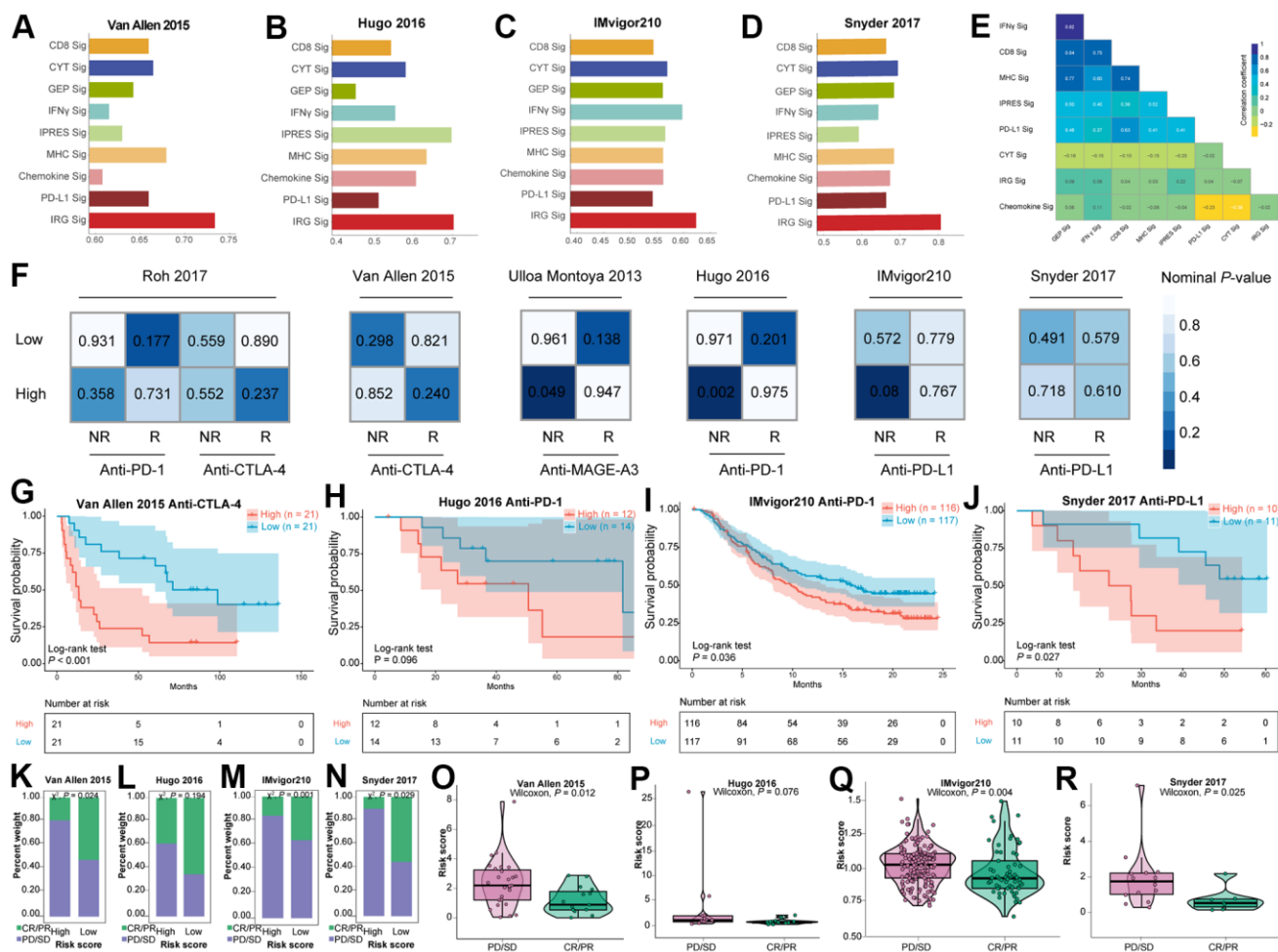


**Figure 5. The immunotherapeutic benefit of the IRGs-based risk score in immunotherapeutic treatment cohorts.** (A–D) Comparison of AUC values between IRGs-based signature and other eight previous published immune related signatures in four immunotherapeutic datasets. (E) Similarity comparison between IRGs-based signature and other seven previous signatures. (F) SubMap analysis utilizing six immunotherapy datasets. Kaplan-Meier survival curve of OS for patients with high- and low- risk score subtypes for (G) Van Allen et al. (2015) dataset, (H) Hugo et al. (2016) dataset, (I) IMvigor210 dataset, and (J) Snyder et al. (2017) dataset. Bar graph illustrated the treatment response to immunotherapy within high- and low- risk score subtypes in (K) Van Allen et al. (2015) dataset, (L) Hugo et al. (2016) dataset, (M) IMvigor210 dataset, and (N) Snyder et al. (2017) dataset. Violin plots illustrated the distribution of risk score for patients with different immunotherapy responses in (O) Van Allen et al. (2015) dataset, (P) Hugo et al. (2016) dataset, (Q) IMvigor210 dataset, and (R) Snyder et al. (2017) dataset.

The IRGs-based risk score was found to be significantly correlated with OS in CRCs and remained significant after adjustment for clinical and pathological parameters. To characterize the TIME immune infiltration, we explored the divergent immune cell subpopulation via the CIBERSORT algorithm between subgroups. The higher pro-tumor immunocytes encompassing Tregs, macrophage M0, and macrophage M2 were observed in the high-risk group, in contrast, immune cells orchestrating anti-tumor responses including CD4<sup>+</sup> memory resting T cells, CD4<sup>+</sup> memory activated T cells, activated DCs, and neutrophils accumulated in the low-risk group. Imbalances in immune cell components are associated with undesirable prognosis and inferior survival outcomes in cancer patients [70, 71]. Toor et al. documented the aggregation of CD4<sup>+</sup> and FoxP3<sup>+</sup> TILs in CRC tissues, compared to para-carcinoma normal tissues [72]. In humans, the accumulation of Tregs within TIME is regarded as a disadvantageous prognostic factor in a plethora of cancers [73]. However, Tregs infiltration in CRC tissues is incapable of predicting the prognosis [74, 75]. Elevated infiltration of Tregs could trigger low tumor differentiation and aggrandized involvement of lymph node [74]. In contrast, enhanced Tregs densities have also been correlated with better relapse-free survival (RFS) [76, 77]. Some heterogeneous subsets of Tregs facilitate CRC progression, covering CD8<sup>+</sup> Tregs [78] and RORγt<sup>+</sup> Tregs [79]. Macrophage polarization plays a prominent role in tumor pathogenesis. In response to distinct microenvironments, primary macrophages (M0) migrate out of vessels and could be polarized toward pro-inflammatory (M1) macrophages or anti-inflammatory (M2) macrophages, while resting macrophages undergo diverse functional alterations [80, 81]. To some extent, M2 macrophage infiltration is closely linked with increased involvement of CRC liver metastasis and malignant lesion in the liver [82]. Moreover, cancer-associated fibroblasts (CAFs) in CRC fuel tumor-associated macrophages (TAMs) infiltration and macrophages M2 polarization in TIME, subsequently impairing the function of NK cells [83]. The increased level of CD4<sup>+</sup> TILs has been deemed as favorable clinical outcome in CRC [84], highlighting the crucial role of CD4<sup>+</sup> cells in regulating immune system to exert anti-neoplastic activity. In CRCs, elevated expression of Th1 transcripts is correlated with beneficial prognosis, whereas the elevated expression of Th17 transcripts is correlated with poor clinical outcome [85]. Additionally, effector and memory Th1 CD4<sup>+</sup> T cells are pivotal in effective anti-tumor immunity and that CD4<sup>+</sup> T cells induce more durable immune responses than CD8<sup>+</sup> T cells [86]. DCs act a key role in presenting tumor antigens and eliciting tumoricidal processes of T cells [87], and activated DCs might potentiate immunotherapeutic efficacy in advanced

CRCs [88]. On the contrary, inhibited functions of DCs in cancer patients lead to the suppression of protective immune responses and facilitating disease progression [89]. An increased intra-tumoral abundance of neutrophil has been shown in CRC [90], and elevated neutrophil/lymphocyte ratio (NLR) in peripheral blood of advanced CRCs is related to unfavorable prognostic aspects [91]. By frequently colocalizing with CD8<sup>+</sup> T cells, neutrophils could also irritate CD8<sup>+</sup> T cell response to T cell receptor priming, thus reflecting that neutrophils might have notably anti-oncogenic efficacy [92]. Thus far, the roles of neutrophils and other immune cells in CRC progression have not been fully elucidated. The investigation in-depth, presented herein, opens new avenues for understanding the relationship between immune cells and the progression of CRC.

Among the seven IRGs in the classifier, NRG1 was considered as a protective factor for CRCs while FABP4, AMH, GRP, INHBB, UCN and MC1R were risk factors for CRCs. These IRGs have been previously reported to be involved in tumorigenesis. The growth factor neuregulin 1 (NRG1) comprises of an epidermal growth factor (EGF)-like domain that binds to human tyrosine kinases of the ErbB/HER receptor family, contributing to heterodimerization and activation of the ErbB-mediated downstream signaling pathways [93]. CRC is an NRG1 fusion-positive tumor [94, 95], in which the expression of NRG1 III is significantly upregulated and negatively correlated with lymph node metastasis [96], implying a satisfactory prognosis. Primarily expressed in the adipocytes and macrophages [97], fatty acid binding protein 4 (FABP4) is involved in lipid transfer between adipocytes and tumor cells, provoking the fatty acid oxidation to induce tumor growth [98, 99]. The elevated expression of FABP4 was confirmed as a robust risk factor for the progression of CRC in a Chinese cohort [100], while an *in-silico* study also uncovered that FABP4 imposed conceivably poor prognosis on CRCs [25]. Herein, FABP4 harbored detrimental effects on CRCs and the strong interaction between the FABP4 expression and macrophages was also manifested in our study, supporting FABP4's crosstalk with macrophages in the TIME. As a corticotropin-releasing factor-related peptide, urocortin (UCN) participated in gastrointestinal motor and visceral pain during stress response [101]. In the current study, UCN was correlated with poor CRC prognosis, in tandem with anteriorly proposed CRC signature [25, 102, 103]. The melanocortin-1 receptor (MC1R) has been regarded as an adverse parameter for survival in CRC [102]. Nevertheless, the specific implication of MC1R in CRC is rarely known. Patients carrying the MC1R variants are presented with elevated melanoma risk, and MC1R had been a therapeutic target for melanoma [104, 105]. Consequently, preclinical studies



on the importance of MC1R in the development of CRC are needed. Anti-Müllerian hormone (AMH) is a member of the TGF $\beta$  family that engages in cell proliferation, differentiation, and apoptosis in normal tissues [106]. AMH was positively related to the risk of breast cancer [107], and the downregulation of AMH lower the risk of CRC was forecasted in two bioinformatic analyses [108, 109]. The inhibin subunit beta B (INHBB) is a subunit of the activin B, a functional cytokine of the TGF $\beta$  superfamily [110, 111]. INHBB is upregulated and exerts tumorigenic activity in a variety of malignant tumors ranging from oral cancer [112] to endometrial cancer [113], prostate cancer [114], and thyroid cancer [115]. In our model, elevated INHBB expression predicted an adverse outcome. Analogously, Yuan et al. indicated that the expression of INHBB was enhanced in CRC tissue, bringing about worse OS and disease-free survival (DFS) [116]. As a subtribe of the bombesin (BN)-like peptide family, gastrin-releasing peptide (GRP) is principally served as gastrointestinal hormone and neurotransmitter [117, 118]. GRP modulates the growth and differentiation of numerous human tumors including CRC [119, 120]. The GRP receptor (GRPR) has been shown to be overexpressed in human CRCs, when compared to normal colonic epithelial cells [121, 122]. Moreover, GRP and the co-expression of GRPR acted in differentiation, with the highest levels observed in well-differentiated CRC cells [123]. BN/GRP antagonists, such as RC-3095 and RC-3940-II, have been reported to exert anti-tumor activities in *in-vitro* and *in-vivo* mouse xenografts [124, 125]. RC-3940-II also exerted potent anti-neoplastic activity on the human CRC cell lines both *in vitro* and *in vivo* [126]. Li et al. pointed out that GRP could predict the prognosis of DFS in CRC [127], uncovering its involvement in the prognosis and survival of CRC. Bedke et al. demonstrated that GRP and GRPR were mainly expressed by TAMs in renal cell carcinomas (RCC) [128], accordantly, the current study indicated that the expression of GRP was positively correlated with the degree of macrophage infiltration. Briefly, these compelling evidences for the significance of GRP show great potential at unmasking the malignancy-associated roles of TAMs in CRC.

Three drugs, including AZD4547, Cytochalasin B, and S-crizotinib, harbored more notable anti-neoplastic activity in the immune risk score-high group. Intriguingly, high-risk specific agents are all anti-tumor targeted compounds, and a striking consistency was shown between the mechanism of action (MOA) of these chemical entities and enriched signatures obtained from GSEA. As prominent segment in the TME composed of cancer cells and stromal or immune cells, CAFs crosstalk with tumor cells contributes to the progression of tumor [129]. Overexpression of the

fibroblast growth factor receptor-1 (FGFR-1) has been correlated with liver metastasis in CRC [130]. The fibroblast growth factor 1 (FGF1)/FGFR-3 signaling mediates migration and invasion in CRC, and activated fibroblasts upregulate the expression of FGF1 [131]. AZD4547 is an orally potent and highly selective tyrosine kinase inhibitor (TKI) targeted FGFR 1-3 [132]. Preclinical data recapitulates that AZD4547 possesses anti-oncogenic activity against various tumors, such as gastric [133], lung [134], and pancreatic [135] cancers. Yao et al. reported that AZD4547 delayed CRC tumor growth *in vitro*, and its activity was in close interaction with the expression level of FGFR [136]. In our study, the infiltration of fibroblasts was apparently higher in high-risk score CRCs, compellingly argue for clinical investigations of AZD4547 for treating high-risk specific CRCs. Cytochalasin B is a common microfilament-disrupting compound that impacts various cellular physiological processes mediated by F-actin, encompassing cell motility, endocytosis and adherence [137–139]. Treating human CRC SW480 cells with cytochalasin B attenuated the downregulation of E-cadherin expression [140]. Indeed, the loss or dysregulation of E-cadherin expression expedites the growth, invasion, and drug resistance in CRC cells [141, 142]. EMT, a morphogenetic process whereby epithelial cells transform to the mesenchymal phenotype, critically engaged in tumorigenesis and cancer progression [143]. In tumor, the expression of epithelial markers, E-cadherin particularly, is downregulated during the process of EMT, ultimately destroying cell adhesion, promoting cell motility and stages of cancer [144, 145]. Conversely, inhibited EMT as evidenced by the elevated expression of E-cadherin exerts suppressive effects on the growth and invasion of human CRC via the Wnt/ $\beta$ -catenin signaling [146, 147]. c-MET/RON activation initiates many facets of cellular responses covering motility, proliferation, EMT, and angiogenesis [148, 149]. Typically, c-Met and RON signaling irritate angiogenesis through the interplay with vascular endothelial growth factor (VEGF) stimulated by hypoxia-inducible factor 1-alpha (HIF-1 $\alpha$ ). Crizotinib is an extensively functioning, small-molecule TKI clinically approved for treating non-small-cell lung cancer (NSCLC) patients [150]. In a three-dimensional CRC culture system, Li et al. found that crizotinib restored cetuximab sensitivity in the HCA-7 CRC cell line [151]. By inhibiting c-MET/RON/ALK/MTH1, S-crizotinib is an optical isomer of a clinical anticancer compound, R-crizotinib, with inhibited efficacy in suppressing MTH1 compared to S-crizotinib [152, 153]. Previous evidence suggests that MTH1 inhibition via S-crizotinib induced an increase in DNA single strand breaks as well as activated DNA repair in SW480 cells [153]. In human cells, acute MTH1 inhibition enables p53-dependent cellular senescence upon hyperoxia

[154]. Moreover, MTH1 is pivotal in RAS-driven oncogenesis and its overexpression accelerates the spectrum of RAS-driven carcinogenic transformation [155]. Notably, elevated expression of MTH1 enhances the transformation of immortalized cells through RAS and maintains pro-oncogenic phenotype, EMT [156, 157]. Collectively, we postulate that AZD4547, Cytochalasin B and S-crizotinib are attractive compounds for further pre-clinical investigations and could be promising novel anti-cancer agents for IRGs risk score-high CRCs.

Immunotherapy, with special regard to ICIs, has attracted great interest in oncotherapy and has been applied in clinical practice for a variety of malignancies. Pembrolizumab and nivolumab that inhibited PD-1 and ipilimumab targeted CTLA-4 have been approved by the United States Food and Drug Administration (FDA) as second-line treatment in MSI-high and dMMR advanced CRCs. Focused on the findings from KEYNOTE 028 [13] and CheckMate 142 [11], solely a modest percentage of advanced CRCs harbored a persistent and stable response during the ICI therapy, with response rate at 30-55%. Therefore, it is of great clinical significance to develop a biomarker for predicting immunotherapeutic efficacy. In this study, we confirmed that CRCs with a low-risk immune signature were markedly related with enhanced response to ICIs targeted PD-1, PD-L1 and CTLA-4, while the immune score-high CRCs exhibited nonresponse to PD-1 inhibitor and MAGE-A3 based immunotherapy. These findings illustrated that the IRGs-based risk score could be served as a practical tool for assessing immunotherapeutic efficacy in CRC, in accordance with a recent study on the immune signature score for colon cancer [24]. Compared to the immune high-risk subclass, the low-risk subclass exhibited significantly higher infiltration of anti-tumor immune cells and expression of immune checkpoint genes, which may account for diverse responses between the two subclasses. Furthermore, the GSEA of hallmark gene sets indicated that the upregulated genes in the high-risk subgroup were enriched in Wnt/ $\beta$ -catenin signaling, consistent with previous findings that the activation of tumor-intrinsic  $\beta$ -catenin pathway could induce T-cell exclusion, thereby causing resistance to PD-L1 or CTLA-4 blockade immunotherapy [158]. Thus, altered Wnt/ $\beta$ -catenin signaling activation may be associated with immunotherapeutic resistance in CRC.

However, there are still some limitations in this study. Firstly, we attempted to obtain abundant CRC cohorts to achieve more reliable results with sufficient sample size. But the intra-tumor or intra-patient heterogeneity of the TIME in CRCs was not fully considered, which impacted the effect of chemotherapy and immunotherapy. Secondly, the median cutoff of IRGs

risk score was utilized to stratify the CRC samples into high-risk subtype and low-risk subtype, and the optimal cutoff of the risk score is needed to best classify the CRCs. Thirdly, all the conclusions in this study were inferred from *in-silico* analyses, and further *in-vitro* or *in-vivo* experiments and clinical validations are needed to promote the clinical application of our findings. Finally, due to the paucity of CRC cohorts treated with immunotherapy, more prospective clinical studies are required to further verify this novel IRGs-based signature in CRCs.

## CONCLUSIONS

The IRGs signature is valuable for its correlation with immune infiltration, and the association between the risk score and OS in the integrated analysis of CRC cohorts suggests that it is a robust prognostic biomarker for CRC. This IRGs model harbors crucial clinical practicality in both high- and low- risk CRCs who had failed first-line treatment or progressed. For immune low-risk score patients, clinicians could adopt ICIs targeted PD-1, PD-L1 and CTLA-4 as well as MAGE-A3 immunotherapy strategies to avoid excessive treatment, so these CRCs could acquire a better quality of life with a favorable prognosis. For immune high-risk score patients, AZD4547, Cytochalasin B and S-crizotinib might be used in cases of immunotherapeutic resistance. Generally, our finding provides new insights into determining the prognosis of CRCs, and sheds new light on tailoring CRCs with precise treatment.

## AUTHOR CONTRIBUTIONS

WY, and JC designed and edited this study; YL and ZJX searched the databases and collected data; YL, YYL, ZJX, DZ, XMC, XYW, and JL analyzed the data and wrote the manuscript. WY and JC critically revised the article for essential intellectual content and administrative support. All authors read and approved the final version of the manuscript. All authors reviewed and revised the manuscript.

## ACKNOWLEDGMENTS

We would like to thank our researchers for their hard work and the reviewers for their valuable advice. We thank Home for Researchers editorial team (<https://www.home-for-researchers.com>) for language editing service.

## CONFLICTS OF INTEREST

The authors declare no conflicts of interest related to this study.

## FUNDING

This research was supported by the National Key R&D Program of China (2019YFA0110300, 2020YFA0509400); the National Natural Science Foundation of China (82071745); the Science and Technology Program of Guangzhou (202002030069); and the Guangdong project (2019QN01Y212).

## REFERENCES

1. Bray F, Ferlay J, Soerjomataram I, Siegel RL, Torre LA, Jemal A. Global cancer statistics 2018: GLOBOCAN estimates of incidence and mortality worldwide for 36 cancers in 185 countries. *CA Cancer J Clin*. 2018; 68:394–424.  
<https://doi.org/10.3322/caac.21492>  
PMID:30207593
2. Dekker E, Tanis PJ, Vleugels JL, Kasi PM, Wallace MB. Colorectal cancer. *Lancet*. 2019; 394:1467–80.  
[https://doi.org/10.1016/S0140-6736\(19\)32319-0](https://doi.org/10.1016/S0140-6736(19)32319-0)  
PMID:31631858
3. Inamura K. Colorectal Cancers: An Update on Their Molecular Pathology. *Cancers (Basel)*. 2018; 10:26.  
<https://doi.org/10.3390/cancers10010026>  
PMID:29361689
4. Schmoll HJ, Van Cutsem E, Stein A, Valentini V, Glimelius B, Haustermans K, Nordlinger B, van de Velde CJ, Balmana J, Regula J, Nagtegaal ID, Beets-Tan RG, Arnold D, et al. ESMO Consensus Guidelines for management of patients with colon and rectal cancer. a personalized approach to clinical decision making. *Ann Oncol*. 2012; 23:2479–516.  
<https://doi.org/10.1093/annonc/mds236>  
PMID:23012255
5. Condamine T, Ramachandran I, Youn JI, Gabrilovich DI. Regulation of tumor metastasis by myeloid-derived suppressor cells. *Annu Rev Med*. 2015; 66:97–110.  
<https://doi.org/10.1146/annurev-med-051013-052304>  
PMID:25341012
6. Hinshaw DC, Shevde LA. The Tumor Microenvironment Innately Modulates Cancer Progression. *Cancer Res*. 2019; 79:4557–66.  
<https://doi.org/10.1158/0008-5472.CAN-18-3962>  
PMID:31350295
7. Mlecnik B, Tosolini M, Kirilovsky A, Berger A, Bindea G, Meatchi T, Bruneval P, Trajanoski Z, Fridman WH, Pagès F, Galon J. Histopathologic-based prognostic factors of colorectal cancers are associated with the state of the local immune reaction. *J Clin Oncol*. 2011; 29:610–8.  
<https://doi.org/10.1200/JCO.2010.30.5425>  
PMID:21245428
8. Pagès F, Mlecnik B, Marliot F, Bindea G, Ou FS, Bifulco C, Lugli A, Zlobec I, Rau TT, Berger MD, Nagtegaal ID, Vink-Börger E, Hartmann A, et al. International validation of the consensus Immunoscore for the classification of colon cancer: a prognostic and accuracy study. *Lancet*. 2018; 391:2128–39.  
[https://doi.org/10.1016/S0140-6736\(18\)30789-X](https://doi.org/10.1016/S0140-6736(18)30789-X)  
PMID:29754777
9. Galon J, Costes A, Sanchez-Cabo F, Kirilovsky A, Mlecnik B, Lagorce-Pagès C, Tosolini M, Camus M, Berger A, Wind P, Zinzindohoué F, Bruneval P, Cugnenc PH, et al. Type, density, and location of immune cells within human colorectal tumors predict clinical outcome. *Science*. 2006; 313:1960–4.  
<https://doi.org/10.1126/science.1129139>  
PMID:17008531
10. Xiao Y, Freeman GJ. The microsatellite instable subset of colorectal cancer is a particularly good candidate for checkpoint blockade immunotherapy. *Cancer Discov*. 2015; 5:16–8.  
<https://doi.org/10.1158/2159-8290.CD-14-1397>  
PMID:25583798
11. Le DT, Durham JN, Smith KN, Wang H, Bartlett BR, Aulakh LK, Lu S, Kemberling H, Wilt C, Luber BS, Wong F, Azad NS, Rucki AA, et al. Mismatch repair deficiency predicts response of solid tumors to PD-1 blockade. *Science*. 2017; 357:409–13.  
<https://doi.org/10.1126/science.aan6733>  
PMID:28596308
12. Overman MJ, Lonardi S, Wong KY, Lenz HJ, Gelsomino F, Aglietta M, Morse MA, Van Cutsem E, McDermott R, Hill A, Sawyer MB, Hendlish A, Neyns B, et al. Durable Clinical Benefit With Nivolumab Plus Ipilimumab in DNA Mismatch Repair-Deficient/Microsatellite Instability-High Metastatic Colorectal Cancer. *J Clin Oncol*. 2018; 36:773–9.  
<https://doi.org/10.1200/JCO.2017.76.9901>  
PMID:29355075
13. Overman MJ, McDermott R, Leach JL, Lonardi S, Lenz HJ, Morse MA, Desai J, Hill A, Axelson M, Moss RA, Goldberg MV, Cao ZA, Ledeine JM, et al. Nivolumab in patients with metastatic DNA mismatch repair-deficient or microsatellite instability-high colorectal cancer (CheckMate 142): an open-label, multicentre, phase 2 study. *Lancet Oncol*. 2017; 18:1182–91.  
[https://doi.org/10.1016/S1470-2045\(17\)30422-9](https://doi.org/10.1016/S1470-2045(17)30422-9)  
PMID:28734759
14. Hersom M, Jørgensen JT. Companion and Complementary Diagnostics-Focus on PD-L1 Expression Assays for PD-1/PD-L1 Checkpoint Inhibitors in Non-Small Cell Lung Cancer. *Ther Drug Monit*. 2018; 40:9–16.

<https://doi.org/10.1097/FTD.0000000000000460>  
PMID:29084031

15. Garon EB, Rizvi NA, Hui R, Leighl N, Balmanoukian AS, Eder JP, Patnaik A, Aggarwal C, Gubens M, Horn L, Carcereny E, Ahn MJ, Felip E, et al, and KEYNOTE-001 Investigators. Pembrolizumab for the treatment of non-small-cell lung cancer. *N Engl J Med*. 2015; 372:2018–28.  
<https://doi.org/10.1056/NEJMoa1501824>  
PMID:25891174
16. Le DT, Uram JN, Wang H, Bartlett BR, Kemberling H, Eyring AD, Skora AD, Lubner BS, Azad NS, Laheru D, Biedrzycki B, Donehower RC, Zaheer A, et al. PD-1 Blockade in Tumors with Mismatch-Repair Deficiency. *N Engl J Med*. 2015; 372:2509–20.  
<https://doi.org/10.1056/NEJMoa1500596>  
PMID:26028255
17. Rooney MS, Shukla SA, Wu CJ, Getz G, Hacohen N. Molecular and genetic properties of tumors associated with local immune cytolytic activity. *Cell*. 2015; 160:48–61.  
<https://doi.org/10.1016/j.cell.2014.12.033>  
PMID:25594174
18. Kreiter S, Vormehr M, van de Roemer N, Diken M, Löwer M, Diekmann J, Boegel S, Schrörs B, Vascotto F, Castle JC, Tadmor AD, Schoenberger SP, Huber C, et al. Mutant MHC class II epitopes drive therapeutic immune responses to cancer. *Nature*. 2015; 520:692–6.  
<https://doi.org/10.1038/nature14426> PMID:25901682
19. Mlecnik B, Bindea G, Angell HK, Maby P, Angelova M, Tougeron D, Church SE, Lafontaine L, Fischer M, Fredriksen T, Sasso M, Bilocq AM, Kirilovsky A, et al. Integrative Analyses of Colorectal Cancer Show Immunoscore Is a Stronger Predictor of Patient Survival Than Microsatellite Instability. *Immunity*. 2016; 44:698–711.  
<https://doi.org/10.1016/j.immuni.2016.02.025>  
PMID:26982367
20. Bruni D, Angell HK, Galon J. The immune contexture and Immunoscore in cancer prognosis and therapeutic efficacy. *Nat Rev Cancer*. 2020; 20:662–80.  
<https://doi.org/10.1038/s41568-020-0285-7>  
PMID:32753728
21. Jansen AM, van Wezel T, van den Akker BE, Ventayol Garcia M, Ruano D, Tops CM, Wagner A, Letteboer TG, Gómez-García EB, Devilee P, Wijnen JT, Hes FJ, Morreau H. Combined mismatch repair and POLE/POLD1 defects explain unresolved suspected Lynch syndrome cancers. *Eur J Hum Genet*. 2016; 24:1089–92.  
<https://doi.org/10.1038/ejhg.2015.252>  
PMID:26648449
22. Domingo E, Freeman-Mills L, Rayner E, Glaire M, Briggs S, Vermeulen L, Fessler E, Medema JP, Boot A, Morreau H, van Wezel T, Liefers GJ, Lothe RA, et al, and Epicolon consortium. Somatic POLE proofreading domain mutation, immune response, and prognosis in colorectal cancer: a retrospective, pooled biomarker study. *Lancet Gastroenterol Hepatol*. 2016; 1:207–16.  
[https://doi.org/10.1016/S2468-1253\(16\)30014-0](https://doi.org/10.1016/S2468-1253(16)30014-0)  
PMID:28404093
23. Ganesh K, Stadler ZK, Cercek A, Mendelsohn RB, Shia J, Segal NH, Diaz LA Jr. Immunotherapy in colorectal cancer: rationale, challenges and potential. *Nat Rev Gastroenterol Hepatol*. 2019; 16:361–75.  
<https://doi.org/10.1038/s41575-019-0126-x>  
PMID:30886395
24. Li X, Wen D, Li X, Yao C, Chong W, Chen H. Identification of an Immune Signature Predicting Prognosis Risk and Lymphocyte Infiltration in Colon Cancer. *Front Immunol*. 2020; 11:1678.  
<https://doi.org/10.3389/fimmu.2020.01678>  
PMID:33013820
25. Lin K, Huang J, Luo H, Luo C, Zhu X, Bu F, Xiao H, Xiao L, Zhu Z. Development of a prognostic index and screening of potential biomarkers based on immunogenomic landscape analysis of colorectal cancer. *Aging (Albany NY)*. 2020; 12:5832–57.  
<https://doi.org/10.18632/aging.102979>  
PMID:32235004
26. Bhattacharya S, Andorf S, Gomes L, Dunn P, Schaefer H, Pontius J, Berger P, Desborough V, Smith T, Campbell J, Thomson E, Monteiro R, Guimaraes P, et al. ImmPort: disseminating data to the public for the future of immunology. *Immunol Res*. 2014; 58:234–9.  
<https://doi.org/10.1007/s12026-014-8516-1>  
PMID:24791905
27. Ghandi M, Huang FW, Jané-Valbuena J, Kryukov GV, Lo CC, McDonald ER 3rd, Barretina J, Gelfand ET, Bielski CM, Li H, Hu K, Andreev-Drakhlin AY, Kim J, et al. Next-generation characterization of the Cancer Cell Line Encyclopedia. *Nature*. 2019; 569:503–8.  
<https://doi.org/10.1038/s41586-019-1186-3>  
PMID:31068700
28. Roh W, Chen PL, Reuben A, Spencer CN, Prieto PA, Miller JP, Gopalakrishnan V, Wang F, Cooper ZA, Reddy SM, Gumbs C, Little L, Chang Q, et al. Integrated molecular analysis of tumor biopsies on sequential CTLA-4 and PD-1 blockade reveals markers of response and resistance. *Sci Transl Med*. 2017; 9:eaah3560.  
<https://doi.org/10.1126/scitranslmed.aah3560>  
PMID:28251903
29. Van Allen EM, Miao D, Schilling B, Shukla SA, Blank C, Zimmer L, Sucker A, Hillen U, Foppen MH, Goldinger



- SM, Utikal J, Hassel JC, Weide B, et al. Genomic correlates of response to CTLA-4 blockade in metastatic melanoma. *Science*. 2015; 350:207–11.  
<https://doi.org/10.1126/science.aad0095>  
PMID:26359337
30. Ulloa-Montoya F, Louahed J, Dizier B, Gruselle O, Spiessens B, Lehmann FF, Suciu S, Kruit WH, Eggermont AM, Vansteenkiste J, Brichard VG. Predictive gene signature in MAGE-A3 antigen-specific cancer immunotherapy. *J Clin Oncol*. 2013; 31:2388–95.  
<https://doi.org/10.1200/JCO.2012.44.3762>  
PMID:23715562
31. Hugo W, Zaretsky JM, Sun L, Song C, Moreno BH, Hu-Lieskovan S, Berent-Maoz B, Pang J, Chmielowski B, Cherry G, Seja E, Lomeli S, Kong X, et al. Genomic and Transcriptomic Features of Response to Anti-PD-1 Therapy in Metastatic Melanoma. *Cell*. 2016; 165:35–44.  
<https://doi.org/10.1016/j.cell.2016.02.065>  
PMID:26997480
32. Mariathasan S, Turley SJ, Nickles D, Castiglioni A, Yuen K, Wang Y, Kadel EE II, Koeppen H, Astarita JL, Cubas R, Jhunjhunwala S, Banchereau R, Yang Y, et al. TGFβ attenuates tumour response to PD-L1 blockade by contributing to exclusion of T cells. *Nature*. 2018; 554:544–8.  
<https://doi.org/10.1038/nature25501>  
PMID:29443960
33. Snyder A, Nathanson T, Funt SA, Ahuja A, Buros Novik J, Hellmann MD, Chang E, Aksoy BA, Al-Ahmadie H, Yusko E, Vignali M, Benzeno S, Boyd M, et al. Contribution of systemic and somatic factors to clinical response and resistance to PD-L1 blockade in urothelial cancer: An exploratory multi-omic analysis. *PLoS Med*. 2017; 14:e1002309.  
<https://doi.org/10.1371/journal.pmed.1002309>  
PMID:28552987
34. Ritchie ME, Phipson B, Wu D, Hu Y, Law CW, Shi W, Smyth GK. limma powers differential expression analyses for RNA-sequencing and microarray studies. *Nucleic Acids Res*. 2015; 43:e47.  
<https://doi.org/10.1093/nar/gkv007>  
PMID:25605792
35. Yu G, Wang LG, Han Y, He QY. clusterProfiler: an R package for comparing biological themes among gene clusters. *OMICS*. 2012; 16:284–7.  
<https://doi.org/10.1089/omi.2011.0118>  
PMID:22455463
36. Liberzon A, Birger C, Thorvaldsdóttir H, Ghandi M, Mesirov JP, Tamayo P. The Molecular Signatures Database (MSigDB) hallmark gene set collection. *Cell Syst*. 2015; 1:417–25.  
<https://doi.org/10.1016/j.cels.2015.12.004>  
PMID:26771021
37. Hänzelmann S, Castelo R, Guinney J. GSVA: gene set variation analysis for microarray and RNA-seq data. *BMC Bioinformatics*. 2013; 14:7.  
<https://doi.org/10.1186/1471-2105-14-7>  
PMID:23323831
38. Eide PW, Bruun J, Lothe RA, Sveen A. CMScaller: an R package for consensus molecular subtyping of colorectal cancer pre-clinical models. *Sci Rep*. 2017; 7:16618.  
<https://doi.org/10.1038/s41598-017-16747-x>  
PMID:29192179
39. Thorsson V, Gibbs DL, Brown SD, Wolf D, Bortone DS, Ou Yang TH, Porta-Pardo E, Gao GF, Plaisier CL, Eddy JA, Ziv E, Culhane AC, Paull EO, et al, and Cancer Genome Atlas Research Network. The Immune Landscape of Cancer. *Immunity*. 2018; 48:812–30.e14.  
<https://doi.org/10.1016/j.immuni.2018.03.023>  
PMID:29628290
40. Yoshihara K, Shahmoradgoli M, Martínez E, Vegesna R, Kim H, Torres-García W, Treviño V, Shen H, Laird PW, Levine DA, Carter SL, Getz G, Stemke-Hale K, et al. Inferring tumour purity and stromal and immune cell admixture from expression data. *Nat Commun*. 2013; 4:2612.  
<https://doi.org/10.1038/ncomms3612> PMID:24113773
41. Xiao Y, Ma D, Zhao S, Suo C, Shi J, Xue MZ, Ruan M, Wang H, Zhao J, Li Q, Wang P, Shi L, Yang WT, et al, and AME Breast Cancer Collaborative Group. Multi-Omics Profiling Reveals Distinct Microenvironment Characterization and Suggests Immune Escape Mechanisms of Triple-Negative Breast Cancer. *Clin Cancer Res*. 2019; 25:5002–14.  
<https://doi.org/10.1158/1078-0432.CCR-18-3524>  
PMID:30837276
42. Sanchez-Vega F, Mina M, Armenia J, Chatila WK, Luna A, La KC, Dimitriadou S, Liu DL, Kantheti HS, Saghafeinia S, Chakravarty D, Daian F, Gao Q, et al, and Cancer Genome Atlas Research Network. Oncogenic Signaling Pathways in The Cancer Genome Atlas. *Cell*. 2018; 173:321–37.e10.  
<https://doi.org/10.1016/j.cell.2018.03.035>  
PMID:29625050
43. Barros L, Pretti MA, Chicaybam L, Abdo L, Boroni M, Bonamino MH. Immunological-based approaches for cancer therapy. *Clinics (Sao Paulo)*. 2018; 73:e429s.  
<https://doi.org/10.6061/clinics/2018/e429s>  
PMID:30133560
44. Bindea G, Mlecnik B, Tosolini M, Kirilovsky A, Waldner M, Obenauf AC, Angell H, Fredriksen T, Lafontaine L, Berger A, Bruneval P, Fridman WH, Becker C, et al.



- Spatiotemporal dynamics of intratumoral immune cells reveal the immune landscape in human cancer. *Immunity*. 2013; 39:782–95.  
<https://doi.org/10.1016/j.immuni.2013.10.003>  
PMID:24138885
45. Geeleher P, Cox N, Huang RS. pRRophetic: an R package for prediction of clinical chemotherapeutic response from tumor gene expression levels. *PLoS One*. 2014; 9:e107468.  
<https://doi.org/10.1371/journal.pone.0107468>  
PMID:25229481
  46. Guinney J, Dienstmann R, Wang X, de Reyniès A, Schlicker A, Soneson C, Marisa L, Roepman P, Nyamundanda G, Angelino P, Bot BM, Morris JS, Simon IM, et al. The consensus molecular subtypes of colorectal cancer. *Nat Med*. 2015; 21:1350–6.  
<https://doi.org/10.1038/nm.3967>  
PMID:26457759
  47. Chen J, Gong C, Mao H, Li Z, Fang Z, Chen Q, Lin M, Jiang X, Hu Y, Wang W, Zhang X, Chen X, Li H. E2F1/SP3/STAT6 axis is required for IL-4-induced epithelial-mesenchymal transition of colorectal cancer cells. *Int J Oncol*. 2018; 53:567–78.  
<https://doi.org/10.3892/ijo.2018.4429>  
PMID:29901191
  48. Chen T, Li Q, Wu J, Wu Y, Peng W, Li H, Wang J, Tang X, Peng Y, Fu X. *Fusobacterium nucleatum* promotes M2 polarization of macrophages in the microenvironment of colorectal tumours via a TLR4-dependent mechanism. *Cancer Immunol Immunother*. 2018; 67:1635–46.  
<https://doi.org/10.1007/s00262-018-2233-x>  
PMID:30121899
  49. Kikuchi Y, Tokita S, Hiramata T, Kochin V, Nakatsugawa M, Shinkawa T, Hirohashi Y, Tsukahara T, Hata F, Takemasa I, Sato N, Kanaseki T, Torigoe T. CD8<sup>+</sup> T-cell Immune Surveillance against a Tumor Antigen Encoded by the Oncogenic Long Noncoding RNA PVT1. *Cancer Immunol Res*. 2021; 9:1342–53.  
<https://doi.org/10.1158/2326-6066.CIR-20-0964>  
PMID:34433589
  50. Shao Q, Wang L, Yuan M, Jin X, Chen Z, Wu C. TIGIT Induces (CD3<sup>+</sup>) T Cell Dysfunction in Colorectal Cancer by Inhibiting Glucose Metabolism. *Front Immunol*. 2021; 12:688961.  
<https://doi.org/10.3389/fimmu.2021.688961>  
PMID:34659197
  51. Spranger S. Mechanisms of tumor escape in the context of the T-cell-inflamed and the non-T-cell-inflamed tumor microenvironment. *Int Immunol*. 2016; 28:383–91.  
<https://doi.org/10.1093/intimm/dxw014>  
PMID:26989092
  52. Hakelius M, Reyhani V, Rubin K, Gerdin B, Nowinski D. Normal Oral Keratinocytes and Head and Neck Squamous Carcinoma Cells Induce an Innate Response of Fibroblasts. *Anticancer Res*. 2016; 36:2131–7.  
PMID:27127114
  53. Tang J, Shalabi A, Hubbard-Lucey VM. Comprehensive analysis of the clinical immuno-oncology landscape. *Ann Oncol*. 2018; 29:84–91.  
<https://doi.org/10.1093/annonc/mdx755>  
PMID:29228097
  54. Angelova M, Charoentong P, Hackl H, Fischer ML, Snajder R, Krogsdam AM, Waldner MJ, Bindea G, Mlecnik B, Galon J, Trajanoski Z. Characterization of the immunophenotypes and antigenomes of colorectal cancers reveals distinct tumor escape mechanisms and novel targets for immunotherapy. *Genome Biol*. 2015; 16:64.  
<https://doi.org/10.1186/s13059-015-0620-6>  
PMID:25853550
  55. Wishart DS, Feunang YD, Guo AC, Lo EJ, Marcu A, Grant JR, Sajed T, Johnson D, Li C, Sayeeda Z, Assempour N, Iynkkaran I, Liu Y, et al. DrugBank 5.0: a major update to the DrugBank database for 2018. *Nucleic Acids Res*. 2018; 46:D1074–82.  
<https://doi.org/10.1093/nar/gkx1037>  
PMID:29126136
  56. Fang S, Dong L, Liu L, Guo J, Zhao L, Zhang J, Bu D, Liu X, Huo P, Cao W, Dong Q, Wu J, Zeng X, et al. HERB: a high-throughput experiment- and reference-guided database of traditional Chinese medicine. *Nucleic Acids Res*. 2021; 49:D1197–206.  
<https://doi.org/10.1093/nar/gkaa1063>  
PMID:33264402
  57. Herr R, Köhler M, Andrlová H, Weinberg F, Möller Y, Halbach S, Lutz L, Mastroianni J, Klose M, Bittermann N, Kowar S, Zeiser R, Olayioye MA, et al. B-Raf inhibitors induce epithelial differentiation in BRAF-mutant colorectal cancer cells. *Cancer Res*. 2015; 75:216–29.  
<https://doi.org/10.1158/0008-5472.CAN-13-3686>  
PMID:25381152
  58. Whittaker SR, Cowley GS, Wagner S, Luo F, Root DE, Garraway LA. Combined Pan-RAF and MEK Inhibition Overcomes Multiple Resistance Mechanisms to Selective RAF Inhibitors. *Mol Cancer Ther*. 2015; 14:2700–11.  
<https://doi.org/10.1158/1535-7163.MCT-15-0136-T>  
PMID:26351322
  59. Herr R, Halbach S, Heizmann M, Busch H, Boerries M, Brummer T. BRAF inhibition upregulates a variety of receptor tyrosine kinases and their downstream effector Gab2 in colorectal cancer cell lines. *Oncogene*. 2018; 37:1576–93.

- <https://doi.org/10.1038/s41388-017-0063-5>  
PMID:29326440
60. Zhang S, Deng Z, Yao C, Huang P, Zhang Y, Cao S, Li X. AT7867 Inhibits Human Colorectal Cancer Cells via AKT-Dependent and AKT-Independent Mechanisms. *PLoS One*. 2017; 12:e0169585.  
<https://doi.org/10.1371/journal.pone.0169585>  
PMID:28081222
  61. Ponnuram S, Standing D, Rangarajan P, Subramaniam D. Tandutinib inhibits the Akt/mTOR signaling pathway to inhibit colon cancer growth. *Mol Cancer Ther*. 2013; 12:598–609.  
<https://doi.org/10.1158/1535-7163.MCT-12-0907>  
PMID:23427297
  62. Liu Q, Li A, Wang L, He W, Zhao L, Wu C, Lu S, Ye X, Zhao H, Shen X, Xiao X, Liu Z. Stomatin-like Protein 2 Promotes Tumor Cell Survival by Activating the JAK2-STAT3-PIM1 Pathway, Suggesting a Novel Therapy in CRC. *Mol Ther Oncolytics*. 2020; 17:169–79.  
<https://doi.org/10.1016/j.omto.2020.03.010>  
PMID:32346607
  63. Lee SJ, Lee I, Lee J, Park C, Kang WK. Statins, 3-hydroxy-3-methylglutaryl coenzyme A reductase inhibitors, potentiate the anti-angiogenic effects of bevacizumab by suppressing angiopoietin2, BiP, and Hsp90α in human colorectal cancer. *Br J Cancer*. 2014; 111:497–505.  
<https://doi.org/10.1038/bjc.2014.283> PMID:24945998
  64. Wächtershäuser A, Akoglu B, Stein J. HMG-CoA reductase inhibitor mevastatin enhances the growth inhibitory effect of butyrate in the colorectal carcinoma cell line Caco-2. *Carcinogenesis*. 2001; 22:1061–7.  
<https://doi.org/10.1093/carcin/22.7.1061>  
PMID:11408350
  65. Xiong D, Wang Y, You M. A gene expression signature of TREM2<sup>hi</sup> macrophages and γδ T cells predicts immunotherapy response. *Nat Commun*. 2020; 11:5084.  
<https://doi.org/10.1038/s41467-020-18546-x>  
PMID:33033253
  66. Ayers M, Lunceford J, Nebozhyn M, Murphy E, Loboda A, Kaufman DR, Albright A, Cheng JD, Kang SP, Shankaran V, Piha-Paul SA, Yearley J, Seiwert TY, et al. IFN-γ-related mRNA profile predicts clinical response to PD-1 blockade. *J Clin Invest*. 2017; 127:2930–40.  
<https://doi.org/10.1172/JCI91190> PMID:28650338
  67. Thompson JC, Hwang WT, Davis C, Deshpande C, Jeffries S, Rajpurohit Y, Krishna V, Smirnov D, Verona R, Lorenzi MV, Langer CJ, Albelda SM. Gene signatures of tumor inflammation and epithelial-to-mesenchymal transition (EMT) predict responses to immune checkpoint blockade in lung cancer with high accuracy. *Lung Cancer*. 2020; 139:1–8.  
<https://doi.org/10.1016/j.lungcan.2019.10.012>  
PMID:31683225
  68. Lauss M, Donia M, Harbst K, Andersen R, Mitra S, Rosengren F, Salim M, Vallon-Christersson J, Törnngren T, Kvist A, Ringnér M, Svane IM, Jönsson G. Mutational and putative neoantigen load predict clinical benefit of adoptive T cell therapy in melanoma. *Nat Commun*. 2017; 8:1738.  
<https://doi.org/10.1038/s41467-017-01460-0>  
PMID:29170503
  69. Messina JL, Fenstermacher DA, Eschrich S, Qu X, Berglund AE, Lloyd MC, Schell MJ, Sondak VK, Weber JS, Mulé JJ. 12-Chemokine gene signature identifies lymph node-like structures in melanoma: potential for patient selection for immunotherapy? *Sci Rep*. 2012; 2:765.  
<https://doi.org/10.1038/srep00765> PMID:23097687
  70. Ali HR, Chlon L, Pharoah PD, Markowitz F, Caldas C. Patterns of Immune Infiltration in Breast Cancer and Their Clinical Implications: A Gene-Expression-Based Retrospective Study. *PLoS Med*. 2016; 13:e1002194.  
<https://doi.org/10.1371/journal.pmed.1002194>  
PMID:27959923
  71. Bense RD, Sotiriou C, Piccart-Gebhart MJ, Haanen JB, van Vugt MA, de Vries EG, Schröder CP, Fehrmann RS. Relevance of Tumor-Infiltrating Immune Cell Composition and Functionality for Disease Outcome in Breast Cancer. *J Natl Cancer Inst*. 2016; 109:djw192.  
<https://doi.org/10.1093/jnci/djw192>  
PMID:27737921
  72. Toor SM, Murshed K, Al-Dhaheer M, Khawar M, Abu Nada M, Elkord E. Immune Checkpoints in Circulating and Tumor-Infiltrating CD4<sup>+</sup> T Cell Subsets in Colorectal Cancer Patients. *Front Immunol*. 2019; 10:2936.  
<https://doi.org/10.3389/fimmu.2019.02936>  
PMID:31921188
  73. Huang Y, Liao H, Zhang Y, Yuan R, Wang F, Gao Y, Wang P, Du Z. Prognostic value of tumor-infiltrating FoxP3<sup>+</sup> T cells in gastrointestinal cancers: a meta analysis. *PLoS One*. 2014; 9:e94376.  
<https://doi.org/10.1371/journal.pone.0094376>  
PMID:24827118
  74. Zhuo C, Xu Y, Ying M, Li Q, Huang L, Li D, Cai S, Li B. FOXP3<sup>+</sup> Tregs: heterogeneous phenotypes and conflicting impacts on survival outcomes in patients with colorectal cancer. *Immunol Res*. 2015; 61:338–47.  
<https://doi.org/10.1007/s12026-014-8616-y>  
PMID:25608795
  75. Sideras K, Galjart B, Vasaturo A, Pedroza-Gonzalez A, Biermann K, Mancham S, Nigg AL, Hansen BE, Stoop

- HA, Zhou G, Verhoef C, Sleijfer S, Sprengers D, et al. Prognostic value of intra-tumoral CD8<sup>+</sup> /FoxP3<sup>+</sup> lymphocyte ratio in patients with resected colorectal cancer liver metastasis. *J Surg Oncol*. 2018; 118:68–76. <https://doi.org/10.1002/iso.25091> PMID:29878369
76. Kuwahara T, Hazama S, Suzuki N, Yoshida S, Tomochika S, Nakagami Y, Matsui H, Shindo Y, Kanekiyo S, Tokumitsu Y, Iida M, Tsunedomi R, Takeda S, et al. Intratumoural-infiltrating CD4 + and FOXP3 + T cells as strong positive predictive markers for the prognosis of resectable colorectal cancer. *Br J Cancer*. 2019; 121:659–65. <https://doi.org/10.1038/s41416-019-0559-6> PMID:31488881
  77. Salama P, Phillips M, Grieco F, Morris M, Zeps N, Joseph D, Platell C, Iacopetta B. Tumor-infiltrating FOXP3+ T regulatory cells show strong prognostic significance in colorectal cancer. *J Clin Oncol*. 2009; 27:186–92. <https://doi.org/10.1200/JCO.2008.18.7229> PMID:19064967
  78. Chaput N, Louafi S, Bardier A, Charlotte F, Vaillant JC, Ménégau F, Rosenzweig M, Lemoine F, Klatzmann D, Taieb J. Identification of CD8+CD25+Foxp3+ suppressive T cells in colorectal cancer tissue. *Gut*. 2009; 58:520–29. <https://doi.org/10.1136/gut.2008.158824> PMID:19022917
  79. Blatner NR, Mulcahy MF, Dennis KL, Scholtens D, Bentrem DJ, Phillips JD, Ham S, Sandall BP, Khan MW, Mahvi DM, Halverson AL, Stryker SJ, Boller AM, et al. Expression of RORγt marks a pathogenic regulatory T cell subset in human colon cancer. *Sci Transl Med*. 2012; 4:164ra159. <https://doi.org/10.1126/scitranslmed.3004566> PMID:23241743
  80. Reddy JP, Atkinson RL, Larson R, Burks JK, Smith D, Debeb BG, Ruffell B, Creighton CJ, Bambhroliya A, Reuben JM, Van Laere SJ, Krishnamurthy S, Symmans WF, et al. Mammary stem cell and macrophage markers are enriched in normal tissue adjacent to inflammatory breast cancer. *Breast Cancer Res Treat*. 2018; 171:283–93. <https://doi.org/10.1007/s10549-018-4835-6> PMID:29858753
  81. Martinez FO. Regulators of macrophage activation. *Eur J Immunol*. 2011; 41:1531–4. <https://doi.org/10.1002/eji.201141670> PMID:21607943
  82. Guo L, Wang C, Qiu X, Pu X, Chang P. Colorectal Cancer Immune Infiltrates: Significance in Patient Prognosis and Immunotherapeutic Efficacy. *Front Immunol*. 2020; 11:1052. <https://doi.org/10.3389/fimmu.2020.01052> PMID:32547556
  83. Zhang R, Qi F, Zhao F, Li G, Shao S, Zhang X, Yuan L, Feng Y. Cancer-associated fibroblasts enhance tumor-associated macrophages enrichment and suppress NK cells function in colorectal cancer. *Cell Death Dis*. 2019; 10:273. <https://doi.org/10.1038/s41419-019-1435-2> PMID:30894509
  84. Kuwahara T, Hazama S, Suzuki N, Yoshida S, Tomochika S, Nakagami Y, Matsui H, Shindo Y, Kanekiyo S, Tokumitsu Y, Iida M, Tsunedomi R, Takeda S, et al. Correction: Intratumoural-infiltrating CD4 + and FOXP3 + T cells as strong positive predictive markers for the prognosis of resectable colorectal cancer. *Br J Cancer*. 2019; 121:983–4. <https://doi.org/10.1038/s41416-019-0605-4> PMID:31624318
  85. Tosolini M, Kirilovsky A, Mlecnik B, Fredriksen T, Mauger S, Bindea G, Berger A, Bruneval P, Fridman WH, Pagès F, Galon J. Clinical impact of different classes of infiltrating T cytotoxic and helper cells (Th1, Th2, Treg, Th17) in patients with colorectal cancer. *Cancer Res*. 2011; 71:1263–71. <https://doi.org/10.1158/0008-5472.CAN-10-2907> PMID:21303976
  86. Melssen M, Slingsluff CL Jr. Vaccines targeting helper T cells for cancer immunotherapy. *Curr Opin Immunol*. 2017; 47:85–92. <https://doi.org/10.1016/j.coi.2017.07.004> PMID:28755541
  87. Palucka K, Banchereau J. Cancer immunotherapy via dendritic cells. *Nat Rev Cancer*. 2012; 12:265–77. <https://doi.org/10.1038/nrc3258> PMID:22437871
  88. Du XH, Liu HL, Li L, Xia SY, Ning N, Zou ZY, Teng D, Xiao CH, Li R, Xu YX. Clinical significance of immunotherapy with combined three kinds of cells for operable colorectal cancer. *Tumour Biol*. 2015; 36:5679–85. <https://doi.org/10.1007/s13277-015-3242-4> PMID:25764087
  89. Hargadon KM. Strategies to Improve the Efficacy of Dendritic Cell-Based Immunotherapy for Melanoma. *Front Immunol*. 2017; 8:1594. <https://doi.org/10.3389/fimmu.2017.01594> PMID:29209327
  90. Rao HL, Chen JW, Li M, Xiao YB, Fu J, Zeng YX, Cai MY, Xie D. Increased intratumoral neutrophil in colorectal carcinomas correlates closely with malignant phenotype and predicts patients' adverse prognosis. *PLoS One*. 2012; 7:e30806. <https://doi.org/10.1371/journal.pone.0030806> PMID:22295111

91. Chua W, Charles KA, Baracos VE, Clarke SJ. Neutrophil/lymphocyte ratio predicts chemotherapy outcomes in patients with advanced colorectal cancer. *Br J Cancer*. 2011; 104:1288–95.  
<https://doi.org/10.1038/bjc.2011.100> PMID: [21448173](#)
92. Governa V, Trella E, Mele V, Tornillo L, Amicarella F, Cremonesi E, Muraro MG, Xu H, Droeser R, Däster SR, Bolli M, Rosso R, Oertli D, et al. The Interplay Between Neutrophils and CD8<sup>+</sup> T Cells Improves Survival in Human Colorectal Cancer. *Clin Cancer Res*. 2017; 23:3847–58.  
<https://doi.org/10.1158/1078-0432.CCR-16-2047> PMID: [28108544](#)
93. Mei L, Xiong WC. Neuregulin 1 in neural development, synaptic plasticity and schizophrenia. *Nat Rev Neurosci*. 2008; 9:437–52.  
<https://doi.org/10.1038/nrn2392> PMID: [18478032](#)
94. Laskin J, Liu SV, Tolba K, Heining C, Schlenk RF, Cheema P, Cadranell J, Jones MR, Drilon A, Cseh A, Gyorffy S, Solca F, Duruisseaux M. NRG1 fusion-driven tumors: biology, detection, and the therapeutic role of afatinib and other ErbB-targeting agents. *Ann Oncol*. 2020; 31:1693–703.  
<https://doi.org/10.1016/j.annonc.2020.08.2335> PMID: [32916265](#)
95. Cadranell J, Liu SV, Duruisseaux M, Branden E, Goto Y, Weinberg BA, Heining C, Schlenk RF, Cheema P, Jones MR, Drilon A, Trombetta D, Muscarella LA, et al. Therapeutic Potential of Afatinib in NRG1 Fusion-Driven Solid Tumors: A Case Series. *Oncologist*. 2021; 26:7–16.  
<https://doi.org/10.1634/theoncologist.2020-0379> PMID: [32852072](#)
96. Guo Y, Duan Z, Jia Y, Ren C, Lv J, Guo P, Zhao W, Wang B, Zhang S, Li Y, Li Z. HER4 isoform CYT2 and its ligand NRG1III are expressed at high levels in human colorectal cancer. *Oncol Lett*. 2018; 15:6629–35.  
<https://doi.org/10.3892/ol.2018.8124> PMID: [29616125](#)
97. Fujii K, Kondo T, Yokoo H, Yamada T, Iwatsuki K, Hirohashi S. Proteomic study of human hepatocellular carcinoma using two-dimensional difference gel electrophoresis with saturation cysteine dye. *Proteomics*. 2005; 5:1411–22.  
<https://doi.org/10.1002/pmic.200401004> PMID: [15751005](#)
98. Nieman KM, Kenny HA, Penicka CV, Ladanyi A, Buell-Gutbrod R, Zillhardt MR, Romero IL, Carey MS, Mills GB, Hotamisligil GS, Yamada SD, Peter ME, Gwin K, Lengyel E. Adipocytes promote ovarian cancer metastasis and provide energy for rapid tumor growth. *Nat Med*. 2011; 17:1498–503.  
<https://doi.org/10.1038/nm.2492> PMID: [22037646](#)
99. Nieman KM, Romero IL, Van Houten B, Lengyel E. Adipose tissue and adipocytes support tumorigenesis and metastasis. *Biochim Biophys Acta*. 2013; 1831:1533–41.  
<https://doi.org/10.1016/j.bbali.2013.02.010> PMID: [23500888](#)
100. Zhang Y, Zhao X, Deng L, Li X, Wang G, Li Y, Chen M. High expression of FABP4 and FABP6 in patients with colorectal cancer. *World J Surg Oncol*. 2019; 17:171.  
<https://doi.org/10.1186/s12957-019-1714-5> PMID: [31651326](#)
101. Martinez V, Wang L, Million M, Rivier J, Taché Y. Urocortins and the regulation of gastrointestinal motor function and visceral pain. *Peptides*. 2004; 25:1733–44.  
<https://doi.org/10.1016/j.peptides.2004.05.025> PMID: [15476940](#)
102. Chen H, Luo J, Guo J. Development and validation of a five-immune gene prognostic risk model in colon cancer. *BMC Cancer*. 2020; 20:395.  
<https://doi.org/10.1186/s12885-020-06799-0> PMID: [32375704](#)
103. Wang J, Yu S, Chen G, Kang M, Jin X, Huang Y, Lin L, Wu D, Wang L, Chen J. A novel prognostic signature of immune-related genes for patients with colorectal cancer. *J Cell Mol Med*. 2020; 24:8491–504.  
<https://doi.org/10.1111/jcmm.15443> PMID: [32564470](#)
104. Scherer D, Nagore E, Bermejo JL, Figl A, Botella-Estrada R, Thirumaran RK, Angelini S, Hemminki K, Schadendorf D, Kumar R. Melanocortin receptor 1 variants and melanoma risk: a study of 2 European populations. *Int J Cancer*. 2009; 125:1868–75.  
<https://doi.org/10.1002/ijc.24548> PMID: [19585506](#)
105. Chen S, Zhu B, Yin C, Liu W, Han C, Chen B, Liu T, Li X, Chen X, Li C, Hu L, Zhou J, Xu ZX, et al. Palmitoylation-dependent activation of MC1R prevents melanomagenesis. *Nature*. 2017; 549:399–403.  
<https://doi.org/10.1038/nature23887> PMID: [28869973](#)
106. MacLaughlin DT, Donahoe PK. Müllerian inhibiting substance/anti-Müllerian hormone: a potential therapeutic agent for human ovarian and other cancers. *Future Oncol*. 2010; 6:391–405.  
<https://doi.org/10.2217/fon.09.172> PMID: [20222796](#)
107. Clendenen TV, Ge W, Koenig KL, Afanasyeva Y, Agnoli C, Brinton LA, Darvishian F, Dorgan JF, Eliassen AH, Falk RT, Hallmans G, Hankinson SE, Hoffman-Bolton J, et al. Breast cancer risk prediction in women aged 35–50 years: impact of including sex hormone concentrations in the Gail model. *Breast Cancer Res*. 2019; 21:42.



<https://doi.org/10.1186/s13058-019-1126-z>  
PMID:[30890167](https://pubmed.ncbi.nlm.nih.gov/30890167/)

108. Gong B, Kao Y, Zhang C, Sun F, Gong Z, Chen J. Identification of Hub Genes Related to Carcinogenesis and Prognosis in Colorectal Cancer Based on Integrated Bioinformatics. *Mediators Inflamm.* 2020; 2020:5934821.  
<https://doi.org/10.1155/2020/5934821>  
PMID:[32351322](https://pubmed.ncbi.nlm.nih.gov/32351322/)
109. Pang B, Xu X, Lu Y, Jin H, Yang R, Jiang C, Shao D, Liu Y, Shi J. Prediction of new targets and mechanisms for quercetin in the treatment of pancreatic cancer, colon cancer, and rectal cancer. *Food Funct.* 2019; 10:5339–49.  
<https://doi.org/10.1039/c9fo01168d> PMID:[31393490](https://pubmed.ncbi.nlm.nih.gov/31393490/)
110. Namwanje M, Brown CW. Activins and Inhibins: Roles in Development, Physiology, and Disease. *Cold Spring Harb Perspect Biol.* 2016; 8:a021881.  
<https://doi.org/10.1101/cshperspect.a021881>  
PMID:[27328872](https://pubmed.ncbi.nlm.nih.gov/27328872/)
111. Wijayarathna R, de Kretser DM. Activins in reproductive biology and beyond. *Hum Reprod Update.* 2016; 22:342–57.  
<https://doi.org/10.1093/humupd/dmv058>  
PMID:[26884470](https://pubmed.ncbi.nlm.nih.gov/26884470/)
112. Kita A, Kasamatsu A, Nakashima D, Endo-Sakamoto Y, Ishida S, Shimizu T, Kimura Y, Miyamoto I, Yoshimura S, Shiiba M, Tanzawa H, Uzawa K. Activin B Regulates Adhesion, Invasiveness, and Migratory Activities in Oral Cancer: a Potential Biomarker for Metastasis. *J Cancer.* 2017; 8:2033–41.  
<https://doi.org/10.7150/jca.18714> PMID:[28819404](https://pubmed.ncbi.nlm.nih.gov/28819404/)
113. Mylonas I. Inhibin-alpha, -betaA and -betaB subunits in uterine non-endometrioid carcinomas: prognostic significance and clinical implications. *Eur J Cancer.* 2010; 46:2485–93.  
<https://doi.org/10.1016/j.ejca.2010.06.001>  
PMID:[20599374](https://pubmed.ncbi.nlm.nih.gov/20599374/)
114. Hofland J, van Weerden WM, Steenbergen J, Dits NF, Jenster G, de Jong FH. Activin A stimulates AKR1C3 expression and growth in human prostate cancer. *Endocrinology.* 2012; 153:5726–34.  
<https://doi.org/10.1210/en.2011-2065>  
PMID:[23024260](https://pubmed.ncbi.nlm.nih.gov/23024260/)
115. Matsuo SE, Ebina KN, Kulcsar MA, Friguglietti CU, Kimura ET. Activin betaB expression in rat experimental goiter and human thyroid tumors. *Thyroid.* 2003; 13:239–47.  
<https://doi.org/10.1089/105072503321582033>  
PMID:[12729472](https://pubmed.ncbi.nlm.nih.gov/12729472/)
116. Yuan J, Xie A, Cao Q, Li X, Chen J. INHBB Is a Novel Prognostic Biomarker Associated with Cancer-Promoting Pathways in Colorectal Cancer. *Biomed Res Int.* 2020; 2020:6909672.  
<https://doi.org/10.1155/2020/6909672>  
PMID:[33083477](https://pubmed.ncbi.nlm.nih.gov/33083477/)
117. Pansky A, DE Weerth A, Fasler-Kan E, Boulay JL, Schulz M, Ketterer S, Selck C, Beglinger C, VON Schrenck T, Hildebrand P. Gastrin releasing peptide-preferring bombesin receptors mediate growth of human renal cell carcinoma. *J Am Soc Nephrol.* 2000; 11:1409–18.  
<https://doi.org/10.1681/ASN.V1181409>  
PMID:[10906154](https://pubmed.ncbi.nlm.nih.gov/10906154/)
118. Thomas RP, Hellmich MR, Townsend CM Jr, Evers BM. Role of gastrointestinal hormones in the proliferation of normal and neoplastic tissues. *Endocr Rev.* 2003; 24:571–99.  
<https://doi.org/10.1210/er.2002-0028>  
PMID:[14570743](https://pubmed.ncbi.nlm.nih.gov/14570743/)
119. Glover SC, Tretiakova MS, Carroll RE, Benya RV. Increased frequency of gastrin-releasing peptide receptor gene mutations during colon-adenocarcinoma progression. *Mol Carcinog.* 2003; 37:5–15.  
<https://doi.org/10.1002/mc.10117>  
PMID:[12720295](https://pubmed.ncbi.nlm.nih.gov/12720295/)
120. Schally AV, Szepeshazi K, Nagy A, Comaru-Schally AM, Halmos G. New approaches to therapy of cancers of the stomach, colon and pancreas based on peptide analogs. *Cell Mol Life Sci.* 2004; 61:1042–68.  
<https://doi.org/10.1007/s00018-004-3434-3>  
PMID:[15112052](https://pubmed.ncbi.nlm.nih.gov/15112052/)
121. Chave HS, Gough AC, Palmer K, Preston SR, Primrose JN. Bombesin family receptor and ligand gene expression in human colorectal cancer and normal mucosa. *Br J Cancer.* 2000; 82:124–30.  
<https://doi.org/10.1054/bjoc.1998.0888>  
PMID:[10638978](https://pubmed.ncbi.nlm.nih.gov/10638978/)
122. Patel O, Dumesny C, Giraud AS, Baldwin GS, Shulkes A. Stimulation of proliferation and migration of a colorectal cancer cell line by amidated and glycine-extended gastrin-releasing peptide via the same receptor. *Biochem Pharmacol.* 2004; 68:2129–42.  
<https://doi.org/10.1016/j.bcp.2004.08.009>  
PMID:[15498503](https://pubmed.ncbi.nlm.nih.gov/15498503/)
123. Matkowskyj KA, Keller K, Glover S, Kornberg L, Tran-Son-Tay R, Benya RV. Expression of GRP and its receptor in well-differentiated colon cancer cells correlates with the presence of focal adhesion kinase phosphorylated at tyrosines 397 and 407. *J Histochem Cytochem.* 2003; 51:1041–8.  
<https://doi.org/10.1177/002215540305100807>  
PMID:[12871985](https://pubmed.ncbi.nlm.nih.gov/12871985/)
124. Rick FG, Schally AV, Block NL, Nadji M, Szepeshazi K, Zarandi M, Vidaurre I, Perez R, Halmos G, Szalontay L.



- Antagonists of growth hormone-releasing hormone (GHRH) reduce prostate size in experimental benign prostatic hyperplasia. *Proc Natl Acad Sci USA*. 2011; 108:3755–60.  
<https://doi.org/10.1073/pnas.1018086108>  
PMID:21321192
125. Schally AV, Comaru-Schally AM, Nagy A, Kovacs M, Szepeshazi K, Plonowski A, Varga JL, Halmos G. Hypothalamic hormones and cancer. *Front Neuroendocrinol*. 2001; 22:248–91.  
<https://doi.org/10.1006/frne.2001.0217>  
PMID:11587553
  126. Rick FG, Buchholz S, Schally AV, Szalontay L, Krishan A, Datz C, Stadlmayr A, Aigner E, Perez R, Seitz S, Block NL, Hohla F. Combination of gastrin-releasing peptide antagonist with cytotoxic agents produces synergistic inhibition of growth of human experimental colon cancers. *Cell Cycle*. 2012; 11:2518–25.  
<https://doi.org/10.4161/cc.20900>  
PMID:22751419
  127. Li C, Shen Z, Zhou Y, Yu W. Independent prognostic genes and mechanism investigation for colon cancer. *Biol Res*. 2018; 51:10.  
<https://doi.org/10.1186/s40659-018-0158-7>  
PMID:29653552
  128. Bedke J, Hemmerlein B, Perske C, Gross A, Heuser M. Tumor-associated macrophages in clear cell renal cell carcinoma express both gastrin-releasing peptide and its receptor: a possible modulatory role of immune effectors cells. *World J Urol*. 2010; 28:335–41.  
<https://doi.org/10.1007/s00345-009-0492-z>  
PMID:20012906
  129. Ribatti D, Vacca A, Rusnati M, Presta M. The discovery of basic fibroblast growth factor/fibroblast growth factor-2 and its role in haematological malignancies. *Cytokine Growth Factor Rev*. 2007; 18:327–34.  
<https://doi.org/10.1016/j.cytogfr.2007.04.011>  
PMID:17537668
  130. Sato T, Oshima T, Yoshihara K, Yamamoto N, Yamada R, Nagano Y, Fujii S, Kunisaki C, Shiozawa M, Akaike M, Rino Y, Tanaka K, Masuda M, Imada T. Overexpression of the fibroblast growth factor receptor-1 gene correlates with liver metastasis in colorectal cancer. *Oncol Rep*. 2009; 21:211–16.  
PMID:19082464
  131. Henriksson ML, Edin S, Dahlin AM, Oldenborg PA, Öberg Å, Van Guelpen B, Rutegård J, Stenling R, Palmqvist R. Colorectal cancer cells activate adjacent fibroblasts resulting in FGF1/FGFR3 signaling and increased invasion. *Am J Pathol*. 2011; 178:1387–94.  
<https://doi.org/10.1016/j.ajpath.2010.12.008>  
PMID:21356388
  132. Gavine PR, Mooney L, Kilgour E, Thomas AP, Al-Kadhimi K, Beck S, Rooney C, Coleman T, Baker D, Mellor MJ, Brooks AN, Klinowska T. AZD4547: an orally bioavailable, potent, and selective inhibitor of the fibroblast growth factor receptor tyrosine kinase family. *Cancer Res*. 2012; 72:2045–56.  
<https://doi.org/10.1158/0008-5472.CAN-11-3034>  
PMID:22369928
  133. Jang J, Kim HK, Bang H, Kim ST, Kim SY, Park SH, Lim HY, Kang WK, Lee J, Kim KM. Antitumor Effect of AZD4547 in a Fibroblast Growth Factor Receptor 2-Amplified Gastric Cancer Patient-Derived Cell Model. *Transl Oncol*. 2017; 10:469–75.  
<https://doi.org/10.1016/j.tranon.2017.03.001>  
PMID:28501555
  134. Paik PK, Shen R, Berger MF, Ferry D, Soria JC, Mathewson A, Rooney C, Smith NR, Cullberg M, Kilgour E, Landers D, Frewer P, Brooks N, André F. A Phase Ib Open-Label Multicenter Study of AZD4547 in Patients with Advanced Squamous Cell Lung Cancers. *Clin Cancer Res*. 2017; 23:5366–73.  
<https://doi.org/10.1158/1078-0432.CCR-17-0645>  
PMID:28615371
  135. Guan Z, Lan H, Sun D, Wang X, Jin K. A potential novel therapy for FGFR1-amplified pancreatic cancer with bone metastasis, screened by next-generation sequencing and a patient-derived xenograft model. *Oncol Lett*. 2019; 17:2303–7.  
<https://doi.org/10.3892/ol.2018.9876>  
PMID:30719110
  136. Yao TJ, Zhu JH, Peng DF, Cui Z, Zhang C, Lu PH. AZD-4547 exerts potent cytostatic and cytotoxic activities against fibroblast growth factor receptor (FGFR)-expressing colorectal cancer cells. *Tumour Biol*. 2015; 36:5641–8.  
<https://doi.org/10.1007/s13277-015-3237-1>  
PMID:25691251
  137. Scherlach K, Boettger D, Remme N, Hertweck C. The chemistry and biology of cytochalasins. *Nat Prod Rep*. 2010; 27:869–86.  
<https://doi.org/10.1039/b903913a>  
PMID:20411198
  138. Van Goietsenoven G, Mathieu V, Andolfi A, Cimmino A, Lefranc F, Kiss R, Evidente A. *In vitro* growth inhibitory effects of cytochalasins and derivatives in cancer cells. *Planta Med*. 2011; 77:711–7.  
<https://doi.org/10.1055/s-0030-1250523>  
PMID:21058241
  139. MacLean-Fletcher S, Pollard TD. Mechanism of action of cytochalasin B on actin. *Cell*. 1980; 20:329–41.  
[https://doi.org/10.1016/0092-8674\(80\)90619-4](https://doi.org/10.1016/0092-8674(80)90619-4)

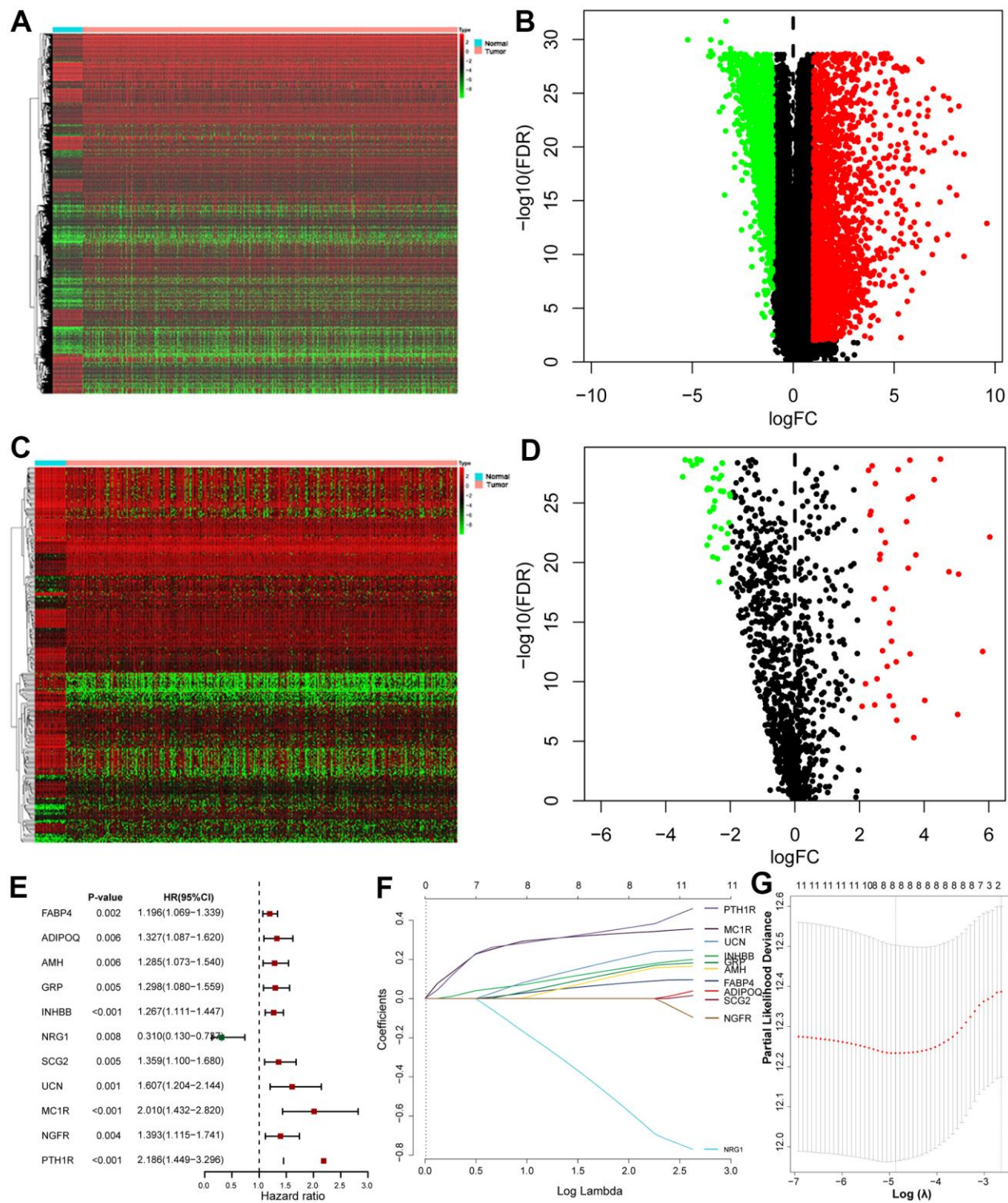
PMID:[6893016](#)

140. Foran E, McWilliam P, Kelleher D, Croke DT, Long A. The leukocyte protein L-plastin induces proliferation, invasion and loss of E-cadherin expression in colon cancer cells. *Int J Cancer*. 2006; 118:2098–104. <https://doi.org/10.1002/ijc.21593> PMID:[16287074](#)
141. Karatzas G, Karayiannakis AJ, Syrigos KN, Chatzigianni E, Papanikolaou S, Riza F, Papanikolaou D. E-cadherin expression correlates with tumor differentiation in colorectal cancer. *Hepatogastroenterology*. 1999; 46:232–5. PMID:[10228798](#)
142. Chen X, Wang Y, Xia H, Wang Q, Jiang X, Lin Z, Ma Y, Yang Y, Hu M. Loss of E-cadherin promotes the growth, invasion and drug resistance of colorectal cancer cells and is associated with liver metastasis. *Mol Biol Rep*. 2012; 39:6707–14. <https://doi.org/10.1007/s11033-012-1494-2> PMID:[22311018](#)
143. Lamouille S, Xu J, Derynck R. Molecular mechanisms of epithelial-mesenchymal transition. *Nat Rev Mol Cell Biol*. 2014; 15:178–96. <https://doi.org/10.1038/nrm3758> PMID:[24556840](#)
144. Kalluri R, Weinberg RA. The basics of epithelial-mesenchymal transition. *J Clin Invest*. 2009; 119:1420–8. <https://doi.org/10.1172/JCI39104> PMID:[19487818](#)
145. Thiery JP, Acloque H, Huang RY, Nieto MA. Epithelial-mesenchymal transitions in development and disease. *Cell*. 2009; 139:871–90. <https://doi.org/10.1016/j.cell.2009.11.007> PMID:[19945376](#)
146. Gu J, Cui CF, Yang L, Wang L, Jiang XH. Emodin Inhibits Colon Cancer Cell Invasion and Migration by Suppressing Epithelial-Mesenchymal Transition via the Wnt/ $\beta$ -Catenin Pathway. *Oncol Res*. 2019; 27:193–202. <https://doi.org/10.3727/096504018X15150662230295> PMID:[29301594](#)
147. Marjaneh RM, Rahmani F, Hassanian SM, Rezaei N, Hashemzahi M, Bahrami A, Ariakia F, Fiuji H, Sahebkar A, Avan A, Khazaei M. Phytosomal curcumin inhibits tumor growth in colitis-associated colorectal cancer. *J Cell Physiol*. 2018; 233:6785–98. <https://doi.org/10.1002/jcp.26538> PMID:[29737515](#)
148. Zhang J, Jiang X, Jiang Y, Guo M, Zhang S, Li J, He J, Liu J, Wang J, Ouyang L. Recent advances in the development of dual VEGFR and c-Met small molecule inhibitors as anticancer drugs. *Eur J Med Chem*. 2016; 108:495–504. <https://doi.org/10.1016/j.ejmech.2015.12.016> PMID:[26717201](#)
149. Chang K, Karnad A, Zhao S, Freeman JW. Roles of c-Met and RON kinases in tumor progression and their potential as therapeutic targets. *Oncotarget*. 2015; 6:3507–18. <https://doi.org/10.18632/oncotarget.3420> PMID:[25784650](#)
150. Kwak EL, Bang YJ, Camidge DR, Shaw AT, Solomon B, Maki RG, Ou SH, Dezube BJ, Jänne PA, Costa DB, Varella-Garcia M, Kim WH, Lynch TJ, et al. Anaplastic lymphoma kinase inhibition in non-small-cell lung cancer. *N Engl J Med*. 2010; 363:1693–703. <https://doi.org/10.1056/NEJMoa1006448> PMID:[20979469](#)
151. Li C, Singh B, Graves-Deal R, Ma H, Starchenko A, Fry WH, Lu Y, Wang Y, Bogatcheva G, Khan MP, Milne GL, Zhao S, Ayers GD, et al. Three-dimensional culture system identifies a new mode of cetuximab resistance and disease-relevant genes in colorectal cancer. *Proc Natl Acad Sci USA*. 2017; 114:E2852–61. <https://doi.org/10.1073/pnas.1618297114> PMID:[28320945](#)
152. Niu Y, Pan D, Shi D, Bai Q, Liu H, Yao X. Influence of Chirality of Crizotinib on Its MTH1 Protein Inhibitory Activity: Insight from Molecular Dynamics Simulations and Binding Free Energy Calculations. *PLoS One*. 2015; 10:e0145219. <https://doi.org/10.1371/journal.pone.0145219> PMID:[26677850](#)
153. Huber KV, Salah E, Radic B, Gridling M, Elkins JM, Stukalov A, Jemth AS, Göktürk C, Sanjiv K, Strömberg K, Pham T, Berglund UW, Colinge J, et al. Stereospecific targeting of MTH1 by (S)-crizotinib as an anticancer strategy. *Nature*. 2014; 508:222–7. <https://doi.org/10.1038/nature13194> PMID:[24695225](#)
154. Rai P, Onder TT, Young JJ, McFaline JL, Pang B, Dedon PC, Weinberg RA. Continuous elimination of oxidized nucleotides is necessary to prevent rapid onset of cellular senescence. *Proc Natl Acad Sci USA*. 2009; 106:169–74. <https://doi.org/10.1073/pnas.0809834106> PMID:[19118192](#)
155. Rai P, Young JJ, Burton DG, Giribaldi MG, Onder TT, Weinberg RA. Enhanced elimination of oxidized guanine nucleotides inhibits oncogenic RAS-induced DNA damage and premature senescence. *Oncogene*. 2011; 30:1489–96. <https://doi.org/10.1038/onc.2010.520> PMID:[21076467](#)

156. Rai P. Human Mut T Homolog 1 (MTH1): a roadblock for the tumor-suppressive effects of oncogenic RAS-induced ROS. *Small GTPases*. 2012; 3:120–5.  
<https://doi.org/10.4161/sgtp.19556> PMID:[22790201](https://pubmed.ncbi.nlm.nih.gov/22790201/)
157. Giribaldi MG, Munoz A, Halvorsen K, Patel A, Rai P. MTH1 expression is required for effective transformation by oncogenic HRAS. *Oncotarget*. 2015; 6:11519–29.  
<https://doi.org/10.18632/oncotarget.3447>  
PMID:[25893378](https://pubmed.ncbi.nlm.nih.gov/25893378/)
158. Spranger S, Bao R, Gajewski TF. Melanoma-intrinsic  $\beta$ -catenin signalling prevents anti-tumour immunity. *Nature*. 2015; 523:231–5.  
<https://doi.org/10.1038/nature14404>  
PMID:[25970248](https://pubmed.ncbi.nlm.nih.gov/25970248/)

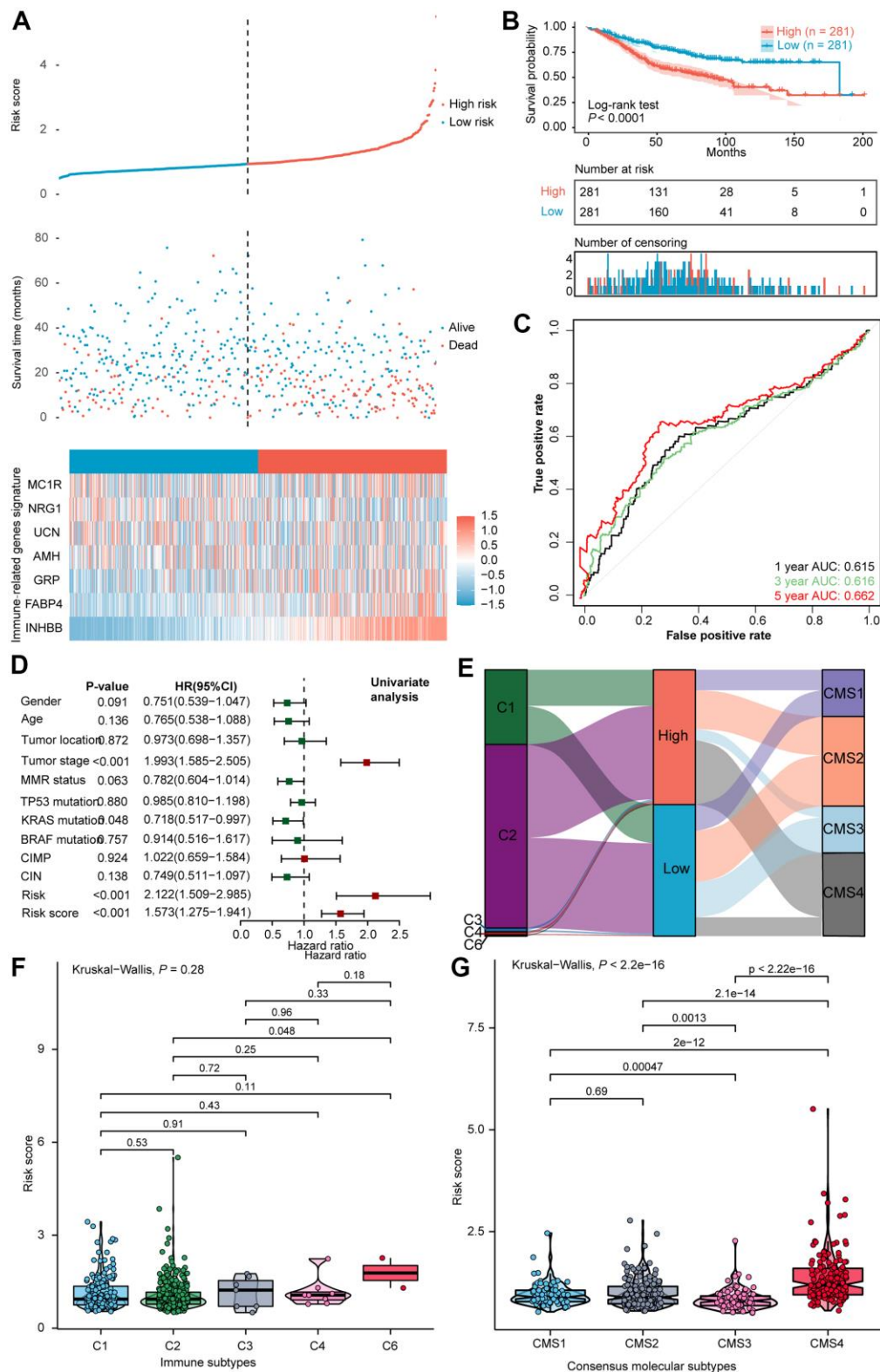
SUPPLEMENTARY MATERIALS

Supplementary Figures



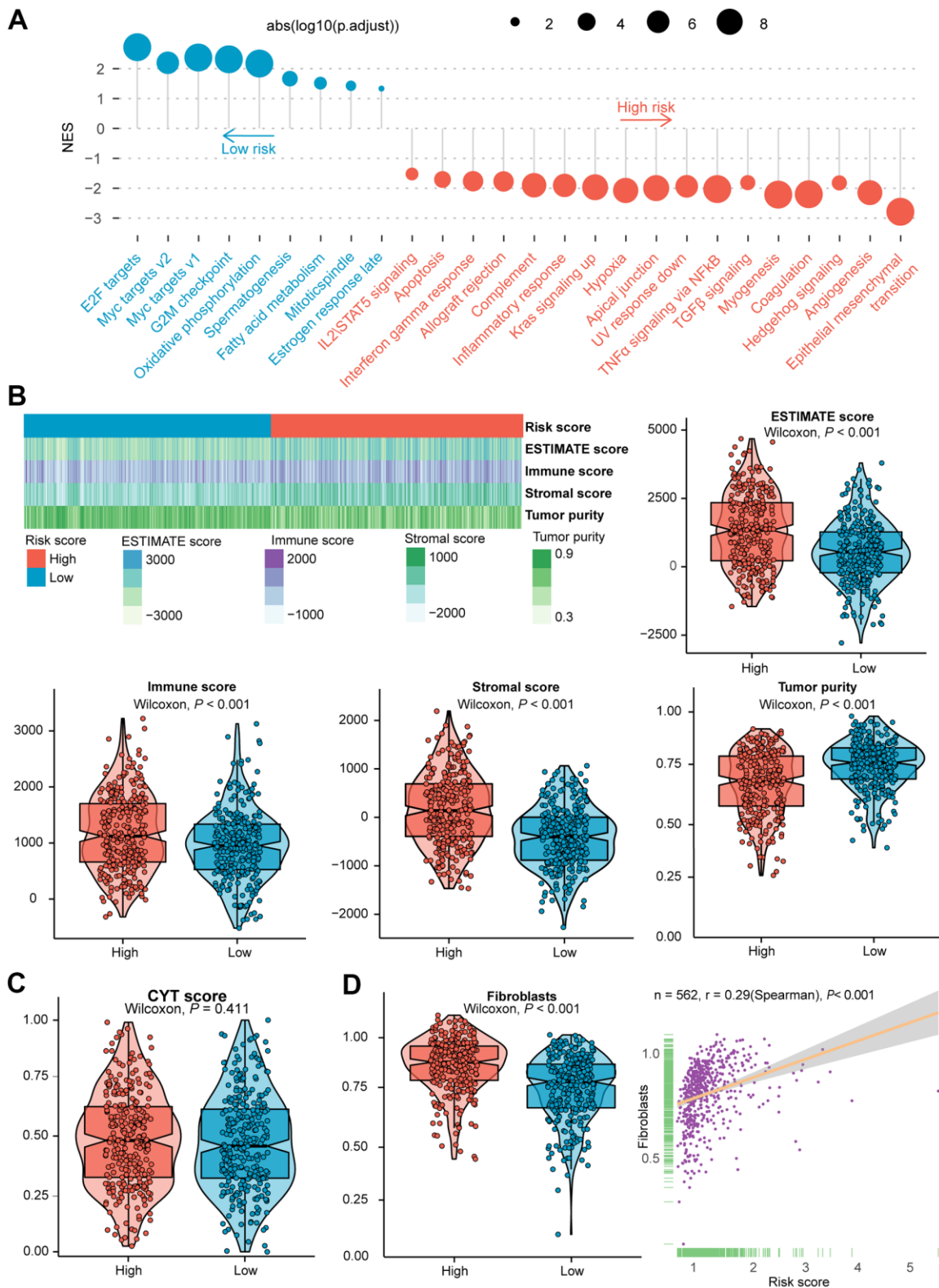
**Supplementary Figure 1. Construction of the IRGs-based risk score model through TCGA training cohort. (A, B)** Differentially expressed genes in CRC. **(C, D)** Differentially expressed IRGs in CRC. **(E)** Forest plot of PRIRGs via univariate Cox regression analysis. **(F)** lasso coefficient profiles of 11 PRIRGs. **(G)** Partial likelihood deviance of variables estimated by the lasso regression algorithm. CRC, colorectal cancer; IRGs, immune-related genes; PRIRGs, prognosis-related IRGs.



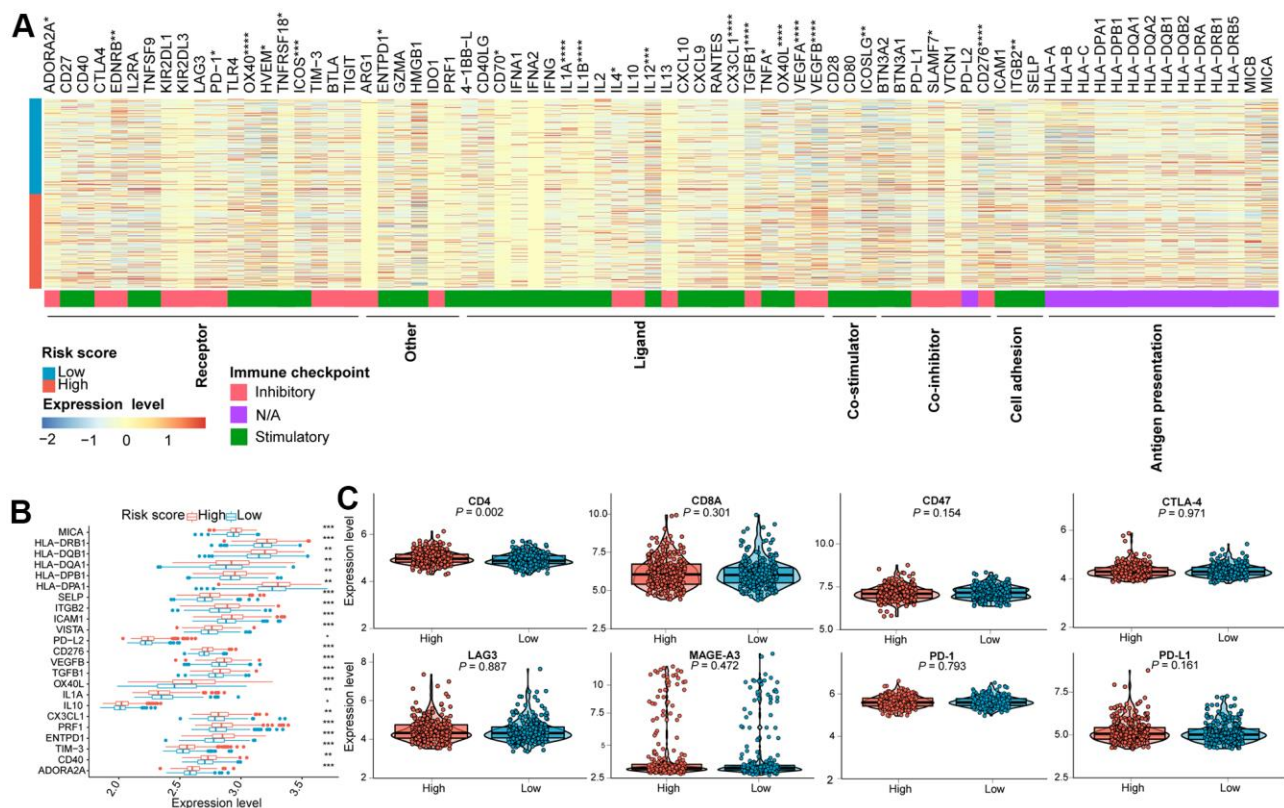


**Supplementary Figure 2. Exploration of the predictive power and clinical characteristics of seven IRGs signature in the validation cohort.** (A) Distribution of risk score, survival status, and the expression of seven IRGs of CRCs. (B) Kaplan-Meier survival curve of the high- and low-risk subgroups. (C) ROC curve analysis of IRGs in the validation cohort. (D) Univariate Cox analysis of prognostic factors and OS of CRCs. (E) Alluvial diagram for the two subtypes versus different immune subtypes and CMS. (F) Violin plot illustrated the correlation between risk score and immune subtypes, and (G) CMS. AUC, area under the curve; OS, overall survival; CRC, colorectal cancer; IRGs, immune-related genes; ROC, receiver operating characteristic; CMS, consensus molecular subtypes.

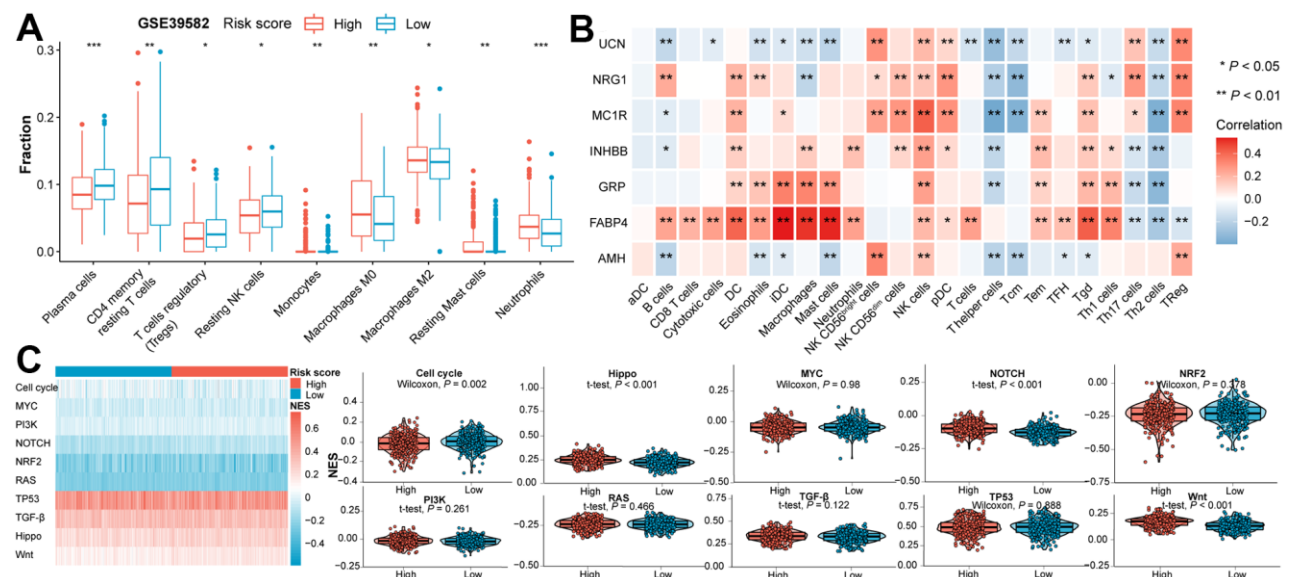




**Supplementary Figure 3. Evaluation of the role of the risk score in the validation cohort.** (A) Results of GSEA of the high-risk group (red) compared with the low-risk group (blue). Color toward gray represents no statistical significance. (B) Heatmap and violin plots of the ESTIMATE score, immune score, stromal score, tumor purity between high- and low- risk subtypes. (C) Violin plot of the CYT score between high- and low- risk subtypes. (D) Violin plot of fibroblasts between two subtypes, and the association between risk score and the NES of fibroblasts. Statistical significance at the level of ns  $\geq$  0.05, \*  $<$  0.05, \*\*  $<$  0.01 and \*\*\*  $<$  0.001. GSEA, gene set enrichment analysis; CYT, cytolytic activity; NES, normalized enrichment score.



**Supplementary Figure 4.** (A) The differential expression levels of immune checkpoint molecules within distinctive subgroups in the TCGA CRCs. (B) The differential expression level of immune checkpoint molecules between two subclasses with statistical significance in the validation cohort. (C) Violin plots of the CD4, CD8A, CD47, CTLA4, LAG3, MAGE-A3, PD-1 and PD-L1 expression levels for two subtypes in the validation cohort.



**Supplementary Figure 5.** (A) Immune infiltration between high- and low- risk subtypes with statistical significance in the validation cohort. (B) Correlation analysis between the expression of seven IRGs and the infiltration of immune cells in the validation cohort. (C) Heatmap and violin plots of the NES of 10 oncogenic pathways between two subtypes in the validation cohort. Statistical significance at the level of ns  $\geq$  0.05, \*  $<$  0.05, \*\*  $<$  0.01 and \*\*\*  $<$  0.001.

## Supplementary Tables

Please browse Full Text version to see the data of Supplementary Tables 1, 5, 6.

### Supplementary Table 1. IRGs retrieved from the ImmPort database.

### Supplementary Table 2. Eight PRIRGs filtered out by lasso regression.

IRGs	Coefficient
FABP4	0.0813685612698171
AMH	0.131513420971701
GRP	0.146281413219288
INHBB	0.160968056160568
NRG1	-0.582958093399237
UCN	0.213129186143968
MC1R	0.335915826080654
PTH1R	0.363374360149091

### Supplementary Table 3. Overall information of seven IRGs in the signature.

Ensembl ID	IRGs	Coefficient	HR (95% CI)	P-value
ENSG00000170323	FABP4	0.139	1.15 (1.021-1.294)	0.021
ENSG00000104899	AMH	0.176	1.193 (0.962-1.479)	0.109
ENSG00000134443	GRP	0.207	1.229 (1.014-1.491)	0.036
ENSG00000163083	INHBB	0.211	1.235 (1.064-1.433)	0.006
ENSG00000157168	NRG1	-0.691	0.501 (0.216-1.164)	0.108
ENSG00000163794	UCN	0.274	1.315 (0.929-1.863)	0.122
ENSG00000258839	MC1R	0.366	1.442 (0.952-2.183)	0.084

**Supplementary Table 4. Clinical characteristics of the TCGA cohort and the GSE39582 cohort.**

TCGA cohort				GSE39582 cohort			
Variable	Low (n = 208)	High (n = 229)	Overall (n = 437)	Variable	Low (n = 220)	High (n = 222)	Overall (n = 442)
<b>Gender</b>				<b>Gender</b>			
Male	113 (54.3%)	119 (52.0%)	232 (53.1%)	Male	122 (55.5%)	117 (52.7%)	239 (54.1%)
Female	95 (45.7%)	110 (48.0%)	205 (46.9%)	Female	98 (44.5%)	105 (47.3%)	203 (45.9%)
<b>Race</b>				<b>Age</b>			
White	107 (51.4%)	124 (54.1%)	231 (52.9%)	>= 65	135 (61.4%)	147 (66.2%)	282 (63.8%)
Black or african american	25 (12.0%)	30 (13.1%)	55 (12.6%)	<65	85 (38.6%)	75 (33.8%)	160 (36.2%)
Others	76 (36.5%)	75 (32.8%)	151 (34.6%)	<b>Tumor location</b>			
<b>Age</b>				Proximal	83 (37.7%)	96 (43.2%)	179 (40.5%)
>= 65	107 (51.4%)	139 (60.7%)	246 (56.3%)	Distal	137 (62.3%)	126 (56.8%)	263 (59.5%)
<65	101 (48.6%)	90 (39.3%)	191 (43.7%)	<b>Tumor stage</b>			
<b>History of colon polyps</b>				I	14 (6.4%)	14 (6.3%)	28 (6.3%)
No	133 (63.9%)	134 (58.5%)	267 (61.1%)	II	113 (51.4%)	104 (46.8%)	217 (49.1%)
Yes	48 (23.1%)	54 (23.6%)	102 (23.3%)	III	73 (33.2%)	76 (34.2%)	149 (33.7%)
NA	27 (13.0%)	41 (17.9%)	68 (15.6%)	IV	20 (9.1%)	28 (12.6%)	48 (10.9%)
<b>Tumor site</b>				<b>MMR status</b>			
Left	130 (62.5%)	117 (51.1%)	247 (56.5%)	pMMR	168 (76.4%)	168 (75.7%)	336 (76.0%)
Right	78 (37.5%)	112 (48.9%)	190 (43.5%)	dMMR	34 (15.5%)	27 (12.2%)	61 (13.8%)
<b>Tumor stage</b>				NA	18 (8.2%)	27 (12.2%)	45 (10.2%)
I	48 (23.1%)	29 (12.7%)	77 (17.6%)	<b>TP53 mutation</b>			
II	79 (38.0%)	79 (34.5%)	158 (36.2%)	Mutant	68 (30.9%)	70 (31.5%)	138 (31.2%)
III	59 (28.4%)	73 (31.9%)	132 (30.2%)	Wildtype	69 (31.4%)	55 (24.8%)	124 (28.1%)
IV	22 (10.6%)	48 (21.0%)	70 (16.0%)	NA	83 (37.7%)	97 (43.7%)	180 (40.7%)
<b>MSI status</b>				<b>KRAS mutation</b>			
MSI-H	33 (15.9%)	24 (10.5%)	57 (13.0%)	Mutant	86 (39.1%)	90 (40.5%)	176 (39.8%)
MSI-L	31 (14.9%)	42 (18.3%)	73 (16.7%)	Wildtype	134 (60.9%)	132 (59.5%)	266 (60.2%)
MSS	144 (69.2%)	163 (71.2%)	307 (70.3%)	<b>BRAF mutation</b>			
<b>MMR status</b>				Mutant	19 (8.6%)	23 (10.4%)	42 (9.5%)
pMMR	133 (63.9%)	140 (61.1%)	273 (62.5%)	Wildtype	201 (91.4%)	199 (89.6%)	400 (90.5%)
dMMR	25 (12.0%)	29 (12.7%)	54 (12.4%)	<b>CIMP</b>			
NA	50 (24.0%)	60 (26.2%)	110 (25.2%)	Negative	176 (80.0%)	188 (84.7%)	364 (82.4%)
<b>TP53 mutation</b>				Positive	44 (20.0%)	34 (15.3%)	78 (17.6%)
Mutant	126 (60.6%)	143 (62.4%)	269 (61.6%)	<b>CIN</b>			
Wildtype	82 (39.4%)	86 (37.6%)	168 (38.4%)	Negative	57 (25.9%)	45 (20.3%)	102 (23.1%)
<b>KRAS mutation</b>				Positive	163 (74.1%)	177 (79.7%)	340 (76.9%)
Mutant	82 (39.4%)	110 (48.0%)	192 (43.9%)				
Wildtype	126 (60.6%)	119 (52.0%)	245 (56.1%)				
<b>BRAF mutation</b>							
Mutant	24 (11.5%)	25 (10.9%)	49 (11.2%)				
Wildtype	184 (88.5%)	204 (89.1%)	388 (88.8%)				
<b>EGFR mutation</b>							
Mutant	1 (0.5%)	8 (3.5%)	9 (2.1%)				
Wildtype	207 (99.5%)	221 (96.5%)	428 (97.9%)				
<b>NRAS mutation</b>							
Mutant	8 (3.8%)	18 (7.9%)	26 (5.9%)				
Wildtype	200 (96.2%)	211 (92.1%)	411 (94.1%)				
<b>APC mutation</b>							
Mutant	169 (81.2%)	177 (77.3%)	346 (79.2%)				
Wildtype	39 (18.8%)	52 (22.7%)	91 (20.8%)				

**Supplementary Table 5. Correlation analysis between the expression of seven IRGs and the infiltration of immune cells.**

**Supplementary Table 6. Lists of drugs in CTRP and PRISM.**

**Supplementary Table 7. List of potential therapeutic agents for CRC patients with IRGs signature high-risk score.**

Name	Source	MOA	Target	Evidence for CRC treatment
AT7867	CTRP	Akt inhibitors	Akt	PMID: 28081222
AZD4547	CTRP	FGFR inhibitors	FGFR	PMID: 25691251
BRD-K16147474	CTRP	NA	NA	NA
cytochalasin B	CTRP	excitatory proteins inhibitors	cytoskeleton/endocytosis	PMID: 16287074
PLX-4032	CTRP	B-raf <sup>V600E</sup> inhibitors	B-raf	PMID: 29326440
SGX-523	CTRP	Met kinase inhibitors	c-Met	NA
PLX-4720	CTRP	B-raf <sup>V600E</sup> inhibitors	B-raf	PMID: 25381152/26351322
TG-101348	CTRP	JAK2 inhibitors	JAK2/STAT3/PIM1 pathway	PMID: 32346607
lovastatin	CTRP	HMG-CoA reductase inhibitors	HMG-CoA reductase	PMID: 24945998
BRD-K37390332	CTRP	NA	NA	NA
AMG458	PRISM	MET/RON inhibitors	MET/RON	NA
LE135	PRISM	RAR $\beta$ antagonist	RAR $\beta$	NA
mevastatin	PRISM	HMG-CoA reductase inhibitors	HMG-CoA reductase	PMID: 11408350
creatine	PRISM	NA	NA	NA
S-crizotinib	PRISM	ALK/RON/c-MET, MTH1 inhibitors	ALK/RON/c-MET, MTH1	PMID: 24695225/28320945
colforsin daproate	PRISM	adenylate cyclase agonist	adenylate cyclase	NA
erythritol	PRISM	NA	cytidyltransferase	NA
CHIR-98014	PRISM	GSK3 inhibitors	GSK-3 $\alpha$ and GSK-3 $\beta$	NA
epinephrine	PRISM	adrenergic receptor agonist	adrenergic receptor	NA
tandutinib	PRISM	FLT3 inhibitors	Akt/mTOR pathway	PMID: 23427297

MOA, mechanism of action.



## TIMP-2 regulates 5-Fu resistance via the ERK/MAPK signaling pathway in colorectal cancer

Guolin Zhang<sup>1,2,\*</sup>, Xin Luo<sup>1,\*</sup>, Zian Wang<sup>1,3,\*</sup>, Jianbin Xu<sup>4</sup>, Wei Zhang<sup>1</sup>, Engeng Chen<sup>1</sup>, Qing Meng<sup>1</sup>, Di Wang<sup>1</sup>, Xuefeng Huang<sup>1</sup>, Wei Zhou<sup>1</sup>, Zhangfa Song<sup>1</sup>

<sup>1</sup>Department of Colorectal Surgery, Sir Run Run Shaw Hospital of Zhejiang University, Hangzhou, China

<sup>2</sup>Department of Gastrointestinal Surgery, Shaoxing People's Hospital, Shaoxing Hospital, Zhejiang University School of Medicine, Shaoxing, Zhejiang Province, China

<sup>3</sup>Department of Colorectal Surgery, Shaoxing People's Hospital, Shaoxing Hospital, Zhejiang University School of Medicine, Shaoxing, Zhejiang Province, China

<sup>4</sup>Zhejiang Province Key Laboratory of Biological Treatment, Hangzhou, China

\*Equal contribution as co-first authors

**Correspondence to:** Wei Zhou, Zhangfa Song; **email:** [weizhou\\_srrsh@zju.edu.cn](mailto:weizhou_srrsh@zju.edu.cn), [songzhangfa@zju.edu.cn](mailto:songzhangfa@zju.edu.cn)

**Keywords:** TIMP-2, ERK/MAPK signaling pathway, 5-Fu, drug resistance, colorectal cancer

**Received:** July 1, 2021

**Accepted:** December 3, 2021

**Published:** January 12, 2022

**Copyright:** © 2021 Zhang et al. This is an open access article distributed under the terms of the [Creative Commons Attribution License](https://creativecommons.org/licenses/by/3.0/) (CC BY 3.0), which permits unrestricted use, distribution, and reproduction in any medium, provided the original author and source are credited.

### ABSTRACT

5-Fluorouracil (5-Fu) is the first-line chemotherapeutic option for colorectal cancer. However, its efficacy is inhibited by drug resistance. Cytokines play an important role in tumor drug resistance, even though their mechanisms are largely unknown. Using a cytokine array, we established that tissue inhibitor metalloproteinase 2 (TIMP-2) is highly expressed in 5-Fu resistant colorectal cancer patients. Analysis of samples from 84 patients showed that elevated TIMP-2 expression levels in colorectal patients were correlated with poor prognostic outcomes. In a 5-Fu-resistant patient-derived xenograft (PDX) model, TIMP-2 was also found to be highly expressed. We established an autocrine mechanism through which elevated TIMP-2 protein levels sustained colorectal cancer cell resistance to 5-Fu by constitutively activating the ERK/MAPK signaling pathway. Inhibition of TIMP-2 using an anti-TIMP-2 antibody or ERK/MAPK inhibition by U0126 suppressed TIMP-2 mediated 5-Fu-resistance in CRC patients. In conclusion, a novel TIMP-2-ERK/MAPK mediated 5-Fu resistance mechanism is involved in colorectal cancer. Therefore, targeting TIMP-2 or ERK/MAPK may provide a new strategy to overcome 5-Fu resistance in colorectal cancer chemotherapy.

### INTRODUCTION

Colorectal cancer (CRC), particularly advanced colorectal cancer, poses a significant challenge in clinical management and is associated with high mortality rates [1]. Moreover, the prognostic outcomes for patients with advanced CRC is poor [2]. 5-fluorouracil (5-Fu), which acts by interfering with cellular DNA synthesis and histone deacetylation, is recommended as a first-line chemotherapeutic option for CRC [3, 4]. Clinically, administration of 5-Fu combined with irinotecan or oxaliplatin is considered to

be a relatively standard chemotherapeutic regimen [5]. Most patients show an initial effective response to 5-Fu, however, they later develop tumor progression, which is indicative of resistance [6–8]. The potential mechanisms of 5-Fu drug resistance have been reported [9–11]. However, specific molecular mechanisms of 5-Fu drug resistance have not been established.

Tumor resistance is closely associated with miRNAs dysregulation [12], promoter hypermethylation [13], and abnormal expressions of cell cycle-related proteins [14]. Due to the role of cytokines in physiological and

pathological cell activities, studies are evaluating their potential roles in tumor drug resistance [15–19]. Cytokines are involved in drug metabolism, delivery, targeting and resistance [16, 20, 21].

As endoproteases, matrix metalloproteinases (MMPs) affect the integrity of extracellular matrix components [22]. Particularly, matrix metalloproteinase 2 (MMP-2) is associated with movement, migration, and metastasis of malignant cells [23–25]. Tissue inhibitor of matrix metalloproteinase 2 (TIMP-2) is a natural inhibitor of MMP-2 [26, 27]. TIMP-2 plays a dual role in cell physiology regulation. It promotes tumor growth via angiogenesis and, through apoptosis, it is also involved in inhibition of malignant cell proliferation [28–31]. TIMP-2 is also associated with tumor malignancy and resistance to chemotherapy in hepatoma, melanoma, and breast cancer [32–34]. In a previous study, Zhang et al. found that TIMP-2 siRNA effectively inhibited colorectal tumor cells (HCT116) invasion *in vitro* [35]. Clinical reports suggest that MMP-2 and TIMP-2 are more prevalent in CRC tissues than in normal tissues, with elevated expression levels in metastatic CRC compared to non-metastatic CRC [36–38]. Elevated TIMP-2 levels have particularly been reported in CRC patients with unfavourable chemotherapeutic responses [36]. However, it has not been established whether it has the same effects in all other tumors, and specific mechanisms of action have not been elucidated. Therefore, there is a need to evaluate the role of TIMP-2 in tumor cell resistance to 5-Fu therapy.

The ERK/MAPK signaling pathway is present in various types of cells. It is activated by dual phosphorylation of MAPKK kinase, catalyzed by the Thr-X-Tyr motif [39, 40]. Then, MAPKK is activated through the phosphorylation of MAPK kinase (MAPKKK) after which MAPKKK is activated by interactions with small GTPase and/or other proteases, thereby combining MAPK with cell surface receptors and with extracellular signals. Upon activation, MAPKs phosphorylate several protein kinases and transcription factors, including ERK1/2, JNK, p38MAPK, ERK5, NF- $\kappa$ B, and SOS [41, 42]. This signaling pathway regulates many critical physiological processes, such as cell growth, signal transduction, stress, and inflammatory responses [35, 43].

Various cytokines simultaneously activate ERK1/2 and ERK5, which then affect cell proliferation and differentiation [44–47]. Peng et al. found that the ERK1/2 signaling pathway plays an important regulatory role in CRC invasion and metastasis [48]. With regards to drug resistance in tumors, the ERK/MAPK signaling pathway plays an essential role in melanoma prognosis [49–51]. However, combined

administration of BET and MEK inhibitors can significantly inhibit the growth of NRAS mutant melanoma and improve survival outcomes for cancer patients [50]. Moreover, these signaling pathways reactivate and play an important role in metastatic melanoma resistance to BRAF inhibition [51]. However, their roles in CRC 5-Fu resistance have not been established.

In this study, we investigated differences in cytokine expression profiles in serum samples of 5-Fu drug-resistant CRC patients. We found that 5-Fu resistant CRC patients exhibited elevated TIMP-2 levels, which were correlated with poor clinical prognoses. TIMP-2 was also found to be highly expressed in 5-Fu resistant CRC PDX models. Furthermore, TIMP-2 promoted CRC cell resistance to 5-Fu *in vitro*. Mechanistic analyses revealed that the ERK/MAPK signaling pathway is actively involved in 5-Fu resistance caused by TIMP-2, and its inhibitor, U0126, inhibits this resistance. From our findings, we hypothesized that TIMP-2 and the ERK/MAPK signaling pathway are excellent therapeutic targets for overcoming 5-Fu resistance in CRC.

## MATERIALS AND METHODS

### Antibodies and reagents

5-Fluorouracil (5-Fu) was obtained from MedChemExpress. Recombinant TIMP-2 was obtained from PeproTech (diluted to 10 ng/mL in the experiment). The antibody for TIMP-2 neutralization was obtained from R&D systems (diluted to 5  $\mu$ g/mL in the experiment). Antibodies to MAPK (Erk1/2) (Cat No.4695), phospho-MAPK (Erk1/2) (Thr202/Tyr204) (Cat No.4370), Erk5 (Cat No.3552), phospho-Erk5 (Thr218/Tyr220) (Cat No.3371) and GAPDH (Cat No. 97166) were purchased from Cell Signaling Technology (CST). In the WB experiment, the above antibodies were diluted 1:1000. HRP-conjugated antibodies were obtained from Hangzhou Fude Biological Technology.

### Enzyme-linked immunosorbent assay (ELISA)

Cell culture supernatants or serum TIMP-2 levels were measured using a sandwich ELISA kit (Elabscience) according to the manufacturer's instructions. Samples were assayed in triplicates.

### Ethical considerations

Ethical approval for this study was obtained from the ethical committee of Sir Run Run Shaw Hospital, School of Medicine, Zhejiang University (study

number: 20140213-19). All animal experiments were in accordance with standard animal care guidelines.

### Study participants

Serum samples were obtained from CRC patients at the Key Laboratory of Biotherapy of Zhejiang province, Sir Run Run Shaw Hospital, School of Medicine, Zhejiang University. Samples were collected from 2008 to 2018. Serum was collected during chemotherapy after patients had been determined to be resistant to 5-Fu. To prevent cytokine decomposition, after extracting the serum from the blood, it was stored at  $-80^{\circ}\text{C}$ . Two experienced pathologists analyzed cancer cell contents, histological tissue types, as well as tumor staging. 5-Fu based chemotherapy was administered to CRC patients, who were then operated on by senior surgeons. World Health Organization (WHO) approved indices for Overall survival (OS) and Disease-free survival (DFS) were used to evaluate treatment efficacies. A total of 84 patients were included in this study. Responses to 5-Fu were divided into two categories; 5-Fu sensitive and 5-Fu resistant CRC. Each group had 42 patients. This classification was based on tumor regression within six months following 5-Fu administration. During chemotherapy with 5-Fu-based chemotherapeutic drugs, if the patient is not checked for tumor progression, we identify these patients as sensitive to 5-Fu, otherwise the patient is considered to be resistant to 5-Fu. Regarding the PDX model, tumor cells were extracted from a 66-year-old male rectal cancer patient, who had been diagnosed with pathologic stage III adenocarcinoma. This patient was untreated and had received neither chemotherapy nor radiotherapy before surgery. Subsequent chemotherapy showed that the tumor was sensitive to 5-Fu.

### Cytokine array

Serum cytokine levels were determined by a protein cytokine array using the Human Cytokine Antibody Array-Membrane (ab193656), purchased from Abcam, Cambridge, UK. This technique is based on the principle of sandwich immunoassay. It comprises 120 coupled target anti-cytokines and the appropriate controls in duplicate. DLD-1 5-FuS and DLD-1 5-FuR cells were cultured in RPMI-1640 medium without fetal bovine serum and incubated at  $37^{\circ}\text{C}$  in a 5%  $\text{CO}_2$  environment for 24 h. Then, membranes were exposed to the chemiluminescence imaging system (LUMIPULSE G1200). Conditioned medium containing cytokines were evaluated according to manufacturer's protocols. Results were normalized using internal controls, and relative protein levels determined across four biological replicates.

### Cell cultures

Two CRC cell lines (DLD-1 cells and HCT116 cells) were obtained from the American Type Culture Collection (ATCC, Manassas). They were respectively cultured in RPMI-1640 (Genom) or Dulbecco's Modified Eagle Medium (DMEM) with higher glucose levels (Genom) containing 10% fetal bovine serum (GIBCO). Incubation was done at  $37^{\circ}\text{C}$  in a 5%  $\text{CO}_2$  atmosphere.

To generate 5-FU resistant cell lines, DLD-1 and HCT116 cells in the logarithmic growth phase were plated into a 6-well plate, at a density of  $1 \times 10^6$  cells per well. The starting 5-Fu concentration in the corresponding culture medium in each well was  $0.1 \mu\text{M}$ . Incubation was done at  $37^{\circ}\text{C}$  in a 5%  $\text{CO}_2$  atmosphere for 2 days. Then, the cell culture medium was replaced with a culture medium that does not contain 5-Fu, and further incubated. Upon achievement of original cell growth rates, 5-Fu concentrations of the corresponding culture medium was adjusted to 2–3 times the original in each well. Further incubation was done for 2 days, after which the above experimental process was continued. CCK-8 was used to assess cell viability and to calculate the  $\text{IC}_{50}$  value. After about half a year, a tumor cell line that can survive normally at a stable concentration of 5-Fu was screened.

### Cell viability assay

Cell viability was determined using the Cell-Counting Kit-8 (CCK8) (Dojindo Molecular Technologies), following the manufacturers' instructions. Absorbance was measured at 450 nm using a microplate reader. Experiments were performed in triplicates.

### RNA isolation and RT-qPCR

Total RNA was extracted from cells using the Trizol reagent (Invitrogen). cDNA was synthesized using the cDNA reverse transcriptase kit (Takara). LightCycler 480 real-time PCR system (Roche, Mannheim) was used to perform SYBR Green-based (Takara) quantitative real-time PCR (RT-qPCR). Glyceraldehyde-3-phosphate dehydrogenase (GAPDH) was used as the internal control. The  $2^{-\Delta\Delta\text{Cq}}$  relative quantification method was used to determine mRNA levels of target genes.

### siRNA interference

Small interfering RNA (siRNA) against TIMP-2 was obtained from Thermo Fisher Scientific. Transient transfection assays were performed using Lipofectamine 2000 (Thermo Fisher Scientific) following the

manufacturers' instructions. Cellular drug resistance and cytokine secretion were analyzed by treating cells with 30 pg/ml TIMP-2 siRNA for two days.

### Western blot analysis

Cells were lysed using a RIPA lysis buffer (Solarbio Life Sciences). Protein concentrations were determined by Bicinchoninic acid assay (BCA, Beyotime Institute of Biotechnology). Proteins from each sample (25 µg) were separated by 10% SDS-PAGE (Beyotime Institute of Biotechnology) and transferred to polyvinylidene fluoride membranes (Immobilon-P). Membranes were blocked using 5% dried skimmed milk for 1 h at room temperature and incubated in the presence of primary antibodies at 4°C overnight. Subsequently, IgG conjugated goat anti-rabbit or IgG conjugated goat anti-mouse secondary antibodies were added and incubated for 1 h at room temperature. Blots were developed using an enhanced chemiluminescence detection reagent (Hangzhou Fude Biological Technology).

### Animal experiments

Four week old female BALB/c- nude mice from SiBeiFu Biotechnology Co., Ltd (Beijing) were used in this study. Briefly, tumor cells from CRC patients were subcutaneously implanted in the groins of nude mice. Then, mice were assigned into three groups of 6 mice each: Veh group (injection of saline), 5-FuS group (injection of 5-Fu but no drug resistance), 5-FuR group (injection of 5-Fu and develop resistance). The experimental group (5-FuS and 5-FuR group) was intraperitoneally administered with 5-Fu (30 mg/kg/dose) three times a week, while the Veh group was intraperitoneally administered with the same dose of saline. An initial reduction in tumor size in the experimental group followed by a re-growth of more than 2.0 cm diameter represented a successful establishment of a PDX model of colorectal tumor that is resistant to 5-Fu, which was defined as the 5-FuR group. After 5-Fu treatment, subcutaneous tumors of some mice continued to decrease in size, and this was defined as the 5-FuS group. Mice that were subcutaneously administered with saline as the control were the Veh group. At that time, the mice were injected with 5-Fu or saline about 12 times. Once the PDX model was obtained, blood samples were collected from eyelids of nude mice after which mice were sacrificed to obtain tumor tissues.

### Immunohistochemistry

Tumor tissue samples were fixed in 4% buffered paraformaldehyde solution, dehydrated and immersed in paraffin, then sliced into 4 µm thick sections. Epitope

retrieval was performed by cooking the de-paraffinized sections under pressure in Tris-EDTA buffer (pH 9.0) for 20 min. Hydrogen peroxide (3%) in methanol solution was applied for 10 min to block endogenous peroxidase activity. Normal goat serum (10%) was then used to prevent non-specific binding for 30 min. Slides were incubated for 1 h at 4°C in TIMP-2 antibody solution diluted at 1:20 followed by incubation with a secondary antibody for 30 min at room temperature. Then, sections were developed using a DAB kit (Shanghai Gene Co., Ltd) and counterstained with hematoxylin (Sigma). For semi-quantitative assay of IHC staining, staining intensity was scored from 0 to 4 (0, absent; 1, weak; 2, moderate; 3, intense; 4, extremely intense). Final IHC score for each sample was determined by three independent senior pathologists. By observing multiple visual fields, each pathologist gave two average scores.

### Statistical analysis

Data from three independent experiments tested in triplicates are presented as means ± SD. Data were analyzed using SPSS (version 22.0), Image J (version 2.0) and GraphPad Prism (version 7.0) software. A Combination index (CI) of 1.0 indicated an additive effect, while CI<1 suggested synergy. Alternative CI values indicated antagonism. Experimental data were examined for consistency to a normal distribution using the one-sample Kolmogorov-Smirnov test. An independent sample *t*-test or non-parametric test was used to analyze the experimental results. Comparisons between survival curves were tested for statistical significance using either a Log-rank test or COX regression analysis. In all cases, *p* values were two-sided. *p* ≤ 0.05 was considered significant.

### Ethical approval and consent to participate

This study was approved by the local ethics committee of Sir Run Run Shaw Hospital, School of Medicine, Zhejiang University (study number: 20140213-19). All animal experiments were in accordance with standard animal care guidelines.

### Availability of data and materials

The data supporting these findings are available from the Department of colorectal surgery, Sir Run Run Shaw Hospital of Zhejiang University but restrictions apply to the availability of these data, which were used under license for the current study, and are therefore, not publicly available. Data are, however, available from the authors upon reasonable request and with permission from the Department of colorectal surgery, Sir Run Run Shaw Hospital of Zhejiang University.



**Table 1. Characteristics of patients involved in cytokine screening.**

Patient	Age (years)	Sex	Stage	Histology	Chemotherapy
P0221	78	M	IVA	Adenocarcinoma	5-Fu + Oxaliplatin + Bevacizumab
P0258 <sup>#</sup>	69	F	IIIB	Adenocarcinoma	5-Fu + Oxaliplatin + Bevacizumab
P0378 <sup>#</sup>	57	F	IVA	Mucus adenocarcinoma	5-Fu + Oxaliplatin + Bevacizumab
P0855	64	M	IIIC	Adenocarcinoma	5-Fu + Irinotecan + Oxaliplatin + Cetuximab
P1061	60	F	IIIB	Adenocarcinoma	5-Fu + Oxaliplatin + Bevacizumab
P1392 <sup>#</sup>	77	M	IIIC	Adenocarcinoma	5-Fu+Irinotecan + Oxaliplatin + Cetuximab

<sup>#</sup>Refers to colorectal cancer patients resistant to 5-Fu.

## RESULTS

### **TIMP-2 was elevated in 5-FU resistant CRC patients and correlated with poor prognosis**

Cytokines are important in drug resistance. First, we clinically selected three typical 5-Fu-resistant and three typical 5-Fu-sensitive CRC patients. Patient characteristics are shown in Table 1. In this study, cytokines such as TIMP-2, GRO, ANGPT2, and EGF, among others, were found to be significantly elevated in serum from 5-Fu-resistant patients (Figure 1A). Since TIMP-2 exhibited the greatest change in expression levels, we hypothesized that TIMP-2 is the key cause of CRC resistance to 5-Fu. To validate our hypothesis, we evaluated TIMP-2 serum levels in nine 5-Fu-resistant and nine 5-Fu-sensitive CRC patients using ELISA. Serum TIMP-2 protein levels in 5-Fu resistant CRC patients was 73.61 ng/ml, 5.3 times higher than those of 5-Fu sensitive CRC patients (13.57 ng/ml) (Figure 1B). Patient characteristics are shown in Table 2. Prognostic outcomes for clinical patients are of great concern to oncologists. Therefore, we evaluated protein levels of TIMP-2 in serum of 84 CRC patients undergoing 5-Fu-based chemotherapy and correlated it with prognosis. Characteristics of these patients are shown in Table 3. Median follow-up time was 54.4 months. Using the median value (36.60 ng/ml) of TIMP-2 protein expression level as the cut-off, patients were assigned into two groups: TIMP-2 high expression group ( $n = 42$ ) and TIMP-2 low expression group ( $n = 42$ ). According to major clinical outcomes of Overall survival (OS) and Disease-free survival (DFS), TIMP-2 high expression group exhibited worse prognostic outcomes, relative to TIMP-2 low expression group (Figure 1C and 1D).

### **TIMP-2 levels were upregulated in 5-Fu resistant CRC cells and in PDX models**

By gradually increasing 5-Fu concentrations in the culture medium, we developed resistant cell lines from two CRC cell lines, DLD-1 and HCT116 [52]. These were named DLD-1 5-FuR and HCT116 5-FuR,

respectively, while primary cells lines were named DLD-1 5-FuS and HCT116 5-FuS. Cell activity data obtained at different concentrations were used to determine the 50% inhibitory concentration ( $IC_{50}$ ).  $IC_{50}$  value for 5-Fu was 11.8-fold in DLD-1 5-FuR, compared to DLD-1 5-FuS. In HCT116 5-FuR and HCT116 5-FuS,  $IC_{50}$  was 3.81-fold (Figure 2A and 2B). Given the relationship between cytokines and tumor resistance [15, 53], we designed a cell culture medium (CM) exchange experiment to verify the effects of cytokines on tumor cell resistance. We used the DLD-1 5-FuR cell culture medium to culture DLD-1 5-FuS cells. These experiments showed that DLD-1 5-FuS cells co-cultured in DLD-1 5-FuR medium were more tolerant to different 5-Fu concentrations than those cultured in the conditioned medium (Figure 2C). The same experiment was repeated in HCT116 5-FuS cells, and similar results were obtained (Figure 2D). It was found that 5-Fu-resistant cell lines secrete cytokines that cause drug resistance.

To determine whether TIMP-2 protein is involved in drug-resistance, we assessed the expression levels of TIMP-2 by real-time quantitative PCR and ELISA. Semi-quantitative mRNA analysis showed that TIMP-2 transcription levels in drug-resistant cell lines were significantly higher than those of sensitive cell lines (Figure 2E). Assessment of TIMP-2 protein levels by ELISA showed that it was highly secreted in drug-resistant cell lines, including DLD-1 5-FuR and HCT116 5-FuR (Figure 2F).

To further show that TIMP-2 was also up-regulated during 5-Fu treatment *in vivo*, we used patient-derived xenograft (PDX) models. The PDX model maintains the donor's original biological behaviors and molecular characteristics [54–57]. Following the necessary construction processes, we constructed a PDX model of colorectal tumor with resistance to 5-Fu (Figure 3A). When the experimental group was treated with 5-Fu, subcutaneous tumors in the experimental group (5-FuS and 5-FuR group) began to be under control. After about 4 weeks of treatment, subcutaneous tumors of



5-FuS group PDX mice began to be resistant to 5-Fu, implying that the PDX model of colorectal tumor with resistance to 5-Fu had successfully been constructed (Figure 3B). TIMP-2 protein levels in the serum of 5-Fu-resistant PDX models were found to be significantly higher than those of sensitive strains (Figure 3C).

Immunohistochemical (IHC) analysis showed that tumor tissues, which showed elevated TIMP-2 expression levels exhibited resistance to 5-Fu (Figure 3D). Semi-quantitative immunohistochemical analysis further affirmed these results (Figure 3E). Similar results were obtained from tested patient serum.

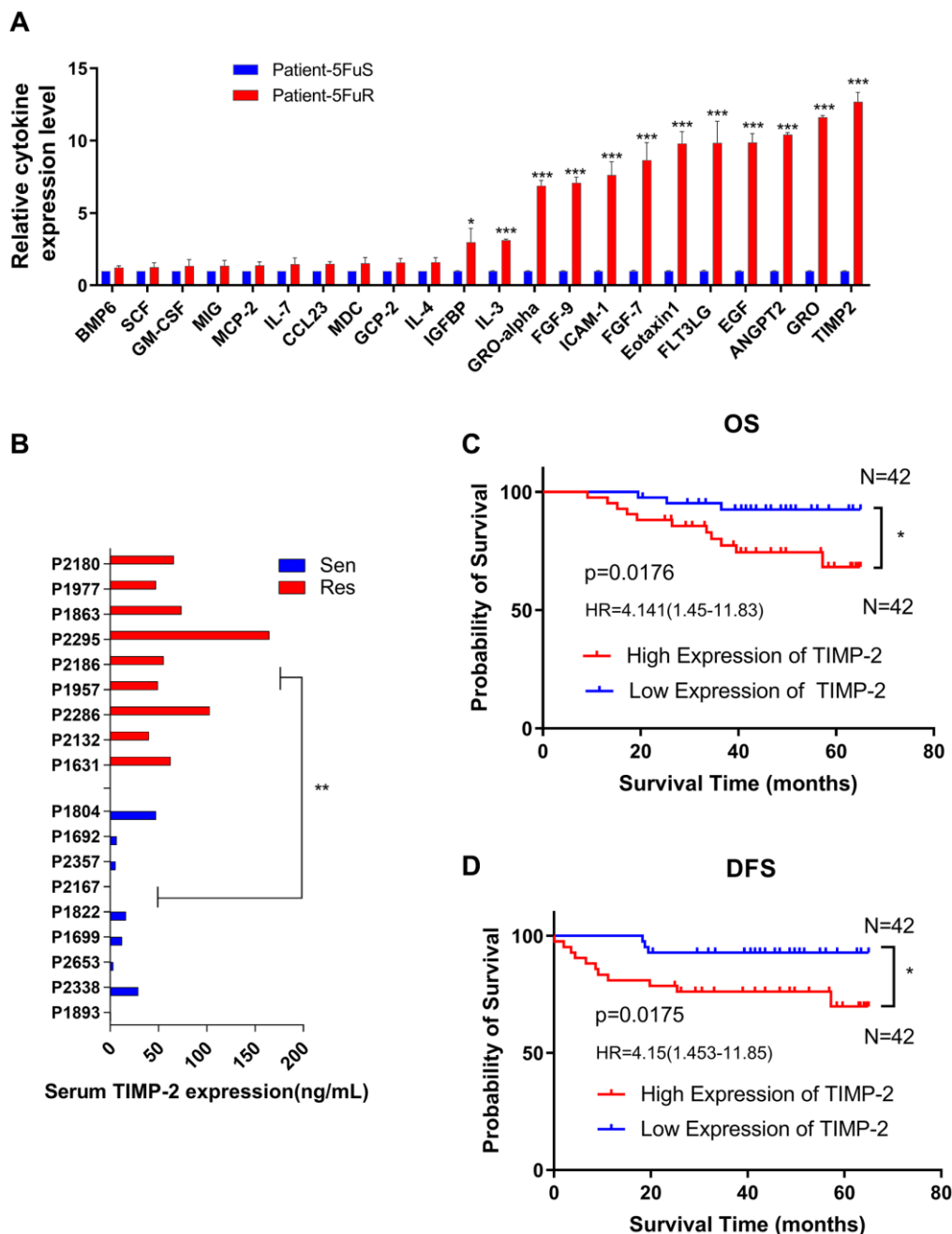


**Figure 1. TIMP-2 is elevated in 5-Fu resistant CRC patients and predicts clinical outcomes.** (A) Relative cytokine expression levels in the serum of 5-Fu sensitive and resistant patients. Patient details are shown in Table 1. Sen, sensitive patients. Res, resistant patients. (B) Differences in TIMP-2 protein expression levels in non-resistant ( $n = 9$ ) and resistant patients ( $n = 9$ ) with colorectal cancer. Patient details are shown in Table 2. Sen, sensitive patients. Res, resistant patients. (C) 6-year OS Kaplan–Meier survival curves for 84 colorectal cancer patients, differential grouping based on TIMP-2 expression (36.6 ng/ml) in serum. Table 3 shows patient information. (D) 6-year DFS Kaplan–Meier survival curves for 84 colorectal cancer patients, differential grouping based on TIMP-2 expression (36.6 ng/ml) in serum. Table 3 shows patient information. (A, B)  $*p < 0.05$ ,  $**p < 0.01$ ,  $***p < 0.001$  by unpaired Student's  $t$ -test. (C, D)  $*p < 0.05$  by logrank (Mantel-Cox), HRs are shown in the figures.

**Table 2. Characteristics of patients involved in assessment of 5-Fu sensitivity or resistance.**

Patient	Age (years)	Sex	Stage	Histology	Chemotherapy
P1631 <sup>#</sup>	66	M	IVA	Adenocarcinoma	5-Fu + Irinotecan + Oxaliplatin + Bevacizumab
P1692	61	F	IVA	Adenocarcinoma	5-Fu + Irinotecan + Oxaliplatin + Bevacizumab
P1699	78	F	IVA	Mucus adenocarcinoma	5-Fu + Oxaliplatin + Bevacizumab
P1804	21	F	IIIC	Mucus adenocarcinoma	5-Fu + Irinotecan + Oxaliplatin
P1822	76	M	IVB	Adenocarcinoma	5-Fu + Irinotecan + Oxaliplatin + Bevacizumab
P1863 <sup>#</sup>	47	F	IVB	Mucus adenocarcinoma	5-Fu + Irinotecan + Oxaliplatin + Bevacizumab
P1893	55	M	IVA	Adenocarcinoma	5-Fu + Oxaliplatin
P1957 <sup>#</sup>	55	M	IVB	Adenocarcinoma	5-Fu + Irinotecan + Oxaliplatin + Cetuximab
P1977 <sup>#</sup>	51	F	IVB	Adenocarcinoma	5-Fu + Irinotecan + Oxaliplatin + Bevacizumab
P2132 <sup>#</sup>	55	M	IVB	Adenocarcinoma	5-Fu + Irinotecan + Oxaliplatin + Bevacizumab
P2167	66	M	IVA	Adenocarcinoma	5-Fu + Irinotecan + Oxaliplatin + Bevacizumab
P2180 <sup>#</sup>	53	F	IVB	Adenocarcinoma	5-Fu + Oxaliplatin
P2186 <sup>#</sup>	65	M	IIIC	Adenocarcinoma	5-Fu + Irinotecan + Oxaliplatin
P2286 <sup>#</sup>	59	M	IVA	Adenocarcinoma	5-Fu + Irinotecan + Oxaliplatin + Cetuximab + Bevacizumab
P2295 <sup>#</sup>	48	M	IIIC	Adenocarcinoma	5-Fu + Irinotecan + Oxaliplatin + Bevacizumab
P2338	66	M	IVB	Adenocarcinoma	5-Fu + Irinotecan + Oxaliplatin + Cetuximab
P2357	70	M	IIIB	Adenocarcinoma	5-Fu + Irinotecan + Bevacizumab
P2653	65	M	IIIC	Adenocarcinoma	5-Fu + Irinotecan + Oxaliplatin + Cetuximab

<sup>#</sup>Refers to colorectal cancer patients resistant to 5-Fu.

**Table 3. Correlations between patient serum TIMP-2 levels and clinical characteristics.**

Characteristics	Total	serum TIMP-2 levels		OR	95% CI	p-value
		<36.6 ng/ml	≥36.6 ng/ml			
All Cases	84	42 (39.0%)	42 (61.0%)			
Age (years)						
≥65	45	19 (42.2%)	26 (57.8%)			
<65	39	23 (59.0%)	16 (41.0%)	0.508	0.213–1.214	0.189
Gender						
Male	48	19 (39.6%)	29 (60.4%)			
Female	36	23 (63.9%)	13 (36.1%)	0.37	0.151–1.043	0.179
Stage						
IIIA	7	3 (42.9%)	4 (57.1%)			
IIIB	62	33 (53.2%)	29 (46.8%)			
IIIC	10	6 (60.0%)	4 (40.4%)			
IVA	3	0	3 (100%)			
IVB	2	0	2 (100%)			0.215
Histological type						
Adenocarcinoma	67	33 (49.3%)	34 (50.7%)			
Mucus adenocarcinoma	14	8 (57.1%)	6 (42.9%)			
Others	3	1 (33.3%)	2 (66.7%)			0.728

p-value calculated by the Chi-square test.

## TIMP-2 promotes CRC cell resistance to 5-Fu through an autocrine mechanism

We have confirmed that TIMP-2 is elevated in 5-Fu resistant CRC patients and is correlated with poor prognostic outcomes. Furthermore, we confirmed that TIMP-2 is closely associated with 5-Fu resistance in

CRC cells. Next, we set to confirm that it is TIMP-2 and not other cytokines that cause 5-Fu resistance. This assay was done by adding recombinant TIMP-2 to the culture medium of 5-Fu sensitive cell lines and adding the neutralization TIMP-2 antibody to the culture medium of 5-Fu resistant cell lines. Following treatment of CRC cell lines (DLD-1 5-FuS and HCT116 5-FuS)

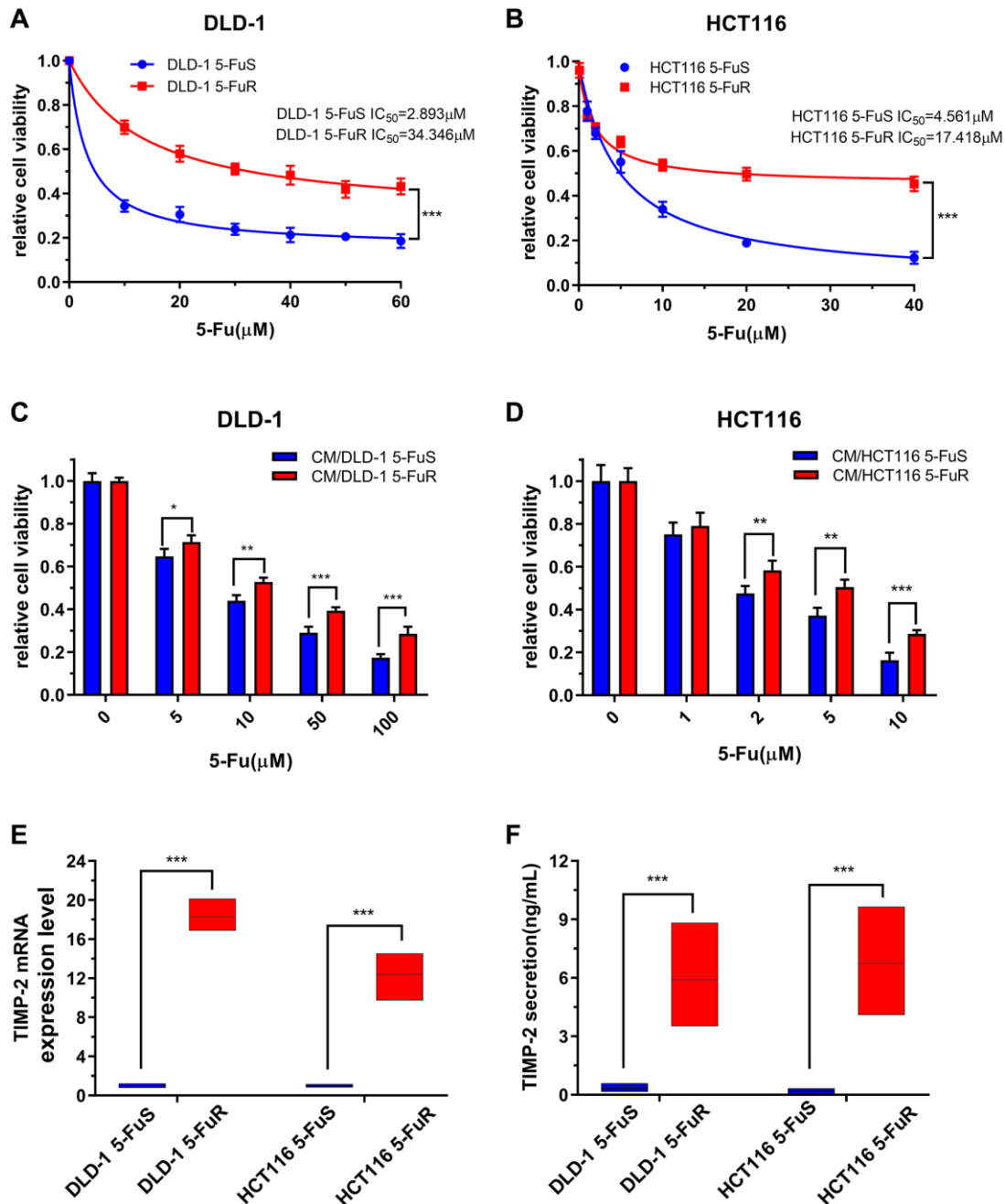


**Figure 2. Upregulation of TIMP-2 in 5-Fu resistant CRC cells *in vitro*.** (A, B) Relative cell viabilities of DLD-1 5-FuS cells and DLD-1 5-FuR cells, HCT116 5-FuS cells and HCT116 5-FuR cells under increasing concentrations of 5-Fu for 3 days. (C, D) Relative cell viabilities of DLD-1 5-FuS cells and HCT116 5-FuS cells in increasing concentrations of 5-Fu for 3 days after culture in conditioned medium of DLD-1 5-FuR cells or HCT116 5-FuR cells for 2 days. (E) mRNA expression levels of TIMP-2 in paired DLD-1 5-FuS cells and DLD-1 5-FuR cells, HCT116 5-FuS cells and HCT116 5-FuR cells. (F) Differences in TIMP-2 protein expression levels in paired DLD-1 5-FuS cells and DLD-1 5-FuR cells, HCT116 5-FuS cells and HCT116 5-FuR cells. Data from triplicate wells in 3 independent experiments. (A, B) \*\*\* $p < 0.001$  by 2 way ANOVA test. (C-F) \* $p < 0.05$ , \*\* $p < 0.01$ , \*\*\* $p < 0.001$  by Student's *t*-test.

with recombinant TIMP-2, changes in TIMP-2 protein levels in cell culture medium (CM) of DLD-1 5-FuS cells and HCT116 5-FuS cells were determined. TIMP-2 protein levels were elevated for 3 days, comparable to levels in the culture medium of 5-Fu resistant cell lines (Figure 4A). Interestingly, after the addition of TIMP-2,

less sensitivity to 5-Fu and increased IC<sub>50</sub> was observed in the 5-Fu sensitive cell lines (Figure 4B and 4C). When the TIMP-2 neutralization antibody was added to the culture medium of DLD-1 5-FuR and HCT116 5-FuR cells, TIMP-2 protein levels were significantly suppressed (Figure 4D). Consistent with our prediction,

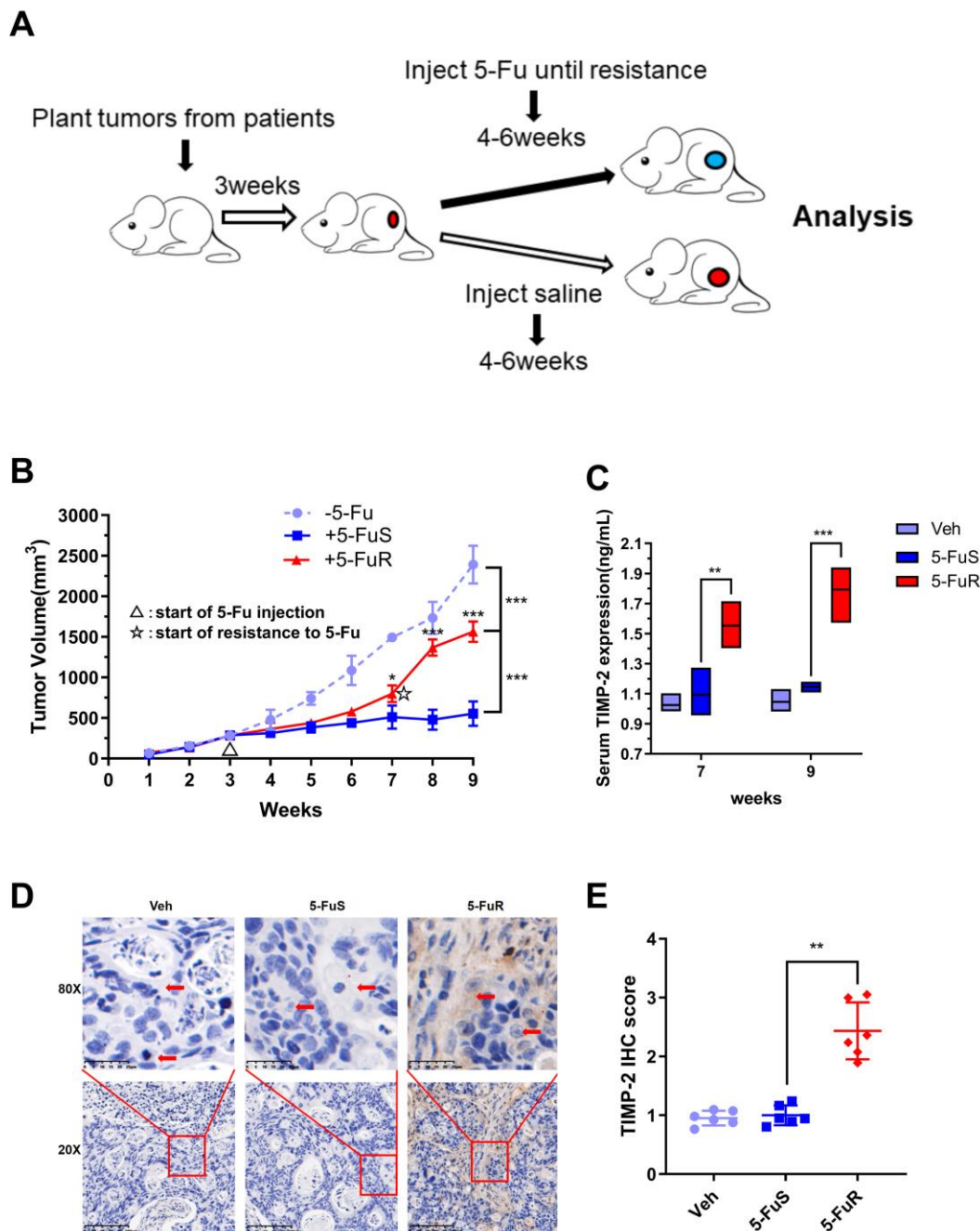


**Figure 3. Activation of TIMP-2 in 5-Fu resistant PDX models of CRC *in vivo*.** (A) Schematic presentation of the constructing of a PDX-drug resistance model. (B) Changes in tumor volumes for Veh, 5-FuS and 5-FuR group PDX mice models during the experiment. (C) Differences in TIMP-2 protein levels in Veh, 5-FuS and 5-FuR group PDX mice models. (D) IHC for typical TIMP-2 staining images of subcutaneous tumors formed in Veh, 5-FuS and 5-FuR group PDX mice models. (E) Semi-quantitative IHC staining scores for TIMP-2 as shown in Figure 3C. Data is presented as mean ± SD. Three mice and 6 tumors per experimental group. \**p* < 0.05, \*\**p* < 0.01, \*\*\**p* < 0.001 by Student's *t*-test or two-way ANOVA.

IC<sub>50</sub> of both 5-Fu resistant cell lines were significantly decreased, indicative of increased sensitivity of cells to drugs (Figure 4E and 4F).

To validate the relationship between 5-Fu resistance and TIMP-2 protein expression levels in colorectal tumors, we used small interfering RNA (siRNA) to knock down

TIMP-2 expression in cell lines. siRNA against TIMP-2 showed excellent knock-down efficiency in DLD-1 5-FuR and HCT116 5-FuR cells (Figure 5A). Besides, DLD-1 5-FuR and HCT116 5-FuR cells regained sensitivity to 5-Fu after knock-down of TIMP-2 expression by siRNA (Figure 5B and 5C). Remarkably, the higher the concentration of 5-Fu in the culture

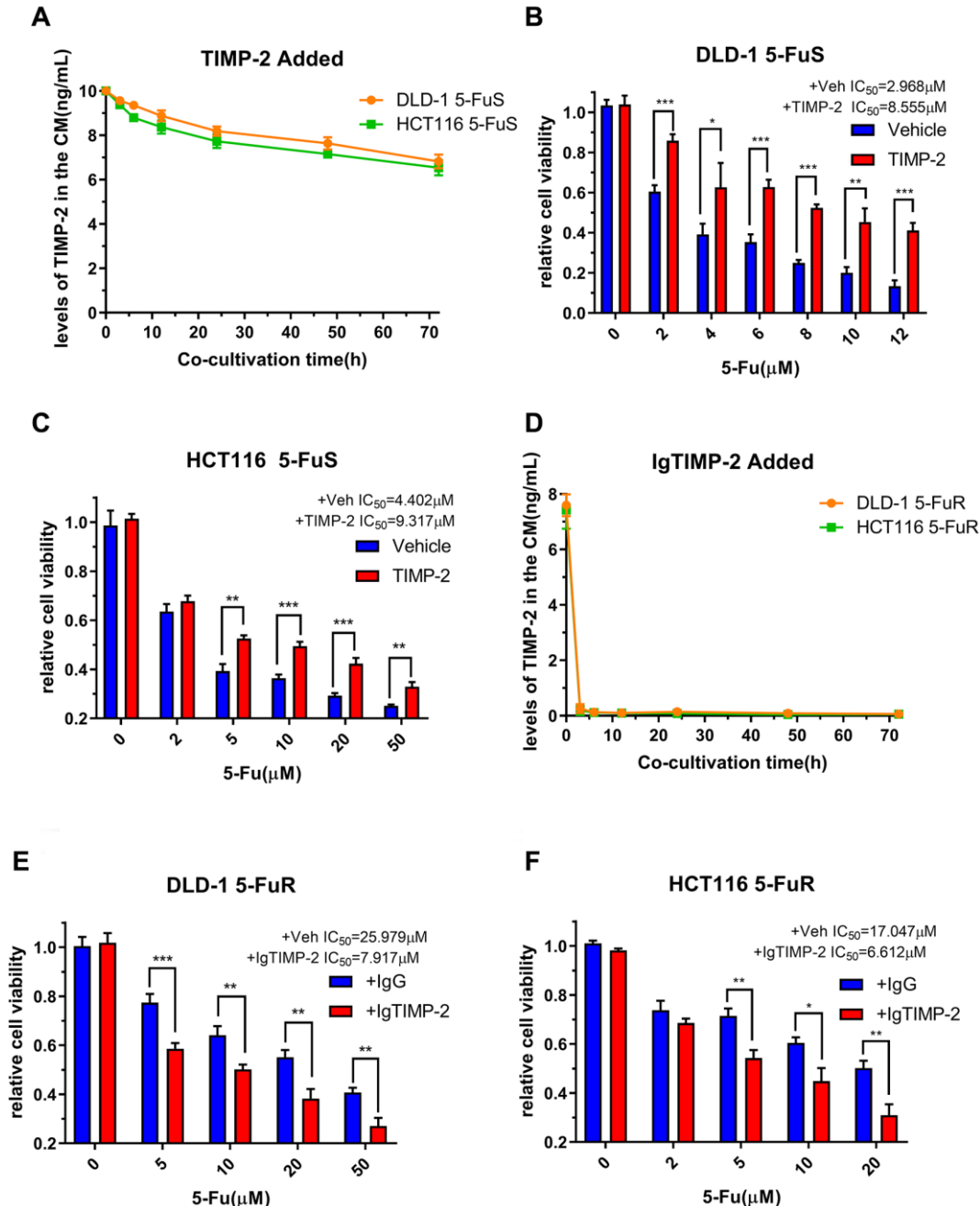


**Figure 4. TIMP-2 promotes CRC cell resistance to 5-Fu through an autocrine mechanism.** (A) Changes in TIMP-2 protein levels in the cell culture medium (CM) of DLD-1 5-FuS cells and HCT116 5-FuS cells 3 days after treatment with 10 ng/mL of recombinant TIMP-2. (B, C) Relative cell viabilities of DLD-1 5-FuS cells and HCT116 5-FuS cells under increasing concentrations of 5-Fu for 3 days after culture with 10 ng/mL of recombinant TIMP-2. (D) Changes in TIMP-2 protein levels in the cell culture medium (CM) of DLD-1 5-FuR cells and HCT116 5-FuR cells for 3 days of culture with 5  $\mu$ g/mL of TIMP-2 neutralizing antibody. (E, F) Relative cell viabilities of DLD-1 5-FuR cells and HCT116 5-FuR cells under increasing concentrations of 5-Fu for 3 days of culture with control IgG or 5  $\mu$ g/mL of TIMP-2 neutralizing antibody. Data from triplicate wells for 3 independent experiments. \* $p$  < 0.05, \*\* $p$  < 0.01, \*\*\* $p$  < 0.001 by Student's  $t$ -test or one-way ANOVA.



solution, the more apparent the above effect. Addition of recombinant TIMP-2 protein to the siRNA-treated DLD-1 5-FuR and HCT116 5-FuR cells restored the resistance of cell lines to 5-Fu (Figure 5B and 5C). The  $IC_{50}$  for each group of cells in the above experiment are shown in Figure 5D. These results show that TIMP-2 induces 5-Fu resistance in CRC cells.

### TIMP-2 induces 5-Fu resistance by activating ERK/MAPK in CRC cells

We further determined the signaling pathway involved in TIMP-2 induced 5-Fu resistance in CRC. It has been reported that TIMP-2 mediates endothelial proliferation, formation of a capillary tube in obesity, and promotes tumor invasion in advanced squamous cell carcinomas [58, 59] by activating the ERK/MAPK signaling pathway. The role of the ERK/MAPK signaling pathway in tumor resistance has been widely reported [60–62]. Therefore, we explored the underlying mechanisms through which TIMP-2 mediates drug resistance by analyzing the expression levels of key proteins in the ERK/MAPK signaling pathway.

When compared to DLD-1 5-FuS and HCT116 5-FuS cells, levels of p-ERK1/2/ERK1/2 and p-ERK5/ERK5 were found to be significantly elevated in DLD-1 5-FuR and HCT116 5-FuR cells, implying that activation of ERK1/2 was accompanied by ERK5 phosphorylation (Figure 6A). Since Erk1/2 and pErk1/2 antibodies can recognize Thr202 and Tyr204 sites of Erk1 and Thr185 as well as Tyr187 sites of Erk2, double bands are shown in the Figure 6.

To confirm the effects of the ERK/MAPK signaling pathway on drug resistance in CRC, we performed a series of experiments. U0126 is an ERK/MAPK signaling pathway inhibitor. Phosphorylation of ERK1/2 and ERK5 in both DLD-1 5-FuR and HCT116 5-FuR cells were markedly inhibited by U0126 treatment (Figure 6B). Moreover, we evaluated the role of TIMP-2 in activation of the ERK/MAPK signaling pathway in CRC cells. Recombinant TIMP-2 treatment significantly enhanced ERK1/2 and ERK5 phosphorylation in both DLD-1 5-FuS and HCT116 5-FuS cells (Figure 6C). However, addition of TIMP-2 neutralization antibody resulted in significantly

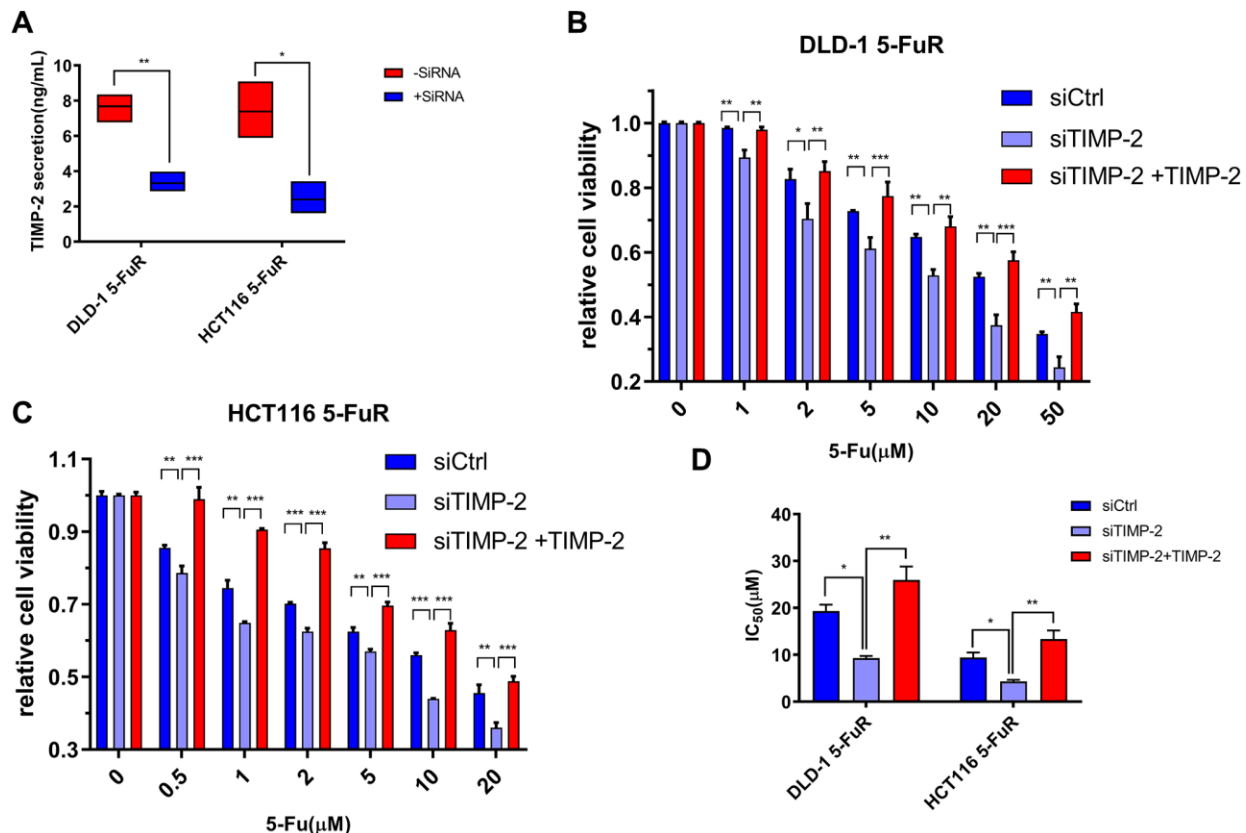


**Figure 5. Knockdown of TIMP-2 overcomes 5-Fu resistance in CRC cells.** (A) Changes in expression levels of TIMP-2 in DLD-1 5-FuR cells and HCT116 5-FuR cells after control siRNA or TIMP-2 siRNA (30 pg/ml) transfections. (B, C) Relative cell viabilities of DLD-1 5-FuR cells and HCT116 5-FuR cells under increasing concentrations of 5-Fu for 3 days of culture with TIMP-2 siRNA (30 pg/ml) or TIMP-2 siRNA (30 pg/ml) and recombinant TIMP-2 (10 ng/ml) together. (D) Differences in 5-Fu concentrations for 50% inhibition of cell growth ( $IC_{50}$ ) between the six groups of cells in Figure 5B and 5C above. Data from triplicate wells for 3 independent experiments. \* $p < 0.05$ , \*\* $p < 0.01$ , \*\*\* $p < 0.001$  by Student's *t*-test or one-way ANOVA.

decreased phosphorylation levels of ERK1/2 and ERK5 in both resistant cell lines (Figure 6D).

### U0126 inhibits 5-Fu resistance in CRC through the ERK/MAPK signaling pathway

We have shown that the ERK/MAPK signaling pathway is vital for 5-Fu resistance in CRC, therefore, we

determined whether U0126 can inhibit the drug resistance process. Synergistic effects were used to analyze the impact of U0126 on the ERK/MAPK signaling pathway in CRC cell resistance. Treatment of CRC resistant cell lines using different concentrations of 5-Fu and U0126, alone or in combination, exhibited different effects. Therefore, we calculated the Combination index (CI) values, which we used to

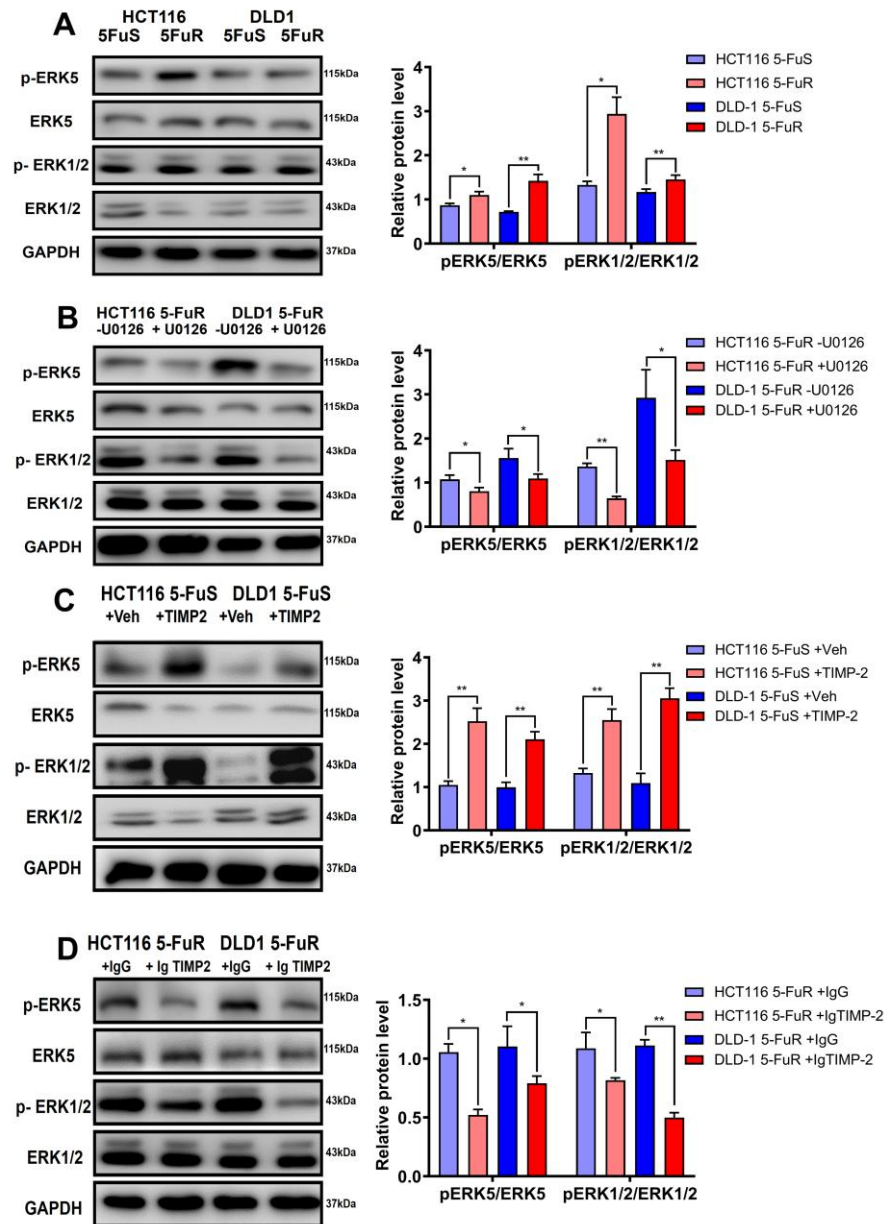


**Figure 6. TIMP-2 sustains the activation of ERK/MAPK in CRC cells.** (A) Immunoblotting of phosphorylated ERK1/2 and ERK5 in DLD-1 5-FuS cells and DLD-1 5-FuR cells, HCT116 5-FuS cells and HCT116 5-FuR cells. (B) Immunoblotting of phosphorylated ERK1/2 and ERK5 in DLD-1 5-FuR cells and HCT116 5-FuR cells cultured with 5  $\mu$ M of U0126 for 2 days, which down-regulates ERK/MAPK signaling. (C) Immunoblotting of phosphorylated ERK1/2 and ERK5 in DLD-1 5-FuS cells and HCT116 5-FuS cells cultured with 10 ng/mL of recombinant TIMP-2 for 6 h. (D) Immunoblotting of phosphorylated ERK1/2 and ERK5 in DLD-1 5-FuR cells and HCT116 5-FuR cells cultured with control IgG or 5  $\mu$ g/mL of TIMP-2 neutralizing antibody for 6 h. Band intensities of western blotting for p-ERK5/ ERK5 and p-ERK1/2/ERK1/2 were analyzed. \* $p < 0.05$ , \*\* $p < 0.01$ , \*\*\* $p < 0.001$  by Student's  $t$ -test.

quantitatively determine interactions between the two drugs, for evaluating the combined effects of U0126 and 5-Fu. There was a strong synergistic effect from the combined U0126 and 5-Fu on both DLD-1 5-FuR and HCT116 5-FuR cells (Figure 7A and 7B).

To further determine that U0126 can reverse TIMP-2-induced 5-Fu resistance in CRC through the ERK/MAPK signaling pathway, we downregulated ERK/MAPK in DLD-1 5-FuS and HCT116 5-FuS cells using U0126. Then, cells were treated with recombinant TIMP-2, followed by increasing the concentrations of 5-Fu in the culture (Figure 7C and 7D). Even though the addition of recombinant TIMP-2 induced resistance to 5-Fu in DLD-1 5-FuS and HCT116 5-FuS cells containing ERK/MAPK, TIMP-2 did not induce 5-Fu resistance in CRC cells with downregulated ERK/MAPK signaling pathway (Figure 7C and 7D). These findings suggest that the ERK/MAPK signaling pathway plays a pivotal role in TIMP-2 mediated resistance of colorectal cancer cells to 5-Fu. When the

ERK/MAPK signaling pathway is blocked, TIMP-2 induced 5-Fu resistance is significantly inhibited. The inhibitor of the ERK/MAPK signaling pathway, U0126, effectively inhibited 5-Fu resistance in colorectal cancer cells. This finding provides a basis for future development of small molecule drugs that antagonize 5-Fu resistance in tumors.

## DISCUSSION

In recent years, global incidences of CRC have gradually increased, especially among the elderly. Advanced CRC has been attributed to 5-Fu resistance. Cytokines in the para cancerous and circulating systems affect immune responses, occurrence, and metastasis of tumors as well as tumor drug resistance [15–18]. We found that TIMP-2 serum levels in 5-Fu resistant CRC patients were elevated.

TIMP-2 belongs to the tissue inhibitor of metalloproteinase (TIMP) family. This gene family

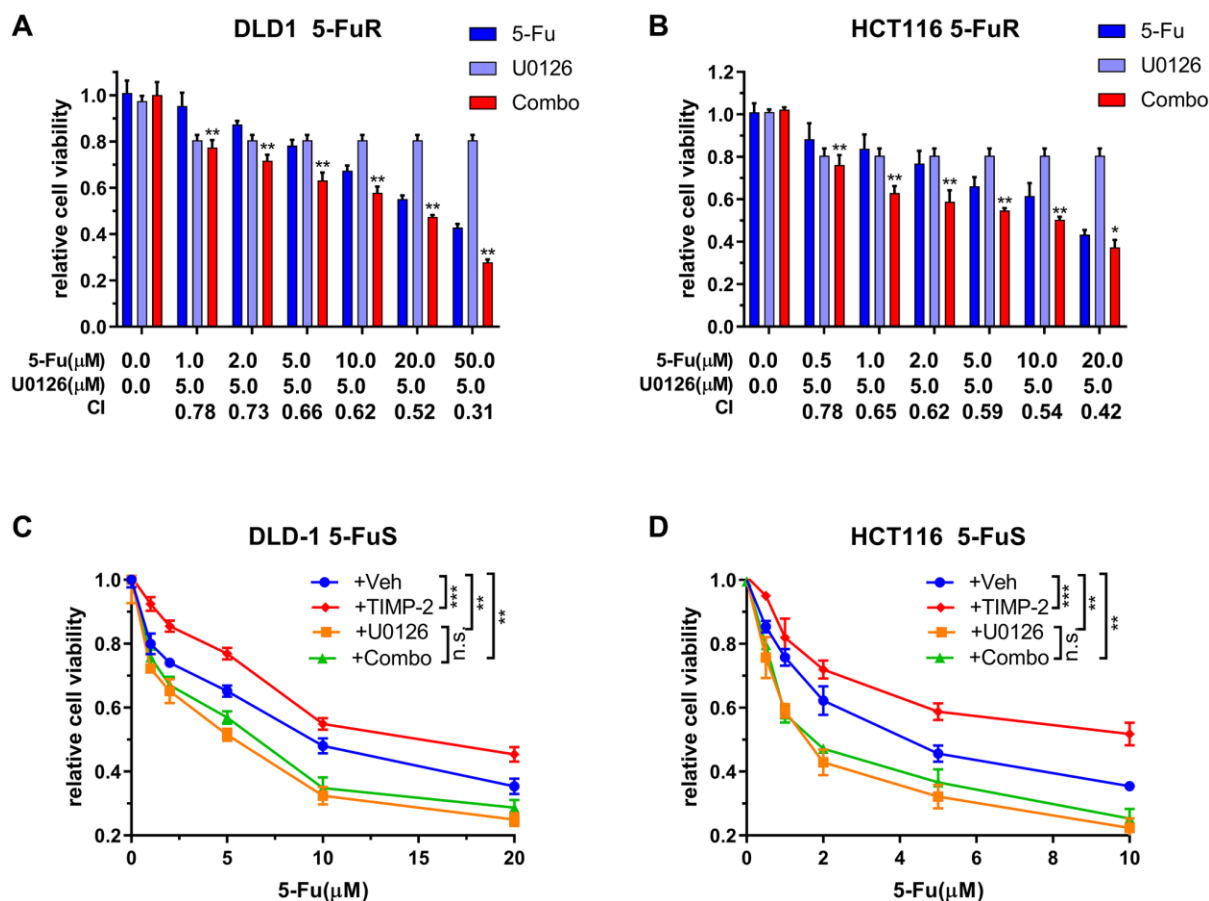


**Figure 7. U0126 inhibits 5-Fu resistance in CRC through the ERK/MAPK signaling pathway.** (A, B) Synergistic effects of U0126 and 5-Fu on DLD-1 5-FuR and HCT116 5-FuR cells. Combo = 5-Fu + U0126. (C, D) Knockdown ERK/MAPK by U0126 blocks TIMP-2 induced 5-Fu resistance in CRC cells. DLD-1 5-FuS and HCT116 5-FuS cells were cultured with 5 μM of U0126 for 24 h and then cultured with recombinant TIMP-2 (10 ng/ml) for 6 h, followed by increasing concentrations of 5-Fu treatment for 3 days. Combo = TIMP-2 + U0126. Combination index (CI) is presented below the bars. Data from triplicate wells of 3 independent experiments. (A, B) \**p* < 0.05, \*\**p* < 0.01 by Student's *t*-test between group +5Fu and group Combo. (C, D) \**p* < 0.05, \*\**p* < 0.01, \*\*\**p* < 0.001 by one-way ANOVA or two-way ANOVA.

encodes natural inhibitors of matrix metalloproteinases (MMPs), a group of peptidases involved in degradation of the extracellular matrix (ECM). Moreover, encoded proteins have a unique role in suppressing endothelial cell proliferation, inhibition of protease activities in tissues undergoing remodeling of the extracellular matrix, and possessing erythroid-potentiating activities [63–66]. High expression levels of TIMP-2 in breast cancer are associated with poor prognosis [67], whereas low expressions of TIMP-2 in lung cancer are correlated with poor prognosis [68]. In addition, high expression levels of TIMP-2 in tumor tissues and serum of liver cancer patients were associated with decreased metastases [69]. However, the roles of TIMP-2 in CRC prognosis and CRC drug resistance have not been elucidated.

We found that CRC patients with elevated TIMP-2 levels exhibited poor overall survival (OS), disease-free survival (DFS) and disease outcomes. These findings were a confirmation of preliminary clinical and 5-Fu-resistant PDX model results that showed a high expression of TIMP-2 in drug-resistant CRC. Therefore, TIMP-2 is a potential marker for 5-Fu drug resistance in CRC patients. Since elevated TIMP-2 levels inform the prognosis of 5-Fu-resistant CRC patients, it is important to evaluate TIMP-2 levels in blood during chemotherapy to assess 5-Fu resistance as early as possible. Elevated TIMP-2 expression levels are accompanied by changes in patient's 5-Fu resistance status. Consequently, doctors can act appropriately to prevent tumor progression. However, studies should elucidate on the relationship between TIMP-2 expression levels and clinical patient characteristics to ascertain these findings.

Our cellular experiments confirmed the ability of TIMP-2 to cause resistance in CRC cells. Li et al. reported a new autocrine cytokine expression following drug resistance in leukemia [70]. Therefore, we aimed at determining whether TIMP-2 induces 5-Fu resistance through this mechanism. 5-Fu sensitive cells co-cultured with 5-Fu resistant cells with a survival advantage were used to determine the cytokines endowing CRC with 5-Fu resistance. Effects of recombinant TIMP-2 treatment on CRC cells revealed that secreted TIMP-2 acts as an autocrine factor to induce 5-Fu resistance. Inhibition of TIMP-2 by neutralization antibodies or siRNA reversed drug resistance in 5-Fu resistant cells. Therefore, up-regulation, down-regulation and rescue experiments proved that an autocrine mechanism is involved in TIMP-2 induced colorectal cancer cell resistance to 5-Fu. These findings elucidate on the role of anti-TIMP-2 antibody in preventing CRC patients from acquiring resistance to 5-Fu drugs during treatment. Moreover,

serum TIMP-2 levels in CRC patients are potential biomarkers for evaluating potential resistance of patients to 5-Fu treatment.

A small-molecule inhibitor (U0126) has been shown to target key proteins in the ERK/MAPK signaling pathway [44, 45]. We found that TIMP-2 mediates 5-Fu resistance through the ERK/MAPK signaling pathway in CRC cells. Targeting the ERK/MAPK signaling pathway can re-sensitize 5-Fu resistant CRC cells to 5-Fu. From our results, we infer that U0126 can efficiently switch 5-Fu-resistant CRC cells to 5-Fu sensitive CRC cells due to its ability to inhibit the ERK/MAPK signaling pathway and to block the TIMP-2 autocrine mechanism involved in 5-Fu resistance.

Therefore, combined use of an agent targeting TIMP-2 and 5-Fu has the potential for preventing or treating CRC resistance to 5-Fu in CRC patients. Alternatively, small molecule inhibitors that target the ERK/MAPK signaling pathway, such as U0126, can effectively cut off the pathway, thereby increasing sensitivity of colorectal tumors to 5-Fu. However, studies involving animal experiments and clinical trials should be performed to ascertain these findings.

## CONCLUSIONS

TIMP-2 is overexpressed in CRC patients, which promotes drug resistance to 5-Fu through the EPK/MAPK signaling pathway. This elevation is indicative of poor disease prognosis. CRC resistance to 5-Fu can be regulated by inhibition of TIMP-2 or ERK/MAPK signaling pathway. Finally, combined administration of TIMP-2 or ERK/MAPK signaling pathway inhibitors and 5-Fu is a promising chemotherapeutic option for the treatment of first time CRC patients as well as relapsed CRC patients previously treated using 5-Fu-based chemotherapy.

## AUTHOR CONTRIBUTIONS

Study design: Zhou W, Song Z, Huang X; Experimental operation: Zhang G, Luo X, Zhang W; Data analysis: Xu J, Chen E; Data collection: Meng Q, Wang D.

## CONFLICTS OF INTEREST

The authors declare no conflicts of interest related to this study.

## FUNDING

This study was financially supported by the National Natural Science Foundation of China (No.81771502, 81701820, 81402580), the Natural Science Foundation

of Zhejiang Province (No. LH19H160001, LY20H180014) and the Department of Health of Zhejiang Province (No. 2018KY473 and 2018PY025).

## REFERENCES

- Bray F, Ferlay J, Soerjomataram I, Siegel RL, Torre LA, Jemal A. Global cancer statistics 2018: GLOBOCAN estimates of incidence and mortality worldwide for 36 cancers in 185 countries. *CA Cancer J Clin.* 2018; 68:394–424.  
<https://doi.org/10.3322/caac.21492>  
PMID:30207593
- Center MM, Jemal A, Smith RA, Ward E. Worldwide variations in colorectal cancer. *CA Cancer J Clin.* 2009; 59:366–78.  
<https://doi.org/10.3322/caac.20038>  
PMID:19897840
- Du C, Huang D, Peng Y, Yao Y, Zhao Y, Yang Y, Wang H, Cao L, Zhu WG, Gu J. 5-Fluorouracil targets histone acetyltransferases p300/CBP in the treatment of colorectal cancer. *Cancer Lett.* 2017; 400:183–93.  
<https://doi.org/10.1016/j.canlet.2017.04.033>  
PMID:28465257
- Lawrence W Jr, Terz JJ, Horsley S 3rd, Donaldson M, Lovett WL, Brown PW, Ruffner BW, Regelson W. Chemotherapy as an adjuvant to surgery for colorectal cancer. *Ann Surg.* 1975; 181:616–23.  
<https://doi.org/10.1097/0000658-197505000-00016>  
PMID:1130879
- Saltz LB, Cox JV, Blanke C, Rosen LS, Fehrenbacher L, Moore MJ, Maroun JA, Ackland SP, Locker PK, Pirotta N, Elfring GL, Miller LL, and Irinotecan Study Group. Irinotecan plus fluorouracil and leucovorin for metastatic colorectal cancer. *N Engl J Med.* 2000; 343:905–14.  
<https://doi.org/10.1056/NEJM200009283431302>  
PMID:11006366
- Panczyk M. Pharmacogenetics research on chemotherapy resistance in colorectal cancer over the last 20 years. *World J Gastroenterol.* 2014; 20:9775–827.  
<https://doi.org/10.3748/wjg.v20.i29.9775>  
PMID:25110414
- Wu Q, Yang Z, Nie Y, Shi Y, Fan D. Multi-drug resistance in cancer chemotherapeutics: mechanisms and lab approaches. *Cancer Lett.* 2014; 347:159–66.  
<https://doi.org/10.1016/j.canlet.2014.03.013>  
PMID:24657660
- Iyer AK, Singh A, Ganta S, Amiji MM. Role of integrated cancer nanomedicine in overcoming drug resistance. *Adv Drug Deliv Rev.* 2013; 65:1784–802.  
<https://doi.org/10.1016/j.addr.2013.07.012>  
PMID:23880506
- Marjaneh RM, Khazaei M, Ferns GA, Avan A, Aghaee-Bakhtiari SH. The role of microRNAs in 5-FU resistance of colorectal cancer: Possible mechanisms. *J Cell Physiol.* 2019; 234:2306–16.  
<https://doi.org/10.1002/jcp.27221>  
PMID:30191973
- Akhdar H, Loyer P, Rauch C, Corlu A, Guillouzo A, Morel F. Involvement of Nrf2 activation in resistance to 5-fluorouracil in human colon cancer HT-29 cells. *Eur J Cancer.* 2009; 45:2219–27.  
<https://doi.org/10.1016/j.ejca.2009.05.017>  
PMID:19524433
- Zhang N, Yin Y, Xu SJ, Chen WS. 5-Fluorouracil: mechanisms of resistance and reversal strategies. *Molecules.* 2008; 13:1551–69.  
<https://doi.org/10.3390/molecules13081551>  
PMID:18794772
- Xie T, Huang M, Wang Y, Wang L, Chen C, Chu X. MicroRNAs as Regulators, Biomarkers and Therapeutic Targets in the Drug Resistance of Colorectal Cancer. *Cell Physiol Biochem.* 2016; 40:62–76.  
<https://doi.org/10.1159/000452525>  
PMID:27842308
- Shen Y, Tong M, Liang Q, Guo Y, Sun HQ, Zheng W, Ao L, Guo Z, She F. Epigenomics alternations and dynamic transcriptional changes in responses to 5-fluorouracil stimulation reveal mechanisms of acquired drug resistance of colorectal cancer cells. *Pharmacogenomics J.* 2018; 18:23–8.  
<https://doi.org/10.1038/tpj.2016.91>  
PMID:28045128
- Lee JH, Yun CW, Lee SH. Cellular Prion Protein Enhances Drug Resistance of Colorectal Cancer Cells via Regulation of a Survival Signal Pathway. *Biomol Ther (Seoul).* 2018; 26:313–21.  
<https://doi.org/10.4062/biomolther.2017.033>  
PMID:28822989
- Butera G, Pacchiana R, Donadelli M. Autocrine mechanisms of cancer chemoresistance. *Semin Cell Dev Biol.* 2018; 78:3–12.  
<https://doi.org/10.1016/j.semcdb.2017.07.019>  
PMID:28751251
- Chow MT, Luster AD. Chemokines in cancer. *Cancer Immunol Res.* 2014; 2:1125–31.  
<https://doi.org/10.1158/2326-6066.CIR-14-0160>  
PMID:25480554
- Miller MA, Sullivan RJ, Lauffenburger DA. Molecular Pathways: Receptor Ectodomain Shedding in Treatment, Resistance, and Monitoring of Cancer. *Clin Cancer Res.* 2017; 23:623–9.  
<https://doi.org/10.1158/1078-0432.CCR-16-0869>  
PMID:27895032



18. Zhou W, Sun W, Yung MMH, Dai S, Cai Y, Chen CW, Meng Y, Lee JB, Braisted JC, Xu Y, Southall NT, Shinn P, Huang X, et al. Autocrine activation of JAK2 by IL-11 promotes platinum drug resistance. *Oncogene*. 2018; 37:3981–97.  
<https://doi.org/10.1038/s41388-018-0238-8>  
PMID: [29662190](#)
19. Jones VS, Huang RY, Chen LP, Chen ZS, Fu L, Huang RP. Cytokines in cancer drug resistance: Cues to new therapeutic strategies. *Biochim Biophys Acta*. 2016; 1865:255–65.  
<https://doi.org/10.1016/j.bbcan.2016.03.005>  
PMID: [26993403](#)
20. Zahreddine H, Borden KL. Mechanisms and insights into drug resistance in cancer. *Front Pharmacol*. 2013; 4:28.  
<https://doi.org/10.3389/fphar.2013.00028>  
PMID: [23504227](#)
21. Brooks KM, George JM, Pau AK, Rupert A, Mehaffy C, De P, Dobos KM, Kellogg A, McLaughlin M, McManus M, Alfaro RM, Hadigan C, Kovacs JA, Kumar P. Cytokine-Mediated Systemic Adverse Drug Reactions in a Drug-Drug Interaction Study of Dolutegravir With Once-Weekly Isoniazid and Rifapentine. *Clin Infect Dis*. 2018; 67:193–201.  
<https://doi.org/10.1093/cid/ciy082>  
PMID: [29415190](#)
22. Wagenaar-Miller RA, Gorden L, Matrisian LM. Matrix metalloproteinases in colorectal cancer: is it worth talking about? *Cancer Metastasis Rev*. 2004; 23:119–35.  
<https://doi.org/10.1023/a:1025819214508>  
PMID: [15000153](#)
23. Kabashima A, Maehara Y, Kakeji Y, Baba H, Koga T, Sugimachi K. Clinicopathological features and overexpression of matrix metalloproteinases in intramucosal gastric carcinoma with lymph node metastasis. *Clin Cancer Res*. 2000; 6:3581–4.  
PMID: [10999748](#)
24. Nabeshima K, Inoue T, Shimao Y, Sameshima T. Matrix metalloproteinases in tumor invasion: role for cell migration. *Pathol Int*. 2002; 52:255–64.  
<https://doi.org/10.1046/j.1440-1827.2002.01343.x>  
PMID: [12031080](#)
25. Schwartz GK. Invasion and metastases in gastric cancer: in vitro and in vivo models with clinical correlations. *Semin Oncol*. 1996; 23:316–24.  
PMID: [8658215](#)
26. Kähäri VM, Saarialho-Kere U. Matrix metalloproteinases and their inhibitors in tumour growth and invasion. *Ann Med*. 1999; 31:34–45.  
<https://doi.org/10.3109/07853899909019260>  
PMID: [10219712](#)
27. Kandasamy AD, Chow AK, Ali MA, Schulz R. Matrix metalloproteinase-2 and myocardial oxidative stress injury: beyond the matrix. *Cardiovasc Res*. 2010; 85:413–23.  
<https://doi.org/10.1093/cvr/cvp268>  
PMID: [19656780](#)
28. Stetler-Stevenson WG. Tissue inhibitors of metalloproteinases in cell signaling: metalloproteinase-independent biological activities. *Sci Signal*. 2008; 1:re6.  
<https://doi.org/10.1126/scisignal.127re6>  
PMID: [18612141](#)
29. Saghatelian A, Jessani N, Joseph A, Humphrey M, Cravatt BF. Activity-based probes for the proteomic profiling of metalloproteases. *Proc Natl Acad Sci U S A*. 2004; 101:10000–5.  
<https://doi.org/10.1073/pnas.0402784101>  
PMID: [15220480](#)
30. Jezierska A, Motyl T. Matrix metalloproteinase-2 involvement in breast cancer progression: a mini-review. *Med Sci Monit*. 2009; 15:RA32–40.  
PMID: [19182722](#)
31. Butler GS, Butler MJ, Atkinson SJ, Will H, Tamura T, Schade van Westrum S, Crabbe T, Clements J, d'Ortho MP, Murphy G. The TIMP2 membrane type 1 metalloproteinase "receptor" regulates the concentration and efficient activation of progelatinase A. A kinetic study. *J Biol Chem*. 1998; 273:871–80.  
<https://doi.org/10.1074/jbc.273.2.871>  
PMID: [9422744](#)
32. Bjørnland K, Lehne G, Johansen HT, Fodstad O, Rugstad HE, Aasen AO, Ree AH. Human hepatoma cells rich in P-glycoprotein display enhanced in vitro invasive properties compared to P-glycoprotein-poor hepatoma cells. *Oncol Res*. 1998; 10:255–62.  
PMID: [9802060](#)
33. Tavakoli F, Jahanban-Esfahlan R, Seidi K, Jabbari M, Behzadi R, Pilehvar-Soltanahmadi Y, Zarghami N. Effects of nano-encapsulated curcumin-chrysin on telomerase, MMPs and TIMPs gene expression in mouse B16F10 melanoma tumour model. *Artif Cells Nanomed Biotechnol*. 2018; 46:75–86.  
<https://doi.org/10.1080/21691401.2018.1452021>  
PMID: [29607740](#)
34. Waleh NS, Murphy BJ, Zaveri NT. Increase in tissue inhibitor of metalloproteinase-2 (TIMP-2) levels and inhibition of MMP-2 activity in a metastatic breast cancer cell line by an anti-invasive small molecule SR13179. *Cancer Lett*. 2010; 289:111–8.  
<https://doi.org/10.1016/j.canlet.2009.08.006>  
PMID: [19751965](#)

35. Avruch J. MAP kinase pathways: the first twenty years. *Biochim Biophys Acta*. 2007; 1773:1150–60.  
<https://doi.org/10.1016/j.bbamcr.2006.11.006>  
PMID:17229475
36. Gentner B, Wein A, Croner RS, Zeittraeger I, Wirtz RM, Roedel F, Dimmler A, Dorlaque L, Hohenberger W, Hahn EG, Brueckl WM. Differences in the gene expression profile of matrix metalloproteinases (MMPs) and their inhibitors (TIMPs) in primary colorectal tumors and their synchronous liver metastases. *Anticancer Res*. 2009; 29:67–74.  
PMID:19331134
37. Groblewska M, Mroczo B, Gryko M, Pryczynicz A, Guzińska-Ustymowicz K, Kędra B, Kemon A, Szmítowski M. Serum levels and tissue expression of matrix metalloproteinase 2 (MMP-2) and tissue inhibitor of metalloproteinases 2 (TIMP-2) in colorectal cancer patients. *Tumour Biol*. 2014; 35:3793–802.  
<https://doi.org/10.1007/s13277-013-1502-8>  
PMID:24395652
38. Park KS, Kim SJ, Kim KH, Kim JC. Clinical characteristics of TIMP2, MMP2, and MMP9 gene polymorphisms in colorectal cancer. *J Gastroenterol Hepatol*. 2011; 26:391–7.  
<https://doi.org/10.1111/j.1440-1746.2010.06504.x>  
PMID:21261731
39. Wagner EF, Nebreda AR. Signal integration by JNK and p38 MAPK pathways in cancer development. *Nat Rev Cancer*. 2009; 9:537–49.  
<https://doi.org/10.1038/nrc2694>  
PMID:19629069
40. Chang L, Karin M. Mammalian MAP kinase signalling cascades. *Nature*. 2001; 410:37–40.  
<https://doi.org/10.1038/35065000>  
PMID:11242034
41. Soleimani A, Rahmani F, Saeedi N, Ghaffarian R, Khazaei M, Ferns GA, Avan A, Hassanian SM. The potential role of regulatory microRNAs of RAS/MAPK signaling pathway in the pathogenesis of colorectal cancer. *J Cell Biochem*. 2019; 120:19245–53.  
<https://doi.org/10.1002/jcb.29268>  
PMID:31512778
42. Yong HY, Koh MS, Moon A. The p38 MAPK inhibitors for the treatment of inflammatory diseases and cancer. *Expert Opin Investig Drugs*. 2009; 18:1893–905.  
<https://doi.org/10.1517/13543780903321490>  
PMID:19852565
43. Morrison DK, Davis RJ. Regulation of MAP kinase signaling modules by scaffold proteins in mammals. *Annu Rev Cell Dev Biol*. 2003; 19:91–118.  
<https://doi.org/10.1146/annurev.cellbio.19.111401.091942>  
PMID:14570565
44. Cavanaugh JE, Ham J, Hetman M, Poser S, Yan C, Xia Z. Differential regulation of mitogen-activated protein kinases ERK1/2 and ERK5 by neurotrophins, neuronal activity, and cAMP in neurons. *J Neurosci*. 2001; 21:434–43.  
<https://doi.org/10.1523/JNEUROSCI.21-02-00434.2001>  
PMID:11160424
45. Nishimoto S, Nishida E. MAPK signalling: ERK5 versus ERK1/2. *EMBO Rep*. 2006; 7:782–6.  
<https://doi.org/10.1038/sj.embor.7400755>  
PMID:16880823
46. Sarközi R, Miller B, Pollack V, Feifel E, Mayer G, Sorokin A, Schramek H. ERK1/2-driven and MKP-mediated inhibition of EGF-induced ERK5 signaling in human proximal tubular cells. *J Cell Physiol*. 2007; 211:88–100.  
<https://doi.org/10.1002/jcp.20909>  
PMID:17131384
47. Vaseva AV, Blake DR, Gilbert TSK, Ng S, Hostetter G, Azam SH, Ozkan-Dagliyan I, Gautam P, Bryant KL, Pearce KH, Herring LE, Han H, Graves LM, et al. KRAS Suppression-Induced Degradation of MYC Is Antagonized by a MEK5-ERK5 Compensatory Mechanism. *Cancer Cell*. 2018; 34:807–22.e7.  
<https://doi.org/10.1016/j.ccell.2018.10.001>  
PMID:30423298
48. Peng L, Xing X, Li W, Qu L, Meng L, Lian S, Jiang B, Wu J, Shou C. PRL-3 promotes the motility, invasion, and metastasis of LoVo colon cancer cells through PRL-3-integrin beta1-ERK1/2 and-MMP2 signaling. *Mol Cancer*. 2009; 8:110.  
<https://doi.org/10.1186/1476-4598-8-110>  
PMID:19930715
49. Brummer C, Faerber S, Bruss C, Blank C, Lacroix R, Haferkamp S, Herr W, Kreutz M, Renner K. Metabolic targeting synergizes with MAPK inhibition and delays drug resistance in melanoma. *Cancer Lett*. 2019; 442:453–63.  
<https://doi.org/10.1016/j.canlet.2018.11.018>  
PMID:30481565
50. Echevarría-Vargas IM, Reyes-Urbe PI, Guterres AN, Yin X, Kossenkova AV, Liu Q, Zhang G, Krepler C, Cheng C, Wei Z, Somasundaram R, Karakousis G, Xu W, et al. Co-targeting BET and MEK as salvage therapy for MAPK and checkpoint inhibitor-resistant melanoma. *EMBO Mol Med*. 2018; 10:e8446.  
<https://doi.org/10.15252/emmm.201708446>  
PMID:29650805

51. Lu H, Liu S, Zhang G, Wu B, Zhu Y, Frederick DT, Hu Y, Zhong W, Randell S, Sadek N, Zhang W, Chen G, Cheng C, et al. PAK signalling drives acquired drug resistance to MAPK inhibitors in BRAF-mutant melanomas. *Nature*. 2017; 550:133–6.  
<https://doi.org/10.1038/nature24040>  
PMID: [28953887](https://pubmed.ncbi.nlm.nih.gov/28953887/)
52. Murakami Y, Kazuno H, Emura T, Tsujimoto H, Suzuki N, Fukushima M. Different mechanisms of acquired resistance to fluorinated pyrimidines in human colorectal cancer cells. *Int J Oncol*. 2000; 17:277–83.  
<https://doi.org/10.3892/ijo.17.2.277>  
PMID: [10891536](https://pubmed.ncbi.nlm.nih.gov/10891536/)
53. Singh A, Settleman J. EMT, cancer stem cells and drug resistance: an emerging axis of evil in the war on cancer. *Oncogene*. 2010; 29:4741–51.  
<https://doi.org/10.1038/onc.2010.215>  
PMID: [20531305](https://pubmed.ncbi.nlm.nih.gov/20531305/)
54. Gao H, Korn JM, Ferretti S, Monahan JE, Wang Y, Singh M, Zhang C, Schnell C, Yang G, Zhang Y, Balbin OA, Barbe S, Cai H, et al. High-throughput screening using patient-derived tumor xenografts to predict clinical trial drug response. *Nat Med*. 2015; 21:1318–25.  
<https://doi.org/10.1038/nm.3954>  
PMID: [26479923](https://pubmed.ncbi.nlm.nih.gov/26479923/)
55. Hidalgo M, Amant F, Biankin AV, Budinská E, Byrne AT, Caldas C, Clarke RB, de Jong S, Jonkers J, Mælandsmo GM, Roman-Roman S, Seoane J, Trusolino L, Villanueva A. Patient-derived xenograft models: an emerging platform for translational cancer research. *Cancer Discov*. 2014; 4:998–1013.  
<https://doi.org/10.1158/2159-8290.CD-14-0001>  
PMID: [25185190](https://pubmed.ncbi.nlm.nih.gov/25185190/)
56. Li S, Shen D, Shao J, Crowder R, Liu W, Prat A, He X, Liu S, Hoog J, Lu C, Ding L, Griffith OL, Miller C, et al. Endocrine-therapy-resistant ESR1 variants revealed by genomic characterization of breast-cancer-derived xenografts. *Cell Rep*. 2013; 4:1116–30.  
<https://doi.org/10.1016/j.celrep.2013.08.022>  
PMID: [24055055](https://pubmed.ncbi.nlm.nih.gov/24055055/)
57. Siolas D, Hannon GJ. Patient-derived tumor xenografts: transforming clinical samples into mouse models. *Cancer Res*. 2013; 73:5315–9.  
<https://doi.org/10.1158/0008-5472.CAN-13-1069>  
PMID: [23733750](https://pubmed.ncbi.nlm.nih.gov/23733750/)
58. Munshi HG, Wu YI, Mukhopadhyay S, Ottaviano AJ, Sassano A, Koblinski JE, Platanias LC, Stack MS. Differential regulation of membrane type 1-matrix metalloproteinase activity by ERK 1/2- and p38 MAPK-modulated tissue inhibitor of metalloproteinases 2 expression controls transforming growth factor-beta1-induced pericellular collagenolysis. *J Biol Chem*. 2004; 279:39042–50.  
<https://doi.org/10.1074/jbc.M404958200>  
PMID: [15247230](https://pubmed.ncbi.nlm.nih.gov/15247230/)
59. Adya R, Tan BK, Pun A, Chen J, Rande HS. Visfatin induces human endothelial VEGF and MMP-2/9 production via MAPK and PI3K/Akt signalling pathways: novel insights into visfatin-induced angiogenesis. *Cardiovasc Res*. 2008; 78:356–65.  
<https://doi.org/10.1093/cvr/cvm111>  
PMID: [18093986](https://pubmed.ncbi.nlm.nih.gov/18093986/)
60. Duan S, Tsai Y, Keng P, Chen Y, Lee SO, Chen Y. IL-6 signaling contributes to cisplatin resistance in non-small cell lung cancer via the up-regulation of anti-apoptotic and DNA repair associated molecules. *Oncotarget*. 2015; 6:27651–60.  
<https://doi.org/10.18632/oncotarget.4753>  
PMID: [26313152](https://pubmed.ncbi.nlm.nih.gov/26313152/)
61. Navarro P, Bueno MJ, Zagorac I, Mondejar T, Sanchez J, Mourón S, Muñoz J, Gómez-López G, Jimenez-Renard V, Mulero F, Chandel NS, Quintela-Fandino M. Targeting Tumor Mitochondrial Metabolism Overcomes Resistance to Antiangiogenics. *Cell Rep*. 2016; 15:2705–18.  
<https://doi.org/10.1016/j.celrep.2016.05.052>  
PMID: [27292634](https://pubmed.ncbi.nlm.nih.gov/27292634/)
62. Wang T, Xiao M, Ge Y, Krepler C, Belser E, Lopez-Coral A, Xu X, Zhang G, Azuma R, Liu Q, Liu R, Li L, Amaravadi RK, et al. BRAF Inhibition Stimulates Melanoma-Associated Macrophages to Drive Tumor Growth. *Clin Cancer Res*. 2015; 21:1652–64.  
<https://doi.org/10.1158/1078-0432.CCR-14-1554>  
PMID: [25617424](https://pubmed.ncbi.nlm.nih.gov/25617424/)
63. Chirco R, Liu XW, Jung KK, Kim HR. Novel functions of TIMPs in cell signaling. *Cancer Metastasis Rev*. 2006; 25:99–113.  
<https://doi.org/10.1007/s10555-006-7893-x>  
PMID: [16680576](https://pubmed.ncbi.nlm.nih.gov/16680576/)
64. Goldberg GI, Marmer BL, Grant GA, Eisen AZ, Wilhelm S, He CS. Human 72-kilodalton type IV collagenase forms a complex with a tissue inhibitor of metalloproteases designated TIMP-2. *Proc Natl Acad Sci U S A*. 1989; 86:8207–11.  
<https://doi.org/10.1073/pnas.86.21.8207>  
PMID: [2554304](https://pubmed.ncbi.nlm.nih.gov/2554304/)
65. Stetler-Stevenson WG, Bersch N, Golde DW. Tissue inhibitor of metalloproteinase-2 (TIMP-2) has erythroid-potentiating activity. *FEBS Lett*. 1992; 296:231–4.  
[https://doi.org/10.1016/0014-5793\(92\)80386-u](https://doi.org/10.1016/0014-5793(92)80386-u)  
PMID: [1370805](https://pubmed.ncbi.nlm.nih.gov/1370805/)

66. Stetler-Stevenson WG, Brown PD, Onisto M, Levy AT, Liotta LA. Tissue inhibitor of metalloproteinases-2 (TIMP-2) mRNA expression in tumor cell lines and human tumor tissues. *J Biol Chem.* 1990; 265:13933–8.  
[https://doi.org/10.1016/S0021-9258\(18\)77438-3](https://doi.org/10.1016/S0021-9258(18)77438-3)  
PMID:[2380196](https://pubmed.ncbi.nlm.nih.gov/2380196/)
67. Visscher DW, Höyhty M, Ottosen SK, Liang CM, Sarkar FH, Crissman JD, Fridman R. Enhanced expression of tissue inhibitor of metalloproteinase-2 (TIMP-2) in the stroma of breast carcinomas correlates with tumor recurrence. *Int J Cancer.* 1994; 59:339–44.  
<https://doi.org/10.1002/ijc.2910590308>  
PMID:[7927938](https://pubmed.ncbi.nlm.nih.gov/7927938/)
68. Gouyer V, Conti M, Devos P, Zerimech F, Copin MC, Crème E, Wurtz A, Porte H, Huet G. Tissue inhibitor of metalloproteinase 1 is an independent predictor of prognosis in patients with nonsmall cell lung carcinoma who undergo resection with curative intent. *Cancer.* 2005; 103:1676–84.  
<https://doi.org/10.1002/cncr.20965>  
PMID:[15754326](https://pubmed.ncbi.nlm.nih.gov/15754326/)
69. Giannelli G, Bergamini C, Marinosci F, Fransvea E, Quaranta M, Lupo L, Schiraldi O, Antonaci S. Clinical role of MMP-2/TIMP-2 imbalance in hepatocellular carcinoma. *Int J Cancer.* 2002; 97:425–31.  
<https://doi.org/10.1002/ijc.1635>  
PMID:[11802202](https://pubmed.ncbi.nlm.nih.gov/11802202/)
70. Li S, Ferguson MJ, Hawkins CJ, Smith C, Elwood NJ. Human telomerase reverse transcriptase protects hematopoietic progenitor TF-1 cells from death and quiescence induced by cytokine withdrawal. *Leukemia.* 2006; 20:1270–8.  
<https://doi.org/10.1038/sj.leu.2404251>  
PMID:[16673017](https://pubmed.ncbi.nlm.nih.gov/16673017/)

# Binding of the angiogenic/senescence inducer CCN1/CYR61 to integrin $\alpha_6\beta_1$ drives endocrine resistance in breast cancer cells

Ingrid Espinoza<sup>1,\*</sup>, Lin Yang<sup>1,\*</sup>, Travis Vander Steen<sup>1</sup>, Luciano Vellon<sup>2</sup>, Elisabet Cuyàs<sup>3,4</sup>, Sara Verdura<sup>3,4</sup>, Lester Lau<sup>5</sup>, Javier A. Menendez<sup>3,4</sup>, Ruth Lupu<sup>1,6,7</sup>

<sup>1</sup>Department of Laboratory Medicine and Pathology, Division of Experimental Pathology, Mayo Clinic, Rochester, 55905 MN, USA

<sup>2</sup>Stem Cells Laboratory, Institute of Biology and Experimental Medicine (IBYME-CONICET), Buenos Aires C1428ADN, Argentina

<sup>3</sup>Program Against Cancer Therapeutic Resistance (ProCURE), Metabolism and Cancer Group, Catalan Institute of Oncology, Girona 17005, Spain

<sup>4</sup>Girona Biomedical Research Institute, Salt, Girona 17190, Spain

<sup>5</sup>Department of Biochemistry and Molecular Genetics, College of Medicine, The University of Illinois at Chicago, Chicago, IL 60607, USA

<sup>6</sup>Department of Biochemistry and Molecular Biology Laboratory, Mayo Clinic Minnesota, Rochester, MN 55905, USA

<sup>7</sup>Mayo Clinic Cancer Center, Rochester, MN 55905, USA

<sup>8</sup>Current address: Department of Preventive Medicine, John D. Bower School of Population Health, University of Mississippi Medical Center, Jackson, MS 39216, USA

<sup>9</sup>Current address: Cancer Institute, School of Medicine, University of Mississippi Medical Center, Jackson, MS 39216, USA

\*Equal contribution

**Correspondence to:** Javier A. Menendez, Ruth Lupu; email: [jmenendez@idibgi.org](mailto:jmenendez@idibgi.org), [lupu.ruth@mayo.edu](mailto:lupu.ruth@mayo.edu)

**Keywords:** matricellular proteins, CYR61, integrins, estrogen receptor, tamoxifen

**Received:** March 5, 2021

**Accepted:** January 29, 2022

**Published:** February 11, 2022

**Copyright:** © 2022 Espinoza et al. This is an open access article distributed under the terms of the [Creative Commons Attribution License](https://creativecommons.org/licenses/by/3.0/) (CC BY 3.0), which permits unrestricted use, distribution, and reproduction in any medium, provided the original author and source are credited.

## ABSTRACT

CCN1/CYR61 promotes angiogenesis, tumor growth and chemoresistance by binding to its integrin receptor  $\alpha_v\beta_3$  in endothelial and breast cancer (BC) cells. CCN1 controls also tissue regeneration by engaging its integrin receptor  $\alpha_6\beta_1$  to induce fibroblast senescence. Here, we explored if the ability of CCN1 to drive an endocrine resistance phenotype in estrogen receptor-positive BC cells relies on interactions with either  $\alpha_v\beta_3$  or  $\alpha_6\beta_1$ . First, we took advantage of site-specific mutagenesis abolishing the CCN1 receptor-binding sites to  $\alpha_v\beta_3$  and  $\alpha_6\beta_1$  to determine the integrin partner responsible for CCN1-driven endocrine resistance. Second, we explored a putative nuclear role of CCN1 in regulating ER $\alpha$ -driven transcriptional responses. Retroviral forced expression of a CCN1 derivative with a single amino acid change (D125A) that abrogates binding to  $\alpha_v\beta_3$  partially phenocopied the endocrine resistance phenotype induced upon overexpression of wild-type (WT) CCN1. Forced expression of the CCN1 mutant TM, which abrogates all the T1, H1, and H2 binding sites to  $\alpha_6\beta_1$ , failed to bypass the estrogen requirement for anchorage-independent growth or to promote resistance to tamoxifen. Wild-type CCN1 promoted estradiol-independent transcriptional activity of ER $\alpha$  and enhanced ER $\alpha$  agonist response to tamoxifen. The  $\alpha_6\beta_1$ -binding-defective TM-CCN1 mutant lost the ER $\alpha$  co-activator-like behavior of WT-CCN1. Co-immunoprecipitation assays revealed a direct interaction between endogenous CCN1 and ER $\alpha$ , and *in vitro* approaches confirmed the ability of recombinant CCN1 to bind ER $\alpha$ . CCN1 signaling via  $\alpha_6\beta_1$ , but not via  $\alpha_v\beta_3$ , drives an endocrine resistance phenotype that involves a direct binding of CCN1 to ER $\alpha$  to regulate its transcriptional activity in ER+ BC cells.



## INTRODUCTION

CCN1 (also named cysteine-rich angiogenic inducer 61 [CYR61]) is an archetypal component of the CCN (CYR61, CTGF, NOV) family of matricellular proteins [1–4]. CCN1 has diverse developmental functions in early life (e.g., placental angiogenesis, vascular integrity, and cardiac morphogenesis) and also plays critical roles in inflammation, wound healing, and tissue repair in the adult [5–13]. Aberrantly expressed CCN1 correlates with numerous chronic inflammation-related diseases, including cancer [14–20]. The ability of CCN1 to interact directly with multiple binding partners, particularly cell-surface integrin receptors but also as-yet-unidentified proteins, underlies its functional versatility [21, 22]. Crucially, the multifunctionality of CCN1 can be

attributed to its multimodular architecture, in which the location of several receptor-binding sites throughout the modular domains of CCN1 physically links CCN1-triggered signaling events to biological activities in a cell- and context- (physiological versus pathological) dependent manner [reviewed in 23, 24]. For instance, the interaction of the V2 functional site at the von Willebrand factor type C repeat (vWC) domain of CCN1 with integrin  $\alpha_v\beta_3$  in endothelial and cancer cells is critical for angiogenic and proliferative activities in embryonic development and tumor growth. By contrast, the interaction of the T1, H1, and H2 functional sites at the carboxy-terminal (CT) domain with integrin  $\alpha_6\beta_1$  (T1) and heparan sulfate proteoglycans (H1, H2) in fibroblasts is critical for apoptosis and cellular senescence phenomena during fibrosis and wound healing [25–28] (Figure 1).

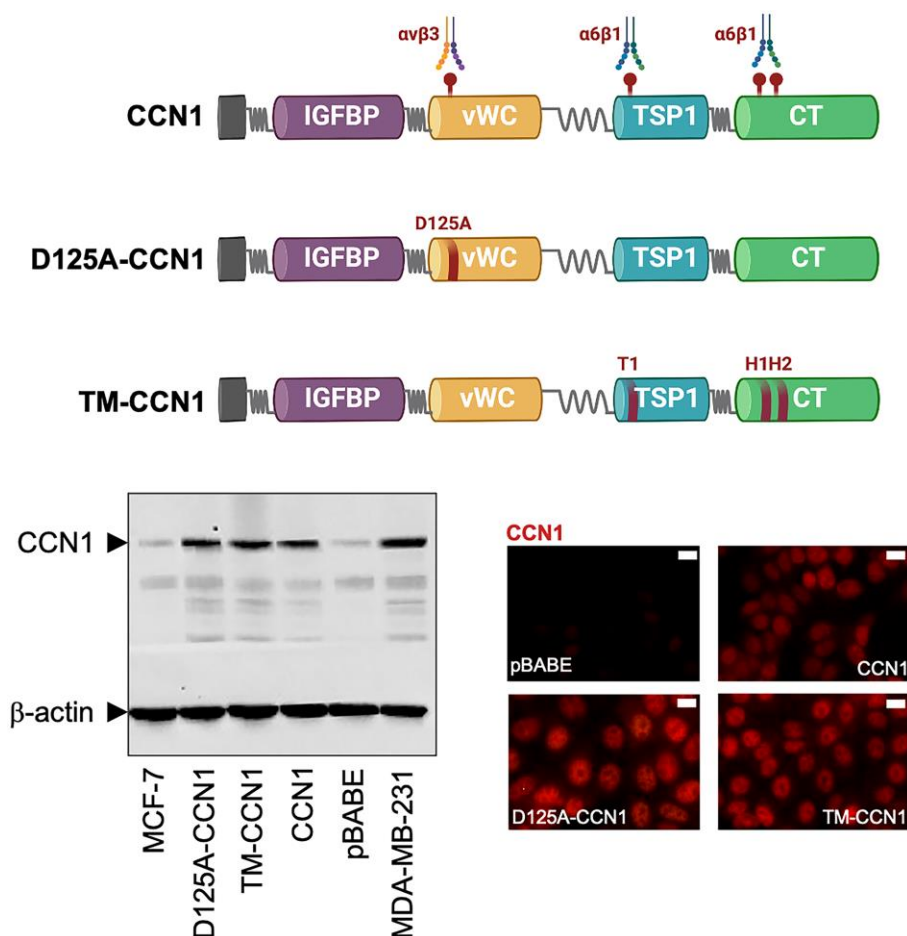


**Figure 1. Expression of CCN1 and CCN1 mutants in MCF-7 breast cancer cells.** Top: Schematic diagram showing the modular domain structure of wild-type CCN1 with the localization of several identified integrin-binding sites, and mutants either bearing the D125A mutation in vWC (D125A-CCN1) or combined mutations in T1, H1, and H2 in TSP1 and TC domains (TM-CCN1). *IGFBP*, insulin-like growth factor binding protein; *vWC*, von Willebrand factor type C repeats; *TSP-1*, thrombospondin type 1; *CT*, C-terminus. Bottom: Immunoblotting assessment of endogenous CCN1 protein in CCN1-overexpressing MDA-MB-231 cells and in MCF-7 cells retrovirally transduced with an empty vector (pBABE) or a vector containing either wild-type CCN1 or D125A-CCN1 and TM-CCN1 mutants. Microphotographs show representative *in situ* immunofluorescence staining of CCN1 in MCF-7/pBABE, MCF-7/CCN1, MCF-7/D125A-CCN1, and MCF-7/TM-CCN1 cells. Scale bar is 10  $\mu$ m. Results are representative of three independent experiments.

Our own previous studies and those of others have established a significant correlation between elevated levels of CCN1 and more advanced disease and metastatic phenotypes in *in vitro* breast cancer models and in patients [14–17, 20, 29–33]. Specifically, we demonstrated that the ability of CCN1 to drive breast tumor initiation, vascularization, and invasiveness, as well as to provide protection of breast cancer cells against chemotherapy-induced apoptosis, was largely mediated through binding to integrin  $\alpha_v\beta_3$ , whose expression is also induced by CCN1 [30, 34, 35]. *In vitro* studies have also clarified the ability of CCN1 to overcome estrogen dependency and elicit resistance to the selective estrogen receptor (ER) modulators and down-regulators (SERMs/SERDs) tamoxifen and fulvestrant in ER-positive breast cancer cells [15–17, 29, 31]. Patients with CCN1-overexpressing, hormone-dependent breast cancer respond poorly to the aromatase inhibitor letrozole [32]. In this context, a recent study has highlighted a role for CCN1 in the development of endocrine resistance in patients with breast cancer [33], identifying it as a potential therapeutic target to overcome refractoriness to a wide-range of antiestrogen therapies. Nonetheless, it is not clear whether the ability of CCN1 to bypass estrogen-dependence and drive resistance to endocrine therapy relies on the interaction with its cell-surface integrin receptors ( $\alpha_v\beta_3/\alpha_v\beta_5$  and  $\alpha_6\beta_1$ ) and/or with potential nuclear functions of CCN1 [36–38] that might affect ER $\alpha$ -driven transcriptional activity.

In the present study, we used previous mutational analyses showing that distinct integrin-binding sites of CCN1 can function independently of one another [25–28] to determine the signaling pathway through which CCN1 mediates endocrine resistance in breast cancer. We first employed site-specific CCN1 mutations specifically abolishing the receptor-binding sites to either  $\alpha_v\beta_3/\alpha_v\beta_5$  or  $\alpha_6\beta_1$  to delineate the integrin partner responsible for CCN1-driven endocrine resistance in breast cancer. Also, given the intriguing possibility that the nuclear localization of CCN1 may regulate gene transcription, we explored a putative nuclear role for CCN1 in regulating ER $\alpha$ -driven transcriptional responses.

## RESULTS

### Generation of ER-positive breast cancer cells overexpressing CCN1 and $\alpha_v\beta_3/\alpha_6\beta_1$ -binding-defective CCN1 mutants

Estrogen-dependent MCF-7 breast cancer cells, which naturally express very low levels of CCN1, were engineered to stably overexpress either wild-type CCN1 or the mutational derivatives D125A-CCN1, which

exhibits a disrupted  $\alpha_v\beta_3$ -binding site through the D125A mutation, and TM-CCN1, which abrogates all the T1, H1, and H2 binding sites to  $\alpha_6\beta_1$  (Figure 1) [25–28]. Immunoblotting procedures, which were performed following cell starvation to prevent the serum effect on CCN1 expression, confirmed that CCN1 was almost undetectable in MCF-7 parental and MCF-7/pBABE control cells but was noticeably elevated in MCF-7/CCN1, MCF-7/D125A-CCN1, and MCF-7/TM-CCN1 cells (Figure 1). CCN1 protein levels in MCF-7/CCN1, MCF-7/D125A-CCN1, and MCF-7/TM-CCN1 cells were comparable to those of MDA-MB-231 cells, a triple-negative breast cancer model naturally overexpressing CCN1 [15, 16]. Immunofluorescence analysis of CCN1 protein revealed that, in addition to its cytoplasmic location, CCN1 exhibited an apparent nuclear-staining pattern in the majority of MCF-7 breast cancer cell lines, with no evident differences between wild-type and mutant CCN1 (Figure 1).

### D125A-CCN1, but not TM-CCN1, phenocopies wild-type CCN1 to drive long-term acquisition of an estrogen-independent phenotype

We assessed whether specific modification of CCN1-integrin(s) binding would impact the ability of CCN1 to modulate estrogen dependency of ER-positive breast cancer cells. To do this, we first compared short-term (10 days) anchorage-independent growth of MCF-7/pBABE, MCF-7/CCN1, MCF-7/D125A-CCN1, and MCF-7/TM-CCN1 cells by colony formation assays in soft agar (Figure 2A, left panel). Forced expression of wild-type CCN1 promoted robust anchorage-independent growth of MCF-7/CCN1 cells in the absence of estradiol supplementation. By contrast, neither MCF-7/D125A-CCN1 nor MCF-7/TM-CCN1 cells formed colonies in the absence of estradiol (Figure 2A, left panel). Addition of estradiol failed to increase further the already strong colony formation capacity of MCF-7/CCN1 cells. E<sub>2</sub> supplementation augmented the anchorage-independent growth in MCF-7/D125A-CCN1 cells beyond that observed in E<sub>2</sub>-treated MCF-7/pBABE control cells (Figure 2A, left panel). Conversely, the estradiol-driven potentiation of anchorage-independent growth in MCF-7/TM-CCN1 cells was indistinguishable from that produced in MCF-7/pBABE control cells (Figure 2A, left panel).

We then re-assessed the patterns of anchorage-independent growth in the long-term absence of estrogens (up to 18 days in soft-agar). MCF-7/D125A-CCN1 cells were capable of strikingly circumvent estradiol requirement to form a similar number of colonies to those generated by MCF-7/CCN1 cells in the long-term (Figure 2A, right panel). The ability of

D125A-CCN1 to drive long-term acquisition of an estrogen-independent phenotype was much less pronounced with the TM-CCN1 derivative. Thus, although capable of forming colonies after long-term culture in the absence of estradiol, MCF-7/TM-CCN1 cells failed to fully recapitulate the highly-aggressive, estrogen-independent phenotype of MCF-7/CCN1 and MCF-7/D125A-CCN1 cells (Figure 2A, right panel).

## TM-CCN1, but not D125A-CCN1, loses the capacity of wild-type CCN1 to promote resistance to anti-estrogens

We next assessed whether modulation of CCN1 expression and/or specific modification of CCN1-integrin(s) binding would affect the anti-estrogen sensitivity of ER-positive breast cancer cells.

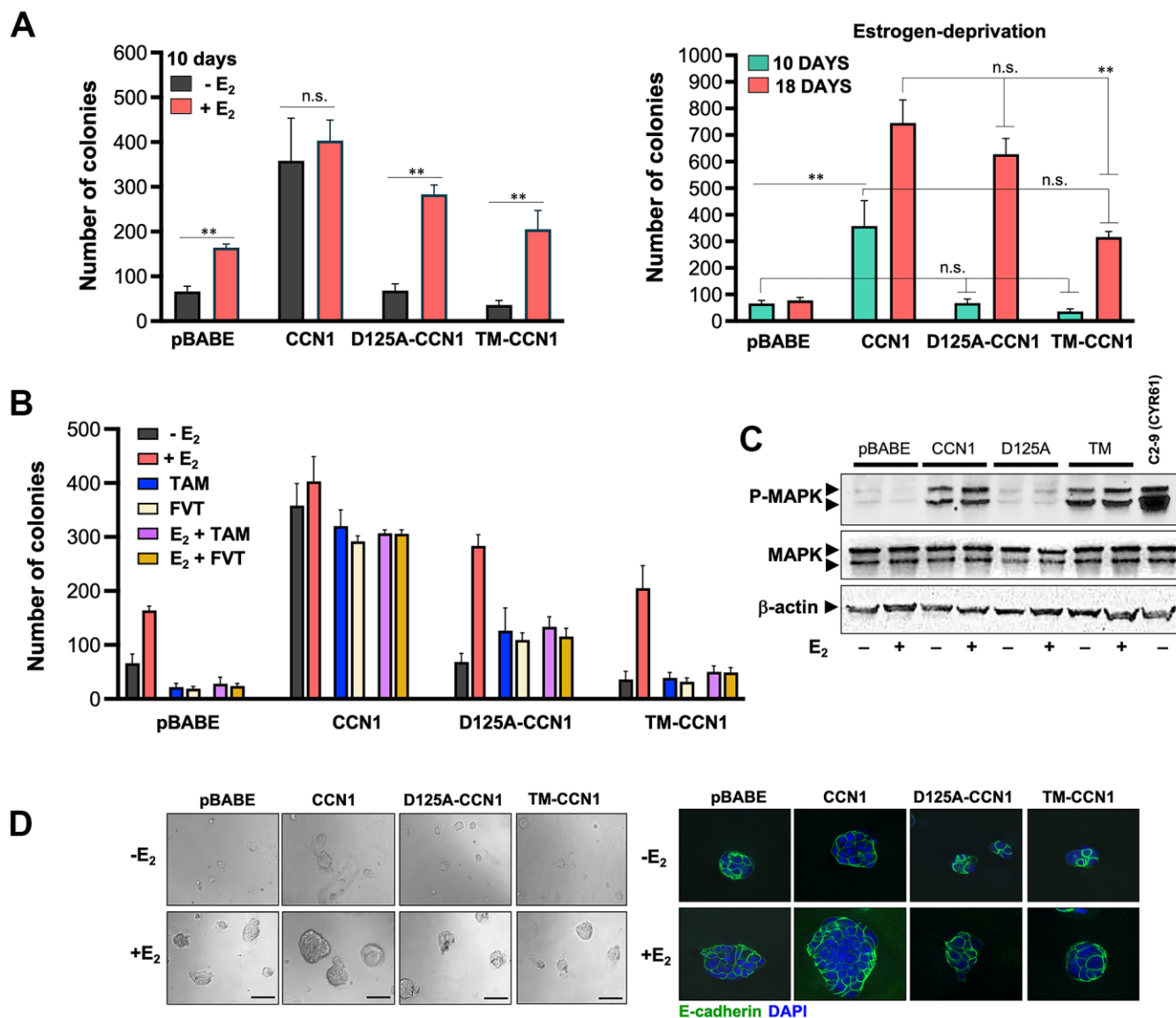


**Figure 2. CCN1 and D125A-CCN1, but not TM-CCN1, promote acquisition of an endocrine resistance phenotype in MCF-7 breast cancer cells.** (A, B) Estradiol (E<sub>2</sub>)-depleted cells were plated in soft agarose either containing or not E<sub>2</sub> (10<sup>-9</sup> M), tamoxifen (10<sup>-7</sup> M), fulvestrant (10<sup>-7</sup> M), their combinations, or vehicles only for either 10 or 18 days. Colony formation (≥50 μm) was assessed using a colony counter. Each experimental value represents the mean colony number (columns) ± S.D. (bars) from at least three separate experiments in which triplicate dishes were counted. (C) Immunoblot analyses of total and activated (phosphorylated) MAPK protein levels in MCF-7/pBABE, MCF-7/CCN1, MCF-7/D125A-CCN1, and MCF-7/TM-CCN1 cells. Blots were reprobed with an antibody for β-actin to control for protein loading and transfer. Results are representative of three independent experiments. (D) Phase contrast images of MCF-7/pBABE, MCF-7/CCN1, MCF-7/D125A-CCN1, and MCF-7/TM-CCN1 cells cultured in Matrigel® in the absence or presence of E<sub>2</sub> (10<sup>-9</sup> M). Scale bar is 100 μm. 3D cultures were stained for E-cadherin and nuclei were counterstained with DAPI.

Tamoxifen and fulvestrant completely inhibited the estradiol-stimulated anchorage-independent growth of MCF-7/pBABE cells, whereas forced expression of CCN1 fully abrogated the inhibitory effects of tamoxifen and fulvestrant on soft-agar colony formation irrespective of the presence or absence of estradiol (Figure 2B). Estradiol-independent colony formation capacity in MCF-7/D125A-CCN1 cells was weakly but significantly stimulated by tamoxifen and fulvestrant; such agonist effects on the anchorage-independent growth of MCF-7/D125A-CCN1 cells were not further enhanced by estradiol (Figure 2B). MCF-7/TM-CCN1 cells retained a *bona fide* endocrine-sensitive phenotype in which tamoxifen and fulvestrant failed to exhibit any agonist effect on the estradiol-independent colony formation capacity and estradiol stimulation failed to promote anchorage-independent growth in the presence of anti-estrogens (Figure 2B).

Because  $\alpha_v\beta_3$ -dependent activation of the MAPK pathway was previously found to drive CCN1-directed cell survival and chemoresistance [30], we explored whether specific modulation of the CCN1-integrin(s) binding differentially altered ERK1/ERK2 activity in breast cancer cells. The activation status of MAPK was significantly higher in MCF-7/CCN1 cells than in matched control MCF-7/pBABE cells by immunoblotting analysis (Figure 2C). Abrogation of CCN1 binding to  $\alpha_v\beta_3$  fully prevented CCN1-driven MAPK hyperactivation in MCF-7/D125-CCN1 cells, but the abrogation of CCN1 binding to  $\alpha_6\beta_1$  fully retained the ability of wild-type CCN1 to activate MAPK in MCF-7/TM-CCN1 cells (Figure 2C).

### CCN1-driven endocrine resistance does not alter 3D breast cancer colony morphology

Because cell culture in three-dimensional (3D) extracellular matrix (ECM) is considered as a more relevant model system to evaluate cancer cell behavior [39, 40], we evaluated the size, form, and E-cadherin distribution of colonies formed by MCF-7/pBABE, MCF-7/CCN1, MCF-7/D125A-CCN1, and MCF-7/TM-CCN1 cells cultured in Matrigel®. MCF-7/CCN1 cells formed larger colonies than MCF-7/pBABE, MCF-7/D125A-CCN1, and MCF-7/TM-CCN1 cells, an effect that was more notable in the presence of estradiol (Figure 2D, left panels). Despite the obvious differences in their colony sizes when grown on top an ECM gel, the expression of E-cadherin was not down-regulated in none of the CCN1-overexpressing cell models (Figure 2D, right panels). Overexpression of wild-type CCN1 and abrogation of CCN1 binding to  $\alpha_v\beta_3$  in MCF-7/D125-CCN1 cells and to  $\alpha_6\beta_1$  in MCF-7/TM-CCN1 cells were insufficient to promote the formation of branching colonies in 3D Matrigel cultures – a hallmark

of the invasive mesenchymal phenotype. Accordingly, MCF-7/pBABE, MCF-7/CCN1, MCF-7/D125A-CCN1, and MCF-7/TM-CCN1 cells all exhibited a mass-like morphology with disorganized nuclei and filled colony centers characteristic of luminal-like breast cancer cells [39, 40] (Figure 2D, right panels).

### CCN1 drives the constitutive activation of estrogen receptor transcriptional activity

To evaluate the effects of CCN1 expression and/or specific modification of CCN1-integrin(s) binding on ER $\alpha$ -transactivation and estradiol responsiveness, we transfected MCF-7/pBABE, MCF-7/CCN1, MCF-7/D125A-CCN1, and MCF-7/TM-CCN1 cells together with a Luciferase reporter gene linked to the consensus Estrogen Response Element (ERE-Luciferase). Transfected cells were then evaluated for changes in the levels of basal (estradiol-independent) and induced (estradiol-stimulated) ER $\alpha$  activity in the absence or presence of anti-estrogens. MCF-7/CCN1 cells showed a very strong constitutive activation of ER $\alpha$  transcriptional activity in the absence of estradiol stimulation, which was largely reduced in MCF-7/D125A-CCN1 cells and fully prevented in MCF-7/TM-CCN1 cells (Figure 3A). Both tamoxifen and fulvestrant failed to suppress the constitutive hyperactivation of ER $\alpha$ -driven transcription in MCF-7/CCN1 cells irrespective of the presence or absence of estradiol. Fulvestrant, but not tamoxifen, suppressed estradiol-induced activation of ERE activity in MCF-7/D125A-CCN1 cells (Figure 3A). Similar to MCF-7/pBABE control cells, MCF-7/TM-CCN1 cells were exquisitely responsive to the ability of tamoxifen and fulvestrant to suppress estradiol-induced agonist transactivation of ER $\alpha$  transcriptional activity (Figure 3A).

### CCN1 directly interacts with the estrogen receptor

Given the nuclear staining pattern of CCN1 in MCF-7/CCN1 cells, we envisioned that CCN1 might interact with ER $\alpha$ . Double immunofluorescence staining of CCN1 and ER $\alpha$  suggested a nuclear co-localization of these proteins in MCF-7/CCN1 cells (Figure 3B, top panels). Co-immunoprecipitation assays of whole cell extracts using anti-ER $\alpha$ , anti-CCN1, and nonspecific IgG antibodies confirmed the interaction between endogenous CCN1 and ER $\alpha$  in MCF-7/CCN1 cells (Figure 3B, bottom panels). Such a strong CCN1-ER $\alpha$  interaction was not detected in immunoblot analyses of immunoprecipitates from CCN1-negative MCF-7/pBABE cells. *In vitro* approaches confirmed the specific ability of recombinant GST-CCN1 to bind recombinant poly-histidine-tagged ER $\alpha$  (Figure 3C).



## DISCUSSION

We show that CCN1/CYR61 signaling via  $\alpha_6\beta_1$ , but not via  $\alpha_v\beta_3/\alpha_v\beta_5$ , drives an endocrine resistance phenotype that involves the unforeseen direct binding of CCN1 to ER $\alpha$  to regulate its transcriptional activity in breast cancer cells.

Increased expression of CCN1 might promote angiogenesis, deregulated proliferation, enhanced cell survival and tumor invasiveness, and chemoresistance in breast cancer cells by activating integrin  $\alpha_v\beta_3$ -driven cellular signaling [14, 17, 30, 41]. While accumulating evidence indicated that CCN1 serves a role in the development and maintenance of endocrine-resistant

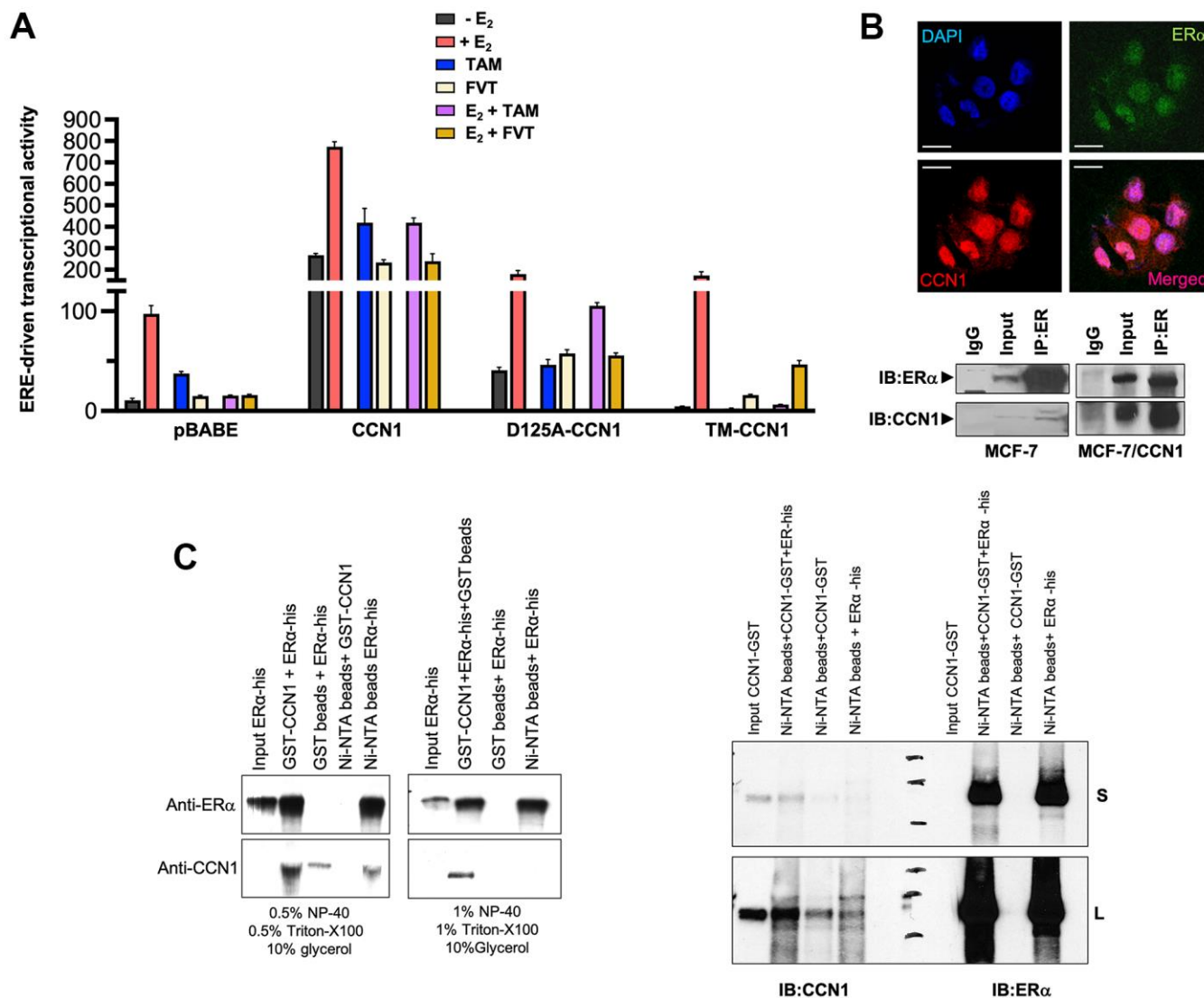


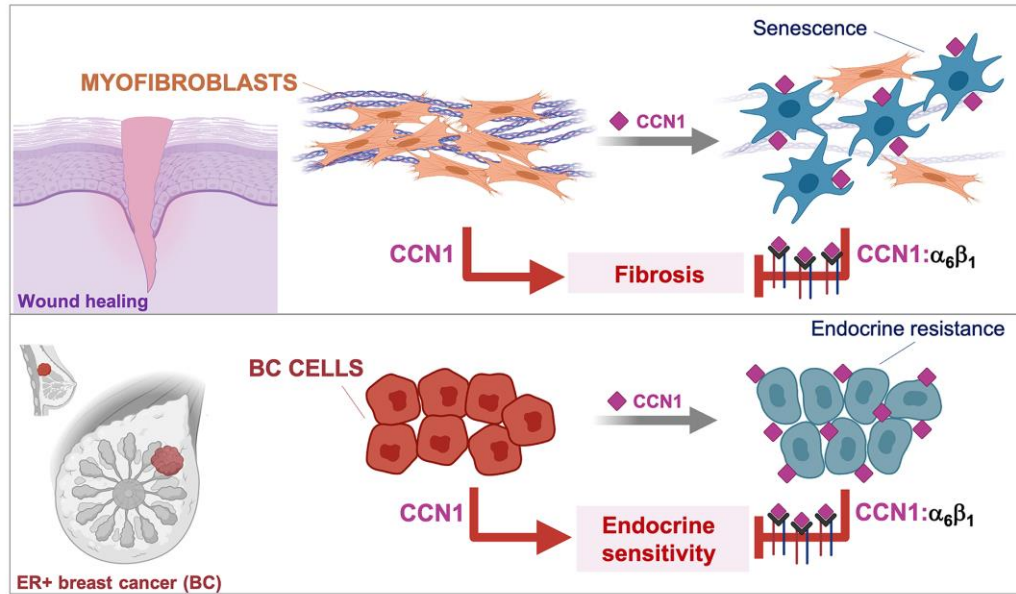
**Figure 3. CCN1 directly binds the estrogen receptor and regulates its transcriptional activity.** (A) MCF-7/pBABE, MCF-7/CCN1, MCF-7/D125A-CCN1, and MCF-7/TM-CCN1 cells were transiently with an ERE-Luciferase reporter (the ERE-containing reporter plasmid) and pRL/CMV (an internal reporter plasmid to control for transfection efficiency). Cells were incubated in the absence or presence of estradiol (E<sub>2</sub>, 10<sup>-9</sup> M), tamoxifen (10<sup>-7</sup> M), fulvestrant (10<sup>-7</sup> M), their combinations, or vehicles for 24 h, and cell extracts were analyzed for Luciferase activity. Data shown represent mean (columns)  $\pm$  S.D. (bars) (n=3). (B) Top: Microphotographs show representative *in situ* immunofluorescence staining of CCN1 and/or estrogen receptor (ER $\alpha$ ) in MCF-7/CCN1 cells. Scale bar is 10  $\mu$ m. Bottom: ER $\alpha$  in the cell lysates of MCF-7 and MCF-7/CCN1 cells was immunoprecipitated and immunoblotted with anti-ER $\alpha$  and anti-CCN1 antibodies. (C) Representative immunoprecipitation results of His-tagged ER $\alpha$  and GST-CCN1 using immobilized Ni<sup>2+</sup>. Purified GST-CCN1 protein was incubated with human recombinant ER $\alpha$ -His protein and Ni-NTA His•Bind resin beads. As controls, ER $\alpha$ -His protein was incubated with GST-only beads or GST-CCN1 was incubated with Ni-NTA beads alone. Proteins retained in the beads were denatured and blotted with the indicated antibodies. Results in (B, C) are representative of three independent experiments. (S: Short exposure; L: Long exposure).



phenotypes in ER-positive breast carcinomas [16, 17, 29, 32, 33], it remained untested whether the anti-estrogen activities of CCN1 were similarly mediated through binding to integrin  $\alpha_v\beta_3$  and/or to another integrin receptor such as  $\alpha_6\beta_1$ . To identify and dissect the differential functional roles of the CCN1-integrin interactions, we used a molecular strategy based on the specific disruption of integrin receptor-binding sites to test integrin-specific CCN1 functions in endocrine resistance. Importantly, CCN1 mutants employed in this study are biologically active, and their functional defects are indeed due to mutation of the specific receptor binding sites rather than structural perturbations [28]. Thus, whereas disruption of the CCN1  $\alpha_v\beta_3$ -binding site (D125A) specifically abolishes  $\alpha_v\beta_3$ - but not  $\alpha_6\beta_1$ -driven functions, a triple-CCN1 mutant disrupting all the  $\alpha_6\beta_1$ -binding sites (TM-CCN1) specifically abolishes  $\alpha_6\beta_1$ -dependent functions without affecting any of the  $\alpha_v\beta_3$ -mediated activities of CCN1 [23, 28]. We show that a single amino acid mutation in the  $\alpha_v\beta_3$  binding site within a 20-amino acid sequence (V2) in CCN1 failed to suppress the endocrine resistance phenotype induced by overexpressing the wild-type form of CCN1 in ER-positive MCF-7 breast cancer cells. Because D125A does not impair the binding of CCN1 to  $\alpha_6\beta_1$ , but fully prevents  $\alpha_v\beta_3$ -mediated intracellular signaling including induction of MAPK—which was previously demonstrated to drive chemoresistance in breast cancer cells [30]—CCN1-driven activation of MAPK appears to be dispensable for CCN1-driven endocrine resistance in breast cancer. Conversely, the CCN1 mutant TM, which abrogates all the T1, H1, and H2 binding sites to  $\alpha_6\beta_1$  but maintains its capacity to bind  $\alpha_v\beta_3$  (enabling the sustained activation of MAPK), fails to bypass the estrogen requirement for anchorage-independent growth or to promote resistance to tamoxifen. To our knowledge, this is first demonstration that the interaction between CCN1 with  $\alpha_6\beta_1$ , which is known to induce apoptosis or cellular senescence in fibroblasts to regulate the inflammatory response and control fibrosis during wound healing [11–13, 23], can be co-opted by ER-positive breast cancer cells to over-ride estrogen dependency and evade the growth-inhibitory effects of anti-estrogens (Figure 4A). Stimulation of breast cancer cell proliferation by estrogen and ER $\alpha$  might be, in part, due to the inhibition of senescence-like growth induced by oncogenic events in ER-positive breast cancer cells [42]. Suppressing ER $\alpha$  signaling with anti-estrogens such as tamoxifen is known to induce senescence-like phenotypes via induction of reactive oxygen species (ROS) [43]. Future studies are required to clarify whether the conversion of CCN1-overexpressing ER-positive breast cancer cells to an antiestrogen-resistant phenotype might associate with a shift toward a pro-oxidant environment as a result of the robust augmentation of ROS levels through binding of CCN1 to integrin  $\alpha_6\beta_1$  [44–46].

Despite the absence of a classical nuclear localization signal, CCN1 has unexpectedly been detected in the nucleus of cells [36]. Earlier studies suggested the intriguing possibility that CCN1 might regulate nuclear gene transcription through direct binding to DNA and/or to DNA-binding proteins [23, 36–38]. Here we found that overexpression of wild-type CCN1 promoted estradiol-independent transcriptional activity of ER $\alpha$  and enhanced ER $\alpha$  agonist response to tamoxifen. Moreover, we identified CCN1 as a previously unrecognized ER $\alpha$ -interacting protein and co-localizing with ER $\alpha$  in cell nuclei. Because the balance of coactivator and corepressor proteins in a cell may determine the response of the ER $\alpha$  to a particular ligand, these findings, overall, appear to illuminate an unforeseen coactivator-like behavior of nuclear CCN1 that could reduce the antagonist activity of tamoxifen-bound ER $\alpha$ . Intriguingly, whereas secreted wild-type CCN1 significantly modified ER $\alpha$  transcriptional activity, the tested secreted CCN1 mutants that failed to interact with either  $\alpha_v\beta_3$  or  $\alpha_6\beta_1$  notably differed in their ability to alter ER $\alpha$ -driven gene transcription (Figure 4B). The  $\alpha_v\beta_3$ -binding-defective D125A-CCN1 mutant was less potent than wild-type CCN1 at promoting estradiol-independent ER $\alpha$  transcriptional activity, but still retained its capacity to promote an ER $\alpha$  agonist response to tamoxifen in the presence of estradiol. It cannot, therefore, be excluded that bi-directional cross-talk between integrin  $\alpha_v\beta_3$  and ER $\alpha$  via ERK1/ERK2 activation in membrane-associated and/or cytosol localizations, which may result in the phosphorylation of nuclear tamoxifen-liganded ER $\alpha$  and its associated coactivators, might be part of the CCN1-driven endocrine resistant phenotype in breast cancer cells. It is noteworthy that connective tissue growth factor (CTGF), another archetypal member of the CCN family of matricellular proteins, has been shown to physically and functionally associate with ER $\alpha$  to inhibit its transcriptional activity as well as the expression of estradiol-responsive genes [47]. The interaction between the CTGF thrombospondin type I repeat, a cell attachment motif, and the DNA-binding domain of ER $\alpha$  was required for the repression of estrogen-responsive transcription by CTGF [47]. Here we show that the  $\alpha_6\beta_1$ -binding-defective TM-CCN1 protein entirely lacked the ability of wild-type CCN1 to exhibit an ER $\alpha$  co-activator-like behavior. While these data might suggest that binding to  $\alpha_6\beta_1$  is largely responsible for the capacity of CCN1 to regulate ER $\alpha$  transcriptional activity in an endocrine-resistant phenotype, future studies will be needed to clarify whether a direct interaction between CCN1 and ER $\alpha$ , which might be disrupted in the case of TM-CCN1, is required for the activation of estrogen/tamoxifen-responsive transcription by CCN1 in endocrine-resistant breast cancer cells (Figure 4).

A



B

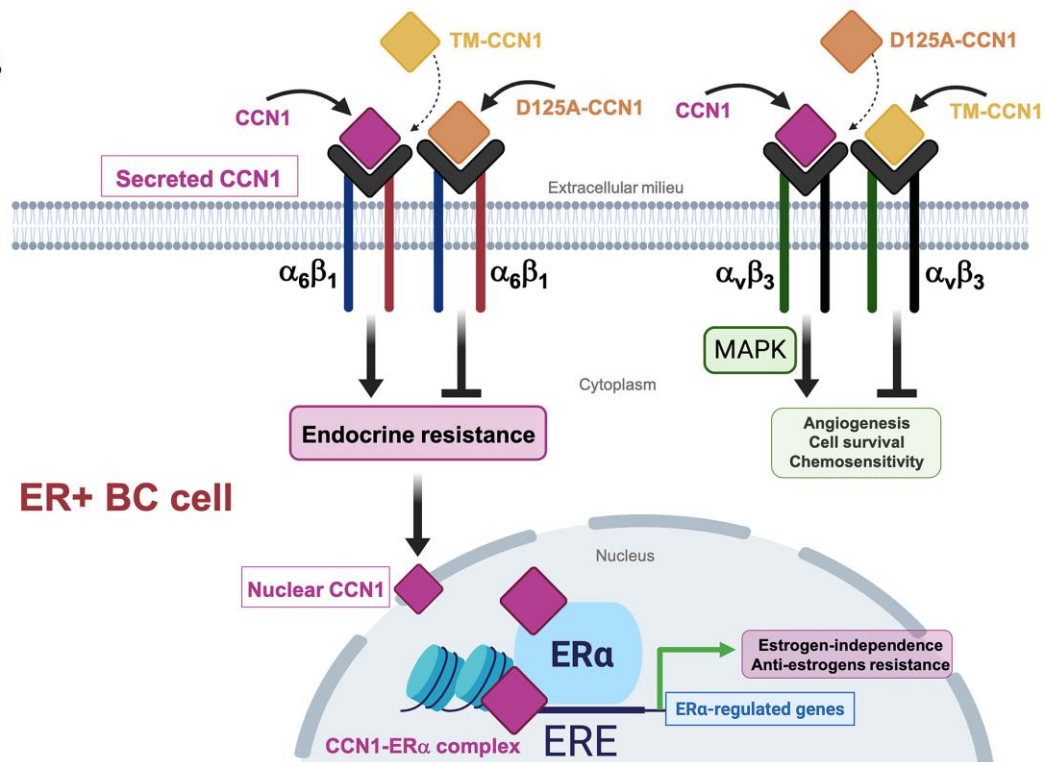


**Figure 4. Binding of the angiogenic/senescence inducer CCN1/CYR61 to integrin  $\alpha_6\beta_1$ , but not to  $\alpha_v\beta_3$ , drives endocrine resistance in breast cancer cells.** (A) Top: The binding of CCN1/CYR61 to its  $\alpha_6\beta_1$  receptor promotes myofibroblast senescence to impose self-limiting control on fibrogenesis during wound healing, thereby allowing tissue regeneration [11–13, 23, 48]. Bottom: CCN1 signaling via  $\alpha_6\beta_1$ , but not via  $\alpha_v\beta_3$ , drives an endocrine resistance phenotype in ER+ breast cancer cells. (B) The interaction between CCN1 and  $\alpha_v\beta_3$  is critical for angiogenic activities in endothelial cells and MAPK-related cell survival/chemosensitivity signaling in breast cancer cells. The interaction of CCN1 with  $\alpha_6\beta_1$  in fibroblasts is known to induce apoptosis or cellular senescence and has been widely regarded as a tumorigenesis-suppressing signaling mechanism. Here, we unveil the unforeseen capacity of CCN1 to signal through  $\alpha_6\beta_1$  in breast cancer cells to drive an endocrine resistant phenotype that might involve direct binding of CCN1 to ER $\alpha$  to regulate transcriptional events underlying estrogen-independence and anti-estrogen resistance in ER $\alpha$ -positive breast cancer cells. (ERE: Estrogen Response Elements).

CCN1/CYR61 might promote enhanced angiogenesis and deregulated proliferation and chemoresistance in breast tumors by binding to and activating  $\alpha_v\beta_3$  integrin signaling. CCN1/CYR61 promotes resolution of tissue fibrosis through induction of cellular senescence in myofibroblasts by engaging integrin  $\alpha_6\beta_1$  [11–13, 23]. Our present description of a novel role for the angiogenic/senescence inducer CCN1 in driving antiestrogen-resistance via  $\alpha_6\beta_1$  might provide a starting point to accelerate the development of CCN1/ $\alpha_6\beta_1$  integrin antagonists to therapeutically prevent the emergence of endocrine resistant phenotypes in ER-positive breast carcinomas.

## MATERIALS AND METHODS

### Cell culture

MCF-7 breast cancer cells were obtained from the American Type Culture Collection (ATCC) and were grown in phenol red-containing improved MEM (IMEM, Biosource International, Camarillo, CA, USA) supplemented with 5% fetal bovine serum (FBS) and 2 mM L-glutamine at 37° C in a humidified atmosphere of 95% air and 5% CO<sub>2</sub>. MCF-7 cells were authenticated to ensure their identity using a short tandem repeat profiling method provided by the Genotyping Shared Resource at Mayo Clinic Rochester.

MCF-7 cells were engineered to overexpress either wild-type CCN1 or CCN1 mutants with a single amino acid change (D125 to A), which abrogates binding to  $\alpha_v\beta_3/\alpha_v\beta_5$ -dependent activities (CCN1-D125A) or CCN1 disrupted in all three T1, H1, and H2 sites that completely abolishes  $\alpha_6\beta_1$ -mediated activities (CCN1-TM), which were generated as described [25–28]. For virus production, TSA54 cells were grown in 10-cm dishes until 70–80% confluency and were transfected using FuGENE 6 (Roche Biochemicals, Indianapolis, IN, USA) with pBABE-Puro Retroviral Vector (10  $\mu$ g) or CCN1 mutants cloned into the pBABE-Puro vector (10  $\mu$ g) plus packaging plasmid PIK (10  $\mu$ g). Twenty-four hours after transfection, the medium containing viral particles was collected and filtered through a 0.45- $\mu$ m filter. MCF-7 cells growing at 70–80% confluency were infected twice with the viral particles and selected with 2.5  $\mu$ g/ml puromycin. Stable transfected pools were maintained in puromycin-containing media for 4 weeks. CCN1/CYR61 expression levels were monitored by immunoblotting and immunofluorescence. Cells were regularly tested to confirm the absence of mycoplasma using the MycoAlert® Mycoplasma Detection Kit (Lonza, Walkersville, MD, USA).

### Immunoblotting analysis of CCN1

Cells were serum-starved overnight, washed twice with phosphate buffered saline (PBS) and lysed in a buffer (20 mM Tris, pH 7.5, 150 mM NaCl, 1 mM EDTA, 1 mM EGTA, 1% Triton X-100, 2.5 mM sodium pyrophosphate, 1 mM  $\beta$ -glycerolphosphate, 1 mM Na<sub>3</sub>VO<sub>4</sub>, 1  $\mu$ g/mL leupeptin, 1 mM phenyl-methylsulfonylfluoride) for 30 min on ice. Lysates were cleared by centrifugation (15 min at 14,000 rpm at 4° C). Protein content was determined against a standardized control using the Pierce Protein Assay Kit (Rockford, IL, USA). Equal amounts of protein (50  $\mu$ g) were resuspended in 5 $\times$  Laemmli sample buffer and denatured for 5 min at 99° C. Proteins were resolved by electrophoresis in 10% SDS-PAGE gels, and transferred to PVDF membranes (Amersham Biosciences Ltd., Little Chalfont, Bucks, UK). Non-specific binding was minimized by blocking membranes with PBS-T (PBS and 0.5% Tween 20) containing 5% (w/v) non-fat dry milk for 1 h at room temperature. Membranes were washed in PBS-T and incubated overnight with a 1:2000 dilution of a rabbit anti-CCN1 polyclonal antibody (ab2026, Novus Biologicals, Inc., Littleton, CO, USA) at 4° C. After three washes with PBS-T, blots were incubated with 1:2000 dilution of a horseradish peroxidase-linked donkey anti-rabbit IgG secondary antibody for 45 min, and immunoreactive bands of CCN1 were detected using the enhanced chemiluminescence reagent (Pierce). Blots were re-probed with an antibody for  $\beta$ -actin goat polyclonal antibody (Santa Cruz Biotechnology, Santa Cruz, CA, USA). Densitometric values of CCN1 protein bands were quantified using the Scion Imaging software (Scion Corp., Frederick, MD, USA).

### In situ immunofluorescence staining

Cells were seeded at a density of  $5 \times 10^3$  cells/well in an 8-well chamber slide (Nalge Nunc International, Rochester, NY, USA). After 24 h of incubation, cells were washed with PBS, fixed in 4% paraformaldehyde in PBS for 15 min at room temperature, permeabilized with 0.2% Triton X-100/PBS for 15 min, and stored overnight at 4° C with 10% horse serum in PBS. Cells were then washed and then incubated for 1 h with an anti-CCN1 antibody diluted 1:200 in 5% BSA. After extensive washes, the cells were incubated for 1 h with a TRITC-conjugated anti-rabbit IgG secondary antibody (Jackson ImmunoResearch Labs, West Grove, PA, USA) diluted 1:200 in 5% BSA. The cells were washed five times with PBS and mounted with VECTASHIELD+DAPI (Vector Laboratories, Burlingame, CA, USA). As controls, cells were stained with primary or secondary antibody alone. No significant fluorescence was found in control experiments (data not shown). Indirect immuno-



fluorescence was recorded on a Zeiss microscope (Jena, Germany). Images were noise-filtered, corrected for background, and prepared using Adobe Photoshop (San Jose, CA, USA).

### Soft agar colony formation assays

The efficiency of colony formation in liquid culture was determined by monitoring anchorage-independent cell growth in soft-agar. Cells were grown in phenol red-free IMEM and 5% charcoal calf serum (CCS) for 5 days in T-75 flasks to deplete estrogen. A bottom layer of 1.5 mL (2×) phenol red-free IMEM containing 1.2% agar and 10% CCS was prepared in 6 well plates. After the bottom layer solidified, cells (20,000 cells/well) were added in a 1 mL top layer containing either estradiol ( $10^{-9}$  M) and/or the anti-estrogens 4-OH-tamoxifen ( $10^{-7}$  M) or fulvestrant ( $10^{-7}$  M) in 0.7% agar and 10% CCS. Plates were incubated in a humidified 5% CO<sub>2</sub> incubator at 37° C, and colonies measuring  $\geq 50$   $\mu$ m were counted after 10–18 days using a cell colony counter (Optonix GelCount™, Abingdon, UK) after staining with nitroblue tetrazolium (Sigma-Aldrich, St. Louis, MO, USA). Assays were carried out in triplicate.

### Three-dimensional culture on Matrigel®

Single-cell suspensions of cells were prepared using trypsin. Cells ( $2 \times 10^3$ /well) in 0.4 mL of 2% Matrigel® in 1× IMEM were then plated on top of a polymerized layer of 100% Matrigel® using 8-well chamber slides. Cells were treated with estradiol and medium was replenished every 3 days. Control wells were maintained in medium containing 5% FBS. Cultures were kept for 5 days. Phase-contrast images were obtained under  $\times 100$  magnification.

### ERE-Luciferase activity

ER transcriptional activity was assessed using an ERE-driven reporter assay. Cells were propagated in estradiol-deprived (phenol red-free) IMEM supplemented with 5% CCS for 4 days before the onset of experiments, thereby ensuring the complete depletion of estradiol-like compounds from the medium. For experiments, cells were seeded into 12-well plates at  $1 \times 10^5$  cells/well. Cells were transfected using FuGENE 6 (Roche Biochemicals) with 0.75  $\mu$ g/well of the estrogen-responsive reporter (ERE), containing a *Xenopus* vitellogenin A<sub>2</sub>-derived ERE, along with 0.05  $\mu$ g/well of the internal control plasmid pRL-CMV, employed to correct for transfection efficiency. After 18 h, the transfected cells were washed and then incubated in fresh medium containing 5% CCS, supplemented with estradiol ( $10^{-9}$  M), tamoxifen ( $10^{-7}$  M), fulvestrant ( $10^{-7}$  M), or their

combinations, as specified. Approximately 24 h after treatments, Luciferase activity from cell extracts was measured using a Dual Luciferase Assay System (Promega, Madison, WI, USA) on a TD-20/20 luminometer (Turner Designs, Sunnyvale, CA, USA). The magnitude of activation in ERE-Luciferase-transfected cells treated with the vehicle was determined after normalization to the activity of pRL-CMV and was defined as 1.0-fold. This control value was used to calculate the relative (fold) change in transcriptional activities of ERE-Luciferase-transfected cells in response to treatments after normalization to pRL-CMV activity. All data were normalized as the ratio of raw light units to pRL-CMV unit corrected for pRL-CMV activity, and were shown as the mean  $\pm$  SD from three separate experiments performed in triplicate.

### In vitro binding assays

The CCN1 coding sequence was cloned in-frame with the glutathione S-transferase (GST) gene at the EcoRI and SalI sites in the pGEX-4T1 vector. Production and purification of the CCN1-GST fusion protein was carried out as described [49]. Recombinant human estrogen receptor alpha (His-tag) (ab240853) was purchased from Abcam (Cambridge, UK). Ni-NTA His•Bind Resin, a high-performance Ni<sup>2+</sup>-charged agarose used for rapid one-step purification of proteins containing a His•Tag sequence by metal chelation chromatography, was purchased from Sigma-Aldrich (70666-3). Pierce™ Glutathione Agarose was obtained from ThermoFisher Scientific (San Jose, CA, USA) (16102BID). GST-CCN1 fusion protein was incubated with recombinant human estrogen receptor His-tagged protein and Ni-NTA His beads in the incubation buffer (pH 7.35, 150 mM NaCl, 0.5 mM EDTA, 50 mM Tris-HCl and 0.5% NP-40) at 4° C for 4 hours. After the incubation, the beads were washed for 15 min with washing buffer (pH 7.35, 0.5–1% NP-40+0.5–1% Triton-X100+10% glycerol) on a shaker in the cold room 5 times. The protein complexes bound to the beads were separated with SDS-PAGE and blotted with the indicated antibodies.

### Statistical analysis

For all experiments, at least 3 independent experiments were performed with  $n \geq 3$  replicate samples per experiment. Data were presented as mean  $\pm$  S.D. Comparisons of means of  $\geq 3$  groups were performed by one-way analysis of variance and Dunnett's t-test for multiple comparisons using GraphPad Prism (GraphPad Software, San Diego, CA, USA). In all studies, p-values  $< 0.05$  and  $< 0.005$  were considered to be statistically significant (denoted as \* and \*\*, respectively). All statistical tests were two-sided.

## AUTHOR CONTRIBUTIONS

Ingrid Espinoza: Investigation, Validation, Formal analysis, Data Curation. Lin Yang: Investigation, Validation, Formal analysis, Data Curation. Travis Vander Steen: Investigation, Validation, Formal analysis, Data Curation. Luciano Vellon: Investigation, Formal analysis, Data Curation. Elisabet Cuyàs: Investigation, Formal analysis, Data Curation. Sara Verdura: Investigation, Formal analysis, Data Curation. Lester Lau: Conceptualization, Methodology, Resources, Supervision. Javier A. Menendez: Conceptualization, Validation, Formal analysis, Writing -Original Draft-, Writing -Review and Editing, Funding acquisition. Ruth Lupu: Conceptualization, Methodology, Validation, Resources, Writing -Original Draft-, Writing -Review and Editing-, Supervision, Funding acquisition. All authors have read, revised, and agreed to the submitted version of the manuscript.

## CONFLICTS OF INTEREST

The authors declare that the research was conducted in the absence of any commercial or financial relationships that could be construed as a potential conflict of interest.

## FUNDING

This work was supported by the NIH National Cancer Institute Grants R01 CA118975 and R01 CA116623 (to Ruth Lupu) and by the U.S. Department of Defense (DOD)-Breakthrough 3 Grants BC151072 and BC151072P1 (to Ruth Lupu). Work in the Menendez laboratory is supported by the Spanish Ministry of Science and Innovation (Grant PID2019-10455GB-I00, Plan Nacional de I+D+I, funded by the European Regional Development Fund, Spain) and by an unrestricted research grant from the Fundació Oncolliga Girona (Lliga catalana d'ajuda al malalt de càncer, Girona). Elisabet Cuyàs holds a research contract "Miguel Servet" (CP20/00003) from the Instituto de Salud Carlos III, Spanish Ministry of Science and Innovation (Spain). The authors would like to thank Kenneth McCreath for editorial support.

## REFERENCES

1. Perbal B. CCN proteins: multifunctional signalling regulators. *Lancet*. 2004; 363:62–4.  
[https://doi.org/10.1016/S0140-6736\(03\)15172-0](https://doi.org/10.1016/S0140-6736(03)15172-0)  
PMID:14723997
2. Bleau AM, Planque N, Perbal B. CCN proteins and cancer: two to tango. *Front Biosci*. 2005; 10:998–1009.  
<https://doi.org/10.2741/1594> PMID:15769600
3. Holbourn KP, Acharya KR, Perbal B. The CCN family of proteins: structure-function relationships. *Trends Biochem Sci*. 2008; 33:461–73.  
<https://doi.org/10.1016/j.tibs.2008.07.006>  
PMID:18789696
4. Perbal B. The concept of the CCN protein family revisited: a centralized coordination network. *J Cell Commun Signal*. 2018; 12:3–12.  
<https://doi.org/10.1007/s12079-018-0455-5>  
PMID:29470822
5. O'Brien TP, Yang GP, Sanders L, Lau LF. Expression of *cyr61*, a growth factor-inducible immediate-early gene. *Mol Cell Biol*. 1990; 10:3569–77.  
<https://doi.org/10.1128/mcb.10.7.3569-3577.1990>  
PMID:2355916
6. O'Brien TP, Lau LF. Expression of the growth factor-inducible immediate early gene *cyr61* correlates with chondrogenesis during mouse embryonic development. *Cell Growth Differ*. 1992; 3:645–54.  
PMID:1419914
7. Kireeva ML, Mo FE, Yang GP, Lau LF. *Cyr61*, a product of a growth factor-inducible immediate-early gene, promotes cell proliferation, migration, and adhesion. *Mol Cell Biol*. 1996; 16:1326–34.  
<https://doi.org/10.1128/MCB.16.4.1326>  
PMID:8657105
8. Wong M, Kireeva ML, Kolesnikova TV, Lau LF. *Cyr61*, product of a growth factor-inducible immediate-early gene, regulates chondrogenesis in mouse limb bud mesenchymal cells. *Dev Biol*. 1997; 192:492–508.  
<https://doi.org/10.1006/dbio.1997.8766>  
PMID:9441684
9. Kireeva ML, Latinkić BV, Kolesnikova TV, Chen CC, Yang GP, Abler AS, Lau LF. *Cyr61* and *Fisp12* are both ECM-associated signaling molecules: activities, metabolism, and localization during development. *Exp Cell Res*. 1997; 233:63–77.  
<https://doi.org/10.1006/excr.1997.3548>  
PMID:9184077
10. Kolesnikova TV, Lau LF. Human *CYR61*-mediated enhancement of bFGF-induced DNA synthesis in human umbilical vein endothelial cells. *Oncogene*. 1998; 16:747–54.  
<https://doi.org/10.1038/sj.onc.1201572>  
PMID:9488038
11. Jun JI, Lau LF. The matricellular protein CCN1 induces fibroblast senescence and restricts fibrosis in cutaneous wound healing. *Nat Cell Biol*. 2010; 12:676–85.  
<https://doi.org/10.1038/ncb2070> PMID:20526329
12. Kim KH, Chen CC, Monzon RI, Lau LF. Matricellular protein CCN1 promotes regression of liver fibrosis



- through induction of cellular senescence in hepatic myofibroblasts. *Mol Cell Biol*. 2013; 33:2078–90.  
<https://doi.org/10.1128/MCB.00049-13>  
PMID:23508104
13. Jun JI, Lau LF. Cellular senescence controls fibrosis in wound healing. *Aging (Albany NY)*. 2010; 2:627–31.  
<https://doi.org/10.18632/aging.100201>  
PMID:20930261
  14. Babic AM, Kireeva ML, Kolesnikova TV, Lau LF. CYR61, a product of a growth factor-inducible immediate early gene, promotes angiogenesis and tumor growth. *Proc Natl Acad Sci USA*. 1998; 95:6355–60.  
<https://doi.org/10.1073/pnas.95.11.6355>  
PMID:9600969
  15. Tsai MS, Hornby AE, Lakins J, Lupu R. Expression and function of CYR61, an angiogenic factor, in breast cancer cell lines and tumor biopsies. *Cancer Res*. 2000; 60:5603–7.  
PMID:11059746
  16. Tsai MS, Bogart DF, Castañeda JM, Li P, Lupu R. Cyr61 promotes breast tumorigenesis and cancer progression. *Oncogene*. 2002; 21:8178–85.  
<https://doi.org/10.1038/sj.onc.1205682>  
PMID:12444554
  17. Menéndez JA, Mehmi I, Griggs DW, Lupu R. The angiogenic factor CYR61 in breast cancer: molecular pathology and therapeutic perspectives. *Endocr Relat Cancer*. 2003; 10:141–52.  
<https://doi.org/10.1677/erc.0.0100141>  
PMID:12790776
  18. Gery S, Xie D, Yin D, Gabra H, Miller C, Wang H, Scott D, Yi WS, Popoviciu ML, Said JW, Koeffler HP. Ovarian carcinomas: CCN genes are aberrantly expressed and CCN1 promotes proliferation of these cells. *Clin Cancer Res*. 2005; 11:7243–54.  
<https://doi.org/10.1158/1078-0432.CCR-05-0231>  
PMID:16243794
  19. Watari H, Xiong Y, Hassan MK, Sakuragi N. Cyr61, a member of ccn (connective tissue growth factor/cysteine-rich 61/nephroblastoma overexpressed) family, predicts survival of patients with endometrial cancer of endometrioid subtype. *Gynecol Oncol*. 2009; 112:229–34.  
<https://doi.org/10.1016/j.ygyno.2008.09.039>  
PMID:19007976
  20. Huang YT, Lan Q, Lorusso G, Duffey N, Rüegg C. The matricellular protein CYR61 promotes breast cancer lung metastasis by facilitating tumor cell extravasation and suppressing anoikis. *Oncotarget*. 2017; 8:9200–15.  
<https://doi.org/10.18632/oncotarget.13677>  
PMID:27911269
  21. Lau LF, Lam SC. The CCN family of angiogenic regulators: the integrin connection. *Exp Cell Res*. 1999; 248:44–57.  
<https://doi.org/10.1006/excr.1999.4456>  
PMID:10094812
  22. Lau LF. Cell surface receptors for CCN proteins. *J Cell Commun Signal*. 2016; 10:121–7.  
<https://doi.org/10.1007/s12079-016-0324-z>  
PMID:27098435
  23. Lau LF. CCN1/CYR61: the very model of a modern matricellular protein. *Cell Mol Life Sci*. 2011; 68:3149–63.  
<https://doi.org/10.1007/s00018-011-0778-3>  
PMID:21805345
  24. Kim KH, Won JH, Cheng N, Lau LF. The matricellular protein CCN1 in tissue injury repair. *J Cell Commun Signal*. 2018; 12:273–9.  
<https://doi.org/10.1007/s12079-018-0450-x>  
PMID:29357009
  25. Grzeszkiewicz TM, Kirschling DJ, Chen N, Lau LF. CYR61 stimulates human skin fibroblast migration through Integrin alpha vbeta 5 and enhances mitogenesis through integrin alpha vbeta 3, independent of its carboxyl-terminal domain. *J Biol Chem*. 2001; 276:21943–50.  
<https://doi.org/10.1074/jbc.M100978200>  
PMID:11287419
  26. Leu SJ, Liu Y, Chen N, Chen CC, Lam SC, Lau LF. Identification of a novel integrin alpha 6 beta 1 binding site in the angiogenic inducer CCN1 (CYR61). *J Biol Chem*. 2003; 278:33801–8.  
<https://doi.org/10.1074/jbc.M305862200>  
PMID:12826661
  27. Chen N, Leu SJ, Todorovic V, Lam SC, Lau LF. Identification of a novel integrin alphavbeta3 binding site in CCN1 (CYR61) critical for pro-angiogenic activities in vascular endothelial cells. *J Biol Chem*. 2004; 279:44166–76.  
<https://doi.org/10.1074/jbc.M406813200>  
PMID:15308622
  28. Leu SJ, Chen N, Chen CC, Todorovic V, Bai T, Juric V, Liu Y, Yan G, Lam SC, Lau LF. Targeted mutagenesis of the angiogenic protein CCN1 (CYR61). Selective inactivation of integrin alpha6beta1-heparan sulfate proteoglycan coreceptor-mediated cellular functions. *J Biol Chem*. 2004; 279:44177–87.  
<https://doi.org/10.1074/jbc.M407850200>  
PMID:15322081
  29. Xie D, Miller CW, O’Kelly J, Nakachi K, Sakashita A, Said JW, Gornbein J, Koeffler HP. Breast cancer. Cyr61 is overexpressed, estrogen-inducible, and associated with more advanced disease. *J Biol Chem*. 2001; 276:14187–94.

- <https://doi.org/10.1074/jbc.M009755200>  
PMID:11297518
30. Menendez JA, Vellon L, Mehmi I, Teng PK, Griggs DW, Lupu R. A novel CYR61-triggered 'CYR61-alpha(v)beta3 integrin loop' regulates breast cancer cell survival and chemosensitivity through activation of ERK1/ERK2 MAPK signaling pathway. *Oncogene*. 2005; 24:761–79.  
<https://doi.org/10.1038/sj.onc.1208238>  
PMID:15592521
  31. Menendez JA, Vellon L, Espinoza I, Lupu R. The metastasis inducer CCN1 (CYR61) activates the fatty acid synthase (FASN)-driven lipogenic phenotype in breast cancer cells. *Oncoscience*. 2016; 3:242–57.  
<https://doi.org/10.18632/oncoscience.314>  
PMID:27713913
  32. Jia X, Liu G, Cheng J, Shen Z, Shao Z. CYR61 Confers the Sensitivity to Aromatase Inhibitor Letrozole in ER Positive Breast Carcinoma. *Curr Cancer Drug Targets*. 2017; 17:191–7.  
<https://doi.org/10.2174/1568009616666160426125058> PMID:27113745
  33. Mayer S, Erbes T, Timme-Bronsert S, Jaeger M, Rücker G, Kuf F, Stickeler E, Gitsch G, Hirschfeld M. Clinical relevance of Cyr61 expression in patients with hormone-dependent breast cancer. *Oncol Lett*. 2017; 14:2334–40.  
<https://doi.org/10.3892/ol.2017.6406>  
PMID:28789451
  34. Vellon L, Menendez JA, Lupu R. AlphaVbeta3 integrin regulates heregulin (HRG)-induced cell proliferation and survival in breast cancer. *Oncogene*. 2005; 24:3759–73.  
<https://doi.org/10.1038/sj.onc.1208452>  
PMID:15782133
  35. Vellon L, Menendez JA, Lupu R. A bidirectional "alpha(v)beta(3) integrin-ERK1/ERK2 MAPK" connection regulates the proliferation of breast cancer cells. *Mol Carcinog*. 2006; 45:795–804.  
<https://doi.org/10.1002/mc.20242>  
PMID:16705745
  36. Tamura I, Rosenbloom J, Macarak E, Chaqour B. Regulation of Cyr61 gene expression by mechanical stretch through multiple signaling pathways. *Am J Physiol Cell Physiol*. 2001; 281:C1524–32.  
<https://doi.org/10.1152/ajpcell.2001.281.5.C1524>  
PMID:11600415
  37. Leng E, Malcolm T, Tai G, Estable M, Sadowski I. Organization and expression of the Cyr61 gene in normal human fibroblasts. *J Biomed Sci*. 2002; 9:59–67.  
<https://doi.org/10.1007/BF02256579> PMID:11810026
  38. Sabbah M, Prunier C, Ferrand N, Megalophonos V, Lambein K, De Wever O, Nazaret N, Lachuer J, Dumont S, Redeuilh G. CCN5, a novel transcriptional repressor of the transforming growth factor  $\beta$  signaling pathway. *Mol Cell Biol*. 2011; 31:1459–69.  
<https://doi.org/10.1128/MCB.01316-10>  
PMID:21262769
  39. Kenny PA, Lee GY, Myers CA, Neve RM, Semeiks JR, Spellman PT, Lorenz K, Lee EH, Barcellos-Hoff MH, Petersen OW, Gray JW, Bissell MJ. The morphologies of breast cancer cell lines in three-dimensional assays correlate with their profiles of gene expression. *Mol Oncol*. 2007; 1:84–96.  
<https://doi.org/10.1016/j.molonc.2007.02.004>  
PMID:18516279
  40. Luca AC, Mersch S, Deenen R, Schmidt S, Messner I, Schäfer KL, Baldus SE, Huckenbeck W, Piekorz RP, Knoefel WT, Krieg A, Stoecklein NH. Impact of the 3D microenvironment on phenotype, gene expression, and EGFR inhibition of colorectal cancer cell lines. *PLoS One*. 2013; 8:e59689.  
<https://doi.org/10.1371/journal.pone.0059689>  
PMID:23555746
  41. Espinoza I, Menendez JA, Kvp CM, Lupu R. CCN1 promotes vascular endothelial growth factor secretion through  $\alpha v \beta 3$  integrin receptors in breast cancer. *J Cell Commun Signal*. 2014; 8:23–7.  
<https://doi.org/10.1007/s12079-013-0214-6>  
PMID:24338441
  42. Liu Z, Wang L, Yang J, Bandyopadhyay A, Kaklamani V, Wang S, Sun LZ. Estrogen receptor alpha inhibits senescence-like phenotype and facilitates transformation induced by oncogenic ras in human mammary epithelial cells. *Oncotarget*. 2016; 7:39097–107.  
<https://doi.org/10.18632/oncotarget.9772>  
PMID:27259243
  43. Lee YH, Kang BS, Bae YS. Premature senescence in human breast cancer and colon cancer cells by tamoxifen-mediated reactive oxygen species generation. *Life Sci*. 2014; 97:116–22.  
<https://doi.org/10.1016/j.lfs.2013.12.009>  
PMID:24361399
  44. Chen CC, Young JL, Monzon RI, Chen N, Todorović V, Lau LF. Cytotoxicity of TNF $\alpha$  is regulated by integrin-mediated matrix signaling. *EMBO J*. 2007; 26:1257–67.  
<https://doi.org/10.1038/sj.emboj.7601596>  
PMID:17318182
  45. Chen CC, Juric V, Lau LF. The extracellular matrix protein CCN1 dictates TNF $\alpha$  and FasL cytotoxicity *in vivo*. *Adv Exp Med Biol*. 2011; 691:595–603.

[https://doi.org/10.1007/978-1-4419-6612-4\\_63](https://doi.org/10.1007/978-1-4419-6612-4_63)

PMID:[21153366](https://pubmed.ncbi.nlm.nih.gov/21153366/)

46. Juric V, Chen CC, Lau LF. TNF $\alpha$ -induced apoptosis enabled by CCN1/CYR61: pathways of reactive oxygen species generation and cytochrome c release. *PLoS One*. 2012; 7:e31303.

<https://doi.org/10.1371/journal.pone.0031303>

PMID:[22363611](https://pubmed.ncbi.nlm.nih.gov/22363611/)

47. Cheng L, Yang Z, Wang X, Jiao Y, Xie X, Lin J, Zhang H, Han J, Jiang K, Ye Q. Suppression of estrogen receptor transcriptional activity by connective tissue growth factor. *PLoS One*. 2011; 6:e20028.

<https://doi.org/10.1371/journal.pone.0020028>

PMID:[21629692](https://pubmed.ncbi.nlm.nih.gov/21629692/)

48. Feng T, Meng J, Kou S, Jiang Z, Huang X, Lu Z, Zhao H, Lau LF, Zhou B, Zhang H. CCN1-Induced Cellular Senescence Promotes Heart Regeneration. *Circulation*. 2019; 139:2495–8.

<https://doi.org/10.1161/CIRCULATIONAHA.119.039530>

PMID:[31107624](https://pubmed.ncbi.nlm.nih.gov/31107624/)

49. Harper S, Speicher DW. Purification of proteins fused to glutathione S-transferase. *Methods Mol Biol*. 2011; 681:259–80.

[https://doi.org/10.1007/978-1-60761-913-0\\_14](https://doi.org/10.1007/978-1-60761-913-0_14)

PMID:[20978970](https://pubmed.ncbi.nlm.nih.gov/20978970/)

# Mechanisms of action of triptolide against colorectal cancer: insights from proteomic and phosphoproteomic analyses

Xinqiang Song<sup>1,2</sup>, Huanhuan He<sup>1</sup>, Yu Zhang<sup>1</sup>, Jinke Fan<sup>1</sup>, Lei Wang<sup>1</sup>

<sup>1</sup>College of Life Sciences, Xinyang Normal University, Xinyang 464000, China

<sup>2</sup>College of Medicine, Xinyang Normal University, Xinyang 464000, China

**Correspondence to:** Xinqiang Song, Lei Wang; **email:** [xqsong2012@126.com](mailto:xqsong2012@126.com), <https://orcid.org/0000-0001-8119-8597>; [wangleibio@126.com](mailto:wangleibio@126.com), <https://orcid.org/0000-0003-2402-2338>

**Keywords:** colorectal cancer, triptolide, proteomic, phosphoproteomic, molecular docking

**Received:** January 18, 2022

**Accepted:** March 26, 2022

**Published:** April 2, 2022

**Copyright:** © 2022 Song et al. This is an open access article distributed under the terms of the [Creative Commons Attribution License](https://creativecommons.org/licenses/by/3.0/) (CC BY 3.0), which permits unrestricted use, distribution, and reproduction in any medium, provided the original author and source are credited.

## ABSTRACT

Triptolide is a potent anti-inflammatory agent that also possesses anticancer activity, including against colorectal cancer (CRC), one of the most frequent cancers around the world. In order to clarify how triptolide may be effective against CRC, we analyzed the proteome and phosphoproteome of CRC cell line HCT116 after incubation for 48 h with the drug (40 nM) or vehicle. Tandem mass tagging led to the identification of 403 proteins whose levels increased and 559 whose levels decreased in the presence of triptolide. We also identified 3,110 sites in proteins that were phosphorylated at higher levels and 3,161 sites phosphorylated at lower levels in the presence of the drug. Analysis of these differentially expressed and/or phosphorylated proteins showed that they were enriched in pathways involving ribosome biogenesis, PI3K–Akt signaling, MAPK signaling, nucleic acid binding as well as other pathways. Protein–protein interactions were explored using the STRING database, and we identified nine protein modules and 15 hub proteins. Finally, we identified 57 motifs using motif analysis of phosphosites and found 16 motifs were experimentally verified for known protein kinases, while 41 appear to be novel. These findings may help clarify how triptolide works against CRC and may guide the development of novel treatments.

## INTRODUCTION

Colorectal cancer (CRC) is one of the most frequent cancers, with more than 1.2 million new cases and 500,00 deaths annually around the world, the cornerstones of therapy are surgery, radiotherapy (for patients with rectal cancer), and chemotherapy [1]. Triptolide, the major active component of *Tripterygium wilfordii* Hook. f, works against CRC by inhibiting colon cancer cell proliferation, colony formation, and organoid growth *in vitro* [2, 3]. The triptolide analog minnelide markedly inhibits the growth of CRC xenografts and the metastasis of CRC to liver, more than doubling the median survival of animals whose CRC has metastasized to the liver [4]. Triptolide also appears to inhibit the epithelial-mesenchymal transition and growth of colon cancer stem cells [5].

Thus, triptolide shows strong potential to treat CRC, but how it works is controversial.

Here we explored protein expression and phosphorylation in CRC cells treated with triptolide in an effort to identify the molecules and pathways that may mediate the drug's anticancer effects. We applied quantitative proteomics and phosphoproteomics based on tandem mass tagging and nanospray liquid chromatography-tandem mass spectrometry. Proteomics allows global analysis of complex changes in protein expression [6, 7], and tandem mass tagging allows high-throughput, high-resolution quantification of changes in protein levels and their phosphorylation [8–10]. Our analyses may help clarify the anticancer mechanism of triptolide and identify druggable targets.

## RESULTS

### Proteome and phosphoproteome in HCT-116 cells

Using tandem mass tagging of total proteins as well as enrichment for phosphopeptides, followed by tandem mass spectrometry (Figure 1A), we identified 33,390 unique peptides corresponding to 5,860 proteins, of which 5,710 proteins could be quantified in triptolide-treated and control groups (Supplementary Table 1 and Supplementary Figures 1, 2A). Of these, 962 proteins were differentially expressed: 403 were present at higher levels and 559 proteins at lower levels in the presence of triptolide (Figure 1B). Triptolide was also associated with higher levels of phosphorylation at 3,110 sites in proteins and lower phosphorylation at 3,161 sites (Figure 1D). Most differentially expressed and/or phosphorylated proteins localized to the nucleus and cytoplasm (Figure 1C, 1E).

### Functional analysis of differentially expressed proteins in CRC

A total of 5710 quantitative proteins were identified in the proteome analysis (Supplementary Figure 2A). We defined proteins that were significantly different (Student's t-test,  $p < 0.05$ ) and used the criterion of 1.2-fold or greater change as the criteria to screen candidate proteins, finally we identified 403 proteins with higher levels and 559 proteins with lower levels in the triptolide-treated group than in the control group (Figure 2A). Heatmaps were applied to indicate the expression levels of the differentially expressed proteins screened by the volcano map in three replicate samples of the triptolide-treated group and the control group (Figure 2B). The potential functions of these proteins were explored based on enrichment in GO terms (Figure 2C and Supplementary Figure 3A–3C). They were enriched in the following GO biological processes: rRNA processing, ribosome biogenesis, keratinocyte proliferation, maturation of SSU-rRNA, regulation of keratinocyte proliferation, RNA phosphodiester bond hydrolysis, and endonucleolysis. The differentially expressed proteins were enriched in the following GO cellular components: preribosome, small-subunit processome, 90S preribosome, MCM complex, intrinsic components of the plasma membrane, intrinsic components of the membrane, integral components of the plasma membrane, and nucleolus. The differentially expressed proteins were enriched in the following GO molecular functions: peptidase inhibitor activity, endopeptidase inhibitor activity, peptidase regulator activity, translation repressor activity, olfactory receptor activity, metalloendopeptidase inhibitor activity, transcription corepressor activity, signaling receptor activity and transmembrane signaling receptor activity.

### Analysis of differentially expressed proteins for enrichment in domains and KEGG pathways, protein-protein interactions and modules

Differentially expressed proteins were enriched with the following domains (Figure 3A and Supplementary Figure 3E): PHD-finger, leucine-rich repeat, N-terminal MCM, CHRromatin Organisation MOdifier (“Chromo”), MCM2/3/5 family, MCM OB, and EGF-like. We identified several KEGG pathways that were enriched in upregulated proteins: chemical carcinogenesis, bile secretion, complement and coagulation cascades, prostate cancer and drug metabolism-cytochrome P450 (Figure 3B and Supplementary Figure 3D). Several KEGG pathways were enriched in downregulated proteins: PPAR signaling, mucin type O-glycan biosynthesis, starch and sucrose metabolism, various types of N-glycan biosynthesis, hedgehog signaling, basal transcription factors and longevity-regulating pathway.

We predicted interactions among differentially expressed proteins using STRING and Cytoscape (Figure 3C), and the protein-protein interaction network revealed four critical protein groups (Figure 3D–3G): MCODE 1 (MCODE score = 37.436), consisting of 40 nodes and 730 edges; MCODE 2 (score = 7.5), consisting of 9 nodes and 306 edges; MCODE 3 (score = 5.667), comprising 7 nodes and 17 edges; and MCODE 4 (score = 3.333), consisting of 4 nodes and 5 edges. Four classification methods in CytoHubba were used to identify the top 10 proteins (Supplementary Table 1), which when combined with the analysis of MCODE modules identified seven proteins as hub proteins: IMP3, BYSL, PDCD11, PNO1, NSA2, RRS1 and RPF2 (Supplementary Figure 6A).

### Functional analysis of differentially phosphorylated proteins in CRC

A total of 3410 quantitative proteins were identified in the experimental group and the control group (Supplementary Figure 2B). Similarly, we identified 3110 proteins with higher phosphorylation levels and 3161 proteins with lower phosphorylation levels in triptolide-treated cells group than in the control group (Figure 4A). Besides, a total of 17,056 phosphosites were identified, of which 88.22% were serines, 11.33% were threonines, and 0.45% were tyrosines (Supplementary Figure 4). The R package “pheatmap” was used to draw a heatmap (Figure 4B), which shows the expression levels of the differentially expressed proteins at the phosphorylation site screened by the volcano map.

Analysis of differentially phosphorylated proteins showed enrichment of the following GO biological



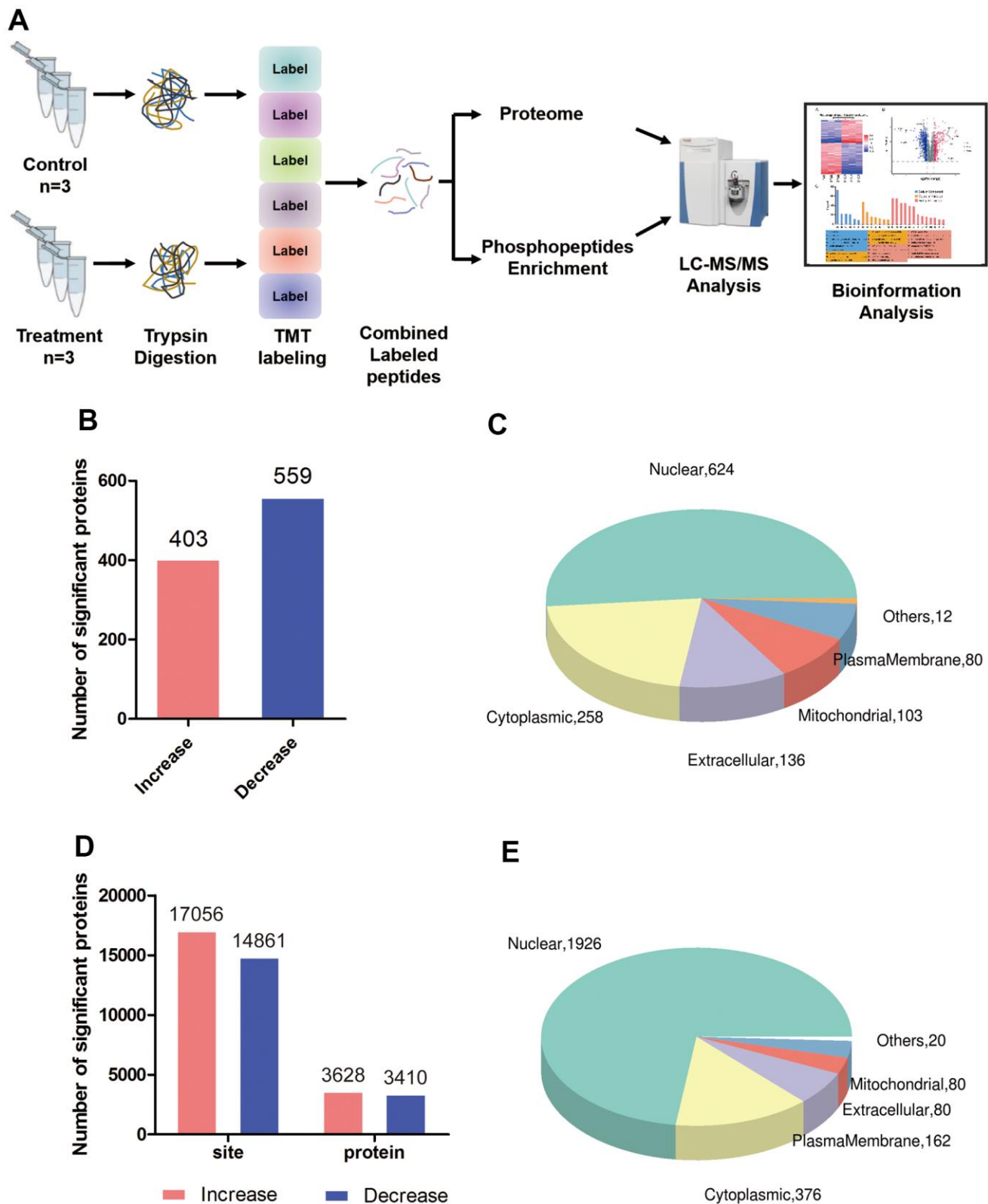


**Figure 1. Global proteomic and phosphoproteomic analysis of colorectal cancer cells.** (A) Schematic of the experimental workflow; LC, liquid chromatography; MS, mass spectrometry; TMT, tandem mass tags. (B) Numbers of proteins whose levels were significantly higher (red) or lower (blue) in triptolide-treated cell cultures than in control cultures. (C) Numbers of differentially expressed proteins in different subcellular compartments. (D) Numbers of sites in proteins whose phosphorylation was significantly higher (red) or lower (blue) in triptolide-treated cell cultures than in control cultures. (E) Numbers of differentially phosphorylated proteins in different subcellular compartments.

processes (Figure 4C and Supplementary Figure 5A–5C): cellular processes, biological regulation of biological processes, regulation of cellular processes, response to stimulus, cellular response to stress, and nucleic acid metabolism. The proteins were enriched in the following GO cellular components: nucleus, organelles, intracellular space,

membrane-enclosed lumen, and nuclear lumen. Differentially phosphorylated proteins were enriched in the following GO molecular functions: binding, catalytic activity, heterocyclic compound binding, organic cyclic compound binding, nucleic acid binding, protein binding, RNA binding and cytoskeletal protein binding.

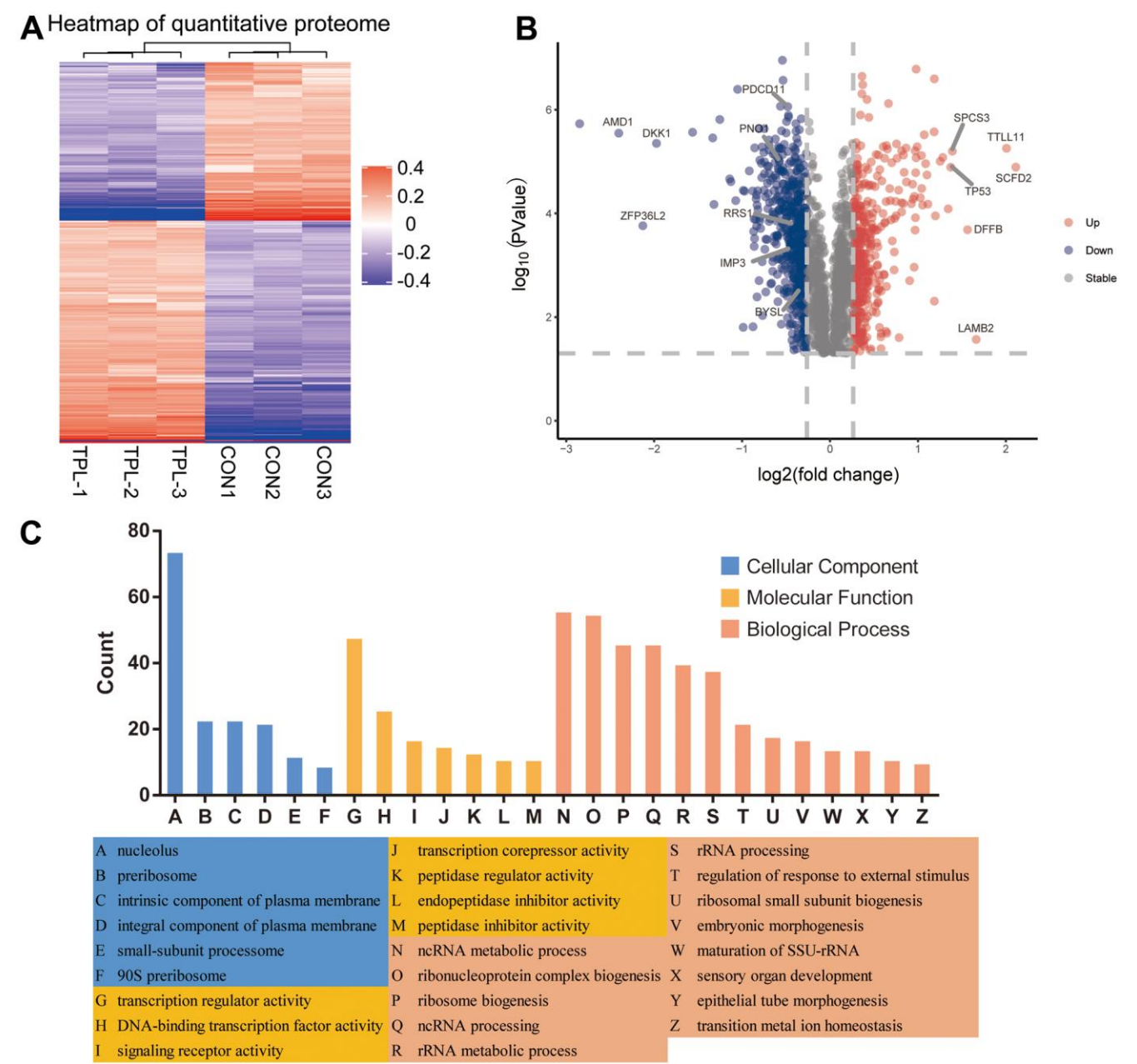


**Figure 2. Differential expression levels of the quantitative proteome and their enrichment in Gene Ontology terms.** (A) Heatmap of the quantitative proteome based on fold differences in expression. (B) Volcano plot of the differences in protein levels. The volcano map was drawn based on the expression of FC and P value (T-test). The significantly down-regulated proteins were blue (FC< 0.83 and P < 0.05), the significantly up-regulated proteins were red (FC>1.2 and P < 0.05), and the proteins with no difference were gray. (C) Classification of differentially expressed proteins based on Gene Ontology biological processes, cellular components and molecular functions.

## Analysis of differentially phosphorylated proteins for enrichment in domains and KEGG pathways, protein-protein interactions and modules

Differentially phosphorylated proteins were enriched in several domains (Figure 5A and Supplementary Figure 5E): protein kinase, RNA recognition motif, WD, G-beta repeat, PDZ, LIM, PHD-finger, and KH.

The proteins were enriched in the following KEGG pathways (Figure 5B and Supplementary Figure 5D): proteoglycans in cancer, human immunodeficiency virus 1 infection, regulation of actin cytoskeleton, tight junction, pathogenic *Escherichia coli* infection, animal autophagy, cGMP-PKG signaling, renal cell carcinoma, AMPK signaling, and axon guidance.

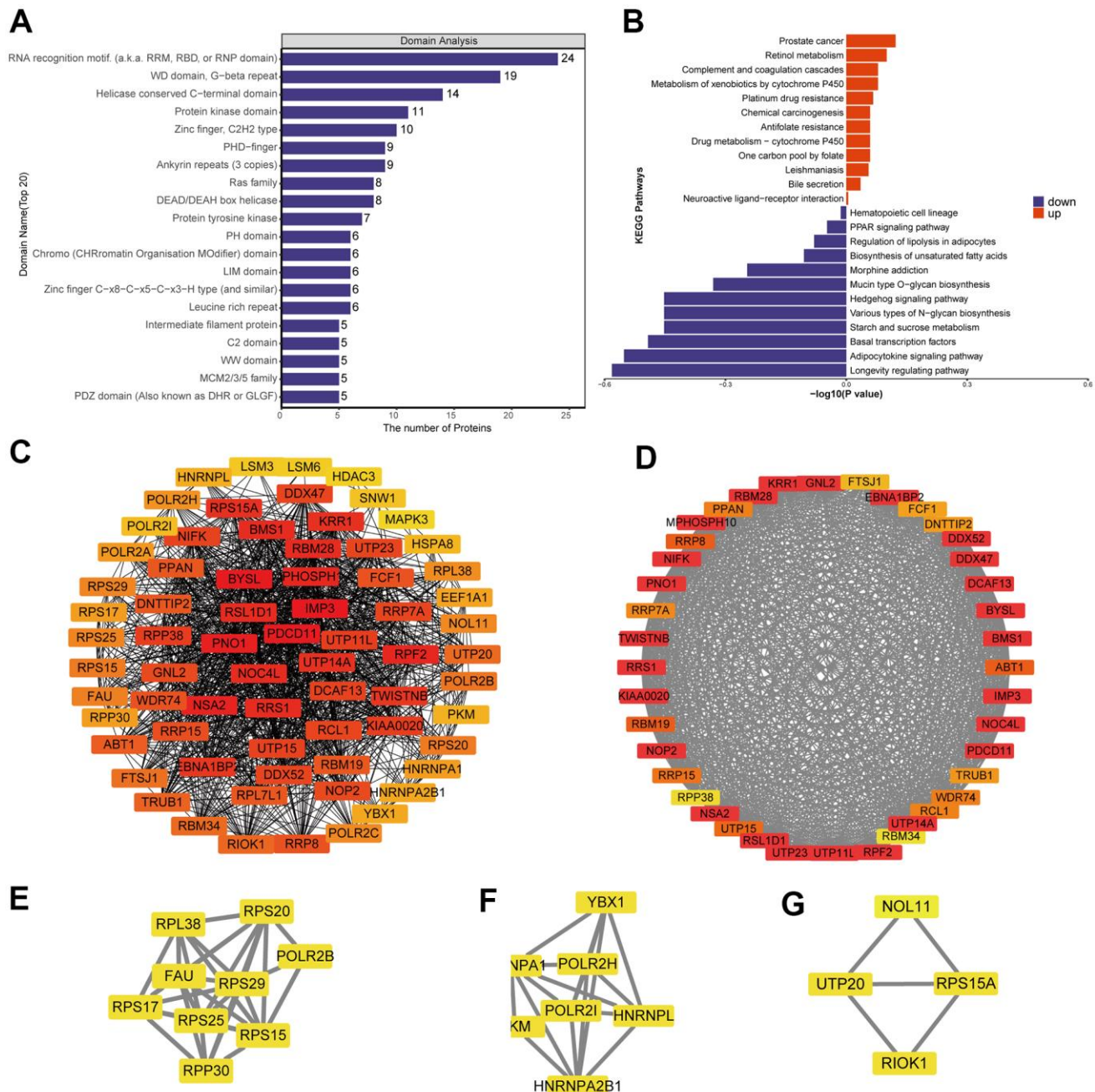


**Figure 3. Analysis of predicted interactions among differentially expressed proteins.** The four most significant modules were identified by the molecular complex detection (MCODE) algorithm. (A) Enrichment of domains in differentially expressed proteins. (B) Enrichment of KEGG pathways in differentially expressed proteins. (C) Interaction network of differentially expressed proteins. (D–G) The four most significant MCODE modules.



A network of potential interactions among differentially phosphorylated proteins (Figure 5C) led to the identification of five critical groups (Figure 5D–5H): MCODE 1 (MCODE score = 19.778), consisting of 28 nodes and 267 edges; MCODE 2 (score = 9.81), consisting of 22 nodes and 103 edges; MCODE 3 (score = 7.459), comprising 38 nodes and 138 edges; MCODE

4 (score = 4.286), comprising 8 nodes and 15 edges; and MCODE 5 (score = 4), comprising 4 nodes and 6 edges. The four classification methods in CytoHubba (Supplementary Table 2) converged on the following eight proteins as hub phosphorylated proteins: SRSF1, HNRNPC, NCBP1, HNRNPA1, DHX9, DDX5, RBM25 and SF3B1 (Supplementary Figure 6B).

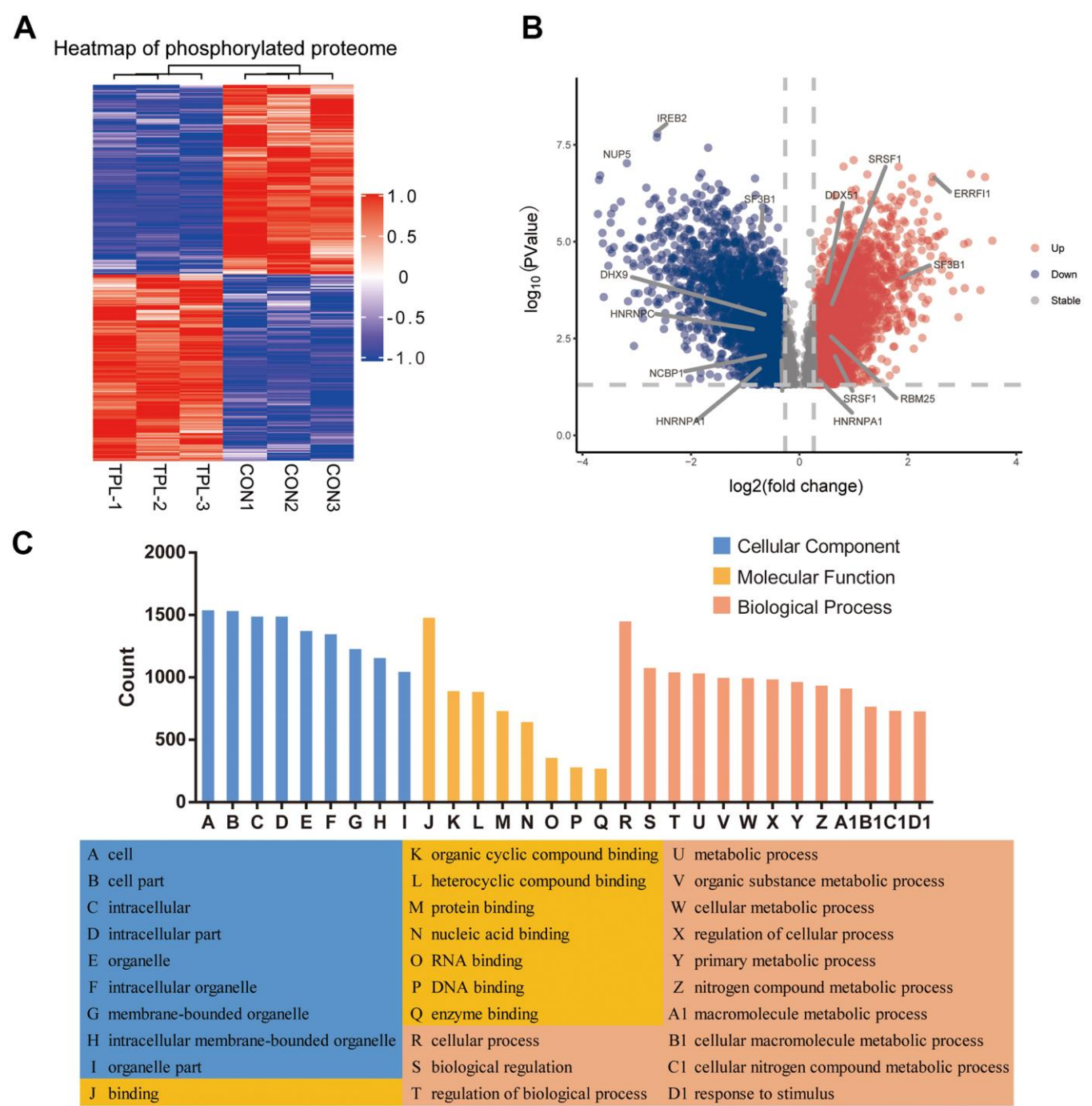


**Figure 4. Differential phosphorylation of the quantitative proteome and enrichment in Gene Ontology terms.** (A) Heatmap based on differential phosphorylation levels. (B) Volcano plot of the differences in phosphorylation levels. (C) Classification of differentially phosphorylated proteins based on Gene Ontology biological processes, cellular components and molecular functions.

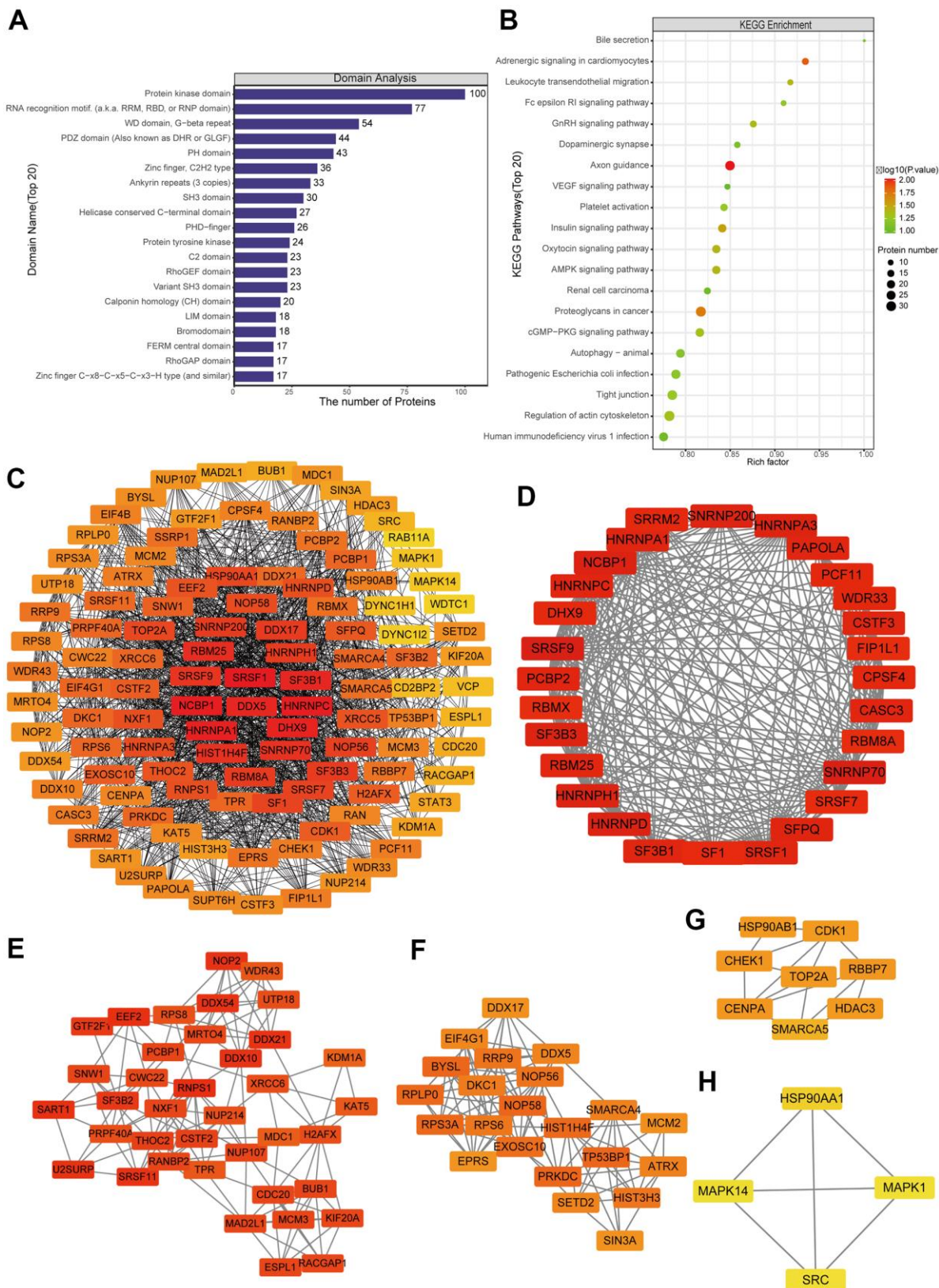


**Figure 5. Protein-protein interaction (PPI) network analyses of PDEPs were performed, and the four most significant modules were identified by the molecular complex detection (MCODE) algorithm. (A) Enrichment of domains in differentially expressed proteins. (B) Enrichment of KEGG pathways in differentially expressed proteins. (C) Interaction network of differentially expressed proteins. (D–H) The five most significant MCODE modules.**



## Motif analysis of the phosphosites

Among the protein sequences differentially phosphorylated between triptolide and control CRC cultures, we identified 50 conserved motifs in which a serine was phosphorylated and 7 conserved motifs in which a threonine was phosphorylated (Supplementary Table 2). Several of the motifs were upregulated by triptolide (Figure 6A), while other motifs were downregulated (Figure 6B). Based on motif score, we identified the top six hub motifs that were down- or upregulated (Figure 6C, 6D).

According to the Human Protein Reference Database (HPRD), 16 phosphorylation motifs have previously been verified as substrates of certain protein kinases, while 41 have not yet been linked to kinases (Supplementary Table 2). Particularly conserved motifs were [xpSxxxx\_pS\_PxxxxK] (motif 1), [xxpSxxx\_pS\_PxxxxK] (motif 3), [xxpSxxx\_pS\_PpTxxx] (motif 5), [xxxRpSx\_pS\_xpSxxx] (motif 15) and [xxxxSx\_pS\_ExExxx] (motif 24). All these motifs scored > 40.00. Several motifs have previously been shown to be phosphorylated by casein kinase II [11–14]: [xxxxxx\_S\_xExxxx] (motif 8), [xxxxxx\_S\_DxExxx] (motif 16), [xxxxxx\_S\_EEExxx] (motif 25), [xxxxxx\_S\_xDxxxx] (motif 40), [xxxSxx\_S\_xxxxxx] (motif 50), [xxxxxx\_T\_xxExxx] (motif 55), and [xxxxSx\_T\_xxxxxx] (motif 56). Casein kinase II is upregulated in numerous cancers, and it has been proposed as a therapeutic target in CRC [15–17]. Meanwhile, elevated Casein kinase II activity play a role in transcriptional regulator of cell cycle and PI3K-promoting genes [18]. The motifs [xxxxxx\_S\_Pxxxxx] (motif 26) and [xxxxxx\_T\_Pxxxxx] (motif 54) are known to be phosphorylated by kinases containing a WW domain [19–21]. The motif [xLxRxx\_S\_xxxxxx] (motif 29), for its part, is phosphorylated by calmodulin-dependent protein kinase II [22], which may be a therapeutic target in cancer [23]. In this way, our findings identify several kinases that may help mediate the effects of triptolide against CRC.

## Verification with molecular docking

To further validate potential targets in triptolide, we performed molecular docking with hub genes. Docking analysis successfully predicted binding energy ( $\Delta G_b$ ), which were all negative and less than  $-5$ , between quercetin and the hub genes. The scores of triptolide-AMD1, -IMP3, -HNRNPC, -DHX9 was  $-5.7634$ ,  $-6.1944$ ,  $-5.5740$  and  $-5.4239$  kcal/mol, respectively (Supplementary Table 3). Docked compounds showed hydrogen bonds in the active site. These selected compounds bind to the hub genes protein by interacting with different amino acid residues, such as Arg20, Lys

3, Asn146, Arg17 and Thr 216. Overall, molecular docking results indicated that triptolide had good binding activities to AMP1, IMP3, HNRNPC and DHX9, as shown in Figure 7.

## DISCUSSION

Globally CRC is the third most frequent cancer and the second most frequent cause of cancer-related deaths [24]. Triptolide has been reported to affect CRC in various ways, such as by arresting the cell cycle [4, 25] and decreasing vascular endothelial growth factor expression to inhibit migration [26]. Since CRC onset and progression likely involve complex interactions among many genes and proteins [27, 28], we did not focus here on specific proteins but instead examined the entire (phospho)proteomic landscape using liquid chromatography-tandem mass spectrometry [29]. We identified 559 proteins whose expression was downregulated and 403 proteins whose expression was upregulated by triptolide.

For example, we found that triptolide downregulated ZFP36L2, consistent with previous studies [30, 31]. In the case of pancreatic ductal adenocarcinoma, high expression of ZFP36L2 predicts shorter survival, and silencing it inhibits cancer cell aggressiveness [31]. We also found that triptolide downregulated AMD1, which is upregulated in many cancers and is associated with patient prognosis [32, 33]. Similarly, triptolide downregulated the RNA helicase DHX9, which is highly expressed in several cancers and is involved mainly in RNA splicing and processing, ribosome synthesis, as well as translation and transcription [34]. Triptolide downregulated the RNA-binding protein HNRNPC. This protein is upregulated in various cancers, and its inhibition slows cancer cell proliferation and tumor growth [35]. Our research highlights that triptolide can directly or indirectly phosphorylate HNRNPC and it is down regulated in triptolide treated group. Therefore, we attribute that triptolide may mediate the proliferation of tumor by HNRNPC. These indicates that triptolide plays a critical role in a variety of cellular processes, especially in cell growth, cell migration and immunoreactivity.

Many of the GO terms enriched in the proteins whose expression was altered by triptolide localized to the nucleus and were related to the ribosome. An important feature of cancer cells is increased ribosomal production and strong disruption of ribosome biogenesis [36, 37]. The production of functional ribosomes begins in the nucleolus [38–40], so this may be an important site of triptolide anticancer activity.

Triptolide downregulated hedgehog signaling, and it altered the phosphorylation of proteins involved in

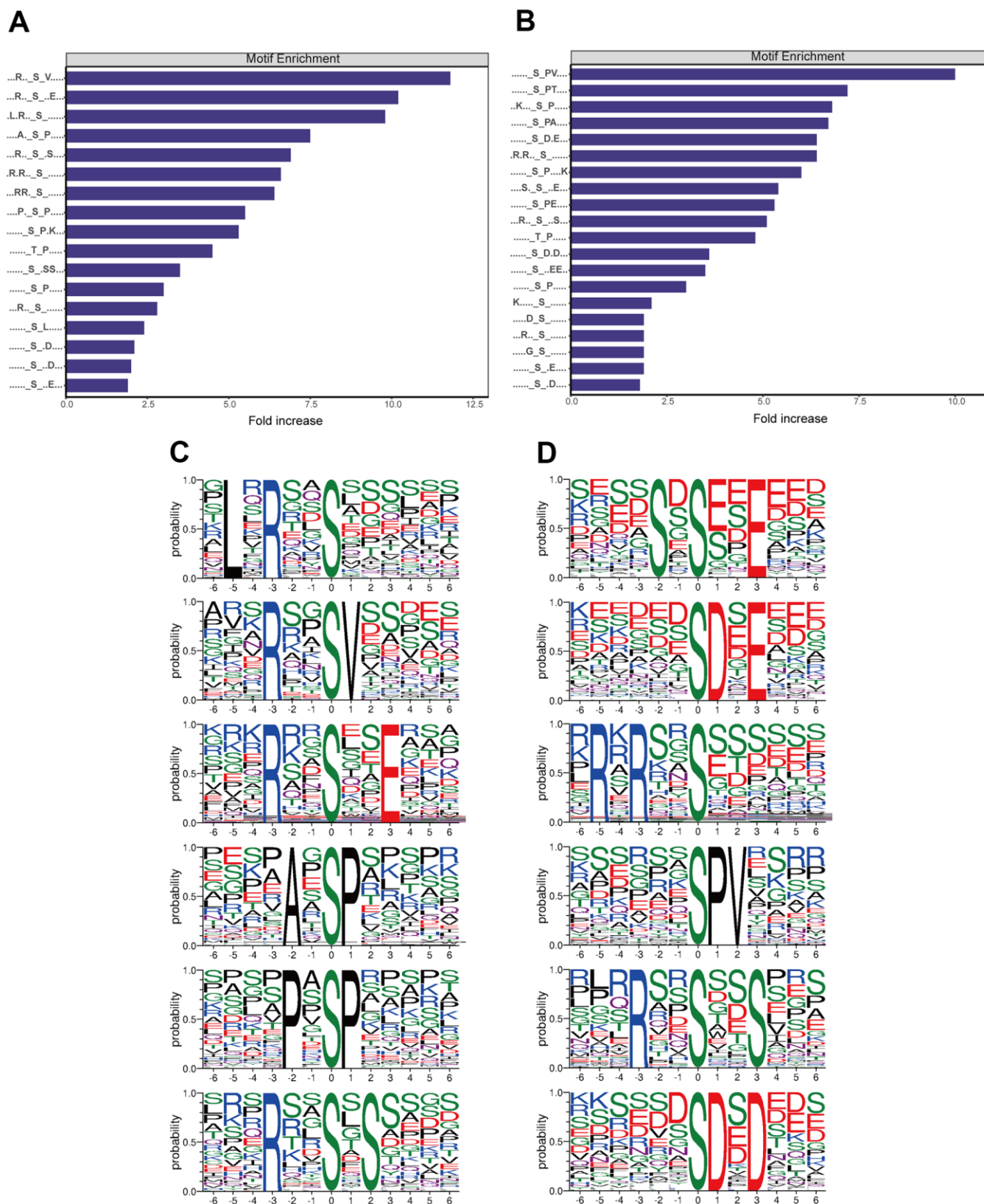


**Figure 6. Analysis of motifs differentially phosphorylated between CRC cultures treated with triptolide or vehicle. (A)** Motifs whose phosphorylation is upregulated by triptolide. **(B)** Motifs whose phosphorylation is downregulated by triptolide. **(C)** Ranking of the top six motifs upregulated by triptolide. **(D)** Ranking of the top six motifs downregulated by triptolide.



PI3K–Akt signaling and MAPK signaling. Hedgehog signaling has been linked to cancer, in particular for maintaining tumor-initiating/stem cells [41]. The pathway contributes to tumorigenesis and tumor growth through several mechanisms [42, 43], including processes affecting cell proliferation, survival and angiogenesis [44]. The pathway can be activated by TNF- $\alpha$ , KRAS–MAPK/ERK, and PI3K–Akt [45–47]. In fact, PI3K activates Akt to regulate hedgehog signaling during the specification of neuronal fate [48]. Our results suggest that triptolide acts partly through hedgehog and associated signaling pathways.

We found that triptolide downregulated the RNA-binding protein IMP3, which is required for ribosomal RNA processing and may predict prognosis in many cancers [49–51]. In breast cancer, IMP3 activates TAZ, a transcriptional co-activator of Hippo signaling that helps drive breast cancer stem cell function [49]. In prostate cancer, IMP3 is overexpressed, and it accelerates the cancer's progression by increasing SMURF1-mediated PTEN ubiquitination, which in turn activates PI3K/AKT/mTOR signaling [50]. In CRC, IMP3 regulates MEKK1 to activate MEK1/ERK signaling, driving cancer progression [52]. Our results suggest that triptolide acts in part through IMP3 and associated pathways. Clinical therapeutic effect need to be further validated in controlled clinical trials.

Altogether, our analysis identifies several pathways through which triptolide may suppress CRC proliferation, including pathways involving IMP3/ PI3K/AKT/mTOR, Hedgehog/ PI3K/AKT and ZFP36L2, AMD1, DHX9 and HNRNPC. These results may help optimize the anticancer efficacy of triptolide as well as develop new druggable targets against CRC.

## MATERIALS AND METHODS

### Cell culture and treatment

The human colon carcinoma cell line HCT 116 was obtained from National Infrastructure of Cell Line Resource (Beijing, China). Cells were treated for 48 h with triptolide (40 ng/ml) dissolved in DMSO or DMSO vehicle. The medium for all cell culture was RPMI 1640 (Life Technologies, Shanghai, China) supplemented with 10% fetal bovine serum (FBS; Thermo Scientific, Shanghai, China). Cultures were incubated at 37° C in an atmosphere of 5% CO<sub>2</sub>.

### Protein extraction and preparation

HCT116 cells were cultured to 70% confluence, then lysed using a buffer containing 100 mM Tris-HCl (pH 7.6), 4% SDS, 1 mM DTT. Protein concentration were

quantified using the BCA assay (Bio-Rad, Hercules, California, USA). The protein solution was sequentially diluted (5 mmol/L dithiothreitol for 30 min at 56° C) and alkylated with 11 mmol/L iodoacetamide for 15 min. These procedures were performed in darkness at room temperature. Then, the assembled protein sample was diluted to a urea concentration of less than 2 mol/L. Finally, trypsin was added to initiate overnight digestion (the ratio of trypsin to the protein mass ratio was 1:50) at 37° C and a subsequent 4 h digestion (the ratio of trypsin to protein mass was 1:100). The resulting peptides were desalted on a Empore™ SPE C18 cartridge (standard density, 7 mm inner bed diameter, 3 ml volume; Sigma, Shanghai, China). The eluted peptides were concentrated by vacuum centrifugation and reconstituted in 40  $\mu$ l of 0.1% (v/v) formic acid.

### Tandem mass tagging and enrichment of phosphopeptides

Tryptic peptide mixtures were labeled with TMT Reagent (Thermo Fisher Scientific) according to the manufacturer's instructions. Three independent cultures of untreated HCT116 were tagged (tags 126, 127 and 128), as well as three independent cultures of triptolide-treated HCT116 cells (tags 129, 130 and 131). Peptide mixtures were enriched for phosphorylated peptides using the High-Select™ Fe-NTA Kit (Thermo Scientific) according to the manufacturer's instructions. The resulting phosphopeptide mixtures were lyophilized, then resuspended in 20  $\mu$ L of 0.1% (v/v) formic acid.

### Liquid chromatography-tandem mass spectrometry

Total peptide and phosphopeptide-enriched samples were loaded onto an Acclaim PepMap100 nanoViper C18 reverse-phase trap column (Thermo Scientific; dimensions, 100  $\mu$ m x 2 cm) connected to an Easy C18 reverse-phase analytical column (Thermo Scientific; inner diameter, 75  $\mu$ m; length, 10 cm; resin diameter, 3  $\mu$ m) in buffer A (0.1% formic acid). Peptides were separated using a linear gradient of buffer B (84% acetonitrile, 0.1% formic acid) at a flow rate of 300 nl/min.

The separated peptides were then subjected to tandem mass spectrometry on a Q Exactive mass spectrometer (Thermo Scientific) for 60–90 min, operated in positive ion mode. Data were acquired using a data-dependent top10 method that dynamically selected the most abundant precursor ions from the survey scan (300–1800 m/z) for Higher energy Collision Induced Dissociation (HCD) fragmentation. The system was operated in peptide recognition mode, and the following device parameters were used: automatic gain control



target, 3e6; maximum injection time, 10 ms; dynamic exclusion duration, 40.0 s; survey scan resolution, 70,000 at *m/z* 200; HCD spectrum resolution, 17,500 at *m/z* 200; isolation width, 2 *m/z*; normalized collision energy, 30 eV; and underfill ratio (minimum percentage of the target value likely to be reached at maximum fill time), 0.1%.

### Database search

The resulting MS/MS data were processed using the MASCOT engine (Matrix Science, London, UK; version 2.2) embedded into Proteome Discoverer 2.4. The data were searched against the database “Homo\_sapiens\_194324” and against a library of common protein contaminants (for filtering out contaminant proteins), and an anti-database was added to assess the false discovery rate (FDR) due to random matches. The following system parameters were applied: restriction enzyme digestion method, trypsin/P; number of missed cleavage sites, 2; peptide mass tolerance,  $\pm 20.0$  ppm; fragment mass tolerance, 0.1 Da; fixed modification, carbamidomethyl (C); variable modifications, “Oxidation (M)”, “Phospho(ST)”, “Phosp (Y)”; and FDR, 1%.

Only proteins whose levels differed  $> 2$ -fold or  $< 0.83$ -fold between cultures treated with triptolide or vehicle (in association with  $p < 0.05$ ) were considered in subsequent bioinformatics analyses. A similar criterion was applied to select phosphorylation sites in the proteome.

### Bioinformatic analyses

Differentially expressed proteins were searched against the NCBI BLAST+ database (ncbi-blast-2.2.28+-win32.exe) and homologous sequences were identified using InterProScan. Potential functions of the proteins were explored using Gene Ontology (GO) terms and annotated using Blast2GO (<https://www.blast2go.com/>) according to GO biological processes, cellular components and molecular functions.

After annotation, proteins were mapped to Kyoto Encyclopedia of Genes and Genomes (KEGG) pathways (<http://www.genome.jp/kegg/>). Their subcellular localizations were predicted using CELLO (<http://cello.life.nctu.edu.tw>). In addition, the InterPro (providing resources for functional analysis of protein sequence family classification, prediction of structural domains and special sites) database was used to analyze the enrichment of functional domains of differentially expressed proteins. Enrichment of a given differentially expressed protein or protein domain was defined as  $p < 0.05$  in a two-tailed Fisher's exact test. We examined enrichment in terms of GO terms, KEGG and domains.

Categories that contained at least one enriched cluster and that were associated with  $p < 0.05$  were considered significant.

The STRING database (version 10.5) was used to create a protein-protein interaction network, and interactions with a confidence score  $> 0.7$  were considered probable. Finally, we integrated databases and protein-protein interaction network, then explored densely connected regions using MCODE and Cytohubba.

Phosphorylation motifs were analyzed using MeMe (<http://meme-suite.org/index.htm>). We extracted amino acid sequences containing the phosphorylated residue as well as six residues upstream and six downstream. Only when the minimum number of occurrences was set to 20 and the statistical test P value is less than 0.000001, the characteristic sequence form is considered to be a motif of the modified peptide. Finally, we estimate the molecular binding capacities of the compounds with the target proteins. The structures of triptolide were downloaded from the TCMSP database. Then, the downloaded structures were converted to three dimensional (3D) structures, and the energy of them was minimized through the Molecular Operating Environment (MOE) 2019.10 software. Molecular docking analysis was conducted for comparing the combined action between the compounds and the crystal structures of AMD1 (PDB ID: 3DZ7), IMP3 (PDB ID: 6FQR), HNRNPC (PDB ID: 2MZ1), DHX9 (PDB ID: 3VYX) using MOE. For each molecular compounds, a number of placements called poses. Among the placement of the compounds, the best pose with the lowest binding energy ( $\Delta G_b$ ) was selected as the output result.

### AUTHOR CONTRIBUTIONS

Conceived and designed the experiments: Xinqiang Song. Performed the experiments: Huanhuan HE. Analyzed the data: Yu Zhang, Jinke FAN, Lei Wang. Wrote the paper: Xinqiang Song.

### ACKNOWLEDGMENTS

We thank Shanghai Applied Protein Technology Co., Ltd. for technological assistance.

### CONFLICTS OF INTEREST

The authors declare no conflicts of interest.

### FUNDING

This work was supported by the National Natural Science Foundation of China (U1804179); the Henan Science and



Technology Innovation Team, Investigation of Plant Resources in Dabie Mountains, and the Study and Utilization of Active Components of Special Plants (2017083); the Henan Key Scientific and Technological Project (202102310190).

## REFERENCES

- Wang Y, Yu F, Liu MY, Zhao YK, Wang DM, Hao QH, Wang XL. Isolation and Characterization of a Human Intestinal Bacterium Eggerthella sp. AUH-JLD49s for the Conversion of (-)-3'-Desmethylyarctigenin. *J Agric Food Chem*. 2017; 65:4051–6.  
<https://doi.org/10.1021/acs.jafc.7b00114>  
PMID:28493688
- Liang X, Xie R, Su J, Ye B, Wei S, Liang Z, Bai R, Chen Z, Li Z, Gao X. Inhibition of RNA polymerase III transcription by Triptolide attenuates colorectal tumorigenesis. *J Exp Clin Cancer Res*. 2019; 38:217.  
<https://doi.org/10.1186/s13046-019-1232-x>  
PMID:31122284
- Qi Y, Li J. Triptolide inhibits the growth and migration of colon carcinoma cells by down-regulation of miR-191. *Exp Mol Pathol*. 2019; 107:23–31.  
<https://doi.org/10.1016/j.yexmp.2019.01.008>  
PMID:30684462
- Oliveira A, Beyer G, Chugh R, Skube SJ, Majumder K, Banerjee S, Sangwan V, Li L, Dawra R, Subramanian S, Saluja A, Dudeja V. Triptolide abrogates growth of colon cancer and induces cell cycle arrest by inhibiting transcriptional activation of E2F. *Lab Invest*. 2015; 95:648–59.  
<https://doi.org/10.1038/labinvest.2015.46>  
PMID:25893635
- Acikgoz E, Tatar C, Oktem G. Triptolide inhibits CD133+/CD44+ colon cancer stem cell growth and migration through triggering apoptosis and represses epithelial-mesenchymal transition via downregulating expressions of snail, slug, and twist. *J Cell Biochem*. 2020; 121:3313–24.  
<https://doi.org/10.1002/jcb.29602> PMID:31904143
- Jiang L, Yin X, Chen YH, Chen Y, Jiang W, Zheng H, Huang FQ, Liu B, Zhou W, Qi LW, Li J. Proteomic analysis reveals ginsenoside Rb1 attenuates myocardial ischemia/reperfusion injury through inhibiting ROS production from mitochondrial complex I. *Theranostics*. 2021; 11:1703–20.  
<https://doi.org/10.7150/thno.43895> PMID:33408776
- Nusinow DP, Szpyt J, Ghandi M, Rose CM, McDonald ER 3rd, Kalocsay M, Jané-Valbuena J, Gelfand E, Schweppe DK, Jedrychowski M, Golji J, Porter DA, Rejtar T, et al. Quantitative Proteomics of the Cancer Cell Line Encyclopedia. *Cell*. 2020; 180:387–402.e16.  
<https://doi.org/10.1016/j.cell.2019.12.023>  
PMID:31978347
- Wang H, Dey KK, Chen PC, Li Y, Niu M, Cho JH, Wang X, Bai B, Jiao Y, Chepyala SR, Haroutunian V, Zhang B, Beach TG, Peng J. Integrated analysis of ultra-deep proteomes in cortex, cerebrospinal fluid and serum reveals a mitochondrial signature in Alzheimer's disease. *Mol Neurodegener*. 2020; 15:43.  
<https://doi.org/10.1186/s13024-020-00384-6>  
PMID:32711556
- Mertins P, Tang LC, Krug K, Clark DJ, Gritsenko MA, Chen L, Clauser KR, Clauss TR, Shah P, Gillette MA, Petyuk VA, Thomas SN, Mani DR, et al. Reproducible workflow for multiplexed deep-scale proteome and phosphoproteome analysis of tumor tissues by liquid chromatography-mass spectrometry. *Nat Protoc*. 2018; 13:1632–61.  
<https://doi.org/10.1038/s41596-018-0006-9>  
PMID:29988108
- Moulder R, Bhosale SD, Goodlett DR, Laheesmaa R. Analysis of the plasma proteome using iTRAQ and TMT-based Isobaric labeling. *Mass Spectrom Rev*. 2018; 37:583–606.  
<https://doi.org/10.1002/mas.21550> PMID:29120501
- Schwartz D, Gygi SP. An iterative statistical approach to the identification of protein phosphorylation motifs from large-scale data sets. *Nat Biotechnol*. 2005; 23:1391–8.  
<https://doi.org/10.1038/nbt1146> PMID:16273072
- Roach PJ. Multisite and hierarchal protein phosphorylation. *J Biol Chem*. 1991; 266:14139–42.  
PMID:1650349
- Kuenzel EA, Mulligan JA, Sommercorn J, Krebs EG. Substrate specificity determinants for casein kinase II as deduced from studies with synthetic peptides. *J Biol Chem*. 1987; 262:9136–40.  
PMID:3474230
- Keshava Prasad TS, Goel R, Kandasamy K, Keerthikumar S, Kumar S, Mathivanan S, Telikicherla D, Raju R, Shafreen B, Venugopal A, Balakrishnan L, Marimuthu A, Banerjee S, et al. Human Protein Reference Database—2009 update. *Nucleic Acids Res*. 2009; 37:D767–72.  
<https://doi.org/10.1093/nar/gkn892> PMID:18988627
- Nitta RT, Gholamin S, Feroze AH, Agarwal M, Cheshier SH, Mitra SS, Li G. Casein kinase 2 $\alpha$  regulates glioblastoma brain tumor-initiating cell growth through the  $\beta$ -catenin pathway. *Oncogene*. 2015; 34:3688–99.  
<https://doi.org/10.1038/onc.2014.299> PMID:25241897
- O-charoenrat P, Rusch V, Talbot SG, Sarkaria I, Viale A, Socci N, Ngai I, Rao P, Singh B. Casein kinase II alpha subunit and C1-inhibitor are independent predictors of

- outcome in patients with squamous cell carcinoma of the lung. *Clin Cancer Res.* 2004; 10:5792–803.  
<https://doi.org/10.1158/1078-0432.CCR-03-0317>  
PMID:15355908
17. Izeradjene K, Douglas L, Delaney A, Houghton JA. Influence of casein kinase II in tumor necrosis factor-related apoptosis-inducing ligand-induced apoptosis in human rhabdomyosarcoma cells. *Clin Cancer Res.* 2004; 10:6650–60.  
<https://doi.org/10.1158/1078-0432.CCR-04-0576>  
PMID:15475455
  18. Song C, Gowda C, Pan X, Ding Y, Tong Y, Tan BH, Wang H, Muthusami S, Ge Z, Sachdev M, Amin SG, Desai D, Gowda K, et al. Targeting casein kinase II restores Ikaros tumor suppressor activity and demonstrates therapeutic efficacy in high-risk leukemia. *Blood.* 2015; 126:1813–22.  
<https://doi.org/10.1182/blood-2015-06-651505>  
PMID:26219304
  19. Yaffe MB, Elia AE. Phosphoserine/threonine-binding domains. *Curr Opin Cell Biol.* 2001; 13:131–8.  
[https://doi.org/10.1016/s0955-0674\(00\)00189-7](https://doi.org/10.1016/s0955-0674(00)00189-7)  
PMID:11248545
  20. Lu PJ, Zhou XZ, Shen M, Lu KP. Function of WW domains as phosphoserine- or phosphothreonine-binding modules. *Science.* 1999; 283:1325–8.  
<https://doi.org/10.1126/science.283.5406.1325>  
PMID:10037602
  21. Sudol M, Chen HI, Bougeret C, Einbond A, Bork P. Characterization of a novel protein-binding module--the WW domain. *FEBS Lett.* 1995; 369:67–71.  
[https://doi.org/10.1016/0014-5793\(95\)00550-s](https://doi.org/10.1016/0014-5793(95)00550-s)  
PMID:7641887
  22. Stokoe D, Caudwell B, Cohen PT, Cohen P. The substrate specificity and structure of mitogen-activated protein (MAP) kinase-activated protein kinase-2. *Biochem J.* 1993; 296:843–9.  
<https://doi.org/10.1042/bj2960843> PMID:8280084
  23. Yu-Ju Wu C, Chen CH, Lin CY, Feng LY, Lin YC, Wei KC, Huang CY, Fang JY, Chen PY. CCL5 of glioma-associated microglia/macrophages regulates glioma migration and invasion via calcium-dependent matrix metalloproteinase 2. *Neuro Oncol.* 2020; 22:253–66.  
<https://doi.org/10.1093/neuonc/noz189>  
PMID:31593589
  24. Bray F, Ferlay J, Soerjomataram I, Siegel RL, Torre LA, Jemal A. Global cancer statistics 2018: GLOBOCAN estimates of incidence and mortality worldwide for 36 cancers in 185 countries. *CA Cancer J Clin.* 2018; 68:394–424.  
<https://doi.org/10.3322/caac.21492>  
PMID:30207593
  25. Liu J, Shen M, Yue Z, Yang Z, Wang M, Li C, Xin C, Wang Y, Mei Q, Wang Z. Triptolide inhibits colon-rectal cancer cells proliferation by induction of G1 phase arrest through upregulation of p21. *Phytomedicine.* 2012; 19:756–62.  
<https://doi.org/10.1016/j.phymed.2012.02.014>  
PMID:22464014
  26. Jiang X, Cao G, Gao G, Wang W, Zhao J, Gao C. Triptolide decreases tumor-associated macrophages infiltration and M2 polarization to remodel colon cancer immune microenvironment via inhibiting tumor-derived CXCL12. *J Cell Physiol.* 2021; 236:193–204.  
<https://doi.org/10.1002/jcp.29833> PMID:32495392
  27. Stratton MR, Campbell PJ, Futreal PA. The cancer genome. *Nature.* 2009; 458:719–24.  
<https://doi.org/10.1038/nature07943> PMID:19360079
  28. Alexandrov LB, Nik-Zainal S, Wedge DC, Aparicio SA, Behjati S, Biankin AV, Bignell GR, Bolli N, Borg A, Børresen-Dale AL, Boyault S, Burkhardt B, Butler AP, et al, and Australian Pancreatic Cancer Genome Initiative, and ICGC Breast Cancer Consortium, and ICGC MMML-Seq Consortium, and ICGC PedBrain. Signatures of mutational processes in human cancer. *Nature.* 2013; 500:415–21.  
<https://doi.org/10.1038/nature12477> PMID:23945592
  29. Banerjee S, Kar A, Mukherjee PK, Haldar PK, Sharma N, Katiyar CK. Immunoprotective potential of Ayurvedic herb Kalmegh (*Andrographis paniculata*) against respiratory viral infections - LC-MS/MS and network pharmacology analysis. *Phytochem Anal.* 2021; 32:629–39.  
<https://doi.org/10.1002/pca.3011> PMID:33167083
  30. Liu Y, Easton J, Shao Y, Maciaszek J, Wang Z, Wilkinson MR, McCastlain K, Edmonson M, Pounds SB, Shi L, Zhou X, Ma X, Sioson E, et al. The genomic landscape of pediatric and young adult T-lineage acute lymphoblastic leukemia. *Nat Genet.* 2017; 49:1211–8.  
<https://doi.org/10.1038/ng.3909> PMID:28671688
  31. Yonemori K, Seki N, Kurahara H, Osako Y, Idichi T, Arai T, Koshizuka K, Kita Y, Maemura K, Natsugoe S. ZFP36L2 promotes cancer cell aggressiveness and is regulated by antitumor microRNA-375 in pancreatic ductal adenocarcinoma. *Cancer Sci.* 2017; 108:124–35.  
<https://doi.org/10.1111/cas.13119> PMID:27862697
  32. Zabala-Letona A, Arruabarrena-Aristorena A, Martín-Martín N, Fernandez-Ruiz S, Sutherland JD, Clasquin M, Tomas-Cortazar J, Jimenez J, Torres I, Quang P, Ximenez-Embun P, Bago R, Ugalde-Olano A, et al. mTORC1-dependent AMD1 regulation sustains polyamine metabolism in prostate cancer. *Nature.* 2017; 547:109–13.  
<https://doi.org/10.1038/nature22964> PMID:28658205

33. Xu L, You X, Cao Q, Huang M, Hong LL, Chen XL, Lei L, Ling ZQ, Chen Y. Polyamine synthesis enzyme AMD1 is closely associated with tumorigenesis and prognosis of human gastric cancers. *Carcinogenesis*. 2020; 41:214–22.  
<https://doi.org/10.1093/carcin/bgz098>  
PMID:[31140554](https://pubmed.ncbi.nlm.nih.gov/31140554/)
34. Abdelhaleem M, Maltais L, Wain H. The human DDX and DHX gene families of putative RNA helicases. *Genomics*. 2003; 81:618–22.  
[https://doi.org/10.1016/s0888-7543\(03\)00049-1](https://doi.org/10.1016/s0888-7543(03)00049-1)  
PMID:[12782131](https://pubmed.ncbi.nlm.nih.gov/12782131/)
35. Wu Y, Zhao W, Liu Y, Tan X, Li X, Zou Q, Xiao Z, Xu H, Wang Y, Yang X. Function of HNRNPC in breast cancer cells by controlling the dsRNA-induced interferon response. *EMBO J*. 2018; 37:e99017.  
<https://doi.org/10.15252/embj.201899017>  
PMID:[30158112](https://pubmed.ncbi.nlm.nih.gov/30158112/)
36. Prakash V, Carson BB, Feenstra JM, Dass RA, Sekyrova P, Hoshino A, Petersen J, Guo Y, Parks MM, Kurylo CM, Batchelder JE, Haller K, Hashimoto A, et al. Ribosome biogenesis during cell cycle arrest fuels EMT in development and disease. *Nat Commun*. 2019; 10:2110.  
<https://doi.org/10.1038/s41467-019-10100-8>  
PMID:[31068593](https://pubmed.ncbi.nlm.nih.gov/31068593/)
37. Belin S, Beghin A, Solano-González E, Bezin L, Brunet-Manquat S, Textoris J, Prats AC, Mertani HC, Dumontet C, Diaz JJ. Dysregulation of ribosome biogenesis and translational capacity is associated with tumor progression of human breast cancer cells. *PLoS One*. 2009; 4:e7147.  
<https://doi.org/10.1371/journal.pone.0007147>  
PMID:[19779612](https://pubmed.ncbi.nlm.nih.gov/19779612/)
38. Baßler J, Hurt E. Eukaryotic Ribosome Assembly. *Annu Rev Biochem*. 2019; 88:281–306.  
<https://doi.org/10.1146/annurev-biochem-013118-110817> PMID:[30566372](https://pubmed.ncbi.nlm.nih.gov/30566372/)
39. Kressler D, Hurt E, Bassler J. Driving ribosome assembly. *Biochim Biophys Acta*. 2010; 1803:673–83.  
<https://doi.org/10.1016/j.bbamcr.2009.10.009>  
PMID:[19879902](https://pubmed.ncbi.nlm.nih.gov/19879902/)
40. Pelletier J, Sonenberg N. The Organizing Principles of Eukaryotic Ribosome Recruitment. *Annu Rev Biochem*. 2019; 88:307–35.  
<https://doi.org/10.1146/annurev-biochem-013118-111042> PMID:[31220979](https://pubmed.ncbi.nlm.nih.gov/31220979/)
41. Harris PJ, Speranza G, Dansky Ullmann C. Targeting embryonic signaling pathways in cancer therapy. *Expert Opin Ther Targets*. 2012; 16:131–45.  
<https://doi.org/10.1517/14728222.2011.645808>  
PMID:[22239436](https://pubmed.ncbi.nlm.nih.gov/22239436/)
42. Tostar U, Malm CJ, Meis-Kindblom JM, Kindblom LG, Toftgård R, Undén AB. Dereglulation of the hedgehog signalling pathway: a possible role for the PTCH and SUFU genes in human rhabdomyoma and rhabdomyosarcoma development. *J Pathol*. 2006; 208:17–25.  
<https://doi.org/10.1002/path.1882>  
PMID:[16294371](https://pubmed.ncbi.nlm.nih.gov/16294371/)
43. Xie J, Murone M, Luoh SM, Ryan A, Gu Q, Zhang C, Bonifas JM, Lam CW, Hynes M, Goddard A, Rosenthal A, Epstein EH Jr, de Sauvage FJ. Activating Smoothed mutations in sporadic basal-cell carcinoma. *Nature*. 1998; 391:90–2.  
<https://doi.org/10.1038/34201> PMID:[9422511](https://pubmed.ncbi.nlm.nih.gov/9422511/)
44. Amakye D, Jagani Z, Dorsch M. Unraveling the therapeutic potential of the Hedgehog pathway in cancer. *Nat Med*. 2013; 19:1410–22.  
<https://doi.org/10.1038/nm.3389> PMID:[24202394](https://pubmed.ncbi.nlm.nih.gov/24202394/)
45. Jagani Z, Mora-Blanco EL, Sansam CG, McKenna ES, Wilson B, Chen D, Klekota J, Tamayo P, Nguyen PT, Tolstorukov M, Park PJ, Cho YJ, Hsiao K, et al. Loss of the tumor suppressor Snf5 leads to aberrant activation of the Hedgehog-Gli pathway. *Nat Med*. 2010; 16:1429–33.  
<https://doi.org/10.1038/nm.2251> PMID:[21076395](https://pubmed.ncbi.nlm.nih.gov/21076395/)
46. Wang Y, Ding Q, Yen CJ, Xia W, Izzo JG, Lang JY, Li CW, Hsu JL, Miller SA, Wang X, Lee DF, Hsu JM, Huo L, et al. The crosstalk of mTOR/S6K1 and Hedgehog pathways. *Cancer Cell*. 2012; 21:374–87.  
<https://doi.org/10.1016/j.ccr.2011.12.028>  
PMID:[22439934](https://pubmed.ncbi.nlm.nih.gov/22439934/)
47. Takebe N, Miele L, Harris PJ, Jeong W, Bando H, Kahn M, Yang SX, Ivy SP. Targeting Notch, Hedgehog, and Wnt pathways in cancer stem cells: clinical update. *Nat Rev Clin Oncol*. 2015; 12:445–64.  
<https://doi.org/10.1038/nrclinonc.2015.61>  
PMID:[25850553](https://pubmed.ncbi.nlm.nih.gov/25850553/)
48. Riobó NA, Lu K, Ai X, Haines GM, Emerson CP Jr. Phosphoinositide 3-kinase and Akt are essential for Sonic Hedgehog signaling. *Proc Natl Acad Sci USA*. 2006; 103:4505–10.  
<https://doi.org/10.1073/pnas.0504337103>  
PMID:[16537363](https://pubmed.ncbi.nlm.nih.gov/16537363/)
49. Samanta S, Guru S, Elaimy AL, Amante JJ, Ou J, Yu J, Zhu LJ, Mercurio AM. IMP3 Stabilization of WNT5B mRNA Facilitates TAZ Activation in Breast Cancer. *Cell Rep*. 2018; 23:2559–67.  
<https://doi.org/10.1016/j.celrep.2018.04.113>  
PMID:[29847788](https://pubmed.ncbi.nlm.nih.gov/29847788/)
50. Zhang X, Wang D, Liu B, Jin X, Wang X, Pan J, Tu W, Shao Y. IMP3 accelerates the progression of prostate cancer through inhibiting PTEN expression in a

SMURF1-dependent way. J Exp Clin Cancer Res. 2020; 39:190.

<https://doi.org/10.1186/s13046-020-01657-0>  
PMID:[32938489](https://pubmed.ncbi.nlm.nih.gov/32938489/)

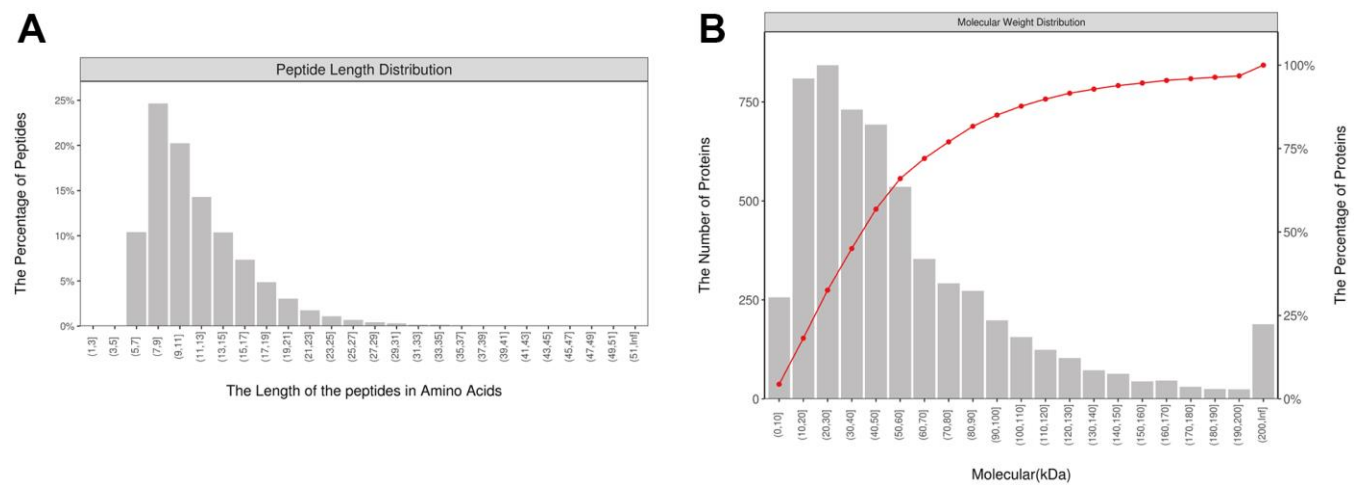
51. Zhang Y, Zhao L, Yang S, Cen Y, Zhu T, Wang L, Xia L, Liu Y, Zou J, Xu J, Li Y, Cheng X, Lu W, et al. CircCDKN2B-AS1 interacts with IMP3 to stabilize hexokinase 2 mRNA and facilitate cervical squamous cell carcinoma aerobic glycolysis progression. J Exp Clin Cancer Res. 2020; 39:281.

<https://doi.org/10.1186/s13046-020-01793-7>  
PMID:[33308298](https://pubmed.ncbi.nlm.nih.gov/33308298/)

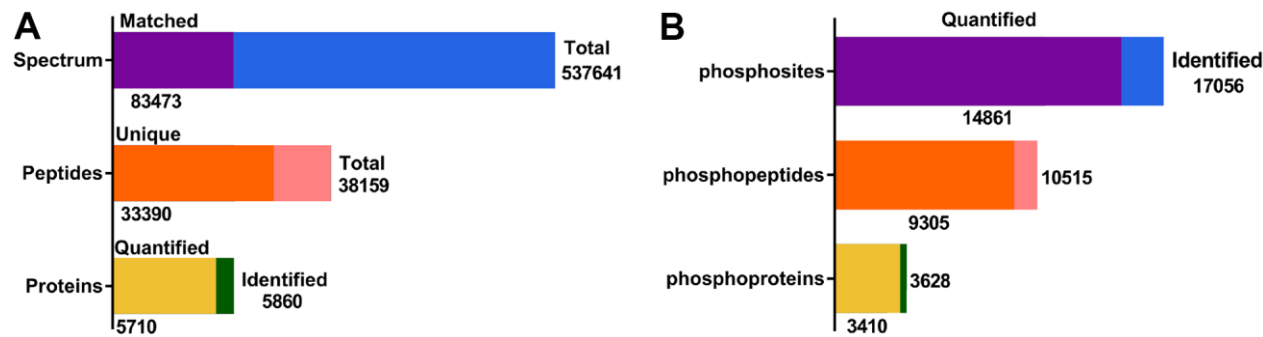
52. Zhang M, Zhao S, Tan C, Gu Y, He X, Du X, Li D, Wei P. RNA-binding protein IMP3 is a novel regulator of MEK1/ERK signaling pathway in the progression of colorectal Cancer through the stabilization of MEK1 mRNA. J Exp Clin Cancer Res. 2021; 40:200.  
<https://doi.org/10.1186/s13046-021-01994-8>  
PMID:[34154626](https://pubmed.ncbi.nlm.nih.gov/34154626/)

SUPPLEMENTARY MATERIALS

Supplementary Figures

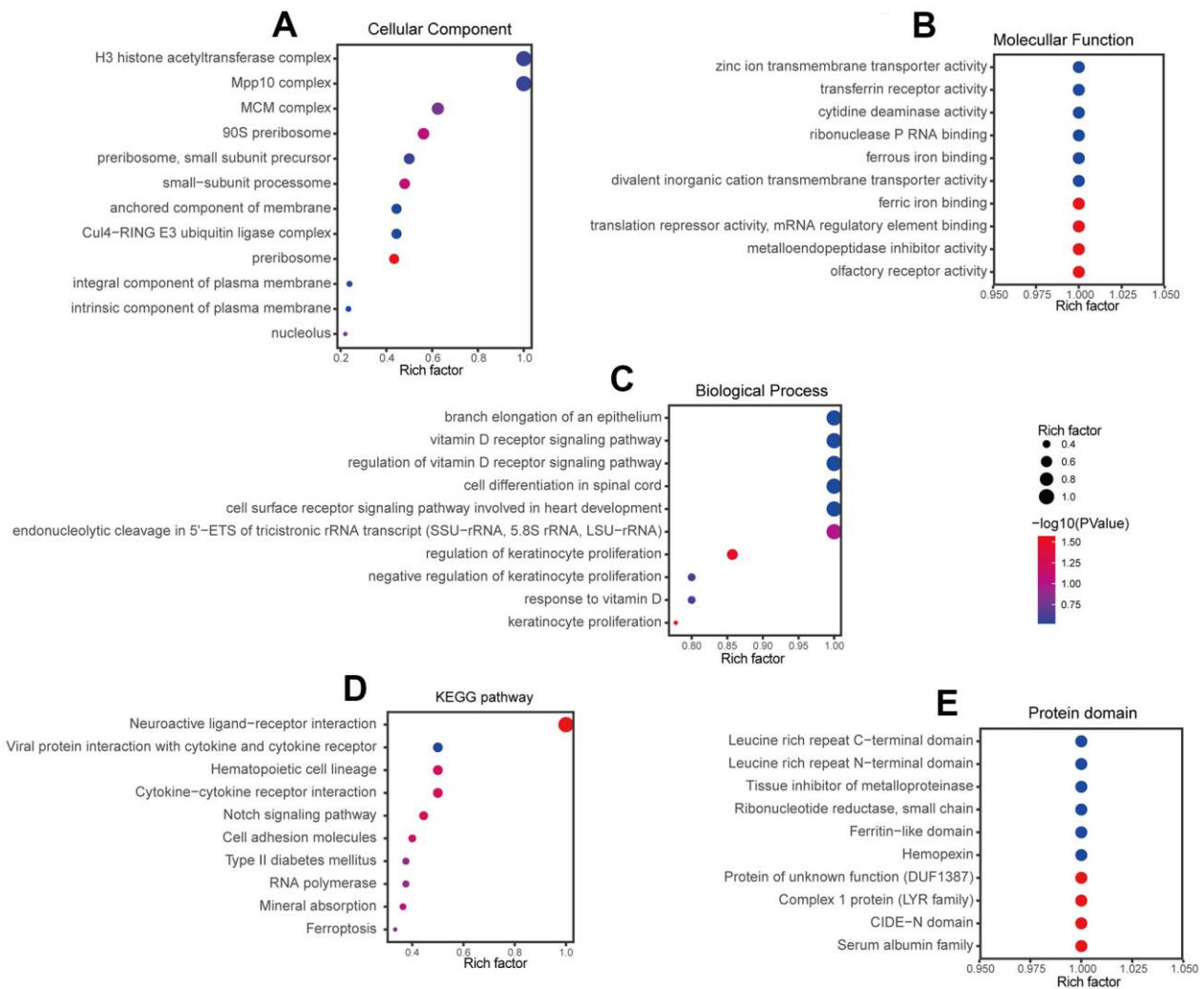


**Supplementary Figure 1.** (A) Distribution of peptide lengths identified by mass spectrometry. (B) Distribution of molecular weights of all proteins identified.

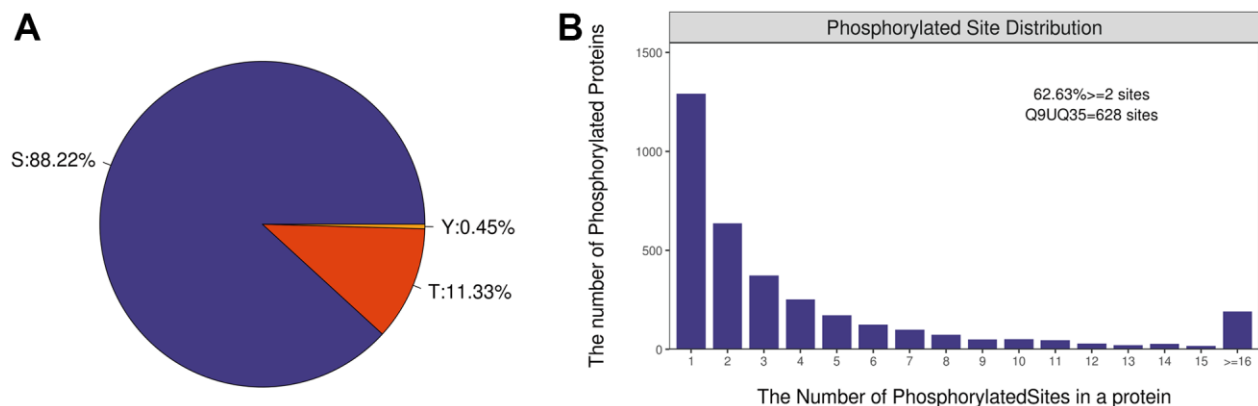


**Supplementary Figure 2.** (A) Results of proteome quantitation. (B) Results of phosphoproteome quantitation.

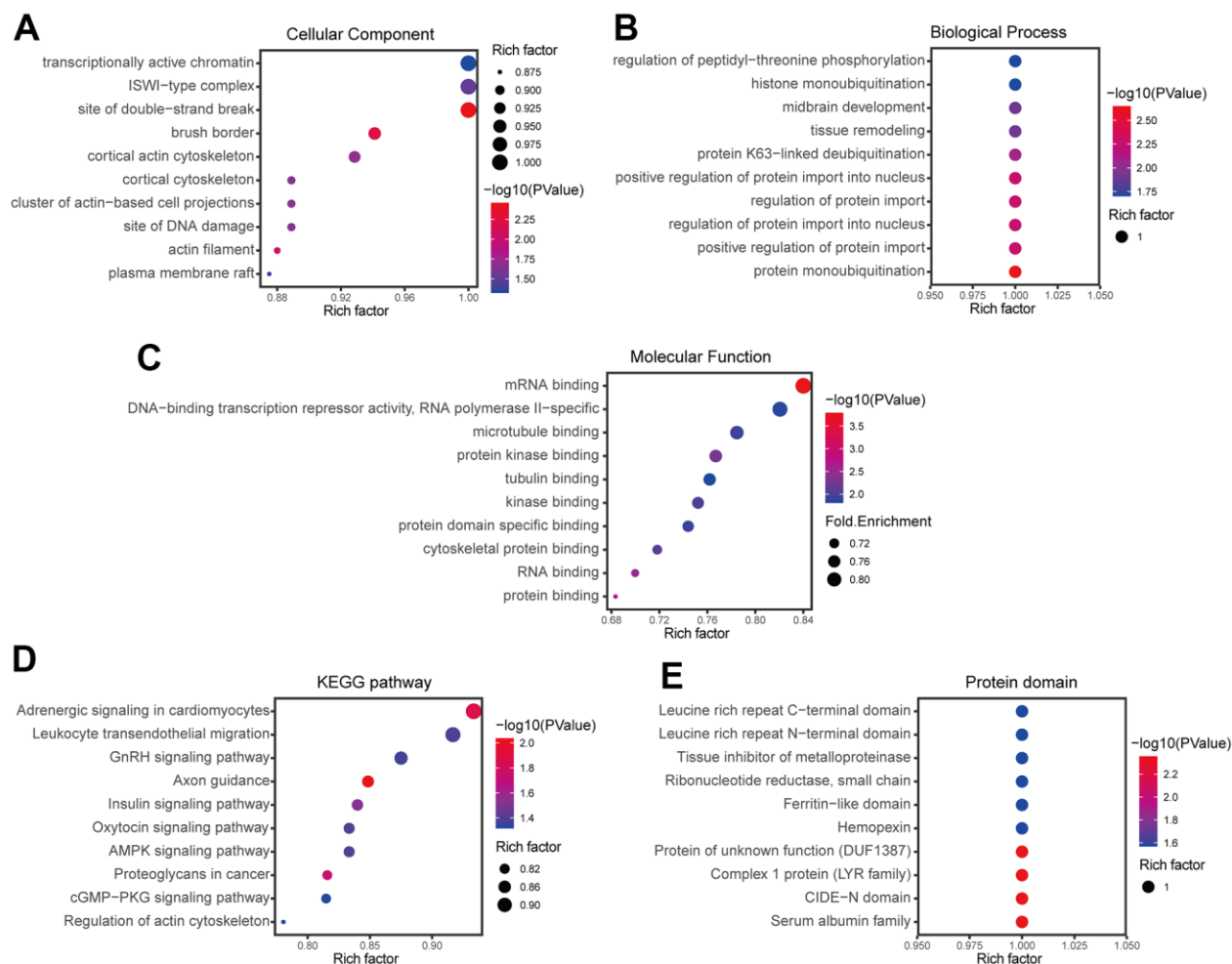




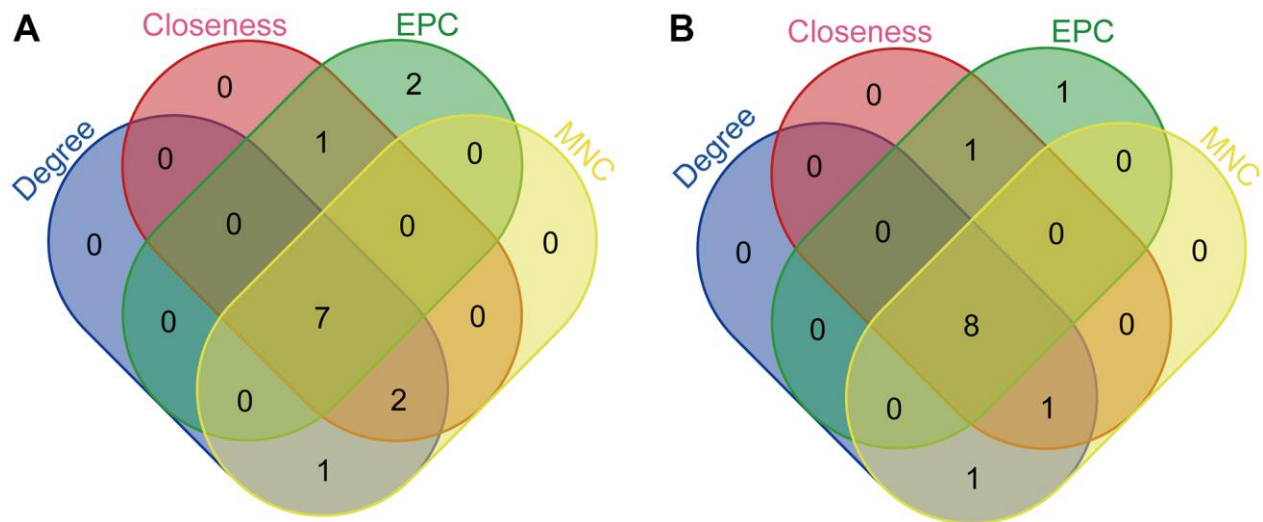
**Supplementary Figure 3.** (A) Clustering of differentially expressed proteins based on enrichment in Gene Ontology (GO) cellular components. (B) Clustering of differentially expressed proteins based on enrichment in GO molecular functions. (C) Clustering of differentially expressed proteins based on enrichment in GO biological processes. (D) Clustering of differentially expressed proteins based on enrichment in Kyoto Encyclopedia of Genes and Genomes (KEGG) pathways. (E) Clustering of differentially expressed proteins based on protein domains.



**Supplementary Figure 4.** (A) Distribution of serine (S), threonine (T) and tyrosine (Y) phosphorylation among all phosphoproteins identified by mass spectrometry. (B) Distribution of phosphoproteins based on number of phosphorylation sites per protein.



**Supplementary Figure 5.** (A) Clustering of differentially phosphorylated proteins based on enrichment in Gene Ontology (GO) cellular components. (B) Clustering of differentially phosphorylated proteins based on enrichment in Gene Ontology (GO) biological processes. (C) Clustering of differentially phosphorylated proteins based on enrichment in Gene Ontology (GO) molecular functions. (D) Clustering of differentially phosphorylated proteins based on enrichment in Kyoto Encyclopedia of Genes and Genomes (KEGG) pathways. (E) Clustering of differentially phosphorylated proteins based on enrichment in protein domains.



**Supplementary Figure 6.** (A) Venn diagram of differentially expressed proteins screened by four classification methods in order to identify hub proteins. (B) Venn diagram of differentially phosphorylated proteins screened by four classification methods in order to identify hub phosphorylated proteins.

## Supplementary Tables

**Supplementary Table 1. The top ten proteins screened by four classification methods.**

Degree	Closeness	EPC	MNC
IMP3	IMP3	IMP3	IMP3
BYSL	PDCD11	BYSL	BYSL
PDCD11	BYSL	PDCD11	PDCD11
PN01	PN01	RRS1	PN01
NSA2	NSA2	RPF2	NSA2
MPHOSPH10	MPHOSPH10	BMS1	MPHOSPH10
RPF2	RPF2	NOC4L	RPF2
RSL1D1	RRS1	NSA2	RSL1D1
RBM28	NOC4L	PN01	RBM28
RRS1	RSL1D1	KIAA0020	RRS1

**Supplementary Table 2. The top ten phosphorylation modified proteins screened by four classification methods.**

Degree	Closeness	EPC	MNC
SRSF1	SRSF1	SRSF1	SRSF1
NCBP1	HNRNPC	HNRNPC	NCBP1
HNRNPC	NCBP1	HNRNPA1	HNRNPC
HNRNPA1	HNRNPA1	NCBP1	HNRNPA1
DHX9	DHX9	DHX9	DHX9
SF3B1	SF3B1	SF3B1	SF3B1
DDX5	DDX5	RBM25	DDX5
RBM25	HIST1H4F	SRSF9	RBM25
SNRNP70	RBM25	DDX5	SNRNP70
HIST1H4F	SRSF9	SF3B3	HIST1H4F

**Supplementary Table 3. Interaction of hub genes with triptolide.**

Gene name	PDB ID	Herbs	$\Delta G_b$	H-Bonds
				Type amino acid
AMD1	3DZ7	Triptolide	-5.2803--5.7650	H-donor Arg A-20
IMP3	6FQR	Triptolide	-5.6453--6.1944	H-donor Lys A-3 H-donor Asn B-146 H-acceptor Asn B-146
HNRNPC	2MZ1	Triptolide	-5.0554--5.8036	H-donor Arg 17
DHX9	3VYX	Triptolide	-5.3092--5.4239	H-donor Thr 216

# Synergistic blocking of RAS downstream signaling and epigenetic pathway in *KRAS* mutant pancreatic cancer

Xiaofei Zhang<sup>1</sup>, Tiebo Mao<sup>1</sup>, Haiyan Xu<sup>1</sup>, Shumin Li<sup>1</sup>, Ming Yue<sup>1</sup>, Jingyu Ma<sup>1</sup>, Jiayu Yao<sup>1</sup>, Yongchao Wang<sup>1</sup>, Xiao Zhang<sup>1</sup>, Weiyu Ge<sup>1</sup>, Yanling Wang<sup>1</sup>, Daiyuan Shentu<sup>1</sup>, Liwei Wang<sup>1</sup>

<sup>1</sup>State Key Laboratory of Oncogenes and Related Genes, Shanghai Cancer Institute, Department of Oncology, Renji Hospital, School of Medicine, Shanghai Jiao Tong University, Shanghai, China

Correspondence to: Liwei Wang; email: [liweiwang@shsmu.edu.cn](mailto:liweiwang@shsmu.edu.cn)

Keywords: pancreatic ductal adenocarcinoma, MEK inhibitor, BET inhibitor, synergistic effect, autophagy

Received: December 28, 2021

Accepted: April 12, 2022

Published: April 25, 2022

Copyright: © 2022 Zhang et al. This is an open access article distributed under the terms of the [Creative Commons Attribution License](https://creativecommons.org/licenses/by/3.0/) (CC BY 3.0), which permits unrestricted use, distribution, and reproduction in any medium, provided the original author and source are credited.

## ABSTRACT

**Background:** Pancreatic ductal adenocarcinoma (PDAC) is a highly fatal malignancy and lacks effective therapeutic targets. Trametinib is considered to be a promising potential indirectly targeted *KRAS* inhibitor in PDAC. However, the clinical outcomes were poor. JQ1 displayed a significant synergistic effect when combined with chemotherapy or potential targeted therapy in pancreatic cancer. The impact of Trametinib and JQ1 combination treatment in PDAC remains to be fully elucidated.

**Methods:** The efficacy of trametinib and JQ1 on cell proliferation and cytotoxicity was assayed in 7 *KRAS* mutant pancreatic cancer cell lines. The cytotoxic effects of drugs either alone or in combination were evaluated using a luminescent cell viability assay. Immunoblot analysis was carried out to investigate changes in p62 and autophagy.

**Results:** We found that either trametinib or JQ1 alone inhibited the proliferation of some pancreatic cancer cell lines with *KRAS* alterations, irrespective of the mutational loci of *KRAS* and the aberrant status of the other driver genes. The synergistic effects of combination treatment of trametinib and JQ1 were observed in both trametinib-resistant and trametinib-sensitive cells. In trametinib-sensitive PDAC cells, the combined treatment definitely inhibited p62 expression compared with trametinib alone, while LC3 expression at high levels changed little. In trametinib-resistant PDAC cells, the combination of MEK/BET inhibitor dramatically decreased p62 expression compared with single agent, while p62 expression increased after anti-autophagic therapy was added.

**Conclusions:** Blocking RAS downstream signaling and epigenetic pathway synergistically increases the antiproliferative activity in *KRAS* mutant PDAC cells. Combination therapeutic synergism may induce different cell death modes in different pancreatic cancer subtypes.

## INTRODUCTION

Pancreatic ductal adenocarcinoma (PDAC) is a highly fatal malignancy with a rapid incidence rate worldwide [1]. Approximately 80–85% of PDAC patients have unresectable or metastatic disease at the time of diagnosis [2]. In addition, the genetic and heterogeneity of PDAC make for a lack of effective therapeutic

options, leading to a 5-year survival rate of less than 10% worldwide [3]. It is estimated that pancreatic cancer will become the second leading cause of cancer death by 2030 [4].

Studies have revealed that up to 90% of PDAC patients harbor oncogene *KRAS* activating alterations, which play an essential role in PDAC initiation and



maintenance [5]. Directly inhibiting *KRAS* seems to be a desirable approach for specifically treating PDAC patients with *KRAS* mutations. However, with the exception of *KRAS* p.G12C specific inhibitors (a mutation merely accounts for 1% of PDAC patients), various attempts to directly inhibit *KRAS* have been unsuccessful [6]. As an alternative approach, targeting *KRAS* downstream effectors has been clinically explored [7]. Trametinib, as a highly selective MEK1/2 inhibitor, targets mitogen-activated protein kinase (MAPK) signaling which is a main pathway downstream of *KRAS*; however, a clinical study has been less encouraging when combined with chemotherapy in PDAC patients [8]. The failure of trametinib in PDAC is probably due to the activation of adaptive signaling, resulting in acquired drug resistance. However, whether there are potential epigenetic-based mechanisms regulating drug sensitivity remains to be fully elucidated.

JQ1, an epigenetic reader protein BET inhibitor of bromodomain-containing protein 4 (BRD4) has emerged as a potential modulation agent [9]. In pancreatic cancer, JQ1 has been reported to exert a synergistic effect and induce tumor regression when combined with gemcitabine, HDAC inhibitors, or even PARP inhibitors [10, 11]. Combination therapy based on BET inhibitors is considered to have promising therapeutic potential for pancreatic cancer [12].

In this study, we aimed to explore the impact of trametinib and/or JQ1 on *KRAS* mutant pancreatic cancer and address the potential mechanism.

## RESULTS

### MEK inhibitor trametinib suppresses pancreatic cancer cells

First, we demonstrated the structure of trametinib (Figure 1A) and the main genetic alterations in our human PDAC cell lines (Table 1). We found that all 7-cell lines carried *KRAS* and *TP53* mutations. AsPC-1 also had *SMAD4* and *CDKN2A* alterations. PSN1 and CFPAC-1 had *SMAD4* copy number variation (CNV) loss alterations, while Mia PaCa-2, PANC-1, HuP-T3, and HuP-T4 carried *CDKN2A* CNV loss alterations. Then we treated all PDAC cell lines with a decreasing concentration gradient of trametinib. Cytostatic responses were observed in all PDAC cell lines, but the effectiveness was totally different in different cell lines from the fitting curve (Figure 1B). AsPC-1, PSN1, and Mia PaCa-2 cells were relatively sensitive to trametinib, and their half maximal inhibitory (IC<sub>50</sub>) values were 1.046 nM, 3.866 nM, and 9.167 nM, respectively (Supplementary Table 1). The IC<sub>50</sub> values of CFPAC-1 and PANC-1 was 61.22 nM and 1031 nM, respectively, which were relatively resistant to trametinib. However, the IC<sub>50</sub> values of HuP-T3 and HuP-T4 were not reached when treated with the maximum concentration of 10  $\mu$ M trametinib.

### BET inhibitor JQ1 suppresses pancreatic cancer cells

To identify sensitivity or resistance to BET inhibitors, we demonstrated the structure of JQ1 (Figure 2A) and

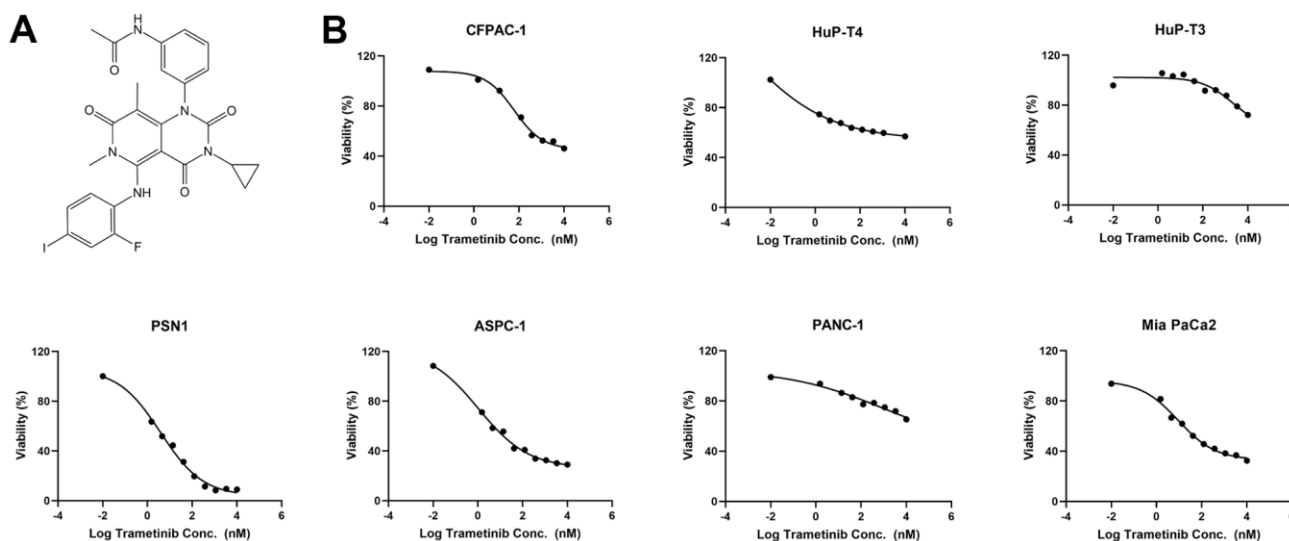


**Figure 1. The MEK inhibitor trametinib suppresses *KRAS* mutant pancreatic cancer cells.** (A) The structure of the MEK inhibitor trametinib. (B) Fitting curve of cytostatic responses illustrated a decreasing concentration gradient of trametinib in 7 *KRAS* mutant pancreatic cancer cell lines (AsPC-1, MIA PaCa-2, PANC-1, HuP-T4, HuP-T3, PSN1, and CFPAC-1).

**Table 1. Main mutation analysis of the PDAC cell lines.**

Cell lines	KRAS	TP53	SMAD4	CDKN2A
AsPC-1	p.G12D	p.C135fs	p.R100T	p.L78fs
MIA PaCa-2	p.G12C	p.R248W	wild type	CNV Loss
PANC-1	p.G12D	p.R273H	wild type	CNV Loss
HuP-T4	p.G12V	p.I255T	wild type	CNV Loss
HuP-T3	p.G12R	p.R282W	wild type	CNV Loss
PSN1	p.G12R	p.K132Q	CNV Loss	wild type
CFPAC-1	p.G12V	p.C242R	CNV Loss	wild type

Abbreviations: p, protein; fs, frame shift; CNV, copy number variations.

examined the antiproliferative activity of JQ1 in 7 PDAC cell lines. Cytostatic responses were also observed in all cell lines (Figure 2B). We observed that the IC<sub>50</sub> values of AsPC-1, PANC-1, HuP-T3, and PSN1 were not reached even if the maximum concentration of 10  $\mu$ M JQ1 was used (Supplementary Table 2). The IC<sub>50</sub> values of the other three cell lines (HuP-T4, Mia PaCa-2, CFPAC-1) were 177.6 nM, 238.7 nM, and 362.3 nM, respectively.

### Synergistic effects elicited by combined trametinib and JQ1 treatment in pancreatic cancer

To confirm the inhibitory effect of blocking the RAS downstream pathway and BET epigenetic transcriptional pathway, we screened the activity of BET/MEK inhibitor combinations in human *KRAS* mutant PDAC

cell lines. In trametinib-sensitive cell lines (AsPC-1 and PSN1), the combination of trametinib and JQ1 substantially reduced the percentage of cell viability, in AsPC-1 cells matching the multiplicative expectation and in PSN1 cells exceeding that which would be expected if monotherapy effects were multiplied (Figure 3A). In trametinib-resistant cells (CFPAC-1 and PANC-1), trametinib had little impact on cell viability. However, combined trametinib/JQ1 treatment resulted in a significantly greater reduction in cell viability than trametinib alone. In CFPAC-1 cells, the effect of trametinib and JQ1 combined was even stronger than would be expected if a single agent was used (Figure 3B). In PANC-1 cells, the effect of trametinib at a low concentration and JQ1 combination treatment still slightly exceeded expectations (Figure 3B). The following isobologram and combination

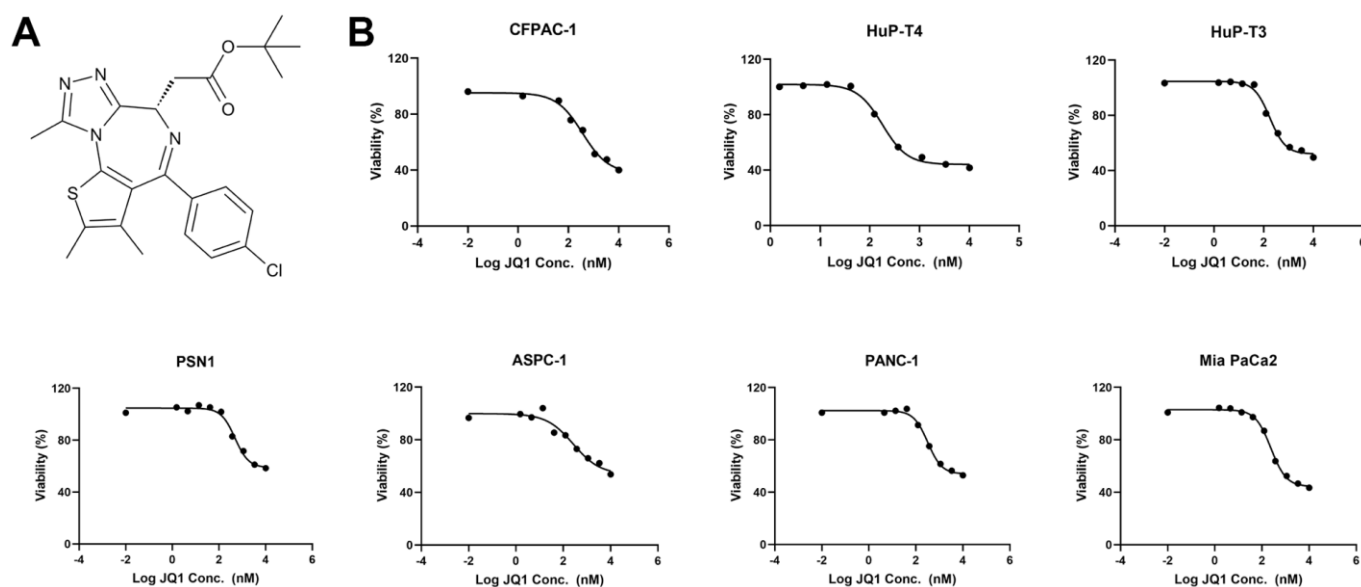


**Figure 2. The BET inhibitor JQ1 suppresses *KRAS* mutant pancreatic cancer cells.** (A) The structure of the BET inhibitor JQ1. (B) Fitting curve of cytostatic responses illustrated a decreasing concentration gradient of JQ1 treated with 7 *KRAS* mutant pancreatic cancer cell lines (AsPC-1, MIA PaCa-2, PANC-1, HuP-T4, HuP-T3, PSN1, and CFPAC-1).

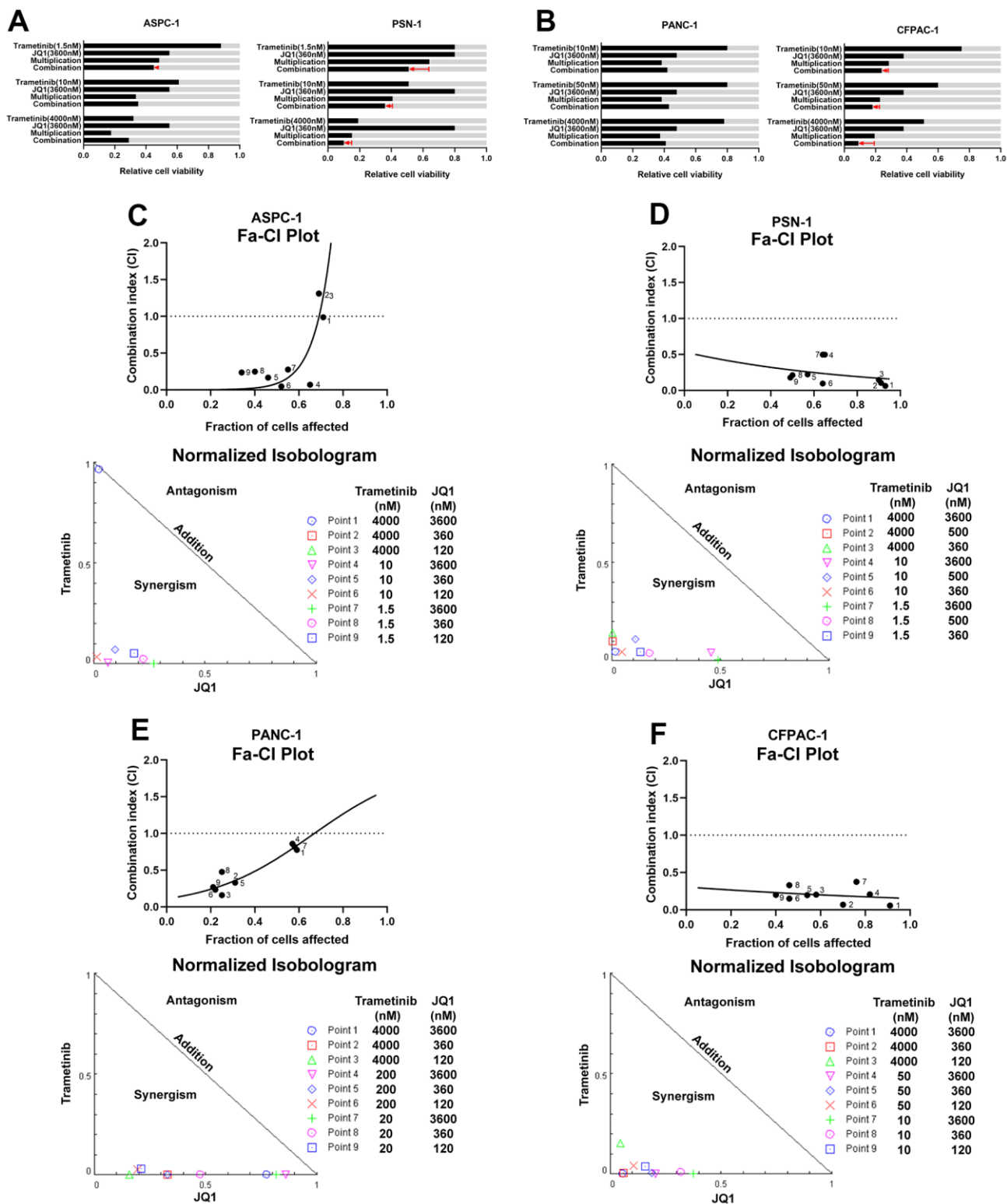


**Figure 3. Synergistic effects elicited by combined treatment trametinib and JQ1 in pancreatic cancer.** (A) Effect of trametinib and/or JQ1 on the percentage of cells in relative trametinib-sensitive PDAC cell lines (ASPC-1 and PSN-1). Light gray bars show control values. "Multiplication" indicates the expected effect of combined treatment if single-agent effects were multiplied; the red arrow indicates the actual effect of the combination. (B) Effect of trametinib and/or JQ1 on the percentage of cells in relative trametinib-resistant PDAC cell lines (PANC-1 and CFPAC-1). (C–F) Combination index (CI) (top) and isobologram (bottom) analyses reveal the synergistic effect of trametinib and JQ1 not only in trametinib-sensitive PDAC cell lines (ASPC-1 and PSN-1), but also in trametinib-resistant PDAC cell lines (PANC-1 and CFPAC-1). Fraction affected (Fa)-CI plots (top) and normalized isobolograms (bottom) are shown.

index (CI) analyses demonstrated that combined trametinib/JQ1 treatment had synergistic inhibitory effects on both trametinib-sensitive and trametinib-resistant *KRAS* mutant PDAC cell growth for most concentration pairings (Figure 3C–3F). Except for AsPC-1 treated with a high concentration of trametinib, trametinib-sensitive cell lines with different combined treatment concentrations showed strongly synergistic inhibition with CI < 0.5 (Figure 3C, 3D). Interestingly, trametinib-resistant PDAC cell lines also displayed potent synergistic inhibitory effects of trametinib/JQ1 combination therapy (Figure 3E, 3F). It is worth mentioning that PANC-1 cells had almost no response to trametinib treatment alone, but there was a strong synergistic effect of combination therapy when JQ1 was used at low and median concentrations (Figure 3E). Together, the combined inhibition of the RAS downstream pathway and BET family proteins results in a potent synergistic antitumoral response to *KRAS* mutant pancreatic cancer cells.

### The combination of trametinib and JQ1 via different cell death modes inhibits pancreatic cancer

Recently, it has been reported that inhibition of the RAS-MEK-ERK signaling pathway induces protective autophagy in pancreatic cancer cells preventing the cytotoxic effects of *KRAS* pathway inhibition [13]. Next, we preliminarily explored the mechanisms between autophagy and MEKi resistance and the synergistic effect with BET inhibitors. We examined the expression of autophagy-related proteins after

treatment in the relative trametinib-sensitive cell line PSN-1 and the relative trametinib-resistant cell line CFPAC-1 by immunoblotting. We observed high expression of LC3 and accumulation of p62/SQSTM1 in PSN-1 cells treated with trametinib alone, JQ1 alone or the combination treatment, respectively (Figure 4A). Compared with trametinib alone, p62 expression was more increased in the combination treatment. It was suggested that the synergistic effect of PSN1 combined therapy inhibited autophagy, thus strengthening the apoptotic pathway. For the trametinib-resistant cell line CFPAC-1, the expression levels of LC3 and p62 did not change after treatment with trametinib alone (Figure 4B). Interestingly, the expression levels of LC3 were not altered in a time-dependent manner when combined with trametinib and JQ1 but were much lower than those of trametinib alone. However, p62 expression disappeared after combined treatment. The synergistic effect of CFPAC-1 combined therapy mainly activated autophagy-dependent cell death instead of apoptosis. To investigate whether the synergistic effect of the two different cell lines on combination therapy was involved in autophagy-dependent cell death, we added the autophagy inhibitor HCQ to PSN1 and CFPAC1 combination therapy. We found that the expression of p62 in PSN1 was slightly enhanced, while that in CFPAC1 was re-expressed after combined therapy plus HCQ (Figure 4A, 4B). This result indicated that autophagy-dependent cell death was mainly induced by the synergistic effect of combined therapy in trametinib-resistant cells but not in trametinib-sensitive cells.

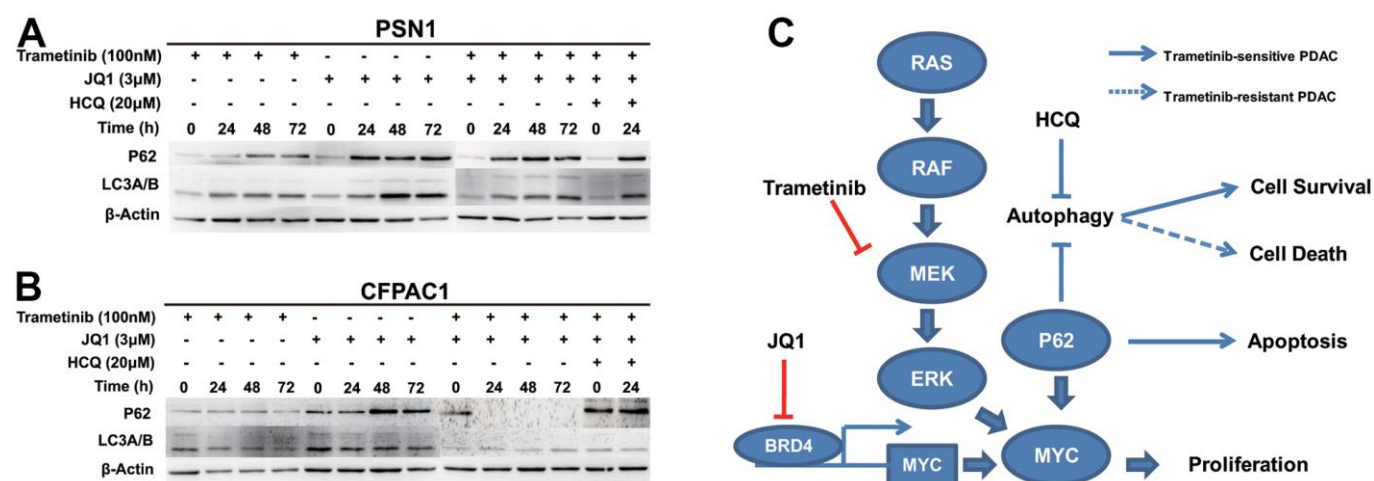


**Figure 4. The combination of trametinib and JQ1 via different cell death modes inhibits pancreatic cancer.** (A) Cell lysates prepared from PSN-1 cells treated with trametinib alone, JQ1 alone, trametinib+JQ1, and trametinib+JQ1+HCQ over a time course were analyzed by immunoblotting for p62, LC3, or actin, as indicated. (B) Cell lysates prepared from CFPAC-1 cells treated with trametinib alone, JQ1 alone, trametinib+JQ1, and trametinib+JQ1+HCQ over a time course were analyzed by immunoblotting for p62, LC3, or actin, as indicated. (C) Model of the synergistic effects induced by the combination treatment of trametinib and JQ1 in *KRAS* mutant pancreatic cancer.

## DISCUSSION

In this study, we screened the inhibitory effects of the MEK inhibitor trametinib and BET inhibitor JQ1 on 7 different pancreatic cancer *KRAS* mutant cell lines. Four cell lines that were relatively sensitive and resistant to trametinib were respectively tested for combination therapy. We observed a synergistic interaction from combination therapy on all cell lines, especially trametinib-resistant CFPAC-1 and trametinib-sensitive PSN1. Further mechanistic analysis showed that the combination therapy synergistic effect of trametinib-sensitive PDAC cells mainly came from apoptosis, while that of trametinib-resistant PDAC cells mainly activated autophagy-dependent cell death. This study was the first to clarify that combined trametinib and JQ1 treatment had a synergistic effect on *KRAS* mutant PDAC cells and elucidate that synergism induced different mechanisms of cell death in different PDAC cell lines.

Trametinib, an MEK1 and MEK2 kinase inhibitor, blocked ERK phosphorylation which downregulated MYC protein causing G1 cell cycle arrest and inducing apoptosis [14]. JQ1 a selective small-molecule bromodomain inhibitor, downregulated *MYC* transcription which produced a potent antiproliferative effect associated with cellular senescence and cell cycle arrest [9]. Combined treatment with BET and MEK inhibitors was reported to promote anaplastic thyroid tumors and colorectal cancer regression via synergistic suppression of *MYC* transcription [15, 16]. Recently, it has been demonstrated that combined MEK/BET inhibitors are much more effective depending on some biomarker in triple-negative breast cancer (TNBC) and in *KRAS* mutant non-small cell lung cancer (NSCLC) [17, 18]. However, the combinational effect of BET and MEK inhibitors has not been systematically evaluated in PDAC.

In our study, we found that either trametinib or JQ1 alone could inhibit the proliferation of some pancreatic cancer cell lines with *KRAS* alterations, irrespective of the mutational loci of *KRAS* and the mutational status of the other driver genes. Further studies demonstrated synergistic effects of the combination treatment of trametinib and JQ1 in both trametinib-resistant and trametinib-sensitive cell lines. It was shown that the BET inhibitor not only further enhanced the sensitivity of trametinib in trametinib-sensitive PDAC cells, but also improved the sensitivity of trametinib in trametinib-resistant PDAC cells. Finally, we preliminarily explored the mechanisms mediating the synergistic effects of the combination therapy in PDAC.

In the trametinib-sensitive PDAC cell line, the combined treatment definitely inhibited MYC, leading

to an increase in p62 expression compared with trametinib alone, while LC3 expression at high levels changed little. It was elucidated that the synergistic effect of MEK/BET inhibitors mainly induced apoptosis in trametinib-sensitive cells, despite slight protective autophagy. In the trametinib-resistant PDAC cell line, the combination of MEK inhibitor and BET inhibitor dramatically decreased p62 expression compared with single drug, while p62 expression increased after anti-autophagy therapy was added. This result revealed that the synergistic effect of combination therapy mainly elicited autophagy-dependent cell death in trametinib-resistant cells. P62/SQSTM1, a ubiquitin-binding multifunctional protein linked to the extrinsic apoptosis pathway promoting programmed cell death, binds directly to LC3 family proteins to negatively regulate autophagy as a marker to study autophagic flux [19]. Autophagy is considered a mechanism by which cancer cells maintain high metabolic levels in poor nutritious environments [20]. Protective autophagy has generally emerged as a drug resistance mechanism inducing metabolic stress for cell survival when pancreatic cancer cells are treated with MEK or ERK inhibitors [13, 21]. However, under certain conditions such as anticancer treatment, autophagy can directly or indirectly induce cell death [20]. Our studies demonstrated that the synergistic effect of trametinib and JQ1 combined therapy might induce different ways of cancer cell death in different pancreatic cancer subtypes (Figure 3C). This indicates that the current clinical exploration of autophagy inhibitors combined with chemotherapy or trametinib in PDAC patients may encounter some bottlenecks [22]. We believe that only screening pancreatic cancer patients who produce protective or adaptive autophagy after treatment could obtain real benefits from anti-autophagic therapy.

Our study also has some limitations. We have not tested the synergistic effect of combination therapy *in vivo*. Animal assays to evaluate the safety and immune effect of trametinib/JQ1 combination therapy have been confirmed in other tumors [17, 18]. We preliminarily verified that blocking the *KRAS* downstream pathway combined with an anti-epigenetic BET inhibitor has a favorable synergistic effect in *KRAS* mutant PDAC cells. In addition, *KRAS* wild-type pancreatic cancer and the detailed regulatory molecular mechanism of different cell death modes induced by combined therapy should be explored and confirmed in the future. Finally, the mechanism of trametinib/JQ1/HQ1 combined treatment is complex, and the antiproliferative effect and the cell death mode need strict designed experiments to be further evaluated.

In summary, our findings show that blocking RAS downstream signaling and epigenetic pathway



synergistically increases the antiproliferative activity in *KRAS* mutant pancreatic cancer cells. Combination therapeutic synergism induces autophagy-dependent cell death in some pancreatic cancer subtypes. This suggests that trametinib and JQ1 can be viewed as potential combination therapeutic options for PDAC patients with *KRAS* alterations. Treatment containing anti-autophagic regimens requires screening suitable pancreatic cancer patients, which needs to be further verified.

## MATERIALS AND METHODS

### Cell culture

The human pancreatic cancer cell lines AsPC-1, MIA PaCa-2, PANC-1, HuP-T4, HuP-T3, PSN1, and CFPAC-1 were purchased from American Type Culture Collection (ATCC) and provided by Suzhou Truway Biotechnology Inc. All cell genetic information was analyzed and downloaded from the Cancer Cell Line Encyclopedia (CCLE) or Catalogue of Somatic Mutations in Cancer (COSMIC) database. Cells were cultured in RPMI 1640, McCoy's 5a, MEM or DMEM supplemented with 10% fetal bovine serum (FBS) and 1% penicillin/streptomycin under the recommended conditions. The ATCC has performed morphological, cytogenetic and DNA profile analyses for characterization of these cell lines. The cell passages were limited to 15 generations for all experiments in this study. Mycoplasma contamination was excluded using the antibiotic mycoplasma (InvivoGen) and was periodically examined using a MycoFluor Mycoplasma Detection Kit (Invitrogen, #M7006).

### Compounds

Trametinib (GSK1120212, MEK inhibitor, APEXBio Technology, Shanghai, China), JQ1 (BET bromodomain inhibitor, APEXBio Technology, Shanghai, China), and hydroxychloroquine (HCQ, autophagy inhibitor, APEXBio Technology, Shanghai, China) were dissolved in DMSO.

### Cell viability assay

Cell viability assays were carried out using the CellTiter-Glo® Luminescent Cell Viability Assay (Promega, USA). Cells were seeded into 96-well cell culture plates at a density of 5000 cells per well in 100  $\mu$ L of culture medium and treated with the indicated drugs at various concentrations. After 72 h of incubation, the cells were lysed with CellTiter Glo reagent (Promega, #G7573), and the luminescence signals produced by ATP molecules from live cells were measured using a SPARK microplate reader

(TECAN, Switzerland) after 30 min of incubation at room temperature. The dose-response curve was fitted based on the relative survival cell percentage in nonlinear fitness (curve fit) using GraphPad Prism 8 software (<http://www.graphpad.com/scientific-software/prism/>). The software build-in analyses “nonlinear regression (curve fit)” and equation “log (inhibitor) vs. response-variable slope” were used for the data analysis and IC50 calculation.

### Immunoblot analysis

Cultured cells were extracted with RIPA buffer containing protease inhibitors and a phosphatase inhibitor cocktail (Roche). The protein concentration was determined by the BCA assay (Pierce). Proteins were resolved by SDS-PAGE, transferred to PVDF membranes (Millipore) and analyzed by immunoblotting. The antibodies used were as follows: LC3A/B antibody (#4108, 1:2000) and SQSTM1/p62 antibody (#5114, 1:2000) were purchased from Cell Signaling Technology, and  $\beta$ -actin (#A5316, 1:2500) was purchased from GenScript.

### Statistical analysis

All statistical analyses were performed using GraphPad Prism 8 (San Diego, CA, USA). Student's unpaired t-tests were used to compare two independent groups before and after different treatments as appropriate. P values less than 0.05 were considered to be statistically significant.

### Abbreviations

PDAC: pancreatic ductal adenocarcinoma; MAPK: mitogen-activated protein kinase; TNBC: triple-negative breast cancer; NSCLC: non-small cell lung cancer; CCLE: Cancer Cell Line Encyclopedia; COSMIC: Catalogue of Somatic Mutations in Cancer; FBS: fetal bovine serum.

## AUTHOR CONTRIBUTIONS

XFZ and LWW designed the study. XFZ created the study methodology. XFZ, TBM, HYX, SML, MY, JYM, JYY, YCW, XZ, YLW, DYST, and WYG cultured cells, tested drug sensitivity and processed the immunoblots. XFZ wrote the manuscript. XFZ and LWW obtained funding. LWW supervised the study. All authors reviewed and approved the manuscript.

## ACKNOWLEDGMENTS

The authors thank Suzhou Truway Biotechnology Inc. providing pancreatic cancer cell lines.

## CONFLICTS OF INTEREST

The authors declare no conflicts of interest.

## FUNDING

This work was supported by a senior investigator LWW's funding from the Innovation Group Project of Shanghai Municipal Health Commission (2019CXJQ03), National Natural Science Foundation of China (81874048, 82171824), Shanghai Municipal Commission of Health and Family Planning (2018ZHYL0223), Fostering Fund of Renji Hospital Affiliated to Shanghai Jiao Tong University School of Medicine (PYIV-17-001), Clinical Research Plan of SHDC (No. SHDC2020CR1035B), Shanghai Key Clinical Specialty (Oncology), Shanghai Leading Talents Project, and Innovative Research Team of High-level Local Universities in Shanghai. Additionally, supported by XFZ's grant from Clinical plus Excellence Project (2020ZYA003) from Shanghai Nucleic Acid Chemistry and Nanomedicine Key Laboratory. The funders had no role in the study design, data collection and analysis, decision to publish, or preparation of the manuscript.

## REFERENCES

1. Mizrahi JD, Surana R, Valle JW, Shroff RT. Pancreatic cancer. *Lancet*. 2020; 395:2008–20.  
[https://doi.org/10.1016/S0140-6736\(20\)30974-0](https://doi.org/10.1016/S0140-6736(20)30974-0)  
PMID:32593337
2. Casolino R, Braconi C, Malleo G, Paiella S, Bassi C, Milella M, Dreyer SB, Froeling FE, Chang DK, Biankin AV, Golan T. Reshaping preoperative treatment of pancreatic cancer in the era of precision medicine. *Ann Oncol*. 2021; 32:183–96.  
<https://doi.org/10.1016/j.annonc.2020.11.013>  
PMID:33248227
3. Siegel RL, Miller KD, Jemal A. Cancer statistics, 2020. *CA Cancer J Clin*. 2020; 70:7–30.  
<https://doi.org/10.3322/caac.21590> PMID:31912902
4. Tsai S, Evans DB. Therapeutic Advances in Localized Pancreatic Cancer. *JAMA Surg*. 2016; 151:862–8.  
<https://doi.org/10.1001/jamasurg.2016.1113>  
PMID:27276001
5. Buscail L, Bournet B, Cordelier P. Role of oncogenic KRAS in the diagnosis, prognosis and treatment of pancreatic cancer. *Nat Rev Gastroenterol Hepatol*. 2020; 17:153–68.  
<https://doi.org/10.1038/s41575-019-0245-4>  
PMID:32005945
6. Hong DS, Fakih MG, Strickler JH, Desai J, Durm GA, Shapiro GI, Falchook GS, Price TJ, Sacher A, Denlinger CS, Bang YJ, Dy GK, Krauss JC, et al. KRASG12C Inhibition with Sotorasib in Advanced Solid Tumors. *N Engl J Med*. 2020; 383:1207–17.  
<https://doi.org/10.1056/NEJMoa1917239>  
PMID:32955176
7. Roberts PJ, Der CJ. Targeting the Raf-MEK-ERK mitogen-activated protein kinase cascade for the treatment of cancer. *Oncogene*. 2007; 26:3291–310.  
<https://doi.org/10.1038/sj.onc.1210422>  
PMID:17496923
8. Infante JR, Somer BG, Park JO, Li CP, Scheulen ME, Kasubhai SM, Oh DY, Liu Y, Redhu S, Stepwski K, Le N. A randomised, double-blind, placebo-controlled trial of trametinib, an oral MEK inhibitor, in combination with gemcitabine for patients with untreated metastatic adenocarcinoma of the pancreas. *Eur J Cancer*. 2014; 50:2072–81.  
<https://doi.org/10.1016/j.ejca.2014.04.024>  
PMID:24915778
9. Filippakopoulos P, Qi J, Picaud S, Shen Y, Smith WB, Fedorov O, Morse EM, Keates T, Hickman TT, Felletar I, Philpott M, Munro S, McKeown MR, et al. Selective inhibition of BET bromodomains. *Nature*. 2010; 468:1067–73.  
<https://doi.org/10.1038/nature09504>  
PMID:20871596
10. Mazur PK, Herner A, Mello SS, Wirth M, Hausmann S, Sánchez-Rivera FJ, Lofgren SM, Kuschma T, Hahn SA, Vangala D, Trajkovic-Arsic M, Gupta A, Heid I, et al. Combined inhibition of BET family proteins and histone deacetylases as a potential epigenetics-based therapy for pancreatic ductal adenocarcinoma. *Nat Med*. 2015; 21:1163–71.  
<https://doi.org/10.1038/nm.3952>  
PMID:26390243
11. Miller AL, Fehling SC, Garcia PL, Gamblin TL, Council LN, van Waardenburg RC, Yang ES, Bradner JE, Yoon KJ. The BET inhibitor JQ1 attenuates double-strand break repair and sensitizes models of pancreatic ductal adenocarcinoma to PARP inhibitors. *EBioMedicine*. 2019; 44:419–30.  
<https://doi.org/10.1016/j.ebiom.2019.05.035>  
PMID:31126889
12. Miller AL, Garcia PL, Yoon KJ. Developing effective combination therapy for pancreatic cancer: An overview. *Pharmacol Res*. 2020; 155:104740.  
<https://doi.org/10.1016/j.phrs.2020.104740>  
PMID:32135247
13. Kinsey CG, Camolotto SA, Boespflug AM, Guillen KP, Foth M, Truong A, Schuman SS, Shea JE, Seipp MT, Yap JT, Burrell LD, Lum DH, Whisenant JR, et al. Protective autophagy elicited by RAF→MEK→ERK inhibition suggests a treatment strategy for RAS-driven cancers. *Nat Med*. 2019; 25:620–7.

<https://doi.org/10.1038/s41591-019-0367-9>  
PMID:30833748

14. Infante JR, Fecher LA, Falchook GS, Nallapareddy S, Gordon MS, Becerra C, DeMarini DJ, Cox DS, Xu Y, Morris SR, Peddareddigari VG, Le NT, Hart L, et al. Safety, pharmacokinetic, pharmacodynamic, and efficacy data for the oral MEK inhibitor trametinib: a phase 1 dose-escalation trial. *Lancet Oncol.* 2012; 13:773–81.  
[https://doi.org/10.1016/S1470-2045\(12\)70270-X](https://doi.org/10.1016/S1470-2045(12)70270-X)  
PMID:22805291
15. Zhu X, Holmsen E, Park S, Willingham MC, Qi J, Cheng SY. Synergistic effects of BET and MEK inhibitors promote regression of anaplastic thyroid tumors. *Oncotarget.* 2018; 9:35408–21.  
<https://doi.org/10.18632/oncotarget.26253>  
PMID:30459933
16. Ma Y, Wang L, Neitzel LR, Loganathan SN, Tang N, Qin L, Crispi EE, Guo Y, Knapp S, Beauchamp RD, Lee E, Wang J. The MAPK Pathway Regulates Intrinsic Resistance to BET Inhibitors in Colorectal Cancer. *Clin Cancer Res.* 2017; 23:2027–37.  
<https://doi.org/10.1158/1078-0432.CCR-16-0453>  
PMID:27678457
17. Schafer JM, Lehmann BD, Gonzalez-Ericsson PI, Marshall CB, Beeler JS, Redman LN, Jin H, Sanchez V, Stubbs MC, Scherle P, Johnson KN, Sheng Q, Roland JT, et al. Targeting MYCN-expressing triple-negative breast cancer with BET and MEK inhibitors. *Sci Transl Med.* 2020; 12:eaaw8275.  
<https://doi.org/10.1126/scitranslmed.aaw8275>  
PMID:32161105
18. Guerra SL, Maertens O, Kuzmickas R, De Raedt T, Adeyemi RO, Guild CJ, Guillemette S, Redig AJ, Chambers ES, Xu M, Tiv H, Santagata S, Jänne PA, et al. A Deregulated HOX Gene Axis Confers an Epigenetic Vulnerability in KRAS-Mutant Lung Cancers. *Cancer Cell.* 2020; 37:705–19.e6.  
<https://doi.org/10.1016/j.ccell.2020.03.004>  
PMID:32243838
19. Moscat J, Diaz-Meco MT. p62 at the crossroads of autophagy, apoptosis, and cancer. *Cell.* 2009; 137:1001–4.  
<https://doi.org/10.1016/j.cell.2009.05.023>  
PMID:19524504
20. Piffoux M, Eriau E, Cassier PA. Autophagy as a therapeutic target in pancreatic cancer. *Br J Cancer.* 2021; 124:333–44.  
<https://doi.org/10.1038/s41416-020-01039-5>  
PMID:32929194
21. Bryant KL, Stalnecker CA, Zeitouni D, Klomp JE, Peng S, Tikunov AP, Gunda V, Pierobon M, Waters AM, George SD, Tomar G, Papke B, Hobbs GA, et al. Combination of ERK and autophagy inhibition as a treatment approach for pancreatic cancer. *Nat Med.* 2019; 25:628–40.  
<https://doi.org/10.1038/s41591-019-0368-8>  
PMID:30833752
22. Karasic TB, O'Hara MH, Loaiza-Bonilla A, Reiss KA, Teitelbaum UR, Borazanci E, De Jesus-Acosta A, Redlinger C, Burrell JA, Laheru DA, Von Hoff DD, Amaravadi RK, Drebin JA, O'Dwyer PJ. Effect of Gemcitabine and nab-Paclitaxel With or Without Hydroxychloroquine on Patients With Advanced Pancreatic Cancer: A Phase 2 Randomized Clinical Trial. *JAMA Oncol.* 2019; 5:993–8.  
<https://doi.org/10.1001/jamaoncol.2019.0684>  
PMID:31120501

## SUPPLEMENTARY MATERIALS

### Supplementary Tables

**Supplementary Table 1. Parameters of proliferation curve fitting with trametinib in PDAC.**

Cell lines	Bottom	Top	LogIC50	HillSlope	IC50(nM)
AsPC-1	26.22	122	0.01952	-0.3883	1.046
MIA PaCa-2	32.94	96.05	0.9622	-0.5241	9.167
PANC-1	42.92	104.9	3.013	-0.2029	1031
HuP-T4	54.26	194.6	-3.236	-0.2279	-
HuP-T3	61.18	102.2	3.335	-0.6284	-
PSN1	3.702	106	0.5873	-0.4583	3.866
CFPAC-1	45.41	107.8	1.787	-0.6881	61.22

Abbreviations: PDAC, pancreatic ductal adenocarcinoma.

**Supplementary Table 2. Parameters of proliferation curve fitting with JQ1 in PDAC.**

Cell lines	Bottom	Top	LogIC50	HillSlope	IC50(nM)
AsPC-1	53.65	99.85	2.423	-0.7698	-
MIA PaCa-2	44.3	102.9	2.378	-1.33	238.7
PANC-1	53.97	102.4	2.506	-1.448	-
HuP-T4	44.01	101.9	2.25	-1.738	177.6
HuP-T3	52.07	104.6	2.244	-1.375	-
PSN1	58.84	104.7	2.681	-1.478	-
CFPAC-1	37.7	95.25	2.559	-0.8447	362.3

Abbreviations: PDAC, pancreatic ductal adenocarcinoma.

# microRNA-569 inhibits tumor metastasis in pancreatic cancer by directly targeting NUSAP1

Xiaohui Guo<sup>1,2,3,4</sup>, Yatian Li<sup>1,2,3,4</sup>, Xiaofang Che<sup>1,2,3,4</sup>, Kezuo Hou<sup>1,2,3,4</sup>, Xiujuan Qu<sup>1,2,3,4,\*</sup>, Ce Li<sup>1,2,3,4,\*</sup>

<sup>1</sup>Department of Medical Oncology, The First Hospital of China Medical University, Shenyang 110001, China

<sup>2</sup>Key Laboratory of Anticancer Drugs and Biotherapy of Liaoning Province, The First Hospital of China Medical University, Shenyang 110001, China

<sup>3</sup>Liaoning Province Clinical Research Center for Cancer, The First Hospital of China Medical University, Shenyang 110001, China

<sup>4</sup>Key Laboratory of Precision Diagnosis and Treatment of Gastrointestinal Tumors, Ministry of Education, The First Hospital of China Medical University, Shenyang 110001, China

\*Equal contribution

**Correspondence to:** Xiujuan Qu, Ce Li; **email:** [xiqu@cmu.edu.cn](mailto:xiqu@cmu.edu.cn), [celi@cmu.edu.cn](mailto:celi@cmu.edu.cn)

**Keywords:** miR-569, NUSAP1, pancreatic cancer, metastasis, ZEB1

**Received:** June 14, 2021

**Accepted:** March 14, 2022

**Published:** April 28, 2022

**Copyright:** © 2022 Guo et al. This is an open access article distributed under the terms of the [Creative Commons Attribution License](https://creativecommons.org/licenses/by/3.0/) (CC BY 3.0), which permits unrestricted use, distribution, and reproduction in any medium, provided the original author and source are credited.

## ABSTRACT

MicroRNAs (miRNAs) are known to be involved in the development and progression of pancreatic cancer (PC). In this study, the prognostic significance and mechanistic role of microRNA-569 in PC were explored. Quantitative real-time PCR was used to detect the expression of microRNA-569 in PC tissues and cell lines. Scratch test and Transwell assay were conducted to detect migration and invasion ability. The xenograft nude mice model was used to determine tumor metastasis *in vivo*. The direct targets of microRNA-569 were determined by using bioinformatics analysis and a dual-luciferase reporter assay. The expression level of microRNA-569 was down-regulated in PC patients with a poor prognosis. *In vitro* and *in vivo* experiments indicated that over-expression of microRNA-569 inhibited the migration and invasion of PC cells. MicroRNA-569 negatively regulated NUSAP1 by directly binding its 3'-untranslated region. Further mechanism research implied that the ZEB1 pathway was involved in microRNA-569/NUSAP1 mediation of the biological behaviors in PC. These data demonstrated that microRNA-569 may exert a tumor-suppressing effect in PC and maybe a potential therapeutic target for PC patients.

## INTRODUCTION

Pancreatic cancer is often referred as the “king of cancers”, with a very poor prognosis, and is the fourth leading cause of cancer death in the world [1]. The main causes for the poor prognosis are its high aggressiveness, early metastasis, and profound chemoresistance [2, 3]. Due to the lack of specific diagnostic methods, more than 80% of patients with PC were found to have locally unresectable or metastatic diseases [4]. Even for patients who underwent a successful operation or good response to chemotherapy, most patients will eventually have local

recurrence or metastasis [5]. PC is prone to metastasize to the liver, lung, lymph nodes, and bones, which is closely related to patient death [6]. Thus, exploring the potential core gene affecting the malignant progression of pancreatic cancer is very crucial.

MicroRNAs (miRNAs), containing 22 to 25 nucleotides, belong to single-stranded ribonucleic acid and exert function by degrading or inhibiting the translation of other proteins to regulate gene expression [7]. Dysregulation of miRNAs were closely associated with the occurrence of various diseases, especially



cancers [8–12]. In lung cancer, miRNA-569 can be used as a tumor suppressor to induce apoptosis [13]. In mammary cancer, over-expression of miRNA-569 has a poor prognosis, and it could inhibit cancer progression by down-regulating TP53INP1 [14], however, there are no reports available on the effect of miR-569 in PC.

Nucleolar and spindle-associated protein 1 (NUSAP1), mainly modulates spindle assembly and stability during mitosis [15]. Previous studies have reported abnormal NUSAP1 expression presenting in multiple malignant tumors. The expression of NUSAP1 was up-regulated in colon cancer, which demonstrated a poor prognosis [16]. Fang et al. that NUSAP1 was significantly up-regulated in renal cell carcinoma, which strengthened a series of malignant biological behaviors of tumor cells [17]. However, NUSAP1 is rarely reported in pancreatic cancer.

Our research is the first to investigate the miRNA-569 expression in PC and reveal its relation with clinical outcomes. Furthermore, the biological role of miRNA-569 and its potential molecular mechanisms were investigated. miRNA-569 directly targets NUSAP1, which in turn regulates ZEB1 expression and inhibits PC cell migration and invasion.

## RESULTS

### microRNA-569 is an indicator of good prognosis

Patients with pancreatic cancer were divided into the following two groups: poor prognosis, 12 months or less; and good prognosis, above 21 months according to the survival time. As shown in Figure 1A, the high miRNA-

569 expression has a good prognosis, suggesting that miR-569 could serve as a good prognostic marker. Furthermore, the overall survival of PC patients with low miRNA-569 expression is shorter (Figure 1B). The median survival time of the low expression group was 10.6 months, while the high-expression group was 24.0 months.

### microRNA-569 over-expression suppresses migration and invasion in PC cells

PC is prone to metastasis in the late stage, especially liver metastasis, leading to a poor prognosis. The expression levels of miR-569 after transfection of mimics in SW1990 and Capan-2 cells were confirmed. As expected, miR-569 levels were significantly up-regulated after transfection of mimics (Figure 2A). Scratch assay and Transwell experiment indicated that, compared to miR-NC, the exogenous increase of miRNA-569 expression can inhibit the migration of PC cells (Figure 2B, 2C). Furthermore, the Transwell invasion assay also helped to confirm that overexpression of miRNA-569 could inhibit cell invasion (Figure 2D), thus, these data revealed that miRNA-569 has an obvious anti-metastatic effect.

### microRNA-569 inhibits PC liver metastasis *in vivo*

Then, we focus on the antitumor effect of miRNA-569 *in vivo*. Capan-2 was transfected with agomir-569 and control, respectively. Transfected cells were injected into the spleen of mice to establish the liver metastasis model, and the metastatic focus was evaluated ten weeks later (Figure 3A). *Ex vivo* luciferase imaging demonstrated that miRNA-569 overexpression significantly reduced liver metastasis in Capan-2 cells

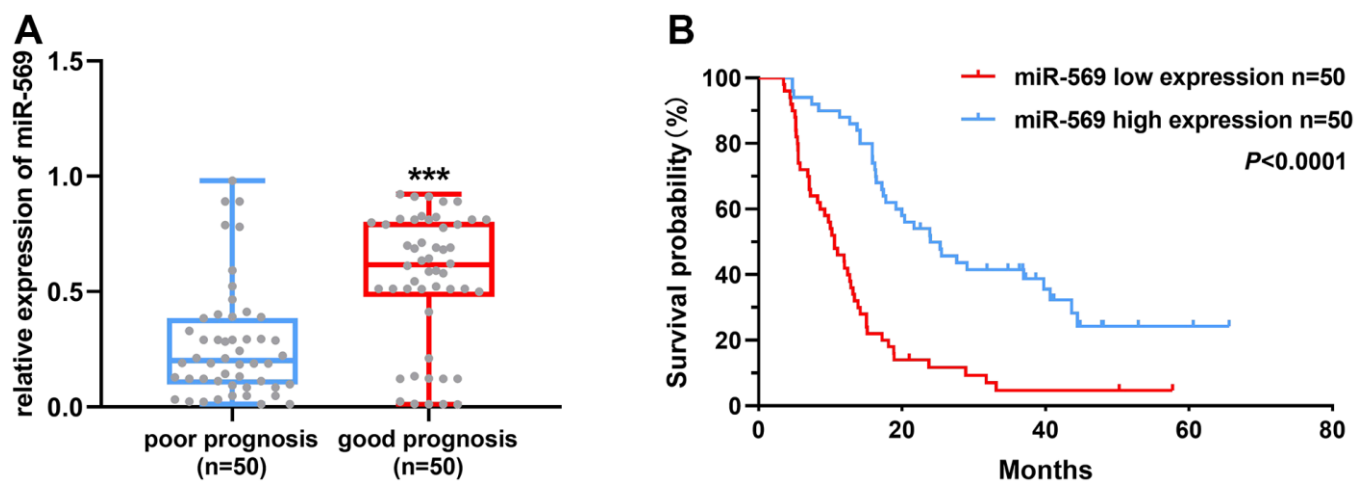


**Figure 1. miR-569 was down-regulated in PC tissues and patients with high miR-569 expression had a good prognosis.** (A) Analysis of miR-569 expression in PC tissues; (B) Kaplan-Meier Plotter analysis of the effect of miR-569 on PC patient survival.

compared with negative control (Figure 3B). The number of metastatic foci in mice injected with agomir-569 cells decreased significantly (Figure 3C). As indicated in Figure 3D, the hepatic metastatic foci

were stained by hematoxylin and eosin (HE). In summary, it can be inferred that miRNA-569 can inhibit liver metastasis of PC, which might have certain clinical significance.

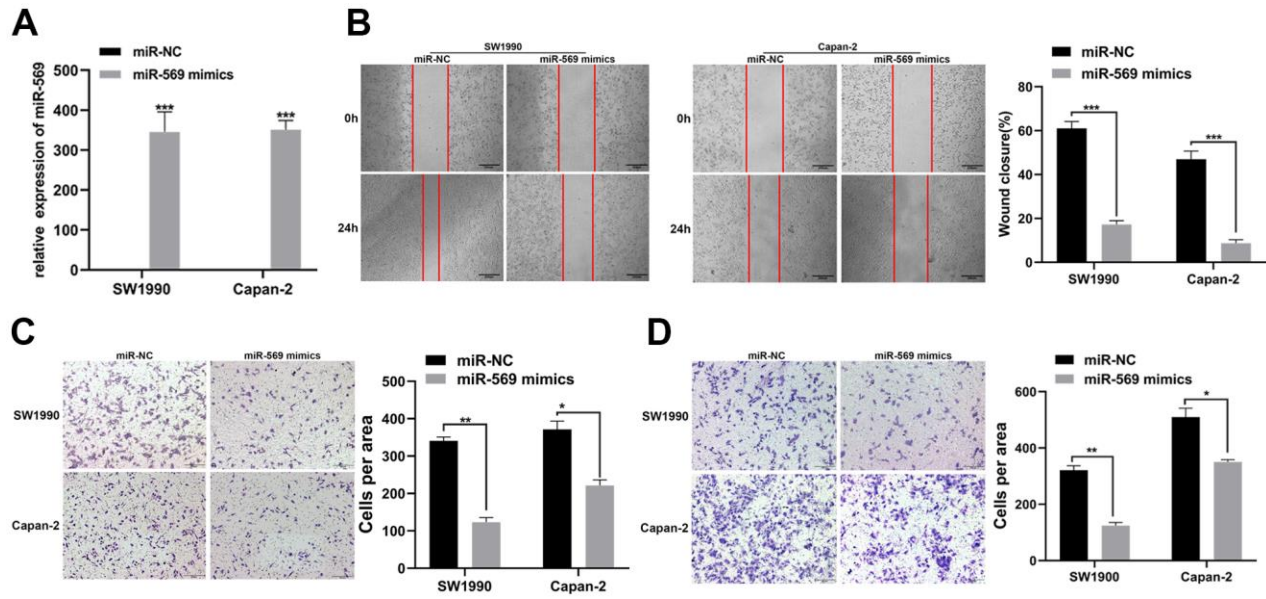


**Figure 2. miR-569 inhibited the migration and invasion of PC cells *in vitro*.** (A) RT-qPCR showed the miR-569 transfection efficiency. (B) Wound healing assay demonstrated migratory abilities of PC cells after over-expression of miR-569; (C) Transwell assay showed migratory abilities of PC cells after over-expression of miR-569; (D) Transwell assay indicated invasive abilities of PC cells after over-expression of miR-569. (\*  $p < 0.05$ , \*\*  $p < 0.01$ , \*\*\*  $p < 0.001$ ,  $n = 3$ , Student's *t*-test, means  $\pm$  95% CI).

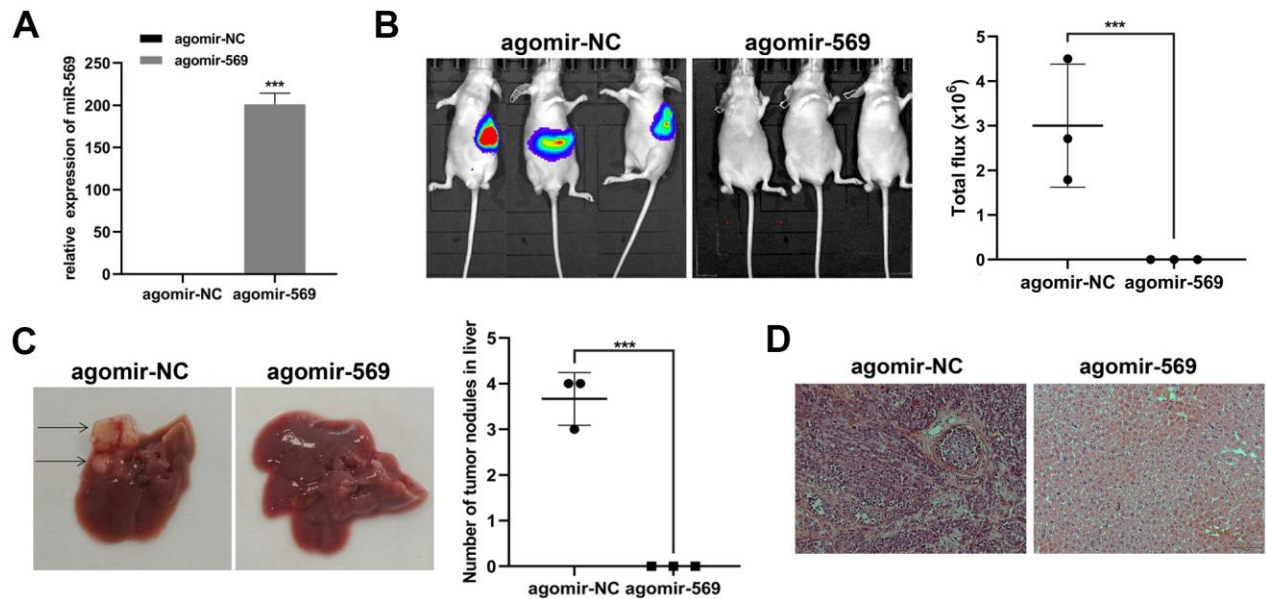


**Figure 3. miR-569 inhibited PC cell metastasis *in vivo*.** (A) RT-qPCR showed miRNA agomir transfection efficiency. (B) *In vivo* bioluminescence imaging of representative animals from each treatment group 10 weeks after tumor cell inoculation. (C) Representative images of the liver of nude mice. Black arrows show metastatic tumor colonies in the liver. (D) HE staining of metastatic tumor colonies in the liver, magnification  $\times 100$ . (\*  $p < 0.05$ , \*\*  $p < 0.01$ ,  $n = 5$ , Student's *t*-test, means  $\pm$  95% CI).

## Prediction and screening of target genes

TargetScan was used for the prediction of the target genes. Then by interaction with up-regulated genes as evidenced by the TCGA database, 141 target genes were identified and viewed in the form of a Venn diagram (Figure 4A). GO and KEGG analyses were applied to clarify the function of miRNA-569. GO analysis is composed of Biological processes (BPs), cellular components (CCs), and molecular functions (MFs) [18], which mainly concentrated on the extracellular matrix organization, focal adhesion, and GTPase activity, which were critical in the processes of cell biology (Figure 4B). For KEGG analysis, the PI3K-Akt signaling pathway and MAPK signaling pathway were reported to be closely related to the cancerous process of PC (Figure 4C). To screen hub genes, we constructed a protein-protein interaction network that consists of 399 nodes and 1499 edges, and we then focused on the 16 hub genes in the network highlighted by cytoHubba according to their degree of overexpression (Figure 4D, 4E). Since miRNA-569 was closely associated with prognosis, the LASSO Cox analysis was used to limit the possible choices of hub genes to facilitate the

selection of only the most useful target genes. This allowed us to identify two genes (ECT2 and NUSAP1) (Figure 5A–5C). The biological function of ECT2 in pancreatic cancer had been discussed in our previous work [19], so we mainly focused on NUSAP1 during subsequent research.

## Verification of target genes

By analyzing data available within the Oncomine database, NUSAP1 was found to be up-regulated in PC tissues relative to normal control (Figure 6A). High expression of NUSAP1 significantly shortened the overall survival time and disease-free survival time (Figure 6B). The base pairing was observed between mature miR-569 and the 3'-UTR region of the NUSAP1 gene-seed sequence (Figure 6C). A dual-luciferase experiment was then performed: as shown in Figure 6D, for the NUSAP1-3'-UTR-WT group, compared with miR-NC, the luciferase activity of miR-569 mimics was weakened. However, there was no significant difference in the NUSAP1-3'-UTR-MT group. In addition, miR-569 could block the expression of NUSAP1 protein (Figure 6E).

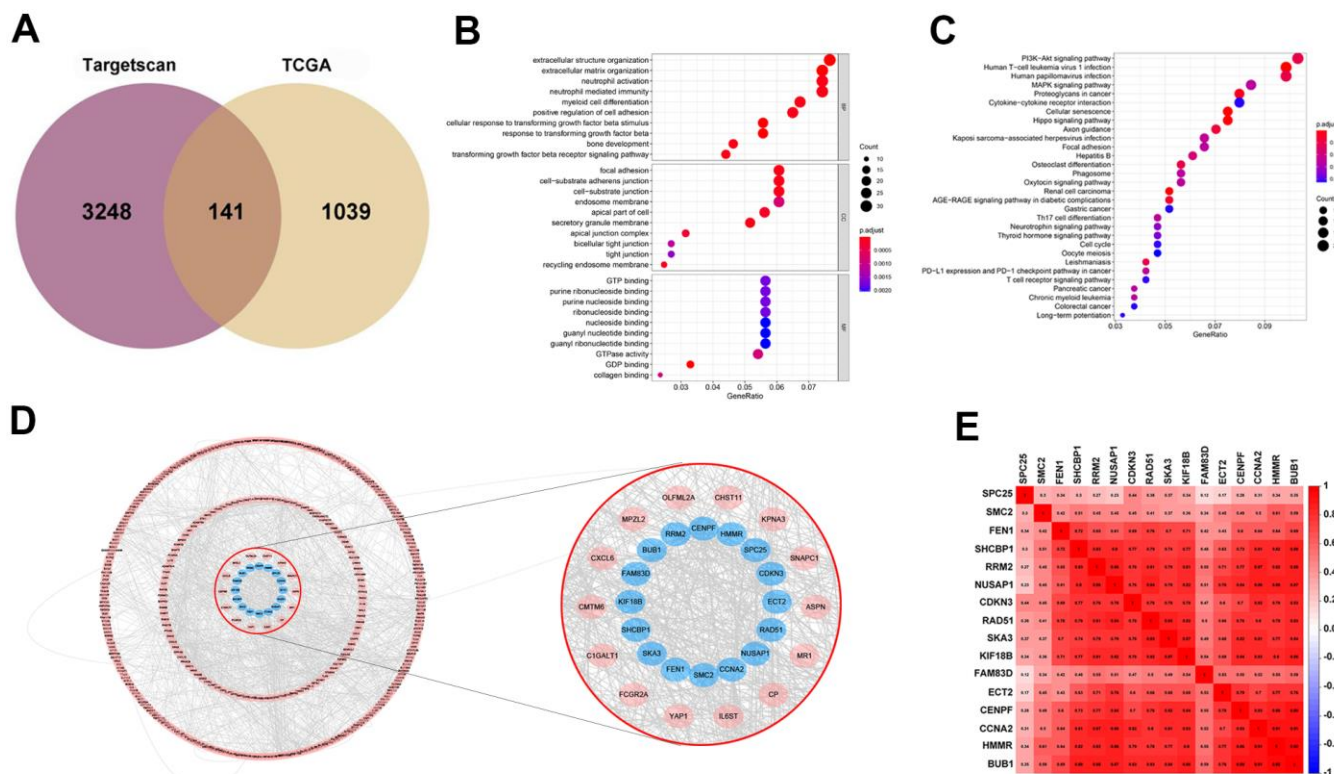


**Figure 4. Prediction and screening of the target gene of miR-569 through bioinformatics analysis.** (A) Venn diagram for the intersections between DEGs and miRNA target genes. (B, C) GO and KEGG analysis shows pathways in which the miR-569 target gene participates. (D) Protein-protein interaction networks of the miR-569 target genes using the Cytoscape database. (E) Correlation heatmap of hub genes.



## NUSAP1 knockdown suppresses PC cell migration and invasion

Then, we explored the influence of changes in the expression of NUSAP1 on the malignant biological behavior of PC. PCR and Western blot assay were carried out to validate the knockdown efficiency (Figure 7A, 7B). As expected, NUSAP1 knockdown significantly inhibited PC cell migration (Figure 7C). In addition, Transwell experiment demonstrated that knockdown of endogenous NUSAP1 expression inhibited migration and invasion of SW1990 and Capan-2 (Figure 7D, 7E).

## The miRNA-569/NUSAP1/ZEB1 axis is involved in the metastasis of PC cells

A functional rescue experiment was performed to further determine whether miRNA-569 inhibits the metastasis of PC cells by targeting NUSAP1. As shown in Figure 8A, 8B, NUSAP1 over-expression reversed the suppression of miRNA-569 up-regulation on PC cell migration. Meanwhile, the reintroduction of NUSAP1 reversed the repression of miRNA-569 on PC cell invasion (Figure 8C). Those results showed that NUSAP1 was involved in mediating the inhibitory effect of miRNA-569 on tumor metastasis. Zinc finger E-box binding homeobox 1 (ZEB1), was also related to tumor metastasis by promoting cell migration and invasion [20]. The GEPIA database showed a significantly positive correlation between NUSAP1 and ZEB1 in PC tissues (Figure 8D). We speculated that miRNA-569/NUSAP1 probably changes the aggressiveness of PC cells by co-regulating ZEB1. As expected, Western blot assay showed that miRNA-569 up-regulation decreased ZEB1 protein levels, whereas over-expressing NUSAP1 restored ZEB1 expression (Figure 8E, 8F). Collectively, these data suggested that NUSAP1 can promote metastasis via ZEB1 up-regulation, while the NUSAP1/ZEB1 axis can be inhibited by miRNA-569.

## DISCUSSION

PC remains one of the deadliest cancer in the world, mainly because most patients are already in the advanced stage when diagnosed [21]. Therefore, exploring new biomarkers and clarifying the potential mechanism of PC progression is very important to developing new PC treatments. An increasing number of literature reports that miRNA can perform a key function in cancer as onco-miRNAs or tumor-inhibited miRNAs during the development of PC [22, 23]. According to a previous study, microRNA-569 expression increased because of 3q26.2 amplification in epithelial cancers, which down-regulated TP53INP1 mRNA expression and enhanced the sensitivity of tumor cells to cisplatin [24]. Zheng et al. revealed that microRNA-569 downregulation occurred in lung cancer, while microRNA-569 overexpression leads to decreased proliferation and migration ability, inducing cell cycle arrest and apoptosis [13]. In addition, microRNA-569 can also be sponged by circ\_0001721 to participate in the progression of osteosarcoma [25]. First of all, we observed that miRNA-569 downregulation predicted a poor prognosis in PC. MiRNA-569 was found to act as a suppressive miRNA in PC by directly targeting NUSAP1 to down-regulate ZEB1 expression, thus impeding PC metastasis and progression. These data indicated that microRNA-569 may be a potential therapeutic target for PC.

NUSAP1, a protein binding with microtubules and chromatin, can unite DNA with mitotic spindles and promote microtubule cross-linking during mitosis. It has been reported that NUSAP1 is abnormally expressed in various cancers [26–28]. Li et al. found that NUSAP1 accelerated epithelial-mesenchyme transition (EMT) progression and enhanced cancer stem cell (CSC) signature through the Wnt/ $\beta$ -catenin signal pathway, which led to cervical cancer [26]. Moreover, by activating the TGF- $\beta$  signaling pathway, NUSAP1 can

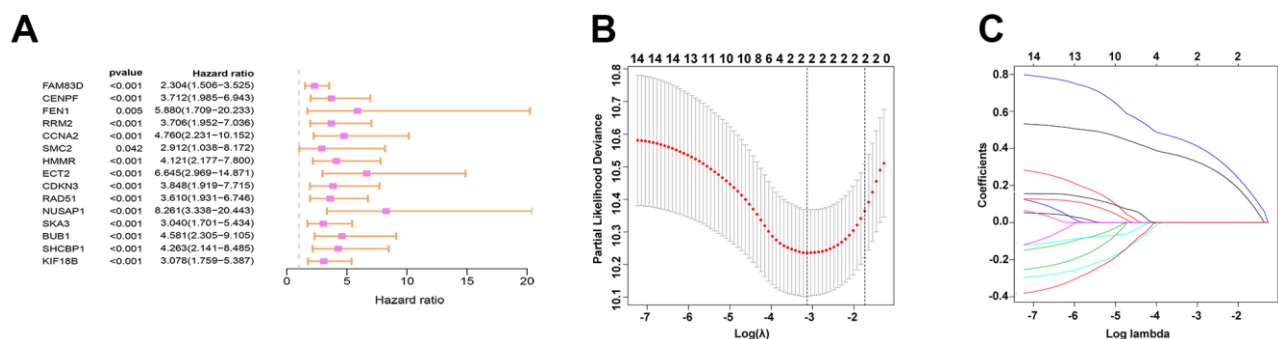


**Figure 5. Prediction and screening of the target gene of miR-569 through bioinformatics analysis. (A)** Forest plot for hazard ratios of survival-associated hub genes in PC. **(B)** Partial likelihood deviance versus log ( $\lambda$ ) was drawn using a LASSO Cox regression model. **(C)** Coefficients of selected features are shown in the terms of  $\lambda$ .

enhance the proliferation, migration, invasion, and chemotherapy resistance of bladder cancer cells [29]. Furthermore, several previous researches revealed that microRNAs can target and regulate NUSAP1 expression [30, 31]. In our study, we found that NUSAP1 is highly expressed in pancreatic cancer, which is an indicator of poor prognosis. NUSAP1 promoted tumor cell migration and invasion, while microRNA-569 over-expression could reverse this effect by directly binding with its 3'-

UTR. These findings suggested that the microRNA-569/NUSAP1 axis functions as a pivotal role in the PC progression.

ZEB1, the member of the ZHF family, could regulate the expression of multiple oncogenes, thereby promoting the initiation and development of cancer [32, 33]. ZEB1 also was the common and important target of a range of signaling pathways (including miRNA signaling) which

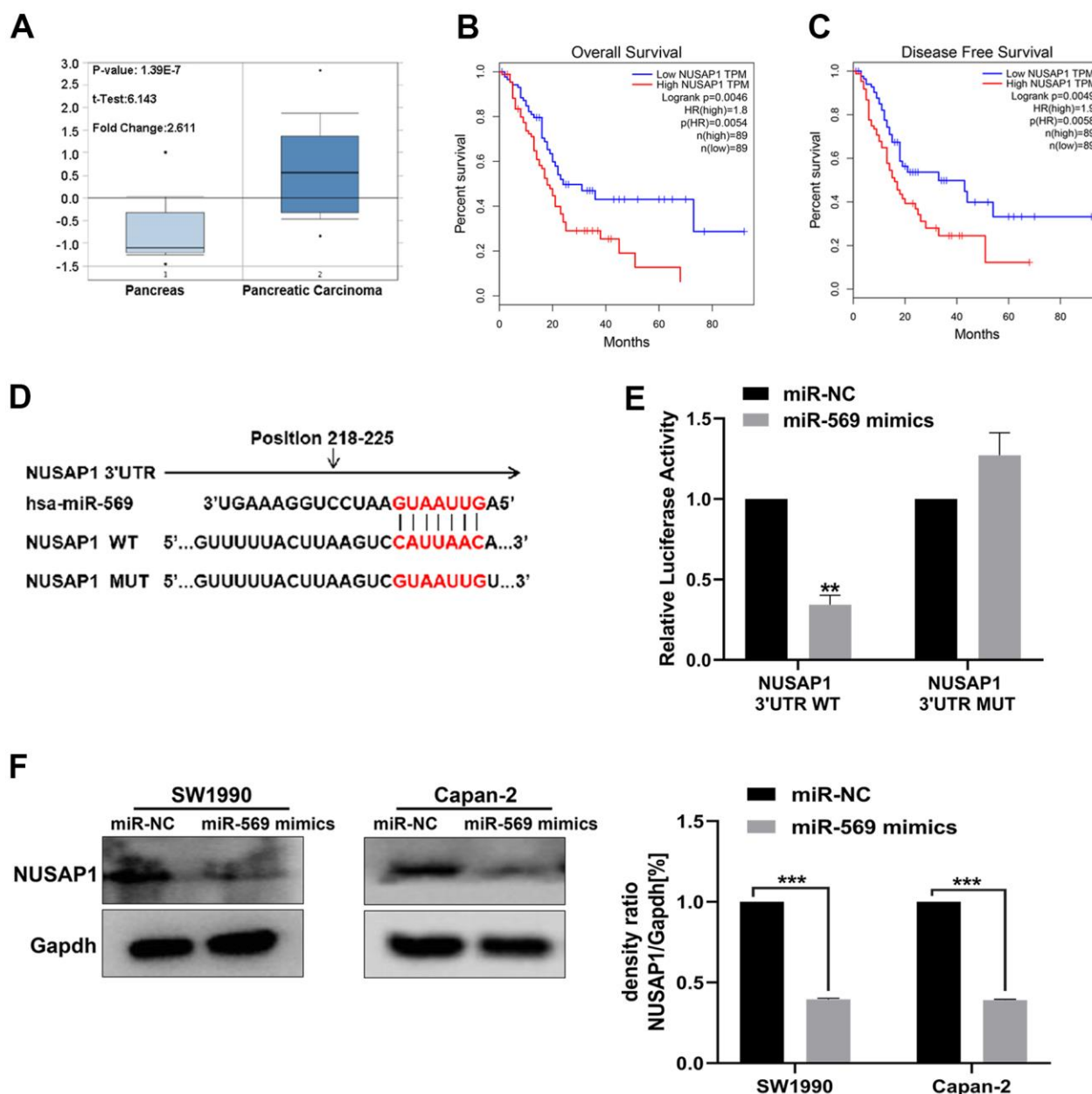


**Figure 6. miR-569 directly targeted NUSAP1.** (A) Oncomine database showing NUSAP1 mRNA expression level in PC and normal tissues. (B, C) Kaplan-Meier overall survival and disease-free survival curves for patients with PC stratified by high and low expression of NUSAP1. (D) Putative miR-569 target sequence in wild-type (WT) and mutated (MUT) 3'UTR of NUSAP1 was generated as indicated. (E) Relative luciferase activity of NUSAP1 3'UTR co-transfected with the indicated reporters and miR-569 mimic oligonucleotides. (F) Western blot assay demonstrated NUSAP1 protein level after over-expression of miR-569. (\*  $p < 0.05$ , \*\*  $p < 0.01$ ,  $n = 5$ , Student's  $t$ -test, means  $\pm$  95% CI).



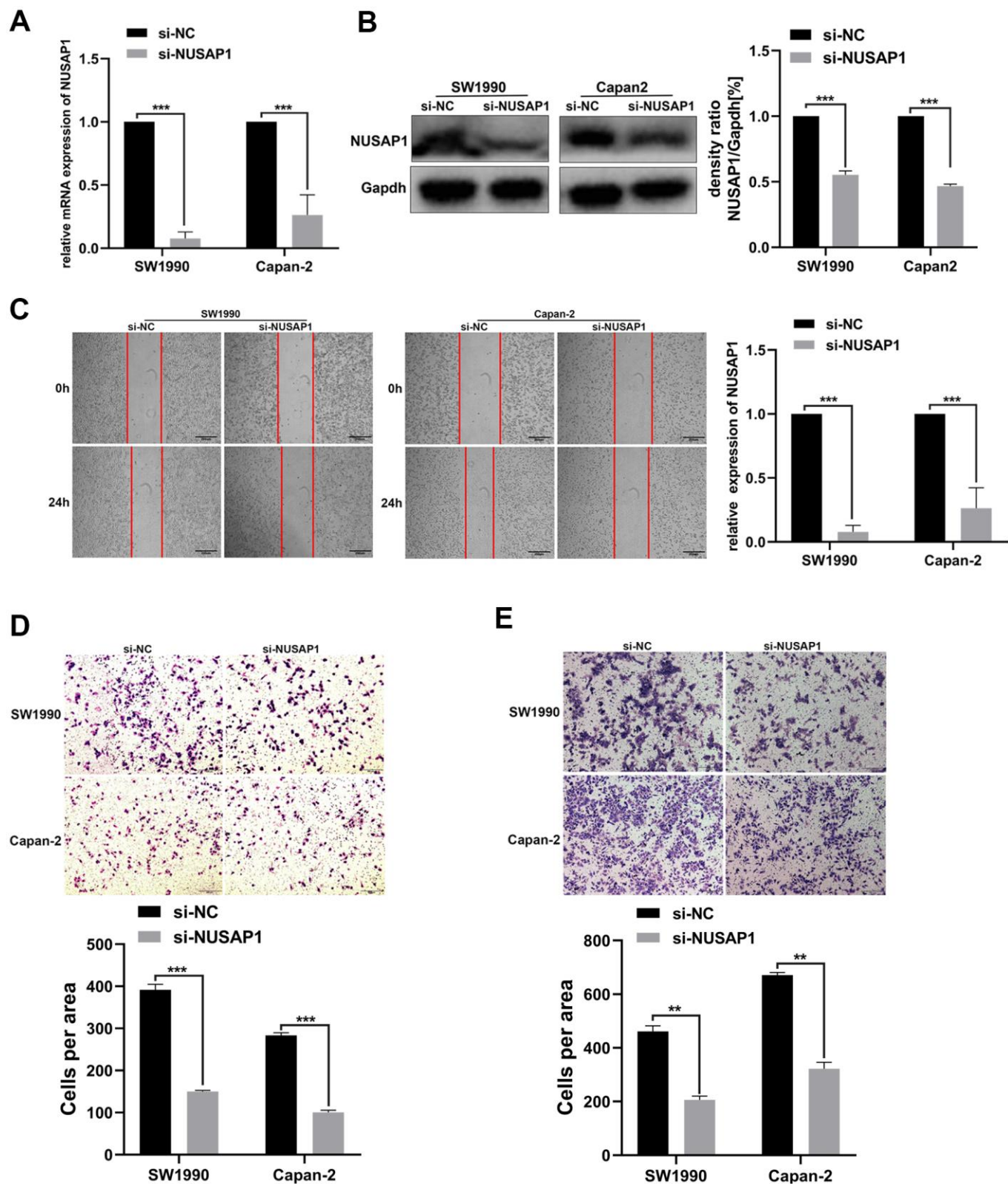


**Figure 7. NUSAP1 promoted the migration and invasion of PC cells.** (A) Western blot and (B) qRT-PCR were performed to verify transfection efficiency (\* $p < 0.05$ ). (C) Wound healing assay showed migratory abilities of PC cells after knocking down NUSAP1; (D) Transwell assay indicated migratory abilities of PC cells after knocking down NUSAP1; (E) Transwell assay showed invasive abilities of PC cells after knocking down NUSAP1. GAPDH was used as a loading control in Western blot assay. (\* $p < 0.05$ , \*\* $p < 0.01$ , \*\*\* $p < 0.001$ ,  $n = 3$ , Student's  $t$ -test, means  $\pm$  95% CI).

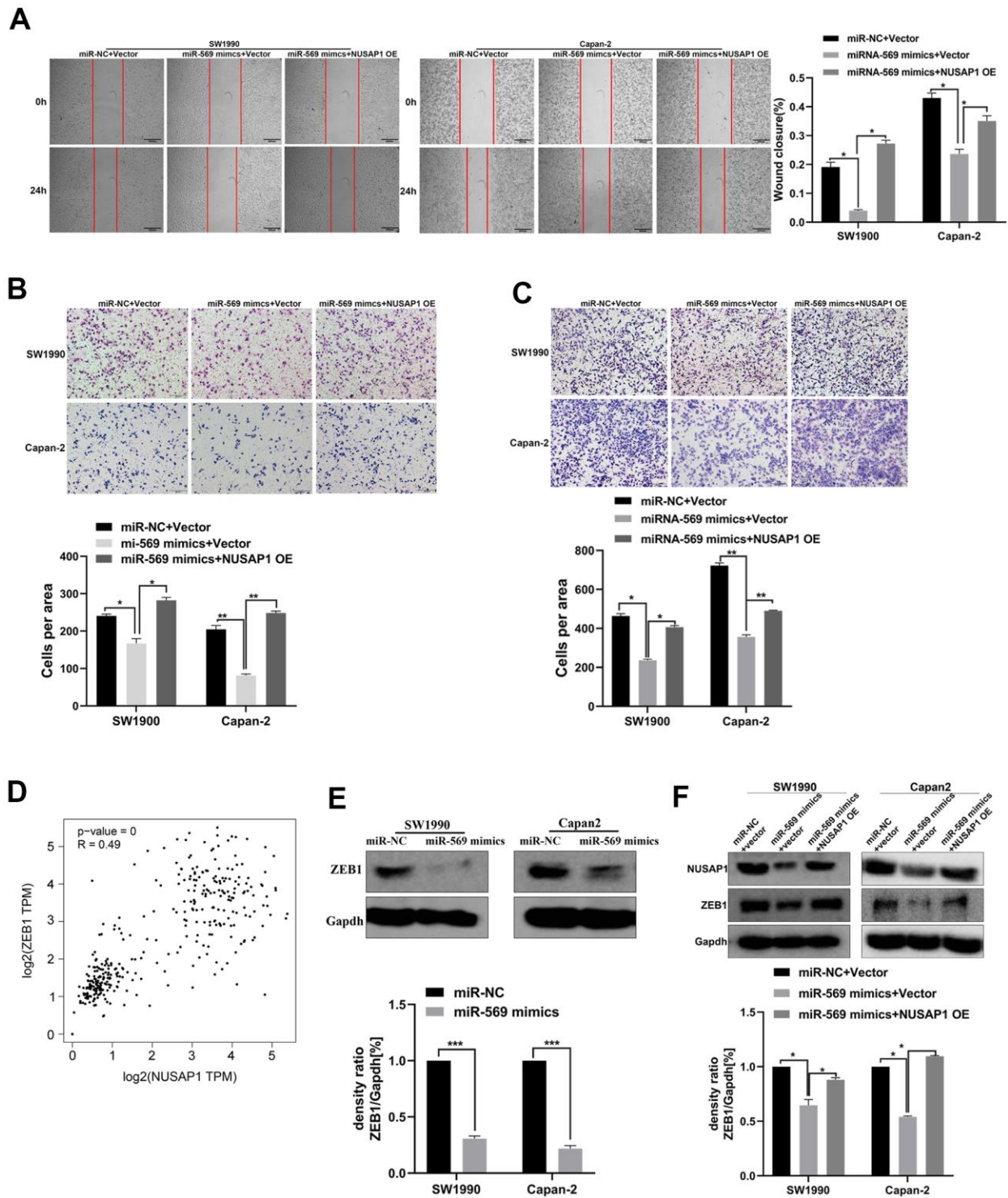


**Figure 8. miR-569/NUSAP1/ZEB1 axis involved in the metastasis of PC cells.** (A) Wound healing showed the migratory abilities of PC cells transfected with a combination of miR-NC and vector, or miR-569 mimics and vector, or miR-569 mimics and NUSAP1 OE; (B) Transwell assay showed the migratory abilities of PC cells transfected with a combination of miR-NC and vector, or miR-569 mimics and vector or miR-569 mimics and NUSAP1 OE; (C) Transwell assay demonstrated the invasive abilities of PC cells transfected with a combination of miR-NC and vector, or miR-569 mimics and vector or miR-569 mimics and NUSAP1 OE; (D) The GEPIA database showed that a significant positive correlation between NUSAP1 and ZEB1 could be observed in PC tissues. (E) Western blot assay showed the ZEB1 protein expression level after over-expression of miR-569. (F) Western blot assay showed the protein expression levels of PC cells transfected with a combination of miR-NC and vector, or miR-569 mimics and vector or miR-569 mimics and NUSAP1 OE; (\*  $p < 0.05$ , \*\*  $p < 0.01$ ,  $n = 5$ , Student's  $t$ -test, means  $\pm$  95% CI).

can regulate cell differentiation, proliferation, plasticity, and survival [34]. For instance, the hepatocyte growth factor activates ERK/MAPK-ZEB1 signal axis to enhance the invasion ability of prostate cancer cells [35]. In the process of bone metastasis of lung cancer, ZEB1, as the downstream target of Wnt/ $\beta$ -catenin, leads to the decrease of E-cadherin expression, which further aggravates EMT [36]. ZEB1 expression was regulated by the well-known transcription factor GRHL2, which can form a double-negative feedback loop with the miR-200 family and ZEB1 [37]. In this study, the microRNA-569/NUSAP1 axis was found to be involved in the process of PC migration and invasion, partly by regulating the ZEB1 signaling pathway. Furthermore, a previous study showed that NUSAP1 contains a DNA binding domain, so it is possible that NUSAP1 acts directly as a transcriptional regulator [38], so we speculated that NUSAP1 protein may directly bind to the ZEB1 promoter and suppress the transcription and promotional activity of ZEB1; however, the binding pattern (direct or indirect) and regulatory mechanism of NUSAP1 and ZEB1 require further experimental verification, perhaps by chromosome co-precipitation or immunoprecipitation.

To sum up, we firstly identified the biological role and regulatory mechanism of miRNA-569 during PC carcinogenesis. Our data concluded: miRNA-569 modulates the NUSAP1/ZEB1 signaling axis, exert anti-tumor function, which is expected to be the clinical therapeutic target of pancreatic cancer.

## MATERIALS AND METHODS

### Cell cultures and tissue samples

The Capan-2(#SUER0449) and SW1990(#TCHu201) were acquired from Suer Biological Technology (Shanghai, China) and the Type Culture Collection of the Chinese Academy of Sciences (Shanghai, China), respectively. Both the cell lines were cultured in DMEM containing 10% FBS, 100 units/ml penicillin-streptomycin at 37° C containing 5% CO<sub>2</sub>. PC tissue specimens were gathered from the Department of Pathology, the Affiliated Shengjing Hospital, China Medical University, and confirmed by histopathological examination by two pathologists. More detailed patient information has been described in the earlier paper [39].

### RNA isolation and RT-PCR

Total RNA of cultured cells was extracted with Trizol reagent according to the manufacturer's instructions, and the RNA was stored at -80° C. The concentration and purity of RNA were measured (RNA purity =A260/A280), and the One Step PrimeScript® miRNA

cDNA Synthesis kit was used for reverse transcription (RT). Quantitative real-time PCR was performed on ABI 7500 Real-time PCR system (Applied Biosystems) using SYBR Premix Ex Taq II. All the reactions were performed for triplicates. Primer sequences were listed in Table 1.

### Transient transfection

NUSAP1 siRNA was designed and synthesized by GENEWIZ (Beijing, China). The NUSAP1 plasmid was purchased from GeneChem (Shanghai, China). miRNA-569 mimics and its control were synthesized and gained from RiboBio (Guangzhou, China). Cells were transiently transfected *in vitro* using jetPRIME reagent (Polyplus) according to protocol.

The siRNA sequences of NC and NUSAP1 were listed:

siNUSAP1-1: 5'-GGAAGACUCUCUGUGGUUTT-3'  
 siNUSAP1-2: 5'-CCAAGACUCCAGCCAGAAATT-3'  
 NC siRNA: 5'-AATTCTGCGAACGAGTCACGT-3'

As shown in Supplementary Figure 1, siNUSAP1-1 was more efficient than siNUSAP1-2, which was selected for the follow-up experiments.

### Scratch assay

When the transfected cells reached sufficient confluency, the cell monolayers were scratched across with a 200- $\mu$ L pipette tip to create a linear wound. Then the supernatant at each well was replaced with a fresh medium without FBS. Migration images were captured at 0, 24 h after scratching by using an inverted bright-field microscope.

### Migration and invasion assay

As for the migration assay: 200  $\mu$ L serum-free medium containing  $3 \times 10^4$  cells was placed in the upper chamber, and 500  $\mu$ L medium containing 10% fetal bovine serum was added to the lower chamber. As for the invasion assay: the Matrigel was diluted with precooled serum-free medium at a ratio of 1:30, and added 50  $\mu$ L into the upper chamber. Other procedures were the same as the migration assay. 24 hours later, the chamber was taken out and fixed with 75% ethanol. After staining with Reyes-Giemsa, put it under a fluorescence microscope (Olympus, Tokyo, Japan) for observation and take photos.

### Western blot analysis

Western blot was conducted as previously described [40]. The primary antibodies used are as follows: anti-NUSAP1 (#ab137230), anti-ZEB1(#4650), anti-GAPDH



**Table 1. Primer sequences.**

Name	Forward primer (5'->3')	Reverse primer (5'->3')
miR-569	CCCGTAATGAATCCTGGAAAGT	
U6	GCTTCGGCAGCACATATACTAAAAT	CGCTTCACGAATTTGCGTGTTCAT
NUSAP1	CAGCCCATCAATAAGGGAGGG	AGTGACCCCTTCAGACCCAA
ZEB1	CAATGATCAGCCTCAATCTGCA	CCATTGGTGGTTGATCCCA
18S	CCCGGGGAGGTAGTGACGAAAAAT	CGCCCGCCCGCTCCCAAGAT

(#25778). Horseradish peroxidase coupled goat anti-rabbit secondary antibody was diluted in TBST at 1:2000. Enhanced chemiluminescence reagent was applied to detect protein bands. Finally, Western blot results were analyzed by NIH Image J software.

### Dual-luciferase reporter assay

Dual-luciferase reporter assays were performed as we previously described [39]. Briefly, NUSAP1 3'UTR containing the predicted wild-type (WT) or mutated (Mut) binding sites of miR-569 were cloned into the pGL3 vector. At 48h after co-transfection of miR-569 mimics and luciferase reporter vector into cells, luciferase activity was detected.

### In vivo metastasis assay

Female BABL/c nude mice (n=10, 4–6 weeks old) were got from Vitalriver (Beijing, China). Capan-2 cells ( $1 \times 10^6$ ) were labeled with luciferase ahead of time. After transfection with agomir-NC (5 $\mu$ M) or agomir-569 (5 $\mu$ M), transfected cells were injected into the mouse spleen (n=5 in each group), respectively. 10 weeks after injection, the mice were killed according to the requirements, and the liver tissues were collected and embedded in paraffin. Then HE staining and pathological analysis was performed. The relevant experimental scheme and content were approved by the Ethics Committee of China Medical University (Approval no. 2020322).

### Bioinformatics

The public database TargetScan ([http://www.targetscan.org/vert\\_72/](http://www.targetscan.org/vert_72/)) was used to determine the potential miR-mRNA interactions. The predicted target genes are intersected with aberrantly expressed data from the TCGA portal (<http://tumorsurvival.org/>) database displayed by a Venn diagram. GO annotation and KEGG pathway of target genes were performed by DAVID 6.8 software (<https://david.ncifcrf.gov/>). The results were visualized with the “clusterProfiler \_3.11.0” package of the R 3.6.0 language. PPI networks were generated by STRING 11.0 (<http://string-db.org>), which aimed to

assess and integrate proteins from prediction or experiments. The interaction network was visualized by Cytoscape 3.8.1 and the MCODE plugin was conducted to screen potential clusters. In the process of selecting model parameters, the minimum absolute contraction and LASSO regression methods are widely used. The “glmnet 4.1.2” package was selected for modeling research. The Oncomine database (<http://www.oncomine.org>) was applied to analyze the transcription expression level of the NUSAP1.

### Statistical analysis

GraphPad Prism 8.0.1 and R 3.6.0 were selected to analyze the experimental data, and presented as the means  $\pm$  standard deviations (SD). All experiments were carried out in triplicate. Group comparison was performed by Student's t-test and the threshold of significant difference was  $p < 0.05$ .

### AUTHOR CONTRIBUTIONS

X.G. and Y.L. designed the experiments and wrote the manuscript. X.G. performed the experiments. Y.L. performed the bioinformatics analysis. X.C. and C.L. analyzed data. K.H. provided provide technical support. X.Q. revised it critically for important intellectual content. All authors contributed to the study design and data interpretation and have reviewed the final version of the manuscript.

### CONFLICTS OF INTEREST

The authors declare that they have no conflicts of interest.

### FUNDING

This work was supported by the Key Research and Development Program of Liaoning Province (2018225060).

### REFERENCES

1. Siegel RL, Miller KD, Jemal A. Cancer statistics, 2019. *CA Cancer J Clin.* 2019; 69:7–34. <https://doi.org/10.3322/caac.21551> PMID:30620402

2. Jurcak N, Zheng L. Signaling in the microenvironment of pancreatic cancer: Transmitting along the nerve. *Pharmacol Ther.* 2019; 200:126–34.  
<https://doi.org/10.1016/j.pharmthera.2019.04.010> PMID:31047906
3. Yachida S, Jones S, Bozic I, Antal T, Leary R, Fu B, Kamiyama M, Hruban RH, Eshleman JR, Nowak MA, Velculescu VE, Kinzler KW, Vogelstein B, Iacobuzio-Donahue CA. Distant metastasis occurs late during the genetic evolution of pancreatic cancer. *Nature.* 2010; 467:1114–7.  
<https://doi.org/10.1038/nature09515> PMID:20981102
4. Klein AP. Pancreatic cancer epidemiology: understanding the role of lifestyle and inherited risk factors. *Nat Rev Gastroenterol Hepatol.* 2021; 18:493–502.  
<https://doi.org/10.1038/s41575-021-00457-x> PMID:34002083
5. Kleeff J, Reiser C, Hinz U, Bachmann J, Debus J, Jaeger D, Friess H, Büchler MW. Surgery for recurrent pancreatic ductal adenocarcinoma. *Ann Surg.* 2007; 245:566–72.  
<https://doi.org/10.1097/01.sla.0000245845.06772.7d> PMID:17414605
6. Sasaki T, Sato T, Nakai Y, Sasahira N, Isayama H, Koike K. Brain metastasis in pancreatic cancer: Two case reports. *Medicine (Baltimore).* 2019; 98:e14227.  
<https://doi.org/10.1097/MD.00000000000014227> PMID:30681602
7. Croce CM. Causes and consequences of microRNA dysregulation in cancer. *Nat Rev Genet.* 2009; 10:704–14.  
<https://doi.org/10.1038/nrg2634> PMID:19763153
8. Hiraide S, Takahashi M, Yoshida Y, Yamada H, Komine K, Ishioka C. Tumor suppressor miR-193a-3p enhances efficacy of BRAF/MEK inhibitors in BRAF-mutated colorectal cancer. *Cancer Sci.* 2021; 112:3856–70.  
<https://doi.org/10.1111/cas.15075> PMID:34288281
9. Wu D, Deng S, Li L, Liu T, Zhang T, Li J, Yu Y, Xu Y. TGF- $\beta$ 1-mediated exosomal lnc-MMP2-2 increases blood-brain barrier permeability via the miRNA-1207-5p/EPB41L5 axis to promote non-small cell lung cancer brain metastasis. *Cell Death Dis.* 2021; 12:721.  
<https://doi.org/10.1038/s41419-021-04004-z> PMID:34285192
10. Todeschini P, Salviato E, Romani C, Raimondi V, Ciccarese F, Ferrari F, Tognon G, Marchini S, D’Incalci M, Zanotti L, Ravaggi A, Odicino F, Sartori E, et al. Comprehensive Profiling of Hypoxia-Related miRNAs Identifies miR-23a-3p Overexpression as a Marker of Platinum Resistance and Poor Prognosis in High-Grade Serous Ovarian Cancer. *Cancers (Basel).* 2021; 13:3358.  
<https://doi.org/10.3390/cancers13133358> PMID:34283087
11. Bagheri M, Khansarinejad B, Mosayebi G, Moradabadi A, Mondanizadeh M. Alterations in The Plasma Expression of mir-15b, mir-195 and the Tumor-Suppressor Gene DLEU7 in Patients with B-Cell Chronic Lymphocytic Leukemia. *Rep Biochem Mol Biol.* 2021; 10:20–9.  
<https://doi.org/10.52547/rbmb.10.1.20> PMID:34277865
12. Di Y, Jiang Y, Shen X, Liu J, Gao Y, Cai H, Sun X, Ning D, Liu B, Lei J, Jin S. Downregulation of miR-135b-5p Suppresses Progression of Esophageal Cancer and Contributes to the Effect of Cisplatin. *Front Oncol.* 2021; 11:679348.  
<https://doi.org/10.3389/fonc.2021.679348> PMID:34277424
13. Zheng YP, Wu L, Gao J, Wang Y. Tumor suppressive role of miR-569 in lung cancer. *Oncol Lett.* 2018; 15:4087–92.  
<https://doi.org/10.3892/ol.2018.7869> PMID:29541173
14. Nishimoto M, Nishikawa S, Kondo N, Wanifuchi-Endo Y, Hato Y, Hisada T, Dong Y, Okuda K, Sugiura H, Kato H, Takahashi S, Toyama T. Prognostic impact of TP53INP1 gene expression in estrogen receptor  $\alpha$ -positive breast cancer patients. *Jpn J Clin Oncol.* 2019; 49:567–75.  
<https://doi.org/10.1093/jjco/hyz029> PMID:30855679
15. Mills CA, Suzuki A, Arceci A, Mo JY, Duncan A, Salmon ED, Emanuele MJ. Nucleolar and spindle-associated protein 1 (NUSAP1) interacts with a SUMO E3 ligase complex during chromosome segregation. *J Biol Chem.* 2017; 292:17178–89.  
<https://doi.org/10.1074/jbc.M117.796045> PMID:28900032
16. Liu Z, Guan C, Lu C, Liu Y, Ni R, Xiao M, Bian Z. High NUSAP1 expression predicts poor prognosis in colon cancer. *Pathol Res Pract.* 2018; 214:968–73.  
<https://doi.org/10.1016/j.prp.2018.05.017> PMID:29853313
17. Fang L, Zhang M, Chen L, Xiong H, Ge Y, Lu W, Wu X, Heng B, Yu D, Wu S. Downregulation of nucleolar and spindle-associated protein 1 expression suppresses cell migration, proliferation and invasion in renal cell carcinoma. *Oncol Rep.* 2016; 36:1506–16.  
<https://doi.org/10.3892/or.2016.4955> PMID:27461786
18. Lu Y, Rosenfeld R, Simon I, Nau GJ, Bar-Joseph Z. A probabilistic generative model for GO enrichment analysis. *Nucleic Acids Res.* 2008; 36:e109.  
<https://doi.org/10.1093/nar/gkn434> PMID:18676451
19. Li C, Peng Z, Wang Y, Lam G, Nissen N, Tang J, Yuan X, Lewis M, Greene MI, Pandol SJ, Wang Q. Epithelial cell



transforming 2 is regulated by Yes-associated protein 1 and mediates pancreatic cancer progression and metastasis. *Am J Physiol Gastrointest Liver Physiol*. 2021; 320:G380–95.

<https://doi.org/10.1152/ajpgi.00185.2020>  
PMID:33501895

20. Zhang W, Shi X, Peng Y, Wu M, Zhang P, Xie R, Wu Y, Yan Q, Liu S, Wang J. HIF-1 $\alpha$  Promotes Epithelial-Mesenchymal Transition and Metastasis through Direct Regulation of ZEB1 in Colorectal Cancer. *PLoS One*. 2015; 10:e0129603.  
<https://doi.org/10.1371/journal.pone.0129603>  
PMID:26057751
21. Satyananda V, Gupta R, Hari DM, Yeh J, Chen KT. Advances in Translational Research and Clinical Care in Pancreatic Cancer: Where Are We Headed? *Gastroenterol Res Pract*. 2019; 2019:7690528.  
<https://doi.org/10.1155/2019/7690528>  
PMID:30863442
22. Fathi M, Ghafouri-Fard S, Abak A, Taheri M. Emerging roles of miRNAs in the development of pancreatic cancer. *Biomed Pharmacother*. 2021; 141:111914.  
<https://doi.org/10.1016/j.biopha.2021.111914>  
PMID:34328099
23. Tarasiuk A, Mackiewicz T, Małecka-Panas E, Fichna J. Biomarkers for early detection of pancreatic cancer - miRNAs as a potential diagnostic and therapeutic tool? *Cancer Biol Ther*. 2021; 22:347–56.  
<https://doi.org/10.1080/15384047.2021.1941584>  
PMID:34224317
24. Chaluvally-Raghavan P, Zhang F, Pradeep S, Hamilton MP, Zhao X, Rupaimoole R, Moss T, Lu Y, Yu S, Pecot CV, Aure MR, Peugeot S, Rodriguez-Aguayo C, et al. Copy number gain of hsa-miR-569 at 3q26.2 leads to loss of TP53INP1 and aggressiveness of epithelial cancers. *Cancer Cell*. 2014; 26:863–79.  
<https://doi.org/10.1016/j.ccell.2014.10.010>  
PMID:25490449
25. Li L, Guo L, Yin G, Yu G, Zhao Y, Pan Y. Upregulation of circular RNA circ\_0001721 predicts unfavorable prognosis in osteosarcoma and facilitates cell progression via sponging miR-569 and miR-599. *Biomed Pharmacother*. 2019; 109:226–32.  
<https://doi.org/10.1016/j.biopha.2018.10.072>  
PMID:30396080
26. Wang H, Liu Z, Wu P, Wang H, Ren W. NUSAP1 Accelerates Osteosarcoma Cell Proliferation and Cell Cycle Progression via Upregulating CDC20 and Cyclin A2. *Onco Targets Ther*. 2021; 14:3443–54.  
<https://doi.org/10.2147/OTT.S295818>  
PMID:34079289
27. Ling B, Wei P, Xiao J, Cen B, Wei H, Feng X, Ye G, Li S, Zhang Z, Liang W, Huang S, Huang W. Nucleolar and spindle-associated protein 1 promotes non-small cell lung cancer progression and serves as an effector of myocyte enhancer factor 2D. *Oncol Rep*. 2021; 45:1044–58.  
<https://doi.org/10.3892/or.2020.7918> PMID:33650655
28. Guo H, Zou J, Zhou L, Zhong M, He Y, Huang S, Chen J, Li J, Xiong J, Fang Z, Xiang X. NUSAP1 Promotes Gastric Cancer Tumorigenesis and Progression by Stabilizing the YAP1 Protein. *Front Oncol*. 2021; 10:591698.  
<https://doi.org/10.3389/fonc.2020.591698>  
PMID:33489890
29. Gao S, Yin H, Tong H, Zhan K, Yang G, Hossain MA, Li T, Gou X, He W. Nucleolar and Spindle Associated Protein 1 (NUSAP1) Promotes Bladder Cancer Progression Through the TGF- $\beta$  Signaling Pathway. *Onco Targets Ther*. 2020; 13:813–25.  
<https://doi.org/10.2147/OTT.S237127> PMID:32099387
30. Chen Y, Zhang W, Kadier A, Zhang H, Yao X. MicroRNA-769-5p suppresses cell growth and migration via targeting NUSAP1 in bladder cancer. *J Clin Lab Anal*. 2020; 34:e23193.  
<https://doi.org/10.1002/jcla.23193> PMID:31901150
31. Roy S, Hooiveld GJ, Seehawer M, Caruso S, Heinzmann F, Schneider AT, Frank AK, Cardenas DV, Sonntag R, Luedde M, Trautwein C, Stein I, Pikarsky E, et al. microRNA 193a-5p Regulates Levels of Nucleolar- and Spindle-Associated Protein 1 to Suppress Hepatocarcinogenesis. *Gastroenterology*. 2018; 155:1951–66.e26.  
<https://doi.org/10.1053/j.gastro.2018.08.032>  
PMID:30165047
32. Bi C, Wang G. LINC00472 suppressed by ZEB1 regulates the miR-23a-3p/FOXO3/BID axis to inhibit the progression of pancreatic cancer. *J Cell Mol Med*. 2021; 25:8312–28.  
<https://doi.org/10.1111/jcmm.16784> PMID:34363438
33. Fratini L, Jaeger M, de Farias CB, Brunetto AT, Brunetto AL, Shaw L, Roesler R. Oncogenic functions of ZEB1 in pediatric solid cancers: interplays with microRNAs and long noncoding RNAs. *Mol Cell Biochem*. 2021; 476:4107–16.  
<https://doi.org/10.1007/s11010-021-04226-x>  
PMID:34292482
34. Zhang Y, Xu L, Li A, Han X. The roles of ZEB1 in tumorigenic progression and epigenetic modifications. *Biomed Pharmacother*. 2019; 110:400–8.  
<https://doi.org/10.1016/j.biopha.2018.11.112>  
PMID:30530042
35. Han Y, Luo Y, Wang Y, Chen Y, Li M, Jiang Y. Hepatocyte growth factor increases the invasive potential of PC-3 human prostate cancer cells via an ERK/MAPK and Zeb-1 signaling pathway. *Oncol Lett*. 2016; 11:753–9.

<https://doi.org/10.3892/ol.2015.3943>

PMID:[26870279](https://pubmed.ncbi.nlm.nih.gov/26870279/)

36. Yang X, Li L, Huang Q, Xu W, Cai X, Zhang J, Yan W, Song D, Liu T, Zhou W, Li Z, Yang C, Dang Y, Xiao J. Wnt signaling through Snail1 and Zeb1 regulates bone metastasis in lung cancer. *Am J Cancer Res*. 2015; 5:748–55.

PMID:[25973312](https://pubmed.ncbi.nlm.nih.gov/25973312/)

37. Nishino H, Takano S, Yoshitomi H, Suzuki K, Kagawa S, Shimazaki R, Shimizu H, Furukawa K, Miyazaki M, Ohtsuka M. Grainyhead-like 2 (GRHL2) regulates epithelial plasticity in pancreatic cancer progression. *Cancer Med*. 2017; 6:2686–96.

<https://doi.org/10.1002/cam4.1212> PMID:[28960866](https://pubmed.ncbi.nlm.nih.gov/28960866/)

38. Gordon CA, Gong X, Ganesh D, Brooks JD. NUSAP1 promotes invasion and metastasis of prostate cancer. *Oncotarget*. 2017; 8:29935–50.

<https://doi.org/10.18632/oncotarget.15604>

PMID:[28404898](https://pubmed.ncbi.nlm.nih.gov/28404898/)

39. Li C, Dong Q, Che X, Xu L, Li Z, Fan Y, Hou K, Wang S, Qu J, Xu L, Wen T, Yang X, Qu X, Liu Y. MicroRNA-29b-2-5p inhibits cell proliferation by directly targeting Cbl-b in pancreatic ductal adenocarcinoma. *BMC Cancer*. 2018; 18:681.

<https://doi.org/10.1186/s12885-018-4526-z>

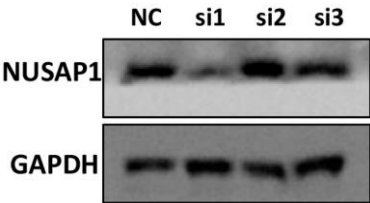
PMID:[29940895](https://pubmed.ncbi.nlm.nih.gov/29940895/)

40. Zang D, Zhang C, Li C, Fan Y, Li Z, Hou K, Che X, Liu Y, Qu X. LPPR4 promotes peritoneal metastasis via Sp1/integrin  $\alpha$ /FAK signaling in gastric cancer. *Am J Cancer Res*. 2020; 10:1026–44.

PMID:[32266108](https://pubmed.ncbi.nlm.nih.gov/32266108/)

SUPPLEMENTARY MATERIALS

Supplementary Figure



Supplementary Figure 1. Western blot of NUSAP1 knockdown.

# Hallmarks of cancer and hallmarks of aging

Mikhail V. Blagosklonny<sup>1</sup>

<sup>1</sup>Roswell Park Comprehensive Cancer Center, Buffalo, NY 14263, USA

**Correspondence to:** Mikhail V. Blagosklonny; **email:** [Blagosklonny@oncotarget.com](mailto:Blagosklonny@oncotarget.com), [Blagosklonny@rapalogs.com](mailto:Blagosklonny@rapalogs.com)

**Keywords:** oncology, carcinogenesis, geroscience, mTOR, rapamycin, hyperfunction theory

**Received:** February 14, 2022

**Accepted:** May 2, 2022

**Published:** May 9, 2022

**Copyright:** © 2022 Blagosklonny. This is an open access article distributed under the terms of the [Creative Commons Attribution License](https://creativecommons.org/licenses/by/3.0/) (CC BY 3.0), which permits unrestricted use, distribution, and reproduction in any medium, provided the original author and source are credited.

## ABSTRACT

A thought-provoking article by [Gems and de Magalhães](#) suggests that canonic hallmarks of aging are superficial imitations of hallmarks of cancer. I took their work a step further and proposed hallmarks of aging based on a hierarchical principle and the hyperfunction theory.

To do this, I first reexamine the hallmarks of cancer proposed by Hanahan and Weinberg in 2000. Although six hallmarks of cancer are genuine, they are not hierarchically arranged, i.e., molecular, intra-cellular, cellular, tissue, organismal and extra-organismal. (For example, invasion and angiogenesis are manifestations of molecular alterations on the tissue level; metastasis on the organismal level, whereas cell immortality is observed outside the host).

The same hierarchical approach is applicable to aging. Unlike cancer, however, aging is not a molecular disease. The lowest level of its origin is normal intracellular signaling pathways such as mTOR that drive developmental growth and, later in life, become hyperfunctional, causing age-related diseases, whose sum is aging. The key hallmark of organismal aging, from worms to humans, are age-related diseases. In addition, hallmarks of aging can be arranged as a timeline, wherein initial hyperfunction is followed by dysfunction, organ damage and functional decline.

## Hallmarks of cancer: comparing apples and oranges

As depicted by Hanahan and Weinberg in 2000 [1], the circle schema of six hallmarks of cancer somewhat compares apples and oranges [https://els-jbs-prod-cdn.jbs.elsevierhealth.com/cms/attachment/428dbc2e-657c-429d-98f4-9910c7df1678/gr1\\_lrg.jpg](https://els-jbs-prod-cdn.jbs.elsevierhealth.com/cms/attachment/428dbc2e-657c-429d-98f4-9910c7df1678/gr1_lrg.jpg).

The hallmarks themselves are exact, but they are not equal. For example, limitless replicative potential (cell immortality) cannot be directly compared to sustained angiogenesis. Cell immortality is revealed outside the host (extra-organismal level), for example, in cell culture where clonal cell lines can proliferate indefinitely without interaction with normal tissues. In contrast, sustained angiogenesis requires interaction of cancer cells with normal cells of several tissues.

Angiogenesis can be only understood on the tissue level.

Second, cancer cells undergo Darwinian-type selection [2] for resistance to anti-growth signals, resistance to apoptosis and self-sufficiency in mitogenic signals. This trio represents three out of six hallmarks of cancer [1]. They can be combined in one super-hallmark: resistance to growth-limiting conditions [3]. (Note: The definition of oncogenic resistance to growth-limiting conditions was discussed previously [4]). Not only resistance to apoptosis and anti-growth signals but also self-sufficiency in mitogenic signals render cells resistant to growth-limiting conditions. Examples of growth-limiting conditions include lack of external mitogenic signals, cytostatic cytokines such as TGF-beta, cytotoxic carcinogens such as tobacco smoke, anti-cancer drugs, contact inhibition, glucose deprivation, cellular senescence, hypoxia, absence of nutrients and

growth factors [5, 6]. For example, glucose deprivation selects for oncogenic Ras [6].

Whereas normal cells do not proliferate in growth-limiting conditions, cancer cells do. Resistance to growth-limiting conditions provides an immediate selective advantage. But what immediate advantages can be provided by cellular immortality? The cell cannot tell the future, that it will live in cell culture one day. Cellular immortality is selected indirectly as derived hallmarks [3], because the same mutations that provide resistance to growth-limiting conditions also make cells immortal, angiogenic, invasive and metastatic [1, 7, 8]. Cellular immortality, angiogenesis, invasion and metastasis are derived hallmarks.

Third, molecular alterations (e.g., DNA mutations) are absent in the six-hallmark circle by Hanahan and Weinberg [1]. As discussed by Gems and de Magalhães, the hallmarks do not include mutations (or genetic instability) because this hallmark is implicitly taken for granted [9]. In fact, Hanahan and Weinberg called it an enabling hallmark in their revised paper published in 2011 [7].

In 2005, I explicitly included the molecular hallmark (mutations) and suggested the hierarchical principle to arrange these hallmarks from molecular to organismal levels [5].

**Hierarchical model of hallmarks of cancer: arranging the oranges**

Here I present the hallmarks of cancer, depicted as a circle by Hanahan and Weinberg [1], not as the circle but hierarchically, from molecular levels to the organism (Figure 1).

**Molecular level: Somatically inheritable molecular alterations.**

Genome instability is an enabling hallmark of cancer because it enables the acquisition of molecular alterations, such as DNA mutations, aneuploidy and epigenetic alterations [7]. Vogelstein et al. suggested that a typical human tumor contains relatively few driver gene mutations that each confers a growth advantage of 0.4% and numerous passenger gene mutations that confer no selective advantage [8, 10].

**Intracellular signaling pathways: Oncogenic translation of ambivalent signaling**

Signal-transduction pathways are ambivalent, causing opposite outcomes depending on cellular context. Oncogenic mutations re-wire signal transduction pathways. For example, MAPK pathways can simultaneously induce cyclin D1 and CDK inhibitors, leading either to cellular proliferation or senescence

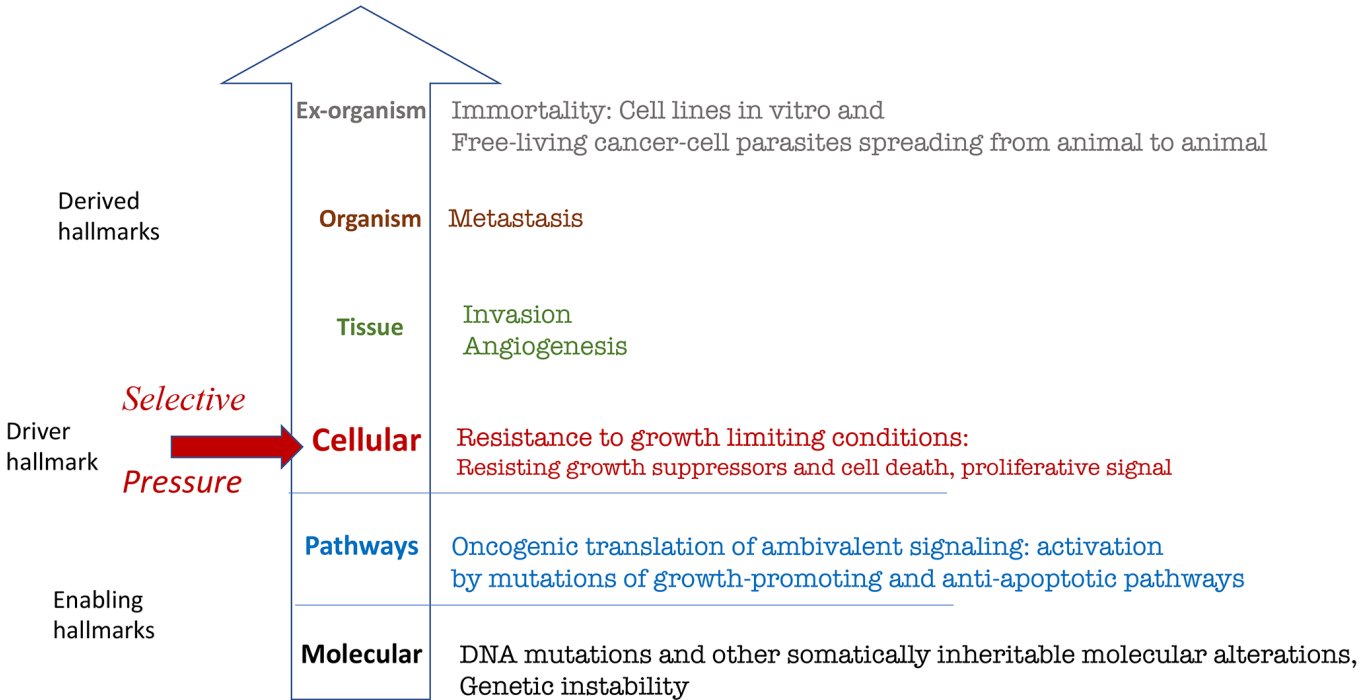


**Figure 1. Hierarchical representation (from molecular to organismal levels) of the original hallmarks of cancer based on Hanahan and Weinberg. See text for explanation.**



[11]. Inactivation of CDK inhibitors such as p16 may translate this ambivalent signaling into proliferation [3, 12]. TGF-beta inhibits normal cell proliferation, but in cancer it can induce proliferation and invasion [7, 13].

Growth-promoting and mitogen/nutrient-sensing signaling pathways are constantly activated by mutations to promote growth and proliferation as well as self-sufficiency in mitogen signaling. This, in turn, is manifested as three hallmarks of cancer on the next hierarchical level: cellular. This trio can be combined as one super-hallmark of resistance to growth-limiting conditions.

#### **Cellular level: Resistance to growth-limiting conditions**

Oncogenic mutations make cancer cells resistant to growth-limiting conditions (a definition of oncogenic-type of resistance was discussed previously [4]). This is the driver hallmark of cancer because it provides a selective advantage to cancer cells. Cells, capable of proliferation, are unicellular organisms in a Darwinian sense [2, 14, 15]. Selection can be “natural” (during carcinogenesis) and “artificial” (during cancer therapy) [14, 16]. For example, selection for therapy resistance increases oncogenic properties of cancer cells because many mutations in oncogenes and tumor suppressors that render cells drug-resistant also make them more oncogenic [5, 17–19]. Simultaneously, the same combination of mutations enables metastasis and other higher-level hallmarks. There is no direct selection for metastatic potential, angiogenesis and immortality. They are derived hallmarks.

#### **Tissue level: Invasion and angiogenesis**

Cancer cells produce cytokines and enzymes, which enable the cells to invade and to attract normal cells of different tissues in order to sustain angiogenesis [7].

#### **Organismal level: Metastasis**

Metastasis is the deadliest hallmark of cancer. Yet, there is no direct selection for metastatic potential. Direct selection for metastatic potential could take place only if metastases produced new metastases; in other words, if metastases reproduce. Simply, selection for cells resistant to growth-limiting conditions (survival and proliferation) brings about mutations that confer not only resistance, but also metastatic potential. There are no specific “metastasis” genes [8, 20]. They are the same oncogenes and tumor suppressors that act on cellular levels for the “trio” hallmark. Let us consider an analogy. If we select people for their ability to run faster, these selected people will also jump higher than

average, although selection was not for jumping ability. The fastest runners are the farthest jumpers.

#### **Extra-organismal level: Cellular immortality**

Some cancer cell lines live for more than half of a century in cell culture and for thousands of years in the wild. Originating in one animal, viable cancer cells are directly transmitted into unrelated hosts in a process similar to metastasis [21, 22]. Transmissible cancers have been observed in domestic dogs, the Tasmanian devil, hamsters and six bivalve species such as the soft-shell clam [23]. Canine transmissible venereal tumors (transmitted during sexual intercourse) may have originated thousands of years ago from the cells of a wolf or East Asian breed of dog [21–25]. The Tasmanian devil facial tumor disease [24] spreads through the Tasmanian devil population by transfer of cancer cells through biting [22]. [26]. Derived from a single original clam, leukemia-like cancer spreads among marine bivalves through sea water, leading to massive population loss [23, 27].

#### **Six levels rather than six hallmarks**

The number of hallmarks of cancer is arbitrary. Some can be combined, and others can be added. Numerous authors have re-visited the hallmarks of cancer, adding hallmarks or suggesting a new set of hallmarks [28–37].

Some hallmarks of cancer may be pseudo-hallmarks. For example, visiting an oncologist is a “hallmark” of cancer. We can be 99% sure that if someone has 20 appointments in an oncology clinic, then this person has cancer. However, it would be ridiculous to include this pseudo-hallmark in Figure 1. And the hierarchical principle makes this impossible, because there is no level (among the six levels) to include it.

#### **Hallmarks of aging**

To start with, let us depict the hallmarks of aging suggested by López-Otín et al. [38] based on the hierarchical principle. This representation renders hallmarks tangible but reveals three shortcomings (Figure 2).

First is the lack of hallmarks on the organismal level. Yet, the main hallmark of organismal aging is age-related diseases in all species from *C. elegans* [39–42] to humans [39, 43]. Aging is the sum of all age-related diseases, which cause death “from aging”.

Second, the relationship between hallmarks on different levels are unclear.

Third, the inclusion of genetic instability as a hallmark is based on the theory that aging is caused by accumulation of molecular damage. The molecular damage theory was refuted by key experiments, as discussed in detail [44–51].

Yes, damage accumulates and is harmful and potentially lethal [52–55] but it is not life-limiting because aging caused by hyper-functional signaling terminates life first. The reason why mTOR-driven aging is life-limiting has been discussed [49, 56, 57].

It was also suggested that the levels of DNA repair needed to avoid cancer at a young age greatly exceeds the levels that are needed to prevent damage-induced aging during a normal lifetime [58]. As previously discussed, the role of molecular damage in cancer supports the role of mTOR-driven hyperfunction in aging [59].

Let us depict hallmarks of aging, according to the hyperfunction theory of aging (Figure 3).

### Hallmarks of aging and hyperfunction theory

The hyperfunction theory of aging was extensively reviewed previously [44, 45, 49, 56, 57, 60–66], and

responses [60, 67] to its critics [68, 69] were also provided.

According to hyperfunction theory, aging is a continuation of developmental and reproductive programs that were not turned off upon their completion. Continuously active signaling pathways that initially drive developmental growth, drive aging later in life. Signaling pathways establish feedback loops, involving also gene expression and epigenetic modifications. These pathways become hyperfunctional, meaning that their activity is higher than optimal for longevity.

How does normal function become a deadly hyperfunction? Consider an analogy. When you pump air into an inflatable balloon, it grows in size. But when it reaches its intended size and you continue to pump air at the same rate, it will not grow further but instead will burst. This event can be compared with a stroke due to hypertension, resulting in brain damage. The brain is not damaged by life-long accumulation of molecular damage, but by hyperfunction, such as hypertension and hypercoagulation, thrombosis.

Hyper-function does not necessarily mean increased function. Even unchanged or slightly decreased activity

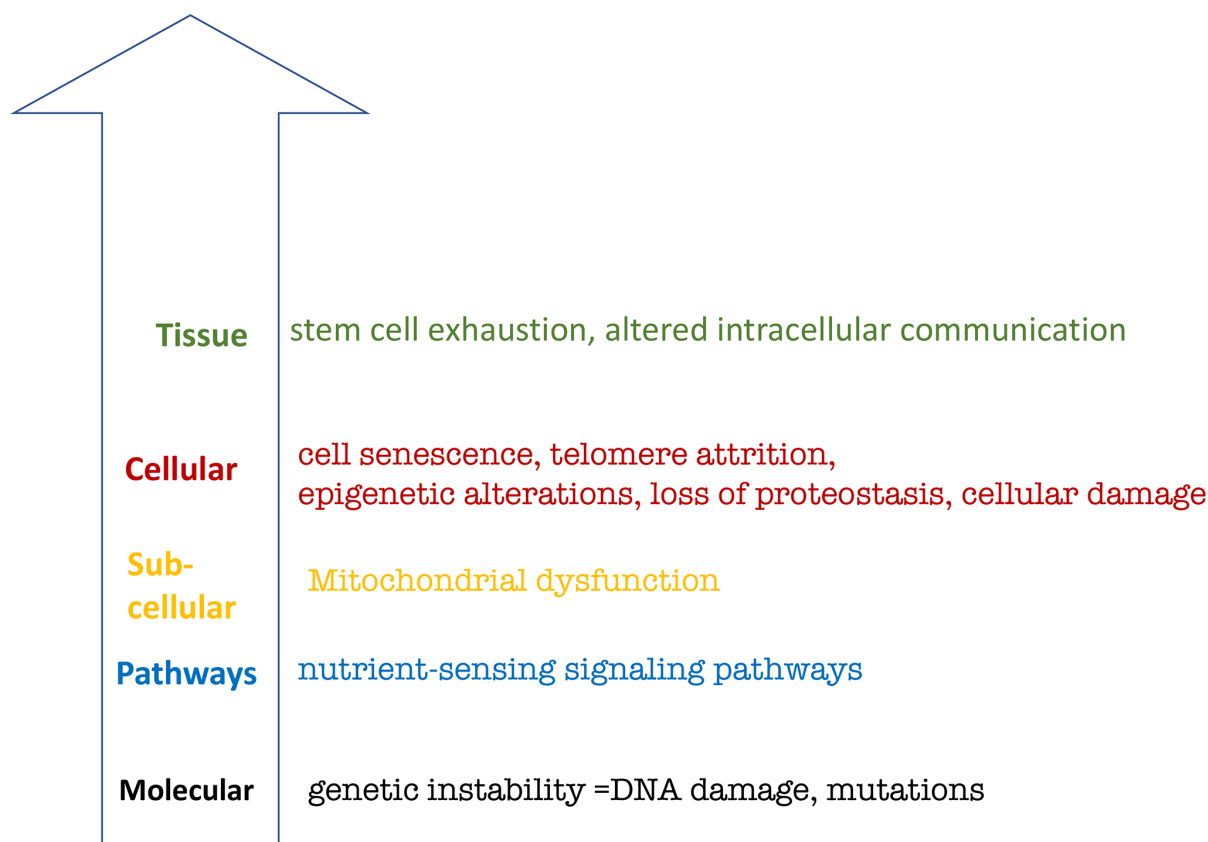


Figure 2. Hierarchical representation of the hallmarks of aging based on López-Otín et al. See text for explanation.

of growth-promoting pathways, such as mTOR, can be hyperfunctional when developmental growth is completed. As an analogy, 55 mph on the highway is not speeding, but even 40 mph on the driveway is too fast.

Hyperfunction causes organ damage and functional decline. The accumulation of molecular damage is associated with decline, but it is hyperfunction that causes decline during a normal lifetime.

Unlike cancer, aging is not a molecular disease. Development is not driven by accumulation of molecular damage or mutations in signaling pathways, and aging is not either. Nutrient-sensing pathways (e.g., mTOR) are not altered by random mutations.

The lowest level of hallmarks of aging is a continuous activation of normal signal transduction pathways. Deactivation of these pathways by knockout of a single gene extends lifespan in animals [70–73]. Rapamycin, a drug that inhibits normal mTOR signaling, extends lifespan [74–77].

Hyperfunctional signaling directly drives age-related diseases. There are no longevity pathways/mechanisms inhibitable by pro-aging pathways such as mTOR. Pro-

aging pathways do not drive aging by inhibiting longevity mechanisms. Why would nature create something that inhibits longevity mechanisms? Pro-aging pathways such as mTOR directly drive age-related diseases because they are a continuation of development.

**The key to understanding aging: life-limiting vs. non-life-limiting hallmarks**

Among numerous harmful processes, only one can be life-limiting in a particular individual. If an animal dies from one cause, it cannot die from another cause even a day later. If quasi-programmed (e.g., mTOR-driven) aging is life-limiting, then accumulation of random damages cannot kill the organism.

López-Otín et al. [38] suggested three criteria for hallmarks of aging but two of them are criteria for both life-limiting and non-life-limiting processes: (1) hallmarks are observed during normal aging and (2) its experimental aggravation should decrease lifespan. However, experimental aggravation can make any process life-limiting. Telomere shortening becomes life-limiting in mice lacking telomerase, but their symptoms are drastically different from normal age-related

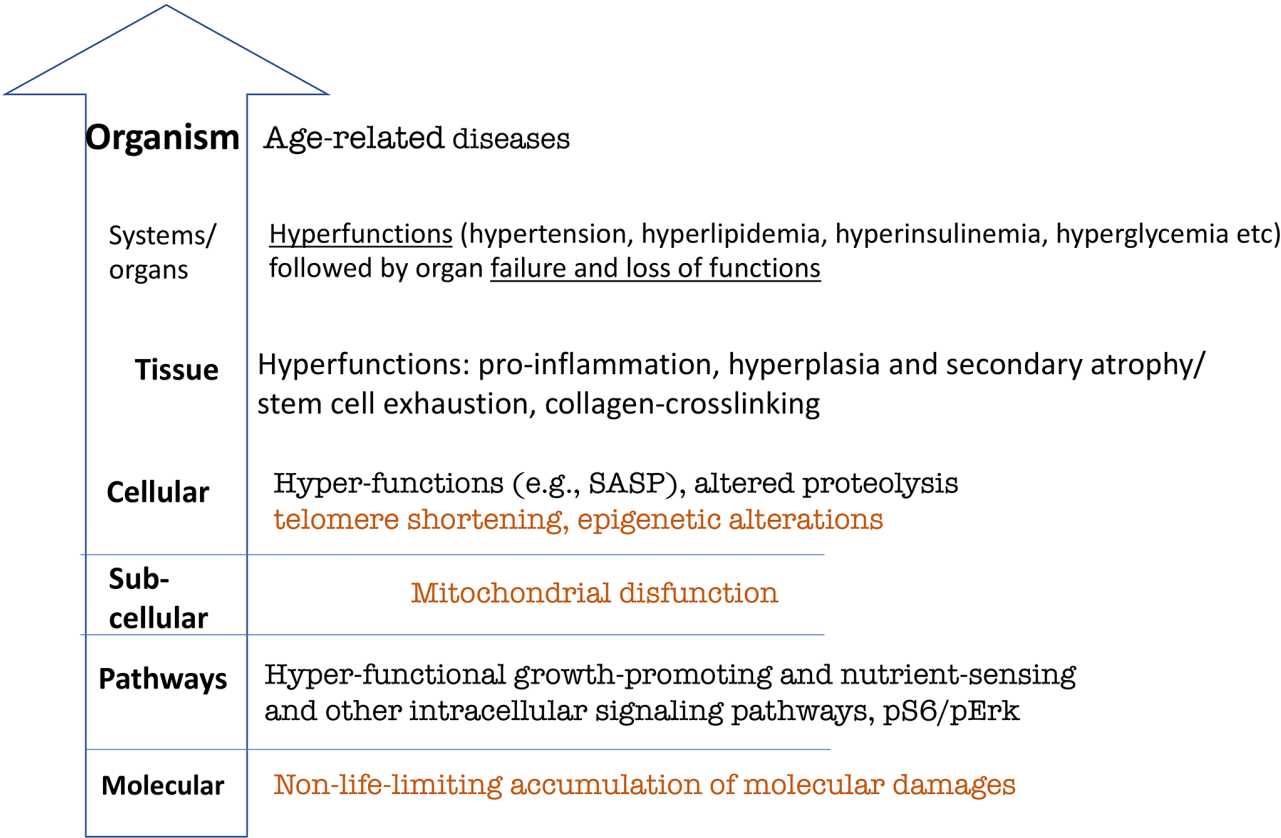


**Figure 3. Hierarchical hallmarks of aging based on hyperfunction theory, applicable to humans.** Non-life-limiting hallmarks are shown in brown color. See text for explanation.

diseases [78]. Although telomere shortening is associated with cardiovascular disease (CVD) in humans, patients with dyskeratosis congenita (DKC), a condition caused by short telomeres, do not die from CVD but from bone marrow failure (which is not a typical age-related disease) [79]. Hyperfunction theory explains how hyper-functional signaling leads to CVD in humans [80]. But telomere shortening cannot explain it.

Anything can shorten lifespan including starvation and the atomic bomb but they are not causes of aging. Only the third criterion matters: (3) its experimental amelioration should slow down aging and increase healthy lifespan. Not surprisingly, “the last criterion is the most difficult to achieve and not all of the hallmarks are fully supported yet by interventions,” as noted by López-Otín et al. [38]. In other words, they are not hallmarks of normal aging.

(Note: Even the third criterion is not sufficient to define a life-limiting hallmark.

Besides interventions may have off-target effects. For example, NAC, an antioxidant, is also a mTOR inhibitor [81]).

In conclusion, numerous deadly processes develop in parallel but only a few (or one) are life-limiting.

Therefore, non-limiting hallmarks are not included in the version of life-limiting hallmarks of aging (Figure 4). This final re-presentation is generic and can be applied to any species, from *C. elegans* to humans.

**Aging as a selective force for cancer**

Common cancers are age-related diseases. This cannot be explained by simple accumulation of mutations with age. For example, melanoma and lung cancer in smokers have atypically high mutation burden [8] but still develop at old age. Centenarians, who age slower, are protected from cancer. Rapamycin and calorie restriction slow aging in mice and prevent cancer.

As discussed, the selective force driving carcinogenesis is growth-limiting conditions, also named micro-environmental constraints in aging [16]. For example, the aging hematopoietic system selects for robust hematopoietic cells and such a preleukemic clone can originate leukemic clone [82]. Specifically, chronic inflammatory microenvironments in old age may select for cells harboring oncogenic mutations [83].

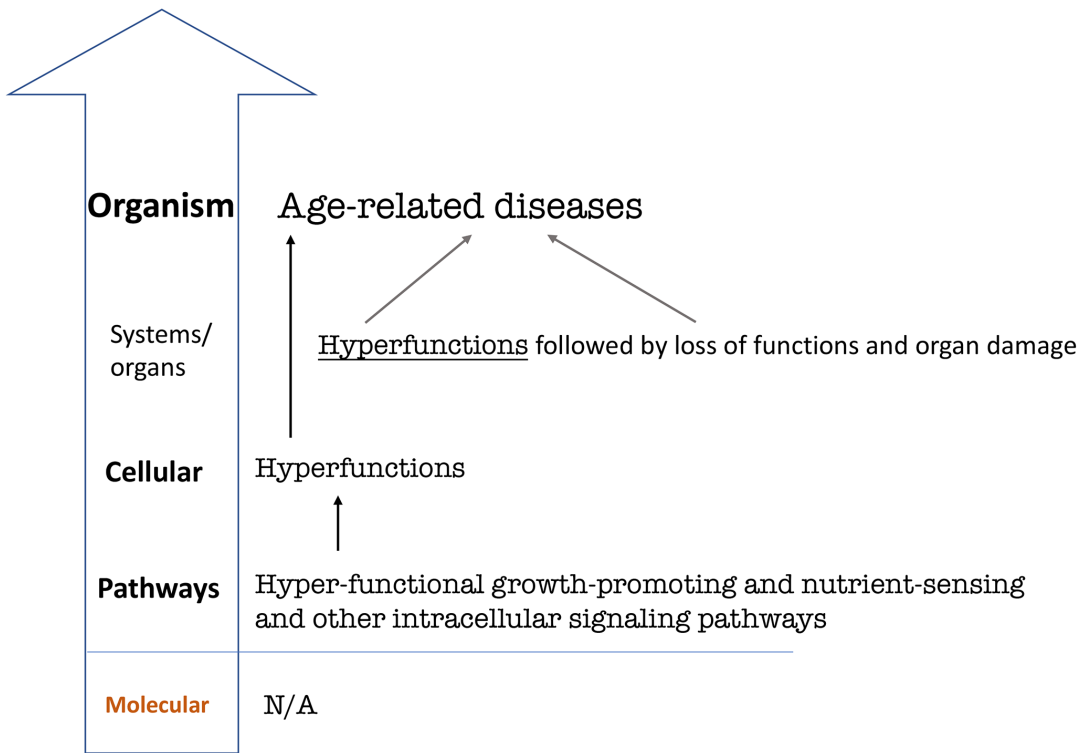


**Figure 4. Hierarchical hallmarks of aging based on hyperfunction theory, universal.** Hyperfunction of intracellular signaling pathways leads to cellular and systemic hyperfunctions, which in turn lead to age-related diseases on the organismal level [56]. Specific hyperfunctions and diseases may be different in different species and therefore are not shown. For example, human systemic hyperfunctions (e.g., hypertension, hyperlipidemia, hyperglycemia) and diseases (e.g., cardio-vascular diseases) differ from diseases in *C. elegans* [40, 41].

Chronic inflammation is a hyper-function and is in part mTOR-dependent [84–88]. An aging microenvironment puts stem cells on the path of hyper-activation [89] and geroconversion [90–92], leading to their exhaustion [89–92].

Mutations are necessary (with a few exceptions) but not sufficient for inducing cancer. The second requirement is selective force, favoring these mutations. Aging is a leading selective force.

One of the potential mechanisms of growth-limiting conditions that drive cancer progression is mTOR-dependent cellular senescence.

### Common hallmarks of cancer, aging and cell senescence

Cellular senescence is a two-step process: cell cycle arrest followed by geroconversion [93]. Like organismal aging, geroconversion is a continuation of growth driven in part by hyperfunctional mTOR. When the cell cycle is blocked by p21/p16, but growth-promoting pathways such as mTOR and MAPK are active, the cells become hypertrophic (large cell morphology) and hyperfunctional: beta-Gal staining (lysosomal hyperfunction) and SASP. A hallmark of cellular senescence is active mTOR pathway in non-proliferating cells. Rapamycin suppresses geroconversion to senescence [93–97]. Figuratively, organismal aging is a quasi-growth after developmental growth is completed.

In cancer, the PI3K/mTOR pathway is almost universally activated by mutations [98–100]. Figuratively, cancer cells are proliferating senescent cells. In organismal aging, cancer and cellular senescence, the same key signaling pathways, such as mTOR, are involved. This is why the same drugs, such as rapamycin, can suppress all of them.

### CONFLICTS OF INTERESTS

The authors declare no conflicts of interest related to this study.

### REFERENCES

1. Hanahan D, Weinberg RA. The hallmarks of cancer. *Cell*. 2000; 100:57–70. [https://doi.org/10.1016/s0092-8674\(00\)81683-9](https://doi.org/10.1016/s0092-8674(00)81683-9) PMID:10647931
2. Cahill DP, Kinzler KW, Vogelstein B, Lengauer C. Genetic instability and darwinian selection in tumours. *Trends Cell Biol*. 1999; 9:M57–60. PMID:10611684
3. Blagosklonny MV. Molecular theory of cancer. *Cancer Biol Ther*. 2005; 4:621–7. <https://doi.org/10.4161/cbt.4.6.1818> PMID:15970666
4. Blagosklonny MV. Oncogenic resistance to growth-limiting conditions. *Nat Rev Cancer*. 2002; 2:221–5. <https://doi.org/10.1038/nrc743> PMID:11990858
5. Blagosklonny MV. Carcinogenesis, cancer therapy and chemoprevention. *Cell Death Differ*. 2005; 12:592–602. <https://doi.org/10.1038/sj.cdd.4401610> PMID:15818400
6. Yun J, Rago C, Cheong I, Pagliarini R, Angenendt P, Rajagopalan H, Schmidt K, Willson JK, Markowitz S, Zhou S, Diaz LA Jr, Velculescu VE, Lengauer C, et al. Glucose deprivation contributes to the development of KRAS pathway mutations in tumor cells. *Science*. 2009; 325:1555–9. <https://doi.org/10.1126/science.1174229> PMID:19661383
7. Hanahan D, Weinberg RA. Hallmarks of cancer: the next generation. *Cell*. 2011; 144:646–74. <https://doi.org/10.1016/j.cell.2011.02.013> PMID:21376230
8. Vogelstein B, Papadopoulos N, Velculescu VE, Zhou S, Diaz LA Jr, Kinzler KW. Cancer genome landscapes. *Science*. 2013; 339:1546–58. <https://doi.org/10.1126/science.1235122> PMID:23539594
9. Gems D, de Magalhães JP. The hoverfly and the wasp: A critique of the hallmarks of aging as a paradigm. *Ageing Res Rev*. 2021; 70:101407. <https://doi.org/10.1016/j.arr.2021.101407> PMID:34271186
10. Bozic I, Antal T, Ohtsuki H, Carter H, Kim D, Chen S, Karchin R, Kinzler KW, Vogelstein B, Nowak MA. Accumulation of driver and passenger mutations during tumor progression. *Proc Natl Acad Sci U S A*. 2010; 107:18545–50. <https://doi.org/10.1073/pnas.1010978107> PMID:20876136
11. Blagosklonny MV. A node between proliferation, apoptosis, and growth arrest. *Bioessays*. 1999; 21:704–9. [https://doi.org/10.1002/\(SICI\)1521-1878\(199908\)21:8<704::AID-BIES10>3.0.CO;2-5](https://doi.org/10.1002/(SICI)1521-1878(199908)21:8<704::AID-BIES10>3.0.CO;2-5) PMID:10440867
12. Maley CC, Galipeau PC, Li X, Sanchez CA, Paulson TG, Reid BJ. Selectively advantageous mutations and hitchhikers in neoplasms: p16 lesions are selected in Barrett's esophagus. *Cancer Res*. 2004; 64:3414–27.



- <https://doi.org/10.1158/0008-5472.CAN-03-3249>  
PMID:15150093
13. Liu X, Sun Y, Ehrlich M, Lu T, Kloog Y, Weinberg RA, Lodish HF, Henis YI. Disruption of TGF-beta growth inhibition by oncogenic ras is linked to p27Kip1 mislocalization. *Oncogene*. 2000; 19:5926–35.  
<https://doi.org/10.1038/sj.onc.1203991>  
PMID:11127824
  14. Nowell PC. The clonal evolution of tumor cell populations. *Science*. 1976; 194:23–8.  
<https://doi.org/10.1126/science.959840>  
PMID:959840
  15. Merlo LM, Pepper JW, Reid BJ, Maley CC. Cancer as an evolutionary and ecological process. *Nat Rev Cancer*. 2006; 6:924–35.  
<https://doi.org/10.1038/nrc2013>  
PMID:17109012
  16. Greaves M, Maley CC. Clonal evolution in cancer. *Nature*. 2012; 481:306–13.  
<https://doi.org/10.1038/nature10762>  
PMID:22258609
  17. Blagosklonny MV. Antiangiogenic therapy and tumor progression. *Cancer Cell*. 2004; 5:13–7.  
[https://doi.org/10.1016/s1535-6108\(03\)00336-2](https://doi.org/10.1016/s1535-6108(03)00336-2)  
PMID:14749122
  18. Blagosklonny MV. Why therapeutic response may not prolong the life of a cancer patient: selection for oncogenic resistance. *Cell Cycle*. 2005; 4:1693–8.  
<https://doi.org/10.4161/cc.4.12.2259>  
PMID:16294046
  19. Pastò A, Pagotto A, Pilotto G, De Paoli A, De Salvo GL, Baldoni A, Nicoletto MO, Ricci F, Damia G, Bellio C, Indraccolo S, Amadori A. Resistance to glucose starvation as metabolic trait of platinum-resistant human epithelial ovarian cancer cells. *Oncotarget*. 2017; 8:6433–45.  
<https://doi.org/10.18632/oncotarget.14118>  
PMID:28031535
  20. Reiter JG, Baretta M, Gerold JM, Makohon-Moore AP, Daud A, Iacobuzio-Donahue CA, Azad NS, Kinzler KW, Nowak MA, Vogelstein B. An analysis of genetic heterogeneity in untreated cancers. *Nat Rev Cancer*. 2019; 19:639–50.  
<https://doi.org/10.1038/s41568-019-0185-x>  
PMID:31455892
  21. Murchison EP. Clonally transmissible cancers in dogs and Tasmanian devils. *Oncogene*. 2008 (Suppl 2); 27:S19–30.  
<https://doi.org/10.1038/ncr.2009.350>  
PMID:19956175
  22. Murchison EP, Schulz-Trieglaff OB, Ning Z, Alexandrov LB, Bauer MJ, Fu B, Hims M, Ding Z, Ivakhno S, Stewart C, Ng BL, Wong W, Aken B, et al. Genome sequencing and analysis of the Tasmanian devil and its transmissible cancer. *Cell*. 2012; 148:780–91.  
<https://doi.org/10.1016/j.cell.2011.11.065>  
PMID:22341448
  23. Lister NC, Milton AM, Hanrahan BJ, Waters PD. Between the Devil and the Deep Blue Sea: Non-Coding RNAs Associated with Transmissible Cancers in Tasmanian Devil, Domestic Dog and Bivalves. *Noncoding RNA*. 2021; 7:72.  
<https://doi.org/10.3390/ncrna7040072>  
PMID:34842768
  24. Ostrander EA, Davis BW, Ostrander GK. Transmissible Tumors: Breaking the Cancer Paradigm. *Trends Genet*. 2016; 32:1–15.  
<https://doi.org/10.1016/j.tig.2015.10.001>  
PMID:26686413
  25. Cohen D. The canine transmissible venereal tumor: a unique result of tumor progression. *Adv Cancer Res*. 1985; 43:75–112.  
[https://doi.org/10.1016/s0065-230x\(08\)60943-4](https://doi.org/10.1016/s0065-230x(08)60943-4)  
PMID:3887857
  26. McCallum H, Jones M, Hawkins C, Hamede R, Lachish S, Sinn DL, Beeton N, Lazenby B. Transmission dynamics of Tasmanian devil facial tumor disease may lead to disease-induced extinction. *Ecology*. 2009; 90:3379–92.  
<https://doi.org/10.1890/08-1763.1>  
PMID:20120807
  27. Metzger MJ, Reinisch C, Sherry J, Goff SP. Horizontal transmission of clonal cancer cells causes leukemia in soft-shell clams. *Cell*. 2015; 161:255–63.  
<https://doi.org/10.1016/j.cell.2015.02.042>  
PMID:25860608
  28. Hanahan D. Hallmarks of Cancer: New Dimensions. *Cancer Discov*. 2022; 12:31–46.  
<https://doi.org/10.1158/2159-8290.CD-21-1059>  
PMID:35022204
  29. Fouad YA, Aanei C. Revisiting the hallmarks of cancer. *Am J Cancer Res*. 2017; 7:1016–36.  
PMID:28560055
  30. Senga SS, Grose RP. Hallmarks of cancer-the new testament. *Open Biol*. 2021; 11:200358.  
<https://doi.org/10.1098/rsob.200358>  
PMID:33465324
  31. Munkley J, Elliott DJ. Hallmarks of glycosylation in cancer. *Oncotarget*. 2016; 7:35478–89.  
<https://doi.org/10.18632/oncotarget.8155>  
PMID:27007155
  32. Flavahan WA, Gaskell E, Bernstein BE. Epigenetic plasticity and the hallmarks of cancer. *Science*. 2017;

- 357:eaal2380.  
<https://doi.org/10.1126/science.aal2380>  
PMID:[28729483](https://pubmed.ncbi.nlm.nih.gov/28729483/)
33. MacCarthy-Morrogh L, Martin P. The hallmarks of cancer are also the hallmarks of wound healing. *Sci Signal*. 2020; 13:eaay8690.  
<https://doi.org/10.1126/scisignal.aay8690>  
PMID:[32900881](https://pubmed.ncbi.nlm.nih.gov/32900881/)
34. Kroemer G, Pouyssegur J. Tumor cell metabolism: cancer's Achilles' heel. *Cancer Cell*. 2008; 13:472–82.  
<https://doi.org/10.1016/j.ccr.2008.05.005>  
PMID:[18538731](https://pubmed.ncbi.nlm.nih.gov/18538731/)
35. Colotta F, Allavena P, Sica A, Garlanda C, Mantovani A. Cancer-related inflammation, the seventh hallmark of cancer: links to genetic instability. *Carcinogenesis*. 2009; 30:1073–81.  
<https://doi.org/10.1093/carcin/bgp127>  
PMID:[19468060](https://pubmed.ncbi.nlm.nih.gov/19468060/)
36. Baraks G, Tseng R, Pan CH, Kasliwal S, Leiton CV, Shroyer KR, Escobar-Hoyos LF. Dissecting the Oncogenic Roles of Keratin 17 in the Hallmarks of Cancer. *Cancer Res*. 2022; 82:1159–66.  
<https://doi.org/10.1158/0008-5472.CAN-21-2522>  
PMID:[34921015](https://pubmed.ncbi.nlm.nih.gov/34921015/)
37. Rassy E, Assi T, Pavlidis N. Exploring the biological hallmarks of cancer of unknown primary: where do we stand today? *Br J Cancer*. 2020; 122:1124–32.  
<https://doi.org/10.1038/s41416-019-0723-z>  
PMID:[32042068](https://pubmed.ncbi.nlm.nih.gov/32042068/)
38. López-Otín C, Blasco MA, Partridge L, Serrano M, Kroemer G. The hallmarks of aging. *Cell*. 2013; 153:1194–217.  
<https://doi.org/10.1016/j.cell.2013.05.039>  
PMID:[23746838](https://pubmed.ncbi.nlm.nih.gov/23746838/)
39. Gems D. The aging-disease false dichotomy: understanding senescence as pathology. *Front Genet*. 2015; 6:212.  
<https://doi.org/10.3389/fgene.2015.00212>  
PMID:[26136770](https://pubmed.ncbi.nlm.nih.gov/26136770/)
40. Ezcurra M, Benedetto A, Sornda T, Gilliat AF, Au C, Zhang Q, van Schelt S, Petrache AL, Wang H, de la Guardia Y, Bar-Nun S, Tyler E, Wakelam MJ, Gems D. *C. elegans* Eats Its Own Intestine to Make Yolk Leading to Multiple Senescent Pathologies. *Curr Biol*. 2018; 28:2544–56.e5.  
<https://doi.org/10.1016/j.cub.2018.06.035>  
PMID:[30100339](https://pubmed.ncbi.nlm.nih.gov/30100339/)
41. Wang H, Zhang Z, Gems D. Monsters in the uterus: teratoma-like tumors in senescent *C. elegans* result from a parthenogenetic quasi-program. *Aging (Albany NY)*. 2018; 10:1188–9.  
<https://doi.org/10.18632/aging.101486>  
PMID:[29923830](https://pubmed.ncbi.nlm.nih.gov/29923830/)
42. Wang H, Zhao Y, Ezcurra M, Benedetto A, Gilliat AF, Hellberg J, Ren Z, Galimov ER, Athigapanich T, Girstmair J, Telford MJ, Dolphin CT, Zhang Z, Gems D. A parthenogenetic quasi-program causes teratoma-like tumors during aging in wild-type *C. elegans*. *NPJ Aging Mech Dis*. 2018; 4:6.  
<https://doi.org/10.1038/s41514-018-0025-3>  
PMID:[29928508](https://pubmed.ncbi.nlm.nih.gov/29928508/)
43. Blagosklonny MV. Validation of anti-aging drugs by treating age-related diseases. *Aging (Albany NY)*. 2009; 1:281–8.  
<https://doi.org/10.18632/aging.100034>  
PMID:[20157517](https://pubmed.ncbi.nlm.nih.gov/20157517/)
44. Gems D, de la Guardia Y. Alternative Perspectives on Aging in *Caenorhabditis elegans*: Reactive Oxygen Species or Hyperfunction? *Antioxid Redox Signal*. 2013; 19:321–9.  
<https://doi.org/10.1089/ars.2012.4840>  
PMID:[22870907](https://pubmed.ncbi.nlm.nih.gov/22870907/)
45. Gems D, Partridge L. Genetics of longevity in model organisms: debates and paradigm shifts. *Annu Rev Physiol*. 2013; 75:621–44.  
<https://doi.org/10.1146/annurev-physiol-030212-183712>  
PMID:[23190075](https://pubmed.ncbi.nlm.nih.gov/23190075/)
46. Doonan R, McElwee JJ, Matthijssens F, Walker GA, Houthoofd K, Back P, Matscheski A, Vanfleteren JR, Gems D. Against the oxidative damage theory of aging: superoxide dismutases protect against oxidative stress but have little or no effect on life span in *Caenorhabditis elegans*. *Genes Dev*. 2008; 22:3236–41.  
<https://doi.org/10.1101/gad.504808>  
PMID:[19056880](https://pubmed.ncbi.nlm.nih.gov/19056880/)
47. Ng LF, Ng LT, van Breugel M, Halliwell B, Gruber J. Mitochondrial DNA Damage Does Not Determine *C. elegans* Lifespan. *Front Genet*. 2019; 10:311.  
<https://doi.org/10.3389/fgene.2019.00311>  
PMID:[31031801](https://pubmed.ncbi.nlm.nih.gov/31031801/)
48. Blagosklonny MV. Aging: ROS or TOR. *Cell Cycle*. 2008; 7:3344–54.  
<https://doi.org/10.4161/cc.7.21.6965>  
PMID:[18971624](https://pubmed.ncbi.nlm.nih.gov/18971624/)
49. Blagosklonny MV. DNA- and telomere-damage does not limit lifespan: evidence from rapamycin. *Aging (Albany NY)*. 2021; 13:3167–75.  
<https://doi.org/10.18632/aging.202674>  
PMID:[33578394](https://pubmed.ncbi.nlm.nih.gov/33578394/)
50. Lapointe J, Hekimi S. When a theory of aging ages badly. *Cell Mol Life Sci*. 2010; 67:1–8.  
<https://doi.org/10.1007/s00018-009-0138-8>

PMID:[19730800](https://pubmed.ncbi.nlm.nih.gov/19730800/)

51. Ristow M, Schmeisser S. Extending life span by increasing oxidative stress. *Free Radic Biol Med*. 2011; 51:327–36.  
<https://doi.org/10.1016/j.freeradbiomed.2011.05.010>  
PMID:[21619928](https://pubmed.ncbi.nlm.nih.gov/21619928/)
52. Gladyshev VN. The free radical theory of aging is dead. Long live the damage theory! *Antioxid Redox Signal*. 2014; 20:727–31.  
<https://doi.org/10.1089/ars.2013.5228>  
PMID:[24159899](https://pubmed.ncbi.nlm.nih.gov/24159899/)
53. Golubev A, Hanson AD, Gladyshev VN. Non-enzymatic molecular damage as a prototypic driver of aging. *J Biol Chem*. 2017; 292:6029–38.  
<https://doi.org/10.1074/jbc.R116.751164>  
PMID:[28264930](https://pubmed.ncbi.nlm.nih.gov/28264930/)
54. Schumacher B, Pothof J, Vijg J, Hoeijmakers JHJ. The central role of DNA damage in the ageing process. *Nature*. 2021; 592:695–703.  
<https://doi.org/10.1038/s41586-021-03307-7>  
PMID:[33911272](https://pubmed.ncbi.nlm.nih.gov/33911272/)
55. MacRae SL, Croken MM, Calder RB, Aliper A, Milholland B, White RR, Zhavoronkov A, Gladyshev VN, Seluanov A, Gorbunova V, Zhang ZD, Vijg J. DNA repair in species with extreme lifespan differences. *Aging (Albany NY)*. 2015; 7:1171–84.  
<https://doi.org/10.18632/aging.100866>  
PMID:[26729707](https://pubmed.ncbi.nlm.nih.gov/26729707/)
56. Blagosklonny MV. Aging and immortality: quasi-programmed senescence and its pharmacologic inhibition. *Cell Cycle*. 2006; 5:2087–102.  
<https://doi.org/10.4161/cc.5.18.3288>  
PMID:[17012837](https://pubmed.ncbi.nlm.nih.gov/17012837/)
57. Blagosklonny MV. The hyperfunction theory of aging: three common misconceptions. *Oncoscience*. 2021; 8:103–7.  
<https://doi.org/10.18632/oncoscience.545>  
PMID:[34549076](https://pubmed.ncbi.nlm.nih.gov/34549076/)
58. de Grey AD. Protagonistic pleiotropy: Why cancer may be the only pathogenic effect of accumulating nuclear mutations and epimutations in aging. *Mech Ageing Dev*. 2007; 128:456–9.  
<https://doi.org/10.1016/j.mad.2007.05.005>  
PMID:[17588643](https://pubmed.ncbi.nlm.nih.gov/17588643/)
59. Blagosklonny MV. Molecular damage in cancer: an argument for mTOR-driven aging. *Aging (Albany NY)*. 2011; 3:1130–41.  
<https://doi.org/10.18632/aging.100422>  
PMID:[22246147](https://pubmed.ncbi.nlm.nih.gov/22246147/)
60. Blagosklonny MV. Response to the Thought-Provoking Critique of Hyperfunction Theory by Aubrey de Grey. *Rejuvenation Res*. 2021; 24:170–2.  
<https://doi.org/10.1089/rej.2021.0018>  
PMID:[33784825](https://pubmed.ncbi.nlm.nih.gov/33784825/)
61. Gems D. The hyperfunction theory: An emerging paradigm for the biology of aging. *Ageing Res Rev*. 2022; 74:101557.  
<https://doi.org/10.1016/j.arr.2021.101557>  
PMID:[34990845](https://pubmed.ncbi.nlm.nih.gov/34990845/)
62. Lind MI, Ravindran S, Sekajova Z, Carlsson H, Hinas A, Maklakov AA. Experimentally reduced insulin/IGF-1 signaling in adulthood extends lifespan of parents and improves Darwinian fitness of their offspring. *Evol Lett*. 2019; 3:207–16.  
<https://doi.org/10.1002/evl3.108>  
PMID:[31007945](https://pubmed.ncbi.nlm.nih.gov/31007945/)
63. Berman AE, Leontieva OV, Natarajan V, McCubrey JA, Demidenko ZN, Nikiforov MA. Recent progress in genetics of aging, senescence and longevity: focusing on cancer-related genes. *Oncotarget*. 2012; 3:1522–32.  
<https://doi.org/10.18632/oncotarget.889>  
PMID:[23455653](https://pubmed.ncbi.nlm.nih.gov/23455653/)
64. Iseghohi SO, Omeke K. How ageing increases cancer susceptibility: A tale of two opposing yet synergistic views. *Genes Dis*. 2016; 3:105–9.  
<https://doi.org/10.1016/j.gendis.2016.04.002>  
PMID:[30258879](https://pubmed.ncbi.nlm.nih.gov/30258879/)
65. Scialò F, Sriram A, Naudí A, Ayala V, Jové M, Pamplona R, Sanz A. Target of rapamycin activation predicts lifespan in fruit flies. *Cell Cycle*. 2015; 14:2949–58.  
<https://doi.org/10.1080/15384101.2015.1071745>  
PMID:[26259964](https://pubmed.ncbi.nlm.nih.gov/26259964/)
66. Biliński T, Paszkiewicz T, Zadrag-Tecza R. Energy excess is the main cause of accelerated aging of mammals. *Oncotarget*. 2015; 6:12909–19.  
<https://doi.org/10.18632/oncotarget.4271>  
PMID:[26079722](https://pubmed.ncbi.nlm.nih.gov/26079722/)
67. Blagosklonny MV. Answering the ultimate question "what is the proximal cause of aging?". *Aging (Albany NY)*. 2012; 4:861–77.  
<https://doi.org/10.18632/aging.100525>  
PMID:[23425777](https://pubmed.ncbi.nlm.nih.gov/23425777/)
68. Zimniak P. What is the Proximal Cause of Aging? *Front Genet*. 2012; 3:189.  
<https://doi.org/10.3389/fgene.2012.00189>  
PMID:[23056007](https://pubmed.ncbi.nlm.nih.gov/23056007/)
69. de Grey ADN. Programs, Hyperfunction, and Damage: Why Definitions and Logic Matter So Much in Biogerontology. *Rejuvenation Res*. 2021; 24:83–5.  
<https://doi.org/10.1089/rej.2021.0015>  
PMID:[33784821](https://pubmed.ncbi.nlm.nih.gov/33784821/)
70. Kenyon CJ. The genetics of ageing. *Nature*. 2010;

464:504–12.

<https://doi.org/10.1038/nature08980>

PMID:20336132

71. Vellai T, Takacs-Vellai K, Zhang Y, Kovacs AL, Orosz L, Müller F. Genetics: influence of TOR kinase on lifespan in *C. elegans*. *Nature*. 2003; 426:620.  
<https://doi.org/10.1038/426620a>  
PMID:14668850
72. Bartke A, Quainoo N. Impact of Growth Hormone-Related Mutations on Mammalian Aging. *Front Genet*. 2018; 9:586.  
<https://doi.org/10.3389/fgene.2018.00586>  
PMID:30542372
73. Selman C, Tullet JM, Wieser D, Irvine E, Lingard SJ, Choudhury AI, Claret M, Al-Qassab H, Carmignac D, Ramadani F, Woods A, Robinson IC, Schuster E, et al. Ribosomal protein S6 kinase 1 signaling regulates mammalian life span. *Science*. 2009; 326:140–4.  
<https://doi.org/10.1126/science.1177221>  
PMID:19797661
74. Harrison DE, Strong R, Sharp ZD, Nelson JF, Astle CM, Flurkey K, Nadon NL, Wilkinson JE, Frenkel K, Carter CS, Pahor M, Javors MA, Fernandez E, Miller RA. Rapamycin fed late in life extends lifespan in genetically heterogeneous mice. *Nature*. 2009; 460:392–5.  
<https://doi.org/10.1038/nature08221>  
PMID:19587680
75. Anisimov VN, Zabezhinski MA, Popovich IG, Piskunova TS, Semchenko AV, Tyndyk ML, Yurova MN, Antoch MP, Blagosklonny MV. Rapamycin extends maximal lifespan in cancer-prone mice. *Am J Pathol*. 2010; 176:2092–7.  
<https://doi.org/10.2353/ajpath.2010.091050>  
PMID:20363920
76. Bitto A, Ito TK, Pineda VV, LeTexier NJ, Huang HZ, Sutlief E, Tung H, Vizzini N, Chen B, Smith K, Meza D, Yajima M, Beyer RP, et al. Transient rapamycin treatment can increase lifespan and healthspan in middle-aged mice. *Elife*. 2016; 5:e16351.  
<https://doi.org/10.7554/eLife.16351>  
PMID:27549339
77. Strong R, Miller RA, Bogue M, Fernandez E, Javors MA, Libert S, Martinez PA, Murphy MP, Musi N, Nelson JF, Petrascheck M, Reifsnnyder P, Richardson A, et al. Rapamycin-mediated mouse lifespan extension: Late-life dosage regimes with sex-specific effects. *Aging Cell*. 2020; 19:e13269.  
<https://doi.org/10.1111/acer.13269>  
PMID:33145977
78. Herrera E, Samper E, Martín-Caballero J, Flores JM, Lee HW, Blasco MA. Disease states associated with telomerase deficiency appear earlier in mice with short telomeres. *EMBO J*. 1999; 18:2950–60.  
<https://doi.org/10.1093/emboj/18.11.2950>  
PMID:10357808
79. Gramatges MM, Bertuch AA. Short telomeres: from dyskeratosis congenita to sporadic aplastic anemia and malignancy. *Transl Res*. 2013; 162:353–63.  
<https://doi.org/10.1016/j.trsl.2013.05.003>  
PMID:23732052
80. Blagosklonny MV. Prospective treatment of age-related diseases by slowing down aging. *Am J Pathol*. 2012; 181:1142–6.  
<https://doi.org/10.1016/j.ajpath.2012.06.024>  
PMID:22841821
81. Lai ZW, Hanczko R, Bonilla E, Caza TN, Clair B, Bartos A, Miklossy G, Jimah J, Doherty E, Tily H, Francis L, Garcia R, Dawood M, et al. N-acetylcysteine reduces disease activity by blocking mammalian target of rapamycin in T cells from systemic lupus erythematosus patients: a randomized, double-blind, placebo-controlled trial. *Arthritis Rheum*. 2012; 64:2937–46.  
<https://doi.org/10.1002/art.34502>  
PMID:22549432
82. Shlush LI, Minden MD. Preleukemia: the normal side of cancer. *Curr Opin Hematol*. 2015; 22:77–84.  
<https://doi.org/10.1097/MOH.0000000000000111>  
PMID:25575035
83. Henry CJ, Casás-Selves M, Kim J, Zaberezhnyy V, Aghili L, Daniel AE, Jimenez L, Azam T, McNamee EN, Clambey ET, Klawitter J, Serkova NJ, Tan AC, et al. Aging-associated inflammation promotes selection for adaptive oncogenic events in B cell progenitors. *J Clin Invest*. 2015; 125:4666–80.  
<https://doi.org/10.1172/JCI83024>  
PMID:26551682
84. Laberge RM, Sun Y, Orjalo AV, Patil CK, Freund A, Zhou L, Curran SC, Davalos AR, Wilson-Edell KA, Liu S, Limbad C, Demaria M, Li P, et al. MTOR regulates the pro-tumorigenic senescence-associated secretory phenotype by promoting IL1A translation. *Nat Cell Biol*. 2015; 17:1049–61.  
<https://doi.org/10.1038/ncb3195>  
PMID:26147250
85. Choi YJ, Moon KM, Chung KW, Jeong JW, Park D, Kim DH, Yu BP, Chung HY. The underlying mechanism of proinflammatory NF- $\kappa$ B activation by the mTORC2/Akt/IKK $\alpha$  pathway during skin aging. *Oncotarget*. 2016; 7:52685–94.  
<https://doi.org/10.18632/oncotarget.10943>  
PMID:27486771
86. Wang R, Sunchu B, Perez VI. Rapamycin and the

- inhibition of the secretory phenotype. *Exp Gerontol*. 2017; 94:89–92.  
<https://doi.org/10.1016/j.exger.2017.01.026>  
 PMID:[28167236](#)
87. Wang R, Yu Z, Sunchu B, Shoaf J, Dang I, Zhao S, Caples K, Bradley L, Beaver LM, Ho E, Löhr CV, Perez VI. Rapamycin inhibits the secretory phenotype of senescent cells by a Nrf2-independent mechanism. *Aging Cell*. 2017; 16:564–74.  
<https://doi.org/10.1111/acer.12587>  
 PMID:[28371119](#)
  88. Bent EH, Gilbert LA, Hemann MT. A senescence secretory switch mediated by PI3K/AKT/mTOR activation controls chemoprotective endothelial secretory responses. *Genes Dev*. 2016; 30:1811–21.  
<https://doi.org/10.1101/gad.284851.116>  
 PMID:[27566778](#)
  89. Rodgers JT, King KY, Brett JO, Cromie MJ, Charville GW, Maguire KK, Brunson C, Mastey N, Liu L, Tsai CR, Goodell MA, Rando TA. mTORC1 controls the adaptive transition of quiescent stem cells from G0 to G(Alert). *Nature*. 2014; 510:393–6.  
<https://doi.org/10.1038/nature13255>  
 PMID:[24870234](#)
  90. Sousa-Victor P, Gutarra S, García-Prat L, Rodriguez-Ubrea J, Ortet L, Ruiz-Bonilla V, Jardí M, Ballestar E, González S, Serrano AL, Perdiguero E, Muñoz-Cánoves P. Geriatric muscle stem cells switch reversible quiescence into senescence. *Nature*. 2014; 506:316–21.  
<https://doi.org/10.1038/nature13013>  
 PMID:[24522534](#)
  91. Sousa-Victor P, Perdiguero E, Muñoz-Cánoves P. Geroconversion of aged muscle stem cells under regenerative pressure. *Cell Cycle*. 2014; 13:3183–90.  
<https://doi.org/10.4161/15384101.2014.965072>  
 PMID:[25485497](#)
  92. Yue F, Bi P, Wang C, Li J, Liu X, Kuang S. Conditional Loss of Pten in Myogenic Progenitors Leads to Postnatal Skeletal Muscle Hypertrophy but Age-Dependent Exhaustion of Satellite Cells. *Cell Rep*. 2016; 17:2340–53.  
<https://doi.org/10.1016/j.celrep.2016.11.002>  
 PMID:[27880908](#)
  93. Blagosklonny MV. Rapamycin, proliferation and geroconversion to senescence. *Cell Cycle*. 2018; 17:2655–65.  
<https://doi.org/10.1080/15384101.2018.1554781>  
 PMID:[30541374](#)
  94. Demidenko ZN, Zubova SG, Bukreeva EI, Pospelov VA, Pospelova TV, Blagosklonny MV. Rapamycin decelerates cellular senescence. *Cell Cycle*. 2009; 8:1888–95.  
<https://doi.org/10.4161/cc.8.12.8606>  
 PMID:[19471117](#)
  95. Dulic V. Senescence regulation by mTOR. *Methods Mol Biol*. 2013; 965:15–35.  
[https://doi.org/10.1007/978-1-62703-239-1\\_2](https://doi.org/10.1007/978-1-62703-239-1_2)  
 PMID:[23296649](#)
  96. Houssaini A, Breau M, Kebe K, Abid S, Marcos E, Lipskaia L, Rideau D, Parpaleix A, Huang J, Amsellem V, Vienney N, Validire P, Maitre B, et al. mTOR pathway activation drives lung cell senescence and emphysema. *JCI Insight*. 2018; 3:93203.  
<https://doi.org/10.1172/jci.insight.93203>  
 PMID:[29415880](#)
  97. Maskey RS, Wang F, Lehman E, Wang Y, Emmanuel N, Zhong W, Jin G, Abraham RT, Arndt KT, Myers JS, Mazurek A. Sustained mTORC1 activity during palbociclib-induced growth arrest triggers senescence in ER+ breast cancer cells. *Cell Cycle*. 2021; 20:65–80.  
<https://doi.org/10.1080/15384101.2020.1859195>  
 PMID:[33356791](#)
  98. Mossmann D, Park S, Hall MN. mTOR signalling and cellular metabolism are mutual determinants in cancer. *Nat Rev Cancer*. 2018; 18:744–57.  
<https://doi.org/10.1038/s41568-018-0074-8>  
 PMID:[30425336](#)
  99. Millis SZ, Jardim DL, Albacker L, Ross JS, Miller VA, Ali SM, Kurzrock R. Phosphatidylinositol 3-kinase pathway genomic alterations in 60,991 diverse solid tumors informs targeted therapy opportunities. *Cancer*. 2019; 125:1185–99.  
<https://doi.org/10.1002/cncr.31921>  
 PMID:[30582752](#)
  100. Schmidt-Kittler O, Zhu J, Yang J, Liu G, Hendricks W, Lengauer C, Gabelli SB, Kinzler KW, Vogelstein B, Huso DL, Zhou S. PI3Kα inhibitors that inhibit metastasis. *Oncotarget*. 2010; 1:339–48.  
<https://doi.org/10.18632/oncotarget.166>  
 PMID:[21179398](#)